Journal of Vacuum Science & Technology B

JVST B

Second Series
Volume 18, Number 4
July/August 2000

Microelectronics and Nanometer Structures

Processing, Measurement, and Phenomena

Papers from the 27th Conference on the Physics and Chemistry of Semiconductor Interfaces

20020107 220

An official journal of the American Vacuum Society
Published by the Society through the American Institute of Physics

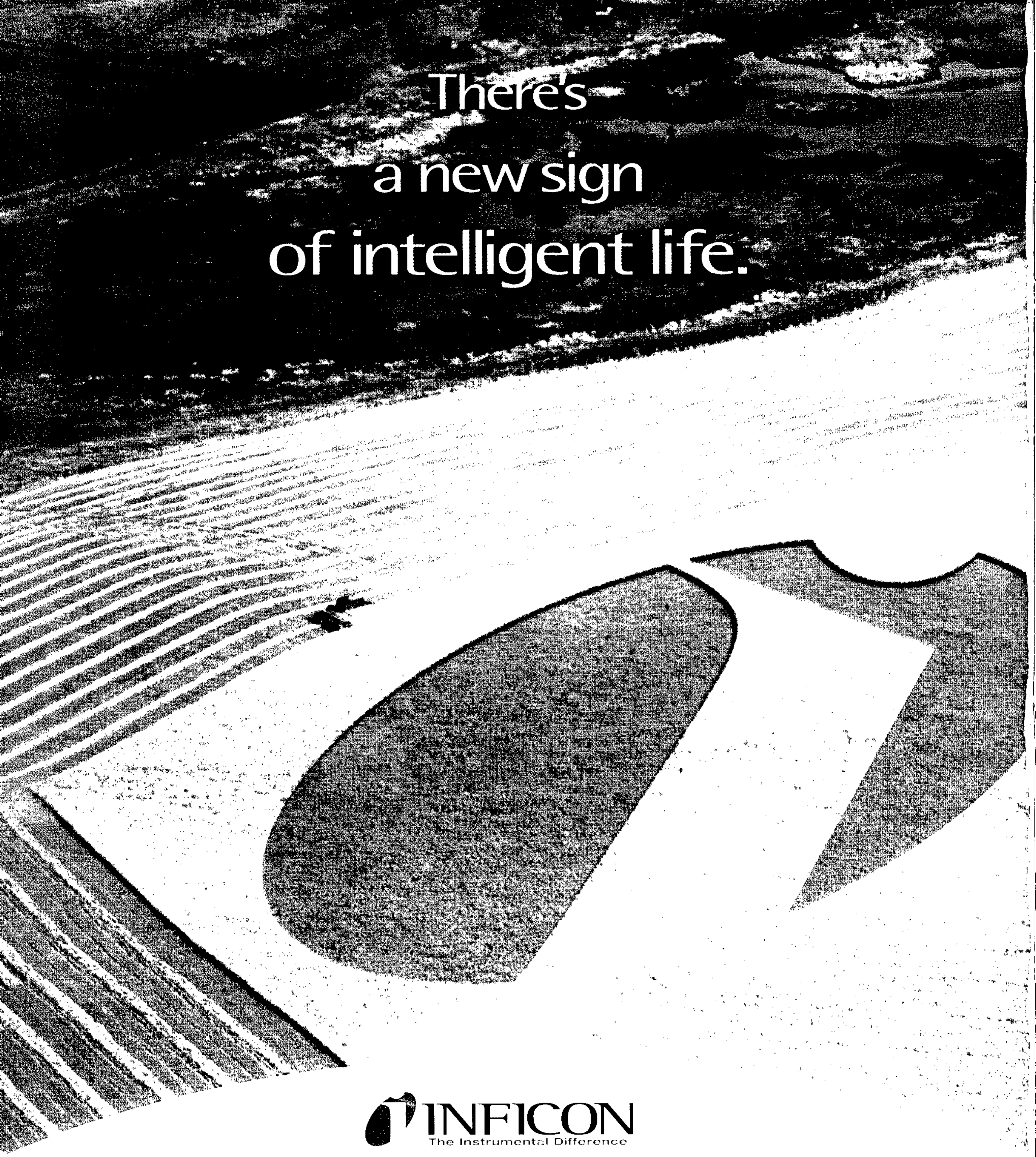

No need to investigate this one. INFICON is the new name of a worldwide leader in gas analysis and sensor integration systems, vacuum gauges, leak detectors, and lead frame cleaning for semiconductor production. Formed from the merger of Leybold Inficon, instrumentation from Leybold, and Balzers Instruments, INFICON is cropping up everywhere with intelligent ways to help processes and fabs run more profitably. That makes INFICON a very logical choice—no matter what planet you're from.

UNITED STATES TAIWAN JAPAN KOREA SINGAPORE GERMANY LIECHTENSTEIN FRANCE UNITED KINGDOM HONG KONG

For more sales and service offices worldwide, visit www.inficon.com

reachus@inficon.com

©2000 INFICON Inc.

OFFICE OF NAVAL RESEARCH

FINAL REPORT

For

Grant No. N00014-00-1-0058

PR Number 00PR01018-01

Twenty-seventh Annual Conference on the Physics and Chemistry of Semiconductor Interfaces

Under the direction of

C. R. Schulte
Institute for Postdoctoral Studies
P. O. Box 36
Scottsdale, Arizona 85252-0036

Reproduction in whole or in part is permitted for any purpose of the United States Government.

*This document has been approved for public release and sale; its distribution is unlimited.

Twenty-seventh Annual Conference on the Physics and Chemistry of Semiconductor Interfaces

Under the direction of
C. R. Schulte
Institute for Postdoctoral Studies
P. O. Box 36
Scottsdale, Arizona 85252-0036

Conference

The Twenty-seventh Annual Conference on the Physics and Chemistry of Semiconductor Interfaces was held in Salt Lake City, Utah in January of 2000, and was attended by over 100 workers in the field of semiconductor interfaces, including researchers from all over the world.

The Twenty-eighth Annual Conference on the Physics and Chemistry of Semiconductor Interfaces was held in Orlando, Florida in January of 2001, and was attended by approximately 77 workers in the field of semiconductor interfaces, including researchers from all over the world.

Both conferences featured extensive discussion sessions and a workshop format, and were judged a success by their attendees – largely because it facilitated informal discussion among the attendees, and especially involving young attendees (e.g., graduate students) interacting with senior scientists.

Publications

The Proceedings of the conference are enclosed, and feature the papers presented which have been published in the Journal of Vacuum Science and Technology.

Expenditure of funds

The following represents the expenditure of Department of Defense funds for this conference.

EXPENDITURES OF DEPARTMENT OF DEFENSE FUNDS: ONR

	PCSI-27	PCSI-28	Total for 27/28
A. Travel	710.17	2936.79	3646.96
B. Secretarial Services	5450.00	7000.00	12450.00
C. Publications	1980.00		1980.00
D. Graphics, Printing	436.92	758.43	1195.35
E. Communications	444.46	135.58	582.04
F. Postage	114.62	47.60	162.22
G. Mailing Services	250.00	300.00	550.00
H. Audio-visual equipment I. and related facilities	387.27	531.80	919.07
J. Other conference facilities K. and services	516.95		516.95
J. Accounting, overhead, and K. Misc. services–a flat fee	750.00	750.00	1500.00
K. **GRAND TOTAL ---- ONR**	**11040.39**	**12460.20**	**23500.59**

REPORT DOCUMENTATION PAGE

Form Approved
OMB No. 0704-0188

Public reporting burden for this collection of information is estimated to average 1 hour per response, including the time for reviewing instructions, searching data sources, gathering and maintaining the data needed, and completing and reviewing the collection of information. Send comments regarding this burden estimate or any other aspect of this collection of information, including suggestions for reducing this burden to Washington Headquarters Service, Directorate for Information Operations and Reports, 1215 Jefferson Davis Highway, Suite 1204, Arlington, VA 22202-4302, and to the Office of Management and Budget, Paperwork Reduction Project (0704-0188) Washington, DC 20503.
PLEASE DO NOT RETURN YOUR FORM TO THE ABOVE ADDRESS.

1. REPORT DATE *(DD-MM-YYYY)*: 31 December 2001

2. REPORT DATE: Final

3. DATES COVERED *(From - To)*: 01 Oct 99 through 30 Sep 01

4. TITLE AND SUBTITLE

Final Report:
Twenty-seventh Annual Conference on the Physics and Chemistry of Semiconductor Interfaces

5a. CONTRACT NUMBER

5b. GRANT NUMBER: N00014-00-1-0058

5c. PROGRAM ELEMENT NUMBER

5d. PROJECT NUMBER

5e. TASK NUMBER

5f. WORK UNIT NUMBER

6. AUTHOR(S)

C. R. Schulte

7. PERFORMING ORGANIZATION NAME(S) AND ADDRESS(ES)

Institute for Postdoctoral Studies
P. O. Box 36
Scottsdale, AZ 85252-0036

8. PERFORMING ORGANIZATION REPORT NUMBER: F1-2001

9. SPONSORING/MONITORING AGENCY NAME(S) AND ADDRESS(ES)

Larry R. Cooper
Office of Naval Research
Ballston Centre Tower One
800 North Quincy Street
Arlington, VA 22217-5660

10. SPONSOR/MONITOR'S ACRONYM(S)

11. SPONSORING/MONITORING AGENCY REPORT NUMBER

12. DISTRIBUTION AVAILABILITY STATEMENT

Approved for public release; distribution is Unlimited.

13. SUPPLEMENTARY NOTES

14. ABSTRACT

The Twenty-seventh Annual Conference on the Physics and Chemistry of Semiconductor Interfaces was held in Salt Lake City, Utah while the Twenty-eighth Annual Conference on the Physics and Chemistry of Semiconductor Interfaces was held in Orlando, Florida. The enclosed report contains abstracts of papers presented at both conferences.

15. SUBJECT TERMS

Semiconductor Interfaces

16. SECURITY CLASSIFICATION OF: a. REPORT	b. ABSTRACT	c. THIS PAGE	17. LIMITATION OF ABSTRACT	18. NUMBER OF PAGES	19a. NAME OF RESPONSIBLE PERSON
U	U	U	UU	395	C. R. Schulte
					19b. TELEPONE NUMBER *(Include area code)* 480 423 8540

Standard Form 298 (Rev. 8-98)
Prescribed by ANSI-Std Z39-18

INTRODUCING A REVOLUTION IN THIN FILM TECHNOLOGY- DIRECT METAL ION BEAM DEPOSITON.

SKION OMNIPOTENT™ METAL SPUTTER ION BEAM SYSTEM

Produce Amorphous Diamond Films

- Hardness more than 40 Gpa
- Transparent
- Ultra-Smooth less than 1nm Ra.
- No hydrogen, no particulates
- Deposition rate more than 5 A/sec.
- Uniformity: +/- 5% over 8" diameter area

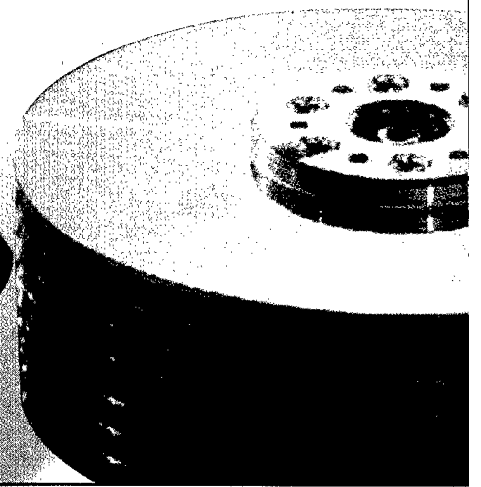

OMNIPOTENT 2000

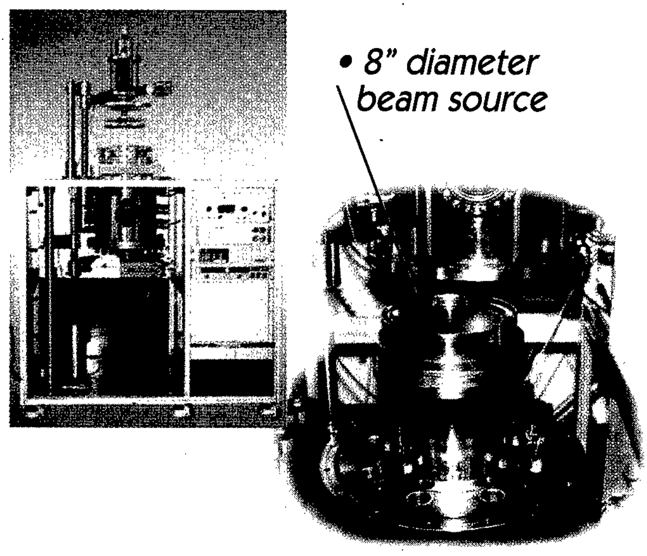

- 8" diameter beam source

OMNIPOTENT 5000

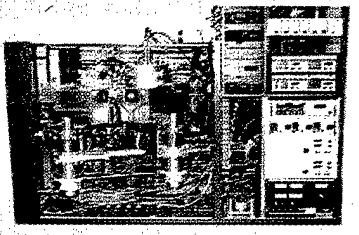

- High throughput robot arm sample transfer

SKION CORPORATION

50 Harrison St., Hoboken, NJ 07030 • Tel: 201-963-5450 Fax: 201-963-5449
E-mail: info@skion.com

Journal of Vacuum Science & Technology B

JVST B

ISSN: 0734-211X
CODEN: JVTBD9

Microelectronics and Nanometer Structures

Processing, Measurement, and Phenomena

Editor: G. E. McGuire,
MCNC, Research Triangle Park, NC 27709. Telephone: (919) 248-1910

Supervisor Editorial Office: Rebecca York,
Editorial Assistant: Estella K. Stansbury,
Journal of Vacuum Science and Technology, Caller Box 13994, 10 Park Plaza, Ste. 4A,
Research Triangle Park, NC 27709, Telephone: (919) 361-2787 and (919) 361-2342;
FAX: (919) 361-1378; E-mail: jvst@jvst.org

Associate Editors:
Eric Kay, Review Articles
D. Bonnell (2001) Univ. of Pennsylvania
S. Felch (2000) Varian Associates
J. P. McVittie (2000) Stanford University
G. Owen (2000) Hewlett Packard Labs.
C. C. Williams (2002) University of Utah
Y. Yasuda (2001) Nagoya University

JVST Publication Committee:
Dorota Temple, Chair, MCNC
John E. Crowell, UC San Diego
J. William Rogers, Jr., Pacific Northwest Natl. Lab.
Pete Sheldon, NREL
Philip Yashar, Intel

JVST Editorial Board:
J. C. Bean (2001) Univ. of Virginia
J. Chapple-Sokol (2002) IBM Corp., Essex Junction
A. Czanderna (2000) NREL
M. Kushner (2000) Univ. of Illinois
T. Mayer Sandia Natl. Labs
D. Monroe (2000) Lucent Bell Labs
J. Theil (2002) Agilent Technologies
P. A. Thiel (2001) Iowa State Univ.

JVST Editorial Staff at AIP: Editorial Supervisor: Deborah McHone; Journal Coordinator: Margaret Reilly; Chief Production Editor: Mary Ellen Mormile

The Journal of Vacuum Science & Technology B is published six times annually (Jan/Feb, Mar/Apr, May/Jun, Jul/Aug, Sep/Oct, Nov/Dec) by the American Vacuum Society (AVS) through the American Institute of Physics (AIP). It is an official publication of the AVS and is received by all members of the Society. It is devoted to reports of original research and Review articles. The *JVST B* has been established to provide a vehicle for the publication of research dealing with microelectronics and nanometer structures. The emphasis will be on processing, measurement, and phenomena, and will include vacuum processing, plasma processing, materials and structural characterization, microlithography, and the physics and chemistry of submicron and nanometer structures and devices. This journal will publish the proceedings of conferences and symposia that are sponsored by the AVS and its divisions.

Submit Manuscripts to the Editorial Office of the *Journal of Vacuum Science & Technology*, 10 Park Plaza, Caller Box 13994, Research Triangle Park, North Carolina 27709-3994; e-mail jvst@jvst.org. Manuscripts of papers presented at AVS-sponsored conferences and symposia and being submitted to *JVST B* should be sent to the Guest Editor appointed for that particular conference. Before preparing a manuscript, authors should read "Information for Contrbutors," printed in the first issue of each volume of the journal. Submission of a manuscript is a representation that the manuscript has not been published previously nor currently submitted for publication elsewhere. Upon receipt of a manuscript the Editor will send the author a Transfer of Copyright Agreement form. This must be completed by the author and returned *only* to the Editorial Office prior to publication of an accepted paper in the *Journal of Vacuum Science & Technology B*. This written transfer of copyright, which previously was assumed to be implicit in the act of submitting a manuscript, is necessary under the 1978 copyright law in order for the AVS and AIP to continue disseminating research results as widely as possible. Further information may be obtained from AIP.

Publication Charge: To support the cost of wide dissemination of research results through the publication of journal pages and production of a database of articles, the author's institution is requested to pay a *page charge* of $95 per page (with a one-page minimum). The charge (if honored) entitles the author to 100 free reprints. For Errata the minimum page charge is $10, with no free reprints.

Electronic Physics Auxiliary Publication Service (EPAPS): EPAPS is a low-cost electronic depository for material that is supplemental to a journal article. For a nominal fee, authors may submit multimedia (e.g., movie files, audio files, 3D rendering files), color figures, data tables, etc. Retrieval instructions are footnoted in the related published paper. Direct requests to the Editor; for additional information see http://www.aip.org/pubservs/epaps.html.

Advertising Rates will be supplied on request from AIP's Advertising Division, Suite 1NO1, 2 Huntington Quadrangle, Melville, NY 11747-4502. Telephone: (516) 576-2440. Fax: (516) 576-2481. E-mail: advtsg@aip.org. All insertion orders and advertising material should be sent to that division.

Copying: Single copies of individual articles may be made for private use or research. Authorization is given (as indicated by the Item Fee Code for this publication) to copy articles beyond the use permitted by Sections 107 and 108 of the U.S. Copyright Law, provided the copying fee of $17 per copy per article is paid to the Copyright Clearance Center, 222 Rosewood Drive, Danvers, MA 01923, USA. Persons desiring to photocopy materials for classroom use should contact the CCC Academic Permissions Service. The Item Fee Code for this publication is 0734-211X/2000 $17.00.

Authorization does not extend to systematic or multiple reproduction, to copying for promotional purposes, to electronic storage or distribution, or to republication in any form. In all such cases, specific written permission from AIP must be obtained.

Permission for Other Use: Permission is granted to quote from the journal with the customary acknowledgment of the source. To reprint a figure, table, or other excerpt requires the consent of one of the authors and notification to AIP.

Requests for Permission: Address requests to AIP Office of Rights and Permissions, Suite 1NO1, 2 Huntington Quadrangle, Melville, NY 11747-4502; Telephone: (516) 576-2268; Fax: (516) 576-2450; E-mail: rights@aip.org.

Copyright © 2000 American Vacuum Society. All rights reserved.

American Vacuum Society

Officers

Paula Grunthaner, *President*
Jet Propulsion Lab., Caltech

Stephen Rossnagel, *Immediate Past-President*
IBM T. J. Watson Research Center

Joseph E. Greene, *Secretary*
University of Illinois

John W. Coburn, *Treasurer*
Univ. of CA, Berkeley

Directors

Cammy R. Abernathy
University of Florida

Gregory J. Exarhos
Pacific Northwest National Lab.

Calvin Gabriel
Advanced Micro Devices

Howard Patton
LLNL

Peter M. A. Sherwood
Kansas State University

Dorota Temple
MCNC

JVST

G. Lucovsky, *Editor-in-Chief*
North Carolina State University

AVS Membership Information may be obtained from

Angela Mulligan
AVS Member Services Coordinator
120 Wall Street
32nd Floor
New York, NY 10005
(212) 248-0200
angela@vacuum.org
www.vacuum.org

Be Highly Selective in Your Choice of Plasma RIE System

Selective plasma etching is the key to successful fabrication of most III-V devices. Our new range of plasma systems are designed specifically for highly selective, homogeneous, low damage etching processes. The image (right) shows selective etching of an HBT structure with high selectivity between InGaAs, GaAs and InGaP. The multilayer structure (below right) is a Bragg reflector of a VCSEL device. Note the steep smooth sidewall and lack of under-etch. Both devices were etched in a SI591 parallel plate RIE system. The SI591 is a ready-to-use parallel plate reactor complete with a computerized control system and a unique end point detector which is so accurate it can stop the etching precisely on any layer of a multilayer structure such as the Bragg reflector shown here.

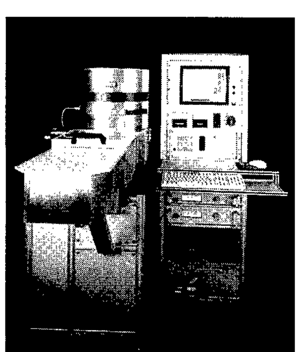

More Data in Less Time

SE850 Spectroscopic Ellipsometer

for All Your Multilayer Films

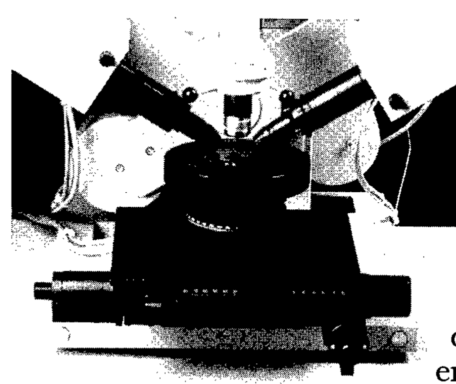

With an SE-850 Spectroscopic Ellipsometer you can measure the thickness and optical constants of multilayer structures with astonishing precision. The SE850 uses a unique compensator which enables the instrument to read the full range of the ellipsometric parameter delta from 0 - 360 degrees enabling you to take readings even on transparent substrates and layers. The SE850 is also very fast, using FT- IR ellipsometry to achieve high speed measurements with outstanding signal to noise ratio. Performance is further enhanced by the use of a diode array detection system in the UV-VIS. As an example, the Bragg reflector shown above, with more than 30 layers, can easily be analyzed in the NIR to verifiy the thickness of each layer.

To find out more about these remarkable products contact:

Micro Photonics Inc
PO Box 3129 Allentown PA 18106
Tel: (610) 366-7103 Fax: (610) 366-7105
Email: info@microphotonics.com
Internet: www.microphotonics.com

SENTECH

Sentech Instruments GmbH
Carl-Scheele-Strasse 16, D12489 Berlin Germany.
Tel: +49 30 63 92 55 20 Fax: +49 30 63 92 55 22
Email: info@sentech.de Internet: www.sentech.de

ABSOLUTE

XUV SILICON PHOTODIODES

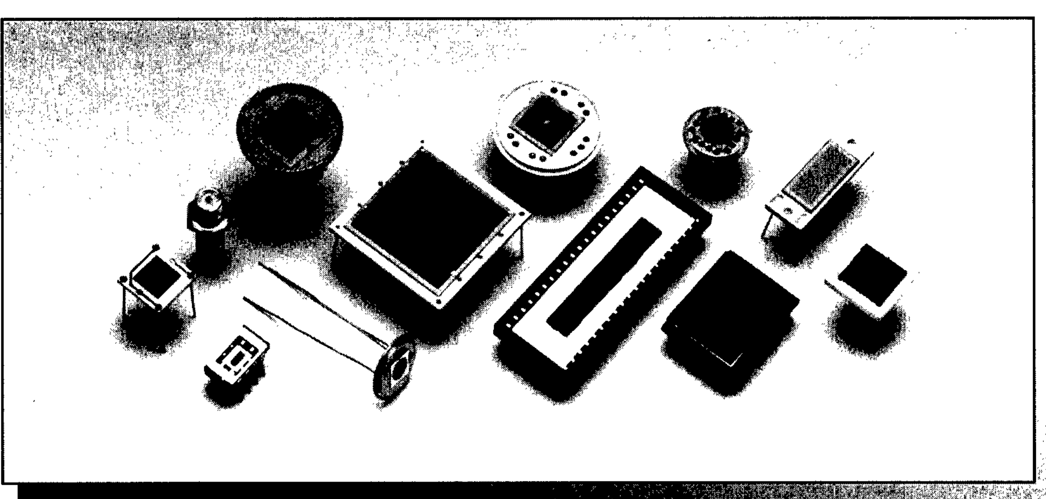

Features

- 100% Internal Collection Efficiency
- 8 Decades of Linearity
- No Change in QE with 100 Mrad (Si) 124 eV Photons
- May be Operated Without Bias
- Cryogenically and UHV Compatible
- With Integrated Bandwidth Limiting Filters

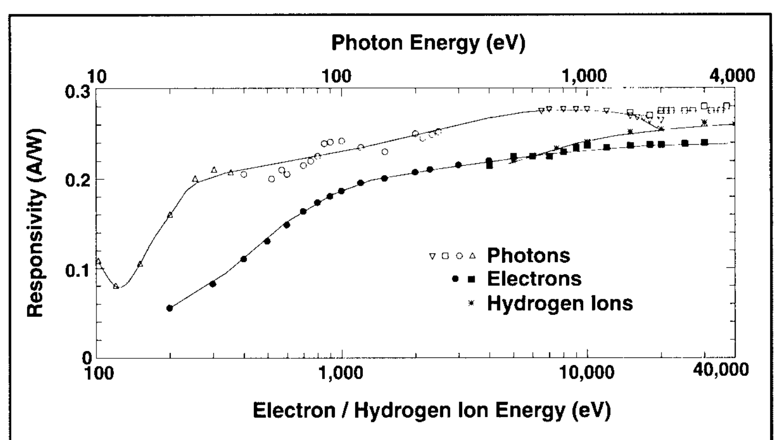

TYPICAL RESPONSIVITY OF AXUV PHOTODIODES TO PHOTONS, ELECTRONS AND HYDROGEN IONS

SXUV Series Photodiodes are Available for Infinite Hardness to XUV Photons

INTERNATIONAL RADIATION DETECTORS INC.
2545 West 237th Street, Unit I ◆ Torrance, California 90505-5229
(310) 534-3661 ◆ FAX (310) 534-3665 ◆ email: irdinc@earthlink.net
http://www.ird-inc.com

DEVELOPED IN COLLABORATION WITH NIST, NIH, LLNL, LANL, NCAR

Journal of Vacuum Science & Technology B

JVST B

Microelectronics and Nanometer Structures

Processing, Measurement, and Phenomena

Second Series
Volume 18, Number 4
Jul/Aug 2000

Regular Articles

Effects of surface oxides on field emission from silicon
Jonathan Shaw **1817**

Studies on the interaction between thin film materials and Mo field emitter arrays
Babu R. Chalamala and Robert H. Reuss **1825**

Emission sensitivity to tip position of Spindt-type field emitters
Chenggang Xie, Yi Wei, Rudy Lucero, and Robert Woodburn **1833**

Electron field emission from amorphous carbon nitride synthesized by electron cyclotron resonance plasma
X. W. Liu, S. H. Tsai, L. H. Lee, M. X. Yang, A. C. M. Yang, I. N. Lin, and H. C. Shih **1840**

Self-assembled gold silicide wires on bromine-passivated Si(110) surfaces
B. Rout, B. Sundaravel, Amal K. Das, S. K. Ghose, K. Sekar, D. P. Mahapatra, and B. N. Dev **1847**

Mechanism of laser-induced nanomodification on hydrogen-passivated Si(100) surfaces underneath the tip of a scanning tunneling microscope
Z. H. Mai, Y. F. Lu, S. M. Huang, W. K. Chim, and J. S. Pan **1853**

(Continued)

Journal of Vacuum Science & Technology B (ISSN: 0734-211X) is published six times annually (Jan/Feb, Mar/Apr, May/Jun, Jul/Aug, Sep/Oct, Nov/Dec) by the American Vacuum Society through the American Institute of Physics, Suite 1NO1, 2 Huntington Quadrangle, Melville, NY 11747-4502. 2000 subscription rates are: US$835. POSTMASTER: Send address changes to *Journal of Vacuum Science & Technology B,* SLACK Inc., 6900 Grove Road, Thorofare, NJ 08086. Periodicals postage paid at Thorofare, NJ 08086, and at additional mailing offices.

Membership in the American Vacuum Society includes $17.50 from membership dues to be applied towards a subscription to *Journal of Vacuum Science & Technology B.*

Subscription Prices (2000)

	U.S.A. and Poss.	Can., Mex., Central & S. America & Caribbean	Europe, Asia, Africa & Oceania*
JVST B†	$835	$868	$891
JVST B‡	$960	$990	$1017
JVST A and B†	$960	$1024	$1070
JVST A and B#	$960	$990	$990
JVST A and B‡	$1086	$1150	$1196

†Print and online.
‡Print and CD-ROM.
#CD-ROM only.
*Nonmember subscriptions include air-freight service.

Back-number Prices: 2000 single copy: $155. Prior to 2000 single copies: $105.

Subscriptions, renewals, and address changes should be addressed to *Subscription Fulfillment Division, SLACK Inc., 6900 Grove Road, Thorofare, NJ 08086.* Allow at least six weeks advance notice. For address changes please send both old and new addresses, and, if possible, include a label from the plastic mailing wrapper of a recent issue. Missing issue requests will be honored only if received within six months of publication date (nine months for Australia and Asia).

Single-copy orders (current and back issues) should be addressed to American Institute of Physics, Circulation and Fulfillment Division, Suite 1NO1, 2 Huntington Quadrangle, Melville, NY 11747-4502; Telephone 800-344-6902 (or 516-576-2230 outside the U.S.A.), Fax at 516-349-9704, or E-mail at subs@aip.org.

Reprints: Reprints can be ordered with or without covers only in multiples of 50 (with a minimum of 100 in each category) from AIP, Circulation and Fulfillment/Reprints, Suite 1NO1, 2 Huntington Quadrangle, Melville, NY 11747-4502; Fax: 516-349-9704; Telephone: 800-344-6909 (U.S. and Canada) or 516-576-2230.

Document Delivery: Copies of journal articles can be ordered for online delivery from the Buy An Article online document delivery service (http://ojps.aip.org/jhtml/artinphys/).

Microform: *Journal of Vacuum Society & Technology B* is available on microfiche issued at the same frequency as the printed journal and annually on microfilm. Direct requests to AIP, Circulation and Fulfillment/Single Copy Sales, Suite 1NO1, 2 Huntington Quadrangle, Melville, NY 11747-4502; Fax: 516-349-9704; Telephone: 800-344-6908 (U.S. and Canada) or 516-576-2230.

Online Access: The *Journal of Vacuum Science and Technology B* is available online to AVS members at no additional charge; for details, please see http://ojps.aip.org/jvstb/. Abstracts of journal articles are available from AIP's SPIN Web Service (http://ojps.aip.org/spinweb/).

Enhancement of resolution of DNA on silylated mica using atomic force microscopy
Jing Tang, Junwei Li, Chen Wang, and Chunli Bai 1858

New polymer materials for nanoimprinting
H. Schulz, H.-C. Scheer, T. Hoffmann, C. M. Sotomayor Torres, K. Pfeiffer, G. Bleidiessel, G. Grützner, Ch. Cardinaud, F. Gaboriau, M.-C. Peignon, J. Ahopelto, and B. Heidari 1861

Bilayer, nanoimprint lithography
Brian Faircloth, Henry Rohrs, Richard Tiberio, Rodney Ruoff, and Robert R. Krchnavek 1866

Determination of coupled acid catalysis-diffusion processes in a positive-tone chemically amplified photoresist
F. A. Houle, W. D. Hinsberg, M. Morrison, M. I. Sanchez, G. Wallraff, C. Larson, and J. Hoffnagle 1874

Statistical considerations of the overlay error in laser driven point source x-ray lithography
Detlev H. Tiszauer 1886

Comparison of Cl_2 and F-based dry etching for high aspect ratio Si microstructures etched with an inductively coupled plasma source
W. -C. Tian, J. W. Weigold, and S. W. Pang 1890

Control of surface reactions in high-performance SiO_2 etching
T. Tatsumi, M. Matsui, M. Okigawa, and M. Sekine 1897

Electron cyclotron resonance plasma etching of InP through-wafer connections at >4 μm/min using Cl_2/Ar
Y. W. Chen, B. S. Ooi, G. I. Ng, and C. L. Tan 1903

Patterning of tantalum pentoxide, a high epsilon material, by inductively coupled plasma etching
L. B. Jonsson, J. Westlinder, F. Engelmark, C. Hedlund, J. Du, U. Smith, and H.-O. Blom 1906

Anisotropic etching of RuO_2 and Ru with high aspect ratio for gigabit dynamic random access memory
Takashi Yunogami and Kazuo Nojiri 1911

Transmission electron microscope investigation of $SrBi_2Ta_2O_9$ memory capacitors on Si with silicon dioxide and silicon nitride as buffers
A. Ils, M. Cantoni, J.-M. Sallese, P. Fazan, J.-P. Han, X. Guo, and T. P. Ma 1915

Stability and chemical composition of thermally grown iridium-oxide thin films
Babu R. Chalamala, Yi Wei, Robert H. Reuss, Sanjeev Aggarwal, Scott R. Perusse, Bruce E. Gnade, and R. Ramesh 1919

Effects of $(Ba, Sr)TiO_3$ film thickness on electrical properties of $(Ba, Sr)TiO_3/(Ba, Sr)RuO_3$ capacitor
Se Hoon Oh, Kyung Woong Park, Jeong Hee Park, Boum Seock Kim, and Duck Kyun Choi 1923

Effects of composition and N_2 plasma treatment on the barrier effectiveness of chemically vapor deposited WSi_x films
M. T. Wang, M. H. Chuang, L. J. Chen, and M. C. Chen 1929

Study of forming a p^+ poly-Si gate by inductively coupled nitrogen plasma nitridation of the stacked poly-Si layers
M. H. Juang 1937

Ion-bombardment effects on PtSi/*n*-Si Schottky contacts studied by ballistic electron emission microscopy
Guo-Ping Ru, Xin-Ping Qu, Shi-Yang Zhu, Bing-Zong Li, C. Detavernier, R. L. Van Meirhaeghe, F. Cardon, R. A. Donaton, and K. Maex 1942

Effect of ramp rate on the C49 to C54 titanium disilicide phase transformation from Ti and Ti(Ta)
Paul Martin Smith, Glenn Bailey, Yao Zhi Hu, and Sing Pin Tay 1949

Mosaic structure of various oriented grains in $CoSi_2$/Si(001)
Tae Soo Kang, Jung Ho Je, Gi Bum Kim, Hong Koo Baik, and Sung-Man Lee 1953

Effect of the first antimony layer on AuZn ohmic contacts to *p*-type InP
Akira Yamaguchi, Hirokuni Asamizu, Takeshi Okada, Yasuhiro Iguchi, Tadashi Saitoh, Yasuo Koide, and Masanori Murakami 1957

Design and implementation of optoelectronic interfaces for high-speed burst-mode transmissions
André Boyoguéno Bendé 1962

Electroreflectance and photoreflectance studies of surface Fermi level and surface state densities of InP SIN^+ structures
W. C. Hwang, Y. J. Cheng, Y. C. Wang, and J. S. Hwang 1967

Passivation of the Ge/InP(110) interface by As interlayers: Interface reactions and band offsets
A. B. Preobrajenski, S. Schömann, R. K. Gebhardt, and T. Chassé 1973

(Continued)

RGA for the Masses

Systems from $3750 (U.S. list)

- 100 and 200 amu systems
- Partial pressure to 10^{-14} Torr
- 6 orders of magnitude dynamic range in a single scan
- Real-time Windows® software
- Mass spectra, leak detection and pressure vs. time modes
- Multi-head operation
- Optional Electron Multiplier

Residual gas analyzers from SRS offer uncompromised performance at half the price of the competition. Our systems provide mass ranges to 200 amu, detectable partial pressures to 10^{-14} Torr and better than 1 amu resolution. With our interactive Windows® software package you can fully control the RGA sensor, acquire data and analyze your vacuum system in real-time. The simple, rugged quadrupole mass spectrometer attaches directly to a 2 3/4" CF flange. A dual ThO_2Ir filament and a unique continuous dynode electron multiplier provide increased stability and longer life than other designs. Both are field replaceable in a matter of minutes – a first for RGAs! If your application involves residual gas analysis, leak detection or vacuum processing, contact us for a copy of our RGA systems brochure and demo software package.

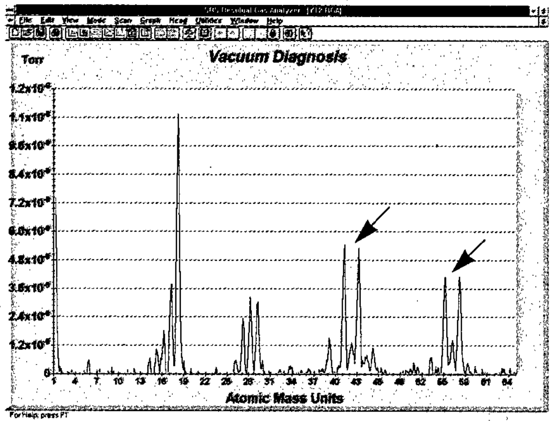

The RGA is an invaluable vacuum diagnostic tool. Shown above is the mass spectrum of a vacuum chamber contaminated with oil.

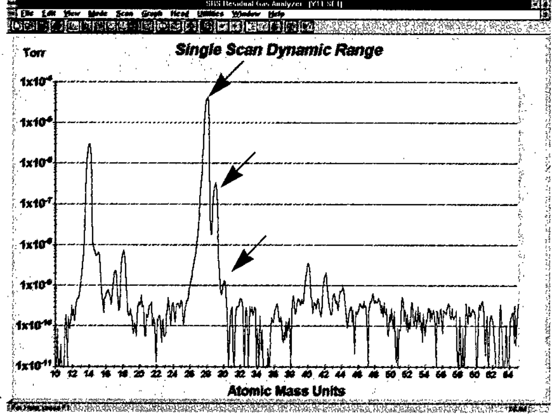

With dynamic range that spans 6 orders of magnitude, three isotopes of Nitrogen ($^{14}N_2$, $^{14}N\,^{15}N$, $^{15}N_2$) are clearly detected in a single scan.

Stanford Research Systems
1290-D Reamwood Avenue, Sunnyvale, CA 94089
Telephone (408)744-9040 • FAX (408)744-9049
Email: info@thinkSRS.com • WWW: www.thinkSRS.com

Windows is a registered trademark of Microsoft Corporation

Polarized laser light scattering applied to surface morphology characterization of epitaxial III–V semiconductor layers
M. U. González, J. A. Sánchez-Gil, Y. González, L. González, and E. R. Méndez **1980**

Reduction of indium segregation in InGaAs/GaAs quantum wells grown by molecular beam epitaxy on vicinal GaAs(001) substrates
S. Martini, A. A. Quivy, A. Tabata, and J. R. Leite **1991**

Structural and electrical properties of chemical vapor deposited diamond films doped by B^+ implantation
S. B. Wang, H. X. Zhang, P. Zhu, and K. Feng **1997**

Preparation of C_{60}-doped silica aerogels and the study of photoluminescence properties
Bin Zhou, Jue Wang, Li Zhao, Jun Shen, Zhongsheng Deng, and Yufen Li **2001**

Brief Reports and Comments

Chlorination of Si surfaces under strain conditions
Timur Halicioglu **2005**

Stability of boron and phosphorus implanted tungsten silicide structures at high temperatures
R. Bashir and F. Hebert **2008**

Rapid Communications

Low temperature inorganic chemical vapor deposition of Ti–Si–N diffusion barrier liners for gigascale copper interconnect applications
Eric Eisenbraun, Allan Upham, Raj Dash, Wanxue Zeng, Johann Hoefnagels, Sarah Lane, Dalaver Anjum, Katharine Dovidenko, Alain Kaloyeros, Barry Arkles, and John J. Sullivan **2011**

Plasma-enhanced atomic layer deposition of Ta and Ti for interconnect diffusion barriers
S. M. Rossnagel, A. Sherman, and F. Turner **2016**

Observation of fine structures of nanodomains in donor-modified $Pb(Zr,Ti)O_3$ ferroelectrics
Qi Tan and Jianxing Li **2021**

Shop Notes

Sheet resistance nonuniformity for ionized titanium deposition
Keith A. Ross and Peter Thimm **2024**

Time-stability measurement and compensation of a scanning probe microscope instrument
Wenhao Huang, Wenwei Wang, Andong Xia, Nong Jin, and ZhiQiang Hu **2027**

Errata

Erratum: "Ion-etch produced damage on InAs(100) studied through collective-mode electronic Raman scattering" [J. Vac. Sci. Technol. B 18, 144 (2000)]
T. A. Tanzer, P. W. Bohn, I. V. Roshchin, and L. H. Greene **2030**

Papers from the 27th Conference on the Physics and Chemistry of Semiconductor Interfaces

Preface **2033**

Spin Dependent Effects and Novel Interface Phenomena

Scanning capacitance microscopy imaging of silicon metal-oxide-semiconductor field effect transistors
R. N. Kleiman, M. L. O'Malley, F. H. Baumann, J. P. Garno, and G. L. Timp **2034**

Ferromagnetic III–V heterostructures
H. Ohno **2039**

Nickel layers on indium arsenide
C. J. Hill, R. A. Beach, and T. C. McGill **2044**

Interfacial scattering of hot electrons in ultrathin Au/Co films
R. P. Lu, B. A. Morgan, K. L. Kavanagh, C. J. Powell, P. J. Chen, F. G. Serpa, and W. F. Egelhoff, Jr. **2047**

Ferromagnetic MnAs grown on GaAs(001): *In situ* investigations
M. Kästner, F. Schippan, P. Schützendübe, L. Däweritz, and K. Ploog **2052**

(Continued)

AES
AFM
ARUPS
CITS
ESCA
HREELS
ISS
LEED
MBE
MFM
PEEM
RHEED
SAM
SEM
SEMPA
SNOM
SPA-LEED
SPLEED
STM
STS
UPS
XPD
XPS

www.omicron-instruments.com and www.omicron.de

High-Definition Electron Spectroscopy

New 'EIS' Electron & Ion Spectroscopy Software

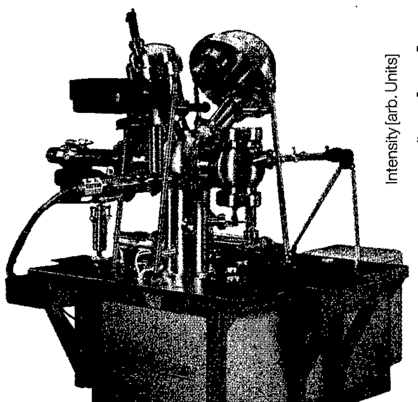

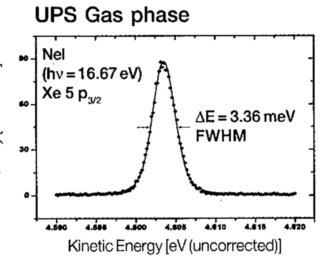

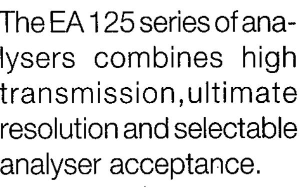
The EA 125 series of analysers combines high transmission, ultimate resolution and selectable analyser acceptance.

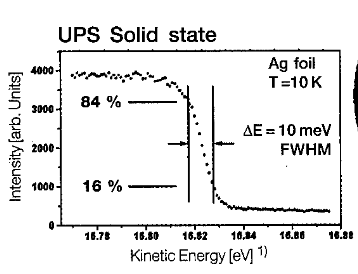

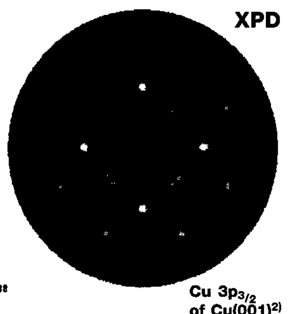

Cu $3p_{3/2}$ of Cu(001)[2]

[1] B. Grimm, H. Hövel, C. Quitmann, and B. Reihl, Univ. of Dortmund, Germany
[2] O. Gröning, P. Gröning, P. Ruffieux, P. Schwaller, and L. Schlapbach; Institut de Physique, Université de Fribourg, Switzerland

Headquarters:
OMICRON VAKUUMPHYSIK GmbH
Tel./Fax +49 (0) 6128 9 87 - 0 / - 185
E-mail: info@omicron.de

USA:
OMICRON Associates
Tel./Fax (412) 831-2262 /-9828
E-mail: omiassoc@sgi.net

GEIB REFINING CORPORATION

Precious Metal Reclamation for Thin Film

• TARGETS • SCRAPINGS
• SANDBLAST MEDIA • REJECTED PARTS

"We build relationships one settlement at a time."

Gold • Silver • Platinum • Palladium

399 Kilvert Street, Warwick, RI 02886
1-800-288-GOLD (4653)
1-401-738-8560 • FAX 1-401-732-2841
www.geibrefining.com sales@geibrefining.com

Plasma Characterization

Quantify your plasma environment:
- Ion mass & energy
- Ion & electron density
- Positive ions/ negative ions
- Plasma & floating potential
- Neutrals & radicals
- Electron temperature & energy distribution

Instruments for Exact Science

E-mail: info@hiden.demon.co.uk
Web site: http://www.hiden.co.uk

Epitaxial ferromagnetic metal/GaAs(100) heterostructures
L. C. Chen, J. W. Dong, B. D. Schultz, C. J. Palmstrøm, J. Berezovsky, A. Isakovic, P. A. Crowell, and N. Tabat 2057

Enhanced magneto-optical effect in a GaAs:MnAs nanoscale hybrid structure combined with GaAs/AlAs distributed Bragg reflectors
H. Shimizu, M. Miyamura, and M. Tanaka 2063

Interface Strain Effects and Atomic Level Characterization

Strain relaxation of InGaAs by lateral oxidation of AlAs
S. K. Mathis, P. Chavarkar, A. M. Andrews, U. K. Mishra, and J. S. Speck 2066

Scanning tunneling microscopy study of organometallic molecules adsorbed on a GaAs(001)-2×4 surface
Hiromi Kuramochi, Jie Cui, Hidekazu Iwai, and Masashi Ozeki 2072

Reflectance anisotropy spectroscopy of the growth of perylene-3,4,9,10-tetracarboxylic dianhydride on chalcogen passivated GaAs(001) surfaces
T. U. Kampen, U. Rossow, M. Schumann, S. Park, and D. R. T. Zahn 2077

Schottky barrier height and electron affinity of titanium on AlN
B. L. Ward, J. D. Hartman, E. H. Hurt, K. M. Tracy, R. F. Davis, and R. J. Nemanich 2082

Quantitative theory of scattering in antimonide-based heterostructures with imperfect interfaces
M. J. Shaw, E. A. Corbin, M. R. Kitchin, J. P. Hagon, and M. Jaros 2088

Interface control and band offset at the $Ga_{0.52}In_{0.48}P$ on GaAs heterojunction
C. Cai and M. I. Nathan 2096

Effects of gap states on scanning tunneling spectra observed on (110)- and (001)-oriented clean surfaces and ultrathin Si layer covered surfaces of GaAs prepared by molecular beam epitaxy
Hideki Hasegawa, Noboru Negoro, Seiya Kasai, Yasuhiko Ishikawa, and Hajime Fujikuwa 2100

Spin-dependent resonant tunneling in double-barrier magnetic heterostructures
A. G. Petukhov, D. O. Demchenko, and A. N. Chantis 2109

Band Alignment Tuning in Contacts and Heterostructures

Schottky barrier tuning with heterovalent interlayers: Al/Ge/GaAs versus Al/Si/GaAs
C. Berthod, N. Binggeli, and A. Baldereschi 2114

Tunable Schottky barrier contacts to $In_xGa_{1-x}As$
C. Marinelli, L. Sorba, M. Lazzarino, D. Kumar, E. Pelucchi, B. H. Müller, D. Orani, S. Rubini, A. Franciosi, S. De Franceschi, and F. Beltram 2119

Photoemission results on intralayer insertion at III-V/III-V junctions: A critical appraisal of the different interpretations
M. Moreno, M. Alonso, M. Höricke, R. Hey, K. Horn, J. L. Sacedón, and K. H. Ploog 2128

Insulators: Epitaxial Films and Alternative Dielectrics

Epitaxial oxide thin films on Si(001)
Z. Yu, J. Ramdani, J. A. Curless, C. D. Overgaard, J. M. Finder, R. Droopad, K. W. Eisenbeiser, J. A. Hallmark, W. J. Ooms, and V. S. Kaushik 2139

Epitaxial thin films of MgO on Si using metalorganic molecular beam epitaxy
F. Niu, B. H. Hoerman, and B. W. Wessels 2146

Hot carrier transport effects in Al_2O_3-based metal-oxide-semiconductor structures
R. Ludeke, M. T. Cuberes, and E. Cartier 2153

Mechanism of dopant segregation to SiO_2/Si(001) interfaces
J. Dabrowski, R. A. Casali, H.-J. Müssig, R. Baierle, M. J. Caldas, and V. Zavodinsky 2160

Roughening of the Si/SiO_2 interface during SC1-chemical treatment studied by scanning tunneling microscopy
M. Gotoh, K. Sudoh, and H. Iwasaki 2165

***E′* centers and leakage currents in the gate oxides of metal oxide silicon devices**
P. M. Lenahan and J. J. Mele 2169

Photoemission spectroscopy of platinum overlayers on silicon dioxide films
J. W. Keister, J. E. Rowe, J. J. Kolodziej, and T. E. Madey 2174

(Continued)

VAT®

All-metal Angle Valve
for UHV and extreme UHV

For pump and gauge isolation under UHV conditions

- **Closing to mechanical stop; eliminates torque wrench requirement**
- **High conductance**
- **VATRING «hard to hard» all-metal sealing for 1,000 maintenance-free cycles**

ONLY $495! (USD price valid in USA/Canada only)

Ask for our catalogue «VAT Vacuum Valves 2000» for detailed information on more than 1000 standard products.

Visit our website at www.vatvalve.com

Swiss Headquarters
Tel ++41 81 771 61 61
Fax ++41 81 771 48 30
Email reception@vat.ch

VAT France
Tel 01 69 20 69 11
Fax 01 69 20 90 08
Email france@vatvalve.com

VAT Germany
Tel (089) 46 50 15
Fax (089) 46 37 65
Email deutschland@vatvalve.com

VAT U.K.
Tel 0208 346 1999
Fax 0208 343 1104
Email uk@vatvalve.com

VAT Japan
Tel (045) 333 11 44
Fax (045) 333 70 24
Email info@vatskk.co.jp

VAT USA
Tel (781) 935 1446
Fax (781) 935 3940
Email usa@vatvalve.com

NANO-MASTER, Inc.
3019 Alvin Devane Blvd • Suite 220 • Austin, TX 78741 • Tel: (512)385-4552
Fax (512)385-4900 • email: main@nanomaster.com • www.nanomaster.com

NANO-MASTER is proud to introduce Custom Built Sputter Coaters and PECVD Systems. These machines are designed for most demanding single wafer processing applications in an R&D environment.

NPE-2001
PECVD System

- Compact, PLC Controlled
- Aluminum Chamber
- Heated 8" Platen
- Hallow Cathode RF Electrode with Fractal Gas Distribution Shower Head
- 200 l/sec. Turbomolecular & 3.5 cfm Mech. Pump
- Mass Flow Controllers

NSC-2000
Sputter Coater

- Compact, PLC Controlled
- 2-4" Single Magnetron DC Sputtering
- 80 l/sec. Turbomolecular & 3.5 cfm Mech. Pump
- 12" Pyrex Chamber, Water Cooled 8" Platen

Options:
- RF package
- Thickness Monitor
- Multiple Magnetrons with Rotating Platen

Precision Surface Science

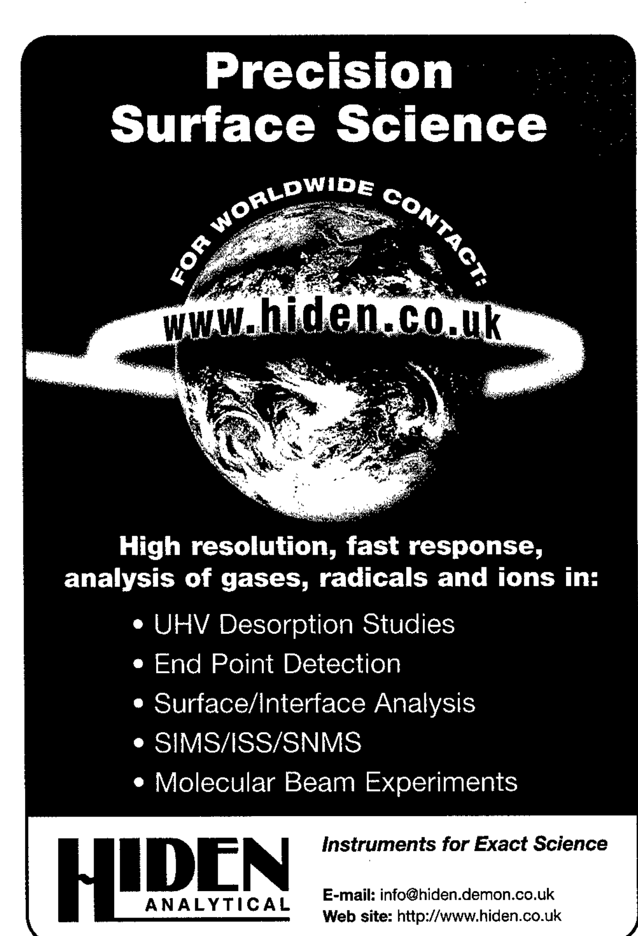

High resolution, fast response, analysis of gases, radicals and ions in:

- UHV Desorption Studies
- End Point Detection
- Surface/Interface Analysis
- SIMS/ISS/SNMS
- Molecular Beam Experiments

HIDEN ANALYTICAL

Instruments for Exact Science

E-mail: info@hiden.demon.co.uk
Web site: http://www.hiden.co.uk

Intrinsic limitations on ultimate device performance and reliability at (i) semiconductor–dielectric interfaces and (ii) internal interfaces in stacked dielectrics
G. Lucovsky, H. Yang, H. Niimi, M. F. Thorpe, and J. C. Phillips **2179**

Quantum Dots and Self-Assembled Interface Structures

Strain-induced self-organized growth of nanostructures: From step bunching to ordering in quantum dot superlattices
J. Stangl, T. Roch, V. Holý, M. Pinczolits, G. Springholz, G. Bauer, I. Kegel, T. H. Metzger, J. Zhu, K. Brunner, G. Abstreiter, and D. Smilgies........ **2187**

Controlled ordering and positioning of InAs self-assembled quantum dots
H. Lee, J. A. Johnson, J. S. Speck, and P. M. Petroff........ **2193**

Growth and microstructure of self-assembled ErAs islands in GaAs
C. Kadow, J. A. Johnson, K. Kolstad, J. P. Ibbetson, and A. C. Gossard........ **2197**

Evolution of Si-on-GaAs (001) surface morphology towards self-organized ordered Si structures
Z. M. Wang, L. Däweritz, P. Schützendübe, and K. H. Ploog **2204**

Atomic structure and composition of the (2×4) reconstruction of InGaP(001)
P. Vogt, K. Lüdge, M. Zorn, M. Pristovsek, W. Braun, W. Richter, and N. Esser **2210**

Interface Optical Properties

Understanding reflectance anisotropy: Surface-state signatures and bulk-related features
W. G. Schmidt, F. Bechstedt, and J. Bernholc **2215**

***In situ* reflectance-difference spectroscopy of doped CdTe and ZnTe grown by molecular beam epitaxy**
R. E. Balderas-Navarro, K. Hingerl, W. Hilber, D. Stifter, A. Bonanni, and H. Sitter........ **2224**

Surface-induced optical anisotropy of Si and Ge
U. Rossow, L. Mantese, and D. E. Aspnes **2229**

In-plane optical anisotropy of quantum well structures: From fundamental considerations to interface characterization and optoelectronic engineering
S. Cortez, O. Krebs, and P. Voisin **2232**

Optical properties of bulk and thin-film $SrTiO_3$ on Si and Pt
Stefan Zollner, A. A. Demkov, R. Liu, P. L. Fejes, R. B. Gregory, Prasad Alluri, J. A. Curless, Z. Yu, J. Ramdani, R. Droopad, T. E. Tiwald, J. N. Hilfiker, and J. A. Woollam **2242**

Method for atomic-layer-resolved measurement of polarization fields by nuclear magnetic resonance
James G. Kempf and Daniel P. Weitekamp........ **2255**

Heteroepitaxy and III-Nitride Materials

ZnSe/CdTe/ZnSe heterostructures
S. Rubini, B. Bonanni, E. Pelucchi, A. Franciosi, A. Garulli, A. Parisini, Y. Zhuang, G. Bauer, and V. Holý **2263**

Anisotropic strain in (100) ZnSe epilayers grown on lattice mismatched substrates
Z. Yang, I. K. Sou, and Y. H. Chen........ **2271**

GaInAsP grown on GaAs substrate by solid source molecular beam epitaxy with a valve phosphorous cracker cell
D. H. Zhang, X. Z. Wang, H. Q. Zheng, W. Shi, S. F. Yoon, and C. H. Kam........ **2274**

Interface tuning of the InAs/AlSb heterostructure-based quantum wells
V. M. Ichizli, K. Mutamba, M. Droba, A. Sigurdardóttir, and H. L. Hartnagel........ **2279**

Surface structures and growth kinetics of InGaN(0001) grown by molecular beam epitaxy
Huajie Chen, R. M. Feenstra, J. E. Northrup, T. Zywietz, J. Neugebauer, and D. W. Greve **2284**

Growth of high-quality (Al,Ga)N and (Ga,In)N heterostructures on SiC(0001) by both plasma-assisted and reactive molecular beam epitaxy
K. H. Ploog, O. Brandt, R. Muralidharan, A. Thamm, and P. Waltereit **2290**

Point defect modification in wide band gap semiconductors through interaction with high-energy electrons: Is reflection high-energy electron diffraction truly benign?
T. H. Myers, A. J. Ptak, B. L. VanMil, M. Moldovan, P. J. Treado, M. P. Nelson, J. M. Ribar, and C. T. Zugates........ **2295**

X-ray studies of group III-nitride quantum wells with high quality interfaces
P. F. Fewster, N. L. Andrew, O. H. Hughes, C. Staddon, C. T. Foxon, A. Bell, T. S. Cheng, T. Wang, S. Sakai, K. Jacobs, and I. Moerman........ **2300**

(Continued)

Surface Analysis Components and Systems Since 1985

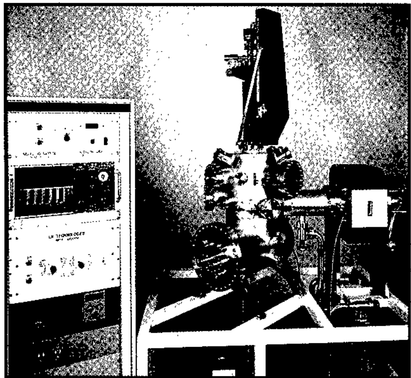
Custom UHV Systems

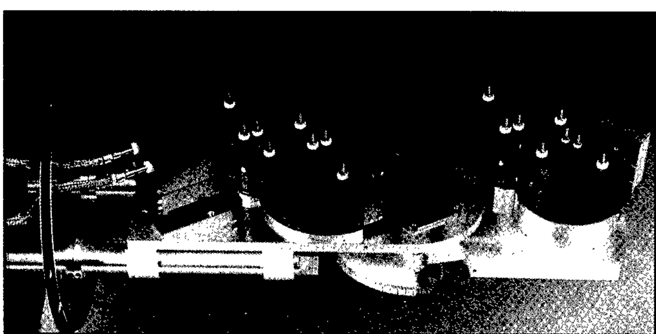
ELS3000 HREELS

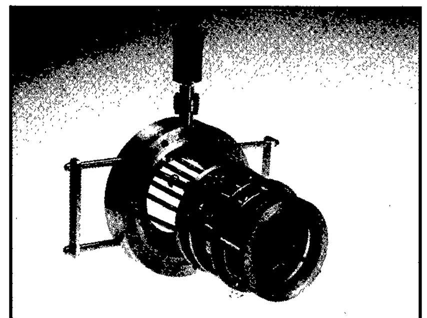
LEED/Auger

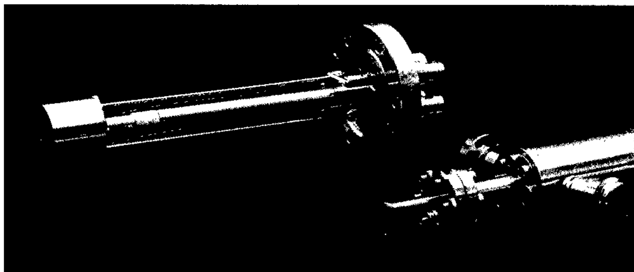
NGI3000 ion guns and *EG3000* electron guns

LK Technologies, Inc.
3910 Roll Avenue, Bloomington, IN 47403
Tel (812) 332-4449
Fax (812) 332-4493
http: //www.lktech.com
e-mail: lktech@lktech.com

Learn Vacuum Technology from the Experts ...

Buy an *AVS Classic Series* reference book—out-of-print references by industry-founding experts:

- *Vacuum Technology and Space Simulation—Santeler, Holkeboer, Jones, and Pagano*
- *Field Emission and Field Ionization—Gomer*
- *Handbook of Electron Tube and Vacuum Techniques—Rosebury*
- *The Physical Basis of Ultrahigh Vacuum—Redhead, Hobson, and Kornelsen*
- *Ionized Gases—von Engel*
- *Vacuum Sealing Techniques—Roth*
- *Basic Data of Plasma Physics: The Fundamental Data on Electrical Discharges in Gases—Brown*
- *Handbook of Materials and Techniques for Vacuum Devices—Kohl*
- *Plasma Diagnostics—Lochte-Holtgreven*
- *Quadrupole Mass Spectrometry—Dawson*

Order your Classic today! Call 1-800-777-4643 to order.

Vacuum Technology Resources for Only $15!

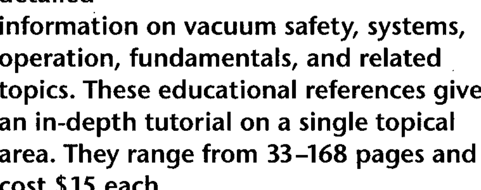

The AVS offers a variety of monographs, providing detailed information on vacuum safety, systems, operation, fundamentals, and related topics. These educational references give an in-depth tutorial on a single topical area. They range from 33–168 pages and cost $15 each.

Call the AVS at 212-248-0200 for a list of monographs.

Charging effects in AlGaN/GaN heterostructures probed using scanning capacitance microscopy
K. V. Smith, X. Z. Dang, E. T. Yu, and J. M. Redwing **2304**

Depth-resolved spectroscopy of interface defects in AlGaN/GaN heterostructure field effect transistors device structures
A. P. Young, J. Bae, L. J. Brillson, M. J. Murphy, and W. J. Schaff **2309**

ZnO/GaN heterointerfaces and ZnO films grown by plasma-assisted molecular beam epitaxy on (0001) GaN/Al_2O_3
S. K. Hong, H. J. Ko, Y. Chen, T. Hanada, and T. Yao **2313**

Polarization effects and transport in AlGaN/GaN system
Yifei Zhang, Yulia Smorchkova, C. Elsass, Stacia Keller, James Ibbetson, Steven DenBaars, Umesh Mishra, and Jasprit Singh **2322**

CUMULATIVE AUTHOR INDEX **2328**

Surface Science Spectra

An International Journal Devoted to Archiving Surface Science Spectra of Technological and Scientific Interest

Add a cost-effective tool to your lab or library by subscribing to ***Surface Science Spectra*** - the definitive international reference guide to spectral data. Applications range from routine identification work to current research in industrial, government, and university labs. Surface Science Spectra offers scientists, engineers, and analysts easy and convenient access to high-quality spectra and related data with every quarterly issue.

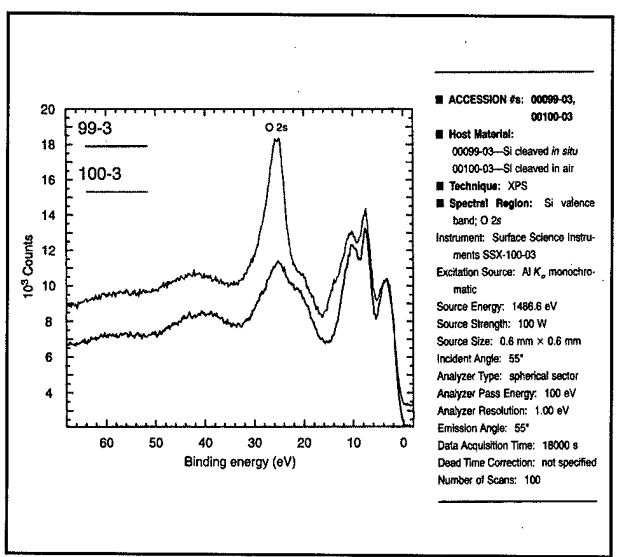

Surface Science Spectra is the most comprehensive source available of complete spectral data. An official journal of the American Vacuum Society, *Surface Science Spectra* currently publishes XPS, Auger, UPS, SIMS and EELS/HREELS spectra from a wide range of fields. Features include:

- Extensive Experimental Details Provided
- The Only Peer Reviewed Spectral Archive
- More Spectra Than in Other Journals
- Focused-Topic Issues and Consolidated References on Specific Materials
- Reference, Comparison, and Technical Spectra
- Spectra in Hard Copy and Electronic Format
- Electronic Database Access with Subscription
- Spectral Data Records from Over 60 Labs Worldwide

** * * Become a part of * * **

this evolving standard today!

Surface Science Spectra

SSS

An international journal devoted to archiving surface science spectra of technological and scientific interest

Surface Science Spectra

To Subscribe or Contribute

Fax or mail this form to SSS, Caller Box 13994, Research Triangle Park, NC 27709, Fax (919)361-1378 Phone(919)361-2498. E-Mail: sss@jvst.org or located at: http://www.vacuum.org/sss.html

Name ____________________

Organization ____________________

Address/Mail Stop ____________________

City/State/Zip ____________________

Country ____________________

E-Mail ____________________

The American Vacuum Society Is ...

Partnering with industry.

The exhibition, held in conjunction with the AVS' annual symposium, is the largest display of the latest innovations in vacuum and deposition equipment, analysis systems, and related services.

Advancing technology worldwide.

Scientists and engineers from universities, government labs, research institutes, and industry gather each fall to attend the week-long AVS National Symposium and learn about the latest developments in their field and exchange ideas with professionals from around the world.

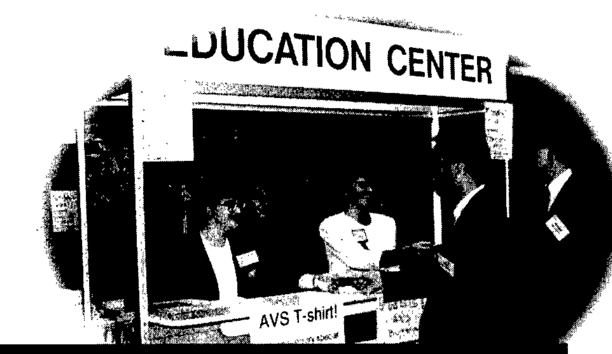

Educating the science community.

Our Educational Center at the annual symposium offers a wide variety of cost-effective educational resources covering vacuum and related technologies.

Providing practical job training.

AVS short courses train more than 3,000 engineers, managers, technicians, and others annually in vacuum technology, surface science, materials and materials characterization, and thin films and processing.

Recognizing outstanding achievements.

AVS awards encourage excellence in graduate students, providing grants for further research, and honor the scientific pioneers among AVS members.

For more information, contact the AVS, 120 Wall Street, 32nd Floor, New York, NY 10005, 212-248-0200, fax 212-248-0245, e-mail avsnyc@vacuum.org, http://www.vacuum.org.

Don't Lose Your Technical Edge ...

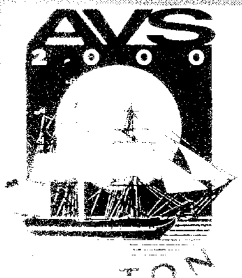

Attend the premier annual symposium on materials, surfaces, interfaces, and processes!

American Vacuum Society 47th International Symposium: Vacuum, Thin Films, Surfaces/Interfaces, Processing & NANO-6

October 2–6, 2000, Boston, Massachusetts

The AVS 47th International Symposium presents leading-edge technical symposia in science and technology for the following areas:

- Biomaterial Interfaces
- Dielectrics
- Electronics
- Flat Panel Displays
- Industrial Ecology
- Magnetic Interfaces and Nanostructures
- Manufacturing Science and Technology
- Material Characterization
- MEMS
- Nanotubes: Science and Applications
- Organic Films and Devices
- Photonics
- Plasma Science and Technology
- Processing at the Nanoscale
- Semiconductors
- Surface Engineering
- Surface Science
- Thin Films
- Vacuum Technology

In addition, the week-long annual

50 Short Courses

- Applied Vacuum Technology
- Surface Analysis and
- Materials, Thin Films, and

150+ Exhibitors

- Vacuum and Deposition
- Analysis Systems
- Vacuum-Related

For more information on the AVS
at **www.vacuum.org**, or contact the
fax 212-248-0245

Advertisers Direct Response

Journal of Vacuum Science & Technology B

Microelectronics and Nanometer Structures, Processing, Measurement, and Phenomena

Listed below are the companies that have advertised in this issue. If you would like to know more about a product or service please complete the information below and fax this form to the appropriate company.

◊ JULY/AUGUST 2000 ◊

ADVERTISERS:

A9 Geib Refining Corp
Fax: (401) 732-2841

A9,11 Hiden Analytical, Inc.
Fax: (603) 924-5009

Cov 2 INFICON
Fax: (315) 437-3803

A4 International Radiation Detectors Inc.
Fax: (310) 534-3665

A13 LK Technologies
Fax: (812) 332-4493

A3 Micro Photonics Inc.
Fax: (610) 366-7105

A11 Nano-Master
Fax: (512) 385-4900

A9 Omicron Associates
Fax: (412) 831-9828

Cov 3 Pfieffer Vacuum
Fax: (603) 578-6650

Cov 4 Quad Group, Inc.
Fax: (509) 458-4555

A1 Skion Corp.
Fax: (201) 963-5449

A7 Stanford Research
Fax: (408) 744-9049

A15 Surface Science Spectra
Fax: (919) 361-2498

A11 Vat Inc.
Fax: (781) 935 3940

FROM:

Your Name

Title

Institution/Dept.

Address

City/State/Zip

Phone/Fax

1. Specialty:
- a. □ Applied Surface Science
- b. □ Electronic Mat'l. & Processing
- c. □ Nanotechnology
- d. □ Plasma Science & Technology
- e. □ Surface Science
- f. □ Thin Film
- g. □ Vacuum Metallurgy
- h. □ Vacuum Technology
- i. □ Other: ____________

2. Need for information:
j. □ Immediate k. □ Future

3. Purchasing Authority
l. □ Specialty m. □ Recommend

Effects of surface oxides on field emission from silicon

Jonathan Shaw[a)]
Naval Research Laboratory, Washington, DC 20375

(Received 17 March 2000; accepted 26 May 2000)

This report documents energy distribution measurements of field emission from single-tip Si field emitter arrays. The emission energy distributions are much broader than clean metal distributions, extending several volts below the Fermi level and often including multiple peak structure. The peak positions typically move to lower energy as the gate voltage is increased, however, the emission history as well as the emission current and/or gate voltage can change the energy as well as intensity of the energy distributions. Changes in the distribution including shifts to higher energy occur suddenly and spontaneously as well as slowly during emission. These results show that the emission comes from oxide and interface states, which refill at a finite rate, limiting the emission current. Changes in the local electric potential due to single charges becoming trapped in the oxide account for large and discrete changes in the emission distribution. [S0734-211X(00)07604-6]

I. INTRODUCTION

The emitting surfaces of field emitter arrays (FEAs) are typically not atomically clean during operation, either because of less than ideal vacuum conditions or because the surface layer cannot be removed without damaging the structures. In most cases the surface consists of a dielectric layer with thickness comparable to or greater than the tunneling barrier. The presence of an insulator with any significant thickness on the surface of a field emitter would be expected to drastically reduce the tunneling probability. Since emission does occur from air-exposed Si emitters, one must assume either that the oxide is removed, or that emission occurs from the oxidized layer itself. The oxide thickness and dielectric quality are very difficult to determine directly since the emission area is so small ($<100\ nm^2$). However, the energy distribution of the emitted electrons can provide some clues about the surface electronic properties and emission mechanism.

FEAs often exhibit significant shifts in the emitted current versus gate voltage, while the arrays are operated.[1,2] The current typically increases during the first minutes to hours after the gate voltage is first increased to a point where emission can be detected. The average emission current from large arrays then becomes relatively stable. However, the individual emitter currents continue to fluctuate. These results have been interpreted previously in terms of changes in the emitter work function caused by adsorption and desorption.[1,3]

According to standard theory, the energy distribution of the field-emitted electrons reflects the density of occupied states near the surface convolved with the tunneling transmission function.[4] If the tunneling transmission function changes as a result of an overall change in field or work function, only the intensity, but not the energy, of the distribution will be affected. Thus, any changes in the shape of the emission distribution reflect either changes in the distribution of occupied states, or a change in the tunneling probability that is specific to a portion of the distribution.

Previous studies of the emission energy distribution from Si FEAs[5] showed that multiple peaks occurred up to four or more volts below the Fermi level when the tips had become contaminated. Tips that had been cleaned showed emission from a single peak near E_F, but the multiple peak distribution soon returned as a result of emission. Increasing the gate voltage reduced the peak energies in linear proportion to the gate voltage. The peak intensities were also reduced as the peak energy decreased, and a new peak sometimes appeared closer to the Fermi level at the highest gate voltages. Similar results were obtained from molybdenum tip arrays.[6] These results were in marked contrast to the sharp peak just below E_F typically obtained from clean macroscopic specimens of W or Mo.[7,8] These results show that the electronic structure at the surface of these microfabricated emitters is much different than that of bulk Si or W. Although it is hardly surprising that the surface electronic structure is much different than the bulk, it is not clear what the properties of a very thin oxide will be (especially after the emitter has been operated), and what effect they will have on the field emission.

II. EXPERIMENT

The single-tip field emitter arrays analyzed were fabricated from 0.02 Ω cm n-type single-crystal silicon at the Microelectronics Center of North Carolina (MCNC). The fabrication process made use of oxidation sharpening as reported previously.[9] The gate aperture diameter was about 1.5 μm, the gate metal was 0.5-μm-thick Pt, and the tip height was about 1 μm. The tip apex radii of similarly prepared specimens were about 5 nm. Specimens were loaded into an ion-pumped ultrahigh vacuum (UHV) chamber without baking via load lock. The platform where the FEA die was placed could be heated. We were unable to measure the die temperature while the platform was heated; however, it appeared that the die was considerably cooler than the platform. The temperatures given are estimates based on the platform temperature. The chamber pressure was typically $1-2\times10^{-10}$ Torr during

a)Electronic mail: jon.shaw@nrl.navy.mil

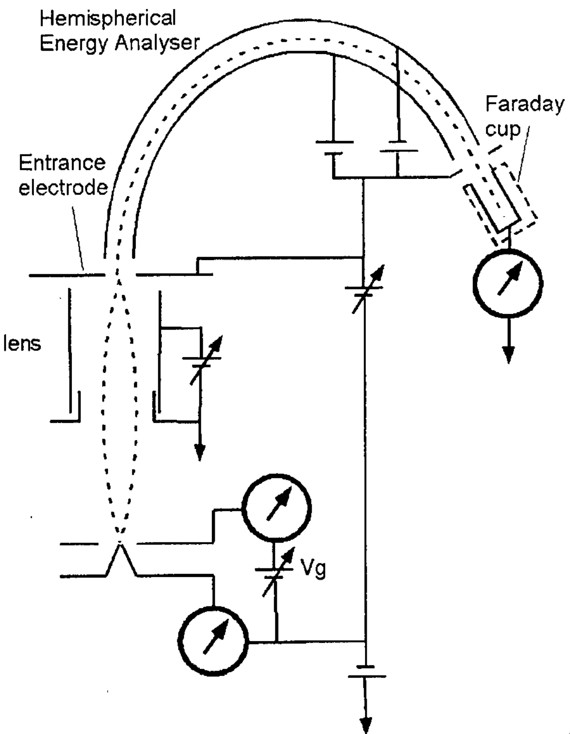

FIG. 1. Schematic diagram of the equipment used to measure the emitter and gate currents and energy distributions. The emitter contact was placed at negative potential with respect to the vacuum chamber. The chamber walls, including parts of the energy analyzer served as the electron collector.

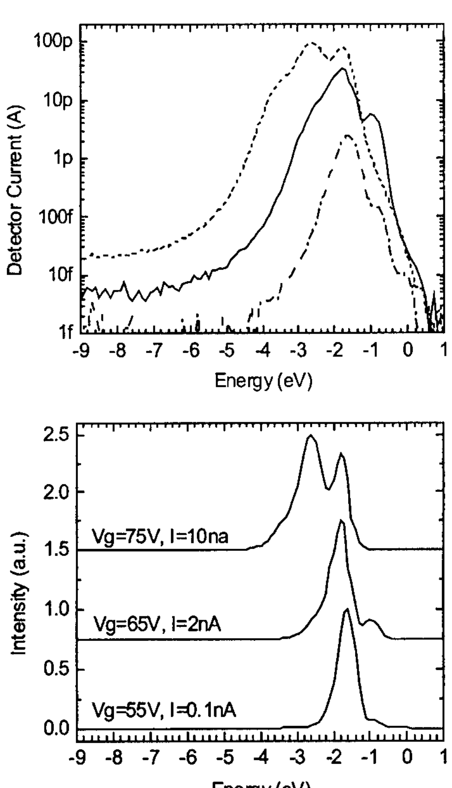

FIG. 2. Energy distributions measured from a silicon field emitter tip at gate voltages of 55, 65, and 75 V. The same three distributions are plotted on a semilog scale on the top and in normalized form using a linear scale on the bottom.

measurements. The die contained several individually gated "arrays" having only one tip and gate aperture. Wire probes mounted on manipulators were used to contact the substrate and one of the gates *in situ*. Current–voltage ($I-V$) measurements made between two substrate contacts verified that the contact potential and resistive loss was insignificant at currents well above the emission currents used. Measurements made on heavily doped and moderately doped specimens showed similar behaviors, again showing that any potential drop within the bulk or tip shank was not significant.

The spectra were made at a resolution full width at half maximum of ~0.025 eV using a VG CLAM 100 spherical sector analyzer operated with constant pass energy set at 5 eV. We verified that the analyzer resolution did not significantly broaden the spectra by comparing spectra measured using higher pass energies. Commercial instruments (Keithley models 237, 2001, and 6517) generated the gate and analyzer voltages and measured currents at the substrate, gate, and Faraday cup detector. The electrical connections are shown in Fig. 1. The acquisition time for a single spectrum was typically 1–2 min. The energy distributions are measured with respect to the vacuum level at the analyzer's entrance electrode. The Fermi level of the system is assumed to be 4.6±0.1 eV below the vacuum level at the entrance electrode, based on the typical work function of a gold plated electrode and verified by field emission energy distribution measurements of metallic surfaces. The electron energy is plotted with respect to the system Fermi energy.

III. RESULTS

Three energy distributions measured from a single-tip Si FEA are plotted in Fig. 2. Energy distributions measured at gate voltages of 55, 65, and 75 V are plotted on both linear and logarithmic scales. This tip was measured in the condition it was received, i.e., it had not been baked or processed. The emitter had been operated at $V_g = 80$ V for 25 min before measuring the first data plotted (at $V_g = 75$ V). All three distributions have threshold energies at E_F, showing that any potential drop in the Si or contacts was negligible. The distribution measured at 55 V shows two additional emission thresholds about -0.4 and -1.2 eV. The distribution measured at 65 V has emission thresholds at nearly the same energies, plus a shoulder below the largest peak suggesting a threshold at approximately -2 eV. The magnitude of the peak centered at about -0.8 eV increased relative to the largest peak centered at -1.8 eV. In the distribution measured at 75 V, an emission threshold near E_F is still evident, but the rest of the distribution shifted about 0.9 eV to lower energy. The peak that had been at -0.8 eV in the 65 V distribution is centered at -1.7 eV in the 75 V distribution, and its magnitude increased further relative to the largest peak such that the two peaks now have similar magnitude.

The presence and charging of oxide states can account for

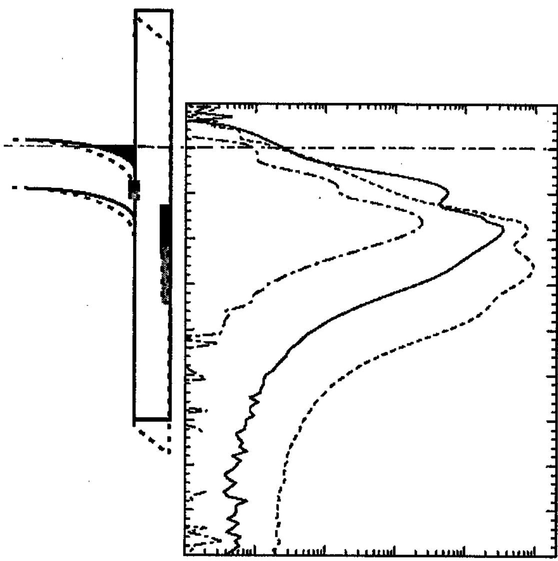

FIG. 3. Same energy distributions shown in Fig. 2 are compared with the potentials of the silicon conduction and valence bands near the emitter surface, the surface oxide, and oxide states. The lines used to draw the silicon and oxide bands are solid in the case when the oxide surface is not charged (i.e., during the spectrum measured with the gate at 55 V). The dotted lines represent the silicon and oxide bands when the surface is charged positive (i.e., during the spectrum measured with the gate at 75 V).

the multiple peaks in the emission energy distribution and the shift in energy. Figure 3 shows a simplified band diagram of the silicon substrate and oxide, including sets of oxide states placed at energies corresponding to the measured emission distributions of Fig. 2. The oxide conduction and valence bands are drawn assuming the conduction band offset at the $Si-SiO_2$ interface is 3 eV and the band gap of SiO_2 is 9 eV. The silicon may be accumulated (E_F up to several tenths of a volt above the conduction band minimum) or not, depending on the charge density in the interface and oxide as well as the gate voltage. If the oxide lacked any charge, the electric field in the oxide would be determined by positive charge at the gate and negative charge in the silicon conduction band and in Si/SiO_2 interface states. Changes in the interface charge will shift the entire oxide potential, but will not change the oxide field. Charge trapped in oxide states can change the oxide field and the potential at neutral oxide states. For simplicity, a uniform charge only at the oxide surface is assumed in Fig. 3. Emission of electrons coming from three types of initial states can be identified according to how their energy might be changed due to changes in trapped charge or gate voltage. If the surface is accumulated, emission can come from conduction band electrons between the Fermi level and the conduction band minimum. The interface potential will not shift by more than 0.5 eV as the surface accumulation changes, assuming the surface does not deplete. Emission from the conduction band will shift less than that since it will be centered near the Fermi level. Emission from interface states will shift strictly with the interface potential, i.e., by less than 0.5 eV. States at the oxide surface will shift by the sum of the interface potential and the potential supported by the oxide. The potential across the oxide will increase with the gate voltage, but can also be either increased or reduced by charge in the oxide. Localized charge in the oxide may create local potential changes.

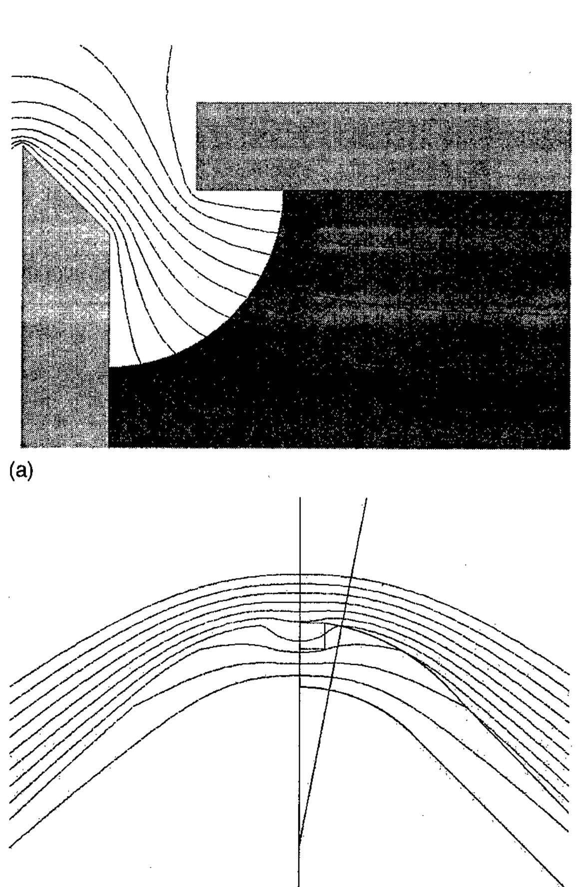

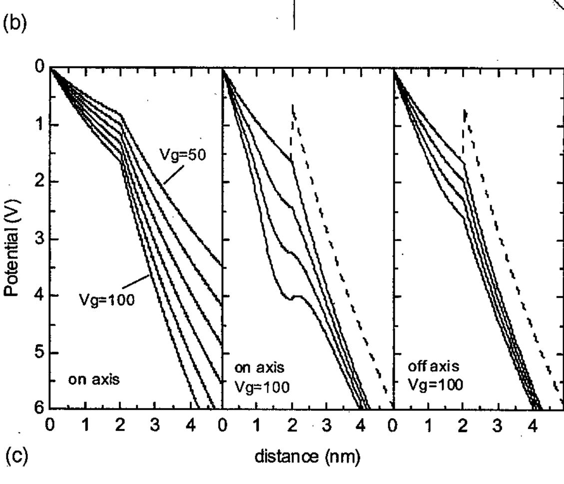

FIG. 4. (a) Model field emitter tip and gate, drawn in cross section along the radius from the axis of rotational symmetry. (b) The apex region of the same field emitter tip, showing the hemispherical portion of the conductor tip with 5 nm radius, covered with a dielectric coating 2 nm thick. The potentials plotted in part (c) calculated along the vertical line on the axis of symmetry and the line drawn 22° off-axis.

All three of the energy distributions show emission thresholds at or above the Fermi level and do not change with the gate voltage, thus the emission at these energies appears to come from initial states in the conduction band. In contrast, the emission structure at lower energies does shift

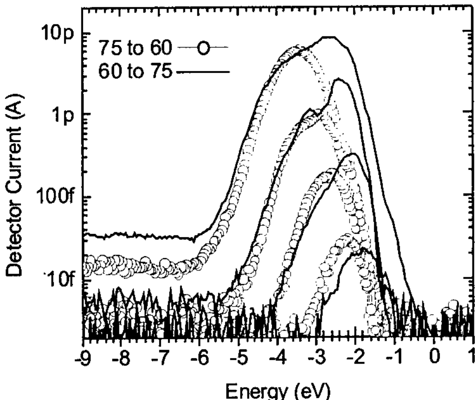

FIG. 5. Energy distributions measured from a silicon field emitter tip at gate voltages of 60, 65, 70, and 75 V. The distributions plotted in open circles were measured after the emitter had been operated at high voltage and as the gate voltage was reduced. The distributions plotted in solid lines were measured after the emitter had been operated at low voltage and as the voltage was increased.

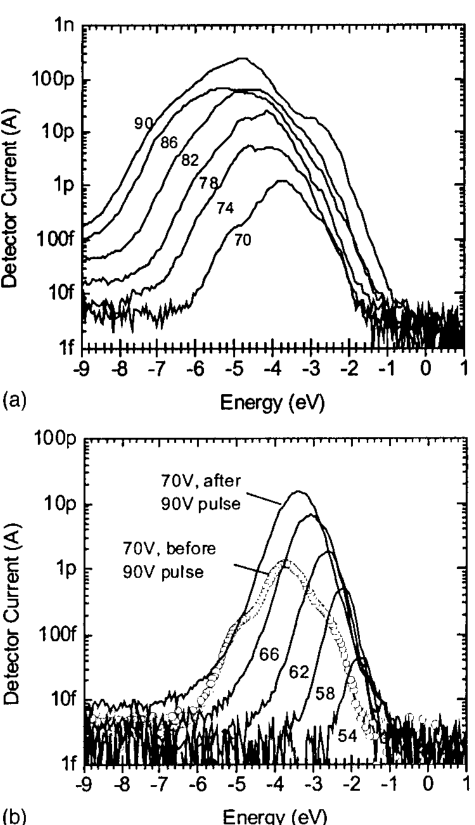

FIG. 6. Energy distributions measured as the gate voltage was reduced from 90 to 70 V. The final 70 V distribution is replotted in part (b), in open circles. The remaining distributions plotted in solid lines in part (b) were measured after the gate had been pulsed to 90 V.

with gate voltage, by as much as 0.9 eV. Such a large shift cannot be supported in the Si because the conduction band density of states becomes too high. Thus, it appears that the lower energy emission comes from oxide states. Note that although this emission occurs at low energy relative to the Fermi level, the potential barrier to tunneling from oxide states may be less than the barrier seen by electrons in the silicon conduction band because the conduction band electrons must tunnel though the oxide.

To help quantify the effect of the electric fields expected near a field emitter tip on the oxide potential, we modeled the potentials in an emitter structure with commercial two-dimensional electrostatic software.[10] Drawings of the model are shown in Figs. 4(a) and 4(b). The model FEA cell had gate radius 1 μm, gate voltage 50–100 V, and a conical 45° tip terminated in a spherical section. The radius of the conductive part of the tip apex is 5 nm. A 2-nm-thick dielectric coating with relative dielectric constant 3.9 increases the radius to 7 nm. A discrete number (0–3) of positive charges are assumed to be uniformly distributed in a small volume (0.8 nm radius cylinder 0.8 nm high) on the symmetry axis at the apex. (The volume assumed to contain the charge is merely a guess, there does not appear to be any good theory to calculate the effective volume of a charge trapped in a dielectric.[11] Of course, the volume chosen has a significant effect on the local potential.) Figure 4(b) shows the potential contours near the apex calculated assuming a single positive charge. A vertical line on the axis of rotation and a line 30° off-axis are shown in Fig. 4(b). The potentials along these lines, starting from the conductor surface and extending through the dielectric into vacuum, are drawn in Fig. 4(c). The curves on the left-side plot were calculated assuming no charge in the oxide and with gate potentials increasing from 50 to 100 V. In this case the potential at the oxide surface changes by about 0.8 eV by increasing the gate voltage from 50 to 100 V, or about 0.16 V for a change of 10 V. This value is in agreement with the shift observed between the distributions of Fig. 2, measured at 55 and 65 V. The center plot shows the potentials along the vertical axis where the gate potential is 100 V and the volume contains 0, 1, 2, and 3 positive charges. The vacuum level for the zero charge case (assuming the electron affinity of the oxide is +1 eV and neglecting image charge effects) is indicated by the dotted line. These plots show that a single charge can change the surface potential very significantly, in this case by 0.8 eV per charge. This shift is very close to the shift in the energy distributions at $V_g = 65$ vs 75 V of Fig. 2. Thus, it appears that the main emission peaks in Fig. 2 come from oxide states, and that the shift must be caused by oxide charge rather than the increased gate field. The *discrete* shift between the 65 and 75 V distributions support the idea that a single oxide charge is responsible. The curves on the right-side plot show the oxide potentials along the off-axis line, adjacent to the volume containing charge. These plots show that the potential of the dielectric changes rapidly relative to the dimensions of the tip apex.

Figure 5 shows two sets of four energy distributions measured sequentially at $V_g = 60$, 65, 70, and 75 V. In one case (open circles) the gate voltage had been held at 75 V for 2 h prior to making measurements, and measurements were made by reducing the gate voltage. In the other case (solid lines) the gate voltage was held at 55 V for half an hour prior to making measurements, and the gate voltage was increased after each measurement.

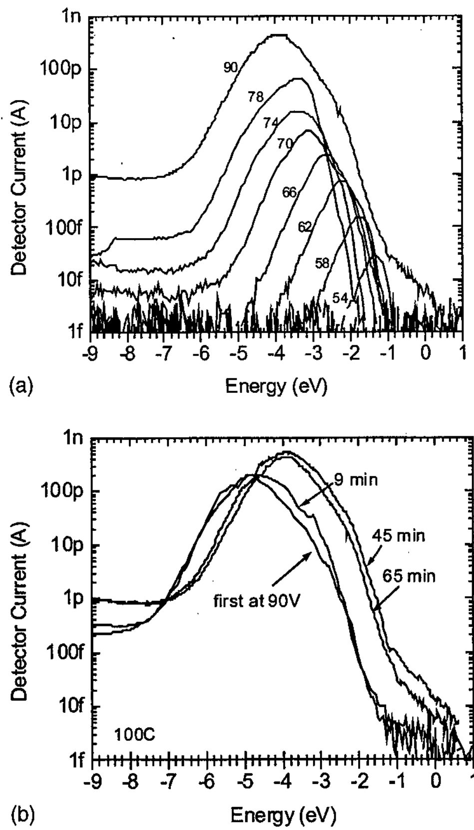

FIG. 7. (a) Energy distributions measured as the gate voltage was increased from 54 to 78 V. The distributions measured above 78 V became very noisy. The gate voltage was kept at 90 V for over an hour while distributions were measured periodically. Four of these distributions are plotted in (b) after the times indicated. The distribution measured after waiting 65 min is plotted in (a) for comparison.

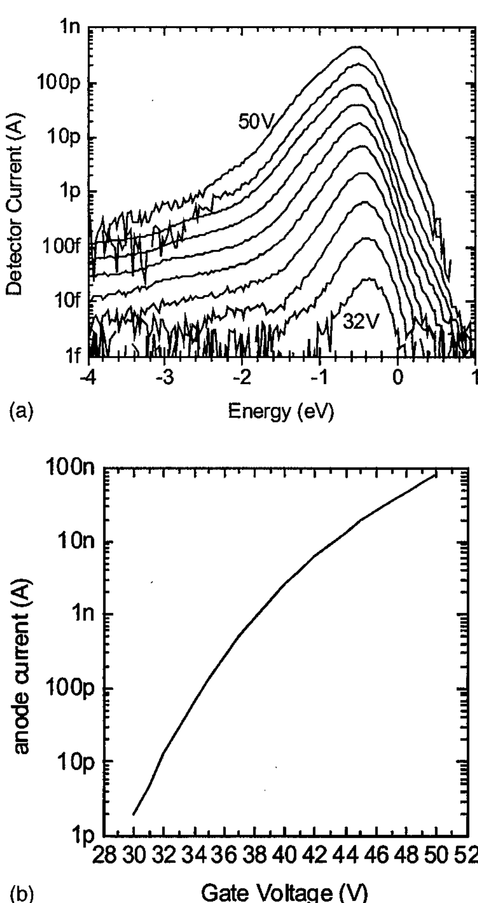

FIG. 8. Measurements made after the tip had been emitting for many hours while the die was heated to approximately 300 °C. (a) Energy distributions; (b) $I-V$ characteristic.

These distributions (and each of the remaining example distributions in Figs. 6–8) were produced by a different tip than those of Fig. 2, but on the same die. The die had been outgassed prior to making these measurements by heating to 300 °C in UHV for 3 h (before contacting the gate), then cooling.

The distributions measured after holding the gate voltage low (solid lines) appear to be composed of two broad and overlapping peaks. However, the higher energy peak is largely suppressed in the distributions measured after holding the gate voltage high (circles). The last distribution measured as the gate voltage was increased shows evidence of a third emission band at higher energy. Thus, the emission appears to come from three discrete sets of states, of which the states at highest energy are the least persistent. This behavior would not occur from a conducting surface, since states closest to the vacuum level have the highest probability of emission. The gate voltage does not appear to cause any energy shift in these distributions. The lack of any shift with gate voltage indicates that all the emission comes from states in good electric contact with the bulk, yet the low emission energy and lack of any emission near E_F indicates that the initial state energies are very different from the bulk band structure. Within the context of a surface oxide model (Fig. 3), this behavior can be explained as emission from interface states through a potential barrier which is modified by charge in the oxide. When the gate has been at low voltage for some time, the oxide becomes positively charged, reducing the potential barrier to tunneling. When the emission current is held high, the oxide net charge is made more negative, increasing the tunnel barrier. The three-dimensional character of the emitting surface must be included in the model in order to explain why the lower energy emission persists in both cases. The lower energy emission may be located near a portion of the emitting surface far from the oxide trap being charged, whereas the higher energy emission band originated from a state near the trap site. Thus, the change in oxide potential is very local to the trap site [as suggested in Fig. 4(b)] and adjacent emission areas are not affected.

The lack of any emission at energies near the Fermi level indicates that no emission is coming from the silicon conduction band. This might be due to an excessively thick oxide, or perhaps because the silicon surface is not accumulated. The lack of emission energy shift with gate voltage indicates that the emission is coming from interface states yet there is no emission from bulk states. Thus, if the oxide is thick enough to prevent emission from bulk states, the "interface" must be taken to include states in the oxide which are in good electrical communication with the bulk

silicon, but significantly closer to the oxide surface than the electrons in the bulk silicon band structure.

Alternatively, the charge in interface states may be sufficiently dense to cause Fermi level pinning or upward band bending in the silicon. If the silicon bands were bent up as in a Schottky diode, free conduction band electrons would be removed from the surface. In that case emission from states above the valence band would be suppressed. In fact, most of the high-energy emission thresholds of the distributions in Fig. 5 are about 1.1–1.5 eV below E_F, in reasonable agreement with the valence band energy. The distribution measured just after setting $V_g = 75$ V shows some emission from states closer to E_F, suggesting that the band bending was reduced enough to populate some states above the valence-band maximum (VBM) in that case. It is qualitatively reasonable that the Fermi level should be moved closer to the conduction band in that case, since the gate voltage is highest and the oxide charge is relatively positive. The charge density needed to screen electric fields typical of field emission, i.e., on the order of 4×10^7 V/cm, and the interface charge density needed to produce some upward band bending, are both about $10^{13}/\text{cm}^2$. A single charge assumed to occupy a space of about 3 nm^2 also creates a local charge density on the order of $10^{13}\,\text{cm}^2$. Thus, the oxide charge in addition to the gate field can account for a shift in the Fermi level position at the interface.

Figure 6 shows another example of an energy distribution change caused by operating the emitter. Figure 6(a) shows some of the distributions recorded while the gate voltage was reduced from 90 to 70 V two volts at a time. As in Fig. 5, all of the distrubutions shown in Fig. 6 start at energies below the VBM, again indicating Fermi level pinning due to interface charge. The emission threshold shifted to lower energy in two discrete steps as the gate voltage was reduced. The discrete increases in threshold energy with increasing gate voltage is consistent with discrete movements of the Fermi level at the oxide interface to energies closer to the conduction band, populating higher energy interface states. Most of these distributions in Fig. 6(a) have shoulders suggestive of emission from separate bands of initial states. The final 70 V distribution is replotted in Fig. 6(b), in open circles. After the measurements shown in Fig. 6(a) were finished, the gate voltage was set to 90 V for 1 s, then returned to 70 V. The distributions measured after the 90 V pulse are shown in Fig. 6(b) as solid lines. In these distributions, the emission threshold shifted back up to the energy previously observed at gate voltages of 86 and 82 V, and remained steady during the subsequent measurements at gate voltages less than 70 V. The change induced by the 90 V pulse can be explained as the effect of a change in the Fermi level position at the interface, caused by the creation of a new interface state during the high current pulse, or perhaps simply by population of an electron trap.

Figure 7 illustrates a case where the energy distribution shifted with gate voltage and in time. The distributions in Fig. 7(a) were measured as the gate voltage was increased from 54 to 90 V. The emission threshold was always well below E_F and shifted smoothly to lower energies as the gate voltage was increased from 54 to 78 V. The smooth shift suggests that the initial states were located in the oxide and moved to lower energy due to increasing field penetration. After the gate voltage was increased above 78 V, the energy distribution became unstable. Upon reaching 90 V, the gate voltage was held constant for over an hour. Some of the energy distributions recorded during that time are shown in Fig. 7(b). As shown, the entire distribution shifted about 1 eV toward *higher* energy and increased in magnitude during that time. The shifted distribution is also plotted in Fig. 7(a) for comparison. Since the gate voltage was held constant, and since the energy shift was to higher energy, it is clear that a change in the oxide charge was responsible, as opposed to field penetration. The shift was approximately 0.8 eV, in agreement with the shift expected from a single charge based on the model of Fig. 4. Even after the shift, the threshold energy remained below the VBM, suggesting Fermi level pinning by surface states as in the previous two examples.

A final set of energy distributions is shown in Fig. 8(a). The measurements correspond to gate voltages from 32 to 50 V in 2 V steps. The distributions were unchanged by the order in which they were measured. The anode current obtained at the same voltages is plotted in Fig. 8(b). These measurements were made while the chip was heated to approximately 300 °C and after emitting for many hours. In this condition there is little shift in the energy distributions. The peak position shifts by 0.2 eV as the emission current changes from 2 pA to 100 nA. The threshold energy is consistent with accumulation or a flatband condition at the interface. After the chip was cooled and the emitter had been off for several hours, the $I-V$ curve and energy distributions degraded dramatically, requiring over 100 V to produce significant emission. The reduced performance may be the result of oxidation of the emitter surface.

IV. DISCUSSION

Field emission through an oxidized silicon surface is similar to high field leakage of metal–oxide–semiconductor (MOS) devices in that the current passing through both devices increases spontaneously over time. Although field emission from a curved surface through an oxide into vacuum is not completely analogous to transport between flat surfaces through oxide, the wealth of data on MOS devices makes the comparison worthwhile.

In the case of MOS devices, neutral oxide states increase the leakage current, presumably by allowing stepwise tunneling.[12] Since oxide states increase the current, the fractional increase in current is a measure of the state density in the oxide. Bias voltages over 5 V are typically required to produce transport through device oxides (>5 nm thick). In this case the fractional increase in current is linearly proportional to the total charge passed through the oxide over several orders of magnitude.[12] Because the leakage current increases more quickly with total charge when higher bias voltages are applied, it is concluded that trap states are cre-

ated by energy deposited in the oxide by hot electrons and by other energy loss processes.[12] The rate of increase in the leakage current drops nearly to zero as the bias voltage drops below 5 V. The 5 V minimum is explained as the sum of the potential required to move the oxide conduction band down to the silicon conduction band (the Si/SiO_2 conduction band offset is 3 eV), plus additional potential needed to create hot electrons with energies at least 2 eV. Other energy loss processes such as recombination of (trapped) electron hole pairs producing as little as 1.5 eV[13] have been suggested. Thus, the release of some minimum energy (about 2 eV) is required to create oxide states. Presumably, the energy is required to break bonds in the oxide, and the broken bonds form oxide states. The atomic origin of the states is not clear, but exposure to atomic hydrogen increases the leakage current,[14] and the state creation process is suppressed at low temperature.

In thin MOS oxides (<5 nm), significant leakage currents can be obtained at bias voltage below 5 V and even less than 3 V,[15] too low to inject electrons into the oxide conduction band and less than typically required to create oxide states. However, the oxide current still increases with time (but not correlated to total charge), indicating that states are still being created.[15] As in the case of thicker oxides, low temperatures (<150 K) suppress the current increase through thin oxide.[15]

The emission current obtained from a silicon field emitter tip often increases in time at constant gate voltage, in a manner similar to the increase in leakage current through oxide films. The fractional field emission increase typically occurs very rapidly when the emission current is barely detectable, e.g., in the picoampere range or below. The field emission current typically increases several orders of magnitude within a few seconds to several minutes. The current eventually saturates, similar to the MOS devices.

In the case of MOS devices, the density of oxide states typically saturates at levels near $10^{13}\,cm^{-2}$. Assuming the density of oxide states at the field emitter apex is $10^{13}\,cm^2$, and assuming the emission comes from an area on the order of $10^{-12}\,cm^2$, the number of oxide states near the apex of a field emitter is about 10. If the actual number of states at a given tip were only 2 or 3, discrete emission bands such as in Fig. 2, and observable effects due a change in the charge of a single oxide state, such as shown in Figs. 5, 6, and 7, are expected.

All of the energy distributions shown in Figs. 2, 5, 6, and 7 show measurable currents emitted more than 2 eV below E_F, in some cases more than 8 eV below E_F. This energy is available to create oxide states. Thus by analogy to MOS devices, it is reasonable to assume that oxide states are created by the energy dissipated during field emission. Energy distributions measured during the initial moments after turn-on often show emission at energies further below E_F, in accord with the notion that the oxide contains a relatively low density of states at that point, and that new states are being created with relatively high efficiency.

In most cases the current emitted near the high energy threshold does not increase with gate voltage. Instead the current density from a given energy range saturates and the additional current is emitted at lower energies. This behavior is most obvious in cases where the oxide is not charging, such as the open circles in Fig. 5, and the lines in Fig. 6(b). The current saturation is consistent with emission from a limited number of states, distributed in energy, which require a finite time to refill. That is, the current density is limited by the rate the oxide states can refill. This is fundamentally different than field emission from a metal surface, where the emission current is given by the product of the Fermi function and the tunneling probability, i.e., the current emitted at a given energy increases indefinitely with the tunneling probability. Thus, the energy distributions shown in Figs. 5 and 6(b) show that direct (one step) tunneling from the bulk silicon into vacuum (as assumed in deriving the Fowler–Nordheim equation) does *not* occur at these oxidized surfaces. Instead, the emission occurs from intermediate states at energies below E_F, which require time to refill. The energy dissipated when the states are refilled is available to break oxide bonds.

The field emission energy distributions in Fig. 8 are much different than in the previous figures, showing little shift toward lower energies with current. This behavior is closer to what would be expected if tunneling occurred directly from bulk states, i.e., the emission current is not limited by transport into intermediate oxide states. Since this behavior occurred while the field emitter was hot, it may be that the higher temperature reduced the time required to refill the oxide states. However, heating other field emitters to the same temperature did not reproduce this type of emission. Heating in UHV for many hours while the tip is emitting appears to be required. The combination of heat and emission over a long period may have simply thinned the oxide to the point where it no longer creates a distinct dielectric layer. Similarly, the density of states in the oxide may have been increased to a point where essentially metallic conduction could take place. The evidence provided by measurements on MOS devices suggests that this is the case. The production of oxide states in MOS devices is thermally activated and stimulated by the presence of hydrogen (the partial pressure of hydrogen and other residual gases in the chamber are slightly elevated while the specimen is heated). In spite of this more metallic behavior, the distributions are still much broader than clean metal tips.

The energy distributions of in Fig. 8 show significant emission at energies up to 1 eV above E_F. This emission is greater than expected from instrumental broadening. 1 eV also appears to be too great an energy to be induced by thermal excitation. One possible explanation is that the emission comes from oxide states above E_F, filled by a kind of Auger process. That is, when electrons in states below E_F are emitted, the energy released when those states are refilled can be transferred to other electrons, allowing them to populate the higher energy oxide states.

Although it may appear to be desirable to achieve the surface condition of Fig. 8, the more metallic surface condi-

tion appears to have contributed to greater oxidation than originally present after the emitter was turned off and allowed to cool. In contrast, emission characteristics such as shown in Fig. 2 could be reproduced after storing the emitter in UHV or in air. Thus, the native oxide appears to be useful and desirable in that it forms a stable surface.

V. CONCLUSIONS

The energy distribution measurements of the field emission from single silicon field emitters presented show that the most of the emission comes from oxide or interface states, rather than directly from the silicon conduction or valence bands. The current emitted from these states is limited by the time required to refill them in addition to the tunneling probability. The energy released when the interface and oxide states are refilled is sufficient to create oxide states, if the exposed oxides behave similarly to MOS structures. The emission sometimes appears in discrete energy bands, suggesting that only a few discrete oxide states are involved in emission. On occasion the energy distributions shift either up or down, indicating that a change in the oxide potential occurred due to a change in the oxide charge. Both positive and negative energy shifts occur. In some cases only a portion of the energy distribution is enhanced, showing that the emission is affected very locally by oxide charge. Under some conditions, particularly when the emitter is hot, the energy distribution indicates a more metallic surface. However, this condition is not stable and the emission is severely reduced after storing the emitter in UHV at room temperature.

ACKNOWLEDGMENTS

Thanks to NRL, ONR, and DARPA-ETO for providing funding. Thanks to Dorota Temple and MCNC for providing the field emitter specimens. Special thanks go to the late Henry Gray for encouragement and enthusiasm.

[1]P. R. Schwoebel and I. Brodie, J. Vac. Sci. Technol. B **13**, 1391 (1995).
[2]J. L. Shaw and H. F. Gray, International Vacuum Microelectronics Conference Technical Digest, 17–21 August 1997, Kyongju, Korea, p. 743.
[3]D. Temple, W. D. Palmer, L. N. Yadon, J. E. Mancusi, D. Vellenga, and G. E. McGuire, J. Vac. Sci. Technol. A **16**, 1980 (1998).
[4]A. Modinos, *Field, Thermionic, and Secondary Electron Emission Spectroscopy* (Plenum, New York, 1984), Chap. 1.
[5]J. Miller and R. Johnston, J. Phys.: Condens. Matter **3**, S231 (1992).
[6]S. T. Purcell, V. T. Binh, and R. Baptist, J. Vac. Sci. Technol. B **15**, 1666 (1997).
[7]J. W. Gadzuk and E. W. Plummer, Rev. Mod. Phys. **45**, 487 (1973).
[8]N. Ernst, J. Unger, H. W. Fink, M. Grunze, H. U. Muller, B. Volkl, M. Hofmann, and C. Woll, Phys. Rev. Lett. **70**, 2503 (1993).
[9]D. Temple, C. A. Ball, W. D. Palmer, L. N. Yadon, D. Vellenga, J. Mancusi, G. E. McGuire, and H. F. Gray, J. Vac. Sci. Technol. B **13**, 150 (1995).
[10]We solved a rotationally symmetric electrostatic model using "Electro" boundary element software: Integrated Engineering Software, 300 Cree Cresent, Winnipeg, Manitoba, Canada R3J 3W9.
[11]R. Resta and S. Sorella, Phys. Rev. Lett. **82**, 370 (1999).
[12]D. J. DiMaria, Solid-State Electron. **41**, 957 (1997); D. J. DiMaria, E. Cartier, and D. Arnold, J. Appl. Phys. **73**, 3367 (1993).
[13]S.-I. Takagi, N. Yasuda, and A. Toriumi, IEEE Trans. Electron Devices **46**, 348 (1999).
[14]D. J. DiMaria and E. Cartier, J. Appl. Phys. **78**, 3883 (1995).
[15]K. R. Farmer, C. P. Debauche, A. R. Giordano, P. Lundgren, M. O. Anderson, and D. A. Buchanan, Appl. Surf. Sci. **104/105**, 369 (1996); K. R. Farmer, M. O. Andersson, and O. Engstrom, Appl. Phys. Lett. **60**, 730 (1992).

Studies on the interaction between thin film materials and Mo field emitter arrays

Babu R. Chalamala[a] and Robert H. Reuss[b]
Flat Panel Display Division, Motorola Incorporated, 7700 South River Parkway, Tempe, Arizona 85284

(Received 17 February 2000; accepted 7 April 2000)

A simple method for the evaluation of materials suitable for the fabrication of field emission vacuum microelectronic devices is presented. Since there can be a wide range of electron and ion interactions with the device, it is important to be able to quickly assess if a material may have a particular adverse effect on emission performance under operational conditions. The technique is based on the sensitivity of a large field emitter array to the outgassing or desorption of gas species from thin films under electron beam excitation. We found that Mo field emitter arrays degraded rapidly with stainless steel anodes coated with various oxide materials. The extent of degradation was found to be the most rapid with SiO_2, Si_3N_4, and MoO_3 thin films. Stainless steel anodes with Mo and Nb thin films show a faster degradation rate than stainless steel anodes, most likely because of native oxides grown during processing and handling. The emission behavior in the presence of Ir, Pd, Al, Zn, and Ti metal films and barrier materials like C and TaN is similar to stainless steel reference data. We find that once the oxide films are covered with barrier layers like C and TaN, emission decay rates approach the values obtained with stainless steel reference anodes. The observed emission current degradation is consistent with a model based on the liberation of oxygen from the surface of electron beam bombarded materials. Using controlled oxygen exposure experiments, we have determined the equivalent local oxygen pressures in the presence of various thin films. We found that with thin films of Nb, ZrO_2, Ta_2O_5, MgO, Nb_2O_5, and Al_2O_3, the emission degradation is akin to having a local O_2 partial pressure in the $1\times10^{-7}-1\times10^{-6}$ Torr range and with Mo, MoO_3, Si_3N_4, and SiO_2, this is equivalent to having local O_2 pressures of 1×10^{-5} Torr. © *2000 American Vacuum Society.* [S0734-211X(00)01204-X]

I. INTRODUCTION

Field emission vacuum microelectronic devices are based on the electron emission by tunneling under extremely high electric field across micron and submicron vacuum gaps. Examples of functional devices based on this quantum mechanical behavior include Spindt-tip field emitter arrays and nanogap electron sources.[1,2] An important application of field emitter arrays is as matrix addressable electron sources in field emission flat panel displays. Field emission vacuum microelectronic devices also find applications in directly modulated microwave tubes and multicolumn electron beam lithography columns.[3]

Field emission displays are an area with immense commercial promise as high brightness light weight flat panel displays. Field emission displays are similar to cathode ray tubes in that light is generated by the electron beam excitation of inorganic phosphor particles. In these devices, even though the electron beam is directed toward the phosphor screen, a small percentage of electrons does bombard other parts of the displays including dielectric materials on the anode surface, dielectrics, and other electron beam sensitive materials on the field emitter array, ceramic spacers which are used as mechanical supports between the field emitter array and the phosphor screen, and vacuum gettering materials used for maintaining the desired vacuum level in the tube. In the case of phosphors, electron beam bombardment is done by design, but electron impact on other parts of the displays occurs inadvertently.

It is evident from published literature that field emitter arrays made from metals like Mo and Nb are prone to oxidation in the presence of oxygenic gases like O_2, CO_2, and H_2O.[4,5] This has been found to be true for silicon field emitter arrays also.[6] Electron bombardment of various materials has been shown to result in the desorption of gases from their surfaces.[7] Outgassing of gases from thin film surfaces under electron bombardment can result from many different processes. These may include thermal effects causing trapped or adsorbed gases to be liberated, chemical decomposition of the thin films (in the case of compound thin film materials), and the electron stimulated surface reactions. However, very little information has been published as to whether these processes actually impact field emission display (FED) performance under operational conditions.

There is ample evidence in the published literature pointing to processes leading to compositional and morphological changes on surfaces under electron bombardment.[8,9] Field emission displays are typically fabricated on glass substrates. Electron beam bombardment of glass results in the release of oxygen from the surface. Irradiation of silicate glass surfaces has been found to result in surface layer leaching as a result of thermal diffusion and desorption processes under limited component inflow from the bulk glass.[10] Degradation of ZnS phosphors is caused by the displacement of S by O in ZnS,

[a]Electronic mail: babu.chalamala@motorola.com
[b]Electronic mail: bob.reuss@motorola.com

leading to loss of luminescence and a color shift.[11] Electron beam induced breakdown of silicon oxide is well known.[12] Electron beam bombardment of SiO_2 leads to the breakup of the Si–O bond, leading to the spontaneous release of two O atoms. Another important electron beam induced process is the electron stimulated desorption of adsorbates from surfaces. In all these processes, the net result is the release of gases, thus leading to an increase in the local pressure inside FED vacuum packages.

II. EXPERIMENTAL CONCEPT

To minimize the potential for degradation of materials under electron beam bombardment and to limit the resulting increase in package pressure, a simple and reliable means to identify thin film materials that have either minimal impact on device performance or act as coatings that provide maximum protection when applied as barrier-type layers is needed. Ideally, an electron beam source capable of producing electrons with the desired energy and current density and coupled to a gas analysis system should yield the desired information. However, experience has shown that such methods do not provide the desired results because the amount of gas liberated is generally too small to detect. A sensitive means by which to detect the impact of outgassing from materials on the emission characteristics of a field emitter array is needed.

Field emitter arrays (FEAs) that are used in large area field emission displays contain millions of individual emitter cones. Such a large array can be used as a high sensitivity detector to determine the effects of desorption from various thin films. Field emission current changes provide the sensitivity by which to evaluate the differences in materials subjected to electron bombardment. In this case, the field emitter array is used as both the electron source and gas detector. The material under test is coated onto an "inert" anode (stainless steel plate, 1 mm thick) support. The thickness of the film is such (~200 Å) that charge can bleed off vertically to the stainless steel anode support. A standard vacuum chamber field emitter array test procedure at a base pressure of $\sim 10^{-9}$ Torr is then initiated with the thin film material under test functioning as the anode. Rate of emission current degradation is then determined and rates for various materials can be measured and compared. Selection of optimum materials can be made and performance projections can be made by comparison to a stable baseline from an inert anode. Anode voltage and the anode–cathode spacing can also be varied to evaluate their impact on the gas liberated.

Since a FEA is used as the analytical probe, a direct measurement of FED performance of the effect of outgassing from a given material is possible. The method provides an extremely sensitive measure of outgassing because of the well documented sensitivity of emission current to contamination sources. Field emitter tips are extremely sensitive to surface adsorbates or surface chemical changes. Measurement techniques based on gravimetric or spectroscopy detection of liberated gases induced by electron bombardment suffer from sensitivity limitations. Use of a FEA as a high sensitivity probe also directly indicates the effect of the electron beam impact on thin films on the field emission characteristics of the array. Since the method is simple and utilizes test equipment similar to that of a regular device test, this method is of greater significance to FED operation than alternative techniques.

III. EXPERIMENTAL APPARATUS

Experiments were performed in an (UHV) ultrahigh vacuum chamber with a base pressure of 2×10^{-9} Torr during device operation. The device is operated in a pulsed mode with a pulse width of 100 μs and a periodicity of 16.6 ms. For all the measurements reported here, the amplitude of the gate pulse is 80 V and the anode voltage is 300 V. Anode current measurements are done by determining the voltage drop across a 100 Ω resistor using a high voltage differential probe. Test and data acquisition electronics are controlled by a personal computer using LabView. The spacing between the anode and FEA is 1 mm. Prior to evaluating device performance with the thin film coated anodes, each FEA was operated for a period of 80–100 h with the stainless steel reference anodes to obtain baseline emission current stability. Once baseline data are obtained with stainless steel reference anodes, the reference anodes are replaced with the thin film coated anode plates. The vacuum system is thoroughly baked again before emission characterization with the thin films. For each thin film under study, a new Mo field emitter array is used.

Multiple devices are run to determine characteristics of the emitter array interactions with various thin film anodes as a function of time. Experimental conditions of interest include gate voltage, emission current, pulse width, pulse repetition rate, anode voltage, and baseline vacuum pressure. The data acquisition software was developed using LabView. Virtual instruments are built for each test module and linked together to perform the desired test procedure. The basic test sequence is as follows. Devices are operated in a pulsed mode at a fixed duty cycle and gate voltage. The data acquisition function monitors gate voltage, anode voltage, and anode current for all the devices under test. Triggering and data acquisition are done sequentially. The anode potential is constant at 300 V. A gate pulse is generated for each device and the corresponding anode current is recorded. Individual devices are pulsed in this sequence. When one device is triggered on, the remaining devices are turned off. This sequence is continued for each device. Once the data logging parameters are set up, data logging is done automatically at the desired intervals.

The apparatus is also configured with a high resolution quadrupole mass spectrometer (Stanford Research Systems model: RGA300) with a 10^{-13} Torr partial pressure detection capability for monitoring changes in the background partial pressures during device operation. It is also used as a process monitor to determine the quality of gas species introduced into the system. Introduction and maintenance of gases into the system allow determination of the gases and

their effective partial pressures which give degradation characteristics similar to those observed with various thin films.

IV. RESULTS AND DISCUSSION

Experiments were performed with three sets of thin film materials. These can be broadly classified as metal films: noble metals like Ir and Pd, oxidation prone metal films like Al, Zn, Ti, Mo, and Nb; thin films of various oxides of interest, namely, MgO, Al_2O_3, SiO_2, ZnO, TiO_2, ZrO_2, Nb_2O_5, MoO_3, and Ta_2O_5; and barrier materials like Si_3N_4, TaN, and sputter deposited C.

A. Thin film fabrication

Thin film materials of interest were deposited on 1 mm thick stainless steel plates. The approximate thickness of the films is 200 Å. Ir, Pd, Al, Zn, Ti, Mo, and Nb thin films were deposited by electron beam evaporation of metal targets. Al_2O_3, MoO_3, and Nb_2O_5 films were fabricated by first depositing a 200 Å metal film on stainless steel plates, followed by oxidation of the film in a oxygen plasma source. ZrO_2, TiO_2, and Ta_2O_5 were prepared by reactive sputtering of respective metal targets in O_2 ambient. For example, to obtain TiO_2 films, Ti was sputter deposited in a 50:50 Ar/O_2 ambient at 300 mTorr for 5 min. TaN films were prepared by reactive sputtering of Ta in a nitrogen ambient. Amorphous Si, SiO_2, and Si_3N_4 films were prepared by plasma enhanced chemical vapor deposition. MgO films were prepared by the following process: first, a thin film of magnesium nitrate was deposited on stainless steel anodes, followed by oxidation of the film. ZnS films were deposited by sputter deposition from a ZnS target.

Surface analyses of as grown Ir and Pd films do not show any evidence of oxidation. On the other hand, as grown Mo, Nb, and Al films tend to have a small amount of oxygen on the surface, indicating that the surface layers get partially oxidized as soon as they are moved from the deposition chamber into the ambient. Sputter depth profiling of TaN and Si_3N_4 layers shows a surface layer of oxynitride on these films.

B. Emission current measurements

Prior to performing emission characterization, the vacuum system is baked at a temperature of 120 °C for 8 h under UHV conditions. This process, in addition to reducing the overall pressure of the system, removes physisorbed gases from the thin film surfaces. Typical base pressure in the system after the bakeout and during device operation is approximately 2×10^{-9} Torr. Prior to evaluating device performance with the thin film coated anodes, each FEA was operated for a period of 80–100 h with stainless steel reference anodes. Once baseline data are obtained with stainless steel reference anodes, the reference anodes are replaced with the thin film coated anode plates. The vacuum system is thoroughly baked again before emission characterization with the thin films. For each thin film under study, a new Mo field emitter array was used.

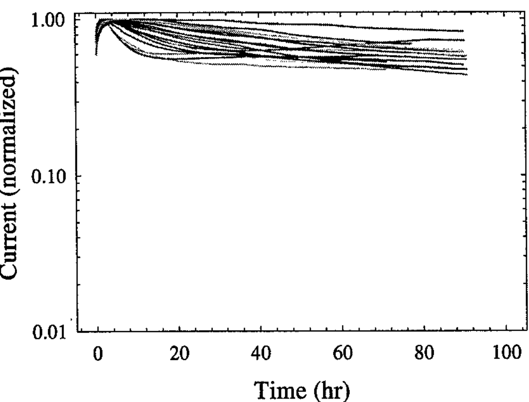

FIG. 1. Emission characteristics of Mo field emitter arrays with stainless steel anodes. The data show the emission characteristics of 24 arrays. The emission current is normalized to the peak value after the initial activation. The total emission current values prior to normalization varied from device to device, but the typical values are between 50 and 120 mA.

1. Emission characterization with stainless steel anodes (reference measurements)

Initial experiments to determine the emission stability of Mo field emitter arrays were performed using 1 mm thick, polished stainless steel plates acting as anode electrodes. Experiments were performed on field emission arrays with an active area of approximately 28 cm^2 (corresponding number of tips). The cathode (emitter) lines are grounded and the gate voltage is set at 80 V. Under these conditions, the devices tested produced emission currents in the 50–100 mA range (corresponding to a current density of 1.8–3.6 mA/cm^2). A total of 24 individual FEAs was studied for baseline and thin film anode studies and a summary of the emission current changes as a function of operational time over a period of 90 h is shown in Fig. 1. The data shown in Fig. 1 are normalized to the peak emission current. The reproducibility of the data between FEAs is adequate for evaluation of thin films of interest. The average emission current after 90 h of continuous operation drops to $57\pm13\%$ of the initial value.

With stainless steel anode plates, devices tested showed an initial activation period of 3–4 h. During this initial activation period, emission current rises rapidly (by about 30%–50%). This process is referred to as initial burn in. The average emission current with 24 devices after 90 h of operation with stainless steel anodes reaches 0.57 ± 0.13 of its initial value.

2. Emission characteristics with metal films

With metal film coated anodes, emission current falls into two broad categories. The emission characteristics with anodes coated with Pd, Ir, Al, Zn, and Ti films are in line with the reference emission data with stainless steel (SS) anodes. With these materials, devices show an initial activation period of 3–4 h, where the initial emission current rapid rises by about 30%–50% during the initial burn-in period. The emission data with metal film anodes for a total operational of time of 90 h are shown in Fig. 2. In contrast to Ir, Pd, Ti,

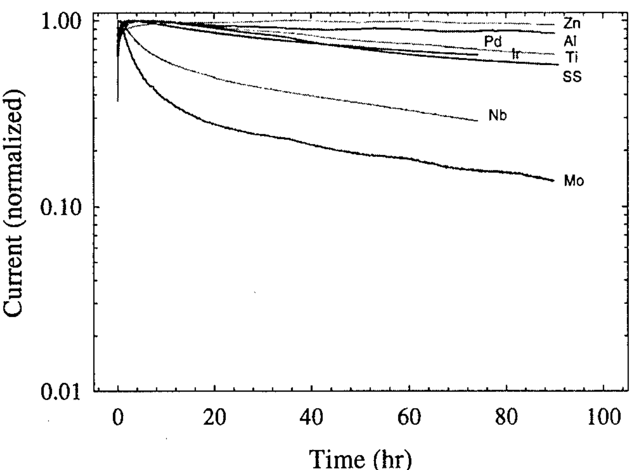

FIG. 2. Emission characteristics of Mo field emitter arrays with stainless steel anodes coated with 200 Å thin films of Pd, Ir, Al, Ti, Zn, Nb, and Mo. The emission current is normalized to the peak value after the initial activation.

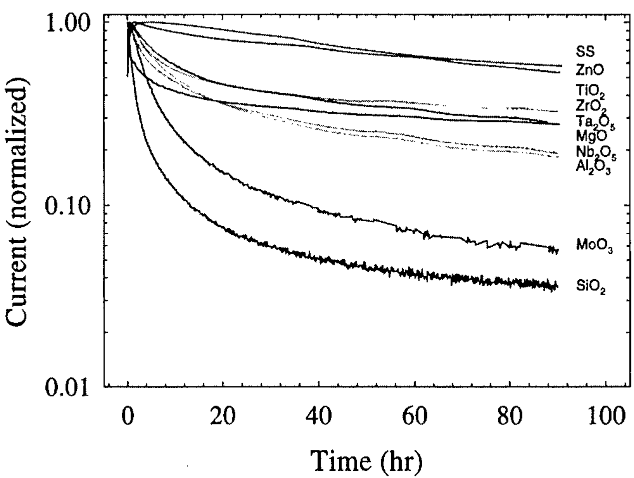

FIG. 3. Emission characteristics of Mo field emitter arrays with stainless steel anodes coated with 200 Å films of various metal oxides. The emission current is normalized to the peak value after the initial activation.

Zn, and Al results, emission current degrades rapidly with Nb and Mo coated anodes. When compared to the reference data, the rate of degradation is about four times faster with Nb and over six times faster with Mo films. In addition, devices with Mo and Nb coated anodes do not initially show current activation, indicating that emission degradation starts immediately after turning on the device. The emission current continued to drop from the onset of the testing process, pointing to the continuous contamination of FEAs. We observe that the emission behavior with Mo and Nb films is quite similar to the behavior with metal oxides (see below). Thus, it appears that the degradation is due to native oxides that form on these metal films. Emission current behavior with Al films is very similar to the reference anodes.

3. Emission characteristics with oxide films

Emission current characteristics as a function of time with various oxide film anodes are summarized in Fig. 3. With the exception of ZnO and TiO_2, in the presence of all other oxide films emission current was found to degrade rapidly during device operation. The emission characteristics with ZnO and TiO_2 coated anodes are similar to the stainless steel reference anode data. On the other hand, the emission characteristics with the remaining oxides are much worse. Emission degradation is much faster than with the respective metal films. In addition, we find that emission current behavior with these oxide thin films showed no initial activation period. Based on our limited data, we observe that the emission characteristics fall into two distinct groups. The decay curves with MgO, Al_2O_3, ZrO_2, Nb_2O_5, and Ta_2O_5 are distinctly different from the curves for SiO_2 and MoO_3. With MgO, Al_2O_3, ZrO_2, Nb_2O_5, and Ta_2O_5, it takes 2–3 h for emission current to reach 50% of the peak emission current value whereas with SiO_2 and MoO_3 films, this happens in less than 1 h. When compared to stainless steel anodes, the rate of degradation with MgO, ZrO_2, Ta_2O_5 is about 4 times faster and with Mo_xO_y and SiO_2, it is over 10 times larger.

Further, relatively stable behavior at ~40% of I_0 is observed with MgO, ZrO_2, and Ta_2O_5 (almost two times less than SS reference anodes), while MoO_3 degrades by an order of magnitude compared to SS reference anodes.

4. Emission characteristics with C, Si_3N_4, and TaN

So far, all the data seem to suggest that Mo field emitter arrays degrade rapidly from the electron beam bombardment of oxide thin films and metal films that are prone to oxidation. A method to eliminate this problem is to deposit a stable barrier film. With this in mind, we looked at the emission characteristics in the presence of nonoxide films, namely, C, TiN, TaN, and Si_3N_4. We deposited 200 Å thick films of TaN and C on SiO_2 and studied the emission characteristics with these films on the anodes. Emission current behavior with C, TiN, TaN, and Si_3N_4 films is summarized in Fig. 4. When compared to the reference stainless steel anode data, we observed no noticeable emission decay with

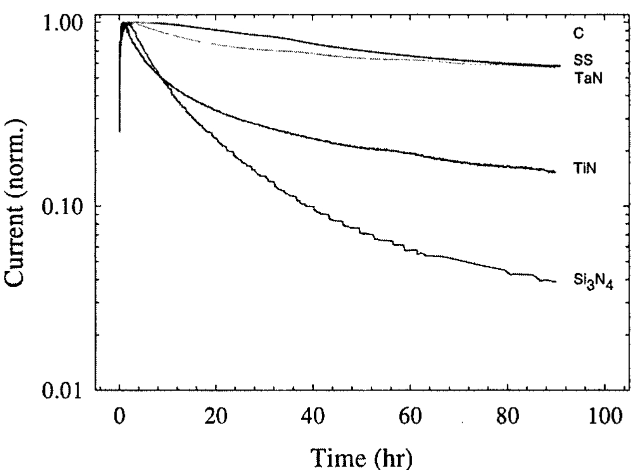

FIG. 4. Emission characteristics of Mo field emitter arrays with stainless steel anodes coated with 200 Å films of C, TiN, TaN, Si_3N_4, and TiN. The emission current is normalized to the peak value after the initial activation.

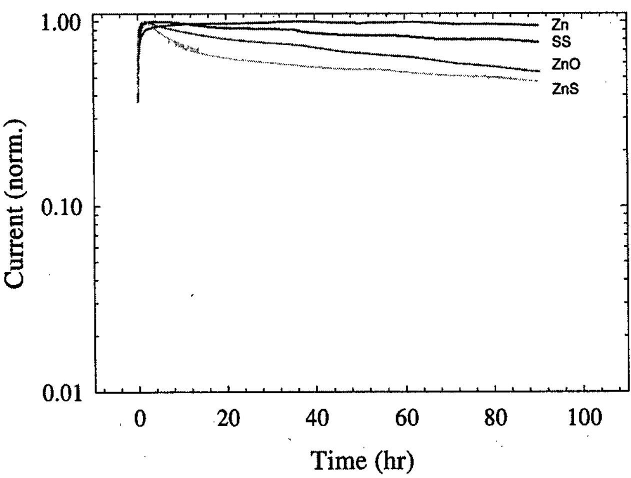

FIG. 5. Emission characteristics of Mo field emitter arrays with stainless steel anodes coated with 200 Å films of ZnS.

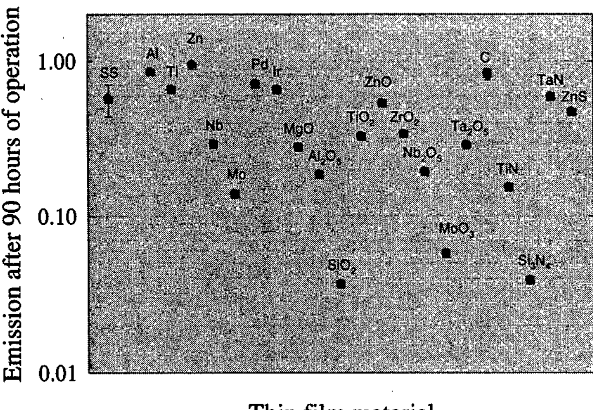

FIG. 6. Relative emission current in the presence of various thin film materials after 90 h of continuous device operation.

C and TaN whereas emission current decays rapidly with Si_3N_4 films. Emission current changes with Si_3N_4 films are similar to those observed with SiO_2 films. This is not totally surprising since Si_3N_4 thin films have a native oxide or oxynitride on the surface. In addition, chemical vapor deposition (CVD) grown Si_3N_4 films tend to have a higher density of defects, leading to the incorporation of OH radicals in the lattice. The data from Fig. 4 show that, in the presence of thin films with no oxygen, Mo field emitter arrays behave well.

5. Emission characteristics with ZnS coated anodes

We also looked at the emission characteristics in the presence of ZnS thin films on the anodes. Emission stability in the presence of ZnS is of interest because ZnS is an efficient phosphor. The emission changes in the presence of ZnS thin films are not very different from those in the ZnO thin film anode data. The emission current changes with Zn, ZnO, and ZnS thin film coated anodes are summarized in Fig. 5. The normalized value of emission current after 90 h of continuous operation with ZnO coatings is 0.54, whereas with ZnS thin film coatings, emission current was found to reach 0.47 times the initial current. The emission current values with ZnS and ZnO are within the device to device emission current variation. But, the fact that the devices behave similarly with ZnO and ZnS anodes is surprising. ZnS has been reported to cause a detrimental effect on the emission characteristics of Mo field emitter arrays.[13]

C. Emission characteristics with various thin film anodes: Discussion

The relative emission current at the end of 90 h of device operation with various materials is summarized in Fig. 6. The data are summarized into three groups: simple metals, metal oxides, and materials without oxygen in them. With most metal films, the emission current remains above or within the range of reference data. The exceptions are Nb and Mo films. In the case of various oxide films, emission current reaches well below the reference values. Among the oxides, the only exception is ZnO. The emission current reaches 3%–5% of the initial values with SiO_2 and MoO_3 films.

Emission current degrades by over 40% with stainless steel anode plates. The emission drop with Pd and Ir films is also significant. Such a large emission current drop (under UHV conditions) with stainless steel anodes and anodes with noble film coatings is surprising. To understand the issues, we looked at the residual gases using a quadrupole mass spectrometer. With a base pressure of 2.0×10^{-9} Torr, residual gas analysis using a quadrupole mass spectrometer shows that principal gases in the system are H_2, H_2O, CO, and CO_2 with partial pressures of 9×10^{-10}, 4×10^{-10}, 2×10^{-10}, and 2×10^{-10} Torr, respectively. The level of O_2 in the background is well below 10^{-10} Torr. Even though, we do not see measurable quantities of O_2 in the system at these base pressures, published results indicate that emission degradation in the presence of oxygenic gases like O_2, CO_2, and H_2O is very similar. Clear estimates of the local pressures in the proximity of the emitters are difficult. We could only speculate on the value of the absolute pressures and what effect these might have on emission performance. With a total oxygen gas pressure of 8×10^{-10} Torr (the sum of H_2O, CO, and CO_2 partial pressures), under static conditions it would take approximately 1000 s for a monolayer formation on the emitter surfaces. At the duty cycles we are operating (0.6% on time versus 99.4% off time), it would be possible that kinetics favor adsorption processes.

There has been speculation about the formation of surface oxides on metal films, which could cause deleterious effects on the emission characteristics. Using x-ray photoelectron spectroscopy (XPS) depth profile analysis, we have determined the amount of oxygen on surfaces of various metal films. For example, for Al films, we estimate the surface oxide to be approximately 35 Å thick. In the case of Mo and Nb films, the surface oxide thickness is approximately 20–30 Å. Ir and Pd are not known to form any oxides at room temperature.

The anomalous result with ZnO and TiO_2 may be ex-

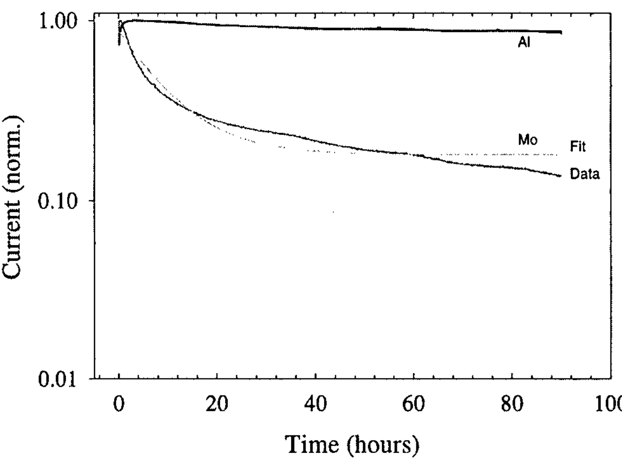

FIG. 7. Current degradation characteristics of Mo field emitter arrays follow a simple equation model given by an equation of the form $I=a+b \exp \times(-Rt)$, where a and b are constant and R is the decay rate. The lines corresponding to the experimental and the fit are indicated.

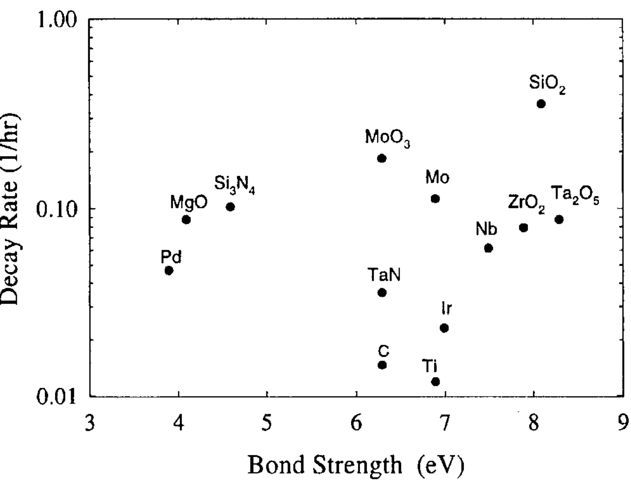

FIG. 8. Bond strength values vs rate of emission current decay. We find no direct correlation between emission decay and the heat of formation.

plained based on the sorption characteristics of ZnO and TiO_2 films. There is ample evidence in the published literature showing that metal oxides like ZnO and TiO_2 tend to be oxygen deficient.[14,15] For example, TiO_2 reduces to $TiO_{x(x=0-2)}$ upon annealing to around ~350 °C. Oxygen deficient TiO_x can work as a distributed getter, thus showing properties similar to the reference anodes. But, again there is continuous competition between oxide breakdown due to electron bombardment and gettering by the metal rich thin film oxide.

D. Emission characteristics: An empirical model

We found that the emission current characteristics of Mo field emitter arrays can be explained using a simple rate equation model. Emission current degradation due to contamination can be explained from a surface coverage model, where the magnitude of the emission current degradation depends on the pressure-time product. Once complete coverage is achieved, then the pressure·time $(P \cdot t)$ product has no further effect on the emission characteristics.[16] Emission current degradation of field emitters follows a first order rate equation given by $I=I_0 \exp(-Rt)$, where R is a rate constant for the given system. This model has been used previously to determine pressure in ultrahigh vacuum systems and extreme vacuum environments.[17] Once the device is activated during the initial burn in, emission current starts to degrade. Using such a simple rate equation model, we could describe the emission characteristics of Mo field emitter arrays in the presence of various thin films and in the presence of gaseous species like oxygen.

The rate of degradation (per h) varies from 0.0117 for Ti, 0.014 for C, and 0.181 for MoO_3 to 0.352 for SiO_2 thin films. Examples of data and the corresponding fitted data are shown in Fig. 7. We also find that a fitting of the form $I=a \exp(-R_1 t)+b \exp(-R_2 t)$ provides much better fittings to all the data. Such a model may indicate two separate processes happening at the same time, for example, a process corresponding to a fast rate corresponding to initial coverage followed by much slower surface chemical changes.

E. Materials issues: Bond strength and penetration depths

In the case of thin films, outgassing or breakdown of the film is a direct function of beam energy, fluence, and total bombardment time. The bond strength of the material is an important factor in determining material stability under electron bombardment. However, bond strength alone does not correlate with stability. The bond strength values were obtained from reference tables.[18] For materials without reference values, we estimated the bond strength from their binding energy data and heat of formation data. The typical bond strength values for the materials tested are in the range of 3–8 eV. For example, the bond strength values (in eV) are the following: for MgO: 4.1, SiO_2: 8.1, TiO_2: 6.9, ZrO_2: 7.9, TaN: 6.3, and ZnO: 2.9. Based on these values, electrons with a kinetic energy of 300 eV are capable of breaking the chemical bond in all the materials that we have studied. A plot of bond strength versus the degradation rate for various materials is shown in Fig. 8. Based on these data, we do not find any correlation between heat of formation or bond strength values and the rate at which emission current decays.

In addition to the bond strength, another parameter of interest is the penetration depth of electrons in a given material. For a given electron energy, penetration depth depends on the density and atomic number of the material. The effective range of travel inside the material is determined by the travel range determined by the empirical relation, $r=25(A/\rho)(E_0/Z^{1/2})^n$ where $n=1.2/(1-0.29 \log_{10} Z)$, A is the molecular weight, Z is the atomic number or the number of electrons in the molecule, and ρ is the density of the material.[19] The electron beam energy E_0 is in keV, and r is given in nanometers. Based on this empirical equation, we estimate that the penetration depth for 300 eV electrons in the above materials ranges from 30 Å for C, 7 Å for SiO_2,

and 3 Å for TiO_2. For materials like Ta, Nb_2O_5, and TaN which have a high density, electrons do not penetrate beyond the first monolayer.

From bond strengths values and penetration depth data, we can conclude that under continuous electron bombardment, surface layers are continuously reduced to their elemental forms. This process, in the case of oxide materials, could result in the evolution of oxygen from the film. Oxygen thus produced can reach the cathode either by diffusion or energetic transport, thus causing emission current degradation. We also find that with barrier layers like C and TaN, emission decay rates approach the values obtained with the reference anodes.

F. Determination of local oxygen partial pressure: Controlled experiments

Our data show that molybdenum field emitter arrays degrade continuously in the presence of oxide thin films on the anode. This led us to ask to several questions. What is the effective partial pressure of oxygen when the thin films are bombarded with the 300 eV electron beam? How does the degradation depend on the material composition? How does it depend on the bond strength of the material and penetration depth of electrons? What is the most important parameter in determining device life?

We cannot directly measure the partial pressure of oxygen within the narrow gap between the FEA and the anode plate. Because of the volumetric issues, no significant change in the pressure of the experimental system due to device operation can be precisely determined. However, we can simulate the O_2 pressures necessary to give emission degradation results similar to the behavior we observed with various thin films.

We performed experiments with stainless anodes with various levels of O_2 in the system. Ultrahigh purity (99.999% purity) O_2 was introduced into the vacuum system using a sapphire sealed variable leak valve. The partial pressure of O_2 was maintained at a constant level during the test period of over 90 h. The emission changes as a function of exposure time at oxygen partial pressures of 1×10^{-9}, 1×10^{-8}, 1×1^{-7}, 1×10^{-6}, and 1×10^{-5} Torr are shown in Fig. 9. After 90 h of continuous operation under ultrahigh vacuum conditions ($<2\times10^{-9}$ Torr with no O_2 introduced), the average emission current level degrades to 57±13% of its initial value. Under dynamically controlled O_2 partial pressures of 1×10^{-8}, 1×10^{-7}, 1×10^{-6}, and 1×10^{-5} Torr, the emission reaches 32±3, 22±2, 17±1, and 4.7 ±0.2% of the initial value at the end of 90 h of continuous operation. A summary of these data is presented in Fig. 10.

Fitting the oxygen exposure data to the first order rate equation, $I=a+b\exp(-Rt)$, gives the following rate constants (per h) at different O_2 partial pressures: 0.066±0.003 at 1×10^{-8} Torr, 0.089±0.009 at 1×10^{7} Torr, 0.197±0.046 at 1×10^{-6} Torr, and 0.341±0.341 at 1×10^{-5} Torr of O_2. Oxygen exposure at 1×10^{-8} Torr produces emission degradation similar to the behavior observed with Al, Ti, Zn, Ir, and Pd metal films. The emission degradation with 1×10^{-9} Torr levels is akin to baseline emission degradation with stainless steel plates. We find that with thin films of Nb, ZrO_2, Ta_2O_5, MgO, Nb_2O_5, and Al_2O_3, the emission degradation is akin to having a local O_2 partial pressure in the 1×10^{-7}–1×10^{-6} Torr range. The degradation rates with Mo, MoO_3, Si_3N_4, and SiO_2 approach the rate constants obtained with 1×10^{-5} Torr O_2 exposures.

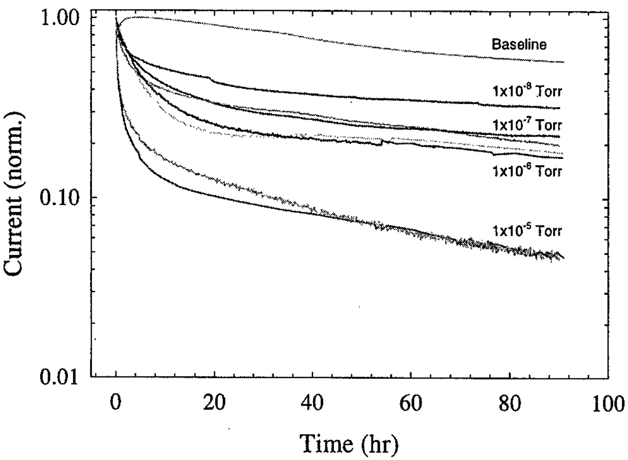

FIG. 9. Emission characteristics of Mo field emitter arrays with stainless steel anodes in the presence of presence of O_2. The emission current is normalized to the peak value after the initial activation.

To understand how coverage affects emission characteristics, the emission current data in Fig. 9 are plotted as a function of total oxygen coverage in Fig. 11. Figure 11 also shows data for two devices that were operated with a 40 mm cathode–anode spacing at vacuum pressures of 2.0×10^{-9} and 1.3×10^{-8} Torr (base pressures in the two test chambers), respectively, for 3500 and 1400 h, respectively. The emission behavior of these devices also falls within the coverage model. Figure 11 again indicates that the emission changes follow a first order rate equation of the form $I=I_0\exp(-Rt)$ for total exposures up to 0.1 Torr s. For total exposure beyond this value, the emission characteristics show a different degradation rate. For this high coverage

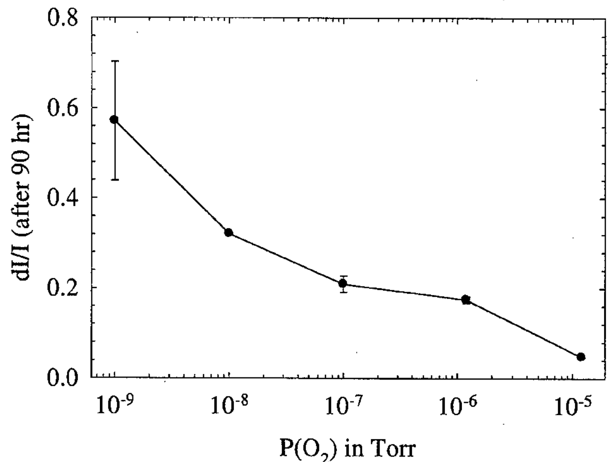

FIG. 10. Summary of emission degradation after 90 h of operation in O_2 at various partial pressure levels.

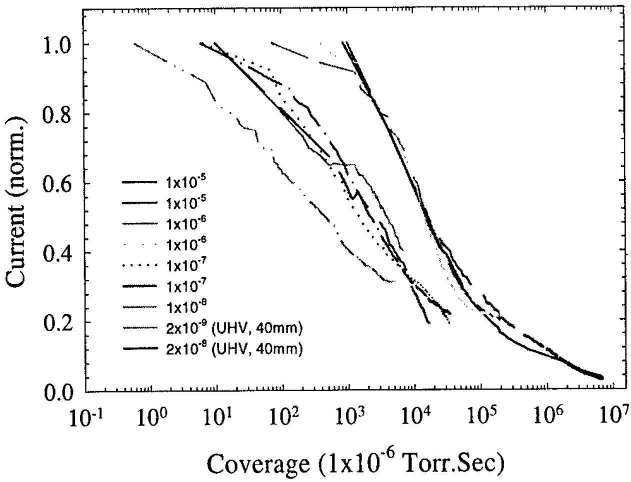

FIG. 11. Emission changes as a function of total O_2 coverage. Coverage is obtained by multiplying O_2 partial pressure by time in seconds. In addition to the data from Fig. 9, also shown here are data for two devices which operated continuously for periods of 3500 and 1400 h, respectively.

regime, the slope of the curve decreases significantly. This could be an indication that the surfaces are reaching either full coverage or are undergoing surface-chemical modifications.

If the total partial pressure of oxygenic gases is 2×10^{-9} Torr, this condition is reached for a total operational time of 14 000 h. For devices operating with a 40 mm gap, the emission versus (time/s) curve does not show saturation behavior after 4000 h of continuous operation. Whereas, when the devices are operated with an O_2 partial pressure of 1×10^{-5} Torr, the time required for full coverage is $\sim$2.8 h (this is simplistic, since this does not take desorption into consideration).

V. CONCLUSIONS

We demonstrated a simple method for the evaluation of thin film materials suitable for the fabrication of field emission displays. The technique is based on the sensitivity of a large field emitter array to the outgassing or the desorption of residual gas species from thin films under electron beam excitation. We demonstrated the usefulness of the method for evaluating the effect of thin film materials on emission characteristics of Mo field emitter arrays. We found that Mo field emitter arrays degraded rapidly with stainless steel anodes coated with various oxide materials. The extent of degradation was found to be the most rapid with SiO_2, Si_3N_4, and MoO_3 thin films. Stainless steel anodes with Mo and Nb thin films show a faster degradation rate than stainless steel anodes, most likely because of native oxides that grow during processing and handling. The emission behavior in the presence of Ir, Pd, Al, Zn, and Ti metal films and barrier materials like C and TaN is similar to that of stainless steel reference data. The observed degradation is consistent with a model based on the liberation of oxygen from the surface of electron beam bombarded materials. Using controlled oxygen exposure experiments, we have determined the equivalent local oxygen pressures in the presence of various thin films. We found that, with thin films of Nb, ZrO_2, Ta_2O_5, MgO, Nb_2O_5, and Al_2O_3, the emission degradation is akin to having a local O_2 partial pressure in the 1×10^{-7}–1×10^{-6} Torr range and with Mo, MoO_3, Si_3N_4, and SiO_2, this is equivalent to having local O_2 pressures of 1×10^{-5} Torr.

ACKNOWLEDGMENTS

The authors want to thank Gene Rossi, Emmett Howard, and Joe Bonanno for thin film deposition and Dave Uebelhoer for technical support.

[1] C. A. Spindt, I. Brodie, L. Humphrey, and E. R. Westerberg, J. Appl. Phys. **47**, 5248 (1976).
[2] K. Sakai *et al.*, Proceedings of the 16th International Display Res. Conference, EuroDisplay '96, 1996, p. 569.
[3] For a comprehensive review of vacuum microelectronic devices, see, for example, D. Temple, Mater. Sci. Eng., R. **24**, 185 (1999).
[4] S. Itoh, T. Niiyama, and M. Yokoyama, J. Vac. Sci. Technol. B **11**, 647 (1993).
[5] B. R. Chalamala, R. M. Wallace, and B. E. Gnade, J. Vac. Sci. Technol. B **16**, 2859 (1998).
[6] D. Temple, Mater. Sci. Eng., R. **24**, 185 (1999).
[7] R. D. Ramsier and J. T. Yates, Jr, Surf. Sci. Rep. **12**, 243 (1991).
[8] S. Ichimura and R. Shimizu, J. Appl. Phys. **50**, 6020 (1979).
[9] S. E. Thompson and T. Nishida, J. Appl. Phys. **72**, 4683 (1992).
[10] Y. V. Dudko, A. A. Kravchenko, and D. I. Cherednichenko, J. Non-Cryst. Solids **188**, 87 (1995).
[11] H. C. Swart, J. S. Sebastian, T. A. Trottier, S. L. Jones, and P. H. Holloway, J. Vac. Sci. Technol. A **14**, 1697 (1996).
[12] S. Thomas, J. Appl. Phys. **45**, 161 (1974).
[13] J. S. Sebastian, H. C. Swart, T. A. Trottier, S. L. Jones, and P. H. Holloway, J. Vac. Sci. Technol. A **15**, 2349 (1997).
[14] M. Grunze, W. Hirschwald, and E. Thull, Thin Solid Films **37**, 351 (1976).
[15] W. Gopel, J. Vac. Sci. Technol. **15**, 1298 (1978).
[16] For a review of the original literature, see, for example, W. P. Dyke and W. W. Dolan, Adv. Electron. Electron Phys. **8**, 90 (1956); J. W. Gadzuk and E. W. Plummer, Rev. Mod. Phys. **45**, 487 (1973), and the references therein.
[17] T. Iwata and K.-S. Chang, Appl. Surf. Sci. **76/77**, 31 (1994).
[18] *CRC Handbook of Physics and Chemistry* (Chemical Rubber, Boca Raton, FL, 1998).
[19] C. Feldman, Phys. Rev. **117**, 455 (1960).

Emission sensitivity to tip position of Spindt-type field emitters

Chenggang Xie,[a] Yi Wei, Rudy Lucero, and Robert Woodburn
Flat Panel Display Division, Motorola, Incorporated, 7700 South River Parkway, Tempe, Arizona 85284

(Received 10 December 1999; accepted 4 April 2000)

The emission characteristics of the Spindt-type field emitter are investigated as a function of the tip position with respect to the gate. The tip position is varied by either changing the hole diameter in the photomask or the dielectric layer thickness. Under low anode field, the measured emission current is sensitive to the tip position and drops quickly as the tip rises above the middle of the gate, which is consistent with the computer simulation result. Under high anode field, the computer simulation result shows that the emission increases for some distance above the gate electrode and then slowly falls off with increasing tip height. There is a ''flat'' region where emission is less sensitive to the tip position. The array with tall tips shows better emission uniformity. Two different types of emission patterns are observed for short and tall tips. The short tips show large blurry spots and the tall tips small sharp spots. © *2000 American Vacuum Society.* [S0734-211X(00)01804-7]

I. INTRODUCTION

The field emission phenomenon has been known for many years. Since Spindt and his co-workers at SRI first developed gated field emitter technology using micro-fabrication techniques in the 1960s,[1] many studies have been performed to understand field emission device characteristics.[2–5] In these studies, the emission current was found to be strongly dependent on the distance from the tip of an emitter to the gate.[6,7] After studying field emission properties of Spindt emitters with emitter tips in a region extending from the gate top surface to 0.7 μm below the gate top surface, researchers concluded improved emission quality was obtained when the emitter tips were located between the center and top of the gate. The tip position was varied by either adjusting the aluminum lift-off layer thickness, which in turn changes the well diameter during tip deposition,[6] or by varying the fabrication process.[7]

Busta *et al.* studied the emission characteristics of a field emission device with the tips well above the gate.[8] By placing the gate below the tip, the device could be initiated by the collector (anode) voltage and modulated by the gate voltage with a swing of only ± 20 V.

In this study, the dependence of emission characteristics on tip position for Spindt-type field emitters is investigated for tips located in a range from below the gate layer to well above the gate. The tip position is varied by adjusting the hole diameter in the photomask or the thickness of the dielectric layer between the gate and base. The tip position is measured by atomic force microscopy (AFM) as well as by scanning electron microscopy (SEM). Besides the emission current measurement, field emission patterns from the field emitter arrays with different tip positions are also studied.

II. EXPERIMENT

The field emitter array used in this study is fabricated using a process similar to Spindt tip technology.[9] Details of the fabrication process have been covered in the literatures.[10–12] Figure 1(a) shows a schematic diagram of a Spindt-type field emission structure. Figure 1(b) is a SEM micrograph of the real field emitter structure. The device has a molybdenum emitter cone and a molybdenum gate electrode. Between the metal gate and the metal tip contact layer is the dielectric layer (SiO_2). Under the tip deposition process, the aspect ratio of tip height to tip base diameter of the Mo tip is about 1:1. Thus, the tip position relative to the gate level can be altered by changing the hole diameter in the photomask or the dielectric thickness between the gate and the tip contact layer shown in Fig. 1(a). In this study, the hole diameter in the mask is varied from 1.0 to 1.6 μm, and the dielectric layer thickness is varied from 0.7 to 1.1 μm. These parameter variations result in tip positions that change from below the bottom of the gate to well above the top surface of the gate. The emission current sensitivity is studied with respect to variation in the well diameters with the SiO_2 layer thickness fixed. Also studied are the emission current sensitivity and emission uniformity as a function of the SiO_2 layer thickness with a fixed well diameter.

The field emitter arrays in this study typically contain about four million tips. The assembly of the anode and cathode, with 1 mm separation, is mounted in a vacuum chamber with a base pressure below 5×10^{-7} Torr. A nonpixelated ZnO coated anode is used for measuring the field emission pattern. The total emission current is measured via a sensing resistor under an anode electric field of 0.4 V/μm.

Computer simulation of emission current sensitivity to tip position is performed using a commercially available three-dimensional (3D) field solver, Coulomb, developed by Integrated Engineering Software.[13]

III. RESULTS AND DISCUSSION

A. Emission sensitivity to tip position: Different well diameters

Keeping the depth of the well (=thickness of the SiO_2 layer + thickness of the gate) constant, different tip positions can be achieved by varying the well diameter. Four different well diameters are used in this study. AFM is used to mea-

[a]Electronic mail: a775aa@email.mot.com

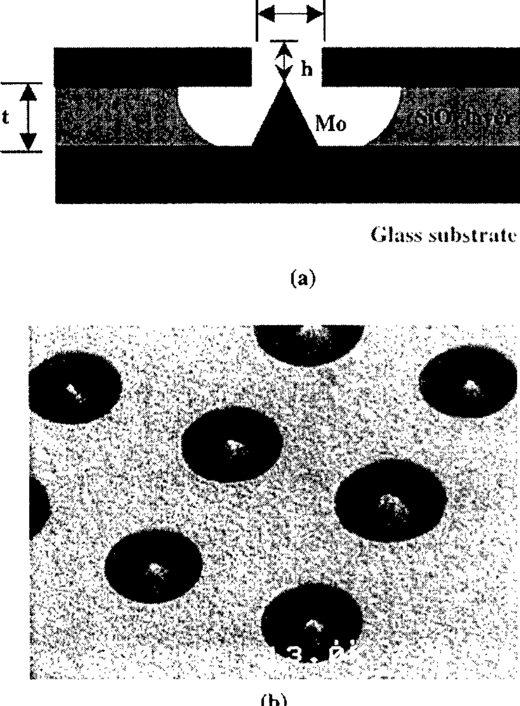

FIG. 1. (a) Schematic diagram showing a Spindt-type field emission structure. The device has a molybdenum emitter cone and a molybdenum gate electrode. *CD* is the well diameter, *h* is the tip to gate surface distance (which sometimes is referred to as tip position in the text: positive *h* means the tip is above the gate surface, negative *h* means the tip is below the gate), both are measured by AFM. *t* is the thickness of the dielectric (SiO_2) layer. (b) SEM of a field emitter array.

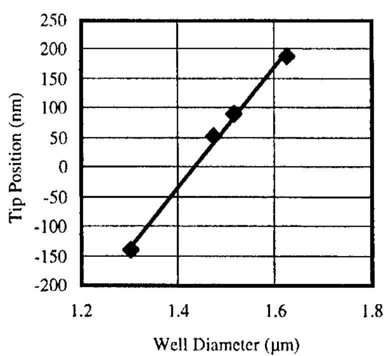

FIG. 3. Empirical relationship between the tip position and the well diameter. The tip position moves up linearly with the increase in well diameter.

sure the well diameter and tip position by measuring the distance between the tip and the gate top surface as shown in Fig. 1(a). Standard position measuring software included with the Digital Instruments AFM control computer is used to measure the tip position. Figure 2 shows two three-dimensional AFM images of the emitter tips and wells with different tip positions. The average tip to gate surface distance is found to depend linearly upon the well diameter as shown in Fig. 3. These arrays with different well diameters and tips from below the gate to well above the gate are used to understand the current sensitivity of the field emitter arrays.

In Fig. 4, the measured emission current is plotted against the well diameter and the average tip position measured by

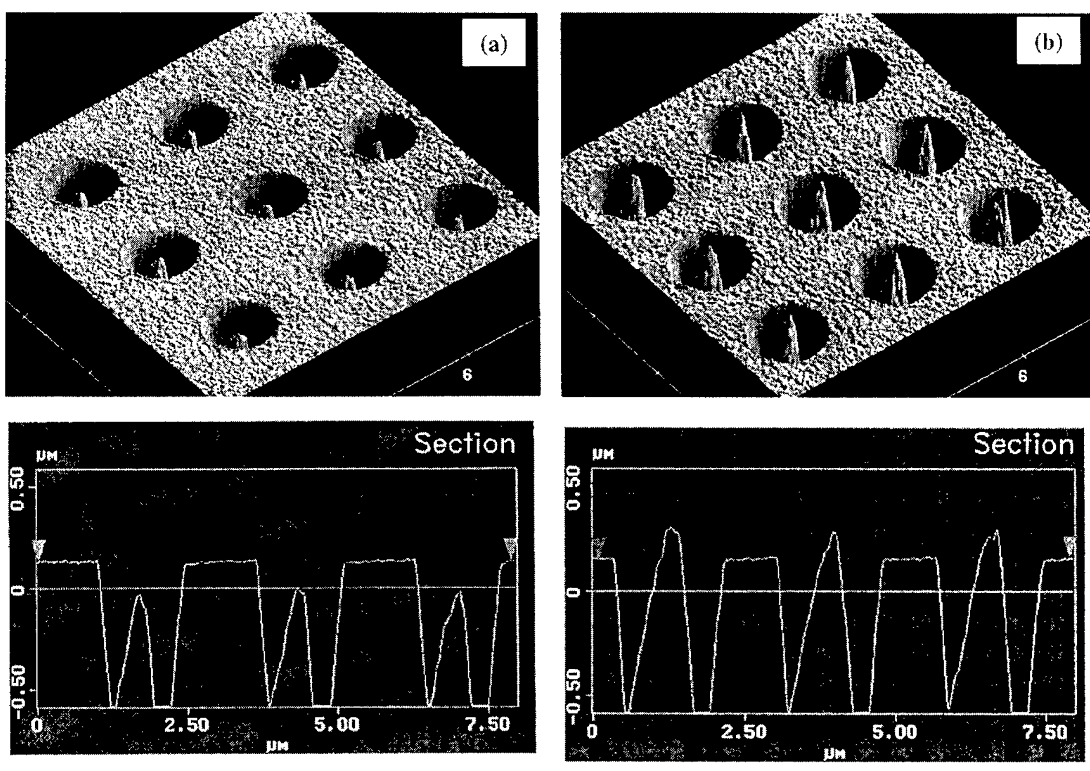

FIG. 2. 3D AFM images of field emitters with tips below and above the gate surface and the corresponding profiles.

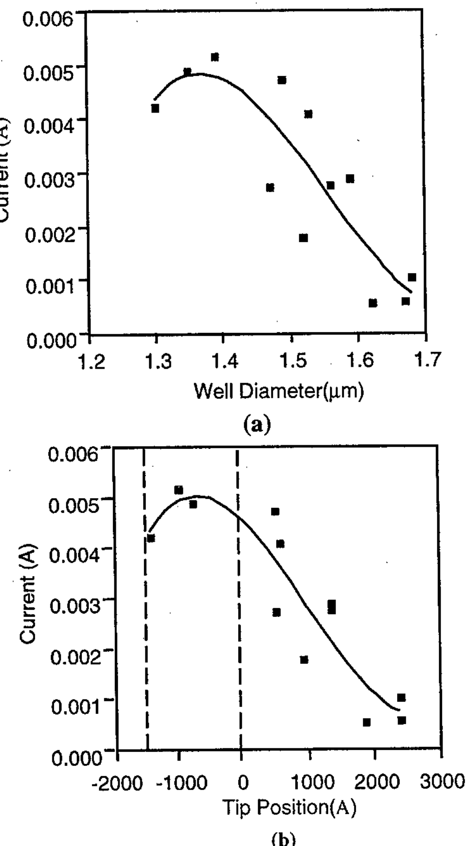

FIG. 4. (a) Measured emission current is plotted vs the well diameter and (b) the average tip position measured by AFM. The tip's position is measured with respect to the gate's top surface. Positive tip position means that the tip is higher than the gate. The gate thickness is 0.30 μm. The gate voltage is 65 V.

AFM. The emission current is sensitive to the well diameter. A small variation in the well diameter can cause a significant change in emission current. To better understand this relationship, a term defining the current sensitivity to well diameter, *CD*, is introduced:

$$I_{CD}=\frac{10\ \log(I_2/I_1)}{CD_2-CD_1}, \tag{1}$$

where *CD* is the well diameter and $10\log(I_2/I_1)$ is the current gain or loss in dB. The average current sensitivity to the well diameter is about -19.4 dB/μm based on the data shown in Fig. 4. In order to achieve less than a 3% variation in the emission current, the *CD* tolerance must be within 0.0066 μm. Thus, this tolerance provides the baseline process control for manufacturing emitter arrays used in the arrays for the field emission displays. Very tight control over the well diameter is desired for better quality field emission cathodes. Regarding tip position dependence, the emission current changes little when the tips are placed at the middle of the gate layer. However, the current drops rapidly once the tips are above the middle of the gate. To study tip position dependence, the current sensitivity to tip position is defined by

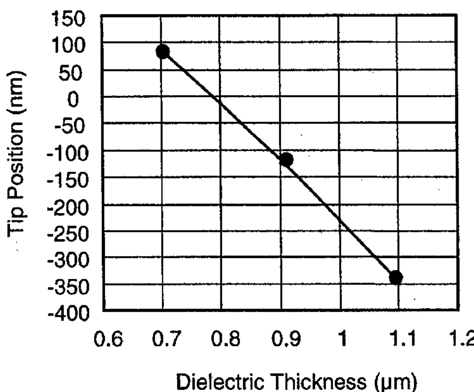

FIG. 5. Measured tip position as a function of dielectric thickness.

$$I_h=\frac{10\log(I_2/I_1)}{h_2-h_1}, \tag{2}$$

where h stands for the tip position with respect to the gate. Ignoring the fact that the well diameter also changes, the current sensitivity to the tip position is about -27.9 dB/μm when the tips are placed above the middle of the gate. Hence, the emission current is very sensitive to the tip position. Besides well diameter, the tip position is also dependent on the deposition temperature, the tip material, and the thickness of the lift-off layer. This poses a significant challenge for process control since small variations in the tip position produce large current variations across a large panel.

In order to optimize the manufacturing process, it is probably necessary to understand the relationship between the well diameter and the emission current. But for academic study of the effect of tip position on the emission current, it is not a wise choice to adjust the well diameter since changing the well diameter to achieve different tip positions changes two variables: well diameter and tip position. To better understand the effect of the tip position on the emission characteristics, we must fix one variable: the well diameter.

B. Emission sensitivity to tip position: with a fixed well diameter

In the experiment discussed above, changing the hole diameter on the photomask not only varies the tip position but the well diameter as well. To separate these two variables, field emitter arrays are fabricated with a different dielectric thickness, while keeping all other variables fixed. Using a well diameter target of 1.0 μm, three different dielectric thicknesses are chosen: 0.7, 0.9, and 1.1 μm. The tip position relative to the gate top surface depends linearly on the thickness of the dielectric layer as shown in Fig. 5. Measured at low anode voltage (400 V), the emission current increases as the dielectric thickness increases or the tip position decreases, as seen in Fig. 6. The field emitter array with the tips 0.35 μm below the top gate surface (slightly below the bottom of the gate since the gate is about 0.30 μm thick) emits five times more current at low anode voltage than the arrays with the tips 0.2 μm above the gate. The current sensitivity

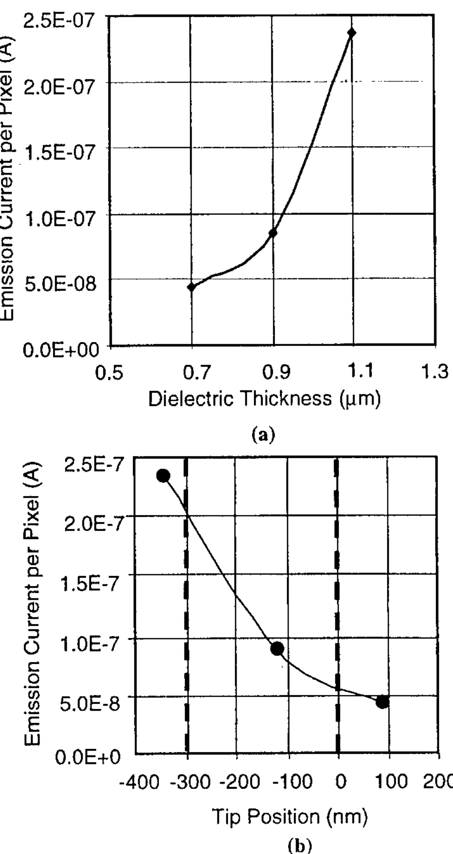

FIG. 6. Measured emission current plotted as a function of the tip position and the dielectric layer thickness. In this case, the gate thickness is 0.3 μm. The dashed lines indicate the top and bottom surfaces of the gate.

to dielectric thickness is about -17.5 dB/μm for a dielectric thickness ranging from 0.7 to 1.1 μm. Thus, increasing the dielectric thickness by 0.1 mm results in an emission current increase of 49%. Such current variation due to dielectric thickness variation may not be a problem for small-scale uniformity since the thickness of the deposited film can be controlled very precisely over a small area. However, large-scale uniformity may be affected by the variation of dielectric thickness. For a typical display, the required brightness variation from one corner to the other is less than 30%. In order to achieve this performance with field emitter array, the dielectric thickness variation must be less than 0.065 μm, equivalent to 6.5% with dielectric thickness of 1 μm.

C. Computer modeling

Computer simulation of emission current sensitivity to tip position is performed using a commercially available 3D-field solver, Coulomb, developed by Integrated Engineering Software.[13] The field solver is based on the boundary element method. Figure 7 shows a 3D model of one quarter of the field emitter. In the model, the anode (not shown Fig. 7) at a fixed potential is located 1 mm from the cathode. The grid size used on the apex of the microtip is 50 Å. The solver is used to compute the electric field along the surface 50 Å above the tip surface. Then, the Fowler–Nordheim equation

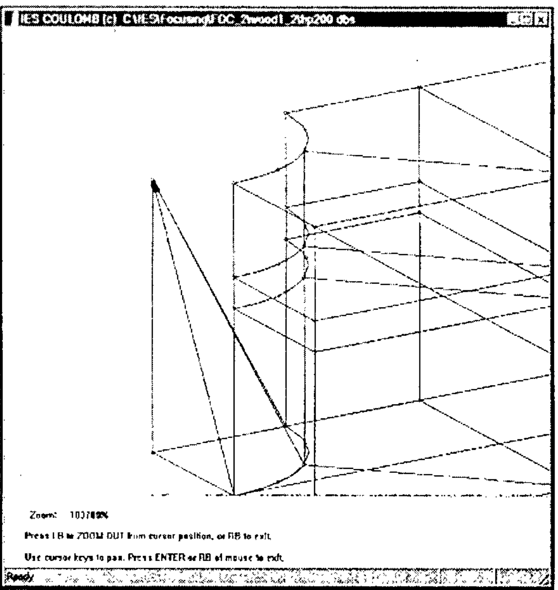

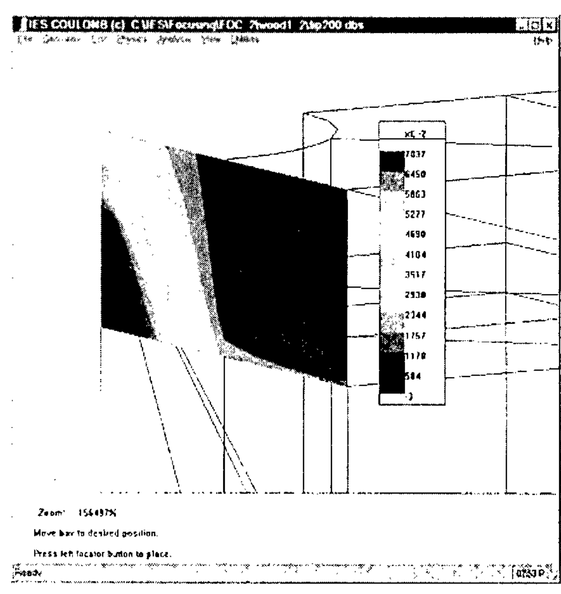

FIG. 7. 3D model of a quarter of a field emitter and the voltage contours near the tip.

is used to calculate emission current assuming the average work function of molybdenum is about 4.55 eV.[14]

Physical parameters used for the model include a tip radius of 200 Å, well diameter of 1.0 μm, gate thickness of 0.3 μm, and total dielectric thickness of 0.7 μm. The distance between the gate top surface and the emitter base is 1 μm. In this study, the tip position is varied from 0.65 to 1.55 μm and the rest of the parameters are kept constant. At an anode voltage of 400 V, the electric field and emission current are found to be a strong function of the tip position, as seen in Fig. 8. When the tip is placed near or above the top gate's surface, the current sensitivity to the tip position is approximately 100 dB/μm, which is much larger than the experimental results. The maximum current is achieved when the tip is placed in the middle of the gate, which is similar to the

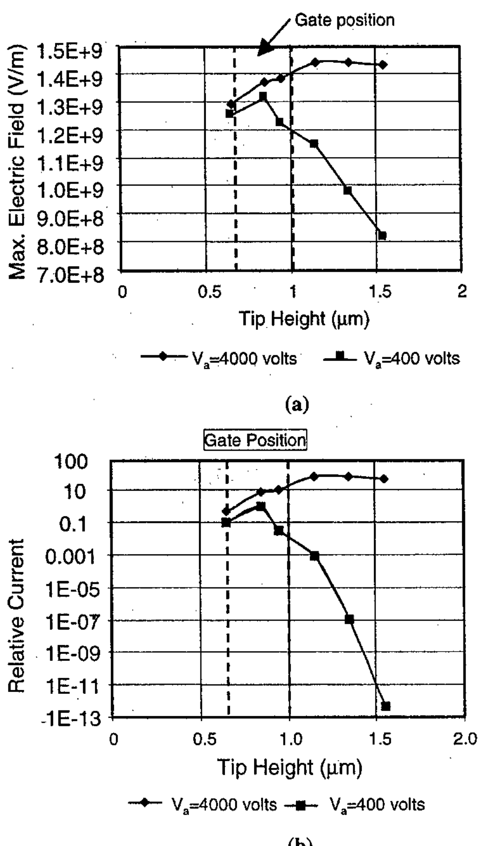

FIG. 8. (a) Maximum electric field as a function of the tip position; (b) relative current as a function of tip position under low and high anode fields.

simulation results obtained by the others.[5] The reason for the discrepancy between the experimental and simulation results is still unknown.

Under the influence of a high anode electric field, the simulation results are significantly different from those at low anode voltage. When the tips are placed at or below the bottom of the gate, there is little difference in the maximum electric field near the emission surface for either high and low anode electric fields. However, as the tip position rises above the gate, the difference between the maximum electric field near the tip apex for high and low anode fields also widens. In the high anode field case, the current is less sensitive to the tip position when the tip is placed slightly above the gate. The current sensitivity for this case is 32 dB/μm when the tip position is varied from 0.85 to 1.15 μm (0.15 μm below the gate's top surface to 0.15 μm above the gate's top surface). However, the current sensitivity to tip position drops to 3.3 dB/μm when the tip is placed further above the gate (0.35–0.5 μm above the gate's top surface). Under low anode voltage, the gate potential largely determines the electric field near the apex because of a small influence of anode electric field. However, under high anode electric field (5 V/μm or higher), the influence of anode potential on the tip apex becomes significant. As the tip rises above the gate, the weight of the electric field on the tip shifts from the field produced by the gate to the field generated by the anode potential. Figure 8 illustrates this effect as a shift of the maximum electric field from 0.15 μm below the gate top surface to 0.35 μm above the gate. Correspondingly, the emission current peaks when the tip is placed 0.35 μm above the top gate's surface. For a proximity focusing scheme (high anode field case), the tips should be placed above the gate to improve the uniformity and maximize emission current. However, if an electrostatic focusing lens is used to narrow the electron beam, the tips are shielded by the focusing electrode from the anode potential and even worse, the focusing electrode imposes a negative electric field relative to the gate field. Therefore, the tips should be placed at the middle of the gate to maximize the current if an electrostatic focusing lens is used.

In the case of varying dielectric thickness, no current peak is observed experimentally for tip positions ranging from 0.35 μm below the top gate surface to 0.1 μm above the top gate surface as shown in Fig. 6(a). This is different from the computer modeling result shown in Fig. 8(b) for the 400 V anode voltage case. One possible explanation is that the emission current measured is composed of two components: primary emission and secondary electron emission first discovered by Purcell and Binh.[15] The primary emission is the conventional field emission governed by Fowler–Nordheim theory. Primary electron emission originates at the apex of the field emitter where the maximum electric field occurs. The initial kinetic energy of the primary electrons is in the neighborhood equivalent to the gate voltage. The secondary electron emission comes from the sidewall of the gate bombarded by the primary electrons emitted from the tips. As the tips recede from the gate, more and more electrons could bombard the gate. Therefore, more secondary electrons emit from the gate. The overall emission current could be higher when the tips are placed below the gate, which is contrary to the simulation result that only accounts for the primary electron emission. The observation of two types of field emission patterns supports the hypothesis of the existence of two types of emission from the Spindt emitter array, which will be discussed in Sec. III. However, more work is needed to understand the mechanisms of those two field emissions.

D. Observation of field emission patterns of the arrays with different dielectric thickness

Experimentally, one common characteristic of the emission pattern generated by secondary electrons is a distorted comet-like spot.[15] Such an emission pattern is a result of a combination of low energy electron emission and highly nonuniform electric fields in the cathode/gate cavity that result from charging of the dielectric layer below the gate. The emission patterns of the field emitter arrays with different tip positions controlled by varying the dielectric thickness were recorded using a charge coupled device (CCD) camera in the same test system at an anode voltage of 3000 V. The field emitter arrays used in this study are made of many four tip clusters which are separated by 110 μm in order to show detailed emission patterns between the tip clusters. Figure 9 shows emission patterns from the field emitter arrays with the tips 0.20 μm above the gate surface, 0.12 μm below the

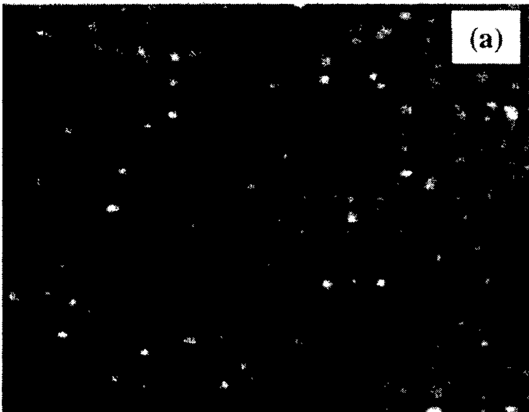

0.2 μm above gate surface
Well defined spots

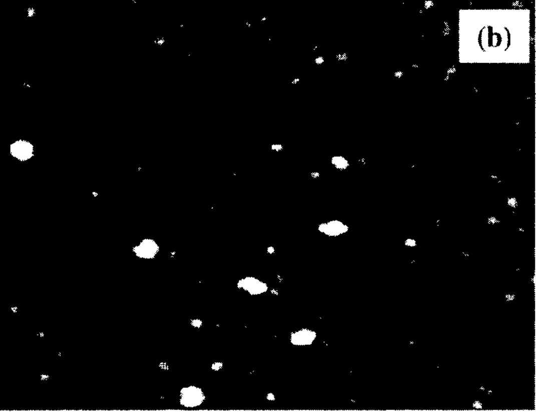

0.12 μm below gate surface
Most of the spots are well defined,
but blur spots start to appear

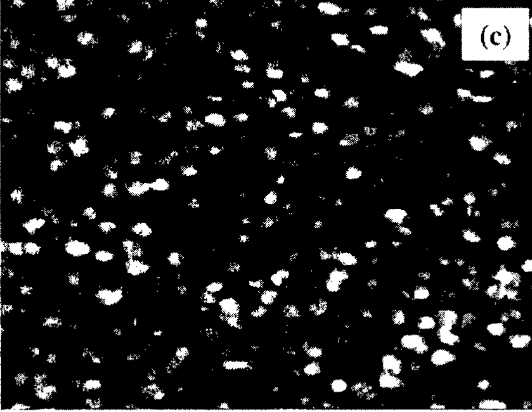

0.35 μm below gate surface
(0.05 μm below bottom of the gate)
Most of the spots are blur

FIG. 9. Emission patterns of the field emitters with different tip positions. The tip positions are (a) 0.1 μm above the gate top surface, (b) 0.12 μm below the gate top surface; and (c) 0.05 μm below the gate bottom surface.

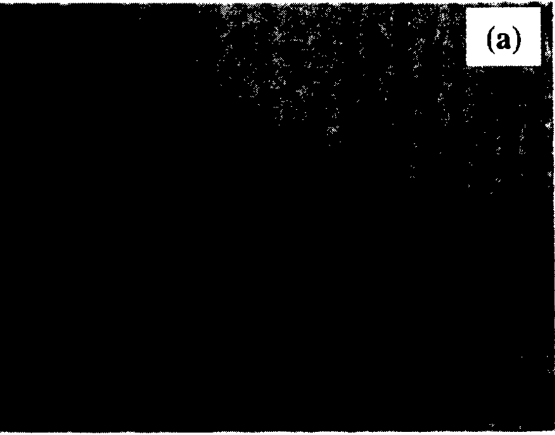

Tip above the gate

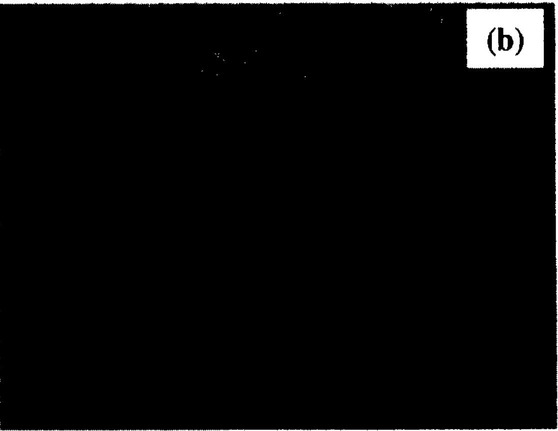

Tip below the gate

FIG. 10. Emission image of fully functional arrays obtained by the CCD camera; a ZnO phosphor coated screen was used. (a) Tips above the gate, and (b) tips below the gate.

gate surface, and 0.05 μm below the gate bottom surface. From Fig. 9, clearly there are two different types of the emission patterns: small sharp spots and large blurry spots. For the tip below the gate, about a half of the spots are large and blurry. However, for the tips above the gate, almost all of the spots are sharp and small. When the tip is located in the middle of the gate, the emission pattern has a mixture of both kinds of spots. The blurry spots could be the emission pattern produced by secondary electron emission from the gate, because these low energy electrons are easily distorted by a local highly nonuniform electric field, as discussed by Purcell and Binh.[15] Since more primary electrons strike the gate when the tip is below the gate bottom surface, the secondary electron emission can be significant. In fact, the secondary electron emission current can be a few times higher than the primary emission current, depending on the secondary electron yield of the gate layer. As the position of the tip apex is shifted upward, fewer electrons strike the gate. Therefore, the secondary electron emission becomes insignificant and is less sensitive to the gate electric field and more dependent on the relative position between the tip and the gate. A possible source of discrepancy between measured and simulated re-

sults is that the conventional field emission theory used to compute the emission current does not include the secondary electron emission.

As suggested by simulation results, under high anode voltage, there is a ''flat'' region where the change in tip position does not have much effect on the emission current and the emission current is less sensitive to tip position. Therefore, the emission variation due to tip position variation, caused by other variations in the process, is minimized. The field emitter arrays with the tall tips placed above the gate should have better uniformity. In addition, a small and well-defined emission pattern of tall tips also helps emission uniformity. Based on the findings in this study, the field emitter arrays fabricated with tall tips show a significant improvement in uniformity. Figure 10 shows the emission pattern of the full pixels. Compared to the short tip array, the tall tip array exhibits improved uniformity and well-defined lines.

IV. SUMMARY AND CONCLUSIONS

The emission characteristics of the Spindt-type field emitter were investigated as a function of the tip position with respect to the gate. The tip position is varied by either changing the hole diameter in the photomask or the dielectric layer thickness. The tip position is found to depend linearly on the well diameter and dielectric layer thickness. Under low anode field, the measured emission current is sensitive to the tip position and drops quickly as the tip rises above the middle of the gate, which is consistent with the computer simulation result. Under high anode field, the computer simulation result shows that the emission increases for some distance above the gate electrode and then slowly falls off with increasing tip position. There is a flat region where emission is less sensitive to the tip position. Although due to the difficulty of the high voltage current measurement no measured current data are obtained that either confirm or deny the simulation result, the field emitter array with tall tips shows better emission uniformity experimentally. Two different types of emission patterns are observed: small sharp spots and large blurry spots. The large blurry spots occur in the field emitter arrays fabricated with tips below the gate and small well-defined spots are found in the arrays with the tips placed above the gate.

ACKNOWLEDGMENTS

The authors would like to express their thanks to the cathode fabrication team and test group for their support.

[1]C. A. Spindt, K. R. Shoulders, and L. N. Heynick, U.S. Patent No. 3,755,704 (filed 1973).
[2]C. A. Spindt, I. Brodie, L. Humphrey, and E. R. Westerberg, J. Appl. Phys. **47**, 5248 (1976).
[3]P. R. Schwobel and I. Brodie, J. Vac. Sci. Technol. B **13**, 1391 (1995).
[4]N. A. Cade, R. Johnson, A. J. Miller, and C. Patel, J. Vac. Sci. Technol. B **13**, 549 (1995).
[5]A. A. Talin, T. E. Felter, and D. J. Devine, J. Vac. Sci. Technol. B **13**, 448 (1995).
[6]S. Itoh, T. Watanabe, K. Ohtsu, M. Tanguchi, S. Uzawa, and N. Nishmura, J. Vac. Sci. Technol. B **13**, 487 (1995).
[7]J. H. Jung, H. R. Chung, B. H. Chung, S. Y. Hwang, S. Y. Han, J. H. Han, M. W. Nam, N. Y. Lee, and S. Ahn, Technical Digest of the 12th IVMC'99, 1999, p. 48.
[8]H. H. Busta, D. W. Jenkin, B. J. Zimmerman, and J. E. Pogemiller, IEEE Trans. Electron Devices **39**, 2616 (1992).
[9]C. A. Spindt, J. Appl. Phys. **39**, 3504 (1968).
[10]L. E. Tannas, Jr., *Flat-Panel Displays and CRT* (Van Norstrand Reinhold, New York, 1985).
[11]B. Gnade and J. Levine, SID'95 Seminar, 1995 (SID, 1995).
[12]B. R. Chalamala, Y. Wei, and B. E. Gnade, IEEE Spectr. **34**, 42 (1998).
[13]Integrated Engineering Software, Winnipeg, Manitoba R3H OX4, Canada.
[14]J. C. Riviere, *Solid State Surface Science*, edited by M. Green (Marcel Dekker, New York, 1969).
[15]S. T. Purcell and V. T. Binh, J. Vac. Sci. Technol. B **15**, 1666 (1997).

Electron field emission from amorphous carbon nitride synthesized by electron cyclotron resonance plasma

X. W. Liu, S. H. Tsai, L. H. Lee, M. X. Yang, and A. C. M. Yang
Department of Materials Science and Engineering, National Tsing Hua University, Hsinchu, Taiwan 300, Republic of China

I. N. Lin
Materials Science Center, National Tsing Hua University, Hsinchu, Taiwan 300, Republic of China

H. C. Shih[a]
Department of Materials Science and Engineering, National Tsing Hua University, Hsinchu, Taiwan 300, Republic of China

(Received 19 August 1999; accepted 14 April 2000)

Amorphous carbon nitride thin films were synthesized using an electron cyclotron resonance chemical vapor deposition system in which a direct current (dc) bias was applied to the silicon substrate and a mixture of C_2H_2, H_2, and Ar was used as precursors. The films prepared in this way were further treated in an argon plasma to increase their surface roughness thereby creating a more efficient electron emitter. An onset emission field as low as ~3.5 V μm^{-1} can be achieved (after Ar^+ plasma sputtering for 3 min), significantly lower than other carbon-based electron field emitters. This low value is mainly attributed to the increase of film roughness, decrease of film thickness, and removal of hydrogen from the film. The structural and compositional modification induced by Ar^+ plasma post-treatment along with the application of a negative dc bias to the synthesized film were analyzed by Fourier-transformation infrared spectroscopy, Raman spectroscopy, x-ray photoelectron spectroscopy, atomic force microscopy, and field emission scanning electron microscopy. © *2000 American Vacuum Society.* [S0734-211X(00)02104-1]

I. INTRODUCTION

The carbon-based electron field emitters have rapidly won worldwide attention as a new electron source for flat panel display, electronic and optoelectronic devices, and so on.[1–4] Recently, electron field emission from bulky materials, such as diamond,[5–10] nitrogenated diamond,[11–14] cesiated diamond,[13] diamondlike carbon (DLC),[8,15] and amorphous carbon (*a*-C)[16,17] have been reported at moderately low electric fields. These low fields are believed to result from their unique properties such as negative electron affinity,[18–22] high thermal conductivity, extreme hardness, and good chemical stability.[8] Also, space-charge-induced band bending of the carbon films could be important in both amorphous carbon[19,22] and diamond films[23] for the enhancement of the field emission.

However, the mechanism of electron emission from diamond is not clearly understood yet. Also, using typical plasma processes and hydrocarbon precursors, diamond grows only in faceted grains, not in a uniform and smooth layer.[8] On the other hand, DLC can be deposited microscopically smooth, following the morphology of the emitter tips. One of the most important advantages of DLC application over diamond is its lower deposition temperatures, ranging from room temperature to 250 °C.[24,25] In addition, high emission currents are possible because of its high thermal conductivity.[20,21]

Recent reports[4,9,10,16,17,25] indicate that amorphous carbon films have received considerable attention over the last decade due to their unique diamondlike chemical, electrical, optical, and mechanical properties. Because of their very low (sometimes even negative) electron affinity,[4,22] they are also considered promising candidates for field emitters.

Since it was proposed that the bulk modulus of a hypothetical material, β-C_3N_4 (4.83 Mbar) might be greater than that of diamond (4.43 Mbar),[26,27] the effect of nitrogen incorporated into *a*-C films has been extensively studied.[28–30] The stress, electrical resistivity, work function[31,32] and optical band gap[17,24] of the resulting material can be significantly lower than the equivalent values for the undoped films. Besides, nitrogen is the best *n*-type dopant, because its atomic size is similar to that of carbon and is a shallow donor below the conduction band in *a*-C.[20,32] Also, the negative electron affinity (NEA) of CN is suggested for enhancing the emission current of amorphous carbon (*a*-C) which has a similar bonding configuration to that of diamond;[9] many nitrides like AlN and BN also show NEA characteristics.[8] The threshold field is much lower in the N-doped *a*-C than in the P- or B-doped *a*-C films.[30] Therefore, nitrogenated amorphous carbon (*a*-C:N) is considered a superior field emission material to *a*-C.[4,17,32,33]

The superior field emission characteristics of *a*-C:N films were synthesized for the first time by an electron cyclotron resonance chemical vapor deposition (ECR–CVD) system by applying a negative direct current (dc) bias to a silicon substrate and using a mixture of C_2H_2, N_2, and Ar as precursors. A process involving Ar^+ plasma sputtering was utilized as the post-treatment to study the effect of surface

[a]Author to whom correspondence should be addressed; electronic mail: hcshih@mse.nthu.edu.tw

roughness of the carbon nitride film on the electron field emission.

II. EXPERIMENT

A. Process equipment

A schematic illustration of the ECR plasma system used in this work is shown in Fig. 1(a). Briefly, the source (plasmodule stream) is mounted on the flange of a stainless steel vacuum chamber. Plasma, generated by microwave excitation at 2.45 GHz by a magnetron (Tepla GmbH) passes through a waveguide and is fed perpendicularly through a quartz dome into an 875 G magnetic field, generated by the coils surrounding the resonance volume, that creates the ECR condition. A negative dc bias is simultaneously applied to the substrate. The deposition chamber is pumped down to the base pressure of 6.7×10^{-4} Pa (5×10^{-6} Torr) with a turbomolecular pump, backed by a rotary mechanical pump.

The substrates, Si (2×2 cm^2) wafer, were degreased in trichloroethane (CH_3CCl_3) and acetone. The samples were prepared under the following conditions: total gas pressure of 1.1 Pa (8×10^{-3} Torr); microwave power at 800 W; 20 sccm of C_2H_2; 20 sccm of N_2; 10 sccm of Ar; negative dc bias at -400 V; and deposition time of 3 min, temperature 100–150 °C. The effects of creating a sputtered surface on the efficacy of the field emission from these samples was also investigated. To this end, Ar^+ plasma sputtering was used under the ECR condition with the application of a negative dc bias to the substrate. The Ar^+ sputtered *a*-C:N films deposited on Si wafer were prepared under the following conditions: microwave power at 600 W; 10 sccm of Ar; negative dc bias at -500 V; and sputtering time of 0–3 min. The electron field emission characteristics of *a*-C:N thin films were studied by varying the Ar^+ sputtering time. Figure 1(b) shows the flow chart of the sample being prepared for the electron field emission studies.

B. Characterization and analysis

The surface morphology and mean roughness of the sample was characterized by an atomic force microscope [(AFM) DI Nanoscope IIIA]. The thickness of the sample was measured by a field emission scanning electron microscopy [(FE–SEM) Hitachi Model S-4000]. The structure of the deposited carbon nitride films was examined using Raman spectroscopy (Renishaw Ramanscope Model 2001). All samples were qualitatively analyzed by Fourier-transform infrared [(FTIR) BOMEN Model DA8.3 SNV] from 500 to 4000 cm^{-1} with a 2 cm^{-1} resolution while utilizing a globar as the infrared light source. The absorption features of the samples were recorded by subtracting the absorption spectra of a blanket Si substrate (background signals).

The relevant chemical elements of the specimen were characterized by [x-ray photoelectron spectroscopy (XPS) Perkin Elmer model PHI 1600] using a single Mg K_α x-ray operating at 250 W. An *in situ* 3 kV Ar^+ ion gun was applied to sputter the samples. Energy calibration was done using the Au $4f_{7/2}$ peak at 83.8 eV and the energy resolution is 1.6 eV

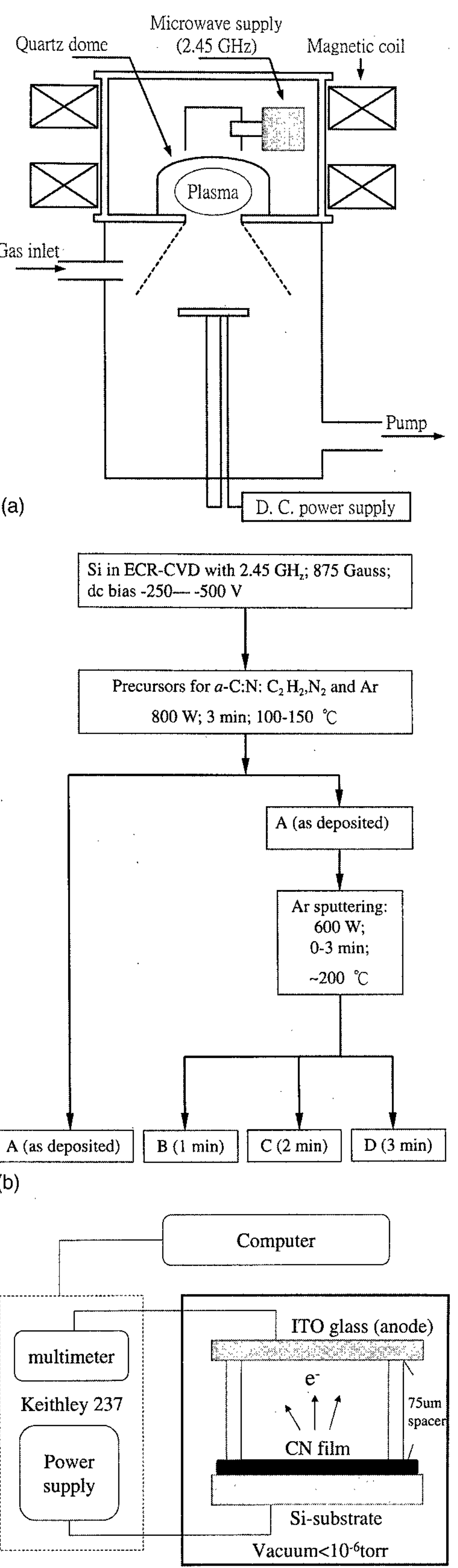

FIG. 1. Experimental setup and specimen preparation, (a) schematic illustration of the ECR–CVD system, (b) flow chart and for sample preparation designation, and (c) diode method (Keithley 237) for field emission measurements.

for survey scan spectra and 0.2 eV for core-level spectra. All peaks of core-level spectra were fitted with the same value for the full width at half maximum. The N/C ratios were obtained by integrating the core-level peak area of N(1s) and C(1s), corrected by the atomic sensitivity factors [(ASF) C: 0.296 and N: 0.477] based upon the empirical peak area values[30,34] modified for the system's transmission function. The resultant films indicate that the N/C ratio could reach as high as 35%.

C. Field emission

The electron field emission characteristics of the amorphous carbon nitride thin films were measured by the conventional diode method[35] at an ambient pressure of 1.3 $\times 10^{-3}$ Pa (10^{-5} Torr). The films (0.5×0.5 cm^2) were separated from the anode by indium tin oxide (ITO) coated glass, where the glass fiber spacer was maintained at 75 μm from the cathode, as shown in Fig. 1(c). The current density and electric field ($J-E$) characteristics were measured using an electrometer (Keithley 237). The results were reproducible over periods of weeks and the films did not degrade with exposure to atmospheric conditions. The electron field emission properties were analyzed using the Fowler–Nordheim (F–N) model,[36] viz., $I = aV^2 \exp(-b\Phi_e^{3/2}/V)$, where a and b are constants. The turn-on voltage was estimated as the voltage deviates from $\ln(I/V^2) - I/V$ curve. The effective work function ($\Phi_e = \Phi/\beta$) of the films was calculated from the slope of the F–N plot, where β is the field enhancement factor and Φ is the true work function of the material.

III. RESULTS AND DISCUSSION

$J-E$ curves and F–N plots for the a-C:N film as deposited on Si by the ECR plasma (sample A) and after the subsequent Ar^+ plasma sputtering treatments from 1 to 3 min (samples B, C, and D) are shown in Figs. 2(a) and 2(b), respectively. Ten specimens for each specific condition were prepared as statistical evidence and a scattering within ±0.1 eV were found for the calculated onset field and effective work function of the a-C:N films. The onset field of the a-C:N films occurs at about 3.5 V/μm and an emission current density of up to 0.4 mA/cm^2 at 12.2 V/μm for same Ar^+ plasma sputtering treatments is shown in Fig. 2(a). The onset field is defined here as the applied macroscopic electric field at which a steady-state emission current of 1 nA is measured for a given film.[37] Linear F–N characteristics indicate that the field emission is responsible for the acquired currents, as shown in Fig. 2(b). Our calculation of the applied field is simply the applied voltage divided by the anode to cathode separation as in a parallel plane geometry. In our case, the onset field is 3.5 V μm^{-1} and the distance from ITO to specimen is 75 μm [Fig. 1(c)]. The applied voltage is therefore the product of 3.5 V μm^{-1} and 75 μm; a value of 263 V is directly recorded on an electrometer (Keithley 237).

It is apparent that the onset field of Ar^+ plasma sputtered a-C:N films (samples B, C, and D) is lower than for the film as deposited without Ar^+ sputtering (sample A). The lowest onset field (~3.5 V μm^{-1}) was obtained from the a-C:N films treated by Ar^+ plasma sputtering for 3 min (sample D). For this sample, an emission current density up to 0.4 mA/cm^2 at 12.2 V μm^{-1} was observed. The film's effective work function (Φ_e), calculated from the slope of the F–N plot, was found as low as 0.99 eV (Table I). However, sputtering times longer than 3 min often led to an increase of the onset field for electron emission. In this study, the F–N relation was clearly established and the slope of which gives the value directly related to the work function of the a-C:N film [Fig. 2(b)]. A tendency of the increase of the work function resulting from the increase of the onset field is therefore obtained and listed in Table I.

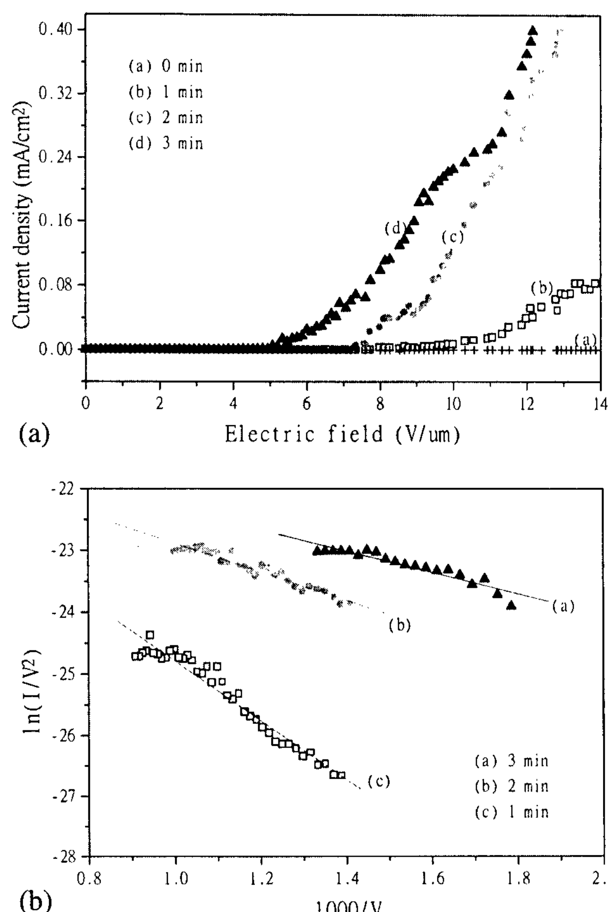

FIG. 2. a-C:N films as deposited (sample A) and with subsequent Ar^+ sputtering for 1 min (sample B), 2 min (sample C), and 3 min (sample D): (a) $J-E$ characteristics and (b) F–N plots.

The AFM examination of sample A indicates that the film surface is relatively smooth (<10 nm), as shown in Fig. 3(a). The mean roughness over an area of 20×20 μm^2 is 4.89 nm (root mean square, R_{rms} 6.1 nm). The maximum roughness in this study can reach a value of 44.2 nm which is however much smaller than the gap (75 μm) between anode and cathode and is apparently dependent on the length of the Ar^+ sputtering time. The AFM surface morphology of the Ar^+ plasma sputtered films for samples B, C, and D is shown in Figs. 3(b), 3(c), and 3(d), respectively.

The thickness of these films measured by FE–SEM de-

TABLE I. Onset field, effective work function, thickness, and mean and maximum roughness of the *a*-C:N films as a function of Ar^+ sputtering time.

Ar^+ sputtering time	Onset field ($\pm$0.1 V/μm)	Effective work function ($\pm$0.1 eV)	Thickness (μm)	Mean roughness (nm)	Maximum roughness (nm)
As-deposited	···	···	1.53	4.89	18.31
1 min	6.67	2.84	1.03	28.40	67.87
2 min	5.87	1.92	0.88	14.02	31.40
3 min	3.55	0.99	0.83	22.26	44.21

creases with increasing Ar^+ plasma sputtering time due to the ion bombardment of the film surface under the applied negative dc bias voltage. The thinner film seems more favorable for the field emission because the film can be more fully depleted,[31] thus an electron can gain enough energy with respect to the conduction band at low thickness for them to be able to surmount the emission barrier to vacuum.[37] Also, a thinner film is beneficial in that it reduces the scattering of electrons and increases the probability that an electron will be emitted through the emission barrier of the *a*-C:N/vacuum interface.[31] Therefore, the high-energy ions can promote the migration and rearrangement of atoms of the *a*-C:N substrate. Taking into consideration that atom mobility can be enhanced by the substrate bias voltage, it may conclude that progressive growth of the graphitic domains occurred in the films under the influence of the higher negative substrate bias voltages (−500 V) chosen in this study.[38] The field emission characteristics can be enhanced by increasing the graphitic content.[39] The values of mean roughness, maximum roughness, thickness, effective work function, and onset field are listed in Table I as a function of Ar^+ plasma sputtering time.

The Raman spectra of *a*-C:N films are given in Fig. 4(a) as a function of Ar^+ plasma sputtering time. The spectra

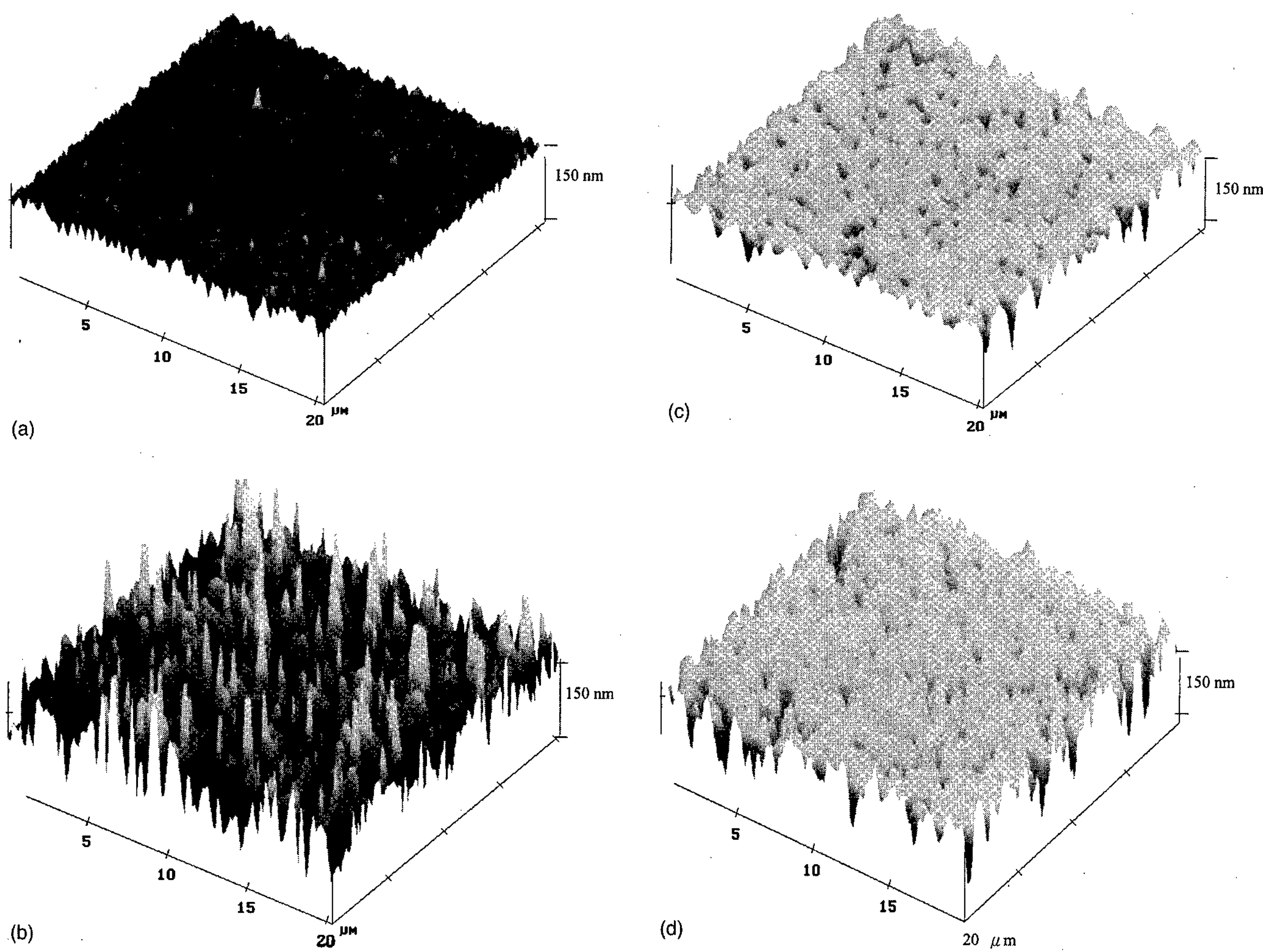

FIG. 3. AFM images of *a*-C:N films: (a) as-deposited (sample A), (b) 1 min (sample B), (c) 2 min (sample C), and (d) 3 min (sample D).

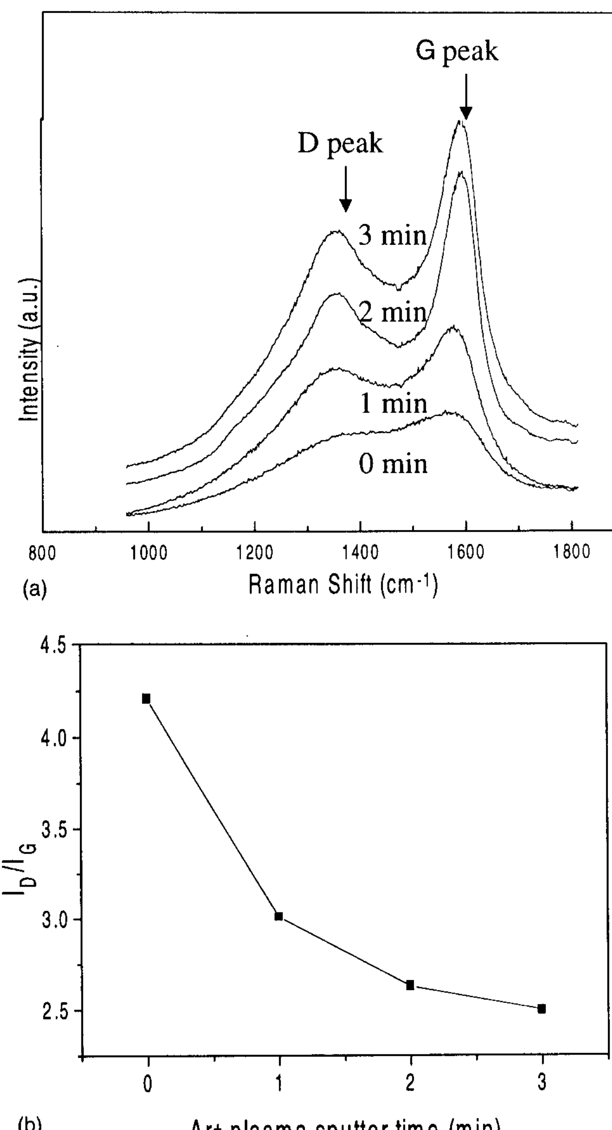

FIG. 4. Analysis and deconvolution of the Raman spectrum for a-C:N, (a) specimens as deposited and after Ar^+ sputtering from 1 to 3 min. (b) The change of intensity ratio I_D/I_G as a function of Ar^+ sputtering time.

shows two distinct peaks around 1373 cm^{-1} (D band) and 1580 cm^{-1} (G band) which are characteristic of disorder and graphitic carbon. The sp^2 contents of a-C:N were also characterized by Raman spectroscopy. Apparently, as the sp^2 content of the film increases, the ratio of the intensity of the disorder peak at 1373 cm^{-1} to the graphite carbon peak at 1580 cm^{-1} (I_D/I_G ratio) decreases, as shown in Fig. 4(b). This ratio reduction is a result of an increasing substrate temperature with an increasing Ar^+ sputtering time.

Recent studies[21] indicate that the damage on the a-C:N film surface caused by Ar^+ plasma sputtering results in the conversion of sp^3 to sp^2 due to reduction of the band gap. The sp^2 structure acts as a conduction part of the amorphous network,[10,15,17] and the graphitic carbon formation is due to the presence of the sp^2 structure.[40] Consequently, electron emission could be from the sp^2 cluster edges[37] brought about by lowering the work function and raising the Fermi level

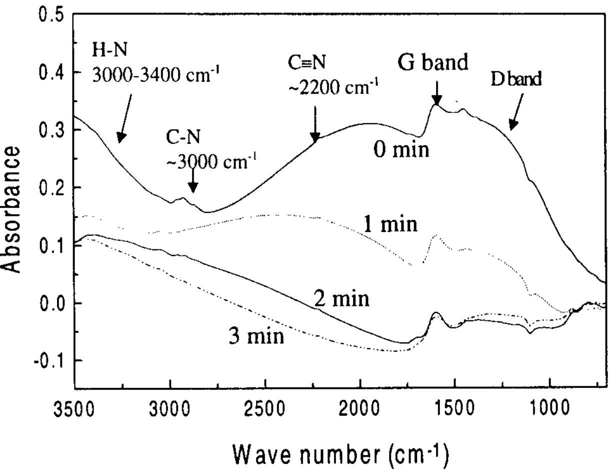

FIG. 5. FTIR spectra of the a-C:N films for as-deposited and after subsequent Ar^+ plasma sputtering from 1 to 3 min.

toward the conduction band. The latter is due to a defect-induced energy band and impurity desorption created by sp^2 content which is reasonable for the field emission enhancement.[39]

FTIR spectra obtained from as-deposited a-C:N films and after Ar^+ plasma sputtering are shown in Fig. 5. The spectra can be divided into four regions. The first region includes the C–C, C–N, and C–H modes from 1000 to 1700 cm^{-1} wherein the broad absorption band is the strongest evidence of the incorporation of nitrogen atoms into the amorphous carbon network.[41] The second region contains two subregions at 2100–2150 and 2065–2260 cm^{-1} that were assigned, respectively, to the nitrile and isonitrile C≡N and C≡C stretching vibrations.[42] The third region contains C–H stretching modes from 2800 to 3050 cm^{-1}, and the fourth region, at 3100–3400 cm^{-1} is associated with to NH, OH, or CH stretching vibrations.[43] These spectra indicate that a large amount of bonded hydrogen is reduced in the films. The FTIR results provide evidence that, in the films studied here, nitrogen is incorporated into the carbon network, in a manner similar to that reported previously.[17] Figure 5 indicates that the main change in the a-C:N film after Ar^+ plasma sputtering is the significant decrease of $C(sp^3)-H$ adsorption. This is consistent with the removal of hydrogen from the film as a result of bombardment with the energetic Ar^+ plasma. The decrease of hydrogen presumably causes the increase of sp^2-bonded carbon fraction which corresponds to the increasing intensity of the G band in Raman spectra. But, in FTIR spectra, such changes could not be analyzed quantitatively. The signal sizes in the wave number ranges of 3100–3400 cm^{-1} (NH, OH, or CH stretching modes) and 2800–3050 cm^{-1} (C–H stretching modes) decrease with increasing Ar^+ sputtering time. So the extent of emission current increase and the onset field decrease, occurring with decreasing H content in the Ar^+ plasma surface-treated a-C:N film, are affected by raising the Fermi level and by decreasing the electron resistivity and optical band gap due to the decreasing H content.[38]

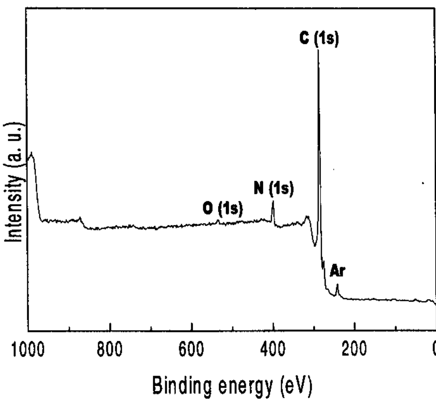

FIG. 6. XPS survey spectra ranging from 0 to 1000 eV for an *a*-C:N film after 3 min Ar^+ plasma sputtering with the application of a negative dc bias of −500 V.

Figure 6 shows the XPS survey scan spectra ranging from 0 to 1000 eV (5 min *in situ* Ar sputtering in XPS) for an *a*-C:N film after 3 min Ar^+ plasma sputtering (sample D). The N/C ratio was obtained by integrating the core-level peak area of N(1*s*) and C(1*s*), corrected by the ASF (C: 0.296 and N: 0.477) which are based upon the empirical peak area values[30] modified for the system's transmission function. Such calculations indicated that the N/C ratio could reach as high as 35%. A recent study[44] indicated that the emission current increase and the onset field decrease are due to the formation of a film with a higher concentration of N possessing a larger percentage of π bonds of carbon (C_π); this could lead to an increase in the carbon sp^2 content. It may also suggest that nitrogenation leads to triple bonded C–N sites.

IV. CONCLUSIONS

In summary, the field emission characteristics of *a*-C:N films were measured by the conventional diode method. The lowest onset field (~3.5 V μm^{-1}) was obtained from the *a*-C:N film after Ar^+ plasma sputtering for 3 min. This film was associated an emission current density up to 0.4 mA/cm^2 at 12.2 V μm^{-1}. The corresponding Φ_e value of this film was calculated from the slope of the F–N plot and found to be as low as 0.99 eV. The reasons for the reduction of the onset field and Φ_e as Ar^+ plasma sputtering time increased include a decreasing film thickness, an increasing film roughness, an increasing graphitic (sp^2) content and an increasing removal of hydrogen. Also, the NEA of *a*-C:N is suggested for enhancing emission current. In addition, XPS measurements indicated that the N/C ratio in the resultant films could reach as high as 35%.

ACKNOWLEDGMENT

This research was supported by the National Science Council of the Republic of China under the contract number of NSC 88-2216-E-007-029.

[1]I. Brodie and C. A. Spindt, Adv. Electron. Electron Phys. **83**, 1 (1992).
[2]I. Brodies and P. R. Schwoebel, Proc. IEEE **82**, 1006 (1994).
[3]J. E. Jaskie, Mater. Res. Bull. **21**, 59 (1996).
[4]S. R. P. Silva, G. A. J. Amaratunga, and J. R. Barnes, Appl. Phys. Lett. **71**, 1477 (1997).
[5]M. W. Geis, J. A. Gregory, and B. B. Pate, IEEE Trans. Electron Devices **38**, 619 (1991).
[6]M. W. Geis, J. C. Twichell, J. Macaulay, and K. Okano, Appl. Phys. Lett. **67**, 1328 (1995).
[7]N. S. Xu, R. V. Latham, and Y. Tzeng, Electron. Lett. **29**, 1596 (1993).
[8]E. J. Chi, J. Y. Shim, H. K. Baik, and S. M. Lee, Appl. Phys. Lett. **71**, 324 (1997).
[9]G. A. J. Amaratunga and S. R. P. Silva, Appl. Phys. Lett. **68**, 2529 (1996).
[10]A. Weber, U. Hoffmann, and C.-P. Klages, J. Vac. Sci. Technol. A **16**, 919 (1998).
[11]K. Okano, S. Koizumi, S. R. P. Silva, and G. A. J. Amaratunga, Nature (London) **381**, 140 (1996).
[12]P. Lerner, N. M. Miskovsky, and P. H. Cutler, J. Vac. Sci. Technol. B **16**, 919 (1998).
[13]M. W. Geis, J. C. Twichell, N. N. Efremow, K. Krohn, and T. M. Lyszczarz, Appl. Phys. Lett. **68**, 2294 (1996).
[14]K. Okano, A. Hiraki, T. Yamada, S. Koizumi, and J. Itoh, Ultramicroscopy **73**, 43 (1998).
[15]O. Groning, O. M. Kuttel, P. Groning, and L. Schlapbach, Appl. Phys. Lett. **71**, 2253 (1997).
[16]B. S. Satyanarayana, A. Hart, W. I. Milne, and J. Robertson, Appl. Phys. Lett. **71**, 1430 (1997).
[17]E. J. Chi, J. Y. Shim, D. J. Choi, and H. K Baik, J. Vac. Sci. Technol. B **16**, 1219 (1998).
[18]F. J. Himpsel, J. A. Knapp, J. A. Van Vechten, and D. E. Eastman, Phys. Rev. B **20**, 624 (1979).
[19]B. B. Pate, Surf. Sci. **165**, 83 (1986).
[20]K. C. Park, J. H. Moon, S. J. Chang, and J. H. Jang, J. Vac. Sci. Technol. B **15**, 454 (1997).
[21]J. H. Jung, B. K. Ju, H. Kim, M. H. Oh, S. J. Chung, and J. Jang, J. Vac. Sci. Technol. B **16**, 705 (1998).
[22]G. A. J. Amaratunga and S. R. P. Silva, J. Non-Cryst. Solids **198–200**, 611 (1996).
[23]E. I. Givargizov, V. V. Zhirnov, A. V. Kuznestov, and P. S. Plekhanov, J. Vac. Sci. Technol. B **74**, 2030 (1996).
[24]J. Chen *et al.*, J. Vac. Sci. Technol. B **16**, 697 (1998).
[25]S. L. Sung, T. G. Tsai, K. P. Huang, J. H. Huang, and H. C. Shih, Jpn. J. Appl. Phys., Part 2 **37**, L148 (1998).
[26]A. Y. Liu and M. L. Cohen, Science **245**, 841 (1989).
[27]A. Y. Liu and M. L. Cohen, Phys. Rev. B **55**, 10727 (1997).
[28]S. L. Sung, S. H. Tsai, C. H. Tseng, X. W. Liu, and H. C. Shih, Appl. Phys. Lett. **74**, 197 (1999).
[29]S. L. Sung, S. H. Tsai, X. W. Liu, and H. C. Shih, J. Mater. Res. **15**, 502 (2000).
[30]S. L. Sung, C. H. Tseng, X. J. Guo, F. K. Chiang, X. W. Liu, and H. C. Shih, Thin Solid Films **340**, 169 (1999).
[31]L. K. Cheah, X. Shi, B. K. P. Silva, and Z. Sun, Diamond Relat. Mater. **7**, 640 (1998).
[32]K. C. Park, J. H. Moon, S. J. Chang, and J. H. Jang, J. Vac. Sci. Technol. B **15**, 431 (1997).
[33]A. Modinos and J. P. Xanthakis, Appl. Phys. Lett. **73**, 1874 (1998).
[34]S. H. Tsai, C. W. Chao, C. L. Lee, X. W. Liu, I. N. Lin, and H. C. Shih, Electrochem. Solid-State Lett. **2**, 247 (1999).
[35]F. Y. Chuang, C. Y. Sun, T. T. Chen, and I. N. Lin, Appl. Phys. Lett. **69**, 3504 (1996).
[36]Y. H. Chen, C. T. Hu, and I. N. Lin, Appl. Phys. Lett. **84**, 3890 (1998).
[37]R. D. Forrest, A. P. Burden, S. R. P. Silva, L. K. Cheah, and X. Shi, Appl. Phys. Lett. **73**, 3784 (1998).
[38]J. H. Kim and Y. H. Kim, Thin Solid Films **289**, 79 (1996).
[39]W. P. Kang, A. Wisitsora-at, J. L. Davidson, D. V. Kerns, Q. Li, J. F. Xu,

and C. K. Kim, J. Vac. Sci. Technol. B **16**, 684 (1998).
[40]I. T. Han, N. Lee, S. W. Lee, S. H. Kim, and D. Jeon, J. Vac. Sci. Technol. B **16**, 2052 (1998).
[41]J. H. Kaufman, S. Metin, and D. D. Saperstein, Phys. Rev. B **39**, 13053 (1989).
[42]D. L. Vien, N. B. Colthup, W. G. Fateley, and J. G. Grasselli, *The Handbook of Infrared and Raman Characteristic Frequencies of Organic Molecules* (Academic, New York, 1991).
[43]C. W. Ong, X. A. Zhao, and Y. C. Tsang, Thin Solid Films **1–4**, 280 (1996).
[44]K. C. Park, J. H. Moon, S. J. Chang, M. H. Oh, W. I. Miline, and J. Jang, J. Vac. Sci. Technol. B **15**, 428 (1997).

Self-assembled gold silicide wires on bromine-passivated Si(110) surfaces

B. Rout, B. Sundaravel,[a] Amal K. Das, S. K. Ghose, K. Sekar,[b] D. P. Mahapatra, and B. N. Dev[c]
Institute of Physics, Sachivalaya Marg, Bhubaneswar 751005, India

(Received 14 February 2000; accepted 28 April 2000)

Thin Au films (~45 nm) deposited by thermal evaporation under high vacuum on bromine-passivated Si(110) substrates, upon annealing showed the formation of long gold silicide wire-like islands on top of a thin uniform layer of gold silicide in a self-assembled Stranski–Krastanov growth process. Optical micrographs showed long, straight and narrow islands with aspect ratios as large as 200:1. Scanning electron microscopy images revealed the presence of facets. The islands are aligned along the $[\bar{1}10]$ direction on the Si(110) surface. Rutherford backscattering spectrometry measurements with an ion microbeam identified the islands to possess varying thickness across a single island as one would expect for islands having facets and also showed the uniform silicide layer over the Si substrate to be very thin (~1.5 nm). The observed alignment of the gold silicide islands on the Si(110) surface has been explained in terms of the lattice mismatch between gold–silicide and silicon and invoking the theory of shape transition in heteroepitaxial growth. We have observed islands as long as 200 μm and as narrow as 100 nm in this nonultrahigh vacuum growth on chemically passivated Si(110) surfaces. The method, with properly optimized parameters, may provide a way to grow *quantum wires*. © *2000 American Vacuum Society.* [S0734-211X(00)04404-8]

I. INTRODUCTION

Passivation of silicon surfaces ((111) and (110)) against oxidation by adsorbed bromine, observed in x-ray standing wave studies[1–4] and theoretical calculations,[5] has raised a number of questions and possibilities of both scientific and technological significance. These include the possibility that such passivated surfaces might permit bonding and even epitaxy of thin overlayer films on silicon without the expensive and, from a production standpoint, unacceptable need for ultrahigh vacuum (UHV) processing. The Br/Si interface has proven to be an extremely stable system for non-UHV analysis.[6] In addition, the nature and extent of apparent passivation, the puzzling absence of bromine passivation on Si(100) surfaces and the interaction of the passivated surface with overlayer films required further careful studies. In recent years many studies were done to address these questions. The difference in passivation for the (111) and (100) surfaces apparently arises from the difference in the number of dangling bonds per surface Si atom and their orientations.[7] Upon Br adsorption the chemical changes incorporating oxygen are much faster with concomitant higher rate of Br desorption for the Si(100) surfaces, in comparison to Si(111) surfaces.[8] Recently the studies of growth on chemically bromine-passivated Si(111) (denoted hereafter by Br–Si(111)) surfaces have shown many interesting results. Thin Cu films deposited under high vacuum on Br–Si(111) surfaces showed interdiffusion behavior across the interface similar to that for Cu films deposited under UHV on an atomically clean Si(111) (7×7) surface.[7,9] An Au/Br–Si(111) system, annealed around the Au–Si eutectic temperature (363 °C) under high vacuum showed the formation of epitaxial eutectic gold silicide islands[10] and an epitaxy-driven fractal structure of Au.[11] Many of the growth features are similar to those obtained in UHV experiments.[12] Small silicide islands have been found to grow in the form of equilateral triangles following the threefold symmetry of the Si(111) surface. Large islands show a triangle-to-trapezoid shape transition associated with strain relaxation in this gold–silicide/silicon heteroepitaxial structure.[13] On the vicinal substrate a directional growth of these elongated islands was obtained along the step directions. The interface sharpness, the chemical nature of the silicide and the interface Br diffusion upon annealing have also been studied for this system.[14] On the phenomenon of shape transition in heteroepitaxial systems the first experimental results were provided with epitaxial growth on the Br–Si(111) surface.[13] This phenomenon was later reported for another system where ion implantation was used to prepare a heteroepitaxial system.[15] To complete the study of noble metal films on Br–Si(111), epitaxial Ag layers have also been grown on Br–Si(111) surfaces.[16]

The formation of self-assembled silicide islands on Br–Si(111) surfaces following the substrate symmetry and the transition to an elongated structure[13] made us believe that long wire-like structures could be formed on a surface with a twofold symmetry, such as a Si(110) surface. On a surface with a twofold symmetry, anisotropic diffusion can also give rise to wire-like structures.[17] Since passivation of Si(110) surfaces with bromine has been possible,[1,3] we have under-

[a]Present address: Department of Electronic Engineering and Materials Technology Research Center, Chinese University of Hong Kong, Shatin, Hong Kong.
[b]Present address: Department of Materials Science & Engineering, University of Virginia, Charlottesville, VA 22903.
[c]Author to whom correspondence should be addressed; electronic mail: bhupen@iopb.res.in

 ©2000 American Vacuum Society

taken a growth study on Br–Si(110) surfaces. Here we present the growth and analysis of wire-like gold silicide structures on Br–Si(110) surfaces. In this work we have used optical and scanning electron microscopy to study the morphology of the surface and the wire-like islands, Rutherford backscattering spectrometry (RBS) and secondary electron imaging with ion microbeam measurements to study the thickness and composition of the islands and the spatial distribution of Au and Si over the islands. Finally conventional RBS and channeling measurements were used to probe the crystalline nature of the silicide islands.

II. EXPERIMENT

Br-passivated symmetric Si(110) substrates were prepared using the procedure as described below. First the substrates were cleaned thoroughly with de-ionized (resistivity ~18.2 MΩ cm) distilled water and then rinsed in methanol. This was followed by another cleaning with trichloroethylene and a final rinse in methanol. The substrates were then pull dried. In order to remove the native oxide layers the cleaned substrates were etched in hydrofluoric acid (48% HF) for 5 min. As the substrates were pulled out of HF, a 0.05% bromine–methanol solution was squirted onto them from a squirt bottle taking care that the surfaces were not exposed to atmosphere prior to being wet by this solution. Then the substrates were rinsed in methanol to remove the unbonded Br and finally dried with dry nitrogen gas. Thin Au films were deposited by thermal evaporation under high vacuum ($\sim 2 \times 10^{-6}$ mbar). The samples were then annealed at 360 ±10 °C, i.e., around the Au–Si eutectic temperature (363 °C), for 30 min under high vacuum conditions ($\sim 2 \times 10^{-5}$ mbar).

Optical microscopy, scanning electron microscopy and RBS experiments were performed. For the RBS studies we used the ion microbeam facility at the State University of New York at Albany.[18,19] A 3.3 MeV He^+ beam of ~2 μm diameter full width half maximum (FWHM) was used for the RBS studies. Conventional RBS and channeling (RBS/C) experiments were performed with a 1.052 MeV He^+ beam of ~1.5 mm diameter, using the 3 MV Pelletron accelerator facility in our laboratory. Details of the RBS/C techniques[20,21] and the experimental setup in our laboratory[9,21] may be obtained elsewhere.

III. RESULTS AND DISCUSSIONS

A. Optical microscopy and scanning electron microscopy (SEM)

The optical micrograph of an annealed Au/Br–Si(110) sample, which had a uniform Au layer of 45 nm thickness before annealing, is shown in Fig. 1, where formation of long narrow straight wire-like structures are seen. Aspect ratios of some of these long islands as large as 200:1 have been observed. Growth of elongated structures on Si surfaces has also been observed in earlier studies. For example, in the case of gold silicide islands grown on Br–Si(111), an aspect ratio as large as 15:1 was observed in the case of islands with a uniform width[13] and 30:1 in the case of islands with a slightly nonuniform width.[10] Rod shaped gold silicide islands with rounded corners have been observed by Mundschau *et al.*[12] in their low energy electron microscopy studies of annealed gold films on an atomically clean Si(111) surface. Mo *et al.*[22] observed an elongated growth of Ge on the Si(001) surface with an aspect ratio ~60:1. Also growth of pure metal like Ag on Si(001) in wire-like structures has been observed.[23] The major cause of growth of such elongated islands has been identified with relaxation of strain which is associated with heteroepitaxial growth. In heteroepitaxial growth small islands can grow following the symmetry of the substrate. Larger islands can undergo a shape transition to form elongated islands as shown in the theoretical work by Tersoff and Tromp[23] and in the experimental work by Sekar *et al.*[13] Anisotropic diffusion on the surface can also lead to formation of elongated structures.[17] On a Si(110) surface, with its twofold symmetry and structural openness along one direction, the anisotropic diffusion process is likely to be significant. This may be partly responsible for the long wire-like growth.

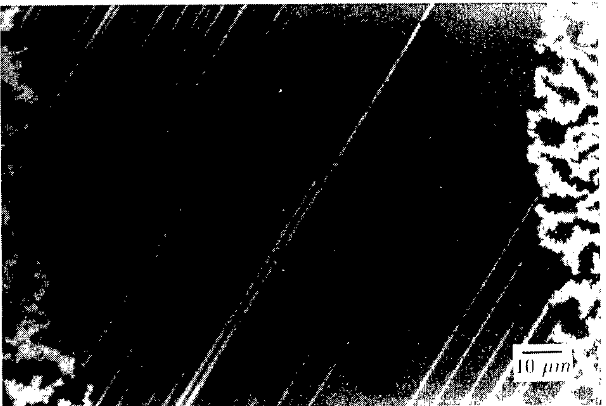

FIG. 1. An optical micrograph of an annealed Au/Br–Si(110) sample showing the formation of wire-like islands. The initial thickness of the uniform Au film was about 45 nm.

On a Si(111) surface, besides the formation of epitaxial silicide islands, concomitant formation of gold fractal structures was observed,[11,13] where this has been called epitaxy driven fractal growth.[11] Here we also observe some stringy structures of gold as seen along the left and the right edges of Fig. 1. For a gold film of higher initial thickness (~85 nm), wider straight islands also appear to form. One such case is shown in Fig. 2, where island facets also are clearly seen. The longer edges of the islands are aligned along the [$\bar{1}$10] direction. The wire-like island growth is not uniform over all the surface. This may be due to the nonuniformity of the Br-passivated surface.

B. RBS and secondary electron images with an ion microbeam

Secondary electrons have been generated from the sample surface by an incident 3.3 MeV He^+ ion microbeam of ~2 μm (FWHM) diameter. The ion beam was scanned on the sample surface and the backscattered secondary electrons

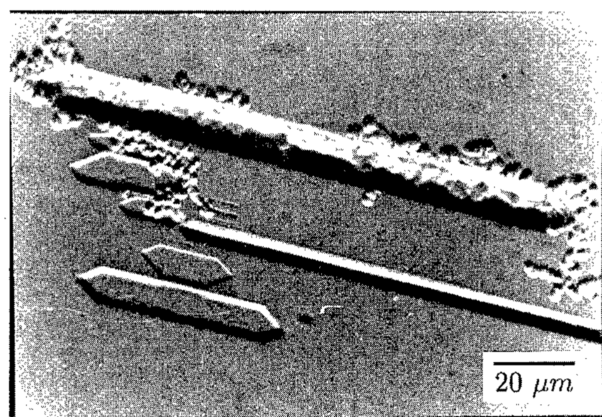

FIG. 2. SEM micrograph of an annealed sample showing facets in the case of a relatively larger initial thickness of Au (~85 nm).

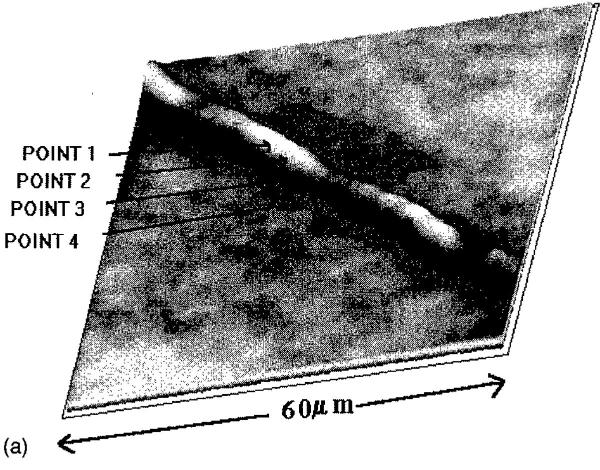

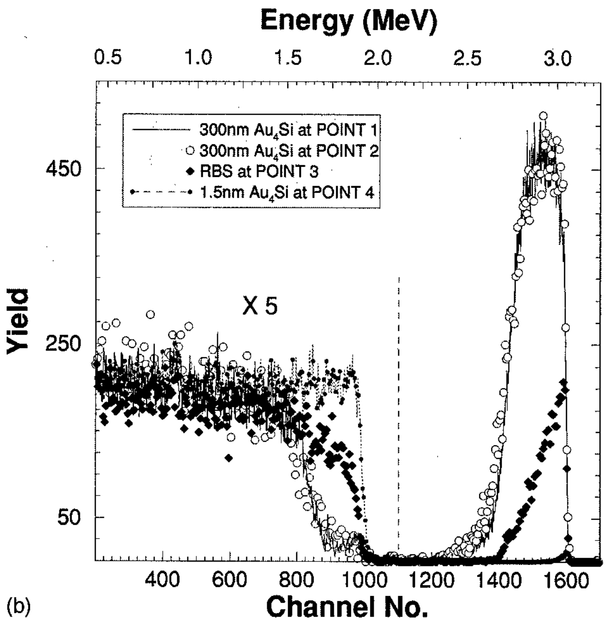

FIG. 3. (a) A secondary electron image of a part of a long island obtained with a scanning ion microbeam. (b) RBS spectra with the ion microbeam incident at several points indicated in (a).

were collected and processed to obtain a quick image of the surface, which shows the wire-like structures such as those in Fig. 1. After an island has been located the backscattered He^+ ions are detected in a surface barrier detector, by scanning the ion beam over a region around the island, and collecting data in a three dimensional array with the third dimension corresponding to channel number (energy) of the backscattered ions. This provides a RBS spectrum at each position coordinate (x,y) on the sample surface. Taking the intensities in the RBS spectra over an appropriate energy window a depth distribution map for a given species (elemental map) is obtained. Generally it takes about 10–30 min to obtain a good quality (statistics) elemental map. A backscattered secondary electron image of the sample surface can be obtained within 10–15 s, and it provides only the surface topographic information.

A backscattered secondary electron image of a part of a long island is shown in Fig. 3(a). Figure 3(b) shows the RBS spectra for the ion beam incident at several points shown in Fig. 3(a). At the middle of the island (points 1 and 2), as the spectrum simulation[24] suggests, the RBS spectra are consistent with a 300 nm Au_4Si layer on a Si substrate. Near the edge of the island (point 3), the layer thickness is much smaller and the shape of the spectrum is representative of a rounded structure, i.e., the region under the ion beam has a variation in thickness. At this position a large part of the ion beam falls on the flat surface. Away from the island on the flat surface (point 4), there is still a 1.5 nm thick silicide present on silicon. This layer-plus-island (Stranski–Krastanov) growth was also seen for the case of silicide growth on Br–Si(111) surfaces.[10,13] Ion microbeam measurements have also been carried out on gold silicide islands grown on Br–Si(111) surfaces, showing similar results. One should note that the silicide thickness at the middle of the wire-like island is >3 times the initial uniform thickness (85 nm) of the deposited Au layer. Br passivation hinders the oxide growth on the surface and thus reduces the diffusion barrier across the interface.[9] This allows Si to diffuse into the Au layer easily and form the Au_4Si eutectic composition at the eutectic temperature. As the silicide islands grow in height, more Au is supplied into it by lateral diffusion of Au, the Si supply being continued from the substrate. This is how the island height can grow much taller than the initial Au layer thickness. The silicide island growth process, consistent with the RBS results in Fig. 3(b), is schematically shown in Fig. 4. The gold silicide/silicon interface is found to be sharp, as the lower edge of the gold signal from the silicide layer falls abruptly [spectra at points (1) and (2) of Fig. 3(b)], which is consistent with our secondary ion mass spectrometry (SIMS) analysis[14] done on gold silicide islands grown on Si(111) surfaces. The thickness of the uniform gold silicide layer varied somewhat for several samples. A gold elemental mapping image of a part of a long and narrower island is shown in Fig. 5. The image was obtained by collecting the integrated gold RBS signal up to 100 nm from the top surface of the sample.

As shown schematically in Fig. 4(b), lateral diffusion of

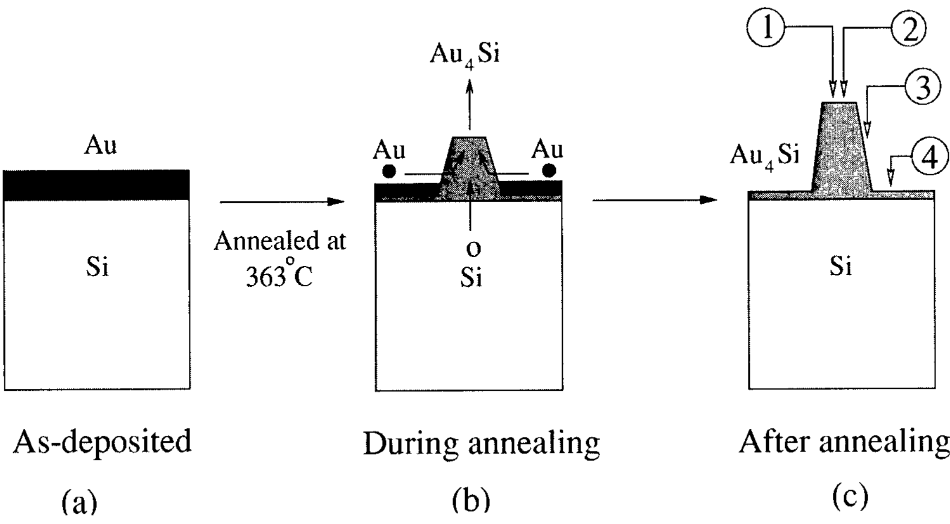

FIG. 4. Gold–silicide growth process upon annealing at the Au–Si eutectic temperature (363 °C) is shown schematically. Points (1), (2), (3), (4) in (c) correspond approximately to those in Fig. 3(a).

Au is necessary for the formation of gold silicide islands. In the process of lateral diffusion of Au, stringy patterns are also formed due to Au aggregation as seen on the left and the right edges of Fig. 1. This aggregation phenomenon along with Monte Carlo simulations has been presented in Ref. 11. A small portion of a stringy structure, obtained in a RBS map with backscattering signal from Au, is shown in Fig. 6.

C. Crystallinity and epitaxy of the silicide: RBS and channeling results

Evidence of the crystallinity of the silicide islands comes from the observation of facets in the islands. It is possible to determine the crystallinity of the silicide islands and their crystallographic relationship with the substrate by RBS and channeling experiments. Of course it would be nice to get a collimated (parallel) microbeam for channeling experiments. However, in the microbeam facility we used, axial channeling measurement is practically impossible as a very tight focusing of the ion beam is employed to obtain a microbeam. A conventional RBS/C experiment uses a beam diameter of ~1 mm. As seen from Fig. 1, for this sample, a 1 mm diam beam would not only see the wire-like islands, but also see unreacted gold in the stringy structure. This would make it difficult to observe the channeling effect in the silicide islands. One possibility is to remove the unreacted Au by etching the sample in aqua regia. In that case the Au signal will come only from gold silicide. However, it would be weak as the surface coverage of silicide islands is low. We have not performed RBS/C experiments for the gold silicide on the Br–Si(110) substrate. However, we have done that for gold silicide on the Br–Si(111) substrate, where we obtained a higher surface coverage of islands.[25] RBS/C experiments have been performed with the ion beam alignment along Si [111] as well as [110] (35.26° tilted with respect to [111]) directions. In both cases, the aligned RBS spectra show lower yield, indicating epitaxy of silicide with substrate Si. The RBS/C spectra for [110] axial channeling are shown in Fig. 7. The yield above channel No. 680 is due to Au in gold silicide islands. We notice a reduction in the Au yield for ion beam incidence along the [110] indicating that the silicide is crystalline. Also simultaneous reduction of the Si yield (below channel No. 680) indicates the epitaxy of the silicide islands on silicon. From this observed alignment along the [110] direction, we expect that the silicide islands on the Si(110) surfaces are also epitaxial. The peak on the aligned spectrum in Fig. 7 around channel No. 220 is due to carbon probably accumulated on the surface during etching in aqua regia.

Green and Bauer studied gold silicide growth in a Au film deposited on a Si(111) surface under UHV conditions.[26]

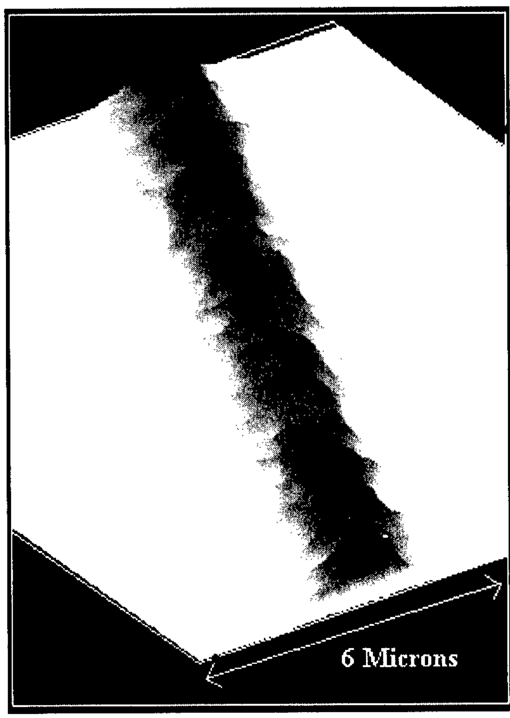

FIG. 5. Gold elemental mapping image of a part of a long island obtained by collecting integrated gold RBS signal up to 100 nm from the top surface of the sample. RBS intensity along with its color coding (white to black indicates increasing intensity) is shown in the third dimension.

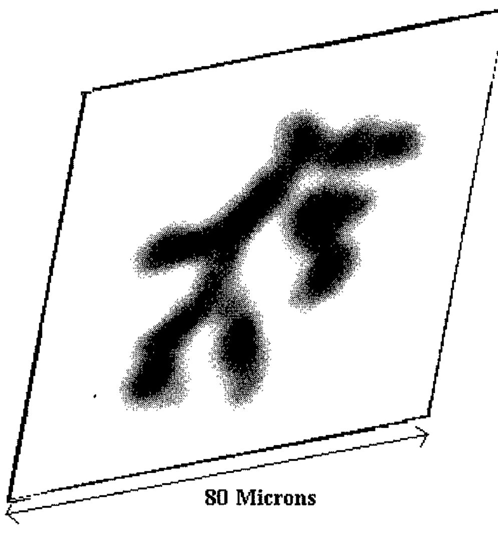

FIG. 6. Gold elemental mapping image of the stringy structures obtained by collecting gold RBS signals from 200 nm below the top surface of the sample. White to black indicates increasing intensity.

They obtained a silicide composition (17% Si, 83% Au) which is close to the eutectic composition and a rectangular unit cell with lateral periodicities of $a^s=0.935$ and $b^s=0.735$ nm in the silicide layer. Either the [01] or the [10] direction in the silicide is parallel to the $[1\bar{1}0]$ direction of the Si substrate. Three-dimensional crystalline gold silicide has also been studied by many workers. Nevertheless, detailed structures of gold silicide are not known. Various structures have been proposed. For gold silicide precipitates in silicon an orthorhombic structure with $a^s=0.960$, $b^s=0.768$ and $c^s=0.690$ nm has been proposed by Baumann and Schroeter.[27] However, they could not determine the atomic positions in the unit cell. They observed that the lattice vector b^s is aligned with a Si[110] direction. The lattice vector b^s is just twice the interatomic distance (2×0.384 nm) along the $[1\bar{1}0]$ direction on an ideal Si(111) surface — a favorable condition for epitaxy of the silicide grown on a Si(111) surface. Thus the observed b^s on the Si(111) surface and the b^s in the precipitate are nearly 2×0.384 nm along a $\langle110\rangle$ direction.

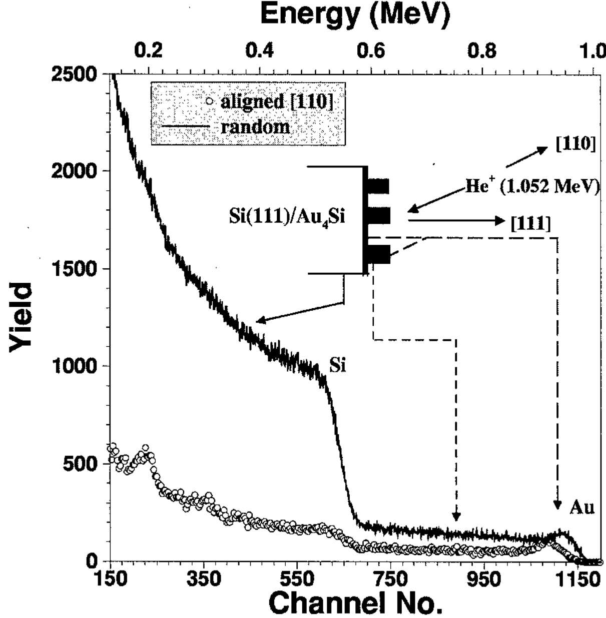

FIG. 7. Random and aligned RBS/C spectra for a gold silicide on Br–Si(111) sample with the ion beam incident along the [110] axial direction. Reduction in the aligned yield with respect to the random case indicates the crystalline nature of the silicide islands as well as its epitaxy with the Si substrate. (From Ref. 25.)

On a Si(110) surface a rectangular unit cell is defined with $a^{si}=0.543$ nm ($\|[00\bar{1}]$), $b^{si}=0.384$ nm ($\|[\bar{1}10]$) (Fig. 8). For epitaxial growth on a Si(110) surface, the fact that $2\times b^{si}\simeq b^s$ and the lattice matching is worse (a^s is 12% smaller than $2a^{si}$ or c^s is 27% larger than a^{si}) in the other direction $[00\bar{1}]$ would cause anisotropic strain in the epitaxial growth, and the strain-relief via shape transition[23] would favor the growth of elongated islands along the $[\bar{1}10]$ direction because of smaller or practically no strain along that direction. This is what is observed here. Of course anisotropic diffusion might also be partially responsible for the growth of long unidirectional islands on a surface with twofold symmetry like Si(110). Growth of Cu on the Pd(110) surface, which has a twofold symmetry, shows the formation of one-dimensional monatomic Cu wires along the $[\bar{1}10]$ direction, because of the Cu migration barrier anisotropy (0.76 and 0.51 eV for the orthogonal $[00\bar{1}]$ and $[\bar{1}10]$ directions, respectively).[17] For the Si(110) surface, from the positions of the surface Si atoms (Fig. 8), we notice that there are open channels along $[\bar{1}10]$ directions. So, like the Pd(110) surface, the migration barrier along the $[\bar{1}10]$ direction is expected to be lower compared to the $[00\bar{1}]$ direction. This would favor elongated growth along the $[\bar{1}10]$ direction. Thus both shape transition and anisotropic diffusion would lead to elongated island growth along the $[\bar{1}10]$ direction. Perhaps, this is the reason for the growth of unusually long silicide wires observed here.

A natural question is: what happens to the interfacial Br when the annealing takes place? As such the amount of Br on the Br–Si(111) or Br–Si(110) substrates is <1/3 monolayer, i.e., $<2\times10^{14}$ atoms/cm^2. It has been shown by SIMS analysis that Br tends to diffuse toward the surface upon annealing,[14] a behavior reminiscent of *surfactant mediated growth* where the *surfactant* layer floats on the thin films.

IV. CONCLUSIONS

Thin Au films deposited on Br–Si(110) surfaces and annealed at 363 °C (Au–Si eutectic temperature) have produced long wire-like gold silicide islands in a self-assembled growth process. The long straight islands as seen from the optical micrographs are narrow with an aspect ratio as large as 200:1. In the case of gold film of higher initial thickness, wider and straight islands are observed with clear faceting of islands. RBS measurements with the ion microbeam taken on a single island showed various thicknesses across the island.

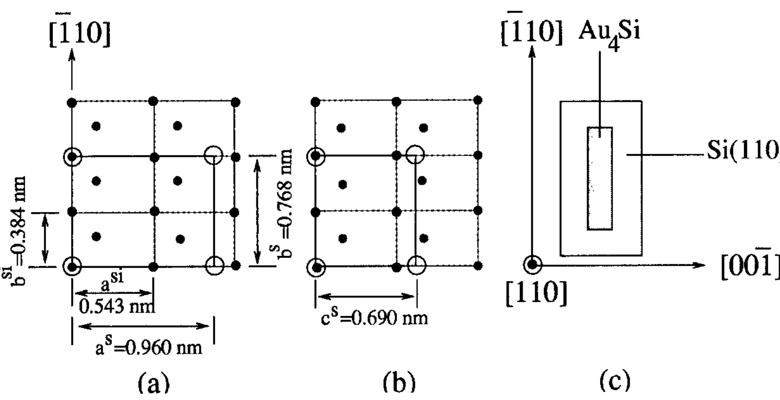

FIG. 8. Possible structural relationship between gold silicide (○) and Si (●). Either a^s (a) or c^s (b) of the silicide unit cell is along the Si[00$\bar{1}$] direction. Approximate lattice matching along the [$\bar{1}$10] direction ($b^s \approx 2 \times b^{Si}$) would produce a smaller strain along the [$\bar{1}$10] direction, causing an elongated island growth (c) along [$\bar{1}$10] through shape transition.

The thickness at the middle of the silicide wire-like islands is greater than three times the initial thickness of the deposited Au layer. The islands have grown on a thin uniform layer of silicide in a Stranski–Krastanov growth process. The thickness of the uniform layer over the Si substrate has been determined to be about 1.5 nm. The silicide/silicon interface is found to be abrupt. Starting from chemically passivated Si(110) substrates and non-UHV growth conditions, we have been able to show the possibility of producing long wire-like crystalline islands in a self-assembled growth process. Unfortunately, we could not identify thinner wires below the resolution limit of SEM. Such islands could be easily observed with atomic force microscopy. We believe it would be possible to grow *quantum wires* by this method with proper optimization of growth parameters. We have grown nanostructural Ge *dots* on deposited Ge layers on bromine-passivated silicon substrates.[28]

ACKNOWLEDGMENTS

The authors thank Professor W. M. Gibson and Professor H. Bakhru for offering their microbeam facility and A. W. Haberl for help with the experiments. They also thank Professor Bakhru and Mr. Haberl for their help in setting up an ion microbeam facility in the authors' laboratory. They also acknowledge the help of Dr. Vijaylakshmi for the SEM micrographs. The work was partially supported by Indo-US Project Nos. USIF 9403-01 and 9405.

[1]P. L. Cowan, J. A. Golovchenko, and M. F. Robbins, Phys. Rev. Lett. **44**, 1680 (1980).
[2]J. A. Golovchenko, J. R. Patel, D. R. Kaplan, P. L. Cowan, and M. J. Bedzyk, Phys. Rev. Lett. **49**, 560 (1982).
[3]M. J. Bedzyk, W. M. Gibson, and J. A. Golovchenko, J. Vac. Sci. Technol. **20**, 634 (1982).
[4]B. N. Dev, V. Aristov, N. Hertel, T. Thundat, and W. M. Gibson, Surf. Sci. **163**, 457 (1985).
[5]S. M. Mohapatra, B. N. Dev, K. C. Mishra, N. Sahoo, W. M. Gibson, and T. P. Das, Phys. Rev. B **38**, 12556 (1988).
[6]D. E. Aspnes and A. A. Studna, Proc. Soc. Photo-Opt. Instrum. Eng. **276**, 227 (1981); Appl Phys. Lett. **39**, 316 (1981).
[7]K. Sekar, P. V. Satyam, G. Kuri, D. P. Mahapatra, and B. N. Dev, Nucl. Instrum. Methods Phys. Res. B **71**, 308 (1992).
[8]K. Sekar, G. Kuri, D. P. Mahapatra, B. N. Dev, J. V. Ramana, S. Kumar, and V. S. Raju, Surf. Sci. **302**, 25 (1994).
[9]K. Sekar, P. V. Satyam, G. Kuri, D. P. Mahapatra, and B. N. Dev, Nucl. Instrum. Methods Phys. Res. B **73**, 63 (1993).
[10]K. Sekar, G. Kuri, P. V. Satyam, B. Sundaravel, D. P. Mahapatra, and B. N. Dev, Surf. Sci. **339**, 96 (1995).
[11]K. Sekar, P. V. Satyam, G. Kuri, D. P. Mahapatra, and B. N. Dev, Solid State Commun. **96**, 871 (1995).
[12]M. Mundschau, E. Bauer, W. Telieps, and W. Swiech, Surf. Sci. **213**, 381 (1989).
[13]K. Sekar, G. Kuri, P. V. Satyam, B. Sundaravel, D. P. Mahapatra, and B. N. Dev, Phys. Rev. B **51**, 14330 (1995).
[14]B. Sundaravel, K. Sekar, G. Kuri, P. V. Satyam, B. N. Dev, Santanu Bera, S. V. Narasimhan, P. Chakraborty, and F. Caccavale, Appl. Surf. Sci. **137**, 103 (1999).
[15]S. H. Brongersma, M. R. Castell, D. D. Petrovic, and M. Zinke-Allmang, Phys. Rev. Lett. **80**, 3795 (1998).
[16]B. Sundaravel, Amal K. Das, S. K. Ghose, K. Sekar, and B. N. Dev, Appl. Surf. Sci. **137**, 11 (1999).
[17]H. Roeder, E. Hahn, H. Brune, J. P. Bucher, and K. Kern, Nature (London) **366**, 141 (1993).
[18]W. G. Morris, W. Katz, H. Bakhru, and A. W. Haberl, J. Vac. Sci. Technol. B **3**, 391 (1985).
[19]W. G. Morris, S. Fesseha, and H. Bakhru, Nucl. Instrum. Methods Phys. Res. B **24/25**, 635 (1987).
[20]See for example, L. C. Feldman and J. W. Mayer, *Fundamentals of Surface and Thin Film Analysis* (North-Holland, New York, 1986).
[21]K. Sekar, G. Kuri, P. V. Satyam, B. Sundaravel, D. P. Mahapatra, and B. N. Dev, Indian J. Phys. **68A**, 1 (1994).
[22]Y. W. Mo, D. E. Savage, B. S. Swartzentruber, and M. G. Lagally, Phys. Rev. Lett. **65**, 1020 (1990).
[23]J. Tersoff and R. M. Tromp, Phys. Rev. Lett. **70**, 2782 (1993).
[24]The RBS spectra were simulated using GISA-3.95 ion scattering code; J. Saarilahti and E. Rauhala, Nucl. Instrum. Methods Phys. Res. B **64**, 734 (1992).
[25]B. Sundaravel, K. Sekar, P. V. Satyam, G. Kuri, B. Rout, S. K. Ghose, D. P. Mahapatra, and B. N. Dev, Indian J. Phys. **70A**, 687 (1996).
[26]A. K. Green and E. Bauer, J. Appl. Phys. **47**, 1284 (1976).
[27]F. H. Baumann and W. Schroeter, Philos. Mag. Lett. **57**, 75 (1988).
[28]Amal K. Das, S. K. Ghose, B. N. Dev, G. Kuri, and T. R. Yang, Appl. Surf. Sci. (in press).

Mechanism of laser-induced nanomodification on hydrogen-passivated Si(100) surfaces underneath the tip of a scanning tunneling microscope

Z. H. Mai, Y. F. Lu,[a] S. M. Huang, and W. K. Chim
Laser Microprocessing Laboratory, Department of Electrical Engineering and Data Storage Institute, National University of Singapore, 10 Kent Ridge Crescent, Singapore 119260

J. S. Pan
Institute of Materials Research and Engineering, National University of Singapore, 10 Kent Ridge Crescent, Singapore 119260

(Received 27 January 2000; accepted 14 April 2000)

Laser-induced nanomodification on hydrogen (H)-passivated Si(100) surfaces has been carried out underneath the tip of a scanning tunneling microscope (STM) in ambient air. The created features were characterized using STM, atomic-force microscopy (AFM), and Auger electron spectroscopy (AES). The features appeared as depressed regions in STM images, while they appeared as protruded regions in AFM images. Oxygen was detected in a modified $2\times2\ \mu m^2$ square region by AES, while no oxygen was detected elsewhere on the same sample surface. The experiment results and mechanism are discussed. Nano-oxide patterns, such as lines and dots, have been created. Dependence of oxide apparent depth on laser intensity, laser pulse numbers, tunneling current during modification, and laser incidence angle has been investigated. © *2000 American Vacuum Society.* [S0734-211X(00)02304-0]

I. INTRODUCTION

Nanofabrication is required in nanoelectronics, x-ray optics, and high-density data storage. Electron-beam lithography is a traditional technique for nanofabrication. However, the proximity effect limits the resolution. In response to the challenge in nanofabrication, scanning probe microscope (SPM)-based nanolithography has been studied extensively. One approach is based on nano-oxidation on hydrogen (H) -passivated Si surfaces using a SPM by applying a voltage between the sample and the tip.[1–6] In ambient air with humidity between 60% and 80%, oxidizing agents, such as O^- and OH^-, exist in the absorbed water layer. In a large electric field, the hydrogen atoms desorbe from the surface and are replaced by O^- or OH^-, forming the first monolayer of oxide. Then, O^- and OH^- drift across the oxide layer under the influence of the high electric field produced by the voltage between the tip and the sample, increasing oxide thickness.[7,8] At positive sample–tip bias, which is in the regime of anodic oxidation, the electric field not only enhances OH^- formation but also enhances the diffusion of OH^- through the oxide layer. At negative sample–tip bias, which was in the regime of cathodic oxidation, the electric field only enhances the OH^- formation. A reflection-mode scanning near-field optical microscope can also locally oxidize a H-passivated amorphous-silicon surface using a krypton laser with a wavelength of 350.7 nm.[9] It is believed that the Si–H bonds on the Si surface are directly broken by photons. Mullenborn *et al.*,[10] using a continuous-wave argon laser with the UV option, optically generated wafer-scale oxide patterns on H-passivated silicon, which can be used to connect the produced nanostructures to the macroscopic world.

In this study, we demonstrated that hydrogen-passivated Si surfaces could be locally oxidized in nanometer scale by 532 nm laser irradiation underneath the tip of a scanning tunneling microscope (STM). Chemical components of modified features were analyzed by Auger electron spectroscopy (AES). Nano-oxide patterns, such as lines and dots, were created. Experimental results and the mechanism are discussed. Dependence of oxide apparent depth on laser intensity, laser pulse numbers, tunneling current during modification, and laser incidence angles has been investigated.

II. EXPERIMENT

The experiment setup is shown in Fig. 1. A commercial STM was operated in air. The STM probe head has an open architecture, which allows an external laser beam being directly introduced to the tip–sample gap from 0° to 90°. During imaging and modification, the tip is fixed and the sample moves via a tube scanner. Tunneling voltages are provided by the tip bias, while the sample is grounded. A vertically polarized 532 nm Nd:YAG pulsed laser with a pulse duration of 7 ns and a maximum repetition rate of 10 Hz was focused to the tip–sample gap through a 100 mm planoconvex lens. The laser pulse energy is adjustable. The spot size of the focused laser beam is approximately 150 μm. An electrical shutter is inserted to switch the laser beam on and off during surface modification. Laser alignment was performed under a high-power optical charge-coupled-device (CCD) microscope by observing diffraction rings from the tip. During modification, the tube scanner and the electrical shutter are controlled by a commercial nanolithography software.

STM tips were homemade from a tungsten wire ($\Phi=0.25$ mm), using the electrochemical (EC) method.[11–13] The radii of curvature of the EC tungsten tips, which are determined by the cutoff time, are in the range from 10 to 50 nm. Tip aspect ratios and tip/meniscus shapes, which are determined

[a]Electronic mail: eleluyf@nus.edu.sg

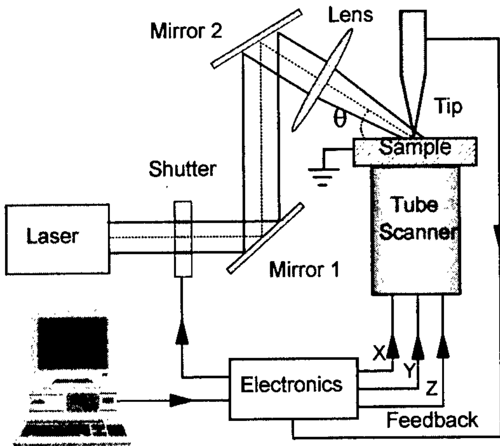

FIG. 1. Experimental arrangement.

by the length of wire in the solution, were observed under a high-power CCD optical microscope. *n*-type Si(100) samples with a resistivity of 10 Ω cm were passivated in a 5% HF solution for 30 s and then dried with a continuous nitrogen flow without water rinsing.

The scanner moves in a constant-current mode during imaging and modification. For H-passivated Si surfaces, a tunneling voltage of 1 V and a tunneling current, ranged from 0.1 to 3 nA, were used for both imaging and modification. No electric-field-induced oxidation was observed with these parameters.

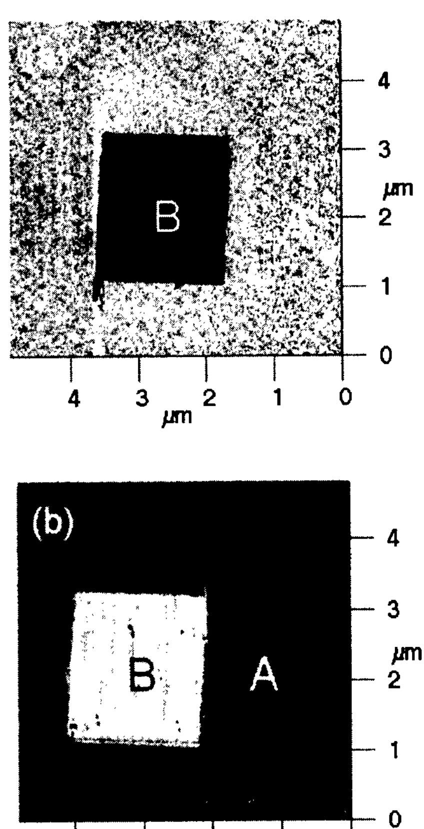

FIG. 2. STM (a) and AFM images (b) of a modified square region used for the AES analysis.

III. RESULTS AND DISCUSSION

The modified square region in Fig. 2 was created at a laser intensity of 3 MW/cm^2. The square region includes 256 lines modified with a scan rate of 10 s per line. The laser repetition rate was 10 Hz. A fast scan rate can be expected using a laser with a high repetition rate. The incident laser beam was in parallel with the sample surface. The feature topography was characterized by both STM and the scanning atomic-force microscope (AFM). Although the square region appeared as a depressed feature in the STM image, it appeared as a protruded feature in an AFM image of the same region. If we assume that the modified region was oxidized, it can be explained that the STM image of the modified region is due to its low conductivity and the AFM image shows it actually protruded topography. To confirm our assumptions, chemical components of the modified region were analyzed by AES. Figure 3 shows two Auger spectra, one for the unmodified region (labeled A), and the other for the locally modified region (labeled B). Carbon peaks, which are due to contamination in air, appear in both of the two spectra. The modified region clearly shows the oxygen peaks at 466, 482, and 503 eV, respectively, the chemically shifted SiO_2 peaks from the oxide layer.[14] There is no oxygen peak in the Auger spectra of the unmodified region. From the two spectra we can conclude that SiO_2 was formed after the H-passivated Si surface was modified in air.

Oxidation by laser irradiation on the H-passivated Si surface underneath the STM tip is due to desorbing hydrogen atoms from the Si surface. On a H-passivated Si(100) surface, Si atoms are bonded to hydrogen atoms forming a monohydride phase[14] or a dihydride phase[15] or a combination of the two phases.[16] To be sure, the hydrogen coverage is very close to 1 ML. Under laser irradiation, the adsorbed hydrogen atoms will thermally be desorbed as H_2 due to laser heating or as H^+ due to direct breaking of the Si–H bond.[17] After hydrogen atoms desorbed from the surface, O^- and OH^- groups, replacing the hydrogen atoms, are ad-

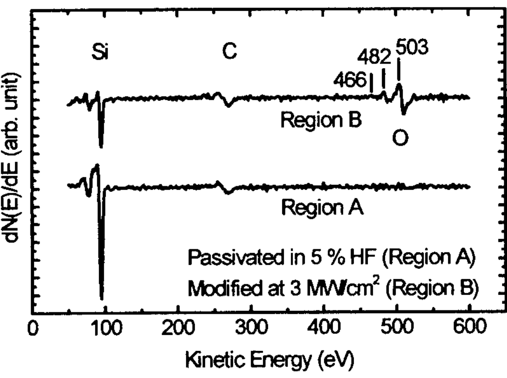

FIG. 3. AES of the modified region and the unmodified region in Fig. 2.

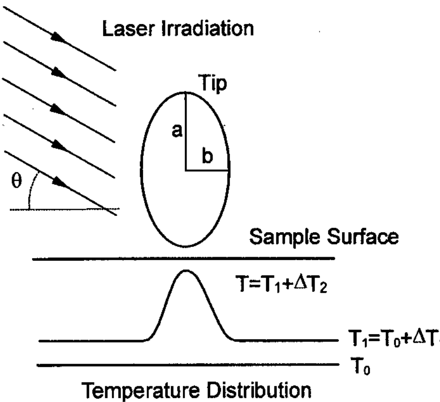

FIG. 4. Laser-induced thermal process on the sample surface underneath the STM tip.

sorbed on Si dangling bonds. Oxygen atoms, then, diffuse into the bulk of Si, forming an oxide layer with a certain thickness.

The binding energy of Si–H bonds on the H-passivated Si surface is approximately 3 eV.[9,16] Under laser irradiation with a wavelength of 532 nm, which has a photon energy of 2.33 eV, a Si–H bond cannot be directly broken by one photon. Therefore, desorption of hydrogen atoms from the Si surface is mainly due to the thermal effect. Both the original laser irradiation and the tip-enhanced laser irradiation contribute to the thermal process on the sample surface underneath the tip. The temperature rise on the sample surface is the sum of the temperature rises induced by both of the optical fields. The thermal process is depicted in Fig. 4. The tip–sample geometry is modeled to a prolate metal spheroid over a plane. The metal spheroid is characterized by an aspect ratio of a/b. The a and b are the half length of the major and minor axis of the ellipsoid, respectively. T_0 is the room temperature, T_1 is the temperature on the sample surface, and T is the temperature on the sample surface underneath the tip. ΔT_1 is the temperature rise due to the original laser irradiation and ΔT_2 is the temperature rise induced by the tip-enhanced laser irradiation underneath the tip. We consider an ideal case, that the size of the tip is much smaller than the laser wavelength. A linear-polarized pulsed laser with a wavelength of 532 nm and a pulse duration of 7 ns is used in our study. Under these assumptions, an electrostatic solution can be used. The optical field enhancement factor can be expressed by[18]

$$\alpha = \frac{E_{\text{tip}}}{E_0} = \frac{1}{1+[\varepsilon(\omega)/\varepsilon_m - 1]A}, \tag{1}$$

where E_0 is the electric field of the incident laser irradiation, E_{tip} is the electric field at the tip apex in the direction of the major axis, $\epsilon(\omega)$ and ϵ_{m} are the dielectric constants of the tip material and the medium material, respectively, and A is the geometry-dependent depolarization factor which is a solution of elliptic integrals of the second kind. If we consider the optical field at the tip apex closest to the sample surface, A is[19]

$$A = \frac{ab^2}{2}\int_0^\infty \frac{ds}{(s+a^2)^{3/2}(s+b^2)}. \tag{2}$$

In the case of a tungsten tip and a Si sample, no surface plasmon (SP) can occur in the gap between the tip and the sample. The necessary condition for SP excitation is that the dielectric constants of both the tip and the sample must be equal to or less than -1.

The temperature rise induced by pulsed-laser irradiation is a nonsteady state[20] and can be expressed by

$$\Delta T_1 = \frac{(1-R_\theta)F\sin\theta}{\sqrt{l_{\text{opt}}^2 + 4D_T\tau}}, \tag{3}$$

where F is the laser fluence, θ is the laser incident angle, R_θ is the reflectance of the sample at the laser incident angle, l_{opt} is the optical absorption length, D_T is the thermal diffusivity of the sample material, and τ is the laser pulse duration.

For the thermal conduction in the nanometer scale, $w_0^2/(4D_T)$ is usually much less than 1 ns. The w_0 is the spot size of the tip-enhanced laser irradiation. Therefore, the steady-state case[19] can be considered in the thermal process induced by the tip-enhanced laser irradiation using either a continuous-wave (cw) laser or a pulsed laser with a pulse duration in the nanosecond scale. If we assume that the radius of the spot size of the tip-enhanced laser irradiation is approximately the curvature radius of the tip, the temperature rise induced by the enhanced optical field underneath the tip is approximately

$$\Delta T_2 = \frac{\sqrt{\pi}\alpha^2 F(1-R_0)w_0\cos\theta}{8\kappa_T\tau}, \tag{4}$$

where R_0 is the optical reflectance of the sample at normal incidence and κ_T is the thermal conductivity of the sample. Equation (4) shows that the temperature rise induced by the tip-enhanced laser irradiation is proportional to the laser intensity F/τ. Therefore, a pulsed laser with short pulse duration and a high repetition rate is preferred in this technique.

The total temperature rise is

$$\Delta T = \Delta T_1 + \Delta T_2 = \frac{(1-R_\theta)F\sin\theta}{\sqrt{l_{\text{opt}}^2 + 4D\tau}} + \frac{\sqrt{\pi}\alpha^2 F(1-R_0)w_0\cos\theta}{8\kappa_T\tau}. \tag{5}$$

When the laser beam is in parallel with the sample surface, ΔT_1 is zero. The thermal effect by the original laser irradiation can be neglected. When the laser beam is perpendicular to the sample surface, no tip-enhanced laser irradiation generates and the temperature rise is totally induced by direct heating of the incident laser beam. No nano-oxidation can be observed in this case. In reality, the tip meniscus may block the laser beam at large incidence angles. Hence, the maximum of the laser incidence angle is limited by tip geometry. In our experiments, we found that the maximum incidence angle is around 45°.

In order to obtain continuous lines using a pulsed laser, the scanning speed must be slow enough. Figure 5 shows

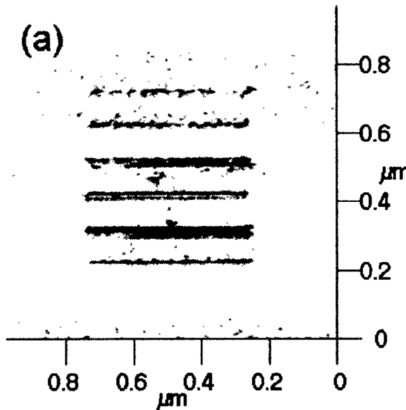

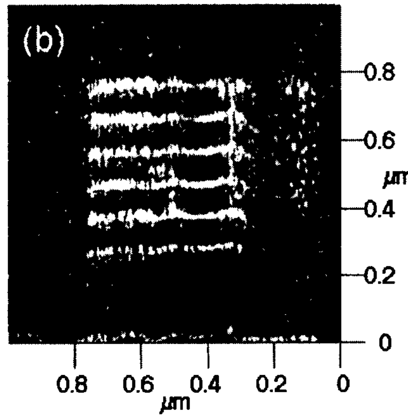

FIG. 5. STM (a) and AFM images (b) of a created oxide line array.

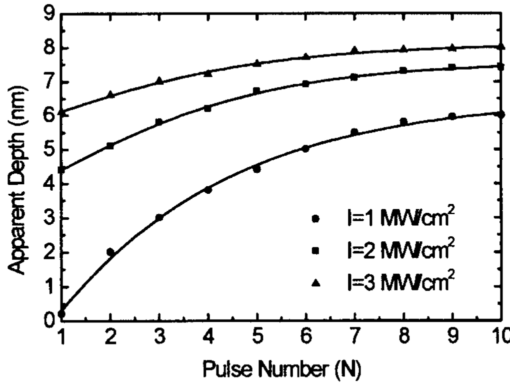

FIG. 7. Dependence of oxide apparent depth on laser pulse number.

STM and AFM images of a series of created lines. The laser beam with an intensity of 3 MW/cm^2 and a repetition of 10 Hz is in parallel with the sample surface. The scanning speed is 0.025 μm/s. The width of the lines is less than 30 nm and the average apparent depth is 3 nm. The AFM image shows an average real height of 0.8 nm. The STM image is taken using the same tip after writing. The AFM image is taken after the STM image in the time scale before the native oxidation occurs, ensuring that the AFM image reveals the real height of the created oxide patterns.

Dependence of apparent depth on intensity is shown in Fig. 6. The apparent depths were measured from the oxide dots created by single laser pulses with different laser intensities. An obvious threshold of laser intensity can be observed. Compared to the nano-oxidation induced by an electrical field,[1] which has a linear dependence of apparent depth on bias voltage, the apparent depth induced by laser irradiation has a fast increase with intensity above the threshold and tends to saturation at high intensity. At much higher laser intensity, we observed that the tip was probably damaged after laser processing. Further studies on the modified regions using AFM showed that these regions had irregular features. This might be surface damage at high intensity. When the sample surface is damaged due to high laser intensity, very thick oxide forms and the tip will touch the sample surface in these regions. This may damage the tip. The relationship between the apparent depth and the pulse number is presented in Fig. 7. The apparent depth also tends to saturation after several laser shots. This is because the amount of adsorbed hydrogen decreases with the increase of laser shots until all the hydrogen atoms are desorbed. The number of laser shots for maximum oxide thickness is dependent on intensity. At high intensity, the hydrogen desorption rate is high, therefore, fewer laser shots are needed for complete desorption of the adsorbed hydrogen atoms.

Another important issue is the dependence of apparent depth on tunneling current. Although oxidation does not seem to be current dependent, apparent depth increases with

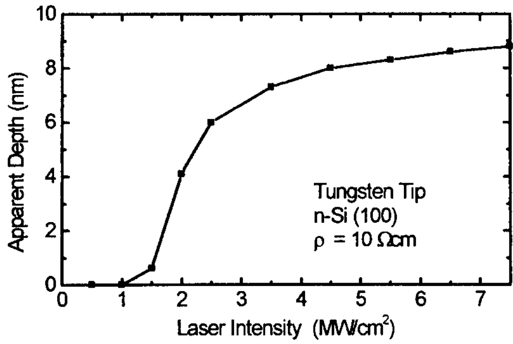

FIG. 6. Dependence of oxide apparent depth on laser intensity.

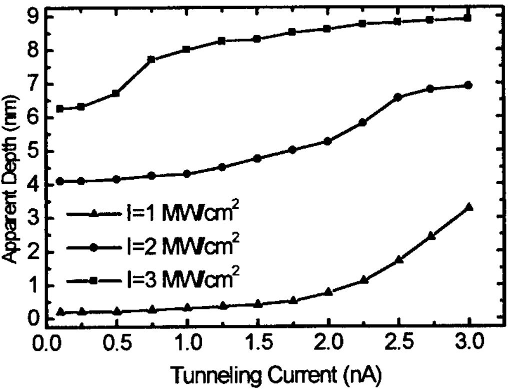

FIG. 8. Dependence of oxide apparent depth on tunneling current during modification.

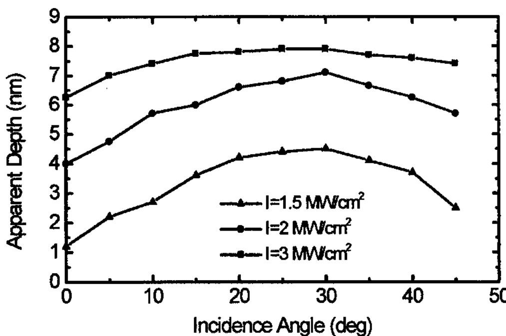

FIG. 9. Dependence of oxide apparent depth on laser incidence angle.

tunneling current, as shown in Fig. 8. This effect is due to the logarithmic dependence of the tip-to-sample distance on tunneling current. Increasing tunneling current reduces the tip-to-sample distance, which results in large optical enhancement on the sample surface.

The apparent depth was also measured for different laser incidence angles, as shown in Fig. 9. Observed under the high-power CCD microscope, the laser beam has an elliptical spot on the sample surface. In this study, we kept the minor axis of the ellipse in a dimension of 150 μm, ensuring that the intensity at the tip–sample gap is the same at all the incidence angles. We observed that for the p-polarized laser, there is an optimum incidence angle for the maximum apparent depth. This can be explained by Eq. (5). The temperature rise generated by the tip-enhanced laser irradiation decreases when θ increases, while the temperature rise generated by original laser irradiation increases, resulting in a maximum temperature rise at an optimum incidence angle.

The temperature rises induced by the laser irradiation ΔT_1, and that by the tip-enhanced laser irradiation ΔT_2, were estimated from Eq. (5). The dielectric constants of tungsten and silicon are $4.85+19.04i$ and $17.14+0.37i$, respectively. At the incidence angle of 30°, R_θ and R_0 are 0.425 and 0.59, respectively. A tungsten tip with a/b of 4 has an optical enhancement α^2 of 100. For Si, 1_{opt} is 940 nm, D is 0.82 cm^2/s, and κ_T is 1.4 W/(cmK) at 300 K. The w_0 is set as 30 nm, which is approximately the width of the oxide lines in Fig. 5. The pulse duration τ is 7 ns. Under the laser irradiation with the intensity of 1.5 MW/cm^2, ΔT_1 is approximately 17 °C, and ΔT_2 is approximately 62 °C. With the laser intensity of 6 MW/cm^2, ΔT_1 is approximately 68 °C, and ΔT_2 is approximately 248 °C.

IV. CONCLUSION

Nano-oxidation on H-passivated Si(100) surfaces were carried out by laser irradiation under a STM tip. Oxygen was detected by AES in a 2×2 μm^2 modified square region, while no oxygen was detected elsewhere on the sample surface. AES shows that after modification, a SiO_2 layer was formed on the H-passivated Si(100) surface. Under laser irradiation with a wavelength of 532 nm, the hydrogen desorption is mainly due to the thermal effect. Both the original laser irradiation and tip-enhanced laser irradiation contribute to the temperature rise on the sample surface underneath the tip.

ACKNOWLEDGMENTS

The authors thank H. L. Koh and Y. W. Goh for their kind help in installation of the SPM system and other facilities in our experiments. The work was supported by the National University of Singapore under Grant No. RP3972692.

[1] J. A. Dagata, J. Schneir, H. H. Harary, C. J. Evans, M. T. Postek, and J. Bennet, Appl. Phys. Lett. **56**, 2001 (1990).
[2] L. A. Nagahara, T. Thundat, and S. M. Lindsay, Appl. Phys. Lett. **57**, 270 (1990).
[3] S. T. Yau, X. Zheng, and M. H. Nayfeh, Appl. Phys. Lett. **59**, 2457 (1991).
[4] N. Barniol, F. Perez-Murano, and X. Aymerich, Appl. Phys. Lett. **61**, 462 (1992).
[5] H. C. Day and D. R. Allee, Appl. Phys. Lett. **62**, 2691 (1993).
[6] E. S. Snow and P. M. Campbell, Appl. Phys. Lett. **64**, 1932 (1994).
[7] M. Heim, R. Eschrich, A. Hillebrand, H. F. Knapp, R. Guckenberger, and G. Cevc, J. Vac. Sci. Technol. B **14**, 1498 (1996).
[8] G. Abadal, E. Perez-Murano, N. Barniol, and X. Aymerich, Appl. Phys. A: Mater. Sci. Process. **66A**, s791 (1998).
[9] S. Madsen, M. Mullenborn, K. Birkelund, and F. Grey, Appl. Phys. Lett. **69**, 544 (1996).
[10] M. Mullenborn, K. Birkelund, F. Grey, and S. Madsen, Appl. Phys. Lett. **69**, 3013 (1996).
[11] J. P. Ibe, P. P. Bey, Jr., S. L. Brandow, R. A. Brizzolara, N. A. Burnham, D. P. DiLella, K. P. Lee, C. R. K. Marrian, and R. J. Colton, J. Vac. Sci. Technol. A **8**, 3570 (1990).
[12] M. Fotino, Rev. Sci. Instrum. **64**, 159 (1993).
[13] *Handbook of Auger Electron Spectroscopy* (Jeol, 1982).
[14] J. Boland, Phys. Rev. Lett. **67**, 1539 (1991).
[15] S. Ciraci, R. Butz, E. M. Oellig, and H. Wagner, Phys. Rev. B **30**, 711 (1984).
[16] Y. J. Chabal and K. Raghavachari, Phys. Rev. Lett. **54**, 1055 (1985).
[17] S. Vijayalakshmi, H. T. Liu, and Z. Wu, Phys. Rev. B **58**, 7377 (1998).
[18] P. W. Barber, R. K. Chang, and H. Massoudi, Phys. Rev. B **27**, 7251 (1983).
[19] P. F. Liao and A. Wokaun, J. Chem. Phys. **76**, 751 (1982).
[20] D. J. Ehrlich and J. Y. Tsao, *Laser Microfabrication—Thin Film Processes and Lithography* (Academic, San Diego, CA, 1989).

Enhancement of resolution of DNA on silylated mica using atomic force microscopy

Jing Tang, Junwei Li, Chen Wang, and Chunli Bai[a)]
Institute of Chemistry, The Chinese Academy of Sciences, Beijing 100080, China

(Received 27 October 1999; accepted 21 April 2000)

It is demonstrated that the mica surface covered with a nanometer-thick, well connected silane film can appreciably improve the lateral resolution of DNA molecules in comparison with that on bare mica using atomic force microscopy. A typical value width of 4 nm can be obtained. We propose that the nanometer dimensioned porous surface provides an approach to eliminate the hydrated salt layer associated with the condensation of DNA strands, and leads to the enhancement of lateral resolution. © *2000 American Vacuum Society.* [S0734-211X(00)02904-8]

I. INTRODUCTION

Atomic force microscopy (AFM) has been shown to be an important tool for structural biology due to its potential of high resolution imaging capability. One of the primary interests in this field is in imaging DNA by AFM.[1] With the developments of many new specimen preparation methods and imaging techniques, stable DNA images have been routinely obtained both in air and in fluids such as water,[2] ethanol,[3] propanol,[2,4] and *n*-butanol,[5] etc. Among AFM examinations of DNA on mica, the disparity is widely acknowledged between helix diameter determined by AFM and by classical crystallographic methods. X-ray diffraction studies indicate the common *B*-form of DNA to be a double stranded helix about 2.0 nm in diameter.[6] However, numerous papers on measuring DNAs on mica by AFM indicate that the average height of DNA to be less than 1 nm (typically 0.1–0.3 nm), and the average width to be much wider than 2 nm, typically above 10 nm. Many arguments have been proposed to account for the discrepancy in lateral width of DNA by AFM measurements. Prevalent arguments[7–14] have attributed the effect largely to the finite tip radius or the convolution of tip geometry while others[15,16] suggested that the most important factor limiting the resolution of DNA is the adhesion force between the tip and substrate. One should notice that the above mentioned effects are convoluted together in the experimental conditions on an atomically flat surface, therefore making it difficult to differentiate them. A surface of porous nature would be ideal in this respect to bring out the effects solely due to the tip geometry.

In this article, we present AFM images of DNA on silylated mica and obtained a significant improvement on lateral resolution, compared to the images of DNA on plain mica imaged under the same sample preparation and imaging conditions. The nanometer sized porous-like surface is considered to function in analogue to ''molecular sieving'' of the salt deposits within the original solution. Combining the structure and adhesion force analysis, we conclude that the existence of a salt layer wrapping the DNA strands is one of the dominating factors that leads to the observed large width of DNA by AFM.

II. EXPERIMENTS

Freshly cleaved slabs of mica were exposed to an 3-aminopropyl triethoxysilane (APTES) vapor by suspending them in a weighing disk which contained a small pool (300 μl) of APETS for 40 min to 2 h depending on the ambient temperature and humidity. After being kept in a glass desiccator for 8 h, the substrate was then heated at 383 K for 3 h in order to allow the silane molecules to cross link and form the desirable network structure. The surface will be referred as AP-mica hereafter.

DNA(Promega Corporation) was diluted in water to the concentration of 1 hg/μl and a drop of this DNA solution was pipetted to the prepared substrate. The specimen was incubated at room temperature for 1–2 min and then compressed nitrogen gas was applied to it in a way as described by Li *et al.*[17] to stretch the DNA strands. The AFM images were obtained by Nanoscope III AFM (Digital Instruments Inc., Santa Barbara, CA). with Si_3N_4 tip (which has a rectangular shape cantilever of 125 μm long with ~50 N/m force constant and ~300 kHz resonant frequency). All images were obtained in the tapping mode.

III. RESULTS AND DISCUSSIONS

The structure of the AP-mica is illustrated in Fig. 1. As can be seen, the chains of silane molecules are crosslinked with each other and form a network of connecting molecules with nanometer sized pores. The scan sizes of Fig. 1 are 2 μm×2 μm, while the pore structure is more evident in Fig. 2(a) which has higher resolution. The film extends uniformly over the entire surface of mica. As a whole, the substrate has a mean root-mean-square (rms) roughness of 0.16 nm, and this makes it ideal for AFM imaging of DNAs. But between the chains small valley-like regions which are much lower than the other parts. The network, or the porous nature, of the film is essential to reduce the salt accumulation that is inevitable during the drying process of DNA solutions.

[a)]Author to whom correspondence should be addressed; electronic mail: clbai@infoc3.icas.ac.cn

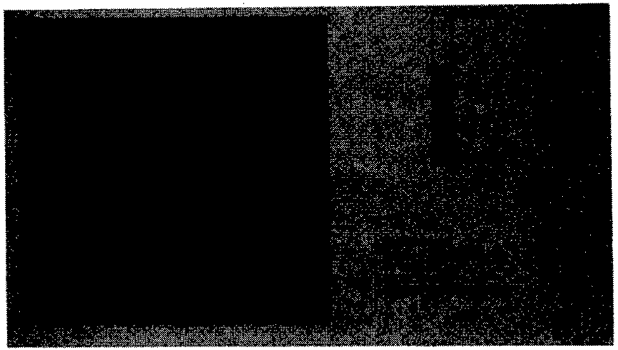

FIG. 1. AFM image of silylated mica (2 μm$\times$2 μm).

When imaging DNA on AP-mica, we discovered a substantial reduction in the measured width of DNA compared to that of DNA on bare mica. Figure 2(a) is a representative image of DNA on the AP-mica while Fig. 2(b) shows one of the typical images of DNA strands on bare mica which we have obtained under the same sample preparation and imaging conditions. On the AP-mica, the width of DNA in some places can be less than 5 nm, and it is much better than the best lateral resolution—about 10 nm, we have obtained on bare mica under optimal condition. In addition, on the AP-mica the DNA strands usually located in the valley-like regions display less lateral dimension than those located on the top of the silane domains.

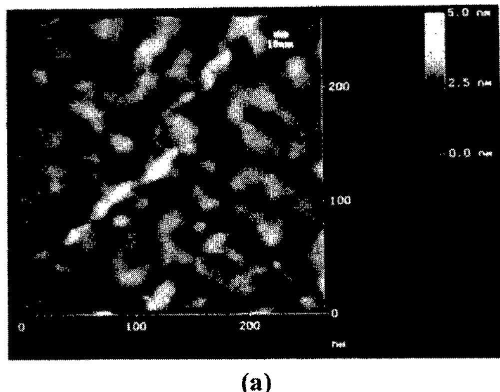

(a)

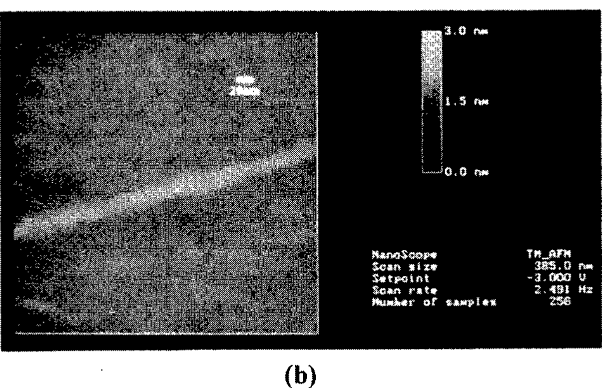

(b)

FIG. 2. (a) Representative DNA image on AP-mica. (b) Typical image of DNA on bare mica we have obtained under the same sample preparation and imaging conditions.

The drastic difference in the lateral resolution of DNA between the two substrates could provide clues to the origin of the anomalously large DNA width on bare mica measured by AFM. It is well known that the width of DNA measured by AFM on bare mica is typically more than 10 nm. This has led to the suspicion that the DNA strands normally observed by AFM are actually embedded within a salt layer. As a result, the apparent width of the DNA molecule is much larger than they should be. Even though the dimension of the salt layer is not significant, its effect could be long range, since the inclusion of ions in the polar solvents could significantly increase the magnitude of the adhesion force.[18] The observed results are supportive to this view. Due to the common practice of separation and purification of DNA, it is almost impossible to obtain DNA samples without any salts or other residue proteins (for example, the DNA buffer solution used in this study is provided in a buffer solution of 10 mM Tris-HCl, 10 mM NaCl, and 1 mM EDTA). Therefore, it is inevitable that DNA will be covered by a layer of salt. Moreover, in ambient air, water coats most surfaces and the salt layer which wraps DNA strands should be hydrated. When the salt-wrapped DNAs adsorbed on the AP-mica which has many nanometer pores on the most outer layer, a large fraction of salt will be deposited into the bottom of the pores, although some of salt will still be associated with the DNA strands to compensate the charge of the phosphate backbone. Especially, when the DNA strands happen to pass across the valley-like region, the strands will be fully suspended and thus salt contents will deposit more easily to the bottom. Hence, the observed DNAs would be nearly ideal ones and be manifested by the appreciably improved lateral width measured with AFM. Actually. It is proposed that the network structure of the mica functions similarly to a molecular sieve, which sieves most of the excess salt contents into the bottom of the substrate exposing the more real DNA to us, as illustrated in Fig. 3.

Furthermore, since the AP-mica is much more hydrophobic than mica, the adhesion force is lower than that on bare mica. As Yang and Shao[15] and Lyubchenko *et al.*[16] have proposed, the decrease in adhesion force might also contribute to the resolution improvement of DNA on AP-mica. But as the demonstrated here, we believe that the removal of the salt layer is the major factor that leads to the improved resolution.

As to the height of DNAs, we find that the height falls into the range of 0.4–0.8 nm while on mica the corresponding range is 0.1–0.3 nm. It also suggests that with a reduced salt layer, the height of the exposed DNA strands could appear close to its real value. However, in AFM images the height of DNA strands on AP-mica is still less than the actual dimension of 2 nm because of the adhesion force between DNA molecule and the surface. This is consistent with the results obtained by Vesenka *et al.*,[2] who attributed the dependence of DNA height on humidity to the hydration of a

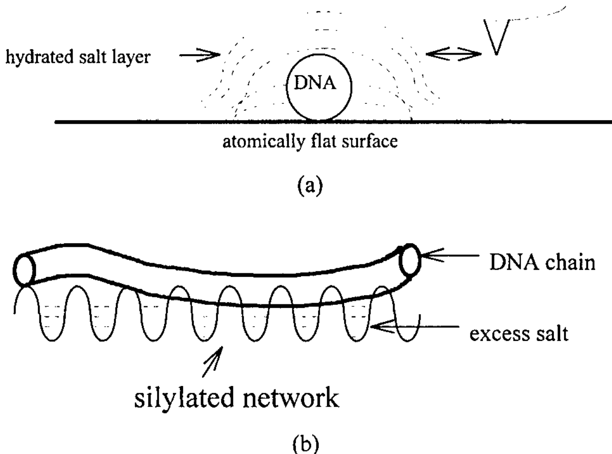

FIG. 3. (a) Schematic diagram showing a linear DNA chain on an atomically flat surface (bare mica) embedded in a salt containing hydration layer due to the drying treatment. (b) Similar schematic diagram of a DNA chain on the surface of a nanometer-sized porous medium whereas the excess salt is sieved and deposited to the "valley" regions of the medium.

salt layer over the mica surface in which the DNA is embedded.

IV. CONCLUSIONS

Using the silylated mica, we obtained AFM images of DNA with widths much smaller than those on bare mica. It is proposed that the surface bound networks formed by cross-linked silane molecules helped to reduce the excess salt content at the immediate vicinity of the DNA chains, therefore reducing the long range adhesion interactions with the probe. From the structure and adhesion force analysis, we concluded that the existence of a hydrated salt layer enclosing the DNA strands should be one of the dominating factors that leads to the usual low resolution of DNA images by AFM.

[1]H. G. Hansma, J. Vesenka, C. Sienerist, G. Kelderman, H. Morrett, R. L. Sinsheimer, V. Elings, C. Bustamante, and P. K. Hansma, Science **256**, 1180 (1992).

[2]J. Vesenka, S. Manne, G. Yang, C. Bustamante, and E. Henderson, Scanning Microsc. **7**, 781 (1993).

[3]H. G. Hansma, R. L. Sinsheimer, S. A. C. Gould, A. L. Weisenhorn, H. E. Gaub, and P. K. Hansma, AIP Conf. Proc. 136 (1991).

[4]J. Vesenka, H. Hansma, C. Siegerist, G. Siligardi, E. Schabtach, and C. Bustamante, Proc. SPIE **1639**, 127 (1992).

[5]H. G. Hansma and P. K. Hansma, Proc. SPIE **189**, 66 (1993).

[6]R. R. Sinden, *DNA Structure and Function* (Academic, San Diego, CA, 1994).

[7]H. G. Hansma, Bezannilla, F. Zenhausem, M. Adrian, and R. L. Sinsheimer, Nucleic Acids Res. **21**, 505 (1993).

[8]T. Thundat, D. P. Allison, R. J. Warmack, G. M. Brown, K. B. Jacobson, J. J. Schrick, and T. L. Ferrell, Scanning Microsc. **6**, 911 (1992).

[9]J. Vesenka, M. Guthold, C. L. Tang, D. Keller, E. Delaine, and C. Bustamante, Ultramicroscopy **42–44**, 1243 (1992).

[10]E. Henderson, Nucleic Acids Res. **21**, 445 (1992).

[11]C. Bustamante, J. Vesenka, L. Tang, W. Rees, M. Guthold, and D. Keller, Biochemistry **31**, 22 (1992).

[12]T. Thundat, D. P. Allison, R. J. Warmack, and T. L. Ferrell, Ultramicroscopy **42–44**, 1101 (1992).

[13]Y. L. Lyubchenko, B. L. Jacobs, and S. M. Lindsay, Nucleic Acids Res. **20**, 3983 (1992).

[14]T. Thundat, D. P. Allison, R. J. Warmack, and K. B. Jacobson, Scanning Microsc. **8**, 23 (1994).

[15]J. Yang and Z. Shao, Ultramicroscopy **50**, 157 (1993).

[16]Y. L. Lyubchenko, P. I. Oden, D. Lampner, S. M. Lindsay, and K. A. Dunker, Nucleic Acids Res. **21**, 1117 (1993).

[17]J.-W. Li, C.-L. Bai, C. Wang, C.-F. Zhu, Z. Lin, Q. Li, and E.-H. Cao, Nucleic Acids Res. **26**, 4785 (1998).

[18]J. Tang, C. Wang, M.-Z. Liu, M. Su, and C.-L. Bai, Chin. Sci. Bull. (to be published).

New polymer materials for nanoimprinting

H. Schulz, H.-C. Scheer,[a] T. Hoffmann, and C. M. Sotomayor Torres
Department of Electrical Engineering and Institute of Materials Science, University of Wuppertal, Germany

K. Pfeiffer, G. Bleidiessel, and G. Grützner
Micro Resist Technology, Berlin, Germany

Ch. Cardinaud, F. Gaboriau, and M.-C. Peignon
Institute for Materials Science, University Nantes, France

J. Ahopelto
VTT Electronics, Espoo, Finland

B. Heidari
Nanostructure Consortium, University Lund, Sweden

(Received 1 June 1999; accepted 27 April 2000)

We have investigated new aromatic polymers for nanoimprint and subsequent dry etching, namely thermoset and thermoplastic compounds. They were tested in a SiO_2 patterning process under low pressure and high plasma density conditions and feature a selectivity about twice as high as poly(methylmethacrylate) (PMMA). The imprint behavior is comparable to PMMA and, in particular, the thermoplastic polymers show excellent imprint quality. This was demonstrated by replication of large arrays of lines down to 50 nm width. The thermoset polymers showed excellent dry etch stability and Teflon-like antisticking layers helped to imprint them without sticking.
© *2000 American Vacuum Society.* [S0734-211X(00)04504-2]

I. INTRODUCTION

Volume production in microelectronics still relies on planar sequences, where deposition of layers and layer patterning are performed repeatedly in order to implement device and circuit functionality on the semiconductor surface. Patterning typically involves a lithography process for pattern definition in a polymer (resist) mask and a subsequent dry etch process to transfer the pattern to the underlying substrate or the surface layer. So far electron beam writing is the only production-proven technique for pattern definition in the nanometer scale. However, decreasing pattern size and increasing accuracy are coupled to a lower throughput. There is still a lack of cost efficient techniques for large area mass production of nanometer patterns.

Recently, a number of imprint-like techniques[1–3] have been investigated as alternatives for pattern definition in the nanometer range. We focus on a technique, where parallel pattern transfer from a rigid stamp is achieved under pressure and temperature, known as ''nanoimprint lithography'' (see Ref. 1) or ''hot embossing'' (see Ref. 4). The most frequently used polymer for nanoimprinting is (poly)methylmethacrylate (PMMA), a well known electron beam resist, which is well suited for an imprint process at temperatures below 200 °C. On the other hand, PMMA is not the best choice with respect to dry etching. The objective of this work is to present results on the development and evaluation of new polymer materials in view of the overall patterning process: imprint lithography and subsequent dry etching. We also attempt to establish criteria for the type of polymers suitable for nanoimprinting.

[a]Electronic mail: scheer@ween01.elektro.uni-wuppertal.de

II. APPROACH

New polymers can be evaluated by comparing their etch stability and flow properties to those of PMMA. The good imprint properties of PMMA are determined by its viscoelastic properties, e.g., those of an amorphous thermoplastic. This type of thermoplastic is characterized by entangled polymer chains which set up a temporary network of physical crosslinks. This leads to a strong temperature dependence of the mobility of entire polymer chains and the related time-dependent viscoelastic response of the polymer to external forces. At temperatures sufficiently above the glass transition temperature T_g the mobility of entire polymer chains will allow irreversible flow on the time scale of the imprint.

In contrast, duromers and to a lesser degree elastomers have a network which is set up by chemical crosslinks which strongly hinder any viscous flow. Semicrystalline thermoplastics consist of microcrystallites and amorphous parts where the crystallites act as a fixed network up to their melting temperature. Thus, of all polymers the amorphous thermoplastics are expected to be the most suitable for the imprint step. In practical terms, good flow which enables the filling of stamp features even over larger distances and different feature sizes is obtained at about 90 °C above the glass transition temperature.[5–7] For example, PMMA has a glass transition temperature of about 105 °C and good imprints are obtained at temperatures between 190 and 200 °C. To obtain shorter imprint times it would be desirable to have an amorphous thermoplastic with a lower glass transition temperature as PMMA. Additionally, the polymer should be stable up to temperatures above the imprint temperature.

A criterion for the choice of polymers regarding the dry etching step may be derived from the experience that aro-

matic polymers, like, e.g., Novolak, are promising candidates for dry etching masks. Moreover, the thermal stability of the polymer has implications for the pattern quality obtained in the dry etching pattern transfer process. Thus, it would be favorable to use either aromatic thermoplastics with higher glass transition temperature or aromatic duromeres with high decomposition temperature.

In this work we have chosen two specific polymer types to balance both demands determined by imprinting and dry etching: (i) aromatic amorphous thermoplastic polymers with expected improved etch stability but similar flow behavior with respect to PMMA and (ii) aromatic thermoset polymers, the latter being imprinted as a thermoplastic prepolymer to maintain good flow properties and subsequently crosslinked to obtain enhanced etch stability. The crosslinking can be carried out by chemical initiation, photoinitiation, or a thermal treatment. In view of the imprint process thermal crosslinking appears most attractive since the dry etch step is determined by the layers to be patterned and the pattern quality required, thus offering only limited flexibility for optimization of the polymer mask. Therefore, we investigated first the dry etch stability of new polymer materials and then, using polymers with satisfactory mask selectivity, we optimized the imprint process.

III. EXPERIMENTAL AND RESULTS

A. Polymer synthesis and characterization

1. Thermoplastic polymers

Linear poly(methacrylic acid arylesters) were synthesised by free-radical polymerization in a solution using α,α-azoisobutyronitrile as an initiator, followed by a cleaning procedure in methyl and a drying process at 80 °C in a vacuum oven. Different aromatic groups were incorporated in the various polymers which allowed the tuning of the glass transition temperature depending on the amount of incorporated aromatic groups. The glass transition temperature was determined by differential scanning calorimetry (DSC). We investigated the etch and imprint behavior of two particular polymers with a T_g of 49 °C (PBM) and 107 °C (PPM), the latter being comparable to that of PMMA. A molecular weight of about 2.5×10^5 g/mol was found by gel chromatography for both polymers. Both polymers are stable up to processing temperatures of 200 °C and were spin coated from solutions of propylene-glycol-monoethylester-acetate.

2. Thermoset polymers

Soluble, branched prepolymers were obtained from poly-benzene-dicarboxylic-diallylesters. The prepolymers are based on diallyl-phthalate, boiling point 169 °C, which was distilled directly before polymerization. The free-radical polymerization was performed at 80 °C initiated by benzoyl-peroxide. The process was controlled by refractometry and interrupted by cooling before the gel point was reached, precipitated in methyl alcohol, cleaned in acetone and hexane, and dried under vacuum at 40 °C. The branched prepolymer

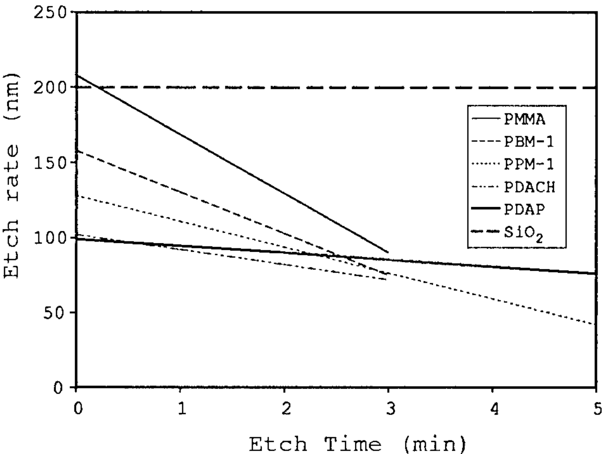

FIG. 1. Etch rates for nonpatterned polymers PPM, PBM, PDAP, PDACH, and PMMA as monitored by *in situ* multiwavelength ellipsometry. The etch rate of SiO_2 is depicted for comparison and determination of the selectivity of the polymers.

prepared in this way is soluble in conventional solvents, has good spinning characteristics and features a molecular weight of 1.8×10^5 g/mol. Two different thermoset prepolymers with glass transition temperatures of 39 °C (PDACH) and 63 °C (PDAP) were prepared for the imprint step.

For further crosslinking about 30% of the initial amount of double bonds remains. A significant crosslinking of the two prepolymers starts at a temperature of about 120 °C. Thermal treatment below 180 °C and for 1 h result in a partial crosslink which is detected by an increase of the glass transition temperature. After a treatment of 1 h at 180 °C no glass transition is detected by DSC, thus the crosslinking is completed. These thermoset polymers remain stable up to at least 280 °C. To characterize the etch stability of blanket layers prepolymers were spin coated and thermally crosslinked for 1 h at 180 °C.

B. Dry Etching

The etching of SiO_2 in a CHF_3 low pressure high density plasma was used as a reference process to compare the polymers under test. The experiments were performed with an inductively coupled plasma at 1500 W, at 150 V substrate bias, and an operating pressure of 10 mTorr. The wafer was mounted on a mechanic chuck and was cooled to an initial temperature of 20 °C. The dynamic evolution of the etch rate was monitored using *in situ* multiwavelength ellipsometry. Scanning electron microscopy (SEM) was used to check changes in surface morphology subsequent to etching.

In a basic test nonpatterned polymers were investigated. Figure 1 reports the real time etch rates for SiO_2, PMMA, and the polymers under test. In contrast to SiO_2, a decrease of the etch rate is noted for all polymers, as they probably suffer from energetic ion impingement. The etch rate decrease of the thermoset polymers (PDAP, PDACH) is substantially smaller than for PMMA, indicating an improved plasma stability. In addition no significant change in the surface morphology is observed (Fig. 2). Concerning the ther-

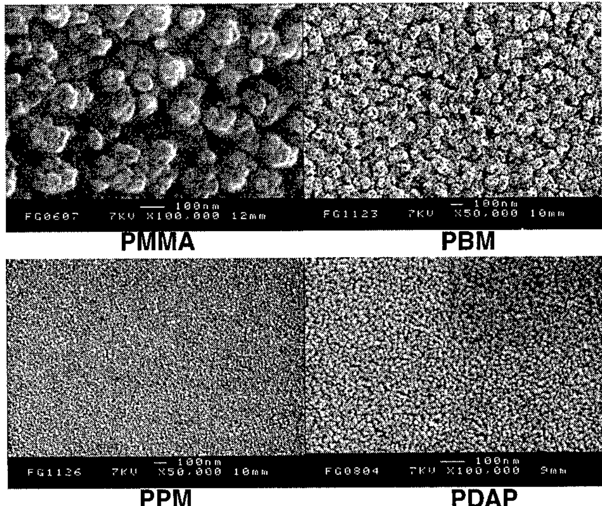

FIG. 2. SEM micrographs of the different polymer surfaces after etching: PMMA (top left) and PBM (top right) show severe degradation whereas PPM (bottom left) and PDAP (bottom right) exhibit less damage of the surface. Note that the magnification differs from image to image.

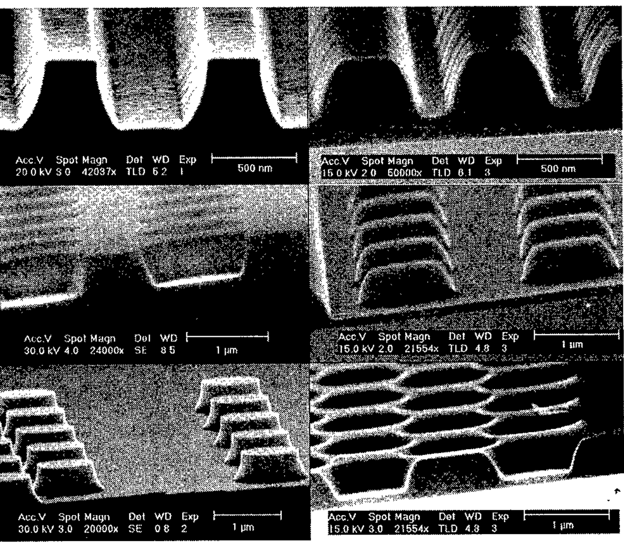

FIG. 3. SEM micrographs of stamp (left) and corresponding patterns (right) as imprinted into polymer PPM. Even smaller details like the surface roughness of the stamp are transferred with high fidelity (see upper left and right). A maximum thickness contrast defined by the ratio of overall resist thickness to that of the remaining bottom layer of about 6:1 is achieved (bottom).

moplastic samples, PPM exhibits an etch rate decrease which is between that of PMMA and that of the duroplasts, but appears to be stable in the plasma (Fig. 2), whereas the behavior of PBM resembles to that of PMMA, e.g., an important decrease of the etch rate is noticed, accompanied by a severe degradation of the surface under plasma exposure. The difference between PBM and PPM could rely in the respective T_g values: although the sample is cooled from the backside during the etching, the sample surface temperature is expected to rise to about 70 °C under plasma exposure. Severe degradation would then occur if the material is brought above T_g in an aggressive plasma environment. Within the first minute, average selectivity of SiO_2: resist is close to one for PMMA and reaches values up to two for the aromatic polymers under test. Figure 1 shows that PDAP features the best selectivity compared to SiO_2.

A further factor of two in the polymer selectivity can be achieved by cooling the wafer to an initial temperature of −20 °C.[8] In addition, decreasing the atomic fluorine concentration in the plasma, e.g., by using a CHF_3–CH_4 gas mixture, can increase resist selectivity further. We expect that a SiO_2: resist selectivity of around 15 can be achieved for the new polymers if needed for special device applications.

C. Nanoimprinting

To test the imprint behavior we use a 2 cm×2 cm stamp. It is made from poly-Si over SiO_2 and features patterns with a lateral geometry from 250 nm to 100 μm and a typical height of 500 nm. In order to evaluate the imprint process independent of a particular pattern, thus eliminating specific material transport characteristics,[6,7] the whole stamp is patterned and the local ratio of positive to negative stamp features is chosen to be close to 50%. In addition to isolated and periodic positive and negative lines and dots, the stamp has a 5 mm×5 mm field of lines and spaces (line 250 nm, pitch 800 nm). The large field size was particularly chosen for the evaluation of imprint quality over large areas. For the evaluation of the high resolution capabilities of nanoimprinting we have used a second stamp that consists of a Cr–Ni layer on silicon. The stamp has 50 μm×50 μm line arrays of decreasing width from 150 nm down to 50 nm.

1. Thermoplastic polymers

The thermoplastic polymers were imprinted in a process guided by our previous findings,[6,7] namely at temperatures 90 °C above T_g and at 100 bar. The imprint was performed into spun layers of PBM and PPM with a thickness of about 300 nm. The quality of replication was found to be similar to that obtained with PMMA and complete transport of the polymer material over large areas for all different types of patterns was observed. In particular, the field of 250 nm lines was replicated with similar quality over the full area of 5 mm×5 mm. By comparing the stamp and the corresponding imprint for PPM (Fig. 3) it can be seen that even the smallest details of the stamp, such as the roughness of the sidewalls are well replicated. This demonstrates clearly the fidelity of pattern transfer obtained by imprinting into amorphous thermoplastic polymers. Replication of lines with 50 nm width was successfully carried out with the second stamp. This is shown for an imprint into PBM in Fig. 4. The thickness contrast obtained under best imprint conditions is approximately 6:1 between the most elevated feature and the remaining bottom layer of the resist. This thickness contrast will help in the subsequent anisotropic dry etch process, where first of all the polymer has to be opened for mask formation. Polymer PBM gave slightly poorer imprint results than PPM most likely due to its low glass transition temperature and thus a low mechanical and thermal stability. Whether this poorer imprint quality is a result of mechanical

FIG. 4. Micrographs of arrays of 50, 70, 100, and 150 nm lines imprinted into PBM (top) and of details of the 50 nm line array (bottom).

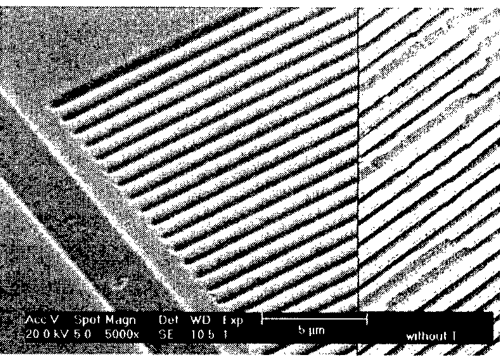

FIG. 5. Imprinted thermoset polymer PDAP with (left) and without (right) use of a Teflon-like antisticking layer on the stamp. A detail of the 5 mm×5 mm field of 250 mm lines is shown.

forces acting during stamp separation or heating by irradiation during examination of the PBM in the SEM remains unclear at present.

2. Thermoset polymers

Imprint of the thermoset polymers turned out to be less straightforward. The major problem is that the optimum temperature for imprinting is above the temperature where crosslinking begins. For PDAP this optimum temperature would be around 153 °C (63+90 °C) and for PDACH 129 °C (39+90 °C), both temperatures are above 120 °C, the point where crosslinking sets in. Under these conditions, severe sticking is observed between the stamp and the sample that hampers their separation after cool down. Manual cleavage with a scalpel induced shear forces to the polymer and often resulted in pull off of a large part of the polymer layer from the sample. This strong adhesion between polymer and stamp is most likely caused by the crosslinking process itself which may lead to the formation of chemical bonds between the reactive prepolymer and the stamp surface. On the other hand, when the imprint temperature is held below the crosslinking temperature, replication of the stamp is feasible with a quality typical of those imprints carried out at temperatures below 90 °C plus T_g which are characterized by limited polymer flow.[6,7]

To overcome this problem an antisticking layer was deposited on the stamp surface using a plasma polymerization process. Characterization of these Teflon-like antisticking layers and process optimization is in progress. In this way the thermoset polymers could be imprinted at 90 °C above T_g with a quality comparable to that of the thermoplastic polymers. Figure 5 shows imprints in PDAP of 250 nm lines in one 5 mm×5 mm field with and without an antisticking layer.

IV. DISCUSSION AND CONCLUSION

As expected the aromatic polymers investigated here showed better etch resistance than PMMA and thus are promising candidates for a dry etch mask. In a SiO_2 patterning process selectivities twice as high as for PMMA were found and best selectivity was found for the thermoset PDAP.

The thermoplastic polymers showed excellent imprint quality, which was demonstrated by replication of patterns with features sizes down to 50 nm lines over large areas. This is primarily caused by their pronounced viscosity decrease above the glass transition temperature. In addition, a thickness contrast of up to 6:1 was achieved which will help in the removal of the residual layer in a subsequent dry etch process. Imprint of the thermoset polymers with comparable quality was demonstrated using a Teflon-like antisticking layer on the stamp. The actual imprint results obtained with all new polymers confirm our previous finding[6,7] that (i) small and periodic features are most easily replicated and (ii) the optimum imprint temperature is about 90 °C above the glass transition temperature of the polymer in question. The best imprint behavior was found for the thermoplastic polymer PPM.

If a high mask selectivity is the most important consideration then PDAP is the most attractive candidate, if a process simplicity is the priority then PPM is preferable, as it could be imprinted without an antisticking layer. The latter will have increasing importance for imprinting with stamps containing features with sizes in the 10 nm range, else antisticking layers will have to be monolayers and at present their long-term stability can hardly be assured.

ACKNOWLEDGMENTS

The author acknowledge financial support from the European Commission ESPRIT funding under Grant No. 28785 ''NANOTECH.'' The authors are grateful to F. Osenberg for the preparation of the antisticking layers.

Presented at the 43rd EIPBN Conference, Mars Island, FL, 1–4 June 1999.

[1]S. Y. Chou *et al.*, Appl. Phys. Lett. **76**, 3114 (1995); J. Vac. Sci. Technol. B **14**, 4129 (1996).
[2]Y. Xia and G. M. Whitesides, Adv. Mater. **9**, 147 (1997); **8**, 1015 (1996).
[3]J. Haisma *et al.*, J. Vac. Sci. Technol. B **14**, 4124 (1996).
[4]R. W. Jaszewski, H. Schift, J. Gobrecht, and P. Smith, Microelectron. Eng. **41/42**, 575 (1998).
[5]K. Pfeiffer, G. Bleidiessel, G. Grützner, H. Schulz, T. Hoffmann, H.-C. Scheer, and C. M. Sotomayor Torres, Proc. Micro- and Nano-Engineering Conference (MNE), Leuven, Sept. 1998.
[6]H.-C. Scheer, H. Schulz, T. Hoffmann, and C. M. Sotomayor Torres, J. Vac. Sci. Technol. B **16**, 3917 (1999).
[7]F. Gottschalch, T. Hoffmann, C. M. Sotomayor Torres, H. Schulz, and H.-C. Scheer, Solid-State Electron. **43**, 1079 (1999).
[8]L. Rolland, M. C. Peignon, Ch. Cardinaud, and G. Turban, J. Vac. Sci. Technol. A (submitted).

Bilayer, nanoimprint lithography

Brian Faircloth
Nuvonyx, Inc., Bridgeton, Missouri 63044

Henry Rohrs
Washington University, St. Louis, Missouri 63130

Richard Tiberio
Cornell University, Ithaca, New York 14853

Rodney Ruoff
Washington University, St. Louis, Missouri 63130

Robert R. Krchnavek[a)]
Rowan University, Glassboro, New Jersey 08028

(Received 3 May 1999; accepted 21 April 2000)

Nanoimprint lithography has been shown to be a viable means of patterning polymer films in the sub-100 nm range. In this work, we demonstrate the use of a bilayer resist to facilitate the metal liftoff step in imprinter fabrication. The bilayer resist technology exhibits more uniform patterns and fewer missing features than similar metal nanoparticle arrays fabricated with single layer resist. The bilayer resist relies upon the differential solubility between poly(methyl methacrylate) and poly(methyl methacrylate methacrylic acid copolymer). Evidence is presented that shows the technique has a resolution of better than 10 nm. © *2000 American Vacuum Society.*
[S0734-211X(00)03104-8]

I. INTRODUCTION

Due to the inevitable transition from the microelectronic to the nanoelectronic age, the demand for sub-100 nm feature sizes in lithographic techniques will increase greatly. As current devices rapidly approach the 100 nm barrier, the microelectronics industry is considering several technologies to overcome this hurdle. Clearly there is an urgent need for fast, reliable, and cost-effective nanolithography. Nanoimprint lithography shows promise in meeting this need.

Nanoimprint lithography is a relatively new lithographic technique that has received considerable attention in recent years.[1–3] It is relatively straightforward. First, an imprinter (mask) is made with the desired sub-100 nm features raised from the surface. Next, the imprinter is coated with a very thin layer of mold release compound to protect it and prevent sticking during the imprinting process. The substrate to be patterned is then coated with a thin film of thermoplastic polymer. The elastomer is heated above its glass transition temperature (T_g) where it becomes viscoelastic. The imprinter is then pressed into the polymer and the system is cooled back down below the polymer's T_g, *freezing* the pattern into the polymer. The mask is then removed and the trenches are cleaned with either an O_2 plasma or with solvents to remove any residual polymer that may remain in the trenches. The imprinter can be reused numerous times thereby providing cost-effective, sub-100 nm lithography.

There are several challenging problems associated with nanoimprint lithography.[4] One critical area is to perform the next level of processing while maintaining the same resolution demonstrated in the polymer resist layer. The formation of patterned metal layers is one application. Finely patterned metal layers are used as interconnects in integrated circuits. They can also be used as catalysts for subsequent layer growth. If the subsequent metal layers cannot readily be etched, e.g., due to crystalline dependent etching rates, an *additive* approach such as *liftoff* is desirable. However, single layer resists are problematic when transferring the pattern via metal liftoff. The nonvertical sidewalls resulting from the imprinting process result in tearing and detachment of the metal film during liftoff. Nonvertical sidewalls occur in imprint lithography if the imprinting element does not have vertical sidewalls. Even if the imprinter does have vertical sidewalls, nonvertical sidewalls are formed in the imprinted film due to a descumming step necessary to remove residual polymer from the bottom of the imprinted feature. Therefore, a technique is required that minimizes the problems associated with metal liftoff using single layer resists.

In this work, we address this issue by considering the fabrication of nanometer-scale metal arrays. We use a bilayer resist technique to provide undercutting that dramatically improves the metal liftoff. We demonstrate high resolution arrays of particles, lines, and crosshatches fabricated from metal liftoff after nanoimprint lithography using a *bilayer* resist.[5]

II. EXPERIMENT

Figure 1 shows a schematic drawing of the imprinting process. The experimental steps involve imprinter (mask) preparation, sample preparation, imprinting, postprocessing, metalization, and liftoff.

[a)]Electronic mail: krchnavek@rowan.edu

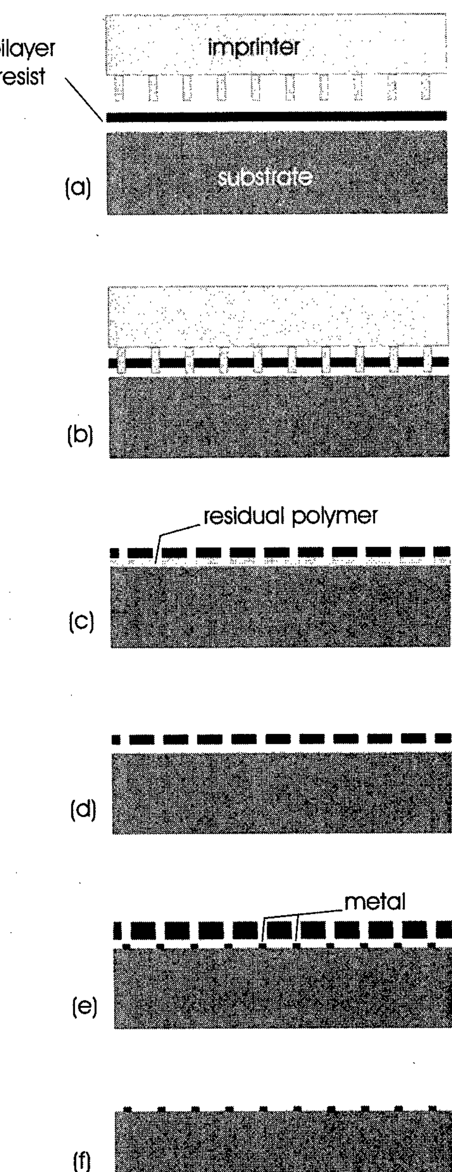

FIG. 1. Schematic illustration of the imprint process. (a) A substrate and imprinter prior to imprinting. The substrate is coated with the bilayer resist and the imprinter is coated with a thin mold-release polymer. (b) Imprinting. Both substrates are heated and cooled during the imprinting process. (c) The imprinter has been pulled back. The residual polymer remains at the bottom of the imprinted features. (d) The residual polymer is removed during a descumming step. This step also undercuts the lower resist layer. (e) Metal is evaporated over the entire surface. (f) After metallization, the polymer layers are dissolved thereby lifting off the undesired metal. The result is a patterned metal layer.

A. Sample preparation

After suitably cleaning a silicon wafer, the bilayer resist is spun on. There are a wide range of thermoplastic elastomer polymers available that should work well for bilayer resists. We chose poly(methyl methacrylate) (1% 495k PMMA in chlorobenzene) and poly(methyl methacrylate methacrylic acid copolymer) [2.2% 73k P(MMA-17.5%MAA) in glycol ether] for this work. These polymers are used as electron beam lithography and x-ray lithography resists and have consistent formulations that spin on uniformly.

To produce the bilayer resist the PMMA is first spin coated onto the wafer (2000 rpm, 60 s) and soft baked to drive out the solvent (170 °C for 60 min). Next, the P(MMA-MAA) copolymer is spin coated (6000 rpm, 60 s) onto the PMMA film and soft baked in the same manner. This results in each layer being approximately 50 nm thick for a total film thickness of approximately 100 nm. It has been shown that these two layers mix neither during the soft baking process nor when heated above their T_g's.[6,7]

B. Mask preparation

Nanoscale imprint lithography requires a suitable mask or imprinter. This is a crucial component of the imprinting process and the fabrication of the imprinter is covered in Ref. 5. It is sufficient to note that our imprinters have been fabricated in both silicon and silicon dioxide, using e-beam lithography and plasma etching. For the work presented here, the imprinter is fabricated in a 500 nm layer of thermally grown silicon dioxide on a silicon wafer.

Prior to use, the imprinter must be coated with a mold release polymer such as the hyperbranched perfluorinated polymer[8] used in this study. A 2 mg/ml solution of the mold release polymer dissolved in chloroform is drawn into a pipette and enough solution is expelled onto the imprinter to form a meniscus (i.e., the entire surface of the imprinter is covered with mold release polymer solution). Since the mold release solution evaporates rapidly, the imprinter is immediately spun at 6000 rpm for 30 s before the concentration on the imprinter has had time to increase significantly. Atomic force microscopy measurements of the resulting film have shown that the thickness is 5–10 nm. The chloroform solvent is removed by placing the imprinter in a vacuum chamber and pumping the chamber down below 50 mTorr.

C. Imprinting

The imprinting apparatus consists of aluminum plates, guide pins, and alignment structures. See Fig. 2. We used carbon tape to fix the sample with respect to the imprinter. This tape serves the dual purpose of holding the sample in place and providing leveling during imprinting. The soft, plastic nature of the tape helps ensure that the imprinter and sample are parallel by deforming to compensate for any macroscopic area pressure gradients. The tape was replaced after every five imprintings due to gradual degradation at the elevated temperatures.

The next step is patterning the bilayer resist polymers. The bilayer-coated substrate is attached to the bottom piece of the imprinting apparatus via the double-sided carbon tape. The entire apparatus is placed into an oven heated to 180 °C. Then the sample and imprinter are brought into intimate contact. A specific amount of force is applied to achieve a desired imprint depth. The force is applied until the oven atmosphere (air) reaches 170 °C. The apparatus is flash cooled and the imprinter is removed. Figure 3 shows a set of scanning electron microscope (SEM) micrographs taken after imprinting. The imprinted sample is now ready for postprocessing.

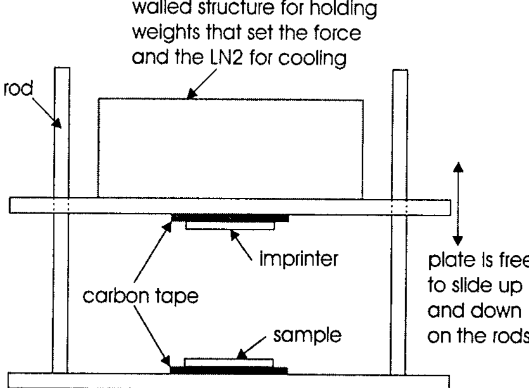

FIG. 2. A drawing of the imprinting apparatus. Brass weights are placed in the walled structure on the top plate to set the applied force. The entire apparatus is placed into an oven for the heating process. Cooling is achieved by pouring liquid nitrogen into the walled structure on the top plate. The sample temperature is assumed to be in equilibrium with the oven temperature.

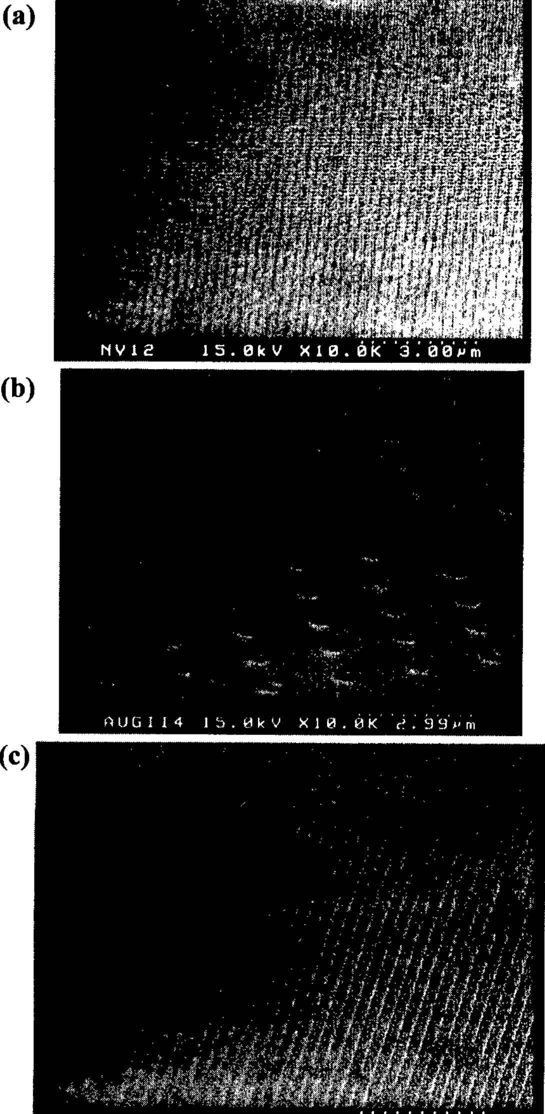

FIG. 3. SEM micrographs of patterns imprinted into a bilayer resist. These samples have been rinsed with toluene to remove any residual mold release polymer. (a) An array of 50-nm-diam dots spaced 250 nm apart. (b) An array of 250 nm dots spaced 2 mm apart. (c) A set of 50-nm-wide parallel lines with a spacing of 500 nm.

D. Postprocessing

After the imprinter is retracted, a small amount of residual polymer remains at the bottom of the trenches. This must be removed if quality reproductions are to be obtained. The residual polymer can be removed by means of a short oxygen plasma etch or by a wet solvent etch. It should be noted that even if the elements of the imprinter have perfectly vertical sidewalls resulting in trenches with perfectly vertical sidewalls, this descumming step will round the edges of the indented structure, resulting in slightly beveled sidewalls. This can lead to the errors already mentioned for single layer resists. The use of an anisotropic oxygen plasma as the descumming agent will reduce this problem somewhat. The bilayer resist is much less sensitive to this effect and can function even when descumming is done using isotropic techniques.

We used two different postprocessing techniques. In the first method, a high pressure is applied during the imprinting process such that the imprinting elements create deep trenches in the bilayer resist. The trench is deep enough to cause considerable compression of the lower PMMA layer. Before the sample can be descummed, any residual mold release polymer must be removed from the surface of the sample so it does not prevent descumming of the thin P(MMA-MAA) film. This is accomplished with a 5 s rinse in toluene. The mold release polymer is very soluble in toluene and a 5 s rinse is more than sufficient. Longer times should be avoided as the toluene will also etch away the lower PMMA layer in areas in which it is exposed. Immediately after rinsing the imprinted sample it was dried with a stream of dry nitrogen.

After removing the residual mold release polymer, there is a thin membrane of P(MMA-MAA) covering the inside of the trench. This thin membrane must be removed otherwise undercutting will be impaired. The membrane can be removed by soaking the imprinted sample in methanol for approximately 5 s and then immediately drying with dry nitrogen. The methanol will etch the P(MMA-MAA) polymer while leaving the lower PMMA polymer unaffected. This is an isotropic etch that not only eliminates the thin P(MMA-MAA) membrane in the trench, but also reduces the thickness of the top layer of the bilayer resist. The final step in preparing the sample for metal deposition and liftoff is to descum the PMMA from the bottom of the trenches while simultaneously creating undercut in the bottom layer. This goal was accomplished by soaking the imprinted sample in a chlorobenzene solution. The chlorobenzene attacks the lower PMMA layer while leaving the upper P(MMA-MAA) unaffected. Typical soak times are 45–60 s.

The second postprocessing technique is used for dense structures in which capillary action upon removal of the imprinter after a deep imprinting results in damage to the poly-

mer films. This damage can be prevented with a shallow imprint. This method will also work with less dense patterns, but is slightly more complex. This technique uses only enough pressure to make indentations that are from 30 to 35 nm deep. After imprinting, the mold release polymer is removed with toluene as described earlier. The pattern must now be transferred deeper into the bilayer resist without the benefit of the imprinter. This is achieved with an anisotropic plasma etch that cuts the pattern deeper into the resist. It is crucial that the final trench depth extend into the bottom layer and that 20–30 nm of P(MMA-MAA) remain. Etching was implemented at the Cornell Nanofabrication Facility using the PlasmaTherm 72 Reactive Ion Etcher. Imprinted samples were etched at a chamber pressure of 15 mTorr, 100 W of power, with gas flows of $CF_4=42$ sccm and $H_2=15$ sccm for 65 s (the etch rate of this plasma chemistry was found to be 29 nm/min). The choice of CF_4/H_2 chemistry was primarily due to its availability in the chamber. It is likely that the primary etch mechanism is sputtering and an inert gas could be used instead. However, the degree to which any polymer deposition may be influencing the etching process will require further study. Oxygen plasmas were also employed, but the etch rate was much higher, making the etching of precise depths difficult.

The final step of this postprocessing method is identical to that of the previous method. A slightly longer soak time in chlorobenzene is needed to ensure that the lower layer PMMA is etched down to the silicon surface. Typical soak times are around 60 s.

E. Metallization

The final step to validate the results is to transfer the pattern imprinted into the resist into a second processing step. We chose to metalize the substrate. Metal evaporation was done using a CVC SC4500 thermal evaporator equipped with a crystal thickness monitor (Cornell Nanofabrication Facility.) The 16 in. throw distance minimizes heating of the substrate which can damage the polymer resist layers.

Once the metal film has been evaporated onto the imprinted sample, liftoff must be done to remove all of the unwanted metal and resist polymers. Liftoff is achieved by soaking the metal-coated sample in a 1:1 mixture of acetone and methylene chloride for 30 min followed by sonication for 3 min. Further sonication in a clean solution of 1:1 acetone:methylene chloride may be required if optical inspection reveals incomplete liftoff.

III. RESULTS AND DISCUSSION

In this work, we have seen that the quality of imprinting depends on the density of the patterns on the imprinter. As patterns become more dense, there is an increasing tendency for the polymer layers to adhere to the imprinter upon removal. This capillary action is reduced with the use of a mold-release polymer, but in dense patterns, it is not eliminated. As discussed in Sec. II, the tendency for the polymer layers to adhere to the imprinter can be reduced by doing a shallow imprint followed by a solvent rinse. The shallow imprint is controlled by the pressure applied to the imprinter. Figure 4 shows the imprint depth as a function of applied pressure. In our system, applied pressure is controlled by weights. The pressure was calculated using the area of the imprinter elements (assuming perfect patterning and vertical etching) and the force due to gravity for the specific weights used. There is a systematic error in these numbers due to the

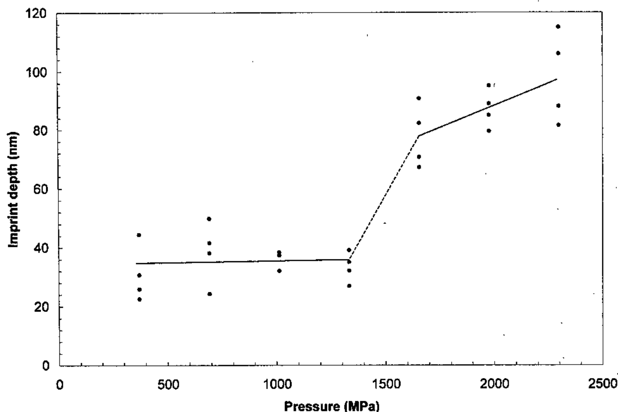

FIG. 4. Imprint depth as a function of applied pressure in a bilayer resist consisting of 50 nm of 495k PMMA (bottom layer) and 50 nm of 73k P(MMA-17.5%MAA)(top layer).

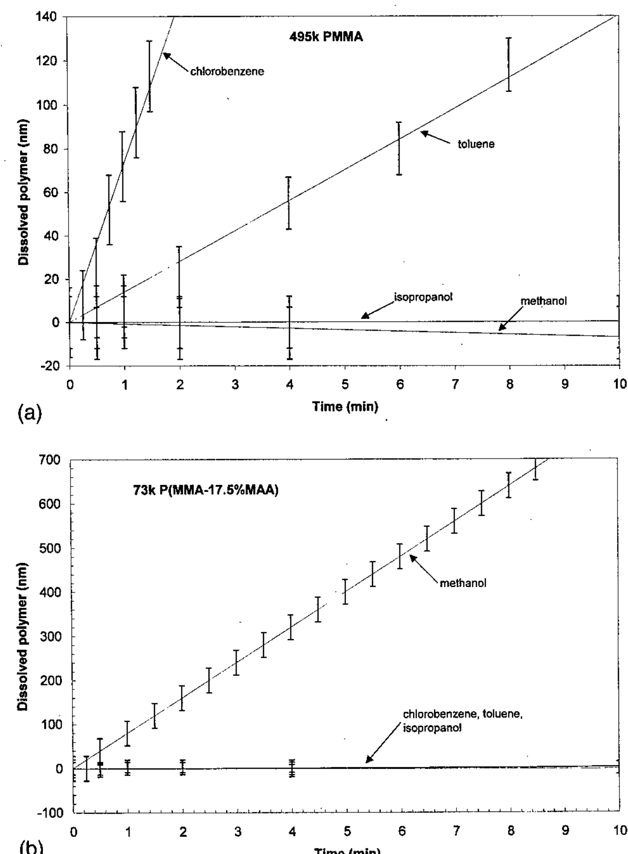

FIG. 5. Polymer thickness removed from a polymer film as a function of time for various solvents. Note that the 495k PMMA is quite soluble in chlorobenzene whereas the 73k P(MMA-17.5%MAA) is essentially insoluble in chlorobenzene.

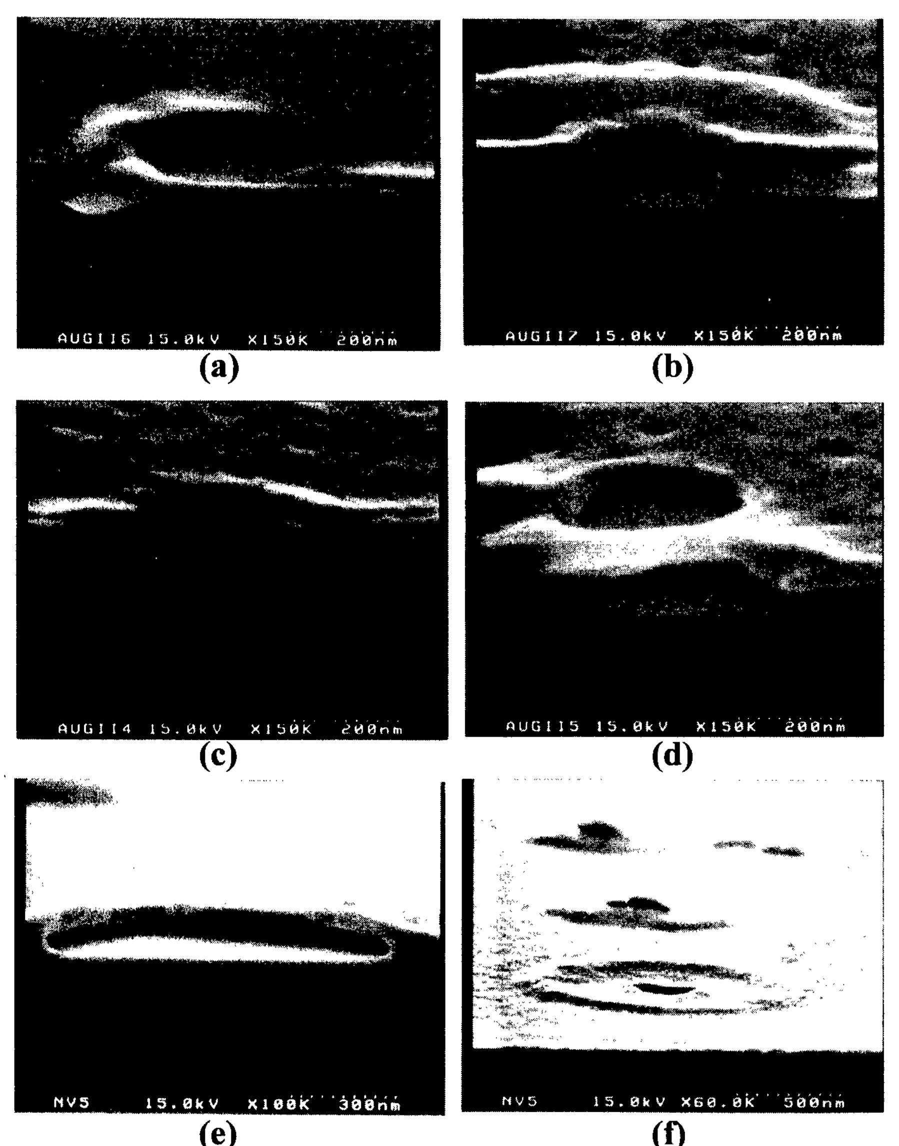

FIG. 6. SEM micrographs of a bilayer resist imprinted with 250 nm dot arrays and soaked in chlorobenzene for (a) 0 s, (b) 30 s, (c) 60 s, (d) 120 s, and (e) 240 s. In (f), the top polymer layer has collapsed because of the extreme undercutting after soaking in chlorobenzene for 240 s.

friction between the rods and the top plate (see Fig. 2) in the imprinting apparatus. The entire imprinting apparatus is brought up to 170 °C before entering the cooling cycle. For the highest pressure shown in Fig. 4, the time to reach 170 °C was approximately 85 min, whereas for the lowest pressure, the imprinting temperature was reached in 40 min. The difference between these times is due to the method we used to apply the pressure. It was simply a set of weights on the top plate of the imprinter apparatus. More pressure requires larger weights, which in turn take longer to heat up. The most striking feature in the data is the nearly constant depth of imprint given by the first four data points. These points cover a wide range of pressures. This phenomenon is most likely a surface effect with several contributing factors. The orientation of the polymer at the surface is almost always different from the interior. In addition, small molecules such as oxygen and water can diffuse deep into the polymer surface due to the large free volume of amorphous polymers. Furthermore, surface oxidation or contamination can exist. For example, P(MMA-MAA), which is the top layer, contains electrolyte side chains which readily attract and react with water molecules creating a contamination layer. Since the imprints are done at a relatively high temperature the diffusion of contaminants into the polymer can be large, resulting in a fairly thick contamination layer.

Very recently it has also been found that the glass transition temperature at the surface of a polymer can be much higher than that for the bulk polymer.[9–11] In addition, in most polymers the surface skin can be from a few nanometers thick to tens of nanometers thick[12] and this can be a sizable fraction of the 50 nm P(MMA-MAA) layer. To complicate matters further, bulk polymers are known to have a skin in the rubbery flow regime due to surface tension effects,[12] but how this skin would manifest itself and what effect it would have upon nanoscopic thin films is uncertain.

It is likely that the relatively constant imprint depth of 35 nm for pressures less than 1400 MPa is due to some combination of the above-mentioned effects. Above 1400 MPa, the surface layer yields to the imprinter elements and they punch through. The yielding pressure is likely to be highly depen-

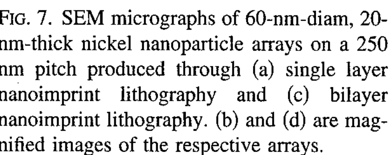

(a) (b) (c) (d)

FIG. 7. SEM micrographs of 60-nm-diam, 20-nm-thick nickel nanoparticle arrays on a 250 nm pitch produced through (a) single layer nanoimprint lithography and (c) bilayer nanoimprint lithography. (b) and (d) are magnified images of the respective arrays.

dent upon the shape and geometry of the imprinting elements, such that a sharp cone like element would easily puncture the surface layer while a flat cylinder like element (a pillar for instance) would have more difficulty. After the surface layer has been compromised the imprinting elements quickly pass through the remaining liquid like P(MMA-MAA) layer and reach the soft elastic PMMA layer below (it is assumed the PMMA layer is in the soft elastic region due to the slope of Fig. 4 coupled with the observation that single layer PMMA films do not show flow upon compression). The rubbery PMMA layer is then compressed with the applied stress from the imprinting elements as shown by the monotonically increasing imprint depth with increasing pressure after 1600 MPa.

Figure 4 demonstrates that one can control the depth of imprinting to a certain extent by controlling the applied pressure. In particular, the two depths (35 and 100 nm) considered in Sec. II are easily obtained by controlling pressure. Note that although the bilayer was nominally 100 nm thick, there is approximately 20% uncertainty in this value resulting in the high-pressure imprint depths exceeding 100 nm.

It is well known that liftoff can be considerably improved when a certain amount of undercutting is produced in the structure. This proves to be the great advantage of using a bilayer resist for imprint lithography. Electron beam lithography and photolithography naturally produce undercutting (in positive resists) due to diffraction spreading effects for photolithography and electron scattering and secondary electron production in the resist for electron beam lithography. In imprint lithography, undercutting must be produced in another way. We achieve this with a bilayer resist. The two polymers used for the bilayer resist, PMMA and P(MMA-MAA), have considerably different chemical properties. There are a wide range of solvents that will attack PMMA, but not P(MMA-MAA) and vice versa (see Fig. 5). The 495k PMMA is highly soluble in chlorobenzene and toluene but quite insoluble in isopropanol and methanol. In contrast, the 73k P(MMA-17.5%MAA) exhibits a high solubility in methanol and low solubility in chlorobenzene, toluene, and isopropanol. After imprinting, the sample is exposed to a solvent that will attack the bottom PMMA layer but not the upper P(MMA-MAA) layer. In this way, undercutting can be produced in the imprinted features and the vapor deposited metal film will not form a continuous film as long as the thickness of the metal is less than that of the bottom layer. The degree of undercutting is easily controlled by timing the solvent rinse. Figure 6 is a series of SEM micrographs showing undercutting in a bilayer resist imprinted with 250-nm-diam holes. The solvent was chlorobenzene and rinse times ranged from 0 to 240 s. Figure 6(a) represents an imprint in which no postprocessing has been done other than a toluene rinse. The continuous nonvertical sidewalls are apparent. Figure 6(b) shows a sample that has been soaked in chlorobenzene for 30 s. The undercut and discontinuity in the

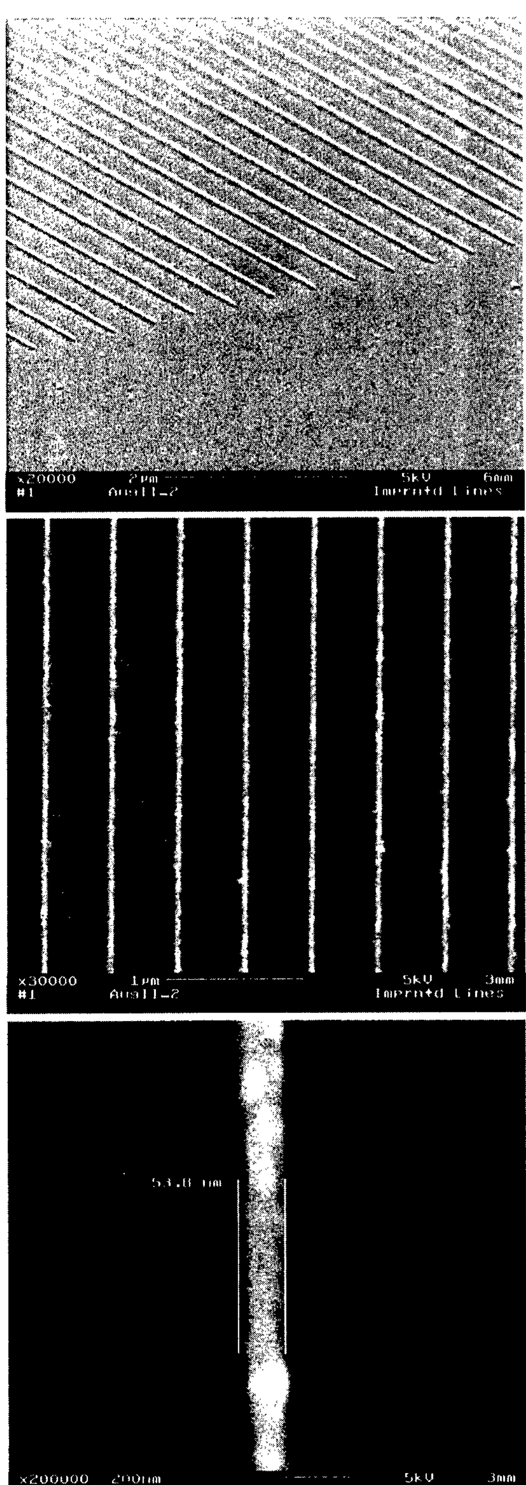

FIG. 8. SEM micrographs of parallel Cr metal lines patterned with bilayer nanoimprint lithography and metal liftoff. The lines are approximately 50 nm wide and 20 nm thick.

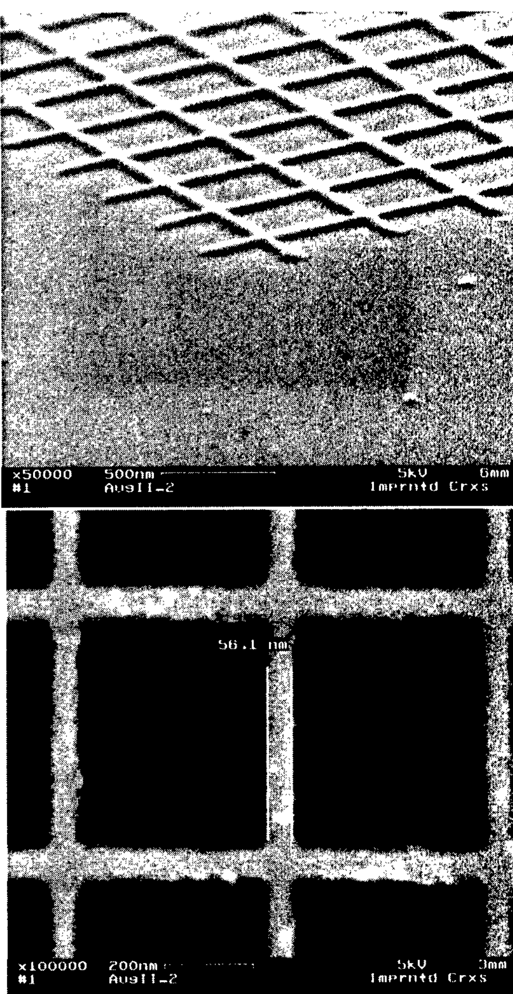

FIG. 9. SEM micrographs of 20-nm-thick Cr crosshatch lines patterned using bilayer nanoimprint lithography and metal liftoff. The lines are approximately 55 nm wide.

sidewalls is now apparent. In Fig. 6(c), the sample has been soaked for 60 s. The undercut is now very noticeable. Figures 6(d) and 6(e) represent samples soaked in chlorobenzene for 120 and 240 s, respectively. In both cases the undercut is extreme. Finally, in Fig. 6(f), in which the sample has been soaked for 240 s, the degree of undercutting is so extreme that the upper, unaffected P(MMA-MAA) layer has collapsed onto the substrate, possibly due to the capillary forces present during solvent evaporation.

One measure of the performance of the bilayer imprinting technique is how well metal liftoff occurs. There were three basic types of patterns originally produced on imprinters — dot arrays, parallel lines, and crosshatch patterns. The first of these patterns is shown in Fig. 7. Figure 7 shows a set of SEM micrographs of 60-nm-diam dots arrays of 20-nm-thick nickel. The 20-nm-thick nickel was thermally evaporated onto the imprinted sample followed by liftoff. Figure 7 compares the single layer imprint lithography [Figs. 7(a) and 7(b)] with the bilayer imprint lithography [Figs. 7(c) and 7(d)]. For the case with the single layer of 495k PMMA resist, the dots are very nonuniform in both size and shape. Additionally, it can be seen in Fig. 7(a) that many of the dots have been completely pulled from the substrate during the liftoff process. Finally, many of the dots appear to have *tails* which are created by metal breaking at an intermediate place on the sidewalls of the trenches.

Figures 7(c) and 7(d) show nickel metal array produced

by imprinting completely through the bilayer resist. It is important to note the high uniformity in size and shape of the 60-nm-diam dots. An additional point can be seen from Fig. 7(c). Our imprinter had an error in the dot array caused by a pattern generator error in the Leica VB-6 electron beam lithography machine. This error produced a subset of the imprinting elements with a spacing of less than 10 nm. As can be seen in the right half of Fig. 7(c), bilayer nanoimprint lithography is capable of distinguishing the two imprinting elements, suggesting that bilayer nanoimprint lithography has a resolution of 10 nm or better.

Two other patterns were evaluated. Figure 8 shows 50-nm-wide parallel lines spaced 500 nm apart. Imprinting was done using the shallow imprinting method and liftoff was performed after thermal evaporation of chromium (20 nm). Figure 9 shows a crosshatch pattern with 50-nm-wide lines spaced 500 nm apart. Shallow imprinting and chromium liftoff were used to fabricate this pattern. In both of these figures, a perspective view is provided to orient the reader and an overhead view is then used to measure the width of the lines. For both the parallel lines and the crosshatch pattern, very few errors can be seen in the SEM images.

IV. CONCLUSIONS

In this work, we demonstrated the advantages of a bilayer resist for nanoimprint lithography. Metal nanoparticle arrays can be fabricated using thermal evaporation and metal liftoff when an appropriate bilayer resist is used. In comparison to a single layer resist, the metal arrays exhibit more uniform patterns and fewer missing features. The bilayer resist relies upon the differential solubility between PMMA and P(MMA-MAA). While gross errors are associated with single layer nanoimprint lithography, bilayer nanoimprint lithography produces much higher quality metal patterns when using liftoff.

We have also demonstrated a shallow imprinting technique in which the bilayer resist is used in conjunction with shallow imprinting to reduce film damage when imprinting dense feature patterns.

Finally, there is evidence that the bilayer resist technique has a resolution of better than 10 nm if an appropriate imprint mask is fabricated. This high resolution coupled with liftoff technology opens up new opportunities for nanoscale research.

ACKNOWLEDGMENTS

The authors would like to thank Lynn Rathbun, Michael Rooks, Jerry Comeau, Mike Skvarla, Jerry Drumheller, Dustin Carr, Jim Clair, and Gary Bordonaro of the Cornell Nanofabrication Facility. This work was performed in part at the Cornell Nanofabrication Facility (a member of the National Nanofabrication Users Network), which is supported by the National Science Foundation under Grant No. ECS-9731293, Cornell University, and industrial affiliates. In addition, we thank Stephen Irons, Nikolay Nemchuk, Anja Mueller, Karen Wooley, and Tomek Kowalewski for numerous technical discussions. This work was supported by a grant from the National Science Foundation (No. DMR-9704644, Periodic Nanotube Arrays).

[1]S. Y. Chou, P. R. Krauss, and P. J. Renstrom, Science **272**, 85 (1996).
[2]J. Haisma, M. Verheijen, and J. van den Berg, J. Vac. Sci. Technol. B **14**, 6 (1996).
[3]X. Sun, L. Zhuang, W. Zhang, and S. Y. Chou, J. Vac. Sci. Technol. B **16**, 6 (1998).
[4]H.-C. Scheer, H. Schultz, T. Hoffmann, and C. M. Sotomayor Torres, J. Vac. Sci. Technol. B **16**, 6 (1998).
[5]B. Faircloth, Master's thesis, Washington University, St. Louis, 1998.
[6]R. C. Tiberio, J. M. Limber, G. J. Galvin, and E. D. Wolf, Proc. SPIE **1089**, 124 (1989).
[7]M. Hatzakis, J. Vac. Sci. Technol. **16**, 6 (1979).
[8]A. Mueller, T. Kowalewski, and K. Wooley, Macromolecules **31**, 3 (1998).
[9]G. B. DeMaggio, W. E. Frieze, D. W. Cidley, M. Zhu, H. A. Hristov, and A. F. Yee, Phys. Rev. Lett. **78**, 1524 (1997).
[10]Y. C. Jean, R. Zhang, H. Cao, J.-P. Yuan, C.-M. Huang, B. Nielson, and P. Asoka-Kumar, Phys. Rev. B **56**, 8459 (1997).
[11]Y. M. Boiko and R. E. Prudhomme, J. Polym. Sci., Part B: Polym. Phys. **36**, 567 (1998).
[12]L. H. Sperling, *Introduction to Physical Polymer Science* (Wiley Interscience, New York, 1992).

Determination of coupled acid catalysis-diffusion processes in a positive-tone chemically amplified photoresist

F. A. Houle,[a] W. D. Hinsberg, M. Morrison, M. I. Sanchez, G. Wallraff, C. Larson, and J. Hoffnagle
IBM Almaden Research Center, 650 Harry Road, San Jose, California 95120

(Received 20 October 1999; accepted 7 April 2000)

Acid diffusion during postexposure baking is viewed to be a limiting factor in the extension of lithography using chemically amplified resists to formation of nanoscale features. Quantification of thermally activated reaction-diffusion kinetics in these materials is therefore an important step in understanding the extendability of this class of resist systems. Previous investigations have addressed this issue, however there is poor agreement among them, and too few data exist in the literature to allow the systematics of the effect of polymer, photoacid generator, added base or other resist components on the diffusion process to be understood. We describe in this article a combined experimental and modeling protocol that is designed to elucidate the chemistry and physics of the reaction-diffusion process. Because it is physically based, not phenomenological, it provides a means of developing a set of predictive, mutually comparable data that will allow new insights to be developed into the nanoscale behavior of chemically amplified resist materials. We apply the protocol to a p-*t*-butyloxycarbonyloxystyrene/bis(*t*-butylphenyl)iodonium perfluorobutanesulfonate positive-tone photoresist system. The resulting kinetics measurements show that diffusion is environment sensistive and describable with two limiting diffusion coefficients. The Arrhenius parameters for the coefficients in p-*t*-butyloxycarbonyloxystyrene are $D_0 = 1.9\times 10^8$ cm^2/s and $E_a = 36.5$ kcal/mol; those for diffusion in the deprotected polymer product p-hydroxystyrene are $D_0 = 9\times 10^{-3}$ cm^2/s and $E_a = 22.1$ kcal/mol. The coefficients are much smaller than previously reported, resulting in a very slow diffusion rate. The model indicates that the considerable image spreading observed during the postexposure bake process is attributable primarily to the efficiency of the catalytic chemistry. Our results suggest that numerical models currently used for prediction of imaging in chemically amplified resists may require refinement in order to be useful for feature sizes below 100 nm and for new classes of resist systems. © *2000 American Vacuum Society.*
[S0734-211X(00)01004-0]

I. INTRODUCTION

It is emphasized frequently in the literature that the image resolution achievable at the nanometer scale using chemically amplified (CA) resists will be limited by diffusion of resist components after exposure to radiation.[1,2] This concern originates from observations of considerable spreading of a latent image during postexposure thermal processing, leading to formation of much broader features after development than had been originally printed.[3] Image spreading is found in both positive- and negative-tone resist systems, and the primary diffuser is thought to be photogenerated acid catalyst in both cases, although diffusion of cross-linking agents in negative-tone systems has also been invoked.[4] For the sake of simplicity, we confine our discussion to positive-tone systems. The impact on these resists of even small changes in local acid concentration would be expected to be large, given the substantial chemical amplification of the initially printed acid image during postexposure processing. The amplification originates from the long catalytic chain caused by each photogenerated acid: a single species can induce hundreds of deprotection events via localized motion in the polymer film before becoming trapped and unreactive.[5]

Numerous investigations of diffusion in positive-tone CA resists during postexposure bake (PEB) have been reported using linewidth measurements,[2,6] multilayer structures of acidified polymer or pure acid on pure polymer,[3,7,8] ionic conductivities[2,9–11] and spectroscopic probes of polymer chemistry changes during or after PEB[2,8,12,13] to elucidate the coupled reaction-diffusion process. Diffusion coefficients are typically extracted from the experimental measurements by one of three ways. The most detailed approach involves modeling the system using coupled reaction-diffusion with diffusion represented by a Fickian process and the deprotection rate dependent on both the acid and remaining protected group concentrations.[7,8,12,14,15] Acid concentrations are not treated as constant, but undergo continuous reduction through loss processes. Simpler treatments involve analysis of ionic conductivities[9–11] or of material loss after development as a function of PEB conditions.[3,6] The diffusion coefficients reported in all of these studies are difficult to compare to each other directly because of the differences in polymer, photoacid generator (PAG), PAG concentration, postapply bake (PAB) conditions and PEB temperatures used, but fall into a range of 10^{-15}–10^{-11} cm^2/s.

When these diffusion coefficients are converted into mean displacements, they predict three-dimensional diffusion

[a]Electronic mail: houle@almaden.ibm.com

lengths of the order of 85–850 nm during a 2 min PEB at 80–100 °C. These distances are large, suggesting that diffusion plays a significant role in determining feature width, particularly at the sub-200 nm scale. Does acid really diffuse this fast? If it does, then it is difficult to explain how chemically amplified resists have been used to fabricate structures 50 nm or less.[1] The coupling between diffusion and acid-catalyzed deprotection must be reconsidered to be sure that the two processes are cleanly distinguished in the analysis of PEB data.

Although rather simple representations of the chemistry have been used in previous studies as noted above, detailed investigations of the acid-catalyzed and noncatalyzed decomposition reactions of CA resist using p-*tert*-butoxycarbonyloxystyrene (PTBOCST) polymer with triphenylsulfonium hexafluoroantimonate as a PAG have shown that the chemistry in this system is actually quite complex.[16] The first order acid catalyzed deprotection reaction to form p-hydroxystyrene (PHOST) is accompanied by acid equilibria between protected and deprotected groups that affect the instantaneous local availability of acid. This is distinct from postulated acid loss processes in that the acid is not permanently removed from the system.[6,8,12–14] The direct thermolysis of the polymer can be described as autoaccelerated in PHOST, becoming more important as a deprotection pathway as the conversion of the polymer proceeds. Throughout the course of these reactions, the volume of the polymer film decreases significantly,[16] assuming rapid relaxation of the polymer, leading to continuously increasing concentrations and thus accelerating deprotection rates. The addition of base to a resist formulation introduces additional rapidly maintained equilibria that dynamically affect the local availability of acid as the composition of the film evolves.[17] All of this chemistry must be included explicitly in any quantitative determinations of diffusion coefficients if an understanding of the role of diffusion in limiting nanoscale lithography is to be developed.

In this article we report a systematic, chemically detailed method for investigation of PEB kinetics in order to make a direct measurement of acid diffusion in a well-defined reacting system. We describe the experimental and simulation methods we have developed for this purpose, and apply them to the specific positive tone photoresist system PTBOCST polymer with bis(para-*t*-butylphenyl)iodonium perfluorobutanesulfonate (PFBS) PAG. This polymer/PAG system was chosen because of the extensive literature that exists on the performance and deprotection chemistry of the resist polymer, and because the PAG, typical of systems currently in use, is a strong acid which obviates the need for including additional acid–base equilibria in the mechanism. It is also the simplest conceivable resist system that will show realistic behavior and can be characterized in detail chemically. The methods we have developed for this study are extendable to other resist systems involving copolymers, residual casting solvent, added base, and PAGs of various acid strengths.

II. EXPERIMENTAL METHODS

All previous acid diffusion studies have sought to start with a well-defined initial acid distribution in order to assess the evolution of the profile during PEB. Two types of approaches have been used: generation of a known acidic latent image in a nearly transparent resist, and juxtaposition of acidic and nonacidic layers in a single structure. In the first method, nonuniformities in initial acid density through the thickness of the film complicate analysis of the data. In the second, the nature of the interface between the layers is unknown, and may introduce additional kinetics that are not accounted for. We use what is essentially a hybrid of both methods with fewer complications in the interpretation of the results. We create a well-defined acidified layer in a resist film by exposure at a wavelength of 193 nm where the polymer is strongly absorbing. The resulting deprotection of PTBOCST during PEB is followed spectroscopically over a wide temperature range. We extract diffusion coefficients by simulation of the experimental data as a reaction-diffusion process using detailed acid-catalyzed and thermal deprotection chemistry.

A. Materials

Experiments were carried out on photoresists using the polymer poly(4-*t*-butoxycarbonyloxystyrene) (PTBOCST) with an average molecular weight $M_n = 52\,434$ and a polydispersity $M_w/M_n = 1.96$ from Kodak. The photoacid generator was bis(*t*-butylphenyl)iodonium perfluorobutanesulfonate (PFBS). It was prepared as described for the camphor sulfonic acid derivative (U.S. Patent 5,585,220) except that the metathesis used the perfluorobutane sulfonic acid derivative. Propylene glycol methyl ether acetate (PM acetate) (IBM, East Fishkill, NY) was used as the casting solvent for all resists.

Resist solutions were prepared using 17.5 wt % PTBOCST in PM acetate and a PAG loading of approximately 0.045 mol/kg of solids. Silicon wafers [25 mm diam wedges, Harrick Scientific, high infrared (IR) transparency] were first spin coated with the antireflection coating BARL 900 (IBM, East Fishkill, NY) at 2400 rpm and postapply baked at 205 °C for 90 s. Resist films were then applied from the PTBOCST solution at 3000 rpm and postapply baked at 130 °C for 90 s. Film thicknesses (~1.20 μm) were measured by profilometry (Tencor, Alpha-Step 200) and optical reflectance (Nanospec).

B. Spectrophotometry

Postexposure bake kinetics were probed using a Nicolet Fourier transform infrared (FTIR) microscope equipped with a heated stage. Temperatures ranged from 45 to 105 °C, controlled to within 1 °C during the experiment. A wafer was exposed at either 254 or 193 nm, then transferred immediately (within 5 min) to the hot stage to induce the acid-catalyzed deprotection reaction. About 30 s was allowed before starting the IR measurements to allow the wafer temperature to rise and equilibrate at the set temperature. This is expected to introduce significant uncertainty into the

data only at temperatures above 110 °C, when the deprotection reaction goes to completion in 1 min or so. A NaCl crystal window separated by a Viton O-ring spacer was used to cover the sample during the measurements. This minimized turbulence due to the N_2 purge, protected the sample from trace contaminants that could interfere with the kinetics, and protected the microscope optics from outgassed products.

The IR absorbance of the carbonyl stretch of PTBOCST (1760 cm^{-1}) was used to monitor the extent of deprotection of the polymer as a function of time. At early times when the PTBOCST decay rate was fastest, each measurement was averaged over eight scans. At later times, measurements were averaged over 64 scans. Background absorbance was measured using a wafer coated with BARL only, and subtracted from all data. The final extent-of-deprotection curves were obtained by dividing the background-corrected data by the background-corrected absorbance of PTBOCST measured prior to exposing the film. These curves were simulated as described below to extract reaction and diffusion rate constants.

C. Irradiation at 254 nm

Experiments using uniformly exposed films to measure the PEB deprotection kinetics in the absence of a diffusion component were carried out using procedures reported previously.[16] Films 1.2 μm thick were exposed under an Optical Associates Incorporated (OAI) deep ultraviolet (DUV) lamp. The light intensity at the wafer plane was measured using a calibrated exposure monitor (OAI 355 and P354), and a 254 nm probe. From preliminary dose-dependence studies it was determined that the rate of deprotection saturated at a dose of 200 mJ/cm^2, and this dose was used for all kinetics measurements. Under these exposure conditions gradients in photogenerated acid concentration and hence acid diffusion can be assumed to be negligible, so the spectrophotometric data reflect deprotection and acid-base kinetics only.

D. Irradiation at 193 nm

Illumination at 193 nm was used to create thin acidified layers in the resist films in order to measure coupled reaction and diffusion kinetics during PEB. The thickness of the layer is determined by the optical density (OD) of the polymer and by the exposure dose.

The absorption coefficient of PTBOCST at 193 nm has not been reported in the literature, and was measured in this work. The procedure used is as follows. Direct absorbance measurements at 193 nm can only be carried out on very thin films because of the high absorptivity of PTBOCST at that wavelength, but absolute thicknesses of very thin films are difficult to measure. Therefore, weaker absorbances at wavelengths where the absorption coefficient was already known were used as an internal standard. Absorbances at 265, 254, 237, 230, and 193 nm were measured for films of nominal thicknesses of 50 nm and 1.2 μm. The resulting absorbance at 193 nm was 13 μm^{-1}, estimated to be accurate to within ± 0.9. We have measured the reflectance of PTBOCST at 193 nm to be 0.147. Although the value of the reflectance may depend on changes in the chemical composition of the surface of the highly absorbing resist film during illumination, errors in this value will not significantly affect our conclusions because the effective quantum yield for acid generation is treated as a fitting parameter (see below).

Open-frame resist exposures were made by placing the coated substrate on a metal plate affixed at the reticle plane of an Integrated Solutions, Incorporated (ISI) 193 nm excimer laser exposure tool. Dose calibrations at the reticle plane were made by measurement of doses to clear for two resist systems at both the reticle plane and at the wafer plane, where calibrated dosimetry is available. The dose used for all the data reported in this work was 70 mJ/cm^2. This high value was chosen in order to create a reproducible acid profile well below the film surface, in a region of the resist film that is most likely to be bulk-like in characteristics and behavior and free of spurious interfacial phenomena. Procedures used to determine the acid profile generated in the resist films are described in Sec. IV.

E. Quantum yield of photoacid generation in PTBOCST films

Quantitative kinetics measurements cannot be made without detailed knowledge of the initial concentrations of all reagents. This is particularly important for the acid catalyst because the catalytic chain length is so long. We made these measurements by titration using bromophenol blue, sodium salt (Aldrich), whose absorbance is a sensitive function of pH. All measurements were made using procedures similar to those reported previously. The amount of photoacid generated was determined as a function of exposure dose (254 nm, 0–200 mJ/cm^2) in films prepared as described above except on 1 in. silicon wafers. Assuming a 1 in. wafer coated by a resist film 1.18 μm thick with 0.0445 molal PFBS in solids and a density for PTBOCST of 1.3 g/cm^3, a maximum of 3.44×10^{-8} moles of acid should be formed at 200 mJ/cm^2. The actual amount of photogenerated acid was determined to be 3.0×10^{-8} moles, corresponding to conversion efficiency of 87%. This method has poor precision at exposure doses below 20 mJ/cm^2 or for measuring less than 1.0×10^{-8} moles of photoacid.

A slightly modified procedure was used in an ultimately unsuccessful attempt to directly measure photoacid yields at 193 nm exposures. We found that over a dose range of 17–70 mJ/cm^2 there was no increase in the amount of photoacid measured by bromophenol blue titration despite the fact that the deprotection kinetics exhibited a strong dose dependence over the same range. This discrepancy indicates that formation of species that interfere with the bromophenol blue color change chemistry occurs on exposure at 193 nm. We attempted to use an alternative route for determining photoacid yield, fluorescence titration with acridine dye, but were also unsuccessful. In this case we conclude that the PAG, an iodonium salt, was interfering with the measurement by quenching the acridine fluorescence. Because of

TABLE I. Parameters used in the simulations.

	254 nm exposure		193 nm exposure
	CKS	VSIM	VSIM
Film thickness	1 μm	0.5 μm	1.2 μm
Film area	5 cm^2	8.5×10^{-10} cm^2	1 cm^2
No. of volume elements	1	85	120
Dose	200 mJ/cm^2	1 mJ/cm^2	70 mJ/cm^2
Initial acid distribution	Homogeneous	Sinusoidal	Layer
Temperature range	45–65 °C	100 °C	65–105 °C
No. of simulation particles	4.4×10^4	10^8	$1\times10^6-3\times10^8$

these difficulties, we used simulations to extract photoacid yields and initial distributions from kinetics data as will be described in Sec. IV.

III. SIMULATION METHODS

A. General model characteristics

All of the PTBOCST PEB deprotection kinetics were analyzed by detailed simulations of the chemistry at constant temperature over the same temperature range as the experiments. In all cases the films were assumed to have an initial acid concentration and distribution appropriate to the PAG concentration and to the exposure dose used; photolysis was not included in the model. The chemical reactions used for acid catalyzed deprotection,

$$\mathrm{PTBOCSTH^+ \rightarrow PHOSTH^+}, \quad (1)$$

$$\mathrm{PTBOCSTH^+ + PHOST \leftrightarrow PTBOCST + PHOSTH^+}, \quad (2)$$

and for uncatalyzed polymer thermolysis,

$$\mathrm{PTBOCST \rightarrow PHOST}, \quad (3)$$

$$\mathrm{PTBOCST + 2\,PHOST \rightarrow 3\,PHOST}, \quad (4)$$

are those reported previously.[16] The suffix H^+ denotes the protonated form. For simplicity, details of the chemistry leading to proton generation[18] were omitted, as were explicit representation of the PFBS anion, and the CO_2 and isobutylene that are released by deprotection and ultimately desorb from the film.[1] Protons were assumed to be always bound to a polymer, and never free as an independent species. Molar densities used for PTBOCST and PHOST were 5.91 and 11.90 mole/l, respectively.[16] Other simulation input is given in Table I.

Three film geometries were modeled. Single slab calculations were made to extract deprotection Arrhenius parameters appropriate to the PFBS/PTBOCST system from measurements of extent of polymer conversion as a function of time and temperature following blanket exposure at 254 nm. Stacked horizontal slabs were used to simulate chemistry coupled to diffusion after exposure at 193 nm. Stacked vertical slabs were used to simulate reaction-diffusion in a line-space-array-exposed film. Spatial inhomogeneities are assumed to be well represented by differences in composition between the slabs, however each individual slab is assumed to be spatially homogeneous at all times. This is a reasonable representation of the system because the slabs are chosen to be very thin.

B. Exposures at 254 nm

The simulator used for most of the 254 nm exposure calculations was a Chemical Kinetics Simulator (CKS), which is described in detail elsewhere.[16,19] Its particular value for the simulations in this work is its capability to carry out highly detailed calculations under variable volume conditions, that is, it allows concentrations to be properly renormalized as the reaction proceeds and the film volume (thickness) changes because of differences between reactant and product polymer densities. It was used to extract reaction kinetics for deprotection of PTBOCST using PFBS PAG. One simulation of PEB at 100 °C of a line-space array exposed at 254 nm was also carried out using Visual Chemical Kinetics Simulator (described below).

C. Exposures at 193 nm

A new version of CKS called Visual Chemical Kinetics Simulator (VSIM) was written for this series of experiments.[20] It uses the same core algorithm as CKS, but treats the system as a set of subvolumes linked by diffusion pathways, with each subvolume undergoing deprotection chemistry according to its initial acid concentration. The stochastic algorithm handles chemical reactions and diffusion events simultaneously in order to maintain an accurate absolute time base, thus allowing experiment and simulations to be compared directly. In the present work, each film was represented as a layered set of 120 10 nm thick slabs with bidirectional diffusion allowed between all adjacent slab pairs. As the deprotection reaction proceeds and the volume of each slab diminishes, film shrinkage is constrained to the thickness dimension only.

The most critical aspect of these simulations is the way in which the acid diffusion is modeled. The species that actually drives the deprotection chemistry is a proton. Our knowledge about the physics involved in motion of a proton through a polymer is quite meager, however the literature on ionic conduction through polymers may be relevant.[21,22] From quantitative PAG-dependent diffusion measurements,[23] we know that migration of a proton is coupled to movement of its anion (perfluorobutanesulfonate in this case), most likely because of local space charge limits, so acid diffusion is more properly describable as ion pair diffusion. This physical picture is supported by an analysis of the relevant Coulombic interactions.[24] Because of its lack of electrons, we expect the proton to interact strongly with its surroundings and never behave as a free species, but the anion's interactions may be more complex. These qualitative notions cannot be transformed into a detailed quantitative model without precise knowledge of exactly how a proton hops from site to site among the oxygen atoms in phenolic and carbonyl groups, where its anion is, and how the polymer responds to movement of charge. In order to avoid making numerous assumptions about the microscopic dynamics

of ion pair diffusion in a phenolic polymer, we have chosen to represent transport of protons as a compound process described by a single number. This allows us to extract Arrhenius coefficients that are sufficiently predictive to model the PEB process and to compare one materials system to another. It must be borne in mind, however, that they represent only the outcome of a number of processes folded together, not an elementary process. From a modeling point of view, our challenge in this work was to find a good description of reversible acid migration between adjacent slabs that would be computationally efficient and that would not require definition of one or more actual independent ionic species that would move under the influence of a concentration gradient. We also needed to ensure that we could simulate diffusion on a chemically relevant timescale (minutes), something that would be essentially impossible if fast trapping-escape kinetics were explicitly included.[25] The model also had to be sufficiently flexible to allow any sensitivity of the diffusion process to local environment (mainly PTBOCST or mainly PHOST depending on the extent of reaction) to emerge from the simulations. Our solution to this challenge was to describe the diffusion process as a simple place exchange between protonated and unprotonated PHOST or PTBOCST groups in two adjacent slabs, n and $n+1$. This process, which we call virtual diffusion, is represented by the steps,

$$\mathrm{PTBOCSTH}^{+}_{(n)} + \mathrm{PTBOCST}_{(n+1)} \leftrightarrow \mathrm{PTBOCST}_{(n)} + \mathrm{PTBOCSTH}^{+}_{(n+1)}, \tag{5}$$

$$\mathrm{PHOSTH}^{+}_{(n)} + \mathrm{PHOST}_{(n+1)} \leftrightarrow \mathrm{PHOST}_{(n)} + \mathrm{PHOSTH}^{+}_{(n+1)}. \tag{6}$$

The rate laws are incorporated as standard Fickian kinetics, not a second order reaction as given by the stoichiometry in steps (5) and (6). The general rate law describing the flux of protonated polymer (occupied traps) $p\text{-H}^+$ between two slabs is

$$\frac{d(p\text{-H}^+)}{dt} = D(T)\frac{A}{y_n - y_{n+1}}\left(\frac{(p\mathrm{H}_n^+)}{V_n} - \frac{(p\mathrm{H}_{n+1}^+)}{V_{n+1}}\right), \tag{7}$$

where $D(T)$ is the temperature-dependent diffusion coefficient, A is the interfacial contact area between the slabs, 1 cm^2 for the geometry used here, y is the vertical position of the center of a slab relative to the top surface, and V is the volume of a slab. Although the slab volumes and thicknesses are initially uniform, each evolves separately depending on local extent of deprotection as the reaction proceeds. Whenever a diffusion event is selected in the simulation, the stoichiometry is updated by trading occupied and unoccupied sites between the slabs, thus keeping the concentrations of PHOST and PTBOCST sites accurate while allowing net migration of ion pairs to take place. It should be noted that this description does not allow a direct pathway for protons to be exchanged between PHOST and PTBOCST pendent groups located in two different slabs. There is a rapid equilibrium (2) exchanging protons among binding sites within a slab, however, which in combination with a virtual diffusion step between two PHOST or two PTBOCST sites is assumed to be a good approximation for interspecies transfer. Virtual diffusion is both a computationally efficient and chemically accurate means of describing acid diffusion. Our ability to implement it is a direct consequence of the flexibility we have to independently prescribe stoichiometry and rate law in stochastic simulations of chemical kinetics.

A VSIM calculation produces as output a full time history of the concentrations of all chemical species and the volume of each slab in the 120 slab stack. In order to compare the simulation results to experiment, the molar amounts of PTBOCST in all slabs are summed for each point in time and normalized to the total, and the resulting fractional amount versus time curve is overlaid on the experimental data. No adjustment or scaling is performed on either the experimental or the simulation results except to make a small offset (1–2 min) in the experimental time base to compensate for the fact that the $t=0$ point of the absorption measurements occurs a little after the wafer is placed on the heated stage, not at the beginning of the reaction, and that the initial reaction rate will be slow because the wafer does not reach the set temperature instantaneously. Diffusion coefficients are obtained from the data by repeatedly estimating values for the diffusion coefficients D_{PTBOCST} and D_{PHOST}, performing a simulation, and comparing the simulation results to experiment. The experimental curves were fit as closely as possible, with goodness of fit being judged visually by closeness of match. The fits we report are actually more precise than the reproducibility of the experimental curves, which is within 5% except for the 105 °C experiments. We found that the goodness of the fits was generally very sensitive to the assumed values of D, with an estimated range of 10% or less in D giving comparable goodness of fit. The exception to this was for the D_{PHOST} coefficients, which in a few cases could vary by a factor of 2 with little effect on the simulated curves.

Stochastic simulators utilize particles to represent moles of reactants and products, with the underlying assumption that the energies of all chemical species are in a Boltzmann distribution, i.e., temperature is defined.[19] The graininess of the simulation depends on the number of particles used: one can never have too many, the calculation will just take longer and statistical effects will be smoothed out, but one can have too few. It is essential to verify that enough particles are specified in the system to properly describe the dynamic range of concentrations and rates of reaction, otherwise the results of the simulations will be incorrect. It is also important to assess the sensistivity of the simulation results to the choice of initial random number seed for the random number generator. When events are initiated by fluctuations or sporadic events, the exact time base depends on the random number chain, and several simulations must be averaged in order to compare results to experiment. We have done both in this work, and have found that they are both important. At the highest temperature simulated, 105 °C, we found that 3×10^{8} particles are required for the simulations because of the large difference in the magnitude of the rates of depro-

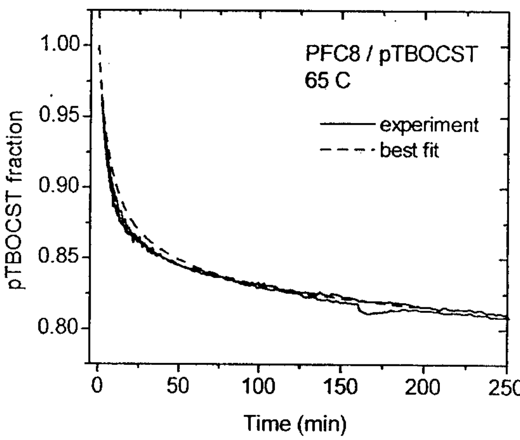

FIG. 1. Spectrophotometric data for deprotection at 65 °C in the PTBOCST/PFC8 system (two separate experiments, solid lines, showing typical experimental reproducibility) and best fit simulation (dashed line).

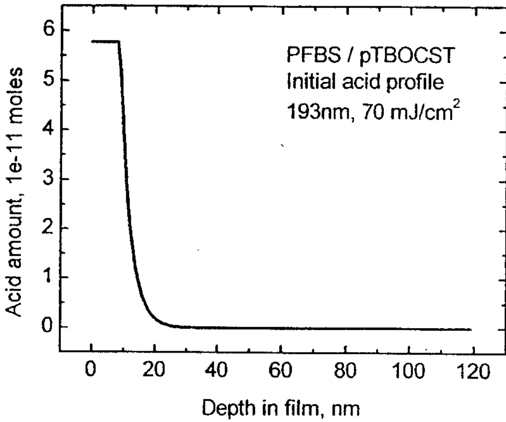

FIG. 2. Initial acid profile generated by irradiation at 193 nm, 70 mJ/cm^2. The top of the film is taken to be the origin of the x axis. Amounts are contained in a 1×10^{-6} cm^3 volume element. Further details are given in the text.

tection and diffusion at long times, while only 1×10^6 were necessary at 65 °C where the rates are more nearly matched. The influence of the initial random number was also most pronounced at 105 °C, giving variations in the simulated curves of about 1%. This reflects the fact that sporadic events become an important means of propagating the reaction at high temperature and long times, as will be discussed more fully below. All simulations were run on microcomputers with 333 MHz Pentium II or 300 MHz K6-2 microprocessors. Simulation runs typically required 2.5–14 h to calculate reaction-diffusion out to 200 min.

D. Estimation of initial acid profile formed by 193 nm irradiation

As discussed in Sec. II E, attempts to measure absolute yields of photoacid at 193 nm were unsuccessful because of interference of unidentified photochemical products with the titration. Therefore we used an indirect method to estimate photoacid yields and distributions.

Referring to Fig. 1, the disappearance curve of PTBOCST as a function of time at constant temperature involves several characteristic time scales. The initial fast decay reflects the deprotection rate at the particular acid concentration and temperature used. As the material surrounding the acid catalyst becomes converted to products, the reaction slows down, forming a distinct elbow in the curve. Past this stage the deprotection reaction will only proceed if the acid catalyst diffuses to regions of the film that have appreciable amounts of starting material, and the shape of the disappearance curve reflects primarily the diffusion process. We have found in our simulations that the extent of the initial fast decay and the shape of the elbow are sensitively dependent on the intrinsic deprotection kinetics, the total acid amount, and the distribution of the acid in the film.

By independently determining the deprotection kinetics and the optical properties of the resist film, we were able to use experimental deprotection curves to obtain a best fit for the initial photogenerated acid profile. This was actually carried out using a different PAG system, bis(t-butylphenyl)iodonium perfluorooctylsulfonate (PFC8) as part of a separate investigation comparing diffusion in several PAG systems.[23] Because the photochemical yield of acid and the optical densities of the films are identical for PFBS and PFC8 PAGs, the acid profile is the same for both systems. Acid diffusion in the PFC8 system is very slow, however, so the shape of the disappearance curve mainly reflects the initial acid distribution.

We assumed that the intensity distribution of light absorbed by the film was given by Beer's law, and have used the values for optical density and reflectance at 193 nm given in Sec. II D to calculate the resulting profile of light intensity penetrating onto the polymer film. Since the polymer as well as the PAG are strongly absorbing at this wavelength, but the polymer is at much higher concentration, the PAG decomposition is most likely due to a sensitization process which will have second order kinetics, not first order as in direct photolysis.[26] We found that, assuming the Perrin formulation for energy transfer[27] or electron transfer sensitization and adjusting the quenching rate to give the same total acid at 70 mJ/cm^2 as with direct absorption-dissociation, the shapes of the acid distributions differed only subtly between the direct and sensitized dissociation cases. Because the sensitization process has not been studied at 193 nm and actual kinetics data are not available, we have approximated the photolysis as a direct process, with a single fitting parameter, the quantum efficiency. The best fit value was determined to be 0.031 ±0.001. The resulting acid profile, shown in Fig. 2, is used to calculate the PTBOCST disappearance curve in Fig. 1. This profile has been used in all simulations performed in our acid diffusion work (wide temperature range and three different photoacid generators), only part of which is presented in this article. All PTBOCST disappearance simulation curves are consistently in agreement with experiment over this wide range of data, indicating that the acid profile is a reasonably accurate representation of the true profile.

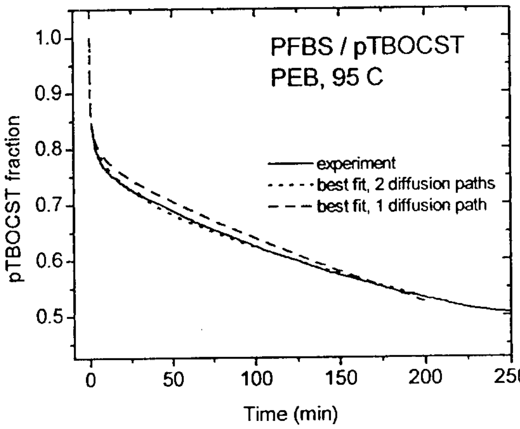

FIG. 3. Assessment of the accuracy of using a single diffusion path for acid diffusion in a reacting polymer instead of an environment-sensitive description. Experimental data and best fit simulations using a single path ($D = 2.8\times 10^{-15}$ cm^2/s) and two diffusion paths ($D_{PTBOCST}=3.5\times 10^{-14}$ cm^2/s and $D_{PHOST}=8\times 10^{-16}$ cm^2/s) are shown for PTBOCST/PFBS at 95 °C.

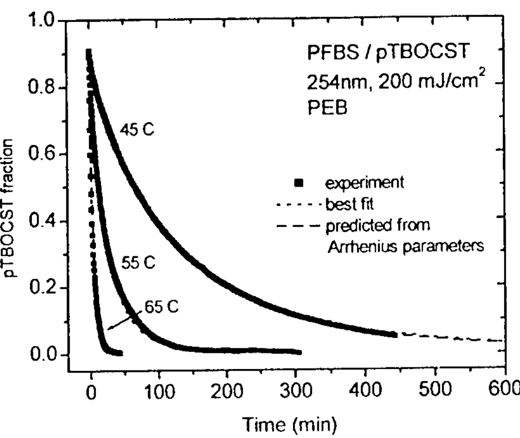

FIG. 4. Experimental data and best fit simulations for acid-catalyzed deprotection in the PTBOCST/PFBS system irradiated at 254 nm, 200 mJ/cm^2. The temperatures are below the threshold for significant uncatalyzed thermolysis. Curves predicted using the Arrhenius parameters extracted from the measurements are also shown.

E. Environmental sensitivity of diffusion

We have provided two independent diffusion paths for simulation of acid diffusion between each pair of layers: migration of acid through a purely PTBOCST environment, and migration of acid through a purely PHOST environment. The best fit diffusion coefficients were allowed to vary independently for the two paths in fitting the experimental data. In order to assess the consequences of this assumption we attempted to use a single diffusion coefficient for both pathways, the physical model being that diffusion is unaffected by chemical changes in the polymer as the deprotection reaction proceeds. This was done for several of the data sets; typical results for PFBS/PTBOCST at 95 °C are shown in Fig. 3. The assumption of a single diffusion coefficient operant at all times is unable to correctly describe the shape of the decay curve for both systems. This provides strong evidence that diffusion is sensitive to local environment during deprotection.

IV. RESULTS

A. Kinetics of acid-catalyzed deprotection in blanket-exposed films

Deprotection curves were measured for 1.2 μm thick films exposed at 254 nm over a temperature range of 45–65 °C and kinetics simulations were used to obtain rate constants for steps (1) and (2). Data and best fit simulations are shown in Fig. 4. The resulting best fit equilibrium constant for step (1) has $\Delta H = 7.85$ kcal/mol and $\Delta S = -2.25$ cal/mol deg. The acidolysis step (2) has the Arrhenius parameters $A = 1.4\times 10^{18}$ s^{-1} and $E_a = 28.67$ kcal/mol. These parameters, together with the Arrhenius parameters for uncatalyzed thermolysis reported previously,[16] were used in all reaction-diffusion simulations. It should be noted that these values are somewhat thickness dependent. Similar measurements in 0.2 μm thick films gave deprotection rates about 20% faster than those determined for the thicker films. The origin of this effect, which may be peculiar to PTBOCST because of its large density change on deprotection, is not known, but may be related to rates of secondary processes such as gas migration through the film.

B. Kinetics of acid-catalyzed deprotection in surface-exposed films

Experimental data and best fit simulations for PFBS-catalyzed deprotection are presented in Fig. 5. All of the experiments were very reproducible except at 105 °C. The origin of the variability in the data at that temperature was not determined. Accordingly, the experimental data in Fig. 5 are actually an average of four separate experimental determinations. The consistently close fits to the data indicate that over the temperature range of 65–95 °C our reaction diffusion model describes the kinetics well at all times. The fit to the 105 °C data is adequate to 50 min. It should be noted that we have not included processes such as acid loss or free

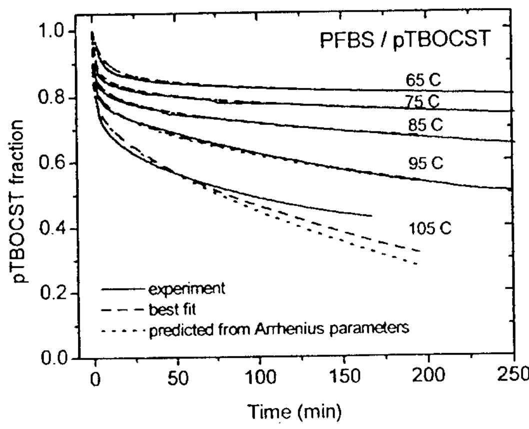

FIG. 5. Experimental data and best fit simulations for acid-catalyzed deprotection in the PTBOCST/PFBS system irradiated at 193 nm, 70 mJ/cm^2. Curves predicted using the Arrhenius parameters extracted from the measurements are also shown.

TABLE II. Best fit diffusion coefficients.

Temperature (°C)	$D_{PTBOCST}$ (cm^2/s)	D_{PHOST} (cm^2/s)
65	5×10^{-16}	4×10^{-17}
75	2.2×10^{-15}	1×10^{-16}
85	1×10^{-14}	4×10^{-16}
95	3.5×10^{-14}	8×10^{-16}
105	1.5×10^{-13}	1×10^{-15}

volume formation in our model,[7,8,12–15,28,29] and their inclusion does not appear to be necessary to fit the data.

Best fit diffusion coefficients are presented in Table II. An Arrhenius plot of these coefficients is shown in Fig. 6. The resulting Arrhenius parameters for diffusion in PHOST are $A=9\times10^{-3}$ cm^2/s and $E_a=22.1$ kcal/mol, and for diffusion in PTBOCST $A=1.9\times10^{8}$ cm^2/s and $E_a=36.5$ kcal/mol. The standard deviations of the parameters are ±2 kcal/mol for the activation energies, and a factor of 3 (for PTBOCST) to 40 (for PHOST) for the pre-exponentials. To check the validity of the Arrhenius parameters, simulations at various temperatures were run for comparison to experiment. The good agreement between the experimental data and the predicted decay curves shown in Fig. 5 provides evidence that the Arrhenius parameters reproduce the best fit curves reasonably well.

V. DISCUSSION

Previous reports of acid diffusion coefficients during PEB of PHOST-rich copolymer resist systems range from 10^{-15} to 10^{-11} cm^2/s at temperatures from 80 to 100 °C. In the present work the range is 1×10^{-14}–3.5×10^{-14} cm^2/s in PTBOCST and 4×10^{-16}–8×10^{-16} cm^2/s in PHOST from 85 to 95 °C. It is evident that the values determined in this work are at the bottom of the range or lower than those obtained using other techniques. These results raise important questions concerning the origin of the discrepancy between the present work and previous studies, the identity of processes leading to spreading of a latent image during PEB, and the nature of the diffusion process itself.

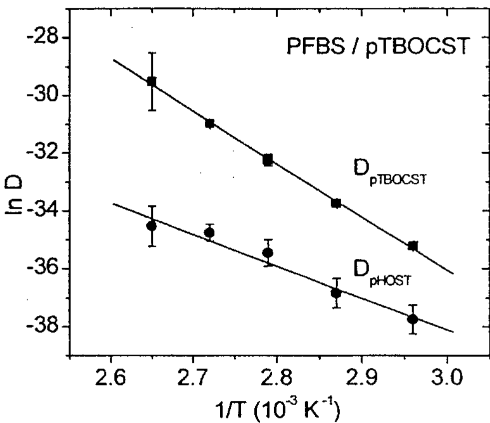

FIG. 6. Arrhenius plot of best fit diffusion coefficients for PTBOCST/PFBS. The values are given in Table II. Error bars reflect the outer limits of the range of diffusion coefficients that can be used to obtain a reasonable fit to the data.

In earlier investigations, acid diffusion was probed using either the extent of reaction measurements (usually resist loss) or ionic conductivity. Although these are fundamentally different types of measurements, there are some underlying similarities in the assumptions made about the physics involved. Conversion of ionic conductivity data into a diffusion coefficient and simple Fickian diffusion analysis of linewidth spreading data both presume acid diffusion to be independent of changes in the polymer as reaction proceeds, and implicitly take the deprotection rate to be linearly proportional to local acid concentration with no catalytic chain. The more realistic coupled reaction-diffusion model also neglects the interaction of the acid with the surrounding polymer during diffusion, but does allow for a catalytic chain. The deprotection reaction rate is dependent on both local protected group concentration and local acid concentration, and the PHOST product is assumed to be chemically inert. The acid concentration has a functional form that includes terms for loss of acid due to diffusion, evaporation, or trapping into unreactive sites. These loss processes are permanent.

If the diffusion coefficients extracted using any model are to be realistic, the model must capture the essential chemistry so that the proper kinetic balance between reaction and diffusion is struck. All previous models neglect critical aspects of the deprotection chemistry and the physics of the interaction between the polymer and the acid however. The catalytic chain length is very long, up to 1000 deprotection events per proton,[5] indicating that if there are permanent loss pathways for acid they are inefficient. Although the protons interact strongly with the resist components, the interactions are best described as coupled reversible equilibria.[5,16–18] The deprotection products are not inert, but act to autoaccelerate a competing nonacid-catalyzed thermolysis pathway. The assumptions made in previous models have profound consequences for analysis of the reaction-diffusion kinetics. Their treatment of local acid concentration and reactivity causes the true acid availability and hence the catalytic deprotection rate to be underestimated. In so doing, the magnitude of the diffusion coefficient must become quite large for the observed extent of reaction to be reproduced. Conversely, when the chemistry of the system is fully described, the calculated diffusion coefficients are much smaller.

The diffusion coefficients in Table II do not of themselves allow us to evaluate the balance between reaction and diffusion in the resist films because they are rate constants, not actual rates which depend also on local reagent concentrations. The chemical transformation of the resist film during PEB can best be understood by examination of the output of the simulations, which generate full concentration versus time curves for all species in the system. Spatial profiles for total acid (bound to PHOST and to PTBOCST) and for PTBOCST at times of 0, 1, 2, and 10 min during PEB at 100 °C are presented in Fig. 7. Two cases have been calcu-

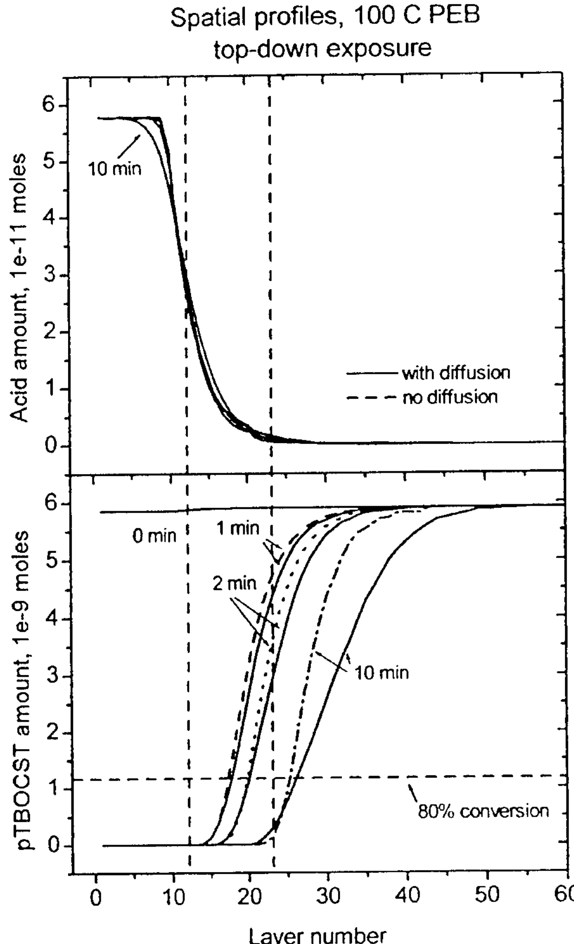

FIG. 7. Simulated total acid and PTBOCST spatial profiles for PEB at 100 °C. Amounts refer to those in each volume element, initially 1×10^{-6} cm^3. Layer 0 is at the top of the film. The solid lines are for calculations with both reaction and diffusion enabled, and the dashed lines are for reaction only. Also shown are dashed lines marking the 80% deprotection level of the polymer, approximately the position of the developable image, and dashed lines indicating the relative positions of the acid profile and the deprotected polymer profile after 2 min of postexposure bake.

lated: reaction with diffusion pathways enabled, and reaction with no diffusion allowed. Also included is a horizontal line denoting the 80% PTBOCST–PHOST conversion level, which is approximately the mixture at which the resist film becomes fully soluble in aqueous base developer.[29] It is interesting to note that at times up to 2 min the position at which PTBOCST is 80% deprotected is essentially independent of whether diffusion is allowed in the simulation or not, and the acid profile is nearly unchanged. The movement of the protected–deprotected PTBOCST boundary is substantial, however, as judged by comparing the initial total acid profile to the deprotected PTBOCST profiles (vertical dashed lines). This is entirely due to the long catalytic chain length: even very small amounts of acid will lead to substantial deprotection under these reaction conditions. As shown in Fig. 7, the deprotection boundary moves about 11 layers down in 120 s. Because PTBOCST and PHOST have molar densities of 5.91 and 11.90 mol/l, respectively,[16] the polymer undergoes a 45% molar density increase during deprotection.

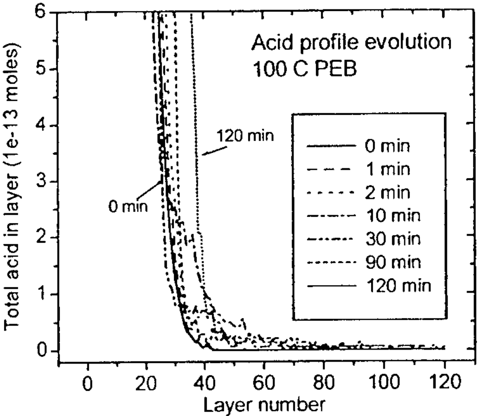

FIG. 8. Total acid profiles from Fig. 7 with additional curves from longer times, showing details of acid movement into the polymer film. The molar amount scale is expanded by a factor of 100.

Therefore, the 11 layers decrease in thickness from 110 to 50 nm over the 2 min period. If acid profile movement alone were responsible for the deprotection boundary position, the apparent acid diffusion coefficient would vary between 1 and 5×10^{-13} cm^2/s, in the middle of the range found in the literature. This analysis does not include the coupling of diffusion to reaction however. Although we find an initial diffusion coefficient of 7.8×10^{-14} cm^2/s when the film is pure PTBOCST, the effective coefficient drops rapidly to 1×10^{-15} cm^2/s as deprotection to PHOST proceeds and the position of the acid profile is essentially unchanged. It is interesting to note that a one-dimensional diffusion coefficient of 10^{-15} cm^2/s gives a mean displacement of about 5 nm, the same as the range estimated from the catalytic chain length.[5,18] This result reinforces the important point made above: if the chemical deprotection rate is not fully included in the analysis, the diffusion rate is overestimated.

The lack of significant relaxation of the acid profile indicates that a sharply defined acid front is not colocated with the deprotected polymer boundary,[8] but it does not mean that acidic species do not move at all. As shown in Fig. 8, amounts of acid at the level of a few percent of the initial maximum are eventually found throughout the thickness of the film. This arises from sporadic escape of acid from the most heavily acidified regions of the film. Although the concentrations are very low, their impact is sure to be felt at long times because of the long catalytic chain length leading to deprotection. Their impact at short times, on the other hand, is negligible. This is in agreement with experiments in which flare has been shown to have little effect on the linewidth of resist features processed under standard conditions.[8]

Taking the origin as the center of an isolated line, the profiles shown in Fig. 7 correspond to formation of highly overexposed, sparse 0.32 μm structures. It is interesting to examine the balance between reaction and diffusion in much smaller, dense structures using a typical line-space pattern and standard exposure and processing conditions to understand image spreading effects at the nanoscale. Accordingly, using the kinetics parameters presented above, we simulated 1 mJ/cm^2, 254 nm exposure of PFBS/PTBOCST resist using

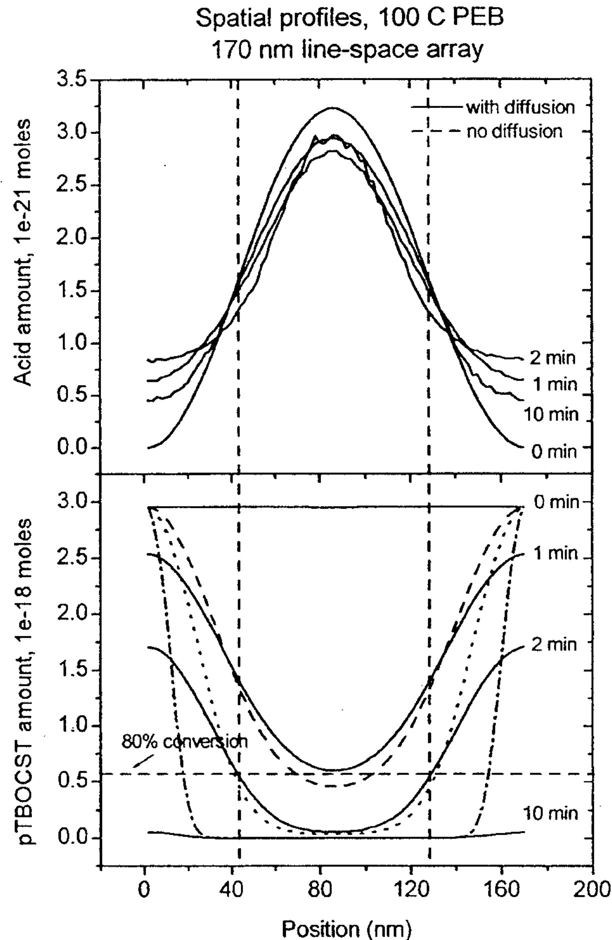

FIG. 9. Simulated total acid and PTBOCST spatial profiles for 100 °C PEB of a 170 nm line-space array exposed at 245 nm, 1 mJ/cm^2. Amounts are those in a single volume clement, initially $5\times10^{-16}\,cm^3$. A single period is shown. The solid lines are for calculations with both reaction and diffusion enabled, and the dashed lines are for reaction only. Also shown are dashed lines marking the 80% deprotection level of the polymer, approximately the position of the developable image, and dashed lines indicating the nominal 85 nm linewidth of the initial acid distribution.

a 170 nm pitch line-space array. Due to numerical constraints in VSIM[30] only one period of the array could be calculated. We used 85 2 nm thick vertical slabs to model this period, and connected the outer two slabs with diffusion paths to enable periodic boundary conditions. A plot of simulation results analogous to that in Fig. 7 is given in Fig. 9.

In this case also diffusion is found to contribute negligibly to the spatial extent of deprotection at 2 min. The acid profile is not static on this length scale, however, but undergoes significant relaxation. The apparently greater change in the acid profile is a result of two factors: the initial feature size is much smaller so concentration gradients and, therefore, initial diffusion rates are larger, and acid diffusing into nominally unexposed regions in an 85 nm line-space array will necessarily be more concentrated—and thus more obvious—than acid leaving a thin top layer and spreading out through 1 μm of resist. As a consequence, even though diffusion does not affect feature size for a standard 2 min PEB at 100 °C (see vertical dashed lines), and the printed linewidth would be nearly ideal, the simulations indicate that the process window is narrow, and the image will be lost very quickly after longer bake times. As a final comment, close inspection of Fig. 9 reveals that increases in acid concentration in the nominally unexposed regions of the resist are not monotonic: at first it increases as expected, but later drops. This very surprising result has as its kinetic origins the rapidly changing gradients of acid bound to PTBOCST and of acid bound to PHOST on this time scale. The simultaneous deprotection reaction changes the relative rates of diffusion between the different regions of the patterned resist in complex ways. It is not known at present whether this prediction is real or is a consequence of the way our reaction-diffusion model is structured. Direct experimental probes of the evolution of a dilute acid profile during reaction on this length scale would be a most useful test of the model.

The diffusion coefficients we report here as single values clearly represent a series of complex events. We really have two time and length scales for diffusion: highly localized movement (approximately 5 nm, affecting chemistry at short times) to propagate a full catalytic chain, and longer range movement (hundreds of nm, affecting chemistry at long times) which must involve migration of both anion and cation in order to maintain charge neutrality. Some insight into the diffusion physics may be gained from consideration of model systems. Recent measurements of trifluoroacetic acid uptake from the vapor phase into unreacting PHOST films gave a time-varying diffusion coefficient in the range of 10^{-10}–$10^{-12}\,cm^2/s$ from 30 to 45 °C.[31] This is many orders of magnitude larger than values determined for the PTBOCST photoresist system, indicating that different physics are involved in this system. The literature on ionic conductivity in polymers, on the other hand, provides some insight into the physics of acid diffusion despite the profound differences in the materials involved. This is clearly not a new idea,[2,9–11] however a detailed consideration of quantitative aspects of the diffusion has not been made. Conductivity data for high concentrations of CsCl in cellulose acetate reveal that typical diffusion coefficients for the cation in the polymer are in the range of $2\times10^{-17}\,cm^2/s$ at 68 °C, with an activation energy of about 24 kcal/mol.[21] Although the PAG anion is larger and heavier, it is interesting that the comparable diffusion coefficient for the acid-PFBS ion pair in PHOST, also an oxygen-rich environment, is $4.6\times10^{-17}\,cm^2/s$ at 65 °C, with an activation energy of 22.1 kcal/mol. Theoretical investigations of the mobility of ions through polymers at temperatures below and above the glass transition temperature have shown that the kinetics of diffusion have Fickian form, but are characterized as a hopping process.[22] Hopping is always a short-range event, confined to a local cage at short times, but leading to net long-range motion as the polymer chains move about and open transient channels. Thus, ion diffusion is dominated by dynamic fluctuations in local density of the polymer host. The present results show that acid diffusion in resist also exhibits statistical hopping behavior (Fig. 8) even though the kinetic rate

law in the model is conventional Fickian diffusion. How the polymer is involved in movement of acid and anion during PEB is not clear beyond the result that some level of environment specificity is required for diffusion in the simulations. It is certain that the details of the accompanying chemical reactions cannot be ignored in the diffusion dynamics. The deprotection reaction generates small, reactive, charged species that ultimately leave the film as stable molecules, but are likely to interact strongly with their environment initially.[32] We can ask whether these products mediate proton movement. The evolution of small molecules in the conversion of PTBOCST to PHOST can be expected to lead to increased free volume in the film at first, but substantial densification occurs once they have left the film. Thus, polymer fluctuation effects on diffusion during deprotection are not likely to be simply describable in terms of characteristic temperatures for types of polymer motion as has been found for nonreacting systems.[33] Experiments that may provide more detailed information on the physics of acid diffusion in resists are in progress.

The results reported here are quantitatively applicable only to the PTBOCST homopolymer. They can be used qualitatively, however, to consider behavior in chemically related resists such as PHOST–PTBOCST copolymers to the extent that deprotection kinetics in the copolymer are dominated by chemical composition and not by possible structural differences between a copolymer and a partially reacted homopolymer. Given the very slow diffusion rate of acid in PHOST, the already small contribution of diffusion to image blurring in the PTBOCST homopolymer can be considered an extreme case; in copolymer-based resists it is likely to be much lower. Extrapolation to other copolymers such as the PHOST–acrylate systems or non-PHOST-based resists is not possible without additional data.

VI. CONCLUSIONS

We have described a combined experimental-modeling approach to determination of acid diffusion coefficients in chemically amplified resist during postexposure bake. The experiments involve creation of a well-defined, thin acid layer in a resist film and following deprotection of the polymer spectrophotometrically. Simulations of the coupled reaction-diffusion system were made using known acid-catalyzed and noncatalyzed deprotection chemistry to extract diffusion coefficients. The method has been applied to the PTBOCST/PFBS resist system over the temperature range of 65–105 °C. Diffusion could not be described by a single coefficient, instead, two diffusion paths specific to diffusion in nonpolar PTBOCST and polar PHOST were required. Concentration profiles as a function of time obtained from simulations of the postexposure bake process reveal that acid diffusion does *not* account for blurring of latent images in this resist system. Rather, image spreading is dominated by the long catalytic chain length characteristic of the deprotection reaction. Diffusion is likely to be even less important for the PHOST-rich PHOST-pTBOCST copolymers more commonly in use for deep-UV lithography, assuming that similar kinetics apply. These results indicate that strategies to minimize resist image spreading during postexposure bake in order to fabricate structures 100 nm or smaller should focus on control of the catalytic chemistry. The data also point to a need for refined photolithography models for prediction of imaging on this length scale.

ACKNOWLEDGMENTS

The authors are grateful to Hiroshi Ito for valuable discussions through the course of this study, to Juliann Opitz, Debra Fenzel-Alexander and Dean Pearson for assistance with the experiments, and to Philip Brock and Gregory Breyta for preparation of bis(*t*-butylphenyl)iodonium perfluorobutanesulfonate. They thank Thomas Clarke for his support and encouragement of the stochastic simulation project that led to writing CKS and VSIM. This research was supported in part by the National Science Foundation Materials Research Science and Engineering Center under Grant No. 9808677 to the Center for Polymer Interfaces and Macromolecular Assemblies.

[1]G. M. Wallraff and W. D. Hinsberg, Chem. Rev. **99**, 1801 (1999).
[2]J. Nakamura, H. Ban, K. Deguchi, and A. Tanaka, Jpn. J. Appl. Phys., Part 1 **30**, 2619 (1991).
[3]L. Schlegel, T. Ueno, N. Hayashi, and T. Iwayanagi, J. Vac. Sci. Technol. B **9**, 278 (1991).
[4]L. Ocola, D. S. Fryer, G. Reynolds, A. Krasnaperova, and F. Cerrina, Appl. Phys. Lett. **68**, 717 (1996).
[5]D. R. McKean, U. Schaedeli, and S. A. MacDonald, J. Polym. Sci., Part A: Polym. Chem. **27**, 3927 (1989).
[6]J. W. Thackeray, T. Adams, M. F. Cronin, M. Denison, T. H. Fedynyshyn, J. Georger, J. M. Mori, G. W. Orsula, and R. Sinta, J. Photopolym. Sci. Technol. **3**, 619 (1994).
[7]H. Watanabe, H. Sumitani, T. Kumada, M. Inoue, K. Marumoto, and Y. Matsui, Jpn. J. Appl. Phys., Part 1 **34**, 6780 (1995).
[8]M. Zuniga, G. Wallraff, and A. R. Neureuther, Proc. SPIE **2438**, 113 (1995).
[9]T. Itani, H. Yoshino, S. Hashimoto, M. Yamana, N. Samoto, and K. Kasama, J. Vac. Sci. Technol. B **14**, 4226 (1996).
[10]T. Itani, H. Yoshino, S. Hashimoto, M. Yamana, N. Samoto, and K. Kasama J. Vac. Sci. Technol. B **15**, 2541 (1997).
[11]T. Itani, H. Yoshino, S. Hashimoto, M. Yamana, N. Samoto, and K. Kasama, Jpn. J. Appl. Phys., Part 1 **35**, 6501 (1996).
[12]A. A. Krasnaperova, M. Khan, S. Rhyner, J. W. Taylor, Y. Zhu, and F. Cerrina, J. Vac. Sci. Technol. B **12**, 3900 (1994).
[13]C. Coenjarts, J. Cameron, N. Deschamps, D. Hambly, G. Pohlers, J. C. Scaiano, R. Sinta, S. Virdee, and A. Zampini, Proc. SPIE **3678**, 1062 (1999).
[14]J. S. Petersen, C. A. Mack, J. Sturtevant, J. D. Byers, and D. A. Miller, Proc. SPIE **2438**, 167 (1995).
[15]M. A. Zuniga and A. R. Neureuther, J. Vac. Sci. Technol. B **14**, 4221 (1996).
[16]G. Wallraff, J. Hutchinson, W. Hinsberg, F. Houle, P. Seidel, R. Johnson, and W. Oldham, J. Vac. Sci. Technol. B **12**, 3857 (1994).
[17]G. M. Wallraff, W. D. Hinsberg, F. Houle, J. Opitz, and D. Hopper, Proc. SPIE **2438**, 182 (1995).
[18]D. R. McKean, R. D. Allen, P. H. Kasai, U. P. Schaedeli, and S. A. MacDonald, Proc. SPIE **1672**, 94 (1992).
[19]The Chemical Kinetics Simulator program package, including supporting documentation, is available for a no-cost license from IBM at http://www.almaden.ibm.com/st/msim/. A reference for the basic algorithm is D. J. Gillespie, J. Comput. Phys. **22**, 403 (1976).
[20]W. D. Hinsberg and F. A. Houle, U.S. Patent Nos. 5,446,870 (issued 1995), and 5,826,065 (issued 1998); for other algorithms for diffusive systems see, for example, F. A. Houle and W. D. Hinsberg, Appl. Phys. A: Mater. Sci. Process. **66**, 143 (1998); P. Hanusse and A. Blanche, J. Chem. Phys. **74**, 6148 (1981).

[21]*Diffusion in Polymers*, edited by J. Crank and G. S. Park (Academic, London, 1968), Chap. 4.

[22]A. Nitzan and M. A. Ratner, J. Phys. Chem. **98**, 1765 (1994); M. C. Lonergan, A. Nitzan, M. A. Ratner, and D. F. Shriver, J. Chem. Phys. **103**, 3253 (1995).

[23]W. D. Hinsberg, F. A. Houle, M. Morrison, G. Wallraff, C. Larson, M. Sanchez, and J. Hoffnagle (unpublished); G. M. Wallraff, W. D. Hinsberg, F. A. Houle, M. Morrison, C. Larson, M. Sanchez, J. Hoffnagle, P. J. Brock, and G. Breyta, Proc. SPIE **3678**, 138 (1999).

[24]X. Shi, J. Vac. Sci. Technol. B **17**, 350 (1999).

[25]M. Toriumi, T. Ohfuji, M. Endo, and H. Morimoto, Proc. SPIE **3678**, 368 (1999).

[26]N. P. Hacker and K. P. Welsh, Macromolecules **24**, 2137 (1991).

[27]N. J. Turro, *Modern Molecular Photochemistry* (Benjamin/Cummings, Menlo Park, CA, 1978), pp. 317–319.

[28]S. Hashimoto, T. Itani, H. Yoshino, M. Yamana, N. Samoto, and K. Kasama, Proc. SPIE **3049**, 248 (1997).

[29]H. Ito, J. Photopolym. Sci. Technol. **11**, 379 (1998).

[30]VSIM is written for a 32 bit word length. This places a constraint on the number of particles that can be used in a simulation to be less than about four billion. The large dynamic range of concentrations and rates in the 254 nm deprotection reaction-diffusion system requires at least one million particles per vertical slab.

[31]K. E. Mueller, W. J. Koros, C. A. Mack, and C. G. Willson, Proc. SPIE **3049**, 706 (1997); P. L. Zhang, A. R. Eckert, C. G. Willson, and S. E. Webber, *ibid.* **3049**, 898 (1997).

[32]H. Ito and M. Sherwood, Proc. SPIE **3678**, 104 (1999); F. A. Houle, G. M. Poliskie, and W. D. Hinsberg (unpublished mass spectrometry data).

[33]D. B. Hall, A. Dhinojwala, and J. M. Torkelson, Phys. Rev. Lett. **79**, 103 (1997); P. Pendzig, W. Dieterich, and A. Nitzan, J. Non-Cryst. Solids **235–237**, 748 (1998); A. A. Gusev and U. W. Suter, J. Chem. Phys. **99**, 2228 (1993).

Statistical considerations of the overlay error in laser driven point source x-ray lithography

Detlev H. Tiszauer[a)]
Laser Science and Technology Dept., Lawrence Livermore National Laboratory, Livermore, California 94550

(Received 4 December 1996; accepted 7 April 2000)

A statistical measure of the point source divergence-induced overlay error over the print field is derived. The assumptions of a wide-sense stationary distribution of gap error and the assumption of a symmetric distribution of overlay sites on the chip field give rise to simple expressions for the overlay error variance. The computations for overlay error are also expressed in the Fourier domain. From this formulation, it is found that these simple results hold for the zero frequency and high frequency limit of gap error in the Fourier domain, even without the assumptions of stationarity.
© *2000 American Vacuum Society.* [S0734-211X(00)01104-5]

I. INTRODUCTION

Point source x-ray lithography (PS-XRL) has been considered a good candidate for extending chip production capabilities to the 0.13 μm feature size area and smaller.[1,2] PS-XRL proximity print introduces errors in overlay and in critical dimension (CD) that are not present for synchrotron x-ray proximity print. Additional errors arise from the spherical wave geometry or divergent rays in the point source used to transfer a pattern from the mask into the resist. Most of the deterministic aspects of these errors can be eliminated by modifications in the pattern written into the mask. Residual random errors can be minimized by reducing the divergence angle of the point source or decreasing the mask-to-wafer gap. Since the optimum gap is set by the depth of focus, in general only the reduction of the point source divergence is left as a means of minimizing the divergence-induced errors. In turn without an x-ray-collimating device the divergence angle can only be reduced by increasing the distance of the x-ray point source from the mask plane. Every increase in distance is accompanied by a corresponding quadratic drop in x-ray power available at the resist. This in turn leads to a significant increase in the cost of the PS-XRL proximity-print tool.

Estimates of the overlay random error ascribable to point source divergence use the maximal ray slope on the print field to predict the transfer of gap error into overlay error. Such estimates have been used to set the acceptable distance for proximity-print, point source x-ray. Because of the significant source cost increase when increasing distance, we look more carefully at the overlay error calculation. We relate the expected overlay error to the statistics of the gap error and find that in certain cases the variance is reduced by a factor of 0.577 compared to use of the maximal ray slope.

II. OVERLAY AND CD ERRORS DUE TO POINT SOURCE PROJECTION GEOMETRY

Point source projection lithography utilizes a spherical wave originating at the x-ray target point to transfer the pattern contained in a planar mask to a planar plate consisting of the resist covered wafer [see Figs. 1(a) and 1(b)]. Given that the point source lies on the optic axis of the projection column at a fixed standoff distance D from the mask and that the mask-to-wafer gap g is a fixed quantity, the field dependent magnification induced by the spherical wave projection is corrected in mask writing. Thus the PS-XRL mask is matched to the specific projection geometry being used in the PS-XRL tool. Since production at and below 0.18 μm feature sizes is sensitive to overlay and CD errors in the few tens of nanometers and the pattern transfer to the resist involves a volumetric exposure process, the net adjustment in the mask needs to account for the specific gap and resist thickness used.[3] For example, at the edge of a centered, 30 mm sized field with a standoff distance D of 22 cm to the wafer and a nominal 20 μm mask–wafer gap, the spherical projection effect is corrected by a 1021.36 μm shift of the features on the mask towards the projection axis. The 20 μm mask–wafer gap accounts for only 0.13% of this total. The size of this correction is scaled linearly as the distance from the axis: from zero to that given at the field edge. An additional field-dependent shift of the mask features is required to account for resist thickness. For example, given a resist thickness of 0.75 μm, and our point source geometry shown in Fig. 1, the additional correction at the edge of the field requires a shift in the mask feature positions of 26 nm away from the axis. Electron beam lithography is developing the capability for achieving accuracies required for such small PS-XRL mask corrections.[4] After these corrections have been implemented in the mask, overlay errors can arise when the mask-to-wafer gap is not constant over the imaging field but contains a random fluctuation that is in general a function of field position. The net gap g can be written as the sum of the gap to the median plane, g_0, and a field dependent residual $\Delta g(x,y)$.

$$g=g_0+\Delta g(x,y). \tag{1}$$

III. OVERLAY ERROR STATISTICS: MATHEMATICAL BASIS

A. Error contributors

Figures 1–3 show the representative point source x-ray proximity print geometry with successive magnifications of

[a)]Electronic mail: tiszauer1@llnl.gov

 0734-211X/2000/18(4)/1886/4/$17.00 ©2000 American Vacuum Society

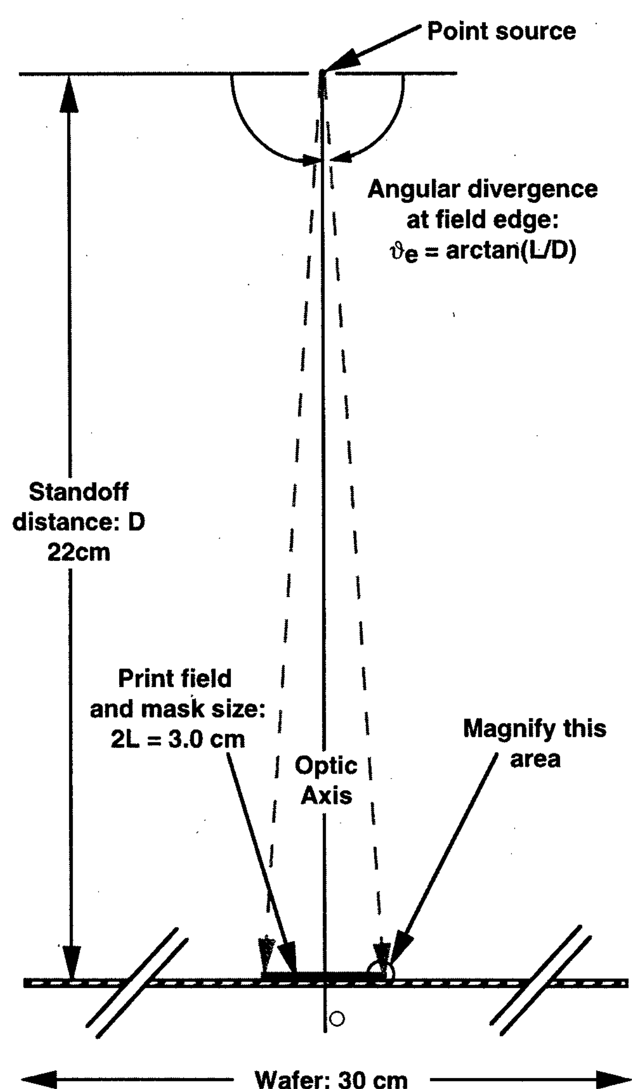

FIG. 1. Geometry of point source proximity print lithography showing the source to mask standoff distance for our nominal system and the maximum divergence angle of the incident x rays at the print mask.

an area near the edge of the print field. Each view preserves the respective scale of the included items. Figure 1 shows that the maximum angle made by x rays at the edge of the 300 mm field is 3.9°. In Fig. 2 a detail near the field edge is shown with the resist surface topography representative of approximately a 0.2 μm root mean square (rms) surface height variation. In Fig. 3 we see how the impinging x ray, targeted for the point at $\bar{x}$ on the mean gap plane, actually intersects the resist at $\bar{x}-\epsilon_x$ due to the local gap error $\Delta g(\bar{x},\bar{y})$. This is the origin of the overlay error considered here.

B. Statistical character

An overlay error is generated at any point (x_o,y_o) inside the print field where a print feature edge that is used as an overlay site for prior or postlithographic layers coincides with a gap error. That is, there are no overlay errors generated in regions in which there are no feature edges, even with

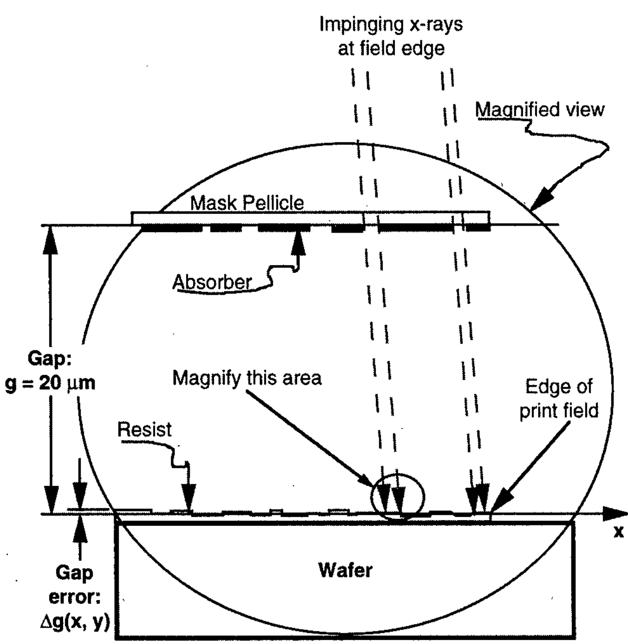

FIG. 2. Magnified view of the mask/wafer area with the gap used for our nominal system and typical gap errors.

gap errors present in those regions. The scaling of overlay error from gap error is through the local projection angle $\theta = \arctan(|\bar{x}|/D)$ as shown in Fig. 3. Using the small-angle approximation for the arctangent, the overlay error distribution function's x and y components, ϵ_x and ϵ_y are given by

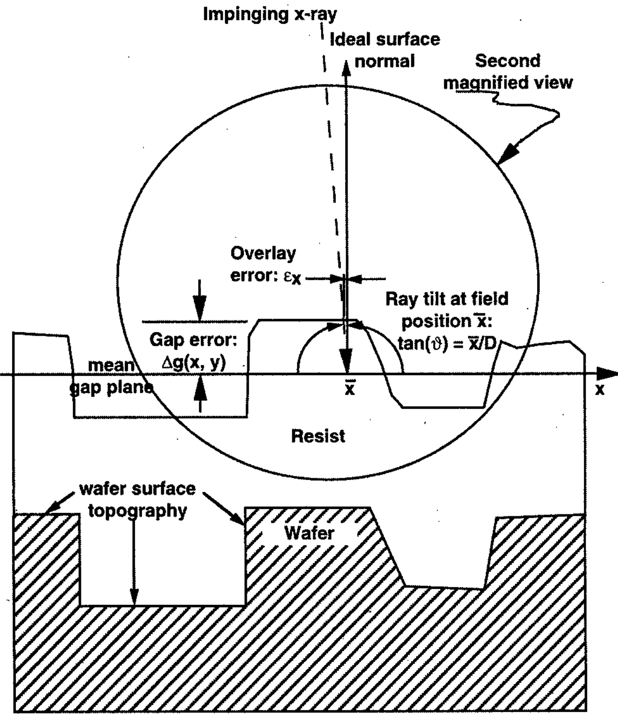

FIG. 3. Closeup of wafer surface and deviations from nominal gap plane in the resist. The overlay error is shown as the shift of the feature edge due to the slanted impinging x ray and the deviation of the resist surface from the nominal gap plane.

$$\epsilon_\xi(x,y)=\frac{\xi}{D}\Delta g(x,y)\,\delta(x-x_o,y-y_o), \tag{2}$$

where $\xi=x$ or y.

We wish to consider the overlay error of all point-source x-ray steppers. The statistical ensemble from which ϵ_x and ϵ_y are derived includes all point-source x-ray steppers having possible gap errors $\Delta g(x,y)$ and all possible chips printed on those steppers having overlay sites at (x_o,y_o).

Since the x and y axes are treated identically, we will only consider the x component of the overlay error distribution function in what follows. The results for the y component follow in analogy from those derived for the x component. The expected overlay error is $\langle\epsilon_x\rangle$:

$$\langle\epsilon_x(x,y)\rangle=\frac{1}{D}\left\langle\left\langle\int_{-\infty}^{\infty}\int_{-\infty}^{\infty}dx\,dy\,x\Delta g(x,y)\times\delta(x-x_o,y-y_o)\right\rangle_F\right\rangle_G, \tag{3}$$

where $\langle\cdot\rangle$ represents an average over the ensemble of possible chips printed. The total ensemble is divided into two disjoint subspaces containing the gap variation and the field position of the overlay. This is represented in the right-hand side of the equality with $\langle\cdot\rangle_F$ representing the average over all possible field positions for the overlay sites and $\langle\cdot\rangle_G$ representing the average over all possible gap errors at any given site. Since the overlay site position is independent of the gap variation we have $\langle\langle\cdot\rangle_F\rangle_G=\langle\langle\cdot\rangle_G\rangle_F$ and

$$\langle\epsilon_x(x,y)\rangle=\frac{1}{D}\left\langle\int_{-\infty}^{\infty}\int_{-\infty}^{\infty}dx\,dy\,x\langle\Delta_g(x,y)\rangle_G\times\delta(x-x_o,y-y_o)\right\rangle_F=\frac{1}{D}\langle x_o\mu_g(x_o,y_o)\rangle_F, \tag{4}$$

where $\mu_g(x_o,y_o)$ is the mean gap error over the ensemble at the overlay site position (x_o,y_o).

For simplicity we drop the "o" subscripts in what follows. If we assume that $\Delta g(x,y)$ is stationary in the wide sense[5] (i.e., the first and second moments of Δg are not deterministic functions of the field positions), then μ_g is independent of (x, y) and can be removed from the average over field position. Since we can reasonably expect the distribution of overlay position to be a symmetric function in the field variable, the average $\langle x\rangle_F$ is zero and therefore the mean overlay error ϵ_x is also zero. We see then that a zero mean overlay error depends on the minimal assumptions of (1) a gap error that is stationary in the wide sense and (2) a distribution of overlay position that is symmetric in each of the field variables x and y.

In general, the overlay error variance $\sigma_{\epsilon x}^2$ is given by

$$\sigma_{\epsilon x}^2=\langle\epsilon_x^2\rangle-\langle\epsilon_x\rangle^2=\frac{1}{D^2}[\langle x^2\langle\Delta g^2(x,y)\rangle_G\rangle_F-\langle x\mu_g(x,y)\rangle_F^2], \tag{5}$$

where we again have used the fact that the position of the overlay site is independent of the gap error. With a stationary gap error Δg and with a symmetric distribution of overlay position, Eq. (5) reduces to

$$\sigma_{\epsilon x}^2=\frac{\sigma_g^2}{D^2}\langle x^2\rangle_F, \tag{6}$$

where σ_g^2 represents the ensemble gap error variance.

C. Effects of nonstationarity at low and high spatial frequencies

Relaxing the assumption of stationarity we consider the random process constituting the gap error more closely. The gap error is defined as the residual gap deviation after the best calibration has been performed on the tool. Topography of resist covering previous lithographic layers, errors in the aligner's out-of-plane positioning of mask and wafer, wafer nonflatness and various mechanical distortions all contribute to the gap error at the field point *(x, y)*. Some of these error sources contribute to local gap variation at the site and others give rise to a constant gap error across the print field. When looked at on a spatial frequency scale, the aligner's residual gap positioning error (residual axial offset of the field and field tilts in x and y) is near zero spatial frequency while topography variations over the field due to prior level features are near the maximum spatial frequency supported by the print resolution. At zero spatial frequency, the gap error is independent of field position and we recover stationarity. Near infinite spatial frequency, the gap error from one point to the next varies in an uncorrelated fashion and therefore the gap statistics are again independent of field position. In either case, the random process is wide-sense stationary and Eq. (6) applies. At frequencies intermediate between zero and infinity and for gap errors that are deterministic functions of the field variables, other considerations need to be made. We treat this more general and more complicated case in Sec. III D.

To proceed further we must specify the distribution for the overlay position. Maintaining symmetry about the origin, we assume that the probability of finding an overlay site within the field is uniformly distributed between the field boundaries. That is, the overlay site is equally likely to be anywhere inside the print field. The average in Eq. (6) then becomes

$$\langle x^2\rangle_F=\int_{-L_y}^{L_y}dy\int_{-L_x}^{L_x}dx\,\frac{1}{2L_xL_y}x^2=\frac{1}{3}L_x^2, \tag{7}$$

where the uniform distribution function,

$$f(x,y)=\begin{cases}\dfrac{1}{2L_x\cdot 2L_y}, & |x|\leq L_x \text{ and } |y|\leq L_y\\ 0, & |x|>L_x \text{ or } |y|>L_y\end{cases}, \tag{8}$$

is used for the overlay site. This then gives the variance of the x-axis overlay error as

$$\sigma_{\epsilon x}^2=\frac{1}{3}\left(\frac{L_x\sigma_g}{D}\right)^2, \tag{9}$$

and the standard deviation of overlay error due to gap in each axis is therefore $1/\sqrt{3}$ (=0.577) times the product of point source divergence at the field edge and gap standard deviation.

$$\sigma_{\epsilon x}=\frac{1}{\sqrt{3}}\left|\frac{L_x}{D}\right|\sigma_g;\quad \sigma_{\epsilon y}=\frac{1}{\sqrt{3}}\left|\frac{L_y}{D}\right|\sigma_g. \tag{10}$$

D. Effects of nonstationarity at arbitrary spatial frequencies

We investigate what happens at an arbitrary spatial frequency when we keep the assumption of a uniform distribution in overlay position and relax the requirement that the gap error is stationary on (x,y). To this end we expand Δg in a double Fourier series with x and y within $(-L,L)$.

$$\Delta g(\mu,\nu)=\sum_{n=-\infty}^{n=\infty}\sum_{m=-\infty}^{m=\infty} a_{n,m}e^{i(n\mu+m\nu)};$$

$$\mu=\pi x/L,\qquad \nu=\pi y/L. \tag{11}$$

After substituting the above result into the general expression for the overlay variance $\sigma_{\epsilon x}^2$ given in Eq. (5) we get, after some algebra,

$$\sigma_{\epsilon x}^2=\frac{L^2}{D^2}\left[\frac{1}{3}\sum_n\sum_m \langle|a_{n,m}|^2\rangle_G + \frac{2}{\pi^2}\sum_n\sum_{p\neq n}\frac{(-1)^{n-p}}{(n-p)^2}\sum_m\langle a_{n,m}a_{p,m}^*\rangle_G - \frac{1}{\pi^2}\sum_{n\neq 0}\sum_{m\neq 0}\langle a_{n,0}a_{m,0}^*\rangle_G\frac{(-1)^{n+m}}{n\cdot m}\right], \tag{12}$$

where all sums are from $-\infty$ to ∞ unless otherwise noted. Without stationarity the above expression cannot be further simplified, and in general we see that the overlay error variance depends on the ensemble average of sums over products of the Fourier amplitudes of the gap error.

While evaluation of Eq. (12) requires specific data of the cross products of the Fourier amplitudes on the print field which are not available to the author at present, we can observe under what conditions Eq. (12) reduces to the stationary result obtained previously. Starting with Eq. (12) and using the definitions of the Fourier amplitudes and Parseval's theorem it can be shown that if $\langle\Delta g(x,y)\rangle_G$ is independent of position (x, y) then the first double sum inside square brackets reduces to σ_g^2 and the last double sum goes to zero. Under the weaker assumption that the ensemble average of the product $\langle\Delta g(x,y)\Delta g(x',y)\rangle_G$ depends only on the difference between x and x', the second term in Eq. (12) involving a triple sum goes to zero. Since these assumptions essentially embody the definition of stationarity in the wide sense we see that this property alone is sufficient to guarantee the results of Eqs. (9) and (10). The results of Sec. III C for low and high spatial frequencies are recovered from Eq. (12) without need of the assumption of stationarity. At zero frequency only the first term in Eq. (12) survives and it becomes the variance σ_g^2 by Parseval's theorem. In the infinite frequency limit the last two terms of Eq. (12) die off for bounded amplitudes $|a_{n,m}|$, and the first term again goes to σ_g^2 by Parseval's theorem. Therefore, while Eq. (12) cannot be evaluated without more data, it is reasonable to expect the results to approximate those of the stationary case if error amplitudes at intermediate spatial frequencies are small.

IV. SUMMARY

Under the simplifying assumptions of a square field upon which an overlay site has a uniform distribution and a gap error that is stationary in the wide sense over the print domain, the rms values of the overlay errors in x and y are independent of field position and are related to the gap variance by a constant multiplier. This multiplier is $1/\sqrt{3}$ times the ray divergence at the field edge L/D, which represents a reduction by 0.577 of the edge-driven overlay error values over the print field.

Without the assumption of stationarity in the wide sense for the gap error on the print field, an expression is derived that involves gap ensemble averages of the product of different gap error component frequencies. If the gap error's major contribution is from zero spatial frequency or very high spatial frequency then the same result is obtained as under the assumption of stationarity of the gap error. The general result derived in the Fourier domain can be applied to any gap error statistics, stationary or not.

ACKNOWLEDGMENTS

Many thanks to Joe Abate and Jerry Guo of AT&T, Frank Gomba and Juan Maldonado of Loral Systems, and Paul Brickmeier and Ralph Amadeo of SVG for their discussions of point-source x-ray overlay error. Thanks also to Franco Cerina of the University of Wisconsin, John Canning, and Gary Escher of Sematech for useful discussions on overlay error accounting methods. Special thanks to Lloyd Hackel and Mike Feit of LLNL for stimulating, motivating discussions of the statistics of the overlay error.

This work was performed under the auspices of the U.S. Department of Energy by University of California Lawrence Livermore National Laboratory under Contract No. W-7405-Eng-48.

[1] *The National Technology Roadmap for Semiconductors* (Semiconductor Industry Association, San Jose, CA, 1994).
[2] H. I. Smith and M. L. Schattenburg, Proc. SPIE **1671**, 282 (1992).
[3] G. Escher, Proc. SPIE **2322**, 409 (1994).
[4] J. Goodberlet, S. Silverman, J. Ferrera, M. Mondol, M L. Schattenburg, and H. I. Smith, Microelectron. Eng. **35**, 473 (1997).
[5] J. S. Bandat and A. G. Piersol, *Random Data: Analysis and Measurement Procedures,* 2nd ed. (Wiley, New York, 1986), p. 11.

Comparison of Cl_2 and F-based dry etching for high aspect ratio Si microstructures etched with an inductively coupled plasma source

W. -C. Tian,[a] J. W. Weigold,[b] and S. W. Pang[c]
Department of Electrical Engineering and Computer Science, The University of Michigan, Ann Arbor, Michigan 48109-2122

(Received 1 March 2000; accepted 26 May 2000)

The differences between Cl_2 and F-based dry etching are compared in this article. Inductively coupled plasma sources have been used to generate plasmas using both Cl_2 and SF_6/C_4F_8 chemistries. Trenches etched using Cl_2 suffered less aspect ratio dependent etching effects because the trenches can be etched at a much lower pressure than with F-based gases. A 1.4 μm wide, 65 μm deep trench can be obtained with an aspect ratio of 46 in 12 h. The average Si etch rate was 90 nm/min and the selectivity to electroplated Ni was 23. The sidewall was vertical and smooth and the trench openings were nearly the same width before and after etching. Adjacent trenches with 0.14 μm mask opening and 2 μm line width were etched using these two etching technologies. With Cl_2 etching, a wider 0.25 μm trench opening, due to the mask erosion effect, with a depth of 5.6 μm was obtained in 50 min. However, the 0.33 μm undercut increased the trench opening to 0.8 μm for 10.7 μm deep trenches after the F-based etching for 55 min. The Si etch rate in a large open area using F-based etching was 1818 nm/min, which is much faster than 201 nm/min when Cl_2 etching was used. However, the Si etch rate, 112 nm/min for Cl_2 and 195 nm/min for F-based gases, was similar when the trench opening was decreased to submicrometer dimensions. This shows that the Cl_2 etching provides better dimension and profile control with comparable Si etch rate to F-based etching when etching submicrometer trenches. The loading effect using Cl_2 chemistry is less than with F-based etching. The Si etch rate was 1.74 μm/min for $\sim$100% Si exposed area and 3.68 μm/min when the exposed Si area was $\sim$0% in F-based etching. Scalloping, which is a periodic undercut near the top of the sidewalls, disappeared when using an electroplated Ni mask. The size and period of the scalloped features decreased as the Si exposed area and etch time increased. © *2000 American Vacuum Society.* [S0734-211X(00)07804-5]

I. INTRODUCTION

Halogens and their compound gases are extensively used in modern plasma etching systems. Currently chlorine (Cl) and fluorine (F)-based gases are widely used for plasma etchers. Many etching processes based on F chemistry have been developed to produce high etch rate, higher selectivity to the mask, and high aspect ratio microstructures in microelectromechanical systems (MEMS).[1–4] However, F atoms react with Si spontaneously and they introduce isotropic etching and cause undercutting below the mask. The Bosch process utilizes a multiplexed etch/passivation cycle that can alleviate this problem significantly.[5] In this switching process, SF_6 will etch the Si substrate in the etch cycle and the sidewall will be coated by C_4F_8 in the passivation cycle to prevent undercutting. Slight undercut below the mask and scalloping, which is a mouse-bite shape on the sidewall, is formed and may affect the etch profile and device performance. Lowering the temperature of the wafer during etching is another way to suppress the spontaneous F etching of Si.[6–8] However, an extra cooling system is needed and this complicates the system design and increases the cost. Even with extensive cooling, the undercut below the mask is large in high aspect ratio trenches with small openings and an enhanced lateral etching near the mask is signficant.[8]

Another widely used gas to etch Si is Cl_2. With Cl_2 etching, many processes were developed for producing vertical sidewalls, smooth surface morphology, fine critical dimension control, and high aspect ratio microstructures for MEMS.[9–14] The main advantage of Cl_2 etching is that etching is anisotropic since it is an ion assisted process rather than a spontaneous etching process. Vertical profile can be easily obtained in Cl_2 etching without polymer passivation or extensive wafer cooling. The disadvantages of this approach are the lower etch rates and lower selectivity to etch mask compared to F-based etching.

In this study, both Cl_2 and F-based etching were used to etch high aspect ratio Si microstructures. Different etch conditions were optimized for these gases. Effects of etch conditions and etch mask on Si etch rate, selectivity, and sidewall morphology were investigated. Etching of 1 and 0.14 μm wide trenches in Cl_2 and F-based systems were compared.

II. EXPERIMENT

Inductively coupled plasma (ICP) systems with Cl_2 and F-based gases were used to etch high aspect ratio microstructures in Si. For Cl_2 etching, the ICP source consisted of a

[a]Electronic mail: wctian@engin.umich.edu
[b]Electronic mail: weigold@eecs.umich.edu
[c]Electronic mail: pang@eecs.umich.edu

four-turn coil around an alumina chamber. Radio frequency (rf) power at 2 MHz was applied to the ICP source and the stage was biased by a separate rf power supply at 13.56 MHz. The distance between the stage and the ICP source could be adjusted from 6 to 25 cm. In order to avoid frequent exposure of the etch chamber to atmosphere, a load lock was used to transfer wafers to the vacuum chamber. For F-based etching, the Bosch process was used by cycling between SF_6 etching and C_4F_8 deposition. The ICP source contained a single-turn coil around the chamber and a power supply at 13.56 MHz. A separate rf power supply, also at 13.56 MHz, was connected to the stage. In both systems, separate power supplies for the ICP source and the stage allow nearly independent control of ion flux and ion energy.

Electroplated Ni, photoresist, and thermal oxide were used as etch masks for Si etching. For the electroplated Ni mask, a thin 20/5 nm Ti/Ni plating base was evaporated and Ni was plated with a current of 50 mA in a Ni sulfamate and boric acid electroplating solution at 50 °C. A 5-μm-thick Ni mask was plated in 3 h. The Ti/Ni plating base was removed by etching in 1:1 HCl:H_2O and BHF. A photoresist mask was formed by patterning Shipley 1827 photoresist to a thickness of 2.9 μm on Si wafers. As for the preparation of the oxide mask, thermal oxide was grown on Si wafers at 1100 °C for 10 h to get a thickness of 2 μm. The oxide was etched in a parallel plate reactive ion etching system using 100 W rf power and 10 sccm CF_4 and CHF_3 at 40 mTorr. Patterns in polymethylmethacrylate (PMMA) with small gaps down to 0.14 μm were defined using electron beam lithography. The PMMA thickness was 0.45 μm and a Ti/Ni etch mask with a thickness of 275 nm was lifted off. This Ti/Ni mask was deposited using electron beam evaporation with 5 periods of 5 nm Ti and 50 nm Ni.

High aspect ratio Si microstructures were etched using Cl_2 and F-based gases. For dry etching in Cl_2, optimized etch conditions were obtained using 265 W source power and 70 W stage power at 7.5 mTorr, 20 sccm Cl_2 gas flow, and 6 cm source to sample distance. The self-induced direct current (dc) bias ($|V_{dc}|$) was 113 V. For the F-based etching, optimized etch conditions were obtained using alternating etch and passivation cycles. In the 12 s etch cycle, 800 W source power and 10 W stage power were used at 30 mTorr with 130 sccm SF_6 and 13 sccm O_2. The $|V_{dc}|$ at the stage was 120 V. In the 6 s passivation cycle, 800 W source power was applied at 15 mTorr with 85 sccm C_4F_8. The stage power was off during the passivation cycle. The pressure was reduced at a rate of 0.2 mTorr/min during the etch. The reduced pressure was useful for etching deep trenches with high aspect ratio.

III. RESULTS AND DISCUSSION

A. Comparison of aspect ratio dependent etching

With aspect ratio dependent etching, Si etch rate usually decreases as the trenching opening decreases, trench depth increases, or aspect ratio (trench depth/trench width) increases. The reduced etch rate is related to the difficulty in the transport of etch species and etch products in and out of high aspect ratio trenches. Several mechanisms have been discussed and many methods have been developed to alleviate it.[15–18] Cl_2-based dry etching suffers less aspect ratio dependent etching because it is typically run at a lower pressure. Since the mean free path is longer at lower pressure, transport of species in and out of the trenches is easier. Another reason for aspect ratio dependent etching is ion shadowing.[15] In Cl_2 etching, the smaller angular ion distribution at lower pressure reduces collisions between the reactive etch species and sidewalls, so it is easier for the reactive etch species to reach the bottom of the trenches.

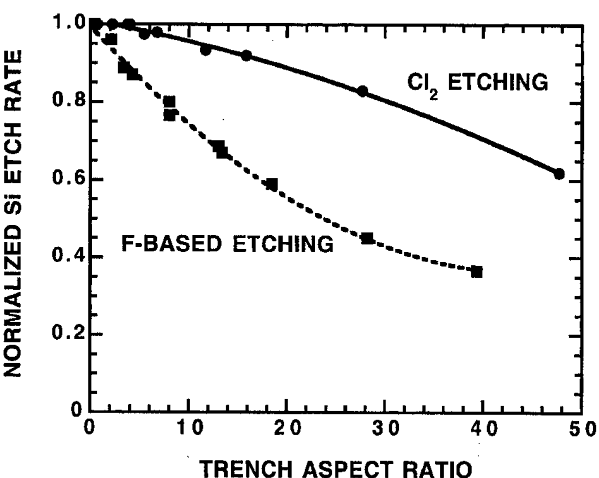

FIG. 1. Si etch rate dependence on feature size and etch depth in Cl_2 and F-based dry etching. For Cl_2 etching, 265 W source power and 70 W stage power were used at 7.5 mTorr, 20 sccm Cl_2 gas flow, and 6 cm source to sample distance. For the F-based etching, alternating etch and passivation cycles were used. In the 12 s etch cycle, 800 W source power and 10 W stage power were used at 30 mTorr with 130 sccm SF_6 and 13 sccm O_2. In the 6 s passivation cycle, 800 W source power was applied at 15 mTorr with 85 sccm C_4F_8.

Figure 1 shows that the normalized Si etch rate decreases as the trench aspect ratio increases. The samples had Ni mask and the optimized etch conditions described earlier were used. The etch depth for Cl_2 and F-based etching were the same in the open areas. For etch depths of 100 and 172 μm in the open areas, the F-based etching required an etch time of 55 and 150 min and the Cl_2 etching required an etch time of 8 and 12 h. The Si etch rate for different trench aspect ratio is normalized to the etch rate in the open area. As shown in Fig. 1, with the same trench aspect ratio, F-based etching suffered a larger etch rate reduction compared to Cl_2 etching. With a trench aspect ratio of 28, the normalized Si etch rate was 0.83 for Cl_2 etching and only 0.45 for F-based etching. The stronger aspect ratio dependent etching in F-based gases is mainly due to the higher pressure (30 mTorr) used during etching compared to Cl_2 etching at a lower pressure of 7.5 mTorr. For the same trench opening, deeper trenches show a larger decrease in the etch rate since the aspect ratio becomes large. It is found that the Si etch rate depends on trench aspect ratio and not just the trench opening or trench depth.[15,18]

Trenches were formed by etching in Cl_2 and F-based gases using the optimized etch conditions as shown in Figs.

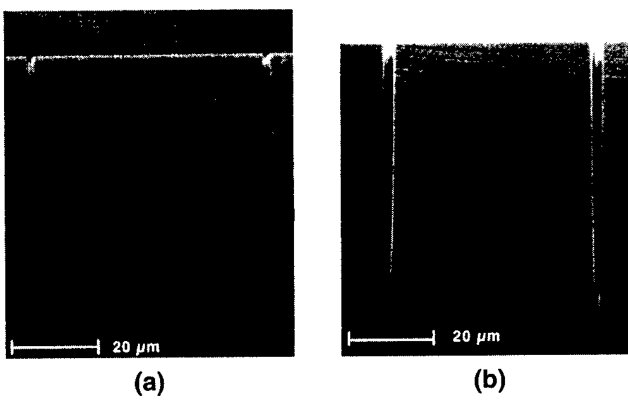

FIG. 2. Etch profile of high aspect ratio Si trenches. In (a), the trench width is 1.4 μm with etch depth of 65 μm in Cl_2 etching after 12 h. In (b), the trench is 1.6 μm wide and 63 μm deep after 55 min in F-based etching.

2(a) and 2(b). Before etching, the Ni etch mask had 1 μm wide openings. Because the trench width changed with depth, trench widths after etching were determined by averaging the top and middle widths of the trenches. Trenches etched in the F-based gases became wider because there was more undercutting compared to Cl_2 etching. Trenches etched in Cl_2 were 1.4 μm wide and 65 μm deep, with an aspect ratio of 46. Trenches etched in F-based gases were 1.6 μm wide and 63 μm deep, with an aspect ratio of 39. Although the etch profile was slightly better using Cl_2 etching due to less undercut, both etches showed narrower trench width near the trench bottom. This tapered etch profile is related to the limited transport of the etch species and etch products in and out of the trenches as the trench depth increases.

With Cl_2 etching, increasing the stage power to increase the ion energy at the end of the etch helps to improve the etch profile. Ions are accelerated with higher ion energy by the higher $|V_{dc}|$ when higher stage power is used. The higher energy ions are more directional since they are not as easily deflected. They also promote faster reactions at the trench bottom for a faster etch rate. Figure 3(a) illustrates the trench profile after etching in the Cl_2 plasma for 5 h under the optimized conditions described earlier. As shown in Fig. 3(b), increasing the stage power from 70 to 300 W for an additional 10 min at the end of the etch widened the width at the trench bottom. The $|V_{dc}|$ was increased from 113 to 325 V for these powers. This two-step etching can be used to improve the etch profile for high aspect ratio trenches. The disadvantage of this second etch step is that the trench width increased from 1 to 1.2 μm due to the mask erosion effect. The higher energy ions etched away the Ni mask faster and the trench width became larger. This etch bias can be taken into account in the mask design. Wet etching using tetramethyl ammonium hydroxide after dry etching has been shown to improve the trench profile.[19] However, wet etching is not easily controllable for high aspect ratio trenches and there is a large increase in trench width.

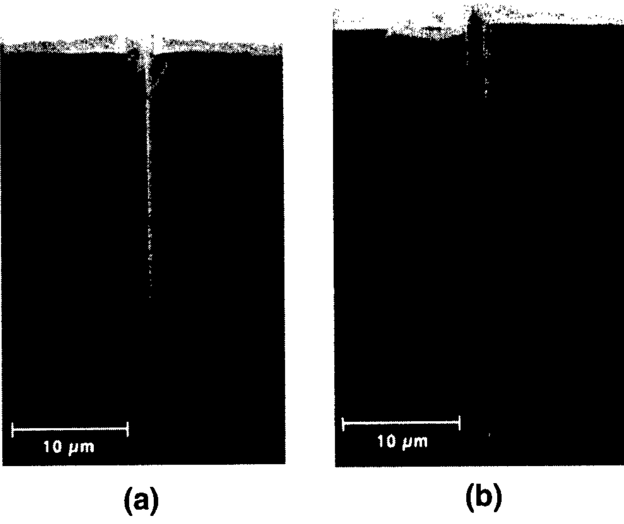

FIG. 3. (a) High aspect ratio trench with tapered profile after Cl_2 etching for 5 h with the optimized etch conditions using a stage power of 70 W. (b) With an additional 10 min etching at a higher stage power of 300 W, the bottom of the trench was widened.

B. Effect of etch gases on Si to mask selectivity

In Cl_2 dry etching, ions and neutrals from the plasma will react with Si on the surface. The energetic ions accelerated by the electrical field between the plasma and the stage will enhance the surface reactions and sputter away the etch products from the surface. This ion assisted etching is anisotropic due to the directionality of the incoming ions. As shown in Table I, Si etch rate in the open area is 201 nm/min and selectivity is 1.2, 8.4, and 50 when using Shipley photoresist 1827, thermal oxide, and electroplated Ni as an etch mask, respectively. Electroplated Ni was chosen as an etch mask for Cl_2 etching because a thick Ni layer can be deposited for deep etching. Low stress Ni can be deposited by electroplating at a low current density.[20] The etch profile is vertical when using the optimized Cl_2 etch conditions.

With F-based etching, electroplated Ni provided the highest selectivity of 909 and even photoresist has a selectivity of 49. As shown in Table I, Si etch rate and selectivity are higher for F-based etching compared to Cl_2 etching. The reasons for the higher selectivity are the faster Si etch rate and lower stage power for F-based etching. Also, the poly-

TABLE I. Dependence of etch rates and selectivity for F-based and Cl_2 dry etching.

	F-based dry etching		Cl_2 dry etching	
	Etch rate (nm/min)	Selectivity	Etch rate (nm/min)	Selectivity
Photoresist (1827)	37	49	170	1.2
Thermal oxide	10	182	24	8.4
Electroplated Ni	2	909	4	50
Si (open area)	1818		201	

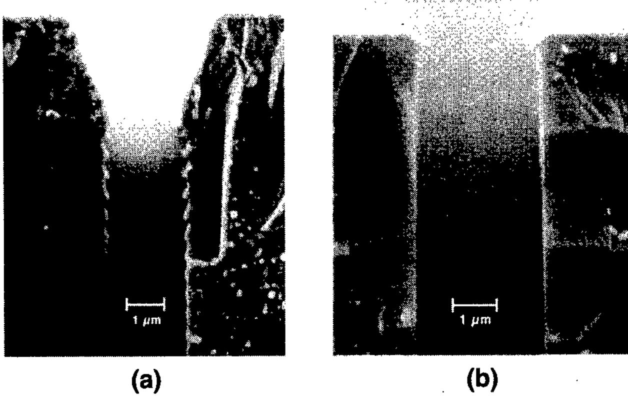

FIG. 4. Scalloping along the sidewalls was observed when a photoresist mask was used in the optimized F-based etching. In (a), the peak to valley height of the scalloping is 0.15 μm and the undercut is 0.25 μm after 5 min of etching. In (b), after a longer etch time of 55 min, the peak to valley height of the scalloping is <30 nm and the trench width was increased from 1.5 to 3.1 μm due to the undercutting and mask erosion effect.

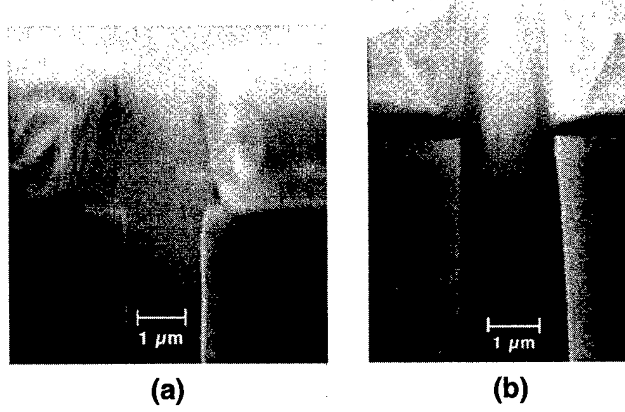

FIG. 5. No scalloping along the sidewalls was found when using an electroplated Ni mask for optimized (a) Cl_2 etching and (b) F-based etching. There was no undercutting after Cl_2 etching and an increased trench width from 0.9 to 2 μm after F-based etching due to undercut.

mer deposited in the passivation cycle during F-based etching helped to increase the selectivity.

Even though the Si etch rate is much faster in F-based etching compared to Cl_2 etching in an open area, the difference in etch rate is substantially less for submicrometer features. For the etching of submicrometer structures, the optimized etch conditions were modified to 80 W source power, 100 W stage power ($|V_{dc}|$ was 197 V), 1 mTorr, 40 sccm Cl_2 gas flow, and 8 cm source to sample distance. The modified etch conditions provide improved etch profile for submicrometer features. For 0.14 μm wide trenches etched to a depth of 5.6 μm, the Si etch rate was 195 nm/min for F-based etching, compared to 112 nm/min in Cl_2 etching. Since these submicrometer trenches have a high aspect ratio, the etch rate reduction in submicrometer trenches compared to large open areas was $<2\times$ in Cl_2 because lower pressure was used. On the other hand, F-based dry etching showed $>9\times$ reduction in Si etch rate for submicrometer trenches.

C. Comparison of undercut and sidewall

In F-based etching, features were formed on the sidewalls due to alternating passivation and etch cycles. Polymer was deposited during the C_4F_8 cycle and Si was etched during the SF_6/O_2 cycle. Often, some undercut occurred during the etch cycle due to spontaneous reaction between F and Si. The repeated cycles resulted in multiple undercuts, known as scalloping, along the sidewalls. Normally, scalloping was more severe near the top of the trenches as shown in Fig. 4(a). After 5 min of etching using a photoresist mask and the optimized etch conditions described earlier, the height of the scalloped features (peak to valley) near the top of the trench is 0.15 μm. However, the height of the scalloped features decreased to <30 nm after etching for 55 min, as shown in Fig. 4(b). The trench opening also expanded from 2 to 3.1 μm due to mask erosion as the etch time was increased from 5 to 55 min. Therefore, there was less scalloping and more undercutting as etch depth increased. The changes in sidewall smoothness and profile with etch depth are related to modifications in the transport of etch species, deposition species, and etch products when the trench aspect ratio becomes larger. The protruding tips of the scalloped features further away from the top of the trenches could be smoothened due to less polymer deposition near the trench bottom and angle dependent sputtering. Therefore, the height of the scalloped features became smaller at a larger etch depth.

Smooth sidewalls were observed in Cl_2 etching for a trench opening of 1.4 μm with an etch time of 12 h, as shown in Fig. 5(a). Ni etch mask and the optimized etch conditions were used. The directional ion-assisted etch mechanism helps to etch very high aspect ratio trenches with vertical sidewalls. Similar sidewall smoothness was obtained for the electroplated Ni, oxide, and photoresist masks. Typically, no undercut was observed and sidewall smoothness was independent of the etch depth.

When a Ni mask was used in the optimized F-based etching, there was no scalloping and less undercut compared to photoresist and oxide mask. Figure 5(b) shows the smooth sidewalls after etching in F-based gases using a Ni mask. The passivation layer along the sidewalls may be a better film to protect against the lateral undercut due to the Ni incorporation. Using a Ni mask, scalloped features can be eliminated in F-based etching, which is important for some electrostatically driven devices in MEMS with small gaps between resonating elements. The smooth sidewalls ensure uniform electrical field between two closely spaced capacitive plates and make it easier to estimate the capacitance between two plates. Besides using a Ni mask, the surface roughness of the sidewalls can also be reduced by thermal oxidation followed by removal of the oxide.[20] Hydrogen annealing at 1100 °C and 80 Torr has been used to smoothen the roughness of the sidewalls.[21] However, these high temperature processes require a high thermal budget which may not be suitable for some MEMS designs.

Adjacent trenches with 0.14 μm spacing and 2 μm line-

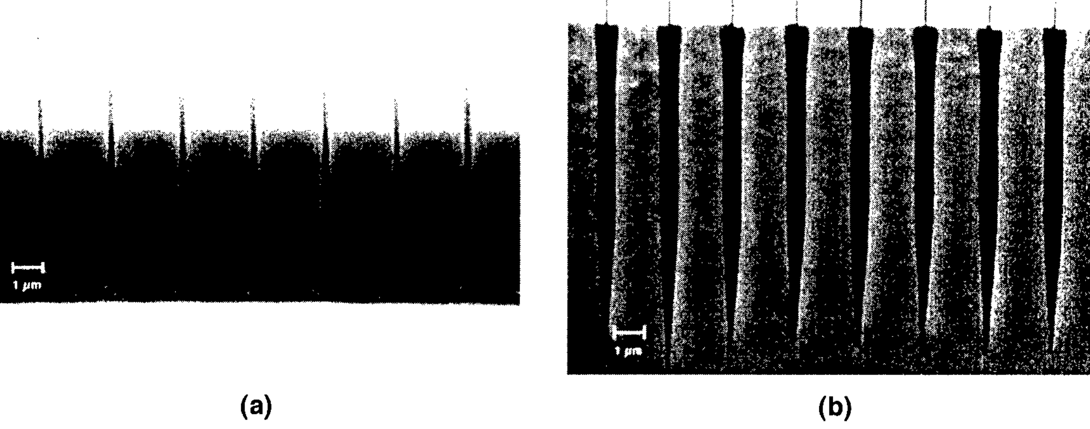

FIG. 6. No undercut was observed in submicrometer trenches when using Cl_2 etching after 50 min, as shown in (a). With F-based etching for 55 min, significant undercut was found as shown in (b).

width were etched. The etch mask was 275-nm-thick Ti/Ni. The modified etch conditions were used with 80 W source power and 100 W stage power at 1 mTorr, 40 sccm Cl_2 gas flow, and 8 cm source to sample distance. As illustrated in Fig. 6(a), the trench opening increased from 0.14 to 0.25 μm due to mask erosion. The etch time was 50 min and the etch depth was 5.6 μm. In F-based etching, the trench width increased from 0.14 to 0.8 μm, as shown in Fig. 6(b). The optimized etch conditions for F-based etching were used and 10.7 μm deep trenches were formed after etching for 55 min. Further development of the F-based etching is needed to minimize the undercut and improve the trench profile for submicrometer trenches. Since F reacts with Si spontaneously, undercut below the mask could be significant for submicrometer features. In addition, the polymer passivation scheme used to prevent undercutting may be less effective for submicrometer trenches due to the limited transport of polymer forming species through the small trench openings.

Besides the undercutting problem for F-based etching, the requirement of polymer passivation may limit the smallest size feature that can be etched. Polymer needed to coat the sidewalls may close or shrink the submicrometer trench opening and the etching may not be able to proceed further. In addition, polymer coating along the sidewalls may not be desirable and a polymer removal step may be needed after the etching is completed. These results show that Cl_2 etching is more suitable for etching submicrometer trenches. It can provide better dimension control with less undercut and smoother sidewalls with no scalloping, even without polymer passivation.

D. Dependence of etch rate and etch profile on Si exposed area

To study the dependence of etch rate on exposed Si area, the so called loading effect, Si carrier wafers with photoresist coverage of ~0%, 25%, 50%, 75%, and 100% were used. A 1 cm×1 cm patterned chip was placed in the center of the carrier wafer with different Si exposed areas. A small amount of vacuum grease was applied at the back of the chip to ensure good thermal conductance between the chip and the carrier wafer. During etching, the etch species could be depleted when a large Si area is exposed to the plasma. As shown in Fig. 7, the Si etch rate decreased from 3.68 μm/min with ~0% exposed Si area to 1.74 μm/min with ~100% exposed Si area after etching in F-based gases. The optimized etch conditions and a photoresist mask were used and the etch time was 5 min. The photoresist etch rate was nearly independent of the Si exposed area and Si to photoresist selectivity decreased from 136 to 34 as the exposed Si area increased.

The exposed area of material being etched, the affinity between the etch species and the material to be etched, the plasma volume, and the lifetime of the etch species are all important in the loading effect.[22] Since F is more reactive with Si compared to Cl, the etch rate is faster in F-based etching. This faster spontaneous reaction rate of F with Si also makes F-based etching more sensitive to the amount of exposed Si area. Conversely, the undesirable loading effect is significantly less in Cl_2 etching. As Si exposed area was changed from ~0% to ~100%, the etch rate only has 45 % variation when Cl_2 was used compared to 139% variation

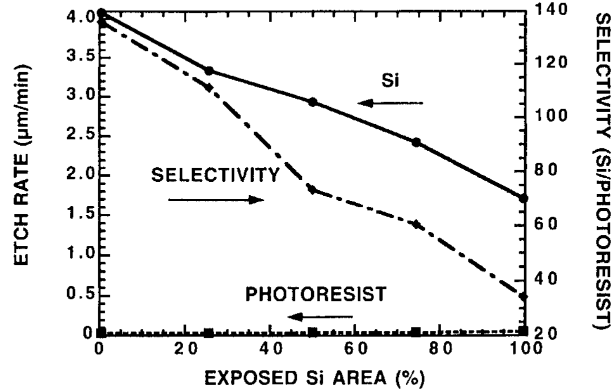

FIG. 7. Dependence of etch rates and selectivity on exposed Si area for F-based etching. The optimized etch conditions and a photoresist mask were used. The etch time was 5 min and Si etch rate decreased with exposed area.

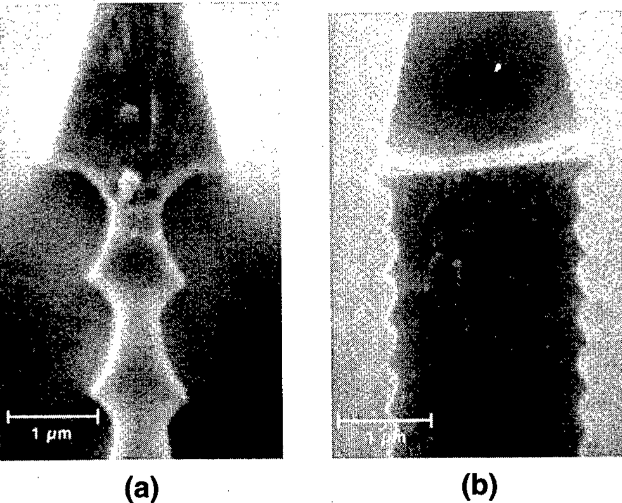

FIG. 8. Size and period of scalloping along the Si sidewalls were changed from 0.3 μm peak to valley height and 1.3 μm peak to peak distance for ~0% exposed Si area as shown in (a) to 0.15 and 0.5 μm for ~100% exposed Si area as shown in (b).

with F-based etching. Therefore, there is a compromise between etch rate and loading effect for these etch conditions.

The undercut below the mask and the scalloped features along the sidewalls also varied with exposed Si area. Figures 8(a) and 8(b) show that the undercut below the mask decreased from 1.1 to 0.25 μm as the exposed Si area was increased from ~0% to ~100%. The optimized F-based etch conditions and a photoresist mask were used. Higher etch rates were achieved with smaller exposed Si area because etch species are not depleted. This higher concentration of etch species will not only increase the etch rate but also enhance the undercut below the mask. The scalloped features have a larger peak to valley height of 0.35 μm for ~0% exposed Si area as shown in Fig. 8(a), compared to a height of 0.15 μm at ~100% exposed Si area as shown in Fig. 8(b). The period of the scalloped features becomes narrower, decreasing from 1.3 to 0.5 μm as the exposed Si area was varied from ~0% to ~100%. The larger undercut and larger period of the scalloped features are due to the increased etch species and lateral etch rate for a smaller exposed Si area.

The etch profile also changed with exposed area. Etch profile is more negative (larger trench opening near bottom) for trenches with larger openings and more positive (larger trench opening near top) for trenches with smaller openings. For deeper trenches, the polymer deposition rate in the passivation cycle was lower at the trench bottom due to increasing aspect ratio. Therefore, more lateral etching could occur due to more limited polymer passivation near the base of the trenches. It has also been suggested that an induced electrical field at the bottom of a trench could enhance lateral etching.[8] For trenches with smaller openings, the transport of etch species is degraded because the aspect ratio becomes larger at a faster rate. In addition, divergent ions are blocked from reaching down to the bottom of narrow trenches due to shadowing. Therefore, etching is reduced near the bottom of narrower trenches and more positive profile is formed.

IV. SUMMARY

In this study, Cl_2 and F-based etching were compared. For bulk micromachining of MEMS, where large portions of the substrate must often be etched, the F-based etching can be used to form deep trenches with high etch rate and high selectivity to a mask. Conversely, Cl_2 etching can be selected for etching small, high aspect ratio feature sizes with a vertical profile in both bulk and surface micromachining. In F-based etching, good profile and high aspect ratio can be obtained for etching deep trenches with opening >2 μm. However, sidewall roughness can be a problem because scalloped features were formed during the etch and passivation cycles. The scalloping was found to be dependent on the etch time, mask material, and the exposed Si area. With Ni as an etch mask, smooth sidewalls without scalloping can be formed. Etching for a longer time with more exposed Si area can also help to reduce scalloping. These findings are important especially when the structures have submicrometer dimensions. For example, in devices driven by electrostatic force with submicrometer dimensions, scalloping on the sidewalls may degrade the uniformity of the electrical field between two closely spaced plates. Cl_2 dry etching exhibits less aspect ratio dependent etching and loading effects, and the sidewalls are very vertical and smooth. Submicrometer structures that were 0.25 μm wide and 5.6 μm deep were fabricated using Cl_2 etching. In contrast to F-based etching of the same features, these submicrometer trenches showed no undercutting or scalloping which is highly desirable. However, for larger features, the lower etch rate and selectivity compared to F-based etching make it harder to etch very deep trenches in a reasonable time and with a practical mask thickness.

ACKNOWLEDGMENT

This work was supported by the Defense Advanced Research Project Agency.

[1]A. A. Ayón, R. A. Braff, R. Bayt, H. H. Sawin, and M. A. Schmidt, J. Electrochem. Soc. **146**, 2730 (1999).
[2]D. C. Hays, K. B. Jung, Y. B. Hahn, E. S. Lambers, S. J. Pearton, J. Donahue, D. Johnson, and R. J. Shul, J. Electrochem. Soc. **146**, 3812 (1999).
[3]K. Kuhl, S. Vogel, U. Schaber, R. Schafflik, and B. Hillerich, Proceedings of the SPIE Conference on Micromachining and Microfabrication Process Technology IV, Santa Clara, CA, 1998, p. 97.
[4]P. -A. Clerc *et al.*, J. Micromech. Microeng. **8**, 272 (1998).
[5]R. Bosch GmbH, U.S. Patent Nos. 4,855,017 and 4,784,720 (1991) and German Patent No. 4241045C1 (1990).
[6]S. Tachi, K. Tsujimoto, S. Arai, and T. Kure, J. Vac. Sci. Technol. A **9**, 796 (1991).
[7]J. K. Bhardwaj and H. Ashraf, Proceedings of the SPIE Conference on Micromachining and Microfabrication Process Technology I, Austin, TX, 1995, p. 224.
[8]S. Aachboun and P. Ranson, J. Vac. Sci. Technol. A **17**, 2270 (1999).
[9]W. H. Juan and S. W. Pang, J. Vac. Sci. Technol. A **14**, 1189 (1996).
[10]J. W. Weigold, W. H. Juan, and S. W. Pang, J. Vac. Sci. Technol. B **15**, 267 (1997).
[11]J. W. Weigold and S. Pang, IEEE J. Microelectromech. **7**, 201 (1998).
[12]M. R. Rakhshandehroo, J. W. Weigold, W. -C. Tian, and S. W. Pang, J. Vac. Sci. Technol. B **16**, 2849 (1998).

[13]S. Swan and G. Hills, Proceedings of the SPIE Conference on Microelectronic Processes, Sensors, and Controls, Monterey, CA, 1994, p. 160.
[14]P. Lange, M. Kirsten, W. Riethmüller, B. Wenk, G. Zwicker, J. R. Morante, F. Ericson, and J. Á. Schweitz, Technical Digest of 8th International Conference on Solid-State Sensors and Actuators, and Eurosensors IX, Stockholm, Sweden, June 1995, p. 202.
[15]R. A. Gottscho, C. W. Jurgensen, and D. J. Vitkavage, J. Vac. Sci. Technol. B **10**, 2133 (1992).
[16]K. Tsujimoto, T. Kumihashi, N. Kofuji, and S. Tachi, J. Vac. Sci. Technol. A **12**, 1209 (1994).
[17]J. Kiihamäki and S. Franssila, J. Vac. Sci. Technol. A **17**, 2280 (1999).
[18]D. Chin, S. H. Dhong, and G. J. Long, J. Electrochem. Soc. **132**, 1705 (1985).
[19]H. P. Kattelus, J. Electrochem. Soc. **144**, 3188 (1997).
[20]W. H. Juan and S. W. Pang, J. Vac. Sci. Technol. B **14**, 4080 (1996).
[21]T. Sato, I. Mizushima, J. Iba, M. Kito, Y. Takegawa, A. Sudo, and Y. Tsunashima, Digest of Technical Papers of 1998 Symposium on VLSI Technology, Honolulu, HI, 1998, p. 206.
[22]C. J. Mogab, J. Electrochem. Soc. **124**, 1262 (1977).

Control of surface reactions in high-performance SiO_2 etching

T. Tatsumi,[a] M. Matsui, M. Okigawa, and M. Sekine
Plasma Technology Laboratory, Association of Super-advanced Electronics Technologies (ASET), 292 Yoshida-cho, Totsuka-ku, Yokohama Kanagawa 244-0817, Japan

(Received 4 October 1999; accepted 15 May 2000)

The relation between SiO_2 etch rates and incident fluxes of reactive species in a dual-frequency (27 MHz and 800 kHz) parallel-plate system was evaluated by using various *in situ* measurements tools. $C_4F_8/Ar/O_2$ was used for etching gases. The steady-state thickness T_{C-F} of a fluorocarbon polymer layer on the etched SiO_2 surface was also measured. The SiO_2 etch rate could be related to total F atom flux $\Gamma_{F\text{-total}}$, which depends on both the incident fluxes of C–F reactive species and the surface reaction probability s. The s is a function of the net energy on the reactive layer (V_{net}). This energy is determined by the incident ion energy and the energy loss at the C–F polymer on the etched surface. A change in V_{net} from 500 to 1450 V was estimated to correspond to a change in s from 0.01 to 0.1. The steady-state thickness of the C–F polymer T_{C-F} increased when excess C–F species were supplied to the etched surface. A thick polymer ($T_{C-F}>1$ nm) decreases the ion energy and slows or stops the etching in fine holes. A polymer 5 nm thick can decrease the ion energy by about 750 V. The T_{C-F} must therefore be controlled when high-aspect contact holes are etched. © *2000 American Vacuum Society.* [S0734-211X(00)05004-6]

I. INTRODUCTION

Manufacturing the next generation of ultralarge scale integrated circuit devices will require the selective etching of contact holes with aspect ratios greater than 10. Etching processes using C_4F_8 plasma have been developed in recent years,[1,2] but the use of highly selective processes often slows the etch rate in fine holes. Hence, the selectivity must be obtained by not only decreasing the etch rate of SiN but also by increasing the etch rate of SiO_2. To do this, we have to understand quantitatively the mechanism of the etching reaction using fluorocarbon plasma. Generally, the etch rate of SiO_2 is controlled by adjusting external parameters such as power, pressure, substrate bias, and gas compositions. They cannot, however, be related straightforwardly to either the incident flux or the surface reaction, and we need to know how to control this flux and reaction at the reactive layer at the bottom of high-aspect contact holes. The purpose of this work is to develop a realistic model that can express the etching performance obtained in the system actually used in mass production. We did this by using various plasma and surface measuring tools and analyzing a high-performance plasma.

The etch rate of SiO_2 depends on (a) the composition of reactive species (including both ion and neutral radicals), (b) the total flux of reactive species, (c) the energy of ions, and (d) the total flux of ions. We have already clarified the relationship between these ''incident fluxes'' and the external parameters. The composition of reactive species (radicals and ions) depends on the gas chemistry,[3] the number of collisions with electrons,[3,4] and the interaction with the wall materials.[3,5,6] We found that the number of collisions with electrons, which can be directly related to the rate of C_4F_8 dissociation, can be assumed to equal $\tau N_e\langle\sigma v\rangle$, where τ is the gas residence time, N_e is the electron density in the bulk plasma, σ is the dissociation collision cross section, and v is electron velocity. The term $\langle\sigma v\rangle$ can be related to electron temperature T_e. The total amount of reactive species can be controlled, independent of their composition, by varying the partial pressure of the parent gas diluted by a large amount of Ar.[7] The incident thermal flux (Γ_{th}) depends on the composition and densities of reactive species near the sheath edge. The reaction energy is supplied to the surface by ions, whose energy can be controlled by adjusting the bias voltages,[8] and the transit time through the sheath.[8] The sheath transit time depends on the ion mass, the sheath thickness, which is a function of the plasma density, and the bias frequency. The ion flux is determined, if we assume the Bohm criterion, by plasma density and electron temperature at the sheath edge.[9] We can already control the amount, composition, and energy of incident fluxes by adjusting the external parameters. The next step is to understand how and why these fluxes are changed as they pass through the surface polymer layer.

II. EXPERIMENT

The etching system used in the present work is shown in Fig. 1. To generate the plasma, radio-frequency (rf) power at 27 MHz was supplied to the top electrode, which was covered with Si, and rf power at 800 kHz was used as the substrate bias. The width of the gap between the two electrodes was fixed at 20 mm. The temperatures of top electrode, bottom electrode, and sidewall were, respectively, kept at 30, −20, and 40 °C. The peak-to-peak voltage (V_{pp}) of the rf-biased bottom electrode was measured using a high-voltage probe, electron density N_e was measured with a 100 GHz microwave interferometer, and electron temperature was measured with a floating probe 10 mm above the bottom electrode. Radicals and ions were measured by infrared-diode laser absorption spectroscopy[10,11] [IRLAS, Laser Pho-

[a]Electronic mail: tatsumi@yrc.aset.or.jp

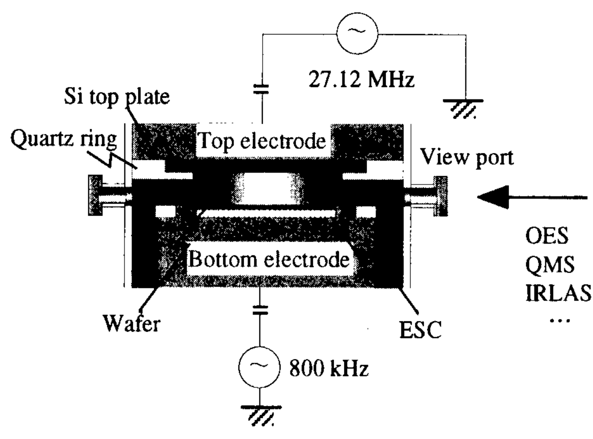

FIG. 1. Configuration of the etching system.

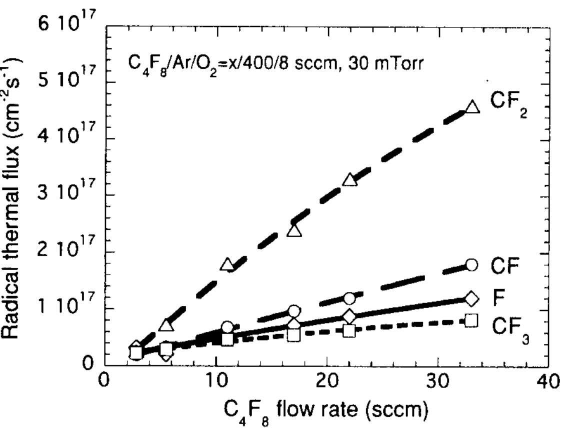

FIG. 2. Radical flux as a function of C_4F_8 flow rate under the same N_e and V_{pp} conditions.

tonics], quadrupole mass spectrometry[12,13] (Hiden Analytical), and optical emission spectroscopy[14–16] (Acton Research). All of these measurement systems could be used without degrading the etching performance, so that the same plasma that is used in the actual manufacturing procedure could be observed. In these experiments, the pressure N_e and residence time were kept at 30 mTorr, $2\times10^{11}\,cm^{-3}$, and 6 ms, respectively, while the gas chemistry (partial pressure of C_4F_8 in the $C_4F_8/Ar/O_2$) was varied. We have previously reported that etch rate of SiO_2 depends mainly on the amount of ions at the high-energy peak in the ion energy distribution function (IED). In this capacitive plasma system, the transit time of ions through the sheath was much shorter than the rf period, because the bias frequency was relatively low at 800 kHz. Hence, the high-energy peak of the IED could be nearly equal to V_{pp} because incident ions subjected to the instantaneous sheath electric field.[7,8] Furthermore, we also evaluated the plasma potential (V_p) under various gas compositions while keeping N_e and V_{pp} at the same value. Under typical conditions, V_p is about 90 V. When we changed the gas composition, the variation of V_p was within 50 V, a voltage much lower than the V_{pp} of 1450 V. Therefore, we assumed that the ion energy was V_{pp}. The direct current bias voltage (V_{dc}) was not measured correctly but it can be estimated to be about a half of V_{pp}. When optimum external parameters were used, it was possible to produce contact holes 0.1 μm in diameter with an aspect ratio of 10, and to etch them with high selectivity relative to the underlying Si layer. The thermal SiO_2 on the 200 mm diameter wafers was used to evaluate the etch rates at both the large area (50 μm$\times$50 μm) and at the bottom of contact holes with aspect ratio ranging from 1 to 15. X-ray photoelectron spectroscopy (VG Scientific) was used to measure the thickness of the C–F polymer on the etched surface. The thickness of the polymer layer was calculated from the ratio of the signal intensity of the Si_{2p} peak (SiO_2) on the etched wafer and that on the untreated SiO_2. The escape depth of photoelectrons in the C–F polymer and Si was assumed to be 3 nm.

III. RESULTS

$C_4F_8/Ar/O_2$ gas chemistry was used, and the flow rates for Ar (400 sccm) and O_2 (8 sccm) were maintained while varying the C_4F_8 flow rate to control the amount of C–F reactive species. Figure 2 shows the radical flux as a function of the flow rate of C_4F_8. The densities of CF, CF_2, and CF_3 were measured by IRLAS, and that of F was measured by an achtinometry method. When we used the constant rf powers, the N_e monotonically decreased with C_4F_8 partial pressure while V_{pp} increased. Therefore, we adjusted both the top and bottom rf powers to obtain the same values of N_e($2\times10^{11}\,cm^{-3}$) and V_{pp} (1450 V). The typical degree of C_4F_8 dissociation was 84.5%, and it was almost constant in this experiment because the number of collisions, $\tau N_e\langle\sigma v\rangle$ was not changed. Fluxes of all C–F radical species and C–F ionic species increased monotonically with the C_4F_8 flow rate, while Ar and Ar^+ fluxes decreased monotonically. As shown in Fig. 3(a) however, the etch rate of SiO_2 did not increase. It once increased (I), reached a peak and then dropped (II) to an almost constant value (III). At C_4F_8 flow rates above those giving the peak etch rate, the thickness of the C–F polymer increased markedly to an almost constant value near 4 nm.

The etch rates at the bottom of contact holes about 1.2 μm deep and with diameters ranging from 0.08 to 0.80 μm were also evaluated and are plotted against aspect ratio in Fig. 3(b). When the C_4F_8 flow rate was relatively low (2.8, 5.5 sccm), the etch rate of SiO_2 was suppressed because of the lack of etchant. Under a C_4F_8 flow rate of 11 sccm, the maximum etch rate was obtained with small reactive ion etching lag. Under the "thick polymer" condition (C_4F_8 flow=33 sccm), however, the etch rate dropped suddenly when the aspect ratio was 5.

IV. DISCUSSION

The surface layer can be assumed to consist of the two layers: the reactive layer (a mixed layer of Si, F, C, and O) and, above it, the C–F polymer layer. A thick C–F polymer seemed to acted as an "inhibitor" that not only slowed the

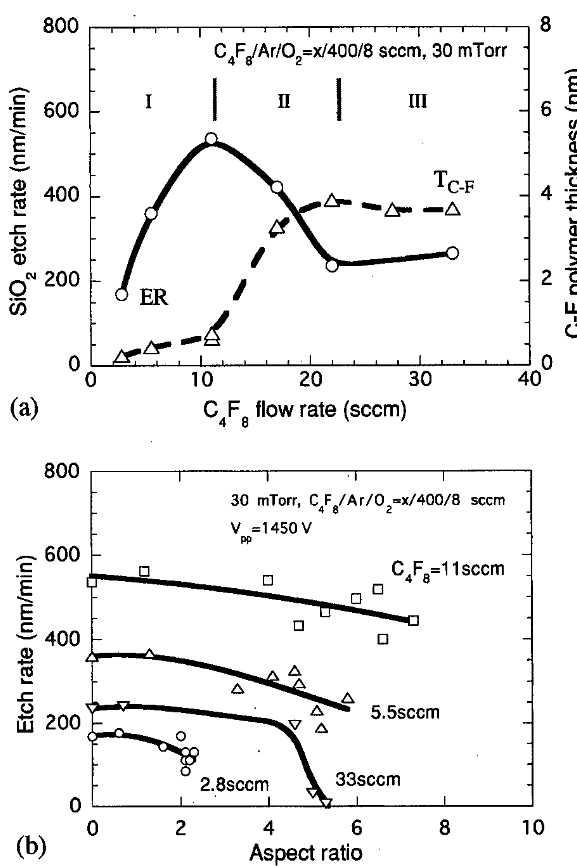

FIG. 3. (a) Etch rate and C–F polymer thickness as a function of the C_4F_8 flow rate. (b) Etch rate as a function of the aspect ratio.

etch rate but also induced the etch stop in the file contact hole. This means that the etch rate is not determined by only the "incident fluxes" but that the polymer affects the energy and the "net flux" at the reactive layer. We have to understand what was changed by the existence of the C–F polymer layer.

A. Basic model for SiO_2 etching

A simple model of SiO_2 etching is used to explain all of the etching results. As previously reported, the etch rate under various "thin polymer" conditions [$T_{C-F}<1$ nm, i.e., region I in Fig. 3(a)] could be well expressed using the total number of incident F atoms, $\Gamma_{F\text{-total}}$ calculated from the net C–F fluxes.[7] So, the $\Gamma_{F\text{-total}}$ at the reactive layer determines the etch rate as

$$ER \propto \Gamma_{F\text{-total}} = \sum_{x,y} \frac{2s}{2-s} \Gamma_{C_xF_y} y,$$

where s is the surface reaction probability and $\Gamma_{C_xF_y}$ is the incident flux of C_xF_y ($x=0-4$, $y=1-8$) species. Under short residence-time conditions, the relative density of large molecules C_xF_y ($x>1$) is low in this system,[6] so $\Gamma_{F\text{-total}}$ can be calculated from the net flux of F, CF, CF_2, and CF_3 radicals

$$ER \propto \Gamma_{F\text{-total}} \approx \sum_x \frac{2s}{2-s} \Gamma_{CF_x} x = \sum_x \frac{2s}{2-s} \tfrac{1}{4} N_{CF_x} v_{CF_x} x,$$

where N_{CF_x} and v_{CF_x} are the density and the thermal velocity, respectively, of F, CF, CF_2, or CF_3 radicals on the sheath edge. Etch rates under $V_{pp}=1450$, 1200, 900, and 600 V are plotted as a function of $\Gamma_{F\text{-total}}$ calculated using $s=0.1$ (assumed not to depend on V_{pp}) as shown in Fig. 4(a). Under low ion-energy conditions ($V_{pp}<1450$ V), the etch rate seemed to be relatively low at the same $\Gamma_{F\text{-total}}$. However, the s is a function of the ion energy, because it must depend on the density of surface sites (dangling bonds) on the reactive layer, which is generated by the ion bombardment. If we assume the surface reaction probability s to have the values as shown in Fig. 4(b), all data in Fig. 4(a) could be plotted on the same line [Fig. 4(c)]. These s values are simply estimated to explain the actual etch rate data, so absolute values may have some errors. The order of the change in s with change in ion energy, however, is not inconsistent with that estimated from beam experiments.[17] Therefore, we conclude that $\Gamma_{F\text{-total}}$ increases with the ion energy, and the etch rate is a function of both the densities of C–F reactive species and the surface reaction probability s which depends on the ion energy supplied on the reactive layer.

B. Effect of a thick polymer

Figure 5 shows the etch rate as a function of $\Gamma_{F\text{-total}}(s=0.1)$ under various T_{C-F} conditions. If excess C–F reactive species are supplied to the etched surface, the steady-state thickness of the C–F polymer T_{C-F} becomes more than 1 nm [Fig. 3(a), II, and III]. Under these conditions, the etch rate is far lower than that estimated from $\Gamma_{F\text{-total}}$ when V_{pp} was 1450 V. For example, under the condition where $\Gamma_{F\text{-total}}$ was calculated to be $2.9\times10^{15}\,cm^{-2}\,s^{-1}$ with $s=0.1$, this number of incident F atoms should enable us to obtain the very high etch rate of about 800 nm/min if the polymer is less than 1 nm thick. But the actual etch rate obtained with a polymer 4 nm thick was only about 250 nm/min. This indicates that the calculation of $\Gamma_{F\text{-total}}$ using $s=0.1$ was not correct under the thick-polymer conditions because the incident ion energy (V_{pp}) decreases while ions pass through the C–F polymer layer. It has been reported that the projection range of ions can be calculated roughly using the Ziegler–Biersack–Littmark (ZBL) model.[18,19] If Ar^+ impinges on the Si surface with an energy of 500 eV, it stops about 5 nm from the top surface. In other words, most of the ion energy was lost within a few nanometers of the top surface.

The T_{C-F} value is less than the (net) projection range in steady state. If not, the deposition rate of the C–F polymer can be observed. The ion energy at the reactive layer [under the C–F polymer layer, see Fig. 6(a)] can be greatly changed according to T_{C-F}. Therefore, the net energy V_{net} used for the determination of the surface reaction probability s must be calculated taking into account energy loss ΔV:

$$V_{net} = V_{pp} - \Delta V(T_{C-F}).$$

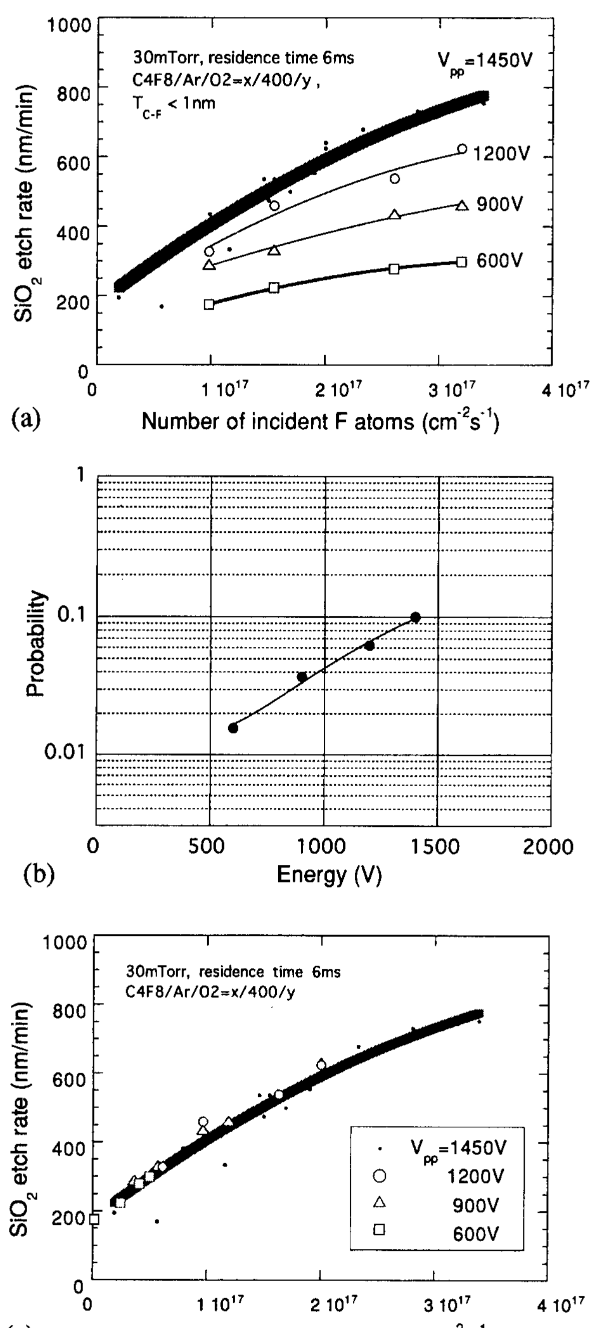

FIG. 4. (a) SiO_2 etch rate under the thin-polymer condition [e.g., Fig. 3(a) region I] plotted against incident number of F atoms calculated from the net flux of radicals (F, CF, CF_2, and CF_3). Surface reaction probability s was assumed to be 0.1 under all V_{pp} conditions. (b) Surface reaction probability s as a function of the incident ion energy (assumed to be V_{pp} under thin-polymer conditions). (c) SiO_2 etch rate under the thin-polymer condition [Fig. 4(a)] replotted against the number of incident F atoms calculated from net flux. Surface reaction probability s was assumed to correspond to ion energy as shown in Fig. 4(b).

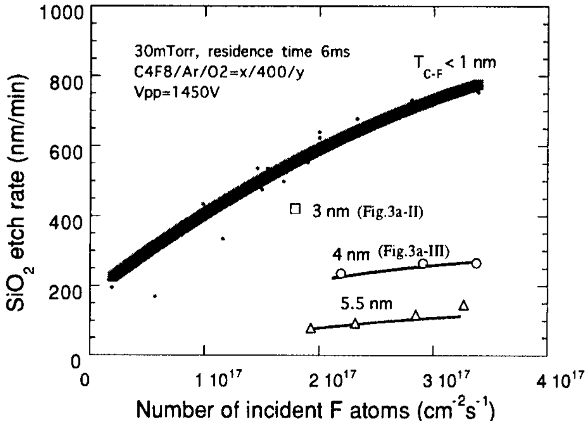

FIG. 5. SiO_2 etch rate plotted against the number of incident F atoms calculated from net flux of radicals (F, CF, CF_2, and CF_3). Surface reaction probability s was assumed to be 0.1 under various polymer-thickness conditions.

Comparing Figs. 4(a) and 5, we can see that the energy loss due to a 4-nm-thick polymer corresponded to the V_{pp} reduction from 1450 to 600 V. The similarly estimated energy loss (ΔV) under many different T_{C-F} conditions is shown in Fig. 6(b), where it is evident that ΔV increases monotonically with T_{C-F}. Consequently, $\Gamma_{F\text{-total}}$ values under the thick-polymer conditions were calculated again using s values less than 0.1, which were estimated from Fig. 4(b) and V_{net} [Fig. 6(a)]. The etch rate under the thick-polymer conditions are now also well expressed by the same function of $\Gamma_{F\text{-total}}$, so we can use the same curve to express all the etch rates under various ion energy and polymer thicknesses.

C. Control of C–F polymer thickness

It is very important to know how the thickness of C–F polymer is determined. The polymer thickness can be correlated to the steady-state density of carbon atoms "above" the reactive layer, which is determined by the balance between the number of incident C atoms in the CF_x fluxes and the C lost through the chemical reaction with oxygen or ion-enhanced reaction with fluorine. We can thus write

$$\rho \frac{dT_{C-F}}{dt} = \Gamma_{C\text{-total}} - L_{ion} - L_O - L_F = 0,$$

where ρ is the density of the C–F polymer, $\Gamma_{C\text{-total}}$ is the total number of incident C atoms in the CF_x fluxes; L_{ion}, L_O, and L_F are, respectively, the rate of C removal (loss term) by ion, oxygen, and fluorine. L_{ion} depends on the ion energy, ion flux, and sputtering yield of the polymer, which depends on the polymer composition, such as the F/C ratio. Chemical reactions with oxygen are the most important in determining the thickness because carbon reacts very easily with oxygen. Oxygen sources are both the incident flux of O from the gas phase ($L_{O\text{-plasma}}$) and the outflux from SiO_2($L_{O\text{-surf}}$):

$$L_O = L_{O\text{-plasma}} + L_{O\text{-surf}}.$$

It is essential to obtain the selectivity to the other materials (Si and SiN), whether outflux contains oxygen or not.[20,21]

In the experiment in which the data shown in Fig. 3(a) was gathered, $\Gamma_{C\text{-total}}$ was increased by increasing the C_4F_8 flow rate, while L_{ion} (N_e and V_{pp}) and $L_{O\text{-plasma}}$ (O_2 flow rate) were kept constant. The excess dissociation of C_4F_8 in this system was suppressed by keeping short residence time and low relative density of F.[3] Therefore, the effect of L_F

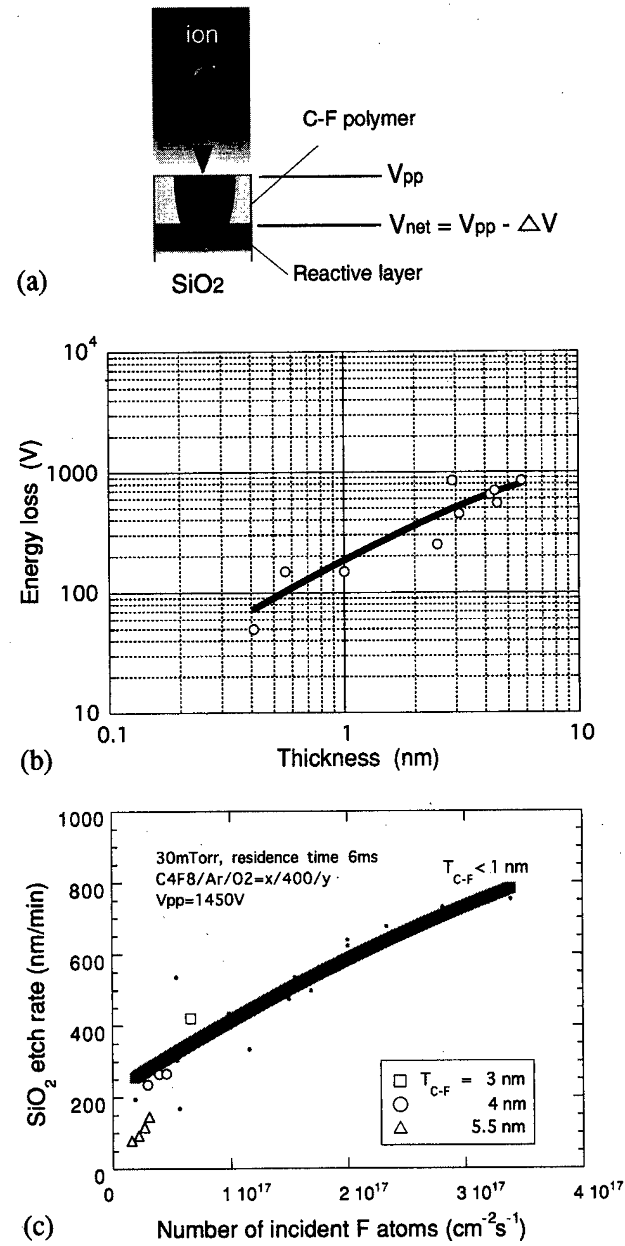

FIG. 6. (a) Images of surface layers. Energy is lost while ions pass through the C–F polymer layer. As a result, the surface reaction probability becomes low. (b) Ion energy loss as a function of the C–F polymer thickness. (c) SiO_2 etch rate under the various polymer conditions (Fig. 5) replotted against the number of incident F atoms calculated from the net flux. Surface reaction probability s was assumed to correspond to net ion energy, as shown in Figs. 4(b) and 6(b).

was small. The steady-state thickness of the C–F polymer T_{C-F} is obtained by solving the earlier rate equation. The increase of the C_4F_8 flow rate means the increase of $\Gamma_{C\text{-total}}$ without changing the loss terms; hence, T_{C-F} increased under the overflux condition (C_4F_8 flow>11 sccm). Similarly, the decrease of the loss term also induces the thick polymer. The detail in these calculation results of the T_{C-F} under various conditions will be reported later.

Etch stop at the high-aspect hole [Fig. 3(b)] is also explained using this rate equation. We have measured the ion

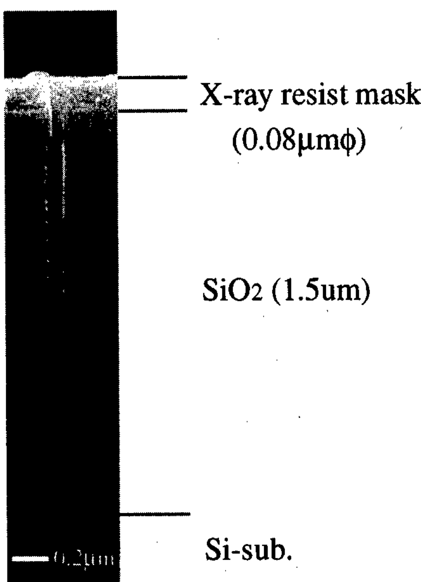

FIG. 7. Profile of a contact hole 0.08 μm in diameter etched under the thin polymer condition. Etch rate was 800 nm/min, and the selectivity (with regard to the resist mask) was about 4.

flux energy distribution through an ''actual-contact-hole-size'' capillary plate 0.2 μm in diameter. Both the energy and flux of ion were decreased in the high-aspect hole,[22] and this can be a reason for smaller loss terms (L_{ion}) at the bottom of the contact hole. Smaller losses (L_{ion}) will result in a thicker polymer, which will reduce the ion energy V_{net}, which will decrease the etch rate (low s, low $\Gamma_{F\text{-total}}$). The lower etch rate will, in turn, result in a smaller outflux of oxygen ($L_{O\text{-surf}}$), and this too will increase the thickness of the polymer. This ''negative spiral'' occurs in an instant, when the T_{C-F} reaches the critical polymer thickness determined by the ion projection range. To suppress the etch stop, we have to suppress the thick-polymer formation even in the high aspect contact holes. To do this, the increase of the loss term by increasing ion flux and oxygen is effective. Under high O_2 flow rate (L_O) with high ion flux (L_{ion}) condition, the ''thin polymer'' process could be realized, that provide the 0.08 μm ϕ contact hole with aspect ratio of 20 with etch rate of about 800 nm/min (Fig. 7).

D. Surface parameters

The results of our experiments clearly show that the information in the gas phase (the amount, composition, and energy of the incident fluxes), which is controlled by adjusting the ''external parameters,'' can be connected with the ''etch rate'' by taking into account of these ''surface parameters:''

(a) T_{C-F} (determined by ''particle balance'' of C),
(b) ΔV (determined by T_{C-F}),
(c) $V_{net}(=V_{pp}-\Delta V)$,
(d) s (function of V_{net}), and
(e) $\Gamma_{F\text{-total}}$ (defined by s and incident flux Γ_{CF_x}).

Using these parameters, the SiO_2 etch rate under various conditions could be expressed as a function of the incident fluxes. Moreover, the selectivity (the etch-rate difference between the materials) and the etched profile (the etch rate at the sidewall and the bottom of the hole) can also be explained using the same etching model.

V. SUMMARY

The relation between SiO_2 etch rates and the incident fluxes of reactive species in a dual-frequency (27 MHz and 800 kHz) parallel-plate system was evaluated.

(1) SiO_2 etch rate could be related to total F atom flux, $\Gamma_{\text{F-total}}$, which depends on both the incident fluxes of C–F reactive species and surface reaction probability s.

(2) The s is a function of the net energy on the reactive layer (V_{net}), which is determined by the incident ion energy (assumed to be V_{pp}) and the energy loss in the C–F polymer on the etched surface. A change in V_{net} from 500 to 1450 V was estimated to correspond to a change in s from 0.01 to 0.1.

(3) The steady-state thickness of the C–F polymer, T_{C-F}, increased when excess C–F species were supplied to the etched surface.

(4) A thick polymer ($T_{C-F}>1$ nm) decreases the ion energy and slows or stops etching reaction in the fine holes because it decreases the reaction energy on the reactive layer V_{net}. A polymer 5 nm thick can decrease the ion energy by about 750 V.

The T_{C-F} must be carefully controlled when high-aspect contact holes are etched.

ACKNOWLEDGMENTS

The authors would like to thank Yosuke Kawai of Tokyo Electron Yamanashi Limited and Yoshimi Kato of Selete Inc. for their helpful technical support. This work was supported by NEDO.

[1] T. Sakai, H. Hayashi, J. Abe, and H. Okano, Proceedings of the 15th Dry Process Symposium, Tokyo, 1993, p. 193.
[2] T. Fukasawa, A. Nakamura, H. Shindo, and Y. Horiike, Jpn. J. Appl. Phys., Part 1 **33**, 2139 (1994).
[3] T. Tatsumi, H. Hayashi, S. Morishita, S. Noda, M. Okigawa, N. Itabashi, Y. Hikosaka, and M. Inoue, Jpn. J. Appl. Phys., Part 1 **37**, 2394 (1998).
[4] H. Hayashi *et al.*, Proceedings of the 15th Symposium on Plasma Processing, Hamamatsu, 1998, p. 577.
[5] M. Okigawa *et al.*, Proceedings of the 15th Symposium on Plasma Processing, Hamamatsu, 1998, p. 454.
[6] S. Morishita, H. Hayashi, T. Tatsumi, Y. Hikosaka, S. Noda, M. Okigawa, and M. Inoue, Jpn. J. Appl. Phys., Part 1 **37**, 6899 (1998).
[7] T. Tatsumi, Y. Hikosaka, S. Morishita, M. Matsui, and M. Sekine, J. Vac. Sci. Technol. A **17**, 1562 (1999).
[8] Y. Hikosaka, H. Hayashi, M. Inoue, T. Tsuboi, M. Endo, N. Nagata, and T. Hayashi, Proceedings of the 15th Symposium on Plasma Processing, Hamamatsu, 1998, p. 581.
[9] S. Noda, K. Kinoshita, H. Nakagawa, M. Okigawa, T. Tatsumi, M. Inoue, and M. Sekine, Proceedings of the 20th Symposium on Dry Process, Tokyo, 1998, p. 235.
[10] M. Magane, N. Itabashi, N. Nishiwaki, T. Goto, C. Yamada, and E. Hirota, Jpn. J. Appl. Phys., Part 1 **29**, L829 (1990).
[11] K. Maruyama, A. Sakaki, and T. Goto, J. Phys. D **26**, 199 (1993).
[12] H. Toyoda, M. Ito, and H. Sugai, Jpn. J. Appl. Phys., Part 1 **36**, 3730 (1997).
[13] K. Kubota, H. Matsumoto, H. Shindo, S. Shingubara, and Y. Horiike, Jpn. J. Appl. Phys., Part 1 **34**, 2119 (1995).
[14] J. W. Coburn and M. Chen, J. Appl. Phys. **51**, 3134 (1980).
[15] J. S. Janq, J. Ding, J. W. Taylor, and N. Hershkowitz, Plasma Sources Sci. Technol. **3**, 154 (1994).
[16] Y. Kawai, K. Sasaki, and K. Kadota, Jpn. J. Appl. Phys., Part 1 **36**, L1261 (1997).
[17] D. C. Gray, Ph.D. thesis, MIT, Dept. of Chemical Engineering, 1992.
[18] J. F. Ziegler, J. P. Biersack, and W. Littmark, *The Stopping and Ranges of Ions in Matter* (Pergamon, New York, 1985), Vol. 4.
[19] M. Matsui, F. Uchida, T. Tokunaga, H. Enomoto, and T. Umezawa, Jpn. J. Appl. Phys., Part 1 **38**, 2124 (1999).
[20] M. Scheapkens, T. E. F. M. Standaert, P. G. M. Sebel, G. S. Oehrlein, and J. M. Cook, J. Vac. Sci. Technol. A **17**, 26 (1999).
[21] M. Matsui, T. Tatsumi, and M. Sekine, Proceedings of the 21st Symposium on Dry Process, Tokyo, 1999, p. 45.
[22] N. Ozawa, S. Noda, Y. Hikosaka, K. Kinoshita, and M. Sekine, Proceedings of the 52nd Gaseous Electronics Conference and 4th International Conference on Reactive Plasmas, Norfolk, 1999, p. 14.

Electron cyclotron resonance plasma etching of InP through-wafer connections at >4 μm/min using Cl_2/Ar

Y. W. Chen, B. S. Ooi, G. I. Ng,[a] and C. L. Tan
Microelectronics Center, School of Electrical and Electronic Engineering, Nanyang Technological University, Singapore 639798

(Received 27 January 2000; accepted 19 May 2000)

We report the development of very high etch rates (>4 μm/min), for InP via hole processes. These processes were developed in an electron cyclotron resonance system using a Cl_2/Ar plasma without heating the sample. The InP etch rates increased as a function of Cl_2 percentage in the Cl_2/Ar mixture, rf power, or microwave power. Via holes, with depths of 100 μm, suitable for monolithic microwave-integrated circuits applications, have been achieved at etch rates as high as 4 μm/min. To the best of our knowledge, this is the highest etch rate ever reported in InP for via hole applications. © *2000 American Vacuum Society.* [S0734-211X(00)06304-6]

I. INTRODUCTION

Through-wafer via hole structures for metal contacts are required to improve the performance of monolithic microwave-integrated circuits (MMICs). The existence of via holes eliminates the need for air bridges that are typically employed in MMICs to connect source pads to drain electrodes. Dry-etching techniques have been developed to produce GaAs via holes.[1–11] The fabrication process of InP via holes using dry etching is, however, not mature and, to date, only very few results have been reported.

The attainment of a very high etch rate (>1 μm/min) and a smooth etched surface with an etched depth of ~100 μm is necessary for via hole applications. CH_4/H_2-based chemistries, which is one of the commonly used mixtures in etching InP, are incapable of producing such a high etch rate. The issue of polymer formation in CH_4/H_2-based processes usually makes the process difficult to control. In the case of Cl_2-based processes, however, heating of an InP substrate to about 150 °C is required to promote desorption of the nonvolatile $InCl_x$ etch products for conventional reactive ion etching (RIE),[12] hence, producing a smooth InP etched surface. The necessity to heat the sample to a temperature >100 °C, however, limits the choice of mask material to either dielectrics or metals.

InP via holes have been demonstrated using wet chemical etching,[13] laser-assisted wet photoelectrochemical etching,[14,15] conventional RIE,[16] and electron cyclotron resonance (ECR) etching.[17,18] Wet-chemical etching is isotropic, which makes the high-density MMIC difficult to realize. A Cl_2/HBr/BCl_3/Ar mixture has been used in a conventional RIE system to achieve InP via holes.[16] An etch rate of 1 μm/min was obtained at a cathode temperature of 160 °C. A similar etch rate has also been obtained using a $Cl_2/CH_4/H_2$/Ar plasma in an ECR system with an electrode temperature of 150 °C.[17] To date, the highest etch rate in InP via hole etching ever reported at room temperature was 2.7 μm/min. This process was developed in an ECR system using a Cl_2/Ar plasma (10 sccm/10 sccm).[18]

In this article, processes giving InP etch rates >4 μm/min are reported. These processes were developed in an ECR system using a Cl_2/Ar plasma. A process with etch rate of ~4 μm/min producing slightly tapered 100-μm-deep InP via holes, suitable for MMIC device fabrication, has been successfully demonstrated.

II. EXPERIMENT

The samples were cleaned prior to resist coating and lithography to define the reversed 70-μm-diam via patterns onto the wafer. Oxygen plasma was used to descum the samples prior to metal mask evaporation. Via patterns with 70-μm-diam were obtained using a lift-off process. Ti/Ni was used as the etch mask as it has relatively high resistance, compared to photoresist, to the plasma etching. After etching, the mask can be easily removed using HF solution.

The plasma is excited in an ECR source operating at 2.45 GHz. The sample position was biased through the application of 13.56 MHz rf power. The sample was placed on a holder which was transferred into the process chamber using a robotic transfer arm. The bottom electrode, where the sample was placed, is not equipped with a He backside cooling or any other cooling system. The vacuum in the process chamber can be maintained at about a 10^{-6} mTorr level for etching processes. Electronic-grade Cl_2 and Ar were introduced into the process chamber through mass-flow controllers.

All experiments were done without intentionally heating the samples. The maximum chuck temperature, after exposing to the plasma for up to 25 min, was about 80 °C. The flow rates of the Cl_2/Ar mixture were fixed at 30 sccm/10 sccm. The average etch rates were obtained from samples etched for 5 min under various process conditions. The effects of rf power, microwave power, and the Cl_2 percentage in the Cl_2/Ar mixture on the InP etch rates were studied. A scanning electron microscope (SEM) was used to study the cross-sectional profiles of the processed samples.

III. RESULTS AND DISCUSSION

The InP etch rate as a function of rf power is shown in Fig. 1. The samples were etched using 1000 W microwave

[a]Electronic mail: EGING@ntu.edu.sg

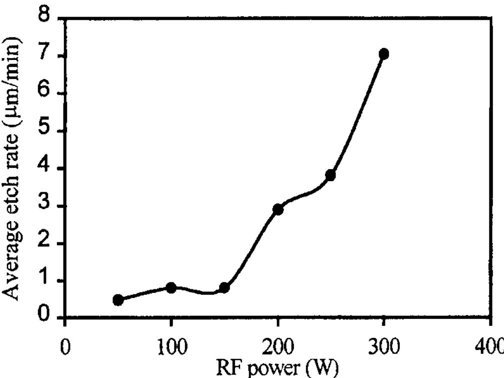

FIG. 1. InP etch rates as a function of rf power. The other parameters were: 1000 W microwave power, 10 mTorr pressure, and 30 sccm Cl_2/10 sccm Ar flow rates.

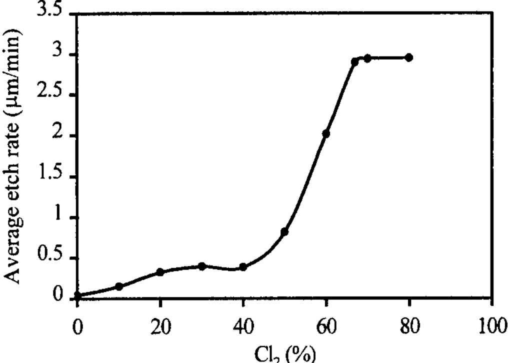

FIG. 3. InP etch rates as a function of Cl_2 percentage in Cl_2/Ar mixture. The other parameters were: 1000 W microwave power, 200 W rf power, 10 mTorr pressure, and 10 sccm Ar flow rate.

power, and 10 mTorr process pressure. The InP etch rates increased as a function of rf power. The etch rates increased from 0.48 to 7.0 μm/min, as the rf power increased from 50 to 300 W. The InP etch rates were >3 μm/min for samples etched using rf powers greater than 200 W. High rf power induces high dc bias. The sample thus subjects to higher rate of ions sputtering, which in turn increases the etch rates by increasing both physical etching and the desorption rate of nonvolatile etched products such as $InCl_x$.

The relationship between the InP etch rate and microwave power is given in Fig. 2. The etching conditions were: 150 W rf power, and 10 mTorr process pressure. From Fig. 2, it is learned that the InP etch rates can also be greatly enhanced by increasing the microwave power. The etch rates were found to increase from 0.07 to 1.1 μm/min as the microwave power increased from 250 to 1500 W. Only a small increase in etch rates was observed from samples etched at low microwave power (0–250 W), whereas at high microwave power ($>$250 W), a significant increase in etch rates has been observed. The ion flux increases with ECR power, which increases sputter desorption of reacted species from the surface. The increased Cl^+ concentration will influence

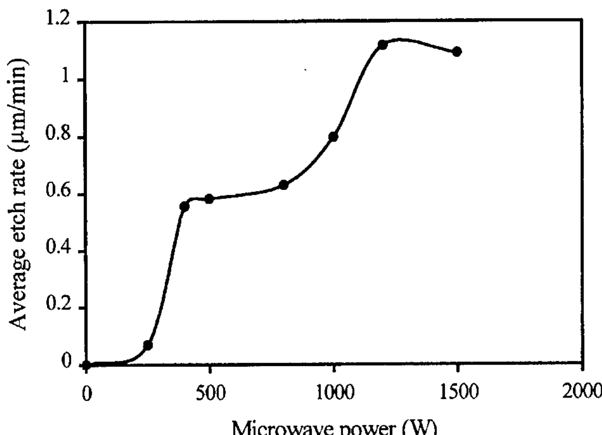

FIG. 2. InP etch rates as a function of microwave power. The other parameters were: 150 W rf power, 10 mTorr pressure, and 30 sccm Cl_2/10 sccm Ar flow rates.

the physical component, while the increase in reactive neutrals (Cl^0) will increase the chemical component of the etching. With a fixed rf power, the dc bias decreases with increasing microwave power as lower voltage is needed to deliver the same rf power at a high plasma density environment. The etching mechanism at high microwave power is, therefore, highly dominated by the chemical reaction between the material and the reactive species from the plasma.

Figure 3 shows the influence of the Cl_2 percentage in the Cl_2/Ar mixture on the InP etch rates. The samples were etched at 1000 W microwave power, 200 W rf power, and 10 mTorr process pressure. The Ar flow rate was fixed at 10 sccm. The etch rates increased from 0.04 to 2.95 μm/min as the Cl_2 percentage in Cl_2/Ar increased from 0% to 80%. Large ion current and relatively high ion energy can be obtained by employing high microwave power (1000 W) and rf power (200 W). As the Cl_2 composition in the Cl_2/Ar chemistry increased, more reactants are made readily available for InP to react. Relatively efficient ion-assisted desorption of the $InCl_3$ can be promoted before it passivates the surface,[19] therefore, the InP etch rates increased.

The etch rates were observed to saturate at 3 μm/min at $Cl_2 > 67\%$. The main function of Ar in the Cl_2/Ar mixture is to enhance the sputtering effect of the plasma and, hence, assist in ion-induced chemical reactions between the Cl reactants and InP, and increase the effect of sputter-assisted desorption of nonvolatile etched products. Although increasing the Cl_2 concentration causes an increase in the concentration of reactants, it reduces the effect of sputter desorption. Hence, the etch rates saturate at high Cl_2 concentration.

A slightly tapered sidewall profile is required for the through-wafer via structure for MMIC applications. This profile is required for facilitating the subsequent metallization step. In addition, in order to increase the throughput and make the process practical, a high InP etch rate ($>$1 μm/min) is needed. Therefore, the effects of process parameters on the via hole profile were also studied. Among the processes investigated, a 100-μm-deep structure with a slightly tapered profile obtained at an etch rate as high as 4 μm/min has been achieved without intentionally heating the electrode during the process (Fig. 4). The etching was done

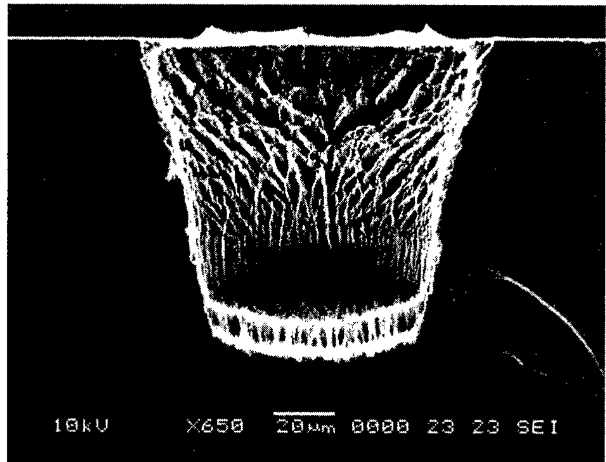

FIG. 4. Cross-sectional SEM micrograph of the InP via hole. The sample was etched at 800 W microwave power, 350 W rf power, and 15 mTorr process pressure for 25 min.

on an InP wafer under the conditions of 800 W microwave power, 350 W rf power, and 10 mTorr process pressure for 25 min. The sidewall was about 77° tapered, which is suitable for the applications in MMIC. To the best of our knowledge, this etch rate is the highest ever reported in InP for similar applications.

IV. CONCLUSIONS

In conclusion, we characterized the etching process of InP vias using a Cl_2/Ar plasma in an ECR system without intentionally heating the electrode. It was found that InP etch rates can be greatly enhanced by increasing the Cl_2 composition in the Cl_2/Ar mixture, microwave power, or rf power. Extremely high InP etch rates (>4 μm/min) have been obtained. This recorded etch rate is believed to be difficult to obtain from CH_4/H_2-based plasma, or conventional RIE Cl_2/Ar plasma without electrode heating. Via hole structure with a 100-μm-deep tapered profile has been obtained using the process with an etch rate as high as 4 μm/min. To the best of our knowledge, this etch rate is the highest ever reported in InP for similar applications.

ACKNOWLEDGMENT

This work was supported by National Sciences and Technology Board (NSTB), Singapore, under Grant No. NSTB/17/2/1.

[1]H. Takano, K. Sumitani, H. Matsuoka, K. Sato, O. Ishihara, and N. Tsubouchi, J. Vac. Sci. Technol. B **14**, 112 (1996).
[2]A. Mitra, C. D. Nordquist, T. N. Jackson, and T. S. Mayer, J. Vac. Sci. Technol. B **16**, 2695 (1998).
[3]S. Salimian, C. B. Cooper III, and M. E. Day, J. Vac. Sci. Technol. B **5**, 1606 (1987).
[4]R. J. Shul, M. L. Lovejoy, J. C. Word, A. J. Howard, D. J. Rieger, and S. H. Kravitz, J. Vac. Sci. Technol. B **15**, 657 (1997).
[5]S. J. Pearton, F. Ren, A. Katz, J. R. Lothian, T. R. Fullowan, and B. Tseng, J. Vac. Sci. Technol. B **11**, 152 (1993).
[6]K. P. Hilton and J. Woodward, Electron. Lett. **21**, 962 (1985).
[7]K. J. Nordheden, D. W. Ferguson, and P. M. Smith, J. Vac. Sci. Technol. B **11**, 1879 (1993).
[8]M. S. Chung, H. R. Kim, J. E. Lee, B. K. Kang, and B. M. Kim, J. Vac. Sci. Technol. B **11**, 159 (1993).
[9]L. G. Hipwood and P. N. Wood, J. Vac. Sci. Technol. B **3**, 395 (1985).
[10]R. J. Shul, A. G. Baca, R. D. Briggs, and G. B. McClellan, Electrochem. Soc. Proc. **2**, 515 (1996).
[11]F. Foulon and M. Green, J. Vac. Sci. Technol. B **11**, 1854 (1993).
[12]T. Yoshikawa, Y. Sugimoto, Y. Sakata, T. Takeuchi, M. Yamamoto, H. Hotta, S. Kohmoto, and K. Asakawa, J. Vac. Sci. Technol. B **14**, 1764 (1996).
[13]S. Trassaert, B. Boudart, S. Piotrowioz, and Y. Crosnier, J. Vac. Sci. Technol. B **16**, 561 (1998).
[14]O. A. Ghandour, R. Scarmozzino, R. M. Osgood, and W. W. Hooper, IEEE Trans. Semicond. Manuf. **6**, 357 (1993).
[15]R. Khare, E. L. Hu, J. J. Brown, and M. A. Melenders, Proceedings of the Fifth International Conference on InP and Related Materials, 1993, p. 537.
[16]K. Y. Hur, B. J. Guerin, and T. E. Kazior, J. Vac. Sci. Technol. B **12**, 1410 (1994).
[17]C. Constantine, C. Barratt, S. J. Pearton, F. Ren, J. R. Lothian, W. S. Hobson, A. Katz, L. W. Yang, and P. C. Chao, Electron. Lett. **29**, 984 (1993).
[18]K. K. Ko and S. W. Pang, J. Electrochem. Soc. **142**, 3945 (1995).
[19]J. W. Lee, J. Hong, and S. J. Pearton, Appl. Phys. Lett. **68**, 847 (1996).

Patterning of tantalum pentoxide, a high epsilon material, by inductively coupled plasma etching

L. B. Jonsson, J. Westlinder, F. Engelmark, C. Hedlund, J. Du, U. Smith,[a)] and H.-O. Blom[b)]
The Ångström Laboratory, Uppsala University, Box 534, SE-751 21 Uppsala, Sweden

(Received 5 October 1999; accepted 26 May 2000)

Integrated capacitors can easily cover a major part of the total chip area which may seriously affect the cost to produce the chip. By using a high epsilon material as the dielectric material, in the capacitor, the size can be reduced significantly. One very promising candidate is tantalum pentoxide (Ta_2O_5) which has a dielectric constant of about 25. This should be compared to silicon nitride which has a dielectric constant of 8. In order to make integrated capacitors the tantalum pentoxide must be patterned. Results of a study on etching of tantalum pentoxide, silicon dioxide, and polysilicon with a high density plasma, using an inductively coupled plasma source, are presented and compared to results obtained by means of reactive ion etching. The gas used, CHF_3, implies a polymerizing chemistry and the deposition of a fluorocarbon layer is shown to play an important role in the etch process. The fluorocarbon deposition onto the substrate surface is not only affected by the temperature of the substrate itself but also by the temperature of all surfaces that are exposed to the plasma. The process parameters with the strongest influence on the process have been found to be pressure and substrate bias voltage. © *2000 American Vacuum Society.*
[S0734-211X(00)08004-5]

I. INTRODUCTION

In some applications integrated capacitors using silicon nitride as the dielectric material may occupy an unreasonably large fraction of the total chip area. Reducing the area of the capacitors by making the dielectric film thinner is usually not possible since the breakdown voltage will decrease and the leakage current will increase which is, of course, unacceptable. A better way to reduce the area of the capacitor is to replace the dielectric material with a material having a higher dielectric constant. The requirements for such a material would be (1) a high dielectric constant; (2) low leakage current; (3) high breakdown voltage; (4) compatible with processing of integrated circuits (ICs). When taking the demands above into account, tantalum pentoxide (Ta_2O_5) seems to be a very promising candidate.[1]

The integrated capacitor can be placed in, or between, different metal layers. This means that the full capacitor structure will be poly-Si/Ta_2O_5/Al or Al/Ta_2O_5/Al. It is possible to wet etch tantalum pentoxide by an etchant consisting of concentrated HF and NH_4F. However, an etchant containing such a high concentration of HF is not suitable because it will also etch other materials used in microelectronic processing. Dry etching is therefore probably the best method to pattern the tantalum pentoxide although the dimensions of the etched features are relatively large. Reactive ion etching (RIE) of tantalum pentoxide has been studied earlier.[2,3] However, available information on the subject is quite limited. Reactive ion etching is also, at present, being phased out and replaced by high density plasma (HDP) etching processes. The most common HDP etching processes uses an inductively coupled plasma (ICP) source, which is a relatively simple and efficient source.

In this article we have studied etching of tantalum pentoxide using an ICP and compared the results with RIE. A special concern has been to find suitable processes that can be used to realize an integrated capacitor structure like, e.g., that in Fig. 1.

II. EXPERIMENT

Tantalum pentoxide films were deposited onto 4 in. silicon wafers by reactive sputtering in a Von Ardenne CS 600S sputtering system. The deposition rate was 160 Å/min. The film composition was analyzed by means of Rutherford backscattering spectroscopy (RBS) and ellipsometry. Stoichiometric films were transparent, with an index of refraction of 2.17 ± 0.01. The dielectric constant was measured using very simple structures consisting of aluminum dots on Ta_2O_5 layers deposited on aluminum. From these measurements the dielectric constant was found to be about 25.

The etching was done both in a standard RIE system and in an ICP system. A schematic of the ICP system used is shown in Fig. 2. It is similar to the system described by Keller *et al.*[4] and consists of a stainless steel chamber with a quartz window, 19 mm thick and 195 mm in diameter, mounted on the top flange. On the quartz window a coil, 140 mm in diameter with three turns, is placed. The coil is connected to a rf generator (Advanced Energy RFXII 1250-W) via a manual matching network. On the bottom flange an electrode, 150 mm in diameter, is mounted. The distance between the quartz window and the substrate is 74 mm. The bottom electrode is connected to a RF generator (Advanced Energy RFX 600A) via an automatic matching network (Advanced Energy ATX) and the setup is used in constant volt-

[a)]Also at MERC, Ericsson Components AB, SE-164 81, Kista, Sweden.
[b)]Electronic mail: hans-olof.blom@angstrom.uu.se

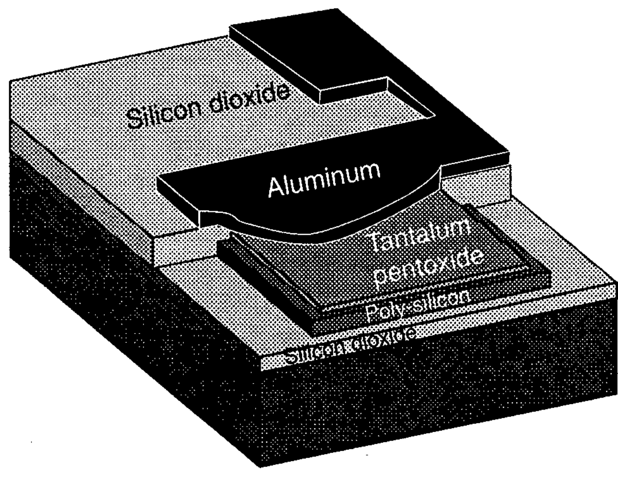

FIG. 1. Schematic of an integrated capacitor structure.

age mode [root mean square (rms)]. The two rf generators are driven in a common exciter mode. A plasma confinement ring consisting of an aluminum cylindrical ring resting on three stainless steel legs is placed between the quartz window and the bottom electrode. To the confinement ring a thermocouple sensor, which is encapsulated in stainless steel, is attached.

The RIE system is similar to the ICP system except that the quartz window with the rf-powered coil is replaced by a grounded electrode and the plasma confinement ring is removed. The bottom electrode is connected to a rf generator (Advanced Energy RFX 600A) via an automatic matching network (Advanced Energy ATX) and the setup is used in constant power mode.

During the etching experiments tantalum pentoxide samples were etched together with samples of thermal silicon dioxide and n^+ polysilicon on silicon dioxide. The samples were placed on the temperature controlled bottom electrode. The temperature was kept constant at 30 °C if not

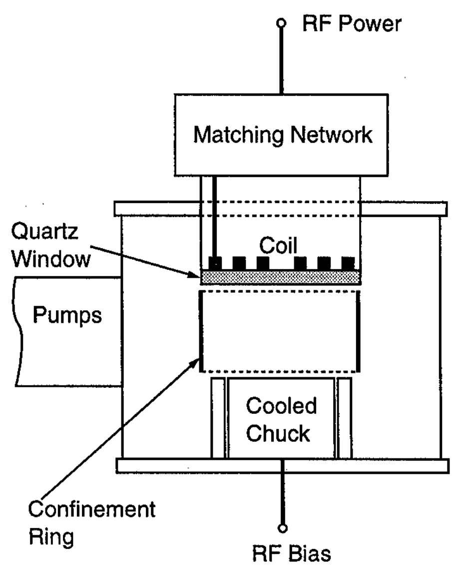

FIG. 2. Schematic of the ICP etching system.

TABLE I. Results from RIE of tantalum pentoxide, polysilicon, and silicon dioxide.

Material	CHF_3 flow (sccm)	Power (W)	Pressure (mTorr)	Rate (Å/min)	Selectivity	
Poly-Si	20	100	20	12	1	···
Ta_2O_5	20	100	20	36	3.1	1
SiO_2	20	100	20	102	8.9	2.9
Poly-Si	33	100	20	12	1	···
Ta_2O_5	33	100	20	41	3.5	1
SiO_2	33	100	20	114	9.7	2.8
Poly-Si	20	200	20	17	1	···
Ta_2O_5	20	200	20	78	4.7	1
SiO_2	20	200	20	233	14	3.0

otherwise stated. In order to increase the heat transfer between the samples and the chuck, some vacuum grease was applied on the backside of the samples.

As etching gas CHF_3 was chosen, since it is one of the most common gases for silicon dioxide etching. The CHF_3 will dissociate in the plasma and form various CF_x radicals and atomic fluorine. The atomic fluorine will react with the tantalum and form TaF_5. The boiling point for TaF_5 is 230 °C which is quite high but a little lower than the boiling point for $TaCl_5$ which is 240 °C.[5] The oxygen in the tantalum pentoxide film will react with CF_x radicals and form CO, CO_2, and COF_2.

The thickness of the samples was measured optically before and after a partial etch using a Leica MPV SP. For some processing conditions a relatively thick fluorocarbon layer will be deposited onto the samples. This fluorocarbon layer will have an index of refraction close to that of SiO_2. This implies that the Leica instrument cannot distinguish between the oxide and the fluorocarbon film. The result is that the thickness measurements for silicon dioxide includes both the oxide film and the fluorocarbon layer. The fluorocarbon film can also cause a problem when measuring the tantalum pentoxide and the polysilicon samples due to the more complex film structure with the extra fluorocarbon layer. The polysilicon samples seem to be especially difficult to measure correctly in the presence of a thick fluorocarbon layer. However, the fluorocarbon deposition mode of the process is considered less interesting since the main purpose of this investigation is to develop an etch process that can be used to realize an integrated capacitor structure.

III. RESULTS AND DISCUSSION

In Table I some results from RIE of tantalum pentoxide, polysilicon, and silicon dioxide are presented. The results are very similar to those obtained earlier by Seki *et al.*[2] and it seems like this process meets the requirements for realizing the capacitor structure in Fig. 1. The silicon dioxide etches faster than the tantalum pentoxide, which is necessary for etching the contact holes down to the tantalum pentoxide. The tantalum pentoxide etches faster than polysilicon so it will be possible to stop the etch on the polysilicon layer that is used as a bottom contact. However, outside the capacitor,

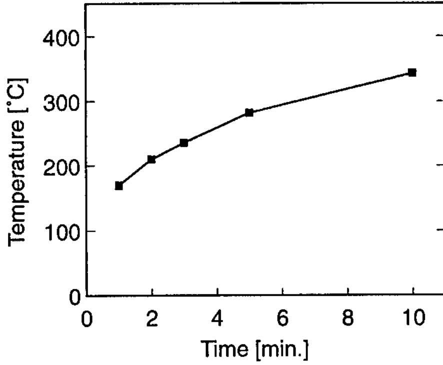

FIG. 3. Temperature of the plasma confinement ring vs time for the etch process after a oxygen warm-up step at an ICP power of 800 W and a pressure of 10 mTorr. For the actual etch process the ICP power was 600 W, the substrate bias was 80 V, the CHF_3 flow was 30 sccm, and the pressure was 10 mTorr.

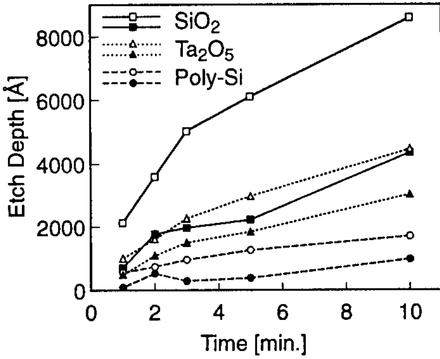

FIG. 4. Etch depth silicon dioxide, tantalum pentoxide, and polysilicon vs time for two starting temperatures (150 °C open symbols and 250 °C solid symbols) on the plasma confinement ring. The ICP power was 600 W, the substrate bias was 80 V, the CHF_3 flow was 30 sccm, the pressure was 10 mTorr, and the substrate temperature was 18 °C.

areas covered with silicon dioxide will be exposed to the etching plasma. During an overetch those areas will etch with a rate about an order of magnitude faster than the polysilicon and about three times faster than the tantalum pentoxide. For this particular structure, this potential problem can easily be avoided by simply etching the tantalum pentoxide before the polysilicon. The etch rate of tantalum pentoxide in a RIE system is very low. By using a high density plasma, like an ICP source, the etch rate can be increased about an order of magnitude.

It is well known that CHF_3 has a polymerizing chemistry and that the formation of a fluorocarbon layer is very temperature dependent.[6] Etching with an ICP tool means that high power is efficiently coupled into the plasma and as a result the chamber walls will heat up rapidly. It was shown by Sugai *et al.*[6] that the concentration of carbon containing radicals in the plasma increases dramatically when the temperature of the chamber walls increases. This wall temperature effect is believed to be due to a decrease in the surface loss of CF_x radicals at hot surfaces. On cold surfaces, i.e., the silicon wafer, the deposition of fluorocarbon will thus increase as the temperature of the chamber walls increases. Despite the large change in the concentration of carbon-containing radicals, the concentration of atomic fluorine is essentially unaffected, resulting in large variations in the F/CF_x ratios. In order to minimize the increase in chamber wall temperature the chamber was, at all times, maintained at 60 °C and a plasma confinement ring, similar to what was used by Schaepkens *et al.*,[7] was placed in the etch system as can be seen in Fig. 2. The purpose of the confinement ring is to very rapidly reach a high temperature, which leads to more stable operating conditions. To get reproducible results the chamber was cleaned with an oxygen plasma, 5 min 800 W at 10 mTorr, before each etch run. This also served as a pre-heating step of the confinement ring. The actual etch step could be performed right after the oxygen cleaning/heating step since only samples without photoresist were used.

The temperature of the confinement ring during a 10 min etch, 600 W ICP power, 30 sccm CHF_3, 10 mTorr is shown in Fig. 3. Here the starting temperature was 150 °C after the oxygen pre-heating plasma. It can be seen that the wall temperature is monotonously increasing with time.

In Fig. 4 the etch depth versus time for silicon dioxide, tantalum pentoxide, and polysilicon is shown. The two sets of curves for each material represent two different starting temperatures, 150 and 250 °C, respectively, on the confinement ring. First it can be noted that the etch depth for 150 °C is about two times larger than that for 250 °C. With a high starting temperature on the confinement ring fewer CF_x radicals are lost at the confinement ring surface and hence a thicker inhibiting fluorocarbon layer is formed on the cooler substrate surface. It can also be noted that after a few minutes the etch rates have reached steady state values although there is a significant difference in the wall temperature. This indicates that other factors like, e.g., the conditions on the walls, i.e., the degree of fluorocarbon deposition, are at least equally important as the temperature. Polysilicon will often only etch in the beginning when the fluorocarbon layer is building up. After about 1 min, the fluorocarbon layer will be thick enough to stop further etching. This means that under such conditions an excessive overetch of a tantalum pentoxide film does not affect an underlying polysilicon layer.

The importance of the fluorocarbon layer is seen in Fig. 5 where the etch rate of tantalum pentoxide and the inverse

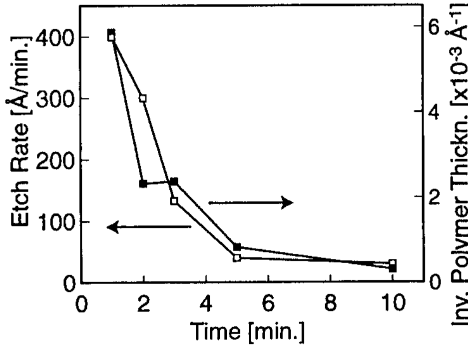

FIG. 5. Etch rate of tantalum pentoxide and the inverse of the thickness of the fluorocarbon layer vs time. The ICP power was 600 W, the substrate bias was 60 V, the CHF_3 flow was 30 sccm, the pressure was 10 mTorr, and the substrate temperature was 18 °C.

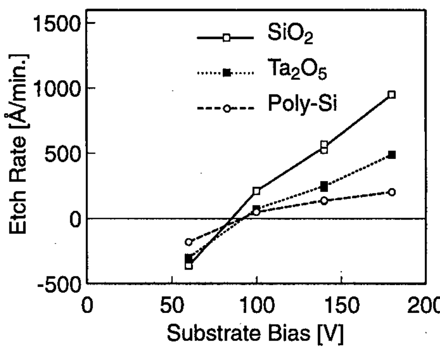

FIG. 6. Etch rates for silicon dioxide, tantalum pentoxide, and polysilicon vs the substrate bias voltage. The ICP power was 400 W, the CHF_3 flow was 30 sccm, and the pressure was 10 mTorr.

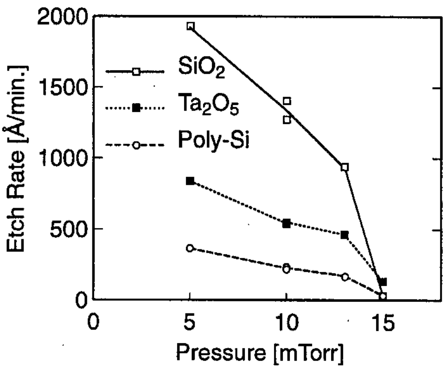

FIG. 8. Etch rates for silicon dioxide, tantalum pentoxide, and polysilicon vs the pressure. The ICP power was 400 W, the substrate bias was 100 V, and the CHF_3 flow was 30 sccm.

thickness of the deposited fluorocarbon layer are plotted versus time. It is interesting to see the strong correlation which is similar to what Oehrlein's group presented.[8]

Since the fluorocarbon deposition on a surface is very temperature dependent, it is essential to control the temperature of all surfaces exposed to the plasma. In the following experiments an oxygen plasma has been used as a combined clean and warm-up step prior to the actual etch step. This means that the starting temperatures of the surfaces exposed to the plasma have been kept constant during the experiments.

Figure 6 shows the etch rates for tantalum pentoxide, silicon dioxide, and polysilicon versus substrate bias voltage. Varying the substrate bias in an ICP system will essentially just vary the ion energy. This is unlike a RIE system where varying the power will change both the ion energy and ion current. However, for a bias $\geqslant$100 V the process seems to behave quite similarly to a RIE process. At low substrate bias voltages the etch rates are negative which means that a fluorocarbon film has been deposited. The reversed order for the etch rates at 60 V bias is mainly due to difficulties in accurately measuring the thickness of the fluorocarbon layer with the Leica MPV SP.

In Fig. 7 etch rates versus the flow of CHF_3 are shown. The influence of the gas flow is relatively small. The small decrease in the etch rates when the flow is increased is probably due to an increase in the fluorocarbon deposition. For small flows the etch rates are low, as expected.

The etch rates versus pressure are shown in Fig. 8. The rapid increase in the etch rate when the pressure is lowered can be explained by a decrease in the fluorocarbon deposition. In a RIE system operating at constant power, a lower pressure usually means a larger ion energy. In this case with an ICP system and the rf-bias generator in constant bias voltage mode this cannot be true. However, the main reason for transferring from RIE to ICP in microelectronics is the possibility to lower the pressure without sacrificing the etch rate. A lower pressure means a larger mean free path for the ions, and hence fewer collisions in the sheet, which will result in a more directional etch. But, the larger mean free path will also alter the ion energy distribution towards a higher average energy by reducing the low energy tail of the distribution. This effect may also contribute to the increase in the etch rates when the pressure is lowered. At very low pressures the etch rates are expected to drop because the production of etchants will decrease. However, this expected drop in the etch rates cannot be seen at 5 mTorr.

Varying the ICP power affects mostly the dissociation and ionization and hence the ion current at the substrate. Increasing the ICP power should therefore just result in an upscaling of the rates which can be seen in Fig. 9. The zero etch rate for silicon dioxide at an ICP power of 400 W is due to an

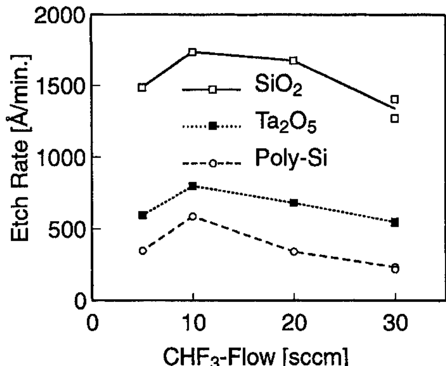

FIG. 7. Etch rates for silicon dioxide, tantalum pentoxide, and polysilicon vs the CHF_3 flow. The ICP power was 400 W, the substrate bias was 100 V, and the pressure was 10 mTorr.

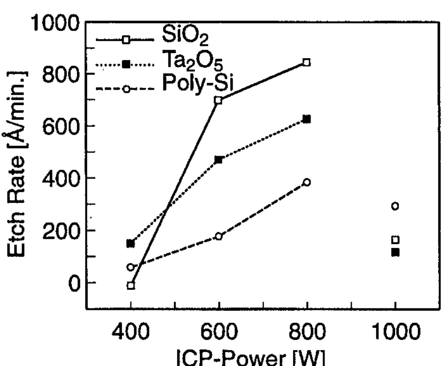

FIG. 9. Etch rates for silicon dioxide, tantalum pentoxide, and polysilicon vs the ICP power. The substrate bias was 60 V, the CHF_3 flow was 30 sccm, and the pressure was 10 mTorr.

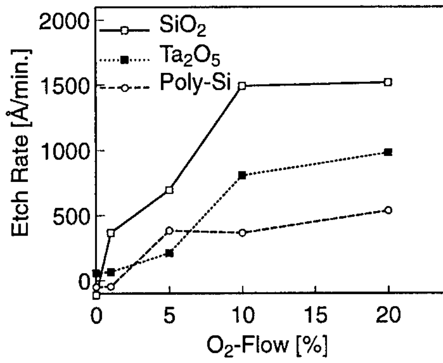

FIG. 10. Etch rates for silicon dioxide, tantalum pentoxide, and polysilicon vs the oxygen addition. The ICP power was 400 W, the substrate bias was 60 V, the CHF_3 flow was 30 sccm, and the pressure was 10 mTorr.

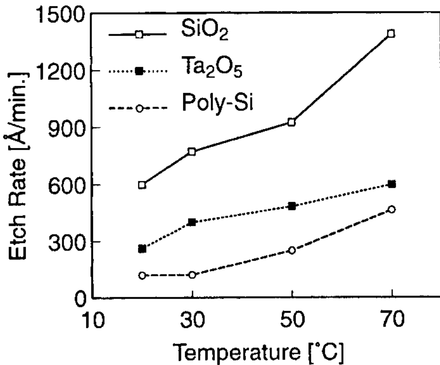

FIG. 11. Etch rates for silicon dioxide, tantalum pentoxide, and polysilicon vs the substrate temperature. The ICP power was 400 W, the substrate bias was 80 V, the CHF_3 flow was 30 sccm, and the pressure was 10 mTorr.

error in the measurement of the film thickness after the etch. This comes about because the Leica MPV SP cannot distinguish between silicon dioxide and a fluorocarbon layer, and the fluorocarbon layer is included in the measurements. For an ICP power of 1000 W a very strange result was obtained. Basically all etch rates dropped. At this high ICP power the confinement ring will be very hot (over 400 °C). Such high temperatures may contribute to the dissociation of the CHF_3 molecule at the confinement ring surface.

Oxygen is often used as an addition in polymerizing chemistries in order to increase the etch rate. However, one drawback with oxygen additions is that the photoresist erosion increases. In Fig. 10 it can be seen that the etch rates increase rapidly for small amounts of oxygen. For larger amounts the effect is relatively small. For very large concentrations of oxygen, the etch rates are expected to decrease because the CHF_3 is diluted and hence less atomic fluorine is produced. It can also be seen that the increase in the etch rate for polysilicon is very large, which together with the increased photoresist erosion makes the addition of oxygen less attractive.

The temperature of surfaces exposed to the plasma has, as shown earlier, a great influence on the etching process. In Fig. 11 the etch rates versus the substrate temperature are shown. It can be seen that an increase in substrate temperature from 20 to 70 °C increases the etch rates two to three times. This means that it is very important to have strict control of the substrate temperature. However, this can easily be obtained in production tools by clamping of the substrate combined with helium backside cooling.

IV. CONCLUSION

Etching of tantalum pentoxide, silicon dioxide, and polysilicon with a high density plasma using an ICP source has been presented and compared to results obtained by RIE.

The deposition of a fluorocarbon layer has been shown to play an important role in the etch process. The fluorocarbon deposition onto the substrate surface is not only affected by the temperature of the substrate itself, but also by the temperature of all surfaces that are exposed to the plasma. Even with a plasma confinement ring that heats up rapidly it can be seen from the data presented that it takes about 1 min before the etch rates reach steady state values. This is can be a problem in production since the total etch time often is in the order of 1 min or less. However, modern production tools, for example, oxide etching, using HDP usually have a temperature control that should be sufficient also for these processes.

From the results presented above it can be seen that in order to obtain high Ta_2O_5/poly-Si selectivity, a process with high pressure and low substrate bias voltage should be chosen. In this process region the etch rate that is measured for the poly-Si is often only due to an initial etching that takes place before an inhibiting fluorocarbon layer has grown thick enough. This means that a prolonged overetch of the tantalum pentoxide layer will not further affect the underlying poly-Si layer.

To obtain high SiO_2/Ta_2O_5 selectivity, a process with low pressure and large substrate bias voltage should be chosen.

A capacitor structure of the type shown in Fig. 1 has been processed successfully using etch processes with parameters chosen according to the recommendations above.

ACKNOWLEDGMENTS

This work was financially supported by the Swedish Research Council for Engineering Sciences (TFR), the Swedish Foundation for Strategic Research (SSF), and the Göran Gustafsson Foundation.

[1] F.-C. Chiu, J.-J. Wang, J. Y. Lee, and S. C. Wu, J. Appl. Phys. **81**, 6911 (1997).
[2] S. Seki, T. Unagami, and B. Tsujiyama, J. Electrochem. Soc. **130**, 2505 (1983).
[3] Y. Kyo, J. Electrochem. Soc. **139**, 579 (1992).
[4] J. H. Keller, J. C. Forster, and M. S. Barnes, J. Vac. Sci. Technol. A **11**, 2487 (1993).
[5] A. J. van Roosmalen, J. A. G. Baggerman, and S. J. H. Brader, *Dry Etching for VLSI* (Plenum, New York, 1991), p. 121.
[6] H. Sugai, K. Nakamura, Y. Hikosawa, and M. Nakamura, J. Vac. Sci. Technol. A **13**, 887 (1995).
[7] M. Schaepkens, R. C. M. Bosch, T. E. F. M. Standaert, G. S. Oehrlein, and J. M. Cook, J. Vac. Sci. Technol. A **16**, 2099 (1998).
[8] N. R. Rueger, J. J. Beulens, M. Schaepkens, M. F. Doemling, J. M. Mirza, T. E. F. M. Standaert, and G. S. Oehrlein, J. Vac. Sci. Technol. A **15**, 1881 (1997).

Anisotropic etching of RuO_2 and Ru with high aspect ratio for gigabit dynamic random access memory

Takashi Yunogami[a] and Kazuo Nojiri
Device Development Center, Hitachi, Ltd., 6-16-3, Shinmachi, Ome-shi, Tokyo 198-8512, Japan

(Received 1 June 1999; accepted 22 February 2000)

Anisotropic RuO_2 and Ru etching technology for gigabit dynamic random access memory has been developed using high density $O_2+10\%$ Cl_2 plasma in an inductively coupled plasma etching system. Under the conditions of low pressure, high gas flow rate, and large overetching times, we have demonstrated 0.2 μm wide patterns in 0.3-μm-thick RuO_2/Ru films and 0.1 μm wide patterns in 0.45-μm-thick Ru films, both with an almost perpendicular taper angle of 89°. © *2000 American Vacuum Society.* [S0734-211X(00)01604-8]

I. INTRODUCTION

Recently, gigabit dynamic random access memory (DRAM) capacitors have been developed using simple stacked structures of high dielectric constant materials, such as barium strontium titanium oxide (BST).[1] Noble metals, such as Pt and Ru, or conductive oxides, such as RuO_2, have been used as electrode materials[2] since they are thermally stable in the high temperature oxygen ambient used for BST deposition. Very high resolution and aspect ratios are needed for the bottom electrode in these structures; the film thickness required for 0.13 μm critical dimensions (CDs) is 0.45 μm, implying an aspect ratio of 3.5:1. The angle of the sidewall taper must be larger than 85°.

It is difficult to achieve the required anisotropic profiles for Pt[3,4] by dry etching because the vapor pressure of the possible reaction products is low.[5] On the other hand, anisotropic etching of Ru and RuO_2 are possible[6,7] by oxygen ion assisted etching through the formation of volatile RuO_3 and RuO_4.[8] The addition of 10% Cl_2 to an O_2 plasma enhances this etch rate[9] further, because 10% Cl_2 increases the concentration of oxygen radicals and ions. In spite of these advances, the etching of Ru or RuO_2 with the required aspect ratio (3.5) and the taper angle (85°) has not yet been demonstrated. The main purpose of this study is to develop a etching process for Ru and RuO_2 with the high aspect ratios required for gigabit DRAM.

II. MECHANISM OF ANISOTROPIC RuO_2 ETCHING

The etching mechanisms of RuO_2 in O_2 plasmas are illustrated in Fig. 1. The Ru etching mechanism is believed to be similar to that of RuO_2. RuO_2 is etched by oxygen ion sputtering and by oxygen ion assisted etching through the formation of volatile RuO_3 and RuO_4. Sidewall coatings may develop through the redeposition of the sputtered component and the decomposition of the volatile compounds into solid Ru or RuO_2. The deposition of these reaction products on the sidewall decreases the taper angle of the etched profile and, thereby, limits the achievable aspect ratio. This effect can be minimized by reducing the partial pressure of the volatile etch products over the wafer, by increasing etching rate of the sidewall deposition with high density oxygen plasma, and by increasing exhaustivity of the reaction products with high gas flow rate and high speed pumping. We therefore implemented the RuO_2 and Ru etching processes in an inductively coupled plasma (ICP) etcher, which can generate a high density plasma with high gas flow rates at low pressure.

III. EXPERIMENTS

The ICP etcher used for RuO_2 and Ru etching experiments was as follows. It has a inductive coil of rectangular cross section placed on the top of a quart window. Radio frequency (rf) power with 13.56 MHz is applied to both the coil and a wafer electrode. Etching gases and productions are exhausted via 2000 little/s turbo molecular pump. The wafer is electrostatically chucked on the electrode.

Samples were prepared with three different layer sequences on 150 mm silicon wafers:

(a) Photoresist (2 μm thick)/plasma-tetraethylorthosilicate (P-TEOS) (200 nm)/RuO_2(250 nm)/Ru(50 nm)/TiN(80 nm)/Ti(50 nm). The CD of the resist pattern was 1 μm.
(b) Electron beam (EB) resist (300 nm thick)/P-TEOS(200 nm)/RuO_2(250 nm)/Ru(50 nm)/TiN(80 nm)/Ti(50 nm). The CD of the EB resist pattern was 0.14 μm.
(c) EB resist (300 nm thick)/P-TEOS(300 nm)/Ru(450 nm)/TiN(80 nm)/Ti(50 nm). The CD of the resist pattern was 0.1 μm.

The bottom layers of TiN/Ti were used for adhesion of RuO_2/Ru and Ru. The resist patterns on all the samples were transferred into the P-TEOS film by dry etching with a CHF_3/CF_4 plasma. The resulting P-TEOS masks were subsequently used to etch the RuO_2/Ru or Ru films in $O_2+10\%$ Cl_2. We first optimized the pressure and $O_2+10\%$ Cl_2 gas flow rate with the (a) samples under the condition of 500 W ICP source power and 200 W rf power. These optimal conditions were used to etch the (b) samples, which were then inspected to determine their anisotropy. Finally, anisotropic etching of Ru was examined using the (c) samples.

[a]Electronic mail: yunogami-takashi@nhmemory.co.jp

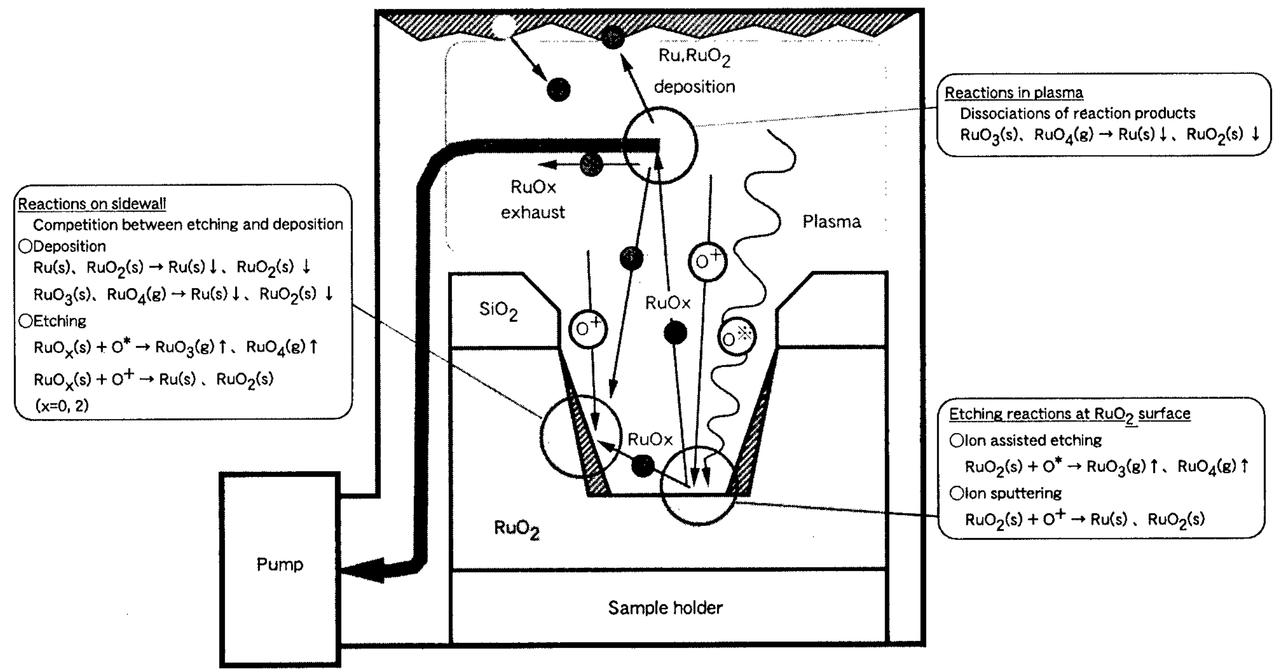

FIG. 1. Etching mechanism of RuO_2 with oxygen-based gas chemistry.

IV. RESULTS AND DISCUSSIONS

A. Optimization of process parameters

At first, pressure and $O_2+10\%$ Cl_2 gas flow rate were optimized for RuO_2/Ru etching using the (a) samples. Figures 2(A) and 3(A) show, respectively, scanning electron micrographs (SEMs) of the etched RuO_2/Ru structures and a summary of the etching characteristics (etch rate, taper angle, and facet width) as functions of pressure. As expected, taper angle increased as pressure decreased. However, reducing the pressure also increased the mask faceting, which leads to shoulder loss of the RuO_2. Based on these results, we chose 15 mTorr as the optimal pressure.

Figures 2(B) and 3(B) show, respectively, SEMs of the RuO_2/Ru etch profiles and a summary of etching characteristics (etch rate, taper angle, and facet width) as a function of $O_2+10\%$ Cl_2 gas flow rate. As again expected, taper angle

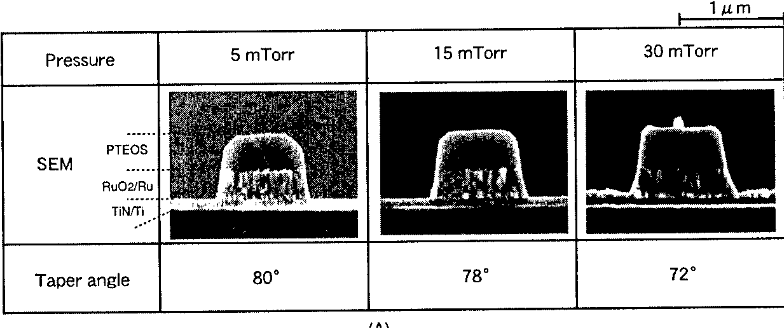

Pressure	5 mTorr	15 mTorr	30 mTorr
SEM (PTEOS, RuO2/Ru, TiN/Ti)			
Taper angle	80°	78°	72°

(A) (scale bar: 1 μm)

O_2/Cl_2 flow rate	100 sccm	360 sccm	800 sccm
SEM (PTEOS, RuO2/Ru, TiN/Ti)			
Taper angle	78°	80°	84°

(B) (scale bar: 1 μm)

FIG. 2. RuO_2/Ru pattern profiles as a function of (A) pressure and (B) $O_2+10\%$ Cl_2 flow rate.

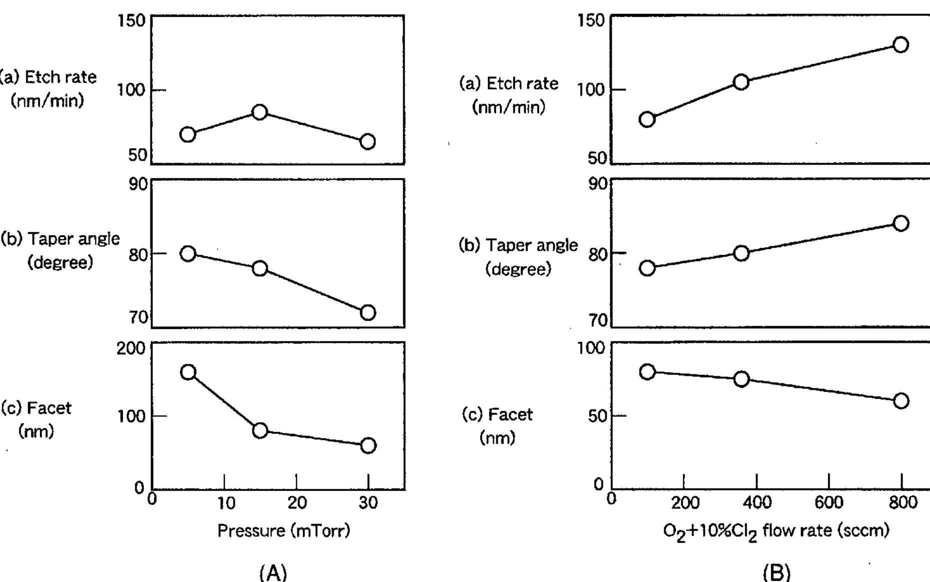

FIG. 3. RuO_2 etching characteristics as a function of (A) pressure and (B) $O_2 + 10\%\ Cl_2$ flow rate.

increased with increasing gas flow rate. When the process conditions were 15 mTorr total pressure and 800 sccm gas flow rate, the taper angle of RuO_2/Ru became 84°, slightly lower than our goal of 85°. Since etch rate and faceting also improved with increasing gas flow rate, the optimal flow rate was chosen as the maximum (800 sccm) that could be achieved at the optimal pressure (15 mTorr).

B. Anisotropic etching of RuO_2/Ru

The high resolution RuO_2/Ru patterns of sample (b) were etched under the optimized conditions discussed earlier. The formation of the P-TEOS mask is shown in Fig. 4: (A) EB resist pattern with a CD of 0.14 μm and a thickness of 0.3 μm, (B) P-TEOS pattern with resist remaining (0.2 μm thick and 0.2 μm CD), and (C) the P-TEOS pattern after resist ashing. A small amount of resist residue remains after the ashing step. The 300-nm-thick RuO_2/Ru stack was then etched with the P-TEOS mask using the optimized conditions (15 mTorr pressure and 800 sccm $O_2 + 10\%\ Cl_2$ flow rate). Figure 5 shows SEM photos of the RuO_2/Ru pattern as a function of percent overetch (OE%), defined as the total etching time less the time required to etch just though the RuO_2/Ru stack expressed as a percentage of the time to etch the stack. The taper angle increases during the overetch period (e.g., with OE%) because RuO_x $(x=0-4)$ no longer evolves from the bottom of the trench but the sidewalls continue to etch. Figure 6 shows a RuO_2/Ru pattern with OE%=100 that has an almost perpendicular taper angle of 89°. Moreover, the CD of the RuO_2/Ru stack was 0.22 μm, corresponding to a CD gain of 20 nm relative to the TEOS mask. This is sufficiently small for current design rules.

C. Anisotropic Ru etching

Finally, Fig. 7 shows a 450-nm-thick Ru film [sample (c)] etched with a P-TEOS mask (0.3 μm thick and 0.1 μm CD) under the same conditions discussed earlier for RuO_2/Ru.

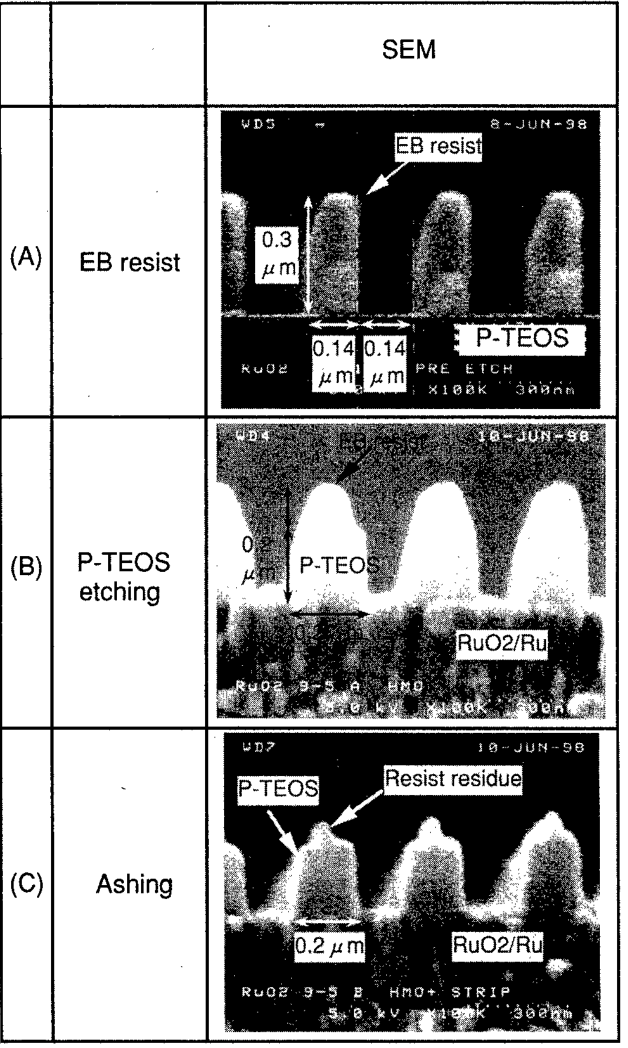

FIG. 4. P-TEOS mask formation. (A) EB resist pattern, (B) P-TEOS etching, and (C) ashing.

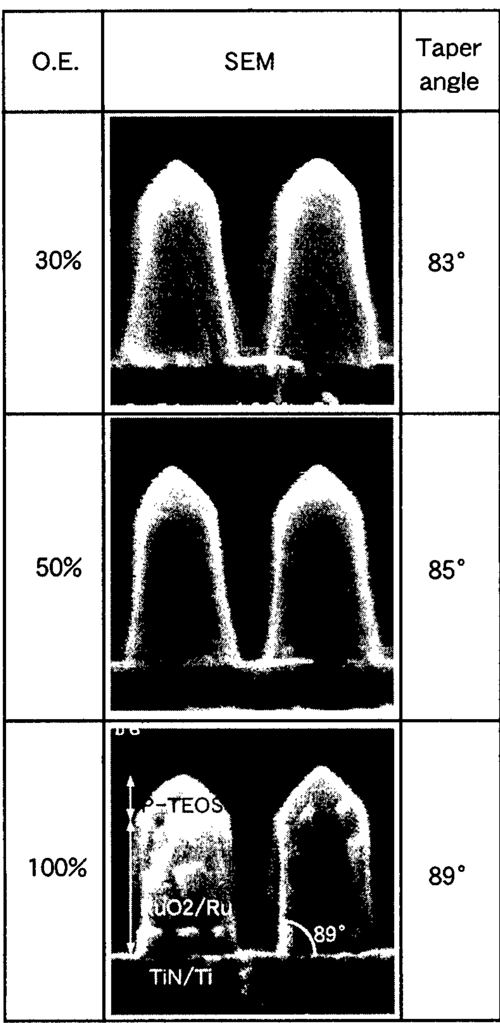

O.E.	SEM	Taper angle
30%		83°
50%		85°
100%		89°

FIG. 5. Taper angle of RuO_2/Ru pattern as a function of overetch percentage.

The resulting Ru pattern is 0.45 μm in height and 0.1 μm wide, corresponding to an aspect ratio of 4.5. The taper angle was 89°, and the CD gain was almost zero.

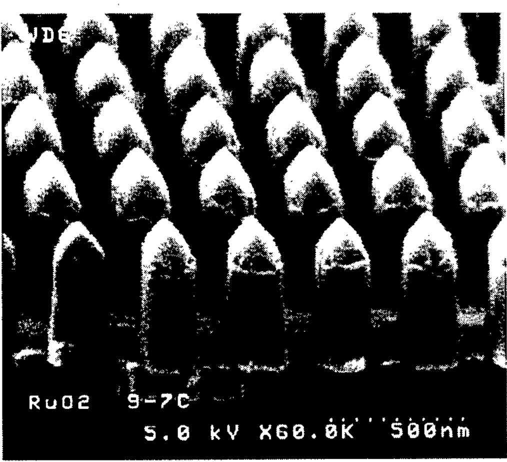

FIG. 6. High aspect ratio RuO_2/Ru profile.

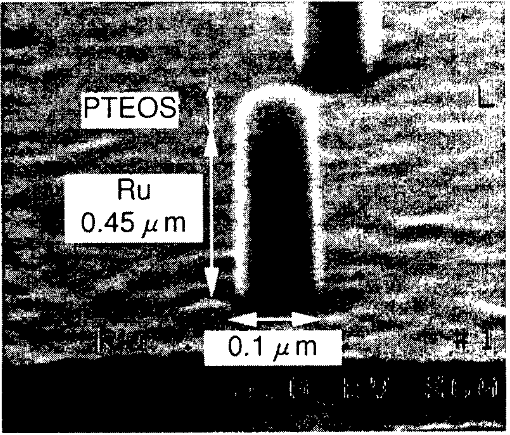

FIG. 7. High aspect ratio Ru profile.

V. CONCLUSIONS

Anisotropic etching technology for RuO_2 and Ru has been developed using a high density O_2 + 10% Cl_2 plasma in an ICP etching system. The taper angle for RuO_2/Ru increased with decreasing pressure, with increasing O_2 + 10% Cl_2 flow rate and with increasing overetch time. Using a low pressure, a high gas flow rate and 100% over etch time resulting in a 0.3-μm thick RuO_2/Ru pattern with 0.2 μm CD and a taper angle of 89°. A 0.45-μm-thick Ru pattern with 0.1 μm CD and a taper angle of 89° was formed using the same etching process. Thus, we have demonstrated a process suitable for etching the electrodes of high-dielectric constant capacitors in gigabit DRAM manufacturing.

ACKNOWLEDGMENTS

The authors wish to thank Sonoko Migitaka, Dr. Yuko Tshuchiya, Toshiyuki Yamamoto, Jiro Yamamoto, Katsuya Hayano, Akira Imai, Norio Hasegawa, Dr. Hiroshi Shiraishi, Dr. Fumio Murai, and Dr. Shinji Okazaki for preparing EB resist mask on Ru and RuO_2.

Presented at the 43rd International Symposium on Electron, Ion, and Photon Beam Technology and Nanofabrication, Marco Island, FL, 1–4 June 1999.

[1]S. Yamamichi, K. Takemura, T. Sakura, H. Watanabe, H. Ono, K. Tokashiki, E. Ikawa, and Y. Miyasaka, *Proceedings of the 1994 IEEE 9th Symposium on the Application of Ferroelectrics* (IEEE, University Park, PA, 1994).
[2]H. Yamaguchi, S. Matsubara, K. Takemura, and Y. Miyasaka, *Proceedings of the 1992 IEEE 8th Symposium on the Application of Ferroelectrics* (IEEE, Piscataway, NJ, 1992), p. 258.
[3]W. J. Yoo, J. H. Hahm, C. S. Hwang, S. O. Park, Y. B. Koh, and M. Y. Lee, Proceedings of the Dry Process Symposium (1995), p. 191.
[4]T. Yunogami and T. Kumihashi, Jpn. J. Appl. Phys., Part 1 **37**, 6934 (1998).
[5]*Handbook of Chemical and Physics*, 76th ed., edited by D. R. Lide (CRC Press, Boston, 1995).
[6]K. Tokashiki, K. Sato, K. Takemura, S. Yamamichi, P. Y. Lesaicherre, H. Miyamoto, E. Ikawa, and Y. Miyasaka, Proceedings of the Dry Process Symposium (1994), p. 73.
[7]K. Nakamura, T. Shibano, and T. Oomori, Proceedings of the Dry Process Symposium (1997), p. 217.
[8]W. E. Bell and M. Tagami, J. Phys. Chem. **67**, 2432 (1963).
[9]E. J. Lee, J. W. Kim, and W. J. Lee, Jpn. J. Appl. Phys., Part 1 **37**, 2634 (1998).

Transmission electron microscope investigation of $SrBi_2Ta_2O_9$ memory capacitors on Si with silicon dioxide and silicon nitride as buffers

A. Ils,[a] M. Cantoni, J.-M. Sallese, and P. Fazan
Electronics Laboratory and Center for Electron Microscopy, Swiss Federal Institute of Technology, CH-1015 Lausanne, Switzerland

J.-P. Han, X. Guo, and T. P. Ma
Department of Electrical Engineering, Center for Microelectronic Materials and Structures, Yale University, New Haven, Connecticut 06520

(Received 5 November 1999; accepted 14 April 2000)

Ferroelectric memory capacitors were made by deposition of $SrBi_2Ta_2O_9$ (SBT) on Si with thin (~40–90 Å) buffer layers of jet vapor deposition (JVD) silicon nitride and oxide. Transmission electron microscope analysis was carried out to compare the microscopic integrity of both films after subsequent processing steps. It was found that the thin SiO_2 buffer layer failed to prevent further oxidation of the Si substrate and furthermore allowed the diffusion of the SBT towards the SiO_2/Si interface. In contrast the silicon nitride layer deposited by the JVD process acted as a good barrier for the diffusion of SBT. It also stopped further oxidation of the Si substrate during subsequent annealing in oxygen. Electrical tests show that the capacitors have large memory windows and that the windows present only slight degradation after 10^{11} switching cycles. The use of JVD nitride as a buffer is encouraging for the further development of ferroelectric memory transistors. © *2000 American Vacuum Society.* [S0734-211X(00)01904-1]

I. INTRODUCTION

$SrBi_2Ta_2O_9$ (SBT) thin films have been investigated intensively for the nonvolatile random access memory applications due to their excellent ferroelectric (FE) properties.[1] At the present time, a FE storage capacitor connected to a pass-gate transistor is the most actively pursued method.[2] However, a memory device based on ferroelectric memory field effect transistor (FET), which can serve both as the storage element and the sensing device, would be highly desirable. The latest trend to this effect is the concept of ferroelectric dynamic random access memories (FEDRAMs).[3] The FEDRAM is derived from the idea of a metal–ferroelectric–insulator–semiconductor FET (MFISFET) structure proposed by Wu *et al.* in 1974 for nonvolatile memory devices.[4] Nevertheless, a major problem that has still held back the progress in this direction is the difficulty in obtaining a good ferroelectric film on Si with good interface properties. Therefore, a working MFISFET is possible only with a thin buffer layer between the ferroelectric film and the silicon substrate. This would allow the deposition of a ferroelectric film on silicon with good interface properties and a large memory window. At the same time, the buffer layer has to be robust enough to maintain its material properties during device processing. The feasibility of the FEDRAM concept can be demonstrated by looking at the result on a ferroelectric gate memory (FEM) capacitor.[2] Although other materials such as $SrTiO_3$ (Refs. 5 and 6) or RuO_2 (Ref. 7) have been investigated as buffers for different FE materials, we have concentrated our investigation on a MFIS structure with SiO_2 and SiN as our selected insulators because both Si–SiO_2 and Si–SiN combinations are believed to be the most stable structures. They are as well fully compatible with standard microelectronics processes. One can precisely control gate the potential of the FET channel due to excellent interface characteristics and obtain high reliability in fatigue and retention time.[8] Unfortunately due to the high temperature processes needed to deposit SBT, the material integrity of some insulators could be compromised, thus rendering the devices unusable.

In this article we will report the result of our transmission electron microscope (TEM) investigation of SBT based capacitors made with jet vapor deposited (JVD) silicon dioxide and silicon nitride as buffers. The integrity of these two buffer materials is discussed. Some electrical results are also presented to support our observations.

II. EXPERIMENT

Nitride (SiN) and oxide (SiO_2) films 4–9 nm thick were deposited by the jet vapor deposition process[9,10] on precleaned *n*-type wafers. A post deposition anneal was performed on these samples for 30 min in nitrogen. SBT films approximately 300 nm thick were then deposited on top of the buffer layers by a spin-on method using a presynthesized metalorganic deposition (MOD) solution. The samples were subsequently annealed at ~900 °C in oxygen for 1 h. This was followed by Au evaporation to form both the gate electrode and the back contact. A postmetal anneal was performed at 400 °C in oxygen to complete the Au/SBT/(nitride) or (oxide)/Si FEM capacitor.

Samples were then prepared for cross-sectional TEM and energy dispersive spectrometry (EDS) analysis. Thinning was done by mechanical polishing followed by Ar^+ ion milling. Philips CM20 and CM300 microscopes working at 200 and 300 keV, respectively, have been used in this study. The beam resolution for EDS was 2 nm.

[a]Electronic mail: amy.ils@epfl.ch

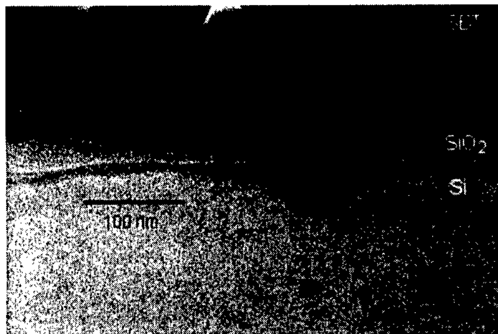

FIG. 1. TEM picture showing the $SBT/SiO_2/Si$ interface. The initial oxide thickness was 40 Å.

III. RESULTS AND DISCUSSION

A. Au/SBT/SiO_2/Si FEM capacitor

Figures 1 and 2 show typical TEM images for the $SBT/SiO_2/Si$ combination at different magnifications. As mentioned previously, one of the most important features in a working device is the integrity of the buffer layer. In this case, it is evident that the SiO_2 layer did not maintain its integrity during the SBT processing.

The final thickness of the oxide is measured to be between 200 to 500 Å. This is approximately the same for both samples with 40 and 80 Å oxide initially which suggests an increase of more than six times the initial layer. It seems that the oxide continued to grow during the SBT annealing in oxygen. In other words, the SBT layer let in oxygen to further oxidize the underlying Si. As illustrated in Fig. 2, we see an undulated interface in some areas between the SiO_2/Si. It is interesting to note that the Si/SiO_2 interface in some cases loosely follows the contour of the SBT grain above it. By and large the interface between the Si and SiO_2 is quite nonuniform and suggests inhomogeneous oxidation of the Si.

Figure 1 shows a SBT grain that has passed through the SiO_2 layer and has come close to the Si interface. This is clearly an indication of SBT diffusion into the buffer layer. The size of the grains is of the order of 150 nm and shows clear preferential orientations.

B. Au/SBT/SiN/Si FEM capacitor

Figures 3(a) and 3(b) show typical images of Au/SBT/SiN/Si FEM capacitor for two thicknesses of SiN buffer. The pictures clearly indicate that the integrity of the nitride film held up during SBT deposition and subsequent annealing. The thicknesses of the films were measured to be approximately 50 and 90 Å, respectively, which are the as-deposited thicknesses. In both cases, the interface between the Si/SiN is quite uniform. This implies that, in contrast to the case of the oxide buffer, the nitride layer has blocked the penetration of oxygen and prevented further oxidation of the silicon.

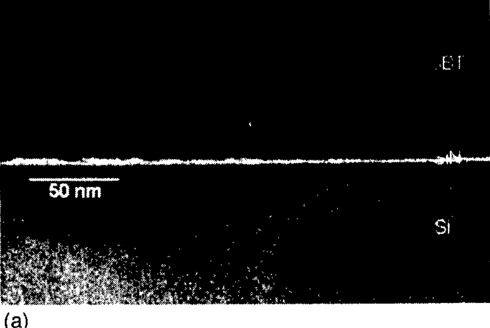

(a)

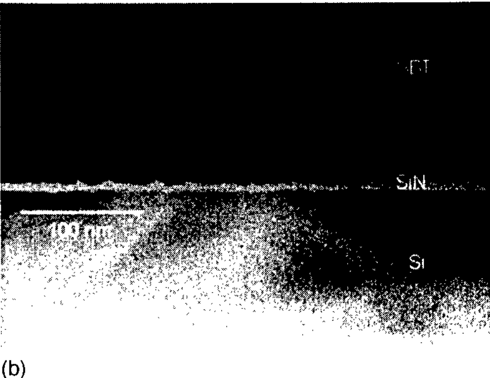

(b)

FIG. 3. TEM picture of the SBT/SiN/Si interface for (a) 50 and (b) 90 Å SiN. Note that there is no diffusion of SBT across the buffer layer.

The grains of the SBT on the SiN show completely different characteristics than those on SiO_2. The typical size of the grains is of the order of 20 nm for the 90 Å nitride. Figure 4 shows a high resolution TEM (HRTEM) image of the SBT/SiN/Si structures. It can be seen from the image that the SBT layer is polycrystalline. The interfaces between SBT/SiN and SiN/Si are clearly defined. Figure 5 shows x-ray diffraction patterns obtain from the SBT film on SiN.

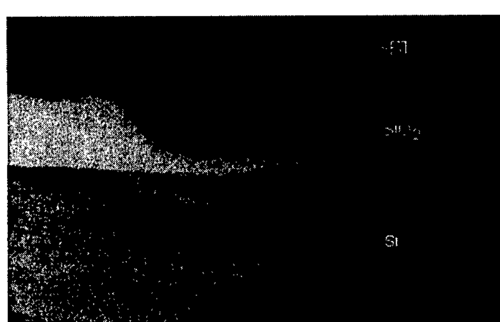

FIG. 2. TEM picture showing how the SiO_2/Si interface follows the contour of the SBT grain.

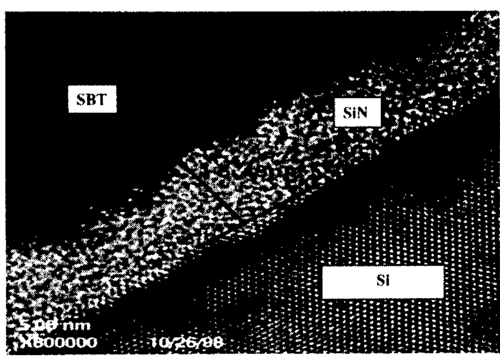

FIG. 4. HRTEM showing the SBT/SiN/Si interface. There are clear interfaces between the three materials.

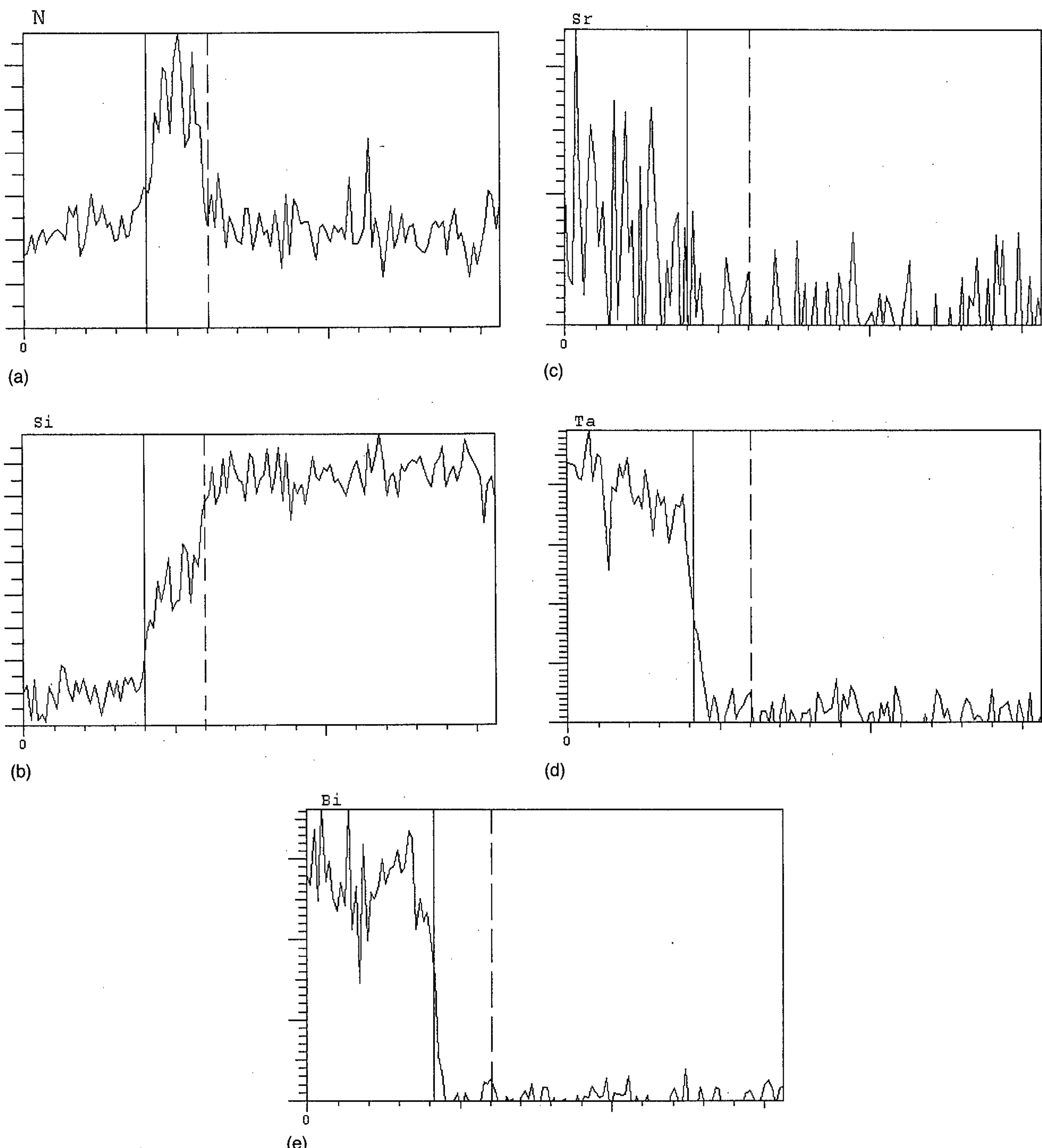

FIG. 5. X-ray diffraction pattern of SBT on the nitride/Si substrate.

Orientations of ⟨110⟩ and ⟨105⟩ are predominantly displayed although ⟨200⟩ and ⟨315⟩ are also visible.

An EDS line scan was taken through these layers and the result is shown in Fig. 6. The different graphs show different elements that are present during the line scan through initially, the SBT layer, then SiN and finally towards the Si substrate. We see that the signals of Sr, Bi, and Ta are strong at the beginning of the sweep. At the SBT/SiN interface, there is a sudden drop in signal from the three elements but an increase in the Si and N signals. Finally as the beam swept towards the Si substrate there is an increase in signal of the Si and a drop in that of N. This analysis was repeated at different regions of the sample and the same results were obtained. We could then conclude that there is almost no diffusion of the SBT into the SiN layer, as there was in the case of the SiO_2 buffer.

C. Discussion

The SiO_2 film reveals that it is not a viable buffer for the high temperature processed SBT film. During the SBT annealing process, oxidation of the underlying silicon layer oc-

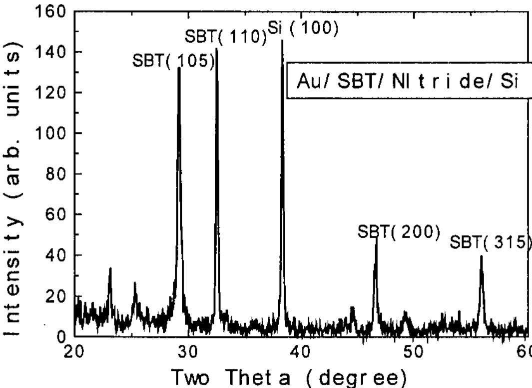

FIG. 6. EDS of the SBT/SiN/Si structure. The solid line indicates the SBT/SiN interface and the dashed line defines the SiN/Si interface. (a) N; (b) Si; (c) Sr; (d) Ta; (e) Bi.

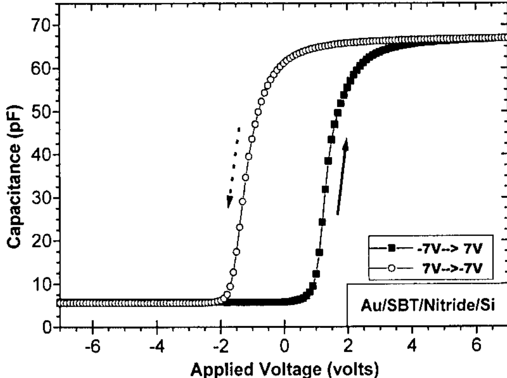

FIG. 7. $C-V$ curves of a FEM capacitor showing hysteresis.

curs since neither the SBT nor the SiO_2 can prevent oxygen penetration. The oxygen is thought to reach the underlying Si layer through the SBT grain boundary. But, it is interesting to note that some traverse the SBT as well to oxidize the Si since in some areas the interface of SiO_2/Si loosely follows the contour of the grain.

The diffusion of the SBT material through the SiO_2 as observed by TEM is another factor that renders SiO_2 unusable for our ferroelectric application. Diffusion can easily occur in the oxide layer during high temperature annealing where the SBT material penetrates the buffer through some defects in the material.

In contrast, the JVD nitride shows excellent material and electrical quality for use as a buffer in SBT device applications. It prevents the penetration of oxygen to underlying materials even during the high temperature process. In addition, no diffusion was observed through the nitride layer, demonstrating that we have a very high quality JVD nitride film to start with. Electrical measurements on the 50 Å nitride capacitor show good capacitance–voltage ($C-V$) characteristics and a large $C-V$ (memory) window as illustrated in Fig. 7. This is an indication of good interface quality between the Si/SiN layers, which is an important criterion for a good buffer. Fatigue tests done on the devices show there was little change in the $C-V$ memory window after 10^{11} cycles of switching. Details of the complete electrical test can be obtained in Refs. 2 and 11.

Finally, a significant difference in SBT grain size can be observed between SiO_2 and SiN samples even though the SBT has been deposited and processed the same way. This disparity is thought to be due to the influence of the buffer layer. It has been reported recently by some research groups that buffer layers play a very important role in the nucleation and growth of high quality ferroelectric film.[12] In particular, the film stoichiometry, microstructure and crystallographic orientation are influenced not only by annealing temperature and time,[13] but by the type of buffer and the corresponding thickness as well. While it would be interesting to investigate the influence of SiN buffer thickness on the grain size and reliability of the device, the focus of this article was to demonstrate the difference between JVD SiN and SiO_2 as buffers. The above topics will be investigated in the future and will be the subject of another paper.

IV. CONCLUSION

We have studied FEM capacitors made with JVD nitride and JVD oxide as buffers. TEM investigation of these structures indicates that the oxide film suffers loss of material integrity during the subsequent high temperature SBT process. The film is neither a good diffusion barrier for the SBT nor a good blocking layer for oxygen penetration. In contrast the integrity of the nitride film was not compromised as a result of high temperature. There was no diffusion of SBT or oxidation through the buffer as indicated by TEM and EDS. It maintains good interfacial quality with the substrate and demonstrates material robustness as shown in the electrical test. Therefore JVD nitride has proven to be a viable buffer for SBT for the next generation of ferroelectric memory devices.

ACKNOWLEDGMENTS

The authors would like to thank Serguei Okhonin, Igor Stolichnov, and Paul Muralt for valuable discussions and Danièle Laub for her assistance in sample preparation.

[1]G. D. Hu, J. B. Xu, I. H. Wilson, W. Y. Cheung, N. Ke, W. K. Chan, and S. P. Wong, Proceedings of the 11th IEEE International Symposium on Applications of Ferroelectrics, August 1998, p. 163.

[2]J.-P. Han and T.-P. Ma, Appl. Phys. Lett. **72**, 1185 (1998).

[3]T.-P. Ma and J.-P. Han, U.S. Patent pending, filed 16 September 1998.

[4]S. Wu, IEEE Trans. Electron Devices **ED-21**, 499 (1974).

[5]E. Tokumitsu, K. Itani, B.-k. Moon, and H. Ishiwara, Jpn. J. Appl. Phys., Part 1 **34**, 5202 (1995).

[6]H.-C. Pan, G. C. Chang, C. C. Chou, and H. F. Cheng, Integr. Ferroelectr. **25**, 179 (1999).

[7]M. Foster, G. R. Bai, J. Vetrone, Y. Huang, and R. Jammy, Integr. Ferroelectr. **14**, 23 (1997).

[8]Y. Matsumuro, H. Sugiyama, M. Noda, and M. Okuyama, Proceedings of the 11th IEEE International Symposium on Applications of Ferroelectrics, August 1998, p. 59.

[9]M. Khare, X. Guo, X. W. Wang, T.-P. Ma, G. J. Cui, T. Tamagawa, B. L. Halpern, and J. J. Schmitt, 1997 Symposium on VLSI Technology Digest of Technical Papers, p. 51.

[10]T.-P. Ma, IEEE Trans. Electron Devices **45**, 680 (1998).

[11]J.-P. Han, X. Guo, and T.-P. Ma, Integr. Ferroelectr. **22**, 213 (1998).

[12]F. Cattan, G. Velu, B. Jaber, D. Remiens, and B. Thierry, Appl. Phys. Lett. **70**, 1718 (1998).

[13]J.-H. Choi and J.-Y. Lee, Appl. Phys. Lett. **74**, 2933 (1999).

Stability and chemical composition of thermally grown iridium-oxide thin films

Babu R. Chalamala,[a] Yi Wei, and Robert H. Reuss
Motorola, Inc., Flat Panel Display Division, 7700 South River Parkway, Tempe, Arizona 85284

Sanjeev Aggarwal, Scott R. Perusse, Bruce E. Gnade,[b] and R. Ramesh
Materials Research Science and Engineering Center, University of Maryland at College Park, College Park, Maryland 20742

(Received 10 December 1999; accepted 14 April 2000)

The effect of growth conditions on the thermal stability and chemical composition of iridium-oxide thin films fabricated by annealing Ir films in O_2 is presented. The oxide growth as a function of anneal temperature was studied by x-ray photoelectron spectroscopy depth profile analysis and the thermal stability was determined using temperature programmed desorption spectroscopy. We observed that with increasing anneal temperature, the surface oxidized to IrO_2 (110) and the thermal stability of the resulting oxide increased. X-ray photoelectron spectroscopy depth profiles showed that IrO_2 starts to form at 600 °C simultaneous with an increase in the surface roughness of the film.
© *2000 American Vacuum Society.* [S0734-211X(00)02204-6]

I. INTRODUCTION

Iridium oxide is a conductive oxide with significant applications in semiconductor and vacuum microelectronic devices. IrO_2 has several useful properties such as low resistivity and excellent diffusion barrier characteristics. For example, iridium oxide is one of the most promising capacitor electrode materials for ferroelectric memories.[1] Other important applications are as optical switching layers in electrochromic display devices,[2] as *p*H-sensing materials,[3,4] and as stable electrode materials for applications in biological, medical,[5,6] and chemically reactive environments.[7]

Most early studies focused on IrO_2 films prepared by wet-electrochemical processes, by reactive sputter deposition of iridium in O_2-rich ambients, or by pulsed-laser ablation of iridium-oxide targets. The determination of the thermal stability of these oxides is limited to chemical analysis using x-ray photoelectron spectroscopy (XPS). Sanjines, Aruchamy, and Levy have shown that sputtered IrO_2 films decompose at about 400 °C in air and 200 °C in vacuum.[8] Partially hydrated films were found to decompose at 350 °C in air and 150 °C in vacuum. The thermal stability of these films was determined by measuring the relative concentrations of O and Ir using XPS after the films were annealed at different temperatures. Peuckert determined that thermally prepared oxidic layers on iridium decompose between 577 and 627 °C in ultrahigh vacuum.[9] Peuckert's results suggest that the surface oxides decompose into the elements at a higher temperature than predicted from thermodynamic data for bulk IrO_2. This is in contrast to the data reported in the literature.[10] Kellogg has used atom probe field ion microscopy to study the stability of thermally grown IrO_2 tips.[11] The IrO_2 films were prepared by heat treating elemental iridium tips in 10 Torr of O_2. The oxides grown at a temperature of 600 °C and above were found to be thermally stable and exhibited some evidence for crystallographic order in the field ion images.

In this article, we report direct measurements on the thermal stability of iridium-oxide films using temperature-programmed desorption (TPD) spectroscopy. The TPD data are complemented with x-ray diffraction (XRD) crystallography measurements and x-ray photoelectron spectroscopy depth profile measurements of the chemical composition of these films.

II. EXPERIMENT

Thin films of iridium were deposited on 1-mm-thick single-crystal lanthanum–aluminum-oxide ($LaAlO_3$) substrates by pulsed-laser ablation (PLD) using a target of iridium metal. The pulsed-laser ablation system is described in detail elsewhere.[12] During deposition, the target was at room temperature and the base pressure of the system was kept at 10^{-5} Torr or below. The excimer laser was operated in the pulsed mode with pulses of 20 ns, peak power density reaching 2 J/cm^2 on the target. The Ir films were then annealed at 600, 700, 800, and 900 °C for 1 h in a furnace with a continuous flow of O_2 at 10 Torr. The work function, crystalline structure, and the surface morphology of thermally oxidized iridium-oxide films have been reported in our recent publication.[13]

III. RESULTS AND DISCUSSION

The as-grown Ir films have a thickness of 100 nm. These films show a preferred (111) orientation. X-ray diffraction data show continuous oxidation of iridium into IrO_2 with increasing temperature. The oxidized films show preferential growth in the (110) direction, but we also see growth in (101) and (200) orientations. This can be seen in the x-ray diffraction data shown in Fig. 1. The surface roughness of the films was found to increase with temperature.[13] Atomic-

[a]Electronic mail: Babu.Chalamala@Motorola.Com
[b]Current address: Department of Materials Science, University of North Texas, Denton, TX 76203.

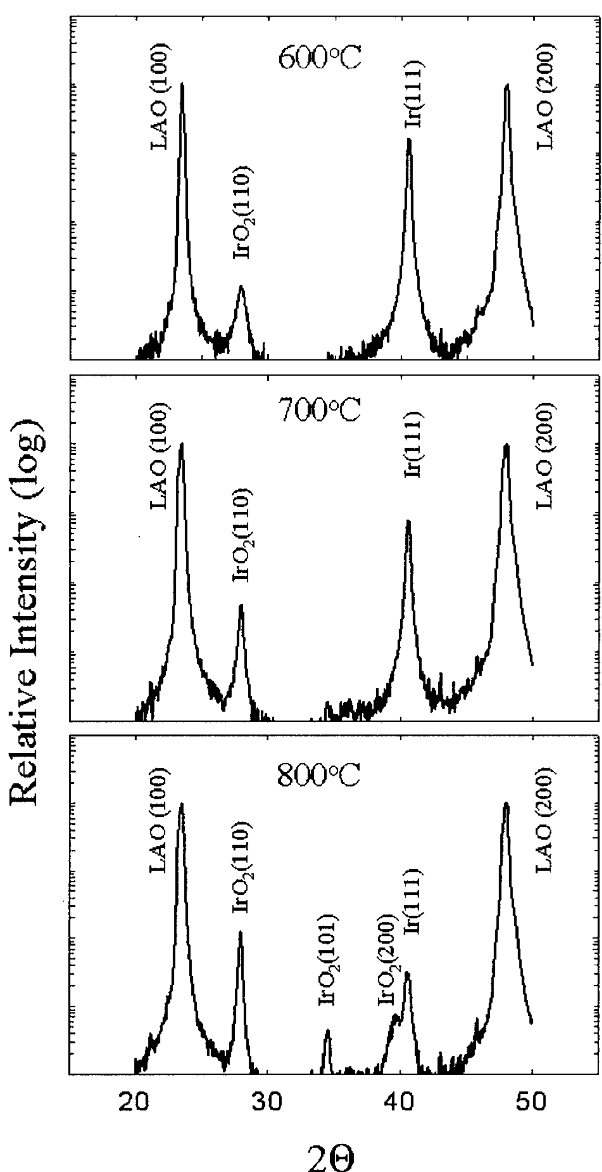

FIG. 1. X-ray diffraction patterns for the iridium films annealed at 600, 700, and 800 °C, respectively.

force microscopy of as-deposited Ir films showed that they were very smooth, with a root-mean-square (rms) roughness of 1.9 Å and a surface height range (low point to high point) of 20.6 Å. The grain size and surface roughness were found to increase with increasing anneal temperature. From the as deposited film to films annealed at 700 °C, the surface rms roughness and height range grow almost linearly, rms roughness from 1.9 to 33.6 Å, height range from 20.6 to 340.6 Å. But, the film annealed at 800 °C in O_2 shows large jumps in the rms roughness and surface height range. The structural changes with increasing annealing temperatures are a result of the growth of IrO_2 crystalline structures.

The chemical composition of the samples was determined using x-ray photoelectron spectroscopy (PHI model 5700 with an Al $K\alpha$ source). XPS provides data about surface composition in conjunction with the chemical bonding information for the elements detected. For the current measurements, the x-ray beam spot size is about 10 μm. Depth profiles were performed by sputter removing material with a 2 keV Ar^+-ion beam. Sputtering conditions that erode thermally grown SiO_2 at an approximate rate of 35 Å per minute were used. The elemental concentrations were measured as a function of depth. Since the sputter rates for Ir and IrO_2 are different from that of SiO_2, the exact thickness of the sputtered film cannot be determined.

TABLE I. Surface chemical composition (in atomic percent) as a function of annealing temperature in 10 Torr of O_2 for 1 h.

Annealing temperature (°C)	C 1*s*	O 1*s*	Al 2*p*	La 3*d*5	Ir 4*f*
As grown	8.1	2.3	···	···	89.0
600	7.5	41.6	-	···	49.0
	4.6	49.0	···	···	43.2
800	5.1	49.8	1.2	1.8	40.9
900	6.2	61.8	15.2	10.0	0.4

The thermal stability of IrO_2 films oxidized at different temperatures was measured by temperature-programmed desorption spectroscopy. In TPD, the desorption of gases as a function of sample temperature is measured.[14] In the present experiment, the temperature was raised at a rate of 18 °C/min. The IrO_2 samples, approximately 1 cm^2 in size, were placed on a heater block. The relative concentration of the desorbed gases was monitored with a mass spectrometer.

Table I shows the atomic concentrations of major elements found on the five surfaces which were annealed in O_2 at different temperatures for 1 h. The atomic concentrations are deduced from the XPS spectra using Physical Electronics Inc., MULTIPAK program[15] and by taking atomic-sensitivity factors into consideration. XPS measurements were done in a system separate from the growth chamber and the samples were exposed to the ambient gases during the transfer process. Due to this, these films had a surface layer of carbonaceous compounds. To remove these surface impurities, a 20-Å-thick layer of the film was sputtered away. The data show that the oxygen content in the films increases with increasing annealing temperature. The ratio of atomic concentrations of oxygen to iridium on the surface increases from 0.85 at 600 °C to 1.22 at 800 °C. However, this ratio is lower than 1 in the bulk of the film, indicating that thermal-oxide growth is diffusion limited. Again, this is consistent with the x-ray diffraction data which shows a (111) Ir peak indicating that not all the Ir is oxidized. The x-ray photoelectron shift in peak energy for iridium to oxygen also indicates that the iridium film surface is converted to IrO_2 after being annealed in O_2 at these temperatures.[13] Annealing the films at 900 °C in O_2 for 1 h resulted in the almost complete loss of iridium from the samples, due to the sublimation of IrO_2 at high temperature. For samples annealed at this temperature, we detect only 0.37 at. % of iridium remaining on the surface. The fact that desorption of the IrO_2 film has occurred is also evident from the detection of substrate elements (Al and La) on these samples.

The results of the XPS depth profiles are shown in Fig. 2.

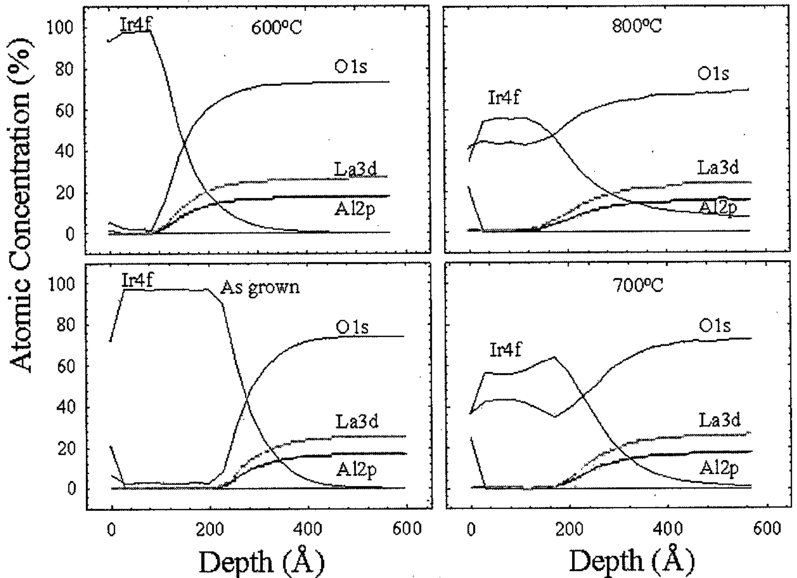

FIG. 2. XPS depth profile measurements of the atomic concentrations of iridium and oxygen in the films as a function of the annealing temperature.

For the as-deposited sample, the film exists primarily as elemental iridium with a low level of surface oxygen. We did not detect a significant amount of oxygen in the bulk of the film. Also, in the as-deposited and -annealed films, carbon was found only on the surface. The carbon and oxygen detected on the surface (about 20–30 at. %, as shown in Table I) is probably due to exposure of the samples to air during sample transport, since the XPS measurements were done *ex situ*. Once the films are annealed in O_2, we observed the formation of oxide layers. After annealing at 600 °C, the oxide layer (IrO_x) exists only near the surface region. At this temperature, we do not find evidence for bulk oxidation. At anneal temperatures of 700 and 800 °C, oxygen starts to diffuse into the bulk of the film. This is consistent with the XRD data, which indicates that there is a considerable amount of Ir below the surface-oxide layer. The amount of Ir reduces with higher temperatures as indicated by the lower intensities of the Ir(111) peak.

The thermal stability of the oxidized films was measured by temperature-programmed desorption spectroscopy. The temperature of the sample was linearly increased with time, and simultaneously the desorbed gas species were monitored with the quadrupole mass spectrometer. The two primary desorbed species have a mass-to-charge ratio of 16 and 32 and were assigned to O and O_2, respectively. During TPD measurements, these two species were monitored as a function of temperature and the desorption data are shown in Fig. 3. The decomposition of the oxide results in the spontaneous release of molecular oxygen (O_2), but not in atomic oxygen (O) form. IrO_2 films grown at 600, 700, and 800 °C temperatures have an O_2 desorption peak at 515, 690, and 665 °C, respectively. This indicates the oxides grown at 600 °C are not as stable as the oxides grown at higher temperatures. The stability and chemical composition of the oxides grown above 700 °C appear to be similar. The thermal desorption data support the XPS depth profile data shown in Fig. 2. For the iridium film annealed at 600 °C in O_2 ambient, the oxide

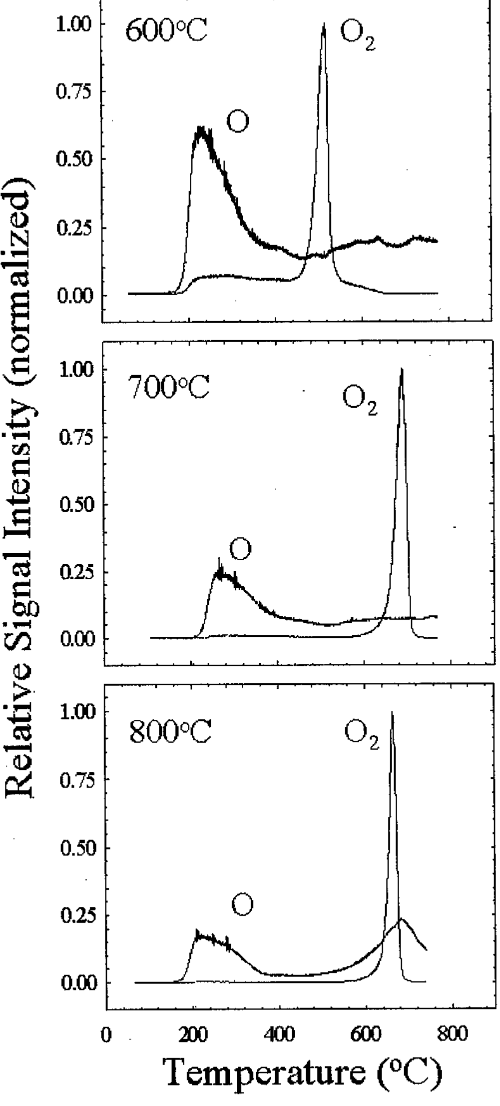

FIG. 3. Thermal decomposition of the IrO_2 films measured using temperature-programmed desorption spectroscopy. The signals are normalized to the peak value of the O_2 signal.

layer was only on the surface, with very little oxygen diffused into the bulk of the film. But, for the iridium films annealed above 700 °C, XPS depth profiles show that oxygen diffused into the bulk, indicating the bulk oxidation of Ir.

The mechanism for the iridium-oxide decomposition is not clear from the known literature. The crystal structure of IrO_2 is rutile with oxygen ions at (1/3, 1/3, 0) and (0.8, 0.2, 1/2), and iridium ions at (1/2, 1/2, 1/2) and (0, 0, 0). Accordingly, the (100) planes have only Ir ions whereas the (200) planes have one Ir and two oxygen ions, that is, a complete IrO_2 molecule. As an IrO molecule is unstable, the IrO_2 bond breakup leads to the simultaneous release of two atomic O species. These atomic oxygen species recombine immediately after desorption, thus forming O_2.

The initial release of atomic oxygen at low-temperature TPD can be explained based on existing models. One possible scenario can be explained by looking at the annealing of Pt in an oxidizing environment. Earlier studies have demonstrated that oxygen diffused through the grain boundaries of Pt and can be trapped in its grain boundaries.[16] Since Ir and Pt are very similar, one can expect to have trapped oxygen at the grain boundaries and during thermal desorption, this oxygen leaves as atomic oxygen species. The height of the atomic oxygen peak decreases by 37% as the annealing temperature is raised from 600 to 800 °C. This again points towards the continued oxidation of Ir with increasing annealing temperature.

IV. SUMMARY

In this article, we have reported direct measurements on the thermal stability of IrO_2. Based on the temperature-programmed desorption measurements, we conclude that films grown at 600 °C are only partially oxidized and completely decompose for temperatures above 515 °C. Films grown at 700 and 800 °C are more stable and decompose at temperatures between 660 and 690 °C. For films grown at these temperatures, the decomposition results in the release of O_2 from the film.

[1] A. Grill and M. J. Brady, Integr. Ferroelectr. **9**, 299 (1995).
[2] W. C. Dautremont-Smith, Displays **3**, 67 (1982).
[3] S. J. Tanghe and K. D. Wise, IEEE J. Solid-State Circuits **27**, 1819 (1992).
[4] K. G. Kreider, M. J. Tarlov, and J. P. Cline, Sens. Actuators B **28**, 167 (1995).
[5] B. Ziaie, M. D. Nardin, A. R. Coghlan, and K. Najafi, IEEE Trans. Biomed. Eng. **44**, 909 (1997).
[6] R. Frohlich, A. Rzany, J. Riedmuller, A. Bolz, and M. Schaldach, J. Mater. Sci.: Mater. Med. **7**, 393 (1996).
[7] K. Kreider, Sens. Actuators B **5**, 165 (1991).
[8] R. Sanjines, A. Aruchamy, and F. Levy, J. Electrochem. Soc. **136**, 1740 (1989).
[9] M. Peuckert, Surf. Sci. **144**, 451 (1984).
[10] *CRC Handbook of Physics and Chemistry* (CRC, Boca Raton, FL, 1999).
[11] G. L. Kellogg, Colloq. Phys. **8**, 297 (1989).
[12] A. M. Dhote, S. Madhukar, D. Young, T. Venkatesan, R. Ramesh, C. M. Cotell, and J. M. Benedetto, J. Mater. Res. **12**, 1589 (1997).
[13] B. R. Chalamala, Y. Wei, R. H. Reuss, S. Aggarwal, B. E. Gnade, R. Ramesh, J. M. Bernhard, E. D. Sosa, and D. E. Golden, Appl. Phys. Lett. **74**, 1394 (1999).
[14] B. R. Chalamala, D. Uebelhoer, and R. H. Reuss, Rev. Sci. Instrum. **41**, 320 (2000).
[15] Physical Electronics, Inc., 6509 Flying Cloud Drive, Eden Prairie, MN 55344.
[16] J. O. Olowolafe, R. E. Jones, Jr., A. C. Campbell, R. I. Hegde, C. J. Mogab, and R. B. Gregory, J. Appl. Phys. **73**, 1764 (1993).

Effects of $(Ba,Sr)TiO_3$ film thickness on electrical properties of $(Ba,Sr)TiO_3/(Ba,Sr)RuO_3$ capacitor*

Se Hoon Oh, Kyung Woong Park,[a] Jeong Hee Park, Boum Seock Kim, and Duck Kyun Choi
Department of Inorganic Materials Engineering, Hanyang University, Seoul 133-791, Korea

(Received 2 December 1999; accepted 21 April 2000)

The electrical properties of $(Ba,Sr)TiO_3/(Ba,Sr)RuO_3$ capacitors as a function of the $(Ba,Sr)TiO_3$ film thickness were investigated. It was found that the electrical properties degraded, as the thickness of the dielectric film decreased. As the thickness of the $(Ba,Sr)TiO_3$ films varied from 30 to 200 nm, the dielectric constants and T_{eq} were 122, 0.96 and 515, 1.5 nm, respectively. The corresponding leakage current densities were 2.7×10^{-5} A/cm^2 at 30 nm and 2.14×10^{-8} A/cm^2 at a 200 nm $(Ba,Sr)TiO_3$ thickness. However, after postannealing at 700 °C, the dielectric constants and T_{eq} of $(Ba,Sr)TiO_3/(Ba,Sr)RuO_3$ capacitors with a 30 nm $(Ba,Sr)TiO_3$ thickness were 230 and 0.51 in N_2 and 200 and 0.59 nm in O_2, respectively, and the leakage current levels were 1.67 $\times10^{-6}$ A/cm^2 in N_2 and 1.64×10^{-7} in O_2. Electrical properties of postannealed specimens improved when compared to those of as-deposited $(Ba,Sr)TiO_3/(Ba,Sr)RuO_3$ capacitors. The dielectric constant and leakage current density annealed in N_2 is a little bit higher than those of the film annealed in an O_2 atmosphere. These differences appear to be attributable to an increased surface roughness and grain boundary defects. Electrical properties such as the leakage current and the relative dielectric constant, are closely related to the surface morphology, in particular, the grain size and grain boundary of the films. © *2000 American Vacuum Society.*
[S0734-211X(00)03304-7]

I. INTRODUCTION

As the dynamic random access memory (DRAM) density increases, silicon dioxide and silicon oxynitride which had been used as dielectric materials for cell capacitors, can no longer be used because of the physical limitations for their structure and thickness. The use of high dielectric constant materials will become inevitable. A few materials with perovskite structures, such as $SrTiO_3$, $(Ba_{1-x}Sr_x)TiO_3$(BST), and $Pb(Zr_xTi_{1-x})O_3$(PZT) have attracted much attention as dielectric materials for charge storage capacitors because they have much higher dielectric constants than silicon dioxide or silicon oxynitride.[1–3]

Among these high dielectric constant oxides, the application of $(Ba,Sr)TiO_3$ to DRAM cell capacitors is an attractive choice, because it has a high dielectric constant, relatively low leakage current and low dielectric loss, properties that can drastically simplify the memory cell capacitor structure.

However, $(Ba,Sr)TiO_3$ has many problems for DRAM application. First, the leakage current of BST thin films is much higher than that found in silicon dioxide and silicon oxynitride; thus BST films must have at least 20–40 nm thickness to obtain the adequate leakage current level. However, it is difficult to squeeze components more than 50 nm thick into post-Gbit DRAM structures.[4] Second, the dielectric constant of BST thin film abruptly decreases as the film thickness decreases.[5] Therefore, it is necessary to investigate variations in the dielectric properties as they are affected by the dielectric film thickness.

Also, when using this material as a dielectric, it is necessary to match in with electrode materials that have certain properties (high metallic conductivity, sufficient resistance against oxidation, good adhesion to BST and interfacial smoothness) to achieve large capacitance and low leakage current density. Recently, some conducting perovskite oxides, such as $SrRuO_3$, $BaRuO_3$, and $(Ca_xSr_{1-x})RuO_3$, which can satisfy such requirements, have been studied as electrodes for BST thin films.[6–8] Because they have the same perovskite structures as a BST thin film, better lattice matching can be expected between BST and the electrodes, which may eliminate interfacial defects and additional electronic states at the interface and may reduce the leakage current and/or dielectric degradation.

The electrical properties of BST thin film were evaluated when deposited on a $(Ba,Sr)RuO_3$(BSR) perovskite electrode in a previous article.[9] In this study, we investigated the variation of electrical properties and causes of electrical properties degradation on BST thickness reduction by introducing a BSR electrode to a chemically and structurally similar BST.

II. EXPERIMENTAL PROCEDURE

BSR thin film was deposited from a cold pressed BSR (Ba/Sr=5/5) target on to a *p*-type (100) Si substrate by a radio-frequency (rf)-magnetron sputtering system. BST thin films with various thicknesses were deposited on BSR (200nm)/Si using a sintered BST target with (Ba+Sr)/Ru =1.025 composition by adding excess BaO and SrO. Detailed deposition conditions are summarized in Table I. Metal–insulator–metal(MIM) structure was performed to

*No proof corrections received from author prior to publication.
[a]Electronic mail: parkkw@hymail.hanyang.ac.kr

TABLE I. Experimental deposition conditions of BST dielectric layer and BSR bottom electrode.

	(Ba,Sr)RuO_3	(Ba,Sr)TiO_3
Sub. temp. (°C)	600	
O_2/Ar ratio	1/9	
Target	3 inch cold-pressed BSR (Ba/Sr=5/5)	3 inch sintered BST [(Ba+Sr)/Ru=1.025]
Work. press. (mTorr)	10	
Base press. (Torr)	2×10^{-7}	
rf power (W)	70	
Thickness (nm)	200	30, 50, 70, 90, 110, 150, 200

evaluate the electrical properties of BST/BSR by using an Al dot top electrode. Crystallinity and crystallographic phases of thin films were measured by standard x-ray diffraction (XRD) ($2\theta=20°-60°$, $\theta=1°$ fixed). The thickness of each film was measured by α step and was cross-checked by a scanning electron microscope (SEM). Surface morphologies were observed by an atomic force microscope (AFM). Auger electron depth profile analysis was performed to investigate the variation of interface layer as BST thickness was reduced. BST/BSR capacitors with 30 nm BST thickness were annealed for 30 min in flowing N_2 and O_2 at 700 °C to investigate the correlation of surface morphology and electrical properties. Capacitance and leakage current were evaluated by an HP 4280A 1 MHz Cmeter/CV plotter and an HP 4155B semiconductor parameter analyzer, respectively.

III. RESULTS AND DISCUSSION

Figure 1 shows XRD spectra for BST thin films with various film thicknesses deposited on BSR substrate at 600 °C. The (110) preferred orientation was observed in the XRD spectra for all the BST thin films irrespective of the film thickness.

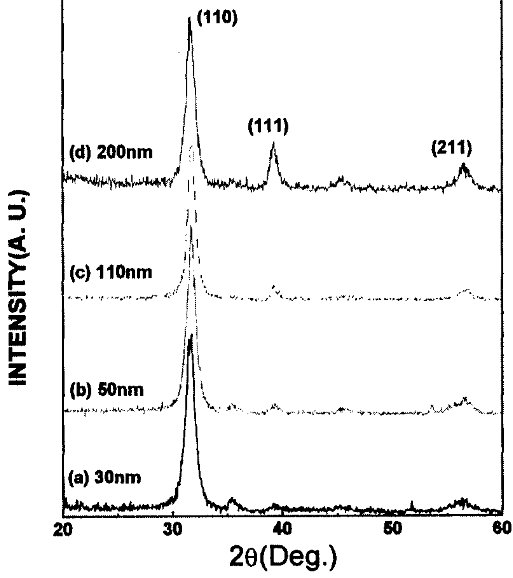

FIG. 1. XRD patterns of BST films as thickness is reduced.

It is interesting to mote that the peak intensities of (111), (211) increased with the increasing BST layer thickness. It is assumed that very thin BST films grow to strongly follow the (110) preferred orientation of BSR thin films, but, as the thickness of the BST thin films increases, crystalline properties of the BST film layer resemble those of bulk BST. This would explain the increasing peak intensities of (111), (211) in BST film with 200 nm thickness. However, no significant change in the intensity and orientation of the diffraction profiles was present as the BST film thickness was varied.

The surface morphology dependence of BST on the film thickness is shown in Fig. 2. As the film thickness decreases, the grain size of the BST thin films decreases markedly. It is generally accepted that the grain size of BST thin films deposited by rf magnetron sputtering decreases as the film thickness decreases.[10] It is observed in Fig. 2 that a BST film of 30 nm thickness is consists of very small grains (less than 50 nm thick). If the grain size of the BST thin films is large, the dielectric constant may be similar to that of the bulk BST. Also, as the grain size decreases, the proportion of grain boundaries in the film which act as leakage current paths increases. Therefore, the small grain size in the 30-nm-thick film may result in a higher leakage current density and a lower dielectric constant than that found in of other thicker films.

Relative dielectric constants of the BST thin films deposited at 600 °C were measured as a function of the film thickness. The results of this are shown in Fig. 3. Relative dielectric constant decreases with varying thickness from 520 at 200 nm to 122 at 30 nm. It is reported that a similar decreasing trend of the relative dielectric constant occurs with decreasing film thickness for BST films.[11]

This dielectric constant degradation can be explained in terms of the decrease in grain size with decreasing film thickness. It is believed that the larger the grain size is, the more the dielectric characteristics approach to those of bulk BST, and the smaller the portion of the BST film is that is occupied by the grain boundaries.

Figure 4 shows variation of the equivalent SiO_2 thickness of the BST film, t_{eq}, with various thicknesses of films. For practical device applications, t_{eq} represents the potential of the dielectrics to store electrical charges, since it includes the terms of relative dielectric constant and the film thickness. It is observed that t_{eq} does not decrease to below about 0.9 nm

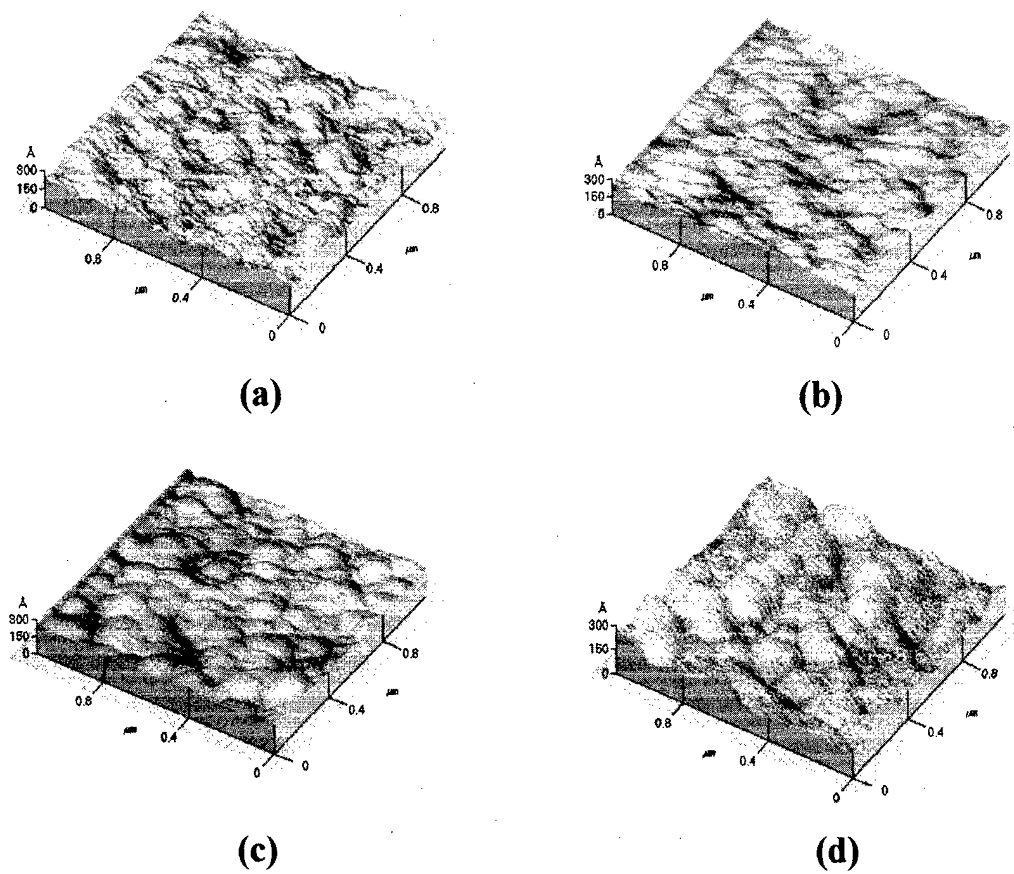

FIG. 2. AFM images of BST thin films with various thicknesses. (a) 30, (b) 50, (c) 110, and (d) 200 nm BST/BSR capacitors.

even with the BST film of thickness smaller than 50 nm, because of the abruptly decreasing relative dielectric constant. Furthermore, BST films with a thickness less than 50 nm are not practically useful because of their high leakage current level (see Fig. 5).

Figure 5 shows variation of the leakage current at +1.5 V as a function of the BST film thickness in the thickness range from 30 to 200 nm. Leakage current density shows a constant value of about 10^{-7} A/cm^2 irrespective of the film thickness down to about 50 nm and then increases abruptly with a further decrease in thickness. The leakage current level of the 30-nm-thick BST films is about 2.7×10^{-3} A/cm^2.

The Auger electron spectroscopy (AES) depth profile of the 30- and 50-nm-thick BST film analysis is not shown here. But since it can be observed that there is no significant difference of AES depth profiles, we can infer that the states of the interfaces of 30- and 50-nm-thick BST films is similar.

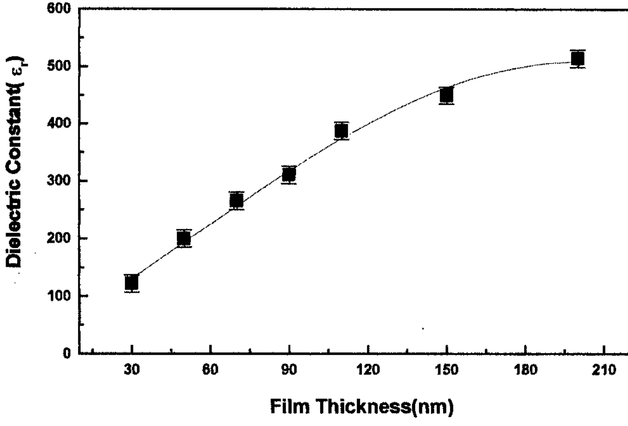

FIG. 3. Dielectric constants of BSR/BSR thin films with various BST film thicknesses.

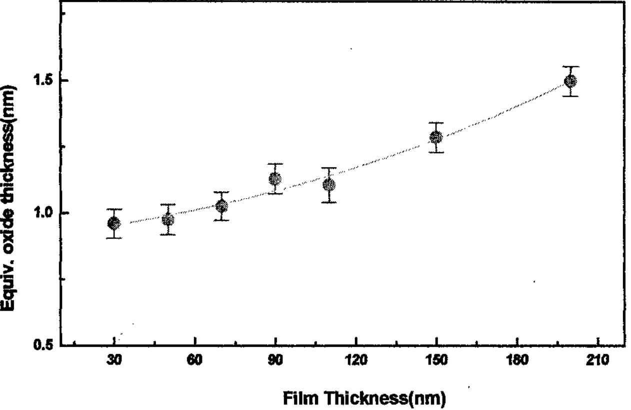

FIG. 4. Variation of T_{eq} in BST/BSR capacitors with varied BST film thicknesses.

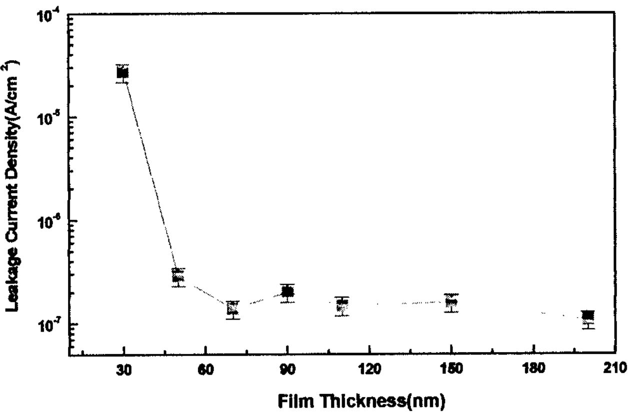

FIG. 5. Leakage current properties of BST/BSR system as affected by BST film thickness.

Therefore, the high leakage currents of the 30-nm-thick films may be correlated with the grain boundaries. The increased proportion of grain boundaries in 30-nm-thick BST film is thought to be the main cause of an abrupt increase in the leakage current. It is reported that grain boundary conduction plays one of the major roles in the leakage current characteristics.[12]

To facilitate investigation of the surface morphology variation, which may be the cause of electrical property degradation in 30-nm-thick BST film, postannealing of the 30-nm-thick BST layer was carried out in N_2 and O_2 atmosphere at 700 °C for 30 min.

The surface morphologies of 30 nm BST layers are shown with postannealing conditions in Fig. 6. It is observed that BST thin films annealed in N_2 and O_2 have relatively larger grain size than as-deposited film, with no difference of grain sizes irrespective of the postannealing atmospheres. However, BST thin films annealed in N_2 atmosphere has a rougher surface than O_2 annealed films.

Variation of the relative dielectric constant and T_{eq} of the BST thin films with postannealing conditions was represented in Fig. 7. The relative dielectric constant of capacitors after annealing in N_2 and O_2 at 700 °C showed an improvement as compared with that of an as-deposited sample. The maximum ϵ_r was 230 in N_2 and 210 in O_2 annealed samples, respectively. The dielectric constant of the film annealed in N_2 atmosphere is a little bit higher than that of the film annealed in an O_2 atmosphere. This difference in the dielectric constant appears to be attributable to an increase in the effective surface area in N_2 annealed BST thin film due to increasing the surface roughness.

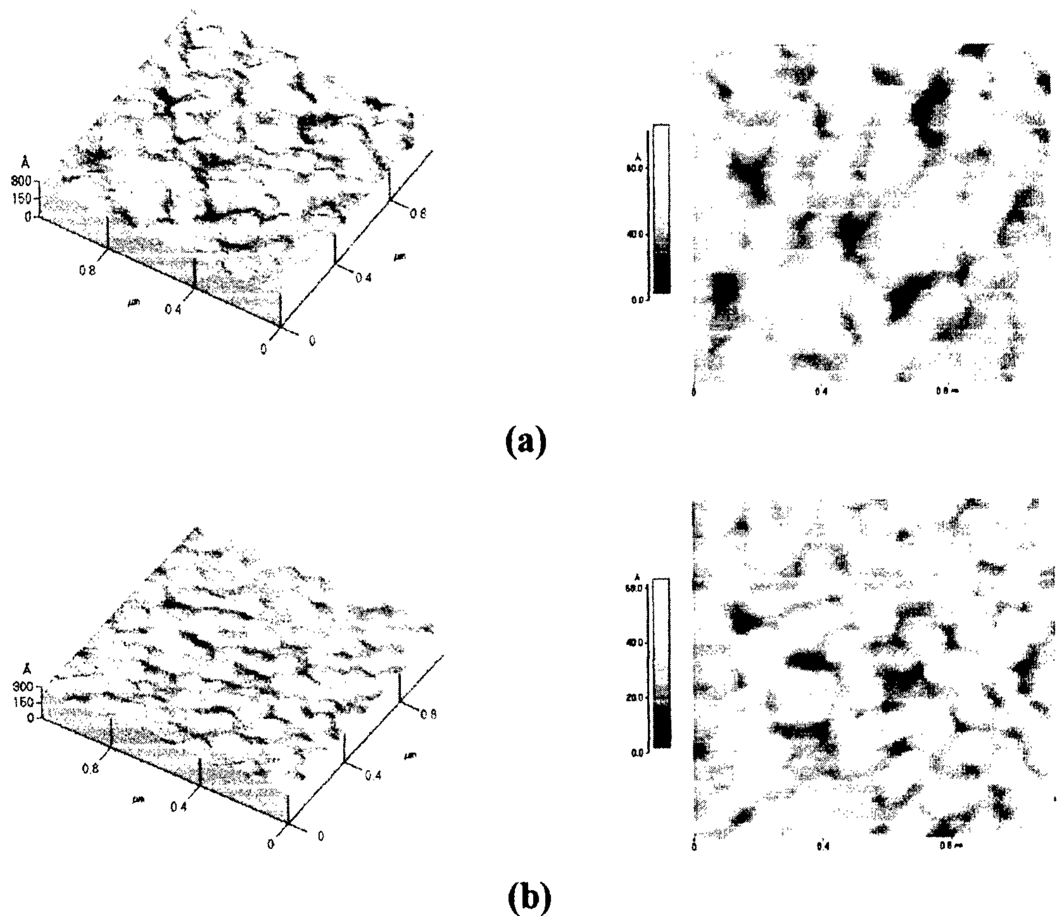

FIG. 6. AFM images of BST/BSR thin films with annealing conditions. (a) N_2 700 °C 30 min, (b) O_2 700 °C 30 min postannealing.

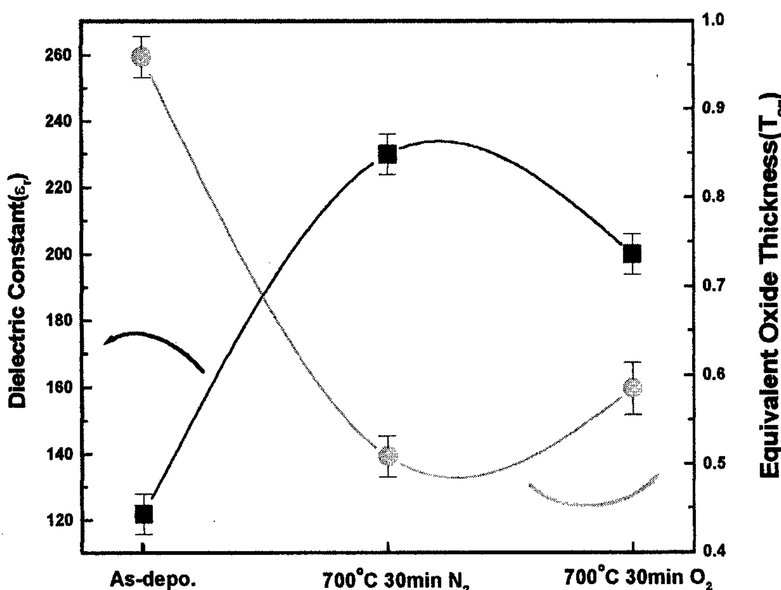

FIG. 7. Dielectric constant and T_{eq} variation of BST (300 Å) thin films with varied annealing conditions.

The leakage current characteristics of the capacitors prepared by N_2 and O_2 flow annealing is also shown in Fig. 8. The BST thin film with N_2 and O_2 annealing at 700 °C had a lower leakage current (2.7×10^{-5} A/cm^2) than that of as-deposited BST thin films. The leakage current level was 1.67×10^{-6} A/cm^2 in N_2 and 1.64×10^{-7} A/cm^2 in O_2 at 1.5 V, respectively.

The capacitors with oxygen flow annealing had leakage current about one order of magnitude lower than that of BST thin film with nitrogen annealing. In this study, the difference in the leakage current could be explained by the variation of the surface morphology and grain boundary defect, which was attributed to the different annealing conditions.

Because of oxygen vacancies in BST films, BST is usually considered an n-type semiconductor.[13] The larger leakage current in the capacitors annealed at 700 °C in N_2 may have been due to the segregation or generation of defects,

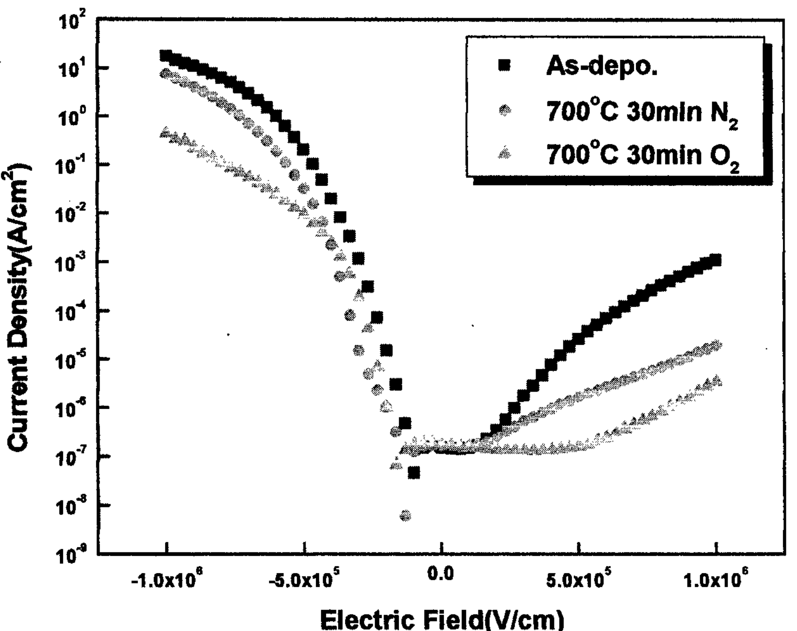

FIG. 8. Leakage current properties of BST (300 Å)/BSR system with various annealing conditions.

such as oxygen vacancies. The grain boundary tends to result in impurities or crystal defects that are energetically unflavored in the bulk of grain.[14] This high-density defect segregation may induce conduction paths at the grain boundary of the BST.[15] Thus, the as-deposited crystalline films may have large O_2 vacancies during the deposition at a high substrate temperature compared to postannealed films. Oxygen vacancy transport along the grain boundary may increase the conductivity of the as-deposited crystalline films. However, in the case of BST thin film with postannealing in O_2 ambient, we observe an improved leakage current property and reduced oxygen vacancy density.

Additional investigation is needed for further quantitative evaluation of postannealing effects in a BST/BSR system.

IV. CONCLUSIONS

BST thin films ranging from 30 to 200 nm thickness were deposited on perovskite BSR thin films by the rf magnetron sputtering method. Electrical properties, such as leakage current and the dielectric constant, are degraded with decreasing dielectric layer thickness due to a reduction of grain sizes. The relative dielectric constant decreases as the thickness is reduced, from 515 at 200 nm to 122 at 30 nm. Leakage current density shows a constant value of about 10^{-7} A/cm^2 irrespective of the film thickness down to about 50 nm. But, the leakage current level of the 30-nm-thick BST films is about 2.7×10^{-5} A/cm^2.

BST thin films annealed in N_2 and O_2 have relatively larger grain size than as-deposited film. However, BST thin films annealed in N_2 atmosphere have a rougher surface than O_2 annealed films. The maximum ϵ_r was 230 in N_2 and 210 in O_2 annealed samples, respectively. The leakage current level was 1.67×10^{-6} A/cm^2 in N_2 and 1.64×10^{-7} A/cm^2 in O_2 at 1.5 V, respectively. It is thought that such a difference with postannealing conditions in the leakage current and dielectric constant is due to the variation of the surface morphology and grain boundary defects which was attributed to the different annealing conditions. As a consequence, the thinner the dielectric film is, the more the electrical properties are influenced by grain size and grain boundary. Improved electrical properties can be expected if very thin dielectric layer have a large grain size.

[1]K. Abe and S. Komatsu, Jpn. J. Appl. Phys., Part 1 **31**, 2985 (1992).
[2]H. Kawano, K. Morii, and Y. Nakayama, J. Appl. Phys. **73**, 5141 (1993).
[3]Y. S. Hwang, S. H. Paek, and J. P. Mah, J. Mater. Sci. Lett. **15**, 1030 (1996).
[4]C. S. Hwang, S. O. Park, C. S. Kang, H. J. Cho, H. K. Kang, S. T. Ahn, and M. Y. Lee, Jpn. J. Appl. Phys., Part 1 **34**, 5198 (1995).
[5]K. Koyama, T. Sakuma, S. Yamamichi, H. Watanabe, H. Aoki, S. Ohya, Y. Miyasaka, and T. Kikkawa, *Proceeding of the International Electron Device Meeting* (IEEE, New York, 1991), p. 823.
[6]M. Izuha, K. Abe, and N. Fukushima, Jpn. J. Appl. Phys., Part 1 **36**, 5866 (1997).
[7]C. Ming Chu and P. Lin, Appl. Phys. Lett. **72**, 1241 (1998).
[8]S. Young Son, B. Seock Kim, and D. Kyun Choi, J. Korean Phys. Soc. **32**, S1517 (1998).
[9]D. Kyun Choi, B. Seock Kim, S. Young Son, S. Hoon Oh, and K. Woong Park, J. Appl. Phys. **86**, 3347 (1999).
[10]S. S. Lee and H. G. Kim, Integr. Ferroelectr. **11**, 137 (1995).
[11]S. Oh Park, C. Seong Hwang, H. Ju Cho, C. Suk Kang, H. Kyu Kang, S. In Lee, and M. Yong Lee, Jpn. J. Appl. Phys., Part 1 **35**, 1548 (1996).
[12]S. H. Paek, J. Won, K. S. Lee, J. S. Choi, and C. S. Park, Jpn. J. Appl. Phys., Part 1 **35**, 5757 (1996).
[13]C. S. Hwang, B. T. Lee, S. O. Park, J. W. Kim, H. J. Cho, C. S. Kang, H. Horii, S. I. Lee, and M. Y. Lee, Integr. Ferroelectr. **13**, 157 (1996).
[14]H. Hu and S. B. Krupanidhi, J. Mater. Res. **9**, 1484 (1994).
[15]R. Hagenbeck and R. Waser, J. Appl. Phys. **83**, 2083 (1998).

Effects of composition and N_2 plasma treatment on the barrier effectiveness of chemically vapor deposited WSi_x films

M. T. Wang[a] and M. H. Chuang
Department of Electronics Engineering, National Chiao-Tung University, Hsinchu, Taiwan

L. J. Chen
Department of Submicron Technology Development, ERSO/ITRI, Hsinchu, Taiwan

M. C. Chen
Department of Electronics Engineering, National Chiao-Tung University, Hsinchu, Taiwan

(Received 1 May 1998; accepted 21 April 2000)

This work investigates the thermal stability of chemically vapor deposited amorphous WSi_x layers used as a diffusion barrier between Cu and Si substrate, in which the WSi_x layers were deposited to a thickness of about 50 nm using the SiH_4 reduction of WF_6 at various SiH_4/WF_6 flow ratios. For 30 min annealing in nitrogen ambient, the effectiveness of the WSi_x layers as barriers between a copper overlayer and a p^+-n junction diode decreases as the Si/W atomic ratio, x, increasing from 1 to 1.3. This composition change is obtained by raising the SiH_4/WF_6 flow ratio from 3 to 50. As deposited, all films are x-ray amorphous. Their resistivity increases roughly linearly with x. The barrier capability of WSi_x layers can be significantly improved by an *in situ* N_2 plasma treatment. The N_2 plasma treatment produces a very thin layer of WSiN (about 5 nm) on the surfaces of WSi_x layers. In particular, the Cu/WSiN/WSi_x/p^+-n junction diodes with the WSi_x layers deposited with a SiH_4/WF_6 flow ratio of 3 were able to remain intact up to at least 600 °C. © *2000 American Vacuum Society.* [S0734-211X(00)03204-2]

I. INTRODUCTION

Copper (Cu) has been extensively studied as a potential metallization material for future ultralarge scale integrated circuits because of its low electrical resistivity, superior electromigration resistance,[1–3] and possibility of deposition by electroplating as well as the chemical vapor deposition (CVD) method.[4–6] Moreover, copper has a better thermal conductivity, higher melting point, and less potential of hillocks' formation than the conventionally used Al alloys.[7] However, Cu metallization is faced with many challenges in practice, such as the lack of a stable self-passivated oxide, poor adhesion to dielectric layers, difficulty of dry etching, and the formation of Cu–Si compounds at low temperatures (about 200 °C).[8] In addition, copper diffuses fast in silicon and causes deep-level trapping;[9] it also drifts through oxide layers under accelerated electric field.[10,11] Therefore, a diffusion barrier between Cu and its underlying layers is considered as a prerequisite for practical applications of Cu metallization.

Various materials have been studied as diffusion barriers between Cu and its underlying layers. Sputter deposited nitride-based diffusion barriers, such as TiN,[12,13] WN,[14,15] TaN,[16–18] MoN,[19,20] and TiWN,[21,22] have attracted extensive attention for a long time. However, these barriers are generally polycrystalline, and grain boundaries in the barriers provide fast paths for Cu diffusion. Typically, the atomic diffusivities in the amorphous phase are orders of magnitude below those of the corresponding polycrystalline phase.[23,24] Thus, the amorphous diffusion barrier is of great interest. In this work, we used chemically vapor deposited amorphous WSi_x (CVD–WSi_x) layers as a diffusion barrier between Cu and Si substrate. The effects of composition on the barrier capability of the amorphous CVD–WSi_x layers were studied using electrical measurements as well as material analyses. We found that the barrier effectiveness depended on the composition of the amorphous WSi_x layers. To improve the barrier capability of the WSi_x layers, we formed a very thin WSiN layer on the surfaces of WSi_x layers using an *in situ* N_2 plasma treatment. The resultant WSiN/WSi_x barrier bilayer was proven to possess a much improved barrier capability against Cu diffusion.

II. EXPERIMENT

The thermal stability of barrier layers was evaluated by measuring the leakage current of thermally annealed Cu/barrier/p^+-n junction diodes. The starting materials used for the diodes fabrication were n-type, (100) oriented silicon wafers with 4–7 Ω cm nominal resistivity. After Radio Corporation of America standard cleaning, the wafers were thermally oxidized to grow a 500 nm oxide layer. Diffusion regions with area sizes of 500×500 and 1000 ×1000 μm^2 were defined on the oxide covered wafers using the conventional photolithographic technique. The p^+-n junctions with a junction depth of about 0.3 μm were formed by BF_2^+ implantation at 40 keV to a dose of $3\times10^{15}\,cm^{-2}$ followed by furnace annealing at 900 °C for 30 min in N_2 ambient.

After the junctions were formed, the wafers were divided into three groups for the preparation of the following devices: Cu/p^+-n, Cu/WSi_x/p^+-n, and Cu/WSiN/WSi_x/

[a]Electronic mail: mcchen@cc.nctu.edu.tw

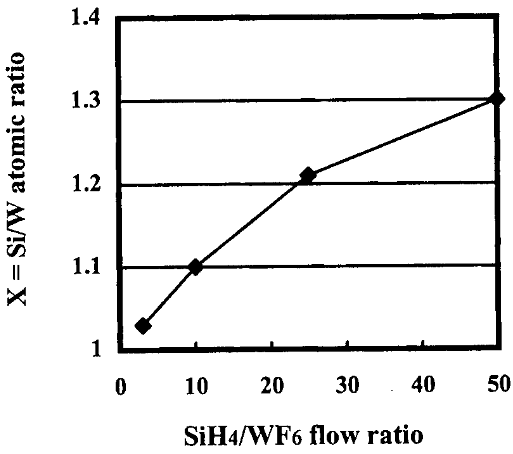

FIG. 1. Si/W atomic ratio, x, of WSi_x films deposited at various SiH_4/WF_6 flow ratios. The films were deposited at a temperature of 250 °C, total gas pressure of 12 mTorr, and WF_6 flow rate of 2 sccm.

p^+-n junction diodes, in which the WSi_x layers were deposited by the CVD method to a thickness of about 50 nm using the SiH_4 reduction of WF_6 at various SiH_4/WF_6 flow rates. In this study, the WSi_x layers were deposited using a load-locked cold wall CVD system with the following deposition conditions: substrate temperature 250 °C, total gas pressure 12 mTorr, WF_6 flow rate 2 sccm, and SiH_4 flow rate ranging from 6 to 100 sccm. For the formation of $WSiN/WSi_x$ barrier bilayers, an *in situ* N_2 plasma treatment was performed on the surfaces of CVD–WSi_x layers without breaking the vacuum. The N_2 plasma treatment was performed with the following conditions: N_2 flow rate 80 sccm, total gas pressure 25 mTorr, plasma power 100 W, and treatment time 300 s. Finally, Cu metallization was applied to all samples.

To investigate the thermal stability of the variously metallized junction diodes, the samples were thermally annealed in N_2 flowing furnace for 30 min at a temperature ranging from 200 to 700 °C. Reverse bias leakage current measurements on the thermally annealed diodes were used to evaluate the barrier capability. An HP-4145B semiconductor parameters analyzer was used for the measurement, and at least 30 diodes were measured in each case. Unpatterned samples of WSi_x/Si, $Cu/WSi_x/Si$, and $Cu/WSiN/WSi_x/Si$ multilayer structures were also prepared for material analysis. Sheet resistance of the multilayer structures was measured using a four point probe. Auger electron spectroscopy (AES) was used to determine the composition of WSi_x films. Rutherford backscattering spectroscopy (RBS) was used to determine the Si/W atomic ratio. Scanning electron microscopy (SEM) was employed to observe the surface morphology and microstructure. X-ray diffraction (XRD) analysis was used for phase identification.

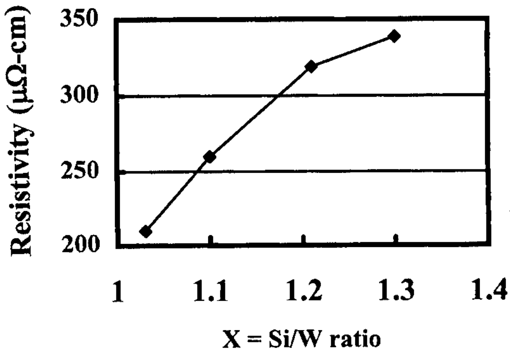

FIG. 2. Resistivity of WSi_x films vs x. The WSi_x films were deposited at a substrate temperature of 250 °C, total gas pressure of 12 mTorr, and WF_6 flow rate of 2 sccm.

III. RESULTS AND DISCUSSION

A. Properties of CVD–WSi_x films

Before investigating the thermal stability of $Cu/WSi_x/p^+-n$ junction diodes, properties of CVD–WSi_x films, including the Si/W atomic ratio, electrical resistivity,

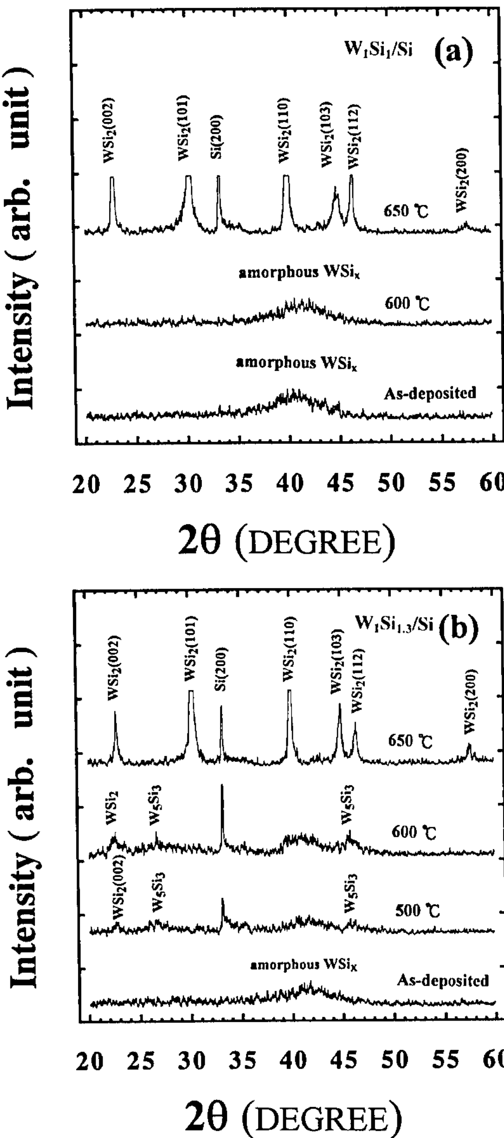

FIG. 3. XRD spectra of (a) W_1Si_1/Si and (b) $W_1Si_{1.3}/Si$ samples before and after annealing at various temperatures. The W_1Si_1 and $W_1Si_{1.3}$ layers are 150 nm thick.

TABLE I. Crystalline phases of CVD–WSi_x films after annealing for 30 min in N_2 ambient at various temperatures.

Annealing temperatures	Si/W atomic ratio x		
	1.0	1.1	1.3
As-deposited	Amorphous	Amorphous	Amorphous
400 °C	Amorphous	Amorphous	Amorphous
500 °C	Amorphous	Amorphous	Weak WSi_2, weak W_5Si_3
600 °C	Amorphous	Weak WSi_2, weak W_5Si_3	Weak WSi_2, weak W_5Si_3
650 °C	WSi_2	WSi_2	WSi_2
800 °C	WSi_2	WSi_2	WSi_2

and crystalline phase were investigated. Figure 1 shows the Si/W atomic ratio of WSi_x layers deposited with various SiH_4/WF_6 flow ratios, as determined by RBS measurements. We found that the Si/W atomic ratio, x, in the WSi_x layer increased from 1.0 to 1.3 as the SiH_4/WF_6 flow ratio was increased from 3 to 50. The resistivity of the WSi_x films also increased with increasing SiH_4/WF_6 flow ratio, as shown in Fig. 2; it increased from 210 to 340 $\mu\Omega$ cm as the SiH_4/WF_6 flow ratio was increased from 3 to 50. The increase in resistivity is presumably due to increasing amount of Si incorporated in the WSi_x layer. Similar results were reported by Kottke *et al.* that higher flow ratios of SiH_4/WF_6 resulted in WSi_x films of higher resistivities and Si/W atomic ratios, although the WSi_x films in their study were deposited at a substrate temperature of 360 °C and a SiH_4/WF_6 flow ratio of 94 to 438, and the resultant WSi_x layers were nonstoichiometric silicon-rich (Si/W atomic ratios larger than 2.0).[25]

The phase of the WSi_x layers was identified by XRD analysis using a 30 keV copper-$K\alpha$ radiation. Figures 3(a) and 3(b) show XRD spectra for the 150-nm-thick films with $x=1$ and 1.3 on silicon substrates before and after annealing at various temperatures. For $x=1$, the as-deposited films were amorphous and the amorphous state remained unchanged even after annealing at 600 °C for 30 min in N_2 ambient [Fig. 3(a)]. It has been reported that the absence of grain boundaries in the amorphous barrier layer contributes to the excellent barrier property, because fast diffusion paths of the grain boundaries are prevented.[26] In this work, the nature of amorphous phase makes the W_1Si_1 layers very attractive in barrier application. Diffraction peaks of WSi_2 phase appeared in the W_1Si_1 samples after annealing at 650 °C for 30 min in N_2 ambient [Fig. 3(a)], indicating silicidation of the layer.

For the $W_1Si_{1.3}$/Si samples, the as-deposited films were also amorphous [Fig. 3(b)]. Weak peaks of tungsten silicides were detected after annealing at 500 °C, and the diffraction peaks slightly intensified after annealing at 600 °C, indicating the grain growth of tungsten silicides. Similar results were reported that Si-rich ($x>2.0$) CVD films converted to tungsten silicides after annealing at 500 °C.[27–29] We found that the crystallization temperature of amorphous CVD–WSi_x layers decreased with increasing Si/W atomic ratio x. Table I summarizes the crystalline states of different CVD–WSi_x films after annealing at various temperatures, as determined by XRD analysis.

B. Composition effects on the barrier capability of CVD–WSi_x films

1. Electrical measurements

Figure 4 illustrates the statistical distributions of reverse bias current density measured at −5 V for the Cu/p^+–n, Cu/W_1Si_1/p^+–n, and Cu/$W_1Si_{1.3}$/p^+–n junction diodes annealed at various temperatures; both layers of W_1Si_1 and $W_1Si_{1.3}$ were 50 nm thick. Since copper reacts with Si at low temperatures (200 °C),[9,10] diodes without a barrier layer between Cu and Si substrate failed after annealing at 200 °C for 30 min [Fig. 4(a)]. With a 50-nm-thick WSi_x barrier layer between Cu and Si substrate, the junction diodes of Cu/W_1Si_1/p^+–n and Cu/$W_1Si_{1.3}$/p^+–n were able to retain their electrical integrity up to 500 and 450 °C, respectively [Figs. 4(b) and 4(c)]. The barrier capability of amorphous WSi_x layers decreased with increasing Si/W atomic ratio, and the decrease in thermal stability of the Cu/$W_1Si_{1.3}$/p^+–n junction diodes correlated with the lower crystallization temperature of the amorphous $W_1Si_{1.3}$ layers.

2. XRD analyses

The drastic increase in sheet resistance of the Cu/WSi_x/Si samples was attributed to the formation of high resistivity η''-Cu_3Si precipitates, as confirmed by XRD analyses shown in Fig. 5. The XRD spectra of as-deposited samples did not reveal the broadband of amorphous WSi_x layers presumably because the WSi_x layers were only 50 nm thick and were covered with 300-nm-thick Cu overlayers. Strong diffraction peaks of Cu_3Si appeared in the XRD spectra of Cu/W_1Si_1/Si and Cu/$W_1Si_{1.3}$/Si samples annealed at 600 and 500 °C, respectively. It is clear that the stability of the WSi_x layers in contact with Cu decreases with increasing Si/W atomic ratio. Furthermore, by comparing the XRD spectra of Cu/W_1Si_1/Si samples [Fig. 5(a)] with those of W_1Si_1/Si samples [Fig. 3(a)], we found that the crystallization temperature of WSi_x layers in the Cu/W_1Si_1/Si samples is about 50 °C lower than that in the W_1Si_1/Si samples. This discrepancy is presumably due to the presence of Cu overlayers for the Cu/W_1Si_1/Si samples. It was reported that the crystallization temperature of $W_{80}Si_{20}$ film on SiO_2 dropped from 800 to 650 °C when the $W_{80}Si_{20}$ film was in contact with a polycrystalline copper layer.[30] It was also reported that the formation temperature of tantalum (Ta) silicide in Ta/Si system dropped from 700 to 650 °C when the Ta film was in contact with a polycrystal-

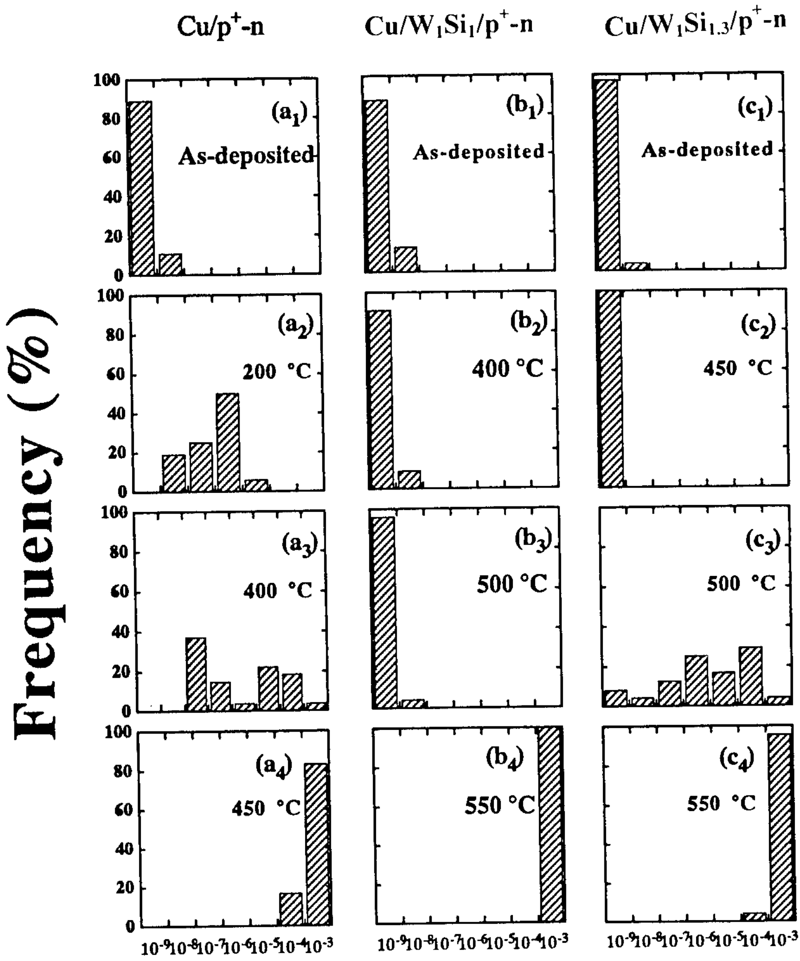

FIG. 4. Histograms showing statistical distributions of reverse bias current density for (a) Cu/p^+-n, (b) $Cu/W_1Si_1/p^+-n$, and (c) $Cu/W_1Si_{1.3}/p^+-n$ junction diodes annealed at various temperatures. The WSi_x layers are 50 nm thick.

line copper layer.[31] In this work, the W_1Si_1/Si samples remained stable up to 600 °C with no detection of tungsten silicide formation [Fig. 3(a)], while diffraction peaks of tungsten silicide phases were detected for the Cu/W_1Si_1/Si samples annealed at the same temperature [Fig. 5(a)]. This suggests that the accelerated crystallization for W_1Si_1 layers was related to the contact with polycrystalline Cu overlayers. The accelerated crystallization is presumably due to the penetration of Cu atoms through W_1Si_1 layers via localized defects, forming Cu_3Si phase and promoting silicidation at the W_1Si_1/Si interface.[31] Table II summarizes the silicides formed on thermally annealed Cu/Si and Cu/WSi_x/Si samples.

3. SEM observations

SEM was used to investigate the surface and cross-sectional morphology of thermally annealed Cu/barrier/p^+-n junction diodes. Figure 6 shows SEM micrographs for the as-deposited as well as 500 °C annealed $Cu/W_1Si_1/p^+-n$ and $Cu/W_1Si_{1.3}/p^+-n$ junction diodes. The barrier structure remained unchanged for the $Cu/W_1Si_1/p^+-n$ diodes after annealing at 500 °C [Fig. 6(b)]; however, large localized Cu_3Si protrusions were observed on the $Cu/W_1Si_{1.3}/p^+-n$ diodes after annealing at the same temperature [Fig. 6(d)]. Failure of the 500 °C annealed $Cu/W_1Si_{1.3}/p^+-n$ diodes is likely associated with these localized Cu_3Si protrusions, which were presumably caused by the diffusion of Cu atoms through the weak points (such as vacancy-accumulated voids and grain boundaries of crystallized $W_1Si_{1.3}$ layers) in the $W_1Si_{1.3}$ barrier layers.

Based on the earlier results, we concluded that the higher the Si/W atomic ratio in WSi_x films is, the lower the crystallization temperature of the WSi_x films becomes (Fig. 3). Accordingly, WSi_x films of higher Si content are not suitable for diffusion barrier application. Moreover, failure of WSi_x barrier layer in the Cu/WSi_x/Si structure was closely related to the presence of Cu_3Si phase, indicating that the barrier failure was due to the interdiffusion of Cu and Si through the WSi_x barrier at elevated temperatures. This suggests that the thermal stability of $Cu/WSi_x/p^+-n$ diodes can be improved if the barrier structure of WSi_x can be modified so as to suppress or retard the interdiffusion of Cu and Si.

C. Effects of N_2 plasma treatment

It was reported that a very thin (4 nm) layer of WSiN formed on the surface of WSi_x by electron cyclotron reso-

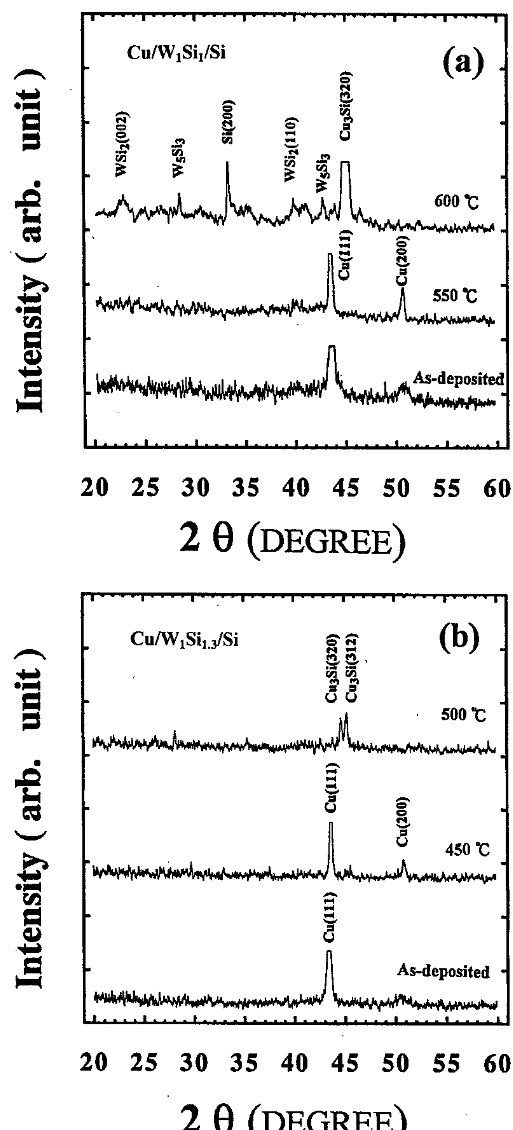

FIG. 5. XRD spectra of (a) $Cu/W_1Si_1/Si$ and (b) $Cu/W_1Si_{1.3}/Si$ samples annealed at various temperatures. The WSi_x layers are 50 nm thick.

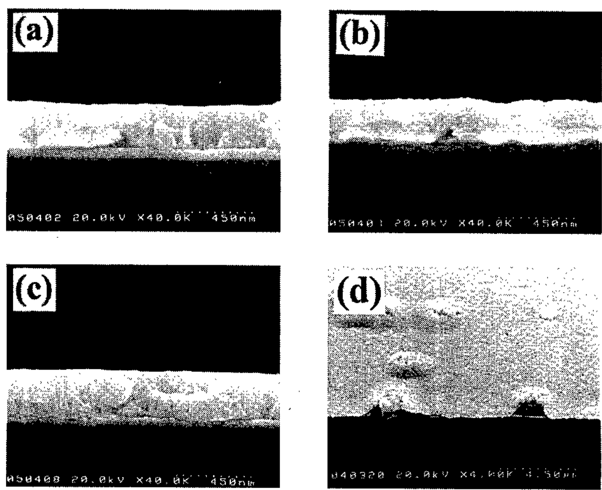

FIG. 6. Cross-sectional view SEM micrographs of $Cu/W_1Si_1/p^+-n$ diodes (a) as-deposited sample and (b) 500 °C annealed sample; SEM micrographs of $Cu/W_1Si_{1.3}/p^+-n$ diodes; (c) cross-sectional view of as-deposited sample; and (d) oblique view of 500 °C annealed sample.

nance N_2 plasma nitridation was able to function as an excellent barrier to dopant diffusion.[32] It was also reported that a WN_x layer about 2 nm thick was formed on the chemically vapor deposited tungsten (CVD–W) surface using a capacitively coupled plasma nitridation, and that the WN_x layer effectively suppressed the increase in resistance of thermally annealed Al/CVD–W/Si interconnects.[33] In addition, we found in a previous study that the barrier effectiveness of a 450-nm-thick selective CVD–W film in the structure of Al/CVD–W/Si can be significantly improved by exposing the W film in an *in situ* N_2 plasma prior to the Al metallization.[34,35] In this study, we insert a very thin WSiN layer between Cu and WSi_x layers to make a structure of $Cu/WSiN/WSi_x/p^+-n$ junction diodes so as to suppress the undesirable interdiffusion between Cu and Si, and thus improve the thermal stability of the junction diodes. The very thin WSiN layer (shown latter in Fig. 8) was formed via an *in situ* N_2 plasma treatment on the surfaces of WSi_x layers.

TABLE II. Silicides formed on Cu/Si and $Cu/WSi_x/Si$ samples.

Annealing temperatures (°C)	Layered structure		
	Cu/Si	$Cu/W_1Si_1/Si$	$Cu/W_1Si_{1.3}/Si$
200	Cu_3Si	×[a]	×
450	Cu_3Si	×	×
500	Cu_3Si	×	Cu_3Si, W_5Si_3
550		Cu_3Si	Cu_3Si, W_5Si_3
600		Cu_3Si, W_5Si_3, WSi_2	Cu_3Si, W_5Si_3, WSi_2
650		Cu_3Si, WSi_2	Cu_3Si, WSi_2

[a]"×" indicates no observation of silicide phase.

1. Electrical measurements

Figure 7 shows the statistical distributions of reverse bias current density for the $Cu/WSiN/W_1Si_1/p^+-n$ and $Cu/WSiN/W_1Si_{1.3}/p^+-n$ junction diodes annealed at various temperatures. All the $Cu/WSiN/W_1Si_1/p^+-n$ junction diodes retained their integrity after annealing at temperatures up to 600 °C, and a large majority of the diodes still remained stable even after annealing at 650 °C [Fig. 7(a)]. This is more than 100 °C improvement in thermal stability over the $Cu/W_1Si_1/p^+-n$ junction diodes [Fig. 4(b)], and is attributed to the very thin (about 5 nm) WSiN layer formed on the WSi_x surfaces by the N_2 plasma treatment, as confirmed by the AES depth profiles shown in Fig. 8. It turned out that the very thin WSiN layer suppressed the diffusion of Cu, thus, the formation of Cu_3Si was retarded and the accelerated crystallization of WSi_x layers was suppressed, which in turn resulted in the improvement of thermal stability for the junction diodes.

For the $Cu/WSiN/W_1Si_{1.3}/p^+-n$ junction diodes, the devices remained stable after annealing at temperatures up to 500 °C, deteriorated slightly after annealing at 550 °C, and failed completely upon annealing at 600 °C [Fig. 7(b)]. This

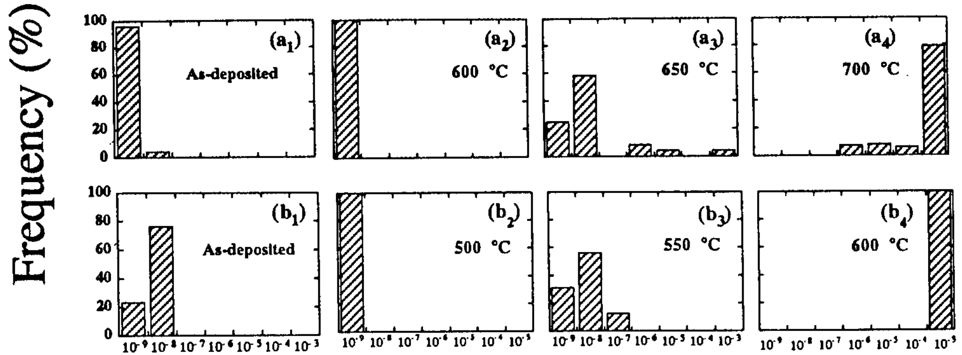

FIG. 7. Histograms showing statistical distributions of reverse bias current density for (a) $Cu/WSiN/W_1Si_1/p^+-n$ and (b) $Cu/WSiN/W_1Si_{1.3}/p^+-n$ junction diodes annealed at various temperatures. The WSi_x layers are 50 nm thick.

is an obvious improvement over the $Cu/W_1Si_{1.3}/p^+-n$ junction diodes without N_2 plasma treatment [Fig. 4(c)]. However, it is clear that the barrier capability of $WSiN/W_1Si_{1.3}$ bilayer is inferior to that of $WSiN/W_1Si_1$ bilayer. Failure of the $WSiN/WSi_x$ barrier bilayers might be correlated with the crystallization temperature of WSi_x layers, which decreased with increasing Si/W atomic ratio in the WSi_x layers (Fig. 3).

2. Sheet resistance measurements and XRD analyses

The normalized change in sheet resistance of annealed sample is defined as

$$\frac{\Delta R_S}{R_S}\% = \frac{R_{S_{\text{after anneal}}} - R_{S_{\text{as-deposited}}}}{R_{S_{\text{as-deposited}}}} 100\%.$$

Figure 9 shows the change in sheet resistance of $Cu/WSi_x/Si$ and $Cu/WSiN/WSi_x/Si$ samples annealed at various temperatures. All WSi_x layers were 50 nm thick. The thermal stability of the $Cu/W_1Si_1/Si$ samples reached 550 °C; however, a drastic increase in sheet resistance was found after annealing at 600 °C [Fig. 9(a)], implying failure of the $Cu/W_1Si_1/Si$ structure. For the $Cu/W_1Si_{1.3}/Si$ samples, the sheet resistance remained unchanged only up to 450 °C, and it increased drastically after annealing at 500 °C. The $Cu/WSi_x/Si$ structure with a WSi_x barrier layer deposited at higher SiH_4/WF_6 flow ratios was obviously less thermally stable. The sheet resistance for all samples of $Cu/WSiN/WSi_x/Si$ remained stable up to 650 °C, as shown in Fig. 9(b). Comparing these results with those of $Cu/WSi_x/Si$ samples shown in Fig. 9(a), we found that the barrier effectiveness of WSi_x layers was improved significantly by forming a thin layer of WSiN on the surfaces of WSi_x via an *in situ* N_2 plasma treatment.

Figure 10 shows the XRD spectra of the $Cu/WSiN/W_1Si_1/Si$ samples after annealing at various temperatures. Instead of the formation of various silicides for the 600 °C annealed $Cu/W_1Si_1/Si$ samples [Fig. 5(a)], no silicide phase was detected for the $Cu/WSiN/W_1Si_1/Si$ samples annealed at 600 °C. This indicates that the accelerated crystallization of WSi_x layers in contact with a polycrystalline Cu overlayer was suppressed by the presence of a thin WSiN layer sandwiched between the Cu and WSi_x layers. It has been reported that a uniform ultrathin (<1 nm) WSiN barrier layer can be formed at the interface of WN/poly-Si by thermal annealing, and the WSiN layer was able to suppress the silicidation reaction between W and poly-Si up to 800 °C.[36] In this study, the very thin but much chemically and thermally stable WSiN layer contributed to retarding the diffusion of copper and suppressing the accelerated crystallization of WSi_x; thus, the barrier effectiveness of the amorphous CVD–WSi_x layers is significantly improved.

3. SEM observations

Figure 11 shows SEM micrographs for the $Cu/WSiN/W_1Si_1/p^+-n$ junction diodes before and after thermal annealing at various temperatures. The barrier structure remained unchanged after annealing at temperatures up to 600 °C [Fig. 11(b)]. After annealing at 650 °C, some of the diodes were degraded while the others remained intact [Fig. 7(a)]. For the diodes that remained intact after annealing, the cross-sectional SEM micrograph shows that the barrier structure remained unchanged [Fig. 11(c)]. Upon annealing at 700 °C, many large openings were found on the diodes' surfaces, and the fully developed Cu_3Si precipitates exhibiting a feature of inverted pyramid shape bounded by Si {111} planes were also observed [Fig. 11(d)]. Thus, failure of the $WSiN/W_1Si_1$ barrier bilayers was likely associated with these highly localized precipitates, which were presumably caused by the diffusion of Cu through the weak points (such

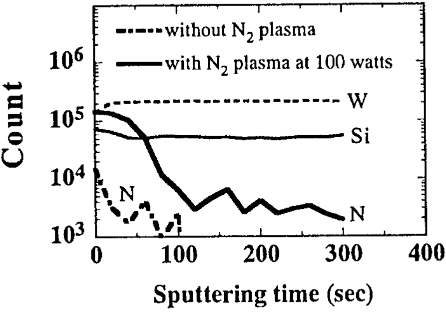

FIG. 8. AES depth profiles of WSi_x/Si samples with and without N_2 plasma treatment showing the difference in nitrogen distribution; the sputtering rate was determined to be about 0.1 nm/s.

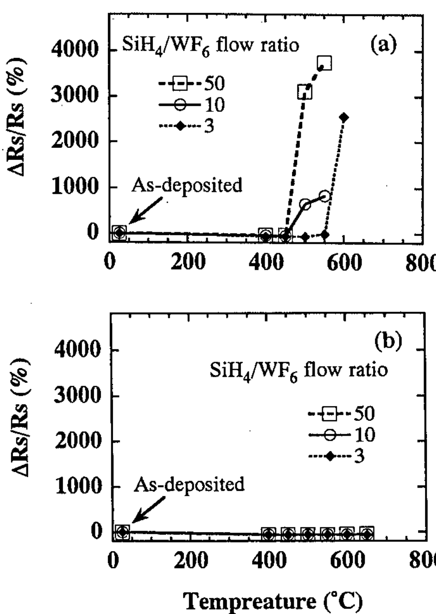

FIG. 9. Change in sheet resistance vs annealing temperature for (a) $Cu/WSi_x/Si$ and (b) $Cu/WSiN/WSi_x/Si$ samples with the WSi_x layers deposited at various SiH_4/WF_6 flow ratios.

as stress-induced microcracks and grain boundaries of the crystallized W_1Si_1 layer) in the thermally annealed barrier layers. The results of SEM observations further confirm that the thermal stability of the $Cu/WSi_x/Si$ structure can be improved significantly by forming a thin layer of WSiN on the surfaces of WSi_x via an *in situ* N_2 plasma treatment. The thermal stability temperatures of WSi_x-based barrier layers determined by various techniques of measurement and/or analysis are summarized in Table III.

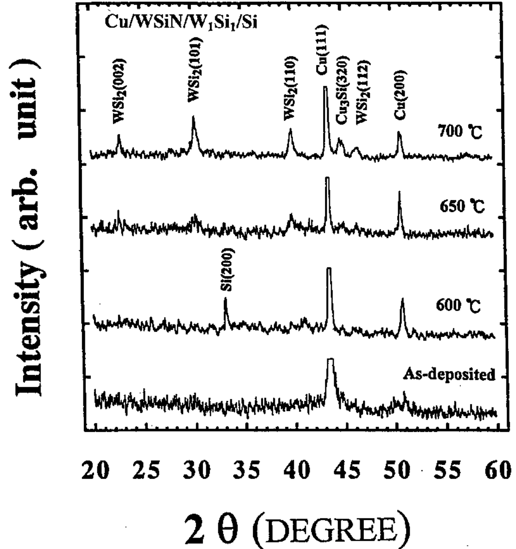

FIG. 10. XRD spectra of $Cu/WSiN/W_1Si_1/Si$ sample annealed at various temperatures.

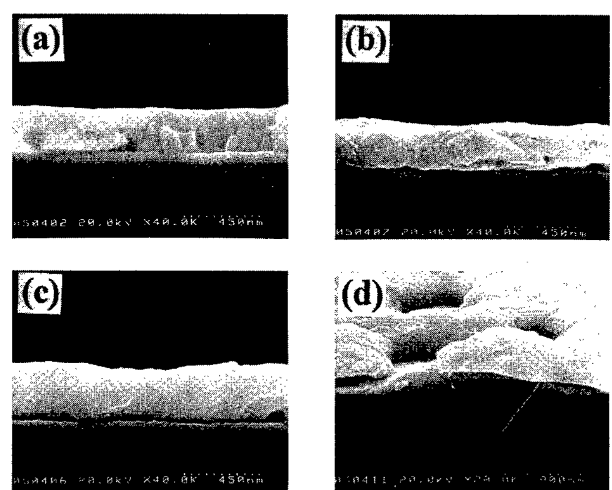

FIG. 11. Cross-sectional and oblique view SEM micrographs for the $Cu/WSiN/W_1Si_1/p^+-n$ junction diodes (a) as-deposited, and (b) 600, (c) 650, and (d) 700 °C annealed.

IV. SUMMARY

The thermal stability of thin amorphous CVD–WSi_x layers, with and without N_2 plasma treatment, was investigated with respect to the capability of diffusion barrier between Cu and Si substrate. We found that the barrier effectiveness depended on the composition of WSi_x films. The amorphous WSi_x films deposited with higher flow ratios of SiH_4/WF_6 have higher Si/W atomic ratios as well as lower crystallization temperatures; thus, the barrier effectiveness of the WSi_x films was lowered. For the 50-nm-thick W_1Si_1 layers deposited with a SiH_4/WF_6 flow ratio of 3, the $Cu/W_1Si_1/p^+-n$ junction diodes were able to sustain a 30 min thermal annealing at temperatures up to 500 °C without causing degradation to the electrical characteristics. The thermal stability was lowered to 450 °C for the $Cu/W_1Si_{1.3}/p^+-n$ junction diodes using the $W_1Si_{1.3}$ barrier layers deposited with a SiH_4/WF_6 flow ratio of 50. The barrier capability of WSi_x films can be efficiently improved by an *in situ* N_2 plasma treatment. The N_2 plasma treatment produced a very thin layer of WSiN on the surfaces of WSi_x layers, and the $WSiN/WSi_x$ bilayers not only suppressed the diffusion of Cu efficiently, but also prevented the accelerated crystallization of WSi_x layers in case of direct contact with the Cu overlayers, resulting in improvement on barrier capability. With an *in situ* N_2 plasma

TABLE III. Thermal stability temperatures of WSi_x-based barrier layers determined by different techniques of measurement/analysis.

	Barrier layers			
Measurement and/or analysis methods	W_1Si_1 (°C)	$W_1Si_{1.3}$ (°C)	$WSiN/W_1Si_1$ (°C)	$WSiN/W_1Si_{1.3}$ (°C)
Reverse current	500	450	600	500–550
Sheet resistance	550	450	650	650
XRD	550	450	600	600
SEM	500	450	600–650	500–550

treatment applied to the W_1Si_1 barrier, the Cu/WSiN/W_1Si_1/p^+-n junction diodes were able to remain intact up to at least 600 °C.

ACKNOWLEDGMENT

This work was supported by the National Science Council (ROC) under Contract No. NSC87-2215-E-009-72.

[1]R. J. Gutmann, T. P. Chow, A. E. Kaloyeros, W. A. Lanford, and S. P. Murarka, Thin Solid Films **262**, 177 (1995).
[2]N. Awaya, H. Inokawa, E. Yamamoto, Y. Okazaki, M. Miyake, Y. Arita, and T. Kobayashi, IEEE Trans. Electron Devices **ED-43**, 1206 (1996).
[3]S. P. Murarka, R. J. Gutmann, A. E. Kaloyeros, and W. A. Lanford, Thin Solid Films **236**, 257 (1993).
[4]V. M. Dubin and Y. S. Diamand, J. Electrochem. Soc. **144**, 898 (1997).
[5]D. H. Kim, R. H. Wentorf, and W. N. Gill, J. Electrochem. Soc. **140**, 3273 (1993).
[6]J. C. Chiou, K. C. Juang, and M. C. Chen, J. Electrochem. Soc. **142**, 177 (1995).
[7]S. Wolf and R. N. Tauber, *Silicon Processing for the VLSI Era* (Lattice, Sunset Beach, CA, 1986), Vol. II, pp. 268, 273.
[8]C. A. Chang, J. Appl. Phys. **67**, 566 (1990).
[9]S. D. Brotherton, J. R. Ayres, A. Gill, H. W. V. Kesteren, and F. J. A. M. Greidanus, J. Appl. Phys. **62**, 1826 (1987).
[10]Y. S. Diamand, A. Dedhia, D. Hoffstetter, and W. G. Oldham, J. Electrochem. Soc. **140**, 2427 (1993).
[11]A. L. S. Loke, C. Ryu, C. P. Yue, J. S. H. Cho, and S. S. Wong, IEEE Electron Device Lett. **EDL-17**, 549 (1996).
[12]J. O. Olowolafe, J. Li, J. W. Mayer, and E. G. Colgan, Appl. Phys. Lett. **58**, 469 (1997).
[13]S. D. Kim, S. G. Jin, M. R. Hong, and C. T. Kim, J. Electrochem. Soc. **144**, 664 (1997).
[14]H. Ono, T. Nakano, and T. Ohta, Jpn. J. Appl. Phys., Part 1 **34**, 1827 (1995).
[15]P. J. Pokela, C.-K. Kwok, E. Kolawa, S. Raud, and M.-A. Nicolet, Appl. Surf. Sci. **53**, 364 (1991).
[16]E. Kolawa, J. S. Chen, J. S. Reid, P. J. Pokela, and M.-A. Nicolet, J. Appl. Phys. **70**, 1369 (1991).
[17]T. Oku, E. Kawakami, M. Uekubo, K. Takahiro, S. Yamaguchi, and M. Murakami, Appl. Surf. Sci. **99**, 265 (1996).
[18]M. Takeyama, A. Noya, T. Sase, and A. Ohta, J. Vac. Sci. Technol. B **14**, 674 (1996).
[19]J. Y. Lee and J. W. Park, Jpn. J. Appl. Phys., Part 1 **35**, 4280 (1996).
[20]V. P. Anitha, A. Bhattacharya, N. G. Patil, and S. Major, Thin Solid Films **236**, 306 (1993).
[21]S. Q. Wang, J. Appl. Phys. **73**, 2301 (1993).
[22]J. C. Chiou, K. C. Juang, and M. C. Chen, J. Electrochem. Soc. **142**, 2326 (1995).
[23]M.-A. Nicolet, Thin Solid Films **107**, 415 (1978).
[24]J. S. Reid, R. Y. Liu, P. M. Smith, R. P. Ruiz, and M.-A. Nicolet, Thin Solid Films **262**, 218 (1995).
[25]M. Kottke, F. Pintchovski, T. R. White, and P. J. Tobin, J. Appl. Phys. **60**, 2835 (1986).
[26]T. Nakano, H. Ono, T. Ohta, T. Oku, and M. Murakami, VMIC Proceedings (1994), p. 407.
[27]Y. Shioya and M. Maeda, J. Appl. Phys. **60**, 327 (1986).
[28]K. C. Saraswat, D. L. Brors, J. A. Fair, K. A. Monnig, and R. Beyers, IEEE Trans. Electron Devices **ED–30**, 1497 (1983).
[29]D. K. Sadana, A. E. Morgan, M. H. Norcott, and S. Naik, J. Appl. Phys. **62**, 2830 (1987).
[30]J. S. Reid, E. Kolawa, R. P. Ruiz, and M.-A. Nicolet, Thin Solid Films **236**, 319 (1993).
[31]K. Holloway, P. M. Fryer, C. Cabral, Jr., J. M. E. Harper, P. J. Bailey, and K. H. Kelleher, J. Appl. Phys. **71**, 5433 (1992).
[32]A. Hirata, T. Hosoya, K. Machida, H. Takaoka, and H. Akiya, J. Electrochem. Soc. **143**, 3747 (1996).
[33]M. Sekiguchi, T. Fujii, and M. Yamanaka, Jpn. J. Appl. Phys., Part 2 **35**, 1111 (1996).
[34]M. T. Wang, P. C. Wang, M. C. Chuang, L. J. Chen, and M. C. Chen, J. Vac. Sci. Technol. B **16**, 2026 (1998).
[35]Y. Shioya, T. Itoh, S. Inoue, and M. Maeda, J. Appl. Phys. **58**, 4194 (1985).
[36]Y. Akasaka *et al.*, VMIC Proceedings (1995), p. 168.

Study of forming a p^+ poly-Si gate by inductively coupled nitrogen plasma nitridation of the stacked poly-Si layers

M. H. Juang[a)]
Department of Electronics Engineering, National Taiwan University of Science & Technology, Kee-Lung Road, Taipei, Taiwan

(Received 9 September 1999; accepted 19 May 2000)

Formation of a p^+ poly-Si gate by using the stacked poly-Si layers that are nitridized by using inductively coupled nitrogen plasma (ICNP) has been studied. The stacked poly-Si gate structure consists of three poly-Si layers with thickness of 50, 50, and 100 nm, respectively. As for the control samples that do not receive nitrogen plasma nitridation, when they are annealed at 900 °C, the gate oxide integrity is significantly degraded and the flat-band voltage (V_{fb}) shift is large, attributable to considerable boron penetration through gate oxide. If the ICNP treatment is directly done with respect to the gate oxide layer, the V_{fb} shift can be considerably reduced, but the resultant gate oxide integrity is even much worse than that for the control samples. However, for the specimens that sustain ICNP treatment immediately after the deposition of the first poly-Si layer, the degradation of gate oxide integrity and the V_{fb} shift are significantly alleviated even at 900 °C. Hence, the process scheme that employs the stacked poly-Si gate nitridized by the ICNP treatment is highly available for forming a p^+ poly-Si gate. © *2000 American Vacuum Society.*
[S0734-211X(00)06504-5]

I. INTRODUCTION

With the scaling of metal-oxide-semiconductor field effect transistor (MOSFET) devices into the deep submicron regime, the *p*-MOSFET using an n^+ poly-Si gate is susceptible to punch-through leakage due to buried-channel operation,[1–3] unless extra well-designed drain and/or channel engineering are employed.[4–6] Therefore, the surface channel *p*-MOS device using a p^+ poly-Si gate appears as a promising candidate for subquarter-micron technology. The penetration of boron through thin gate oxide would cause the shift of flat-band voltage (V_{fb}), the distortion of capacitance–voltage ($C-V$) curve, the increase of subthreshold swing, and the deterioration of gate oxide integrity.

Several methods have been previously reported to suppress the penetration of boron.[7–16] Thermally nitridized gate oxide or reoxidized nitrided oxide could act as a good barrier against the penetration of boron.[8,9] Implantation of BF_2 dopant into bilayered CoSi/*a*-Si films and subsequent annealing, with the CoSi silicide layer as an implantation barrier, can also reduce boron penetration.[13] Large grain size formed by as-deposited amorphous silicon (*a*-Si) films could inhibit the fluorine and boron diffusion.[10] Suppression of boron penetration in a BF_2-implanted p^+ gate can be achieved by trapping of fluorine in an amorphous-Si gate.[11] Incorporation of $TiSi_2$ silicide or a thin polyoxide on the top of a poly-Si gate prior to BF_2 implantation can trap fluorine out from the poly-Si gate.[14] Implantation of nitrogen into the poly-Si gate was reported to suppress the boron penetration, thus achieving high reliability and performance of *p*-MOSFETs.[15] In a stacked gate structure consisting of three *a*-Si or poly-Si layers, lots of boron and fluorine atoms segregate at the interfaces between stack layers during the postimplant annealing process.[16]

However, by the scheme of thermal nitridation of gate oxide, high thermal budget may be required, and also it is difficult to effectively retard the penetration of boron as the gate oxide is thinner than 3 nm. In addition, as for using the *a*-Si gate or the nitridation of the poly-Si gate, the efficiency of suppressing boron penetration may be further enhanced by using the stacked gate structure, instead of a single-layer gate structure. Thus, this scheme may be especially promising for the technology employing a gate oxide thinner than 3 nm, though this scheme needs a relatively long fabrication cycle time.

In this article, formation of a p^+ poly-Si gate by using inductively coupled N_2 plasma (ICNP) nitridation of the stacked poly-Si layers has been studied. Various experimental conditions are performed to examine the effect of ICNP nitridation on the suppression of boron penetration. Extensive electrical characterization with respect to the resultant integrity of gate oxide has been done. Significant suppression of penetration of boron through the gate oxide can be obtained by employing this scheme.

II. EXPERIMENT PROCEDURE

(100)-oriented, 4–6 Ω cm, phosphorus-doped, *n*-type Si wafers were used. Figure 1 shows the primary process flow for fabricating this stacked p^+ poly-Si gate with the ICNP treatment. Field oxides of 400 nm were grown for patterning the active regions of MOS capacitors. Thin gate oxides of 7.5 nm were thermally grown at 900 °C in dry O_2 ambient at the active area. Part of the samples were directly treated by the ICNP nitridation with respect to the gate oxide layer, with a power of 200 W, a flow rate of 40 sccm/min, and a processing time of 10 min. Then, undoped poly-Si films of

[a)]Electronic mail: jmh@et.ntust.edu.tw

Main process flow

- phosphorus-doped n-(100) Si
- field oxidation, 400 nm
- active-area definition
- gate oxidation, 75 Å
- LPCVD poly-Si I, 50 nm
- with or without ICNP treatment
- LPCVD poly-Si II, 50 nm
- LPCVD poly-Si III, 100 nm
- BF_2(40 keV, 5×10^{15} cm^{-2})
- furnace annealing
- Al sputtering
- p^+-poly-Si gate delineation

FIG. 1. Main process flow for this stacked poly-Si gate structure with inductively coupled-nitrogen-plasma (ICNP) treatment.

50 nm thickness, called the poly-Si I layer, were deposited onto all the samples by using low-pressure chemical-vapor deposition (LPCVD) at 620 °C. Part of the as-deposited samples that did not sustain any N_2 plasma treatment were called the control samples. In addition, other samples, except those with the ICNP treatment on the gate oxide, would sustain the ICNP treatment on the poly-Si I layer, called the stacked poly-Si gate with N_2 plasma nitridation. Furthermore, all the samples were then sequentially deposited with undoped poly-Si films of 50 and 100 nm thickness, called the poly-Si II and the poly-Si III layers correspondingly, by using LPCVD at 620 °C. Accordingly, the stacked poly-Si gate structure consists of the poly-Si I, the poly-Si II, and the poly-Si III layers, with a total thickness of 200 nm. The samples were then BF_2 implanted at 40 keV to a dose of $5\times10^{15}\,cm^{-2}$. Reoxidation of the poly-Si layers upon removal from a LPCVD furnace would occur. Hence, prior to the subsequent poly-Si deposition of the stacked poly-Si gate, a dilute HF dip was done to minimize the native oxide. Consequently, no anomalous electrical characteristics are found to be ascribed to the possible reoxidation concern.

The postimplanted samples were annealed at 600–900 °C for 30 min in nitrogen ambient. Thick Al films were then sputtered onto the poly-Si layer, and gate delineation was done. Figure 2 shows a schematic plot of the resultant stacked poly-Si gate structure. The resultant MOS-capacitor characteristics were analyzed by $C-V$ and current–voltage

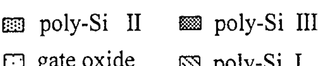

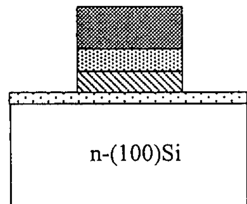

FIG. 2. Schematic plot of the resultant stacked poly-Si gate structure.

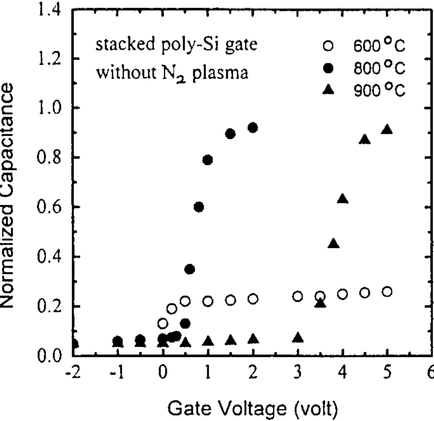

FIG. 3. Normalized high-frequency gate $C-V$ characteristics for the control samples that do not receive any nitrogen plasma nitridation.

($I-V$) methods. The high-frequency $C-V$ profiles were measured at 100 kHz, and the quasistatic $C-V$ curves were obtained at 100 Hz (Fig. 3). The time-zero-dielectric-breakdown (TZDB) characteristics were achieved by the ramping voltage method. The time-dependent-dielectric-breakdown (TDDB) characteristics, including the gate voltage shift and the charge to oxide breakdown, were conducted by using a positive constant gate current stressing of 100 mA/cm^2 at the accumulation mode. The second ion mass spectrometry (SIMS) analyses were also done to examine the distribution profiles of nitrogen and boron atoms.

III. RESULTS AND DISCUSSION

Figure 4 shows the normalized high-frequency gate $C-V$ profiles for the control samples that do not sustain any nitrogen plasma nitridation. The samples annealed at 600 °C show a low accumulation capacitance, reflecting the insufficient dopant activation that causes the poly-Si gate depletion effect. The specimens annealed at 800 °C exhibit a nearly ideal $C-V$ profile, reflecting the formation of a good p^+ poly-Si gate. In addition, the flat-band voltage shift is very small,

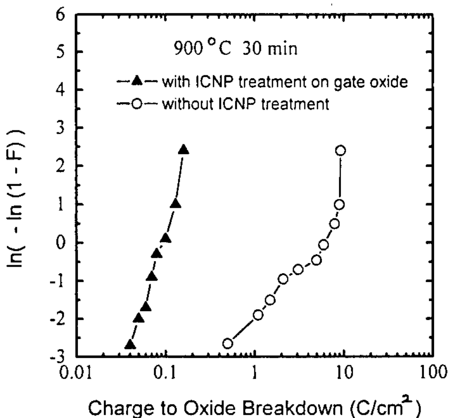

FIG. 4. Weibull plot of the charge-to-oxide-breakdown (Q_{bd}) value for the samples with and without ICNP treatment on the gate oxide layer, respectively, and annealed at 900 °C. The F value is the cumulative fail percentage of the testing devices.

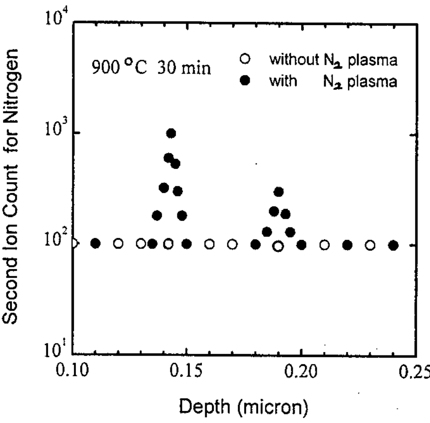

FIG. 5. Depth profiles of nitrogen for the samples with and without ICNP treatment on the poly-Si layer, respectively, and annealed at 900 °C.

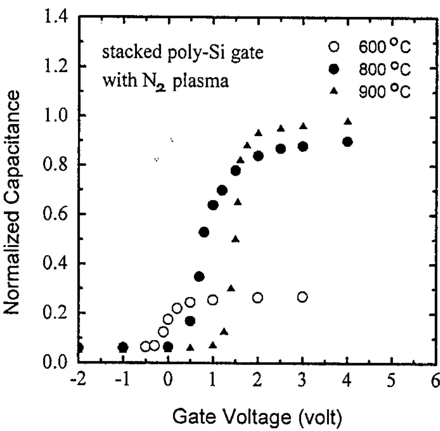

FIG. 6. Normalized high-frequency gate $C-V$ characteristics for the samples that sustain ICNP treatment on the poly-Si I layer.

attributable to very minor penetration of boron through gate oxide. However, the samples annealed at 900 °C exhibit a large V_{fb} shift of about 3 V, due to the considerable penetration of boron. However, when the ICNP treatment is directly done on the gate oxide layer, the V_{fb} shift can be reduced to be about 2 V at 900 °C due to the nitridized gate oxide.

Though the ICNP treatment on the gate oxide layer can enhance the resistance to penetration of boron, the resultant V_{fb} shift is still much larger than 0.5 V at the annealing temperature of 900 °C. In addition, the resultant gate oxide integrity is found to be severely degraded. Figure 4 shows the Weibull plot of the charge-to-oxide-breakdown (Q_{bd}) value for the control samples and the specimens that sustain ICNP treatment on the gate oxide layer, respectively, and annealed at 900 °C. The F value is the cumulative fail percentage of the testing devices. For 900 °C annealing, the gate oxide for the control samples has been actually degraded due to boron penetration, showing a poor Q_{bd} distribution. However, the samples that sustain ICNP treatment on the gate oxide layer cause even much worse gate oxide integrity. This severe deterioration is attributable to the plasma-induced damage on the gate oxide while the above ICNP treatment.

Accordingly, the ICNP treatment can be done immediately after the deposition of the first poly-Si layer, for the alleviation of plasma-induced damages as well as the nitridation of the gate oxide and the poly-Si layer. The samples that sustain N_2 plasma treatment could show better resistance to boron penetration than those without N_2 plasma nitridation. Figure 5 show the depth profiles of nitrogen for the samples that sustain ICNP treatment on the poly-Si I layer and those without N_2 plasma treatment, respectively, and annealed at 900 °C. A nitrogen peak is present near the interface of the poly-Si I and the poly-Si II layers, at the position with a depth of about 0.14–0.15 μm. In addition, the region of gate oxide, at the position with a depth of about 0.19 μm, also manifests a nitrogen peak. As a result after the annealing, the ICNP treatment eventually causes the nitridized gate oxide and the piling-up of nitrogen at the interface of the poly-Si I and the poly-Si II layers. Both the effects would significantly contribute to inhibit the penetration of boron. In addition, the plasma-induced damage could be avoided by using this ICNP process scheme. As a result, the depth profiles of boron also reflect the significantly suppressed penetration of boron through gate oxide by using this ICNP nitridation scheme, as compared to the stacked poly-Si gate without N_2 plasma treatment.

The nitrogen piling-up around the gate oxide region and also near the interface of the poly-Si I and poly-Si II layers may similarly trap the F atoms and retard the boron diffusion, as also can be seen from the resulting distribution profiles of the F atom. Moreover, the INCP treatment performed on the poly-Si I layer is found to result in better suppression of boron penetration than the direct plasma treatment on the gate oxide. For the samples that sustain ICNP treatment on the poly-Si I layer, the segregation of nitrogen near the interface of the poly-Si I and poly-Si II layers could serve as the first barrier to largely reduce the driving force of boron diffusion while annealing. The nitridized gate oxide would serve as the second barrier to further resist penetration of boron. Hence, both the barriers of nitrogen-doped regions are equally important for suppressing penetration of boron. However, for the direct nitridation on gate oxide, the large driving force of boron diffusion is still present, since the driving force cannot be considerably reduced by the weaker barrier of the interface of the poly-Si I and poly-Si II layers without nitrogen incorporation. Hence, the penetration of boron is more easily caused, though the nitride gate oxide can also resist the penetration of boron.

Figure 6 shows the normalized high-frequency gate $C-V$ profiles for the samples with the ICNP treatment on the poly-Si I layer. By this ICNP nitridation scheme, the specimens annealed at 800 °C again exhibit a nearly ideal $C-V$ profile and a negligible flat-band voltage shift. However, as compared to the cases for the control samples and the specimens with ICNP treatment on the gate oxide layer, the samples that sustain ICNP treatment on the poly-Si I layer show a significantly much smaller V_{fb} shift at 900 °C. This result reflects the largely suppressed boron penetration for the stacked poly-Si gate with this ICNP nitridation.

Moreover, Fig. 7 shows the quasistatic gate $C-V$ profiles

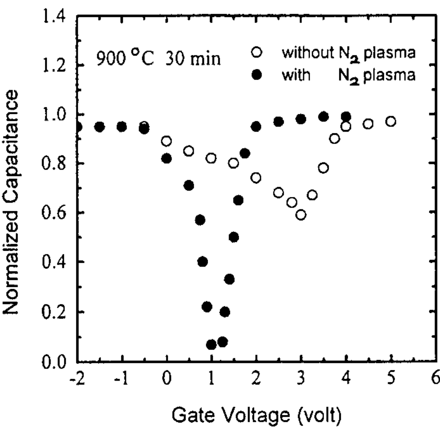

FIG. 7. Quasistatic gate $C-V$ characteristics for the samples with and without ICNP treatment on the poly-Si I layer, respectively, and annealed at 900 °C.

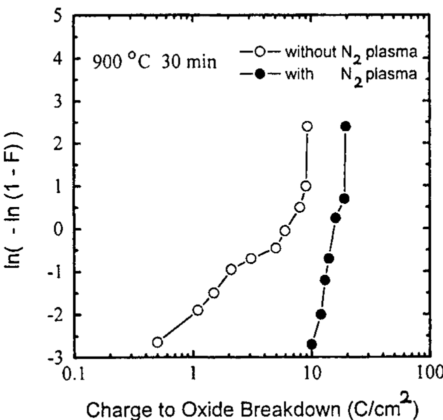

FIG. 9. Weibull plot of the charge-to-oxide-breakdown value for the samples with and without ICNP treatment on the poly-Si layer, respectively, and annealed at 900 °C.

for the samples with and without ICNP treatment on the poly-Si I layer, respectively, and annealed at 900 °C. The stacked poly-Si gate samples with ICNP treatment can cause much better $C-V$ characteristics for high-performance MOSFET operation than those without N_2 plasma treatment. Figure 8 shows the gate voltage shift as a function of the constant-current stressing time for the stacked poly-Si gate samples with and without ICNP treatment on the poly-Si I layer, respectively, and annealed at 900 °C. The samples without plasma nitridation exhibit a larger electron trapping rate than those with the ICNP treatment, reflecting the degraded gate oxide due to considerable boron penetration. Moreover, from the resultant stressing time that leads to oxide breakdown, the samples with the ICNP treatment lead to a much larger charge-to-oxide-breakdown value than the control specimens, which again manifests the good suppression of penetration of boron through gate oxide.

Figure 9 shows the Weibull plot of the charge-to-oxide-breakdown (Q_{bd}) value for the samples with and without ICNP treatment on the poly-Si I layer, respectively, and annealed at 900 °C. The stacked poly-Si gate samples with the ICNP treatment manifest a better and more uniform distribution of the Q_{bd} value than the control ones. Furthermore, the electric breakdown field of oxides (E_{bd}) value for the control samples annealed at 900 °C show a distribution of 8–14 MV/cm, whereas that for the plasma-nitridized specimens can yield a distribution of 13–17 MV/cm. As compared with the previous report[10] that showed a V_{fb} shift smaller than 0.1 V and Q_{bd} value of about 10 C/cm^2, a V_{fb} shift smaller than 0.1 V and Q_{bd} value larger than 10 C/cm^2 can be achieved by using this process scheme. Hence, the stacked poly-Si gate that sustains ICNP treatment on the poly-Si I layer can effectively inhibit the penetration of boron through the gate oxide. A good p^+ poly-Si gate without considerable flat-band voltage shift as well as excellent gate oxide integrity can be achieved by using this scheme.

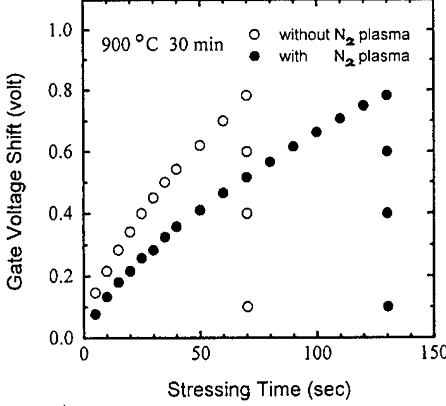

FIG. 8. Gate voltage shift as a function of the stressing time for the samples with and without ICNP treatment on the poly-Si I layer, respectively, and annealed at 900 °C. A constant stress current density of 100 mA/cm^2 is used.

IV. CONCLUSIONS

Formation of a p^+ poly-Si gate by using the stacked poly-Si layers that is nitridized by the ICNP treatment has been studied. As for the control samples that do not receive any nitrogen plasma nitridation, when they are annealed at 800 °C, no considerable V_{fb} shift and gate oxide deterioration is observed. However, when they are annealed at 900 °C, the gate oxide integrity is significantly degraded and the V_{fb} shift is large, attributable to considerable penetration of boron through the gate oxide. If the ICNP treatment is directly done on the gate oxide layer, the V_{fb} shift can be considerably reduced, but the resultant gate oxide integrity is even much worse than that for the control samples, attributable to the plasma-induced damage on the gate oxide. Accordingly, the ICNP treatment should be done on the poly-Si layer but not the gate oxide, for achieving plasma nitridation without causing damage. Hence, as for the specimens that sustain ICNP treatment on the poly-Si I layer, no considerable degradation of gate oxide integrity is observed even at 900 °C. The penetration of boron through gate oxide is largely suppressed, due to the nitridized gate oxide and the segregation of nitrogen near the interface of the poly-Si I and poly-Si II layers.

Hence, the process scheme that employs the stacked poly-Si gate with the ICNP treatment is highly available for forming a p^+ poly-Si gate.

ACKNOWLEDGMENTS

The research was supported in part by the Republic of China National Science Council under Contract No. NSC 89-2215-E011-008. The authors are also grateful for the technical support from S. C. Chu and Dr. W. K. Lai. In addition, the authors would like to thank Dr. H. C. Cheng and Dr. T. F. Liu for valuable discussion.

[1]G. J. Hu and R. H. Bruce, IEEE Trans. Electron Devices **32**, 584 (1985).
[2]F. Matsuoka, H. Iwai, H. Hayashida, and K. Maeguchi, IEEE Trans. Electron Devices **37**, 1487 (1990).
[3]K. Tanaka and M. Fukuma, Tech. Dig. Int. Electron Devices Meet. 628 (1987).
[4]T. Hori and K. Kurimoto, Tech. Dig. Int. Electron Devices Meet. 394 (1988).
[5]M. Miyake, J. Electrochem. Soc. **137**, 2860 (1990).
[6]K. M. Cham and S. Chang, IEEE Trans. Electron Devices **31**, 964 (1984).
[7]H. H. Tseng, M. Orlowski, P. J. Tobin, and R. L. Hance, IEEE Electron Device Lett. **13**, 14 (1992).
[8]G. Q. Lo and D. L. Kwong, IEEE Electron Device Lett. **12**, 175 (1991).
[9]Z. J. Ma, J. C. Chen, Z. H. Liu, J. T. Krick, Y. C. Cheng, C. Hu, and P. K. Ko, IEEE Electron Device Lett. **15**, 109 (1994).
[10]M. Koda, Y. Shida, J. Kawaguchi, and Y. Kaneko, Tech. Dig. Int. Electron Devices Meet. 316 (1993).
[11]C. Y. Lin, C. Y. Chang, and C. C. H. Hsu, IEEE Trans. Electron Devices **42**, 1503 (1995).
[12]C. Y. Lu, J. M. Sung, H. C. Kirsch, S. J. Hillenius, T. E. Smith, and L. Manchanda, IEEE Electron Device Lett. **10**, 192 (1989).
[13]M. H. Juang, Solid-State Electron. **42**, 389 (1995).
[14]V. H. Lin, C. L. Lee, T. F. Lei, and T. S. Chao, IEEE Electron Device Lett. **15**, 164 (1995).
[15]T. Kuroi, S. Kusunoki, M. Shirahata, Y. Okumura, M. Kobayashi, M. Inuishi, and N. Tsubouchi, Int. Symp. on VLSI Technology, 1994 (unpublished), p. 107.
[16]S. L. Wu, C. L. Lee, and T. F. Lei, Tech. Dig. Int. Electron Devices Meet. 329 (1993).

Ion-bombardment effects on PtSi/n-Si Schottky contacts studied by ballistic electron emission microscopy

Guo-Ping Ru,[a] Xin-Ping Qu, Shi-Yang Zhu, and Bing-Zong Li
Department of Electronic Engineering, Fudan University, Shanghai 200433, China

C. Detavernier, R. L. Van Meirhaeghe, and F. Cardon
Department of Solid State Sciences, University of Gent, Krijgslaan 281/S1, B-9000 Gent, Belgium

R. A. Donaton and K. Maex
IMEC, Kapeldreef 75, B-3001 Leuven, Belgium

(Received 7 May 1999; accepted 21 April 2000)

Ballistic electron emission microscopy has been used to study physical damage effects on PtSi/n-Si Schottky contacts. The physical damages are introduced into Si substrates by ion bombardment with well-defined energies in an ion-milling process. Schottky barrier height (SBH) distribution is measured on the subsequently formed PtSi/n-Si Schottky diodes. The results show that mean SBH decreases with ion energy in a square-root relation. A simple SBH model is developed to consider image-force lowering effect for a semiconductor with a step-function distribution of donor concentration. The model is successfully used to explain quantitatively the experimental relation between SBH and ion energy. © *2000 American Vacuum Society.* [S0734-211X(00)02804-3]

I. INTRODUCTION

Dry-etching process-induced damage has attracted much attention in recent studies because dry etching, such as reactive-ion etching (RIE), is one of the major processing steps in very large-scale integrated (VLSI) circuit fabrication.[1,2] Their influence on electronic properties and device characteristics is one of the most important topics because the damage may not be fully removed, even after high-temperature anneals,[1–3] and their effects will be more pronounced in a device with smaller features that the current VLSI technology is moving toward. For example, in a self-aligned silicide process, some amount of substrate Si will be consumed in the reaction, which may contain much damage introduced in an early dry-etching process for opening contact holes. But as the device size is scaled down, less Si will be consumed; therefore, more damage will be left.

An effective way to monitor damage introduced by a dry-etching process is to form a Schottky barrier diode (SBD) on a process-treated substrate and measure its electrical characteristics. Current–voltage ($I-V$), capacitance–voltage ($C-V$), and recently developed ballistic electron emission microscopy (BEEM) techniques have been used to study RIE damage effects on Schottky diodes.[3–9] A general phenomenon observed is that the RIE treatment often lowers the Schottky barrier height (SBH) for a metal contact to n-type Si, whereas it increases the SBH for a metal contact to p-type Si. It is believed that a thin surface layer containing positive charges is formed after RIE treatment.[3,6,9] However, there is no consensus explanation of their nature. Murata *et al.* believed that SiF_3 was the cause of the positive charges, whereas Hwang, Ruzyllo, and Kamieniecki thought the positive charges were related to surface roughness.[6,7] However, those arguments may be incomprehensive, because generally, the RIE process not only introduces chemical impurities, but also introduces structural damage into a substrate. On the other hand, a similar phenomenon of SBH was observed in samples treated by sputter-etching (SE) and ion-milling processes, in which only inert ions, such as Ar ions, are present.[10–12] Moreover, Grusell, Berg, and Andersson detected sputtering-induced traps or donorlike defects in rf-sputtered substrates by the deep-level transient spectroscopy (DLTS) technique, indicating that ion bombardment itself produces additional positive charges accumulated near the surface.[10]

Therefore, it would be interesting if one could show the relation between the sputtering-induced traps and ion-bombardment conditions. In a RIE or SE system, where plasma and the substrate are located closely in the same chamber, ions collide with each other at a certain pressure and are accelerated through random distances before they bombard the substrate. Therefore, the bombardment energy varies widely. In contrast, in an ion-milling system, ions are generated in a confined space and can be accelerated by a fixed voltage before they bombard the substrate.[13] The spread of the ion-bombardment energy is very small, typically several electron volts.[14] In this respect, the ion-milling process is more suitable for a quantitative study on energetic ion-bombardment effects, because it offers precise, as well as independent, control over energy and dose of ions that produce the damage. In a previous paper, we reported BEEM and DLTS measurements of ion-bombardment effects on PtSi/n-Si Schottky diodes in an ion-milling process.[15] We observed a systematic decrease of SBH and an increase of the amount of process-induced deep levels as ion energy increases. In this paper, we develop a simple model to relate the process-modified SBH with ion-bombardment energy, and we give a quantitative explanation of the results obtained by BEEM.

[a]Electronic mail: gpru@fudan.edu.cn

 ©2000 American Vacuum Society

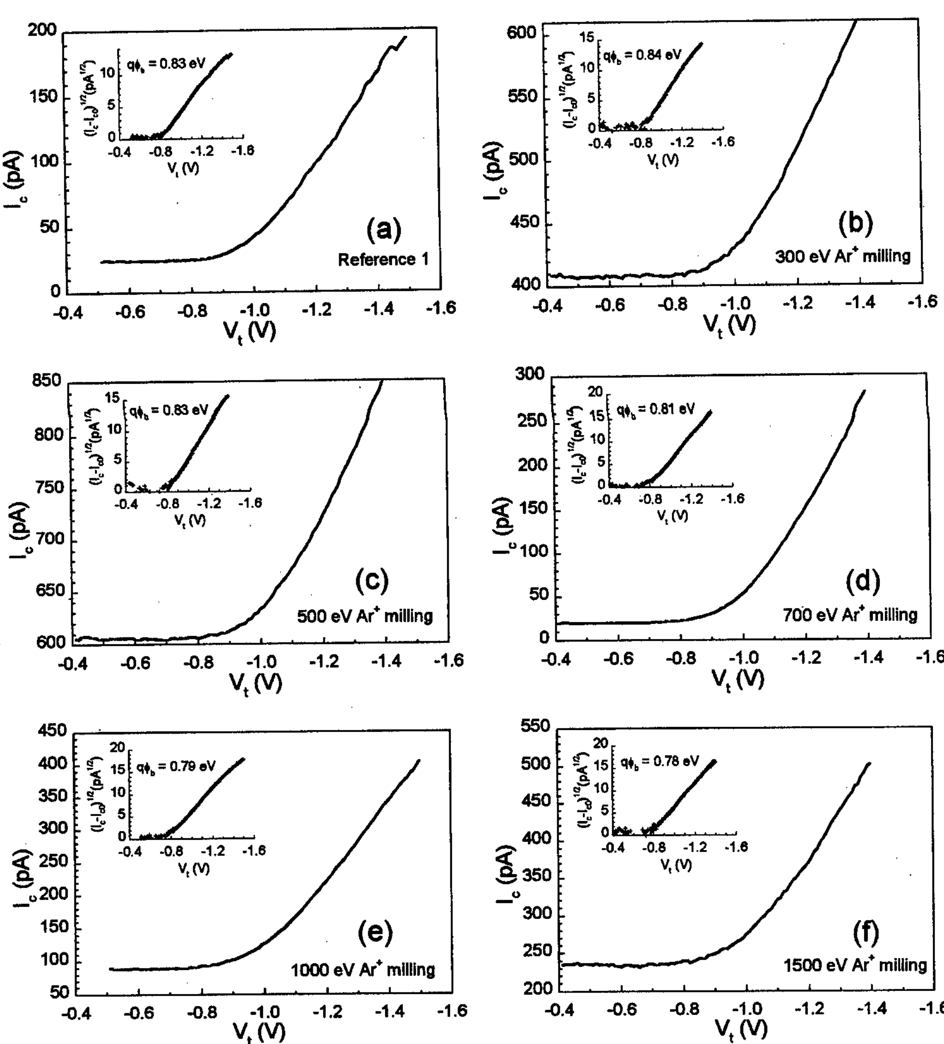

FIG. 1. Ballistic electron emission spectra of PtSi/n-Si diodes on the Si substrate (a) without and with (b) 300 eV, (c) 500 eV, (d) 700 eV, (e) 1000 eV, and (f) 1500 eV Ar ion bombardment. The insets show the square root of the collector current and its linear fit with tip voltage.

II. EXPERIMENT

Ion-milling experiments were performed on n-type Si (100) substrates in an Oxford ion-beam sputtering system. The substrate doping level was $1\times10^{15}\,\mathrm{cm}^{-3}$, as determined by Hall measurements. Ar ions with energies of 300, 500, 700, 1000, and 1500 eV were used to bombard the substrates. Ion current density was fixed around 1 mA/cm^2. The substrates were bombarded for 5 min, which is adequate to remove a thick enough surface layer and illustrate intrinsic behaviors of process-induced damages. An approximately 50-nm-thick Pt layer was deposited on the substrates in a dc magnetron sputtering system. An ultrathin ($\sim$3 nm) PtSi layer was formed by 250 °C (60 s) and 450 °C (60 s) rapid thermal anneals (RTAs) with a selective etch in between.[16] Details of sample preparation can be found elsewhere.[15]

BEEM measurements were performed at room temperature in air by an AIVTB-4B system of Surface/Interface Co. A PtIr tip was used in the experiments. More than 200 ballistic electron emission spectra (BEES) were acquired randomly in every sample. A histogram of SBH was then plotted based on those SBHs for every sample.

III. RESULTS AND DISCUSSION

Besides ion-milled samples, samples without ion milling were also prepared as reference samples in the metal deposition and silicidation processes. Figures 1(a)–1(f) show the BEES (I_c vs V_t) of PtSi/Si diodes on the Si substrate without or with bombardment by 300, 500, 700, 1000, and 1500 eV Ar ions. The insets show the square root of the collector current $(I_c-I_{c0})^{1/2}$ and its linear fit with tip voltage, where I_{c0} is the background current resulting from amplifier offset-bias setting. Clearly a linear relation between $(I_c-I_{c0})^{1/2}$ and tip voltage occurs near the threshold voltage for all the samples, indicating that the BEES can be well described by the Bell-Kaiser model, i.e., a quadratic law.[17] The SBH can then be extracted by fitting the BEES with thermal broadening correction. Figures 2(a) and 2(b) show SBH distributions of two PtSi/Si reference diodes that were prepared under the same conditions but in two runs. Although there are appreciable differences in shape (e.g., width and peak value) between the two distributions, the mean SBHs are essentially

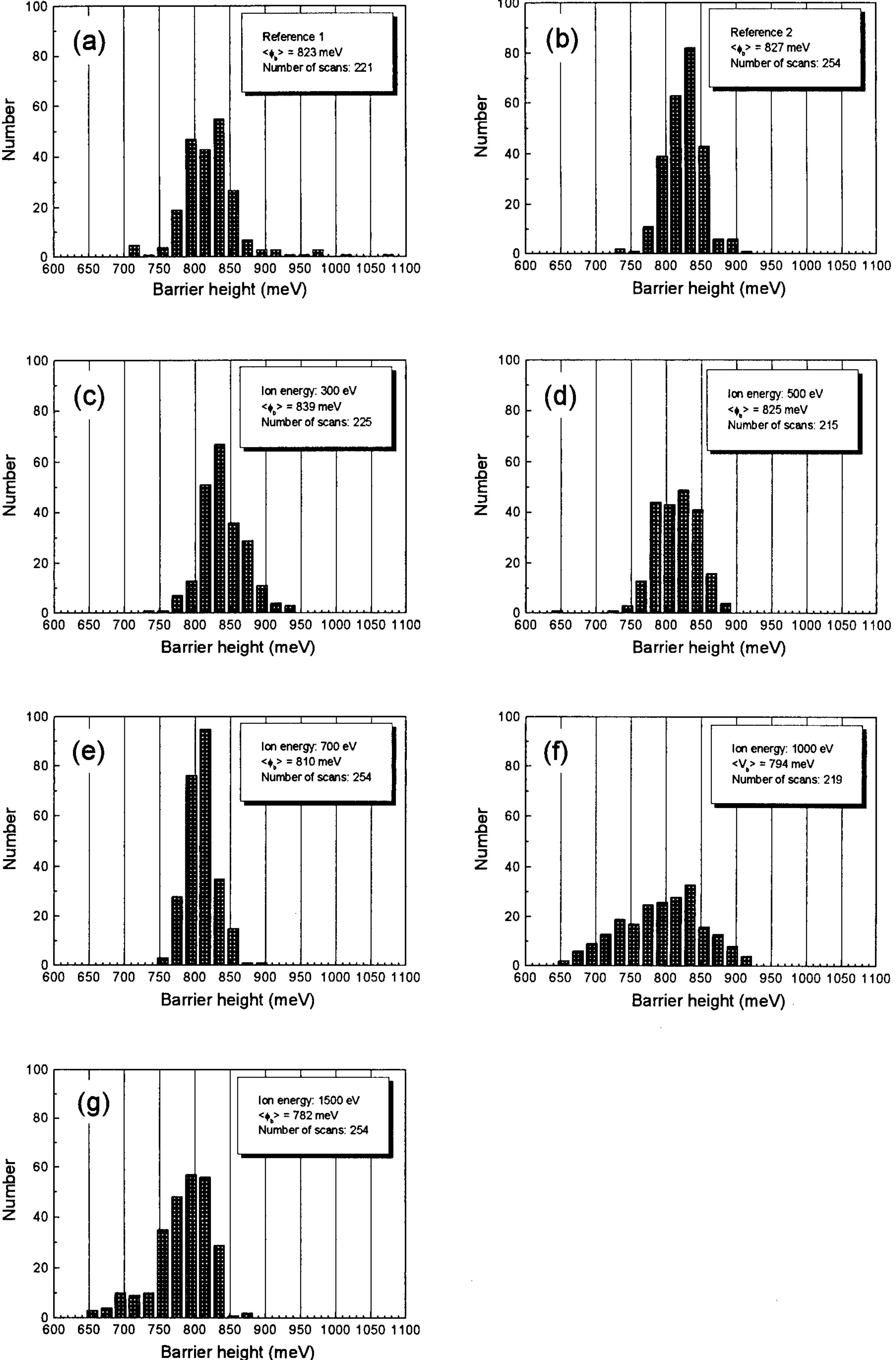

FIG. 2. Schottky barrier height distributions of PtSi/n-Si contacts (a), (b) without and with (c) 300 eV, (d) 500 eV, (e) 700 eV, (f) 1000 eV, and (g) 1500 eV Ar ion bombardment. Each distribution was plotted based on quadratic fitting of BEES acquired at more than 200 random positions of one sample.

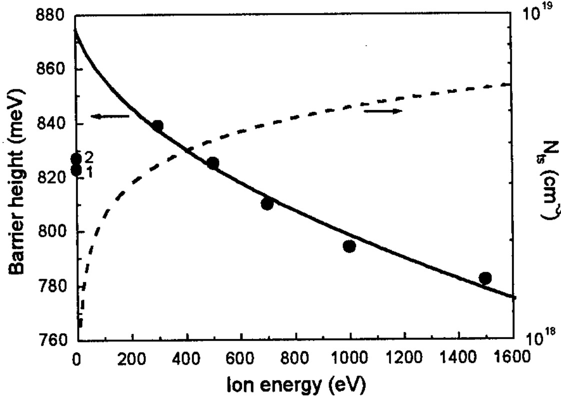

FIG. 3. Mean barrier height as a function of ion energy. The closed circles represent the experimental barrier height, whereas the solid line is its best fitting by Eq. (9). The dashed line, which represents N_{ts}, is calculated by $N_{ts}=kE(W_0/R_p)\cdot N_D$.

the same (823 and 827 meV). The results convinced us to make comparisons of mean SBHs between samples prepared under different conditions.

Figures 2(c)–2(g) show SBH distributions of PtSi/n-Si SBDs, whose substrates were bombarded by Ar ions with energies of 300, 500, 700, 1000, and 1500 eV before Pt deposition. When the mean SBH is plotted as a function of ion energy, as shown by closed circles in Fig. 3, one can see that SBH substantially decreases as ion energy increases, except for the reference samples.

This trend is in agreement with some related studies by other groups, which can be explained by the fact that ion bombardment causes positive charges or donorlike defects near a surface.[9,11] Just as in low-energy ion implantation, ions implanting into a substrate will cause structural damage and produce defects, which may electrically behave as donors.[10] The additional donors close to the metal–semiconductor (M–S) interface will significantly increase the surface field in a semiconductor, therefore reducing the effective barrier height when image-force lowering is considered.[18] It would be ideal to do an analysis if one knows the donor concentration, as well as its distribution, by some techniques. However, techniques now available to do such characterization are quite limited. DLTS can detect deep levels, but is not sensitive to shallow donors that may dominate band bending in a Schottky diode. The $C-V$ carrier profiling technique suffers from the limit of an initial depletion width.

Here, we take an alternative approach by developing a simple SBH model to quantitatively analyze the results. A few assumptions must be made to relate the effective SBH with donorlike defect concentration and its distribution depth. Although defect distribution is assumed to be in an exponential decay form in a few papers,[10,11] damage distribution of ion implantation is calculated to be nearly Gaussian.[19] To the first order of accuracy, a constant distribution with a depth of the projected range R_p is assumed for the donorlike defects in this paper. In fact, the ion energy used in this work is generally much lower than that in conventional ion implantation. The projected range R_p then is quite small, typically tens of angstroms, which, in turn, makes other distributions indistinguishable from the constant distribution.

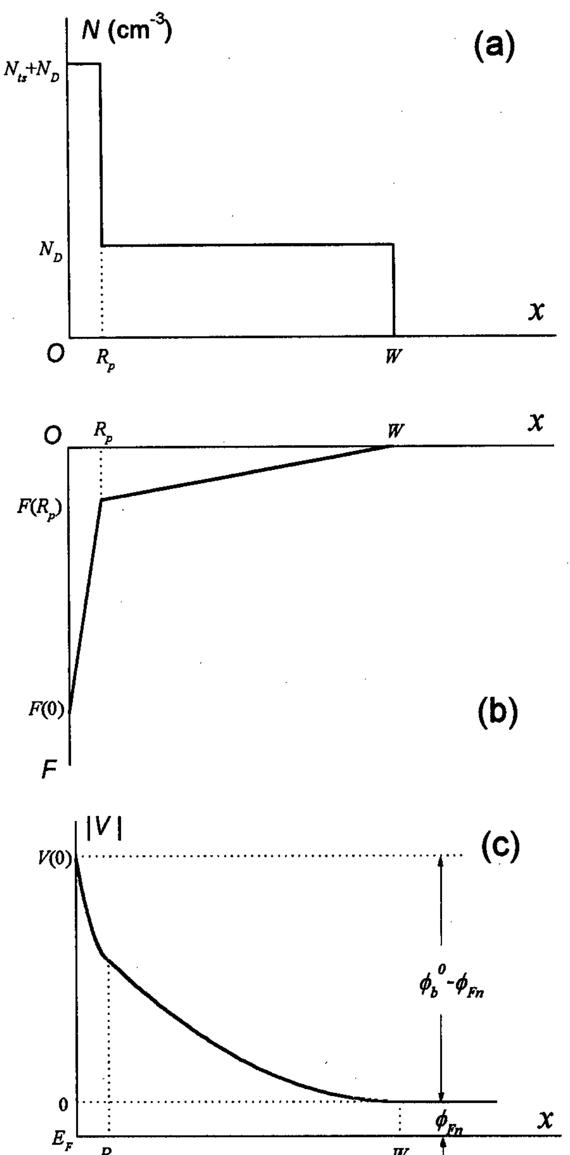

FIG. 4. Distribution of (a) ionized donor concentration, (b) electrical field, and (c) potential in the depletion region of a metal-n^+/n-Si contact.

Figures 4(a)–4(c) show the proposed charge concentration, electrical field, and potential distribution in the depletion region of a metal-n^+/n-Si contact. The donor concentration distributes as a step function. N_{ts} is the concentration of damage-induced donors and N_D is the doping concentration of the substrate. R_p is the depth of damages, which is assumed to be equal to the projected range of Ar ions implanted into Si. W is the width of the depletion region. Then the surface field F_s can be written as [see Eq. (A2)]

$$F_s=\frac{q}{\epsilon_0\epsilon_r}(N_DW+N_{ts}R_p), \tag{1}$$

where q is the electron charge and ϵ_0 and ϵ_r are the absolute permittivity and relative permittivity of a semiconductor, respectively.

The surface potential, equivalently, the band bending, can be expressed as [see Eq. (A4)]

$$V_s=\frac{q}{2\epsilon_0\epsilon_r}(N_D W^2+N_{ts}R_p^2). \tag{2}$$

On the other hand, the band bending V_s is equal to $(\phi_b^0-\phi_{Fn})$, where ϕ_b^0 is the intrinsic SBH without any correction, and ϕ_{Fn} is the Fermi potential of the semiconductor. Thus, the band bending is a constant for a given barrier height and background doping level, and it can be expressed as

$$V_s\equiv\phi_b^0-\phi_{Fn}=\frac{qN_D W_0^2}{2\epsilon_0\epsilon_r}. \tag{3}$$

Here, the physical meaning of W_0 is the width of a depletion region when no other donor except the background donor (N_D) is present in the semiconductor.

For a real M–S contact, the image-force lowering plays an important role in its electrical characteristic, especially when the surface field is high. The image-force lowering of a Schottky barrier can be written as[20]

$$\Delta\phi_{bi}=\left(\frac{qF_s}{4\pi\epsilon_0\epsilon_r}\right)^{1/2}. \tag{4}$$

Substituting F_s from Eqs. (1)–(3) into Eq. (4) by keeping W_0 as a constant, one can obtain

$$\Delta\phi_{bi}=\frac{q}{2\pi\epsilon_0\epsilon_r}\left\{\pi N_D W_0\left[\left(1-\frac{N_{ts}R_p^2}{N_D W_0^2}\right)^{1/2}+\frac{N_{ts}R_p}{N_D W_0}\right]\right\}^{1/2}. \tag{5}$$

To relate defect density with ion energy, we may make the following deduction. First, assume each Ar ion stops at a depth of R_p, and the energy E is uniformly dissipated in the depth. Second, the energy loss of ions is mainly due to nuclear stopping, and it causes defects. Third, the defect density is proportional to ion energy loss per unit length (electron volts per angstrom). Although the defects can only be produced by impingement with a kind of characteristic energy (e.g., 15 eV for Si[19]), the third assumption is still good because in reality ion collision with atoms is a statistical process and the ion energy is broadened after a collision. With these three assumptions, one can obtain $N_{ts}\propto E/R_p$. Let

$$\frac{N_{ts}R_p}{N_D W_0}=kE, \tag{6}$$

where k is a proportionality constant for the bombardment effect on defect density. Then Eq. (5) can be written as

$$\Delta\phi_{bi}=\frac{q}{2\pi\epsilon_0\epsilon_r}\left\{\pi N_D W_0\left[\left(1-kE\frac{R_p}{W_0}\right)^{1/2}+kE\right]\right\}^{1/2}. \tag{7}$$

Now, let us make an estimation of the parameters in Eq. (7). W_0 is on the order of 1 μm (0.89 μm, in our case), whereas R_p is on the order of tens of angstroms, so $R_p/W_0 \ll 1$. As will be shown later, for $E>200\,\text{eV}$, the term kE in Eq. (7) dominates the square brackets, so, the term $kE(R_p/W_0)$ as well as 1 can be neglected for this ion-energy range. For $E\leqslant 200\,\text{eV}$, 1 is comparable to kE, but the $kE(R_p/W_0)$ term will be much smaller than 1. So for the whole ion-energy range, the $kE(R_p/W_0)$ term can be neglected. Then Eq. (7) can be written as

$$\Delta\phi_{bi}=\frac{q}{2\pi\epsilon_0\epsilon_r}[\pi N_D W_0(1+kE)]^{1/2}. \tag{8}$$

And the effective SBH can now be written as

$$\phi_b=\phi_b^0-\frac{q}{2\pi\epsilon_0\epsilon_r}[\pi N_D W_0(1+kE)]^{1/2}. \tag{9}$$

Equation (9) indicates that the effective SBH decreases as ion energy increases in a square-root relationship. By using Eq. (9), we can fit the experimental SBH data within small deviations, except for the reference samples, as shown by the solid line in Fig. 3. The intrinsic SBH of the PtSi/n-Si contact ϕ_b^0 is fitted to be 887 meV, and the parameter k is fitted to be $0.048\,\text{eV}^{-1}$. k^{-1} means a characteristic energy, equal to 20.8 eV. Here we can see that for $E>200\,\text{eV}$, kE will be an order of magnitude larger than 1.

From the k, we can have an estimation of N_{ts} if we know R_p. For low-energy ion implantation, R_p will deviate from the prediction by standard ion-implantation theory, but can be well described by an empirical formula,[13]

$$R_p=\frac{1.1M_t E^{2/3}}{\rho_t(Z_i^{1/4}+Z_t^{1/4})^2}, \tag{10}$$

where M_t and ρ_t are the atomic weight and mass density of the target element, E is the ion energy in electron volts, Z_i and Z_t are the atomic numbers of the ion and target materials, and R_p is the depth in angstroms. Then N_{ts} can be calculated by knowing k and W_0 for all energies. The results are listed in the first five rows of Table I and are also shown by the dashed line in Fig. 3. The last two rows in Table I show RIE and rf SE results obtained by other groups for comparison.[6,10]

Before discussing the fitting results, we must mention an important effect, i.e., the etch effect in ion-milling experiments. In a process where low-energy Ar ions are used to bombard a substrate, surface Si will be etched away at a rate of several angstrom per second for the present beam voltage and current density.[21] So, a surface Si layer of more than 1000 Å was etched away for the samples treated by ion milling in this experiment; then the subsequently formed M–S interface will shift from the initial surface to a deeper position in the substrate. It can be proved that when the etch time is much longer than a characteristic time equal to the damage distribution length divided by the etch rate, the damage concentration near the surface reaches a saturation level. In the present experiments, such a characteristic time is on the order of tens of seconds; 5 min is then long enough for damage concentration to reach such a saturation level. Therefore, our results illustrate a general consequence of ion bombardment. The concentration of ion-milling induced donors is on the

TABLE I. Treatment effects on Schottky diodes. The first five rows show ion-milling influence on PtSi/n-Si Schottky contacts, whereas the last two rows show reactive-ion etching and sputter-etching influence on other Schottky contacts.

E (eV)	$N_{ts}R_p$ (cm^{-2})	R_p (Å)	N_{ts} (cm^{-3})	$\langle\phi_b\rangle$ (meV)	$\frac{N_{ts}R_p^2}{N_D W_0^2}$	$\frac{N_{ts}R_p}{N_D W_0}$
300	1.19×10^{12}	37	3.5×10^{18}	839	0.06	15
500	2.04×10^{12}	53	4.1×10^{18}	825	0.15	24
700	3.19×10^{12}	66	4.6×10^{18}	810	0.25	34
1000	4.69×10^{12}	84	5.2×10^{18}	794	0.46	49
1500	6.01×10^{12}	109	5.9×10^{18}	782	0.88	72
(RIE)[a]	...	...	2.0×10^{19}	...	...	...
0.5–1.5 kV (SE)[b]	...	160	2.5×10^{17}	...	...	...

[a]Reference 6.
[b]Reference 10.

order of $10^{18}\,\text{cm}^{-3}$, which is in the middle of the published RIE and SE data.[6,10] But the results should more essentially illustrate bombardment-induced damage due to the small spread of ion energy in the experiments.

As seen before, the SBH of reference diodes seems to deviate from the above-mentioned model. The cause can be explained as follows. In a usual wafer fabrication process, the wafers should be polished after being cut from an ingot. Mechanical damage is then inevitable near the surface region of the wafers. This damage or defects may also be electrically active. On the other hand, there is possible contamination at the surface, which will also lower SBH when a metal is contacted. As previously pointed out, in an ion-milling process, a surface Si layer with those defects will be removed by the etch effect, and the final M–S interface will shift to a deeper position in the substrate, where the crystal quality is better than that at the surface. So, it is not surprising that the SBH of a 300 eV ion-milled sample is higher than the SBH of a reference because the removal of the existing defects is possibly more than the introduction of the new defects. In a recent study on the rf sputter treatment effect on Pd/n-Si Schottky diodes, Deenapanray, Auret, and Myburg observed an analogous phenomenon — nonmonotonic variation of SBH with treatment time.[22] A similar explanation was proposed by them.

Now we can reexamine the validity for neglecting the $kE(R_p/W_0)$ term in Eq. (7). The term is equivalently written as $N_{ts}R_p^2/N_D W_0^2$ in Table I, and kE is equivalently written as $N_{ts}R_p/N_D W_0$ in the table. From Table I, one can see that $N_{ts}R_p^2/N_D W_0^2$ is always much smaller than $N_{ts}R_p/N_D W_0$. As previously known, for ion energy higher than 200 eV, $(N_{ts}R_p/N_D W_0)$ is an order of magnitude larger than 1. But for ion energy lower than 200 eV, $N_{ts}R_p/N_D W_0$ will decrease to be more and more comparable to 1. So, in Eq. (7), the $N_{ts}R_p^2/N_D W_0^2$ term can always be neglected while 1 can be neglected only for $E > 200\,\text{eV}$. So the term 1 is retained in Eq. (8), to hold the comprehensiveness of the model.

Finally it should be noted that in the preceding discussion we have not considered possible diffusion of defects, for example, in a RTA process. So, even if Eq. (10) accurately describes the damage penetration in as-treated substrates, the real penetration depth of the defects is difficult to know. From Eqs. (8) and (9), which essentially depend on the $N_{ts}R_p$ product, one can see that the $N_{ts}R_p$ product should be more meaningful than N_{ts} itself. It should also be noted that the present model does not include the tunneling effect, which may have an appreciable effect when donor concentration is very high. But after inclusion of image-force lowering in conduction-band bending, the electrical field near the band maximum does not change as drastically with donor concentration as the case where no image-force lowering is considered, so the tunneling effect should be diminished in a real M–S contact.

IV. CONCLUSION

Physical damage effects on PtSi/n-Si Schottky contacts introduced by an ion-milling process have been studied by BEEM. Ion bombardment on a semiconductor results in a thin surface layer with positive charges or donorlike defects, which increases the surface field and reduces the effective SBH. A simple SBH model is developed to relate the effective SBH with ion-bombardment energy. The model predicts the decrease of SBH with ion energy in a square-root relationship, which successfully explains the relation between the mean SBH obtained by BEEM and ion energy. In addition, the model deduces an intrinsic SBH of 887 meV for the PtSi/n-Si contact and defect concentration on the order of $10^{18}\,\text{cm}^{-3}$ for energetic Ar ion (300–1500 eV) bombardment.

ACKNOWLEDGMENTS

This work is supported by a bilateral cooperation project Bil No. 96/74/B017 from the Flemish Ministry of Science and Technology and the Ministry of Science and Technology of China, and, in part, by Natural Science Foundation of China NSFC-69776005. The authors would like to thank L. Van Meirhaeghe for his technical support. C.D. thanks the "Fonds voor Wetenschappelijk Onderzoek—Vlaanderen" for a scholarship.

APPENDIX

With depletion approximation and continuity conditions, the electrical field in the depletion region can be written as

$$|F(x)|=\begin{cases}\frac{qN_D}{\epsilon_0\epsilon_r}(W-x) & R_p\leq x\leq W\\ \frac{q}{\epsilon_0\epsilon_r}[N_D(W-R_p)+(N_{ts}+N_D)(R_p-x)] & \\ =\frac{q}{\epsilon_0\epsilon_r}[N_D(W-x)+N_{ts}(R_p-x)] & \\ 0\leq x<R_p. & \end{cases} \quad \text{(A1)}$$

The surface field F_s can be written as

$$F_s=|F(0)|=\frac{q}{\epsilon_0\epsilon_r}(N_DW+N_{ts}R_p). \quad \text{(A2)}$$

The potential in the depletion region can be written as

$$|V(x)| =\begin{cases}\frac{qN_D}{2\epsilon_0\epsilon_r}(W-x)^2 & R_p\leq x\leq W\\ \frac{1}{2}|F(R_p)|(W-R_p)+\frac{1}{2}[|F(R_p)|+|F(x)|] & \\ \times(R_p-x)=\frac{1}{2}|F(R_p)|(W-x)+\frac{1}{2}|F(x)| & \\ \times(R_p-x) \quad 0\leq x<R_p. & \end{cases} \quad \text{(A3)}$$

Then the surface potential or band bending can be written as

$$\begin{aligned}V_s&=|V(0)|\\ &=\tfrac{1}{2}|F(R_p)|W+\tfrac{1}{2}|F(0)|R_p\\ &=\frac{q}{2\epsilon_0\epsilon_r}[N_D(W-R_p)W+(N_DW+N_{ts}R_p)R_p]\\ &=\frac{q}{2\epsilon_0\epsilon_r}[N_D(W-R_p)W+(N_DW+N_{ts}R_p)R_p]\\ &=\frac{q}{2\epsilon_0\epsilon_r}(N_DW^2+N_{ts}R_p^2).\end{aligned} \quad \text{(A4)}$$

[1]S. J. Fonash, J. Electrochem. Soc. **137**, 3885 (1990).
[2]A. Singh, Microelectron. J. **18**, 13 (1987).
[3]M. Ostling, C. S. Petersson, H. Norstrom, R. Buchta, and H.-O. Bolm, J. Vac. Sci. Technol. B **5**, 586 (1987).
[4]S. Ashok, T. P. Chow, and B. J. Baliga, Appl. Phys. Lett. **42**, 687 (1983).
[5]F. K. Moghadam and X. C. Mu, IEEE Trans. Electron Devices **ED-36**, 1602 (1989).
[6]A. Murata, M. Nakamura, A. Asai, and I. Taniguchi, IEICE Trans. Electron. **75-C**, 990 (1992).
[7]D. K. Hwang, J. Ruzyllo, and E. Kamieniecki, Electrochemical Soc. Proc. **95-20**, 184 (1995).
[8]K.-H. Kwon, H.-H. Park, K.-S. Kim, C.-I. Kim, and Y.-K. Sung, Jpn. J. Appl. Phys., Part 1 **35**, 1611 (1996).
[9]J. G. Couillard, A. Davies, and H. G. Craighead, J. Vac. Sci. Technol. B **10**, 3112 (1992).
[10]E. Grusell, S. Berg, and L. P. Andersson, J. Electrochem. Soc. **127**, 1573 (1980).
[11]L. Quattropani, K. Solt, P. Niedermann, I. M.-Aprile, O. Fischer, and T. Pavelka, Appl. Surf. Sci. **70/71**, 391 (1993).
[12]A. Climent and S. J. Fonash, J. Appl. Phys. **56**, 1063 (1984).
[13]J. M. E. Harper, J. J. Cuomo, and H. R. Kaufman, J. Vac. Sci. Technol. **21**, 737 (1982).
[14]H. R. Kaufman, J. Vac. Sci. Technol. **15**, 272 (1978).
[15]G.-P. Ru *et al.*, Mater. Res. Soc. Symp. Proc. **564**, 201 (1999).
[16]R. A. Donaton, S. Jin, H. Bender, M. Zagrebnov, K. Baert, K. Maex, A. Vantomme, and G. Langouche, Microelectron. Eng. **37/38**, 507 (1997).
[17]L. D. Bell and W. J. Kaiser, Phys. Rev. Lett. **61**, 2368 (1988).
[18]J. M. Shannon, Appl. Phys. Lett. **24**, 369 (1974).
[19]T. E. Seidel, in *VLSI Technology*, edited by S. M. Sze (McGraw–Hill, Auckland, 1983), p. 237.
[20]E. H. Rhoderick and R. H. Williams, *Metal-Semiconductor Contacts*, 2nd ed. (Clarendon, Oxford, 1988), p. 36.
[21]B. Chapman, *Glow Discharge Processes: Sputtering and Plasma Etching* (Wiley, New York, 1980), p. 395. For example, sputtering yield of Ar on Si is 0.31 at 300 eV, which leads to an etch rate of 4 Å/s.
[22]P. N. K. Deenapanray, F. D. Auret, and G. Myburg, J. Vac. Sci. Technol. B **16**, 1873 (1998).

Effect of ramp rate on the C49 to C54 titanium disilicide phase transformation from Ti and Ti(Ta)

Paul Martin Smith[a] and Glenn Bailey
Sandia National Laboratories, Albuquerque, New Mexico 87185

Yao Zhi Hu and Sing Pin Tay
Steag RTP Systems Inc., 4425 Fortran Drive, San Jose, California 95134

(Received 6 October 1999; accepted 12 May 2000)

The C49 to C54 $TiSi_2$ transformation temperature is shown to be reduced by increasing the ramp rate during rapid thermal processing and this effect is more pronounced for thinner initial Ti and Ti(Ta) films. Experiments were performed on blanket wafers and on wafers that had patterned polycrystalline Si lines with Si_3N_4 sidewall spacers. Changing the ramp rate caused no change in the transformation temperature for 60 nm blanket Ti films. For blanket Ti films of 25 or 40 nm, however, increasing the ramp rate from 7 to 180 °C/s decreased the transformation temperature by 15 °C. Studies of patterned lines indicate that sheet resistance of narrow lines is reduced by increased ramp rates for both Ti and Ti(Ta) films, especially as the linewidths decrease below 0.4 μm. This improvement is particularly pronounced for the thinnest Ti(Ta) films, which exhibited almost no linewidth effect after being annealed with a ramp rate of 75 °C/s. © *2000 American Vacuum Society.* [S0734-211X(00)05104-0]

I. INTRODUCTION

Self-aligned titanium silicide (Ti-salicide) has been used for many generations of ultralarge scale integration devices because of its temperature stability and low resistivity.[1,2] Unfortunately, reliably producing low resistivity $TiSi_2$ on lines narrower than ≈0.3 μm is difficult.[1,3–5] If Ti-salicide is to remain a viable technology for ULSI applications, techniques must be found that overcome this difficulty. Toward that end, we show that the ramp rate used for Ti-salicide processing is an important parameter for controlling this linewidth effect.

Titanium disilicide is a polymorphic material that may exist as the C49 phase or as the thermodynamically favored C54 phase.[6] During annealing of thin Ti films in contact with Si the first $TiSi_2$ phase to form is C49, which forms above 500 °C, is metastable, and has a high resistivity (40–90 $\mu\Omega$ cm). Upon continued heating to over 700 °C the C49 transforms to C54, which is stable and has a low resistivity (15–20 $\mu\Omega$ cm).[2,4,6,7] The activation energy for this transformation is ⩾3.7 eV.[6–8]

Typical Ti-salicide processing[2,9] consists of depositing a Ti film on a patterned wafer with regions of exposed Si in a field of dielectric material, typically SiO_2 or Si_3N_4. A rapid thermal process (RTP) is performed at a relatively low temperature, about 700 °C, to react the Ti and exposed Si to form C49 $TiSi_2$ while the remaining Ti is unreacted. This RTP is done in a N_2 ambient, which creates a thin TiN layer over the entire wafer. The low RTP temperature and TiN prevent bridging, or electrical shorting, by reducing lateral Si diffusion.[2] A wet etch is then used to selectively remove only the TiN and unreacted Ti. A second RTP is performed at a relatively high temperature, about 850 °C, to transform the C49 into the desired C54 $TiSi_2$ phase. Thermal budget issues and $TiSi_2$ agglomeration[2,3] limit the temperature of this RTP.

Previous work has shown that the C54 $TiSi_2$ phase selectively nucleates in thin films of C49 $TiSi_2$ at a grain edge (where three grains meet).[10] Once the linewidth shrinks below the size of an average C49 grain (i.e., bamboo structure), grain edges are rare and nucleation of the C54 phase is significantly reduced.[1] This problem is further aggravated by the fact that typical Ti-salicide thicknesses are also decreasing and the problem is actually caused by the limited volume of $TiSi_2$ material being transformed. In order to extend Ti-salicide manufacturing to deep submicron applications there have been many studies of the C49 to C54 transformation.[3–16] The transformation temperature has been shown to be a function of film thickness,[6,17] C49 grain size,[12] dopants in the Si,[3] and other factors. The transformation temperature is reduced by small quantities of refractory metal, such as Mo, Ta, Nb, or W, introduced at or near the Ti/Si interface.[5,7,11,13] Earlier work also showed that the C49 grain size of blanket Ti films on ⟨100⟩ Si can be reduced, and the transformation temperature lowered, by increasing the ramp rate of the first RTP.[12] More recent work showed that higher ramp rates result in lower sheet resistance for deep submicron lines.[14] In this paper we report on varying the as-deposited Ti or Ti(Ta) film thicknesses and ramp rates during RTP of blanket films and patterned lines. The C49 to C54 transformation temperature is reduced by increasing the as-deposited film thickness and by increasing the RTP ramp rate.

II. EXPERIMENT

Blanket samples were prepared by sputtering nominally 25, 40, or 60 nm Ti films onto 300 nm of undoped polycrystalline Si (poly-Si). The poly-Si was deposited on a 12.5 nm

[a]Electronic mail: smithpm@sandia.gov

grown oxide and these substrates were annealed at 600 °C for 60 min and 900 °C for 30 min to fully crystallize the poly-Si and reduce film stress prior to Ti deposition. All of the sputter depositions in this study, on both blanket and patterned samples, were performed with no sputter etch. RTP of the blanket samples was carried out at temperatures ranging from 300 to 1000 °C with ramp rates of 7, 30, 70, and 180 °C/s. The sheet resistance of the as-deposited films and the silicided films were measured by four-point probe. Our definition of the transformation temperature, T_{TR}, follows Lin and Pramanik,[15] and is defined as the temperature where a linear fit to the sheet resistance in the C49 to C54 transformation region intersects a linear fit to the sheet resistance in the C54 region.

Patterned samples of electrically isolated, Ti-salicided lines designed to maximize the linewidth effect were produced on 150 mm Si ⟨100⟩ wafers. The processing started with a 12.5 nm grown thermal oxide followed by 300 nm of deposited poly-Si. The poly-Si was implanted with 8×10^{15} As/cm^2 at 120 keV, capped with 500 nm of deposited oxide, and annealed at 1100 °C in N_2 for 180 min to activate the implant and reduce film stress. The oxide was stripped and the poly-Si was patterned to linewidths of 0.27 μm and greater, as measured by scanning electron microscopy (SEM) after the processing was complete. A 180 nm Si_3N_4 film was deposited on the samples and etched back to form sidewall spacers. The wafers were cleaned in 5:1 H_2SO_4:H_2O_2 for 5 min, SC-1 for 10 min, SC-2 for 5 min, and 30:1 buffered oxide etch for 1 min immediately prior to Ti or Ti(Ta) deposition. The nominally 40 nm Ti film was sputter deposited. The nominally 25 and 40 nm Ti(Ta) films were sputtered from a Ti(Ta) target that was produced by evaporating 300 nm of Ta onto the erosion zone of a pure Ti sputter target. The Ta was evaporated onto the Ti target through a patterned shield and the resulting Ti(Ta) target produced approximately 100 nm of sputtered Ti(Ta) material (≈4 at. % Ta in Ti) before all the Ta was eroded from the sputter target. Approximately 10 nm of material was deposited from the Ti(Ta) target onto a dummy wafer to clean the target and then the 25 and 40 nm of Ti(Ta) was deposited onto the patterned wafers. The composition of the Ti(Ta) was determined by Rutherford backscattering spectrometry on a similarly produced film. The as-deposited sheet resistance of the films was ≈19 Ω/sq for the 40 nm Ti film, ≈25 Ω/sq for the 40 nm Ti(Ta) film, and ≈36 Ω/sq for the 25 nm Ti(Ta) film. The patterned wafers were diced into samples and annealed in a RTP system at 700 °C for 20 s with ramp rates of 5, 30, and 75 °C/s for the Ti film and 30 and 75 °C/s for the Ti(Ta) films. The samples were then etched in SC-1 to remove any TiN and unreacted Ti and the samples were annealed at 850 °C for 30 s with a ramp rate of 30 °C/s.

III. RESULTS AND DISCUSSION

A. Blanket Ti samples

Figure 1 shows sheet resistance versus RTP temperature for the 25, 40, and 60 nm blanket Ti films annealed from 300 to 1000 °C with a ramp rate of 70 °C/s. There are three dis-

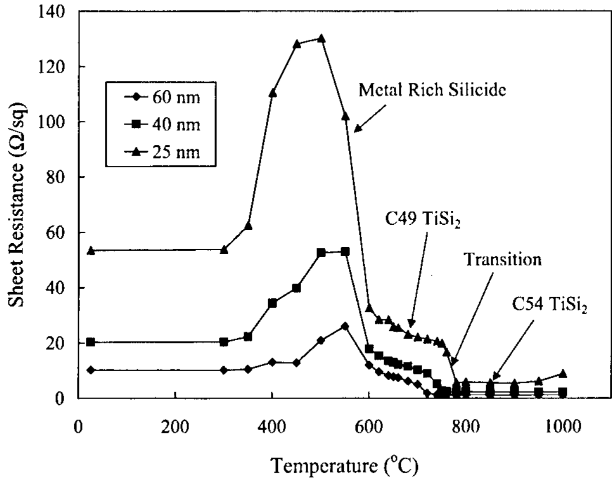

FIG. 1. Sheet resistance as a function of RTP temperature for 25, 40, and 60 nm Ti films on poly-Si. These samples were processed with a ramp rate of 70 °C/s. T_{TR} is the temperature where linear fits to the sheet resistance in the transition region and the C54 region intersect.

tinct transitions for all three thicknesses. The first transition, with increasing temperature, is a resistivity increase that occurs above 300 °C and probably corresponds to the formation of a metal-rich silicide.[18] The second transition corresponds to the C49 formation and occurs by 620 °C in all three cases. The gradual decrease in resistivity between the second and third transitions is probably due to grain coarsening of the C49 phase. The third transition corresponds to the transformation from C49 to C54 and always occurs within a ≈30 °C temperature window, although the window shifts higher in temperature as the Ti film thickness decreases. Once the third transition is complete, at temperature T_{TR}, the resistivity remains stable until agglomeration begins. Note that the thinnest Ti film has both the highest transformation temperature and the lowest agglomeration temperature. This provides a good illustration of why the Ti-salicide process window is narrowing as device geometries decrease.

Blanket samples with Ti thicknesses of 25, 40, and 60 nm were annealed for 20 s at temperatures from 620 to 840 °C with ramp rates of 7, 30, and 180 °C/s. Figure 2 shows the sheet resistances versus RTP temperatures for the 25 and 60 nm blanket Ti films. It is obvious that the transformation temperature of the 60 nm Ti film is not affected by increasing the ramp rate, while the transformation temperature of the 25 nm Ti film is monatonically reduced by increasing the ramp rate. The transformation temperatures, T_{TR}, for all the blanket films are plotted in Fig. 3 as a function of nominal Ti film thicknesses. In all cases, the transformation temperature increased by at least 50 °C as the thickness decreased from 60 to 25 nm. Changing the ramp rate did not significantly affect T_{TR} for the 60 nm Ti films. For the 40 and 25 nm Ti films, however, T_{TR} was reduced by 15 °C as the ramp rate was increased from 7 to 180 °C. This clearly shows that increasing the ramp rate partially compensates for the increase in T_{TR} that occurs as the film thickness decreases. Because the C54 $TiSi_2$ phase is thermodynamically stable, we can be certain that the resistivity increase seen at slower ramp rates

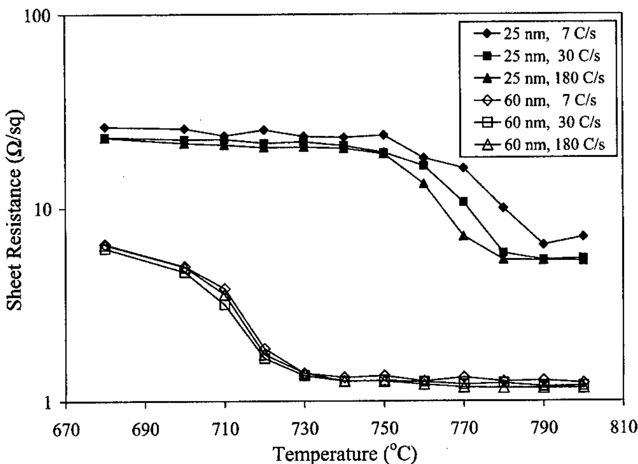

FIG. 2. Sheet resistance as a function of RTP temperature and ramp rate for 60 and 25 nm blanket Ti films on poly-Si. The 70 °C/s data have been omitted for clarity. It is obvious that the ramp rate affects T_{TR} of the 25 nm Ti film but not T_{TR} of the 60 nm film.

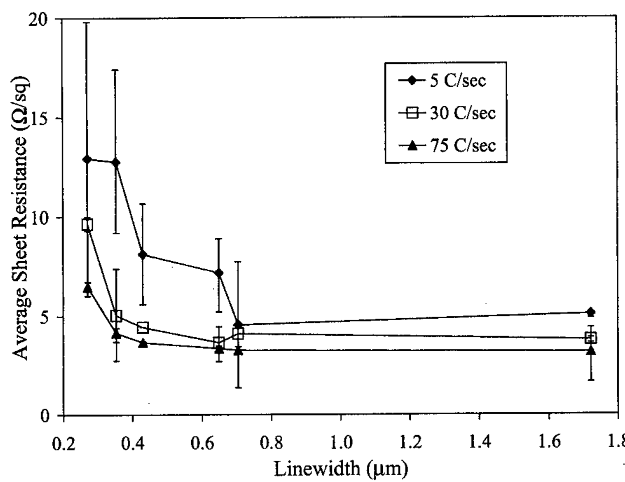

FIG. 4. Sheet resistance vs patterned linewidth of a 40 nm, as-deposited, Ti film after processing at various ramp rates. The error bars indicate the minimum and maximum values of the measured data. It is obvious that the linewidth effect is monotonically reduced by increasing the ramp rate.

is not caused by any effective increase in the time at temperature. Also, because the resistivity increase does not persist to temperatures above the transformation, it could not be produced by agglomeration or other structural changes to the film.

B. Patterned Ti and Ti(Ta) samples

Figure 4 shows sheet resistance as a function of linewidth and ramp rate for the patterned samples with 40 nm Ti. Each data point is an average of two or four measurements and the error bars indicate the maximum and minimum data values. As expected, the sheet resistance increases as the lines narrow, indicating that the transformation is being inhibited by the volume reduction. With a ramp rate of 5 °C/s there is already a significant increase by 0.6 μm and the sheet resistance increases by a factor of ≈2.4× at the minimum linewidth. As the ramp rate increases the linewidth effect progressively decreases. The sheet resistance increase observed for the sample with the 75 °C/s ramp rate was only ≈10% at 0.4 μm and only a factor of ≈1.8× at the minimum linewidth of 0.27 μm.

For the 40 nm Ti(Ta) film, there was no observed linewidth effect. Because this effect is clearly seen for the 40 nm Ti film, the difference is attributed to the ≈4 at. % Ta in the film, which agrees with previously published findings.[6,13] Figure 5 shows the sheet resistance as a function of linewidth and ramp rate for the patterned samples with 25 nm Ti(Ta) films. As in Fig. 4, each data point is an average of two or four measurements and the error bars indicate the maximum and minimum data values. There is an obvious reduction in the linewidth effect due to the increased ramp rate. With a ramp rate of 30 °C/s there is an increase in sheet resistance at 0.7 μm that continues to grow with decreasing linewidth

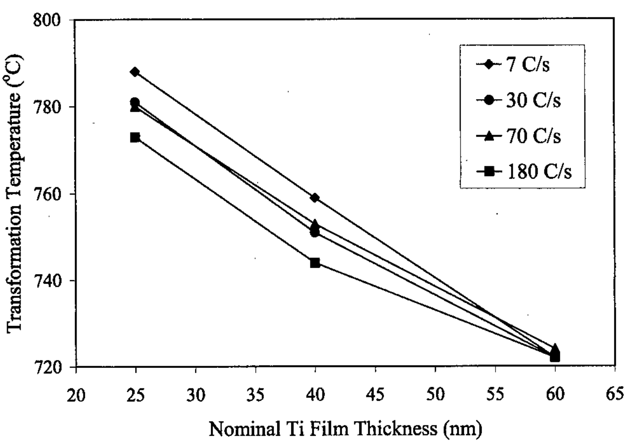

FIG. 3. Transformation temperature, T_{TR}, as a function of nominal, as-deposited, Ti film thickness. Although the transformation temperature always increases with reduced film thickness, increasing the RTP ramp rate minimizes this effect.

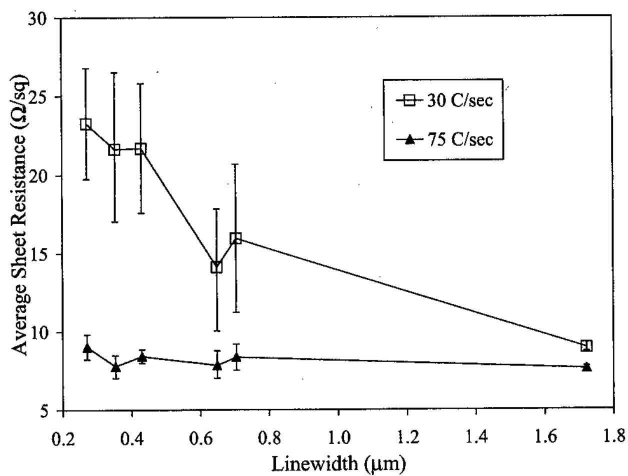

FIG. 5. Sheet resistance vs patterned linewidth of a 25 nm, as-deposited, Ti(≈4 at. % Ta) film after processing at various ramp rates. The error bars indicate the minimum and maximum values of the measured data. The linewidth effect is virtually eliminated by increasing the ramp rate to 75 °C/s.

until it has increased by a factor of ≈2.1× at the minimum linewidth. In sharp contrast, increasing the ramp rate to 75 °C/s has essentially eliminated the linewidth effect and there is only a ≈10% increase in the sheet resistance even at the minimum linewidth.

IV. CONCLUSIONS

This work has shown that the C49 to C54 $TiSi_2$ transformation temperature is increased by reducing the initial Ti film thickness and reduced by increasing the RTP ramp rate. This effect was observed for Ti and Ti(Ta) films. The transformation temperature increased by at least 50 °C for blanket Ti films, from ≈ 720 to over 770 °C, when the film thickness decreased from 60 to 25 nm. The effect of ramp rate on the transformation temperature was strongly affected by the initial film thickness. Varying the ramp rate caused no change in the transformation temperature for the 60 nm blanket Ti films. For blanket films of 25 or 40 nm, however, increasing the ramp rate from 7 to 180 °C/s decreased the transformation temperature by 15 °C. Studies of patterned lines indicate that sheet resistance of narrow lines is also reduced by increased ramp rates for both Ti and Ti(Ta) films, especially as the linewidths decrease below 0.4 μm. This improvement is particularly pronounced for the 25 nm Ti(Ta) film, which exhibited virtually no linewidth effect to below 0.3 μm after being annealed with a 75 °C/s ramp rate. This result may be of significant technological importance as critical dimensions for semiconductor devices continue to decrease.

ACKNOWLEDGMENTS

The authors would like to thank the personnel at Sandia's Microelectronics Development Laboratory (MDL) for wafer processing. Pat Shea produced SEM micrographs for this work. Sandia is a multiprogram laboratory operated by Sandia Corporation, a Lockheed Martin Company, for the United States Department of Energy under Contract No. DE-AC04-94AL85000.

[1]Q. Z. Hong, J. A. Kittl, and M. S. Rodder, in *Advanced Metallization for ULSI Applications in 1995*, edited by R. C. Ellwanger and S.-Q. Wang (Materials Research Society, Pittsburgh, PA, 1996), pp. 431–438.

[2]E. G. Colgan, J. P. Gambino, and Q. Z. Hong, Mater. Sci. Eng., **RA16**, 43 (1996).

[3]E. Ganin, S. Wind, P. Ronsheim, A. Yapsir, K. Barmak, J. Bucchignano, and R. Assenza, in *Rapid Thermal and Integrated Processing II*, edited by J. C. Gelpey *et al.* [Mater. Res. Soc. Symp. Proc. **303**, 109 (1993)].

[4]L. A. Clevenger *et al.*, J. Mater. Res. **10**, 2355 (1995).

[5]C. Cabral, Jr. *et al.*, in *Advanced Metallization and Interconnect Systems for ULSI Applications in 1997*, edited by R. Cheung, J. Klein, K. Tsubouchi, M. Murakami, and N. Kobayashi (Materials Research Society, Warrendale, PA, 1998), p. 557.

[6]Z. Ma and L. H. Allen, Phys. Rev. B **49**, 13501 (1994).

[7]R. W. Mann, G. L. Miles, T. A. Knotts, D. W. Rakowski, L. A. Clevenger, J. M. E. Harper, F. M. D'Heurle, and C. Cabral, Appl. Phys. Lett. **67**, 3729 (1995).

[8]R. W. Mann, L. A. Clevenger, and Q. Z. Hong, J. Appl. Phys. **73**, 3566 (1993).

[9]Q. Xu and C. Hu, IEEE Trans. Electron Devices **45**, 2002 (1998).

[10]Z. Ma, L. H. Allen, and D. D. J. Allman, Thin Solid Films **253**, 451 (1994).

[11]C. Cabral, Jr., L. A. Clevenger, J. M. E. Harper, F. M. d'Heurle, R. A. Roy, K. L. Saenger, G. L. Miles, and R. W. Mann, J. Mater. Res. **12**, 304 (1997).

[12]H. J. W. van Houtum, I. J. M. M. Raaijmakers, and T. J. M. Menting, J. Appl. Phys. **61**, 3116 (1987).

[13]C. Cabral, Jr. *et al.*, Appl. Phys. Lett. **71**, 3531 (1997).

[14]C. C. D. Tan, L. Lu, A. See, S. Y. Chen, L. H. Chua, K. L. T. Chan, and L. Chan, presented at the First International Conference on Advanced Materials and Processes for Microelectronics, San Jose, CA, 15–19 March 1999 (unpublished).

[15]X. W. Lin and D. Promanik, in *Rapid Thermal and Integrated Processing V*, edited by J. C. Gelpey, M. C. Ozturk, R. P. S. Thakur, A. T. Fiory, and F. Roozeboom [Mater. Res. Soc. Symp. Proc. **429**, 181 (1996)].

[16]I. De Wolf, D. J. Howard, A. Lauwers, K. Maex, and H. E. Maes, Appl. Phys. Lett. **70**, 2262 (1997).

[17]H. J. W. van Houtum and I. J. M. M. Raaijmakers, in *Interfaces and Phenomena*, edited by R. J. Nemanich, P. S. Ho, and S. S. Lau [Mater. Res. Soc. Symp. Proc. **54**, 31 (1986)].

[18]S. P. Murarka, *Silicides for VLSI Applications* (Academic, New York, 1983), Chap. 4.

Mosaic structure of various oriented grains in $CoSi_2$/Si(001)

Tae Soo Kang and Jung Ho Je[a)]
Department of Materials Science and Engineering, POSTECH, Pohang 790-784, Korea

Gi Bum Kim and Hong Koo Baik
Department of Metallurgical Engineering, Yonsei University, Seoul, Korea

Sung-Man Lee
Department of Materials Engineering, Kangwon National University, Chunchon, Korea

(Received 24 November 1999; accepted 21 April 2000)

We investigated the mosaic structure of $CoSi_2$/Si(001) film in a synchrotron x-ray scattering experiment. The $CoSi_2$ film, formed by thermal reaction of a 120 Å Co film on Si(001), was composed largely of epitaxial grains of various orientations. In particular, the twin oriented (B-type) $CoSi_2$(111) grains were grown epitaxially on the Si{111} facets that were generated during annealing. Two distinct mosaic structures were observed in the $CoSi_2$ grains; the epitaxial grains of the same orientation with the Si substrate, such as the $CoSi_2$(001) [the $CoSi_2$(111)] grains lying on the Si(001) [the Si{111} facets], showed a small mosaicity of ~0.5° full width at half maximum (FWHM), while those of different orientations demonstrated a rather broad mosaicity of ~2.5° FWHM. We attributed the smaller mosaicity of the epitaxial grains of the same orientation to the reduced interfacial energy due to higher coincidence site density. © *2000 American Vacuum Society.* [S0734-2101(00)03404-7]

I. INTRODUCTION

Metal silicide is presently of interest as a metallic component in ultralarge scale integration (ULSI) because of its low electrical resistivity of 15–20 $\mu\Omega$ cm.[1] In particular, for the fabrication of shallow junctions in ULSI, it is very important for silicide layer to have flat interface and high thermal stability. For that reason, epitaxial $CoSi_2$ is a good candidate of metallic components in ULSI due to its smooth interface and high thermal stability.[2]

Considering the similarity of the crystal structure and the small lattice mismatch between Si and $CoSi_2$, we expect the epitaxial growth of $CoSi_2$(001) layer of Si(001). In reality, it is difficult to grow single-crystalline $CoSi_2$(001) layer on Si(001), mostly due to the concurrent growth of epitaxial $CoSi_2$(011) and $CoSi_2$(122) grains,[3] which have different orientations and large lattice mismatches with Si(001). The $CoSi_2$ films grown by deposition of Co along on Si(001) substrates are commonly found to consistent of grains with various orientations. The extended domain matching (EDM) that forms superlattices by taking larger unit cells for lattice matching explains the epitaxial growth of these grains of large lattice mismatch.[4] Lattice match in EDM is a very similar idea to the concept of coincidence site density in high angle grain boundaries.[5] Here we note that the coincidence site density of EDM grains is much lower than that of one-to-one matching system such as $CoSi_2$(001)/Si(001). This means that the interfacial energy of EDM grains might be higher than that of one-to-one matching grains.

Considerable interest has been directed toward growth of epitaxial films of high quality, i.e., of low mosaicity. Many studies on $CoSi_2$ films were focused on the microstructure affected by various factors, such as annealing temperature, starting surface topography,[6] existence of diffusion barrier,[7] growth technique,[8] etc. The mosaic structure of epitaxial $CoSi_2$ grains, however, has not been studied well, especially in reference to epitaxial relationship.

In this article we present a synchrotron x-ray scattering study of the mosaic structure of various oriented $CoSi_2$ grains on Si(001) substrate. High flux synchrotron x rays are one of the best probes for structural characterization of thin films. Our study demonstrated that there existed two distinct mosaic distributions; the grains with the same orientation as Si showed low mosaic distributions, compared with those of different orientations. We attributed the better epitaxial quality of the grains with the same orientation to the reduced interfacial energy by higher coincidence site density.

II. EXPERIMENTAL PROCEDURES

$CoSi_2$ film was formed by thermal reaction of a 120 Å Co film on Si(001). The substrate used in this study was *p*-type Si(001) wafer with resistivity of 13–15 Ω cm. After a standard cleaning process, the Si substrate was dipped in a diluted HF solution prior to being loaded into an evaporator with a base pressure of 1×10^{-6} Torr, and then 120 Å Co was deposited on the substrate. To form $CoSi_2$ layer, the sample was annealed in 600 °C in forming ambient (N_2+12%H_2) for 30 min.

To examine the microstructure of $CoSi_2$/Si(001) film, we performed x-ray measurements. The synchrotron x-ray scattering experiments were carried out at beamline 5C2 at Pohang Light Source (PLS) in Korea. The incident x rays were vertically focused by a mirror, and monochromatized to the wavelength of 1.447 Å by a double bounce Si(111) monochromator. The monochromator also focused the x rays in

[a)]Author to whom correspondence should be addressed; electronic mail: jhje@postech.ac.kr

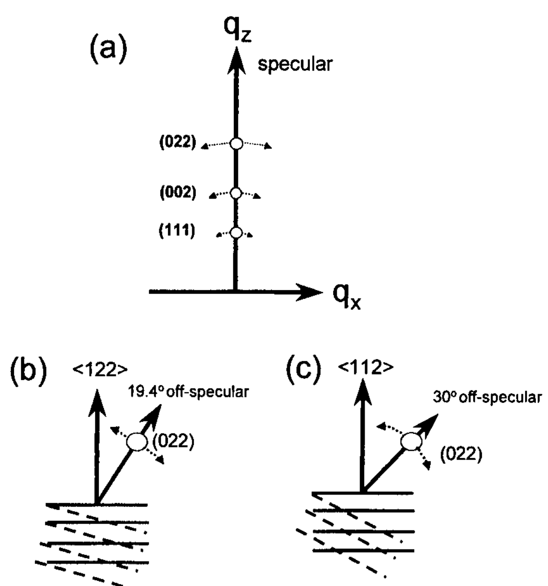

FIG. 1. (a) Scattering geometry used in this experiment. A conventional powder diffraction profile is obtained by measuring the scattering intensity along the specular q_z direction. The schematic diagrams of the inclined (022) planes for (b) the (122) oriented $CoSi_2$ and (c) the (112) oriented $CoSi_2$.

horizontal direction. The momentum transfer resolution was controlled by two pairs of slits on the detector arm, set at 0.001 $Å^{-1}$ in this experiment. To achieve the exact scattering geometry, we employed a four-circle x-ray diffractometer that enabled us to attain arbitrary momentum transfer $\mathbf{q}$ in three-dimensional space. The scattering geometry used in this experiment is illustrated in Fig. 1. The conventional powder diffraction pattern (θ–2θ scan) was obtained scanning along the specular reflection rod q_z. From the diffraction profile along the specular reflection rod, one might obtain the crystal structure and the crystalline orientation of the deposited film. The epitaxial quality in the in-plane and out-of-plane directions was estimated from the rocking curves as described with the dotted lines in Figs. 1(a), 1(b), and 1(c), respectively. Since the angle between the ⟨022⟩ and the ⟨122⟩ is 19.4°, the occurrence of (122)-like reflections in this off-specular direction indicates that the crystalline axis direction in the substrate normal is the ⟨122⟩. Similarly the (112)-like reflection in this 30° off-specular direction indicates that the crystalline axis direction in the substrate normal is the ⟨112⟩, because the angle between the ⟨022⟩ and the ⟨112⟩ is 30°, which are shown in Figs. 1(b) and 1(c). The detailed scattering geometry using a four-circle diffractometer has been well described in Ref. 9.

III. RESULTS AND DISCUSSION

The conventional powder diffraction was measured by varying the momentum transfer q_z along the surface normal to characterize the crystal structure of the $CoSi_2$ film formed at 600 °C from 120 Å Co/Si(001). The powder diffraction pattern shows the $CoSi_2(111)$, the $CoSi_2(002)$, and the $CoSi_2(022)$ Bragg reflections, illustrated in Fig. 2. The intensity ratio of the $CoSi_2(022)$ [$CoSi_2(002)$] to the $CoSi_2(111)$

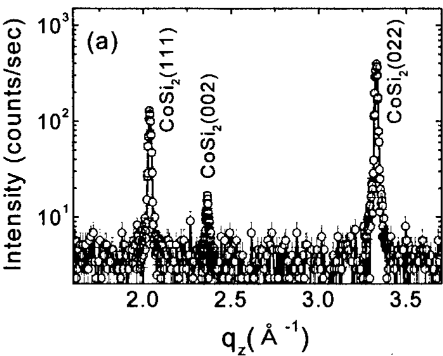

FIG. 2. Powder diffraction profile of the $CoSi_2$/Si(001) film formed from the 120 Å Co/Si(001) by annealing at 600 °C. Note that logarithmic scale was used in y axis to signify the weak scattering feature of the $CoSi_2(002)$ reflection.

reflection was estimated as 3.1 [0.13], about three times higher than those of polycrystalline $CoSi_2[I_{(220)}/I_{(111)} = 1.1, I_{(002)}/I_{(111)} = 0.022$, JCPDS 38-1449]. It follows that the $CoSi_2$ film was grown with the (001) and the (011) preferred orientations in agreement with a previous report.[3]

In fact, the $CoSi_2$ film was composed largely of epitaxial grains of various orientations. To study the epitaxial relationship of the $CoSi_2$ grains, we examined the in-plane orientations of $CoSi_2$ grains relative to those of the Si. The x-ray in-plane measurement (data not shown) revealed that the orientational relationships of the epitaxially grown $CoSi_2(001)$ and $CoSi_2(011)$ grains were $CoSi_2(001)$||Si(001) [$CoSi_2(011)$||Si(011)] and $CoSi_2(011)$||Si(001) [$CoSi_2(100)$||Si(110) with two in-plane rotational variants, respectively, as reported previously.[3] Meanwhile, the in-plane crystalline orientation of the $CoSi_2(111)$ was isotropically distributed, indicating that the $CoSi_2(111)$ grains were not grown epitaxially on the Si(001) substrate. The $CoSi_2(111)$ grains were relatively well aligned in the out-of-plane direction with a mosaic distribution of 3° full width at half maximum (FWHM).

High epitaxial $CoSi_2$ film that has a smooth interface and high thermal stability may be preferable for deep submicron device contacts and lines. It is thus important to know the epitaxial quality, which can be represented by mosaicity. Figures 3(a) and 3(b) show the mosaicity of the $CoSi_2(002)$

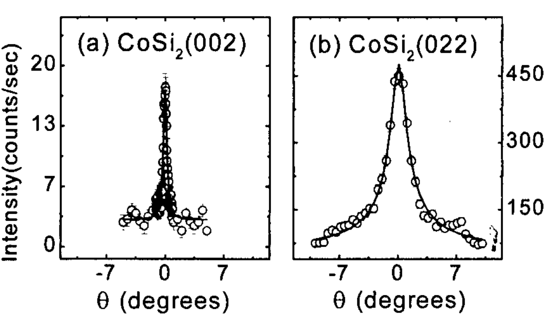

FIG. 3. Rocking curves of (a) the $CoSi_2(002)$ and (b) the $CoSi_2(022)$ Bragg reflections, respectively. The lines are best fit to Gaussian to deduce the width of the reflections.

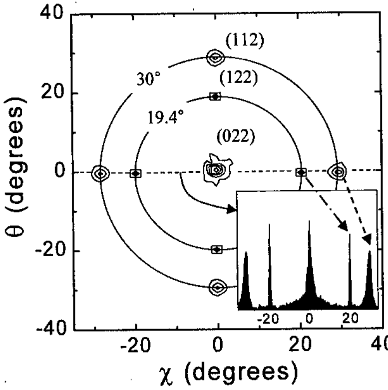

FIG. 4. {011} pole figure of the $CoSi_2$/Si(001) film. Remarkably there were two distinct four-fold reflections of 19.4° and 30° off from the Si⟨001⟩ axis. The well-defined 30° off four reflections indicated that the $CoSi_2$(112) grains were grown epitaxially on the Si(001). The 19.4° off-$CoSi_2$(022) reflections were originated from the $CoSi_2$(111) grains on Si{111} facets. The χ rocking curve of the $CoSi_2$(022) reflection at $q=0°$ is illustrated in the inset.

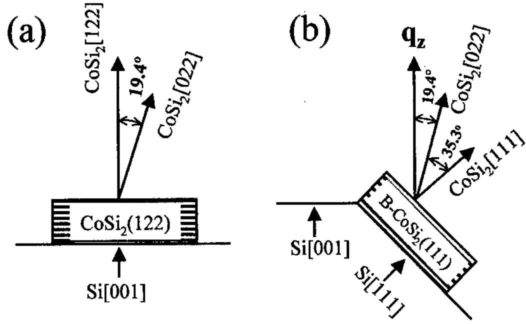

FIG. 5. Schematic illustrations of the possible growth configurations: (a) the growth of the $CoSi_2$(122) on Si(001) and (b) the growth of the $CoSi_2$(111) on Si{111} facets.

and the $CoSi_2$(022) grains. The mosaicity of the $CoSi_2$(002) grains was very small as 0.47° FWHM, compared with that of the $CoSi_2$(011), 2.6° FWHM. The difference of the mosaicity was attributed to the matching relationships of the $CoSi_2$(002)/Si(001) and the $CoSi_2$(022)/Si(001). The $CoSi_2$(002) grains on Si(001) had a one-to-one relationship with a low lattice mismatch of 0.83% at 600 °C. Meanwhile the $CoSi_2$(022)/Si(001) shows EDM wherein 10 Si distance in $CoSi_2$ matches to 7 Si distance in the Si [110] direction.[3] As a result the residual lattice mismatch can be as small as 0.19%, possibly forming the epitaxial (011) grains. Here we note that the coincidence site density of the $CoSi_2$(011)/Si(001) was estimated as ten times higher than that of the $CoSi_2$(011)/Si(001). It was conceivable that high coincidence site density was directly related with low interfacial energy, since the broken or highly distorted bonds between the atoms in the interface were associated with a relatively high energy. Therefore, we attributed the smaller mosaicity or the better alignment of the $CoSi_2$(001) grains to the reduced interfacial energy by higher coincidence site density.

At this point we should not fail to notice the microstructure of the $CoSi_2$ grains with some orientations of which the Bragg reflections are forbidden. The microstructure of the $CoSi_2$ grins with forbidden reflections, such as the $CoSi_2$(112) or the $CoSi_2$(122) grains, can be studied using a {011} pole figure. The x-ray intensities in the {011} zone of the $CoSi_2$ film are plotted in Fig. 4. Remarkably there were two distinct four-fold reflections that were located at 19.4° and 30° off the Si⟨001⟩ axis.

First, we discuss the $CoSi_2$(022) reflections that appeared on the circle 30° off the Si⟨001⟩ axis. Since the angle between the ⟨011⟩ and the ⟨112⟩ is 30°, each pole on the circle was attributed to the $CoSi_2$(112) grains that were grown parallel to the Si(001) planes. The well-defined four reflections indicated that the $CoSi_2$(112) grains were grown epitaxially on the Si(001). From the relative crystallographic directions of the grains and the substrate crystalline axes, we concluded that the epitaxial relationship of the $CoSi_2$(112) grains was $CoSi_2$(112)‖Si(001) [$CoSi_2$(110)‖Si(110)] with two in-plane rotational variants. The mosaicity of the $CoSi_2$(112) grains was rather broad as 2.2° FWHM, similar to that of the $CoSi_2$(011) grains on Si(001), as indicated by the dashed arrow in the inset of Fig. 4. Since the $CoSi_2$(112) grains on Si(001) also showed EDM, wherein 17 Si distance in $CoSi_2$ matches to 14 Si distance in the Si[110] direction, we also attributed the broad mosaicity of the $CoSi_2$(112) grains to the increased interfacial energy by the low coincidence site density.

Back to the $CoSi_2$(022) reflections that appeared on the circle 19.4° off the Si⟨001⟩ axis, two scenarios, schematically illustrated in Figs. 5(a) and 5(b), are possible for the appearance of these reflections. The first is the growth of the $CoSi_2$(122) planes parallel to the Si(001) planes as shown in Fig. 5(a). Since the angle between the ⟨011⟩ and the ⟨122⟩ is 19.4°, the growth of the $CoSi_2$(122) planes parallel to the Si(001) planes makes it possible to generate the 19.4° off-$CoSi_2$(022) reflections as shown in Fig. 4. In this case, the $CoSi_2$(122) grains were matched on Si(001) by EDM and as a result a broad mosaicity was expected due to the low coincidence site density.

The second possibility, shown in Fig. 5(b), is that the $CoSi_2$(111) grains were grown on the Si{111} facets that were generated during the annealing. Since the angle between the $CoSi_2$(011) planes and the $CoSi_2$(111) planes is 35.3° and the angle between the Si(111) planes and the Si(001) planes is 54.7°, and $CoSi_2$(022) reflection can appear at 19.4° off the Si⟨001⟩ axis. In this case, a small mosaicity was expected in the $CoSi_2$(111) grains on the Si{111} facets as a result of its one-to-one matching, similar to the $CoSi_2$(001) grains on the Si(001).

Obviously the mosaicity of the $CoSi_2$ grains that contributed to the 19.4° off-$CoSi_2$(022) reflections, as indicated by the long-dashed dot arrow in the inset of Fig. 4, was relatively small as 0.54° FWHM, similar to that of the $CoSi_2$(001) grains on Si(001). From this result we believed that the 19.4° off-$CoSi_2$(022) reflections were originated from the $CoSi_2$(111) grains grown on the Si{111} facets, i.e., the grains with a one-to-one matching relationship, rather

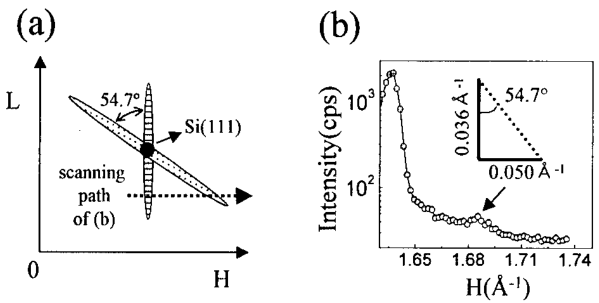

FIG. 6. (a) Schematic diagram of crystal truncation rods of the Si(001) surface and the Si{111} facet in reciprocal space. (b) H scan at $L=1.12$ Å^{-1} near the Si(111) reflection (1.634, 0, 1.156 Å^{-1}). The H direction was defined as the Si⟨110⟩ direction. The peak at $H=1.684$ Å^{-1} indicates that the Si{111} facets were formed during annealing.

than the $CoSi_2(122)$ grains on Si(001). The well-defined four 19.4° off-$CoSi_2(022)$ reflections in Fig. 4 also indicated that the $CoSi_2(111)$ grains were grown epitaxially on the Si{111} facets.

In addition, the existence of the $CoSi_2(022)$ reflections that appeared 19.4° off the Si⟨001⟩ axis clearly demonstrates that the $CoSi_2(111)$ grains were grown with the B-type orientation on the Si{111} facets, since the $CoSi_2(022)$ reflections cannot exist at 19.4° off the Si⟨001⟩ axis for the A-type oriented $CoSi_2(111)$ grains on the Si{111} facets.[10] In fact, the B-type oriented $CoSi_2(111)$ grains are usually grown on the Si(111) substrate.[11]

In silicidation process, it is well known that the Si{111} facets are easily formed and extend over hundreds of angstroms during annealing due to the lower interfacial free energy of the Si(111) plane than that of the Si(001).[12] To confirm the existence of the Si{111} facets in this experiment, we measured the scattering profile of the crystal truncation rods (CTRs) for Si(001) and Si{111} facets. Since the direction of CTR was expanding along the surface normal,[13] the two CTRs were expected to appear 54.7° apart, originated from the Si(001) surface and the Si{111} facets, as illustrated in Fig. 6(a), if the Si{111} facets were generated during the annealing. In Fig. 6(a) the H direction was defined as the Si⟨110⟩ direction. Figure 6(b) shows the scattering profile along the H direction at $L=1.12$ Å^{-1}, below the reciprocal point of the off-specular Si(111) reflection (1.634, 0, 1.156 Å^{-1}). There clearly appeared two peaks at $H=1.634$ Å^{-1} and $H=1.684$ Å^{-1}. Of course, the peak at $H=1.634$ Å^{-1} was originated from the CTR for the Si(001) surface. Another peak $H=1.684$ Å^{-1}, indicated by an arrow, was located at $\Delta H=0.050$ Å^{-1} and $\Delta L=0.036$ Å^{-1} from the reciprocal point of the off-specular Si(111), as shown in Fig. 6(b). It follows that the peak at $H=1.684$ Å^{-1} was placed 54.7° away from the CTR for the Si(001) surface. This immediately indicated that the peak at $H=1.684$ Å^{-1} was originated from the CTR for the Si{111} facets. Considering their surface area, it was conceivable that the scattering intensity of the CTR for the Si{111} facets was very weak compared with that for Si(001). In this way, we confirmed that the Si{111} facets was actually formed during the silicidation in this experiment.

IV. CONCLUSION

In summary, we investigated the mosaic structure of $CoSi_2$/Si(001) film using a synchrotron x-ray scattering experiment. The $CoSi_2$ film, formed by thermal reaction of a 120 Å Co film on Si(001), was composed largely of epitaxial grains of various orientations. In particular, the twin oriented (B-type) $CoSi_2(111)$ grains were grown epitaxially on the Si{111} facets that were generated during annealing.

Two distinct mosaic structures were observed in the $CoSi_2$ grains. The epitaxial grains of the same orientation with the Si substrate, such as the $CoSi_2(002)$ [the $CoSi_2(111)$] grains lying on Si(001) [Si{111} facets], showed a small mosaicity of ~0.5° FWHM. In the meanwhile those of different orientations, such as the $CoSi_2(022)$ and the $CoSi_2(112)$ grains lying on Si(001), demonstrated a rather broad mosaicity of ~2.5° FWHM. We attributed the smaller mosaicity of the epitaxial grains of the same orientation to the reduced interfacial energy by higher coincidence site density. This result might be applicable to a number of other epitaxial silicides which have the matching face relationships between the particular face of silicides and Si substrate.[14,15]

ACKNOWLEDGMENTS

The authors wish to acknowledge the financial support of the Korean Research Foundation made in the program year of 1998. PLS is supported by Korean Ministry of Science and Technology.

[1]S. P. Murarka, *Silicides for VLSI Applications* (Academic, New York, 1983).
[2]S. L. Hsia, T. Y. Tan, P. Smith, and G. E. McGuire, J. Appl. Phys. **70**, 7579 (1991).
[3]C. W. T. Bulle-Lieuwma, A. H. van Ommen, J. Hornstra, and C. N. A. M. Aussems, J. Appl. Phys. **71**, 2211 (1992).
[4]A. Zur and T. C. McGill, J. Appl. Phys. **55**, 378 (1984).
[5]P. H. Pumphrey, in *Grain Boundary Structure and Properties*, edited by G. A. Chadwick and D. A. Smith (Academic, London, 1976).
[6]O. P. Karpenko and S. M. Yalisove, J. Appl. Phys. **80**, 6211 (1996).
[7]M. Lawrence, A. Dass, D. B. Fraser, and C. S. Wei, Appl. Phys. Lett. **58**, 1308 (1991).
[8]J. R. Jimenez, L. M. Hsiung, K. Rajan, L. J. Schowalter, S. Hashimoto, R. D. Thompson, and S. S. Iyer, Appl. Phys. Lett. **57**, 2811 (1990).
[9]J. H. Je, T. S. Kang, and D. Y. Noh, J. Appl. Phys. **81**, 6716 (1997).
[10]R. T. Tung, J. M. Poate, J. C. Bean, J. M. Gibson, and D. C. Jacobson, Thin Solid Films **93**, 77 (1982).
[11]J. M. Gibson, J. L. Batstone, and R. T. Tung, Appl. Phys. Lett. **51**, 45 (1987).
[12]J. P. Sullivan, R. T. Tung, and F. Schrey, J. Appl. Phys. **72**, 478 (1992).
[13]I. K. Robinson and D. J. Tweet, Rep. Prog. Phys. **55**, 599 (1992).
[14]K. H. Kim *et al.*, J. Appl. Phys. **71**, 3812 (1992).
[15]J. E. Mahan, K. M. Geib, G. Y. Robinson, G. G. Long, Y. Xinghua, G. Bai, M. A. Nicolet, and M. Nathan, Appl. Phys. Lett. **56**, 2439 (1990).

Effect of the first antimony layer on AuZn ohmic contacts to *p*-type InP

Akira Yamaguchi[a)]
Analytical Characterization Center, Sumitomo Electric Industries, Ltd., 1-1-1 Koya-kita, Itami, Hyogo 664-0016, Japan

Hirokuni Asamizu
Department of Materials Science and Engineering, Kyoto University, Kyoto 606-8501, Japan

Takeshi Okada, Yasuhiro Iguchi, and Tadashi Saitoh
Opto-electronics Research Laboratory, Sumitomo Electric Industries, Ltd., 1-1-3 Shimaya, Konohana-ku, Osaka 554-0024, Japan

Yasuo Koide and Masanori Murakami
Department of Materials Science and Engineering, Kyoto University, Kyoto 606-8501, Japan

(Received 25 March 1999; accepted 28 April 2000)

The electrical properties of the Sb/Zn/Au/Nb ohmic contacts to *p*-type InP were investigated, where a slash (/) indicates the deposition sequence. The first Sb layer improved the contact resistivity and reduced the optimum annealing temperature, compared with the Au/Zn/Au/Nb contacts whose first layer was Au. The minimum contact resistivity of $4\times10^{-5}\ \Omega\,\mathrm{cm}^2$ was obtained from the Sb(3 nm)/Zn(5 nm)/Au(10 nm)/Nb(50 nm) contacts annealed at 325 °C for 2 min. The interfacial microstructure was studied using the cross-sectional transmission electron microscope. It was considered that the deposited Sb deoxidized and removed the native oxides of the InP surface and that facilitated the upper Au and Zn diffusion into InP. © *2000 American Vacuum Society.*
[S0734-211X(00)04204-9]

I. INTRODUCTION

Indium phosphide and related compounds, such as InGaAsP have been widely used as materials for both opto-electronic devices and high speed electronic devices such as photodiodes, laser diodes and high electron mobility transistors. Fiber-based telecommunication systems are widely used and the requirements for materials and processing of these devices are growing in terms of reliability and mass production. Consequently, low resistance reliable ohmic contacts and simple preparation methods are required. However, it is known that fabricating low resistance ohmic contacts to *p*-InP is difficult because of relatively high Schottky barrier heights ϕ_B and the large effective mass of the carriers. AuZn or AuBe is commonly used as ohmic contacts to *p*-InP. These Au-based ohmic contacts yield satisfactory low resistance of $10^{-5}\ \Omega\,\mathrm{cm}^2$, however they have deep protrusions of the metals into the InP substrates and the annealing temperature is relatively high ($\sim$450 °C) compared with that of typical AuGeNi ohmic contacts to *n*-InP ($\sim$350 °C).[1] In addition to the inherent reaction sequence in which Au and InP form a multiphase layer consisting of both Au_xIn_y and Au_2P_3 compounds,[2] it was reported that the native oxides on the InP led to the protrusions because of low reactivity of Au with the native oxide of the InP surface.[3]

To achieve higher reliability and higher performance, ohmic contacts having low contact resistance of $10^{-5}\ \Omega\,\mathrm{cm}^2$ with a shallow reaction layer of nanoscale range are required. It was reported that while the reduction of the thickness of Au created a shallower reaction layer, the contact resistance increased by an order of magnitude.[1] Therefore, two approaches have been conducted by several authors. One approach was to use near-noble transition metals such as Pd and Ni whose reactivity with the native oxide are relatively high.[4–7] Another approach was to control the native oxide: in the case of AuZn contacts, Au and Zn were expected to diffuse into InP easily at lower temperatures and deep protrusions were not expected to be generated if there was no native oxide layer at the AuZn/InP interface. Prior to deposition several kinds of chemical etching to remove the contaminants and the native oxides grown on the InP surface were tried, however similar characteristics of AuZn (AuBe) contacts were reported.[8–12] It was also reported that reoxidization occurred when the etched wafer was exposed to air.[13] These results indicated that the control of the native oxides was difficult using *ex situ* chemical etching prior to the deposition of metal films. An *in situ* sputter cleaning and deposition in the same vacuum chamber was then conducted on *n*-InP ohmic contacts,[14] however the sputter cleaning on *p*-InP was unsuitable because the sputtering process induced donor-like defects at the surface.[15] Surface passivation using an ammonia sulfide ($(NH_4)_2S_x$) solution was an attractive technique to prevent further oxidation after chemical etching[16] and it was applied to *n*-GaAs ohmic contacts.[17] However, there was concern over cross contamination in the laboratory or plant originating from the H_2S vapor and polysulfide powders generated from the $(NH_4)_2S_x$ solution.

In this article, a novel method to control the surface native oxides has been proposed to fabricate low resistance ohmic contacts with a shallow reaction layer. A few nm thick Sb

[a)]Author to whom correspondence should be addressed; present address: Opto-electronics Research Laboratory, Sumitomo Electric Industries, Ltd., 1 Taya-cho, Sakae-ku, Yokohama 244-8588, Japan; electronic mail: yamaguchi-akira@sei.co.jp

layer was deposited on the p-InP as the first layer of the AuZn ohmic contacts. It was previously reported that Sb deoxidizes In_2O_3 which was a main component of the native oxides during the annealing at 300 °C.[18] If the native oxides were deoxidized and removed by the first Sb layer, it was expected that the upper Au and Zn would diffuse into InP easily and that a low resistance ohmic contact with a shallow reaction layer would be achieved at a low annealing temperature.

II. EXPERIMENTAL PROCEDURES

The wafers used in this study were S doped n-type InP (100) substrates with undoped InP surface layers of 5 μm thickness ($n \sim 5\times10^{15}$ cm^{-3}) prepared by chloride vapor phase epitaxy. Channels of the p-type region were fabricated by the diffusion of Zn into the undoped InP epitaxial layer through the SiN_x masks. The carrier concentration of the InP surface was about 4×10^{18} cm^{-3}. Prior to contact metallization deposition, the surface of the p-InP layer was etched by an H_2SO_4:H_2O:H_2O_2=3:1:1 solution for 5 min at 25 °C followed by a de-ionized water rinse and blown dry by nitrogen before loading into an evaporation chamber. Then, the Sb/Au/Zn/Nb layered structure was deposited in an electron-beam evaporator equipped with a cryo pump. The base pressure was $\sim 5\times10^{-8}$ Torr. The thicknesses of the Au, Zn and Sb layers were varied in the range of 0–10, 3–5 and 1–15 nm, respectively. The thicknesses of the Au and Zn layers were considerably thinner than conventional AuZn contacts in order to obtain a shallow reaction layer. A 50 nm thick Nb was deposited as the top layer. Nb was selected because of its low reactivity with other metals and InP. The Au(5 nm)/Zn(5 nm)/Au(10 nm)/Nb(50 nm) and Sb(10 nm)/Nb(50 nm) structures were also prepared for comparison. Patterning of the metal film was performed using a conventional lift-off process for electrical evaluation. Blanket metallizations were prepared for microstructural analysis. The specimens were then annealed in a conventional furnace from 300 to 500 °C for 2 min in a forming gas (5% H_2:95% N_2). The contact resistivity was determined using the transmission line model.[19] The surface morphology of the Sb deposited surface was observed by a high-resolution scanning electron microscope using Hitachi model S-900. Cross-sectional transmission electron microscopy (XTEM) was performed by a Hitachi model H-9000UHR microscope operated at 300 kV for structural analysis. Elemental composition analysis using a nanoprobe was carried out by a Hitachi model HF-2000 microscope operated at 200 kV equipped with a Philips DX-4 energy dispersive x-ray analyzer (EDX). The electron probe diameter used for chemical composition analysis was about 1 nm and quantitative analysis was undertaken using theoretical "k" factors. The XTEM specimens were prepared by the conventional techniques of mechanical polishing and ion milling.

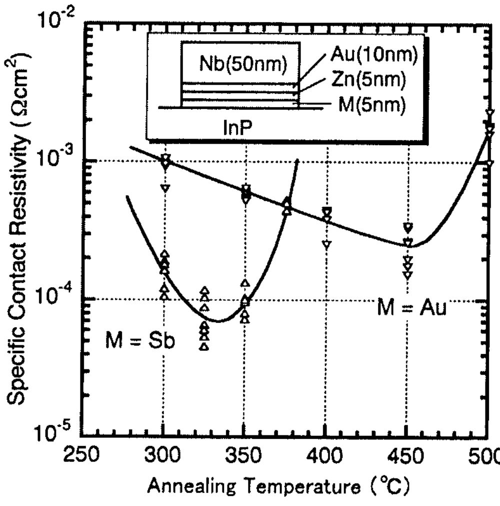

FIG. 1. Results of contact resistivity vs annealing temperature of the Sb(5 nm)/Zn(5 nm)/Au(10 nm)/Nb(50 nm) contacts and the Au(5 nm)/Zn(5 nm)/Au(10 nm)/Nb(50 nm) contacts. Annealing time was 2 min.

III. RESULTS

A. Contact resistivity measurements

First, contact resistances were measured for the Sb(5 nm)/Zn(5 nm)/Au(10 nm)/Nb(50 nm) contacts and Au(5 nm)/Zn(5 nm)/Au(10 nm)/Nb(50 nm) contacts. Figure 1 shows the annealing temperature dependence of these contacts. The annealing time of both specimens was 2 min. In the case of the Sb/Zn/Au/Nb structure, the minimum contact resistivity of 7×10^{-5} Ω cm^2 was obtained at the annealing temperature of 325 °C, while 2×10^{-4} Ω cm^2 at 450 °C was obtained in the case of the Au/Zn/Au/Nb structure whose first layer was Au instead of Sb, indicating a small effect of added Zn in the Au/Zn/Au/Nb contacts. Contact resistance of the Sb(10 nm)/Nb(50 nm) structure which contained no Au nor Zn was also measured, resulting in 2×10^{-4} Ω cm^2 at 450 °C as the minimum contact resistivity.

In order to optimize the thickness of Au, Zn and Sb, contact resistances were measured for various thicknesses and annealing temperatures. Figure 2 shows the thickness dependence of the first Sb layer on the contact resistivities ranging from 3 to 15 nm. The thinner the first Sb layer, the lower the contact resistivity and the contact resistivities below 10^{-5} Ω cm^2 were obtained at 3–5 nm. The minimum value was 4×10^{-5} Ω cm^2 which was the same level as the conventional thick AuZn contacts. The optimum annealing temperatures were 325–350 °C, which were considerably lower than that of the conventional AuZn contacts (~450 °C). The specimens with 1 nm thick Sb did not yield 10^{-5} Ω cm^2 of contact resistivities. Thickness dependence of the Au layer on the contact resistance was also measured in the Sb(5 nm)/Zn(5 nm)/Au(0–10 nm)/Nb(50 nm) structure and a low contact resistivity in the 10^{-5} Ω cm^2 range was obtained in the case of 10 nm. The Sb(5 nm)/Zn(5 nm)/Nb(50 nm) contacts, whose Au layer thickness was 0 nm, did not yield 10^{-5} Ω cm^2 as the minimum contact resistivity, indicating that Au was indispensable. Thickness dependence of the Zn layer

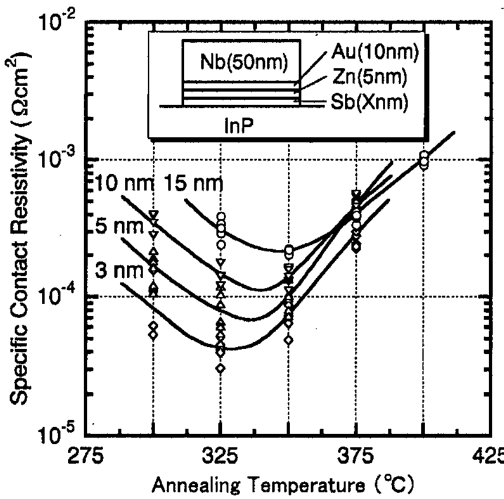

FIG. 2. Sb thickness dependence on the contact resistivity in the Sb(X nm)/Zn(5 nm)/Au(10 nm)/Nb(50 nm) structure. Annealing time was 2 min.

was investigated in the Zn thickness from 3 to 10 nm and the dependence was found to be minimal.

B. Surface observation on Sb deposited InP using high-resolution scanning electron microscopy (HR-SEM)

The microstructure of the metal/InP interface was known to strongly control the electrical properties. Hence, observation by the HR-SEM was conducted in order to observe the Sb deposited InP specimens. Figure 3 shows a HR-SEM image of the Sb 3 nm deposited specimen. It was found that the deposited Sb formed island structures. Islands with 5–30 nm diameters were observed. The heights of the islands were found to be 5–15 nm from cross-sectional observations. The distance between island to island was 10–30 nm in the case of 3 nm. The density of the islands became higher with Sb thickness, and almost continuous films were observed at the thickness of 15 nm, which is shown in Fig. 4.

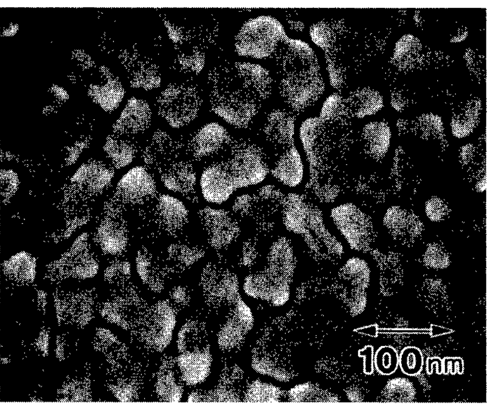

FIG. 4. Typical HR-SEM of Sb deposited InP. The thickness of Sb was 15 nm.

C. Microstructural analysis using XTEM

In order to clarify the effect of the first Sb layer on the electrical properties, the interfacial microstructure was studied using XTEM. Figure 5 shows a typical XTEM image of the Sb(3 nm)/Zn(5 nm)/Au(10 nm)/Nb(50 nm) specimen which was annealed at 325 °C for 2 min. Several small protrusions into InP were observed, indicating the reaction between the metal and InP. The reaction depth was found to be about 20 nm. The EDX measurements and electron diffraction measurements revealed that these protrusions consisted of $AuIn_2$ and a small amount of Zn. Multipoints analysis across the $AuIn_2$/InP interface using a 1 nm ϕ probe were performed, and it was found that Sb was not detected at the $AuIn_2$/InP interface. It was also found that Sb was detected at the Nb/$AuIn_2$ interface. High resolution TEM observation was performed on the metal/InP interface, which is shown in Fig. 6. The native oxides were observed only at the metal/InP interface in which the $AuIn_2$ protrusions were not generated. The abrupt interface was seen at the $AuIn_2$/InP interface on an atomic scale.

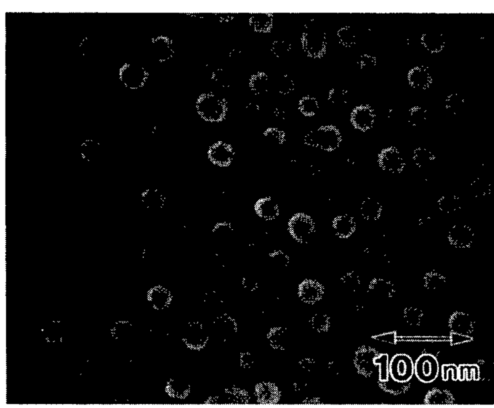

FIG. 3. Typical high resolution scanning electron micrograph of Sb deposited InP. Thickness of Sb was 3 nm.

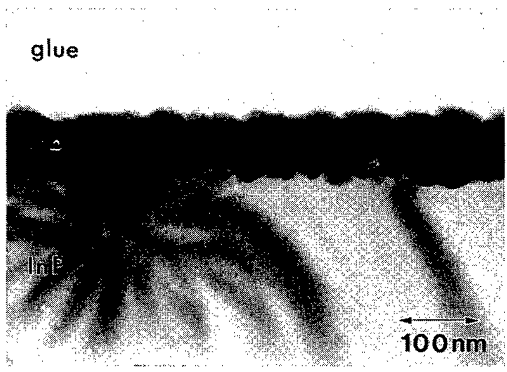

FIG. 5. Typical XTEM of the interfacial structure of the Sb(3 nm)/Zn(5 nm)/Au(10 nm)/Nb(50 nm) specimen which was annealed at 325 °C for 2 min.

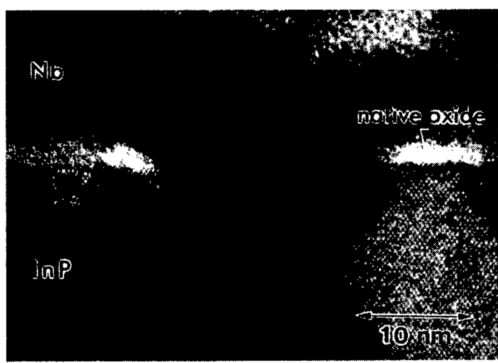

FIG. 6. High resolution transmission electron micrograph on the metal/InP interface of the Sb(3 nm)/Zn(5 nm)/Au(10 nm)/Nb(50 nm) specimen which was annealed at 325 °C for 2 min.

IV. DISCUSSION

A. Ohmic contact formation mechanism

The contact resistivities of thin AuZn contacts which have Nb top layers were measured and they were found to improve considerably by setting an Sb layer of 3–5 nm thickness as the first layer. The function of the added Sb is discussed. The ohmic contacts which have a narrow band gap intermediate semiconductor layer (ISL) such as $InSb_xP_{1-x}$ were previously proposed.[7,20] However, the details of the interfacial microstructure, especially the ISL/InP interfacial structure, were not reported. From the quasibinary phase diagram study on the InP–InSb system, it was reported that solid solutions were formed only in limited regions: x is nearly zero or x is nearly one in the $InSb_xP_{1-x}$ formula.[21] Then, a large lattice mismatch occurred between Sb rich $InSb_xP_{1-x}$ and InP [lattice constant $a_0=0.5869$ nm (InP) and 0.6479 nm (InSb)]. It was therefore believed to be difficult to realize an $InSb_xP_{1-x}$/InP heterostructure. Undeniably, such a metastable $InSb_xP_{1-x}$ grew, as reported by Jou using organometallic vapor-phase epitaxy,[22] however in this study, compounds such as $InSb_xP_{1-x}$ were not observed by XTEM with a 1 nm ϕ probe.

Nobusawa *et al.* reported from their x-ray photoelectron spectroscopy (XPS) study the deoxidization effect of Sb on In_2O_3, which was a main component of the native oxides of InP, with annealing at 300 °C for 10 min[18]

$$Sb+In_2O_3 \rightarrow Sb_2O_3+In. \quad (1)$$

It therefore seems possible that the deoxidization of the native oxides took place and a part of the native oxides was deoxidized by the reaction with deposited Sb under our experimental conditions of annealing at 300–325 °C for 2 min.

From the HR-SEM study on the Sb deposited InP surface, the deposited Sb formed island structures. The heights of the deposited islands or the thickness of Sb film were 5–15 nm, which were thicker than the native oxides. When the thickness of Sb was 3–5 nm, Sb islands were thought to play two roles: one was deoxidizing the native oxides, the other was making Zn stick onto the specimen surface. As discussed above, deoxidation of the native oxides by Sb took place at 300 °C, therefore the deposited Sb islands deoxidized the native oxides and pinhole like defects were thought to be generated in the native oxides, followed by the diffusion of Au and Zn into InP. The XTEM results in which the native oxides remain at the interface where no $AuIn_2$(Zn) protrusion exists supports this process. It was speculated that pinhole like defects generate a local stress on the native oxides. It is known that the sticking coefficient of Zn onto InP was very low. However, it was found that the sticking coefficient of Zn onto Sb (3–5 nm) deposited InP was as high as that of Zn onto metal such as Pd from the results of wet chemical composition analysis of the Sb(3 nm)/Zn(5 nm)/Pd(20 nm) and Sb(3 nm)/Zn(5 nm)/Pd(20 nm) specimen. It was speculated that Sb islands acted as nuclei of Zn deposition. Thus Zn exists closer to the InP substrate, and it was supposed that Zn more easily enhanced the surface hole density during annealing.

If the thickness of Sb was thinner than 3 nm, the sticking coefficient of Zn onto Sb/InP was supposed to be low, indicating that the effects of added Zn were ineffective. If the thickness was over 10 nm, it was found that deposited Sb formed continuous films and that these remained after annealing at the $AuIn_2$/Nb interface. Then these Sb films caused Zn to separate from the InP surface. Furthermore, it was found that if the Sb films were partially oxidized from the results of Auger electron spectroscopic analysis, then these Sb films deteriorated the contact resistance. Therefore it was believed that the optimum thickness is 3–5 nm. A proposed model of an ohmic contact formation mechanism on the Sb/Zn/Au/Nb contacts is illustrated in Fig. 7.

B. Simultaneous annealing for *p*- and *n*-InP ohmic contacts

By setting a thin Sb layer as the first layer of AuZn contacts, low resistance (10^{-5} Ω cm^2) ohmic contacts with a shallow (20 nm) reaction layer were obtained with annealing at moderate temperatures (325–350 °C). It was reported that the annealing temperature was reduced by about 20 °C with the addition of Pd or Ni to AuZn contacts to *p*-InP, while the contact resistivity deteriorated.[10,23] However, the addition of Sb enabled the reduction of the annealing temperature of ~ 100 °C in addition to greatly improving the contact resistivity. To the best of our knowledge, such a significant effect has not been reported previously. The annealing temperature of typical AuGeNi ohmic contacts to *n*-InP was about 350 °C, therefore simultaneous annealing of *p*- and *n*-InP ohmic contacts can be achieved by using the Sb/Zn/Au/Nb contacts, which are assumed to reduce the production cost of the devices. The reaction depth of the Sb/Zn/Au/Nb contacts was about 20 nm, which was about 25 times shallower than that of conventional AuZn contacts (~ 0.5 μm), indicating that the Sb/Zn/Au/Nb contacts are also suitable for devices such as optoelectronic integrated circuits as well as *p-i-n* photodiodes.

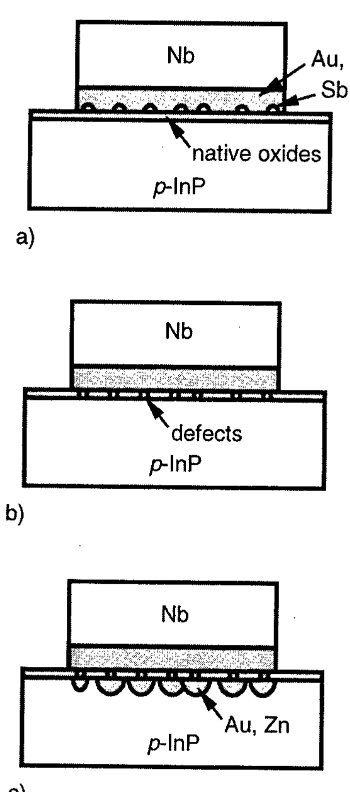

FIG. 7. Schematic diagrams of the proposed reaction sequence of the Sb/Zn/Au/Nb contacts to p-InP at elevated temperatures. (a) Sb was deposited on the InP surface as an island structure. (b) Native oxides were deoxidized by Sb and pinhole-like defects were generated in the native oxides by annealing at about 300 °C. (c) Upper Au and Zn diffused into InP and p^+ regions were generated in the InP surface at 325–350 °C.

V. CONCLUSION

The electrical properties of the Sb/Zn/Au/Nb ohmic contacts to p-type InP were investigated. The Sb first layer improved the contact resistivity and reduced the annealing temperature. The optimum thickness of the Sb layer was 3 nm and the minimum contact resistivity of $4 \times 10^{-5}\ \Omega\ \mathrm{cm}^2$ was obtained from the Sb(3 nm)/Zn(5 nm)/ Au(10 nm)/Nb(50 nm) structure which was annealed at 325 °C for 2 min. The surface structure of the Sb deposited InP surface was studied by a HR-SEM. The interfacial microstructure was also studied by XTEM. It was found that if the deposited Sb islands deoxidized the native oxides and that Au and Zn diffused into InP through pinholes bored in the native oxides, then p^+ regions were generated at the surface of InP, which enable hole tunneling. The reduction of the contact resistivity as well as the optimum annealing temperature were remarkable characteristics of the addition of Sb to p-InP ohmic contacts. Simultaneous annealing of p- and n-InP ohmic contacts will be achieved by using the Sb/Zn/Au/Nb contacts due to low annealing temperature similar to that of typical AuGeNi contacts to n-InP.

ACKNOWLEDGMENTS

The authors wish to thank Dr. Hideki Hayashi, Dr. Naoyuki Yamabayashi, Hitoshi Terauchi, and Dr. Shigeo Murai for their support of this work. They are grateful to Masayuki Nishizawa, Taira Horiuchi, Sanae Takekoshi, and Yoko Yamashita for their fine TEM analysis.

[1]A. Yamaguchi, I. Tonai, H. Okuda, N. Yamabayashi, and M. Shibata, Bunseki Kagaku **40**, 741 (1991).
[2]A. Piotrowska, P. Auvray, B. Guenais, A. Guivarc'h, G. Pelous, and P. Henoc, Electron Tech. **15**, 13 (1982).
[3]M. Ogawa, J. Surf. Sci. Soc. Jpn. **2**, 265 (1981).
[4]D. G. Ivey, P. Jian, L. Wan, R. Bruce, S. Eicher, and C. Blaauw, J. Electron. Mater. **20**, 237 (1991).
[5]L. C. Wang, M. H. Park, F. Deng, A. Clawson, S. S. Lau, D. M. Hwang, and C. J. Palmstrøm, Appl. Phys. Lett. **66**, 3310 (1995).
[6]M. H. Park, L. C. Wang, J. Y. Cheng, F. Deng, S. S. Lau, and C. J. Palmstrøm, Appl. Phys. Lett. **68**, 952 (1996).
[7]M. H. Park, L. C. Wang, J. Y. Cheng, and C. J. Palmstrøm, Appl. Phys. Lett. **70**, 99 (1997).
[8]A. J. Nalois and G. Y. Robinson, Solid-State Electron. **25**, 973 (1982).
[9]C. L. Cheng, L. A. Coldren, B. I. Miller, J. A. Rentschler, and C. C. Shen, Electron. Lett. **18**, 755 (1982).
[10]T. Clausen and O. Leistiko, Microelectron. Eng. **18**, 305 (1992).
[11]O. Oparaku, C. L. Dargan, N. M. Pearsall, and R. Hill, Semicond. Sci. Technol. **5**, 65 (1990).
[12]V. Malina, U. Schade, and K. Vogel, Semicond. Sci. Technol. **9**, 49 (1994).
[13]J. P. Contour, J. Massies, and A. Saletes, Jpn. J. Appl. Phys., Part 2 **24**, L563 (1985).
[14]W. C. Dautremont-Smith, P. A. Barnes, and J. W. Stayt, Jr., J. Vac. Sci. Technol. B **2**, 620 (1984).
[15]K. Tsubaki, S. Ando, K. Oe, and K. Sugiyama, Jpn. J. Appl. Phys. **19**, 1191 (1979).
[16]H. Oigawa, J.-F. Fan, Y. Nannichi, H. Sugahara, and M. Oshima, Jpn. J. Appl. Phys., Part 2 **30**, L322 (1991).
[17]V. Fischer, T. J. Kim, P. H. Holloway, E. Ristolainen, and D. Schoenfield, J. Vac. Sci. Technol. B **12**, 1419 (1994).
[18]H. Nobusawa and H. Ikoma, Jpn. J. Appl. Phys., Part 1 **32**, 3713 (1993).
[19]H. H. Berger, Solid-State Electron. **15**, 145 (1972).
[20]R. Dutta, M. A. Shahid, and P. J. Sakach, J. Appl. Phys. **69**, 3968 (1991).
[21]K. Nakajima, M. Osamura, and Y. Murakami, J. Jpn. Inst. Met. **37**, 1276 (1973).
[22]M. J. Jou, Y. T. Cheng, and G. B. Stringfellow, J. Appl. Phys. **64**, 1472 (1988).
[23]H. Temkin, R. J. McCoy, V. G. Keramidas, and W. A. Bonner, Appl. Phys. Lett. **36**, 444 (1980).

Design and implementation of optoelectronic interfaces for high-speed burst-mode transmissions

André Boyoguéno Bendé[a)]
Microelectronics Research Group, Electrical Engineering Department, Ecole Polytechnique de Montreal (Québec) Canada, CP 6079 succ. Centre-Ville, H3C 3A7, Canada

(Received 13 August 1999; accepted 26 March 2000)

The popularity of internet and multimedia has greatly increased the demand for high-speed transmission networks. The next generation of optical networks will likely request fast packet switching to support multimedia applications. In fact, in such applications, the amplitude and phase of the receiver can be quite different from packet to packet due to different fiber attenuation and the chromatic dispersion caused by the variation of the transmitter's wavelength. Link performance is strongly dependent on both the sensitivity and dynamic range of the receiver circuit. Although emerging lightwave communication technologies are bringing 10 Gb/s systems into commercial use [K. Yukio, A. Yuji, N. Kiyoski, K. Hiroyuki, and Y. Imai, IEEE Trans. Microwave Theory Tech. **43**, 1916 (1995)], optoelectronic interfaces are still limiting factors for better performances. In this article, we address power penalty in high-speed burst-mode operation. Architectures applicable to high-speed systems and insensitive to parasitic input loading are proposed to overcome speed limitations at the receiver's input. A 4.7 GHz bandwidth, a transimpedance of 43 dB Ω and an average input noise current density of 9 $\mathrm{pA}/\sqrt{\mathrm{Hz}}$ have been achieved in simulations with the single-ended version. © *2000 American Vacuum Society.* [S0734-211X(00)01504-3]

I. INTRODUCTION

For fiber optic communication systems, whether for long distances or for busing data over short distances, whether operating at low data rates or at high bit rates, one of the key elements is the receiver. The performance level of the system is established at the receiver input where the signal is at its weakest. So the design of the input optoelectronic interface must be done carefully.

Conventional receivers are not suitable for burst-mode operation because, they cannot instantaneously handle different arriving packets with large difference in optical power and phase alignment. The fundamental differences between traditional receivers and the new burst-mode devices are that, direct current coupling must be used throughout the receiver instead of alternating current coupling due to the low frequency spectral content of the burst-mode data and that they must adapt to the variation in optical power and phase alignment on a burst to burst basis. A large dynamic range and a high gain are desirable in order to allow network flexibility.

Furthermore, one effective approach of improving the input sensitivity of a receiver is to use a preamplifier. However, the bandwidth of the preamplifier is generally not wide enough, so sensitivity degrades at high bit rates. To overcome this problem, we employed a wide-band preamplifier based on the parallel feedback technique using a common-gate (C-G) input stage as shown in Fig. 1 and Fig. 2. Section II of this article addresses issues of how to best choose the input device such that noise added is minimized in the bandwidth of interest. In Sec. III, fabrication issues are discussed; the discussion of simulation results follows in Sec. IV.

II. DESIGN ISSUES

We first analyze the receiver noise mechanism and then its impact on burst-mode operation for high-speed transmission and determine power penalty considering that Gaussian noise approximation holds. The penalty arises from the fact that, the first bit exhibits statistical variations in amplitude, and therefore establishing the threshold based on this bit alone will result in a threshold voltage which shows identical statistical variations. The variations in the threshold voltage will result in a degradation in the bit error rate/signal to noise ratio (BER/SNR). We then present our approach to improve the receiver's sensitivity thus improving power penalty.

A. Noise and sensitivity analysis

As the link performance is strongly dependent on the sensitivity of the receiver circuit, the input stage configuration choice is crucial. In fact, the receiver sensitivity is determined predominantly by the radio frequency (rf) small-signal and noise performance of the device used in the frontend rf analog part. It is important in the design of this rf interface to make an estimation of noise generated by the components of the amplifier.

For example, all resistors (R_s, R_{ds}, R_d, R_L) will generate Johnson or thermal noise due to the random thermal motion of charge carriers. It is a white noise in that, it has a constant power density independent of frequency and can be neglected. The remaining components are the transistors. At low frequencies, each one has at least two major noise sources. The first is the thermal channel noise because the channel resistance of the transistor is finite. For a transistor in the saturation region, the drain thermal noise is

[a)]IEEE Student Member; electronic mail: boyo@grm94.polymtl.ca

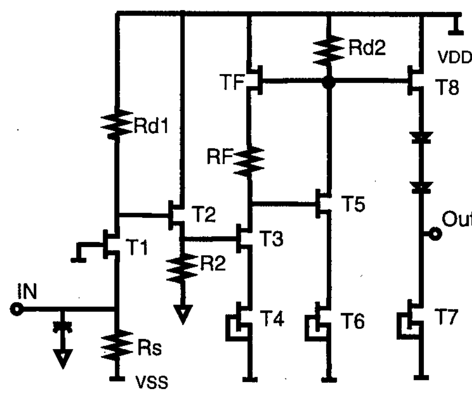

FIG. 1. C-G stage in single ended.

$$\overline{i_{\rm dnt}^2}=4KT\tfrac{2}{3}g_m\Delta f. \quad (1)$$

The second source of noise is called the flicker noise generated by surface states. While there are numerous expressions attempting to accurately describe this noise, the one selected here is by[1] represented by a drain-source current generator

$$\overline{i_{\rm dnf}^2}=K_1\frac{g_m^2}{WLf}\Delta f. \quad (2)$$

Variables W, L, and g_m represent the transistor's width, length, and transconductance, respectively, and K_1 is a constant for a given device. An important point to note here is that, *1/f* noise is inversely proportional to frequency and the transistor area. It is normally the dominant noise at low frequencies; since g_m is proportional to the drain current. To minimize the flicker noise, the input device should be run at low drain current and be made as large as allowed by the monolithic integration.

Considerable effort has been done to estimate the amplifier noise for different front end designs.[2–6] A simple approach that accounts for amplifier noise is by introducing a quantity F_n referred to as amplifier noise figure. Thus, the thermal noise variance can be expressed as

$$\sigma_T^2=\langle i_T^2(t)\rangle=\int_{-\infty}^{\infty}S_T(f)df=(4KT/R_L)F_n\Delta f. \quad (3)$$

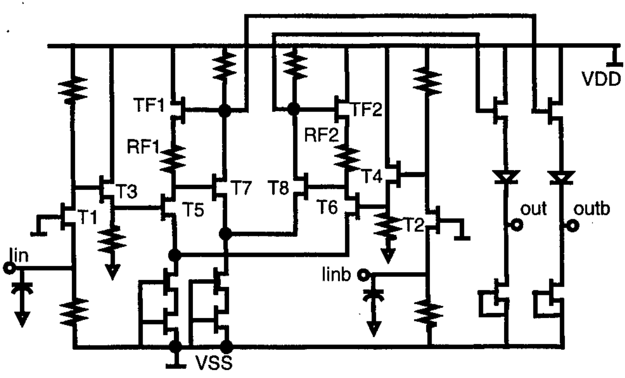

FIG. 2. Novel differential stage based on the C-G configuration.

Physically, F_n represents the factor by which the thermal noise is influenced by various resistors used in the preamplifier and the postamplifier. The total current noise is obtained by adding the contribution of each individual noise source. With approximately Gaussian statistics, the total variance of the current fluctuations is

$$\sigma^2=\sigma_s^2+\sigma_T^2=2q(I_p+I_d)\Delta f+(4KT/R_L)F_n\Delta f, \quad (4)$$

where

$$\sigma_s^2=\langle i_s^2(t)\rangle=\int_{-\infty}^{\infty}S_s(f)df=2qI_p\Delta f \quad (5)$$

stands for the variance of shot noise generated by the photodiode. The SNR is related to the incident optical power as

$$\mathrm{SNR}=\frac{R_p^2P_{\rm in}^2}{2q(R_pP_{\rm in}+I_d)\Delta f+(4KT/R_l)F_n\Delta f}. \quad (6)$$

If the dark current is neglected, this expression becomes

$$\mathrm{SNR}=\frac{\eta P_{\rm in}}{2h\nu\Delta f}. \quad (7)$$

It appears that, the SNR increases linearly with $P_{\rm in}$ in the shot noise limit and depends only on the quantum efficiency η, the noise bandwidth Δf, and the photon energy $h\nu$. In most cases of practical interest, the thermal noise dominates the receiver performance ($\sigma_T^2 \gg \sigma_s^2$) and the SNR can be written as

$$\mathrm{SNR}=\frac{R_LR_p^2P_{\rm in}^2}{4KTF_n\Delta f}. \quad (8)$$

Thus, the SNR varies as $P_{\rm in}^2$ in the thermal noise limit. The power penalty can be improved by increasing the load resistance R_L and minimizing the F_n of the receiver.

B. Problems of conventional preamplifiers

Generally, the amplifier stages used to obtain a required loop gain consist of a combination of inverter and buffer/level shift circuits. Two types of input-stage circuits have always been used for frontend preamplifier of photoreceivers: an inverter type and a cascode type. The inverter input stage is quite attractive for its simple circuit configuration, but it has a large Miller capacitance that increases circuit's input noise. On the other hand, the cascode configuration reduces the Miller capacitance thus reducing the nondominant time constant and, hence, improving the amplifier stability. A simple expression of the noise current at the input stage can be estimated by the following equation:[2,3]

$$\langle i_{\rm ni}^2\rangle=\frac{4KTI_2B}{R_f}+2qI_TI_2B+\frac{4KT\Gamma(2\pi C_T)^2I_3B^3}{g_m}, \quad (9)$$

where B is the bit rate, K is the Boltzman constant, T is the temperature, q is the electron charge, I_T is the average leakage current, I_2 and I_3 are Personick's integrals which relate

the bit rate to the actual circuit bandwidth,[3] C_T is the contribution of the total input capacitances, R_f is the feedback resistance, and Γ is the field-effect transistor (FET) noise factor.

In order to reduce the input noise current, it is desirable to reduce the contribution of $C_T(C_T=C_d+C_{\mathrm{FET}})$, and to increase R_f and g_m. In fact, in the case of the inverter preamplifier, from the Miller effect phenomenon, the capacitance of the input FET C_{FET} is given by $C_{\mathrm{FET}}=C_{gs}+(1+g_mR_L)C_{gd}$. To reduce the contribution of C_T, the desired design should minimize the second term of C_{FET} known as the Miller effect. When the cascode configuration is used, then $C_{\mathrm{FET}}=C_{gs}+2C_{gd}$.

C. Proposed architectures

Figure 1 is the schematic diagram of the proposed preamplifier. The width of the input transistor T1 is optimized for low-noise operation. T2 is an impedance transformer stage. T3 and T5 form the voltage gain stage while, T8 and T7 form the voltage level-shifting stage. For wide-band operation, we adopted a parallel feedback loop based on TF and rf. The use of TF is essential to increase the bandwidth. In fact, a first order approximation of the bandwidth is

$$\mathrm{BW}=\frac{1+A_v}{2\pi R_T C_T}. \tag{10}$$

A_v being the loop gain which is improved by using the parallel feedback, R_T is the equivalent input resistance $C_T=C_d+C_{\mathrm{FET}}$ is minimized by the C-G input stage. Consequently, the bandwidth with this architecture is expected to be much wider than that of a conventional amplifier.

The output of the gain stage is connected to a buffer/level shift circuit which permits smaller capacitive loading, and therefore do not decrease the operating bandwidth. In the absence of the level/shifting, bypass capacitors are necessary; low operating frequency cannot be achieved easily, in this case, unless very large capacitors are used, a requirement which is not compatible with GaAs monolithic integration.

Figure 2 is the differential structure, where the input transistors T1 and T2 are connected in a C-G configuration. Since conventional feedback is not employed in our design, this eliminates a common characteristic of traditional high-speed transimpedance receivers of gain peaking and the bandwidth limitation caused by the interaction of the feedback resistor with the input capacitance time constant.

What is new in this design compare to the previous transimpedance architecture is the use of the C-G configuration for high-speed operation with a perfect isolation of the photodetector capacitance in determining the 3 dB bandwidth combined with the parallel feedback instead of a conventional one.

III. FABRICATION ISSUES

A broad range of foundry processes are available for different types of metal–semiconductor field effect transistor (MESFET) devices, such as high-power, low-noise and, general purpose devices. Integration of several types of active devices on a single chip, including E/D and microwave depletion mode devices also is an important consideration. Most monolithic microwave integrated circuit (MMIC) foundries offer depletion mode MESFET based process technology with 0.5, 1.0 μm, or more gate lengths. TriQuint is the only foundry offering the most extensive product line which includes E/D devices; and for our designs, we have used PSPICE and CADENCE package with TriQuint own models all through the design flow. Care have been put during layout to avoid short-channel effect and backgating. Moreover, active devices in MMIC circuitry are beginning to find more nonstandard applications.

In addition to the device's intended application, power, and frequency range of interest also affect its design even when MESFET devices are to be used as amplifier elements; for example, the optimum device for a low-noise, high-frequency amplifier will be quite different than optimum power device. Two figures of merit are commonly used to characterize transistor speed. The frequency at which the device current gain has decreased to unity known as f_T. As a first order estimation, f_T of a MESFET can be expressed as

$$f_T=\frac{g_m}{2\pi(C_{gs}+C_{gd})}. \tag{11}$$

The transconductance of the device g_m increases approximately linearly as the gate-length dimension is scaled down. The gate capacitances both decrease as the gate length decreases. This results in a desire for short gate lengths for MESFETs. Normally, C_{gs} dominates the denominator of the expression for f_T which decreases linearly with decreased gate length. The frequency of unity power gain $f_{\max}$,

$$f_{\max}=\frac{f_T}{2\sqrt{G_0(R_g+R_s)+2\pi f_T C_{gd}R_d}} \tag{12}$$

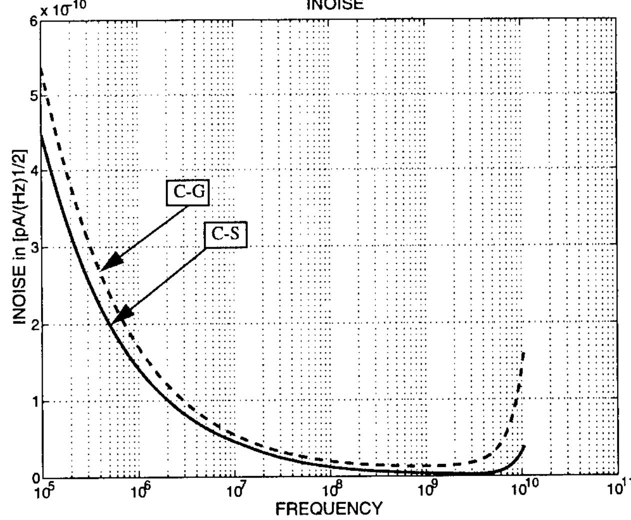

FIG. 3. Comparative input referred noise for high-bit rate.

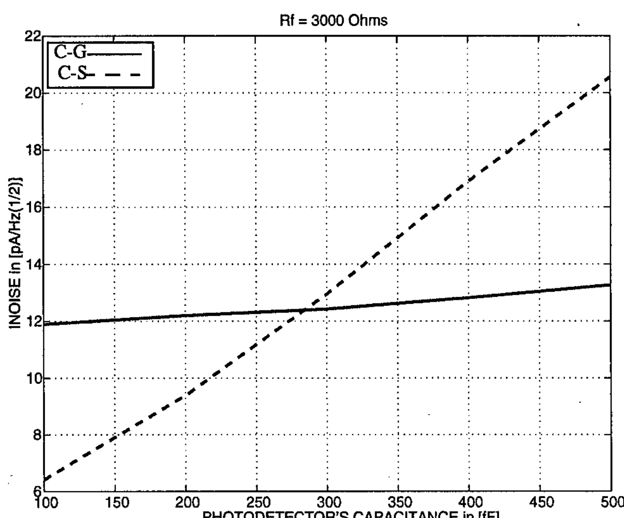

FIG. 4. Influence of the input loading.

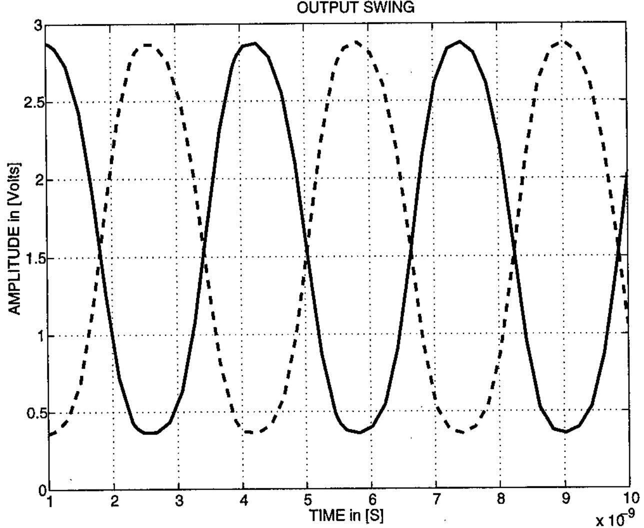

FIG. 6. Transient differential output signals.

is given in terms of the gate resistance (or the base resistance) and gate-drain capacitance (or the base-collector capacitance). These transistors while processing high-speed suffer from threshold variations for their speed. These properties pose significant challenges for the designer. This design has been performed with the TriQuint 0.6 μm gate-length process, with transistors having $f_T=20$ GHz and $I_{DSS}=70$ μA/(μm). Furthermore, fewer noise sources are present in the FET (no shot noise) as compared to the bipolar transistor. Nevertheless, a disadvantage of the GaAs MESFET is the higher $1/f$ noise compared to the silicon bipolar transistor, thus the necessity to exploit them in high-speed applications.

Wire bonding is a common and inexpensive mounting technique, but the large capacitic inductance degrades the IC performance and has to be considered during the design flow. Pad metallization is also another issue to be considered in the circuit design. The parasitic capacitance of the input pad in particular affects the preamplifier performance because the time constant at the input node of a preamplifier largely determines the frequency response. For example, increasing the capacitance of a pad decreases the bandwidth and cause the response to become uneven.

The transimpedance Z_T is approximately given by

$$Z_T=\frac{Z_{T0}}{1+\frac{s}{p_1}+\frac{s^2}{p_1 p_2}}, \tag{13}$$

where $p_1=A_0/R_f C_T$ and $p_2=1/R_L C_{TC}$, C_{CT} is the total parasitic capacitance at the drain of the input transistor. The value of A_0 is given by $A_0\approx g_m R_{\text{load}}$. The ration of the poles p_2/p_1 is a measure of the peaking level which increases with a decrease in the ratio.

We plan to fabricate an optical-transceiver-type module in which the transmitted and receiver will be integrated into a single package contributing remarkably to the incorporation of a compact optical interface module. An optical switch will also be incorporated to modulate optical pulses according to transmitted data, thus providing an E/O conversion.

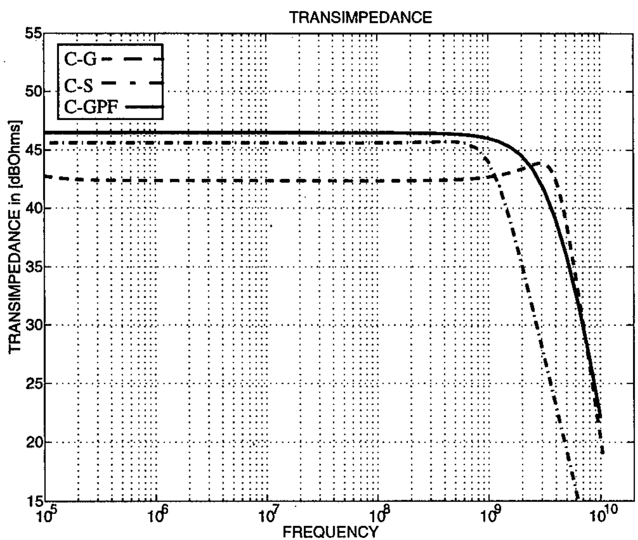

FIG. 5. Comparative study for the three configurations (C-S, C-G with PF, and C-G differential with PF).

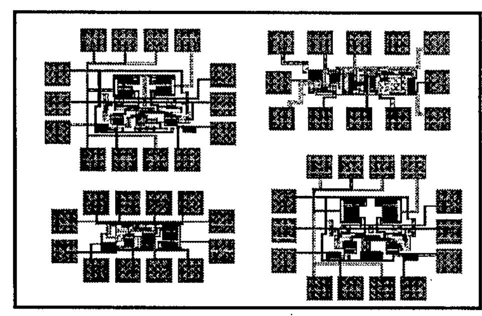

FIG. 7. Layout of designs submitted for fabrication.

IV. DISCUSSION AND RESULTS

In general, the input impedance $1/g_m$ of the input FET is much smaller than the feedback impedance used in the transimpedance amplifier. Since high open-loop gain in a conventional transimpedance amplifier is difficult to maintain due to excessive feedback parasites and limited phase margin at high frequencies, the receiver bandwidth, therefore, can be improved significantly by shifting the dominant pole expressed in Eq. (11) with the proposed design.

To prove the effectiveness of the proposed design, architectures in Figs. 1 and 2 have been investigated. We first present a comparison between the conventional common-source (C-S) configuration and the C-G for the same transimpedance. Figure 3 is the input referred noise for high bit rates of C-S and C-G while, Fig. 4 is the influence of the input loading for the two configurations. It appears that the noise performances are similar, bu the C-G is more stable considering input loading. Figure 5 is a comparative study of three major architecturs: C-S, C-G, and the differential stage as illustrated in Fig. 2 (C-GPF). Figure 6 deals with the transient analysis of the differential C-G amplifier and Fig. 7 is the layout of designs submitted for fabrication. A 350 fF equivalent parasitic capacitance of the photodiode in front of the preamplifier was considered in the transimpedance calculations and simulations. All the simulations were performed with the temperature equal to 80 °C.

V. CONCLUSION

We have presented an effective approach of improving power penalty and therefore input sensibility of a photoreceiver which is less sensitive to data format. The simulation results also demonstrate a higher bandwidth for the proposed C-G differential stage of the same transimpedance gain as compare to the classical stage (C-S). This feature allows multiapplications usage of the circuit with a standard 0.6 μm gate-length GaAs MESFETs technology.

Presented at the Ninth Canadian Semiconductor Technology Conference, Ottawa, Canada, 10–13 August 1999.

[1]P. R. Gray and R. G. Meyer, *Analysis and Design of Analog Integrated Circuits* (Wiley, New York, 1993).
[2]S. D. Personick, Bell Syst. Tech. J. **52**, 843 (1973).
[3]R. G. Smith and S. D. Personick, *Semiconductor Devices for Optical Communications* (Springer, New York, 1980), Chap. 4.
[4]Y. Ota and R. G. Swartz, JLT **8**, 1897 (1990).
[5]C. A. Eldering, JLT **11**, 2145 (1993).
[6]E. Sokolowska, G. Fortin, A. Boyogueno, C. Roy, and B. Kaminska, Canadian Conference on Broadband Research, April 1997, pp. 20–26.

Electroreflectance and photoreflectance studies of surface Fermi level and surface state densities of InP SIN$^+$ structures

W. C. Hwang, Y. J. Cheng, Y. C. Wang,[a] and J. S. Hwang[b]
Department of Physics, National Cheng Kung University, Tainan 70101, Taiwan

(Received 12 April 2000; accepted 5 May 2000)

The built-in electric fields, surface Fermi level, and surface state density of a series of InP surface-intrinsic-n^+ structures are calculated from the Franz–Keldysh oscillations of the modulation spectra of photoreflectance (PR) and electroreflectance (ER). Those results indicate that for samples with similar doping concentrations in the buffer layer and the substrate, the only built-in electric field across the top layer increases as their top layer thickness decreases. The surface Fermi level, however, remains roughly constant. For samples with a semi-insulated substrate, two built-in electric field exist separately in the top layer and at the interface between the buffer layer and the substrate. In addition, ER spectra are taken with the modulation electric field across the top layer. Although the built-in electric field across the top layer derived from the ER spectra increases as the top layer thickness decreases, the surface Fermi level, again, remains roughly constant. An approach of room temperature photoreflectance, based on the thermionic-emission theory and the current transport theory, is employed to estimate the surface state density. The surface state density of the InP SIN$^+$ structure is found to diminish with an increase in the thickness of the top layer. © *2000 American Vacuum Society.* [S0734-2101(00)04305-0]

I. INTRODUCTION

Modulation spectroscopy, particularly photoreflectance (PR) and electroreflectance (ER), has become an important technique for characterizing bulk semiconductors and semiconductor microstructures.[1–7] Any changes in the composition, structures, or doping concentration in bulk and/or surface dramatically alter the PR and ER signals ($\Delta R/R$); therefore, PR and ER have provided an accurate and rapid method for determining the energy gap, quantum transitions,[4–7] built-in surface or interface electric fields,[8–10] and doping concentrations[11,12] in these systems. These advantageous characteristics are common for ER and PR; however, PR is also contactless and nondestructive, requiring no special mounting, and can be performed in a variety of transparent "ambients." These characteristics make PR the prime candidate as a method for quantity and quality control on the electric device mass production line.

In this article, we describe our investigation, using PR and ER techniques, of the built-in electric fields, the surface Fermi level positions, and surface state densities of a series molecular beam epitaxy (MBE) grown InP SIN$^+$ structures. Our studies found that for samples with similar doping concentrations in their substrate and buffer layer, only one electric field exists over the top layer. On the other hand, if the sample has a Fe-doped semi-insulated substrate, two electric fields appear. One exists in the top layer while the other exists at the interface region between the buffer and substrate. The surface Fermi level positions for both categories of structures, however, are identical, and are pinned at 0.35 ± 0.01 eV below the conduction band edge. A new approach to room temperature photoreflectance, based on the thermionic-emission theory and current transport theory, was used to estimate the occupied surface state density. The occupied surface state densities of the InP SIN$^+$ structures were found to decrease with an increase of the thickness of the top layer.

II. THEORY

In PR, the surface electric field is modulated through the photoinjection of electron-hole pairs via chopped incident laser beam. The line shape of the PR signal, $\Delta R/R$, is directly related to the perturbed complex dielectric function. For a moderate electric field, the PR spectrum exhibits a series of oscillations (FKO) originating from the electric field F in the samples. The nth extrema E_n of FKO occurs when[13–16]

$$n\pi=(4/3)[(E_n-E_g)/\hbar\Theta]^{3/2}+\chi, \quad (1)$$

where E_g is the energy gap, χ is an arbitrary factor, and $\hbar\Theta=(e^2\hbar^2F^2/8\mu)^{1/3}$ with e being the electron charge, and μ the reduced effective mass. A plot of $(4/3\pi)(E_n-E_g)^{3/2}$ versus the index number n will yield a straight line with slope $(\hbar\Theta)^{-3/2}$. Therefore, the electric field (F) can be obtained directly from the period of the FKOs.

The surface barrier height is related to the built-in electric field by[17,18]

$$V_b=Fd+kT/e+\varepsilon F^2/2eN+(4/3\pi)(kT/q)(N_c/n^+)\times[F_{3/2}(-\varepsilon F^2/2qn^+)-F_{3/2}(0)], \quad (2)$$

where d is the undoped layer thickness; k the Boltzmann constant; T the temperature; ε the dielectric constant; N the doping concentration; and $F_{3/2}(x)$ the Fermi integral of argument x. For samples investigated, the last term is two or-

[a]Present address: Department of Physics and Chemistry, Chinese Military Academy, Fengshan, Taiwan.
[b]Author to whom all correspondence should be addressed; electronic mail: jshwang@ibm60.phy.ncku.edu.tw

ders of magnitude less than the third term and so can be ignored. The surface Fermi level V_f, measured from the conduction band at the surface, is equal to $V_b + V_s$, where V_s is the photovoltage induced by both pump and probe beam. If both the pump and probe beams are defocused on the sample and maintained at sufficiently low intensities, the photovoltage induced is a small constant and can be neglected. The surface Fermi level V_f is then equivalent to the surface barrier height V_b.

On the other hand, if only the probe beam is defocused on the sample and maintained at sufficiently low intensity, the photovoltage induced by the probe beam can be neglected. The photovoltage and hence the surface barrier height V_b, at a constant temperature, is a function of the pump beam intensity only. The photocurrent density J_{pc} consists of the drift and diffusion currents and can be written as[19]

$$J_{pc} = [eP_m\gamma(1-R_0)/\hbar\omega]\{[1-\exp(-\alpha L)] + \alpha L_d \exp(-\alpha L)/(1+\alpha L_d)\}, \quad (3)$$

where γ is the quantum efficiency, R_0 is the reflectivity of sample surface and $\hbar\omega$ is the photon energy of the pump beam, L is the depletion width equivalent approximately to the top layer thickness d, α is the absorption coefficient,[20] and L_d is the diffusion length of the minority carriers. For cases in which the diffusion length is much larger than the penetration depth, i.e., $\alpha L_d \gg 1$, Eq. (3) is reduced as follows:

$$J_{pc} = eP_m\gamma(1-R_0)/\hbar\omega. \quad (4)$$

According to the current-transport theory, the photovoltage V_s can be expressed as[21,22]

$$V_s = (\eta kT/e)\ln(I_{pc}/I_0 + 1), \quad (5)$$

where η is an ideality factor,[23] I_{pc} equals J_{pc} times the surface area A_{pc} simultaneously illuminated by both pump and probe beams, and $I_0(T)$ is the saturation current. The saturation current depends on the dominant current flow mechanism and is equal to the saturation current density $J_0(T)$ times some effective area A_0, which contributes to the current mechanism. For samples of SIN^+ structure, thermionic emission and diffusion are the major contributions to $J_0(T)$, therefore; J_0 can be expressed as[24,25]

$$J_0(T) = [A^*T^2/(1+BT^{3/2})]\exp[-eV_F(T)/kT], \quad (6)$$

where A^* is the modified Richardson constant defined as[24] $m^*ek^2/(2\pi^2\hbar^3)$ and $B = (k/2\pi m^*)^{1/2}(300/\nu_0)$, where m^* is the effective mass of the electron. By substituting Eqs. (4) and (6) into Eq. (5) with $I_{pc} = A_{pc}J_{pc}$ and $I_0 = A_0J_0$, the surface barrier height is then given by

$$V_b = V_F - (\eta kT/e)\ln[1 + eP_m\gamma(1-R_0) \times (1+BT^{3/2})\exp(eV_F/kT)/\hbar\omega r A^* T^2], \quad (7)$$

where the geometry factor $r \equiv A_0/A_{pc}$ is the fraction of the surface that has surface states.

At constant temperature, the only variable in Eq. (7) is the pump beam intensity P_m. When the surface barrier height V_b as a function of pump beam intensity is least-squares fitted to Eq. (7), V_F, η, and r can be obtained from the fitting parameters. By assuming one surface state per atom at the surface, the surface state density D_s can be calculated from rN_o, where N_o is the number of atoms per unit area of the surface.

TABLE I. Sample identification, substrate type, thickness of buffer layer, and top layer for various samples.

Sample	Doping of substrate	Thickness of buffer layer (μm)	Thickness of top layer (Å)
C331i	Fe	1	100
C332i	Fe	1	500
C333i	Fe	1	1000
C334i	Fe	1	2000
C331n	Sn	1	100
C332n	Sn	1	500
C333n	Sn	1	1000
C334n	Sn	1	2000

III. SAMPLE PREPARATION AND EXPERIMENT

All samples studied in this work were grown by MBE. A typical growth sequence entailed an InP undoped layer with various thickness being grown on 1 μm of a Si-doped, n-type InP buffer which had been previously grown on either a Fe-doped semi-insulated (SI) (110) InP substrate (SI substrate) or a Sn-doped n-type (110) InP substrate with a doping concentration $1\times10^{18}\,\mathrm{cm}^{-3}$ (N^+-doped substrate). The doping concentration in the buffer layer is $1\times10^{18}\,\mathrm{cm}^{-3}$ for all samples. The samples' IDs along with their structures are listed in Table I.

Sample preparation for the electroreflectance measurement involves alternately etching and depositing electrically conductive materials on different layers of the samples. A coating of photoresist was deposited initially on the top layer leaving a small uncoated edge for etching. The structure was then etched to depth below the interface of the top and buffer layer with an etching solution consisting of HCl and H_3PO_4 in a volume ratio of 1:3. The etching rate with this solution is 150 Å/s for InP. We controlled the etching depth by varying the exposure time to the etchant. This process results in a notch in the corner of the structure, exposing a ledge of the buffer material. After cleaning the photoresist with acetone, we deposited additional photoresist so as to expose only a portion of the buffer ledge. Subsequent gold evaporation formed an electrical pad on the buffer ledge. After cleaning the structure a second time, we deposited a final photoresist coating, leaving a window on the top layer for ITO deposition. The structure was then cleaned and electrical leads were attached to the gold and ITO electrical contact pads. An ac bias of 0.5 V at 200 Hz was used to modulated the electric field across the top layer for ER measurement.

A standard arrangement of the PR apparatus was used in this study. For a detailed description of the PR spectroscopy apparatus, refer to Refs. 10 and 21. In the study of surface Fermi level pinning, both the probe and pump beams were defocused on the sample with their intensities maintained below 1 μW/cm² to eliminate the photovoltaic effect. The

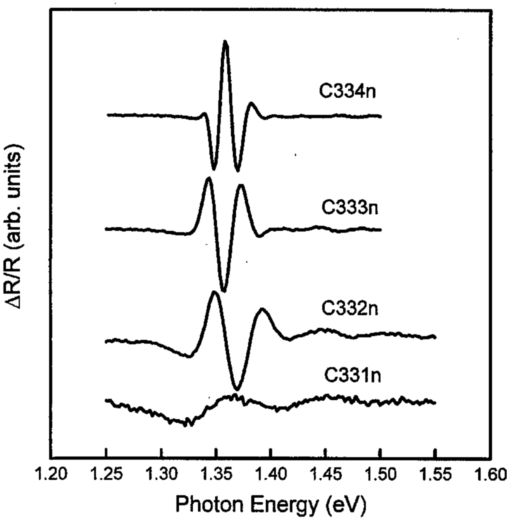

FIG. 1. PR spectra of INP SIN^+ structure with N^+-doped substrate.

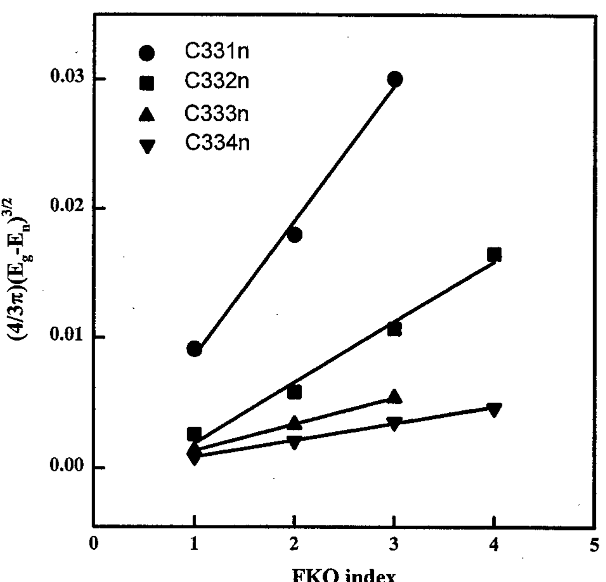

FIG. 3. Plot of $(4/3\pi)(E_n-E_g)^{3/2}$ as a function the FKO extrema index n in Fig. 1.

surface Fermi level, in this case, is approximately the same as the surface barrier height. All measurements were performed at room temperature and at a modulation frequency of 200 Hz. For ER measurements, the pumping beam was replaced by an ac bias of 0.5 V at 200 Hz applying across the top layer. To determine of the surface Fermi level and surface state intensity from the dependence of the surface barrier height on the pump beam intensity, the probe beam intensity was maintained at 0.1 μW/cm^2.

IV. RESULTS AND DISCUSSION

The PR spectra of samples with N^+-doped substrate and SI substrate are displayed in Figs. 1 and 2, respectively. Figures 3 and 4 plot the quantity, $(4/3\pi)(E_n-E_g)^{3/2}$, as a function of the index n of the FKO extrema in the spectra displayed in Figs. 1 and 2, respectively. The solid lines represent the least-squares fits to Eq. (1), with E_g obtained from the three point method.[26] The $\hbar\Theta$ can be obtained from the slope of the line. The built-in electric field F is then deduced from $\hbar\Theta$ and is plotted as a function of the thickness of the top layer in Fig. 5 for both categories of samples. Figure 6 presents the surface Fermi level of each sample with N^+-doped substrate, as calculated from Eq. (2). At this point, assume that the surface Fermi level V_F is the same as V_b, since both the probe and the pump beams were defocused on the sample and their intensities were maintained at 1 μW/cm^2. For the samples with N^+-doped substrate, as the thickness of the top layer increases, the electric field decreases and the surface Fermi level position remains roughly the same, 0.35 ± 0.01 eV below the conduction band edge. This result implies that the FKO feature in the PR spectra originates from the electric field over the top layer. The sur-

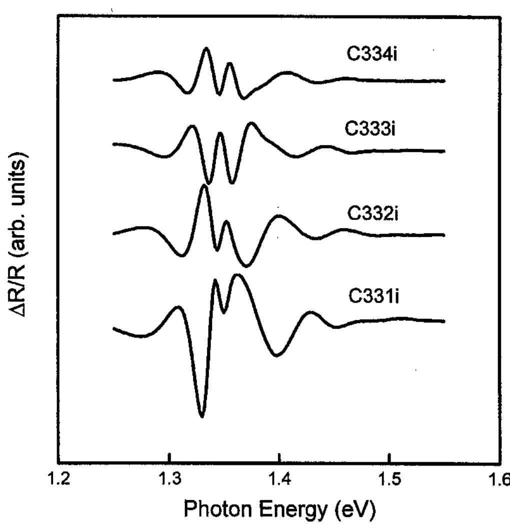

FIG. 2. PR spectra of INP SIN^+ structure with SI substrate.

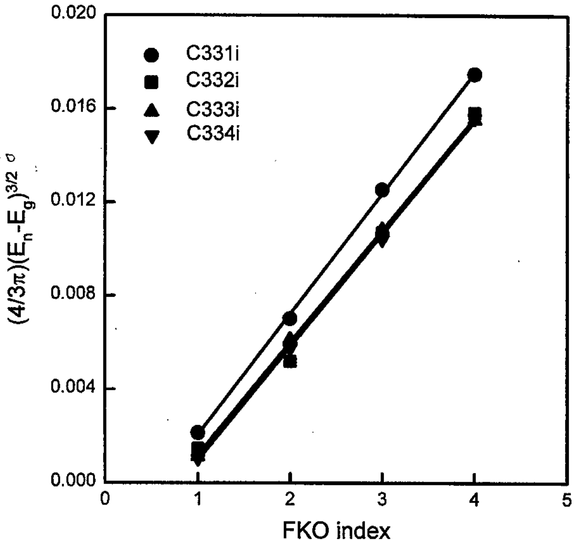

FIG. 4. Plot of $(4/3\pi)(E_n-E_g)^{3/2}$ as a function the FKO extrema index n in Fig. 2.

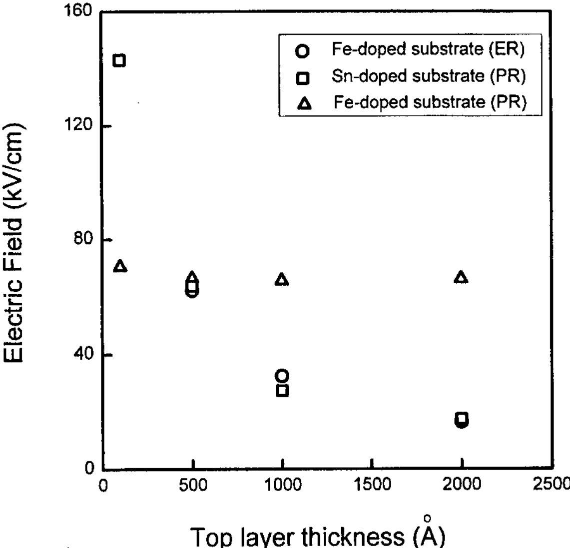

FIG. 5. Built-in electric field as a function of the top layer thickness for all samples measured by ER and PR technique.

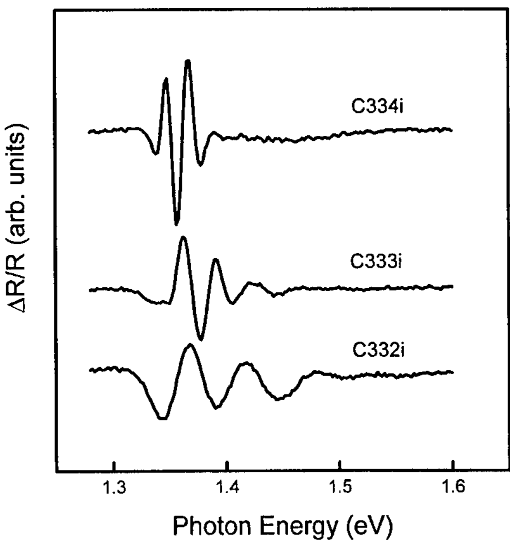

FIG. 7. ER spectra of INP SIN$^+$ structure with SI substrate.

face Fermi level position of this InP SIN$^+$ structure with N$^+$-doped substrate is pinned at the energy band gap. For samples with a SI substrate, however, the built-in electric field is independent of the top layer thickness. This observation can be understood by assuming that the FKO feature in the PR spectra does not simply originate from the electric field across the top layer, but instead, is a superposition of two FKOs arising from the field across the top layer and the field at the interface region of the buffer and the substrate. To investigate the electric field across the top layer and the surface Fermi level position, ER spectra were measured with an ac bias across the top layer. Figure 7 displays the ER spectra of the samples with the Fe-doped SI substrate. Since only the electric field across the top layer is modulated, the FKOs in the ER spectra are a result of the electric field in the top layer. The built-in electric field and the surface Fermi level derived from the ER spectra are also included in Figs. 5 and 6, respectively. The surface Fermi level is notably independent of the top layer thickness and has the same value as the Fermi levels of the samples with the N$^+$-doped substrate that were evaluated from their PR spectra. For the samples with N$^+$-doped substrate, the PR and ER spectra do not significantly differ. The built-in electric fields derived from the PR and ER spectra are almost identical, as are the surface Fermi levels; therefore, the only electric field in this structure exists in the top layer. Since the doping concentration in the buffer and the substrate are identical, no interface charges are accumulated at the interface region.

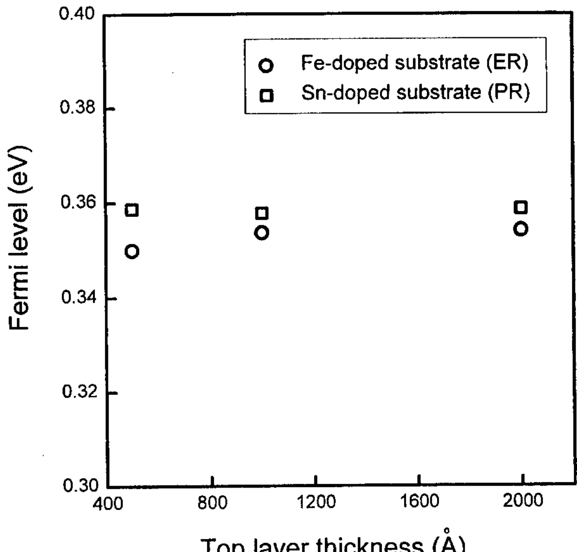

FIG. 6. Measured surface Fermi levels of all samples with different substrates and different top layer thickness.

Room temperature PR spectra of the InP SIN$^+$ structures with N$^+$-doped substrate were measured using various pump beam intensities. Figure 8 displays the PR spectra of the InP SIN$^+$ structure with a top layer thickness of 2000 Å under various pump beam intensities with the probe beam intensity maintained at 0.1 μW/cm^2. Figure 9 depicts with dots the surface barrier height V_b as a function of pump beam intensity for samples C332n, C333n, and C334n. The solid lines in Fig. 9 represent the least-squares fits to Eq. (7). For InP, where $A^* = 10.16\,\mathrm{A/cm^2\,K^2}$, $B = 3.3\times 10^{-4}\,\mathrm{K^{-3/2}}$, $\gamma \cong 1$, $N_o = 5.8\times 10^{14}\,\mathrm{cm^{-3}}$, and $R_0 = 0.31$, the fitting parameters obtained are V_F, η, and r; these parameters are listed in Table II along with the densities of surface states evaluated from $D_s = rN_o$. Fermi levels obtained by this approach are also plotted in Fig. 6. The occupied surface state densities, which are proportional to the surface charge densities, decrease notably with an increase in top layer thickness, because the thicker the top layer, the more difficulty the carriers have moving from the doped layer to the surface.

In this work, the surface state density and the surface Fermi level of semiconductor microstructures were determined simply by varying the intensity of the pump beam while measuring the room temperature photoreflectance.

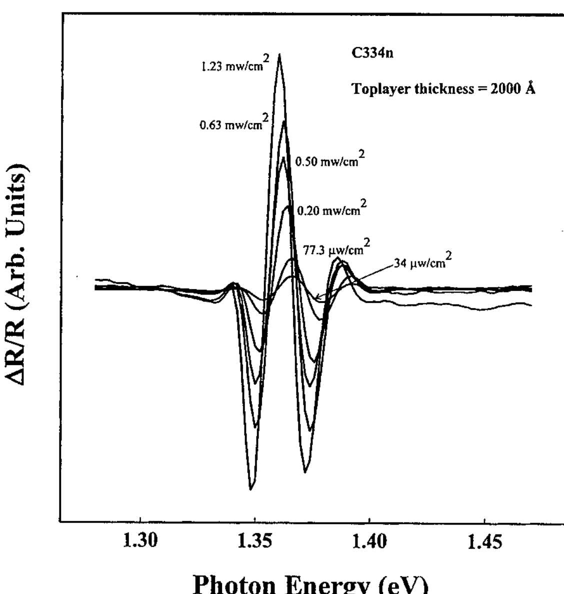

FIG. 8. PR spectra of the C334n InP SIN$^+$ structure with the pump beam intensity varying from 34 μW/cm^2 to 1.23 mW/cm^2.

Since the intensity of the pump beam can be adjusted by simply inserting a gradient neutral density filter in the beam path, using this approach is a much easier and more efficient means than previous methods[10,24] of investigating the surface state density of various semiconductor surfaces or interfaces. Rival methods can be extremely tedious and time consuming.

V. CONCLUSION

This study measured the PR and ER spectra at room temperature from a series of InP SIN$^+$ structures. The electric field in the top layer, and hence the surface Fermi level position, were determined from the FKO analysis. According to our results, the PR and ER spectra of the structures with N$^+$-doped substrate are identical, since the only electric field in this structure exists in the top layer. The significant differences between the PR and ER spectra of the samples with a SI substrate indicates that different electric fields exist separately in the top layer and at the interface of the buffer and the substrate. The surface Fermi level positions for both categories of samples are identical, and independent of their top layer thickness; these positions are pinned at 0.35 ± 0.01 eV below the conduction band edge. A novel approach was developed to find the surface Fermi level and surface state density of semiconductors using room temperature PR spectra under various pump beam intensities. This new approach makes the determination much easier to perform and less time consuming than other approaches.

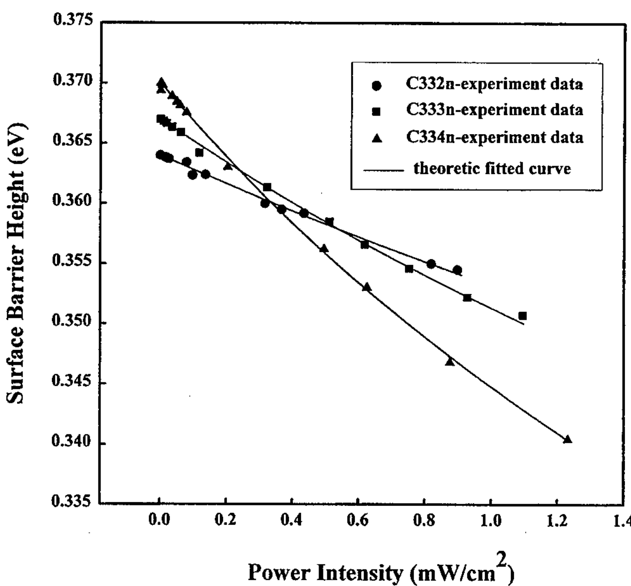

FIG. 9. Measured surface barrier heights V_b as a function of the pump beam intensity. The solid lines are the least-squares fits to Eq. (7).

TABLE II. Surface Fermi level, ideality factor η, geometry factor r, and the surface state densities of InP SIN$^+$ structures obtained from dependence of V_b as a function of pump beam intensity.

Samples	V_F(eV)± 0.02	$\eta \pm 0.2$	$r \pm 1\times 10^{-3}$	D_s(1/cm^2)
C332n	0.36	1.8	9.86×10^{-3}	5.72×10^{12}
C333n	0.37	1.7	8.92×10^{-3}	5.17×10^{12}
C334n	0.37	1.7	8.78×10^{-3}	5.09×10^{12}

ACKNOWLEDGMENT

The authors would like to thank the National Science Council of the Republic of China for financially supporting this research under Contract No. NSC 89-2112-M-006-016.

[1]O. J. Glembocki, Proc. SPIE **1286**, 2 (1990).
[2]J. S. Hwang, Z. Hang, S. L. Tyan, S. W. Ding, J. H. Tung, C. Y. Chen, B. J. Lee, and J. T. Hsu, Jpn. J. Appl. Phys., Part 2 **31**, L571 (1992).
[3]M. Sydor, N. Jahren, W. C. Mitchel, W. V. Lampert, T. W. Haas, M. Y. Yen, S. M. Mudare, and D. H. Tomich, J. Appl. Phys. **67**, 7423 (1990).
[4]H. Shen, S. H. Pan, F. H. Pollak, M. Dutta, and T. R. AuCoin, Phys. Rev. B **36**, 9384 (1987).
[5]S. Moneger, H. Qiang, F. H. Pollak, and T. F. Noble, J. Electron. Mater. **24**, 1341 (1995).
[6]L. Esaki, in *Recent Topics in Semiconductor Physics*, edited by M. Kamimurus and Y. Toyozawa (World Scientific, Singapore, 1983), p. 1.
[7]S. L. Tyan, M. L. Lee, Y. C. Wang, W. Y. Chou, and J. S. Hwang, J. Vac. Sci. Technol. B **13**, 1010 (1995).
[8]R. Bhattacharya, C. Y. Lee, F. H. Pollak, and D. M. Schleich, J. Non-Cryst. Solids **91**, 235 (1987).
[9]H. Shen, F. H. Pollak, and J. M. Woodall, J. Vac. Sci. Technol. B **8**, 413 (1990).
[10]J. S. Hwang, W. Y. Chou, S. L. Tyan, H. H. Lin, and T. L. Lee, Appl. Phys. Lett. **67**, 2350 (1995).
[11]X. Yin, H. M. Chen, F. H. Pollak, Y. Chen, P. A. Montano, J. M. Woodall, P. D. Kirncher, and D. Pettit, Proceedings of the 20th International Conference on the Physics of Semiconductors, Greece, 1990.
[12]M. Kallergi, B. Roughani, J. Aubel, S. Sundaram, T. Chu, S. Chu, and R. Green, J. Vac. Sci. Technol. A **8**, 1907 (1990).
[13]F. H. Pollak and H. Shen, Mater. Sci. Eng., R. **10**, 273 (1993).
[14]D. E. Aspnes and A. A. Studa, Phys. Rev. B **7**, 4605 (1973).
[15]J. S. Hwang and S. L. Tyan, J. Vac. Sci. Technol. A **10**, 3176 (1992).
[16]J. S. Hwang, S. L. Tyan, M. J. Lin, and Y. K. Su, Solid State Commun. **80**, 891 (1991).
[17]H. Shen and M. Dutta, J. Appl. Phys. **78**, 2151 (1995).
[18]X. Yin, H.-M. Chen, F. H. Pollak, Y. Chan, P. A. Montano, P. D. Kirchner, G. D. Pettit, and J. M. Woodall, J. Vac. Sci. Technol. A **10**, 131 (1992).

[19]T. Kanata, M. Matsunaga, H. Takakura, Y. Hamakawa, and T. Nishino, in *Proceedings of the Society of Photo-Optical Instrumentation Engineers* (SPIE, Bellingham, 1990), Vol. 1286, p. 56.
[20]H. Shen, S. H. Pan, Z. Hang, J. Leng, F. H. Pollak, J. M. Woodall, and R. N. Sacks, Appl. Phys. Lett. **53**, 1080 (1988).
[21]J. S. Hwang, S. L. Tyan, W. Y. Chou, M. L. Lee, H. H. Lin, T. L. Lee, D. Weyburne, and Z. Hang, Appl. Phys. Lett. **64**, 3314 (1994).
[22]H. Hovel, in *Semiconductors and Semimetals* (Academic, New York, 1975), Vol. 11, p. 59.
[23]S. M. Sze, in *Semiconductor Devices Physics and Technology* (Wiley, New York, 1985).
[24]X. Yin, H-M. Chen, F. H. Pollak, Y. Chan, P. H. Montano, P. D. Kirchner, G. D. Pettit, and J. M. Woodall, J. Vac. Sci. Technol. A **10**, 131 (1992).
[25]M. Hecht, Phys. Rev. B **41**, 7918 (1990).
[26]See, for example, D. E. Aspnes, in *Handbook on Semiconductors*, edited by M. Balkanski (North-Holland, New York, 1980), Vol. 2, p. 109, and references therein.

Passivation of the Ge/InP(110) interface by As interlayers: Interface reactions and band offsets

A. B. Preobrajenski, S. Schömann, and R. K. Gebhardt
Wilhelm-Ostwald-Institute for Physical and Theoretical Chemistry, University of Leipzig, Linnéstr. 2, D-04103 Leipzig, Germany

T. Chassé[a)]
Wilhelm-Ostwald-Institute for Physical and Theoretical Chemistry, University of Leipzig, Linnéstr. 2, D-04103 Leipzig, Germany and Institute for Surface Modification Leipzig, Permoserstr. 15, D-04303 Leipzig, Germany

(Received 3 February 2000; accepted 12 May 2000)

The formation of the Ge/InP(110) interface at room temperature and the influence of an additional arsenic interlayer on the interface chemistry, the film growth, and the electronic properties of this heterostructure have been investigated using core and valence level photoemission and low-energy electron diffraction. We have shown that an As interlayer at the Ge/InP(110) interface can completely suppress the interface reaction of the Ge with the substrate at room temperature, including partial In–Ge exchange and In segregation. The electronic situation at the interface is characterized by an anomalous evolution of the surface Fermi level with Ge coverage on InP(110) and a high valence band offset of $\Delta E_v = 1.01 \pm 0.07\,\text{eV}$, which is reduced to $\Delta E_v = 0.78 \pm 0.07\,\text{eV}$ for Ge/As/InP(110). We may attribute the differences of the measured valence band offsets to a reaction-induced interface doping of the InP at the real Ge/InP(110) interface, which introduces an interface dipole layer. A calculation of this interface dipole contribution (0.38 eV) using the model of interface induced gap states gives a fair estimate for the experimentally observed difference of the valence band offsets. © *2000 American Vacuum Society.*
[S0734-211X(00)05304-X]

I. INTRODUCTION

The Ge/GaAs and Ge/InP heterostructures have received wide recognition as classical model systems for investigation of peculiarities of semiconductor interface formation. Whereas the Ge/GaAs(110) system with its perfect lattice matching has abrupt and well-defined epitaxial interface, a strong lattice mismatch (~4%) and strong chemical reactions blur the boundary between the constituents in the Ge/InP(110) heterostructure and initiate drastical changes in the surface Fermi-level position (E_F):[1,2] a fast movement of the surface Fermi level E_F from the conduction-band minimum (CBM) into the gap at submonolayer Ge coverages [which is also characteristic for Ge/GaAs(110)] gives way to a slower return of E_F to CBM at higher coverages. Moreover, it has been shown[2] that two different atom distributions with different E_F can be obtained at the same temperature (300 K) and same Ge coverage (0.5 nm) in the Ge/InP(110) system by the room-temperature (RT) deposition and by the deposition at 60 K with subsequent slow annealing to RT. To get clearer insight into the nature of E_F behavior in this system it would be very interesting to passivate the InP(110) surface chemically and electronically before the Ge deposition to prevent interface reactions. Our recent results on the arsenic passivation in some metal–semiconductor systems with the InP(110) surface as a substrate[3,4] have revealed excellent passivating properties of the As monolayer, that is a good reason to use As as an interlayer in the Ge/InP(110) heterostructure as well.

In this study we present the main trends in the formation and evolution of the Ge/As/InP(110) interface with Ge coverage on the basis of photoemission experiments with synchrotron radiation. A detailed comparison of the Ge/InP(110) and Ge/As/InP(110) heterojunctions is performed and the influence of As on interface chemistry, Ge growth mode, Fermi level changes, and magnitude of band discontinuity is analyzed.

II. EXPERIMENT

All photoemission experiments were performed at the TGM 3 beamline of the BESSY I storage ring in Berlin. The total experimental resolution (monochromator plus analyzer) was ~280 meV for the In $4d$, As $3d$, and Ge $3d$ core levels and for the valence bands, and ~500 meV for the P $2p$ core level. To increase the surface sensitivity of the measurements a photon energy of 170 eV was chosen to excite the P $2p$ levels and 75 eV—to excite all other spectra. The n-type InP samples (S doped, $2\times10^{18}\,\text{cm}^{-3}$) were cleaved *in situ* at a base pressure of $4\times10^{-10}\,\text{mbar}$, making use of the double wedge technique. The adsorption of As and the deposition of Ge were carried out using water-cooled Knudsen cells. The required amount of As was controlled by the total As pressure in the preparation chamber. A total As exposure of $50\,\text{L}(1\,\text{L}=1.3\times10^{-6}\,\text{mbar s})$ was used to prepare a completely saturated monolayer of the adsorbate.[5] The evapora-

a)Author to whom correspondence should be addressed; electronic mail: chasse@rz.uni-leipzig.de

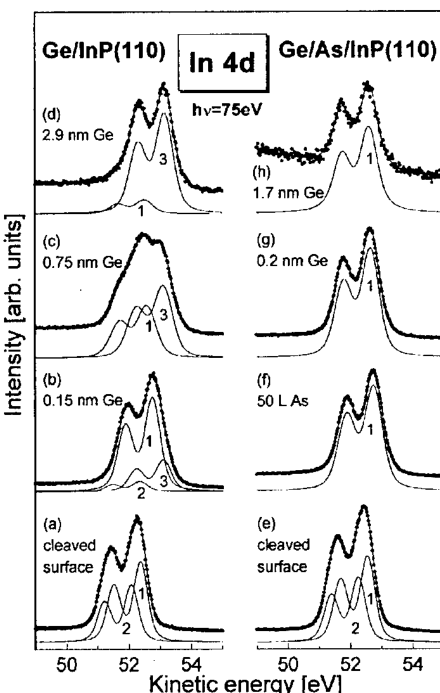

FIG. 1. Surface-sensitive In $4d$ core-level spectra for the Ge/InP(110) interface acquired with increasing Ge coverage without (a)–(d) and with (e)–(h) As interlayer. Components 1, 2, and 3 correspond to signals from bulk, surface, and segregating In atoms, respectively.

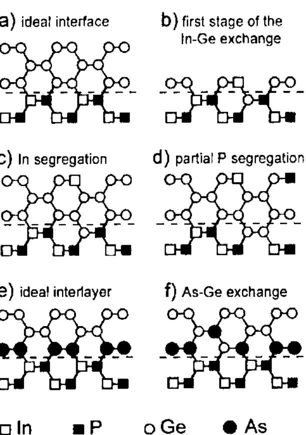

FIG. 2. Schematic models (side views) of the Ge/InP(110) (a)–(d) and Ge/As/InP(110) (e)–(f) interface formation. (a) Ideal Ge/InP(110) interface, (b) first stage of Ge deposition (~1 ML) and partial In–Ge exchange, (c) Ge/InP(110) interface after segregation of the expelled In atoms away from the interface region, (d) possible additional P–Ge exchange with subsequent P removal, (e) ideal Ge/As/InP(110) interface, and (f) Ge/As/InP(110) interface with partial As–Ge intermixing.

tion rate of Ge was 0.08 nm/min as determined by measurements with a quartz microbalance. On the InP(110) surface (surface atom density $8.2\times10^{14}\,cm^{-2}$) one monolayer (1 ML) of Ge corresponds to a nominal layer thickness of 0.185 nm. All deposition experiments were performed at room temperature.

Numerical data analysis was performed by a χ^2 minimization.[6] Typically, for the peak fits all parameters for the main doublet component were allowed to vary, while the line shapes of additional components were constrained to the first one.

III. RESULTS AND DISCUSSION

In order to obtain information on chemical processes at both interfaces of interest the In $4d$, P $2p$, Ge $3d$, and As $3d$ core level spectra were investigated. The energy positions of all the peaks are affected by band bending-induced shifts that will be discussed later. In Fig. 1 In $4d$ spectra are presented without (left) and with (right) As monolayer. Numerical data analysis allows to detect two components in the spectra from the clean cleaved surface [Figs. 1(a) and 1(e)]. They correspond to the bulk In $4d$ signal and to the surface component, which is shifted by 0.31 eV to lower kinetic energies.[5,7,8] Already at submonolayer Ge coverage [Fig. 1(b)] the surface component almost disappears. But another In $4d$ doublet arises with Ge deposition, which is shifted from the bulk signal to higher kinetic energies by 0.3 eV, initially. This new component grows with increasing Ge coverage and dominates the spectrum above nominal layer thickness of 0.5 nm [Figs. 1(c) and 1(d)]. The high energy shift with respect to the bulk component amounts up to 0.65 eV for a 2.9 nm Ge film. We attribute this new signal in the In $4d$ spectrum to released In atoms, resulting from a disruption of the semiconductor surface due to an extensive interface reaction, including exchange of In and Ge atoms. Line shape analysis of the reacted In $4d$ component [Figs. 1(b), 1(c), and 1(d)] does not provide evidence for clustering of the segregated In atoms, because no asymmetry of this line has been found, which would indicate a metallic environment. These results are in analogy with the work of Aldao *et al.*[1] In order to illustrate the atomic arrangements at the interface and their changes due to reaction, exchange, and diffusion processes we have sketched a few simplified models, which are presented in Fig. 2. These models have been developed from the analysis of the core level spectra and reflect bonding and local atomic environment at the interface, but do not intend to predict the exact structure. Note that the low-energy electron diffraction (LEED) patterns disappear quickly after deposition of Ge at room temperature, providing evidence that the Ge layers grow in a disordered fashion rather than pseudomorphically. An ideal Ge/InP(110) interface is shown in Fig. 2(a) while the observed Ge–In exchange at about monolayer coverage is sketched in Fig. 2(b).

The formation of the interface is drastically changed for Ge growth on the As-passivated InP(110). In accordance with our previous work,[3–5] passivation of this surface by an As monolayer results in the disappearance of the surface component in the In $4d$ spectra [Fig. 1(f)]. The In $4d$ line shape is represented by just one single doublet (InP bulk), which does not change at any of the following Ge deposition steps up to the highest coverages used (1.7 nm). This provides unambiguous evidence of the complete suppression of the In–Ge interface exchange by the As interlayer at room temperature. An assumed ideal As monolayer at the interface is sketched in Fig. 2(e).

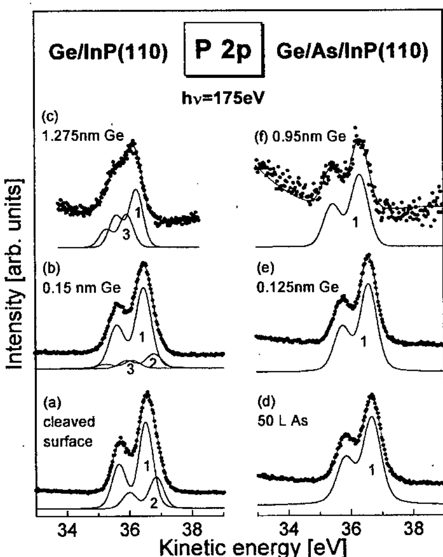

FIG. 3. Surface-sensitive P $2p$ core-level spectra of the Ge/InP(110) interface acquired with increasing Ge coverage without (a)–(c) and with (d)–(f) As interlayer. Components 1 and 2 correspond to signals from bulk and surface P atoms, respectively. Component 3 corresponds to P–Ge reactions and exchange at the interface.

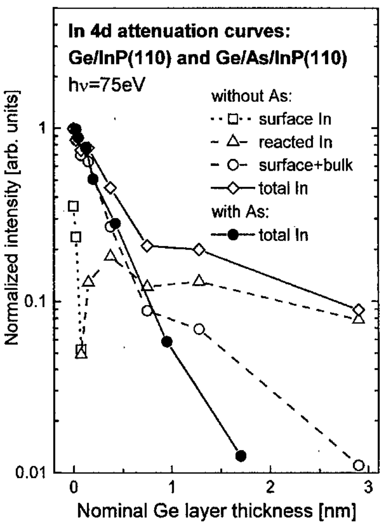

FIG. 4. In $4d$ core-level intensity attenuation due to Ge deposition onto the bare (open symbols) and arsenic-covered (solid circles) InP(110) surface.

An examination of the P $2p$ core level spectra shown in Fig. 3 leads to similar conclusions regarding the interface formation. The clean surface spectra [Fig. 3(a)] reveal the bulk component and the well-known surface component, shifted by 0.34 eV to higher kinetic energy. This surface component disappears rapidly with Ge deposition. After Ge deposition a reacted component occurs in the P $2p$ spectra, which is shifted to higher kinetic energies with respect to the P $2p$ bulk component. This shift reaches 0.42 eV for relatively thick Ge layers [Fig. 3(c)]. This chemical shift indicates a substantial change of the chemical bonding of surface phosphorus atoms due to a P–Ge bonding. But in contrast to the In $4d$ spectra, this reacted component does never dominate the P $2p$ spectra at any of the investigated coverages. This suggests that the reacted phosphorus remains trapped near the interface [see Figs. 2(a), 2(b), and 2(c)]. Pretreatment with As causes a complete suppression of the surface component [Fig. 3(d)] as well as the reacted component also in the case of P $2p$ spectra [Figs. 3(e) and 3(f)], demonstrating suppression of P–Ge reaction at the interface.

In order to study the influence of an As interlayer on the Ge film morphology and growth mode the In $4d$ (Fig. 4) and P $2p$ (not shown) intensity attenuation curves of these substrate-related peaks have been analyzed. The intensity of the In $4d$ surface component vanishes quickly (see Fig. 4). An examination of the intensity of the reacted In component shows that it reaches a maximum at 0.38 nm Ge thickness (~2 ML) but then attenuates very slowly with further Ge deposition onto the InP(110) surface. This insensitivity to the Ge deposition suggests that an extensive segregation of the In atoms takes place, that were released from the InP crystal due to the reaction and expelled from the Ge layer to the surface. Assuming the attenuation length of the In $4d$ electrons in InP at the chosen excitation energy of 75 eV to be between 0.38 nm (from the attenuation of the In $4d$ bulk signal in Fig. 4) and 0.5 nm,[9] the photoelectron intensity from In atoms in the uppermost layer should contribute approximately one third of the whole signal. The intensity of the reacted component at its maximum (at 0.38 nm Ge thickness) is as large as 0.18 of the initial total In $4d$ intensity (see Fig. 4), and therefore it may be concluded that approximately 50% of the In atoms in the uppermost layer of InP ($\frac{1}{4}$ ML) are exchanged with Ge atoms. We can observe a deviation of the intensity attenuation curve of the substrate-related (bulk+surface) In $3d$ signal from a straight line in the semi-log presentation in Fig. 4. Therefore, we may suppose that some Ge islanding occurs beyond 0.75 nm. On the other hand, pretreatment of the InP(110) surface with As prevents evidently any In segregation because of the perfect chemical passivation, as mentioned before. Moreover, As interlayer forces Ge films to grow more evenly, preventing significant islanding at least up to 1.5 nm (see Fig. 4).

The analysis of the attenuation curves for the P $2p$ components (not shown) also supports the occurrence of some Ge islands on the surface without As interlayer, but the P atom redistribution is much weaker in comparison with In. We conclude that P atoms released from the bulk remain generally in the near-interface region. Again, no evidence of Ge island formation has been found on the InP(110) surface preliminary passivated with As.

Complementary information can be obtained from the analysis of the Ge $3d$ spectra in dependence on the nominal film thickness, as shown in Fig. 5. All Ge $3d$ spectra appear broader than expected from the experimental resolution. This observation indicates significant scatter in the local Ge atom environment in the deposited films, which imposes a structurally induced broadening. This is in accordance with the growth of a disordered film as suggested by LEED. The Ge $3d$ peak recorded on the bare interface at submonolayer coverage [Fig. 5(a)] has to be fitted by two doublet components. The intensity of the component at the higher kinetic energy

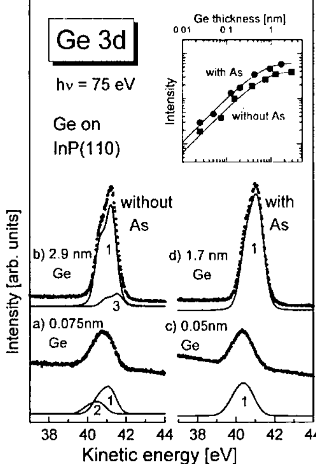

FIG. 5. Surface-sensitive Ge $3d$ core-level spectra of the Ge/InP(110) interface acquired with increasing Ge coverage without (a)–(b) and with (c)–(d) As interlayer. Components 1, 2, and 3 correspond to Ge–Ge, Ge–P, and Ge–In bonds, respectively. Inset shows the evolution of total Ge $3d$ intensity for both cases of interest.

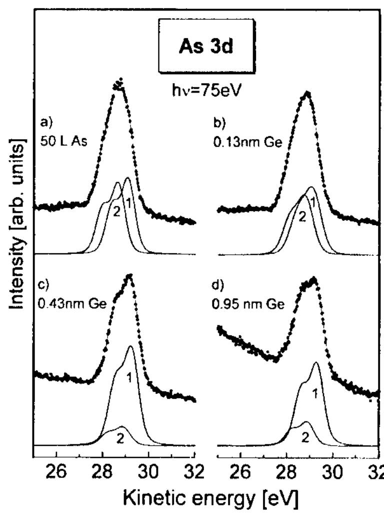

FIG. 6. Surface-sensitive As $3d$ core-level spectra for the Ge/As/InP(110) interface. Components 1 and 2 correspond to arsenic atoms in more cation-like and more anion-like surroundings, respectively.

grows with progressing Ge deposition. This component dominates the spectrum at coverages above 1 ML, while the lower energy component fades away [Fig. 5(b)]. We attribute the lower energy component in Fig. 5(a) to the Ge–P bonding at the interface due to the In–Ge exchange and the higher energy Ge $3d$ component to Ge in the film. Note that the intensity of the lower energy Ge $3d$ component reaches about 1/4 of the total signal at 0.8 ML (not shown). This result supports the earlier estimate of the amount of the In–Ge exchange reaction, which was based on the In $4d$ data. The weak additional, high energy and low-intensity component in Fig. 5(b) may probably originate from Ge surrounded by expelled In atoms.

The Ge $3d$ spectra recorded from the Ge film on the As-saturated surface appear even broader. They can be reasonably fitted with only one broad doublet at all coverages. This is further evidence for the suppression of interface reactions by the arsenic.

The inset in Fig. 5 shows the intensity evolution with nominal Ge coverage in a log–log plot. The initial slopes of the intensity curves from both interfaces correspond to $\sim$1.0 up to about monolayer coverage. This demonstrates that the intensity is strictly proportional to the amount of deposited Ge, in this manner proving the two-dimensional growth in the initial stage of film deposition very clearly. The solid lines in the inset represent exponential curves, which describe the intensity increase towards signal saturation for high Ge film thickness. The good matching of the intensity data and the model curves indicates, that the Ge film may be rather well characterized by a laterally homogeneous growth in layer thickness at least up to about 1 nm Ge, in accordance with the discussion of Fig. 4.

In order to shed more light on the effects of Ge deposition on the As interlayer during the formation of the Ge/As/InP(110) heterostructure we have also analyzed the As $3d$ spectra of this system. A set of As $3d$ spectra is shown in Fig. 6. After adsorption of the As monolayer two As $3d$ doublets of equal intensity with energy separation of 0.43 eV can be distinguished by using a numerical line shape analysis [Fig. 6(a)]. The fitting procedure is found to be very stable giving consequent results for the whole series of the As $3d$ spectra. In accordance with our previous results[5] we attribute the components in the initial spectrum to As species bound to surface P (As–P, at lower kinetic energy) and to As species bound to surface In (As–In, at higher kinetic energy) in the monolayer. The only change of the As $3d$ spectrum at submonolayer Ge coverage is a slight broadening of the two components, which we associate with an influence of randomly distributed Ge atoms on the surface. But the intensity ratio and the energy shift of the As components remain almost constant [Fig. 6(b)]. Above monolayer Ge coverage [Figs. 6(c) and 6(d)] the following significant changes occur in the As $3d$ spectrum: (i) a dramatical change of the intensity ratio in favor of the component with higher kinetic energy; (ii) an additional broadening of this component followed by a narrowing beyond 0.9 nm Ge; and (iii) gradual energy shift of this component from the second one up to 0.53 eV at 1.7 nm Ge. All these changes in the shape of the As $3d$ signal argue for a partial substitution of As atoms, originally attached to surface P by Ge atoms [Fig. 2(f)]. This is clearly illustrated by examination of the attenuation curves of both components in Fig. 7. At nominal Ge thicknesses from 0.1 to 0.4 nm ($\sim$0.5–2 ML) the intensity of the As–P component drops down so rapidly, that it cannot be explained by an exponential attenuation due to an overlayer. In contrast, the intensity of the component attributed to As–In bonding even grows in this range of coverage in spite of the increasing Ge layer thickness. We are thus led to suppose a breaking of some part of the weaker As–P bonds and a limited exchange of As and Ge atoms. The intensity increase of the As component with higher kinetic energy one should understand as occurrence of another (besides As–In) As species in cation-like surroundings, which can contribute to this

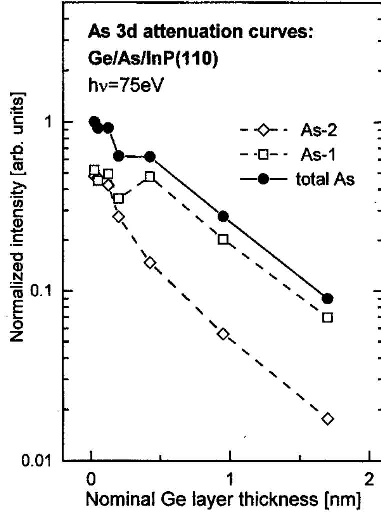

FIG. 7. As $3d$ core-level intensity attenuation due to Ge deposition onto the arsenic-covered InP(110) surface. Open squares represent the signal from As atoms in anion-like surrounding (As-2) and circles are related to the signal from As atoms in cation-like surrounding (As-I).

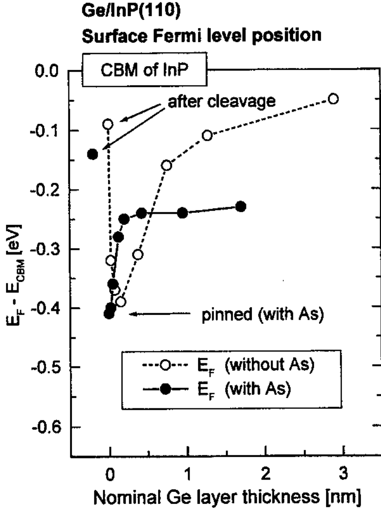

FIG. 8. Evolution of the surface Fermi-level position at the Ge/InP(110) heterostructure with increasing Ge coverage without (open circles) and with (solid circles) As interlayer. Energies are referred to the CBM of InP.

component. In all up to four types of such surroundings of As could be possible as a result of As–Ge exchange: (1) In, Ge, and 2 As, (2) In, 2 Ge, and As, (3) 4 Ge, and (4) In and 3 Ge. So, it would be more correct to denote the high energy component in the As $3d$ spectrum as "As in more cation-like surrounding." Taking into account that this signal can contain up to four components with close energy positions, it is easy to realize why a significant broadening of this signal is observed at an intermediate stage of deposition. (Just to keep a reliability of the numerical fit we treated it as a single component.) Such a nature of the high energy component (As-1) explains also its slight gradual shift from the As–P component (As-2) to higher kinetic energies.

Investigations of As interlayers at metal–semiconductor contacts[3,4] have shown that some part of As atoms can be released from the interlayer and can be expelled to the surface of the growing metal films acting as surfactants. Although in the case of Ge/As/InP heterostructure some As–Ge exchange is also likely to take place (up to 60% of the As–P species, as estimated from Fig. 7), the released As species does not tend to behave as a surfactant. The probable reason for this is the covalent bonding in Ge as well as the similar atom size. It should be emphasized that the presence of the As interlayer still seems to prevent Ge islanding in spite of the lack of surfactant properties.

In Fig. 8 the evolution of the InP(110) surface Fermi level position (E_F) during Ge deposition without (open circles) and with (solid circles) As interlayer is shown. We have used the energy position of the bulk $4d_{5/2}$ component in the In $4d$ spectrum [16.65 eV below the valence-band maximum (VBM) of InP] to determine E_F in the gap of InP. The VBM position of Ge was measured directly. On the clean n-InP(110) surface E_F was found close to the CBM. With increasing deposition of Ge the surface Fermi level moves into the gap, reaching a minimum (≈0.96 eV above VBM) at 0.15–0.20 nm Ge (about 1 ML), and then it retreats slowly towards the CBM. These results on the behavior of E_F as a function of Ge coverage in the Ge/InP system without passivating interlayer (Fig. 8) are very similar to the results of other groups.[1,2,10] In the presence of an As interlayer the behavior of E_F is drastically different. Initially E_F is pinned by the presence of the As monolayer at about 0.94 eV above the VBM, in accordance with previous results.[5] Due to the Ge deposition E_F shifts towards the CBM, reaching a saturation position (≈1.13 eV above the VBM) at 0.2–0.4 nm Ge (~1–2 ML).

In order to account for the changes in E_F position in both cases of interest (Fig. 8) we have to consider the essentially different electronic nature of the respective surfaces before the Ge deposition. The clean cleaved n-InP(110) surface is unpinned and the As-passivated one is pinned by arsenic adatom-induced states at 0.94±0.02 eV above the VBM. This position is in reasonable agreement with the position of the lowest unoccupied As-induced state in the gap of InP calculated in the framework of density-functional theory for As adsorption on InP(110).[11] Because of different electronic properties of the substrate surface before and after As adsorption (unpinned and pinned, respectively) the absolute change of the surface E_F position at the first deposition step (0.025 nm, approximately 0.12 ML Ge) is as large as 210 meV in the Ge/InP(110) system and only 10 meV in Ge/As/InP(110). In the case of unpassivated substrate the surface E_F position tries first to achieve some equilibrium value in the gap pinned by adsorbate induced states of single Ge atoms. The states induced by the In atoms, which are released due to the interface reaction, may also contribute to this tendency. If there would be no interface reactions at all, such a position could be reached already at coverages of some tenth of a ML (or at least at 1 ML in the case of common overshoot effects) but it should not change significantly thereafter. The extensive interface disruption causes a competitive tendency in this movement of the surface Fermi level, driving the E_F position up to the CBM with increasing Ge layer

thickness. We associate this tendency mainly with the In–Ge exchange resulting in a strong *n* doping of the InP substrate by Ge in close proximity to the interface. A similar explanation was proposed by Mahowald *et al.*,[10] who also attributed the E_F reversal to formation of P–Ge donor bonds, but in Ge, as a result of the P–Ge exchange. (There will be no difference at all if we consider the case under study as a heavy donor doping of a thin intermediate region enriched with Ge–P bonds.) The minimum of the surface Fermi-level position is reached at approximately 1 ML Ge as a compromise of two earlier mentioned competitive trends and does not probably achieve the equilibrium position in the gap. This position should be expected somewhat below the overshoot minimum and was achieved in the experiment of Aldao *et al.*[2] with Ge deposition at 60 K and subsequent slow annealing to 300 K, resulting in a nondisruptive interface. In the presence of the As interlayer in the Ge/InP(110) heterostructure both earlier mentioned driving forces of E_F movement are absent: E_F is initially pinned and no interface doping comes into play because of the lack of interface reactions. The only change in the surface E_F position is a movement towards the CBM from the pinning position (0.94 eV above the VBM) to 1.11 eV at 0.2 nm Ge. We attribute this change to enhancement of donor properties of the As monolayer after Ge deposition because of As–Ge donor bonds, resulting in a single positively charged layer localized in the plane of As atoms.

An even more important issue for understanding of the electronic properties of heterocontacts than the evolution of the surface Fermi-level position are the band discontinuities at the interface and in particular the valence band offset ΔE_v. We have derived ΔE_v in the usual manner[1,2,16] from relative energy separations of the InP and Ge valence band edges, which have been corrected for band bending by taking into account the shifts of the related shallow In 4*d* and Ge 3*d* core levels. The In 4*d*–Ge 3*d* energy distance has been observed to be constant at coverages of about 1 nm and above. The measured valence band offset $\Delta E_v = 1.01$ (± 0.07) eV of the Ge/InP(110) interface agrees very well with the value of 1.03 eV reported previously by Aldao *et al.*[1,2] However, the measured discontinuity ΔE_v varies considerably under influence of As interlayer. The determined valence band offset of 0.78 (± 0.07) eV at the Ge/As/InP(110) heterointerface is significantly smaller than on the bare interface. Note that this change of ΔE_v was measured reproducibly in a set of similar independent experiments.

At an ideal abrupt Ge/InP(110) interface in absence of defects, interface reactions and strain effects Tersoff's model of charge neutrality level (CNL) predicts ΔE_v heights as a simple difference in the position of branching points ϕ_{CNL} of Ge and InP, because the electronegativities of the materials are almost equal and no charge transfer occurs at the interface. Using the results of the calculations of Cardona and Christensen[12] of midgap energies for Ge and InP, the theoretical value of ΔE_v for the ideal interface can be estimated as 0.84 eV. Other related theoretical approaches estimate the difference in CNL for InP and Ge as 0.58,[13] 1.14,[14] and 0.63 eV.[15]

But the real Ge/InP(110) heterostructure is characterized by extensive interface reactions and atom exchange, as discussed earlier. This atomic exchange [see also Figs. 2(b), 2(c), and 2(d)] may induce the occurrence of charged electronic defects, leading to an interface doping. From the analysis of the situation at the passivated interface [see also Figs. 2(e) and 2(f)] we suggest that the measured value of valence-band offset in Ge/As/InP(110) (0.78 eV) can be used as a good approximation of the value for the ideal, nonreacted, defect-free, and unstrained Ge/InP interface. The Ge deposition on top of As-passivated InP(110) leads to the occurrence of a positively charged layer of As–Ge donor bonds, which can affect the E_F position, but no doubly charged layer appears and no dipole contribution influences the band offset. The earlier mentioned partial As–Ge exchange shown schematically in Fig. 2(f) (up to 60% of the As–P species or 30% of all As atoms as can be estimated from Fig. 7) does not change the situation: it results only in a slight redistribution of the same positive charge from the As layer to Ge. It should also be noted that our measured value of ΔE_v in case of Ge/As/InP (0.78 eV) is in fact very close to the theoretical value for the neutral valence-band offset in ideal Ge/InP heterostructure (0.84 eV) obtained from by Cardona and Christensen.[12]

Returning to the reacted Ge/InP interface, it is straightforward to ascribe the observed enhancement of $\delta(\Delta E_v) = 0.23\,\mathrm{eV}$ to the influence of defects. This enhancement $\delta(\Delta E_v)$ may be attributed either to charged donors on the InP side or to charged acceptors on the Ge side of the interface. This is consistent with the formation of P–Ge donor bonds on the InP side and In–Ge acceptor bonds on the Ge side as a result of the Ge–In exchange, as discussed earlier. Thus, Ge–In exchange seems to be the main mechanism responsible for increase of ΔE_v in the real Ge/InP heterostructure. Further, it is probably the P–Ge donor bonds, which govern the valence-band offset, because of their localization in the uppermost InP layer whereas In–Ge acceptor bonds are delocalized as a result of In segregation and contribute rather to Ge bulk doping. The electron density released at P–Ge donor bonds fills some part of unoccupied interface-induced gap states (IIGS) on the InP side and creates a doubly charged layer between this negative charge of IIGS and positive charge of P–Ge donors. This doping-induced dipole may be regarded as the main reason for the enhancement of ΔE_v in the real Ge/InP heterostructure.

The value of $\delta(\Delta E_v)$ can be estimated by analogy with the semiempirical approach of Mönch[16] for Schottky barrier heights at metal–semiconductor interfaces

$$\delta(\Delta E_v) = (1-S)[1-f_0(E_{\mathrm{id}}-E_F)]\frac{N_{\mathrm{id}}}{D_{\mathrm{gs}}^{\mathrm{ii}}},$$

where N_{id} is the surface density of interface defects, $D_{\mathrm{gs}}^{\mathrm{ii}}$ is the number of IIGS per unit area and unit energy, $f_0(E_{\mathrm{id}} - E_F)$ is the Fermi–Dirac distribution function, and

$$S=\frac{1}{1+(e_0^2/\epsilon_0\epsilon_i)D_{gs}^{ii}\delta_i}$$

is the slope parameter. Here e_0 is the electronic charge, ϵ_0 is the vacuum permittivity, ϵ_i is the static dielectric constant of the interface, and δ_i is the characteristic thickness of the double charged layer. Although these equations were obtained for the case of metal-induced gap states at metal–semiconductor contacts, their application may be extended to interfaces between two semiconductors, because the nature of the induced gap states is the same: they derive from the virtual gap states of the complex band structure of the semiconductors, and the mechanism of band alignment is similar. The valence band of Ge does not contain narrow-band features, which could induce resonance states in D_{gs}^{ii} of InP.[17] Assuming that the value of D_{gs}^{ii} does not change too much aside from the VBM and CBM, it can be crudely approximated by D_{gs}^{ii}(CNL). δ_i is determined by the penetration depth of IIGS into InP and can be estimated as 0.42 nm.[18] ϵ_i can be written as the average of ϵ_{Ge} and ϵ_{InP}. Provided 50% of the In atoms in the uppermost layer are exchanged with Ge, the density of interface donors N_{id} has to be as much as $2.05\times10^{14}\,cm^{-2}$. Using $\epsilon_i=14.4$, $D_{gs}^{ii}(CNL)=3.45\times10^{14}\,cm^{-2}\,eV^{-1}$,[17] and assuming all donors are charged ($f_0=0$), we obtain $\delta(\Delta E_v)=(0.38\pm0.1)$ eV. This value lies somewhat above the experimental result of 0.23 eV. Strain effects have been reported to increase ΔE_v by 0.2–0.3 eV on pseudomorphically grown Ge/InP(001) interfaces.[19] But these effects are rather unlikely to contribute to a large extent to the band offsets in our experiments since the investigated Ge films are amorphous or polycrystalline and only short-range order still persists in geometrical arrangement of Ge atoms. The difference between theoretical estimate and experimental values might be partly associated with incomplete charge of donor defects, although the E_F position does not seem to be fully pinned by the defect levels (Fig. 8). But a reliable estimate of the extent of such a contribution is hardly possible with the available data. We believe that the discrepancy is most likely due to the partial diffusion of *P* atoms into Ge and/or possible partial desorption of *P* atoms during Ge evaporation with corresponding reduction of density of P–Ge donor bonds on the InP side of the interface, as suggested in Fig. 2(d). Taking into account the complexity of defect structure in the real reacted Ge/InP heterostructure, it can be nevertheless concluded that the concept of interface doping can not only explain the mechanism of valence-band offset enhancement in this system, but it can also predict the magnitude of this enhancement semiquantitatively.

IV. CONCLUSIONS

The Ge/InP(110) interface formation at room temperature is described by a limited interface reaction, including a partial In–Ge exchange and In segregation, essentially, which accompany the growth of a disordered, unstrained Ge film. The electronic situation at the interface is characterized by an anomalous evolution of the surface Fermi level with Ge coverage and a high valence band offset of $\Delta E_v=1.01\pm0.07$ eV. These observations are in good agreement with prior studies.[1,2]

We have shown that an As interlayer at the Ge/InP(110) interface can completely suppress the interface reaction of the Ge with the substrate at room temperature. The evolution of the surface Fermi level with increasing Ge coverage proceeds completely different for the heterostructure with As interlayer due to suppression of the reaction and the absence of interface defects. The valence band offset is also influenced by preliminary As passivation and it is reduced to $\Delta E_v=0.78\pm0.07$ eV for Ge/As/InP(110), which value is in close agreement to theoretical predictions for the ideal Ge/InP interface (0.84 eV).[12] These results let us suggest, that the As-passivated interface provides a reasonable approach for an unreacted, unstrained Ge/InP(110). Therefore we may attribute the differences of the measured valence band offsets to a reaction-induced interface doping of the InP at the real Ge/InP(110) interface, which introduces an interface dipole layer. A calculation of this interface dipole contribution (0.38 eV) using the model of IIGS gives a fair estimate for the experimentally observed difference of the valence band offsets.

ACKNOWLEDGMENTS

This work was supported by the BMBF, Contract No. 05 SE8 OLA, and by the DFG, Graduiertenkolleg ''physical chemistry of interfaces'' at the University of Leipzig. The authors thank K. Horn and his group (FHI Berlin) for support and cooperation at BESSY.

[1] C. M. Aldao, I. M. Vitomirov, F. Xu, and J. H. Weaver, Phys. Rev. B **40**, 3711 (1989).
[2] C. M. Aldao, I. M. Vitomirov, G. D. Waddill, and J. H. Weaver, Phys. Rev. B **43**, 13952 (1991).
[3] S. Schömann, K. Schmidt, H. Peisert, T. Chassé, and K. Horn, Surf. Sci. **352–354**, 855 (1995).
[4] S. Schömann and T. Chassé, J. Vac. Sci. Technol. A **16**, 2990 (1998).
[5] T. Chassé, G. Neuhold, and K. Horn, Surf. Sci. **331–333**, 511 (1994).
[6] R. Hesse, T. Chassé, and R. Szargan, Fresenius J. Anal. Chem. **365**, 48 (1999).
[7] W. Wilke, V. Hinkel, W. Theis, and K. Horn, Phys. Rev. B **40**, 9824 (1989).
[8] A. B. McLean and R. Ludeke, Phys. Rev. B **39**, 6223 (1989).
[9] S. Tanuma, C. J. Powell, and D. R. Penn, Surf. Interface Anal. **20**, 77 (1993).
[10] P. H. Mahowald, T. Kendelevicz, K. A. Bertness, C. E. McCants, M. D. Williams, and W. E. Spicer, J. Vac. Sci. Technol. B **5**, 1258 (1987).
[11] S. Schömann, Ph.D. thesis, Leipzig University, 1997.
[12] M. Cardona and N. E. Christensen, Phys. Rev. B **35**, 6182 (1987).
[13] J. Tersoff, Phys. Rev. B **30**, 4874 (1984).
[14] W. Mönch, Appl. Surf. Sci. **117–118**, 380 (1997).
[15] C. Ohler, C. Daniels, A. Förster, and H. Lüth, Phys. Rev. B **58**, 7864 (1998).
[16] W. Mönch, *Semiconductor Surfaces and Interfaces* (Springer, Berlin, 1995).
[17] E. Louis, F. Yndurain, and F. Flores, Phys. Rev. B **13**, 4408 (1976).
[18] C. Tejedor, F. Flores, and E. Louis, J. Phys. C **10**, 2163 (1977).
[19] D. Rioux, R. Patel, and H. Höchst, Phys. Rev. B **45**, 6060 (1992).

Polarized laser light scattering applied to surface morphology characterization of epitaxial III–V semiconductor layers

M. U. González[a)]
Instituto de Microelectrónica de Madrid (IMM-CNM), Consejo Superior de Investigaciones Científicas, C/Isaac Newton, 8, 28760 Tres Cantos, Madrid, Spain

J. A. Sánchez-Gil
Instituto de Estructura de la Materia, Consejo Superior de Investigaciones Científicas, Serrano, 121, 28006 Madrid, Spain

Y. González and L. González
Instituto de Microelectrónica de Madrid (IMM-CNM), Consejo Superior de Investigaciones Científicas, C/Isaac Newton, 8, 28760 Tres Cantos, Madrid, Spain

E. R. Méndez
División de Física Aplicada, Centro de Investigación Científica y de Educación Superior de Ensenada, Apdo. Postal 2732, Ensenada, Baja California, 22800 México

(Received 12 August 1999; accepted 5 May 2000)

In this paper, we analyze typical morphologies of epitaxial III–V semiconductor layers by using a polarized laser light scattering technique. Crosshatched topographies, which are developed during heteroepitaxial growth, are studied. A sample with an intentionally high density of oval defects is also explored to establish how the laser light scattering pattern is affected by the presence of these defects, which are unavoidable in the epitaxial layers grown by molecular beam epitaxy. The former topographies produce a scattered light pattern that is highly anisotropic, with the intensity concentrated along two preferential directions; the latter defects give rise to a fairly isotropic pattern. Employing a perturbation-theoretical model, whose applicability and consistency are explicitly demonstrated by our results, the surface power spectral density is retrieved from the angle-resolved light scattering experimental data. For the samples exhibiting crosshatched topography, the scattering measurements provide information that allows us to model the roughness of the surface in terms of two quasi-one-dimensional, anisotropic components, and one two-dimensional, isotropic, long-range background. The root mean square heights and the typical lateral distances between ridges are obtained in quantitative agreement with the values extracted from the atomic force microscopy measurements. For the sample presenting oval defects, we consider their contribution to the surface power spectral density by means of a simple model of randomly distributed particles on a surface, and we compare the resulting power spectral density with typical behavior found in the literature for good-morphology GaAs layers. With the help of the *ex situ* information thus obtained, we also discuss the implementation of the light scattering technique for *in situ* monitoring during epitaxial growth. © *2000 American Vacuum Society.*
[S0734-211X(00)04904-0]

I. INTRODUCTION

Epitaxial growth techniques are essential for the fabrication of new and sophisticated electronic devices, such as millimeter and microwave integrated circuits and vertical cavity surface emitting lasers.

The quality of the epitaxially grown structures greatly depends on the deposition parameters, such as substrate temperature, growth rate, and flux ratios. Thus, it is necessary to use real-time control techniques of the epitaxial process. In this situation, the development of *in situ* characterization techniques during growth is crucial. Optical techniques such as dynamic optical reflectance, ellipsometry, differential reflectance spectroscopy, reflectance anisotropy, and light scattering are very powerful tools because they are simple, fast, inexpensive, contact-free, nondestructive and noninvasive, and they do not require vacuum conditions. These techniques can be used in most commonly encountered pressure environments employed in the different epitaxial growth processes.

Laser light scattering (LLS) is an especially interesting technique, due to its sensitivity to surface morphology, which is a critical parameter to obtaining good performance in electronic and optoelectronic devices. Moreover, the monitoring of the surface morphology features that develop during epitaxial growth of different heterostructures provides information about important processes that take place during growth, such as plastic and elastic relaxation, and three-dimensional nucleation, or the formation of quantum dots.

Although the inverse problem in electromagnetic theory is in general a formidable task, it has already been shown that in certain limits the LLS intensity can be related to the mean surface roughness.[1] Under the assumption of smooth rough-

[a)]Electronic mail: ujue@imm.cnm.csic.es

ness and small slopes, the angular distribution of the scattered intensity can be calculated by means of perturbation theories.[1,2] By retaining the lowest-order term in the expansion of the scattering amplitude in powers of the surface profile function, the resulting scattered intensity can be shown to be proportional to the surface power spectral density (PSD), namely, the Fourier transform of the correlation function of the surface topography. This applies not only to the simplest scattering configuration, consisting of a rough interface separating vacuum (or any other propagating medium) from a semi-infinite, dielectric medium (see Refs. 1–3, and references therein); similar proportionality has been found in the case of a rough film on a planar substrate with different dielectric permittivities,[4–8] and even for multilayer structures.[9,10] The criteria for the applicability of such perturbation-theoretical expressions[1,2,11] for the typical surface roughness developed during epitaxial growth are, in most cases, fulfilled as a result of the high smoothness of the surfaces thus generated. This allows us to use the LLS technique for viewing and studying surface features as small as tenths of nanometer in height and with lateral dimensions larger than $\lambda/2$ (Rayleigh limit). It should be mentioned that the latter limit for the optically discernible lateral dimensions can be overcome by using near-field optical microscopy,[12] a technique that unfortunately poses severe difficulties for implementation as a real-time characterization tool.

As demonstrated,[13–17] LLS is a powerful technique for *in situ* monitoring of surface evolution during growth. However, its implementation is complicated by geometrical restrictions imposed by the growth reactor, which does not usually allow obtainment of the full spatial distribution of the scattered intensity. Nevertheless, the time evolution of scattered light at fixed angular positions still yields useful information. Therefore, in order to choose the most appropriate configuration for *in situ* measurements and to achieve a correct interpretation of the results, we have carried out *ex situ* characterization of common surface morphologies that develop during epitaxial growth of III–V systems. Our aims in this paper are to assess the capabilities of the LLS technique to characterize the topography of this kind of systems and to evaluate the validity and utility of the scattering perturbation theory applied to interpret it.

To that end, in Sec. III we present the results from polarized light scattering experiments (the experimental setup being described in Sec. II) of two typical surface topographies developed during epitaxial growth by molecular beam epitaxy (MBE) on (001) III–V semiconductor substrates: the crosshatched surface morphology, and the presence of oval defects. The oval defects are randomly distributed isolated defects, which appear related to two main causes: (i) impurities and particulates on the surface substrate prior to growth, and (ii) liquid-gallium "spitting" and gallium oxides coming from the gallium cell during growth.[18] The formation of oval defects in MBE epitaxial layers is inherent to the growth process, although their density can be significantly reduced with state-of-the-art MBE technology. One of the challenges is analyzing the scattered signal due to the

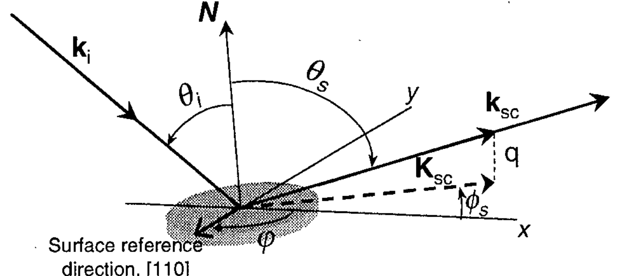

FIG. 1. Schematic of the light scattering geometry for plane-wave incidence.

presence of this kind of defects, which is convoluted with surface roughness contributing to the LLS signal. The crosshatched morphology (see Ref. 14, and references therein) develops during growth of low-strained heteroepitaxial systems (mismatch $\epsilon_0 < 2\%$) and consists of ripples and troughs aligned along [110] and [$1\bar{1}0$] directions. It is associated with local surface diffusion variations caused by the presence of strain fields related to misfit dislocations formed during plastic relaxation.

The LLS experimental data are then evaluated by means of the scattering perturbation theory to obtain the PSDs of the samples under study, providing qualitative and quantitative information of the surface topography; this is discussed in Sec. IV. Finally, our main results (summarized in Sec. V) support the high potential of LLS as an *in situ* characterization technique for monitoring growth.

II. EXPERIMENT

The samples studied in this work consist of 400-nm-thick $In_{0.2}Ga_{0.8}As$ layers grown on GaAs (001) substrates (lattice mismatch $\epsilon_0 = 1.4\%$). One of the layers (sample A) was grown by MBE at a substrate temperature $T_s = 500\,°C$ and the other (sample B) was grown by atomic layer molecular beam epitaxy (ALMBE) at $T_s = 200\,°C$. We have also studied homoepitaxial samples of GaAs on GaAs (001) with different densities of oval defects. Here, we show the results for a 780-nm-thick layer of GaAs grown by MBE at $T_s = 580\,°C$ (sample C), which presents an extremely high density of large oval defects with a broad distribution of lateral size (100 nm$<l<$8 μm) and height (50 nm$<h<$1 μm). The surface morphology of all these layers was studied by polarized laser light scattering and the results were cross-checked with atomic force microscopy (AFM) measurements of the surface topography.

A schematic of the light scattering geometry for plane-wave incidence is shown in Fig. 1. The incident wave vector $\mathbf{k}_i$ and the surface normal $\mathbf{N}$ fix the so-called plane of incidence π_{inc}, whose intersection with the surface plane is taken as the origin for the azimuthal angles. The scattered wave vector direction is determined by the polar, θ_s, and azimuthal, ϕ_s, scattering angles $(-\pi/2 \leq \theta_s \leq \pi/2, -\pi/2 \leq \phi_s \leq \pi/2)$. Only the polar angle of incidence, θ_i, is necessary to determine the incident wave vector direction because of the definition of the origin of azimuthal angles ($\phi_i \equiv 0$). We have also included the "surface azimuthal" angle φ (0

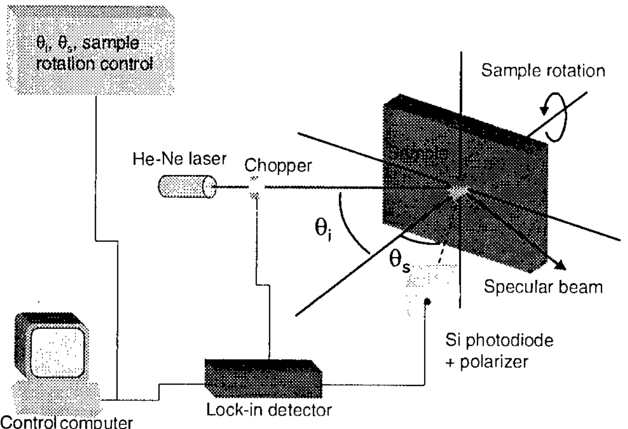

FIG. 2. Experimental setup for the polarized laser light scattering (LLS) measurements. A 10 mW linearly polarized He–Ne laser ($\lambda=633$ nm) is used as incident light. The sample is placed in a goniometer that permits us to change the angle of incidence θ_i between 0° and 60°, and the surface azimuthal angle φ between 0° and 360°. Scattered light is collected with a silicon photodiode situated in the plane of incidence $\pi_{\rm inc}$ and mounted on a rotatable arm that scans between polar scattering angles θ_s of −72° and 72°. We have introduced a polarization analyzer in front of the photodiode to select the polarization of the detected light. We employ lock-in detection to improve the signal-to-noise ratio.

$\leqslant\varphi\leqslant 2\pi$), which accounts for the surface position with respect to the plane of incidence. We define φ as the angle between a reference direction of the surface and the intersection of $\pi_{\rm inc}$ with the surface plane. We have chosen the [110] direction as the surface reference direction.

Our LLS experimental setup is shown in Fig. 2. We use as incident light a 10 mW linearly polarized He–Ne laser ($\lambda=633$ nm), whose spot on the sample has a diameter of 1 mm. The laser can be rotated to select the beam polarization. The sample is placed on a goniometer, which permits us to change the polar angle of incidence θ_i between 0° and 60°, and the surface azimuthal angle φ between 0° and 360°. The scattered light is collected with a silicon photodiode situated in the plane of incidence; thus $\phi_s=0$ in all our measurements. The photodiode is mounted on a rotatable arm that can move in the plane of incidence, scanning polar scattering angles θ_s from −72° to 72°. In front of the photodiode we have introduced a polarization analyzer to select the polarization of the detected light. It should be pointed out that when θ_s is very close to $(-\theta_i)$, the photodiode blocks the He–Ne laser light; consequently, the backscattering information is not available in our experiments. We employ lock-in detection to reject spurious signals and to improve the signal-to-noise ratio. This setup allows us to carry out two types of measurements: angle-resolved light scattering (ARLS) and azimuthal-dependent light scattering (AzLS).

For the AzLS measurements, we choose the angle θ_i and the polarization of the incident beam, place the photodiode at a fixed polar scattering angle θ_s in the plane of incidence, and rotate the sample to obtain the scattered intensity at different surface azimuthal angles. With this kind of measurements, we can distinguish between isotropic scattering, independent of φ, and anisotropic scattering. In the latter case,

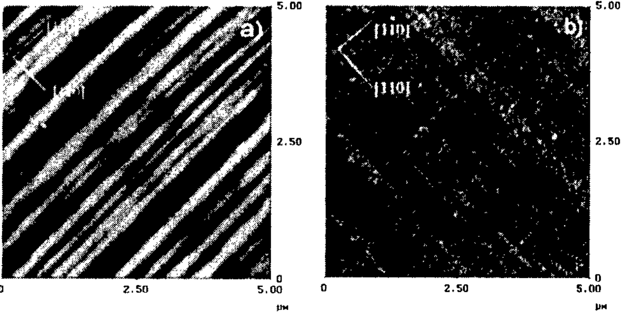

FIG. 3. AFM images of two crosshatched surfaces. (a) Surface of a sample consisting of a 400-nm-thick layer of $In_{0.2}Ga_{0.8}As$ grown by molecular beam epitaxy (MBE) at substrate temperature $T_s=500$ °C on GaAs (001). (b) Surface of a sample consisting of a 400-nm-thick layer of $In_{0.2}Ga_{0.8}As$ grown by atomic layer molecular beam epitaxy (ALMBE) at $T_s=200$ °C on GaAs (001). Both images are printed using the same grayscale.

these measurements also allow us to identify preferential scattering directions.

The other type of measurements we can carry out, ARLS, provides the distribution of scattered light in the plane of incidence. The detector is moved in this plane while keeping constant the polar angle of incidence θ_i, the polarization, and the sample surface azimuthal angle φ. Through a combination of the two main modes of operation of our experimental setup, we can obtain the angular distribution of scattered light for different orientations of the surface. The possibility of changing the surface azimuthal angle φ is of fundamental importance when the surface presents anisotropic roughness. In this work, we performed ARLS measurements at different angles of incidence: $\theta_i=0°$, 10°, 20°, 30°, 40°. We employ both s- and p-polarized incident light and select the desired polarization of the scattered light through the polarization analyzer placed in front of the detector.

III. EXPERIMENTAL RESULTS

Figure 3 shows the topography, as observed by AFM, of the heteroepitaxial $In_{0.2}Ga_{0.8}As$ on GaAs (001) layers studied in this work. Sample A (grown by MBE at $T_s=500$ °C) is shown in Fig. 3(a) and sample B (grown by ALMBE at $T_s=200$ °C) is shown in Fig. 3(b). The AFM images are printed using the same grayscale to distinguish changes in the roughness height by a simple visual inspection. Both surfaces present lines along ⟨110⟩ directions, which is characteristic of crosshatched patterns. However, the distinct growth conditions give rise to noticeable differences in their morphologies. The surface in Fig. 3(a) is clearly anisotropic, with ridges along the [1$\bar{1}$0] direction more closely spaced than those oriented along [110]. The height variations are more pronounced along the [110] direction than along the [1$\bar{1}$0] one. In contrast, Fig. 3(b) shows a smoother surface, still anisotropic, but with similar features along these two preferential perpendicular directions. In Table I, we present data corresponding to the ridge height and the distance between consecutive ridges obtained from the AFM measurements. These parameters were obtained by averaging over

TABLE I. Distances and height values for crosshatched roughness in samples A and B obtained from the AFM and LLS measurements. Distances between ridges running along the $[1\bar{1}0]$ direction and their height are represented by $d_{[110]}$ and $h_{[110]}$, respectively. Distances and height for features along the [110] direction are represented by $d_{[1\bar{1}0]}$ and $h_{[1\bar{1}0]}$, respectively.

		$d_{[110]}$ (μm)	$d_{[1\bar{1}0]}$ (μm)	$h_{[110]}$ (nm)	$h_{[1\bar{1}0]}$ (nm)
AFM	Sample A	0.71	1.3	17.2±0.5	2.3±0.3
	Sample B	Not defined	Not defined	2.5±0.2	2.1±0.2
LLS	Sample A	0.74	1.15	12	3.2
	Sample B	0.33	0.2	1.8	1.7

the AFM profiles taken along the ⟨110⟩ directions, in a rectangular area of the AFM scans of these samples. We have considered as the characteristic lateral feature on the surface, d, the average of the distance between two consecutive peaks. As for the representative feature in the vertical direction, h, we have taken the average of the peak-to-valley values.

The typical crosshatched roughness shown in Fig. 3 produces a characteristic pattern of scattered light. Figure 4 shows such an image, taken with a charge-coupled device (CCD) camera. The sample was illuminated with a He–Ne laser under normal incidence, and the scattered light was projected onto a flat screen placed in front of the sample. A circular hole in the screen allowed the illumination of the sample. We observe that the scattered light is strongly concentrated along two orthogonal lines, parallel to the ⟨110⟩ directions, which indicates that crosshatched topography can be envisioned as a superposition of two perpendicular quasi-one-dimensional (quasi-1D) components. The light scattered along each ⟨110⟩ direction comes from the ridges perpendicular to it. By studying the angular distribution of scattered light along those preferential directions we can obtain further information on the surface roughness characteristics.

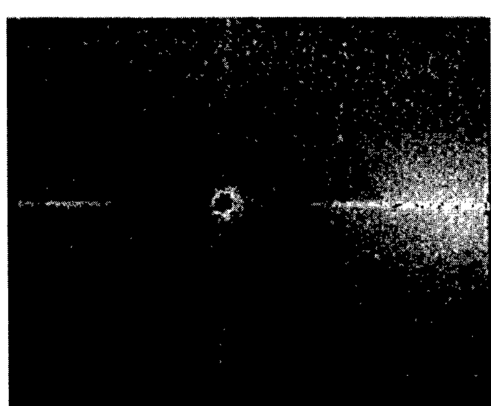

FIG. 4. Light scattered by a crosshatched surface illuminated at normal incidence with a He–Ne laser (λ=633 nm). Image was taken with a CCD camera, projecting the scattered light onto a flat screen situated in front of the sample. A circular hole has been made in the center of the screen to allow the incident beam to reach the sample. The horizontal bright line is parallel to the surface [110] direction and corresponds to light scattered by roughness features perpendicular to it. The vertical bright line comes from features parallel to the [110] direction.

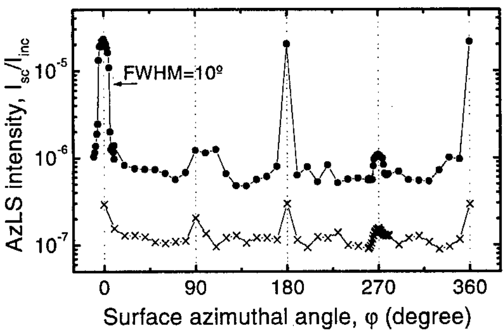

FIG. 5. s-polarized scattered intensity during surface azimuthal-dependent light scattering (AzLS) measurements of samples A (●) and B (×). Data were taken under s-polarized normal incidence (λ=633 nm) at θ_s=30°. Surface azimuthal angles φ=0° and φ=180° correspond to the [110] direction in the plane of incidence. Surface azimuthal angles φ=90° and φ=270° correspond to the $[1\bar{1}0]$ direction in the plane of incidence.

In the following paragraphs, we present representative LLS results leading to a useful description of the surface morphology. Figure 5 shows the AzLS measurements, normalized to the incident intensity, of samples A (●) and B (×) taken at normal incidence with s-polarized light and the detector placed at θ_s=30°. In both cases, we see that the ⟨110⟩ directions are preferential scattering directions. There are narrow peaks in the scattered intensity in those directions, confirming that the crosshatched morphology has two quasi-1D components along them, as mentioned previously. The full width at half-maximum (FWHM) of the AzLS peaks, calculated from data in Fig. 5, is 10°. From the detector angular aperture, we estimate its value to be about 5°. For sample A, we see that the signal at φ=0°, 180° is one order of magnitude larger than that at φ=90°, 270°, revealing that is the [110] direction is rougher than the orthogonal one. From this, we conclude that ridges parallel to the $[1\bar{1}0]$ direction are higher than the perpendicular ones. The intensity of the light scattered from sample B, although highly anisotropic, is considerably lower than that from sample A, showing that sample B is smoother. Moreover, in the case of sample B, the fact that the intensity in the two preferential scattering directions is similar indicates that the roughness in these two directions has similar statistical properties.

Figure 6 presents ARLS data of samples A [Figs. 6(a)–6(c)] and B [Figs. 6(d)–6(f)], taken at θ_i=0° [Figs. 6(a) and 6(d)], θ_i=20° [Figs. 6(b) and 6(e)], and θ_i=40° [Figs. 6(c) and 6(f)]. In all cases, the intensity data shown have been normalized to the incident intensity. The signal coming from sample B was very low, and we increased the detector angular aperture in that case; thus, a direct comparison of intensities between the top and bottom graphs is not possible. However, the signal from sample B is still lower than that from sample A and the qualitative discussion provided in the following still holds. Closed symbols correspond to the s-polarized scattered signal for s-polarized incident light (s-to-s), and open symbols correspond to p-to-p scattering. No depolarization in the scattered light was observed for these samples. The experiments were made by detecting the scattered intensity in the plane of incidence when the [110] (■,

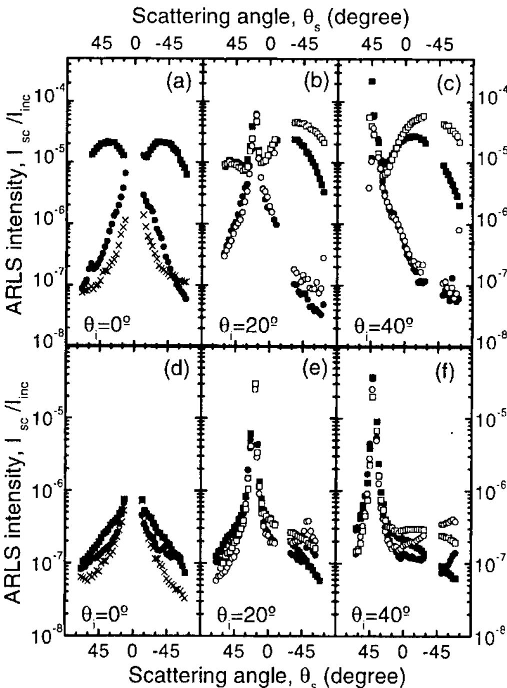

FIG. 6. Angle-resolved light scattered (ARLS) intensity of light ($\lambda=633$ nm) scattered by samples A [(a)–(c)] and B [(d)–(f)]. Data correspond to scattered intensity in the plane of incidence when the [110] (■), [1$\bar{1}$0] (●), and [100] (×) surface directions are contained in it. Measurements were taken at $\theta_i=0°$ [(a), (d)], at $\theta_i=20°$ [(b), (e)], and at $\theta_i=40°$ [(c), (f)]. Closed symbols: *s*-polarized incident and scattered light. Open symbols: *p*-polarized incident and scattered light. In both cases, intensity data have been normalized to the incident power. Direct comparison between top and bottom figures is not possible because the detector angular aperture in measurements from sample B was increased due to the low level of signal.

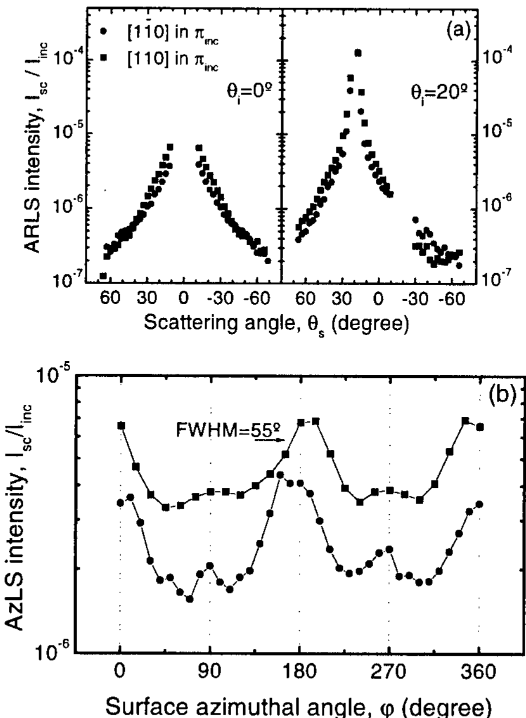

FIG. 7. *s*-polarized light intensity scattered from sample C, which presents a high density of oval defects, illuminated with *s*-polarized light ($\lambda=633$ nm). (a) Angle-resolved light scattering (ARLS) data: $\theta_i=0°$ (left graph) and $\theta_i=20°$ (right graph), for the [110] (■) and [1$\bar{1}$0] (●) directions on π_{inc}, respectively. (b) Azimuthal-dependent light scattering (AzLS) measurements detected at $\theta_s=12°$ for $\theta_i=0°$ (■) and at $\theta_s=30°$ for $\theta_i=10°$ (●).

□), [1$\bar{1}$0] (●, ○), and [100] (×) surface directions are contained in it; we thus obtained the distribution of scattered light both in the preferential scattering directions ([110] and [1$\bar{1}$0]) and in an intermediate one ([100]). As mentioned previously, the light scattered in the plane of incidence when each of the ⟨110⟩ directions are contained in it comes from the surface ridges running along the perpendicular direction. Similar to the AzLS data, from the ARLS data we observe that the scattered light signal for both samples is mainly concentrated on the ⟨110⟩ directions because of the crosshatched nature of the surface. All ARLS data show that sample A scatters more than sample B, indicating that the former is rougher. For sample A, the intensity coming from features along the [1$\bar{1}$0] direction ([110] direction on π_{inc}) is higher, and this means that the height variations are larger than in the orthogonal direction. In the case of sample B, we can conclude that the features are similar in both directions. On the other hand, we observe that although the scattered intensities obtained under different incidence conditions indeed differ, they allow us to extract the same qualitative results.

Figure 7 corresponds to light scattering data, normalized to the incident intensity, from sample C (GaAs on GaAs (001) grown by MBE at $T_s=580\,°C$), whose main morphological characteristic consists of the presence of a huge density of oval defects on a flat GaAs homoepitaxial layer. Figures 7(a) and 7(b) show ARLS and AzLS intensity, respectively. The *s*-polarized scattered intensity data in Fig. 7(a) were taken in the plane of incidence under *s*-polarized illumination, with $\theta_i=0°$ (left graph) and $\theta_i=20°$ (right graph), for the two ⟨110⟩ directions. The curves for other surface azimuthal angles are similar to these, indicating that sample C shows nearly isotropic roughness.

AzLS measurements presented in Fig. 7(b) were done under *s*-polarized incidence, detecting the *s*-polarized scattered signal at $\theta_s=12°$ for $\theta_i=0°$ (■) and at $\theta_s=30°$ for $\theta_i=10°$ (●). We see that the signal has a small dependence on the azimuthal angle φ, and it shows broad peaks (FWHM $=50°$). These broad peaks, centered at $\varphi=0°$ and 180°, could indicate that the defects have a tendency to be elongated along the [1$\bar{1}$0] direction. It is clear that these peaks are not as sharp as those found in the case of the crosshatched surfaces (where FWHM$<10°$) and cannot be related to quasi-1D morphological components. We have not observed depolarization in the light scattered from this sample either.

Using the AzLS technique, we have characterized homoepitaxial GaAs layers with different density and size distribution of oval defects. Although the AzLS plots of these samples are not shown in this work, it is important to note that we always observe broad peaks (FWHM$\approx 50°$) centered at $\varphi=0°$ and 180° (while the level of the LLS signal is characteristic of each sample).

It is obvious that oval defects and crosshatched morphology coexist in low-strained heteroepitaxial MBE samples.

However, we can assume that these two kinds of topographies are not correlated because they originate by different and independent processes: the presence of stress fields in the surface for the crosshatch, and contamination of the substrate or liquid gallium splitting for the oval defects.

The existence of two different and uncorrelated types of roughness on a surface results in a scattered signal that is the sum of light scattered by each type of roughness. Because the presence of a high density of oval defects on a surface considerably increases the amount of scattered intensity, it may mask the scattered signal coming from other types of roughness on our surface. When we try to detect the evolution of a highly anisotropic roughness during growth (as, for example, a crosshatched surface) and we detect an increasing of the scattering signal along the [110] or $[1\bar{1}0]$ directions, we must confirm that the signal really corresponds to that kind of anisotropic morphology by means of AzLS measurements: we can test whether we obtain a sharp distribution of the signal with the azimuth or not. If signal distribution is broad, it could mean that we are merely detecting the signal coming from oval defects on the surface.

The high anisotropy of the AzLS measurements of samples A and B (see Fig. 5) allows us to ensure that the LLS signal detected from these samples is coming from crosshatched features. The LLS signal level due to oval defects in these samples is low enough to be masked by the crosshatched LLS signal.

Our *ex situ* LLS experimental results allow us to identify the type of surface morphology, as well as the relative height of surface features. In Sec. IV we will show that, by using a perturbative scattering theory, we can recover the surface PSDs, thus acquiring quantitative information on the surface that helps us to determine the size of the typical surface features.

In situ implementation of the LLS technique has, as mentioned before, several geometrical constraints that must be considered to obtain the whole spectrum of the ARLS characterization. However, *in situ* recording of the AzLS data for fixed θ_i and θ_s only requires the ability to change the azimuthal surface angle; this is a common feature of sample holders in epitaxial growth systems. From our experimental *ex situ* AzLS results, we know that these kind of measurements provide key information about the degree of isotropy of the sample morphology, which is essential to assess the characteristics of the evolution of the growth front in real time.

IV. SURFACE TOPOGRAPHY FROM ANGLE-RESOLVED LIGHT SCATTERING

The question now arises as to how the ARLS distributions relate to the surface topography. Although the inverse problem cannot be solved in a general manner, there exist certain ranges of the scattering parameters for which relevant information can be extracted from the ARLS data.[1,2] Under the assumption of smooth roughness and small slopes, the electric field amplitude (actually, the scattering amplitude, which is related to the electric field through a Rayleigh expansion) can be expanded in powers of the surface profile function.[2] Basically, we consider a heteroepitaxial system as an interface separating vacuum from a homogeneous, isotropic, semi-infinite dielectric medium (characterized by the dielectric permittivity ϵ). The surface profile function, assumed to constitute a realization of a stationary random process, is denoted by $\zeta(\mathbf{r})$. This function is chosen in such a way that it is a zero-mean function, that is, $\bar{\zeta}(\mathbf{r})=0$. The surface height correlation $W(|\mathbf{r}|)$ is defined by

$$\langle \zeta(\mathbf{r})\zeta(\mathbf{r}')\rangle = \chi^2 W(|\mathbf{r}-\mathbf{r}'|), \tag{1}$$

where the angular brackets here denote an average over the ensemble of realizations of the surface profile function, and $\chi=\langle \zeta^2(\mathbf{r})\rangle^{1/2}$ is the rms height of the surface. At this stage, it is convenient to introduce the Fourier integral representation of $\zeta(\mathbf{r})$,

$$\zeta(\mathbf{r}) = \int_{-\infty}^{\infty} \frac{d\mathbf{K}}{(2\pi)^2} \hat{\zeta}(\mathbf{K}) \exp(i\mathbf{K}\cdot\mathbf{r}), \tag{2}$$

which also represents a zero-mean random process with the property

$$\langle \hat{\zeta}(\mathbf{K})\hat{\zeta}(\mathbf{K}')\rangle = (2\pi)^2 \delta(\mathbf{K}+\mathbf{K}')\chi^2 g(|\mathbf{K}|), \tag{3}$$

where $g(|\mathbf{K}|)$, the power spectral density of the surface roughness, is defined in terms of the surface height autocorrelation function $W(|\mathbf{r}|)$ by

$$g(|\mathbf{K}|) = \int_{-\infty}^{\infty} d\mathbf{r}\, W(|\mathbf{r}|) \exp(i\mathbf{K}\cdot\mathbf{r}). \tag{4}$$

The angular distribution of diffusely scattered intensity normalized to the incident power (also known as the diffuse component of the mean differential reflection coefficient) can be written to lowest order in the rms surface height χ as

$$I_{\alpha\beta}(\mathbf{K}_{sc}) = f_{\alpha\beta}(\mathbf{K}_{sc},\mathbf{K}_i) g(\mathbf{K}_{sc}-\mathbf{K}_i) + O\left[\left(\frac{\chi}{\lambda}\right)^4\right]. \tag{5}$$

The scattered wave vector is (see Fig. 1)

$$\mathbf{k}_{sc} \equiv (\mathbf{K}_{sc}, q) = (2\pi/\lambda)(\sin\theta_s \cos\phi_s, \sin\theta_s \sin\phi_s, \cos\theta_s), \tag{6}$$

where θ_s and ϕ_s are the polar and azimuthal scattering angles; thus, $\mathbf{K}_{sc}$ is the component parallel to the xy plane, and q is the component perpendicular to the xy plane. The incident wave vector $\mathbf{k}_i$ is defined analogously, choosing $\phi_i\equiv 0$ without loss of generality. In this way, $\mathbf{K}_i$ is the component parallel to the xy plane for the incident wave vector. Notice the difference between ϕ_s and the surface azimuthal angle φ, which is defined in order to describe the position of the different (001) surface directions with respect to the plane of incidence (see Fig. 1). In Eq. (5), the factor $f_{\alpha\beta}$ is defined as[3]

$$f_{\alpha\beta}(\mathbf{K}_{sc},\mathbf{K}_i) = \left(\frac{2\pi}{\lambda}\right)^4 \frac{|\epsilon-1|^2}{4(2\pi)^2} \cos^{-1}\theta_i \, |\sigma_{\alpha\beta}(\mathbf{K}_{sc},\mathbf{K}_i)|^2, \tag{7}$$

where α and β denote the polarization state (s,p) of the scattered and incident light, respectively, in such a way that

$$\sigma_{ss}(\mathbf{K}_{sc},\mathbf{K}_i)=T_s(\mathbf{K}_{sc})T_s(\mathbf{K}_i)\cos\phi_s, \quad (8a)$$

$$\sigma_{sp}(\mathbf{K}_{sc},\mathbf{K}_i)=T_s(\mathbf{K}_{sc})T_p(\mathbf{K}_i)\sin\phi_s\frac{(\epsilon-\sin^2\theta_i)^{1/2}}{\epsilon^{1/2}}, \quad (8b)$$

$$\sigma_{ps}(\mathbf{K}_{sc},\mathbf{K}_i)=T_p(\mathbf{K}_{sc})T_s(\mathbf{K}_i)\sin\phi_s\frac{(\epsilon-\sin^2\theta_s)^{1/2}}{\epsilon^{1/2}}, \quad (8c)$$

$$\sigma_{pp}(\mathbf{K}_{sc},\mathbf{K}_i)=T_p(\mathbf{K}_{sc})T_p(\mathbf{K}_i)[\sin\theta_s\sin\theta_i - \epsilon^{-1}\cos\phi_s(\epsilon-\sin^2\theta_s)^{1/2}(\epsilon-\sin^2\theta_i)^{1/2}] \quad (8d)$$

and the Fresnel transmission coefficients T_α are given by

$$T_s(\mathbf{K}_{sc})=\frac{2q}{q+(\epsilon|\mathbf{k}_{sc}|^2-|\mathbf{K}_{sc}|^2)^{1/2}}, \quad (9a)$$

$$T_p(\mathbf{K}_{sc})=\frac{2\epsilon^{1/2}q}{\epsilon q+(\epsilon|\mathbf{k}_{sc}|^2-|\mathbf{K}_{sc}|^2)^{1/2}}. \quad (9b)$$

Because $f_{\alpha\beta}$ depends only on the geometry of the experiment and on the bulk properties of the sample (ϵ), Eq. (5) shows that ARLS data are proportional to the PSD of the illuminated region. In fact, it can be shown that similar perturbative expressions are obtained for multilayer structures,[4–7,9,10] the differences being accounted for by the function $f_{\alpha\beta}$. As we will see in the following, for our purposes the semi-infinite medium assumption suffices. This can be justified on the basis of the optical behavior of the heteroepitaxial systems being studied. Namely, the light reflected back into vacuum from the layer/substrate interface is negligible, as a result of the strong light absorption within the upper layer and the small reflection coefficient at these interfaces due to low index mismatch. However, for smaller epilayer thicknesses (for our heteroepitaxial system $d\leqslant 50$ nm), slight interference effects in the scattered light can be observed, indicating that further refinements of the model should be included to account for the presence of thin layers. Incidentally, we would like to point out that no volume scattering effects stemming from the presence of bulk defects are considered, since no such defects are expected in the type of samples being studied here. If bulk defects were abundant, their contribution to the LLS, and in turn its correlation with the surface scattering contribution, would have to be taken into account. For weak scatterers, this could be done through the first Born approximation, for example, whereas strong scatterers would notably complicate the formalism, possibly making LLS useless as a surface morphology characterization tool.

We will now analyze the experimental ARLS results of Sec. III, exploiting the analytical expression (5). Nonetheless, recall that, inasmuch as the available (detectable) incident and scattered wave vector components are limited in the far field, this technique fails to provide information on roughness lateral dimensions smaller than $\lambda/2$ (Rayleigh limit). This is explicitly demonstrated in Eq. (5) through the maximum spatial frequency appearing in the argument of the PSD. In addition, there is another constraint in our ARLS measurements, namely, the absence of data points near the backscattering direction (as seen in Figs. 6 and 7); this is because the light detector in our sample experimental setup blocks the incident light at such angles. On the other hand, the lack of cross-polarized scattering in the plane of incidence mentioned in Sec. III, predicted by Eqs. (5)–(9b), comes in support of our retaining only the lowest-order term in the perturbation theory.

A. Crosshatched surface morphology

Considering the typical shape of the scattering pattern produced by the crosshatched (CH) surfaces (see Fig. 4) and the relation between the PSD and the scattering pattern [given by Eq. (5)], it is natural to assume that the surface roughness basically contains three random and independent components: two quasi-1D components along the [110] and [$1\bar{1}0$] directions (denoted as the x and y directions, respectively) and a small two-dimensional (2D) isotropic component. The latter is revealed by our ARLS results in directions other than the ⟨110⟩ ones. There is no correlation between the 2D component and either of the quasi-1D ones. The resulting surface roughness profile can be written as follows:

$$\zeta_{\mathrm{CH}}(\mathbf{r})=\zeta_{[110]}(x)+\zeta_{[1\bar{1}0]}(y)+\xi(\mathbf{r}), \quad (10)$$

where, as we mentioned, the three components are assumed to be statistically independent. The PSD thus yields

$$g_{\mathrm{CH}}(\mathbf{K}) =2\pi[g^{1\mathrm{D}}_{[110]}(K_x)\,\delta(K_y)+g^{1\mathrm{D}}_{[1\bar{1}0]}(K_y)\,\delta(K_x)]+g^{2\mathrm{D}}(|\mathbf{K}|). \quad (11)$$

With the aim of calculating all components, we have carried out ARLS experiments, as described in Sec. III, along the [110] and [$1\bar{1}0$] directions for different angles of incidence θ_i. From the ARLS distributions thus obtained, and using Eq.(5) with $\phi_s=0$ (scattering signal always in the plane of incidence), the PSDs along the two relevant perpendicular directions are calculated. However, care must be taken when extracting the 1D and 2D components of the PSD, because they involve different normalization of the ARLS data. The procedure is as follows.

First, the complete PSD is retrieved from the ARLS data along the ⟨110⟩ directions. A careful analysis of this function allows the identification of two different behaviors: one corresponding to the low-spatial-frequency part, and the other to the rest of the frequency range. The low-spatial-frequency region coincides in both ⟨110⟩ directions and can thus be identified as the 2D isotropic component. (Alternatively, the ARLS data along the [100] direction could be used for the calculation of this PSD component, which in our case led to similar results, as expected.) This region of spatial frequencies in the ARLS data is normalized to the solid angle $\Delta\Omega_s$ covered by the detector, and it is then fitted (if possible) to an appropriate PSD. We have obtained reasonable agreement with the following function:[9]

$$g^{2\mathrm{D}}(|\mathbf{K}|)=\frac{2\pi\chi_L^2a_L^2}{(1+a_L^2|\mathbf{K}|^2)^{3/2}}, \quad (12)$$

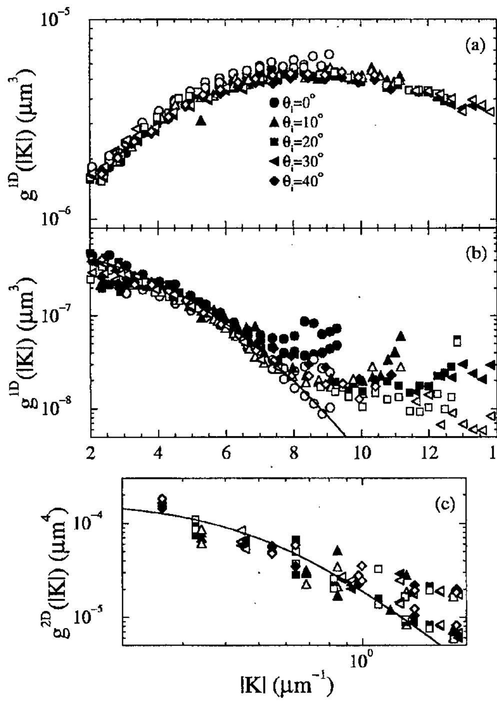

FIG. 8. Power spectral density (PSD) for sample A calculated from angle-resolved light scattering (ARLS) data at different angles of incidence, as those shown in Figs. 6(a)–6(c). Closed symbols: *s*-polarized incident and scattered light. Open symbols: *p*-polarized incident and scattered light. Solid curves are fits to particular functions. (a) 1D PSD along the [110] direction. (b) 1D PSD along the [1̄10] direction. (c) 2D PSD, assumed isotropic, along both directions.

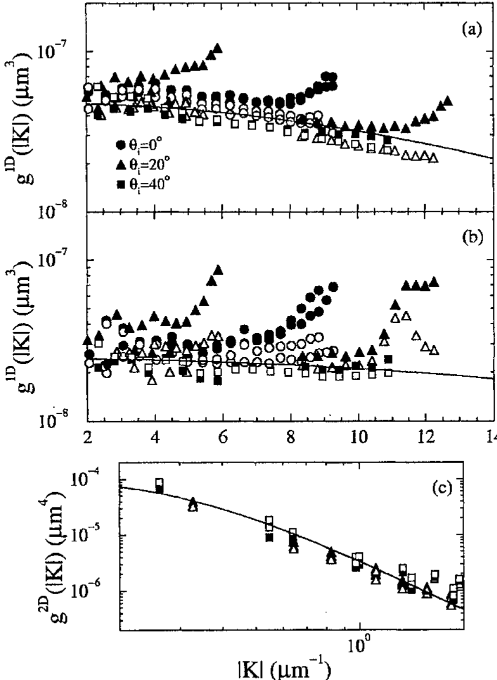

FIG. 9. Power spectral density (PSD) as in Fig. 8, but for sample B [calculated from angle-resolved light scattering data, as those shown in Figs. 6(d)–6(f)].

with a_L and χ_L denoting, respectively, the long-range correlation length and rms height, resulting from a negative exponential surface correlation function.

Next, we subtract this component from the ARLS data and renormalize them by the scattering angle $\Delta\theta_s$ subtended by the detector in the plane of incidence. In this manner, because the detector width in the direction perpendicular to the plane of incidence has been chosen so that it entirely covers the narrow lines of the crosshatched scattered pattern (see Fig. 4), we can formally integrate the PSD along that perpendicular direction. Therefore, even though strictly speaking the expected 1D contribution to the scattered signal is not a delta function as assumed for the PSD model in Eq. (11), the resulting integral can be considered completely equivalent.

The PSD components thus retrieved from the ARLS data are presented in Fig. 8 for sample A and Fig. 9 for sample B. Before analyzing the results in detail, we note that, as expected, there is good agreement between the PSDs obtained from the ARLS data corresponding to the two polarizations and various angles of incidence; this supports the analysis based on the perturbation-theoretical expression (5). The PSD points originating in the region of weak ARLS signals (at large scattering angles) are subjected to larger relative errors, and thus manifest some inconsistencies.

Having a reliable method for obtaining the PSDs, we can extract quantitative information of the surface roughness. Let us first focus on sample A (Fig. 8). The most relevant feature is the broad maximum of the PSD along the [110] direction [see Fig. 8(a)] at $|\mathbf{K}|=8.5\ \mu\text{m}^{-1}$. Roughly speaking, this can be associated with a pseudoperiodicity along the [110] direction with average period $d_{[110]}=2\pi/|\mathbf{K}|=740$ nm. The height of these pseudoperiodic ridges can be estimated by exploring the following property of the PSD:

$$\int \frac{dK^n}{(2\pi)^n}\, g^{nD}(\mathbf{K})=\chi^2, \quad n=1,2. \tag{13}$$

Thus, by integrating the PSD in Fig. 8(a) (including the negative frequencies), the square of the rms height is obtained. Our data yield $\chi_{[110]}=4.3$ nm. If one assumes that the profile is sinusoidal, this rms height is related to the peak-to-valley value $h_{[110]}=2^{3/2}\chi_{[110]}=12$ nm. On the other hand, the PSD along the [1̄10] [see Fig. 8(b)] is basically structureless, with only a monotonic decay with increasing spatial frequency. The fact that no structure can be found along the [1̄10] does not imply that there is no information on the surface. It merely indicates that the 1D roughness component along the [1̄10] is more strongly randomized and weaker in magnitude than the perpendicular component (as revealed by the overall magnitude of the PSDs). Furthermore, we have found that the PSD fits reasonably well the Gaussian correlation function [solid curve in Fig. 8(b)]:

$$g_{[1\bar{1}0]}(K_y)=\pi^{1/2} a \chi^2_{[1\bar{1}0]} \exp\left(-\frac{a^2K_y^2}{4}\right), \tag{14}$$

with $a=450$ nm and $\chi_{[1\bar{1}0]}=0.8$ nm. $\chi_{[1\bar{1}0]}$ is the rms height associated with this roughness component, and in the case of a Gaussian model it is related to the average peak-to-valley heights through the relation $h=4\chi$. The parameter a is called the transverse correlation length and represents the $1/e$ value

of the correlation function. For a Gaussian random process, the correlation length can be related to the mean distance between consecutive valleys or ridges of the profile through[19] $\langle d\rangle=2.56a$, which leads to $\langle d_{[1\bar{1}0]}=1.15$ μm. We point out, however, that the latter parameter is analogous to, but different from, the pseudoperiod found along the [110] direction, because the roughness along the $[1\bar{1}0]$ decorrelates more rapidly and has no remnants of periodicity.

Finally, the 2D isotropic component of the PSD is shown in Fig. 8(c) for our two main perpendicular directions, along with the fit (solid curve) to the long-range function (12), with $a_L=1.8$ μm and $\chi_L=2.9$ nm. Note, in Fig. 8(c), that for spatial frequencies beyond $|\mathbf{K}|=1$ μm^{-1}, as the strong pseudoperiodic 1D component builds in, there is a slight departure of the PSD data from the fit to the long-range function (12) along the [110] direction. With respect to this 2D component, it should be pointed out that its contribution to the total PSD again exceeds that of the 1D short-range Gaussian function for $|K|>10$ μm^{-1}, which could be the origin of the spurious PSD data shown in Fig. 8(b) for such spatial frequencies.

The scattering pattern produced by sample B is not quite as well developed along the two orthogonal directions as the one produced by sample A, although one can still find two preferred directions along which the roughness appears. The PSDs shown in Fig. 9, extracted from the ARLS as mentioned previously, look quite similar for both the [110] and the $[1\bar{1}0]$ directions; they follow a monotonic decrease with increasing spatial frequency. Thus, a strongly randomized component along both perpendicular directions is present, and both PSDs can be fitted to the above-mentioned Gaussian model in Eq. (14). Because the decay of the PSDs is slower than that of sample A along $[1\bar{1}0]$, smaller correlation lengths are inferred: $a_{[110]}=130$ nm and $a_{[1\bar{1}0]}=78$ nm, with similar rms heights, $\chi_{[110]}=0.46$ nm and $\chi_{[1\bar{1}0]}=0.42$ nm, respectively. Nevertheless we note that, particularly along the $[1\bar{1}0]$ direction, the fit is not very accurate, even if the data corresponding to large scattering angles, where the ARLS signals are weak, are eliminated. This is related to the Rayleigh limit, because the region over which the scattering data are available does not permit the retrieval of spatial frequencies corresponding to details smaller than about half a wavelength. Thus, the retrieval of correlation functions with correlation lengths significantly smaller than the wavelength becomes very difficult; the Gaussian exponential decay predicted by the PSD in Eq. (14) is not observable in such a case. Actually, the results in Fig. 9(b) could be fitted to a different PSD, but poor accuracy with respect to the spatial frequency decay would be obtained whatever its particular shape. On the other hand, concerning the 2D isotropic component, good agreement is found [see Fig. 9(c)] with the PSD in Eq. (12) for $a_L=3.2$ μm and $\chi_L=1.4$ nm.

All of these features are summarized in Table I, and they agree quite well with the AFM topographical images shown in Fig. 3 and the resulting parameters included in Table I. With regard to sample A, the pseudoperiodicity along the [110] direction accounts for the large ridges running parallel to the $[1\bar{1}0]$ direction, whereas the Gaussian correlation function along the latter direction describes the weaker random fluctuations along the ridges that decorrelate more rapidly. The weaker crosshatched pattern of sample B predicted from ARLS is also in agreement with AFM data. Furthermore, although less relevant for our purposes, our optically retrieved PSDs can yield long-range information that is absent from the AFM image.

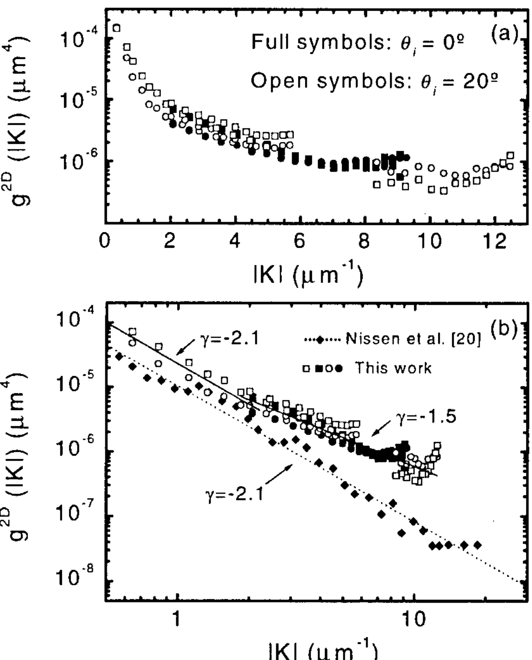

FIG. 10. (a) 2D power spectral density (PSD) for sample C calculated from the angle-resolved light scattering (ARLS) data at two angles of incidence shown in Fig. 7(a) (*s*-polarized incident and scattered light). (□): PSD calculated from ARLS measurements taken with the [110] direction in π_{inc}; (○): PSD from the $[1\bar{1}0]$ direction. (b) Log–log plot of sample C PSD, fitted to two straight lines (—): one of slope $\gamma=-1.5$ in the high-spatial-frequency range and the other of slope $\gamma=-2.1$ for low frequencies. Data from Ref. 20 and their corresponding linear fit (---) have also been plotted for comparison.

B. Presence of oval defects

A similar analysis of crosshatched topography can be made on other kinds of samples. We have performed such a study on sample C, consisting of 780 nm of homoepitaxial GaAs with an extremely high density of randomly distributed oval defects, with a broad dispersion of lateral size (100 nm$<l<$8 μm) and height (50 nm$<h<$1 μm), as observed through AFM and Normarsky measurements.

First of all, as described in Sec. III, from AzLS and ARLS data (Fig. 7) we conclude that there are no quasi-1D roughness components, in spite of the weak anisotropy in scattered intensity with surface azimuthal angle. So, the surface PSD consists of a 2D component, which can be directly calculated through expression (5) with the ARLS data properly normalized by the incident power and the solid angle $\Delta\Omega_s$. The PSD thus obtained is shown in Fig. 10(a). It can be seen that the measured light anisotropy does not imply significant dif-

ferences in the PSD when calculated from the [110] (■,□) and [$1\bar{1}0$] (●,○) directions, confirming again that surface roughness is nearly isotropic.

As mentioned in Sec. IV A, the integral of the PSD yields the square of the rms height. In the case of the PSD data in Fig. 10(a), this 2D integral gives: $\chi_{2D}=3.9$ nm. This value can be compared to those found in the literature for light scattering measurements of good-quality GaAs epilayers grown on GaAs (001).[20,21] This means that, although sample C presents a huge density of oval defects, most of its surface area is flat (free of oval defects), not causing any significant increase of the LLS signal.

In Fig. 10(b), we show a log–log plot of the PSD obtained for this sample with a high density of oval defects. Data corresponding to the low-frequency part can be fitted to a linear behavior with a slope $\gamma=-2.1$, which is the characteristic behavior of the PSD from GaAs grown under good growth conditions, as reported in the literature.[20,22] Data from Ref. 20 are plotted in Fig. 10(b) for comparison. However, for high frequencies the PSD of sample C departs from this behavior, and the experimental data fit to a straight line with slope $\gamma=-1.5$ on a logarithmic scale.

The latter behavior could be explained by taking into account the simple model proposed by Maheswari, Kadono, and Ohtsu[12] for a random distribution of structures (oval defects in our case) on a surface. The PSD resulting from this model is

$$g(\mathbf{K})\approx\rho|\hat{s}(\mathbf{K})|^2, \tag{15}$$

where ρ is the surface density of defects and $\hat{s}$ is the Fourier transform of the surface-defect profile $s(\mathbf{r})$. For identical defects, the PSD is thus given by the square modulus of the Fourier transform of a single defect (proportional to the defect height square). This function typically decays smoothly up to a certain spatial frequency, directly related with the defect lateral dimensions, where the PSD decays abruptly. If several distributions of defects are present, each with a characteristic defect size and density, the final PSD is obtained through the sum of the PSD associated with each particular distribution. In our sample, the oval defects show a broad dispersion of size and density, which indeed leads through averaging in Eq. (15) to a decorrelation of the PSD with respect to that of uniform distribution of defects; the resulting PSD consists of a monotonically decaying function with an abrupt roll-off at the frequency related to the minimum defect lateral size present on the surface. The decay rate of the PSD (the slope of the PSD in a linear fit of a log–log plot), which in sample C corresponds to a value $\gamma=-1.5$, will depend on each particular distribution of defect sizes and densities. The spatial frequency where we would expect a drop of the signal, as related to the defects of 100 nm (minimum defect size observed in sample C by AFM measurements), cannot be reached with our experimental setup.

Our results show that the GaAs layer roughness contribution to the PSD exceeds that of the defects at the low-spatial-frequency range, dominating PSD behavior. For larger spatial frequencies, a change in the PSD slope is detected, most likely indicating that the contribution from oval defects then becomes larger than that from the GaAs layer roughness. This reveals that, depending on their size and density, the contribution of oval defects to the PSD extends over a wide spatial-frequency range available for LLS measurements with visible light and may even be predominant. Therefore, care must be taken during *in situ* MBE LLS measurements because the light scattered from oval defects could mask the signal coming from other types of roughness, which could be our main interest. A test of AzLS behavior could be helpful to know the true origin of the scattered light. However, for good growth conditions and system cleanliness, the density of oval defects is highly reduced and its contribution to the PSD could be neglected.

V. SUMMARY AND CONCLUSIONS

In the preceding sections, we have analyzed typical morphologies of epitaxial III–V compound semiconductor layers, using the polarized laser light scattering (LLS) technique. In particular, we have studied $In_{0.2}Ga_{0.8}As$ surfaces with crosshatched morphology, which typically develops during heteroepitaxial growth of III–V systems with small lattice mismatch ($\epsilon_0<2\%$). To study the influence of oval defects in the scattering pattern produced by different types of roughness, we have also analyzed a surface with a random distribution of these features.

From angle-resolved light scattering (ARLS) data, we have retrieved the power spectral density (PSD) by using a perturbation-theoretical model that appears to be adequate for the III–V heteroepitaxial systems under study. The PSDs thus obtained from data corresponding to both s and p polarizations and various angles of incidence exhibit excellent consistency, thus validating the approximations involved in the model.

One main conclusion is that the analysis of the PSD provides quantitative data on surface morphology, which agree with the AFM results.

We have considered the contribution of the presence of oval defects to the surface power spectral density. We have shown that the presence of a high density of oval defects must be considered, because it could mask the signal coming from another kind of roughness.

All of these results point out the high potential of LLS for use as an *in situ*, real-time technique for monitoring epitaxial growth processes. These results establish the limitations of the technique. Although the *in situ* extraction of the surface PSD has several geometrical constraints, the time evolution of scattered light at a fixed angular position together with AzLS measurements can still yield useful information. On the one hand, the increase of the scattered light indicates that the surface is roughening. On the other hand, *in situ* AzLS measurements give us key information about the degree of isotropy of the sample morphology, which is essential to assess the characteristics of the evolution of the growth front in real time.

We note the advantages of carrying out LLS experiments while varying the incident light wavelength,[23] as this over-

comes the geometrical restrictions imposed by *in situ* measurements and allows us to retrieve the surface PSD, which is indispensable to obtain quantitative information on surface roughness. It is also worth mentioning that the use of ultraviolet light can increase the sensitivity toward high-spatial-frequency components (constrained by the Rayleigh limit). This can be a relevant factor in some cases in which one tries to detect small features, such as the formation of quantum dots[22] on semiconductor surfaces.

ACKNOWLEDGMENTS

The authors are very grateful to Dr. R. García and A. San Paulo for the AFM measurements. The authors wish to acknowledge the Spanish CICYT for financial support under Project No. TIC96-1020-C02. M.U.G. thanks the Consejería de Educación y Cultura de la Comunidad de Madrid for financial support. J.A.S.-G. acknowledges financial support from the Spanish DGESIC Grant No. PB97-1221.

[1]J. M. Benentt and L. Mattson, *Introduction to Surface Roughness and Scattering* (Optical Society of America, Washington, DC, 1989).
[2]J. A. Ogilvy, *Theory of Wave Scattering from Rough Surfaces* (Adam Hilger, Bristol, 1991).
[3]J. J. Greffet, Phys. Rev. B **37**, 6436 (1988).
[4]A. Duparré and S. Kassam, Appl. Opt. **32**, 5475 (1993).
[5]C. Amra, Appl. Opt. **32**, 5481 (1993).; J. Opt. Soc. Am. A **11**, 197, 211 (1994).
[6]J. A. Sánchez-Gil, A. A. Maradudin, J. Q. Lu, V. Freilikher, M. Pustilnik, and I. Yurkevich, Phys. Rev. B **50**, 15353 (1994).
[7]V. Freilikher, M. Pustilnik, I. Yurkevich, and V. I. Tatarskii, Opt. Lett. **19**, 1382 (1994).
[8]J. Q. Lu, J. A. Sánchez-Gil, E. R. Méndez , Z.-H. Gu, and A. A. Maradudin, J. Opt. Soc. Am. A **50**, 185 (1998).
[9]J. M. Elson, J. Opt. Soc. Am. A **12**, 729 (1995).
[10]R. G. Llamas and L. E. Regalado, Appl. Opt. **35**, 5583 (1996).
[11]J. A. Sánchez-Gil, A. A. Maradudin, and E. Méndez, J. Opt. Soc. Am. A **12**, 1547 (1995).
[12]R. U. Maheswari, H. Kadono, and M. Ohtsu, Opt. Commun. **131**, 133 (1996).
[13]T. Pinnington, C. Lavoie, T. Tiedje, B. Haveman, and E. Nodwell, Phys. Rev. Lett. **79**, 1698 (1997).
[14]K. L. Kavanagh, R. S. Goldman, C. Lavoie, B. Leduc, T. Pinnington, T. Tiedje, D. Klug, and J. Tse, J. Cryst. Growth **174**, 550 (1997).
[15]A. R. Boyd, T. B. Joyce, and R. Beanland, J. Cryst. Growth **164**, 51 (1996).
[16]D. J. Robbins, A. G. Cullis, and A. J. Pidduck, J. Vac. Sci. Technol. B **9**, 2048 (1991).
[17]U. Rossow, N. Dietz, K. J. Bachmann, and D. E. Aspnes, J. Vac. Sci. Technol. B **14**, 3040 (1996).
[18]C. T. Lee and Y. C. Chou, J. Cryst. Growth **91**, 169 (1988).
[19]A. A. Maradudin and T. R. Michel, J. Stat. Phys. **58**, 485 (1990).
[20]M. K. Nissen, C. Lavoie, S. Eisebitt, T. Pinnington, and T. Tiedje, Scanning Microsc. **8**, 935 (1994).
[21]V. A. Sterligov, Y. V. Subbota, Y. M. Shirshov, L. P. Pochekaylova, E. F. Venger, R. V. Konakova, and I. Y. Ilyin, Appl. Opt. **38**, 2666 (1999).
[22]T. Pinnington, Y. Levy, J. A. MacKenzie, and T. Tiedje, Phys. Rev. B **60**, 15901 (1999).
[23]E. Chason, M. B. Sinclair, J. A. Floro, J. A. Hunter, and R. Q. Hwang, Appl. Phys. Lett. **72**, 3276 (1998).

Reduction of indium segregation in InGaAs/GaAs quantum wells grown by molecular beam epitaxy on vicinal GaAs(001) substrates

S. Martini, A. A. Quivy,[a] A. Tabata, and J. R. Leite
Instituto de Física da Universidade de São Paulo, CP 66318, 05315-970 São Paulo, SP, Brazil

(Received 23 September 1999; accepted 14 April 2000)

Low-temperature photoluminescence (PL) was used to investigate the optical properties of $In_{0.10}Ga_{0.90}As$/GaAs quantum wells grown on GaAs(001) substrates with a miscut angle of 0° (nominal), 2°, 4° and 6° towards [110]. The luminescence from the quantum wells grown on a vicinal surface exhibited a blueshift compared to the nominal case. An extra emission at low energy was only observed for the nominal sample and was related to In segregation. Its absence from the PL spectrum of quantum wells grown on vicinal surfaces is a strong indication that In segregation is modified on this type of surface. Theoretical calculations confirmed our experimental data.
© *2000 American Vacuum Society.* [S0734-211X(00)01704-2]

I. INTRODUCTION

The growth of strained $In_xGa_{1-x}As$/GaAs quantum wells (QWs) of high quality is very important to the micro- and optoelectronics industry since they can be used in a large range of high-performance devices such as high-mobility transistors and strained-layer lasers operating in the 980 nm region.[1,2] For most of these applications, the In fraction, x, must be less than 0.25 in order to achieve a sufficiently thick strained layer without any structural defects. During the last decade, vicinal substrates became of great technological value because they provide better optical properties due to the smoother interfaces that can be obtained when growing a heterostructure.[3] As a matter of fact, the presence of a high density of steps on their surface, generated by the miscut angle, can switch the growth mode from the usual two-dimensional (2D) nucleation mode to the step-flow mode depending on the growth conditions.[4] It is now also well established that surface segregation of In atoms constitutes the ultimate limitation to the achievement of perfectly abrupt interfaces in the case of $In_xGa_{1-x}As$/GaAs heterostructures grown by molecular beam epitaxy (MBE).[5]

In an effort to minimize this deviation from the intended square-well profile, several techniques, usually involving a variation of the substrate temperature, have been developed to improve the abruptness of the interfaces.[6,7] However, the growth at low temperature (to thermodynamically limit segregation) often results in poorer crystalline quality and usually has a negative influence on the final performance of the devices. On the other hand, the evaporation at high temperature (flash off) of the excess of In atoms at the second interface is generally quite difficult to control in order to avoid extra In evaporation from the well.

Most available data about segregation efficiency of In atoms are related to the GaAs(001) surface and show rather good agreement with each other.[8–11] However, to our knowledge, only a few, and sometimes contradictory, studies have been carried out for other orientations or for vicinal GaAs(001) surfaces since the growth mechanisms are more complex, theoretical calculations are more sophisticated and other physical mechanisms must be taken into account. Ilg and Ploog[12] observed a progressive enhancement of In segregation on GaAs(h11) substrates ($h=1,\ 2,\ 3$) when h decreases (i.e., for increasing angle with respect to the (001) surface), whereas Guimarães *et al.*[13] showed that the GaAs(311)A surface had a smaller segregation tendency than the GaAs(001) surface. López *et al.*[14] and Porto and Sánchez-Dehesa[15] assumed that In segregation was identical on nominal and vicinal GaAs(001) substrates in order to be able to find the contribution of the strain inhomogeneity to the blueshift of their optical data. In the present work, we contribute to this very interesting subject using low-temperature photoluminescence (PL) in order to probe the influence of the miscut angle on the segregation of In atoms, and we show that the segregation efficiency is slightly different for nominal and vicinal substrates.

II. EXPERIMENTAL DETAILS

The samples investigated here were grown in a Mod. Gen. II MBE system from Varian. They consisted of a 0.5 μm thick GaAs buffer grown at 600 °C and a quantum-well structure grown at 520 °C. After growth of the buffer layer, the substrate temperature was ramped down to 520 °C and the first 500 Å thick GaAs barrier was grown, followed by a 100 Å thick $In_{0.10}Ga_{0.90}As$ layer and a second 500 Å thick GaAs barrier. A 20 s growth interruption was realized at each interface. In order to check the influence of the misorientation angle on the In segregation, this structure was simultaneously grown on top of four pieces of GaAs(001) substrates with miscuts of 0° (nominal), 2°, 4° and 6° towards [110]. They were symmetrically fixed on the same Mo block with liquid indium and were rotated during growth in order to optimize the homogeneity of the epitaxial layer. The growth rate was previously determined by reflection high-energy electron diffraction (RHEED) oscillations and was 0.95 and 0.28 monolayer per second (ML/s) for GaAs and

[a]Author to whom correspondence should be addressed; electronic mail: aquivy@macbeth.if.usp.br

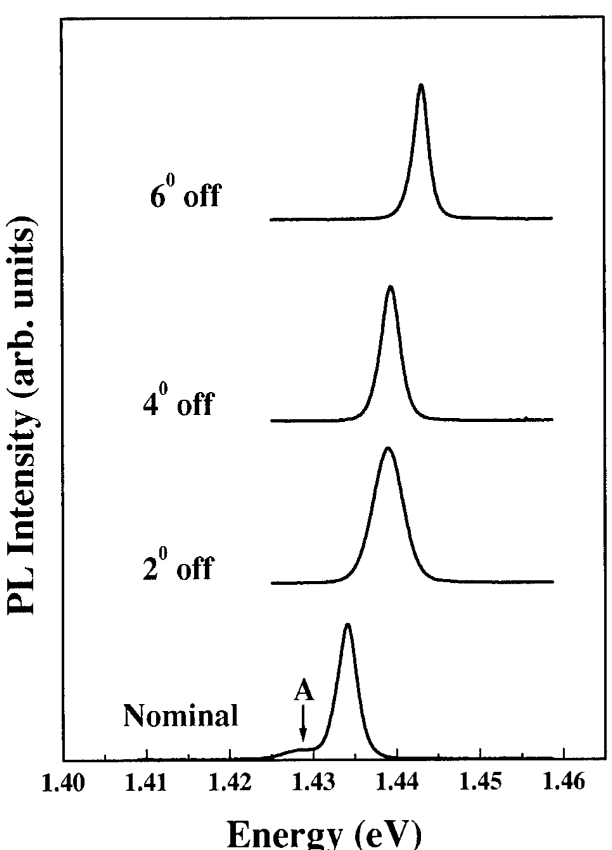

FIG. 1. 1.4 K PL spectra of a 100 Å wide $In_{0.10}Ga_{0.90}As/GaAs$ quantum well simultaneously grown on GaAs(001) substrates with a miscut angle of 0° (nominal), 2°, 4° and 6° towards [110]. The power density was 2.4 W/cm^2.

$In_{0.10}Ga_{0.90}As$, respectively. The PL spectra were recorded by usual lock-in techniques at 1.4 K with the 5145 Å line of an Ar^+ laser.

III. RESULTS AND DISCUSSION

Figure 1 shows the PL spectrum of the four samples. The main emission peak of each sample is related to the fundamental E_1-HH_1 radiative recombination from the quantum well. The spectra display three interesting trends: (1) the full width at half maximum (FWHM) of the main emission of each spectrum depends on the miscut angle; (2) the luminescence energy of the vicinal samples is increasingly blueshifted with respect to the nominal substrate when the misorientation angle increases; (3) an extra emission (peak A) is observed at low energy for the nominal surface only.

The first feature is intrinsically related to the influence of a vicinal substrate on the growth mechanisms. Due to the presence of the high density of steps on these surfaces, the growth mode switches from the usual nucleation mode to the step-flow mode. In order for the system to reach this specific growth mode, the diffusion length of the adatoms must be larger than the distance between two steps in such a way that the atoms can be directly incorporated at the steps instead of forming 2D islands on the terraces. In our case, the terrace widths are, respectively, 81, 40 and 27 Å for the 2°, 4° and 6° off samples, respectively. At a growth temperature of 520 °C, the diffusion length of In adatoms is much larger than that of Ga adatoms, which in turn is expected to be larger than the step separation of the vicinal surfaces (specially for the largest miscut angles). Because the growth front in the step-flow mode is smoother than in the nucleation mode, the interfaces of a heterostructure grown on a vicinal surface are generally smoother than on a nominal substrate, and the FWHM of the PL spectrum is smaller as a consequence of the lower scattering of the excitons at the interfaces. This is consistent with our experimental data that pointed out a FWHM of 3, 4.5, 2.5 and 2 meV for the QWs grown on nominal, 2°, 4° and 6° surfaces, respectively. It was already reported in the literature[14,16] that the FWHM of an InGaAs quantum well grown on a 2° off GaAs(001) sample was larger than that of the same QW grown on a nominal surface, unlike what is expected from the previous explanation. As a matter of fact, for this specific miscut angle, the mean distance between two steps is around 81 Å, but several groups[17,18] already observed a variation of the terrace width from 50 to 120 Å. Although In adatoms are known to have a large diffusion length at 520 °C, Ga adatoms have a much smaller surface mobility at that temperature. Under these conditions, only part of the Ga adatoms can reach the step edges (the ones belonging to the narrower terraces), whereas the rest of them have to nucleate on the largest terraces and form slightly Ga-rich islands. There is thus a larger alloy fluctuation in the material of the well which is known to induce a broadening of the PL spectrum.[19] For larger miscut angles, all Ga and In adatoms can reach the steps since the terraces are narrower, and the alloy fluctuation is smaller. The larger FWHM of the 2° off sample could also be interpreted in terms of step bunching that increases the roughness of the interfaces and induces lateral variation of the In composition in the ternary alloy.[20,21] However, as this effect should be stronger for larger miscut angles, this hypothesis can be discarded since the QWs grown on the 4° and 6° off substrates showed a much smaller FWHM.

The energy blueshift observed in the PL spectrum of the QWs grown on top of the vicinal substrates with respect to the emission energy of the same structure grown on the nominal surface can be explained if the extra strain, due to the presence of the high density of steps at the surface, is taken into account. On a nominal surface, the intrinsic strain present in the InGaAs layer comes from the difference in lattice parameter between the ternary alloy and the GaAs buffer layer. The only way to impose biaxial stress to the epitaxial film is through matching of the lateral lattice parameter at the interface between both materials. At the initial stage of growth, the layers are deposited according to the Franck–van der Merwe growth mode (layer by layer), and the InGaAs layer is biaxially stressed in order to match the x-y lattice parameter of the GaAs substrate. The z lattice parameter of the layer is increased in order to conserve the total volume of the unit cell (tetragonal deformation). When the same structure is deposited on top of a vicinal substrate, the high density of GaAs steps at the surface locally changes the stress from biaxial to hydrostatic. This is due to the fact

that, at the step edges, the first layer of ternary alloy has to match the GaAs lattice parameter in the x-y plane (as before) but also along the z direction (growth direction) because of the presence of the GaAs step where the In and Ga adatoms are preferentially incorporated. This extra strain (hydrostatic instead of biaxial) at the GaAs steps can be treated as a weak perturbative potential since its influence can only be felt laterally over a few unit cells away from the steps, and far from them the strain is biaxial again. The presence of this perturbative potential in the Hamiltonian of the system slightly increases the eigenvalues of the holes and electrons, yielding the observed blueshift with respect to the nominal substrate. This periodic lateral modulation of the strain, together with the increasing number of steps for larger miscut angles, explains the increase of the blueshift with increasing misorientation. The relatively large blueshift of the QW grown on the 2° off substrate with respect to the other vicinal substrates is closely related to the effect previously mentioned for the explanation of the FWHM: as for that misorientation all the Ga adatoms do not reach the step edges, the region near the border of the widest terraces will be slightly In rich and will undergo larger hydrostatic strain, increasing hence the blueshift of the main emission. It is important to emphasize here that the blueshift observed for all the vicinal substrates cannot be attributed to any variation of In desorption with the miscut angle, since it is well known that, at the growth temperature used here, this effect can be neglected.[22,23]

The third feature of the PL spectra in Fig. 1 will be described in more detail since it is intimately related to the scope of this article. Such low-energy emission was already observed in many types of InGaAs layers[24–32] and its most common explanation was generally related to monolayer fluctuation or to incorporation of shallow impurities into the well. ML fluctuation is not compatible with our experimental data because the energy difference between peak A and the main emission is too large (7 instead of 1.8 meV, as calculated for this well width and In content). Trapping of free excitons by impurities present in the well should show saturation of the intensity of peak A with increasing excitation-power density, unlike what happens in our sample (see Fig. 2). More recently, Yu and co-workers[33] attributed its origin to the trapping of free excitons by slightly In-rich islands at the top interface of the QW. This effect is a consequence of In segregation that creates a floating In layer at the top of the growth front[6] from which slightly In-rich regions can be formed when the second GaAs barrier is grown. At that moment, most of the In atoms segregate into the barrier, but a very small quantity is allowed to diffuse back into the InGaAs well and form islands with slightly higher In content.[34]

The main issue of the present work is that the misoriented samples that were grown together with the nominal substrate did not show any emission of this nature. As its origin is related to the formation of In-rich islands, which is a consequence of In segregation, we can deduce that this effect was modified on the vicinal substrates. The main difference between these substrates and the nominal one is the presence of

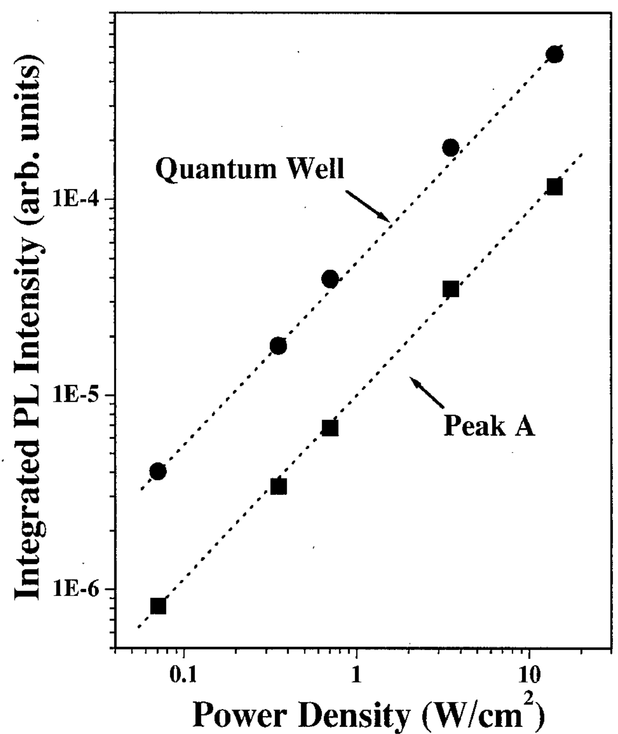

FIG. 2. Integrated PL intensity as a function of laser-power density for the main emission and peak A of the QW grown on the nominal GaAs(001) substrate. The lines are only a guide to the eyes.

a large number of steps on the surface, the density of which increases with the misorientation angle. On these surfaces, growth usually proceeds in the step-flow mode and thus the step edges that are predilected sites for incorporation act as a sink for both types of adatoms and naturally limit their diffusion length. It has been shown[5,35] that In segregation could be reduced by controlling the surface migration or the exchange rate of the process. That is usually achieved by lowering the substrate temperature during growth, but it will also generally decrease the crystalline quality of the layers. In our case, the natural steps present on the surface were used to lower the diffusion length of the adatoms and to consequently reduce the segregation effect. Although these do not act as perfect sinks (i.e., the incorporation probability is not unity), as was thought earlier,[4] their presence is enough to decrease the diffusion length of the adatoms and to slightly modify the segregation process with respect to the nominal case. This influence of terrace edges on growth processes was already demonstrated by Shitara *et al.*[36] who showed that the steps present on the A- (Ga-terminated steps), B- (As-terminated steps) and C-type (both kinds of steps) surfaces of GaAs(001) off-axis substrates were not identical with respect to the incorporation rate. The family-III adatoms can be attached and detached from these steps at a certain rate that depends on the surface type. The activation energy for incorporation at the steps is larger for A than for B surfaces (and is in between both values for the C surface), meaning that the adatoms stick more on B than on A surfaces. As a consequence, the steps and their nature are able

to modify the physical processes occurring at the surface of the sample during growth.

Our experimental results do show that even the Ga-terminated steps, which are expected to have a weaker influence, are able to lower the surface-migration length of the adatoms with respect to the nominal case. This is enough to slightly reduce In segregation as can be seen from the absence of peak A in the optical spectrum of the QW grown on the vicinal substrates. It cannot be attributed to any temperature or In-content variation from sample to sample during growth as all the substrates were symmetrically glued side by side with liquid indium on the same Mo block and continuously rotated during epitaxy. These experimental data clearly indicate that In segregation can no longer be considered the same for both nominal and vicinal surfaces, as was erroneously assumed in the literature until now.[14,15,37] This small segregation difference is generally very difficult to observe in the PL spectrum of these systems since the experimental blueshift with respect to the excitonic emission of a 100 Å wide $In_{0.10}Ga_{0.90}As$/GaAs square quantum well grown on GaAs(001) is due to two different effects: In segregation (which is no longer the same for nominal and vicinal substrates as we just showed) and strain inhomogeneity at the steps that is also dependent on the miscut angle. If In segregation is reduced, we could expect a decrease of the QW transition energy as a consequence of the higher In content in the layer that leads to a smaller energy gap of the material. However, as the contribution of strain inhomogeneity to the blueshift increases with misorientation and In content (and influences the electron and hole energy levels in a stronger way), it competes with the reduction of In segregation (that has a weaker influence), and thus no net decrease of the blueshift will be observed in the PL spectrum. This is why the reduction of In segregation is so difficult to observe on vicinal substrates. It is only possible to see this effect in our case as peak A, which is due to In segregation (there is no doubt about that because ML fluctuation and impurity incorporation could be eliminated by simple physical arguments), disappeared in the spectrum of the vicinal samples.

To support our assumptions and confirm the influence of the miscut angle on In segregation, we performed theoretical calculations that were compared with our experimental data. If we assume (as should be done from now on) that segregation is different on nominal and vicinal substrates, the right procedure to estimate the segregation coefficient for each type of substrate is first to solve the Schrödinger equation of the whole system taking into account the intrinsic (i.e., biaxial) strain of the InGaAs layer and the strain inhomogeneity at the interfaces. Then, the segregation efficiency can be estimated using some theoretical model in the literature.[6,10] The first step is to include the biaxial strain of the ternary alloy and the lateral periodic potential coming from the hydrostatic strain at the GaAs steps in the Hamiltonian of the system that will be used to solve the 2D Schrödinger equation

$$\left\{\frac{\hbar^2}{2m^*_{e,hh}}\left(\frac{\partial^2}{\partial y^2}+\frac{\partial^2}{\partial z^2}\right)+V(y,z)\right\}\Psi(y,z)=E\Psi(y,z), \quad (1)$$

where $m^*_{e,hh}$ are the effective mass of electrons (e) and heavy holes (hh), $V(y,z)$ is the total potential experienced by the particles, and E and $\Psi(y,z)$ are the eigenvalue and wave function, respectively. The solution of Eq. (1) with a realistic potential is a very complex problem. So, as a first approximation, we assumed that the potential $V(y,z)$ can be written as

$$V(y,z)=V(y)+V(z), \quad (2)$$

where $V(z)$ is the quantum-well square potential with a width L_Z and $V(y)$ is the perturbative potential with periodicity l that simulates the well modulation induced by the periodic distribution of GaAs steps present at the interfaces of the QW grown on vicinal surfaces. This assumption is correct as long as the energy variation produced by the steps on the energy levels is much smaller than the eigenvalues of the unperturbed Hamiltonian. Using this approximation, we can write the wave function as $\Psi(y,z)=\Phi(y)\chi(z)$, where $\chi(z)$ are the eigenfunctions of the Schrödinger equation,

$$\left\{\frac{\hbar^2}{2m^*_{e,hh}}\frac{\partial^2}{\partial z^2}+V(z)\right\}\chi(z)=\epsilon_{e,hh}\chi(z), \quad (3)$$

and $\epsilon_{e,hh}$ are the unperturbed eigenvalues. The equation of interest to be solved now is

$$\left\{\frac{\hbar^2}{2m^*_{e,hh}}\frac{\partial^2}{\partial y^2}+V(y)\right\}\Phi(y)=\gamma_{e,hh}\Phi(y), \quad (4)$$

where $\gamma_{e,hh}$ are the perturbed eigenvalues. From a perturbation point of view, the potential $V(y)$ is usually approximated by a Dirac comb[37–39] to take into account the periodic shrinkage of the QW thickness and strain inhomogeneity, both due to the presence of the GaAs steps at the interface. The amplitude of the potential is given by the difference in confinement energy between a $n-1$ ML-wide well bordered by hydrostatically compressed InGaAs and a n ML-wide well under biaxial strain,

$$V(y)=V_0\approx[\epsilon_{e,hh}(n-1)-\epsilon_{e,hh}(n)]. \quad (5)$$

Since the hydrostatic strain at the GaAs steps turns into biaxial strain a few unit cells away from the steps, we approximated this behavior by assuming that the strain was constantly hydrostatic over a distance ξ from the steps and then became suddenly biaxial. That was actually done by assuming a broadening ξ for each of the delta function of the comb. Under these conditions, the secular equation can be written in the form

$$\cos(kl)=\cosh(\xi\rho)\cos[(l-\xi)\kappa]-\frac{\gamma_{e,hh}-\frac{V_0}{2}}{\sqrt{\gamma_{e,hh}(V_0-\gamma_{e,hh})}}\sinh(\xi\rho)\sin[(l-\xi)\kappa], \quad (6)$$

where

$$\rho=\sqrt{\frac{2m^*_{e,hh}(V_0-\gamma_{e,hh})}{\hbar^2}} \quad (7)$$

and

$$\kappa = \sqrt{\frac{2m^*_{e,hh}\gamma_{e,hh}}{\hbar^2}}. \tag{8}$$

The quantum-well energy levels were obtained by solving the Schrödinger equation using the effective-mass approach. The band offset was obtained from the van de Walle model.[40] In this case, each semiconductor is determined in terms of an absolute-energy level and in terms of deformation potentials describing the effects of hydrostatic and biaxial strain on the electronic structure. The calculation was carried out with a homogeneous and isotropic effective mass and the binding energy of the heavy-hole exciton was taken as 7 meV. A value of 13 Å was used for ξ according to the work of López *et al.*[14]

This method is simpler and less time consuming, computationally speaking, than the variational model of Porto and Sánchez-Dehesa[15] and produces exactly the same results within 1 or 2 meV, depending on the miscut angle. It is based on the same idea as that in Refs. 37–39 but is more complete because the decay rate of the hydrostatic strain at the steps is also taken into account. However, the main difference with respect to all these models is that segregation can be treated separately as a function of misorientation, as will be seen below.

In order to obtain the segregation coefficient, we used the model of Muraki *et al.*[6] According to them, the In composition x_n in the nth layer is given by

$$x_n = x_0(1-R^n), \quad \text{for } n \leq N, \tag{9}$$

$$x_n = x_0(1-R^N)R^{n-N}, \quad \text{for } n > N, \tag{10}$$

where x_0 and N are the nominal In composition and the well width in monolayers, respectively. When $n>N$, we are actually estimating the In content of the layers from the second barrier. The segregation coefficient R is a fitting parameter that estimates the strength of the segregation and is adjusted to give the actual In content of the QW that will be used to calculate the heavy-hole and electron confinement energies in order to fit the optical data. On the nominal sample, R was found to be 0.941. Nevertheless, it is more complicated to obtain the value of R for the vicinal substrates since two different effects can yield a blueshift of the optical emissions: In segregation and strain inhomogeneity at the GaAs steps. In the literature, up to now, In segregation was considered the same for nominal and vicinal substrates, so the only physical reason for this blueshift (with respect to the nominal surface) was attributed to strain inhomogeneity.[14,15] However, our experimental data clearly suggest that In segregation can no longer be considered the same on vicinal and nominal surfaces. So, in order to estimate the real value of R on the vicinal substrates, we first have to calculate the confinement energy of the carriers using our model above in order to also take into account the blueshift originating from the strain modulation at the GaAs steps. Then, we can adjust the experimental data, as was done for the nominal substrate, using R as a parameter. For the PL curves in Fig. 1, we obtained a segregation coefficient R of 0.929, 0.925 and 0.918 for the 2°, 4° and 6° off samples, respectively. These coefficients, together with the value obtained for the nominal substrate, are slightly larger than the ones generally encountered in the literature[6,37,41] (around 0.85–0.92 at 520 °C) as a consequence of our particular growth conditions: low InGaAs growth rate (0.28 ML/s) and low V/III flux ratio in order to stay close to the 2×4 (As-rich) to 4×2 (Ga-rich) surface-reconstruction transition during growth. It is well known that kinetics and growth conditions can dramatically influence In segregation: for instance, segregation increases with higher growth temperature and decreases with higher As pressure and growth rate.[6,35] Whatever the absolute values of our coefficients, the important point is that in our set of samples (that were simultaneously grown on the same Mo block) the segregation coefficients monotonically decrease with increasing misorientation, confirming the reduction of In segregation on vicinal surfaces. As can be seen from our calculations, this effect is quite small and would be very difficult to be experimentally observed in PL curves when there is a mixing of several contributions leading to competing blue- and redshifts. This is why the presence of peak A in the PL curve of the nominal sample and its absence in the spectra of the vicinal substrates provide a unique way by which to evidence the difference in In segregation on both types of surface. However, it should be emphasized that peak A is not strictly necessary for this. As a matter of fact, we observed, as already mentioned before by Yu and co-workers,[33] that other samples grown under similar conditions did not show any lower energy emission (peak A). It seems that an uncontrolled parameter (perhaps intrinsically related to local properties of the surface) also plays an important role in the growth and is able to modify or even inhibit the formation of In-rich islands at the second interface. Peak A is a consequence of In segregation, but its absence from the PL curve of the nominal sample does not mean that segregation is the same for all the surfaces. The real and unique physical argument able to confirm any difference in segregation between nominal and vicinal substrates is the comparison of the optical data with the theoretical calculations when the strain inhomogeneity at the steps is taken into account.

IV. CONCLUSIONS

We investigated the influence of vicinal GaAs(001) substrates on the optical properties of an InGaAs/GaAs QW. The PL energy of the QW grown on misoriented surfaces was blueshifted with respect to that of the QW grown on a nominal (001) surface, an effect that was attributed to the additional hydrostatic strain present at the GaAs steps of the interfaces. The FWHM of the main emission peak decreased with increasing miscut angle, as expected from the smoother interfaces obtained on miscut substrates. Larger values of the FWHM and of the blueshift were observed for the 2°-off surface as a consequence of the different diffusion length of In and Ga adatoms that increased the disorder in the ternary alloy. The PL measurements also showed a low-energy emission that was only present in the spectrum of the nominal substrate. This feature was related to the trapping of free

excitons by slightly In-rich islands that were present at the second interface as a result of In segregation. The absence of this emission in the optical spectrum of the vicinal surfaces is an indication that In segregation was slightly reduced on these substrates. The main difference, with respect to the nominal orientation, was the presence of a high density of steps, and we concluded that the step edges limited the surface migration of the adatoms, thus lowering the segregation. Theoretical calculations were carried out and confirmed our experimental observations.

ACKNOWLEDGMENTS

The authors would like to thank FAPESP (Grant Nos. 96/6498-3, 97/9722-4 and 97/07974-6), CNPq and CAPES (Brazilian funding agencies), for partial financial support.

[1]M. Meshkinpour, M. S. Goorsky, B. Jenichen, D. C. Streit, and T. R. Block, J. Appl. Phys. **81**, 3124 (1997).
[2]M. C. Wu, N. A. Olsson, D. Sivco, and A. Y. Cho, Appl. Phys. Lett. **56**, 221 (1990).
[3]R. K. Tsui, J. A. Curless, G. D. Kramer, M. S. Peffley, and D. L. Rode, J. Appl. Phys. **58**, 2570 (1985).
[4]J. H. Neave, P. J. Dobson, B. A. Joyce, and J. Zhang, Appl. Phys. Lett. **47**, 100 (1985).
[5]J. M. Moison, C. Guille, F. Houzay, F. Barthe, and M. Van Rompay, Phys. Rev. B **40**, 6149 (1989).
[6]K. Muraki, S. Fukatsu, Y. Shiraki, and R. Ito, Appl. Phys. Lett. **61**, 557 (1992).
[7]K. Chattopadhyay, J. Aubel, S. Sundaram, J. E. Ehret, R. Kaspi, and K. R. Evans, J. Appl. Phys. **81**, 3601 (1997).
[8]J. G. Belk, C. F. McConville, J. L. Sudijono, T. S. Jones, and B. A. Joyce, Surf. Sci. **387**, 213 (1997).
[9]J. F. Zheng, J. D. Walker, M. B. Salmeron, and E. R. Weber, Phys. Rev. Lett. **72**, 2414 (1994).
[10]J. Nagle, J. P. Landesman, M. Larive, C. Mottet, and P. Bois, J. Cryst. Growth **127**, 550 (1993).
[11]J. M. Gerard and J. Y. Marzin, Phys. Rev. B **45**, 6313 (1992).
[12]M. Ilg and K. H. Ploog, Phys. Rev. B **48**, 11512 (1993).
[13]F. E. G. Guimarães, D. Lubyshev, V. A. Chitta, and P. Basmaji, Mater. Sci. Eng., B **35**, 318 (1995).
[14]C. López, R. Mayoral, F. Meseguer, J. A. Porto, J. Sánchez-Dehesa, M. Leroux, N. Grandjean, C. Deparis, and J. Massies, J. Appl. Phys. **81**, 3281 (1997).
[15]J. A. Porto and J. Sánchez-Dehesa, Phys. Rev. B **51**, 14352 (1995).
[16]A. S. Brown, U. K. Mishra, J. A. Henige, and M. J. Delaney, J. Appl. Phys. **64**, 3476 (1988).
[17]M. D. Pashley, K. W. Haberern, and J. M. Gaines, Appl. Phys. Lett. **58**, 406 (1991).
[18]P. R. Pukite, G. S. Petrich, S. Batra, and P. I. Cohen, J. Cryst. Growth **95**, 269 (1989).
[19]J. Singh and K. K. Bajaj, Appl. Phys. Lett. **44**, 1075 (1984).
[20]K. Hiramoto, T. Tsuchiya, M. Sagawa, and K. Uomi, J. Cryst. Growth **145**, 133 (1994).
[21]J. R. Botha and A. W. R. Leitch, J. Cryst. Growth **169**, 629 (1996).
[22]T. Hayakawa, M. Nagai, H. Horie, and Y. Niwata, J. Cryst. Growth **127**, 532 (1993).
[23]K. Radhakrishnan, S. F. Yoon, R. Gopalakrishnan, and K. L. Tan, J. Vac. Sci. Technol. A **12**, 1124 (1994).
[24]P. B. Kirby, J. A. Constable, and R. S. Smith, Phys. Rev. B **40**, 3013 (1989).
[25]K. Muraki, S. Fukatsu, Y. Shiraki, and R. Ito, Surf. Sci. **267**, 107 (1992).
[26]A. Patanè, A. Polimeni, M. Capizzi, and F. Martelli, Phys. Rev. B **52**, 2784 (1995).
[27]T. G. Andersson, Z. G. Chen, V. D. Kulakovskii, A. Uddin, and J. T. Vallin, Appl. Phys. Lett. **51**, 752 (1987).
[28]N. G. Anderson, W. D. Laidig, R. M. Kolbas, and Y. C. Lo, J. Appl. Phys. **60**, 2361 (1986).
[29]J. P. Reithmaier, H. Cerva, and R. Lösch, Appl. Phys. Lett. **54**, 48 (1989).
[30]W. C. Hsu, S. Z. Chang, and W. Lin, Jpn. J. Appl. Phys., Part 1 **31**, 26 (1992).
[31]J. Pamulapati, J. E. Oh, N. Debbar, and P. Bhattacharya, J. Appl. Phys. **65**, 1361 (1989).
[32]R. Droopad, D. S. Gerber, C. Choi, and G. N. Maracas, J. Cryst. Growth **127**, 606 (1993).
[33]H. Yu, C. Roberts, and R. Murray, Appl. Phys. Lett. **66**, 2253 (1995).
[34]P. N. Fawcett, B. A. Joyce, X. Zhang, and D. W. Pashley, J. Cryst. Growth **116**, 81 (1992).
[35]O. Dehaese, X. Wallart, and F. Mollot, Appl. Phys. Lett. **66**, 52 (1995).
[36]T. Shitara, J. Zhang, J. H. Neave, and B. Joyce, J. Appl. Phys. **71**, 4299 (1992).
[37]M. Leroux, N. Grandjean, C. Deparis, J. Massies, C. López, R. Mayoral, and F. Meseguer, Jpn. J. Appl. Phys., Part 1 **34**, 3437 (1995).
[38]F. Meseguer, N. Mestres, J. Sánchez-Dehesa, C. Deparis, G. Neu, and J. Massies, Phys. Rev. B **45**, 6942 (1992).
[39]B. Chastaingt, M. Leroux, G. Neu, N. Grandjean, C. Deparis, and J. Massies, Phys. Rev. B **47**, 1292 (1993).
[40]C. G. van de Walle, Phys. Rev. B **39**, 1871 (1989).
[41]R. Kaspi and K. R. Evans, Appl. Phys. Lett. **67**, 819 (1995).

Structural and electrical properties of chemical vapor deposited diamond films doped by B^+ implantation

S. B. Wang,[a] H. X. Zhang, P. Zhu, and K. Feng
Institute of Physics, Chinese Academy of Sciences, Beijing 100080, People's Republic of China

(Received 9 September 1999; accepted 21 April 2000)

Chemical vapor deposited diamond films (DF) were prepared on *p*-type Si (100) substrates. The films were doped by 140 keV B^+ implantation to doses between 10^{14}–$6\times10^{16}\,cm^{-2}$. Structural changes were studied by scanning electron microscopy and Raman measurements. The DF become more and more seriously disordered versus dose. Surprisingly, the amorphization process is not as rapid as predicted. Secondary ion mass spectroscopy results show that the implanted B atoms have a strong tendency of outdiffusion during annealing. When experimental parameters are suitable, the B atoms' profiles indicate perfect Gaussian-like shape and the electrical resistance of DF can be decreased ten orders of magnitude. © *2000 American Vacuum Society.* [S0734-211X(00)03004-3]

I. INTRODUCTION

Diamond has many superior properties, such as wide energy band gap, high thermal conductivity, high mechanical hardness, etc.[1,2] Since diamond films (DF) were synthesized successfully using various methods,[2,3] it has been of increasing interest to study the applications potential of DF as electronic and photoelectric materials.[4,5] In practice, it is necessary to realize the doping of *p*- and *n*-type DF. At present, B doped DF, which have been achieved *in situ* during the film growth, show large increases in electrical conductivity.[5,6] However, doping DF by ion implantation is seldom studied. Ion implantation has proven to be an effective method in doping semiconductors and it probably has the potential to reduce the size of electronic and photoelectric devices of DF. Therefore, studying the structure and properties of doped DF by ion implantation is needed.[4] Although previous works corresponding to ion implantation of diamond have been reported, most of them focus on the lattice damage of single crystalline diamond induced by self-ion irradiation.[7,8] In this article, the microstructure and conduction mechanism of B doped DF have been investigated.

II. EXPERIMENT

Hot filament chemical vapor deposited diamond films were prepared on *p*-type Si (100). During deposition the flux ratio of methane to hydrogen was 1:99, and the substrate temperature was 850 °C. These films were implanted with 140 keV B^+ to doses of 10^{14}, 10^{15}, 3×10^{15}, 5×10^{15}, 2×10^{16}, and $6\times10^{16}/cm^2$, respectively. A furnace annealing was performed at various temperatures (ranging from 550 to 850 °C) for different times ($t=4$, 8 min) under N_2 gas ambient. A SPEX-1403 Raman spectrometer was used to characterize the structural changes of DF. During the measurement laser wavelength and power were 514.5 nm and 300 mW, respectively. In addition, scanning electron microscopy (SEM) was used to observe the surface morphology after irradiation. Secondary ion mass spectroscopy (SIMS) measurements were employed to obtain the depth profile of B atoms. Equal-distanced dot electrodes of Ti (50 nm)/Au (200 nm) were deposited on the DF to make ohmic contact. The two terminal method was used to measure the electrical resistance.

[a]Author to whom correspondence should be addressed; electronic mail: przhu@aphy02.iphy.ac.cn

III. RESULTS AND DISCUSSION

Figure 1 shows the Raman spectra of as-deposited, as-implanted ($5\times10^{15}/cm^2$), and annealed samples. It can be seen that the characteristic peak (1332 cm^{-1}) of as-deposited DF is sharp [with a full width at half-maximum (FWHM) of 12 cm^{-1}]. Although there is a small broad peak around 1560 cm^{-1} (corresponding to nondiamond phase), the sharp 1332 cm^{-1} peak shows that high quality DF have been prepared. When implantation was carried out, the characteristic peak becomes wider and weaker. In addition, a large bump (covering a wide range of 1100 cm^{-2}–1640 cm^{-1}) corresponding to amorphous carbon appears. After annealing, the peak intensity of 1332 cm^{-1} is reduced and the background be-

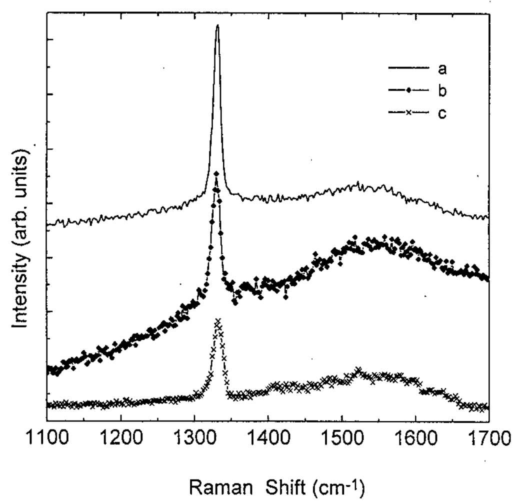

FIG. 1. Raman curves of samples which have been offset along perpendicular axis, from top to bottom, they are samples: (a) as-deposited, (b) as-implanted with $5\times10^{15}/cm^2$ B^+, and (c) implanted followed by annealing at 700 °C for 4 min.

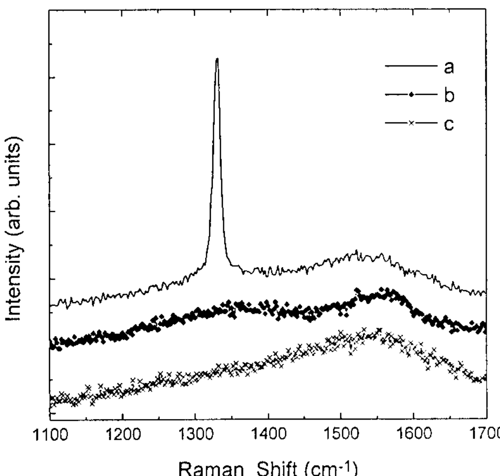

FIG. 2. Raman curves of samples which have been offset along perpendicular axis, from top to bottom, they are samples: (a) as-deposited, (b) as-implanted with $6\times10^{16}/cm^2$ B^+, (c) implanted then annealed at 700 °C for 4 min.

comes intense compared to the as-implanted samples. However, the FWHM of the 1332 cm^{-1} peak is sharper (14 cm^{-1}) than that of the as-implanted samples (18 cm^{-1}). This implies that the damaged lattice of DF may be partially recovered after the annealing.[5]

Figure 2 shows the Raman spectra of samples implanted with B^+ to a dose of $6\times10^{16}/cm^2$. The implantation has created a complete disorder of DF lattice. The 1332 cm^{-1} peak has disappeared. There are two broad peaks (located at 1360 and 1580 cm^{-1}) corresponding to "D" and "G" line of diamond-like carbon films, respectively.[9] Usually, the D line reflects the concentration of microcrystalline graphite, and the G line corresponds to polycrystalline graphite. After annealing the D line becomes indistinguishable; only a broad peak corresponding mainly to the G line of DLC can be observed. This implies that the microcrystalline graphite has increased greatly in size, thus this corresponds to a "graphitization" procedure.[10]

On the other hand, as observed by SEM (see Fig. 3), it is apparent that diamond grains become disordered with the increase of B^+ dose. When $5\times10^{15}/cm^2$ is achieved, the lattice damage seems less serious compared to that of larger doses. For $6\times10^{16}/cm^2$ case, diamond transforms into finer grains with a round shape. Combining Raman results, it is believed that the crystalline diamond has been collapsed under the implantation.

According to the Raman spectrum analysis and SEM observation, it is clear, after the dose ($5\times10^{15}/cm^2$) of implantation the lattice disorder of DF is not very serious. This is not in agreement with the reports on single crystalline diamond which do not maintain crystalline order under an implantation dose of $4-5\times10^{15}/cm^2$ again.[7,11] It is suggested that the polycrystalline DF is more defective in structure than the single-crystalline one. Especially, the polycrystalline DF have a large number of boundaries. This can allow grains to slide along boundaries and change in volume during irradiation. All these may benefit the relaxation of the lattice. Due to these reasons (also other ones), it is thought the lattice of DF can bear a larger implantation dose.

Figure 4 shows the depth profiles of samples implanted by B^+ with various doses at different annealing periods. It can be observed that B atoms have a tendency of outdiffusion. After annealing at 750 °C for 8 min, B atoms are aggregated at the outside surface of DF which has been implanted to smaller dose (1×10^{14} or $1\times10^{15}/cm^2$). It implies that implanted B atoms have experienced a strong outdiffusion in the annealing process. However, for the implantation with $5\times10^{15}/cm^2$ B^+, when the annealing was performed at 700 °C for the same time, B atoms still are in a Gaussian-like profile.

Why does the annealing strongly induce the outdiffusion of B atoms, especially for the low dose case? The effect of lattice stress are assumed as the reasons. Referencing to the TRIM96 simulation, it is clear, for small dose case the lattice damage of DF is lighter after the implantation. Due to a number of dopants existing as interstitials, the local stress produced by dopants' introduction is increased. This is thought to have contribution to the outdiffusion of B atoms during annealing. In fact, it is usually believed that the dense structure of diamond makes B atoms difficult to penetrate inward. On the other hand, less serious damage means that fewer point defects were generated. These point defects may produce an attractive force on the dopants and supply combination sites.[12,13] As a result of interaction, some B atoms can stay in substitution sites rather than outdiffusing. However, a moderate dose of doping firstly supplies richer B atoms in DF. In addition, a large number of point defects which are produced in implantation process may have more trap effects on dopants. More serious damage in the DF suppresses the influences of lattice stress. These reasons may explain the reduction of the outdiffusion of B atoms. In a short annealing time, the withdrawal of B atoms is not rapid

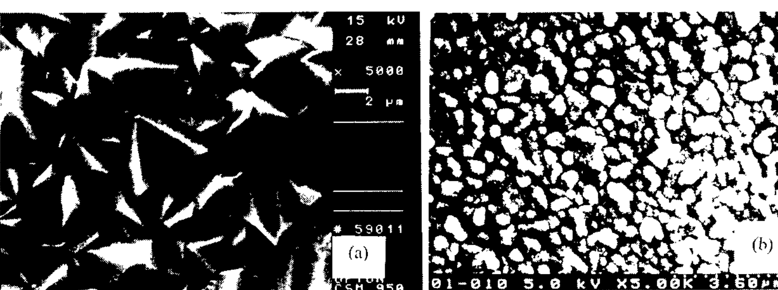

FIG. 3. SEM images of samples: (a) as-implanted with $5\times10^{15}\,cm^{-2}$ B^+ and (b) as-implanted with $6\times10^{16}/cm^2$ B^+.

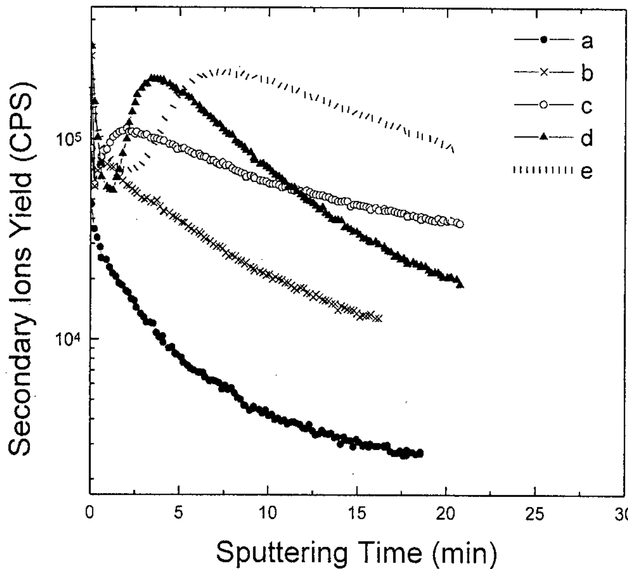

FIG. 4. Depth profiles of B atoms in samples: implanted with $1\times10^{14}/cm^2$ B^+ and annealed at 750 °C for 8 min (a), $1\times10^{15}/cm^2$ B^+ and annealed at 750 °C for 8 min (b), $3\times10^{15}/cm^2$ B^+ and annealed at 700 °C for 8 min (c), $5\times10^{15}/cm^2$ B^+ and annealed at 700 °C for 8 min (d), and as-implanted with $5\times10^{15}/cm^2$ B^+ (e).

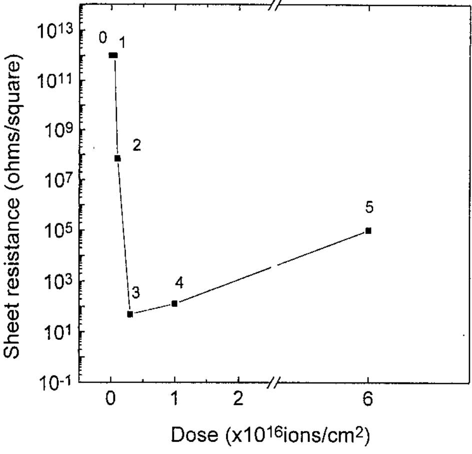

FIG. 6. Change in the sheet resistance of samples implanted and annealed at various conditions: as-deposited (0), implanted with $1\times10^{15}/cm^2$ B^+ and annealed at 750 °C for 8 min (1), $3\times10^{15}/cm^2$ B^+ and annealed at 700 °C for 8 min (2), $5\times10^{15}/cm^2$ B^+ and annealed at 700 °C for 8 min (3), $2\times10^{16}/cm^2$ B^+ and annealed at 700 °C for 8 min (4), $6\times10^{16}/cm^2$ B^+ and annealed at 700 °C for 8 min (5).

enough to move the peak concentration out the DF. The $5\times10^{15}\,cm^{-2}$ doping at different annealing times supports that. Therefore, we suggest that the B atomic profile depends strongly on the implantation and annealing parameters. It is concluded that the implantation with larger dose followed by a rapid anneal is more beneficial in obtaining an optimum profile.

Figure 5 shows the electrical resistance values of samples doped with various doses of B^+ under different annealing temperatures. It seems that 700 °C is the most moderate temperature for the activation of B dopants, for samples annealed at the temperature, medium dose of B doped DF has

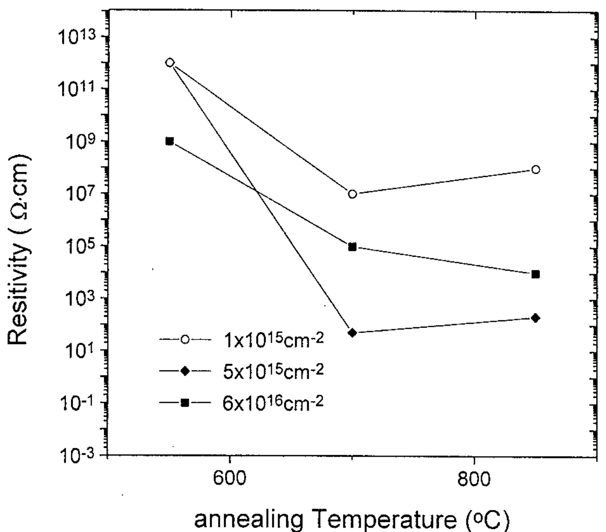

FIG. 5. Change in the electrical resistance values of samples doped with different doses of B^+ under various annealing temperatures.

the smallest resistivity. However, for large dose case, its resistivity decreases continuously versus temperature. This is understandable considering the graphitization process. Figure 6 shows the electrical resistance values of samples doped with various doses of B^+ and annealed at 750 °C/700 °C for 8 min. Combining the results of SIMS, it can be clear, with larger implantation dose and shorter annealing time B atoms mainly distributed in the DF. If most of them are activated, the sheet resistance can be reduced greatly. For $5\times10^{15}/cm^2$ case the decrement in resistance ranges over ten orders of magnitude. However, both low ($<10^{15}/cm^2$) and very larger dose ($6\times10^{16}/cm^2$) of B doped samples have relatively smaller decrease in resistance. For low dose cases especially for those less than $10^{15}/cm^2$, due to strong outdiffusion happens, there are less dopants remained in the DF. In addition, there is a minimum in the resistivity at moderate doping dose. For large dose one, the lattice has been collapsed and more sp^2 configurations are generated. However, the decrease in resistance is further smaller comparing to samples which have moderate implantation fluence.

In general, if B atoms distribute extensively in the DF after annealing, the resistivity can achieve a lower value. Suitable doping dose and annealing parameters are very important in DF's conductivity. At the stage, the B atoms occupy the substitution sites, the energy level of local acceptors would be created. Thus p-type DF has been obtained. Due to the contribution of hole carriers, the resistivity can be reduced greatly.[14,15] Although there is contribution of nondiamond components induced by irradiation, the reduction in resistivity can be mainly attributed to dopants' activation.

IV. CONCLUSIONS

Under various doses of B^+ implantation, the DF are damaged to different degrees. It is found that the profiles of B atoms depend strongly on both implantation and annealing

parameters. Larger implantation dose has more B atoms retained inside the DF. Moreover, it is suggested that moderate annealing temperature can have relatively slighter outdiffusion of B atoms. When the implantation dose achieves $5 \times 10^{15}/cm^2$, after the annealing the B atoms have a Gaussian-like profile. Meanwhile, the samples have small resistivity. By choosing moderate implantation and annealing parameters, the resistivity can be decreased ten orders of magnitude.

ACKNOWLEDGMENTS

The work is supported by the National Natural Science Foundation of China and Committee of 863 High Science and Technology Project Funds. The authors are grateful for help in DF deposition at Surface Laboratory of Institute of Physics. The authors are also very grateful to Professor Y. L. Liu.

[1] B. V. Spitsyn, L. L. Builov, and B. V. Deryagin, J. Cryst. Growth **52**, 219 (1981).
[2] M. Kamo, Y. Sato, S. Matsumoto, and N. Setaka, J. Mater. Sci. **17**, 3106 (1982).
[3] B. V. Deryagin, B. V. Spitsyn, L. L. Builov, A. A. Klochkov, A. E. Gorodetskii, and A. V. Smolyaninov, Sov. Phys. Dokl. **21**, 676 (1976).
[4] B. J. Baliga, IEEE Electron Device Lett. **10**, 455 (1989).
[5] J. H. Won *et al.*, Appl. Phys. Lett. **68**, 2822 (1996).
[6] T. H. Borst and O. Weis, Diamond Relat. Mater. **4**, 948 (1995).
[7] G. Braunstein and R. Kalish, Appl. Phys. Lett. **38**, 416 (1981).
[8] J. F. Prins, Mater. Sci. Rep. **7**, 271 (1992).
[9] J. Robertson, Diamond Relat. Mater. **2**, 984 (1993).
[10] R. Kalish *et al.*, Appl. Phys. Lett. **74**, 2936 (1999).
[11] H. Quintel, K. Bharuth-Ram, H. Hofsass, M. Restle, and C. Ronning, Nucl. Instrum. Methods Phys. Res. B **118**, 72 (1996).
[12] H. Zillgen and P. Ehrhart, Nucl. Instrum. Methods Phys. Res. B **135**, 280 (1998).
[13] V. Raineri and S. U. Campisano, Nucl. Instrum. Methods Phys. Res. B **120**, 56 (1996).
[14] L. X. Yie, *Semiconductor Physics* (Education, 1996), p. 90.
[15] H.-C. Tsai and D. B. Bogy, J. Vac. Sci. Technol. A **5**, 5 (1987).

Preparation of C_{60}-doped silica aerogels and the study of photoluminescence properties*

Bin Zhou and Jue Wang
Pohl Institute of Solid State Physics, Tongji University, Shanghai, People's Republic of China 200092

Li Zhao
Department of Physics, Fudan University, Shanghai, People's Republic of China 200433

Jun Shen and Zhongsheng Deng[a)]
Pohl Institute of Solid State Physics, Tongji University, Shanghai, People's Republic of China 200092

Yufen Li
Department of Physics, Fudan University, Shanghai, People's Republic of China 200433

(Received 7 January 1998; accepted 19 May 2000)

The preparation of C_{60}-doped silica aerogels by the sol-gel process is described in this article. Fourier transfer infrared spectra, time-of-flight mass spectroscopy, and transmission electron microscopy showed that C_{60} was incorporated into silica aerogels, and the C_{60} structure was retained in the preparation process. The C_{60}-doped silica aerogels emitted intense visible light (2.10 eV) under Ar^+ laser (488 nm) excitation at room temperature, and the photoluminescence peak was "blueshifted" when compared with C_{60}'s. The blueshift is explained based on a quantum confinement effect. © *2000 American Vacuum Society.* [S0734-211X(00)06404-0]

I. INTRODUCTION

The optical properties of semiconductor micro crystals are attracting attention because of their potential application in nonlinear optics, ultrafast optical equipment, and lasers. In the early nineties, the quantum confinement effect (QCE), which was responsible for the photoluminescence (PL) of porous silicon, was studied by researchers interested in new types of optical-electric materials.

C_{60} (fullerene) is a nanometer cluster and a molecular semiconductor. The energy gap between the highest occupied molecular orbit (HOMO) and the lowest unoccupied molecular orbit (LUMO) is 1.9 eV; the transition in the gap is forbidden. At room temperature, the neutral C_{60} molecule has a weak photoluminescence at 1.65 eV[1,2] and the PL intensity increases slightly at low temperature. If a zero-dimension fullerene "quantum dot" is embedded in a suitable medium, it may be possible to transform the forbidden transition into an admitted transition by breaking the C_{60}'s transition rules. Based on the influence of the quantum confinement effect, C_{60}'s transition rule and energy gap can be changed. Anderson and his co-researchers[3] had observed singular optical properties in a fullerene-coating porous aluminophosphate composite which was caused by the QCE. Sheng Dai[4] also doped the C_{70} molecule in a silica gel by the sol-gel process, and observed some interesting phenomena, but reported that the C_{60} molecule was difficult to dope in a silica gel.

A silica aerogel is a noncrystalline solid material with porosity from 80% to 99.8%. It is produced by the sol-gel process and a supercritical drying process. The pore size of a silica aerogel is from 1 to 100 nm, its specific surface area is from 20 to 1000 m^2/g, and its density is from 5 to 600 Kg/m^3. A silica aerogel is an ideal porous medium for doping a micro-crystalline semiconductor. In this work, we prepared C_{60}-doped silica aerogels by the sol-gel process and supercritical drying. The samples were dark red and the C_{60} molecule was well distributed in the silica aerogel. The photoluminescence properties of C_{60}-doped silica aerogel were studied. Measurements showed that the C_{60}-doped silica aerogel had a singular photoluminescence phenomenon. A preliminary theoretical model was created to explain this phenomenon.

II. EXPERIMENTS AND MEASUREMENT

A. Sample preparation

"Gold grade" C_{60} powder produced by the Hoechct Company in Germany was used in this experiment. In the preparation process, the C_{60} molecules were completely dissolved in toluene and a purple C_{60}-toluene solution was formed. Tetraethoxysilane (TEOS) was stirred with acetone, water, and HF in a suitable ratio. The typical volume ratio was acetone:TEOS:H_2O:HF$=8:4:1:0.5$. This composition produced a silica gel precursor. When this silica gel precursor was mixed with the C_{60}-toluene solution at room temperature, the solution underwent a series of hydrolysis and condensation reactions to produce the well-distributed C_{60}-doped silica gel. The doping concentration ranged from 0.001 to 0.5 mol%. The gels were dried by supercritical drying using CO_2 ($Tc=31.1\,°C$, $Pc=73.5\,bar$).[5] The structure of the gels did not crack during supercritical drying, and a sample of C_{60}-doped silica aerogel were obtained.

*No proof corrections received from author prior to publication.
[a)]Electronic mail: dengpohk@online.sh.cn

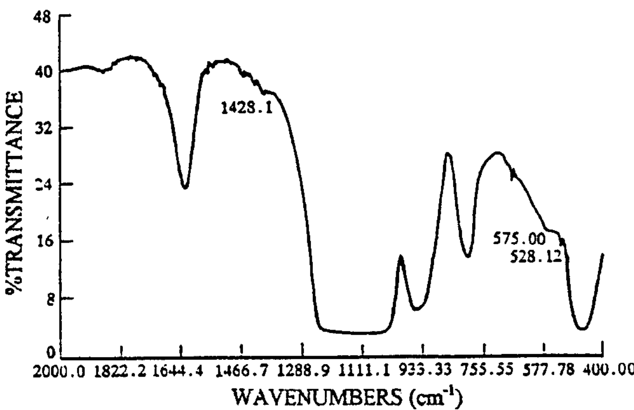

FIG. 1. FTIR of C_{60}-doped silica aerogel (0.3 mol %).

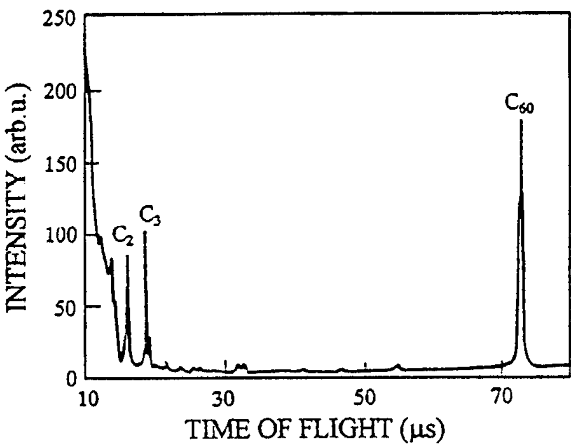

FIG. 2. Time-of-flight mass spectra of negative ions obtained from C_{60}-doped silica aerogels.

B. Measurement

PL, infrared spectra, time-of-flight mass spectra (TOFMS) and transmission electron microscopy (TEM) were used to measure the C_{60}-doped silica aerogels with different concentrations. PL measurements were made directly on the bulk samples using a SPEX 1403 Raman spectrometer at an excitation wavelength of 488 nm (Ar^+ laser). The infrared spectra were obtained on a Fourier transform infrared (FTIR) spectrometer 5DX. Laser ablation combined with TOF mass spectroscopy to verify the doping of C_{60} in silica aerogel was done on an apparatus at Fudan University which was described in an earlier article.[6]

III. RESULTS

A. Fourier transform infrared spectroscopy and time-of-flight mass spectroscopy

FTIR and TOFMS were used to verify the condition of the C_{60} in the C_{60}-doped silica aerogels.

The infrared spectra of the C_{60}-doped silica aerogel (0.3 mol %) showed three distinct characteristic lines at 528, 575, and 1428 cm^{-1} for C_{60}; the peak at 1181 cm^{-1} was overlapped by one broad IR peak for pure silica aerogel in the C_{60}-doped silica aerogel. These un-shifted IR spectral structures of C_{60} in the C_{60}-doped sample, shown in Fig. 1, indicated that C_{60} was incorporated into the silica aerogels.

Laser ablation is an effective method to study various clusters. In this measurement, a 308 nm XeCl excimer laser (~20 ns) was focused onto the sample surface with a 20 cm focal length lens to generate clusters from the C_{60}-doped sample. The ions produced by laser ablation were collected and measured by TOF mass spectrometry. It revealed the presence of C_{60} molecules as shown in Fig. 2. The laser power was about 600 mJ/cm^2 to ensure a small fragment ratio during the laser ablation process.

B. Transmission electron microscopy with electronic diffraction pattern

High resolution transmission electron microscopy (HRTEM) images, together with the corresponding electron diffraction pattern, revealed some interesting features of the C_{60}-doped silica aerogels.

At low C_{60} doping (<0.1 mol %), the TEM image of C_{60}-doped silica aerogels appeared to have the same structure as pure silica aerogels. The C_{60} could not be distinguished by image contrast. The electron diffraction pattern (EDP) showed a diffuse broad ring that indicated an amorphous structure. This meant that the C_{60} molecules were well distributed in the C_{60}-doped silica aerogels.

At heavy C_{60} doping (0.3 mol %), the silica aerogels exhibited a porous structure as shown in Fig. 3. But the typical EDP, as shown in Fig. 4, was made up of a hexagon of symmetric diffraction points and diffraction rings that showed both the C_{60}'s crystalline structure and the silica aerogel's amorphous structure. The EDP of a C_{60} grain showed it had a (110) spacing of the face-centered-cubic structure ($d \approx 5.0$ Å). But with the same sample (0.3 mol %) in another point, in Fig. 4(b), the EDP showed a distinctly different pattern when compared with the former result. It also showed hexagonally symmetric diffraction points, but every group of diffraction points was made up of three points. This phenomenon may be caused by a "small-angle grain boundary" when C_{60} grains form clusters in the preparation process.

FIG. 3. HRTEM of C_{60}-doped silica aerogel (0.3 mol %, ×250 000).

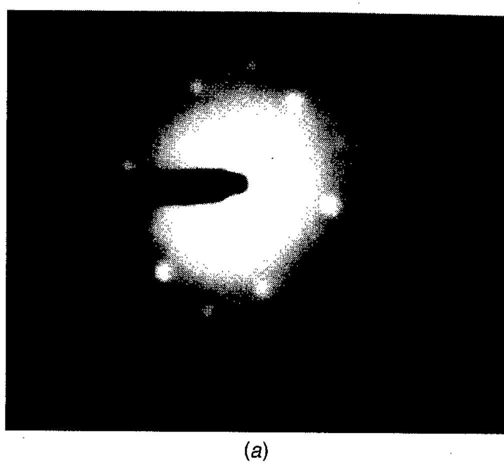

(*a*)

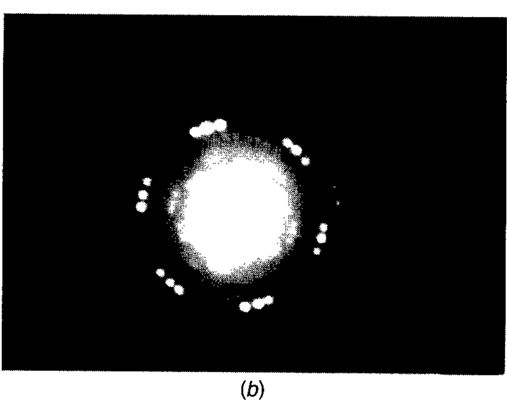

(*b*)

FIG. 4. EDP of C_{60}-doped silica aerogels with heavy doping (0.3 mol %), (a) normal, (b) special.

C. Photoluminescence (PL) properties

At room temperature, under Ar^+ laser (488 nm, 10 mW) excitation, the PL from the C_{60}-doped silica aerogel showed broad visible light emission, while the as-prepared silica aerogel showed no PL at the same experimental conditions as shown in Fig. 5. When samples with different concentrations (ranging from 0.001 to 0.4 mol %) were measured under the same conditions, the PL peaks were all near 2.10 eV (shown in Table I), and the PL peak of C_{60}-doped silica aerogels was obviously "blueshifted" from that of C_{60}. The relative PL intensity of different samples were measured because the absolute PL intensity was difficult to scale.

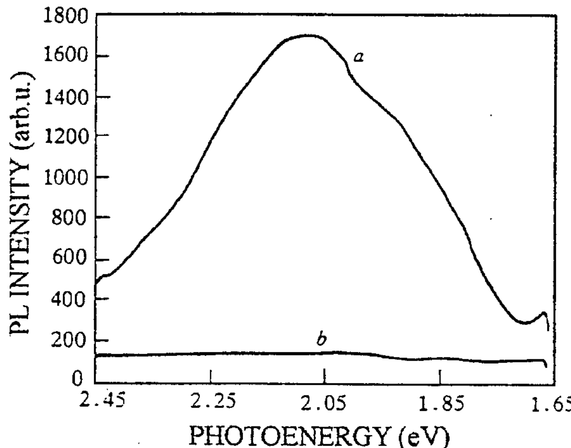

FIG. 5. PL spectra of C_{60}-doped silica aerogels, (a) 0.3 mol %, (b) as-prepared pure silica aerogels.

TABLE I. PL of C_{60}-doped silica aerogels with different concentrations.

Sample number	Concentration (mol %)	PL peak (eV)	Intensity
1	0.0015	2.15	3.6×10^3
2	0.0024	2.11	2.1×10^3
3	0.0042	2.10	4.8×10^3
4	0.0063	2.15	4.8×10^3
5	0.0084	2.06	3.1×10^3
6	0.023	2.07	3.1×10^3
7	0.043	2.13	1.1×10^3
8	0.066	2.11	1.0×10^3
9	0.12	2.15	2.7×10^3
10	0.25	2.14	1.5×10^3
11	0.37	2.16	1.5×10^3

The PL intensity increased after annealing the sample under vacuum. Table II lists the PL characteristics of C_{60}-doped silica aerogels after annealing. The PL intensity increased and the PL peak was more blue shifted after annealing. The explanation for this increase of intensity is that the heat treatment (200 °C, 1 h) effectively removed residual organic molecules and adsorbed gases in the C_{60}-doped silica aerogels which could quench the light emission. We believe the increased blueshift after annealing was caused by strengthening of the quantum confinement effect. When the network of silica aerogels was formed in the sol-gel process, C_{60} grains were embedded in the silica aerogel's backbone. During the heat treatment, the backbone aged and shrank, which increased the confinement of the C_{60}.

IV. DISCUSSION

The study of photoluminescence properties on C_{60}-doped silica aerogels showed that its PL peak was obviously blueshifted and the PL intensity increased compared to that of the pure C_{60} under Ar^+ laser (488 nm). We gave a preliminary explanation of this phenomenon.

The C_{60} powder has a very weak photoluminescence peak at about 1.7 eV. When the C_{60} was doped in silica aerogels, it produced an intense visible light emission at about 2.10 eV, while the PL peak at about 1.65 eV disappeared. The excitation energy (488 nm) is 2.53 eV which is above that forbidden HOMO-LUMO transition of pristine C_{60}, ${}^1T_{1g}-{}^1A_g$ (about 1.9 eV),[7] but below that of the first allowed optical transition, ${}^1T_{1u}-{}^1A_g$ (about 2.9 eV).[8] Thus we think

TABLE II. PL of C_{60}-doped silica aerogels after annealing.

Concentration (mol %)	PL peak (eV)		Intensity	
	Unannealed	Annealed	Unannealed	Annealed
0.023	2.07	2.12	3.1×10^3	8.4×10^3
0.253	2.14	2.20	1.5×10^3	2.4×10^3

that the PL spectra excited at 488 nm of the C_{60}-doped silica aerogels are originating from the HOMO-LUMO transition of C_{60}. Normally the HOMO-LUMO transition is forbidden; therefore, the PL of C_{60} power is extremely low. When C_{60} was doped in silica aerogels, the transition rules were broken due to quantum ''dot'' states. In C_{60}-doped silica aerogels, C_{60} was well distributed in the silica aerogel and formed a ''C_{60} quantum dot.'' The silica aerogel caused a confinement to the C_{60} quantum dot and the band gap of C_{60} was increased due to the quantum confinement effect. When the laser excited the samples, the recombination of excited electrons and holes resulted in an intense blueshift photoluminescence.

In addition, silica aerogels have a surface area of up to 500 m^2/g.[6] There were enormous numbers of surface states in the C_{60}-doped silica aerogels which would also cause photoluminescence. These influences are beyond the scope of this article.

V. CONCLUSION

We reported the successful synthesis of C_{60}-doped silica aerogels by the sol-gel process. FTIR spectra, TOFMS and TEM verified the doping of C_{60} in silica aerogels, and the structure of C_{60} was retained. The C_{60}-doped silica aerogels emitted intense visible light (2.10 eV) and the PL peak was blueshifted when compared with C_{60} under 488 nm excitation. This phenomenon was caused by the quantum confinement effect.

ACKNOWLEDGMENTS

This work is supported by the National Nature Science Foundation of China and High Technology Foundation of China.

[1]C. Rebber *et al.*, J. Phys. Chem. **95**, 2127 (1991).
[2]J. H. Weaver *et al.*, Phys. Rev. Lett. **66**, 174 (1991).
[3]M. W. Anderson *et al.*, The First International Interdisciplinary Colloquium on the Science and Technology of the Fullerenes, Santa Barbara, CA, 1993, p. 155.
[4]Sheng Dai *et al.*, Commun. Am. Ceram. Soc. **75**, 2865 (1992).
[5]J. Shen, J. Wang, and X. Wu, Mater. Sci. Eng. **12**, 1 (1994) (in Chinese).
[6]L. Zhu *et al.*, Phys. Rev. A **49**, 3036 (1994).
[7]Z. Gasyna *et al.*, Chem. Phys. Lett. **183**, 283 (1991).
[8]S. Saito and A. Oshiyama, Phys. Rev. Lett. **66**, 2673 (1991).

BRIEF REPORTS AND COMMENTS

This section is intended for the publication of (1) brief reports which do not require the formal structure of regular journal articles, and (2) comments on items previously published in the journal.

Chlorination of Si surfaces under strain conditions

Timur Halicioglu[a]
Thermosciences Institute, NASA, Ames Research Center, M.S. 230-3, Moffett Field, California 94035

(Received 18 February 2000; accepted 12 May 2000)

Energetics for the chlorination process of Si(100)-(2×1) surfaces with an A-type single step edge were investigated under strain conditions. Strains applied uniaxially in the direction parallel to the exposed surfaces produced little or no effect on the energetics of the first chlorination step leading to fully Cl-covered terraces (one Cl attached to every exposed Si atom). The energy of the second chlorination step (leading to the formation of attached $-SiCl_2$ units) taking place near a step-edge site, however, is affected considerably by the applied strain. The effect was found to be largest for strains applied in the direction perpendicular to the step edge. © *2000 American Vacuum Society.*
[S0734-211X(00)05404-4]

I. INTRODUCTION

One of the important steps in the etching process of silicon by Cl, used in today's microelectronic device fabrication technology, is the adsorption of the Cl species onto Si surfaces. It has been well recognized that silicon surfaces exposed to chlorine atoms (or molecules) become chlorinated, forming attached –SiCl and $-SiCl_2$ species. The degree of surface chlorination, in this case, is an important factor in the overall etching procedure. When a clean Si(100)-(2×1) surface is exposed to Cl, the surface quickly becomes chlorinated, first forming attached –SiCl species (in this case, one terminally bonded Cl for each exposed Si).[1] If the surface is flat and free of defects, the chlorination process at low temperatures stops at this –SiCl level.[2,3] In this first chlorination step, each of the Cl-attached Si atoms is bonded to two nearest-neighbor Si atoms located in the lower layer, and there is also one additional bond with its dimer partner at the top layer. For surface etching purposes, however, this first chlorination step is not sufficient. The desorption of the –SiCl species from the surface is energetically quite costly and it does not occur spontaneously.[1] Studies indicate that further exposure to Cl (at low T) does not necessarily increase the Cl incorporation for defect-free surfaces. This is primarily because of steric effects (i.e., due to repulsive forces among the attached and/or incoming Cl atoms). It has been shown that on flat surfaces $-SiCl_2$ units may form via surface diffusion of Cl atoms. However, this is an uphill process requiring an additional 2.1 eV per Cl atom.[4,5]

If the surface contains defects (such as vacancies, steps, or cracks, etc.), then further chlorination is possible, producing $-SiCl_2$ units at the exposed surface. Temperature programed desorption experiments indicate that the formation of attached $-SiCl_2$ species is the most important step in the overall etching process.[6,7] During this second chlorination step the Si–Si dimer bond is broken, and now each bichlorinated Si atoms is bonded only to two other Si atoms located in the layer below. In this case, the process of $-SiCl_2$ formation is downhill (approximately -1.4 eV) and, accordingly, the desorption (etching) of the $-SiCl_2$ unit becomes energetically more feasible.[1]

The objective of this study is to analyze the effect of strain on the adsorption characteristic of Cl on Si(100) surfaces, which is one of the important steps in the etching process. Strain plays a significant role in the physics of surfaces, as has been shown in experiments.[8] It can alter surface configurations, which in turn may affect the energetics of adsorbing (and desorbing) Cl species. In many cases it may be desirable to have strain as an externally applied and continuous variable. Here, calculations were carried out for Si(100)-(2×1) surfaces with single height A-type steps.[9] In this case, second chlorination takes place spontaneously at step edges forming $-SiCl_2$ units. We considered the chlorination process of terraces and calculated relative formation energies for –SiCl and $-SiCl_2$ species under uniaxial tension and compression conditions.

II. CALCULATIONS

Throughout this study, energies and forces were calculated, employing the empirical potential function developed by Feil, Dieleman, and Garrison for systems containing Si and Cl species.[2] The functional form of this potential is similar to the Stillinger–Weber potential (developed for Si–F systems), but employs a different set of parameters. This function has been used successfully in various simulation studies producing acceptable results.[2,10–12] The computational cell used in this study consisted of 16 layers contain-

[a]Current address: Department of Materials Science and Engineering, Stanford, CA 94305-2205; electronic mail: halicioglu@leland.stanford.edu

ing up to 36 Si atoms per layer. Bottom layers were held rigid and two-dimensional periodic boundary conditions were imposed for continuity to mimic an infinite crystal with an exposed (100)-(2×1) surface. A step edge was created by removing half of the top layer Si atoms in the direction of dimer rows, resulting in a type-A step.[13] Exposed surfaces were fully dimerized and, in this case, dimers in upper and lower terraces are orthogonal to each other. Strain conditions were imposed on the system uniaxially by elongating or compressing the lattice in x and y directions which are parallel to the exposed surfaces. In this case, x and y directions are taken perpendicular and parallel to the step edge, respectively (corresponding to 011 and 101 directions). In this study, we investigated up to 3% tension and up to 2% compression. Percent variation, P_E, in Cl attachment energy due to applied strains was calculated as

$$P_E = 100(e_f/e_f^0 - 1),$$

where e and e^0 denote Cl attachment energies for strained and unstrained systems, respectively.

Calculations were carried out in two steps. First, we used a simulated annealing procedure based on a molecular dynamics method (employing the Verlet leapfrog algorithm).[14] For a complete equilibration, the temperature of the system was first increased (up to approximately 250 K) and then linearly cooled down to a low temperature limit (≈1 K). Typical runs were about 10^4 time steps, corresponding to a picosecond (or longer). Then the lowest energy configuration of the low temperature molecular dynamics result was used as input to a minimization routine based on a quasi-Newton algorithm to find the local minimum. This method is very efficient in finding low-lying minima for systems containing large numbers of moving particles.

III. RESULTS AND DISCUSSIONS

For the first chlorination step, leading to Cl-covered terraces, the attachment energy was calculated as about −4.0 eV per Cl atom. This is in good agreement with earlier reports.[1,2] Present calculations indicate that for Si(100)-(2×1) terraces with a single height step, applied uniaxial strain has little or no effect on the first chlorination step. In both x and y directional strains, variations in the Cl attachment energies leading to the formation of –SiCl units were found to be less than 1%. This is expected because Cl–Cl distances at chlorinated surface regions are relatively large. A schematic side view of singly chlorinated terraces is depicted in Fig. 1(a). On a dimerized surface, chlorine atoms (being attached at the terminal sites) form almost a square array covering the surface with a Cl–Cl nearest-neighbor distance of about 3.8 Å. Accordingly, for small strains, no appreciable steric effects are operational, and in this case calculated Si–Cl binding energies are almost independent of applied strain.

The effect of strain is quite profound during the second chlorination step. Figure 1(b) displays a doubly chlorinated Si atom at the step edge. The attachment energy of the second Cl atom (forming a $-SiCl_2$ unit at the step edge) is

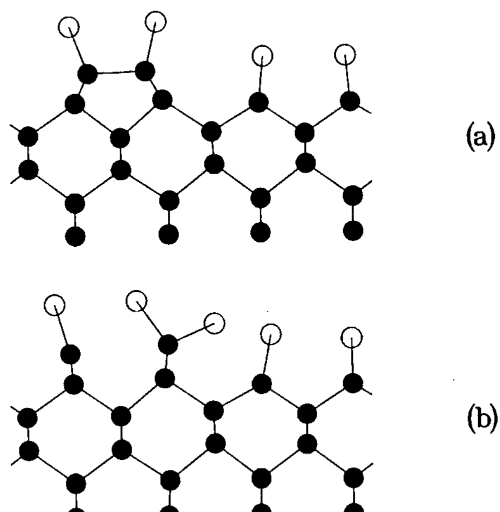

FIG. 1. Side views of chlorinated Si(100)-(2×1) surfaces with single step high edges. Sis and Cl atoms are represented by closed and open circles, respectively. (a) Chlorinated terraces: one Cl atom is attached at the terminal site for each exposed Si atom. On the upper terrace the dimer bond between the edge Si and its neighbor is shown. On the lower terrace, dimer bonds are perpendicular to the view plane. (b) An additional chlorine atom attachment to an edge-site Si atom is depicted. In this case, the dimer bond is broken and the additional Cl atom is at the bridge site, forming an attached $-SiCl_2$ species.

strongly influenced by the applied strain. Calculations indicate that the attachment process, in this case, is energetically more favorable under tension and less favorable under compression than the unstrained case. Percent variations, P_E, in Cl attachment energies are shown in Fig. 2 for uniaxial strains applied in x and y directions. Positive values of P_E here indicate an increase and negative values indicate a decrease in the attachment strength. For the maximum tensile

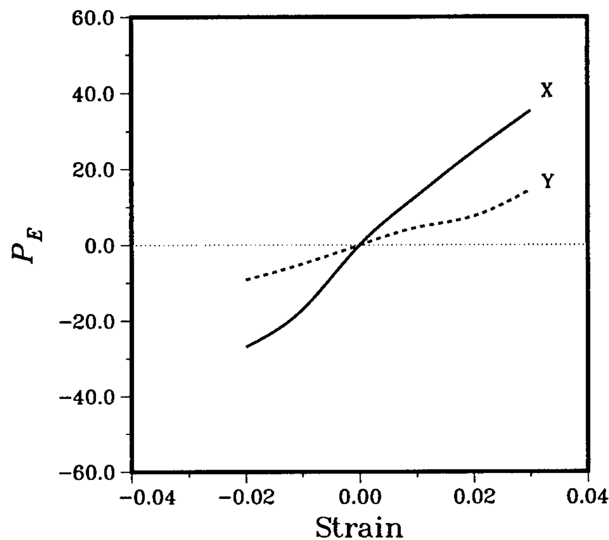

FIG. 2. Percent variation, P_E, in the second chlorination energy of an edge-site Si atom with applied strain. Solid and dashed lines represent variations due to strains applied in the X and Y directions, respectively. Negative values of strain correspond to compression and positive values indicate tension.

strain (0.03) that we used here, the Cl attachment strength was found to increase about 35% and 12% corresponding to tensions applied in x and y directions, respectively. For the compressive strain of -0.02, Cl attachment strength decreases about 25% for compressions applied in the x direction, and 9% for compressions applied in the y direction.

The present calculations also show that the z-directional position of the attached $-SiCl_2$ unit (with respect to the top surface layer) varies with applied strain. Again, the effect is most pronounced for strains in the x direction. The distance between the attached $-SiCl_2$ unit and the upper terrace was found to increase under the compressive strain and decrease under tension. The total change in the distance (for strains applied in the x direction) is about 0.5 Å going from a compressive state of -0.02 to a tension of 0.03. This outcome is quite consistent with the calculated energy values, indicating that under compression the $-SiCl_2$ unit is less strongly bonded to its surface site. The applied strain, in this case, does not alter the general geometry of the $-SiCl_2$ unit. Calculations indicate that the effect of the applied strain on Si–Cl and Cl–Cl distances is rather negligible. The attached $-SiCl_2$ unit is not an isosceles triangle. The Si–Cl distances were calculated as 2.22 and 2.08 Å for Cl atoms located at the bridge and terminal sites, respectively, and Cl–Cl distance was found around 3.4 Å.

IV. CONCLUSIONS

In this study, the role played by external strain on the chlorination process of silicon surfaces was investigated. This is the first systematic study showing the effect of applied strain on the adsorption energetics of Cl atoms on Si surfaces. Here, a Si(100)-(2×1) surface with an A-type step edge was taken into consideration. Percent variations in energies of first and second chlorination steps were calculated as functions of external strain. Results indicate that applied strain has little or no effect on the first chlorination step. The energetics of the second chlorination step, however, were found to be affected considerably by the applied strain. The bond strength of the second Cl atom attached to an edge site Si (forming a $-SiCl_2$ unit) was found to decrease with increasing compression and increase with tension. The effect is more pronounced for strains applied in the direction perpendicular to the step edge. The strain effect on the desorption energetics of Cl-containing Si species is under investigation and the outcome will be included in our next report. Finally, results obtained in this present study show that external strain can be used to control the second chlorination process, which in turn may be instrumental in certain applications related to silicon etching technology.

ACKNOWLEDGMENT

This work was supported by NASA Ames Research Center through Prime Contract No. NAS2-99092 to Eloret.

[1]T. Halicioglu and D. Srivastava, Surf. Sci. **437**, 773 (1999).
[2]H. Feil, J. Dieleman, and B. J. Garrison, J. Appl. Phys. **74**, 1303 (1993).
[3]W. Sesselmann, E. Hudeczek, and F. Bachmann, J. Vac. Sci. Technol. B **7**, 1284 (1989).
[4]G. A. de Wijs, A. De Vita, and A. Selloni, Phys. Rev. B **57**, 10021 (1998).
[5]G. A. de Wijs, A. De Vita, and A. Selloni, Phys. Rev. Lett. **78**, 4877 (1997).
[6]K. Nakayama, C. M. Aldao, and J. H. Weaver, Phys. Rev. B **82**, 568 (1999).
[7]W. Yang, Z. Dohnalek, W. J. Choyke, and J. T. Yates, Jr., Surf. Sci. **392**, 8 (1997).
[8]M. B. Webb, F. K. Men, B. S. Swartzentruber, R. Kariotis, and M. G. Lagally, Surf. Sci. **242**, 23 (1991).
[9]T. W. Poon, S. Yip, P. S. Ho, and F. F. Abraham, Phys. Rev. Lett. **65**, 2161 (1990).
[10]H. Feil, Phys. Rev. Lett. **74**, 1879 (1995).
[11]D. E. Hanson, A. F. Voter, and J. D. Kress, J. Appl. Phys. **82**, 3552 (1997).
[12]M. E. Barone, T. O. Robinson, and D. B. Graves, IEEE Trans. Plasma Sci. **24**, 77 (1996).
[13]D. Srivastava, T. Halicioglu, and T. A. Schoolcraft, J. Vac. Sci. Technol. A **17**, 657 (1999).
[14]E. Clementi, *Modern Techniques in Computational Chemistry: MOTECC-90* (Escom, Leiden, 1990), Chap. 17.

Stability of boron and phosphorus implanted tungsten silicide structures at high temperatures

R. Bashir[a] and F. Hebert[b]
School of Electrical and Computer Engineering, Purdue University, West Lafayette, Indiana 47906

(Received 8 October 1999; accepted 28 April 2000)

We report on the stability of sputter-deposited tungsten silicide ($WSi_{2.6}$) films that were implanted with boron or phosphorus and annealed at high temperatures using rapid thermal annealing. Depending on process conditions, some films were found to be unstable, resulting in peeling and lifting from the substrate. The regime of stability was experimentally determined and found to be a function of the implant dose, species, and anneal temperature. Films implanted with boron were found to be more stable than those implanted with phosphorus. With the appropriate choice of dopant dose, anneal temperature, and capping layer type, the film stacks were found to be stable upon subsequent furnace annealing steps at 900 °C. © *2000 American Vacuum Society.* [S0734-211X(00)04304-3]

I. INTRODUCTION

Since the earlier reports of the use of tungsten silicide for integrated circuit applications,[1,2] there have been numerous reports of the use of this material for bipolar extrinsic base regions,[3] metal–oxide–semiconductor gate structures,[4] EEPROMs,[5] and related applications.[6] Stacks of polycrystalline silicon and silicide (polycides) have the benefit of having a lower resistivity than heavily doped polysilicon. Most popular polycide and silicide structures, however, are not stable at high temperatures. For example, $TiSi_2$ forms a high resistance contact to P+ silicon due to the formation of Ti–B compounds at temperatures above 950 °C. Furthermore, $TiSi_2$ and $CoSi_2$ agglomerate when exposed to temperatures in excess of 1000 °C, resulting in increased sheet resistance. This is inconsistent with the use of such materials for integrated circuit manufacturing.

Tungsten silicide films can be stable up to temperatures in excess of 1100 °C. These films can be formed using chemical vapor deposition (CVD) or rf sputtering. The stability of CVD tungsten silicide films upon furnace oxidation can be improved upon reduction of internal stresses by a rapid thermal processing and by increasing the Si/W ratio to greater than 2.6.[7] Stacking the films in layers of polycrystalline silicon has also shown to improve their stability.[8] These films can also be implanted specifically to be used as a dopant diffusion source, or become implanted inadvertently when being used as a mask. There are no reports in the literature on the stability of tungsten silicide films after ion implantation and rapid thermal annealing.

The purpose of this article is to report, for the first time, on the preliminary experimental results of stability of tungsten silicide films that were implanted and subsequently rapid thermal annealed. A stability regime was experimentally determined and it was a found that boron doped films were more stable than phosphorus doped films.

[a]Author to whom correspondence should be addressed; electronic mail: bashir@ecn.purdue.edu
[b]Now with Linear Technology Corporation, Milpitas, CA.

II. EXPERIMENTS AND RESULTS

The experiments were performed on 5 in. wafers without any patterns. After the deposition of a thin layer of polycrystalline silicon of 1500 Å in thickness on the silicon surface, the tungsten silicide layer was deposited in a sputtering system (Varian model 3280) using a target of composition $WSi_{2.8}$. The resulting film had a composition of about $WSi_{2.6}$. The resistivity was extracted from a series of depositions of increasing time and thickness of the film and was found to be about 7.8×10^{-4} Ω cm. This is consistent with earlier reports of such films. The film thickness used in the experiments here was about 1000 Å. The wafers were then implanted with a series of doses ranging from a dose of 6×10^{14} to 3×10^{16} #/cm^2. The energy of all implants was kept at 20 keV. A capping insulator layer was then deposited over the surface of the film consisting of a 2000 Å undoped oxide layer deposited using thermal decomposition from a tetramethylorthosilicate (TEOS) source. The wafers were then annealed in an AG4108 rapid thermal processor for 30 s each at 1050, 1100, and 1150 °C in an N_2 ambient. The wafers were inspected after anneal and the film was defined to be unstable if the defect density exceeded 1/cm^2. The defects were defined to be any regions where the film had peeled, lifted off, or cracked, as observed visually under a 500× magnification. Figure 1 shows an optical micrograph of the regions showing the regions where the films had cracked and peeled in circular shapes.

The dose of the implant species was found to have a significant effect on the stability. This behavior is shown in Figs. 2 and 3, which are plots showing final annealing temperature versus dopant dose for boron and phosphorus implanted silicide/polycide films. These figures show the regions of stability and instability for the doped films. The graph clearly shows the combinations of anneal temperature and dopant dose which form regions of implanted film stability and instability (peeling). As can be seen from Fig. 2, boron may be used at doses up to approximately 1×10^{16} #/cm^2 to obtain films which are stable at temperatures up to 1100 °C. As shown in Fig. 3, phosphorus can be used at

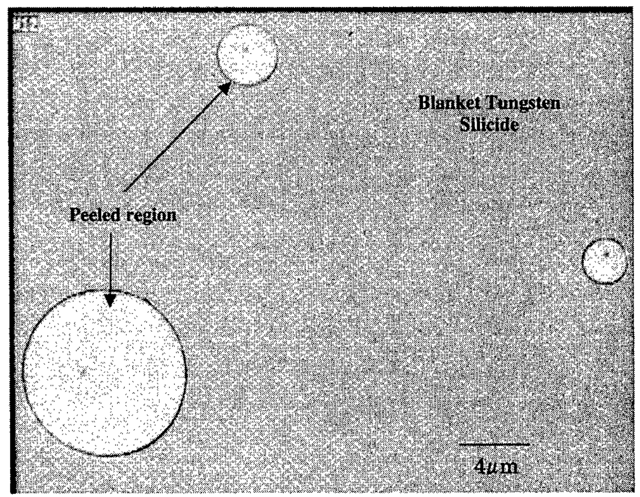

FIG. 1. Optical micrograph (500×) of the region of tungsten silicide peeling.

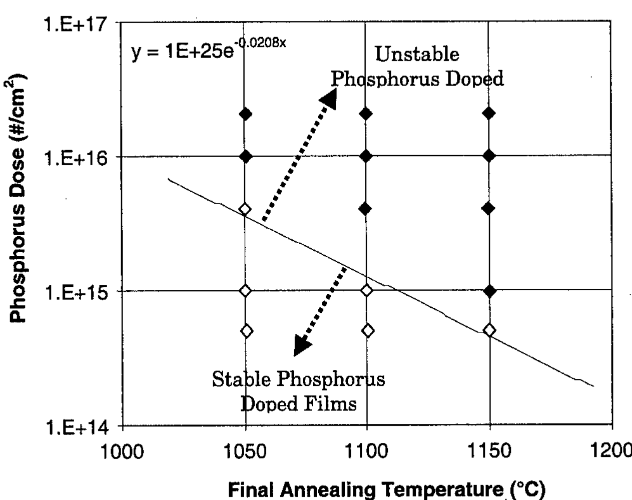

FIG. 3. Phosphorus dose vs final annealing temperature. The region below the dashed line is for stable phosphorus doped $WSi_{2.6}$ films.

doses up to approximately 4×10^{15} #/cm^2 to obtain films which are stable at temperatures up to 1050 °C. The difference in the behavior of phosphorus and boron can be attributed to changes in film stress upon the introduction of these species of different sizes. Boron is a smaller atom than phosphorus and is expected to produce less perturbation and stress in the amorphous structure of the tungsten silicide. Upon substitutional incorporation of boron or phosphorus in single crystal silicon, the damage from boron is typically harder to anneal since the difference in atomic size between boron and silicon is larger than that of the difference between phosphorus and silicon. In amorphous tungsten silicide however, the situation can be different and the real reason for increased stability with boron implantation when compared to phosphorus is not totally clear and needs more investigation. It can however be postulated that the incorporation of phosphorus increases the stress in the films making then more unstable and susceptible to peeling. It should also be pointed out that in the given experiments, undoped tungsten silicide films were stable even when exposed up to 1200 °C for 30 s.

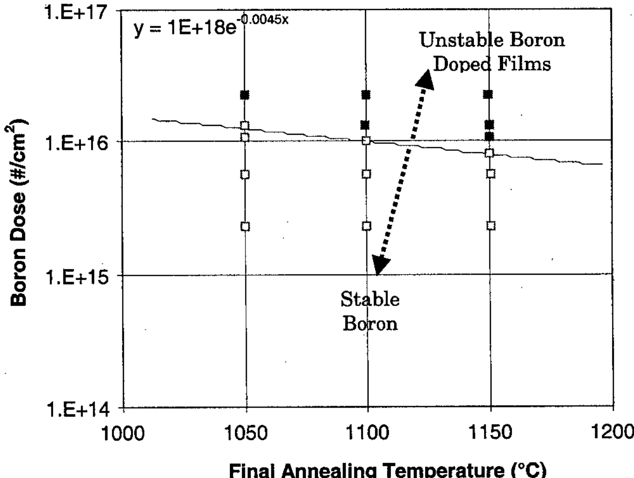

FIG. 2. Boron dose vs final annealing temperature. The region below the dashed line is for stable boron doped $WSi_{2.6}$ films.

It was also found that the composition and thickness of the insulator layer deposited on the silicide/polycide layer had an effect on the stability of the film. When a 2000 Å thick oxide film is deposited from a TEOS source thermal decomposition is used as the insulator on top of the silicide layer, and the stack is stable up to a rapid thermal anneal (RTA) temperature of 1100 °C. When a densification anneal step at 900 °C for 20 min in dry oxygen was used after the deposition of the oxide, the stack/films were not stable at 1100 °C. When the densification step was performed in nitrogen, the stack was stable at 1100° RTA step. The nitride/oxide stack on silicide could be the preferred insulator configuration for the silicide/polycide capping layer since this could possibly permit the use of thinner oxide layers with oxidizing ambients (because the nitride blocks the oxygen diffusion).

III. CONCLUSIONS

In this work, we experimentally determined the regions of stability for sputter deposited tungsten silicide films after implantation and RTA. Boron implanted films were found to be more stable when compared to phosphorus implanted films, possibly due to increased stress in the silicide film after implantation. Experimentally obtained data showing the stability region versus implant dose has also been presented.

ACKNOWLEDGMENT

The work was done at National Semiconductor Corporation, Sunnyvale, CA.

[1]F. Mohammadi and K. C. Saraswat, J. Electrochem. Soc. **127**, 450 (1980).
[2]K. C. Saraswat, D. L. Brors, J. A. Fair, K. A. Monnig, and R. Beyers, IEEE Trans. Electron Devices **30**, 1497 (1983).

[3]K. C. Brown *et al.*, Proc. SPIE **2875**, 48 (1996).
[4]H. Kuo-Ching, F. Yean-Kuen, Y. Dun-Nian, C. Chii-Wen, L. Mong-Song, H. Jang-Cheng, S. Chi-Wen, and K-Y. Lee, IEEE Electron Device Lett. **20**, 36 (1999).
[5]K. Ogier-Monnier, P. Boivin, and O. Bonnaud, Proc. SPIE **3507**, 175 (1998).
[6]S. Wolf, *Silicon Processing for the VLSI Era*, Process Integration, Vol. 2 (Lattice, 1990), pp. 162–169.
[7]A. P. Blosse, Rapid Thermal and Integrated Processing VII, Symposium of the Materials Research Society, 1998, p. 371.
[8]K.-Y. Lee, Y.-K. Fang, C.-W. Chen, M.-S. Liang, and J.-C. Hsieh, IEEE Electron Device Lett. **18**, 181 (1997).

This section is reserved for short submissions which contain important new results and are intended for accelerated publication.

Low temperature inorganic chemical vapor deposition of Ti–Si–N diffusion barrier liners for gigascale copper interconnect applications

Eric Eisenbraun,[a] Allan Upham, Raj Dash, Wanxue Zeng, Johann Hoefnagels, Sarah Lane, Dalaver Anjum, Katharine Dovidenko, and Alain Kaloyeros
The New York State Center for Advanced Thin Film Technology and Department of Physics, The University at Albany–SUNY, Albany, New York 12203

Barry Arkles
Gelest Incorporated, Tullytown, Pennsylvania 19007

John J. Sullivan
MKS Instruments, Incorporated, Andover, Massachusetts 01810

(Received 28 February 2000; accepted 26 May 2000)

A new low temperature inorganic thermal chemical vapor deposition process has been developed for the growth of titanium–silicon–nitride (Ti–Si–N) liners for diffusion barrier applications in ultralarge scale integration copper interconnect schemes. This process employs the thermal reaction of tetraiodotitanium (TiI_4), tetraiodosilane (SiI_4), and ammonia (NH_3) as, respectively, the individual Ti, Si, and N sources. Ti–Si–N films were successfully grown over a broad range of deposition conditions, including wafer temperature, process pressure, and TiI_4, SiI_4, and NH_3 flows ranging, respectively, from 350 to 430 °C, 0.1–1 Torr, and 2.5–8.0, 2.5–12.5, and 100–250 sccm. Film stoichiometry was tightly tailored through independent control of the Ti, Si, and N source flows. Film properties were characterized by x-ray photoelectron spectroscopy, Rutherford backscattering spectrometry, transmission electron microscopy, scanning electron microscopy, x-ray diffraction, and four-point resistivity probe. Resulting findings indicated that the texture and resistivity of the Ti–Si–N system were dependent on composition. In particular, films with a $Ti_{33}Si_{15}N_{51}$ stoichiometry exhibited a nanocrystalline TiN phase within an amorphous SiN matrix, highly dense morphology, resistivity of $\sim 800\ \mu\Omega$ cm for 25 nm thick films, and step coverage of ~50% in 130 nm wide, 10:1 aspect ratio trenches. Oxygen and iodine contaminant levels were below, respectively, 3 and 1.4 at. % each. Preliminary copper diffusion-barrier studies indicated that barrier failure for 25 nm thick $Ti_{34}Si_{23}N_{43}$ films did not occur until after annealing for 30 min at 700 °C. *© 2000 American Vacuum Society.* [S0734-211X(00)07904-X]

Copper based interconnects have almost universally replaced aluminum in high-performance integrated circuitry applications. This transition was driven by copper's lower resistivity and improved electromigration resistance, which allow faster signal propagation speed and higher performance characteristics. However, the successful incorporation of copper into subquarter-micron device generations requires effective chemical, structural, mechanical, and electrical compatibility with the surrounding low dielectric constant insulators. Most of the resulting target specifications could be achieved through the identification of appropriate liners that prevent copper diffusion into the dielectric, and promote viable copper-dielectric interlayer adhesion.[1]

The need for a diffusion barrier and adhesion promoter is further mandated by the high diffusivity of Cu into silicon and its poor adhesion to silicon dioxide and low dielectric constant materials. The presence of copper in silicon results in the formation of deep level traps that cause device degradation and failure. Liner materials are also required to be thermodynamically stable with respect to the copper and dielectric layers, and preferably exhibit an amorphous structure to eliminate the high diffusion pathways typically provided by grain boundaries. More important, they must sustain their desirable properties at extremely reduced thicknesses to ensure that most of the effective volume of the trench and via structures is occupied by the actual copper conductor.[1]

In this respect, ternary refractory metal liners such as the titanium–silicon–nitrogen (Ti–Si–N), tantalum–silicon–nitrogen (Ta–Si–N), and tungsten–boron–nitrogen (W–B–N) systems could act as viable diffusion barriers in copper metallization due to their favorable chemical, structural, and thermal properties. In particular, the Ti–Si–N phase represents a highly desirable option due to the fact that Ti-based liners have already gained wide acceptance in semiconductor fabrication flows. In addition, the availability of Ti–Si–N in amorphous form provides an added incentive, in view of the

[a]Author to whom correspondence should be addressed; electronic mail: ee@cnsvax.albany.edu

TABLE I. Range of CVD TiSiN processing conditions investigated in this work.

Parameter	Processing range investigated
Temperature	350–430 °C
Pressure	0.1–1 Torr
NH_3 flow	100–250 sccm
H_2 flow	100 sccm
TiI_4 vapor flow	2.5–6 sccm
SiI_4 vapor flow	0–12.5 sccm

TABLE III. Optimized CVD TiSiN key processing parameters.

Parameter	First-pass optimized process settings
Temperature	430 °C
Pressure	0.6 Torr
NH_3 flow	250 sccm
H_2 flow	100 sccm
TiI_4 vapor flow	6 sccm
SiI_4 vapor flow	10 sccm

absence of grain boundaries that tend to act as fast diffusion paths for copper migration. In this respect, the amorphous Ti–Si–N phase has been shown to be stable against crystallization at temperatures as high as 1000 °C, with the latter being strongly dependent on film stoichiometry.[2] As a result, various research groups have investigated the formation of Ti–Si–N films by a variety of physical vapor deposition (PVD) and metalorganic chemical vapor deposition (MOCVD) techniques, and documented their resulting performance as copper diffusion barriers.

In the PVD case, most of the diffusion barrier studies employed liners with thicknesses larger than 100 nm, which made the resulting conclusions less applicable to subquarter-micron device structures.[3–5] The MOCVD route, on the other hand, exploited the reaction of tetrakis diethylamido titanium (TDEAT), silane (SiH_4), and NH_3 to deposit Ti–Si–N films over the temperature range from 300 to 450 °C.[6] Barrier thermal stress (BTS) testing was subsequently performed on 10 nm thick $Ti_{23}Si_{14}N_{45}O_3C_3H_{12}$ samples that were MOCVD grown at 400 °C. The samples were shown to possess a mean time to failure (MTTF) approximately 10–100 times that of PVD TiN.[7] More recently, metalorganic atomic layer deposition (MOALD) was employed to deposit conformal Ti–Si–N layers at low substrate temperatures (180 °C). However, no information was available with regard to film purity, resistivity, or barrier properties.[8]

The work presented herein has focused on the development of a low temperature thermal CVD process that employs the thermal reaction of tetraiodotitanium (TiI_4), tetraiodosilane (SiI_4), and ammonia (NH_3) as, respectively, the individual Ti, Si, and N sources. These source precursors are attractive because of their chemical simplicity, low dissociation energy, and reduced decomposition temperature as compared with other inorganic chemistries (such as $TiCl_4$). Additionally, SiI_4 was selected over SiH_4 in order to prevent the possible incorporation of hydrogen into the film as a result of incomplete decomposition of the SiH_4 molecule. The strategy espoused was to grow the Ti–Si–N phase *in situ* through the simultaneous reaction of appropriate mixtures of the Ti, Si, and N sources in the presence of hydrogen. Film stoichiometry was tightly tailored through independent control of the TiI_4, SiI_4, and NH_3 gaseous flows, with the reaction proceeding schematically as follows:

$$TiI_4+SiI_4+NH_3+H_2 \rightarrow Ti_mSi_nN_p+NH_qI_r+HI.$$

Hydrogen was employed to ensure complete passivation and elimination of any free iodide reaction by-products from the reaction zone.

All Ti–SiN films were deposited in a customized, stainless steel, 200 mm wafer capable, warm-wall CVD system equipped with a high vacuum loadlock for wafer transport and handling without exposing the deposition chamber to air. This approach allowed tight control over the process stability and reproducibility. The chamber was also equipped with a parallel-plate-type, radio-frequency (rf) plasma capability for *in situ* wafer plasma cleaning. A Roots blower stack was used for process pumping. The TiI_4 and SiI_4 source precursors, which are solid at room temperature, were delivered to

TABLE II. Selected film properties.

Property	Value
Optimized composition (RBS, XPS)	$Ti_{33}Si_{15}N_{51}$
Iodine incorporation (XPS)	~1.4 at. %
Oxygen incorporation (XPS)	Typical XPS background levels
Texture (XRD, TEM)	Nanocrystalline TiN phase within an amorphous SiN_x matrix
Resistivity (25 nm thick film)	~800 $\mu\Omega$ cm
Conformality (130 nm wide, 10:1 aspect ratio trenches)	50%

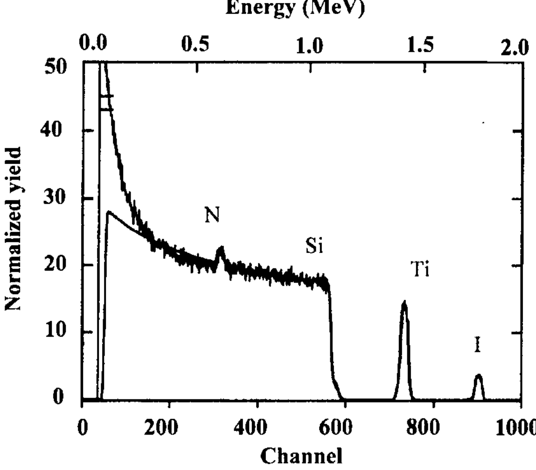

FIG. 1. Typical RBS plot of as-deposited CVD Ti–Si–N film.

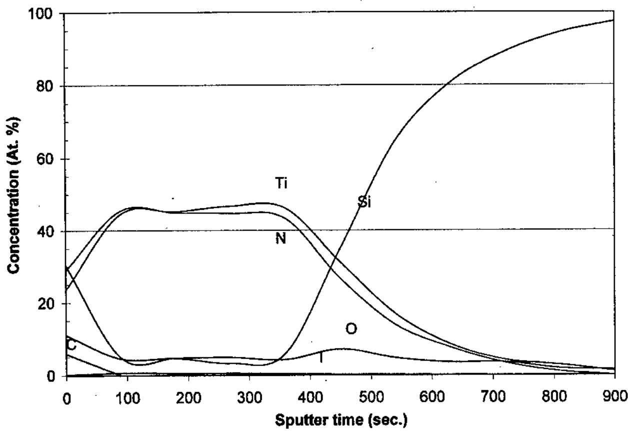

FIG. 2. XPS depth profile of as-deposited CVD $Ti_{36}Si_{12}N_{52}$ film.

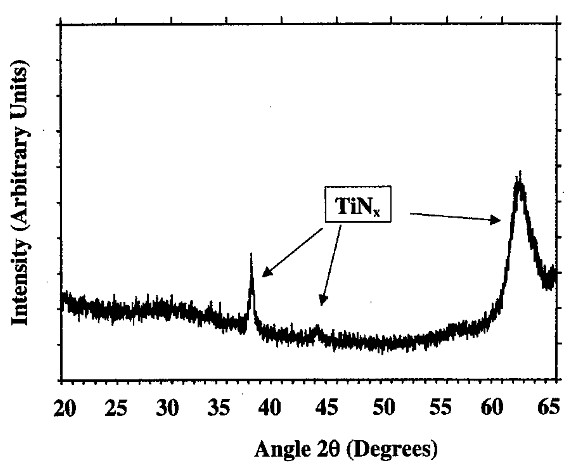

FIG. 3. XRD scan of an as-deposited, 25 nm thick, CVD $Ti_{36}Si_{12}N_{52}$ film.

the reaction chamber using individual MKS model 1153A vapor source delivery systems. Sufficient vapor pressure for delivery to the chamber was achieved by heating each source to $\sim 160\,°C$, with the delivery systems and transport lines being kept at $\sim 180\,°C$ to prevent precursor recondensation. This delivery approach did not require carrier gas, and allowed repeatable and controllable control over reactant flows to the process chamber.

NH_3 and hydrogen (H_2) were used as coreactants. Undesirable gas phase reactions were eliminated through the use of a ''no-mix'' showerhead architecture, where the ammonia line was isolated from all other reactants until introduction into the reaction zone. For all depositions, three types of substrates were employed. Si(100) wafers were employed for thermal diffusion barrier testing, while 500 nm thick thermally grown SiO_2 on Si was applied for composition, resistivity, and texture measurements, and patterned oxide structures were used for assessment of film conformality. Table I summarizes pertinent deposition parameters and corresponding ranges explored in this work.

The composition, microstructure, surface morphology, conformality, and electrical properties of the CVD Ti–Si–N films were analyzed by x-ray photoelectron spectroscopy (XPS), Rutherford backscattering spectrometry (RBS), x-ray diffraction (XRD), transmission electron microscopy (TEM), and four-point resistivity probe. Relevant information regarding these characterization techniques is given elsewhere.[9] In this respect, selected film properties are summarized in Table II, and the corresponding optimized processing conditions are listed in Table III.

Additionally, a preliminary evaluation was carried out of

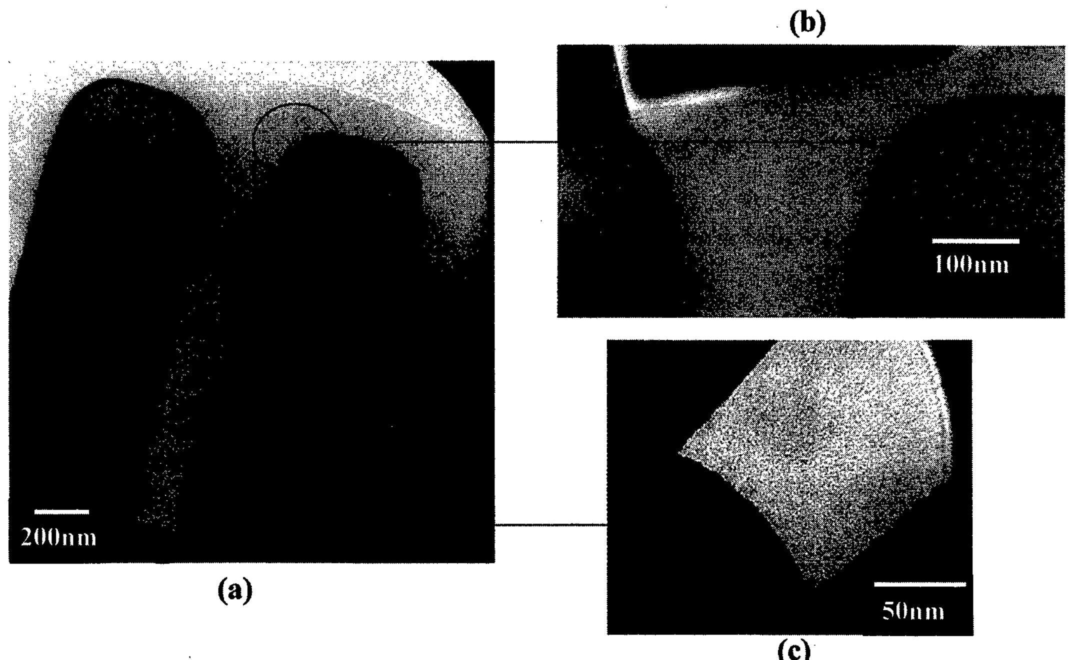

FIG. 4. TEM imaging studies of as-deposited, 10 nm thick, CVD Ti–Si–N film show (a) 50% step coverage in a nominally 130 nm wide, 10:1 aspect ratio, trench structure, (b) no loafing at the top corners of the structure, and (c) no thinning at the bottom corners of the trench structure.

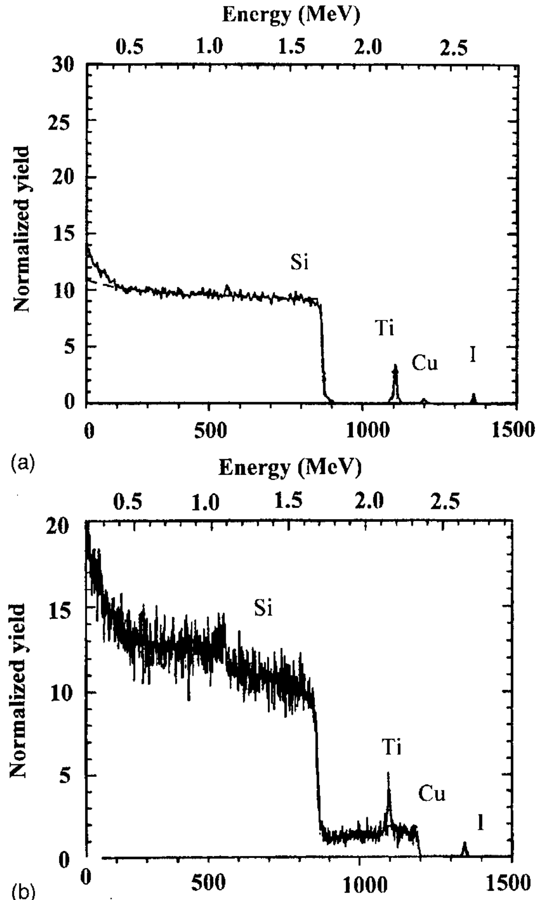

FIG. 5. Typical RBS spectra of sputtered Cu/CVD $Ti_{36}Si_{12}N_{52}$/Si stacks films after annealing at (a) 600 and (b) 700 °C. The data were collected after removal of the top copper layer.

the performance of the CVD Ti–Si–N as a diffusion barrier in copper metallization. For this, 100 nm thick Cu films were *ex situ* sputter deposited onto 25 nm thick CVD $Ti_{33}Si_{15}N_{51}$ films grown on Si. The resulting stacks were annealed in 1 atm argon at 450, 515, 600, and 700 °C for 30 min, along with sputter-deposited Cu/CVD TiN/Si stacks of identical thickness. The latter provided a comparative assessment of barrier performance. After annealing, the copper was stripped off in a diluted nitric acid solution, and the resulting samples were then analyzed by RBS to detect the presence of Cu, either in the liner material or in the underlying Si substrate.

Figure 1 presents a typical RBS spectrum of an 82 nm thick CVD Ti–Si–N film deposited on Si at a wafer temperature of 430 °C. RBS analysis indicated that the films were free of any heavy elemental contaminants, with the exception of ~1.4 at. % I. In this respect, higher NH_3 and SiI_4 flows at constant TiI_4 flow yielded, respectively, increased nitrogen and silicon incorporation into the resulting Ti–Si–N phase. For illustration purposes, Fig. 2 displays the XPS depth profile for the same type sample as that shown in Fig. 1. The XPS depth profile yielded a film composition of $Ti_{33}Si_{15}N_{51}$, and indicated the presence of oxygen levels of ~3 at. %, which was within the typical background levels of the XPS system.

Figure 3 presents a typical XRD spectrum of a 25 nm thick CVD TiSiN film grown on SiO_2. The only XRD peaks detected were ascribed to TiN_x phases. It is believed that this finding indicates that film microstructure consisted of a nanocrystalline TiN phase within an amorphous SiN matrix, in agreement with prior results in the literature on sputter-deposited Ti–Si–N films.[10] It was suggested that this Ti–Si–N microstructure is desirable from a diffusion barrier performance perspective, especially in view of the absence of grain boundaries.[11] The latter tend to act as fast diffusion paths for copper migration.

TEM was used to determine the film conformality in aggressive device structures. In this respect, Fig. 4(a) exhibits the bright field TEM micrograph of 10 nm thick CVD-grown Ti–Si–N in a nominally 130 nm wide, 10:1 aspect ratio, trench structure. In addition, Figs. 4(b) and 4(c) display higher magnification TEM images of film profiles at, respectively, the top and bottom of the trench structure. TEM analysis yielded a film conformality of ~50%, and indicated the absence of thinning or loafing effects at the top and bottom corners of the trench structure. TEM imaging also confirmed the XRD results with respect to the existence of a nanocrystalline structural phase.

In terms of diffusion barrier performance, RBS results indicated the absence of any diffused copper in the CVD Ti–Si–N liner or underlying Si substrates after annealing at 600 °C, as shown in Fig. 5(a). In contrast, RBS detected the onset of copper diffusion for the same film after annealing at 700 °C, as shown in Fig. 5(b).

In summary, a new low temperature inorganic CVD Ti–Si–N process has been developed for applications as a diffusion barrier in copper metallization schemes. This process employs the thermal reaction of TiI_4, SiI_4, and NH_3 as, respectively, the individual Ti, Si, and N sources. Ti–Si–N films were successfully grown over a broad range of deposition conditions, including wafer temperature, process pressure, and TiI_4, SiI_4, and NH_3 flows ranging, respectively, from 350 to 430 °C, 0.1–1 Torr, and 2.5–8.0, 2.5–12.5, and 100–250 sccm. In particular, films with a $Ti_{33}Si_{15}N_{51}$ stoichiometry exhibited a nanocrystalline TiN phase within an amorphous SiN matrix, highly dense morphology, resistivity of ~800 $\mu\Omega$ cm for 25 nm thick films, and step coverage ~50% in 130 nm wide, 10:1 aspect ratio trenches. The oxygen and iodine contaminant levels were below, respectively, 3 and 1.4 at. % each. Preliminary copper diffusion-barrier studies indicated that barrier failure for 25 nm thick $Ti_{33}Si_{15}N_{51}$ films did not occur until after annealing for 30 min at 700 °C. Additional studies are presently underway to further optimize the film conformality through modeling of film profiles in aggressive device topographies using fast simulators and to fully document corresponding diffusion-barrier characteristics by employing barrier thermal stress measurements.

The work presented herein was supported in part by SEMATECH under Contract No. MLMA006, by MKS Instruments, and by the New York State Center for Advanced Thin Film Technology. This support is gratefully acknowledged.

[1] *The International Technology Roadmap for Semiconductors*, 1999 ed. (Semiconductor Industry Association, San Jose, CA, 1999), p. 165.
[2] X. Sun, J. Reid, E. Kolawa, and M. Nicolet, J. Appl. Phys. **81**, 656 (1997).
[3] J. Reid, E. Kolawa, R. Ruiz, and M. Nicolet, Thin Solid Films **236**, 319 (1993).
[4] P. Pokela, E. Kolawa, M. Nicolet, and R. Ruiz, J. Electrochem. Soc. **138**, 2125 (1991).
[5] J. Reid, E. Kolawa, C. Garland, M. Nicolet, F. Cardone, D. Gupta, and R. Ruiz, J. Appl. Phys. **79**, 1109 (1996).
[6] J. Custer, P. Smith, R. Jones, A. Maverick, D. Roberts, J. Norman, and A. Hochberg, *Advanced Metallization and Interconnect Systems for ULSI Applications in 1995* (Materials Research Society, Pittsburgh, PA, 1996), p. 343.
[7] P. Smith *et al.*, in Ref. 6, p. 249.
[8] J. Min, H. Park, and S. Kang, Appl. Phys. Lett. **75**, 1521 (1999).
[9] See, for example, J. Kelsey, C. Goldberg, G. Nuesca, G. Peterson, A. Kaloyeros, and B. Arkles, J. Vac. Sci. Technol. B **17**, 1101 (1999).
[10] X. Sun, E. Kolawa, S. Im, C. Garland, and M. Nicolet, Appl. Phys. A: Mater. Sci. Process. **65**, 43 (1997).
[11] X. Sun, J. Reid, E. Kolawa, M. Nicolet, and R. Ruiz, J. Appl. Phys. **81**, 664 (1997).

Plasma-enhanced atomic layer deposition of Ta and Ti for interconnect diffusion barriers

S. M. Rossnagel
IBM Research, P.O. Box 218, Yorktown Heights, New York 10598

A. Sherman and F. Turner
Sherman and Associates, Menlo Park, California 94025

(Received 28 January 2000; accepted 12 May 2000)

Thin films of inert, refractory materials are used in semiconductor interconnect applications as diffusion barriers, seed, and adhesion layers. A typical example is the use of a thin, conformal Ta or Ti/TiN films on the walls of a dielectric trench or via which reduces or eliminates out-diffusion of the primary conductor, usually Cu, into the dielectric. Atomic layer deposition is a known technique which is intrinsically conformal and is appropriate for this application. Plasma enhancement of the process allows deposition at significantly lower temperatures than conventional chemical vapor deposition, which is a requirement for low-*k* dielectrics. Tantalum films deposited at 25–400 °C using ALD with a $TaCl_5$ precursor and atomic hydrogen as the reactive species at up to a rate of 1.67 Ang/cycle are amorphous, conformal, and show moderate or controllable levels of impurities; primarily oxygen and a small level of Cl. Similar results have been observed for Ti using $TiCl_4$ as a precursor. The process scales to manufacturing dimensions and applications and will facilitate the extension of interconnect technology beyond (below) 100 nm dimensions. © *2000 American Vacuum Society.* [S0734-211X(00)05204-5]

I. INTRODUCTION

The interconnect technology of current-day semiconductor manufacturing is moving rapidly towards a "Damascene" approach, which is characterized by etching trenches and vias in a dielectric, filling the cavities with metal, and using chemical mechanical polishing (CMP) to planarize the now-embedded conductors. This approach differs fundamentally from the past technology, which was based on the reactive ion etching (RIE)-based patterning of blanket metal films followed by dielectric deposition and planarization, in that the metal features are deposited into embedded structures and hence have a much larger, more complicated metal-dielectric surface interaction process. This requires the use of thin, conformal layers on the inner surfaces of the patterned dielectric whose roles may be: adhesion promotion; prevention of out-diffusion of the to-be-deposited metal conductor into the dielectric; prevention of chemical reaction between the materials used for the metal conductor deposition and the dielectric; prevention of in-diffusion of atoms or molecules from the dielectric to the metal conductor; or promotion of deposition chemistry of some subsequent step. This last category includes such things as seed layers for electrodeposition, or specific chemical surfaces for selective deposition of some kind (gas or liquid phase). These types of films are known generically as "liner" films, since their role is to conformally line the sidewalls and bottoms of the various trenches and vias in the interconnect structures.

Thin, liner films are usually deposited by means of sputtering [also known as physical vapor deposition (PVD)], or by chemical vapor deposition (CVD). Due to the somewhat simpler nature and lower cost of PVD technologies, they are used almost exclusively in manufacturing applications. PVD alone, however, is inadequate for conformal deposition in high aspect ratio structures, and has been modified or enhanced by the use of collimators[1,2] or in-flight ionization[3–6] such that the depositing trajectories of the liner atoms can be more controlled and potentially more conformal. PVD-based techniques can lead to adequate conformality in modest aspect ratio features (<5:1) but eventually fail at higher aspect ratio or very thin film thickness due to the intrinsically directional nature of PVD, which limits the total number of atoms which enter the via or trench. CVD techniques can be designed to be completely conformal, but often at the unacceptable cost of either impurity incorporation or high sample temperature. In addition, some CVD techniques have low nucleation rates, requiring the use of a seed layer (usually by PVD) prior to CVD deposition. This increases cost significantly, and the general complexity and cost of many CVD technologies have limited their applicability in semiconductor interconnect manufacturing applications.

Atomic layer deposition (ALD) is in many ways a similar process to CVD, in that it utilizes similar chemistry resulting in the deposition of a film. This general class of deposition technologies has been available for some time,[7–12] but has usually been applied either to dielectrics or semiconductor materials; less often for metals.[13,14] Much like CVD, ALD can be stimulated or enhanced by the use of a plasma, which can result in increased reaction rates on surfaces, increased fragmentation of the precursor molecules, bombardment-enhancement of the removal of product molecules, or some combination of all of these steps, all at lower substrate temperatures than for conventional (i.e., thermal) CVD.

Atomic layer deposition occurs in time-separated steps which are intrinsically self-limited by the nature of the process. A simplified schematic of the process flow is shown in

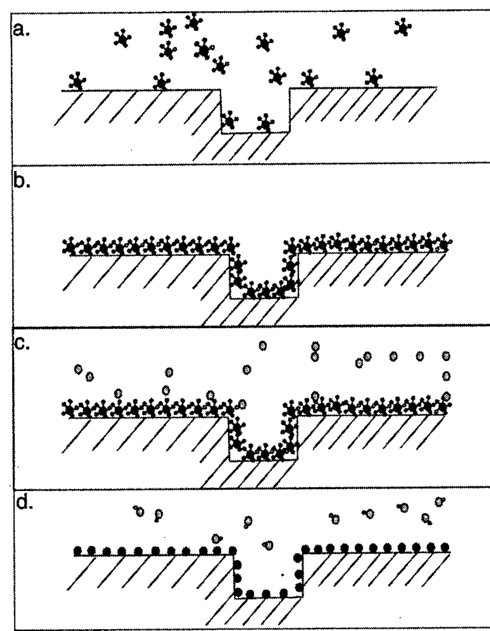

FIG. 1. Idealized schematic of process flow. (a) Exposure of $TaCl_5$, (b) monolayer formation, (c) exposure to atomic hydrogen, and (d) formation and pumping of HCl product molecules.

Figs. 1(a)–1(d). The first ALD step is the exposure of a clean surface to the metal-containing precursor gas [Fig. 1(a)]. After an exposure on the order of 10 000 Langmuirs (1 Langmuir=1 monolayer-equivalent flux, which is roughly equal to a pressure of 10^{-6} Torr for 1 s), the precursor gas is evacuated from the sample chamber. During this exposure, the precursor gas adsorbs on virtually all surfaces within the sample chamber, forming approximately 1 monolayer of surface coverage [Fig. 1(b)]. This is a key component to ALD: the physisorbed monolayer film is moderately stable with time on the surface and does not strongly depend on the deposition conditions. Surfaces which were much colder than room temperature would build up thicker adsorbed layers, but in the temperature range of room temperature to a few hundred degrees C, approximately a single monolayer is adsorbed with a residence time of many seconds or longer. The third step [Fig. 1(c)] is a reaction step which generally uses a reaction between a second, introduced species in the gas phase and the adsorbed monolayer. Under the appropriate conditions, the reaction occurs with all of the adsorbed surface molecules, resulting in the formation of volatile product molecules, which are then pumped away in the gas phase [Fig. 1(d)]. This leaves behind a single layer, generally less than a monolayer, of the desired material (metal) on the film surface.

The ALD process is intrinsically self-limited because it occurs in discrete, time-separated steps. The metal-containing precursor is completely removed from the sample chamber, aside from the adsorbed monolayer, prior to the introduction of the second species which initiates the chemical reaction. Then, the second species, plus the product molecules, are completely removed from the chamber prior to exposure to another pulse of the metal-containing precursor. Each two-pulse cycle can only result in the deposition of a monolayer or less, and films are then built up to controlled thicknesses by increasing the number of cycles. This differs from most conventional film deposition processes used in semiconductor manufacturing, which are usually rate-calibrated and deposited in a dynamic, continuous manner for a time adequate to result in the desired film thickness.

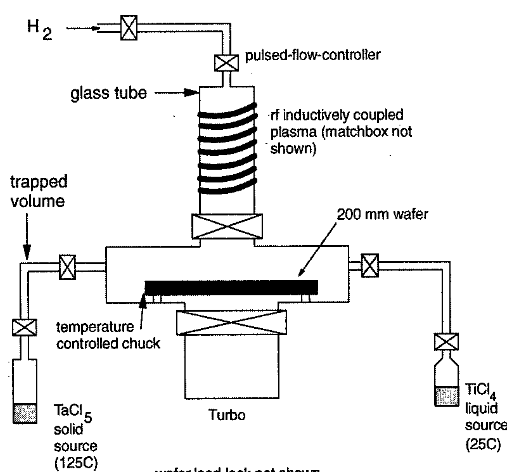

FIG. 2. Schematic of ALD system. Details of loadlock and pumping system not shown.

II. EXPERIMENT

The ALD process uses fairly simple hardware, although the vacuum requirements are fairly stringent. A typical deposition system is shown in Fig. 2. The sample chamber is generally small for practical reasons described below, and might be 6–8 l in volume for a 200 mm wafer sample size. For the experiments described here, the wall temperature can be controlled in the 25–200 °C temperature range. The chamber is usually pumped by a reactive-gas grade turbomolecular pump, and an appropriate size for this 6–8 l volume would be >500 l/s, with a working base pressure of $<10^{-7}$ Torr. For this example, a gate valve is configured between the chamber and the turbo pump. The appropriate flange opening in this case is 150 mm, consistent with an 8 in. conflat flange. A second system has also been used, which has a slightly smaller volume of 4 l, and is pumped via a 300 l/s reactive-gas turbo via a 6 in. conflat gate valve.

For the ALD of Ta, the precursor used is $TaCl_5$, which comes as a fine powder and is stable at room temperature although it reacts readily with water vapor to form tantalum oxide. The second species used is atomic hydrogen, which in this case is formed by means of a plasma, and used downstream at the sample surface. The reaction is then:

$$TaCl_5(g)+5H(atomic,g)\rightarrow Ta(s)+5HCl(g).$$

The key to this reaction, and many similar halogen-based metal precursers, is the scavenging of the Cl atoms from the $TaCl_5$ with atomic hydrogen to form volatile HCl. This re-

action can occur near room temperature, whereas the conventional CVD equivalent process, using H_2, requires temperatures of 800 °C or more.

The $TaCl_5$ source used in this experiment is a heated stainless steel chamber connected to the sample chamber by a pair of valves. The source chamber is heated by heating tape or other resistive means to temperatures on the order of 100–120 °C, which results in a vapor pressure within the source chamber of 2–5 Torr. A pair of valves, with a small, trapped volume between, can be opened sequentially to fill the trapped volume (opening and closing the valve on the source side), and then discharge the trapped volume (opening and closing the valve on the sample side) into the sample region. The valves and tubing are heated to 150–175 °C to prevent condensation of the $TaCl_5$ within the valves.

The $TiCl_4$ source was a glass tube which was not heated. The $TiCl_4$, which is a liquid at room temperature, was placed in the tube, frozen at liquid nitrogen temperature, and evacuated to 1 mTorr. Upon rewarming to room temperature, the vapor from the source was used directly through a timed vacuum valve to provide the working pressure within the chamber of 30–100 mTorr.

The atomic hydrogen source used is a quartz tube connected to the sample chamber by a gate valve and fed from a hydrogen gas supply via a leak valve. The quartz tube is wrapped with a multiple-turn coil powered at 13.56 MHz at a power of 300 to 1200 W. At the bottom of the tube, a small 1–3 mm aperture is used to limit the plasma to the tube region. It should be noted that there are many different types of atomic hydrogen sources, varying from heated tungsten tubes to microwave downstream reactors. The type of hydrogen source should be mostly irrelevant. In the current experiment, a gate valve is used between the sample chamber and the tube region such that the $TaCl_5$ or $TiCl_4$ precursor is not exposed to the tube region, as deposited films would eventually be a problem for radio-frequency (rf) penetration of the dielectric tube.

Once the $TaCl_5$ source is heated to 100–120 °C, the deposition cycle consists of the following steps: (a) filling the trapped volume between the $TaCl_5$ source valves, (b) closing the chamber gate valve and then discharging the trapped volume of $TaCl_5$ into the sample chamber, (c) after exposure of $>10^4$ Langmuirs, opening the chamber gate valve, evacuating the chamber, (d) opening the hydrogen source valves and initiating the rf plasma for a set time, and (e) shutting off the hydrogen source and plasma, allowing the chamber to return to base pressure. This cycle ideally results in the complete reaction of the adsorbed $TaCl_5$ layer, and the deposition of a fraction of a monolayer of Ta. The Ti deposition sequence is similar, except that steps (a) and (b) are replaced with a single, timed valve.

III. RESULTS

The samples used for deposition were thermally oxidized Si wafers or wafer pieces, along with samples of fused silica. The substrates were cleaned with acetone and alcohol, rinsed with deionized water, and dried with clean nitrogen prior to insertion into the system. For the heated samples, the samples were clamped to a heated stage for 1–2 h prior to deposition. There was no *in situ* plasma cleaning of the samples.

The rate of deposition per cycle is dependent on many experimental features, such as the sample temperature and composition, the level of exposure to the precursor, the amount of atomic hydrogen, the pumping speed of the product HCl, and the presence of contaminants or impurities. The deposition rate for the Ta ALD films has been found to range from 0.16 to 0.5 Å cycle at 25 °C to 1.67 Å/cycle at 250–400 °C. It should be noted that this is extremely sensitive to water vapor and/or air exposure, as described below. Under similar circumstances, the deposition of Ti was estimated to be 1.5–1.7 Å/cycle. It is not clear why there should be much, if any dependence on sample temperature in this range. The exposure level of the precursor was generally over 100 000 Langmuirs, which should saturate the surface.

At deposition temperatures of 250 °C and below, no structure can be observed using x-ray diffraction in the deposited Ta at thicknesses of 400 Å. At 400 °C deposition temperature, a weak beta-phase, (111) orientation can be detected. Nicolet has predicted that amorphous Ta may be metastable under some circumstances.[15]

Chemically, the Ta films were analyzed using Auger electron spectroscopy (AES), x-ray photoelectron spectroscopy (XPS), and Rutherford backscattering spectroscopy (RBS). However, no analysis has been possible *in situ*: all films have been exposed to air for extended periods prior to analysis. The primary impurities measured are oxygen, at levels of a few percent up to 26%, and chlorine, at levels of 0.2%–3%. In one case, Cu impurities were also noted, but were traced to an uncoated Cu gasket in the source region. Typically, the Cu gaskets have been coated with Pt or Ni to reduce the Cl reaction.

As mentioned above, the deposition process is very susceptible to contamination by water vapor. These early experiments have been undertaken in a nonload-locked environment, such that the deposition chamber is opened to air (and moisture) to change samples. The presence of water vapor in the vacuum chamber leads to the deposition of Ta oxide, and indeed this reaction is used for the intentional deposition of Ta_2O_5.[12] In addition, the thin Ta films are readily oxidized upon removal from the vacuum chamber. An example of this is a Ta film of 30 Å thickness which was completely converted to Ta_2O_5 after exposure to air for <24 h at room temperature.

Analysis of the Ti films was also complicated by the rapid oxidation of the deposited films upon exposure to air. For films of 20–150 Å thickness, the oxidation occurred at room temperature in as little as a few seconds. It is believed that the thinner films are oxidized by removing oxygen from the underlying silicon dioxide. However, for the thicker films, this should be self-limiting. This general effect of rapid film oxidation is inconsistent with reports of thin, evaporated 4-nm-thick Ti features, which were apparently stable in air.[16] Sputter-deposited Ti films (on silica) of similar thicknesses

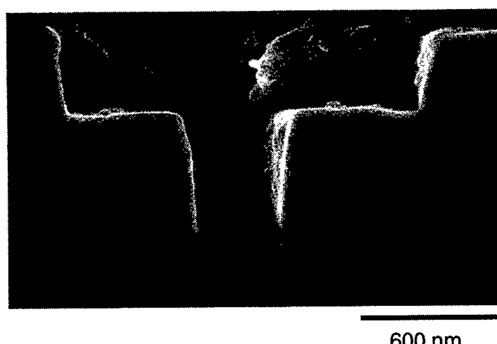

FIG. 3. ALD deposition of Ta film, 400 Å thick (240 cycles) in dual-damascene feature. Deposition temperature=250 °C.

to the current study were observed to oxidize in minutes to an hour. The rapid oxidation of the ALD Ti films in this study suggests that they may be porous or at least underdense. RBS analysis of the oxidized films indicated nearly stoichiometric TiO_2 with Cl impurities in the low percentage range. The optical index was lower than bulk value by 10%–15% for various sample thicknesses. Preliminary results of ALD Ti films deposited on Cu surfaces at 25 °C show much more stable, metallic films. These films appear to be amorphous with XRD.

The conformality of the Ta films when deposited at 250 °C into trenches and vias etched into SiO_2 is good, and an example is shown for a dual damascene structure (trench plus via) in Fig. 3. In this case, the film thickness is quite large (400 Å) such that the film could be easily observed using scanning electron microscopy (SEM). The resultant deposition produced a rather rough surface which is not seen with thinner depositions. The degree of conformality is high, and approached 100% for samples of aspect ratio of up to 6:1 at temperatures at least as low as 250 °C.

IV. DISCUSSION

Atomic layer deposition of Ta and/or Ti (and their nitrides) solves a number of fundamental problems with the future evolution of semiconductor interconnect features. ALD is intrinsically conformal, at least up to 6:1 aspect ratio (AR), and this is a significant advantage over the widely used PVD-based processes. The conformality of directional PVD processes results in an in-feature step coverage for a via which scales as roughly 1/(4 AR). For 5:1 features, therefore, the best step coverage is in the 5%–7% range, which unfortunately then requires thick field deposits for adequate sidewall coverage. For some materials, such as Cu, which has moderate surface mobility at typical process temperatures (25–100 °C), this leads to agglomeration and incomplete surface coverage in deep features, particularly on the sidewall films.

The observed step coverage for Ta at modest temperatures (250 °C) is quite adequate for the 0.1 μm, roughly 1 GHz microprocessor generation, and continuing work is underway to extend these measurements well below 0.1 μm via dimensions as well as to lower deposition temperatures.

Another intrinsic advantage of Ta, Ti, or most halogen-based ALD is the low temperature of operation, particularly compared to similar CVD processes. This is a process and cost advantage since it shortens the preheating and cool-down times, and more importantly facilitates the use of the polymer-based low-*k* dielectrics, many of which are limited in temperature to 200 °C or less.

The apparently amorphous nature of the deposited Ta films is intriguing for their application as diffusion barriers. In most barriers used in semiconductor manufacturing, the primary interdiffusion pathway is by means of grain boundary diffusion or defect diffusion, rather than bulk diffusion through the liner material. While it is expected that amorphous liners will nominally be superior to polycrystalline materials because of the lack of grain boundaries, diffusion through a less-than-100% dense material may occur at a more rapid pace than through a crystallized bulk material. Work is underway to integrate the ALD Ta system with a second, *in situ* deposition for realistic diffusion barrier tests.

The most important advantage, though, of this ALD approach for liners such as Ta or Ti or their nitrides is the atomic-scale control of the deposition. Films can be deposited in units of a fraction of a monolayer under very controlled circumstances. As an example of the scope of this topic, consider a via with a diameter of 1000 Å operating at a frequency of 1 GHz. The best case electrically for this via is if it is 100% Cu atoms, large-grained or single crystal with no impurities, and with no liners or diffusion barriers at its outer perimeter. If a single atomic layer of Ta is used as a liner in this via or a 1:1 aspect ratio line, the total number of Cu atoms in the via is reduced by 1.2%, resulting in roughly a 1% increase in the electrical resistance. If, in the ideal embodiment, circuit speed is limited by the RC time constant of the interconnect structure, this single layer of Ta results in a measureable reduction in operating frequency. Each additional Ta layer displaces another 1% of the Cu, approximately, and results in increased via or line resistance and reduced operating frequency. Therefore, it is imperative for future interconnect generations that the liner be an absolute minimum thickness.

It is expected that future liner technologies in the sub-0.1 μm generation will be intrinsically atomic in nature, and may consist of amorphous 1–3-atom-thick sequential layers of the appropriate metals, nitrides, and perhaps even oxides of materials such as Ta, Ti, and W. With a total thickness of no more than 15–20 Å (6–8 atoms thick), it is not clear that these layers will have any appreciable conductivity in the classic sense, which allows the usage of materials such as oxides which are not appropriate for the thicker barriers and liners used in the >0.13 μm generations. This may also mean, however, that any current-carrying capability of the liner will be minimal. It is likely, however, that an appropriate technique may be needed, in this case, which eliminates the liner from the contact point at the bottom of a via to reduce the resistance of the interconnection or to reduce potential voids due to interface-related electromigration effects that can occur with a Cu diffusion barrier.

[1] S. M. Rossnagel, D. Mikalsen, H. Kinoshita, and J. Cuomo, J. Vac. Sci. Technol. A **9**, 261 (1991).
[2] R. Joshi and S. Brodsky, Proceedings of the 9th International VLSI Multilevel Interconnection Conference, Santa Clara, CA, 1992, p. 253.
[3] S. M. Rossnagel and J. Hopwood, Appl. Phys. Lett. **63**, 3285 (1993).
[4] S. M. Rossnagel and J. Hopwood, J. Vac. Sci. Technol. B **12**, 449 (1994).
[5] M. Dickson, F. Chian, and J. Hopwood, J. Vac. Sci. Technol. A **15**, 340 (1997).
[6] C. A. Nichols, S. M. Rossnagel, and S. Hamaguchi, J. Vac. Sci. Technol. B **14**, 3270 (1996).
[7] T. Suntola, Thin Solid Films **216**, 84 (1992).
[8] M. Ritala, Appl. Surf. Sci. **112**, 223 (1997).
[9] M. Ritala, M. Leskela, E. Rauhala, and P. Haussalo, J. Electrochem. Soc. **142**, 2731 (1995).
[10] T. Suntola and J. Hyarinen, Annu. Rev. Sci. **15**, 177 (1985).
[11] C. Tran, R. Masut, J. Brebner, and M. Jouanne, J. Appl. Phys. **75**, 2398 (1994).
[12] J. Aarik, A. Aidla, K. Kukli, and T. Uustare, J. Cryst. Growth **144**, 116 (1994); K. Kukli, J. Aarik, A. Aidla, O. Kohan, T. Uustare, and V. Sammelselg, Thin Solid Films **260**, 135 (1995).
[13] J. W. Klauss, S. J. Ferro, and S. M. George, paper TF-TuM6, presented at the American Vacuum Society Conference, Seattle WA, October 1999 (unpublished).
[14] P. Martennson and J.-O. Carlson, Chem. Vap. Deposition **3**, 45 (1997); P. Martennson, K. Larsson, and J.-O. Carlson, Appl. Surf. Sci. **148**, 9 (1999).
[15] M. Nicolet (private communication).
[16] R. Martel, T. Schmidt, R. L. Sandstrom, and Ph. Avouris, J. Vac. Sci. Technol. A **17**, 1451 (1999).

Observation of fine structures of nanodomains in donor-modified $Pb(Zr,Ti)O_3$ ferroelectrics

Qi Tan and Jianxing Li
Honeywell Electronic Materials, 15128 E. Euclid Avenue, Spokane, Washington 99216

(Received 3 January 2000; accepted 5 May 2000)

A nanodomain morphology comprising fine structures of less than 5 nm spacing was observed in oxygen deficient lead zirconate titanates modified by La, Ca, and Sr. Oxidation of samples can eliminate the fine structures and facilitate polarization switching. Although grain growth after high temperature annealing results in normal domain morphology and complete polarization switching, irregular and fragmented domains remain. These fine domain structures were explained in terms of local polarization pinning due to oxygen vacancies and antisite substitutents. © *2000 American Vacuum Society.* [S0734-211X(00)04704-1]

Ferroelectric ordering refers to the establishment of a long-range dipole array within a crystal. In materials with displacive transitions such as lead zirconate titanates (PZTs), the ordering is measured by the degree of displacement of certain ions or ionic groups, i.e., the long-range ordering of induced dipoles. Dipolar interactions are long-range Coulombic forces compared with short-range forces (chemical binding, repulsion and van der Waals), which play an important role in ferroelectric transitions. The description of ferroelectric order is usually correlated with domain structural development. Conventionally, normal micron-sized domains are typical of long-range ferroelectric order. When increasing temperature, pressure, or concentration of cation substituents in PZT, domain sizes are decreased typical of a reduced ferroelectric order. For example, higher valent La^{3+} substitutions result in the destruction of domain structures and the stabilization of tweedlike and nanodomain states in PZTs.[1,2] Direct observation of polar nanodomains by transmission electron microscopy (TEM)[3] revealed that these are the small areas of <50 nm having a uniform spontaneous polarization. A large amount of investigation has demonstrated that A- and B-site cation substitution have significant influences on the domain characteristics and properties of ABO_3 structured PZTs. However, the effect of oxygen vacancies on domain structures of fixed PZT compositions was not specifically studied although oxygen vacancies were addressed in lower-valent modified hard PZTs. As a matter of fact, oxygen vacancies are deleterious to ferroelectric properties, particularly in thin film devices because oxygen vacancies were found to cause fatigue and imprint problems.[4–6] Oxygen vacancies can be generated via several possible causes: (1) the presence of lower-valent impurities in raw materials, (2) low oxygen pressure and improper compositional control during thin film deposition, (3) lower-valent ''acceptor'' modification which requires charge compensation, (4) smaller higher-valent ''donor'' modification which results in antisite occupation, and (5) sample processing in reduced oxygen environment.

Oxygen vacancies can be eliminated by using high purity raw materials, donor dopants, and appropriate deposition conditions. For example, a dramatic reduction of imprint was observed in PZT thin film capacitors although remanent polarization was decreased with increasing Nb content.[7] Using isovalent cations such as Ca^{2+} and Sr^{2+} also enhances the resistance to retention and imprint in lanthanum-modified PZT (PLZT) thin film devices.[8,9] However, a remaining problem that was never touched in ferroelectric materials research is the influence of oxygen vacancies generated by vacuum consolidation of donor-doped PZT. The effect of their distribution and the interaction with polarization or domains are an unknown puzzle. Understanding their effect on domain structure-property relations would provide valuable information for ferroelectric property enhancement. In this communication, oxygen vacancies were introduced intentionally by vacuum consolidation of PLZT samples in order to trace the effect of their existence and interaction with polarization. Domain structure-ferroelectric property relationship was studied by performing annealing treatments. It was revealed that penetration of oxygen into PLZT plays dominant role in controlling ferroelectric performance, while further grain growth after annealing at higher temperatures could enhance polarization and ferroelectric properties.

Specimens in these studies are isovalent Ca and Sr modified $(Pb_{0.91}La_{0.02}M_{0.07})(Zr_{0.4}Ti_{0.6})O_3$ base compositions, designated as PLMZT 2/7/40/60, where M refers to Ca and Sr. Excess Pb was added in order to compensate for Pb loss during consolidation. Dense specimens were obtained after vacuum hot pressing at certain high temperatures (proprietary conditions), giving oxygen deficient compositions. Reoxidation of samples was performed in air at 700 °C for 10 h, which was found to incorporate saturated oxygen.[10] Grain growth was induced by annealing at various temperatures for 2 h in air. The P–E behavior was characterized with a Radiant Technology RT 6000HVS system. Grain sizes were measured using scanning electron microscopy (LEO 4300). TEM studies were done on a EDS-attached Phillips EM-420 microscope operating at an accelerating voltage of 120 kV.

Domain structures of vacuum hot-pressed PLMZT 2/7/40/60 were studied using transmission electron microscopy. Figure 1(a) shows a very unusual domain structure in oxygen deficient PLMZT specimens. Normal ferroelectric domains were absent; instead, very dense and irregular domain struc-

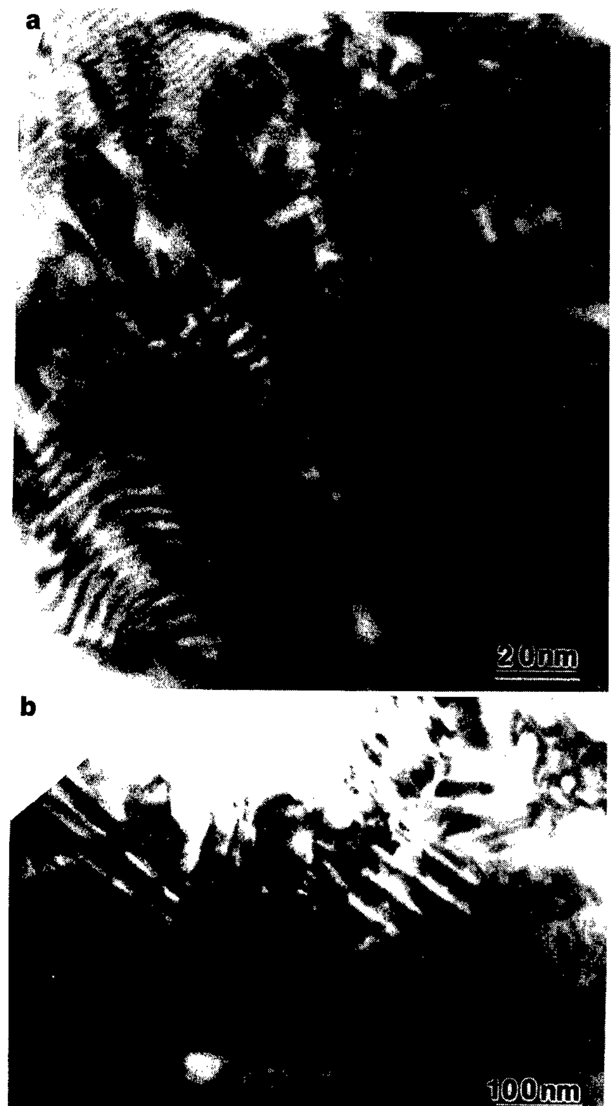

FIG. 1. Bright field image of ferroelectric domains in PLMZT 2/7/40/60. (a) As-hot-pressed and (b) oxidized at 700 °C for 11 h.

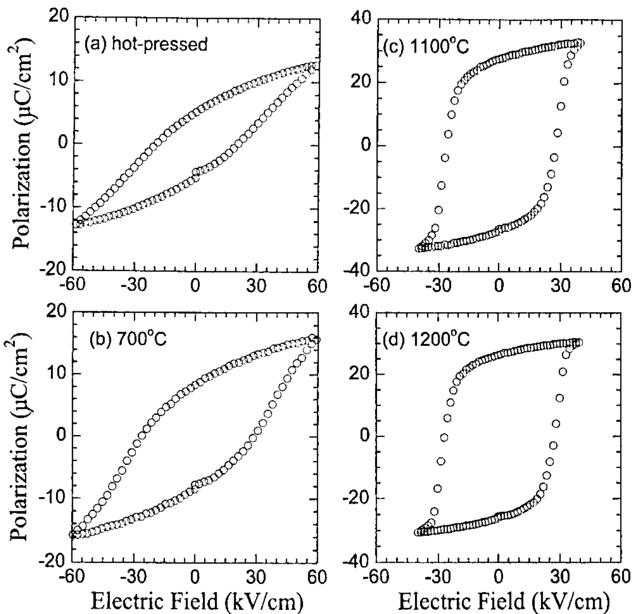

FIG. 2. Room-temperature polarization hystereses after various annealing temperatures. (a) Hot-pressed, (b) 700 °C for 11 h, (c) 1100 °C for 2 h, and (d) 1200 °C for 2 h.

tures were the representative domain morphology. Domain widths are about 2–5 nm and the lengths are about 30–60 nm, indicating a highly anisotropic morphology. These domains were different than conventional equiaxial nanodomains[1,3] that were observed in high La content—PLZTs, lead magnesium niobates (PMN), and lead scandium tantalates (PSTs). Moreover, domains can be viewed as consisting of several different areas. Most of them have closely spaced substructure along certain crystallographic orientations in spite of wavy shape. The substructures in nanodomain areas observed in oxygen deficient PLMZT were not yet observed in other relaxor ferroelectrics. This is related to the interaction between defects and polarization at the atomic scale.

A very interesting phenomenon observed after oxidizing specimens at 700 °C was a pronounced increase in domain scale. However, randomly distributed nanodomain features still remain as shown in Fig. 1(b). The lengths of domains were about 150 nm and their widths were approximately 30 nm now. Comparing with that of oxygen-deficient PLMZT reveals that oxygen vacancies did make things different. Since there is no grain growth at 700 °C, grain sizes do not contribute to the morphological change. It is also known that PZT40/60 modified by lanthanum of up to 12 at. % do not exhibit nanodomains. Consequently, the observed fine structure within nanodomains cannot be attributed to the high-content of higher-valent substituents (La and M).

Figure 2(a) shows the polarization behavior of an oxygen deficient specimen due to vacuum hot pressing. The polarization switching is extremely hard and the remanent polarization is very low. There are two possible reasons for the behavior: one is small grain size due to lower temperature consolidation and the other is oxygen deficiency. Investigations revealed both are playing important roles. After oxidizing at 700 °C for 11 h, the specimen shows an increase in the ease of polarization switching compared with that of the as-hot-pressed specimen, as shown in Fig. 2(b), although very high electric field is still needed for complete polarization switching. This shows the influence of oxygen incorporation. It should be pointed out that the incorporation of oxygen in the annealed specimens was revealed both microscopically using energy dispersive x-ray (EDX) and macroscopically using thermogravimetric method.[10] The pronounced increase in oxygen peak intensity of oxidized specimen (normalized to Pb peak intensity) were observed (data not shown). The polarization characteristics presented above was found to be changed significantly upon annealing at temperatures higher than 800 °C. Figures 2(c) and 2(d) show the polarization–field (P–E) curves corresponding to annealing temperatures of 1100 and 1200 °C, respectively. At 1100 °C, a fully developed hysteresis loop with increased remnant polarization

FIG. 3. Bright field image of ferroelectric domains after annealing at 1100 °C for 2 h.

was observed [Fig. 2(c)]. The coercive field becomes as low as ~30 kV/cm. Further increasing annealing temperature up to 1200 °C does not result in much different polarization hysteresis [Fig. 2(d)]. Average grain size was checked using scanning electron microscopy revealing an increase from ~0.3 μm for the as-hot-pressed specimens to ~1 μm for the specimen annealed at 1100 °C. Such considerable grain growth would release the internal stress field from grain boundaries, and reduce the randomness of overall polarization. Consequently, ease of polarization switching resulted.

Domain structures after annealing at higher temperatures were also observed as shown in Fig. 3. After annealing at 1100 °C, normal domains appear as usually observed. Their lengths and widths grow up to submicrometer and several hundred angstroms, respectively. Clearly, the domain growth is associated with grain growth. However, it was also observed that even within the coarse grain structure there are some areas containing irregular and fragmented domains. This phenomenon further reveals that the irregular domain feature is independent of grain sizes, but rather residual defects may be responsible.

The subdomain structures within nanodomains and their evolution upon oxidation can be understood in terms of local polarization pinning. Vacuum hot-pressing causes oxygen vacancies incorporated into BO_6 octahedra. This structural adjustment results in the change of bonding relationship between octahedra.[11] As a result, long-range-ferroelectric order due to the alignment of dipoles was interrupted. Consequently, finer nanodomain structures and irregularity in domain morphology were resulted and harder polarization switching were observed. Since the number of these oxygen vacancy-acceptor complexes is not sufficient to provide strong pinning, the double-loop-like polarization characteristics as reported earlier by Tan *et al.*[11] were not observed.

After annealing, externally introduced oxygen vacancies were eliminated. The distortion in octahedra, and then, the local polarization pinning, are dramatically decreased. Since A-site substituents have certain occupancy at B-sites due to ionic size consideration according to previous reports,[12,13] it can be conjectured that La, Ca, and Sr cations may have a small amount of antisite occupancy even in fully oxidized specimens. Then, oxygen vacancies are created in order to maintain charge balance. These defect complexes may give rise to local polarization pinning and fragmented domains in some very small area. However, the coexistence of irregular fine domains and normal domains in coarse-grained specimens may degrade ferroelectric properties. Thereby, it is imperative to take some measures to compensate the deleterious contribution of the residual antisite substitutents.

In conclusion, ferroelectric domain structures and polarization behaviors were studied for oxygen deficient and oxidized PLMZT samples. Fine structures characterized by very closely spaced and wavy domain morphology of nanometer size were first observed. Elimination of oxygen vacancies was found to decrease the special domain structure and to increase polarization. Grain growth results in domain growth and fully polarization saturation but does not cause the disappearance of fine nanodomain structures. The introduced oxygen vacancies and antisite occupancy of A-site substituents was suggested to be the cause of fine domain morphology.

The authors would like to thank Tamara White, Tim Scott, Stephen Matthew, Vasanth Mohan in Honeywell Electronic Materials for consolidating samples and technical information. Dr. Z. Xu's consulting work on TEM images is greatly appreciated.

[1]X. H. Dai and D. Viehland, Philos. Mag. B **70**, 33 (1994).
[2]J. F. Li, X. H. Dai, A. Chow, and D. Viehland, J. Mater. Res. **19**, 926 (1995).
[3]C. A. Randall, Ph.D. dissertation, University of Essex, Essex, Colchester, England (1987).
[4]D. M. Smyth, Prog. Solid State Chem. **15**, 145 (1984).
[5]D. Dimos, W. L. Warren, M. B. Sinclair, B. A. Tuttle, and R. W. Schwartz, J. Appl. Phys. **76**, 4305 (1994).
[6]J. Lee, R. Ramesh, V. G. Keramidas, W. L. Warren, G. E. Pike, and J. T. Evans, Jr., Appl. Phys. Lett. **66**, 1337 (1995).
[7]J. T. Evans, Jr. and R. Womack, U.S. Patent No. 5,804,850 (1998).
[8]F. Kulcsar, J. Am. Ceram. Soc. **42**, 49 (1959).
[9]T. D. Hadnagy and T. Davenport, Integr. Ferroelectr. **22**, 183 (1998).
[10]Q. Tan and J. X. Li, J. Am. Ceram. Soc. **83**, 451 (2000).
[11]Q. Tan, Z. Xu, and D. Viehland, J. Mater. Res. **14**, 465 (1999).
[12]P. Gonnard and M. Troccaz, J. Solid State Chem. **23**, 321 (1978).
[13]Q. Tan, Z. Xu, and D. Viehland, Philos. Mag. (in press).

SHOP NOTE

These are "how to do it" papers. They should be written and illustrated so that the reader may easily follow whatever instruction or advice is being given.

Sheet resistance nonuniformity for ionized titanium deposition

Keith A. Ross[a)]
American Microsystems, Inc., Pocatello, Idaho 83204

Peter Thimm
Applied Materials, Lake Oswego, Oregon 97035

(Received 25 February 2000; accepted 19 May 2000)

A combination of recipe power and pressure in an ion metal plasma sputter deposition chamber has reduced average within-wafer sheet resistance nonuniformity approximately 40% to a value of 3.1% ±0.2%. This result was obtained for a new polished target and nonknurled coil assembly operated over one coil life. © *2000 American Vacuum Society.* [S0734-211X(00)06204-1]

I. INTRODUCTION

Ionized physical vapor deposition techniques such as ionized metal plasma (IMP) are becoming critical for achieving sufficient bottom coverage in the high aspect ratio features (>5:1) used in advanced semiconductor devices.[1–5] However, when IMP is tuned for optimal bottom coverage, the deposited film sheet resistance nonuniformity can be higher than that obtained using standard sputter techniques. This value of sheet resistance nonuniformity has been reduced on later version IMP deposition chambers by utilizing modified rf circuitry for the inductively coupled plasma (ICP) coil to achieve sheet resistance nonuniformities of less than 3% at 1 σ for film layers down to 5 nm.[6] However, there are many previously manufactured IMP chambers that would benefit from improved sheet resistance nonuniformity on thicker films. In addition, it has been anecdotally reported that under certain recipe conditions, a transient in sheet resistance nonuniformity can occur over the first 50 μm of deposited material.[7] It is theorized that transport of target material to the ICP coil is enhanced when high-power target conditioning is used. If this deposited titanium (Ti) is more easily sputtered from the coil than the base coil material, low values of film sheet resistance nonuniformity are obtained until this deposited Ti is sputtered away.[7] This nonuniformity then increases to a steady-state value. This article summarizes work done both to decrease the initial transient in sheet resistance nonuniformity and to improve steady-state sheet resistance nonuniformity for thick (~50 nm) films deposited using an Applied Materials Vectra™ IMP Ti deposition chamber.

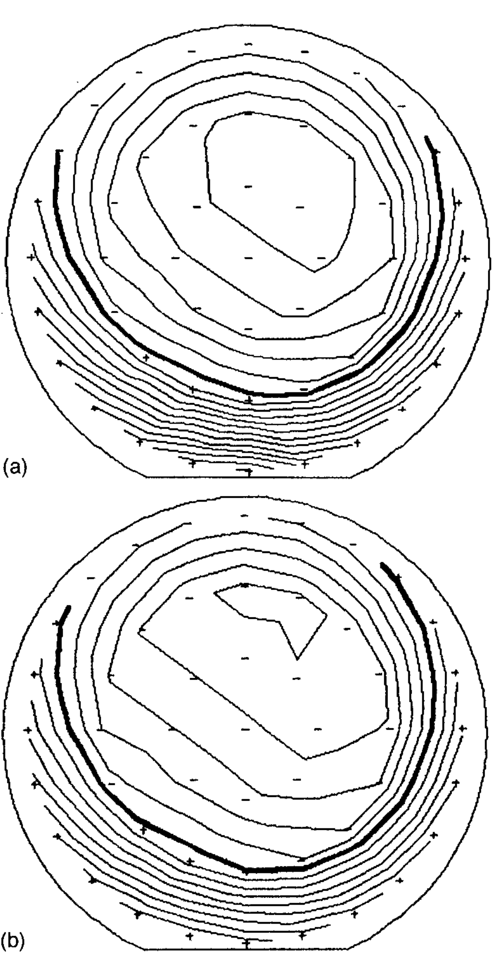

FIG. 1. 49-site polar sheet resistance map for a Ti film using 2.25 kW dc target power and 2.75 kW rf ICP coil power. Wafer bias was approximately 200 W rf and deposition pressure was approximately 21 mTorr. Nonuniformity is approximately 5%, 1σ at (a) 35 kW h and (b) 219 kW h of Ti coil life. The wafer flat corresponds to the region near the coil feedthrough. The contour line interval in the sheet resistance maps is 1%.

II. EXPERIMENT

Since many IMP chambers are used for the deposition of titanium nitride (TiN), a standard Ti ICP coil has a knurled

a)Electronic mail: Keith_Ross@amis.com

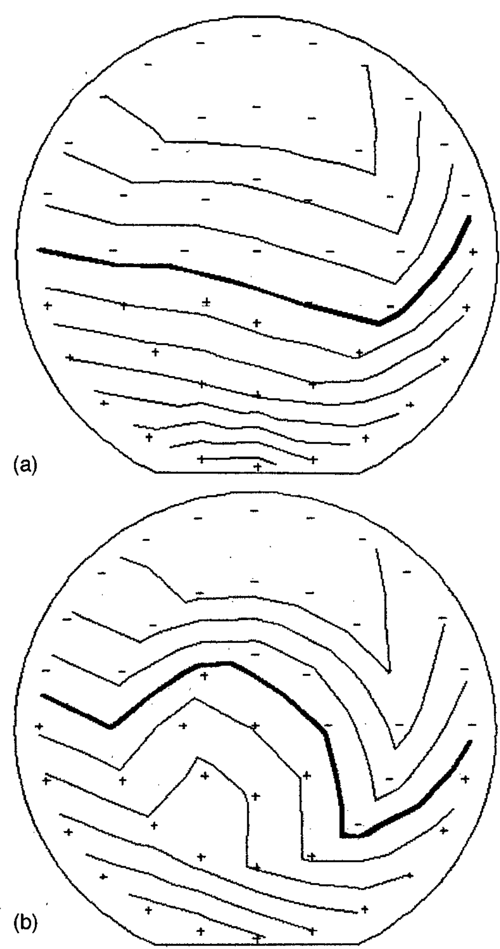

FIG. 2. 49-site polar sheet resistance map for a Ti film using 1.5 kW dc for a polished target and 2.75 kW rf for a nonknurled coil. Wafer bias was approximately 200 W rf and deposition pressure was approximately 13 mTorr. Nonuniformity is approximately 3%, 1σ at (a) 35 kW h and (b) 219 kW h of Ti coil life. The contour line interval in the sheet resistance maps is 1%.

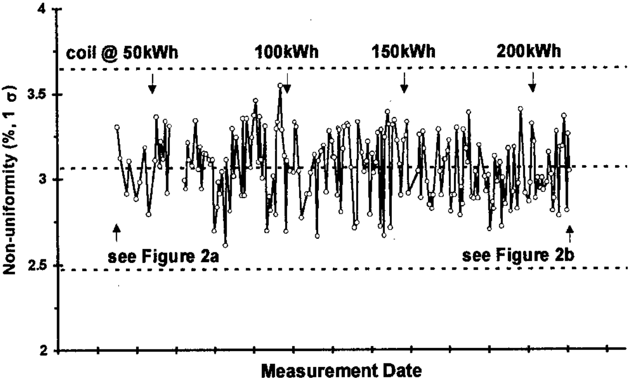

FIG. 3. Ion metal plasma titanium deposition sheet resistance nonuniformity over the period of the first coil life of 219 kW h for approximately 45-nm-thick films. The averages of 49-site polar sheet resistance maps are plotted. Dashed lines represent the calculated overall average value and 3σ process control limits. Average film nonuniformity is $3.1\% \pm 0.2\%$ at 1σ.

(mechanically texturized with a crosshatch pattern) surface to help in the reduction of TiN particulates. Since the application presented is a dedicated Ti deposition, a nonknurled coil was used. Initial testing of IMP Ti nonuniformity used a standard-finish target with standard conditioning which steps target power to 8 kW dc. Films were then deposited with a standard process deposition power of 2.25 kW dc for the target, 2.75 kW rf for the Ti ICP coil, and a deposition pressure of approximately 21 mTorr. The initial film sheet resistance nonuniformity was approximately 2.8%, but after 35 kW h of coil life the nonuniformity increased to approximately 5%. This value is approximately the same at a Ti coil lifetime of 219 kW h, as illustrated in Fig. 1.

In an effort to decrease the transient in-film within-wafer and wafer-to-wafer nonuniformity, a polished Ti target was used. A polished target has a damage layer thickness of 15–20 μm as compared to a standard target damage layer thickness of 20–35 μm.[8] It was anticipated that the smooth and untreated surface finish would reduce burn-in time due to the reduction of surface stress layers that are induced in a standard target manufacturing process. This decreased burn-in requirement was used to reduce Ti deposition from the target onto the coil during initial target and coil conditioning by modification of the conditioning recipe to 2.25 kW dc target power and 2.75 kW rf coil power being applied in six 180 s steps separated by 35 s cooling steps. Deposition pressure for target conditioning was maintained at approximately 21 mTorr. The total time to condition the target was approximately 5.5 h for 15 conditioning wafers. Conditioning was completed before any sheet resistance nonuniformity data were taken. Resultant initial and final film sheet resistance nonuniformity maps for one coil lifetime are illustrated in Fig. 2. Within-wafer sheet resistance nonuniformity data spanning the coil lifetime were taken at regular intervals and are illustrated in Fig. 3. Using a standard [(max−min)/(max+min)] calculation for the data set represented in Fig. 3, wafer-to-wafer sheet resistance nonuniformity was 3.85%.

The recipe used for collection of sheet resistance nonuni-

TABLE I. Approximate deposition rate, bottom coverage, and bulk resistivity for a 100 s Ti deposition for an approximate 450 nm contact with 86° sidewalls and 2.25:1 aspect ratio. Data were taken at approximately 219 kW h of ICP coil life.

Fig.	Deposition power target (kW dc) /coil kW rf)	Deposition pressure (mTorr)	Deposition rate (nm/min)	Bottom coverage (%)	Bulk resistivity ($\mu\Omega$ cm)	Sheet resistance nonuniformity (%, 1σ)
4(a)	2.25 / 2.75	21	70	70	58.7	4.2
4(b)	1.5 / 2.75	21	55	70	59.2	3.5
4(c)	1.5 / 2.75	13	60	50	52.1	2.7

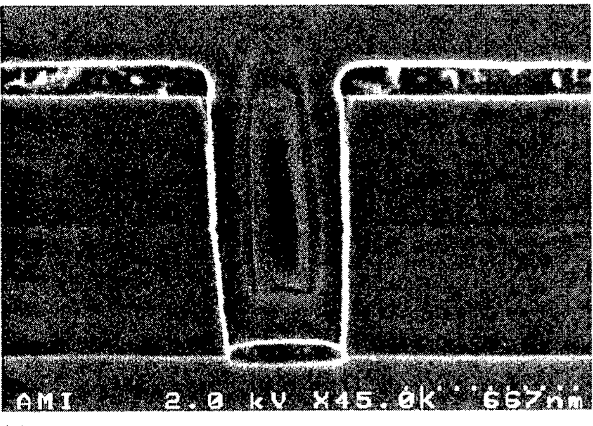

(a)

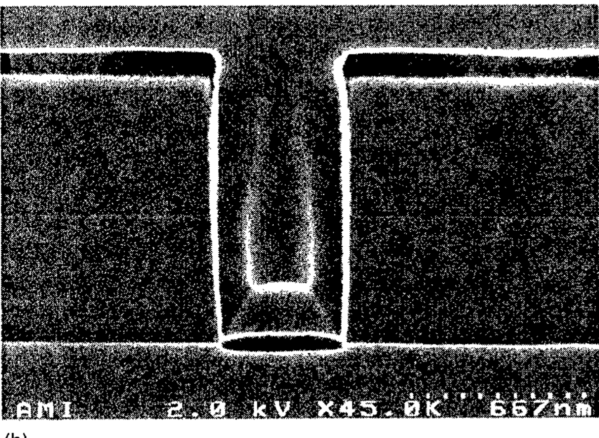

(b)

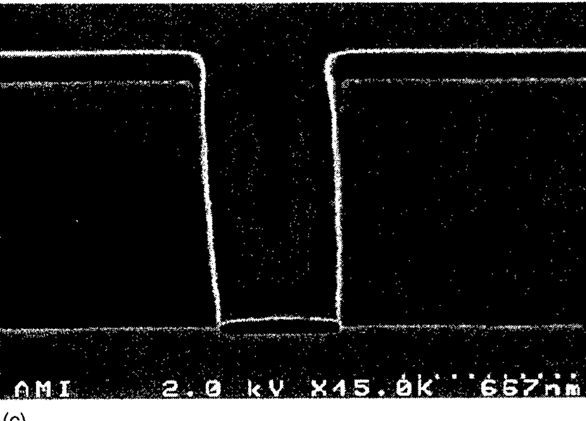

(c)

FIG. 4. Scanning electron microscopy cross sections of approximate 450 nm contacts with 86° sidewalls and 2.25:1 aspect ratio in PETEOS over silicon. Deposition conditions are (a) 2.25 kW dc target power, 2.75 kW rf coil power, and 21 mTorr deposition pressure; (b) 1.5 kW dc target power, 2.75 kW rf coil power, and 21 mTorr deposition pressure; and (c) 1.5 kW dc target power, 2.75 kW rf coil power, and 13 mTorr deposition pressure. Data were taken at approximately 219 kW h of ICP coil life.

formity data given in Figs. 2 and 3 used 1.5 kW target power, 2.75 kW rf coil power, a 200 W rf wafer bias, and a deposition pressure near 13 mTorr. The film thickness for each measurement was approximately 45 nm. Since a decrease in deposition power and pressure usually leads to a decrease in both deposition rate and bottom coverage, approximate deposition rates and resulting bottom coverage were obtained and are illustrated in Fig. 4 and summarized in Table I. These depositions were performed at the end of coil life. The bulk resistivity and sheet resistance nonuniformity in Table I were obtained from film thickness measurements and 49 point polar sheet resistance measurements taken on PETEOS-coated wafers with a blanket Ti deposition at 100 °C pedestal temperature.

III. SUMMARY

Once the Ti that was deposited onto the coil from the target was sputtered away, sheet resistance nonuniformity increased to a steady-state value of approximately 5% for a standard-finished target, standard target conditioning, and standard film deposition parameters. The use of a polished target allowed for the use of low-dc power conditioning that reduced deposition of target material onto the coil. The subsequent use of an almost 1:2 dc:rf power ratio in combination with a relatively low deposition pressure appears to stabilize within-wafer sheet resistance nonuniformity at approximately 3% for a new target and coil throughout coil life. This approximate 40% improvement in nonuniformity comes at the expense of an approximate 15% decrease in deposition rate and an approximate 30% decrease in bottom coverage for the given contact dimensions. This is no surprise since bottom coverage is known to decrease with decreasing deposition pressure and corresponding decreasing metal ionization, and to also decrease with increasing deposition pressure.[9] This degradation in bottom coverage should be more pronounced in higher aspect ratio features. There appears to be an approximate 10% lowering of bulk resistivity of the film deposited with reduced target power and reduced deposition pressure. It is unclear as to whether the lower resistivity is due to an increase in film density or a reduction in argon incorporation.

ACKNOWLEDGMENTS

The authors would like to thank John Forster of Applied Materials and Ray Lappan of American Microsystems for their initial reviews of this manuscript.

[1]S. M. Rossnagel, J. Vac. Sci. Technol. B **16**, 3008 (1998).
[2]G. Zhong and J. Hopwood, J. Vac. Sci. Technol. B **17**, 405 (1999).
[3]Y. Tanaka, E. Kim, J. Forster, and Z. Xu, J. Vac. Sci. Technol. B **17**, 416 (1999).
[4]T. Smy, R. V. Joshi, N. Tait, S. K. Dew, and M. J. Brett, Tech. Dig. Int. Electron Devices Meet., San Francisco, CA, 6–9 December 1998, pp. 311–314.
[5]S. M. Rossnagel, J. Vac. Sci. Technol. B **16**, 2585 (1998).
[6]P. Gopalraja, J. Forster, A. Chan, J. van Gogh, Z. Xu, and F. Chen, *ISSP '99, 16–18 June 1999* (Kanazawa Institute of Technology, Kanazawa, Ishikawa, Japan, 1999), pp. 45–48.
[7]J. Forster, J. van Gogh, and J. Thompson (private communication).
[8]NIMTEC Inc., "Sputter Ready" target data.
[9]R. A. Powell, and S. M. Rossnagel, *PVD For Microelectronics: Sputter Deposition Applied To Semiconductor Manufacturing* (Academic, San Diego, CA, 1999), pp. 250–260.

Time-stability measurement and compensation of a scanning probe microscope instrument

Wenhao Huang[a)]
Open Laboratory of Bond-Selective Chemistry, University of Science and Technology of China, Hefei, Anhui 230026, People's Republic of China and Department of Precision Machinery and Precision Instrumentation, University of Science and Technology of China, Hefei, Anhui 230026, People's Republic of China

Wenwei Wang
Department of Precision Machinery and Precision Instrumentation, University of Science and Technology of China, Hefei, Anhui 230026, People's Republic of China

Andong Xia
Open Laboratory of Bond-Selective Chemistry, University of Science and Technology of China, Hefei, Anhui 230026, People's Republic of China and Department of Precision Machinery and Precision Instrumentation, University of Science and Technology of China, Hefei, Anhui 230026, People's Republic of China

Nong Jin
Department of Precision Machinery and Precision Instrumentation, University of Science and Technology of China, Hefei, Anhui 230026, People's Republic of China

ZhiQiang Hu
Institute of Nuclear Research, Academia Sinica, Shanghai 201800

(Received 27 August 1999; accepted 26 May 2000)

The scanning probe microscope (SPM) is a kind of superprecision instrument with nanometer and even atomic resolution. The time stability of a SPM instrument is an important parameter. We measured the time stability and obtained the drift speed of a commercial SPM instrument quantitatively by using the method of image correlation. Then the drift was fed to the scanning piezotube to compensate. The experiment showed that the drift speed of our instrument was decreased by an order of magnitude during the scanning of 16 images. The possible causes of the drift are also discussed in the article. © *2000 American Vacuum Society.*
[S0734-211X(00)07704-0]

I. INTRODUCTION

Since the invention of the scanning probe microscope (SPM) instruments, their resolution of higher than nanometer scale has attracted scientists greatly. In the view of measurement, it is very important to detect and control the time stability of the instrument quantitatively.[1] Special attention should be paid to these problems during designing and operation of a high temperature SPM.[2,3] Some people have paid attention to the importance of these problems. They usually detected the time stability of the tunnel current (for scanning tunneling microscopy) or the intensity of reflected light from cantilever (for atomic force microscopy) and judged the drift rate of the instrument. However, this drift is only in the vertical direction (z direction). Furthermore, the measuring result mentioned earlier is an average value in a long period (such as an hour), which is also affected by environmental factors. For drift compensation, one method is based on averaging the apparent reciprocal lattice vectors corresponding to consecutive scans obtained in opposite scanning directions,[4] while other are mainly based on matching the materials and dimensions of the SPM elements.[5,6] The online detection and compensation of drift in the horizontal direction has not been reported. To solve this problem, we report an image correlation method to measure and compensate the time stability of a SPM instrument. The experiment showed that the drift speed of our instrument was decreased by an order of magnitude during the scanning of 16 images.

II. PRINCIPLE OF THE IMAGE CORRELATION METHOD (REF. 7)

We assume that the gray signal values of two images are $f(m,n)$ and $g(m+i,n+j)$, respectively, then the correlation coefficient of two images is

$$p(i,j) = \frac{\sum_{m=1}^{M}\sum_{n=1}^{N} f(m,n)g(m+i,n+j)}{[\sum_{m=1}^{M}\sum_{n=1}^{N} f^2(m,n)]^{1/2}[\sum_{m=1}^{M}\sum_{n=1}^{N} g^2(m+i,n+j)]^{1/2}}. \quad (1)$$

If the images are periodical ones, then the correlation function of them is

$$p(i,j) = \sum_{m=1}^{M}\sum_{n=1}^{N} f(m,n)g(m+i,n+j). \quad (2)$$

When $p(i,j)$ is maximum, j and i can be, respectively, regarded as horizontal and vertical drift value of image $g(m+i,n+j)$ with respect to image $f(m,n)$. Whether the sample is periodic or not, we can calculate the values of i and j.

a)Electronic mail: whuang@ustc.edu.cn

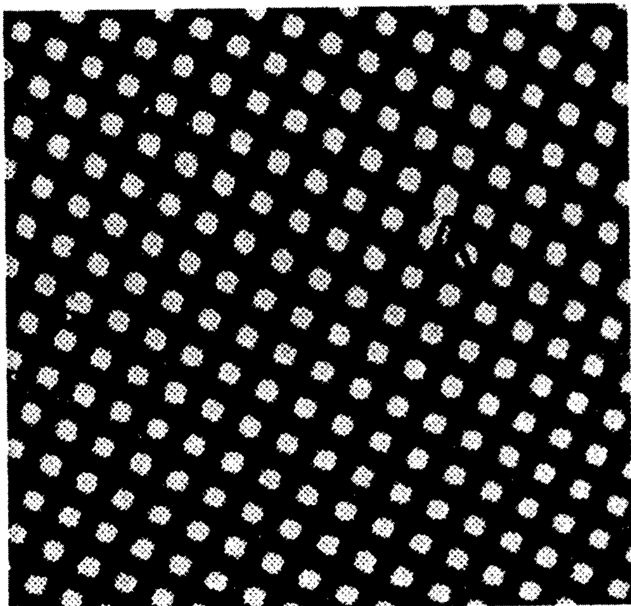

FIG. 1. Surface topography of two-dimensional grating.

III. EXPERIMENT

We did the experiments with a commercial SPM. The sample is a two-dimensional grating which is made by Micro-electronic and Micro-structure Center of France (CNRS) with x, y spacing of 1.3 μm, and a z height of 45 nm.

The topography image of the grating is shown in Fig. 1.

The test mode we used is a tapping mode. After the SPM was on for 2 h, we obtained a series of images f1, f2, ..., f6 continuously. Every image was acquired in 256 s. The scan range is 20 μm×20 μm and the images are shown with 512×512 pixels (about 40 nm per pixel). How can we determine the SPMs drift rate? We usually get the approximate displacement and the direction of drift by watching the movement of point A, but we cannot get the precise drift value of images by this method.

Figure 2 shows the calculated image correlation result between images f1 and f2 (the following unit of this article is pixel if not specified).

The drift value of image f2 with respect to image f1 is

$$\Delta x_1 = -4, \quad \Delta y_1 = -5.$$

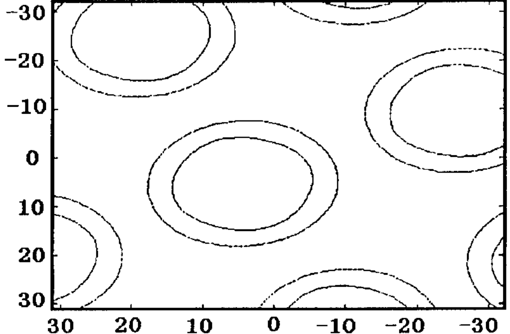

FIG. 2. Contour map of autocorrelation between image f2 and f1.

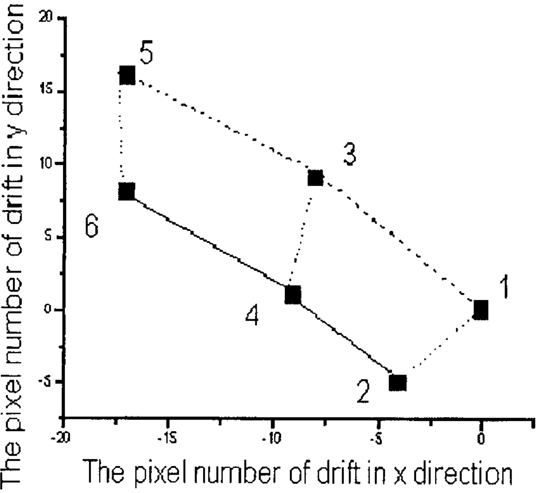

FIG. 3. Drift tendency of the images.

Repeating the process described earlier, we can obtain the drift values of f3, f4, f5, and f6 related to f1. The result is shown in Fig. 3.

In Fig. 3 the scan direction of images f1, f3, f5 is from top to bottom, the scan direction of images f2, f4, f6 is from bottom to top. We can see that the drift of f3 with respect to f1 is almost equal to the drift of f5 with respect to f3, and the drift of f4 with respect to f2 is almost equal to the drift of f6 with respect to f4. However, there is apparently difference in the y direction between the drift of f2, f1 and the drift of f3, f2. We can see the drift, the drifts from f1 to f2, f3 to f4, f5 to f6 are negative, but the drifts from f2 to f3, f4 to f5 is positive. In the x direction, the situation is not the same as that in the y direction, the total drift tendency is much smaller. Figure 4(a) shows the drifts in the x direction. Figure 4(b) shows the drift fluctuation in the y direction. We can see that the drift in the x direction is smaller, around the average value. In the y direction, there is an average tendency with bigger fluctuations, which is related to the scanning directions.

We can see that in the x direction there is an average drift tendency superimposed with small fluctuations. In the y direction, there is also an average drift tendency, but the superimposed fluctuation is obviously bigger than in the x direction. These bigger vibrations are related to the scanning

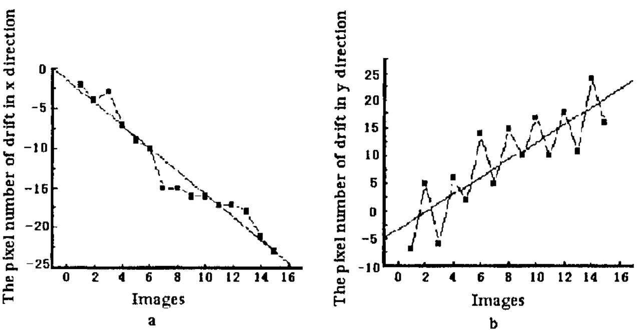

FIG. 4. Drift tendency in the x, y direction.

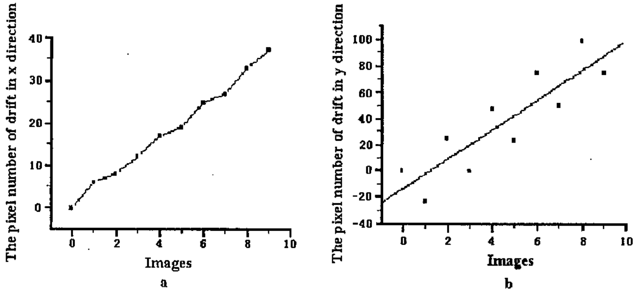

FIG. 5. Drift in the x, y direction before compensation.

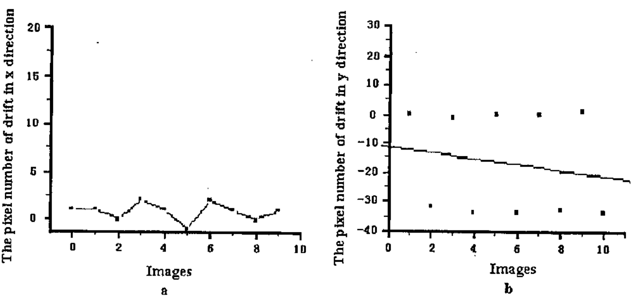

FIG. 7. Drift in the x, y direction after compensation.

directions. In Fig. 4(b), all the images above the average line are from the same y direction (from top to bottom), the images below the average tendency line are from the opposite scanning direction (from bottom to top). This phenomenon is very interesting. We found the same behavior on one homemade SPM. The drifts in the x, y directions are shown in Fig. 5.

One possible explanation is that: the drift of the whole SPM instrument mainly consists of two parts. The first one comes from the thermal effect of the whole system, which corresponds to the average line. The other comes from the hysteresis of the piezoscanner,[8] which corresponds to the superposed fluctuation. In each cycle, the shape of the hysteresis curve is almost the same. In the x direction the piezo scans very quickly, and it is easy to keep the central position. However, in the y direction, it works in half cycle within one image, so the fluctuation will be bigger than in the x direction between the adjacent images. We have not done the experiment to verify the y drift dependence on the speed of the scan, because in the scan manner, the speed of the y scan is far slower than the x scan. However, we believe that if the speed of the y scan can reach the level of the x scan, the drift speed in the y direction will be as small as it is in the x direction.

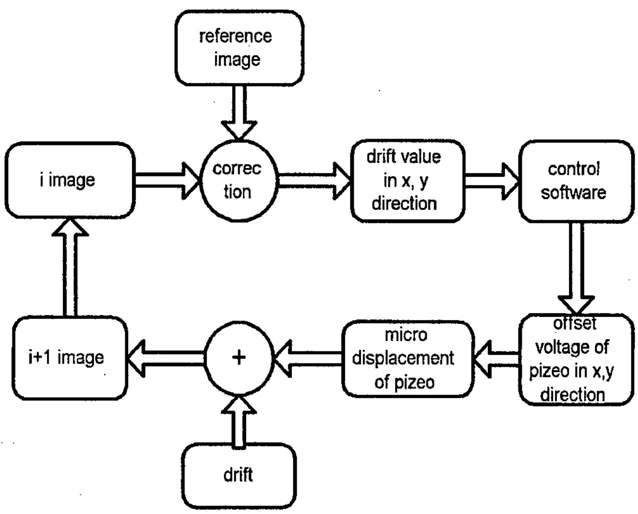

FIG. 6. Principle of real-time drift compensation.

According to the earlier understanding, we arranged the on-line compensation method shown in Fig. 6. Here we chose those images, which were taken all in the same y scanning direction. Comparing each image with the first image (as a reference image) and using the correlation method, we could get the magnitude and direction of the drift. Then they were turned to voltage and fed to the scanner as offset signal respectively before the next image scanning. The drift curves after on-line compensation are shown in Fig. 7. The drift is reduced from 100 pixels in Fig. 5 to 3 pixels in the y direction and from 35 pixels to 3 pixels in the x direction during 10 images.

IV. CONCLUSION

(i) The time stability of a SPM instrument can be measured quantitatively by utilizing the image correlation method.

(ii) The drift of the SPM is strongly related with the scanning direction of the piezoscanner.

(iii) The drift of the SPM consists mainly of two parts: One comes from the thermal effect of the whole system, which corresponds to the average line. The other comes mainly from the hysteresis of the piezoscanner, which causes the superimposed fluctuations on the average line.

(iv) The drift can be reduced greatly using on-line compensation by about an order of magnitude.

ACKNOWLEDGMENTS

This research is supported by National Nature Science Foundation of China. The authors also thank Dr. Z. Z. Wang in CNRS, France for providing the two-dimensional grating.

[1]K. H. Kanazawa *et al.*, J. Vac. Sci. Technol. B **12**, 1681 (1994).
[2]B. Voigtlander, A. Zinner, and T. Weber, Rev. Sci. Instrum. **67**, 2568 (1999).
[3]M. S. Hoogeman *et al.*, Rev. Sci. Instrum. **69**, 2072 (1998).
[4]J. T. Woodward and D. K. Schwartz, J. Vac. Sci. Technol. B **16**, 51 (1998).
[5]D. D. Koleske *et al.*, Rev. Sci. Instrum. **66**, 4566 (1995).
[6]F. Oulevey, G. Gremaud, A. J. Kulik, and B. Guisolan, Rev. Sci. Instrum. **70**, 1889 (1999).
[7]W. Wenwei *et al.*, Proceedings of China-Japan Bilateral Symposium on AME, 1998, pp. 145–148.
[8]J. F. Jorgensen *et al.*, J. Vac. Sci. Technol. B **12**, 1702 (1994).

ERRATA

Erratum: "Ion-etch produced damage on InAs(100) studied through collective-mode electronic Raman scattering" [J. Vac. Sci. Technol. B 18, 144 (2000)]

T. A. Tanzer and P. W. Bohn[a),b)]
Department of Chemistry and Materials Research Laboratory, University of Illinois at Urbana-Champaign, 600 South Mathews Avenue, Urbana, Illinois 61801

I. V. Roshchin and L. H. Greene[a),b)]
Department of Physics and Materials Research Laboratory, University of Illinois at Urbana-Champaign, 1110 West Greet Street, Urbana, Illinois 61801

[S0734-211X(00)07504-1]

In the above paper, L. H. Green should be changed to L. H. Greene.

[a)]Authors to whom correspondence should be addressed.
[b)]Electronic mail: bohn@scs.uiuc.edu; lhg@uiuc.edu

Papers from the 27th Conference on the Physics and Chemistry of Semiconductor Interfaces

16–20 January 2000
Salt Lake City, Utah

Sponsored by
The American Vacuum Society
The Army Research Office
The Office of Naval Research

Editor for the Conference:
J. E. Rowe

Published by the American Vacuum Society through
the American Institute of Physics, New York, 2000

ORGANIZING COMMITTEE

CONFERENCE CHAIR

Chris J. Palmstrom
Univ. Minnesota

PROGRAM COMMITTEE

D. E. Aspnes (North Carolina State Univ.)
L. Cooper (Office of Naval Research)
J. D. Dow (Arizona State Univ.)
R. M. Feenstra (Carnegie Mellon Univ.)
K. L. Kavanagh (Univ. California, San Diego)
G. Lucovsky (North Carolina State Univ.)
J. E. Rowe (Army Research Office)
H. W. M. Salemink (IBM Res. Labs, Zurich)
J. S. Speck (Univ. California, Santa Barbara)
D. J. Wolford (Iowa State Univ.)

CONFERENCE ADMINISTRATION

Carole and John Dow

PREFACE

This volume contains papers presented at the 27th Annual Conference on the Physics and Chemistry of Semiconductor Interfaces (PCSI-27). The Conference was held 16–20 January 2000 at the Salt Lake City Marriott University Park Hotel, Utah. Approximately 96 people attended the conference, which included sessions on Spintronics, Ferromagnet/Semiconductor Heterostructures, Band Alignment Tuning, Insulators, Optical Properties Group III-Nitrides, Schottky Barriers, Epitaxy and Heteroepitaxy, and Novel Techniques. There were 21 invited talks and 60 short oral presentations. All presentations included posters, which were displayed for the full duration of the conference. Time was allotted for extensive viewing of all the posters, which contributed to the workshop atmosphere of the conference.

An informative session was held on Sunday evening on Spintronics, chaired by Jo De Boeck from IMEC, Belgium. The main topic of the session was the incorporation of spin in semiconductors. Keynote speakers at this session were David Awschalom from UC Santa Barbara, Hideo Ohno from Tohoko University, and Jim Allen from UC Santa Barbara. The keynote speakers' and chairman's groups have spearheaded the incorporation of spins in semiconductors. The lively Monday evening session reported on Band Alignment Tuning in Contacts and Heterostructures and included both theory (A. Baldereschi, Ecole Polytechnique Fédérale de Lausanne), and experiment (A. Franciosi, TASC-INFM, Trieste and University of Minnesota) and differing views (M. Moreno, Instituto de Ciencia de Materiales de Madrid and Paul Drude Institut). Other exciting advances reported at the conference include: Epitaxial Oxides on Si (Z. Yu, Motorola), Ferromagnet/Semiconductor Spin Transport (W. Butler, Oak Ridge and J. De Boeck, IMEC), Strain-Induced Self-Organized Nanostructures (G. Bauer, University of Linz), and Piezoelectric effects in Group-III Nitrides (N. Grandjean, CNRS and J. Singh, University of Michigan). All of the presentations were well received and sparked much discussion by the audience which has been a hallmark of the PCSI meetings.

The conference excursion on Tuesday afternoon was to the Alta Ski Resort. Those who participated enjoyed the typical weather of a Scottish ski excursion with wind, hail, and rain. Despite the atypical Utah weather, a wonderful time was had by all. The conference facilities at the Salt Lake City Marriott University Park Hotel were quite suitable for the conference, and many people expressed the opinion that they enjoyed being back at this location again after a one year absence. The conference succeeded through the efforts of many people. We would like to thank particularly the many anonymous reviewers who performed their work carefully and thoroughly, Jack Dow for conference management and Carole Dow for registration management. We also thank Ms. Becky York of the *Journal of Vacuum Science and Technology* and her staff for their help in rapidly processing the manuscript changes and other publication details. Financial support from Larry Cooper of the Office of Naval Research and Jack Rowe of the Army Research Office are gratefully acknowledged. The conference was held under the sponsorship of the American Vacuum Society through the Electronic and Materials Processing Division, the Office of Naval Research, and the Army Research Office.

Jack E. Rowe
Conference Proceedings Editor

Chris J. Palmstrøm
Conference Chairperson

Scanning capacitance microscopy imaging of silicon metal-oxide-semiconductor field effect transistors*

R. N. Kleiman,[a] M. L. O'Malley, F. H. Baumann, J. P. Garno, and G. L. Timp
Bell Laboratories, Lucent Technologies, Murray Hill, New Jersey 07974

(Received 17 January 2000; accepted 31 May 2000)

We have studied cross-sectioned *n*- and *p*-metal-oxide-semiconductor field effect transistors with gate lengths approaching 60 nm using a scanning capacitance microscope (SCM). In a homogeneous semiconductor, the SCM measures the depletion length, determining the dopant concentration. When imaging a real device there is an interaction between the probe tip and the built-in depletion of the *p*-*n* junction. With the help of a device simulator, we can understand the relation between the SCM images and the position of the *p*-*n* junction, making the SCM a quantitative tool for junction delineation and direct measurement of the electrical channel length. © *2000 American Vacuum Society.* [S0734-211X(00)08604-2]

I. INTRODUCTION

With the aggressive scaling of metal-oxide-semiconductor field effect transistors (MOSFETs) approaching gate lengths of <100 nm, the need for direct feedback to process simulation is becoming increasingly important. Scanning capacitance microscopy (SCM) is a promising technique that convincingly provides quantitative information about the junction position in a MOSFET. Consequently, junction depths and effective channel lengths can be measured. While the interpretation of the SCM images is not completely straightforward, with the assistance of process and device simulators we have been able to understand the imaging mechanism in more detail in the vicinity of the junctions, which is the crucial region where quantitative understanding is essential. This understanding allows us, in principle, to determine the entire dopant profile of the device, but it also allows us to develop a simple method for using the SCM to determine junction positions. While the entire dopant profile is unarguably valuable, a simple method for junction profiling addresses many of the crucial needs for device design.

At the same time, the aggressive scaling of MOSFET dimensions places a high demand for steady improvements on the spatial resolution needed for characterization tools. We have attempted to understand the limits to the spatial resolution with SCM, theoretically with simulations, and experimentally by working with smaller probe tips. This has provided us with resolution suitable for sub 100 nm devices.

II. PARALLEL PLATE MOS SIMULATIONS

There has been considerable effort to model the imaging mechanism with the SCM.[1,2] To introduce the technique we first consider the simplest possible geometry, that of the parallel plate capacitor (see Fig. 1). The results for the capacitance, C, as a function of voltage, V, oxide thickness, t_{ox}, and dopant concentration (assumed uniform), n, are well known[3] and will not be repeated here. For a variety of reasons it is more useful to measure dC/dV rather than just C. As a result one parameter is lost, but that is unavailable experimentally anyway due to the extremely low value of the measured capacitance relative to the ambient stray values. For the MOS capacitor there is a peak in dC/dV, which is positive for n-type materials and negative for p-type materials. The peak value of dC/dV is shown in Fig. 2 showing good sensitivity to dopant concentration in the relevant range for modern devices.

III. MEASUREMENT TECHNIQUE

We have used a commercial (Digital Instruments) SCM to obtain the images presented in this investigation. The SCM consists of a contact-mode atomic force microscope with a 915 MHz tuned circuit coupled to the tip-sample capacitance and is configured by a modulation technique to measure dC/dV. Modifications have been made such that both the magnitude and sign of the dC/dV signal are reflected in the data. This is essential to the ability to perceive the difference between n-type and p-type doped regions.

The semiconductor device samples have been cross sectioned using standard techniques, finishing with a colloidal silica emulsion.

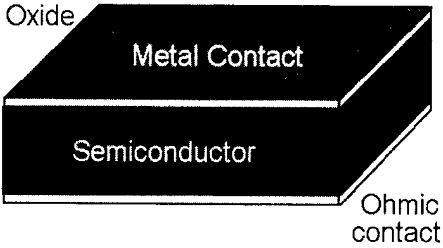

FIG. 1. Device geometry for parallel plate capacitor MOS simulations.

*No proof corrections received from author prior to publication.
[a]Electronic mail: Rafi@lucent.com

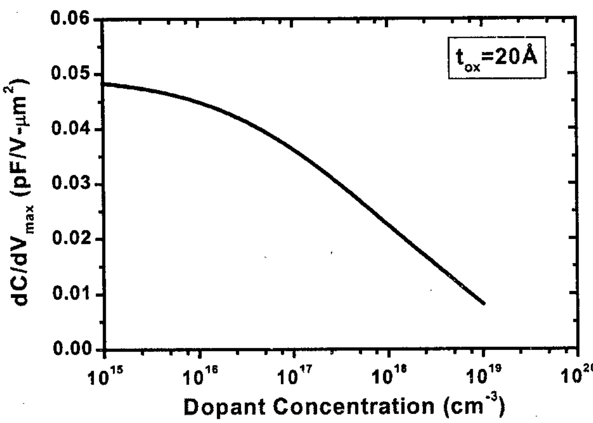

FIG. 2. Calculated peak dC/dV value for a 20-Å-thick SiO_2 dielectric on a silicon substrate of given concentration.

IV. SCM RESULTS ON 0.35 μm PROCESS *n*-MOS DEVICES

We began our investigations by studying a relatively large *n*-MOSFET manufactured in 0.35 μm technology. A typical SCM image of this device is shown in Fig. 3. It clearly shows the source and drain regions, their heavily doped parts with $dC/dV \sim 0$, and their more lightly doped parts in a magenta color. The gate and the insulating region above it both have $dC/dV \sim 0$, the former because it is heavily doped and the latter because it has no carriers to deplete. The SCM image shows excellent contrast between the *n*- and *p*-type regions, clearly delineating the boundary between them, here shown in green and having $dC/dV=0$. The dimensions of the junction depths and of the effective channel length can be easily measured and are in good agreement with expectations.

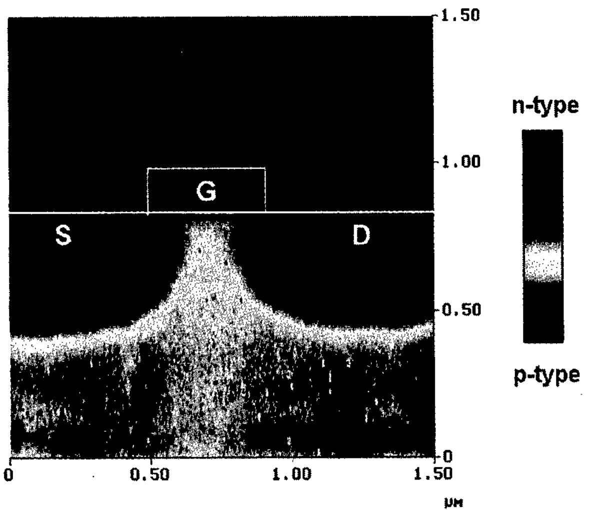

FIG. 3. SCM image of a 0.35 μm process *n*-MOSFET. The source, drain, and gate are labeled. The red/yellow regions are *p* type, the magenta/black regions are *n* type, and the green region corresponds to $dC/dV=0$. The gate and the heavily doped parts of the source and drain have $dC/dV \sim 0$. The apparent junction position is the boundary where $dC/dV=0$.

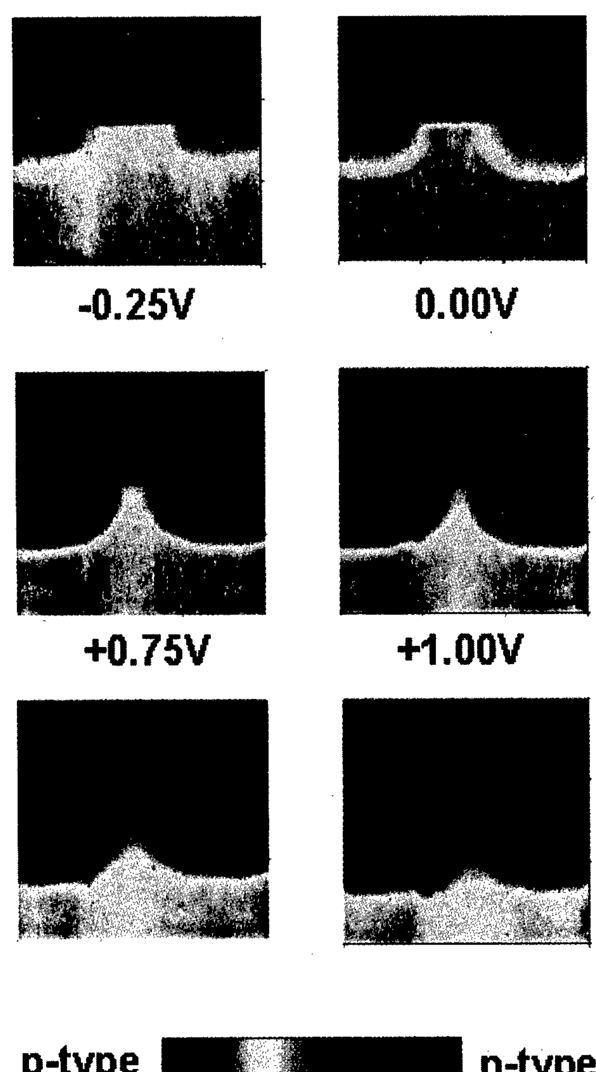

FIG. 4. SCM images of a 0.35 μm process *n*-MOSFET with changing voltage V_B between the tip and the sample. The apparent junction position ($dC/dV=0$) moves significantly with V_B due to the interaction between the tip and the built-in depletion region of the device. The upper portions of each image have $dC/dV=0$, since that region is insulating. When $V_B=+1.5$ V the *p*-*n* junctions have moved to pinch off the channel. When $V_B=-0.75$ V the junctions have moved to meet the heaviest parts of the source/drain implants. At intermediate voltages the junction sits beneath the gate.

However, when we change the voltage between the probe tip and the sample (all of the transistor leads are tied to each other and to the ohmic back contact) we see that the interpretation of the images is considerably more complicated than previously expected (see Fig. 4). The images change in such a way that the apparent *pn* junction (where $dC/dV=0$) moves with bias voltage, and consequently the sign of dC/dV changes in the active regions of the device. Clearly, for the relevant part of devices, SCM cannot be thought of as a simple dopant profiler, where the dopant concentration can be determined by a calibration such as shown in Fig. 2 (modified for the realistic tip geometry). In order to use SCM

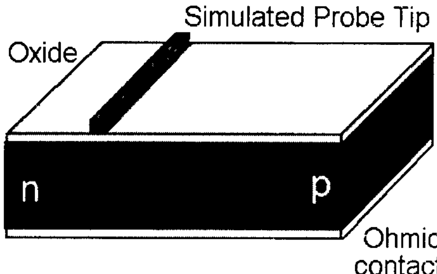

FIG. 5. Device geometry for $2d$ simulations across a pn junction. The probe tip is chosen to be 100 Å wide and infinitely long in our simulations. While this is far from a realistic tip shape, it is sufficient to introduce the new length scale of the tip diameter.

as a quantitative tool we need to understand the change of the images with applied bias voltage.

V. 1*d* MOS SIMULATIONS

The simulated dopant profiles were generated using the process simulator PROPHET that creates a $2d$ doping profile with the subtleties of a fabricated pn junction. The electrostatic state of the system, including the carrier distributions, the potential distribution, as well as C and dC/dV were calculated using PADRE. PADRE simulates semiconductor device behavior, considering both minority and majority carriers and all relevant semiconductor physics while solving Poisson's equation, the continuity, and energy balance equations for the relevant geometry.

While our simulations do not use a realistic tip shape, we believe that they capture the essential device physics to understand the SCM imaging. The geometry we have chosen (see Figs. 5 and 8) introduces the length scale of the tip radius, which must be small compared to typical device dimensions. A $3d$ simulator is only required for device regions with high radius of curvature.

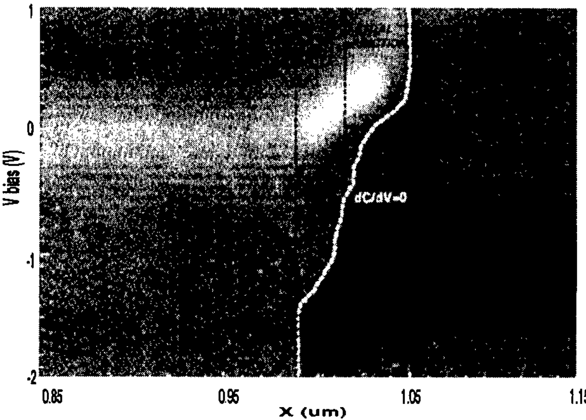

FIG. 6. dC/dV plotted vs electrode position, x, and bias voltage, V_B. The physical p-n junction is at $x=1.015\,\mu$m. The substrate is p type with $n=5\times10^{17}/\text{cm}^3$, while the implant side is n type with $n=3\times10^{18}/\text{cm}^3$. The light region corresponds to $dC/dV>0$, while the dark region corresponds to $dC/dV<0$. The apparent p-n junction where $dC/dV=0$ is the nearly vertical contour separating the light and dark regions. The voltage scale is shifted from the experimental case, due to the work functions of the tip and the bottom electrode.

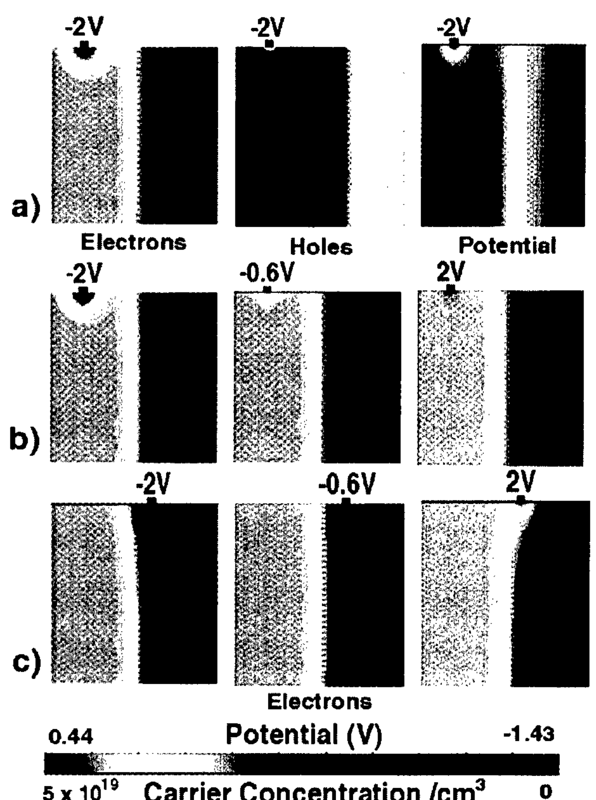

FIG. 7. Simulation data for a pn junction. (a) Electrode placed over the n-type region: at -2 V the electrons under the electrode are depleted, the holes are accumulated, and there is a potential drop across the depletion region. (b) Electrode placed over the n-type region: the electron concentration changes as the electrode bias is changed from -2 V to 2 V. (c) Electrode placed over the depletion region: the real position of the pn junction moves as the electrode bias is changed from -2 V to 2 V.

A. *p-n* junction results

Our simulation results[4] are shown in Fig. 6 for a particular pn junction profile. It clearly simulates the movement of the apparent pn junction with changing bias voltage. Outside of the junction regions we see simple peaks in dC/dV as ex-

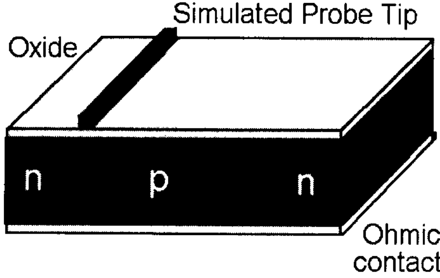

FIG. 8. Device geometry for $1d$ simulations across an n-p-n junction. This geometry is suitable to study the dC/dV response in the channel region. As the junctions get close to one another this simulation geometry is required to study the interaction between the junctions.

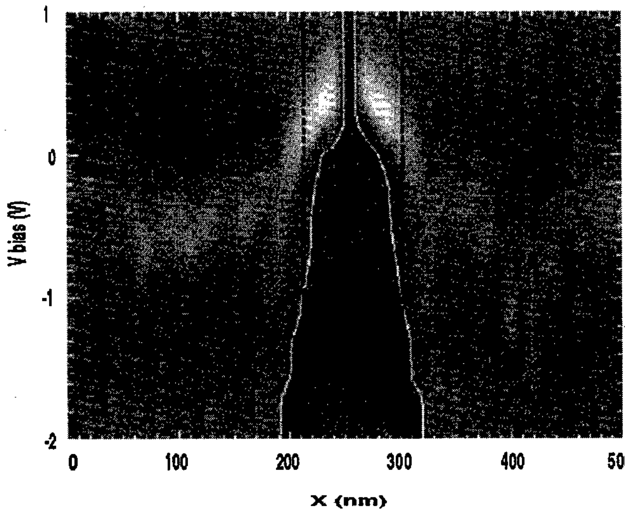

FIG. 9. dC/dV vs electrode position, x, and bias voltage, V_B. The substrate doping is $5\times10^{17}/cm^3$ and the source/drain doping is $2\times10^{19}/cm^3$. The effective channel length, $L_0\sim90$ nm. The p-n junctions are shown as dotted red lines. The light region corresponds to $dC/dV>0$, while the dark region corresponds to $dC/dV<0$. The apparent p-n junctions, where $dC/dV=0$, are the white contours lines. The apparent channel length, L^*, is the spacing between those two lines and changes with V_B.

pected from parallel plate results. In the junction region the sign of dC/dV changes with voltage as observed experimentally.

B. Physical significance of results

To better understand the physical significance of our results, we investigated the carrier distributions at various points of Fig. 6 using our device simulator.[5] Typical results are shown in Fig. 7. Figure 7(c) shows clearly that the junction position is actually moved by the tip, which can easily sweep electrons or holes into the depletion region of the device. However, when the tip voltage is mid band the junction is unperturbed. Note also that in Fig. 6 the $dC/dV=0$ boundary intersects the actual junction position (set in the simulation) when the voltage is roughly midway between the peaks in dC/dV outside of the junction region. This suggests a simple method for correct junction delineation with the SCM: set the voltage midway between the dC/dV peaks in the homogeneous regions (preferably regions with the same concentration), and the resulting $dC/dV=0$ boundary is a good approximation to the electrical junction position.

C. *n-p-n* junction results

Figure 9 shows simulations of an n-p-n structure. These simulations form the quantitative basis for using the SCM for the direct measurement of the effective channel length of a MOSFET. As with the pn junction the correct choice of bias voltage is crucial.[6]

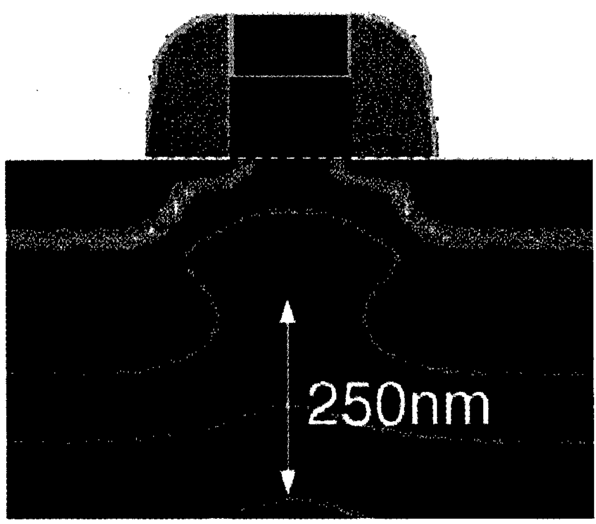

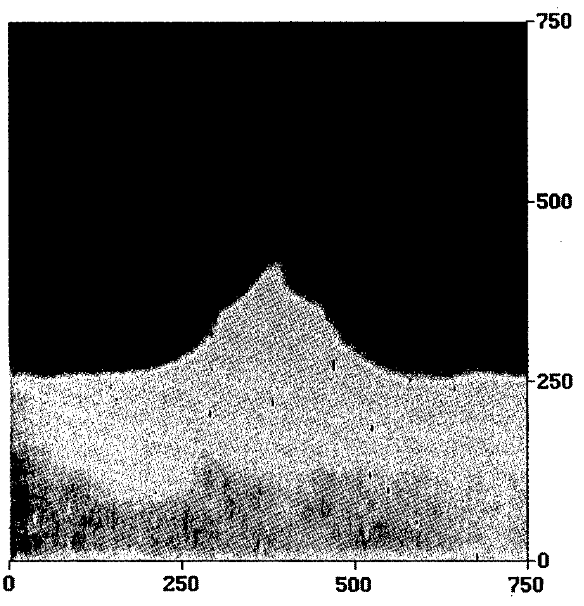

FIG. 10. PROPHET process simulation of the intended doping profile of a 0.15 μm gate length n-MOSFET and a SCM image of the same device at a representative bias voltage. The device is fabricated with an HDD and LLD, whose features are easily observed in the SCM image. The spacing between the junctions at the semiconductor surface is ≈0.12 μm.

VI. SCM RESULTS ON 60 nm PROCESS CMOS DEVICES

Figures 10 and 11 show n-MOS and p-MOS transistors fabricated as part of an effort to understand the limits to conventional complementary metal-oxide-semiconductor.[7] Figure 10 shows nice agreement with process simulation for an n-MOSFET. We investigated a series of p-MOSFETs and the results are shown in Fig. 12. The measurement of the

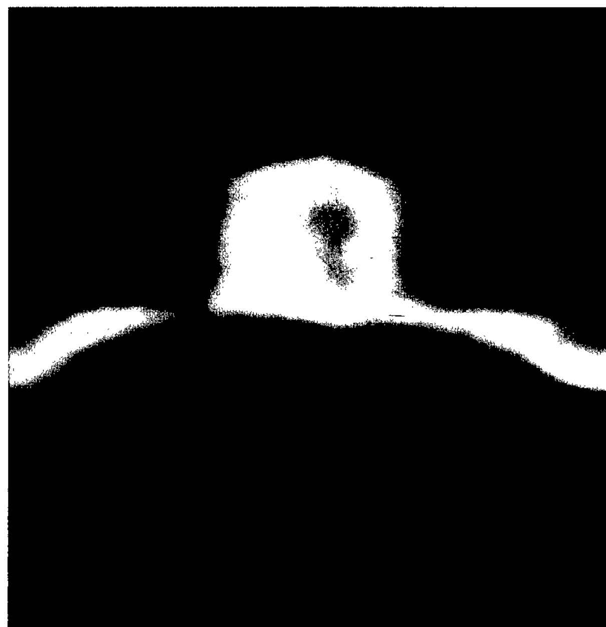

FIG. 11. SCM image of a *p*-MOSFET with a gate length of 80 nm. The image is 400×400 nm. The shallow HDDs and ultrashallow LDDs are easily observable and measurable from these images. The effective channel length is extremely narrow ~35 nm, demonstrating the high spatial resolution attainable.

minimum possible gate length (~53 nm) shows the clear benefit of the direct measurement of the effective channel length using SCM.

VII. ULTIMATE SPATIAL RESOLUTION WITH THE SCM

We have modeled the SCM response for *n*-*p*-*n* structures with varying gate lengths.[6] We find that there is no intrinsic

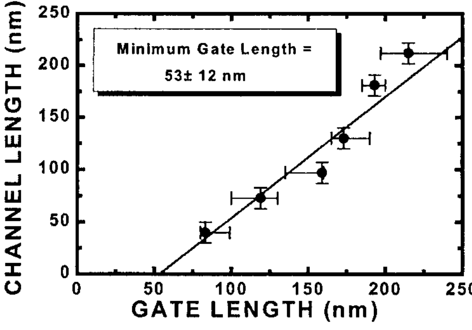

FIG. 12. Effective channel length as determined from SCM imaging, plotted vs gate length as determined from scanning electron microscopy. Studying an array of different gate lengths improves the statistics in determining the minimum attainable gate length. Our measurements show that with the particular *p*-MOS process used the minimum attainable gate length is ~53 nm.

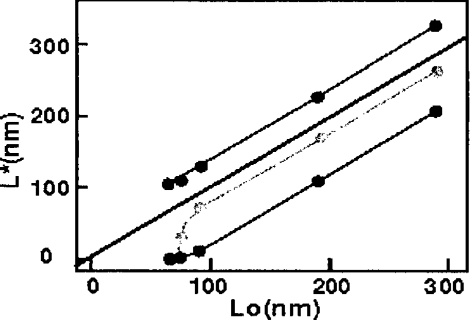

FIG. 13. Apparent channel length, L^*, vs effective channel length, L_0, for different choices of V_B. With $V_B = 1.0$ V (lower), $L^* < L_0$ and the channel pinches off at 80 nm. With $V_B = -0.5$ V (middle), L^* is slightly below L_0 due to tip broadening, but continues to track L_0 down to 80 nm. With $V_B = -2.0$ V (upper), $L^* > L_0$, but the channel structure is washed out.

limit to resolving the channel in a realistic MOSFET structure. Figure 13 shows that L_0 as measured by SCM is reliable until the two depletion boundaries meet. However, sufficiently sharp probe tips must be used to achieve the ultimate resolution.

VIII. CONCLUSIONS

We have shown experimentally that the SCM does not work as a simple dopant profiler in regions of a semiconductor device with *pn* junctions. Nevertheless, our simulation work has given a clear understanding of the interaction between the probe tip and the built-in depletion of the junction region. This forms the quantitative basis for using the SCM to determine junction positions and to directly measure the effective channel length of a device. It has also led us to a simple method for implementing the SCM to measure junction positions.

We have used the SCM to study sub 100 nm state-of-the-art MOSFETs, and have been able to achieve sufficient spatial resolution to study the smallest fabricated devices. We have found from simulations that there is no intrinsic resolution limit when studying MOSFETs, but experimentally this places a demand for suitable probe tips to achieve even higher resolution.

[1] Y. Huang and C. C. Williams, Appl. Phys. Lett. **66**, 344 (1995).
[2] J. J. Kopanski, J. F. Marchiando, and J. R. Lowney, J. Vac. Sci. Technol. B **14**, 242 (1996).
[3] S. M. Sze, *Physics of Semiconductor Devices* (Wiley, New York, 1981).
[4] R. N. Kleiman, M. L. O'Malley, F. H. Baumann, J. P. Garno, and G. L. Timp, Tech. Dig. Int. Electron Devices Meet. 691 (1997).
[5] M. L. O'Malley, G. L. Timp, S. V. Moccio, F. H. Baumann, J. P. Garno, and R. N. Kleiman, Appl. Phys. Lett. **74**, 272 (1999).
[6] R. N. Kleiman, M. L. O'Malley, F. H. Baumann, J. P. Garno, W. Timp, and G. L. Timp, VLSI Tech. Symp. Dig. 138 (1998).
[7] G. L. Timp *et al.*, Tech. Dig. Int. Electron Devices Meet. 615 (1998).

Ferromagnetic III–V heterostructures

H. Ohno[a)]
Laboratory for Electronic Intelligent Systems, Research Institute of Electrical Communication, Tohoku University, Katahira 2-1-1, Aoba-ku, Sendai 980-8577, Japan

(Received 17 January 2000; accepted 22 May 2000)

Properties of the ferromagnetic III–V semiconductor (Ga,Mn)As and heterostructures based on it are reviewed. A model based on hole-mediated ferromagnetic interaction is shown to successfully describe the ferromagnetic transition temperature of (Ga,Mn)As. Spontaneous splitting of resonant tunneling spectra was compared with theory and shown to result from the spin splitting of the valence band. The first demonstration of spin-dependent scattering in magnetic semiconductor trilayers as well as electrical spin injection is also reviewed. © *2000 American Vacuum Society.* [S0734-211X(00)06004-2]

I. INTRODUCTION

Manipulation of the spin degree of freedom in semiconductors has become a focus of interest in recent years. In order to utilize spin in semiconductors, one needs to be able to polarize, inject, transport, manipulate, store, and detect spins. Although polarization of carrier spins can be produced by optical orientation or by application of magnetic fields, it is more versatile if there is a ferromagnetic semiconductor that can be grown epitaxially on a target semiconductor system. The III–V based compound semiconductor system is a good candidate for the target system, not only because it is already in use in everyday electronics but also because it is providing a rich field of solid state physics owing to its capability of producing atomically abrupt heterostructures in a virtually impurity free environment. The discovery of ferromagnetism in (In,Mn)As[1] and later in (Ga,Mn)As[2] has offered an opportunity to explore the combination of the high-purity heterostructures and ferromagnetism. Here I review the properties of thin films and heterostructures of ferromagnetic semiconductors based on III–V's, particularly (Ga,Mn)As which can be grown pseudomorphically on GaAs substrates.

II. PREPARATION AND BASIC PROPERTIES OF FERROMAGNETIC (Ga,Mn)As

In order to observe ferromagnetism in III–V semiconductors, magnetic elements such as transition metals have to be introduced at concentration greater than 1 at. % beyond its solubility limit in III–V's. Low temperature molecular beam epitaxy (LT-MBE) capable of growing metastable crystals was shown to produce III–V's containing substitutionally doped transition metals over its solubility limit.[3,4] Mn is the preferred magnetic element because it serves as a source of magnetic moments due to its half filled *d* shell and of holes due to its acceptor nature; it is the shallowest acceptor among the transition metals. The latter is critical for ferromagnetism, since the ferromagnetic interaction among the magnetic moments is mediated by the presence of a high concentration of holes as a result of Mn acceptor doping. LT-MBE can produce GaAs with Mn concentration as high as 7%, beyond which segregation of Mn takes place during growth. The strain free lattice constant a of the thus produced alloy, (Ga,Mn)As, increases linearly with Mn concentration x as $a=0.566(1-x)+0.598\,x\,(\mathrm{nm})$, and therefore can be grown on GaAs substrates without introducing dislocations up to a critical thickness.

Magnetization as well as magnetotransport measurements revealed the presence of ferromagnetism in the (Ga,Mn)As films.[2] The ferromagnetic transition temperature T_C increases with increasing x as $2000\,x\pm 10$ K ($x<0.05$); below $x=0.005$, however, no ferromagnetism could be detected. The highest T_C so far obtained is 110 K.[5] The magnetic easy axis was in plane due to compressive strain from the GaAs substrate; the easy axis can be made perpendicular by reversal of the strain direction.[6] The low temperature saturation magnetization M_S of (Ga,Mn)As was consistent with the spin of Mn $S=5/2$. Susceptibility χ follows the Curie–Weiss form $\chi=C/(T-\theta)$, where C is the Curie constant and θ the paramagnetic Curie temperature. In fully compensated (Ga,Mn)As samples, however, θ becomes negative (-2 K),[7] showing that the direct exchange among Mn is antiferromagnetic and that the ferromagnetic interaction observed in these films is carrier (hole) induced.

The temperature T dependence of the sheet resistances of six 200-nm-thick (Ga,Mn)As epitaxial films grown on $(\mathrm{Al_{0.9}Ga_{0.1}})$As buffer layers showed that the samples with intermediate Mn composition ($x=0.035$, 0.043, and 0.053) are on the metal side of the metal-insulator transition, whereas low and high x samples are on the insulator side ($x=0.015$, 0.022, and 0.071).[5]

III. ORIGIN OF FERROMAGNETISM

In order to understand the carrier-induced ferromagnetism, a model based on ferromagnetic interactions mediated by holes in the ensemble of localized spins has been put forward.[8] The nature of exchange is represented by an exchange integral $N_0\beta$ (for the valence band; $N_0\alpha$ is used for the conduction band), which was employed successfully to reproduce various optical and magnetic phenomena observed

a)Author to whom correspondence should be addressed; electronic mail: ohno@riec.tohoku.ac.jp

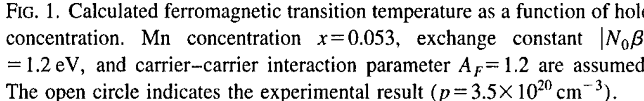

FIG. 1. Calculated ferromagnetic transition temperature as a function of hole concentration. Mn concentration $x=0.053$, exchange constant $|N_0\beta| = 1.2\,\text{eV}$, and carrier–carrier interaction parameter $A_F=1.2$ are assumed. The open circle indicates the experimental result ($p=3.5\times10^{20}\,\text{cm}^{-3}$).

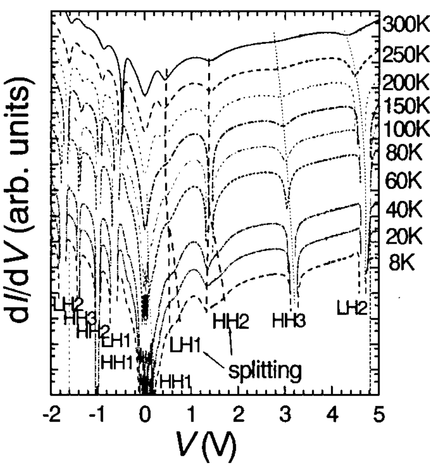

FIG. 2. Temperature dependence of $dI/dV-V$ characteristics of a double barrier resonant tunneling diode with a (Ga,Mn)As emitter layer with no applied magnetic field. Holes are injected from the (Ga,Mn)As side under positive bias. Note the spontaneous splitting of peaks, especially HH2.

in II–VI based paramagnetic semiconductors.[9] The ferromagnetism in the model is driven by the exchange interaction between carriers and localized spins. When the mean distance between the carriers is greater than that between the spins, which is the case for (Ga,Mn)As, the Friedel oscillation of the carrier spin polarization around the localized spins averages to zero. In this limit, the model becomes equivalent to the Ruderman–Kittel–Kasuya–Yosida (RKKY) interaction.[10] T_C is obtained by minimizing the Ginzburg–Landau free-energy functional, comprised of the carrier contribution term and the localized spin term, with respect to M at a given T and hole concentration p. The carrier contribution part is calculated by solving a 6×6 Luttinger Hamiltonian taking into account the presence of the pd interaction and by the integration over the Fermi volume. All the Luttinger parameters for (Ga,Mn)As were assumed to be identical to those of GaAs. Figure 1 shows the hole concentration dependence of T_C, with $N_0\beta=-1.2\pm0.2\,\text{eV}$ from photoemission experiments,[11] Mn concentration of $x=0.053$, and a carrier–carrier interaction enhancement of 1.2.[12] T_C of 130 K at hole concentration of $p=3.5\times10^{20}\,\text{cm}^{-3}$ is in good agreement with the experimental value of 110 K.[5,13] The theory also reproduced the dependence of the easy axis on the strain direction. Note that transport measurement also gives $|N_0\beta|$ ranging from 1.3 to 1.7 eV.[13]

The theory can explain the absence of ferromagnetism in n-type materials; in n-type materials, the small $N_0\alpha$ (about 0.2 eV) makes it difficult for the ferromagnetic interaction to overcome the direct antiferromagnetic coupling among Mn. Ferromagnetism in insulating samples can be understood along the same line, when one considers the difference between the length scales involved in the transport and the magnetism. In insulating samples, the localization length is smaller than the sample size (millimeters) but may still be significantly larger than the length scale of magnetic interactions (nanometers), thus making the adopted approach a good starting point.

IV. FERROMAGNETIC SEMICONDUCTOR HETEROSTRUCTURES

A. Ferromagnetic resonant tunneling heterostructures

Spontaneous magnetization in ferromagnetic semiconductors gives rise to spin splitting in the conduction and valence bands due to the exchange interaction between band electrons and localized spins. When (Ga,Mn)As is used as an emitter of double barrier resonant-tunneling diodes (RTDs), this spin splitting should manifest itself in current–voltage ($I-V$) characteristics. Experiments employing AlAs/GaAs/AlAs double barrier RTDs with a (Ga,Mn)As emitter indeed revealed spontaneous splitting of resonant peaks in the absence of magnetic fields at low temperatures, where (Ga,Mn)As is ferromagnetic.[14,15] Figure 2 shows the temperature dependence of dI/dV vs V curves of such a RTD in the absence of magnetic field, in which clear spontaneous splitting of resonant peaks labeled HH2 and LH1 was observed below the ferromagnetic transition temperature of 60 K. The structure studied here consists of (from the surface side) 150 nm ($Ga_{0.97}Mn_{0.03}$)As/15 nm undoped GaAs spacer/5 nm undoped AlAs barrier/4 nm undoped GaAs quantum well/5 nm undoped AlAs barrier/5 nm undoped GaAs spacer/150 nm Be doped GaAs ($p=5\times10^{17}\,\text{cm}^{-3}$)/150 nm Be doped GaAs ($p=5\times10^{18}\,\text{cm}^{-3}$)/$p^+$ GaAs substrates. Here, positive bias indicates that holes are injected from the (Ga,Mn)As side. Each label in Fig. 2 indicates the resonant state in the GaAs well, where a total of five states are present in the 4 nm GaAs well.

Although splittings in $I-V$ characteristics were observed and interpreted as a result of spin splitting of the bands, it was not clear why the splitting was observed only at specific resonant peaks and not in all the resonant states. In order to understand such resonant tunneling spectra, we have recently calculated $I-V$ characteristics of RTDs with a ferromagnetic (Ga,Mn)As emitter, taking into account the strong k-dependent mixing with the presence of exchange

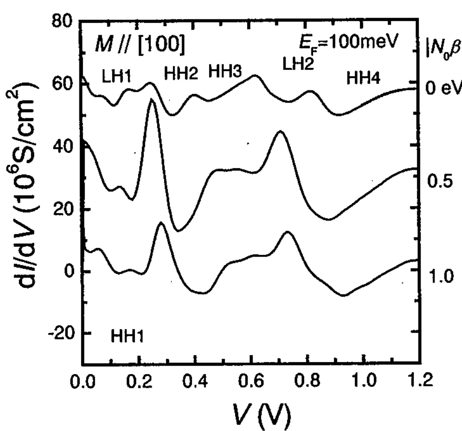

FIG. 3. Calculated $dI/dV-V$ characteristics of (Ga,Mn)As RTD with $N_0\beta$ as a parameter. Fermi energy of 100 meV ($p=1.2\times10^{20}\ \mathrm{cm}^{-3}$) was assumed. No strain is included.

interaction.[16] We have extended previous theoretical approaches to resonant tunneling of holes in III–V semiconductors[17] by using the pd exchange interaction in the 6×6 Luttinger–Kohn Hamiltonian. The resonant states in the GaAs well were calculated using the 4×4 Hamiltonian. The current density for a given hole concentration and voltage was then calculated by the following expression:

$$J_z=\frac{e}{(2\pi)^3\hbar}\sum_{i,j,l=1}^{4}\iiint_{E\leq E_F} d^3k\cdot\left(\frac{\partial E}{\partial k_z}\right)\cdot T^*T_{ij}\cdot[f(E)-f(E-eV)]\cdot c_{il}.$$

Here, T^*T_{ij} is the transmission coefficient from the heavy or light hole states in the emitter to the heavy and light hole states in the collector, $f(E)$ is the Fermi–Dirac distribution function, and c_{il} is the probability amplitude of the jth hole state in the lth band.

Figure 3 shows the calculated $dI/dV-V$ characteristics with $|N_0\beta|$ as a parameter. A thin AlAs barrier of 1 nm is assumed to avoid numerical instability arising from the order-of-magnitude smaller off-resonance transmission coefficients. No strain is considered. The resonant peaks in Fig. 3 show a complex pattern, which reproduces the overall features observed in the experiment. The complexity obtained here is a result of convolution of E-k diagrams of the spin-split ferromagnetic (Ga,Mn)As and of the energy quantized resonant states together with the k-dependent transmission coefficient. Analysis of the complex pattern suggests the importance of including the effect of strain in the calculation. The present $k\cdot p$ calculation indicates that it is necessary to go through rather elaborate calculation to identify the origin of the peaks and their splitting when k-dependent spin splittings are involved.

B. Spin-dependent scattering in ferromagnetic/nonmagnetic semiconductor multilayers

Spin-dependent scattering in metallic ferromagnetic/nonmagnetic multilayers has attracted much attention because of its physics as well as the technological importance of the giant magnetoresistance (MR) effect.[18] When a semiconducting layer is used for the intermediary nonmagnetic layer, the interlayer coupling can be modulated by external parameters such as temperature[19] and light illumination.[20] Multilayer structures made of semiconductor materials alone may have even higher potential advantages over their metal counterparts: one may be able to control electronically the coupling and other properties of multilayers.

To study spin-dependent scattering in all semiconductor ferromagnet/nonmagnet structures, a set of $(\mathrm{Ga_{0.95}Mn_{0.05}})\mathrm{As}/(\mathrm{Al_{0.14}Ga_{0.86}})\mathrm{As}/(\mathrm{Ga_{0.97}Mn_{0.03}})\mathrm{As}$ trilayer structures was prepared on 50-nm-thick $(\mathrm{Al_{0.30}Ga_{0.70}})\mathrm{As}$/1-$\mu$m-thick $(\mathrm{In_{0.15}Ga_{0.85}})\mathrm{As}$/semi-insulating GaAs (001) substrates.[21] The Mn composition of (Ga,Mn)As layers was chosen so that the conductivities of the two layers become comparable at low temperatures. No spin-dependent scattering was observed in previous experiments designed to observe interlayer coupling,[22] most probably because of the three orders of magnitude difference in the resistivities of the employed (Ga,Mn)As layers. The fully lattice relaxed (In,Ga)As buffer layer is designed to have a free-standing lattice constant larger than those of the GaAs and (Ga,Mn)As layers grown on it. Thus the two (Ga,Mn)As layers are tensilely strained, making the easy axis of magnetization perpendicular to the surface. One can then use the Hall effect to monitor the magnetization, since the anomalous Hall effect, that dominates the Hall effect in the relevant temperature and magnetic field ranges in (Ga,Mn)As, is proportional to the magnetization perpendicular to the plane and serves as a sensitive magnetometer. The thickness of the two (Ga,Mn)As layers and (Al,Ga)As layer was set to 30 and 2.8 nm, respectively. The Mn contents x of 0.05 for the top (Ga,Mn)As and 0.03 for the bottom (Ga,Mn)As were used to give different coercive forces. Since the resistivity of $(\mathrm{Ga_{0.95}Mn_{0.05}})\mathrm{As}$ is comparable to that of $(\mathrm{Ga_{0.97}Mn_{0.03}})\mathrm{As}$ at low temperature, transport measurements allow us to observe the properties of both layers at the same time. The parallel or antiparallel spin configuration in the prepared trilayer structure is realized by the use of the difference between the coercivities of the two (Ga,Mn)As layers with different x.

Figure 4 shows the magnetotransport properties of the trilayer structure at 30 K. The step feature in the sheet Hall resistance R_{Hall} observed in Fig. 4 reflects the weighted average of magnetization M of the two (Ga,Mn)As layers with different coercivities. Since the conductivity of the $(\mathrm{Ga_{0.95}Mn_{0.05}})\mathrm{As}$ layer is slightly higher than that of the $(\mathrm{Ga_{0.97}Mn_{0.03}})\mathrm{As}$, the overall feature in the transport properties reflects the behavior of the $(\mathrm{Ga_{0.95}Mn_{0.05}})\mathrm{As}$ layer. The clear increase of sheet resistance R_{sheet} was observed in the step region of 20–60 G of R_{Hall}, where the magnetizations of the two (Ga,Mn)As layers are aligned antiparallel. The result indicates that there is spin-dependent scattering, which results in increase of R_{sheet} just as in metallic multiplayer systems. The MR ratio was about 0.20% and is several orders of magnitude lower than that of the metallic systems, which is partly due to the nonoptimized structure. The ob-

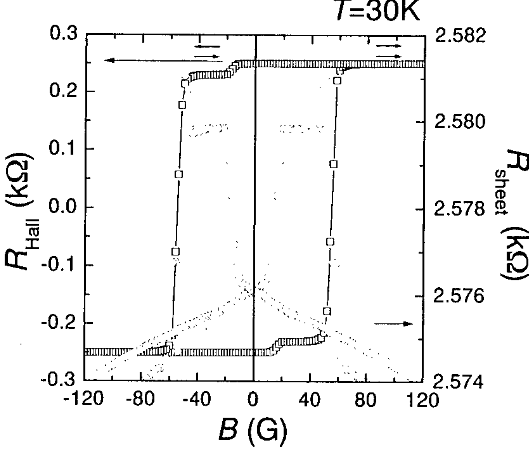

FIG. 4. Hall resistance R_{Hall} and sheet resistance R_{sheet} vs B at 30 K for a $(Ga_{0.95}Mn_{0.05})As/(Al_{0.14}Ga_{0.86})As/(Ga_{0.97}Mn_{0.03})As$ trilayer structure. The clear increase of R_{sheet} was observed in the step region of 20–60 G of R_{Hall}, where the magnetizations of the two (Ga,Mn)As layers are antiparallel. The hysteresis in R_{sheet} extending over the coersive field is due to temperature fluctuation.

servation of spin-dependent scattering in the semiconductor magnetic trilayer structure is an encouraging first step towards monolithic all-semiconductor magnetic sensors.

C. Electrical spin-injection in ferromagnetic semiconductor heterostructures

Electrical spin injection into nonmagnetic semiconductor heterostructures is one of the key elements in manipulating the spin degree of freedom in semiconductors. Since (Ga,Mn)As can epitaxially be incorporated into the GaAs heterostructure system and its spontaneous magnetization results in an imbalance of spin population in the carrier system, it is a good candidate of a spin polarized carrier source for spin injection in GaAs based structures. It has recently been demonstrated, by the use of a light emitting diode structure, that spin injection is indeed possible using (Ga,Mn)As.[23] Holes injected from the p-type (Ga,Mn)As layer through an intrinsic GaAs into an (In,Ga)As quantum well in p-i-n structures retain their spin imbalance information over distances greater than 200 nm and give rise to electroluminescence polarization in the absence of an external magnetic field. The demonstration of electrical spin injection in all semiconductor light emitting structures is believed to open a variety of new possibilities.

V. SUMMARY

Heterostructures based on ferromagnetic III–V semiconductor (Ga,Mn)As were reviewed. The hole-mediated ferromagnetic interaction is put forward in a model which successfully describes the ferromagnetic transition temperature of (Ga,Mn)As. Resonant tunneling structures as well as magnetic all-semiconductor trilayers exhibit pronounced spin-dependent phenomena: spin splitting of tunneling spectra and spin-dependent scattering, both of which are absent in nonmagnetic semiconductor structures. Although not included here, a number of optical studies on (Ga,Mn)As[24–27] have also been carried out as well as studies on magnetic III–V's other than (Ga,Mn)As and (In,Mn)As.[28–31] Ferromagnetic III–V's offer an excellent tool to explore a new field of semiconductor physics and technology, where both charge and spin of electrons play critical roles.

ACKNOWLEDGMENTS

The authors thank F. Matsukura, Y. Ohno, T. Dietl, N. Akiba, T. Omiya, I. Arata, E. Abe, D. Chiba, D. K. Young, B. Beschoten, and D. D. Awschalom for collaboration and valuable discussion. This work was partly supported by the "Research for the Future" Program (No. JSPS-RFTF97P00202) from the Japan Society for the Promotion of Science and by a Grant-in-Aid on Priority Area "Spin Controlled Semiconductor Nanostructures" (No. 09244103) from the Ministry of Education, Science, Sport, and Culture, Japan.

[1]H. Ohno, H. Munekata, T. Penney, S. von Molnár, and L. L. Chang, Phys. Rev. Lett. **68**, 2664 (1992).
[2]H. Ohno, A. Shen, F. Matsukura, A. Oiwa, A. Endo, S. Katsumoto, and Y. Iye, Appl. Phys. Lett. **69**, 363 (1996); See also, H. Ohno, Science **281**, 951 (1998); H. Ohno, J. Magn. Magn. Mater. **200**, 110 (1999).
[3]H. Munekata, H. Ohno, S. von Molnár, A. Segmüller, L. L. Chang, and L. Esaki, Phys. Rev. Lett. **63**, 1849 (1989).
[4]R. Shioda, K. Ando, T. Hayashi, and M. Tanaka, Phys. Rev. B **58**, 1100 (1998).
[5]F. Matsukura, H. Ohno, A. Shen, and Y. Sugawara, Phys. Rev. B **57**, R2037 (1998).
[6]H. Ohno, F. Matsukura, A. Shen, Y. Sugawara, A. Oiwa, A. Endo, S. Katsumoto, and Y. Iye, in *Proceedings of the 23rd International Conference on the Physics of Semiconductors*, edited by M. Scheffler and R. Zimmermann (World Scientific, Singapore, 1996), p. 405.
[7]Y. Satoh, N. Inoue, Y. Nishikawa, and J. Yoshino, Proceedings of the 3rd Symposium on Physics and Application of Spin Related Phenomena in Semiconductors, edited by H. Ohno, J. Yoshino, and Y. Oka, 17–18 Nov. 1997, Sendai, Japan, p. 23.
[8]T. Dietl, H. Ohno, F. Matsukura, J. Cibert, and D. Ferrand, Science **287**, 1019 (2000).
[9]*Semiconductor and Semimetals*, edited by J. K. Furdyna and J. Kossut (Academic, New York, 1988), Vol. 25.
[10]T. Dietl, A. Haury, and Y. Merle d'Aubigné, Phys. Rev. B **55**, R3347 (1997).
[11]J. Okabayashi, A. Kimura, O. Rader, T. Mizokawa, A. Fujimori, T. Hayashi, and M. Tanaka, Phys. Rev. B **58**, R4211 (1998).
[12]T. Jungwirth, W. A. Atkinson, B. H. Lee, and A. H. MacDonald, Phys. Rev. B **59**, 9818 (1999).
[13]H. Ohno, F. Matsukura, T. Omiya, and N. Akiba, J. Appl. Phys. **85**, 4277 (1999); T. Omiya, F. Matsukura, T. Dietl, Y. Ohno, T. Sakon, M. Motokawa, and H. Ohno, Physica E **7**, 976 (2000).
[14]H. Ohno, N. Akiba, F. Matsukura, A. Shen, K. Ohtani, and Y. Ohno, Appl. Phys. Lett. **73**, 363 (1998).
[15]N. Akiba, F. Matsukura, Y. Ohno, A. Shen, K. Ohtani, T. Sakon, M. Motokawa, and H. Ohno, Physica B **256–258**, 561 (1998).
[16]N. Akiba, F. Matsukura, K. Ohtani, Y. Ohno, T. Dietl, and H. Ohno (unpublished).
[17]C. Y.-P. Chao and S. L. Chuang, Phys. Rev. B **43**, 7027 (1991); A. C. Rodrigues Bittencourt, A. M. Cohen, and G. E. Marques, *ibid.* **57**, 4525 (1998).
[18]*Ultrathin Magnetic Structures*, edited by B. Heinrich and J. A. C. Bland (Springer, Verlag Berlin, 1994), Vol. 2, Chap. 2, and references therein.

[19]B. Briner and M. Landolt, Phys. Rev. Lett. **73**, 340 (1994); H. Akinaga, W. Van Roy, S. Miyanishi, and K. Tanaka, J. Appl. Phys. **81**, 5345 (1997).
[20]J. E. Mattson, S. Kumar, E. E. Fullerton, S. R. Lee, C. H. Sowers, M. Grimsditch, S. D. Bader, and F. T. Parker, Phys. Rev. Lett. **71**, 185 (1993).
[21]N. Akiba, D. Chiba, K. Nakata, F. Matsukura, Y. Ohno, and H. Ohno, J. Appl. Phys. **87**, 6436 (2000).
[22]N. Akiba, F. Matsukura, A. Shen, Y. Ohno, and H. Ohno, Appl. Phys. Lett. **73**, 2122 (1998).
[23]Y. Ohno, D. K. Young, B. Beschoten, F. Matsukura, H. Ohno, and D. D. Awschalom, Nature (London) **402**, 790 (1999).
[24]T. Kuroiwa, T. Yasuda, F. Matsukura, A. Shen, Y. Ohno, H. Ohno, and Y. Segawa, Electron. Lett. **34**, 190 (1998).
[25]K. Ando, T. Hayashi, M. Tanaka, and A. Twardowski, J. Appl. Phys. **83**, 6548 (1998).
[26]J. Szczytko, W. Mac, A. Twardowski, F. Matsukura, and H. Ohno, Phys. Rev. B **59**, 12935 (1999).
[27]B. Beschoten, P. A. Crowell, I. Malajovich, D. D. Awschalom, F. Matsukura, A. Shen, and H. Ohno, Phys. Rev. Lett. **83**, 3073 (1999).
[28]E. Abe, F. Matsukura, H. Yasuda, Y. Ohno, and H. Ohno, Physica E (to be published).
[29]M. Yamaura, S. Haneda, K. Hara, S. Hirose, Y. Takatani, S. Harigae, and H. Munekata, Materials Research Society 1999 Spring Meeting Francisco, 5–9 April 1999; J. Yoshino (private communication).
[30]M. Tanaka (private communication).
[31]K. Ando (private communication).

Nickel layers on indium arsenide

C. J. Hill,[a] R. A. Beach, and T. C. McGill
Thomas J. Watson, Sr., Laboratory of Applied Physics, California Institute of Technology, Pasadena, California 91125

(Received 17 January 2000; accepted 25 May 2000)

We report here on the preparation and characterization of InAs substrates for *in situ* deposition of ferromagnetic contacts, a necessary precursor for semiconductor devices based on spin injection. InAs has been grown on InAs(111)*A* and (100) substrates by molecular-beam epitaxy and then metalized *in situ* in order to better understand the mechanisms that inhibit spin injection into a semiconductor. Initial x-ray characterization of the samples indicate the presence of nickel arsenides and indium–nickel compounds forming during deposition at temperatures above room temperature. Several temperature ranges have been investigated in order to determine the effect on nickel-arsenide formation. The presence of such compounds at the interface could greatly reduce the spin-injection efficiency and help elucidate previous unsuccessful attempts at measuring spin injection into InAs. © *2000 American Vacuum Society.* [S0734-211X(00)06804-9]

I. INTRODUCTION

The success of recent attempts to inject spin-polarized currents from a ferromagnetic metal into a semiconductor have been the subject of much debate, and has called into question the quality of the interface.[1-4] Recent theoretical considerations conclude that in the drift-diffusion regime spin-polarized current injection from a ferromagnetic metal into a semiconductor may not be possible.[5] In any case, a detailed look at the interface between the ferromagnetic metal and the semiconductor is a clear prerequisite for understanding what is happening during current injection. In this article, we look at the interface between one of the most widely used ferromagnetic metals, nickel, and InAs, which is often used for its high mobility and negative Schottky barrier when doped *n* type. Nickel was also selected because it offers the additional possibility of a lattice match to (111) and (110) InAs substrates. The matches were identified using the two-dimensional supercell technique developed by Zur.[6] The 0.7% mismatch of cubic Ni on the (111)InAs face is depicted in Fig. 1. Matches of this type have been experimentally demonstrated with CdTe on GaAs.

II. EXPERIMENTAL DETAILS

A. Preparation of samples

Samples were produced from commercially available 1 in. InAs(100) and (111) wafers, *n* type with carrier concentration approximately 1×10^{-16} cm^{-3}. Wafers were degreased in a standard acetone, isopropyl alcohol, deionized water degrease, after which they were placed in HCl for 1 min to remove the native oxide and rinsed in deionized water. After this, the wafers were blown dry and indium bonded to substrate blocks and introduced into vacuum. Unintentionally doped *n*-type InAs was then grown in a Perkin Elmer 430 molecular-beam epitaxy chamber until the reflection high-energy electron diffraction (RHEED) pattern indicated a smooth growth surface. The samples were then transferred *in situ* for x-ray photoelectron spectroscopic (XPS) analysis. Finally, the samples were transferred, again *in situ*, to an UHV metalization chamber for nickel deposition. Film thicknesses were monitored *in situ* by a Leybold–Inficon crystal growth monitor and verified *ex situ* by ellipsometry when possible. Nickel deposition was carried out at a variety of substrate temperatures from room temperature (RT) to 350 °C. The deposition rates were held between 0.5 and 0.7 Å/s.

B. Sample characterization

X-ray diffraction studies were performed on all samples to look for nickel films or reaction by-products produced at the interface. X-ray scans were performed with a low-resolution, high-throughput mode with a receiving slit width of 0.45 mm. Many samples were annealed for 3 min at 650 °C to see if the x-ray peak heights of the reaction products could be improved. Growths on the (100) face were characterized electrically to ensure that electrically insulating layers were not being produced.

III. RESULTS AND DISCUSSION

A. X-ray analysis

X-ray diffraction $\omega-2\theta$ scan results on the (100) samples A, B, and C from Table I are shown in Fig. 2. The addition

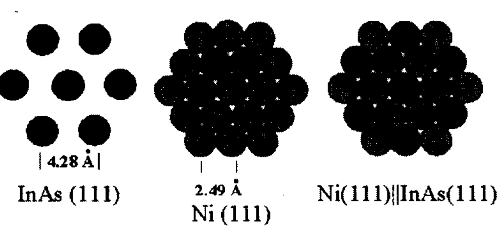

FIG. 1. Geometrical lattice match of the (111) face of nickel on (111)InAs. There is a 0.7% lattice mismatch in the plane.

[a]Electronic mail: cjh@ssdp.caltech.edu

 ©2000 American Vacuum Society

TABLE I. Summary of the samples presented.

Sample	Face	Depositon temperature (°C)	Ni thickness (nm)	Reaction products
A	100	RT	200	InNi,[a]Ni_3In[a]
B	100	150	200	InNi,[a]hex.Ni[a]
C	100	350	200	Ni_5As_2,InNi,$Ni_{11}As_8$
D	111	RT	21	···
E	111	350	1000	NiAs,Ni_5As_2,$Ni_{11}As_8$,hex.Ni

[a]After anneal.

of two extra peaks is clearly visible in the scans of sample C, deposited at a substrate temperature of 350 °C. These peaks were also visible in all other (100) samples grown at 350 °C. No evidence of reaction by-products are visible in the room-temperature growths. Samples A, B, and C were subjected to a rapid thermal annealing process in flowing argon for 2 min at 650 °C. The pre- and postnasal x-ray data are shown in Figs. 2 and 3.

Figure 4 shows the x-ray data for representative growths on the (111) face. Sample D was a 210 Å film of Ni on the (111) face of InAs. Only substrate peaks were visible in the x-ray scans both before and after annealing, as was the case with all thin (100–300 Å) Ni films on the (111) face. Sample D showed no extra peaks after annealing at 650 °C for 3 min. It is most likely that not enough Ni was deposited to form crystals detectable by x-ray analysis, or the film was amorphous. Sample E was prepared on the (111) face and taken repeatedly to 350 °C for Ni deposition and XPS analysis. After four depositions of varying thickness, the sample had roughly 1 μm of Ni on the surface, and showed many extra peaks from reaction by-products.

Few of the peaks found in the annealed x-ray data are exact matches to any of the x-ray lines for the known combinations of In, Ni, and As. Most of them are believed to be from InNi, $Ni_{11}As_8$, Ni_5As_2, $NiAs_2$, and hexagonal nickel with indium incorporated in the lattice. Table I lists the most likely impurity compounds present in each sample.

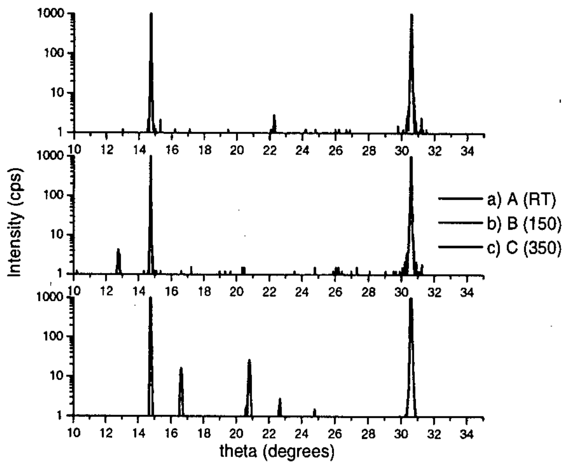

FIG. 2. X-ray diffraction scans of 200 nm Ni films on InAs(100) substrates.

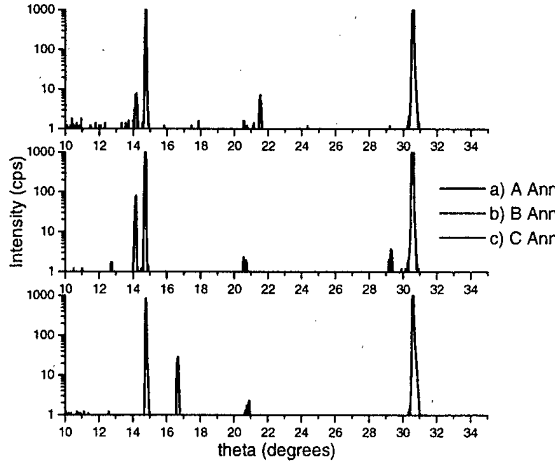

FIG. 3. X-ray diffraction scans of 200 nm Ni films on InAs(100) substrates from Fig. 2 after a rapid thermal anneal of 650 °C for 3 min.

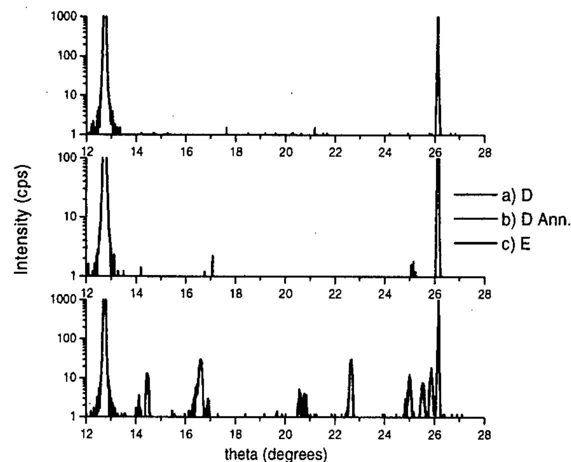

FIG. 4. X-ray diffraction scans of Ni films on InAs(111) substrates. (a) 210 Å Ni film on InAs, substrate temperature 100 °C. (b) Anneal of sample in (a). (c) 1 μm of Ni deposited at 350 °C.

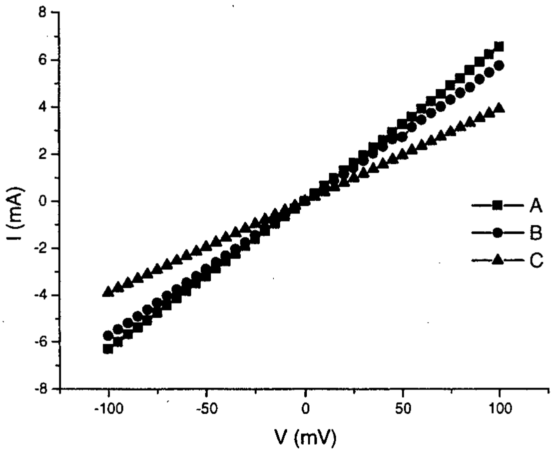

FIG. 5. Ohmic I–V curves of samples A, B, and C for 150 μm radius circular contacts.

B. Electrical characterization

To test that the contacts were indeed Ohmic, electrical measurements were carried out on samples A, B, and C. Linear $I-V$ curves were observed for all three samples and representative curves are shown in Fig. 5. The $I-V$ curves are from 150 μm circular pads with a 50 μm gap etched approximately 1 μm into the surface. The linear $I-V$ curves indicate that no insulating barrier was formed during deposition.

IV. CONCLUSIONS

Ni films grown *in situ* on InAs(100) substrates yield Ohmic contacts at a wide range of substrate temperatures during deposition. No direct evidence of NiAs compounds was observed for room-temperature deposition of Ni on both (100) and (111) faces of InAs, ruling out the presence of interfacial NiAs compounds as an impediment to spin injection. Reaction by-products are only visible upon bringing the sample to higher temperatures. To date, efforts to produce epitaxial nickel on InAs(111) have been unsuccessful. Since it is apparent that low deposition temperatures are necessary to produce clean interfaces, a much lower growth rate may have to be used to offset the lower surface mobility of the deposited atoms at cooler temperatures. Most likely, the addition of an *in situ* diagnostic technique like RHEED will help to facilitate the development of a viable epitaxial growth technique, allowing one to correlate growth temperatures and deposition rates with the onset of noncrystallinity.

ACKNOWLEDGMENTS

The authors would like to thank Professor J. O. McCaldin for many fruitful discussions. This work was supported by Office of Naval Research Grant Nos. N0014-99-1-1006 and N0014-91-1-0492.

[1]P. R. Hammar, B. R. Bennett, M. J. Yang, and M. Johnson, Phys. Rev. Lett. **83**, 203 (1999).
[2]F. G. Monzon and M. L. Roukes, J. Magn. Magn. Mater. **199**, 632 (1999).
[3]H. X. Tang, F. G. Monzon, R. Lifshitz, M. L. Cross, and M. L. Roukes, Phys. Rev. B **61**, 4437 (2000).
[4]M. Oestreich, J. Hubner, D. Hagele, P. J. Klar, W. Heimbrodt, W. W. Ruhle, D. E. Ashenford, and B. Lunn, Appl. Phys. Lett. **74**, 1251 (1999).
[5]G. Schmidt, L. W. Molenkamp, A. T. Filip, and B. J. van Wees (unpublished).
[6]A. Zur and T. C. McGill, J. Appl. Phys. **55**, 378 (1984).

Interfacial scattering of hot electrons in ultrathin Au/Co films

R. P. Lu,[a] B. A. Morgan, and K. L. Kavanagh[b]
Department of Electrical Computer Engineering, University of California San Diego, La Jolla, California 92093-0407

C. J. Powell, P. J. Chen, F. G. Serpa, and W. F. Egelhoff, Jr.
National Institute of Standards and Technology, Gaithersburg, Maryland 20899

(Received 17 January 2000; accepted 1 June 2000)

We have used room-temperature, ballistic electron emission microscopy (BEEM) to measure hot-electron transport through ultrathin Au/Co multilayer structures deposited onto Si. The samples consist of Au/Co/Si or $(Au/Co)_n/Au/Si$ diodes, sputter deposited at 175 or 300 K, where n is the number of repeat layers. The thin-film Co attenuation length, λ_{Co}, is extracted from the BEEM spectra as a function of Co thickness, in single Co layer samples. Similarly, the interface attenuation number, or the number of Co/Au interfaces required for a $1/e$ attenuation, is determined from the multi-interface samples. BEEM barrier heights of Au/Co/Si decrease with increasing Co thickness (for thicknesses <1 nm), as the film becomes continuous and develops a Schottky barrier for Co or $CoSi_2$(<0.7 eV). For these diodes, λ_{Co}, increases from 0.3 to 0.5 nm, each with an estimated uncertainty of 0.1 nm, when the deposition temperature is decreased from 300 to 175K. This result is associated with decreased silicide formation at the lower deposition temperature. When Co is isolated from the Si with a 2 nm Au layer, the barrier height is stable (0.82 eV), and λ_{Co}, increases further to 0.8 ± 0.1 nm. The λ_{Co} values are independent of electron energy over the range measurable (1–1.8 eV). The interface attenuation number was 1.8 and 25 interfaces for 0.6 and 1.2 nm total Co thickness, respectively (in structures with a constant total Au thickness of 8 nm). Thus, significant interface scattering is observed in the thinner sample and negligible scattering when the Co thickness was doubled. Further BEEM measurements on similar superlattices are being carried out to understand these results. © *2000 American Vacuum Society.* [S0734-211X(00)08904-6]

I. INTRODUCTION

Ballistic electron emission microscopy (BEEM) has proven itself in the past decade to be an important tool for the analysis of buried interfaces and the transport properties of thin metal films. BEEM utilizes a scanning tunneling microscope (STM) in which electrons tunnel into thin surface conducting layer, usually a metal. In the simplest sample, the metal is deposited onto a semiconductor forming a buried Schottky barrier. A third terminal is connected through an ohmic contact to the semiconductor. Depending on the bias between the tip and the metal layer, and the thickness of the metal layer, some of the tunneling electrons reach the metal/semiconductor or metal/insulator interface ballistically.[1] In the case of a Schottky diode, they can cross into the semiconductor if the bias exceeds the local Schottky barrier height. Area maps of Schottky barrier heights can be obtained as well as barrier height distributions from a diode.[2,3] More complicated samples consisting of heterostructures or metal–insulator–metal layers[4,5] have also been studied. BEEM has the advantage of nanometer-scale resolution and permits the direct observation of lateral nonuniformities in hot-electron scattering processes.

While electron transport across interface barriers has been a major focus of many previous BEEM studies, BEEM has also been applied to the determination of electron attenuation lengths (ALs), λ. The AL is energy dependent and arises from a combination of elastic and inelastic scattering processes each with their own separate mean free paths. Few AL measurements in the energy range <50 eV have been carried out.[6,7] The behavior in the 5 to 15 eV range above the Fermi level cannot be described by a universal behavior, particularly for transition metals.[8] By measuring the BEEM current, I_B, through a metal/semiconductor sample as a function of metal thickness, t, and electron energy, E, one can obtain the perpendicular AL, λ, for electron transport normal to the interface from $I_B(t,E)=I_B(t=0,E)\exp[-t/\lambda]$. In this way λ (1–6 eV) has been measured for Au,[9–15] Pd,[16] PtSi,[17,18] and $CoSi_2$[11,19] thin films using metal/Si structures. In a similar manner, multilayer samples consisting of different numbers of nominally identical interfaces can be used to investigate the degree of interface scattering. The interface attenuation number λ_i will be defined here as the number of identical interfaces required to reduce the BEEM current by a factor $1/e$.

The effects of interfaces and thin film microstructure on the AL is pertinent to understanding giant magnetoresistance (GMR) in both current-in-plane and current-perpendicular-to-the-plane multilayer structures.[20] Perpendicular transport across such structures is difficult to measure directly because the resistance is very small. Superconducting or microfabricated contacts have been used to obtain data at energies near the Fermi level.[21,22] Measurements of the spin dependent

[a]Electronic mail: rlu@ucsd.edu
[b]Present address: Department of Physics, Simon Fraser University, Burnaby, British Columbia V5A 1S6, Canada; electronic mail: kavanagh@sfu.ca

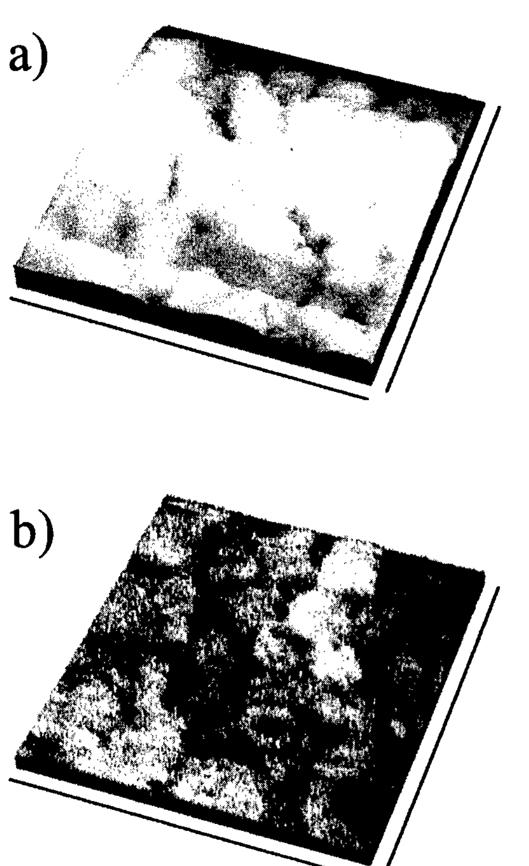

FIG. 1. Surface STM topography 64×64 nm (a) and corresponding BEEM image (b) of a Au(6 nm) Co(0.6 nm)/Au(2 nm)/Si diode. Tip bias, $V_t = -1.2$ V, tunneling current, $I_t = 5$ nA, and BEEM image contrast $0 < I_c < 9$ pA.

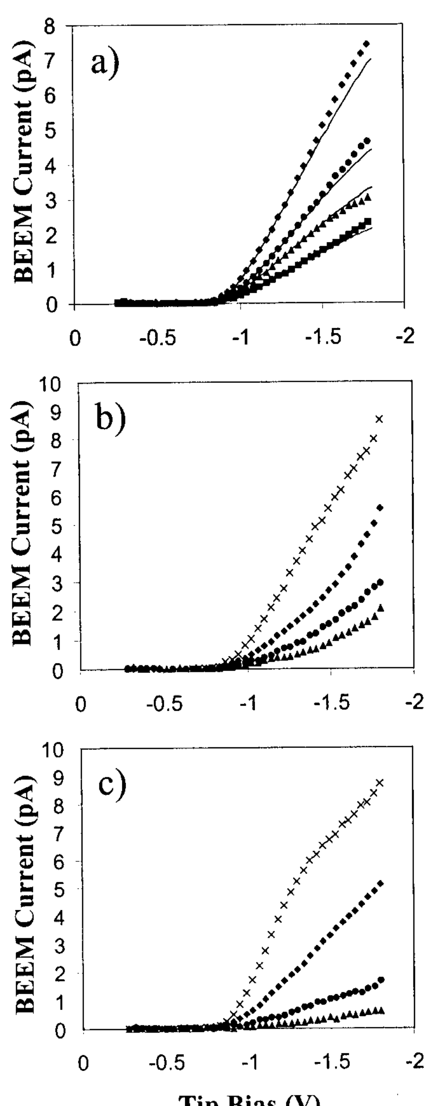

FIG. 2. Average BEEM spectra, from (a) Au(5 nm)/Co/Au(2 nm)Si deposited at 175 K, from Au(5 nm)/Co/Si structures deposited at (b) 175 K, and (c) at room temperature for Co thicknesses of 0.2 nm (crosses), 0.4 nm (diamonds), 0.6 nm (circles), and 0.8 nm (triangles). Solid lines are Bell–Kaiser fits.

transport of hot electrons through single layers[8] and magnetic multilayers has been demonstrated in semiconductor-based, spin-valve structures.[23,24] BEEM is beginning to be applied to magnetic metal structures, including the detection of spin-dependent transport and magnetic-domain imaging.[24–26] Rippard and Buhrman have also reported BEEM measurements of the Co AL for electrons of different spin polarization from Co/Cu/Co multilayers.[27] Previously, we have reported BEEM measurements of the average AL for a selection of magnetic and nonmagnetic metals pertinent to GMR devices.[28] In this article, we describe additional BEEM measurements on Au/Co structures and present initial results on the role of interface scattering in this system.

II. EXPERIMENT

Samples consist of metal multilayers deposited by direct current magnetron sputtering onto n-type Si(001) substrates (phosphorus-doped $7\times10^{14}\,\mathrm{cm}^{-3}$). The Si was prepared for deposition by a cleaning process consisting of a dip into a 6% HF solution, followed by an ultrasonic bath in glassware cleaning solution, and a final rinse in a stream of ultrapure distilled water. They were then loaded into the ultrahigh vacuum sputtering chamber immediately. The ultrasonic bath and distilled water were necessary to reduce the HF residue on the surface, which otherwise could be detected along with particulates under a dark field microscope. *In situ* x-ray photoelectron spectroscopy of the cleaned Si surface showed an ~1 nm mixture of hydrocarbons, fluorine, and water vapor. Heating to 350–400 °C, removed most of this contamination, but a fraction of a monolayer of carbon remains, probably in the form of SiC. Sputter cleaning of the samples was not carried out since this was found to result in undetectable BEEM signals, presumably due to electron trapping at Si interface defects. The metal layers were sputter deposited through a mechanical mask (3 mm diameter holes) to thicknesses ranging from 0.2 to 5 nm. Using a shutter system, Au/Co/Au/Si diodes varying in metal thicknesses could be deposited in a single run. $(\mathrm{AuCo})_n/\mathrm{Au/Si(001)}$ diodes with varying numbers of Au/Co interfaces ($2n$) were also fabri-

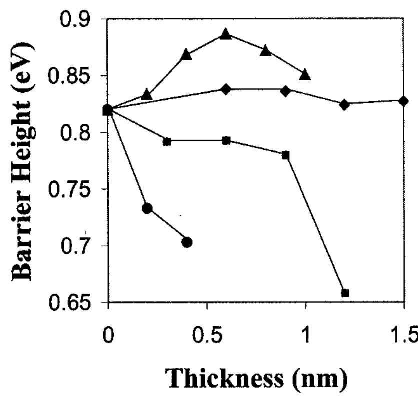

FIG. 3. Barrier heights plotted vs ferromagnet layer thickness for (♦) Au/Co/Au/Si; (●) Au/Ni/Si; (▲) Au/Fe/Si; and (■) Au/Co/Si diodes.

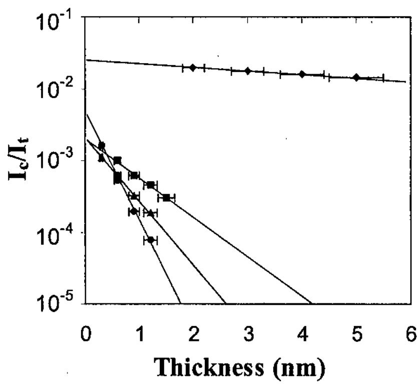

FIG. 4. BEEM current on a logarithmic scale, plotted vs metal-layer thickness for room temperature depositions of (♦) Au/Si; (●) Au/Co/Si; and low-temperature (175 K) depositions of (▲) Au/Co/Si; and (■) Au/Co/Au/Si.

cated as a function of the number of Au/Co repeat layers, n, for constant total metal thicknesses. Diodes were prepared at room temperature and at 175 K.

BEEM studies were performed in air, at room temperature, using a modified Omicron[29] STM Pt–Ir(80:20) wire (0.20 mm diameter) was mechanically cut to produce the tunneling tips. With the sample grounded, negative bias was applied to the tip, and the BEEM current was converted to a voltage by a low-noise, operational amplifier (OPA128).[2,3] At least 256 BEEM spectra were obtained from each diode sample from a 200 nm^2 area on the surface. A Bell–Kaiser[1] fit was performed on the average spectra to extract the barrier height. The BEEM signal from each diode was electronically stable in air for approximately 3 weeks, longer if stored in a refrigerator.

III. RESULTS

A typical STM surface image and the corresponding BEEM current image obtained simultaneously from a Au/Co/Au/Si(6 nm/0.6 nm/2 nm) diode are shown in Fig. 1 (tip bias, $V_t = -1.2$ V and tunneling current, $I_t = 5$ nA). The Au surface shows a spherical grain structure with diameters of approximately 10 nm.[2] The BEEM current image shows grain-dependent contrast, uniform across most grains but decreasing near the grain boundaries, presumably a function of the Au or underlying magnetic-metal grain orientation.

Average BEEM spectra measured from Au(5 nm)/Co/Si and Au(3 nm)/Co/Au(2 nm)/Si structures as a function of Co thickness are shown in Fig. 2 for two substrate temperatures. The noise level on these spectra is less than 0.1 pA. The highest BEEM currents are obtained for the Au/Co/Au/Si diodes deposited at 175 K. Barrier heights determined from fits to spectra (a) and (b) from Fig. 2 and others not shown, as a function of metal thickness are plotted in Fig. 3. We assign an error of less than 0.01 eV to the barrier heights from these fits. The sputtered Au/Co/Au/Si diodes gave stable BEEM thresholds (or Schottky barriers) of 0.82±0.01 eV, consistent with literature reports.[3,30] In diodes where the metal (Co, Fe, Ni, and Cu) is deposited directly onto the Si, the barrier height eventually decreases with coverage towards the values expected for the associated metal or silicide involved.

Logarithmic plots of the BEEM current (tip bias of −1.5 eV) versus Co thickness from the spectra of Fig. 2 are shown in Fig. 4 together with results from Au/Si diodes. The error bars on the BEEM current (typically <0.1 pA) are negligible compared to the uncertainty in the film thicknesses (estimated to ±10%). In each case, the plot is linear to within the error of the measurement. The y intercept for the Au/Si samples corresponds to the room-temperature-deposited Au/Si interface transmission coefficient. The y intercept for the Au/Co samples should be reduced from this value corresponding to the current for a Au(5 nm)/Si sample since all of these samples had a 5 nm Au surface layer. The AL values calculated from the slopes of these curves are summarized in Table I.

Our measurement of λ_{Au} (9.5±1 nm) for room-temperature-deposited Au is slightly less than those from previous BEEM measurements (11–27 nm).[9–15] The value for Co deposited directly onto Si, 0.3 nm, is the smallest AL measured, perhaps an indication that the Co had reacted with the Si forming a silicide. Decreasing the deposition temperature to 175 K increases λ_{Co} to 0.5 nm. Use of a Au interlayer

TABLE I. BEEM attenuation lengths, λ for $E=1.5$ eV, determined from logarithmic plots of BEEM current vs thickness (Fig. 2), with an estimated uncertainty of 10%, and previously reported values.

Sample type	Metal M	Deposition temperature K	Attenuation length λ ±10% nm	Previously reported λ nm
Au(5 nm)/M/Si	Au	300	9.5	12.5[a]
	Co	300	0.3	0.8[b]
		175	0.5	
Au/M/Au/Si (3 nm)M(2 nm)	Co	175	0.8	

[a]Average value of Refs. 9–15, 26 thicknesses 0–20 nm, and $V_t = -1.2$ V.
[b]Reference 8 (photoemission).

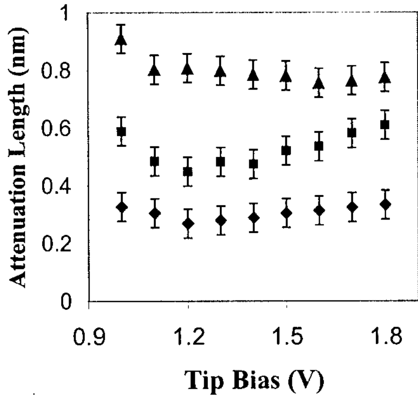

FIG. 5. Attenuation length vs tip bias for (♦) Au/Co/Si deposited at room temperature (■) Au/Co/Si at 175 K; and (▲) Au/Co/Au/Si at 175 K.

between Si and Co further increased the λ_{Co} for Co deposited at 175 K, from 0.5 to 0.8 nm. The AL value obtained for these sputter-deposited materials is slightly less than the average Co AL reported by Rippard and Buhrman[27] (1.4 nm) for electron-beam deposited Co. However, our value is identical to spin-averaged mean free paths (attenuation lengths) reported from low-energy photoemission from Co layers epitaxially grown on W(110).[8]

Attenuation lengths were determined as a function of energy over the energy range of the spectra probed in our BEEM experiments, 1.0–1.8 eV, in a similar manner to that for the 1.5 eV energy. The results, plotted in Fig. 5, show very little variation with energy over this range.

BEEM spectra from two sets of multilayer, $(Au/Co)_n/(Au/Si)$ samples are shown in Fig. 6. Each set consisted of three diodes, with repeat numbers $n=1$, 2 and 3, both designed such that the total Au thickness was 8 nm. The total Co thickness was the only parameter varied, 0.6 or 1.2 nm. Thus, the samples had the same number of Au/Co interfaces but differed by a factor of 2 in the thickness of each Co layer. Not shown are Bell–Kaiser fits to these spectra which gave Au/Si barrier heights, as before. A logarithmic plot of BEEM current, normalized to the tip current, as a function of the number of Co/Au interfaces is shown in Fig. 7. The Au/Co interface attenuation number λ_I is 1.8 and 25 interfaces, for the 0.6 and 1.2 nm samples, respectively. Thus, there is negligible interface scattering for the thicker sample, in agreement with recent results for the Co/Cu/Co system,[27] but a significant degree of scattering occurs in the thinner set.

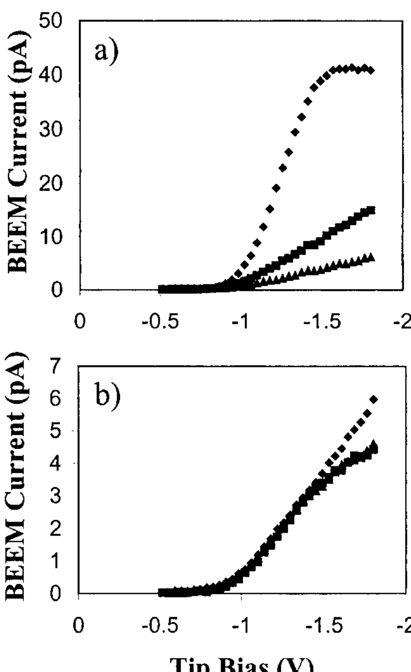

FIG. 6. Average BEEM spectra (256 locations) as a function of number of Co/Au interfaces for $(Au/Co)_n/Au/Si(100)$ diode structures. (a) 0.6 nm Co; and (b) 1.2 nm Co, for (♦) 2, (■) 4, and (▲) 6 interfaces.

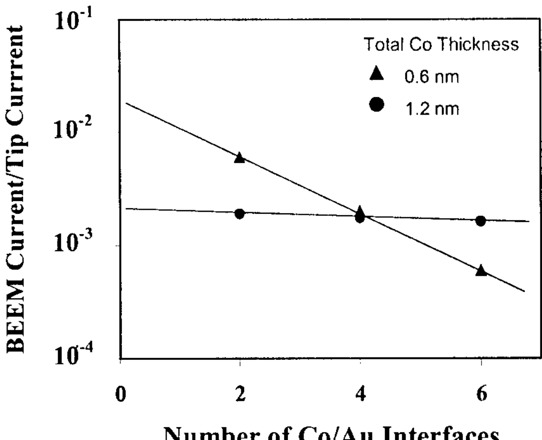

FIG. 7. BEEM current on a logarithmic scale normalized to the tip tunneling current, plotted vs number of Co/Au interfaces, for (▲) 0.6 nm and (●) 1.2 nm total Co. Total Au thickness is 8 nm in both cases.

IV. DISCUSSION

The short attenuation lengths measured for Co deposited directly onto Si at room temperature, compared to deposition at 175 K or when sandwiched between Au, is an indication that there was considerable reaction with the Si to form a silicide. Lowering the deposition temperature would reduce the rate of this reaction and result in less alloy formation, increasing the attenuation lengths as was observed. Adding a Au layer between the metal and the Si is expected to prevent silicide reaction, considering the stable Au/Si barrier height, and further increase the AL as observed.

The BEEM results from the multilayer were puzzling. Every attempt was made to fabricate the two sets of diodes in an identical fashion. However, since the interface attenuation factor varied from severe to negligible when the Co layer thicknesses were doubled, it must be concluded that the interfaces were not identical. There was also a higher-than-expected BEEM current in the thinner set of diodes compared to the thicker set suggesting that the Si interface is different and responsible for changes in the subsequent Au/Co interfaces. Further experiments are required to understand these data.

V. CONCLUSION

In summary, we have used BEEM to measure hot-electron attenuation lengths of thin (<1 nm), Co films deposited directly onto Si or isolated from Si via a Au buffer layer. When deposited directly onto Si, the BEEM barrier height decreased with thickness as the film became continuous. The Co attenuation lengths were shortest (0.3 nm) for films deposited at room temperature and were longer (0.5 nm) for films deposited at lower temperature (175 K); this increase is believed to be due to inhibition of the silicide reaction at the lower temperature. The longest Co attenuation lengths were measured for Au/Co/Au/Si diodes (0.8 nm) deposited at 175 K. The interface scattering measured from multilayer $(Au/Co)_n$/Au/Si diode was severe (attenuation number 1.8 interfaces) for Co layer thicknesses <0.6 nm, while negligible (attenuation number 25 interfaces) when these thicknesses were doubled. Future multilayer experiments are planned to understand these results.

ACKNOWLEDGMENT

R. P. L. and K. L. K. are grateful for partial support of this research from NSF (DMR-9710509).

[1]W. J. Kaiser and L. D. Bell, Phys. Rev. Lett. **60**, 1406 (1988); L. D. Bell and W. J. Kaiser, *ibid.* **61**, 2368 (1988).
[2]A. A. Talin, R. S. Williams, B. A. Morgan, K. M. Ring, and K. L. Kavanagh, Phys. Rev. B **49**, 16474 (1994).
[3]B. A. Morgan *et al.*, Mater. Chem. Phys. **46**, 224 (1996).
[4]B. Kaczer and J. P. Pelz, Phys. Rev. Lett. **77**, 91 (1996); J. Vac. Sci. Technol. B **14**, 2864 (1996).
[5]M.-I. Ke, D. I. Westwood, C. C. Matthai, B. E. Richardson, and R. H. Williams, Phys. Rev. B **53**, 4845 (1996).
[6]M. P. Seah and W. A. Dench, Surf. Interface Anal. **1**, 2 (1979).
[7]C. J. Powell and A. Jablonski, J. Phys. Chem. Ref. Data **28**, 19 (1999).
[8]G. Schönhense and H. C. Siegmann, Ann. Phys. (Leipzig) **2**, 465 (1993).
[9]L. D. Bell, Phys. Rev. Lett. **77**, 3893 (1996).
[10]R. Coratger, R. Pechon, F. Ajustron, and J. Beauvillain, Eur. Phys. J.: Appl. Phys. **5**, 237 (1999).
[11]C. Manke, Y. Bodschwinna, and M. Schulz, Appl. Surf. Sci. **117/118**, 321 (1997).
[12]M. K. Weilmeier, W. H. Rippard, and R. A. Buhrman, Phys. Rev. B **59**, R2521 (1999).
[13]H. Palm, M. Arbes, and M. Schulz, Appl. Phys. A: Solids Surf. **56**, 1 (1993).
[14]A. M. Milliken, S. J. Manion, W. J. Kaiser, L. D. Bell, and M. H. Hecht, Phys. Rev. B **46**, 12826 (1992).
[15]C. A. Ventrice, V. P. LaBella, G. Ramaswany, H.-P. Yu, and L. J. Schowalter, Phys. Rev. B **53**, 3952 (1996).
[16]R. Ludeke and A. Bauer, Phys. Rev. Lett. **71**, 1760 (1993); J. Vac. Sci. Technol. A **12**, 1910 (1994).
[17]L. J. Schowalter and E. Y. Lee, Phys. Rev. B **43**, 9308 (1991).
[18]P. Niedemann and L. Quattropani, Phys. Rev. B **48**, 8833 (1993).
[19]E. Y. Lee, H. Sirringhaus, U. Kafader, and H. von Kanel, Phys. Rev. B **52**, 1816 (1995).
[20]K. G. Ashar, *Magnetic Disk Drive Technology* (IEEE, New York, 1997).
[21]W. Park, R. Loloee, J. A. Caballero, W. P. Pratt, Jr., P. A. Schroeder, J. Bass, A. Fert, and C. Vouille, J. Appl. Phys. **85**, 4542 (1999).
[22]M. A. Gijs and G. E. W. Bauer, Adv. Phys. **46**, 285 (1997).
[23]D. J. Monsma, J. C. Lodder, Th. J. A. Popma, and B. Dieny, Phys. Rev. Lett. **74**, 5260 (1995).
[24]T. Kinno, K. Tanaka, and K. Migushima, Phys. Rev. B **56**, R4391 (1997).
[25]P. N. First, J. A. Bonetti, D. K. Guthrie, L. E. Harrell, and S. S. P. Parkin, J. Appl. Phys. **81**, 5533 (1997).
[26]W. H. Rippard and R. A. Buhrman, Appl. Phys. Lett. **75**, 1001 (1999).
[27]W. H. Rippard and R. A. Buhrman, Phys. Rev. Lett. **84**, 4 (2000).
[28]R. P. Lu, B. A. Morgan, K. L. Kavanagh, C. J. Powell, P. J. Chen, F. G. Serpa, and W. F. Egelhoff, Jr., J. Appl. Phys. **87**, 5164 (2000).
[29]Certain commercial products are identified here to specify the experimental conditions. Such identification is not intended to imply recommendation of endorsement by the National Institute of Standards and Technology, nor is it intended to imply that the product identified is necessarily the best available for the purpose.
[30]E. H. Rhoderick and R. H. Williams, *Metal-Semiconductor Contacts* (Clarendon, Oxford, 1988).

Ferromagnetic MnAs grown on GaAs(001): *In situ* investigations

M. Kästner,[a] F. Schippan, P. Schützendübe, L. Däweritz, and K. Ploog
Paul Drude Institute for Solid State Electronics, 10 117 Berlin, Germany

(Received 17 January 2000; accepted 1 May 2000)

We have grown ferromagnetic α-MnAs layers on GaAs(001) by molecular beam epitaxy. The surface was studied during growth by reflection high-energy electron diffraction (RHEED) and reflectance difference spectroscopy (RDS) and after growth by *in situ* scanning tunneling microscopy (STM). During nucleation on the $c(4\times4)$ reconstructed GaAs(001) surface the RHEED pattern disappears. STM images at this stage show well defined steps and flat terraces, but a disordered structure on the terraces. After deposition of 1.5 ML MnAs small three-dimensional clusters have been observed by STM. For thicker layers several phases of the MnAs($\bar{1}100$) surface with different reconstructions have been observed by RHEED. Intensity oscillations of the specular spot have been found for As-rich growth at 265 °C substrate temperature and deposition rates of 0.2–0.65 ML/s. For temperatures below 360 °C a feature was found in the RD spectra that is sensitive to the surface reconstruction. At higher temperatures the RD spectra did not depend on the surface structure. The (1×2) and (1×1) reconstructions have been cooled down to room temperature. Atomic scale images of these surfaces are presented. The images of the (1×2) structure show asymmetric protrusions, consequently this structure has only onefold symmetry. This leads to the formation of reconstruction domains with opposite orientations of the unit mesh in adjacent domains. The domain boundaries run along the [0001] direction. © *2000 American Vacuum Society.* [S0734-211X(00)03604-0]

I. INTRODUCTION

Manganese arsenide has a ferromagnetic phase at room temperature (α-MnAs) and grows epitaxially on GaAs. It is therefore a promising candidate for successful integration of magnetic materials in semiconductor structures. Moreover, it is a representative of a whole class of materials, the transition metal pnictides. Related materials having the same crystal structure show a large variety of magnetic properties: MnSb and MnBi are also ferromagnetic,[1,2] CrSb, FeSb, and CoSb are antiferromagnetic, TiSb and NiAs are paramagnetic and NiSb is diamagnetic.[3,4] Magnetic and nonmagnetic materials might thus be combined within this material class, offering a number of interesting possibilities for realization of heterostructures. Optimized layers for applications require sophisticated growth procedures and careful analysis and understanding of the growth process. This article is concerned with the growth properties of MnAs studied by *in situ* methods.

II. EXPERIMENT

Growth was performed in a molecular beam epitaxy (MBE) system equipped with standard MBE evaporators for Ga and Mn and a valved cracker cell for As_4. Reflection high-energy electron diffraction (RHEED) and reflectance difference spectroscopy (RDS) were used for *in situ* growth control.

The substrates were commercially available silicon doped GaAs(001) wafers with a miscut of $\pm0.05°$ and a carrier concentration of 2×10^{18} cm^{-3}. For the scanning tunneling microscopy (STM) investigation of nucleation we have used substrates with a misorientation of 2° towards [110] in order to obtain a well defined step structure on the substrate. The temperature was measured by a thermocouple, oxide desorption from the epiready substrate at 580 °C was used to calibrate the temperature scale. After oxide desorption a 250 nm Si doped GaAs buffer layer was grown at 550 °C, with a Si concentration of 7×10^{17} cm^{-3}.

RHEED and RDS measurements were performed *in situ* on the growing surface as well as on the static surface. After growth the samples were cooled down to room temperature and transferred under ultrahigh vacuum conditions to the STM. The RHEED pattern observed at low temperatures ($\leq$330 °C) did not change during cooling to room temperature, unlike the pattern observed at higher temperature, which changed to the low temperature pattern during cooling. Therefore, a special annealing procedure (described elsewhere[5]) was used to prepare the (1×1) structure for the STM measurement.

III. CRYSTAL STRUCTURE AND EPITAXIAL ORIENTATION

The crystal structure of α-MnAs is hexagonal, with the symmetry group $P6_3/mmc$ and lattice constants $a=3.72$ Å and $c=5.71$ Å. [6] Thus, the distance of adjacent atoms of the same kind in the c direction is 2.86 Å. The epitaxial relation between the MnAs film and the GaAs substrate depends on the growth conditions during nucleation. It has been shown that the growth direction and the final crystalline structure of MnAs depends crucially on the growth condition for the first few monolayers.[7,8] If the MnAs film nucleates under Mn-rich conditions, the growth plane [i.e., the lattice plane parallel to the (001) surface of the GaAs substrate] is ($\bar{1}101$) oriented according to Ref. 9. If the film nucleates under As-rich conditions, the growth plane is ($\bar{1}100$) oriented.[9,10] The c axis is

[a]Electronic mail: kaestner@pdi-berlin.de

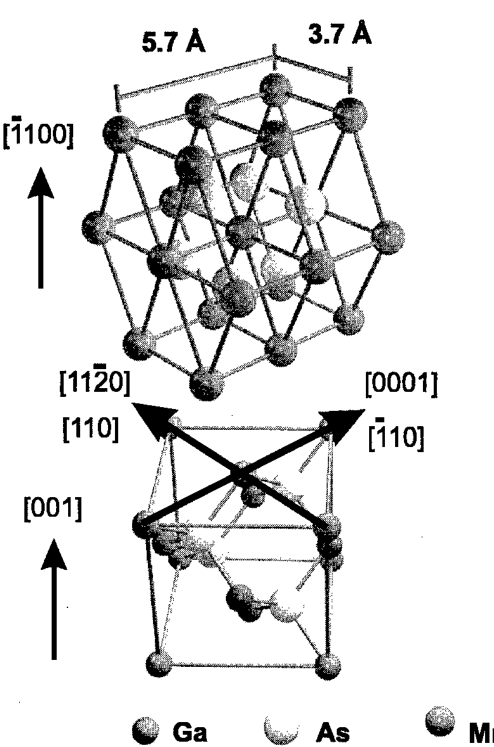

FIG. 1. Epitaxial relationship between MnAs($\bar{1}100$) and GaAs(001) (Ref. 14). The c axis of the hexagonal MnAs unit cell lies in the growth plane.

then parallel to the $[\bar{1}10]$ direction of the GaAs substrate, as shown in Fig. 1. We have chosen As-rich conditions.

The lattice misfit along the c axis of MnAs, defined as

$$f=\frac{d_{\mathrm{MnAs}}\{0001\}-d_{\mathrm{GaAs}}\{\bar{1}10\}}{d_{\mathrm{GaAs}}\{\bar{1}10\}},$$

[where $d_{\mathrm{MnAs}}\{hklm\}$ and $d_{\mathrm{GaAs}}\{hkl\}$ are the distances between corresponding lattice planes] is 43%. Even in the case that a misfit is defined on the base of the distance of adjacent lattice planes of the same kind $[d_{\mathrm{MnAs}}\{0002\}]$, it amounts to -29%. This value is so high that epitaxial growth can hardly be expected. As pointed out, however, already in earlier work,[11] the epitaxial relationship corresponds to a coincident lattice[12] with two units of α-MnAs to three units of GaAs in the $[\bar{1}10]$ direction. The formation of a near coincidence lattice was experimentally confirmed by high-resolution transmission electron microscopy.[10,13] Every fourth {0002} MnAs plane fits every sixth {220} GaAs plane. This 2 to 3 coincident lattice reduces the lattice misfit to -4.8%, which is still large, but small enough to allow epitaxial growth. The lattice misfit along the other in plane direction (perpendicular to the c axis) is -6.9% with a 1 to 1 coincident lattice.[11] This misfit is accommodated by regularly arranged misfit dislocations.[10,13]

IV. MORPHOLOGY

From a *thermodynamical* point of view, because of the strain in a lattice mismatched system, three-dimensional (3D) islanding is expected. Depending on the surface energies of substrate and film γ_s, γ_f and the energy of the substrate–film interface γ_{sf}, 3D islands should form either right from the start (Frank–van der Merve growth if $\gamma_s < \gamma_f + \gamma_{sf}$), or after a two-dimensional (2D) wetting layer has been formed (Stranski–Krastanov growth if $\gamma_s > \gamma_f + \gamma_{sf}$). At low growth rates and high growth temperatures this picture may explain the observed growth morphologies. On the other hand, at high growth rates and low growth temperatures the morphology will be determined by *kinetic* limitations and may therefore be different. One kinetic process that is critical for the evolution of surface morphology is nucleation.

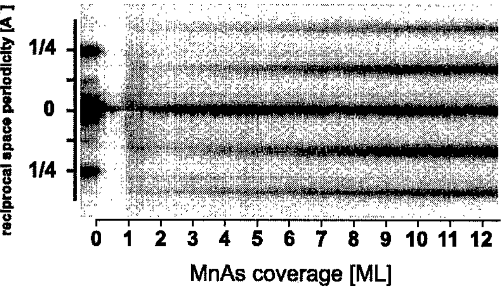

FIG. 2. RHEED intensity profile evolution as a function of MnAs coverage at a substrate temperature of 250 °C.

A. Nucleation

1. Low substrate temperature

Figure 2 shows the evolution of the RHEED pattern when the electron beam is directed along the MnAs[$11\bar{2}0$] direction.[14] The figure was obtained by recording the RHEED intensity along a line across the RHEED pattern as a function of time during growth at constant deposition rate. The growth temperature was 250 °C. After the Mn shutter was opened, the RHEED pattern of the GaAs substrate immediately disappeared, only the diffuse background intensity was observed on the RHEED screen. After deposition of approximately 1 ML the MnAs RHEED pattern appeared.

In agreement with the diffuse RHEED, a rather disordered structure is observed by STM at the early stages of growth. At first irregular shaped 2D clusters appear. Later, 3D clusters are formed, which are more or less rectangular. Figure 3(a) shows the bare GaAs substrate. A number of monolayer steps is observed, separating flat terraces with a mean terrace width of 80 Å in accordance with the 2° misorientation. Figure 3(b) shows the substrate covered with 0.4 ML MnAs. Small clusters are formed on the surface. They do not have a particular form. A similar disordered phase has been observed by RHEED and STM for the growth of epitaxial FeAl films on AlAs/GaAs.[15] From the diffuse RHEED it was concluded, that the crystal structure of the clusters is not very well defined at this stage, or at least that they are not properly oriented on the substrate. If this is true one has to wonder how the order is restored during later stages of growth. Another explanation might be that the size of the clusters is too small to allow the formation of a reconstruction. At a coverage of 1.5 ML 3D islands have formed, as can be seen in Fig. 3(c). Their base planes tend to become rectangular,

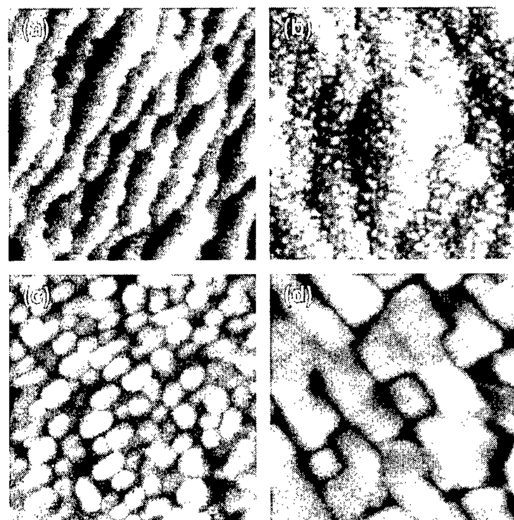

FIG. 3. Evolution of MnAs film morphology with increasing coverage at $T_{sub}=250\,^{\circ}C$: (a) 0 ML (bare substrate, 800 Å×800 Å), (b) 0.4 ML(800 Å ×800 Å), (c) 1.5 ML (1000 Å×1000 Å), (d) 5.5 ML (1000 Å×1000 Å).

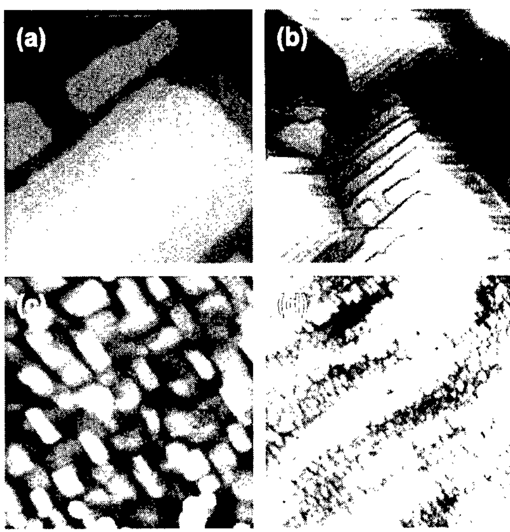

FIG. 5. Roughness and step morphology of 10 nm MnAs grown on GaAs(001) at 250 °C with a As_4/Mn—BEP ratio of 300. (a) 1000 Å×1000 Å, (b) 2700 Å×2700 Å, (c) 0.5 μm×0.5 μm, (d) 2 μm×2 μm. The roughness is of the order 10 Å for a 2 μm×2 μm STM scan.

with the edges oriented along the principal crystallographic axes of the substrate. Their tops appear rounded in the STM images. Due to the increased degree of order in the film, RHEED patterns can be observed at this coverage. Figure 3(d) shows 5.5 ML MnAs deposited on the substrate. Due to coalescence a smooth film has developed from the individual islands. Some portions of the film seem to resist against incorporation, causing deep trenches in the film. Between these trenches, the surface is very flat, and monolayer steps can be observed. At this stage the RHEED patterns are clear and streaky.

2. High substrate temperature

During nucleation at higher temperatures the RHEED patterns of the GaAs substrate fade away more slowly. They remain visible during the deposition of the first monolayer MnAs. At a growth temperature of 380 °C the first new reflections were observed after 1–1.5 ML MnAs was deposited. In contrast to the lower growth temperature, in this case the new reflections were spotty.

Figure 4 shows the morphology of 1.5 ML MnAs grown at 380 °C. Deposition was stopped after the first new reflections were observed by RHEED. Two types of islands can be distinguished. The first, three-dimensional type of islands is typically about 20 Å high and 120 Å wide. The second, two-dimensional type is much flatter and many of these flat islands are very elongated (e.g., 60 Å wide, 270 Å long, 8–12 Å high, lateral aspect ratio 4.5, vertical aspect ratio 6 or 27, respectively). According to this morphology, the spotty RHEED reflections are transmission patterns from the three-dimensional islands.

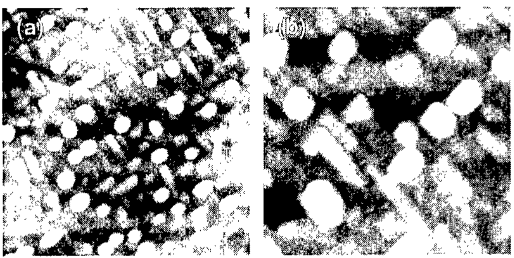

FIG. 4. Morphology of 1.5 ML MnAs grown at 380 °C. (a) 2000 Å×2000 Å, (b) 1000 Å×1000 Å. Two- and three-dimensional islands are observed.

B. Growth

During the growth of thicker layers we have found RHEED intensity oscillations.[16] This is important from a practical point of view because this provides a convenient way of measuring the growth rate *in situ* and with monolayer precision. Moreover, RHEED oscillations can be used to characterize the growth dynamics, and they are indicating layer-by-layer growth.

For the standard growth conditions ($T=250\,^{\circ}C$ and $R=10$ nm/h) RHEED oscillations were not observed. In spite of that, the MnAs layer is very smooth: Atomically flat terraces exist [Fig. 5(a)] and the rms roughness is of the order of 10 Å for a 2μm×2μm STM scan [Fig. 5(d)]. Because the density of 3D islands formed in the nucleation process is high, the islands can coalesce and form a closed film at an early stage of growth while the islands are still small. This leads to the observed smoothness of the MnAs film. Combining these findings we suggest that the best method to grow MnAs layers is to apply a low growth temperature and a low growth rate during the nucleation phase. After nucleation has been completed, temperature and growth rate can be increased in order to achieve high quality layers in reasonable time.

V. SURFACE RECONSTRUCTIONS

Surface reconstructions modify kinetic processes like surface diffusion and adatom incorporation[17,18] which are important during MBE growth, and can therefore have a con-

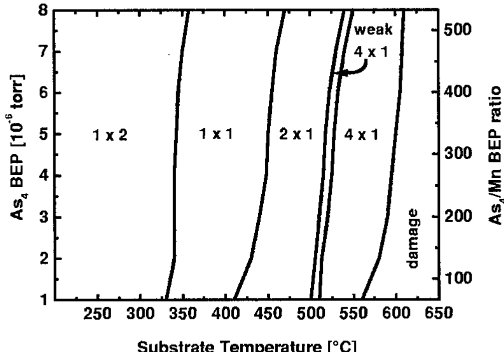

FIG. 6. Surface phase diagram of MnAs($\bar{1}100$) growth from Mn and As_4 beams. MnAs growth rate: 10 nm/h (Ref. 16).

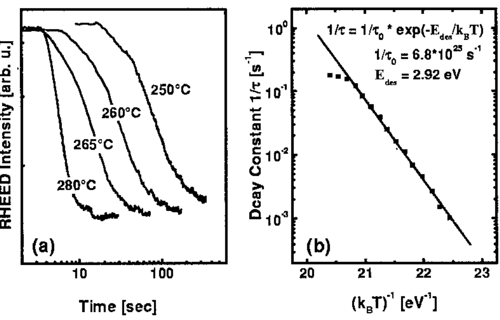

FIG. 7. (a) Example curves for the exponential decay of the intensity of the half-order RHEED spot during (1×2) to (1×1) transition. (b) Arrhenius plot of the decay constants. For comparison: bond energies in diatomic molecules are 2.174 eV for As–Ga and 3.962 eV for As–As bond, respectively.

siderable influence on the growth mode. For the MnAs/GaAs(001) system for example, it was found that MnAs grows best on the As-rich $d(4\times4)$ reconstruction of the substrate.[7,14] During growth of MnAs/GaAs/MnAs trilayer heterostructures on GaAs(111)B the GaAs grows monocrystalline on the As-rich MnAs(0001)–(3×2) surface but polycrystalline on the MnAs(0001)–(2×2) surface.[19]

A. RHEED AND STM

For the MnAs($\bar{1}100$) surface several reconstructions have been observed by RHEED.[16] Which one of them actually occurs depends on the growth conditions. This dependence is summarized in Fig. 6. The reconstruction depends mainly on the growth temperature, but within narrow temperature regions it is also possible to switch between two reconstructions by changing the As_4 beam equivalent pressure (BEP). This shows that the (1×2) surface is probably As terminated.

Consider the following desorption experiment: According to the phase diagram (Fig. 6) a change from high to low As_4 BEP in the temperature range from 330 to 360 °C will change the reconstruction from a (1×2) to a (1×1) structure. Starting from an As_4 BEP of 6×10^{-6} Torr, we have measured the intensity of the half-order spot as a function of time after the As valve was suddenly closed. For all temperatures an exponential decay was observed. Example curves are shown in Fig. 7(a). The decay constants follow an Arrhenius law. The activation energy and especially the pre-exponential factor obtained from the Arrhenius plot [Fig. 7(b)] are unusually large, therefore a direct physical interpretation of these quantities is not obvious. Thus, the transition from the (1×1) to the (1×2) reconstruction takes place by As adsorption, the (1×2) structure is therefore probably As terminated. A similar argument applies to the transition from the (2×1) to the (1×1) structure, so we assume that both, the (1×1) and the (1×2) reconstructed surfaces, are As terminated.

Figure 8 shows two atomic scale STM images of the (1×1) and the (1×2) reconstructions, respectively. The interatomic spacings are 3.8±0.5 Å in the $[11\bar{2}0]$ direction, and 5.8±0.5 Å in the [0001] direction for the (1×1) structure in Fig. 8(a) and 7.3±0.5 Å in the $[11\bar{2}0]$ direction, and 5.8 ±0.5 Å in the [0001] direction for the (1×2) structure in Fig. 8(b). These values agree well with the literature[6] and the results from our RHEED observations.[5,14] It should be noted that the image of the (1×1) reconstruction was taken from a sample that was not fully (1×1) reconstructed. Part of the surface was still (1×2) reconstructed.[5]

An interesting special feature of the (1×2) structure is evident from Fig. 8(b): this structure does not have twofold symmetry as might be expected from the symmetry of the MnAs lattice. The unit mesh has one straight and one curved edge along the $[11\bar{2}0]$ direction, as indicated by the "D" in Fig. 8(b). Therefore the symmetry is only onefold. Because of this asymmetry in the surface unit mesh, the reconstructed surface consists of different domains. In adjacent domains the structure of the surface is rotated about 180°, and the surface lattice is shifted by one half of the lattice constant along the [0001] direction. A domain boundary is indicated by the dashed line in Fig. 8(b). As a consequence, the structure model for the (1×2) reconstruction should reflect this asymmetry, as discussed elsewhere.[5]

B. Reflectance difference spectroscopy

In many studies[20–22] RDS was used to decide which of several existing surface structure models is most realistic. Additionally, RDS provides information on the composition of the surfaces of compound semiconductors. In this sense it

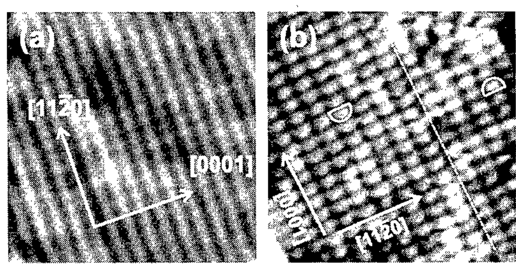

FIG. 8. STM images of MnAs($\bar{1}100$) surfaces: (a) (1×1) reconstructed and (b) (1×2) reconstructed surface. Different domains of the (1×2) reconstruction are visible. Image sizes are (a) 80×80 Å^2 and (b) 100×100 Å^2.

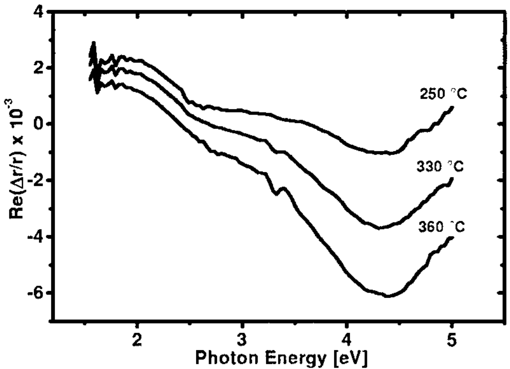

FIG. 9. Reflectance difference spectra, measured at various temperatures. At 360 °C and below the spectra show a temperature dependent optical anisotropy at 4.5 eV that increases with increasing temperature.

is complementary to STM. It is a useful tool for *in situ* growth control and therefore it is interesting to see if it can be used to control the growth of MnAs films.

The reflectance difference spectra in Fig. 9 show a temperature dependent anisotropy at 4.5 eV. The anisotropy increases with the temperature. It is strongest for the fully (1×1) reconstructed surface at 360 °C, and only weak for the (1×2) surface at 250 °C. At 400 °C and higher temperatures the optical anisotropy neither depends on the temperature, nor on the surface reconstruction.[5]

Successful application of RDS is often based on the comparison of experimental data to calculated spectra. Here we have to interpret the observed spectra in terms of simple arguments because calculations of MnAs RD spectra do not exist. Because the anisotropy at 4.5 eV is strongest for the fully (1×1) reconstructed surface, it can be ascribed to the (1×1) reconstruction.[5] In the spectrum at 250 °C, it is weak but still detectable. This shows that while the largest part of the surface is (1×2) reconstructed, as indicated by RHEED, a small fraction of the surface is still (1×1) reconstructed. This cannot be inferred from the RHEED patterns and thus shows that RDS can be used as a very sensitive tool also for *in situ* control of the growth of MnAs.

Additional strong features are not present in the spectrum of the (1×2) reconstructed surface. Many studies report that surface dimers usually lead to pronounced features in the RD spectrum.[20,22] Because such features are not observed, we assume that the (1×2) structure does not contain surface dimers. A more detailed explanation of the RDS spectra based on the comparison to calculated spectra is of course highly desirable and we expect that this would yield valuable information concerning surface structure and composition.

VI. SUMMARY

We have studied nucleation, growth and surface reconstructions of MnAs on GaAs(001) *in situ* with RHEED, RDS, and STM. As expected for lattice mismatched epitaxy, two-dimensional islands are formed for submonolayer deposition, and later three-dimensional islands appear. At $T_{sub}=250$ °C the RHEED patterns disappear in the submonolayer regime, while they persist at $T_{sub}=380$ °C. The corresponding STM images show a high density of irregular shaped two-dimensional clusters at the lower temperature, and a lower density of two-dimensional, rectangular shaped islands at higher temperature. Also the density of 3D islands is higher at lower temperatures, as expected. The high density of 3D islands at 250 °C leads to smooth films. When the temperature is raised to 265 °C, RHEED oscillations can be observed, indicating layer by layer growth.

Atomic scale STM images of the (1×2) and (1×1) reconstructions were presented, showing that the (1×2) surface has an asymmetric unit mesh and therefore different reconstruction domains. At low temperatures ($T\leq360$ °C) a temperature dependent optical anisotropy was found at ~4.5 eV that is indicative of the (1×1) reconstruction.

[1]R. Coehorn, C. Haas, and R. A. de Groot, Phys. Rev. B **31**, 1980 (1985).
[2]R. Coehorn and R. A. de Groot, J. Phys. F: Met. Phys. **15**, 2135 (1985).
[3]J. W. Allen and W. Stutius, Solid State Commun. **20**, 561 (1976).
[4]K. Motizuki, J. Magn. Magn. Mater. **70**, 1 (1987).
[5]M. Kästner, F. Schippan, P. Schützendübe, L. Däweritz, and K. H. Ploog, Surf. Sci. (to be published).
[6]Powder Diffraction File, ICCD, Swartsmoor, Pennsylvania, USA, PDF 280644.
[7]M. Tanaka, J. P. Harbison, M. C. Park, Y. S. Park, T. Shin, and G. M. Rothberg, J. Appl. Phys. **76**, 6278 (1994).
[8]M. Tanaka, J. Harbison, M. Park, Y. Park, T. Shin, and G. Rothberg, Appl. Phys. Lett. **65**, 1964 (1994).
[9]M. Tanaka, Mater. Sci. Eng., B **31**, 117 (1995).
[10]F. Schippan, A. Trampert, L. Däweritz, K. Ploog, B. Dennis, K. Neumann, and K. Ziebeck, J. Cryst. Growth **201/202**, 674 (1999).
[11]C. J. Palmstrøm, Annu. Rev. Mater. Sci. **25**, 389 (1995).
[12]N. Fletcher and K. W. Lodge, in *Epitaxial Growth, Part B*, edited by J. W. Matthews (Academic, New York, 1975), p. 529.
[13]A. Trampert, F. Schippan, L. Däweritz, and K. Ploog, *Int. Phys. Conf. Ser.* (IOP, Bristol, 1999), Vol. 164, p. 305.
[14]F. Schippan, A. Trampert, L. Däweritz, and K. Ploog, J. Vac. Sci. Technol. B **17**, 1716 (1999).
[15]B. E. Ishaug, S. M. Seutter, A. M. Dabiran, P. I. Cohen, R. F. C. Farrow, D. Weller, and S. S. P. Parkin, Surf. Sci. **380**, 75 (1997).
[16]F. Schippan, M. Kästner, L. Däweritz, and K. H. Ploog, Appl. Phys. Lett. **76**, 834 (2000).
[17]B. Voigtländer, M. Kästner, and P. Šmilauer, Phys. Rev. Lett. **81**, 858 (1998).
[18]J. Mysliveček, T. Jarolímek, P. Šmilauer, and M. Kästner, Phys. Rev. B **60**, 13869 (1999).
[19]M. Tanaka, K. Saito, and T. Nishinaga, Appl. Phys. Lett. **74**, 64 (1999).
[20]I. Kamiya, D. E. Aspnes, L. T. Florez, and J. P. Harbison, Phys. Rev. B **46**, 15894 (1992).
[21]W. G. Schmidt, F. Bechstedt, N. Esser, M. Pristovsek, C. Schultz, and W. Richter, Phys. Rev. B **57**, 14596 (1998).
[22]A. I. Shkrebtii, N. Esser, W. Richter, W. G. Schmidt, F. Bechstedt, O. Fimland, A. Kley, and R. Del Sole, Phys. Rev. Lett. **81**, 721 (1998).

Epitaxial ferromagnetic metal/GaAs(100) heterostructures

L. C. Chen,[a] J. W. Dong, B. D. Schultz, and C. J. Palmstrøm
Department of Chemical Engineering and Materials Science, University of Minnesota, Minneapolis, Minnesota 55455

J. Berezovsky, A. Isakovic, and P. A. Crowell
Department of Physics and Astronomy, University of Minnesota, Minneapolis, Minnesota 55455

N. Tabat
Recording Head Operations, Seagate Technology, Minneapolis, Minnesota 55435

(Received 6 April 2000; accepted 26 May 2000)

Ferromagnetic bcc-Fe_xCo_{1-x}(100) films have been successfully grown on GaAs(100) and Sc_yEr_{1-y}As(100) by molecular beam epitaxy. X-ray diffraction combined with reflection high energy electron diffraction and low energy electron diffraction patterns revealed the epitaxial orientation of bcc-Fe_xCo_{1-x}(100)⟨010⟩‖GaAs(100)⟨010⟩ and bcc-Fe_xCo_{1-x}(100)⟨010⟩‖Sc_yEr_{1-y}As(100)⟨010⟩. Rutherford backscattering channeling minimum yields, $\chi_{\rm min}\sim 3\%$, suggest epitaxial films of high crystalline quality. Vibrating sample magnetometry measurements show in-plane uniaxial anisotropy and fourfold in-plane anisotropy for Fe_xCo_{1-x} grown on GaAs(100) and Sc_yEr_{1-y}As(100), respectively. The difference in magnetic anisotropy is interpreted as arising from the Sc_yEr_{1-y}As interlayer altering the surface symmetry from twofold symmetry for GaAs(100) to fourfold symmetry. Misoriented substrates were also used to increase the step density in the [011] direction, which induced an additional uniaxial anisotropy with a [011] easy axis and a $[01\bar{1}]$ hard axis. This step structure symmetry-induced magnetic anisotropy generated a split field ~50 Oe in the hard axis for bcc-Fe_xCo_{1-x}(100) grown on Sc_yEr_{1-y}As(100) surfaces. © *2000 American Vacuum Society.* [S0734-211X(00)07104-3]

I. INTRODUCTION

Ferromagnet/semiconductor heterostructures are of growing interest for the development of spintronic devices.[1] The electronic and magnetic properties of ferromagnets play an essential role in designing ferromagnet/semiconductor heterostructures for spin injection and spin tunneling injection. Ferromagnetic Fe_xCo_{1-x} alloys are technologically important because of their high permeability, saturation magnetization, and magnetocrystalline anisotropy combined with low coercivity.[2] In the bulk, the bcc-Fe_xCo_{1-x} lattice constant,[3] magnetic moment,[4] and easy axis[5] can be adjusted by changing the Fe to Co ratio. Although detailed studies of Fe/GaAs[6–8] and Fe_xCo_{1-x}/ZnSe[9,10] heterostructures have been performed, only recently have Fe_xCo_{1-x} films been grown on GaAs(100).[11,12] For epitaxial growth of elemental metallic films on GaAs, interfacial reactions generally occur. For Fe, the interfacial reactions result in As accumulation on the surface during growth.[13,14] The reactions can be minimized by low temperature growth and the use of an epitaxial diffusion barrier. Sc_yEr_{1-y}As can be grown epitaxially on GaAs and is thermodynamically stable,[15] suggesting it may act as an excellent diffusion barrier between Fe_xCo_{1-x} and GaAs.

The GaAs(100) surface has twofold symmetry due to the sp^3 covalent bonding. The surface of Sc_yEr_{1-y}As(100), which has the NaCl crystal structure, is fourfold symmetric, and can be easily grown on GaAs(100).[15] Therefore, a Sc_yEr_{1-y}As interlayer is expected to convert the surface symmetry from the twofold of GaAs(100) substrate to fourfold.

The substrate surface symmetry has been shown to control the in-plane magnetic anisotropy of ferromagnetic thin films grown on metallic substrates.[16] For GaAs(100), the surface steps run along the ⟨011⟩ directions and are typically one bilayer high (2.83 Å).[17] The step density depends upon the misorientation of the surface with respect to the crystalline plane. Figure 1 shows the schematic drawing of GaAs(100) step structure with miscut $\theta°$ toward (111)A. The GaAs(100) substrate with a 4° miscut towards (111)A will have steps running along the $[01\bar{1}]$ direction with a terrace width ~40 Å and density of $\sim 2.5\times 10^6$ steps/cm in the [011] direction (Fig. 1). This step structure will induce an additional twofold symmetry on the substrate surface.

In this article, the surface symmetry of the GaAs(100) substrate is altered by the use of a Sc_yEr_{1-y}As interlayer and by the use of misorientated substrates. The effects on the magnetic properties of epitaxial Fe_xCo_{1-x} grown on these substrates will be discussed.

II. EXPERIMENTAL TECHNIQUES

n-doped GaAs(100) substrates [nominally 0°, 4°, 6°, 8°, and 10° miscut toward the (111)A surface] were indium bonded to molybdenum sample holders and loaded into the preparation chamber through a load lock of a modified VG Semicon V80H molecular beam epitaxy (MBE) system, which has a base pressure of $\sim 5\times 10^{-11}$ mbar. After outgas-

[a]Author to whom correspondence should be addressed; electronic mail: chenx102@umn.edu

FIG. 1. Twofold surface symmetry of the GaAs(100) vicinal surface with $\theta°$ miscut towards (111)A.

sing at 250 °C in the preparation chamber, the samples were transported to the growth chamber where the depositions were performed. For each substrate, after native oxide removal at 610 °C under an As_4 flux, a 0.5 μm thick Si doped n ($10^{16}/cm^3$) GaAs buffer layer was grown at 585 °C. Each sample was cooled to 95 °C while maintaining the (2×4) surface reconstruction by controlling the valve opening of the arsenic valve cracker during the cooling procedure. For $Sc_yEr_{1-y}As$ interlayers, each sample was cooled to 350 °C under an As_4 flux, at which point 10 monolayers (~28 Å) of $Sc_yEr_{1-y}As$ were grown on the GaAs substrate using high temperature effusion cells for Sc and Er. Further cooling to 95 °C was performed without an As_4 flux. The Fe_xCo_{1-x} alloy films were grown at 95 °C by codeposition from an e-beam evaporation source for Fe and a high temperature effusion cell for Co. The samples were then rotated away from the effusion cells and cooled down to ~0 °C with the help of the liquid-nitrogen cooled cryo panel inside the MBE growth chamber. To protect the films from oxidation, the samples were capped by an ~20 Å Al protective layer deposited at ~0 °C prior to removal from the vacuum system. The alloy films were characterized *in situ* by reflection high energy electron diffraction (RHEED), low energy electron diffraction (LEED), and Auger electron spectroscopy (AES). *Ex situ* structural characterization included Rutherford backscattering spectrometry (RBS) and x-ray diffraction (XRD). The magnetic properties were characterized *ex situ* by vibrating sample magnetometry (VSM) and magneto-optical Kerr effect (MOKE) measurements. The MOKE setup was arranged such that both the longitudinal and transverse polarization could be measured.

III. RESULTS AND DISCUSSIONS

A. Growth and structure characterization

Figures 2 and 3 show the RHEED patterns of Fe_xCo_{1-x}/GaAs and $Fe_xCo_{1-x}/Sc_yEr_{1-y}As$/GaAs heterostructures, respectively. These RHEED patterns were obtained during growth. The RHEED patterns of Fe_xCo_{1-x} films exhibit well-defined Kikuchi lines, indicating high-quality single crystal growth of $Fe_xCo_{1-x}(100)$ on GaAs(100) and $Sc_yEr_{1-y}As(100)$. The spacing of RHEED streaks in the ⟨011⟩ and ⟨010⟩ directions showed a $\sqrt{2}$ ratio, indicating square surface unit cell, which was also observed by LEED. The RHEED patterns showed a 2× reconstruction of Fe_xCo_{1-x} in both [011] and [01$\bar{1}$] directions which is similar to that observed for bcc-Fe/GaAs(100),[13]

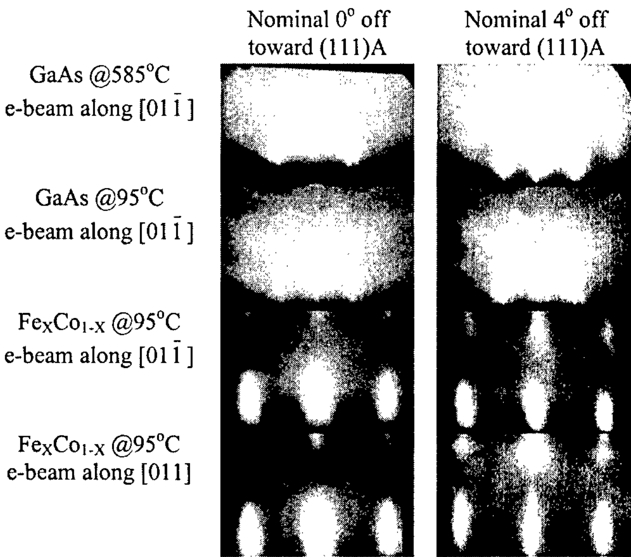

FIG. 2. Reflection high energy electron diffraction patterns of Fe_xCo_{1-x}/GaAs(100) heterostructures with 0° and 4° miscut toward (111)A.

bcc-Co/GaAs(100),[18] bcc-Co/ZnSe(100),[19] bcc-Fe/ZnSe(100),[19] and bcc-Fe_xCo_{1-x}/ZnSe(100).[9,10]

No detectable As, Ga, or other contaminants were detected by AES on ~200 Å thick Fe_xCo_{1-x} films grown directly on GaAs in contrast to the growth of Fe on sputter cleaned and annealed GaAs.[20] Figure 4 shows the XRD patterns of Fe_xCo_{1-x} grown on GaAs(100) and $Sc_yEr_{1-y}As(100)$. The XRD data combined with RHEED and LEED patterns reveal the epitaxial alignment of $Fe_xCo_{1-x}(100)$⟨010⟩‖GaAs(100)⟨010⟩ and $Fe_xCo_{1-x}(100)$ ⟨010⟩‖$Sc_yEr_{1-y}As(100)$⟨010⟩‖GaAs(100)⟨010⟩. The out-of-plane lattice constants of Fe_xCo_{1-x} obtained from XRD are 2.856 Å in both cases, indicating an ~1% mismatch to

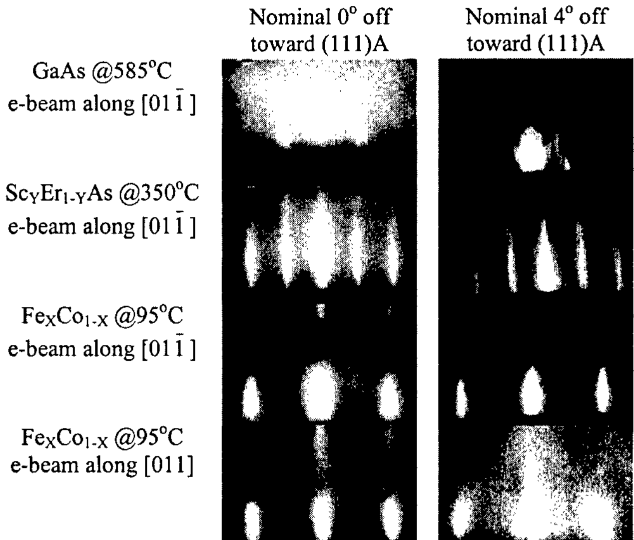

FIG. 3. Reflection high energy electron diffraction patterns of bcc $Fe_xCo_{1-x}(100)/Sc_yEr_{1-y}As(100)$/GaAs(100) heterostructures with 0° and 4° miscut toward (111)A.

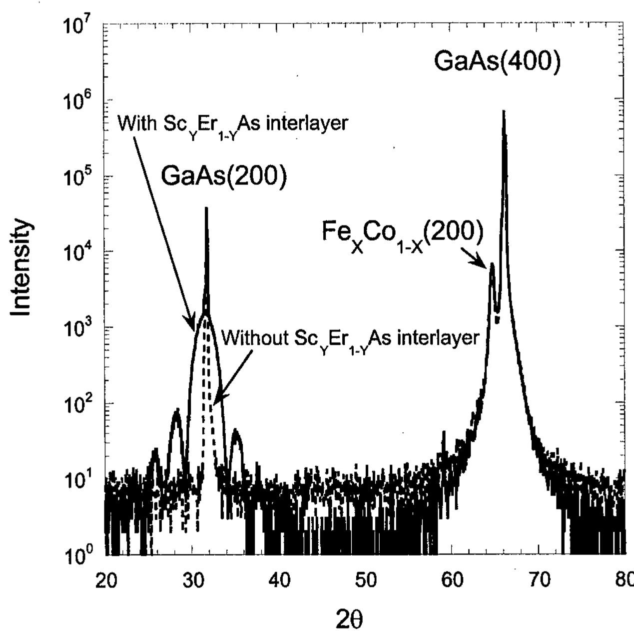

FIG. 4. X-ray diffraction patterns of Fe_xCo_{1-x} thin films grown on GaAs(100) substrates with and without $Sc_yEr_{1-y}As$ interlayer.

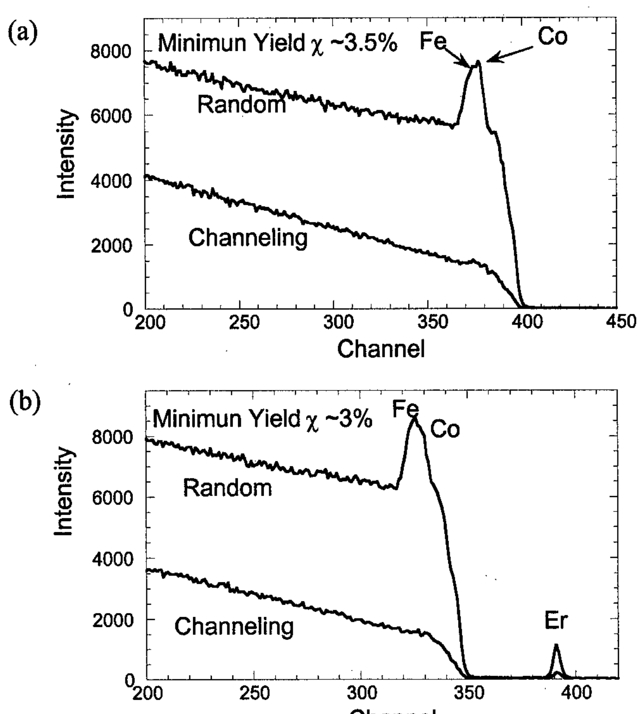

FIG. 5. RBS channeling and random spectra of (a) $Fe_xCo_{1-x}(100)$/GaAs(100)2×4 and (b) $Fe_xCo_{1-x}(100)/Sc_yEr_{1-y}As(100)/n$-GaAs(100).

half the unit cell of both $Sc_yEr_{1-y}As$ and GaAs. The out-of-plane lattice constants obtained from the XRD are close to the lattice constant of bulk bcc-$Fe_{0.5}Co_{0.5}$(2.85 Å),[21] suggesting that the Fe_xCo_{1-x} films are fully relaxed. In the case of Fe_xCo_{1-x} grown on $Sc_yEr_{1-y}As$, the XRD shows a set of satellite peaks around the GaAs(200) peak due to the finite thickness of the $Sc_yEr_{1-y}As$ layer. This indicates abrupt interfaces between Fe_xCo_{1-x}, $Sc_yEr_{1-y}As$, and GaAs.[22,23]

Figure 5 shows the RBS channeling and random spectra of $Fe_xCo_{1-x}(100)$/GaAs(100) and $Fe_xCo_{1-x}(100)/Sc_yEr_{1-y}As(100)$/GaAs(100). The minimum yield (χ_{min}) was obtained from the ratio of Fe_xCo_{1-x} peak area of channeling spectrum to that of random spectrum after background subtraction. The channeling minimum yields of $Fe_xCo_{1-x}(100)$/GaAs(100) and $Fe_xCo_{1-x}(100)/Sc_yEr_{1-y}As(100)$/GaAs(100) were 3.5% and 3%, respectively, which is indicative of high crystalline quality. The ~1:1 composition ratios of Fe_xCo_{1-x} were obtained from the deconvolution of RBS random spectra.

B. Magnetic characterization

VSM hysteresis loops with an applied magnetic field directed along the in-plane ⟨011⟩ and ⟨010⟩ crystalline azimuths for $Fe_xCo_{1-x}(100)/n$-GaAs(100) and $Fe_xCo_{1-x}(100)/Sc_yEr_{1-y}As(100)/n$-GaAs(100) are depicted in Figs. 6(a) and 6(b), respectively. The crystalline azimuths are referred to the GaAs substrate. In Fig. 6(a), it is obvious that the [011] and $[01\bar{1}]$ axes are different. A perfect square hysteresis loop was obtained when the applied field was directed in the [011] direction, suggesting this to be an easy axis. The hysteresis loops with the field along [010] and [001] were identical and are consistent with these being medium hard axes. The hysteresis loop obtained with the field along $[01\bar{1}]$ suggests this to be the hardest axis. This hard axis hysteresis loop has two symmetric split loops which are characterized by a split field (H_s).[24] The split field may result from the combination of magnetocrystalline anisotropy and uniaxial anisotropy.[25] This split field was found to be ~127 Oe.

It has been reported that the in-plane magnetic anisotropy of ferromagnetic metal/semiconductor heterostructures can be altered by surface morphology,[13,26] surface reconstruction,[6–9,13,19,27] and interfacial structures.[9,19,28–30] Since GaAs has a zincblende structure with sp^3 bonding, the bonding on the GaAs(100) surface tends to align in the [011] direction for As atoms or the $[01\bar{1}]$ direction for Ga atoms. Although the reason for the induced uniaxial anisotropy is not known, we believe that the uniaxial anisotropy results from the twofold surface symmetry of GaAs(100)[6–8] resulting from its sp^3 covalent bonding. This is in agreement with the STM studies of Fe grown on GaAs(100).[6–8]

Figure 6(b) shows the hysteresis loops of bcc-$Fe_xCo_{1-x}(100)$ grown on $Sc_yEr_{1-y}As(100)$. The VSM hysteresis loops in [011] and $[01\bar{1}]$ directions are identical, indicating the Fe_xCo_{1-x} films have fourfold anisotropy. Furthermore, the fourfold anisotropy results in no split field ($H_s=0$) in the $Fe_xCo_{1-x}/Sc_yEr_{1-y}As$/GaAs heterostructure. This suggests that the 127 Oe split field in the Fe_xCo_{1-x}/GaAs heterostructure results from the GaAs twofold surface symmetry. This implies that the interfacial structure dominates the magnetic anisotropy. It is unclear why the fourfold in-plane anisotropy of $Fe_xCo_{1-x}/Sc_yEr_{1-y}As$/

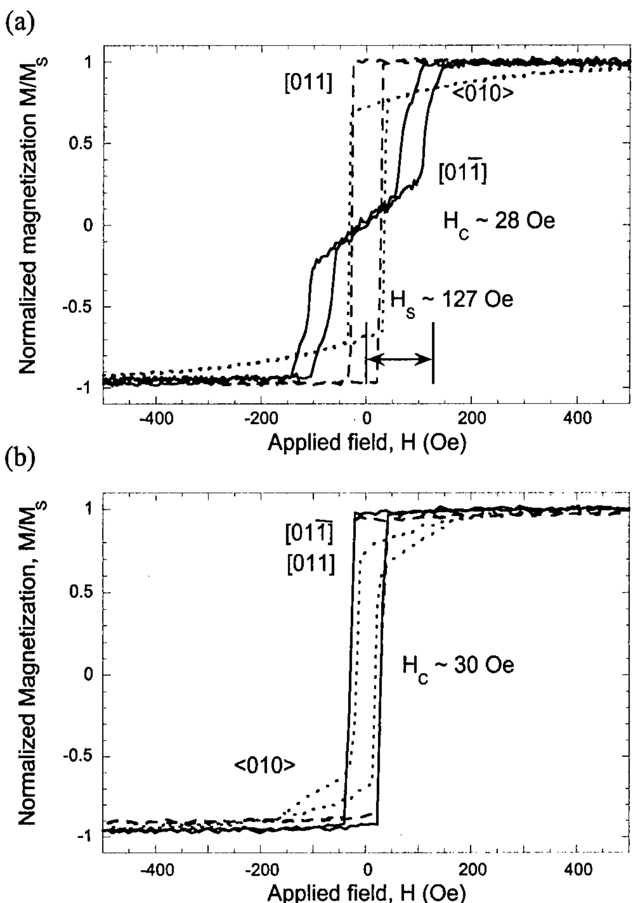

FIG. 6. VSM hysteresis loops of bcc-Fe_xCo_{1-x}(100) grown on GaAs(100) (a) without $Sc_yEr_{1-y}As$ and (b) with a $Sc_yEr_{1-y}As$ interlayer.

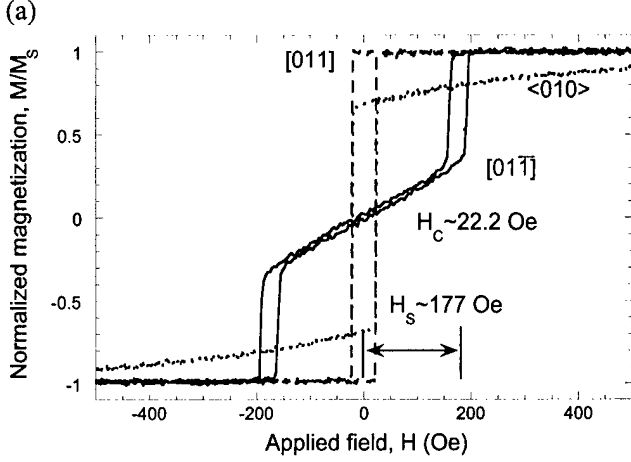

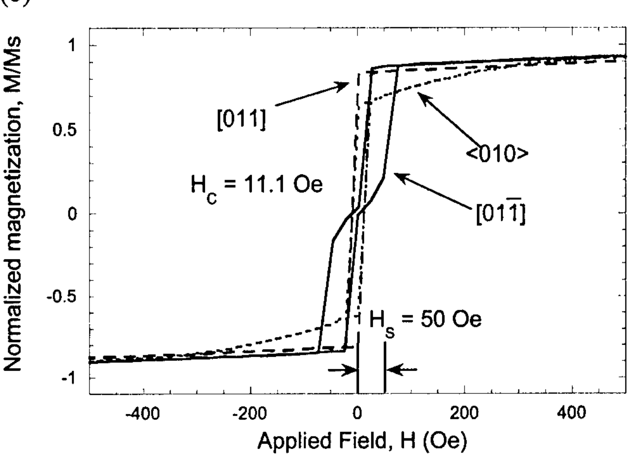

FIG. 7. VSM hysteresis loops of bcc-Fe_xCo_{1-x}(100) grown on GaAs(100) 4° miscut toward (111)A (a) without $Sc_yEr_{1-y}As$ and (b) with $Sc_yEr_{1-y}As$ interlayer.

GaAs(100) has two easy axes in the [011] and [01$\bar{1}$] directions instead of ⟨010⟩ or ⟨111⟩ easy axes as expected for bulk bcc-Fe_xCo_{1-x}.[31] This may result from the $Sc_yEr_{1-y}As$ crystal structure or from the combined effects of shape anisotropy and magnetocrystalline anisotropy.

Stepped surfaces can create symmetry-induced anisotropy in the elemental ferromagnetic thin films grown on the metallic substrates.[16,25,32] By using vicinal GaAs substrates, stepped surfaces can easily be formed. Figure 7(a) shows the hysteresis loops of Fe_xCo_{1-x} grown on GaAs(100) substrate with a 4° miscut toward (111)A. The [011], [01$\bar{1}$], and ⟨010⟩ are easy, hard, and medium hard axes, respectively. The hysteresis loops are similar to those obtained from Fe_xCo_{1-x} grown on GaAs(100) substrate without miscut except that the split field (H_s) increases from ~127 Oe without miscut to ~177 Oe with a 4° miscut in the hard axis. This 50 Oe increase in the split field results from the step symmetry-induced anisotropy. It is equivalent to applying a bias field in the easy axis direction.[24,33] Hence, the misoriented substrate makes the hard axis ([01$\bar{1}$]) require a larger field to saturate the magnetization. Figure 7(b) shows the hysteresis loops of Fe_xCo_{1-x} grown on GaAs(100) substrate with a 4° miscut toward (111)A and with a $Sc_yEr_{1-y}As$ interlayer. The hysteresis loops in the [011] and [01$\bar{1}$] are now different, indicating a uniaxial anisotropy. The easy axis is in the [011] direction and the hard axis is in the [01$\bar{1}$] direction. The hard axis has a set of split loops with ~50 Oe split field. Figure 8 shows the hard axis VSM hysteresis loops of bcc-Fe_xCo_{1-x}/$Sc_yEr_{1-y}As$/GaAs(100) and bcc-Fe_xCo_{1-x}/GaAs(100) with different miscut angles toward (111)A. It is obvious that the higher the misorientation angle, the larger the split field in both cases. The miscut angle dependence of the hard axis hysteresis loops suggests the higher miscut angle, the higher step density, and the stronger uniaxial anisotropy.

The crystal structure symmetry-induced magnetic anisotropy may be considered as an intrinsic anisotropy and the step structure symmetry-induced magnetic anisotropy as an extrinsic anisotropy. The intrinsic anisotropy cannot be changed without modifying the substrate crystal properties but the extrinsic anisotropy can be altered. The GaAs(100)(2×4) creates a uniaxial anisotropy with a [011] easy axis (intrinsic anisotropy) and the GaAs(100) miscut toward (111)A also creates a uniaxial anisotropy with [011] easy axis (extrinsic anisotropy). Therefore, this combination of intrinsic and extrinsic anisotropies induces in-plane magnetic anisotropy in the case of GaAs substrate (twofold crystalline surface symmetry). In the case of the $Sc_yEr_{1-y}As$

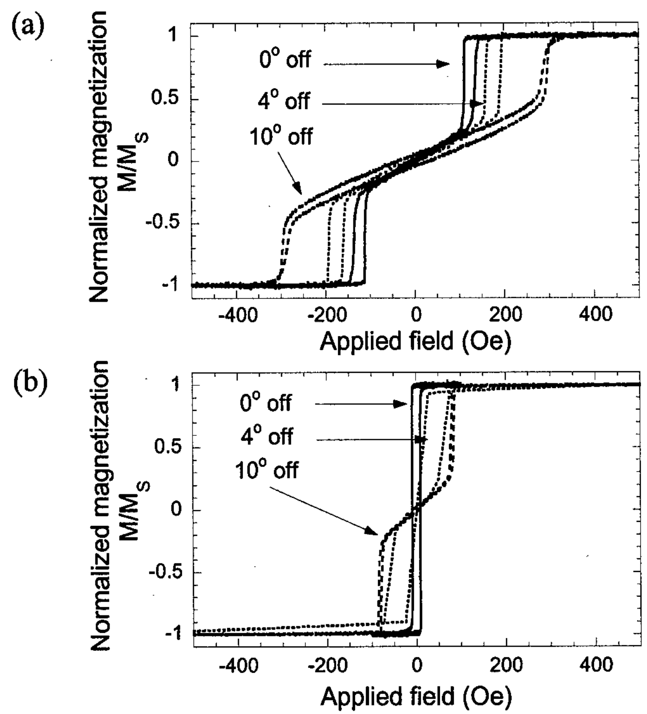

FIG. 8. Miscut angle dependence of VSM hard axis hysteresis loops for (a) bcc-Fe_xCo_{1-x}/n-GaAs(100) and (b) bcc-Fe_xCo_{1-x}/$Sc_yEr_{1-y}As$/n-GaAs(100) with 0°, 4°, and 10° miscut toward (111)A.

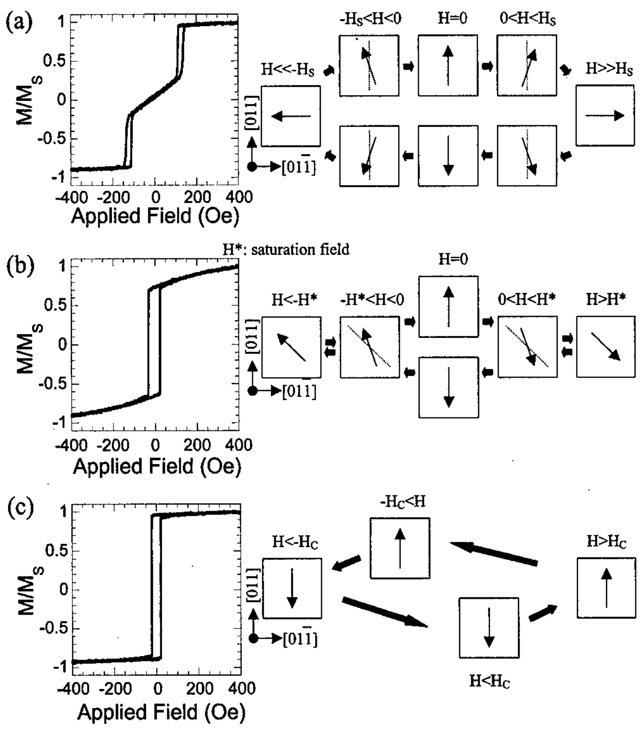

FIG. 10. Magnetic moments switching mechanism of bcc Fe_xCo_{1-x}(100)/GaAs(100). The applied field was directed along (a) $[01\bar{1}]$, the hard axis; (b) ⟨010⟩, the medium hard axes; and (c) [011], the easy axis.

(fourfold crystalline symmetry), the in-plane uniaxial anisotropy results exclusively from the extrinsic twofold surface symmetry.

Figure 9 shows the longitudinal and transverse MOKE spectra from a Fe_xCo_{1-x}/GaAs(100) without miscut. The external field was applied along the hard axis, the $[01\bar{1}]$ direction, and both the longitudinal (parallel to the applied field) and transverse (perpendicular to the applied field) in-plane magnetization were measured as the magnitude of the external field was varied. It is interesting to note that the in-plane magnetization perpendicular to the field increased dramatically when the applied magnetic field is reduced from its maximum values and reaches the split field. This suggests that the magnetic moments flip from being aligned parallel to the applied field and rotate nearly 90° from the hard axis ($[01\bar{1}]$) to the easy axis ([011]) when the uniaxial anisotropy dominates. As the applied field decreases, the linear relationship between in-plane longitudinal magnetization (parallel to the field) and applied field suggests a single domain coherent rotation. The in-plane magnetization perpendicular to the field remains almost the same, suggesting that the coherent rotation angle is too small to make a significant contribution to the longitudinal magnetization.

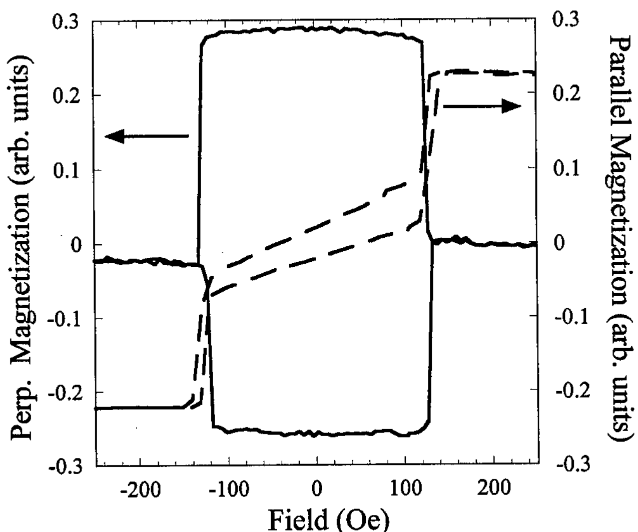

FIG. 9. Longitudinal and transverse magneto-optical Kerr effect (MOKE) spectrum of bcc-Fe_xCo_{1-x}(100)/GaAs(100)-2×4.

Figure 10 shows a possible magnetic moment switching mechanism. As discussed in the previous section, when the applied field is directed along the $[01\bar{1}]$ hard axis direction, the magnetic moments will be aligned under a saturation field; when the applied field is smaller than the split field ($-H_s<H$ or $H_s>H$), the magnetic moments rotate close to the [011] easy axis [as shown in Fig. 10(a)]. As the applied field is directed along the ⟨010⟩ directions [Fig. 10(b)], the magnetic moments will be aligned under a saturation field ($H>H^*$ or $H<-H^*$). The applied field can only partially align the magnetic moments toward the ⟨010⟩ direction and the magnetic moments rotate towards the easy axis (in [011] direction) when the applied field is decreased ($-H^*<H<-H_c$ or $H^*>H>H_c$). Hence, the magnetic moments will point to the [011] direction if there is no applied field. Therefore, the remanence in the ⟨010⟩ direction should be equal to

the projection of magnetic moments in the [011] direction to the ⟨010⟩ direction, which is cos 45° or 0.707. This is in an excellent agreement with the M_R/M_S ratio, which is ~0.7 in the ⟨010⟩ direction.

IV. CONCLUSIONS

Epitaxial single crystal bcc-Fe_xCo_{1-x}(100) thin films have been successfully grown on the GaAs(100) substrate. RHEED, LEED, and XRD data are consistent with the cube-on-cube crystal alignment of bcc-Fe_xCo_{1-x}(100)⟨010⟩‖GaAs(100)⟨010⟩ and bcc-Fe_xCo_{1-x}(100)⟨010⟩‖Sc_yEr_{1-y}As(100)⟨010⟩‖GaAs(100)⟨010⟩. The ~3% RBS minimum yields obtained from the channeling spectra indicate high quality single crystals. For the bcc-Fe_xCo_{1-x}(100)/GaAs(100) heterostructures, VSM hysteresis loops reveal a uniaxial magnetic anisotropy with [011] easy and $[01\bar{1}]$ hard axes. The uniaxial anisotropy was enhanced by increasing step density in the [011] direction. The uniaxial anisotropy can be eliminated by using a Sc_yEr_{1-y}As interlayer with fourfold symmetry. The intrinsic fourfold magnetic anisotropy of bcc-Fe_xCo_{1-x}(100)/Sc_yEr_{1-y}As(100)/GaAs(100) heterostructure can be made uniaxial by growth on vicinal substrates. In summary, we demonstrated the ability to control the magnetic anisotropy of ferromagnet/semiconductor by modifying the surface symmetries.

ACKNOWLEDGMENTS

This work was supported in part by Contract Nos. ONR-N/N00014-99-1-0233, DARPA/ONR-N/N00014-99-1-1005, NSF/DMR 981-9659, and by the Research Corporation (PAC).

[1]G. A. Prinz, Phys. Today **48**, 58 (1995).
[2]G. Y. Chin and J. H. Wernick, in *Ferromagnetic Materials*, edited by E. P. Wohlfarth (North-Holland, Amsterdam, 1980), Vol. 2, p. 55.
[3]K. Schwarz and D. R. Salahub, Phys. Rev. B **25**, 3427 (1982).
[4]T. R. McGuire, J. Appl. Phys. **40**, 1371 (1969).
[5]R. C. Hall, J. Appl. Phys. **31**, 157S (1960).
[6]E. M. Kneedler, P. M. Thibado, B. T. Jonker, B. R. Bennett, B. V. Shanabrook, R. J. Wagner, and L. J. Whitman, J. Vac. Sci. Technol. B **14**, 3193 (1996).
[7]E. M. Kneedler, B. T. Jonker, P. M. Thibado, R. J. Wagner, B. V. Shanabrook, and L. J. Whitman, Phys. Rev. B **56**, 8163 (1997).
[8]E. M. Kneedler and B. T. Jonker, J. Appl. Phys. **81**, 4463 (1997).
[9]C. J. Gutierrez, J. J. Krebs, and G. A. Prinz, Appl. Phys. Lett. **61**, 2476 (1992).
[10]C. J. Gutierrez, V. G. Harris, J. J. Krebs, W. T. Elam, and G. A. Prinz, J. Appl. Phys. **73**, 6763 (1993).
[11]L. C. Chen, J. W. Dong, B. D. Schultz, J. Berezovsky, P. A. Crowell, and C. J. Palmstrøm, presented at the 46th American Vacuum Society Meeting, Seattle, 1999.
[12]M. Dumm, M. Zölfl, R. Moosbühler, and G. Bayreuther, presented at the 44th Magnetism and Magnetic Materials Meeting, San Jose, 1999.
[13]J. J. Krebs, B. T. Jonker, and G. A. Prinz, J. Appl. Phys. **61**, 2596 (1987).
[14]J. R. Waldrop and R. W. Grant, Appl. Phys. Lett. **34**, 630 (1979).
[15]C. J. Palmstrøm and T. Sands, in *Contacts to Semiconductors*, edited by L. J. Brillson (Noyes, Park Ridge, NJ, 1993).
[16]R. K. Kawakami, E. J. Escorcia-Aparicio, and Z. Q. Qiu, Phys. Rev. Lett. **77**, 2570 (1996), and references therein.
[17]M. D. Pashley, K. W. Haberern, W. Friday, J. M. Woodall, and P. D. Kirchner, Phys. Rev. Lett. **60**, 2176 (1988).
[18]G. A. Prinz, Phys. Rev. Lett. **54**, 1051 (1985).
[19]B. T. Jonker, G. A. Prinz, and Y. U. Idzerda, J. Vac. Sci. Technol. B **9**, 2437 (1991).
[20]S. A. Chambers, F. Xu, H. W. Chen, I. M. Vitomirov, S. B. Anderson, and J. H. Weaver, Phys. Rev. B **34**, 6605 (1986).
[21]M. Shiga, in *Physics of Transition Metals—1980*, edited by P. Rhodes (Oxford, New York, 1980), p. 241.
[22]P. F. Miceli, C. J. Palmstrøm, and K. W. Moyers, Appl. Phys. Lett. **61**, 2060 (1992).
[23]P. F. Miceli and C. J. Palmstrøm, Phys. Rev. B **51**, 5506 (1995).
[24]W. Weber, C. H. Back, A. Bischof, Ch. Würsch, and R. Allenspach, Phys. Rev. Lett. **76**, 1940 (1996).
[25]H. P. Oepen, C. M. Schneider, D. S. Chuang, C. A. Ballentine, and R. C. O'Handley, J. Appl. Phys. **73**, 6186 (1993).
[26]M. Gester, C. Daboo, R. J. Hicken, S. J. Gray, A. Ercole, and J. A. C. Bland, J. Appl. Phys. **80**, 347 (1996).
[27]Y. B. Xu, E. T. M. Kernohan, D. J. Freeland, M. Tselepi, A. Ercole, and J. A. C. Bland, J. Magn. Magn. Mater. **198–199**, 703 (1999).
[28]A. Filipe, A. Schuhl, and P. Galtier, Appl. Phys. Lett. **70**, 129 (1997).
[29]A. Filipe and A. Schuhl, J. Appl. Phys. **81**, 4359 (1997).
[30]Y. B. Xu, E. T. Kernohan, M. Tselepi, J. A. C. Bland, and S. Holmes, Appl. Phys. Lett. **73**, 399 (1998).
[31]R. C. Hall, J. Appl. Phys. **31**, 157S (1960).
[32]A. Berger, U. Linke, and H. P. Oepen, Phys. Rev. Lett. **68**, 839 (1992).
[33]W. Weber, R. Allenspach, and A. Bischof, Appl. Phys. Lett. **70**, 520 (1997).

Enhanced magneto-optical effect in a GaAs:MnAs nanoscale hybrid structure combined with GaAs/AlAs distributed Bragg reflectors

H. Shimizu, M. Miyamura, and M. Tanaka[a)]
Department of Electronic Engineering, The University of Tokyo, 7-3-1, Hongo, Bunkyo-ku, Tokyo 113-8656, Japan

(Received 17 January 2000; accepted 19 April 2000)

We present significant enhancement of magneto-optical effect at room temperature in GaAs with MnAs magnetic nanoclusters sandwiched by GaAs/AlAs multilayers acting as distributed Bragg reflectors. The experimentally observed transmissivity and magneto-optical spectra are well explained by theoretical calculations. This new material system will open up the possibility of realizing nonreciprocal magneto-optical devices integrated with semiconductor optoelectronic devices and circuits. © *2000 American Vacuum Society.* [S0734-211X(00)02504-X]

I. INTRODUCTION

Recent advances in epitaxial growth techniques have made it possible to fabricate hybrid materials composed of III–V based semiconductors and magnetic compounds. Among the hybrid materials whose base material is GaAs, (1) ferromagnetic semiconductor (GaMn)As,[1,2] (2) semiconductor/ferromagnet hybrid heterostructures such as MnAs/GaAs,[3,4] and (3) GaAs:MnAs nanoclusters[5] have been synthesized and have attracted much interest from the viewpoint both of condensed matter physics and of novel device applications. These hybrid systems have good compatibility with conventional nonmagnetic semiconductor systems, together with good crystalline quality and atomic-scale controllability of the layer thickness, leading to the formation of III–V based magnetic quantum heterostructures.[6] These merits have enabled one to observe novel phenomena in spin dependent transport properties in (GaMn)As based magnetic quantum heterostructures.[7,8] On the one hand, these hybrid materials were found to show large magneto-optical effect.[9–11] However, for application to practical magneto-optical devices such as optical isolators, it is necessary to enlarge their magneto-optical effect at room temperature. Recently, Inoue *et al.* theoretically and experimentally demonstrated enhancement of the magneto-optical effect in thin Bi-substituted yttrium–iron–garnet (Bi:YIG) films combined with multilayers composed of two different dielectric films by using multiple interference of light, in other words, weak localization of light in the magnetic layer.[12–15] For application to the devices integrated with optoelectronic circuitry, one must design a desired magneto-optical property with a large magneto-optical effect, which must be realized in semiconductor-based thin films rather than in bulk materials or oxide films.

In this article, we present fabrication of a GaAs:MnAs nanoscale hybrid structure combined with GaAs/AlAs distributed Bragg reflectors (DBRs), and show significant enhancement of the magneto-optical effect in this multilayer system at room temperature. In this material system which is composed of all semiconductor-based epitaxial films, a number of unique properties are expected; it will be easy to integrate with III–V optoelectronic devices because the operating wavelength can be tuned in a wide range because of a lot of freedom in the materials design, and because the magneto-optical effect can be enhanced at room temperature at relatively low magnetic field.

II. GROWTH PROCESS AND MAGNETO-OPTICAL PROPERTIES

The samples, whose typical structure is shown in Fig. 1, were grown by molecular-beam epitaxy (MBE). Here we set the operation wavelength at $\lambda = 980$ nm for application to a Faraday rotator in optical isolators for pump laser diodes of erbium doped fiber amplifiers (EDFAs). The growth process consisted of three parts. First, 10 pairs of GaAs (70 nm)/AlAs (83 nm) multilayers (bottom DBR) were grown at 550–580 °C on a 300 nm thick AlGaAs etch-stop layer on a (001) GaAs substrate. The thickness of each layer was designed to be $\lambda/4n$ (n is the refractive index of each layer, 3.52 for GaAs and 2.95 for AlAs at 980 nm). Second, a 139 nm thick $(Ga_{1-x}Mn_x)As$ layer was grown at 250 °C with Mn concentration $x = 0.043$, and then the substrate temperature was raised to 580 °C. Third, 10 pairs of AlAs/GaAs multilayers (top DBR) with the same thickness as the bottom DBR were grown at 550–580 °C. During growth of the top DBR at 550–580 °C (about 3 h), the homogeneous (GaMn)As alloy turned into an inhomogeneous structure, in which MnAs nanoclusters 6–7 nm in diameter are embedded in GaAs, by phase separation.[5] This GaAs:MnAs nanoscale hybrid system shows a superparamagnetic behavior.[5] Here the thickness of the magnetic GaAs:MnAs layer was set at half of the optical path length, $\lambda/2n$, assuming that the refractive index n of the GaAs:MnAs layer is the same as that of GaAs. Since this multilayer structure is essentially a microcavity, a specific standing-wave mode of Bragg wavelength λ is selectively confined in the central magnetic layer, and at the same time the light of λ can be transmitted through the whole structure, hence it is possible to enhance the magneto-optical Faraday effect. Figure 1 shows a cross

a)Author to whom correspondence should be addressed; also at CREST, Japan Science and Technology Corporation; electronic mail: shmz@cryst.t.u-tokyo.ac.jp

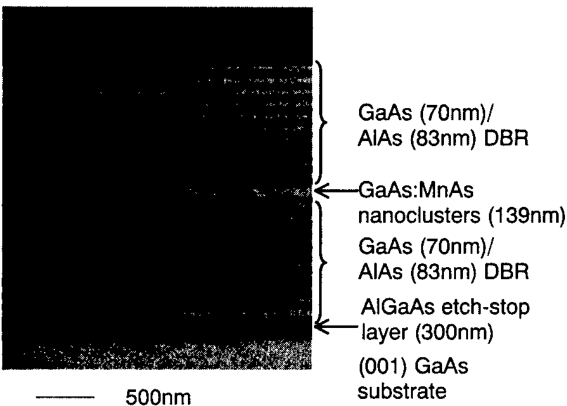

FIG. 1. Cross-sectional view of a GaAs:MnAs nanoscale hybrid structure sandwiched by GaAs/AlAs DBRs taken by a scanning electron microscope.

section of this sample taken by a scanning electron microscope (SEM). Deviation of the thickness between the designed and the fabricated layer is within 5%.

Figures 2(a) and 2(b) show a transmissivity spectrum and a magnetic circular dichroism (MCD) (equal to the Faraday ellipticity) spectrum of this sample measured at room temperature, respectively. The MCD was measured under a magnetic field of 1 T applied perpendicular to the film plane. A MCD spectrum of a 200 nm thick single film of GaAs:MnAs nanoclusters fabricated in the same manner is also shown as a reference in Fig. 2(b). One can see that the transmissivity is low in the range of 900–1040 nm, as shown in Fig. 2(a), which corresponds to the optical stop band (photonic band gap) of this multilayer structure. At a wavelength of 960–970 nm (deviated from the aimed at wavelength of 980 nm, because the GaAs, AlAs, and GaAs:MnAs layers were slightly thinner than designed), a local maximum (~2%) was seen in the transmissivity spectrum [Fig. 2(a)]. At this wavelength, the MCD intensity was significantly enhanced in the sample with the DBR compared with the sample without the DBR from 0.12° to 0.63° [Fig. 2(b)]. If compared with the same magnetic layer thickness, the enhancement factor is 6–7. This peak wavelength of 960–970 nm in the MCD spectrum is consistent with the SEM observation (Fig. 1), which shows that the GaAs/AlAs of the DBR and GaAs:MnAs layer were slightly thinner than designed. Due to the low transmissivity of our multilayer system, we have not yet succeeded in measuring the Faraday rotation, which is one of the most important parameters for optical isolator applications. However, this experiment clearly demonstrates the effective enhancement of the magneto-optical effect in GaAs:MnAs nanoclusters sandwiched by GaAs/AlAs DBRs by multiple interference of light, or the localization of light near the magnetic layer.

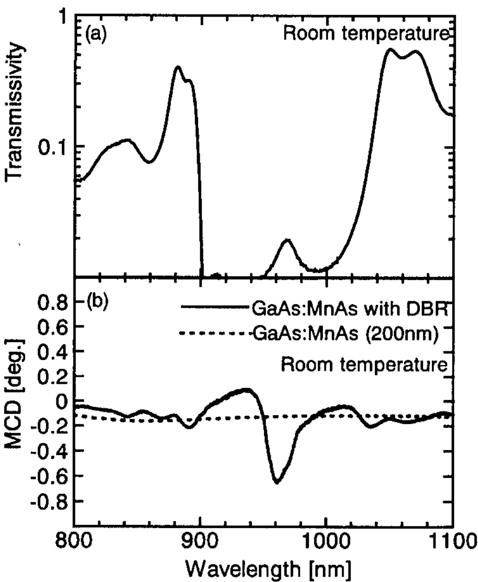

FIG. 2. (a) Transmissivity and (b) transmission MCD (Faraday ellipticity) spectrum of GaAs:MnAs nanoclusters sandwiched by a GaAs/AlAs DBR measured at room temperature. (b) A MCD spectrum of a 200 nm thick GaAs:MnAs single layer without a DBR is shown as a reference by a dotted curve. The MCD was measured under a magnetic field of 1 T applied perpendicular to the film plane.

Furthermore, we have calculated the magneto-optical effect of this structure using the method of Inoue *et al.*[12] which was employed in the Bi:YIG/dielectric multilayers. Since optical parameters such as the dielectric tensor of semiconductor/magnetic hybrid materials of (GaMn)As and GaAs:MnAs have not been reported, we assumed here that the refractive index of GaAs:MnAs is the same as that of GaAs, and extracted nondiagonal elements of the dielectric tensor from the measurements of Faraday rotation and MCD spectra of a single GaAs:MnAs film. In the calculation of magneto-optical properties, we treated the extinction coefficients as a fitting parameter. Figures 3(a)–3(c) show, respectively, calculated transmissivity, MCD, and Faraday rotation spectra of the present structure (dotted curves) compared with the experimental spectra (solid curves). Although the experimental spectra are broader than the calculated ones due to structural inhomogeneity, the calculated spectra fairly nicely reproduced the experimental transmissivity and MCD spectra. From this calculation, Faraday rotation of this sample, which could not be measured due to low transmissivity, is predicted to be about 0.8°.

III. DISCUSSION

At present, the most important problem in our multilayer system is that optical absorption of the magnetic layer is fairly large. Optical absorption of the GaAs:MnAs layer is sensitive to the annealing temperature and annealing time. It is expected that when the annealing temperature is too high or the annealing time is too long, the size of MnAs ferromagnetic metal in a GaAs matrix becomes large and optical loss is increased. Since, for the present sample, the growth time of the upper DBR layers, which is equal to the effective annealing time, is relatively longer than that of the previously reported GaAs:MnAs samples,[5,11] it is essential to optimize the growth temperature of the upper DBR layer so as not to degrade the optical properties both of the GaAs:MnAs and of the DBR layers. Another possible solution would be to reduce the Mn concentration and carrier concentration in

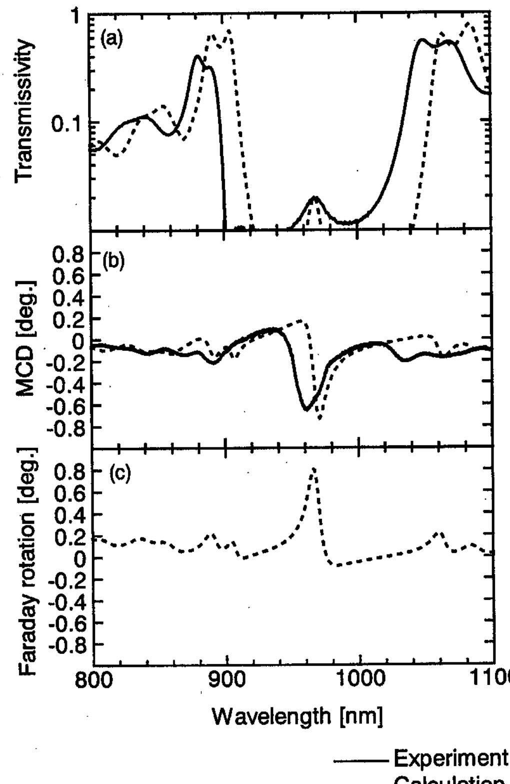

FIG. 3. Theoretical calculation of transmissivity, the MCD, and Faraday rotation spectra (dotted curves). Experimental results are also shown in the transmissivity and MCD spectra (solid curves).

(GaMn)As. Also, more appropriate design of the multilayer structure would be effective to improve the optical and magneto-optical properties, and this will be reported elsewhere.

Since our material system is based on semiconductor epitaxial thin films, some potential strengths are expected. (1) Compared with conventional magneto-optical materials based on garnet, it is easy to fabricate high-quality heterostructures having smooth interfaces, as exemplified by the multilayers of the GaAs:MnAs magnetic layer combined with GaAs/AlAs DBRs. (2) The operating wavelength is tunable in a wide energy range by the materials choices and by adjusting the structural and processing parameters. (3) GaAs:MnAs with GaAs/AlAs DBRs is immediately suitable for integration with conventional III–V based semiconductor-based optoelectronic devices and circuits.

IV. SUMMARY

In summary, we have shown the enhancement of the magneto-optical effect in a GaAs:MnAs nanoscale hybrid structure sandwiched by GaAs/AlAs multilayers acting as distributed Bragg reflectors. The Faraday ellipticity was found to be enhanced six to seven times compared with that of a GaAs:MnAs single layer at room temperature. Theoretical calculations successfully reproduced the experimentally observed transmissivity and MCD spectra. Furthermore, current problems of the present structure and future prospects were discussed for improvement of the optical and magneto-optical properties.

ACKNOWLEDGMENTS

The authors are grateful to Dr. K. Ando for guidance in the magneto-optical measurements, Dr. H. Akinaga for valuable discussions about the properties of GaAs:MnAs nanoclusters, and Professor T. Nishinaga for his support and encouragement. This work was partially supported by the JSPS Research for the Future Program (JSPS-RFTF 97P00202), CREST Program of JST, and by a Grant-in-Aid for Scientific Research on the Priority Area ''Spin-Controlled Semiconductor Nanostructures'' from the Ministry of Education, Science, Sports, and Culture.

[1]H. Ohno, A. Shen, F. Matsukura, A. Oiwa, A. Endo, S. Katsumoto, and Y. Iye, Appl. Phys. Lett. **69**, 363 (1996).
[2]T. Hayashi, M. Tanaka, T. Nishinaga, H. Shimada, and Y. Otuka, J. Cryst. Growth **175/176**, 1063 (1997).
[3]M. Tanaka, Mater. Sci. Eng., B **31**, 117 (1995); Physica E **2**, 372 (1998).
[4]M. Tanaka, K. Saito, and T. Nishinaga, Appl. Phys. Lett. **74**, 64 (1999).
[5]J. De Boeck, R Oesterholt, A. Van Esch, H. Bender, C. Bruynseraede, C. Van Hoof, and G. Borghs, Appl. Phys. Lett. **68**, 2744 (1996).
[6]T. Hayashi, M. Tanaka, K. Seto, T. Nishinaga, and K. Ando, Appl. Phys. Lett. **71**, 1825 (1997).
[7]H. Ohno, N. Akiba, F. Matsukura, A. Shen, K. Ohtani, and Y. Ohno, Appl. Phys. Lett. **73**, 363 (1998).
[8]T. Hayashi, H. Shimada, H. Shimizu, and M. Tanaka, J. Cryst. Growth **201/202**, 689 (1999).
[9]T. Kuroiwa, T. Yasuda, F. Matsukura, A. Shen, Y. Ohno, Y. Segawa, and H. Ohno, Electron. Lett. **34**, 190 (1998).
[10]K. Ando, T. Hayashi, M. Tanaka, and A. Twardowski, J. Appl. Phys. **83**, 6548 (1998).
[11]H. Akinaga, S. Miyanishi, K. Tanaka, W. Van Roy, and K. Onodera, Appl. Phys. Lett. **76**, 97 (2000).
[12]M. Inoue and T. Fujii, J. Appl. Phys. **81**, 5659 (1997).
[13]M. Inoue, K. I. Arai, T. Fujii, and M. Abe, J. Appl. Phys. **83**, 6768 (1998).
[14]M. Inoue, K. I. Arai, T. Fujii, and M. Abe, J. Appl. Phys. **85**, 5768 (1999).
[15]M. Inoue, K. Yayoi, T. Takayama, K. Nakamura, T. Fujii, M. Abe, and K. I. Arai, Proceedings of the 2nd International Symposium on Frontiers in Magnetism 1999.

Strain relaxation of InGaAs by lateral oxidation of AlAs

S. K. Mathis[a)]
Materials Department, University of California, Santa Barbara, California 93106

P. Chavarkar
Electrical and Computer Engineering Department, University of California, Santa Barbara, California 93106

A. M. Andrews
Materials Department, University of California, Santa Barbara, California 93106

U. K. Mishra
Electrical and Computer Engineering Department, University of California, Santa Barbara, California 93106

J. S. Speck
Materials Department, University of California, Santa Barbara, California 93106

(Received 17 January 2000; accepted 5 April 2000)

Strained InGaAs layers grown on AlAs/GaAs have been shown to relax when the AlAs is laterally oxidized. A detailed microscopy study is reported of the InGaAs structure before and after oxidation. Plan-view transmission electron microscopy (TEM) reveals that the misfit dislocation density in the InGaAs/AlAs interface is reduced by 30 times after lateral oxidation. The mechanism proposed for this reduction is the oxidation of the InGaAs interface, including the core regions of the misfit dislocations. Threading dislocation densities in the InGaAs are not measurable by TEM either before or after oxidation for optimized $In_{0.20}Ga_{0.80}As$ and $In_{0.30}Ga_{0.70}As$ layers. Two possible strain relaxation mechanisms are examined: (i) the compressive strain in the InGaAs is relaxed by a tensile stress developing during oxidation in the cap layer; and (ii) the stress is relaxed by the threading dislocation *motion* in the cap layer during oxidation. The removal of misfit dislocations reduces the likelihood of threading dislocation blocking, which prevents threading dislocations from moving across misfit dislocations. © *2000 American Vacuum Society.* [S0734-211X(00)00704-6]

I. INTRODUCTION

Dislocations in semiconductors are detrimental to device performance. Threading dislocations (TDs) and strain-relieving misfit dislocations (MDs) are generated when thin films are grown epitaxially on a lattice-mismatched substrate. However, many III–V materials without a lattice-matched substrate are desirable for improving carrier mobility, reaching different wavelengths, or for achieving useful band offsets. Previously, lattice-mismatched substrates have been used for heteroepitaxial growth by one of two main methods: preventing the formation of MDs and associated TDs by growing thinner than the critical thickness for dislocation generation or by using a buffer layer to first strain relax the film and then reduce the density of threading dislocations that formed as a result of the strain relaxation.[1]

Postgrowth relaxation of a strained layer grown beyond the critical thickness has been demonstrated using lateral oxidation of an underlying layer by Chavarkar *et al.*[2] Strained layers, such as InGaAs on GaAs substrates, may be grown beyond their critical thickness with only partial strain relaxation. This is possible at low substrate temperature due to kinetic constraints on dislocation generation. When a sample of InGaAs/AlAs/GaAs (termed a lattice engineered substrate "template") is patterned and mesas of 100–500 μm are etched, sidewalls of underlying layers of AlAs may be exposed. Lateral oxidation of this AlAs layer may be carried out in a steam furnace at 400–450 °C. This leaves a selectively oxidized structure with nanocrystalline, mesoporous Al_2O_3 beneath the strain relaxed InGaAs. A sample of $In_{0.20}Ga_{0.80}As$/500 Å AlAs/GaAs was shown to be 41% relaxed as grown and 87% relaxed after lateral oxidation at 450 °C.

Strain relaxation by lateral oxidation is affected by the oxidation temperature.[2] The strain relieved increases with increasing oxidation temperature in the range 410–450 °C. Samples merely annealed at the oxidation temperature in an inert or reducing environment do not display strain relaxation. Increasing the nominal misfit strain generally leads to a higher degree of initial strain relaxation during growth and thus limits the possible further strain relaxation during lateral oxidation.

In this article, we describe microstructural studies of the as-grown and oxidized lattice engineered substrate (LES) template structure. This was accomplished using plan-view transmission electron microscopy (TEM) along with x-ray diffraction. Possible strain relaxation mechanisms will be discussed. Regrowths on the template structure have been performed, and structural studies of these regrown structures will be reported.

II. EXPERIMENTAL PROCEDURE

The molecular beam epitaxy (MBE) growths were carried out in a Varian Gen II system equipped with a valved, cracked As_2 source. The lattice engineered substrate tem-

[a)]Electronic mail: smathis@engineering.ucsb.edu

plate structure consisted of InGaAs layers grown on a standard buffer layer structure on GaAs substrates. This layer structure was comprised of 2000 Å of GaAs (undoped) and 500 Å of AlAs grown at the standard growth temperature of 580 °C. The substrate was then cooled to 350–400 °C for InGaAs growth. The low growth temperature was employed to maintain a smooth InGaAs surface and slow rate of strain relaxation.[3,4] The structure was then capped with a 50 Å AlAs etch stop layer and a thin (200 Å) protective GaAs layer for oxidation. The thickness of the InGaAs layers was varied in multiples of the Matthews–Blakeslee equilibrium critical thickness h_c, which is 68 Å for 20% InGaAs (misfit strain $\epsilon_m = 1.41\%$), 44 Å for 30% InGaAs ($\epsilon_m = 2.10\%$), and 27.5 Å for 40% InGaAs ($\epsilon_m = 2.79\%$).[5]

To expose the AlAs layer sidewalls, 100×100 μm mesas were patterned using standard optical lithography and were etched with a phosphoric acid wet etchant. The 500 Å AlAs layer was laterally oxidized in a tube furnace with N_2 flowed through de-ionized water held at 90 °C. The oxidation was complete after ~16 min at a furnace temperature of 450 °C. As has been verified by Choquette *et al.*, the structure of the oxidized AlAs layer is nanocrystalline γ spinel and porous Al_2O_3 with approximately 13% vertical shrinkage.[6]

Regrowths were performed on the oxidized structure. After oxidation, the capping layers were removed by first etching the GaAs in citric acid and the 50 Å AlAs in buffered HF. This AlAs layer is intact since AlAs will not oxidize laterally when it is thinner than 200 Å.[7] The InGaAs surface revealed by this etching develops a native In_2O_3 and Ga_2O_3 oxide layer. This oxide must be removed before epitaxial regrowth. This was accomplished by *in situ* Ar^+ ion sputtering with 80 kV ions in a separate chamber which is connected to the MBE growth system with an ultrahigh vacuum (UHV) transfer line. After ion sputtering, the sample was transferred into the growth chamber and annealed in an As_2 flux at 500 °C to remove any remaining oxide. InGaAs regrowth was performed at 500 °C on the InGaAs template.

As-grown and oxidized structures were characterized by x-ray diffraction (XRD) to determine the composition and strain state of the InGaAs layers in the template structures. This was accomplished by taking the 115 and $\bar{1}\bar{1}5$ rocking curves. The composition and in- and out-of-plane lattice parameters were calculated according to the method in Ref. 8. The 004 reflection was also used to independently verify the 004 interplanar spacing.

Plan-view TEM specimens were prepared by the wedge technique. Samples were mechanically thinned from the substrate side only. When they reached optical transparency, they were chemically mechanically polished using bromine methanol, also only on the substrate side. Finally, a short, final polish was performed using 3.6 keV Ar^+ ions in a Gatan Precision Ion Polisher. Cross-section TEM samples were prepared in the same manner, but they were polished from both sides at each step. The samples were examined in a JEOL 2000FX operating at 200 kV.

Due to the special geometry in thin film growth, MD densities are typically quantified in units of dislocation line length per area. Here, the measurement is made by drawing a line parallel to a ⟨110⟩ direction and counting the number of misfit dislocations intersecting that line. The count is averaged between the two orthogonal ⟨110⟩ directions lying in the (001) plane.

Threading dislocation densities can be measured both by plan-view TEM and etch pit density (EPD) measurements. Etch pits are formed at the site where a TD intersects the wafer surface. Special etchants are required to preferentially attack the dislocations, and the type of etchant depends on the material, its orientation, and on the type of dislocation. For (001)-oriented GaAs, molten KOH has been shown to attack threading dislocations.[9] Etch pit density measurements were made on 1360 Å $In_{0.20}Ga_{0.80}As$/500 Å AlAs/GaAs patterned in 500 μm stripes and oxidized at 450 °C to 90 μm. This was accomplished by placing the sample in the bottom of a nickel crucible and covering it with KOH pellets. The crucible was placed in a furnace held at 400 °C for 5 min. After removing the sample from the molten KOH, it was rinsed with de-ionized water. The dislocation density was estimated using an optical microscope at 1000× magnification.

Two sets of experiments were performed. First, plan-view TEM was used to examine samples with $In_{0.20}Ga_{0.80}As$ grown to $20\times h_c = 1360$ Å and samples of $In_{0.30}Ga_{0.70}As$ grown to $20\times h_c = 880$ Å. The interfaces between the InGaAs and AlAs and the InGaAs and Al_2O_3 were of primary interest. Images were recorded in strong- and weak-beam 220 and 400 diffraction conditions. Second, the effect of InGaAs layer thickness on strain relaxation was investigated to improve upon the efficiency of strain relaxation in the template. Three template samples were grown of $In_{0.29}Ga_{0.71}As$/500 Å AlAs/GaAs with varying InGaAs layer thickness: one sample each of $5\times h_c = 220$ Å, $10\times h_c = 440$ Å, and $15\times h_c = 660$ Å. The growth temperature of the InGaAs was 400 °C. Plan-view TEM was used to image a partially oxidized sample at the oxidation front of each sample. Finally, TEM images of the microstructure InGaAs regrowths will be presented.

III. RESULTS

Figure 1 shows the variation in the measured strain relaxation with growth thickness before and after oxidation. The extent of strain relaxation in as-grown $In_{0.29}Ga_{0.71}As$/AlAs/GaAs varies linearly with thickness h for $h > h_c$. Up to thicknesses of $5\times h_c = 220$ Å, there is not significant strain relaxation in the as-grown sample, and hence a low MD density is expected. Figure 2(a) shows a plan-view TEM image looking through the InGaAs/AlAs interface at the oxidation front. The MD density is too low for reliable density measurement before oxidation. At thicknesses of $10\times h_c = 440$ Å and $15\times h_c = 660$ Å, the MD density increases in the samples before oxidation, which releases more of the misfit strain, as shown in Figs. 2(b) and 2(c). After oxidation, an average of 27% of the total misfit strain is relieved and is nearly constant for each of the three thicknesses. This means that a constant amount of strain (27% of

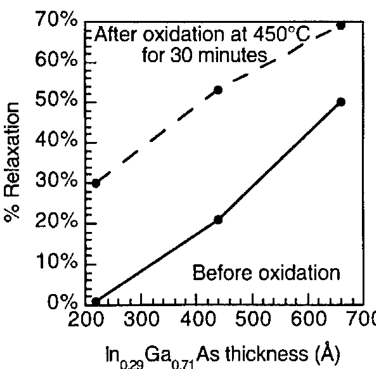

FIG. 1. Strain relaxation variation with $In_{0.29}Ga_{0.71}As$ thickness in the range $5-15\times h_c$. The extent of strain relaxation was measured with x-ray diffraction rocking curves of the 115 and -1-15 reflections. The 500 Å AlAs layer lying immediately beneath the $In_{0.29}Ga_{0.71}As$ layer was laterally oxidized in each sample at 450 °C in a steam environment. An approximately linear relationship is found between the relaxation and strained layer thickness both before and after the oxidation process. An average of 27% of the total misfit strain is relaxed during oxidation.

2.0% strain=0.55%) is relieved in this sample series. This is consistent with our prior samples grown at varying temperatures in the range 350–500 °C and in the composition range of 20%–40% InGaAs, where the strain relieved varies from 0.35%–0.68%.[2]

The detailed microstructural study was carried out on samples of $In_{0.30}Ga_{0.70}As$ and $In_{0.20}Ga_{0.80}As$ grown to $20\times h_c$. As shown in the plan-view TEM of the oxidation front region in Fig. 3(a), a linear MD density of 1.7×10^5/cm before oxidation is reduced to 5.9×10^3/cm after oxidation in $In_{0.20}Ga_{0.80}As$. In the unoxidized region, it is not possible to measure the TD density since the dense MD array dominates the image contrast. In the oxidized region, TD contrast is absent as shown in Fig. 3(b). Typically, threading dislocations have oscillatory contrast due to their inclined line direction with respect to the viewing direction along the [001] zone axis in plan view. The TD density was estimated using etch pit density measurements to be $10^6/cm^2$. The MD segments that remain consist of short, straight segments and some small, bent "elbow" segments.

In Figs. 2(a)–2(c), the $In_{0.29}Ga_{0.71}As$ thickness series samples are consistent with the prior plan-view TEM images. Figure 4(a) shows that the contrast in the unoxidized region is uniform and only contains bend contours. In the oxidized region for this $5\times h_c$ sample, bend contours appear in a higher density. This is attributed to the decreased heat conduction in that part of the sample, since the AlAs semiconductor has been replaced with an oxide. In Figs. 2(b) and 2(c), the oxidized region has a much lower MD density than the unoxidized portion.

Plan-view TEM samples were produced by chemical polishing from the substrate side of the sample. It is possible to mechanically remove all or part of the MD network lying at the interface between the AlAs and InGaAs. This possibility was discounted by imaging Moiré fringes in the oxidized region. For Moiré interference, two or more crystalline layers must be misaligned with respect to one another. This can

(a)

(b)

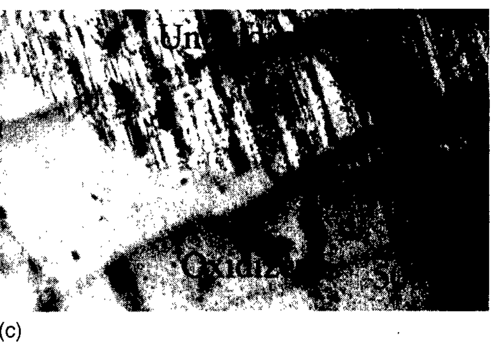

(c)

FIG. 2. Plan-view TEM images of the samples included in the thickness series. In each figure, an image at the oxidation front was taken to identify changes in the structure before and after oxidation. Each structure was $In_{0.29}Ga_{0.71}As$/500 Å AlAs/GaAs substrate with varying InGaAs thickness. (a) $5\times h_c=220$ Å. The misfit dislocation density is immeasurably low before the onset of relaxation. There is no change in the dislocation density before and after oxidation. (b) $10\times h_c=440$ Å. The misfit dislocation density increases in the as-grown area as the misfit strain is relieved. The misfit dislocations are removed upon oxidation. Moiré fringe contrast is present in the oxidized region, along with larger bend contour contrast. (c) $15\times h_c=660$ Å. The misfit dislocation network is dense but is again almost totally removed upon oxidation. The removal of the misfit dislocations happens abruptly at the oxidation front, leaving Moiré fringes in the oxidized regions.

happen either due to a rotation (termed rotational Moiré) or due to a misfit (termed misfit Moiré). In this case, InGaAs and GaAs created misfit Moiré due to different lattice parameters in the direction of the diffraction vector. For misfit Moiré, the spacing of Moiré fringes $d_{\rm tm}$ is inversely related to the difference in the magnitude of the diffraction vectors (**g** vectors, $g_{tm}=g_2-g_1$), and to lattice spacing in the direction of the diffraction vector d by the relation given in Ref. 10.

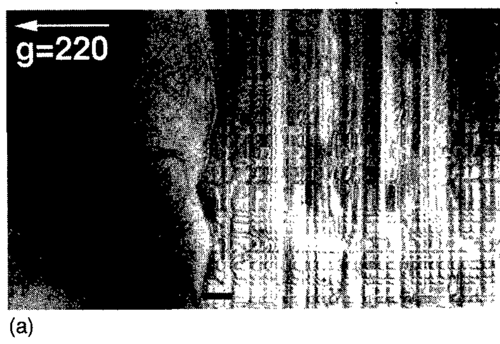

(a)

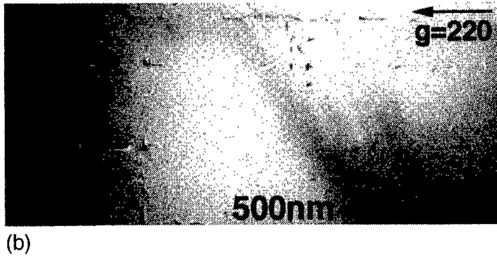

(b)

FIG. 3. Plan-view TEM images of (a) the oxidation front region and (b) 40 μm behind the oxidation front, inside the oxidized region. The sample structure was 1360 Å $In_{0.20}Ga_{0.80}As$/500 Å AlAs/GaAs buffer and substrate.

$$d_{tm}=1/g_{tm}=d_2d_1/(d_1-d_2).$$

The spacing of the Moiré contrast of $In_{0.20}Ga_{0.80}As/Al_2O_3$/GaAs in Fig. 4 correlates with a strain relaxation of ~93%, which is consistent with 87% strain relaxation measured by XRD. Therefore, the Moiré contrast evident in Fig. 4 demonstrates that both the InGaAs and the GaAs buffer layers remain above and below the oxide. This confirms that the InGaAs/oxide interface is still intact and that misfit dislocations were removed only by the oxidation process.

Regrowths were performed on the oxidized template structures. Figure 5(a) shows a typical plan-view TEM image of the regrowth of $In_{0.30}Ga_{0.70}As/In_{0.30}Ga_{0.30}As$ template. TD contrast is clearly evident at a density of $\sim 5\times 10^8/cm^2$. Figure 5(b) shows a cross-section TEM image of the regrown

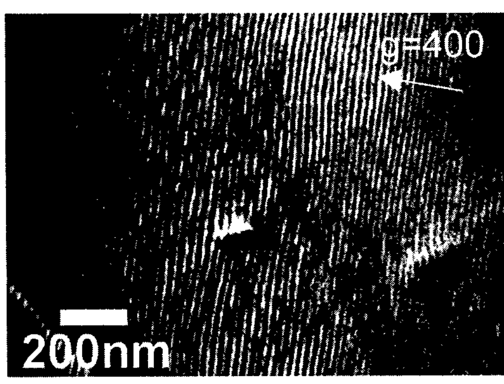

FIG. 4. Moiré fringe contrast imaged by plan-view TEM in 880 Å $In_{0.30}Ga_{0.70}As$/500 Å AlAs/GaAs. The image was taken in the **g**=400 strong beam condition. Moiré contrast indicates that the in-plane lattice parameter of the InGaAs has relaxed from the fully strained condition, and thus interferes with diffraction from the GaAs buffer layer.

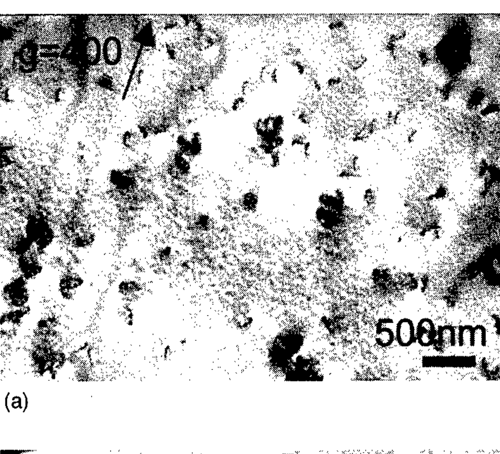

(a)

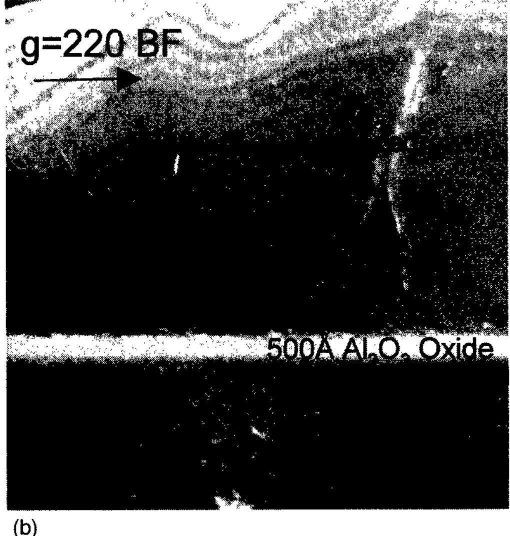

(b)

FIG. 5. TEM images of the regrowth of 5000 Å $In_{0.30}Ga_{0.70}As$ on a template of 380 Å $In_{0.3}Ga_{0.7}As$/500 Å AlAs/GaAs buffer and substrate. (a) Plan-view TEM image of the surface of the regrowth. The threading dislocation density is $3\times 10^8/cm^2$. (b) Cross-section TEM image of the regrown film. The threading dislocations emanate from the interface between the regrowth and the template layer. Since the composition of the regrowth and template layer are the same, the threading dislocations may result from problems with the surface pretreatment.

material for the same sample. The TDs start at the regrowth interface, indicating that they nucleate during regrowth. Current research focuses on improved surface preparation to minimize dislocation formation at the regrowth interface.

IV. DISCUSSION

We propose that the misfit dislocations are removed from the InGaAs/AlAs interface by oxidation of the interface. The cores of the dislocations are effectively ''burned out'' of the layer by oxidation of the surrounding material. Since the misfit dislocations lie at the interface, this interfacial oxidation would not extend far into the InGaAs layer. Interestingly, segments of the misfit dislocations remain in the InGaAs layer after the removal of the single-crystalline interface. Specifically, the elbows that remain in the layer are bent misfit segments that may have been created by TD reactions or cross slip. As a result, the orthogonal misfit dislo-

cations left behind the TD must have a small segment joining them that lies out of the ordinary slip plane. This segment would be immobile and may lie slightly above the InGaAs/oxide interface, making the elbows less likely to be removed upon oxidation.

A consequence of the MD removal is that the motion of threading dislocations may become more likely. Ordinarily, TD motion is hindered, or "blocked," when a TD glides toward a MD lying in its path.[11] By removing the misfit dislocations, a TD can move freely through the film. Additionally, since the crystalline interface has been removed, TD motion does not necessitate the energetically costly creation of misfit dislocation length in its wake, as in ordinary heteroepitaxial interfaces. Therefore, two major obstacles to dislocation motion have been reduced, probably making TD motion more energetically favorable. In a prior article, it was speculated that the strain relief resulted from enhanced dislocation motion due to interfacial voids and an interface that was not single crystalline.[2]

TD motion results in an irreversible plastic deformation of the film. This is due to the translation of the crystal on one side of the dislocation slip plane with respect to the other side of the slip plane by the Burgers vector, **b**. As a result, if enough TDs moved through the mismatched InGaAs layer in an LES structure, the InGaAs layer would relax despite the apparent absence of misfit dislocations. Normally, TD motion and the associated creation of misfit dislocation line length is the method of strain relaxation in two-dimensional heteroepitaxial growth. TD motion without the generation of the high local strain fields associated with MDs is one possibility for explaining the observed strain relaxation during lateral oxidation as well.

A second possible explanation for the strain relaxation in the InGaAs layer may be that stresses developed during the oxidation process that oppose the compressive lattice mismatch. As we calculated in Sec. III, the average compressive in-plane strain relieved due to oxidation was $\Delta\epsilon = 0.55\%$. This strain relief is consistent with the reported tensile strains induced in GaAs when underlying AlAs layers are laterally oxidized. Two groups have used micro-Raman spectroscopy to estimate the strain in GaAs cap layers.[12,13] In the investigation of Landesman *et al.*, micro-Raman spectroscopy was used to measure the deformation of a 1000 Å GaAs cap due to the oxidation of a 1000 Å AlAs layer lying directly beneath the cap. The strain induced in the cap layer was determined to be 0.08%.[12] In the study of Pan *et al.*, a similar structure with an 800 Å AlAs layer and a 600 Å GaAs cap was investigated with micro-Raman, and larger strains were found in the cap layer. These strains were 0.5%–0.6%.[13] The reported strains correspond to approximately the same stress in sign and order of magnitude as the amount of stress relieved in the InGaAs overlayers. While an oxidation stress opposing the compressive misfit stress in the InGaAs layer may relax some of the strain in the layer, these reports of strain have not been correlated with a measured strain by x-ray diffraction. The mechanism of developing an oxidation-related strain was not proposed by either Landesman *et al.* or Pan *et al.* Additionally, the magnitude of the strain reported by Landesman *et al.* is much lower than the amount of strain relieved in our samples.

The presence of interfacial misfit dislocations before oxidation does not affect the amount of strain relief from lateral oxidation. As shown in the thickness study, the sample with a 5 h_c InGaAs layer does not have a significant misfit dislocation density. However, the 5 h_c sample had the same amount of strain relieved by oxidation as the 10 h_c sample and the 15 h_c sample. The thicker samples both had a significant amount of strain relief as grown and a well-developed MD network. This demonstrates that the presence of misfit dislocations and the partial relaxation of the structure *before oxidation* does not dictate the amount of strain relieved during oxidation.

V. CONCLUSION

The results show that the structure of the InGaAs lattice engineered substrate is altered in two main ways by lateral oxidation of underlying AlAs. First, the misfit dislocations are eliminated by the removal of a crystalline interface between the InGaAs and AlAs. This reduces threading dislocation blocking. Second, the remaining misfit strain in the InGaAs layer is relieved. This may happen due to stresses associated with the lateral oxidation process or due to dislocation processes. Finally, the threading dislocation density remains low before and after lateral oxidation, but conditions for regrowth have not yet been optimized.

ACKNOWLEDGMENTS

The authors acknowledge the continued support of the Air Force Office of Scientific Research through the PRET Center at UCSB (Dr. Gerald Witt contract monitor). This work made use of the MRL Central Facilities supported by the National Science Foundation under Award No. DMR96-32716.

[1] R. Beanland, D. J. Dunstan, and P. J. Goodhew, Adv. Phys. **45**, 87 (1996).
[2] P. Chavarkar, L. Zhao, S. Keller, A. Fisher, C. Zheng, J. S. Speck, and U. K. Mishra, Appl. Phys. Lett. **75**, 2253 (1999).
[3] N. Grandjean and J. Massies, J. Cryst. Growth **134**, 51 (1993).
[4] M. Tachikawa and H. Mori, Appl. Phys. Lett. **56**, 2225 (1990); M. Sugo, N. Uchida, A. Yamamoto, and T. Nishioka, J. Appl. Phys. **65**, 591 (1989).
[5] J. W. Matthews and A. E. Blakeslee, J. Cryst. Growth **27**, 118 (1974). Our calculation of the critical thickness used a core cutoff value of $R = 4b$, where $b = a\sqrt{2}/2$ is the dislocation Burgers vector and a is the lattice parameter.
[6] K. D. Choquette, K. M. Geib, C. I. H. Ashby, R. D. Twesten, O. Blum, H. Q. Hou, D. M. Follstaedt, B. E. Hammons, D. Mathes, and R. Hull, IEEE J. Sel. Top. Quantum Electron. **3**, 916 (1997).
[7] R. L. Naone and L. A. Coldren, J. Appl. Phys. **82**, 2277 (1997).
[8] *Optical Characterization of Epitaxial Semiconductor Layers*, edited by G. Bauer and W. Richter (Springer, Berlin, 1996).

[9]J. G. Grabmeier and C. B. Watson, Phys. Status Solidi **32**, K13 (1969).
[10]D. B. Williams and C. B. Carter, *Transmission Electron Microscopy* (Plenum, New York, 1996), Vol. 3.
[11]A. E. Romanov, W. Pompe, S. K. Mathis, G. E. Beltz, and J. S. Speck, J. Appl. Phys. **85**, 182 (1999).
[12]J. P. Landesman, A. Fiore, J. Nagle, V. Berger, E. Rosencher, and P. Puech, Appl. Phys. Lett. **71**, 2520 (1997).
[13]Z. Pan, Y. Zhang, Y. Du, H.X. Han, and R. H. Wu, IEEE Lasers and Electro-optics Society 1998 Annual Meeting, Orlando, FL, 1–4 December 1998. These conference proceedings were distributed at the conference in summary form and can be found online at http://ielimg.ihs.com/ie14/5948/15943/00739549.pdf.

Scanning tunneling microscopy study of organometallic molecules adsorbed on a GaAs(001)-2×4 surface

Hiromi Kuramochi,[a] Jie Cui, Hidekazu Iwai, and Masashi Ozeki
Joint Research Center for Atom Technology (JRCAT)–Angstrom Technology Partnership (ATP), 1-1-4 Higashi, Tsukuba 305-0046, Japan

(Received 17 January 2000; accepted 19 April 2000)

The interaction of tertiarybutylarsine (TBAs), triisobutylgallium (TiBGa) and trisdimethylaminoarsenic (TDMAAs) with the GaAs(001)-2×4 surface is studied by scanning tunneling microscope. No adsorbates were observed after TBAs exposure at room temperature. In the case of TiBGa and TDMAAs, adsorbates were observed on the As dimer rows. They were adsorbed randomly at low coverage and formed a 4×4 structure at a full monolayer. Weak interaction between molecules and the GaAs surface is expected because the 2×4 structure of the clean surface was kept under the adsorbates. © *2000 American Vacuum Society.* [S0734-211X(00)02404-5]

I. INTRODUCTION

Nanofabrication on compound semiconductor surfaces may have great potential for technologies in the next generation, but it also has difficulties of systematical realization due to complexity of the materials. To find a key for the fabrication of nanostructures on compound semiconductor surfaces, it is necessary to understand the fundamental physics and chemistry of source molecules on such surfaces, e.g., adsorption sites and structures, reactivity and the desorption process at the atomic level.

The GaAs(001) surface is the most important and popular for devices. A number of reconstructions are known on the GaAs(001) surface by its surface stoichiometry, but the structural details of most of them are still under discussion.[1–9] The 2×4 surface is the principal surface obtained by molecular beam epitaxy of GaAs(001) and it is the most well defined structure among various phases.[6,10] It is rather inactive for organometallic molecules other than As-rich $c(4\times4)$ and Ga-rich 4×6 surfaces. So the GaAs(001)-2×4 surface is suitable as the first step in the study of essential reactions between source molecules and the GaAs(001) surface.

The essential reactions of source molecules on compound semiconductor surfaces are still uncertain at the atomic/molecular level. Some groups have tried to combine scanning tunneling microscopy (STM) experimental studies with theoretical study [e.g., using trimethylgallium ($TMGa:Ga(CH_3)_3$)] on GaAs(001)-2×4 in (Refs. 11–13) and other experimental methods [using *t*-butylphosphine ($TBP:(CH_3)_3CPH_2$)] on GaP(001)-2×4 (Ref. 14) to investigate the adsorption mechanism. We selected tertiarybutylarsine [($TBAs:(C_4H_9)AsH_2$)], triisobutylgallium {$TiBGa: Ga[CH_2CH(CH_3)_2]_3$} and trisdimethylaminoarsenic {$TDMAAs:As[N(CH_3)_2]_3$} as source molecules to deposit on the GaAs(001)-2×4 surface, because source molecules with low decomposition temperatures are good candidates for practical use.[15–17] TBAs is known as one of the main organometallic As source with low decomposition temperature and high vapor pressure for atomic layer epitaxy[18] and organometallic vapor phase epitaxy.[19] TiBGa is selected not only because of its low decomposition temperature, but also because of its simple reaction process on the GaAs surfaces. It is adsorbed on the GaAs(001)-2×4 surface without dissociation at a sample temperature of 200 °C or less, and it decomposes directly into Ga and isobutyl groups above 300 °C.[17] TDMAAs is a less toxic As source than arsine for metalorganic molecular beam epitaxy, which has a relatively low decomposition temperature due to As–N bonding.[20–23]

The study of selective adsorption of organometallic molecules on a specific site of an As-rich GaAs(001) surface will give us new knowledge and a clue to the technologies for atomic layer epitaxy and nanostructure fabrication. As the first step, we exposed some organometallic molecules on a GaAs(001)-2×4 surface at room temperature and observed the surface structure using STM after that.

II. EXPERIMENT

The experiments were carried out with a variable-temperature scanning tunneling microscope (VTSTM) (Omicron GmbH) in ultrahigh vacuum (UHV). The STM apparatus is composed of two chambers, the STM chamber (base pressure: 4×10^{-11} Torr) equipped with the VTSTM and the preparation chamber (8×10^{-11} Torr) equipped with two sample heating stages. It is connected to the molecular beam epitaxy (MBE) chamber (6×10^{-10} Torr) and the processing chamber (6×10^{-10} Torr) by UHV tunnels ($<3\times10^{-10}$ Torr), so that the samples are transferred to each chamber without contamination.

The sample ($7\times10\times0.35\,mm^3$) was cut from an *N*-type on-axis wafer (Si dopant, $1.6\times10^{-3}\,\Omega\,cm$) and was mounted on a molybdenum holder with indium. The native oxide on the sample surface was removed by annealing at >550 °C in As_4 flux and a GaAs homoepitaxy layer was grown at ~530 °C with an As_4/Ga flux ratio of ~60. Then the sample was annealed at ~510 °C with As_4 flux for more than 60 min until we got a sharp 2×4 reflection high-energy electron diffraction (RHEED) pattern. Keeping the 2×4 RHEED pattern, the sample was cooled down with As_4 flux until 400 °C.

[a]Electronic mail: hiromi@jrcat.or.jp

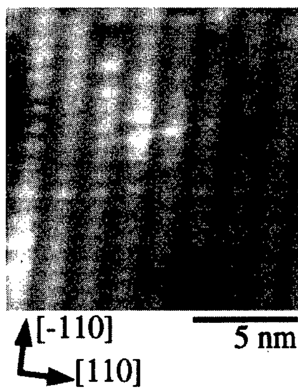

FIG. 1. STM images of a GaAs(001)-2×4 clean surface. $15\times15\,\mathrm{nm}^2$, $V_s=-3.0\,\mathrm{V}$, $I_t=0.21\,\mathrm{nA}$.

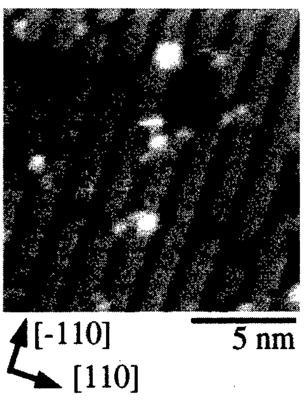

FIG. 2. STM images of the GaAs (001) surface after TBAs exposure. Surface As dimers are still observed. Bright spots on the shoulder of the dimers are considered to be extra As atoms. $15\times15\,\mathrm{nm}^2$, $V_s=-3.2\,\mathrm{V}$, $I_t=0.17\,\mathrm{nA}$.

Then the sample was quenched without As_4 flux and was transferred to the STM chamber through UHV tunnels.

After the STM observation on the clean surface in the STM chamber, the sample was transferred to the processing chamber and was exposed to an organometallic molecular beam at room temperature. The temperature of the bubbler was kept at 40–50 °C and the incident angle of the molecular beam was perpendicular to the surface. Organometallic molecules were supplied to the surface as molecular beam pulses (pulse width: 20–250 ms, interval: 500 ms) or as a continuous beam with a diameter of ~3 mm using an electromagnetic gas valve. The total exposure time was 2–300 s and the beam equivalent pressure was 10^{-8}–10^{-6} Torr. Then the sample was transferred to the STM chamber again and observation of the surface was carried out immediately. All STM observations were done at room temperature. After observation of adsorbates, the sample was heated to 200–250 °C slowly in the preparation chamber and was observed by STM again at room temperature.

III. RESULTS AND DISCUSSION

The GaAs(001)-2×4 clean surface was scanned with a Pt–Ir tip at a sample bias voltage (V_s) of −3.0 V (filled state) and a tunneling current (I_t) of 0.21 nA (Fig. 1). The bright rows and trenches along the [−110] direction correspond to As dimer rows and missing dimer rows, respectively. The distance between the dimer rows along the [110] direction is 1.6 nm. The distance between the bright features is 0.8 nm, and one consists of two As dimers according to previous studies.[1,5,6,10]

A STM image of the GaAs(001) surface ($15\times15\,\mathrm{nm}^2$) after the exposure of TBAs for 2.4 s by molecular beam pulses (pulses width: 20 ms, total exposure: $\sim2.3\times10^{13}$ molecules) at room temperature is shown in Fig. 2. No additional features were observed. The amount of extra As atoms on the shoulder of the As dimers is the same as that on the clean surface, so it is considered that no decomposition occurred on the surface. These results are expected from the quite small sticking coefficient of the TBAs molecule for GaAs(001)-2×4 with this dosage at room temperature[15] and confirmed that no contamination reached the surface during sample transfer and exposure of source molecules.

Although TMGa is well known as a Ga source molecule, TiBGa is used in this work because the decomposition of TiBGa on GaAs is simpler than that of TMGa. The GaAs(001) surface ($30\times30\,\mathrm{nm}^2$) after the exposure of TiBGa for 0.8 s by molecular beam pulses (pulse width: 20 ms, total exposure: $\sim2.4\times10^{12}$ molecules) is observed at room temperature as shown in Fig. 3(a). White features with a round shape appeared on the surface; they were adsorbed randomly, but sat on the As dimer rows not on the missing rows. The density of these features increased as the TiBGa dosage increased. When the dosage was increased up to a full monolayer (exposure time: 11.6 s, total exposure: $\sim3.5\times10^{13}$ molecules), adsorbates formed a 4×4 structure [Fig. 3(b)], which is also confirmed by low-energy electron diffraction (LEED). The distance between rows along the [−110] direction was still the same as that of the clean surface, but no As dimers were observed at this coverage. The features are thought to be TiBGa molecules because TiBGa is adsorbed on the GaAs(001)-2×4 surface without dissociation at room temperature.[17] Their average diameter is 1.2 nm, which is close to the size of the TiBGa molecule estimated from covalent radii of the elements. In Fig. 3(b), the tone of adsorbates is not uniform, although only intact adsorption is expected. The difference of tone of adsorbates in STM images represents the height difference. The average height of bright features is 0.16 nm and that of the rather dusky features is 0.075 nm. It is thought that the difference is due to irregularities in the substrate surface, orientation of the molecules, second layer adsorption, and the difference in interaction with the surface. The average distance between molecules along the [110] direction, 1.6 nm, is just twice the distance between the pairs of As dimers. Along the [−110] direction, adsorbates sat side by side or were shifted ~0.8 nm from their neighboring ones on the next row. Thinking over the GaAs(001)-2×4β2 structure model, these periodicities indicate that one TiBGa molecule was adsorbed per two pairs of top-layer As dimers.

Another candidate as an As source is TDMAAs. Figure

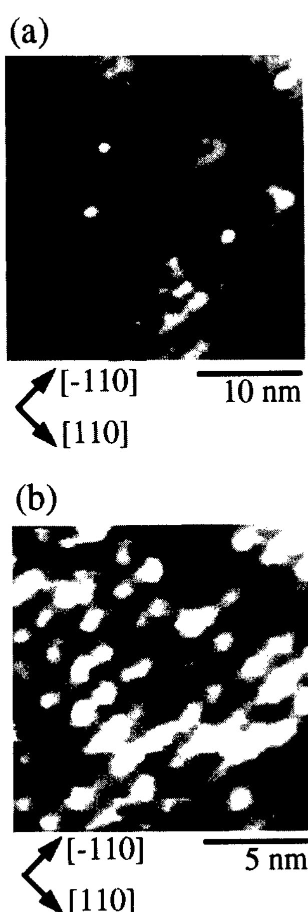

FIG. 3. STM images of the GaAs (001) surface after TiBGa exposure. (a) $30\times30\ nm^2$, total exposure time=20 s, $V_s=-3.0$ V, $I_t=0.20$ nA. (b) 4×4 structure. Each bright feature corresponds to a TiBGa molecule. $15\times15\ nm^2$, total exposure time=300 s (full monolayer), $V_s=-3.0$ V, $I_t=0.20$ nA.

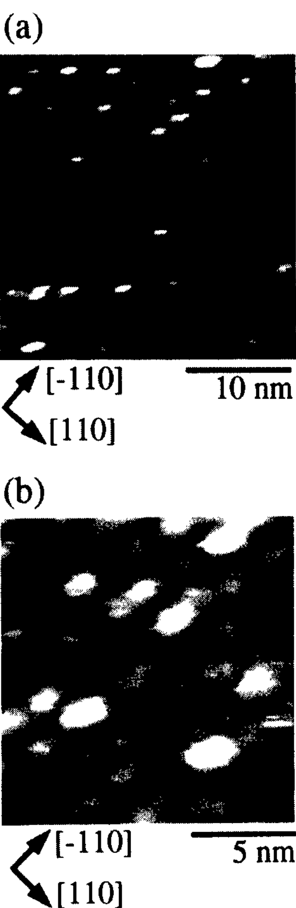

FIG. 4. STM images of the GaAs (001) surface after TDMAAs exposure. (a) $30\times30\ nm^2$, total exposure time=2.4 s, $V_s=-2.2$ V, $I_t=0.27$ nA. (b) 4×4 structure. Each feature is thought to be a TDMAAs molecule. $15\times15 nm^2$, total exposure time=30 s (full monolayer), $V_s=-3.1$ V, $I_t=0.21$ nA.

4(a) shows a STM image of the GaAs(001) surface after the exposure of TDMAAs for 2.4 s by molecular beam pulses (pulse width: 20 ms, total exposure: $\sim1.6\times10^{13}$ molecules) at room temperature. Arsenic dimers were still observed and bright features appeared on the dimer rows. These features increased with increased exposure so they are thought to be TDMAAs molecules and/or their relations, e.g., alkyl groups and partially decomposed molecules such as DDMAAs and MDMAAs. They were adsorbed on the As dimers randomly at low coverage the same as TMGa and TiBGa. The surface structure changed dramatically after TDMAAs exposure of 30 s by molecular beam pulses (pulse width: 250 ms, total exposure: $\sim2.0\times10^{14}$ molecules) as shown in Fig. 4(b). The distance of 1.6 nm between the rows along the [−110] direction did not change, but no As dimers were observed. Instead of As dimers, it is observed that oval or round shaped features covered all of the surface. In Fig. 4(b), the tone of adsorbates is not uniform, some of them are brighter than others. The average height of bright features is 0.15 nm and that of the rather dusky features is 0.08 nm. The difference may be caused by the difference in adsorbates and for the same reasons as for TiBGa. The average diameter of adsorbates is 1.1 nm, and it is close to the estimated size of a TDMAAs molecule. The distances between them along the [110] direction in Fig. 4(b) are 1.6 and 2.4 nm. Along the [−110] direction, molecules sat side by side or were shifted ~0.8 nm from their neighboring ones on the next row. These periodicities indicate that one TDMAAs derived species exist per two or three pairs of As dimers.

The STM image of the surface after adsorption of TDMAAs molecules looks similar to that of the Ga including molecule (TiBGa) on the As-terminated GaAs(001) surface. All adsorbates sat on the dimer rows, not on the shoulder of the As dimers or on the missing rows. It is interesting that the aspects of the structure with adsorbates are the same without regard to the difference in metals included in the molecules. We cannot say the exact adsorption sites from only these results, but we tried to think of possible adsorption sites for these molecules. To consider the possibilities for TiBGa, previous studies on TMGa are profitable. TMGa sat on the top-layer As atoms of the GaAs(001)-2×4 surface through interaction between alkyl group and lone pairs of As dimers.[13] TMGa molecules were adsorbed on GaAs(001)-$c(2\times8)$ dissociatively, and it is thought that DMGa or MMGa bonds to As dimers from the vibrational spectra.[24] From these previous studies, TMGa derived species are ad-

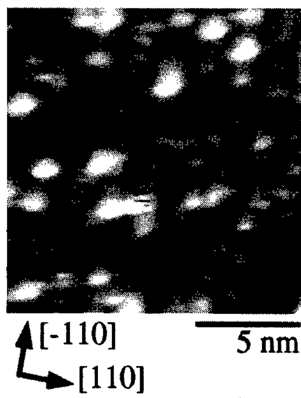

FIG. 5. STM image of the GaAs(001) surface after heating to ~200 °C. Arsenic dimers appeared again. Bright spots on the shoulder of the dimers correspond to extra As atoms. Larger bright features are considered to be As clusters and/or remaining adsorbates. $15\times 15\ nm^2$, $V_s=-2.2$ V, $I_t=0.38$ nA.

sorbed on top-layer As dimers. So it is expected that TiBGa molecules were adsorbed on top-layer As dimers. Two interactions are assumed between the adsorbates and the surface, one is the interaction between the alkyl group and lone pairs of top-layer As dimers in the same manner as that of TMGa and the other is the interaction between As and Ga atoms. On the other hand, more studies are required to identify the TDMAAs derived species. But almost all adsorbates in the STM image were equal, so we assume only one adsorption state for TDMAAs derived species here. TDMAAs molecules are adsorbed on a Ga-rich GaAs(001)-4×6 surface without As–N bond dissociation at 100 °C.[21] The GaAs(001)-2×4 surface is less active for chemical reaction than the 4×6 surface, and therefore these bright features are expected to be TDMAAs molecules. So we assumed only intact adsorption to think of the possible adsorption sites. One possibility is that TDMAAs molecules were adsorbed on top-layer As dimers through interaction between the alkyl group and lone pairs of As dimers the same as for TMGa and TiBGa. Another is that they were adsorbed on the second-layer Ga atoms between the pair of top-layer As dimers through interaction between As and Ga atoms. These arrangements are consistent with observed surface periodicities.

It is expected that adsorbed organometallic molecules are desorbed from the GaAs(001) surface at around 200 °C.[16,17] On the other hand, Ga and As atoms are still likely to remain on the GaAs(001)-2×4 surface over this temperature range. When the samples which adsorbed TiBGa or TDMAAs were heated to ~200 °C at a heating rate of ~0.7 °C/s, the As dimers appeared again. The number of As dimers that reappeared increased as the heating temperature became higher. From these results, it is indicated that the 2×4 structure of the GaAs(001) is kept under adsorbates so quite weak interaction is expected between the surface and the molecules. In the case of TiBGa, an almost clean 2×4 surface appeared after heating. It is considered that all TiBGa molecules were desorbed without decomposition at this heating rate. Figure 5 shows a STM image of the surface after TDMAAs desorption by heating. Large bright features on the As dimers rows in Fig. 5 are considered to be remaining hydrocarbons and/or As clusters. Small bright spots at the edge of the As dimers are thought to be As atoms. Extra As atoms at the same sites were also observed on the clean surface, but the quantity of extra As atoms after heating was much larger than that on the clean surface. The increase of As atoms suggests that the decomposition process occurred on the surface under 200 °C, since an As atom should be supplied from a TDMAAs molecule when it decomposes completely. From the desorption analysis, As–N bonds of TDMAAs molecules were observed to dissociate on the Ga-rich GaAs(001)-4×6 surface even at room temperature, which is much lower than the decomposition temperature in the gas phase (250–300 °C).[21,22] It was impossible to distinguish additional As clusters from the remaining molecules/relations by STM, so we cannot discuss the decomposition process quantitatively here, we only give a rough estimation. The remaining features in Fig. 5 are counted up as 28 arsenic atoms and 18 clusters. It is estimated that ~60 As atoms are supplied for a $15\times 15\ nm^2$ area by complete decomposition of full-monolayer TDMAAs molecules. On the assumption that all of the remaining features are As atoms and clusters, and if two As atoms are included per one cluster, 64 arsenic atoms remained in this area. This means that all TDMAAs molecules decomposed under 200 °C. If the large features are As including molecules/relations, 46 As atoms would finally be supplied and ~14, molecules were desorbed without decomposition. In this case, ~75% of the molecules decomposed under 200 °C. It is less possible that TDMAAs derived species without As atoms remain on the surface after heating. But if the large features are species without As atoms, 28 As atoms are supplied after heating, which means ~45% molecules decomposed under 200 °C. From STM experiments, it is estimated that the decomposition probability of TDMAAs molecules on the GaAs(001)-2×4 surface under 200 °C is at least 45%. More studies of adsorption of TDMAAs on the GaAs(001)-2×4 surface will be required to identify the surface species and to know the surface process exactly using other experimental methods and theoretical calculation.

IV. CONCLUSIONS

TiBGa and TDMAAs molecules were adsorbed on the GaAs(001)-2×4 surface randomly at low coverage. The surface was closely packed with TiBGa molecules or TDMAAs derived species and formed a 4×4 structure at full monolayer. After heating to ~200 °C, they were desorbed from the surface and the As dimers were observed again, therefore it is considered that the surface 2×4 structure is kept under adsorbates. Weak interaction between the surface and molecules is expected. Additional As atoms after desorption of TDMAAs suggests that the probability of decomposition of TDMAAs molecules under 200 °C is at least 45%.

ACKNOWLEDGMENTS

The authors would like to acknowledge useful discussions with Professor Y. Murata of the University of Electro-Communications and Professor Y. Fukuda of Shizuoka Uni-

versity. This work was partly supported by the New Energy and Industrial Technology Development Organization (NEDO), and performed at the Joint Research Center for Atom Technology (JRCAT) under a joint research agreement between the National Institute for Advanced Interdisciplinary Research (NAIR) and the Angstrom Technology Partnership (ATP).

[1]D. J. Chadi, J. Vac. Sci. Technol. A **5**, 834 (1987).
[2]M. D. Pashley, K. W. Haberern, W. Friday, J. M. Woodall, and P. D. Kichner, Phys. Rev. Lett. **60**, 2176 (1988).
[3]D. K. Biegelsen, R. D. Bringans, J. E. Northrup, and L. E. Swartz, Phys. Rev. B **41**, 5701 (1990).
[4]S. L. Skala, J. S. Hubacek, J. R. Tucker, J. W. Lyding, S. T. Chou, and K. Y. Cheng, Phys. Rev. B **48**, 9138 (1993).
[5]J. E. Northrup and S. Froyen, Phys. Rev. B **50**, 2015 (1994).
[6]T. Hashizume, Q. K. Xue, J. Zhou, A. Ichimiya, and T. Sakurai, Phys. Rev. Lett. **73**, 2208 (1994); Phys. Rev. B **51**, 4200 (1995).
[7]Q. K. Xue, T. Hashizume, J. Zhou, T. Sakata, T. Ohno, and T. Sakurai, Phys. Rev. Lett. **74**, 3177 (1995).
[8]I. Chizhov, G. Lee, R. F. Willis, D. Lubyshev, and D. L. Miller, Phys. Rev. B **56**, 1013 (1997); Surf. Sci. **419**, 1 (1998).
[9]G. R. Bell, J. G. Belk, C. F. McConville, and T. S. Jones, Phys. Rev. B **59**, 2947 (1999).
[10]V. P. LaBella, H. Yang, D. W. Bullock, P. M. Thibado, P. Kratzer, and M. Scheffler, Phys. Rev. Lett. **83**, 2989 (1999).
[11]A. R. Avery, A. J. Mayne, C. M. Goringe, J. H. G. Owen, C. W. Smith, M. O. Schweitzer, T. S. Jones, G. A. D. Briggs, and W. H. Weinberg, Mater. Res. Soc. Symp. Proc. **312**, 219 (1993).
[12]A. J. Mayne, C. M. Goringe, C. W. Smith, and G. A. D. Briggs, Surf. Sci. **348**, 209 (1996).
[13]C. M. Goringe, L. J. Clark, M. H. Lee, M. C. Payne, I. Stich, J. A. White, M. J. Gillan, and P. Sutton, J. Phys. Chem. B **101**, 1498 (1997).
[14]Y. Fukuda, T. Sekizawa, and N. Sanada, Surf. Sci. **432**, L595 (1999).
[15]M. Ozeki, J. Cui, and M. Ohashi, Appl. Surf. Sci. **112**, 110 (1997); J. Cui, M. Ozeki, and M. Ohashi, *ibid.* **117/118**, 739 (1997).
[16]J. Cui, M. Ozeki, and M. Ohashi, Appl. Phys. Lett. **71**, 2659 (1997).
[17]J. Cui, M. Ozeki, and M. Ohashi, J. Cryst. Growth **188**, 137 (1998).
[18]C. H. Chen, C. A. Beyler, P. D. Dapkus, J. J. Alwan, and J. J. Coleman, Appl. Phys. Lett. **60**, 2418 (1992).
[19]C. H. Chen, C. L. Larsen, and G. B. Stringfellow, Appl. Phys. Lett. **50**, 218 (1987).
[20]M. H. Zimmer, R. Hovel, W. Brysch, A. Brauers, and P. Balk, J. Cryst. Growth **107**, 348 (1991).
[21]M. Xi, S. Salim, K. F. Jensen, and D. A. Bohling, Mater. Res. Soc. Symp. Proc. **334**, 169 (1994).
[22]J. Cui and M. Ozeki (private communication).
[23]D. A. Bohling, C. R. Abernathy, and K. F. Jensen, J. Cryst. Growth **136**, 118 (1994).
[24]P. E. Gee, H. Qi, and R. F. Hicks, Surf. Sci. **330**, 135 (1995).

Reflectance anisotropy spectroscopy of the growth of perylene-3,4,9,10-tetracarboxylic dianhydride on chalcogen passivated GaAs(001) surfaces

T. U. Kampen[a)]
Institut für Physik, TU Chemnitz, D-09107 Chemnitz, Germany

U. Rossow
Institut für Physik, TU Ilmenau, D-98684 Ilmenau, Germany

M. Schumann, S. Park, and D. R. T. Zahn
Institut für Physik, TU Chemnitz, D-09107 Chemnitz, Germany

(Received 17 January 2000; accepted 5 April 2000)

The properties of organic molecular layers grown from perylene-3,4,9,10-tetracarboxylic dianhydride (PTCDA) on GaAs(001) substrates were investigated using reflectance anisotropy spectroscopy/reflectance difference spectroscopy (RAS/RDS). In an attempt to grow ordered organic layers GaAs(001) surfaces were modified with sulfur prior to the evaporation of PTCDA under ultrahigh vacuum conditions. The chalcogen modification results in a gallium sulfide-like surface layer terminated by S dimers, which shows a (2×1) low-energy electron diffraction pattern. The lines shapes of the RAS spectra of S modified surfaces show sharp derivative-like features at the E_1 gap and broad spectral features at higher energies likely related to E_0' and E_2 gaps of bulk GaAs. For low PTCDA coverages the shape of the spectra in the energy range of the GaAs bulk features is unchanged which indicates a low interaction between substrate and organic layer. Additional features appear in the spectra for PTCDA coverages even below 0.3 nm which can be attributed to transitions between the highest occupied molecular orbital and the lowest unoccupied molecular orbital at 2.23 eV. While the sharp feature due to the E_1 gap of GaAs is essentially unaffected, the optical anisotropy at higher energies is increasing strongly with increasing PTCDA layer thickness which is due to interference effects as shown by a model calculation. © *2000 American Vacuum Society.* [S0734-211X(00)00804-0]

I. INTRODUCTION

Thin films of organic molecules show properties which make them a promising material for optoelectronic devices like light emitting diodes.[1] The advantage of organic materials over conventional semiconductors is the synthetic capabilities of organic chemistry to tailor the molecules and their properties according to what is needed for a certain device. For the structural properties of organic films, which affect the electronic and optical properties, the interaction between the organic film and the substrate at the interface is of importance.

Organic films of different crystalline quality have been grown depending on the type of substrate. Films grown on layered materials, or, in other words, van der Waals crystals, such as graphite or transition metal dichalcogenides showed the best crystalline quality.[2,3] The weak chemical interaction due to van der Waals bonding between the molecules and these surfaces supports an epitaxial growth of the organic molecular layers. Chemically active sites such as dangling bonds, vacancies, or steps greatly affect the molecular ordering at the interface and in the films. One example of the influence of chemically active sites on the properties of the organic layers is the growth of perylene-3,4,9,10-tetracarboxylic dianhydride (PTCDA) on nonpassivated and passivated GaAs(001) surfaces. Investigations of the growth of PTCDA on GaAs(001) surfaces by low-energy electron diffraction (LEED) and reflection high-energy electron diffraction (RHEED) methods showed bulk molecular stacking in the direction perpendicular to the substrate surface.[4] In the plane parallel to the substrate considerable disorder was observed which is attributed to the "pinning" of the organic molecules by chemically active sites in random positions on the GaAs surface. This leads to the presence of small misoriented domains in the deposited films. Passivation of the GaAs surface with Se reduces the density of chemically active sites. The quality of the PTCDA films significantly improved.[5]

In this study we applied reflectance anisotropy spectroscopy/reflectance difference spectroscopy (RAS/RDS)[6–8] to characterize the growth of PTCDA layers on sulfur passivated GaAs(001) surfaces. RAS measures the difference in reflectance $\Delta r/r = 2(r_\alpha - r_\beta)/(r_\alpha + r_\beta)$ between two directions α and β that are perpendicular to each other in the plane of the surface. For cubic materials the bulk is optically isotropic and the signal observed originates at surfaces and interfaces, which have reduced symmetry. For materials of lower (than cubic) symmetry as the organic compound PTCDA the bulk can also contribute if the symmetry in the plane parallel to the surface is lowered. This is

a)Electronic mail: kampen@physik.tu-chemnitz.de

the case when, for example, the molecules are flat on the substrate and are oriented in the same direction or the planes of the molecular films are tilted with respect to the substrate surface. To obtain ordered layers it is necessary to passivate the surface and thus supress chemical reactions between the molecule and the substrate. For GaAs(001) S and Se termination are well known to passivate the surface and ordered growth has been reported for the Se passivation.[9] The advantage of RAS in such studies is that it is thus very sensitive to the growth mode of the layer and also to the interface properties as will be discussed in detail.

II. EXPERIMENT

Homoepitaxial n- and p-type GaAs(001) layers with a doping concentration of $N=P=1\times10^{18}\,\mathrm{cm}^{-3}$ served as substrates in this study. After their growth by molecular beam epitaxy they were covered by a thick amorphous arsenic layer to protect the GaAs(001) surfaces against contamination and oxidation. These samples were transferred into an ultrahigh vacuum (UHV) system with a base pressure of $p<2\times10^{-10}$ mbar. The arsenic layer was then removed by gentle annealing to 380 °C. This leads to an As-rich $c(4\times4)$ surface reconstruction of the GaAs(001) surface as can be judged from the line shape analysis of the measured photoemission spectra and additional (LEED) experiments. For the chalcogen passivation the compound SnS_2 was used as source material in a Knudsen cell since this material decomposes in a well defined temperature range into SnS+S and is thus an ideal source for atomic sulfur.[10] The substrates were kept at room temperature during the chalcogen deposition. The S covered surface was then annealed to 400 °C. The surfaces obtained by this treatment are terminated by sulfur dimers and reveal a (2×1) reconstruction as indicated by LEED.

A sulfur passivation can also be achieved by wet chemical etching in S_2Cl_2.[11,12] This etching procedure consists of four steps. First, the sample is successively cleaned in aceton, ethanol, and ultraclean water for 5 min each using an ultrasonic bath. Second, the sample is etched for 5 s in S_2Cl_2. This step removes the oxide and modifies the surface with S. Third, the sample is dipped into CCl_4 for 5 s. Fourth, the procedure of step 1 is repeated.

PTCDA films were prepared by organic molecular beam deposition (OMBD) from a Knudsen cell under UHV conditions. Before the PTCDA was used in OMBD the source material was purified by thermal gradient sublimation in high vacuum. The evaporation rate determined from a quartz crystal microbalance was about 0.3 nm min^{-1}.

The RDS measurements were done using a spectrometer that operates at near-normal incidence from 1.5 to 5.5 eV.[8] Both real and imaginary parts of $\Delta r/r$ were measured. For convenience only real parts are shown in the following. The eigenaxes α and β are oriented along the $[-110]$ and $[110]$ directions, respectively. The orientation of the samples was checked by LEED.

III. SIMULATION OF $\Delta r/r$

For a better understanding of the measured RAS/RDS spectra we describe the system by a four-phase model: (0): $\epsilon_0=1$, (1): isotropic layer (PTCDA) with ϵ_1, (2): anisotropic interface width d_2 with two dielectric functions $\epsilon_{2\alpha}$ and $\epsilon_{2\beta}$, respectively, (3): isotropic substrate with ϵ_3. Any anisotropy of the PTCDA layer results in an extra contribution to $\Delta r/r$ which is not considered here.

The signal is given by

$$\frac{\Delta r}{r}=\frac{r_\alpha^{(4)}-r_\beta^{(4)}}{1/2(r_\alpha^{(4)}+r_\beta^{(4)})}, \tag{1}$$

where $r_\alpha^{(4)}$ and $r_\beta^{(4)}$ are the Fresnel coefficients for the four-phase model with $\epsilon_{2\alpha}$ and $\epsilon_{2\beta}$, respectively.

Usually $\epsilon_{2\alpha}\approx\epsilon_{2\beta}$ and we can expand the nominator and keep only linear terms in $\Delta\epsilon_2=\epsilon_{2\alpha}-\epsilon_{2\beta}$:

$$r_\alpha^{(4)}-r_\beta^{(4)}=\frac{\partial r^{(4)}}{\partial\epsilon_2}\Delta\epsilon_2. \tag{2}$$

Furthermore, it is easy to show that $1/2(r_\alpha^{(4)}+r_\beta^{(4)})=r^{(4)}\times(\bar\epsilon_2)$ where $\bar\epsilon_2=1/2(\epsilon_{2\alpha}+\epsilon_{2\beta})$.

The Fresnel coefficient for the four-phase model is given by[13]

$$r^{(4)}=\frac{(r_{01}+r_{12}e^{i2\beta_1})+(r_{01}r_{12}+e^{i2\beta_1})r_{23}e^{i2\beta_2}}{(1+r_{01}r_{12}e^{i2\beta_1})+(r_{12}+r_{01}e^{i2\beta_1})r_{23}e^{i2\beta_2}}, \tag{3}$$

where r_{ij} is the Fresnel coefficient for the reflection at the interface from phase (i) to phase (j) which can be expressed by the corresponding dielectric functions ϵ_i and ϵ_j and the angle of incidence ϕ_0:

$$r_{ij}=\frac{\sqrt{\epsilon_i-\epsilon_0\sin^2\phi_0}-\sqrt{\epsilon_j-\epsilon_0\sin^2\phi_0}}{\sqrt{\epsilon_i-\epsilon_0\sin^2\phi_0}+\sqrt{\epsilon_j-\epsilon_0\sin^2\phi_0}}. \tag{4}$$

The phase factors β_i for phase (i) are given by

$$\beta_i=\frac{2\pi d_i E}{hc}\sqrt{\epsilon_i-\epsilon_0\sin^2\phi_0}, \tag{5}$$

where E is the photon energy, hc is the product of Planck's constant and the velocity of light, and d_i the layer thickness.

In the following we neglect the small angle of incidence which is typically below 1°. The derivative of $r^{(4)}$ is then given by

$$\frac{\partial r^{(4)}}{\partial\epsilon_2}=\frac{\partial r^{(4)}}{\partial r_{12}}\frac{\partial r_{12}}{\partial\epsilon_2}+\frac{\partial r^{(4)}}{\partial r_{23}}\frac{\partial r_{23}}{\partial\epsilon_2}+\frac{\partial r^{(4)}}{\partial\beta_2}\frac{\partial\beta_2}{\partial\epsilon_2}. \tag{6}$$

A straightforward calculation yields

$$\frac{\partial r^{(4)}}{\partial\epsilon_2}=\frac{(1-r_{01}^2)e^{i2\beta_1}}{[(1+r_{01}r_{12}e^{i2\beta_1})+(r_{12}+r_{01}e^{i2\beta_1})r_{23}e^{i2\beta_2}]^2}\times\left[(1-r_{23}^2e^{i4\beta_2})\frac{\partial r_{12}}{\partial\epsilon_2}+e^{i2\beta_2}(1-r_{12}^2)\frac{\partial r_{23}}{\partial\epsilon_2}+2ir_{23}e^{i2\beta_2}(1-r_{12}^2)\frac{\partial\beta_2}{\partial\epsilon_2}\right]. \tag{7}$$

Since phase (2) is the interface and (3) is bulk, the dielectric functions are approximately equal and we can neglect r_{23}. Then

$$\bar{r}^{(4)}(r_{23}\approx 0)=\frac{(r_{01}+r_{12}e^{i2\beta_1})}{(1+r_{01}r_{12}e^{i2\beta_1})}. \tag{8}$$

This is exactly valid for the derivative of the Fresnel coefficient in Eq. (7) since the derivative is evaluated for $\Delta\epsilon_2=0$:

$$\frac{\partial r^{(4)}}{\partial\epsilon_2}=\frac{(1-r_{01}^2)e^{i2\beta_1}}{(1+r_{01}r_{12}e^{i2\beta_1})^2}\left[\frac{\partial r_{12}}{\partial\epsilon_2}+e^{i2\beta_2}(1-r_{12}^2)\frac{\partial r_{23}}{\partial\epsilon_2}\right]. \tag{9}$$

Combining Eqs. (9) and (8) we obtain

$$\frac{\Delta r}{r}=\frac{1}{\bar{r}^{(4)}}\frac{\partial r^{(4)}}{\partial\epsilon_2}\Delta\epsilon_2$$

$$=\frac{(1-r_{01}^2)e^{i2\beta_1}}{(r_{01}+r_{12}e^{i2\beta_1})(1+r_{01}r_{12}e^{i2\beta_1})}$$

$$\times\left[\frac{\partial r_{12}}{\partial\epsilon_2}+e^{i2\beta_2}(1-r_{12}^2)\frac{\partial r_{23}}{\partial\epsilon_2}\right]. \tag{10}$$

It is easy to show that

$$\frac{\partial r_{12}}{\partial\epsilon_2}+(1-r_{12}^2)\frac{\partial r_{23}}{\partial\epsilon_2}\approx 0. \tag{11}$$

This follows also from the fact that the signal must vanish if the extension of the interface is zero.

For a very thin interface we can further approximate: $\exp(i2\beta_2)\approx 1+i2\beta_2$. Taken into account Eq. (11) then Eq. (10) becomes

$$\frac{\Delta r}{r}=\frac{(1-r_{01}^2)e^{i2\beta_1}}{(r_{01}+r_{12}e^{i2\beta_1})(1+r_{01}r_{12}e^{i2\beta_1})}$$

$$\times 2i\beta_2(1-r_{12}^2)\frac{\partial r_{23}}{\partial\epsilon_2}\Delta\epsilon_2. \tag{12}$$

Using the Fresnel coefficients the last term can be written as

$$2i\beta_2(1-r_{12}^2)\frac{\partial r_{23}}{\partial\epsilon_2}=\frac{4\pi i d_2 E}{hc}\frac{\sqrt{\epsilon_1}}{(1+\sqrt{\epsilon_1}/\sqrt{\epsilon_2})^2}\frac{1}{\epsilon_3}. \tag{13}$$

Finally

$$\frac{\Delta r}{r}=\frac{(1-r_{01}^2)e^{i2\beta_1}}{(r_{01}+r_{12}e^{i2\beta_1})(1+r_{01}r_{12}e^{i2\beta_1})}$$

$$\times\frac{\sqrt{\epsilon_1}}{(1+\sqrt{\epsilon_1}/\sqrt{\epsilon_2})^2}\frac{4\pi i d_2 E}{hc}\frac{\Delta\epsilon_2}{\epsilon_3}. \tag{14}$$

Now

$$\left(\frac{\Delta r}{r}\right)_{\text{interface}}=-\frac{4\pi i d_2 E}{hc}\frac{\Delta\epsilon_2}{\epsilon_3} \tag{15}$$

is just the interface anisotropy.

We can therefore write

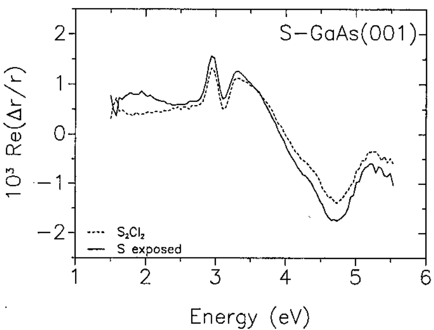

FIG. 1. RAS spectra of two GaAs(001) surfaces passivated by sulfur using a UHV treatment or wet chemical etching.

$$\frac{\Delta r}{r}=\frac{(1-r_{01}^2)e^{i2\beta_1}}{(r_{01}+r_{12}e^{i2\beta_1})(1+r_{01}r_{12}e^{i2\beta_1})}\frac{\sqrt{\epsilon_1}}{(1+\sqrt{\epsilon_1}/\sqrt{\epsilon_2})^2}$$

$$\times(-1)\left(\frac{\Delta r}{r}\right)_{\text{interface}}. \tag{16}$$

For a better understanding of Eq. (16) some further approximations can be done. First, the Fresnel coefficients are smaller than 0.5 and thus the squares can be neglected. Second, the refractive index of PTCDA is smaller than that of GaAs.

Then

$$\frac{\Delta r}{r}\approx\frac{e^{i2\beta_1}}{(r_{01}+r_{12}e^{i2\beta_1})}n_1(-1)\left(\frac{\Delta r}{r}\right)_{\text{interface}}. \tag{17}$$

Note that both Fresnel coefficients r_{01}, r_{12} are negative.

Thus we can separate the RAS/RDS signal in an interference related term, the refractive index of PTCDA, and the interface contribution. The first term can become quite large when $|r_{01}|\approx|r_{12}|$ and the layer is essentially transparent.

IV. RESULTS AND DISCUSSION

In Fig. 1 the RAS spectra of GaAs(001) surfaces passivated by S using both the vacuum deposition procedure and the wet chemical etching are shown. For reasons of comparison the optical anisotropy for the etched sample is offset. The line shapes of both spectra as well as the absolute values agree very well. Therefore, both treatments for the sulfur passivation lead to surfaces with the same optical properties. Bulk-like features are apparent in $\Delta r/r$ if the anisotropic surface modifies the bulk optical response. The sharp derivative-like feature(s) between 2.5 and 3.5 eV is attributed to the E_1 gap of GaAs while the broad feature with a minimum at 4.7 eV is related to E_0' and E_2 gaps of bulk GaAs. A weak shoulder around 3.6 eV is also apparent. A feature at this spectral position has previously been assigned to transitions involving S-S dimer states.[14] A small offset below 2.7 eV is likely due to strain effects in the window. For ideal passivated surfaces we expect a null signal in this spectral range.

The RAS spectra of sulfur modified GaAs(001) covered with PTCDA at room temperature are shown in Figs. 2 and

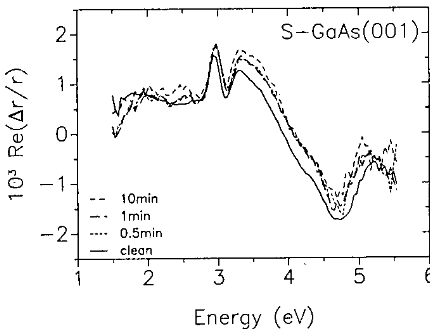

FIG. 2. RAS spectra of a GaAs(001) surface passivated with sulfur by wet chemical etching and after deposition of PTCDA.

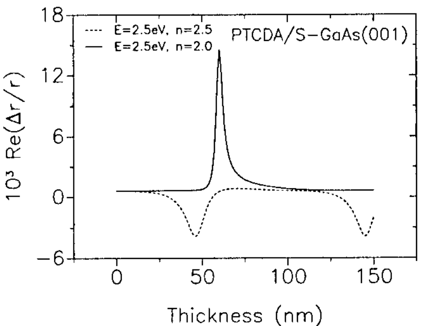

FIG. 4. Simulation of the intensity of the RAS signal at 2.5 eV as a function of the PTCDA layer thickness for two different refractive indices.

3. Here, Fig. 2 presents the spectra for the sulfur treated substrate and for PTCDA exposures of 0.5, 1, and 10 min. For these exposures the features of the GaAs bulk in the RAS spectra remain essentially unchanged. A new feature can be observed at 2.3 eV even for smallest coverages. It can be attributed to the highest occupied molecular orbital-lowest unoccupied molecular orbital (HOMO-LUMO) transitions of PTCDA, which have an energy difference of 2.23 eV. The spectra for higher PTCDA exposures between 25 min and 100 min are displayed in Fig. 3. The PTCDA induced feature at 2.3 eV is more pronounced for exposures above 25 min. The GaAs bulk features due to the E_1 gap are still unchanged while the minimum at 4.7 eV is decreased with increased PTCDA coverage. This dependence of the signal as a function of the PTCDA coverage is due to interference effects. This becomes more obvious by comparing the experimental data with the simulation of the magnitude of the RAS signal at 2.5 and 4.7 eV photon energy displayed in Figs. 4 and 5, respectively. For both photon energies two refractive indices of the PTCDA were used as indicated in the figures and the layer thickness was varied between 0 and 150 nm. The anisotropy as a function of the layer thickness d_1 was then calculated by Eq. (16) with the interface anisotropy determined from the spectra of the S-passivated GaAs surface with offset corrections.

For transparent overlayers Eq. (16) predicts a periodic varying signal at fixed photon energy with increasing layer thickness. At 4.7 eV the minima are much sharper for $n=2.0$ compared to $n=2.5$ and the first minimum occurs at a layer thickness smaller than 25 nm. The signal is amplified by more than a factor of 10. This is not observed in the experimental data. The minimum signal is not reached for the highest exposure (~33 nm). Better agreement with experiment is found for $n=2.0$. The first minimum for 4.7 eV is shifted to higher values and for 2.5 eV the calculation predicts essentially no increase in signal (due to interference effects). The latter is expected because for the passivated surface $\Delta r/r$ should be zero and according to Eq. (16) the total signal would be zero as well. However, the anisotropy of the PTCDA layer induces an additional signal which is also influenced by interference effects and which is not taken into account in the derivation of Eq. (16). For a more realistic calculation we need to separate both effects and must consider the finite absorption of the layers for photon energies around 2.5 eV.

V. SUMMARY

We have investigated the growth of PTCDA on S-passivated GaAs(001) surfaces using RAS. The RAS spectra of GaAs(001) surfaces passivated either by wet chemical etching or S deposition and annealing in UHV are in very good agreement and show features due to the E_1, E_0', and E_2 gaps of the bulk GaAs. For increasing PTCDA coverage we observe a strong increase of the optical anisotropy for photon energies in the range 4.5–5 eV, while a smaller variation was found below 3.5 eV. This behavior can be understood by a simple calculation assuming that the signal originates at the interface and is modified by interferences in a

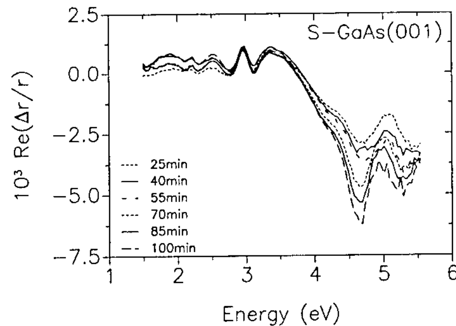

FIG. 3. RAS spectra of a sulfur passivated GaAs(001) with PTCDA exposures between 25 and 100 min.

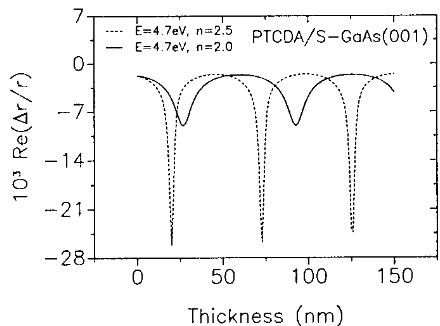

FIG. 5. Simulation of the intensity of the RAS signal at 4.7 eV as a function of the PTCDA layer thickness for two different refractive indices.

transparent, optically isotropic PTCDA overlayer. This also indicates that the interface is unchanged during PTCDA growth in agreement with previous photoemission[15] and Raman specroscopy[16] results. In addition a PTCDA induced feature in the optical anisotropy is observed at photon energies of 2.3 eV which is close to the HOMO-LUMO gap of PTCDA. This contribution is smaller compared to the interface anisotropy. This indicates that the PTCDA films are almost optical isotropic which could be due to an amorphous growth or an at least fourfold symmetry in the PTCDA films.

ACKNOWLEDGMENT

The authors gratefully acknowledge financial support by the Deutsche Forschungsgemeinschaft and the EU funded IHP Research Training Network "DIODE" (Contract No. HPRN-CT-1999-00164).

[1]C. W. Tung and S. A. van Slyke, Appl. Phys. Lett. **51**, 913 (1987).
[2]C. Ludwig, B. Gompf, W. Glatz, J. Petersen, W. Eisenmenger, M. Mobius, U. Zimmermann, and N. Karl, Z. Phys. B: Condens. Matter **86**, 397 (1992).
[3]M. L. Anderson, V. S. Williams, T. J. Schuerlein, G. E. Collins, C. D. England, L.-K. Chau, P. A. Lee, K. W. Nebesny, and N. R. Armstrong, Surf. Sci. **307–309**, 551 (1994).
[4]Y. Hirose, W. Chen, E. I. Haskal, S. R. Forrest, and A. Kahn, J. Vac. Sci. Technol. B **12**, 2616 (1994).
[5]Y. Hirose, S. R. Forrest, and A. Kahn, Appl. Phys. Lett. **66**, 944 (1994).
[6]D. E. Aspnes, J. Vac. Sci. Technol. B **3**, 1498 (1985).
[7]W. Richter, Philos. Trans. R. Soc. London **A344**, 453 (1993).
[8]D. E. Aspnes, J. P. Harbison, A. A. Studna, L. T. Florez, and M. K. Kelly, J. Vac. Sci. Technol. A **6**, 1327 (1988).
[9]Y. Hirose, S. R. Forrest, and A. Kahn, Appl. Phys. Lett. **66**, 944 (1994).
[10]T. Shimada, F. S. Ohuchi, and B. A. Parkinson, J. Vac. Sci. Technol. A **10**, 539 (1992).
[11]D. N. Gnoth, D. Wolfframm, A. Patchett, S. Hohenecker, D. R. T. Zahn, A. Leslie, I. T. McGovern, and D. A. Evans, Appl. Surf. Sci. **123/124**, 120 (1998).
[12]Z. S. Li, W. Z. Cai, R. Z. Su, G. S. Dong, D. M. Huang, X. M. Ding, X. Y. Hou, and X. Wang, Appl. Phys. Lett. **64**, 3425 (1994).
[13]R. M. A. Azzam and N. M. Bashara, *Ellipsometry and Polarized Light* (North-Holland, Amsterdam, 1977).
[14]G. Hughes, C. Springer, U. Resch, N. Esser, and W. Richter, J. Appl. Phys. **78**, 1948 (1995).
[15]S. Park, T. Querner, T. U. Kampen, W. Braun, and D. R. T. Zahn, Appl. Surf. Sci. (submitted).
[16]T. U. Kampen, G. Salvan, M. Friedrich, D. A. Tenne, S. Park, and D. R. T. Zahn, Appl. Surf. Sci. (accepted).

Schottky barrier height and electron affinity of titanium on AlN

B. L. Ward, J. D. Hartman, E. H. Hurt, K. M. Tracy, R. F. Davis, and R. J. Nemanich[a)]
Department of Physics and Department of Materials Science and Engineering, North Carolina State University, Raleigh, North Carolina 27695-8202

(Received 17 January 2000; accepted 6 April 2000)

Approximately 100 or 1000 Å of AlN was deposited on the (0001)Si-face of on-axis n-type 6H–SiC. The surfaces were examined by ultraviolet photoemission spectroscopy (UPS) utilizing the He I α (21.2 eV) and the He II α (40.8 eV) excitation. Experimental difficulties are discussed. Titanium was deposited on the clean surface of *in situ* grown AlN. The titanium–AlN interface was also characterized with UPS. Two approaches are presented to identify the valence band maximum (VBM) and the electron affinity χ of the clean surface of AlN was found to be either 0 to 1 eV depending upon the position of the valence band edge. The same assumptions were applied to the analysis of the Ti/AlN interface and, for the case of $\chi = 0$ eV, the position of the valence band maximum is 3.4 eV below the position of the Fermi level. For the case of $\chi = 1$ eV, the position of the valence band maximum is 4.4 eV below the position of the Fermi level. Therefore, the p-type Schottky barrier height of titanium on AlN is measured to be 3.4 ± 0.2 or 4.4 ± 0.2 eV for $\chi = 0$ eV and $\chi = 1$ eV, respectively. Independent of the selection of the valence band maximum, the observed Schottky barrier differed from that predicted by the Schottky–Mott model by 1.5 ± 0.2 eV. © *2000 American Vacuum Society.* [S0734-211X(00)00104-9]

I. INTRODUCTION

The III-nitride wide band gap semiconductors of AlN–GaN–InN have been considered for a wide range of electronic and optoelectronic applications. Of this group, AlN exhibits the largest band gap with a value of 6.2 eV.[1,2] Several studies have suggested the materials exhibit a low or negative electron affinity.[3–5] Given this small or negative electron affinity of AlN, our interest in exploring the Schottky barrier to AlN is twofold. The first is to explore contacts that could supply electrons to the conduction band, and the second is to determine if a thin metal layer on AlN will result in an effective negative electron affinity as in the case of diamond.[6]

Photoemission spectroscopy has proven to be an indispensable technique in obtaining information about electronic structure. In particular, ultraviolet photoemission spectroscopy (UPS) is especially surface sensitive, making it possible to determine the electron affinity and the surface Fermi level as well as offering information about surface states. These material parameters will have a direct effect on the properties of the interface formed between a metal and a semiconductor. However, these are not the only effects that will determine the value of the Schottky barrier. The complex bonding at the interface contributes to the Schottky barrier through several different effects.

The Schottky barrier is often described in terms of two models. The Schottky–Mott model assumes that the bands are aligned with respect to the vacuum level of the metal and the semiconductor. The n-type Schottky barrier is just the difference between the metal work function and the semiconductor electron affinity. The alternative model is the interface dipole model, where the structure of the interface causes a shift in the bands relative to the predictions of the Schottky–Mott model. This band shift may be interpreted as a change in the interface dipole due to the atomic bonding at the interface.

In understanding the electronic structure of interfaces of wide band gap semiconductors, it is useful to have knowledge of the electron affinity. The electron affinity of a semiconductor is defined as the energy difference between the vacuum level and the conduction band minimum. The value of the electron affinity at the surface of AlN has been the subject of debate in the literature. For example, thin layers of AlN deposited on 6H–SiC by organometallic vapor phase epitaxy (OMVPE) or by gas source molecular beam epitaxy (GSMBE) resulted in a negative electron affinity.[3,4] In another study,[7,8] AlN (0.2 μm thick) films were deposited on Si(111) by molecular beam epitaxy (MBE). The results of this study indicate a positive electron affinity of either 1.9 ± 0.2 or 2.1 ± 0.3 eV. In another study,[9] an epitaxial structure consisting of a 30 nm AlN(0001) layer on GaN on the (0001) face of Al_2O_3 exhibited a positive electron affinity value of 3.2 eV. Another technique[5] for depositing AlN involved first depositing a thick layer (2.7 μm) of n-type silicon-doped GaN and then depositing a thin Al layer via vapor deposition. This structure was then annealed in excess of 800 °C which is the temperature at which nitrogen was released from the underlying GaN. The nitrogen then combined with the Al to form AlN as verified by x-ray photoemission spectroscopy (XPS) and Auger electron spectroscopy (AES). The results indicate a positive electron affinity of 0.6 ± 0.3 eV. A more recent study[10] of reactive magnetron sputtered AlN prepared *in situ* with the analysis indicates that oxygen plays a critical role in determining whether the value of the electron affinity at the surface will be negative or positive.

This study explores the electron affinity of AlN and the Schottky barrier with Ti. The metal Ti has a relatively low

[a)]Electronic mail: robert_nemanich@ncsu.edu

work function with a reported polycrystalline value of 4.3 eV.[11] Our previous studies of Ti on diamond have established that a thin layer of Ti results in an effective negative electron affinity.[6] The results established that with the thin Ti layer the vacuum level is at or below the conduction band minimum of the diamond, and the *p*-type Schottky barrier to the diamond was ~1.0 eV. While other surface layers such as Cs have been considered to induce an effective negative electron affinity, Ti has a significant advantage in stability.

Our study will first explore the experimental difficulties in determining the electron affinity of AlN, and then examine the Schottky barrier of a thin layer of Ti on a clean AlN surface. Comparison of the results will allow the determination of the effect of the interface bonding on the interface dipole layer.

II. EXPERIMENT

The films prepared for this study were 100 and 1000 Å of AlN deposited on the (0001) Si-face of on-axis *n*-type 6H–SiC (hereafter referred to as 6H–SiC) by (GSMBE). The GSMBE is interconnected via a transfer tube with several analysis chambers [AES, low energy electron diffraction (LEED), and UPS] as well as an e-beam evaporation system. The base pressure of the entire system is ~1.0E−09 Torr. AES and LEED were employed before and after each process step in order to monitor any contamination that might result from transfer.

The SiC was received with a thermally grown oxide protective coating. This oxide can be removed with a 10:1 buffered HF dip for 10 min. Once the oxide is removed, a thick layer of tungsten is sputtered onto the backside of the wafer. This is necessary for the radiative heating of the SiC. After the tungsten deposition, the SiC is cleaned with solvents (trichloroethylene, acetone, and methanol), mounted to a molybdenum sample holder with Ta wire, and loaded into the GSMBE for the AlN film growth. The particulars of the GSMBE can be found elsewhere,[12] but certain aspects of the growth will be highlighted here. Once the SiC is loaded into the GSMBE, a final cleaning procedure for the SiC is employed. Each SiC wafer is annealed for 11 min at 1250 °C in a flux of SiH_4.The pressure in the chamber never exceeded 3.0E−05 Torr during this procedure. For the AlN growth, the samples were annealed to 1250 °C. Once this temperature is achieved, the sample is exposed to Al from a Knudsen cell and NH_3 through a leak valve. The temperature of the Al Knudsen cell was 1250 °C. A sustained growth rate of ~1000 Å/h was achieved with a NH_3 leak rate that corresponded to a chamber pressure of ~1.0E−05 Torr. The AlN film was exposed to a constant flow of NH_3 until the sample cooled to a temperature of 600–700 °C.

After the growth process, the sample was transferred into the AES and LEED chamber, and then into the UPS chamber. For the AES measurements, a PHI model 10-155 single pass cylindrical-mirror analyzer was employed to study the chemical composition of the surface of the samples. For the AES measurements, a beam energy of 3 kV was employed for the incident electrons. The AES is operated in the pulse-count, $N(E)$, mode. For the LEED images, a Princeton Research Instruments model RVL 6-120 was employed to image the surface of the samples. For the LEED images, an accelerating potential of 80 V was utilized.

The UPS technique utilizes an Omicron HIS13 noble-gas-discharge lamp. Both the He I α (21.2 eV) and the He II α (40.8 eV) light are accessible with this excitation source. The He II α excitation is particularly useful because of the He I β (23.1 eV) line which can sometimes complicate the determination of the valence band maximum (VBM). The photoexcited electrons were collected by an energy analyzer which was positioned at surface normal. The 50 mm radius hemispherical electron analyzer has an energy resolution of 0.15 eV and a 2° angular resolution. The sample stage is electrically isolated from the rest of the chamber and was biased by up to 6 V. In order for the low-energy electrons to overcome the work function of the analyzer, which is 4.5 eV, a 3–4 V bias is necessary to realize the full width of the spectra. The reason for the higher bias value of 6 V is that, for AlN films, charging effects which will distort the UPS spectra and shift the spectra toward higher binding energies are often encountered. However, if a somewhat higher bias (6 V) is applied to the sample, the full width of the spectra can be realized depending upon the amount of charging. Unfortunately, in the case of charging, the peak positions will be shifted toward higher binding energies, and it is generally impossible to accurately determine the surface Fermi level relative to the valence band maximum (VBM).

Once UPS spectra have been collected from the clean surface of AlN, the sample is transferred to the e-beam evaporation system for titanium deposition. Data are presented for a metal film thickness of 2 Å. The sample is returned to the UPS chamber for further characterization.

III. RESULTS AND DISCUSSION

The results of AES and LEED indicate a clean, 1×1 surface. The carbon signal was at or below the detection limit while there is a small peak due to the presence of oxygen as indicated in Fig. 1.

Photoemission spectra for clean AlN having thicknesses of 100 and 1000 Å are shown in Fig. 2. Since both films were prepared identically, it is unlikely that there is a fundamental difference in the surface Fermi level position. The spectrum of the 1000 Å film is significantly shifted to higher binding energies, and the spectrum is distorted. These effects are attributed to charging of the highly insulating AlN film.

In order to determine the position of the VBM, and hence determine the electron affinity of the sample, it is necessary to find bulk AlN features in the spectra to which all values can be referenced. We consider now the spectra of the 100 Å AlN layer where charging effects are not directly evident. There are three identifiable bulk features in the spectrum shown in Fig. 2(a). The first and most dominant feature is located at ~6.1 eV below the Fermi level. The second feature is located at ~9.3 eV below the Fermi level. The 9.3 eV feature is more evident when the 40.8 eV excitation is employed as indicated in Fig. 3. The third feature, which ap-

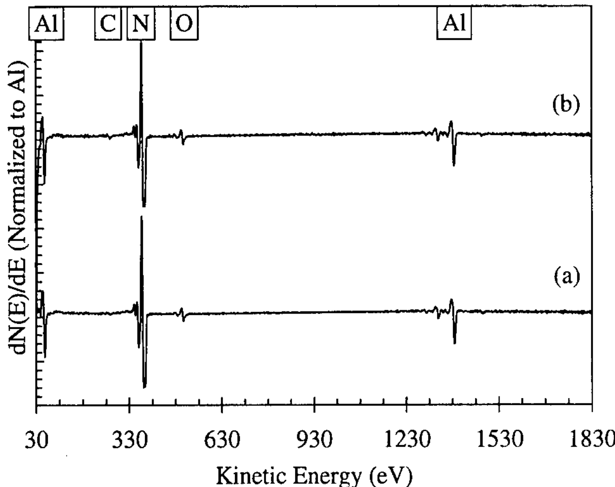

FIG. 1. AES survey spectra of (a) 100 Å AlN on 6H–SiC and (b) 1000 Å AlN on 6H–SiC. The spectra are normalized such that the absolute height of the dominant Al *KLL* peak is one. The peak due to carbon is at or below the detection limit while there is a small peak due to the presence of oxygen.

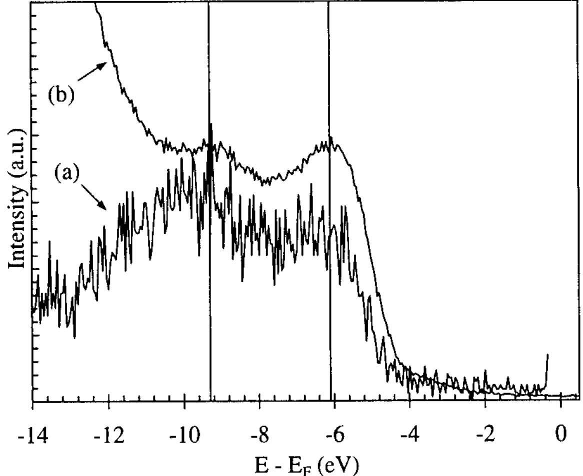

FIG. 3. UPS spectra of 100 Å AlN on 6H–SiC when (a) 40.8 eV excitation and (b) 21.2 eV excitation is incident upon the sample. For (a), the spectrum is multiplied by 45. The vertical lines are located at 9.3 eV below the Fermi level and 6.1 eV below the Fermi level. The peak at 9.3 eV below the Fermi level is enhanced by the 40.8 eV excitation.

pears as a shoulder to the secondary electron peak, is located at ~13 eV below the Fermi level.

In one study,[13] these features are located at 6 and 8.5 eV below the Fermi level. The AlN samples in that study were prepared by N_2^+ ion beam bombardment of high-purity polycrystalline Al. In a similar study on samples prepared in the same manner by the same authors,[14] these peaks are reported to be located at 5 and 8.5 eV below the Fermi level. These peak positions were located at 5.8 and 8 eV below the Fermi level for samples consisting of 1000 Å of Al deposited on (100) Si and subsequently bombarded by N_2^+ ions.[15] In another study,[16] XPS results of AlN prepared by N^+ ion bombardment of monocrystalline (111) aluminum indicates that these peaks are located at 5 and 9 eV. The XPS results were in excellent agreement with the UPS results in that study. These values were also obtained by Bermudez *et al.*[5]

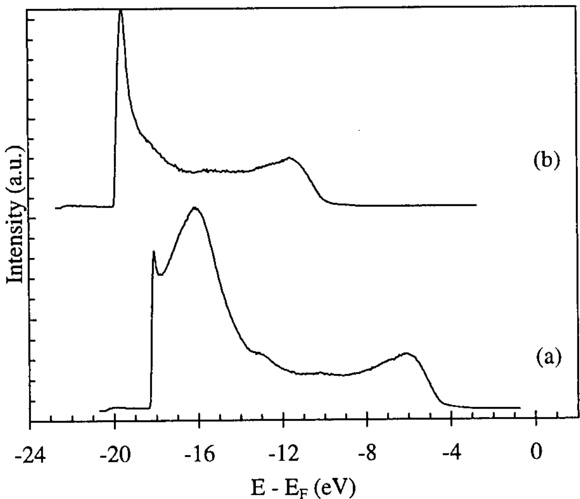

FIG. 2. UPS spectra of (a) 100 Å AlN on 6H–SiC and (b) 1000 Å AlN on 6H–SiC. In (b), the peak positions clearly indicate the presence of charging which will shift the spectrum to higher binding energies.

In addition to surface charging there are several other effects that could lead to shifts in the spectra, which would be reflected as changes in the binding energy. These include band bending due to surface states, a different bulk Fermi level, polarization fields, and nonequilibrium processes such as surface photovoltage.

We note that the spectra plotted in Fig. 2(a) may also exhibit the characteristics of charging or one of the other above mentioned effects since the values for the peak positions disagree with the other reported values by as much as 1 eV. Given the obvious charging effect displayed in Fig. 2(b), it seems likely that surface charging may explain the smaller shifts observed in Fig. 2(a).

Another set of studies[7,8] has focused on the electron affinity and electronic structure of AlN (0.2 μm thick) films deposited on Si(111) by MBE. Their results indicate spectral peaks located at ~7 and ~11 eV below the Fermi level. Comparing their spectra to those presented here and to the prior reports may suggest that the spectra are shifted ~2 eV accordingly to higher binding energies. After shifting the spectra, the peak positions of the 7 eV peak and the 11 eV peak should then be 5 and 9 eV. We note this difference since this study[7,8] had noted a significantly larger electron affinity than prior studies from our laboratory and from other reports.[3–5]

We continue to explore effects in our spectra that are apparently related to charging. Even if the spectrum in Fig. 2(a) is shifted to higher binding energies due to charging, we expect the width (W) of the spectrum to be the same as long as there is enough bias applied to be able to discern the entire spectrum. For Fig. 2(a), a series of scans were collected at different applied sample bias. The spectra were biased up to 5 V in increments of 0.5 V. At a bias value of 3.5 V, the width of the spectra stopped increasing. The spectra presented in Fig. 2(a) were obtained with a bias value of 4 V, and the full width is discernible.

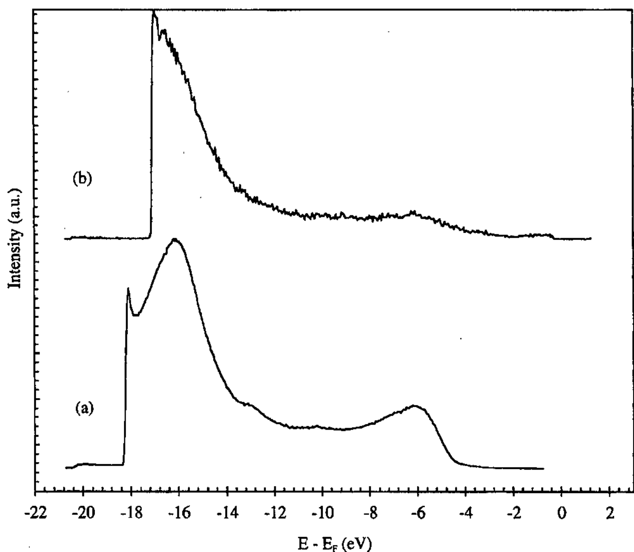

FIG. 4. UPS spectra of (a) AlN (100 Å thickness) deposited on 6H–SiC and (b) 2 Å Ti deposited on 1000 Å AlN deposited on 6H–SiC. Note that as a result of the Ti deposition, the charging effects that were evident in Fig. 2(b) appear to be reduced.

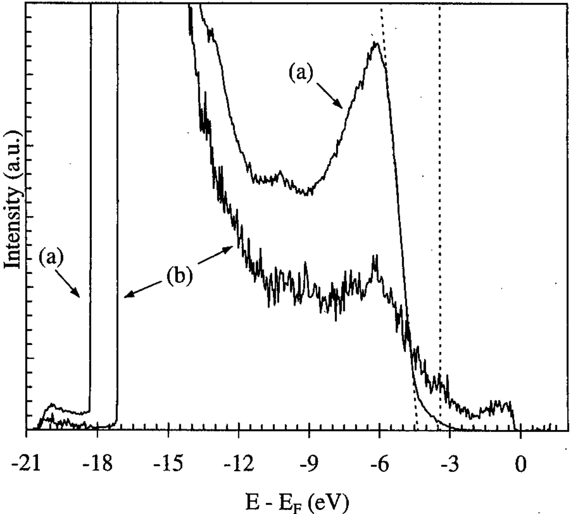

FIG. 5. Expanded view of the spectra shown in Fig. 4(a) AlN (100 Å thickness) deposited on 6H–SiC and (b) 2 Å Ti deposited on 1000 Å AlN deposited on 6H–SiC. The y axis of (b) is scaled with respect to (a) so that the features of the clean surface and the features of the titanium-covered surface can be compared. The dashed lines represent the models utilized in determining the VBM.

Charging in itself does not necessarily affect the width of the spectra unless not enough bias is applied to discern the entire width of the spectra. For example, in Fig. 2(b), a bias of 6 V was applied to the sample, and the full width of the spectra is still not discernible because the spectrum is shifted to higher binding energies by as much as 6 V (the peak that should be located 5 eV below the Fermi level is located at 11 eV below the Fermi level). Therefore, if we were to determine the electron affinity from the spectrum presented in Fig. 2(b), we would erroneously come to the conclusion that the surface has a positive electron affinity of 4.5 eV.

The electron affinity as determined by photoemission has the following relationship:

$$\chi = h\nu - E_g - W, \tag{1}$$

where χ is the electron infinity, $h\nu$ is the energy of the excitation source, E_g is the band gap of the material, and W is the measured width of the spectra from the position of the onset of the emission to the position of the low energy end of the spectra. In all calculations in this study, a value of 6.2 eV is used for the band gap of AlN. Note that this relationship does not apply to the case of a negative electron affinity. In that case, the low energy end of the spectrum defines the position of the conduction band minimum and not the position of the vacuum level. If a surface exhibits a negative electron affinity, this analysis would yield a value of $\chi = 0$. Therefore, the value of an electron affinity which is less than zero cannot be determined from photoemission without other supporting measurements.

We now consider one of the critical aspects in determining the electron affinity from photoemission, namely the determination of the width of the spectrum. In Fig. 4(a), we present the results for the clean surface of AlN (100 Å thickness) deposited on 6H–SiC and in Fig. 5(a) we present an expanded view of the same spectrum. Examination of the spectra shows a strong feature at 6.1 eV with scattering extending up to ~3 eV. We have compared this spectrum to a spectrum from a clean Ni film. In this comparison it is evident that the scattering extending above the 6 eV peak is indeed real and attributable to electronic states of the sample. This scattering is neither broadening due to the instrument nor spectral features associated with the weak 23.1 eV He I β radiation. This additional scattering may or may not be representative of the bulk states of the AlN. We therefore consider two different methods to define the VBM. In the first method, we ignore the additional scattering and line fit the leading edge of the 6.1 eV feature. The extrapolation of this line fit will give the VBM with this approach. The dashed line extrapolated to 4.4 eV below the Fermi level is the result of this analysis.

In the second approach we consider that the scattering extending above the 6.1 eV feature is due to bulk states of the AlN. Rather than a spectral analysis of this feature, we have instead drawn a vertical line on the graph that would indicate the position of the VBM if the surface had a negative electron affinity. This line is drawn at 15.0 eV from the low energy cutoff [as predicted from Eq. (1)]. Visual inspection indicates that this is a reasonable extrapolation under the assumption that these are indeed bulk states.

Wu and Kahn have proposed that this feature is due to contamination related states, particularly oxygen contamination in excess of a few percent as determined by XPS, on their samples.[7,17] However, many of the spectra presented in the literature contain this feature.[5,13–16,18,19] In one study,[20] this feature is attributed to the He I β (23.1 eV) radiation. However, if it were the 23.1 eV radiation, this feature should mimic the corresponding part of the spectra that is lower in energy by 1.9 eV. Indeed, the origin of this feature is difficult to understand.

Given that the low energy cutoff is well defined at 18.4 eV below the Fermi level as indicated in Fig. 5(a), the width of the spectrum can now be determined for these two possible assumptions. We find $\chi=1$ eV for case 1 where the leading edge of the 6.1 eV feature is extrapolated to zero intensity, and we find $\chi=0$ eV for the second case where we consider the weak emission extending up to 3 eV.

We note that independent of our assumptions of the VBM, our data yield a larger spectral width and consequently a smaller electron affinity than those reported by Wu *et al.*[7,8] One possibility that may account for this difference is that the polarity of the films is different (Al or N face), and the different surfaces may have a correspondingly different electron affinity. It remains for future work to determine if the different orientations of AlN exhibit different values of the electron affinity.

The Schottky barrier height (SBH) (Φ_b) can be measured from the photoemission spectra by locating the valence band edge (E_v) of the semiconductor and the Fermi level (E_F) of the metal. The position of the valence band edge is determined as described above. The *p*-type SBH is defined as the energy difference between the Fermi level and the VBM at the interface between the metal and the semiconductor under equilibrium conditions. In the photoemission spectra, this is the value that can be directly measured. The value of the *n*-type SBH can be determined with a knowledge of the band gap. In order to determine the SBH with UPS, it is necessary to deposit an appropriate thickness of metal such that features of the underlying semiconductor are evident in the spectra. It is also extremely difficult to discern the position of the valence band maximum for a metal layer deposited on a semiconductor. Thus, it is necessary to obtain at least two spectra; one spectra obtained from the clean surface of the semiconductor and another spectra obtained from the semiconductor with a thin layer of metal deposited.

In Figs. 4(b) and 5(b), we present the results for the 2 Å Ti deposited on 1000 Å AlN deposited on 6H–SiC. Note that as a result of the Ti deposition, the charging effects that were evident in Fig. 2(b) appear to be reduced. Comparing Figs. 5(a) and 5(b), only the AlN feature located at 6 eV below the Fermi level can be discerned in both spectra.

We consider now the Schottky barrier determined from the spectra presented in Figs. 4 and 5. The width of the combined spectrum now extends from the Fermi level to the low energy cutoff at 17.2 eV. The vacuum level is then determined to be 4.0 eV above the Fermi level (i.e., $E_{vac}=21.2$ eV -17.2 eV). To complete a picture of the band alignments, it is necessary to determine the position of the VBM. Here again we will consider both possibilities noted in the discussion above. The band relations for the two cases, for $\chi=0$ and $\chi=1$, are illustrated in Figs. 6(a) and 6(b), respectively. In constructing this picture, we have also used a value of 4.3 eV for the work function of Ti.

The first aspect to note is that the surface has an increase in the effective electron affinity rather than the hoped for decrease. Here again we note that we define the effective electron affinity as the relationship between the semiconductor conduction band minimum (CBM) and the vacuum level with the metallic overlayer. Thus, depending upon the determination of the VBM, the effective electron affinity after Ti deposition is 1.5 or 2.5 eV. In contrast, to the effect of Ti on diamond, which lowers the effective electron affinity, Ti on AlN results in an increase in the electron affinity.

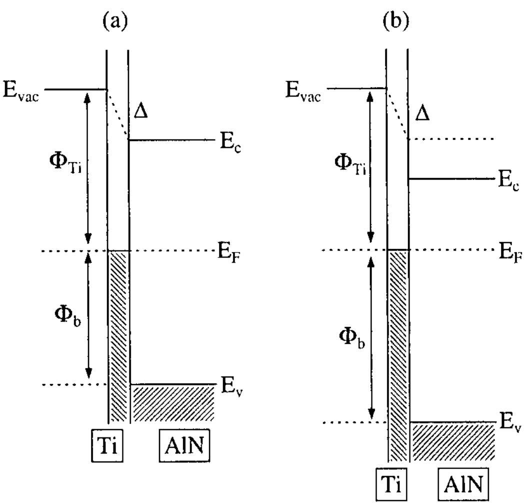

FIG. 6. Schematic of the band relations of the Ti/AlN interface. The two schematics were obtained from different approaches for the analysis of the VBM of the AlN spectrum: (a) is obtained from the analysis yielding χ of 0 eV, and (b) is obtained from the analysis assuming χ is 1 eV. The work function of titanium (Φ_{Ti}) is 4.1 eV. The *p*-type Schottky barrier height (Φ_b) is 3.4±0.2 and 4.4±0.2 eV in (a) and (b), respectively. The amount of band shifting (Δ) is independent of the choice of VBM and is determined to be 1.5±0.2 eV.

An indication that the deposition of a metal overlayer may result in a reduction of the effective electron affinity can be obtained with a comparison of the electronegativity values for the atoms. The electronegativity is defined as the tendency of an atom to attract bonding electrons. Therefore, the difference between the values of the electronegativity for two atoms can provide a useful indicator of the polarity of the resulting dipole that is formed.[11] For an adsorbate atom that has a lower electronegativity value than the surface atoms on the semiconductor, the resulting dipole field that is formed will be directed outward from the semiconductor. Thus, the effective electron affinity would be reduced. In the case of AlN, Ti has a lower electronegativity than either Al or N (1.54 eV for Ti as compared to 1.61 eV for Al and 3.04 eV for N).[11] This is the reason that it was proposed that the deposition of Ti would result in a reduction of the effective electron affinity. This trend was not observed in this experiment.

Independent of the choice of the VBM, the amount of shift in the bands due to the interface dipole (Δ) is 1.5±0.2 eV. This shift then represents the change in the band alignment due to the interface dipole. This change in band alignment is the difference between our measured results and those predicted from the Schottky–Mott model of the barrier. There is a slight discrepancy (almost within the experimental uncertainty) between this analysis shown in Fig. 6 and the amount of shift in the low energy end of the UPS spectra

between the clean and titanium-covered surface which is indicated in Fig. 5. From Fig. 5, the amount of shift in the low kinetic energy end of the spectra is 1.2±0.2 eV toward lower binding energies. One possible explanation for this discrepancy is that if we were to use a lower value for the work function of titanium, we would obtain a correspondingly lower value for the interface dipole in the calculation illustrated in Fig. 6. The justification for using a lower value for the work function of titanium could be reactive bonding of titanium with nitrogen from the AlN. Another possible explanation results from a closer examination of Fig. 5(b). In Fig. 5(b), the spectrum extends to the Fermi level of the system. In fact, the turn-on for the spectrum in Fig. 5(b) is located ~0.2 eV below the Fermi level. The spectrum could be shifted toward higher binding energies by 0.2 eV due to the presence of charging. If this is the case, then the shift in the low kinetic energy end of the spectra should be 1.4±0.2 instead of the observed 1.2±0.2 eV. Both of these explanations would result in values that are in closer agreement with each other.

IV. CONCLUSIONS

We have explored the experimental aspects of photoemission measurements of epitaxial AlN films grown on 6H–SiC. Significant surface charging was observed for 1000 Å films. The choice of the position of the VBM was complicated by the presence of weak scattering that extends beyond the 6.1 eV feature. We have explored two possible methods to analyze the spectra, and we find a value for the VBM that differs by 1 eV depending upon the assumptions. Based on this analysis, we conclude that 100 Å of AlN grown on 6H–SiC has an electron affinity value of either 0 or 1 eV depending upon the choice of the position of the VBM.

Titanium was deposited on the clean surface of *in situ* grown AlN, and was characterized with UPS. For the case of $\chi=0$ eV, the position of the VBM is 3.4 eV below the position of the Fermi level. For the case of $\chi=1$ eV, the position of the valence band maximum is 4.4 eV below the position of the Fermi level. Therefore, the *p*-type Schottky barrier height of titanium on AlN is measured to be 3.4±0.2 or 4.4±0.2 eV for $\chi=0$ and $\chi=1$ eV, respectively. Independent of the selection of the VBM, the observed Schottky barrier differed from that predicted by the Schottky–Mott model by 1.5±0.2 eV. This value of the interface dipole is independent of the choice of the VBM.

ACKNOWLEDGMENTS

The authors wish to thank Dr. Sean W. King, Dr. Mark C. Benjamin, and Dr. Jack E. Rowe for many helpful discussions. This study was supported by the PTS Corporation and the Office of Naval Research.

[1] P. B. Perry and R. F. Rutz, Appl. Phys. Lett. **33**, 319 (1978).
[2] W. M. Yim, E. J. Stofko, P. J. Zanzucchi, J. I. Pankove, M. Ettenberg, and S. L. Gilbert, J. Appl. Phys. **44**, 292 (1973).
[3] M. C. Benjamin, Cheng Wang, R. F. Davis, and R. J. Nemanich, Appl. Phys. Lett. **64**, 3288 (1994).
[4] M. C. Benjamin, M. D. Bremser, T. W. Weeks, Jr., S. W. King, R. F. Davis, and R. J. Nemanich, Appl. Surf. Sci. **104/105**, 455 (1996).
[5] V. M. Bermudez, T. M. Jung, K. Doverspike, and A. E. Wickenden, J. Appl. Phys. **79**, 110 (1996).
[6] J. van der Weide and R. J. Nemanich, J. Vac. Sci. Technol. B **10**, 1940 (1992).
[7] C. I. Wu and A. Kahn, Appl. Phys. Lett. **73**, 1346 (1998).
[8] C. I. Wu and A. Kahn, Appl. Phys. Lett. **74**, 546 (1999).
[9] D. P. Malta, G. G. Fountain, J. B. Posthill, T. P. Humphreys, C. Pettenkofer, and R. J. Markunas, in *Gallium Nitride and Related Materials II*, edited by C. R. Abernathy, H. Amano, and J. C. Zolper, Materials Research Society Symp. Proc. 468 (Materials Research Society, Pittsburgh, 1997), p. 437.
[10] T. Wrase, P. Reinke, and P. Oelhafen, presented at GaN and Related Alloys, Materials Research Society Symposium W, Boston, MA, 1999.
[11] *CRC Handbook of Chemistry and Physics*, 80th ed., edited by David R. Lide (Chemical Rubber, Boca Raton, FL, 1999).
[12] S. W. King, R. F. Davis, C. Ronning, M. C. Benjamin, and R. J. Nemanich, J. Appl. Phys. **86**, 4483 (1999).
[13] F. S. Ohuchi, R. H. French, and R. V. Kasowski, J. Appl. Phys. **62**, 2286 (1987).
[14] R. V. Kasowski and F. S. Ohuchi, Phys. Rev. B **35**, 9311 (1987).
[15] J. Ashley Taylor and J. Wayne Rabalais, J. Chem. Phys. **75**, 1735 (1981).
[16] M. Gautier, J. P. Duraud, and C. Le Gressus, J. Appl. Phys. **61**, 574 (1987).
[17] J. R. Waldrop and R. W. Grant, Appl. Phys. Lett. **68**, 2879 (1996).
[18] C. G. Olson, J. H. Sexton, D. W. Lynch, A. J. Bevolo, H. R. Shanks, B. N. Harmon, W. Y. Ching, and D. M. Wieliczka, Solid State Commun. **56**, 35 (1985).
[19] M. Gautier, J. P. Duraud, and C. Le Gressus, Surf. Sci. **178**, 201 (1986).
[20] S. W. King, C. Ronning, R. F. Davis, M. C. Benjamin, and R. J. Nemanich, J. Appl. Phys. **84**, 2086 (1998).

Quantitative theory of scattering in antimonide-based heterostructures with imperfect interfaces

M. J. Shaw,[a] E. A. Corbin, M. R. Kitchin, J. P. Hagon, and M. Jaros
Department of Physics, The University of Newcastle upon Tyne, Newcastle upon Tyne, United Kingdom

(Received 17 January 2000; accepted 26 May 2000)

We report quantitative calculations of carrier lifetimes in imperfect $Ga_xIn_{1-x}Sb/InAs$ superlattice structures. A microscopic description of imperfections including substitutional anions and interface islands is obtained through a novel strain-dependent empirical pseudopotential calculation. The T matrix of scattering theory is used to take our calculations of scattering lifetimes beyond the Born approximation, including multiple scattering events. Carrier lifetimes are related to the microscopic nature of the defects, their proximity to the interfaces, and the size and shape of interface islands. Anomalous effects due to lattice relaxation are seen to alter hole lifetimes, and their dependence upon position. For isolated isovalent anion defects we predict electron and hole lifetimes as low as 0.2 and 0.8 μs, respectively, for typical defect concentrations. © *2000 American Vacuum Society.*
[S0734-2101(00)07304-8]

I. INTRODUCTION

In recent years considerable attention has been afforded to the electronic and optical properties of antimonide-based heterostructures. These structures, comprising layers containing GaSb, AlSb and InSb, and the near-lattice-matched InAs, have been developed in the search for high-performance infrared optoelectronic devices[1–19] and ultrafast electronics.[20–22] By careful choice of layer widths and compositions these heterostructures may be engineered to exhibit a wide range of properties including fundamental gaps tunable in the mid- to far-infrared region of the spectrum.[23] However, in spite of the well-documented favorable features associated with these materials,[24,25] these materials have yet to achieve widespread technological application. One of the main reasons for this has been the lack of understanding of the microscopic processes which restrict carrier lifetimes in these structures. In order to enable improvements in performance sufficient to displace the existing infrared technologies, it is necessary first to obtain a detailed understanding at the microscopic level of the processes which limit performance at present.

Recent advances in microscopy techniques have presented a detailed microscopic picture of the quality of layers, and in particular, interfaces, which can be attained using state-of-the-art growth techniques.[22,26,27] A recent series of theoretical results obtained from *ab initio* pseudopotential calculations demonstrated the importance of the interaction between impurities and the interfaces of heterostructures.[28,29] However, no quantitative prediction of the effect on the dynamical characteristics of the defects was made. What is required of theory is to provide the link between microscopic imperfections in the vicinity of heterointerfaces and the key device performance indicators such as the carrier lifetimes. To meet this demand a theoretical scheme is required in which an atomistic model of disorder is provided, and from which the essential dynamical information required to calculate lifetimes can be extracted. In a very recent article we presented theoretical results for elastic scattering lifetimes.[30]

In this article we outline the essential features of our theoretical method in which a novel, strain-dependent, empirical pseudopotential calculation is used to obtain the stationary states of the imperfect heterostructure, and the results of scattering theory are applied to obtain the dynamical information. The empirical pseudopotential method (EPM) provides a description of the electronic states in heterostructures in which the microscopic composition of the layers is taken into account. Further, the EPM lends itself to the extension to imperfect systems using perturbation theory, allowing large unit cells to be considered on an atomic scale. Rival formalisms such as the $\mathbf{k}\cdot\mathbf{p}$ theory are unable to correctly reflect the symmetry of the systems and implicitly eliminate some of the band mixings which are known to exist in heterostructures.[31] The use of *ab initio* methods is restricted to relatively small unit cells, and generally imposes higher computational demands. The study of dynamical processes in heterostructure systems has usually been confined to the first-order case, through application of Fermi's golden rule or the Born approximation. This enables the scattering of the perturbed system to be described in the absence of a knowledge of the perturbed states. With the benefit of modern computers, it is now possible to obtain from our EPM calculations a microscopic description of the stationary state wave functions for the imperfect heterostructures. Application of the T matrix of scattering theory enables us to exploit our knowledge of these perturbed states to make quantitative predictions of the scattering properties to nth order.

This article describes a systematic study of the scattering lifetimes for commonly occurring substitutional anion defects in a $Ga_{0.75}In_{0.25}Sb/InAs$ superlattice designed for use as an infrared detector structure.[32] We relate the computed lifetimes to the microscopic details of the disorder, including the location of defects, the relaxation of the lattice around the defects, and the chemical species of the defect. In addition, the effect of clustering of defects into islands at the interfaces is investigated. We find that the full microscopic calculations

[a]Electronic mail: m.j.shaw@ncl.ac.uk

predict features in the scattering properties which cannot be derived from simpler models.

II. THEORY

A. Strain-dependent empirical pseudopotential method

The application of empirical pseudopotentials for the study of heterostructure systems was initially performed for unstrained GaAs–AlGaAs structures,[33,34] and its success in such cases has been well established over many years. However, the extension of the basic EPM to encompass strained heterostructures is not trivial. As we have discussed in full detail in a recent publication,[35] the development of an EPM approach in which strain can be adequately accounted for requires an examination of the very nature of the pseudopotentials used. In this article we shall outline the principles of our strained EPM scheme.

The difficulties associated with the inclusion of strain can be understood most easily by considering the case of a bulk semiconductor. Following the approach of Cohen and Bergstresser,[36] we first neglect the effects of spin-orbit coupling and write the local empirical pseudopotential to be

$$V_p(\mathbf{r})=\sum_{G,i} S_i(\mathbf{G})V_i(\mathbf{G})e^{i\mathbf{G}\cdot\mathbf{r}}. \tag{1}$$

In this equation $\mathbf{G}$ are reciprocal lattice vectors of the crystal, i is a sum over atomic species, and $V_i(\mathbf{G})$ are the Fourier components of the atomic pseudopotential known as form factors. The structure factors $S_i(\mathbf{G})$ contain the information about atomic positions and are written

$$S_i(\mathbf{G})=\frac{1}{N_i}\sum_j e^{-i\mathbf{G}\cdot\mathbf{R}_j^i}, \tag{2}$$

where $\mathbf{R}_j^i$ is the position of the jth atom of species i.

The structure factors are easily computed. The form factors, on the other hand, must be determined by fitting to empirical data. In the usual derivation of the EPM, it is assumed that the atomic pseudopotentials are spherical, with the result that the form factors $V_i(\mathbf{G})$ in fact depend only upon the magnitude of the reciprocal lattice vectors, i.e., $V_i(\mathbf{G})=V_i(|\mathbf{G}|)$. This assumption plays a considerable role in the simplification of the problem—the number of distinct values which must be calculated is radically reduced. Coupled with the observation that the magnitude of the form factors reduced sharply with $|\mathbf{G}|$, it is typically found that only six nonzero independent form factors need to be retained. It is a relatively easy task to adjust these factors in order to fit the gaps predicted by the EPM calculation to available empirical data.

The difficulties which strain introduces originate in the determination of these form factors when the system is strained. The lengths of the reciprocal lattice vectors are no longer symmetric with respect to the crystal axes. This draws into question the validity of the spherical symmetry approximation introduced above—can we justify the use of this now that the crystal is strained? In any case, even with the retention of spherical symmetry one is now required to evaluate $V_i(|\mathbf{G}|)$ for a large number of lengths $|\mathbf{G}|$. A number of methods have, with some success, proceeded by retaining the spherical approximation and using an interpolation to the unstrained form factors to obtain form factors at the strained reciprocal lattice vector lengths.[13,37,38] However, these methods require a considerable effort in the choice of the interpolating function, and are not generally applicable to different materials. There is, in addition, a theoretical difficulty with this approach. The interpolation procedure fails to distinguish between the effects of strain which require the evaluation of V at intermediate values of wavevector, and the effects of increased periodicity which requires intermediate values for the calculations pertaining to, for example, superlattices. There is in principle no reason why these two separate physical effects should be accounted for by a single interpolating function.

In the present method, we relax the spherical symmetry restriction enabling the reduction of symmetry to be fully reflected in the form factors. However, in order to retain only a practical number of fitting parameters, the form factor function is assumed to be separable into components along the crystal axes directions as follows:

$$V(\mathbf{G})=w_xV_x(G_x)+w_yV_y(G_y)+w_zV_z(G_z). \tag{3}$$

In this equation, the functions V_i are the form factors fitted for the material hydrostatically strained to the lattice constant in the i direction of the strained material, and they are evaluated at G_i, the magnitude of the reciprocal lattice vector corresponding to $\mathbf{G}$ in the hydrostatically strained system. The weighting factors w_i reflect the degree to which the vector of interest $\mathbf{G}$ is oriented along the ith direction, i.e., $w_i=(g_i/|\mathbf{G}|)^2$ [where $\mathbf{G}=(g_x,g_y,g_z)$]. Note that the separability of the potential in this way is not a rigorous property, and represents an approximate representation of the empirical pseudopotential.

This method for the calculation of bulk materials is readily extended to the case of superlattices, and in principle to imperfect superlattices, simply by including the atomic positions in the larger unit cell and using reciprocal lattice vectors appropriate to the unit cell in question. Interpolation between the *strained* form factors enables evaluation of the intermediate values required. For imperfect superlattices, however, the number of plane waves in the basis set rapidly becomes too large to treat easily. We therefore turn to perturbation theory to solve for imperfect structures. The wave function of the perturbed system is written as a sum of unperturbed superlattice states

$$\Psi_{\mathbf{k}}^i=\sum_{n\mathbf{k}'} A_{n,\mathbf{k}'}^i\phi_{\mathbf{k}'}^n. \tag{4}$$

Here, $\Psi_{\mathbf{k}}^i$ is the wave function in the ith state of the imperfect superlattice with wavevector $\mathbf{k}$, and $\phi_{\mathbf{k}'}^n$ is the wave function of the unperturbed superlattice in miniband n and at wavevector $\mathbf{k}'=\mathbf{k}+\mathbf{g}$, where $\mathbf{g}$ represents a reciprocal lattice vector of the perturbed unit cell. The coefficients $A_{n,\mathbf{k}'}^i$ are obtained from perturbation theory.

The relationship between this approach and other schemes for the treatment of strained structures with empirical pseudopotentials in the literature[39] is discussed in detail in our earlier article.[35] The key feature of the present method is that the full reduction of symmetry is included in the nature of the pseudopotentials, and that the effects of strain are treated independently from the interpolations associated with the treatment of superlattice pseudopotentials.

B. Elastic scattering from defects

In order to extract the dynamical information from the stationary states obtained by the empirical pseudopotential method described in Sec. II A we turn to the quantum theory of scattering. The elastic scattering rate may be described by the well-known result of scattering theory, which relates the scattering rate $R(\mathbf{k},\mathbf{k}')$ from an initial state $\phi_{\mathbf{k}}^{n}$ to a final state $\phi_{\mathbf{k}'}^{n'}$ to the so-called T matrix by

$$R(\mathbf{k},\mathbf{k}')\propto|\langle\phi_{\mathbf{k}'}^{n'}|T|\phi_{\mathbf{k}}^{n}\rangle|^2\delta(E_{\mathbf{k}}-E_{\mathbf{k}'}). \tag{5}$$

The transition, or T matrix elements are defined

$$\langle\phi_{\mathbf{k}'}^{n'}|T|\phi_{\mathbf{k}}^{n}\rangle=\langle\phi_{\mathbf{k}'}^{n'}|U|\Psi_{\mathbf{k}}^{n}\rangle, \tag{6}$$

where $\Psi_{\mathbf{k}}^{n}$ is the perturbed evolution state of $\phi_{\mathbf{k}}^{n}$ under perturbation U.

Since we are in possession of the wave functions of the states in the perturbed system, $\Psi_{\mathbf{k}}^{n}$, as given by Eq. (4), we may directly evaluate the T-matrix elements. We can define a lifetime for an extended system of N_{sc} scattering centers and show that it is given by the expression

$$(\tau_{n\mathbf{k}})^{-1}=\frac{2\pi}{\hbar}N_{\mathrm{sc}}\sum_{n'\mathbf{K}}\left|\sum_{n,\mathbf{k}''}A_{n,\mathbf{k}''}^{i}\langle\phi_{\mathbf{K}}^{n'}|U|\phi_{\mathbf{k}''}^{n}\rangle\right|^2\rho_{n'\mathbf{K}}(E_{n'K}), \tag{7}$$

while the scattering cross section per scattering center is

$$\sigma_n(\mathbf{k})=\frac{2\pi}{\hbar}\frac{\Omega}{\mathbf{v}_0^{n\mathbf{k}}}\sum_{n'\mathbf{K}}\left|\sum_{n,\mathbf{k}''}A_{n,\mathbf{k}''}^{i}\langle\phi_{\mathbf{K}}^{n'}|U|\phi_{\mathbf{k}''}^{n}\rangle\right|^2\rho_{n'\mathbf{K}}(E_{n'K}). \tag{8}$$

In these expressions $\rho_{n'\mathbf{K}}(E_{n'K})$ is the partial density of states in small volume around wavevector K. Note that following the perturbation calculation for the stationary states, the matrix elements $\langle\phi_{\mathbf{K}}^{n'}|U|\phi_{\mathbf{k}''}^{n}\rangle$ and coefficients $A_{n,\mathbf{k}}^{i}$, are already known, and the scattering result is obtained for a minimal computational effort. An interpolation procedure is invoked to ensure that the expressions for the partial density of states converge.

Equations (7) and (8) include the full expression for the perturbed stationary state wave functions, and include nth order scattering processes. It can easily be seen that restricting the expressions for $\Psi_{\mathbf{k}}^{n}$ to their leading term, namely $\phi_{\mathbf{k}}^{n}$, first-order expressions are obtained as follows:

$$\sigma_n(\mathbf{k})=\frac{2\pi}{\hbar}\frac{\Omega}{\mathbf{v}_0^{n\mathbf{k}}}\sum_{n'\mathbf{K}}|\langle\phi_{\mathbf{K}}^{n'}|U|\phi_{\mathbf{k}}^{n}\rangle|^2\rho_{n'\mathbf{K}}(E_{n'K}), \tag{9}$$

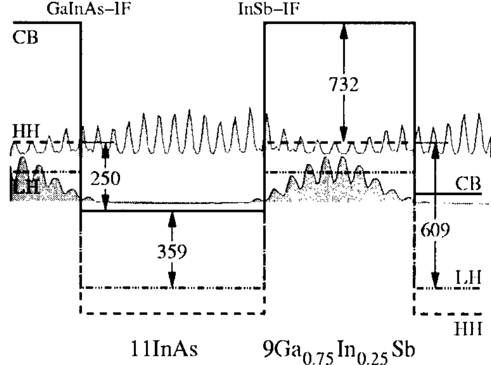

FIG. 1. Schematic diagram of the line-up of the bulk band edges in the $11\mathrm{Ga}_{0.75}\mathrm{In}_{0.25}\mathrm{Sb}/9\mathrm{InAs}$ superlattice. The numerical values (meV) were calculated using the method of Van de Walle (Ref. 41). The conduction (CB), heavy-hole (HH), and light-hole (LH) band edges are shown. The dark shading shows the computed charge density of the uppermost superlattice valence miniband, while the light shading shows the lowest energy conduction miniband charge density.

$$(\tau_{n\mathbf{k}})^{-1}=\frac{2\pi}{\hbar}N_{\mathrm{sc}}\sum_{n'\mathbf{K}}|\langle\phi_{\mathbf{K}}^{n'}|U|\phi_{\mathbf{k}}^{n}\rangle|^2\rho_{n'\mathbf{K}}(E_{n'K}). \tag{10}$$

These are equivalent to the result of Fermi's golden rule, and include only the effects of single scattering processes.

III. IDEALIZED $\mathrm{Ga}_{0.75}\mathrm{In}_{0.25}$SB/InAs SUPERLATTICE

The empirical pseudopotential method outlined in Sec. II A was initially applied to model a detector structure for which experimental absorption data has been obtained by Jack *et al.*[32] The specification for the structure was $11\mathrm{Ga}_{0.75}\mathrm{In}_{0.25}\mathrm{Sb}/9\mathrm{InAs}$, grown on a GaSb substrate, where 9InAs refers to 9 monolayers, 4.5 lattice constants, of InAs. The structure was assumed to have one of each type of interface available in these heterostructures, namely one $\mathrm{Ga}_{0.75}\mathrm{In}_{0.25}$As-like interface and one InSb-like interface. The alloy layers in this structure were treated using the virtual crystal approximation (VCA).[40] In this approximation, the microscopic configuration of atoms within the alloy layer is represented by a single "virtual" crystal which has properties obtained by a weighted average of the constituent materials, and which exhibits the full symmetry of the zinc-blende lattice.

The charge densities of the zone-center conduction and valence band-edge states, as computed using the full EPM calculations described, are shown in Fig. 1, superimposed upon the theoretical bulk band edges. The bulk band edges were computed using the model solid theory and deformation potentials of Van de Walle[41] and available empirical data pertaining to the materials in question.[42] With regard to the optical properties of such a structure, the key feature of the charge densities in Fig. 1 is the clear type II localization. In other words, the localization of the charge in the conduction and valence bands to separate layers. Such a charge distribution results in a generally weak fundamental transition, and a transition which is sensitive to the microscopic structure of the interfaces. Indeed, recent calculations have demonstrated that the presence of alloy disorder at type II

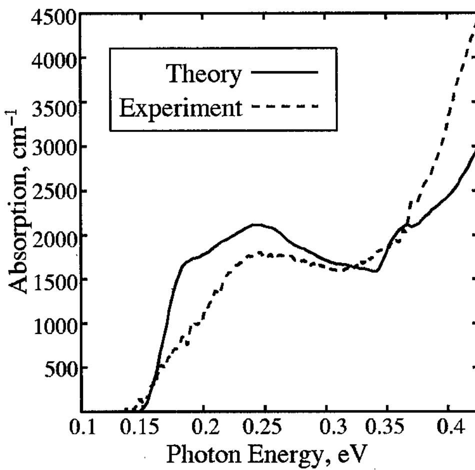

FIG. 2. Variation of the calculated absorption coefficient (cm^{-1}) with photon energy (eV) for the 11InAs/9$Ga_{0.75}In_{0.25}$Sb superlattice is compared with the experimental result of Jack *et al.* (Ref. 32) for a nominally identical structure.

interfaces can significantly alter the emission spectra of type II superlattices.[43] The asymmetry of the interface bond types is also apparent in the charge densities in Fig. 1. This demonstrates the microscopic nature of the EPM calculations, the differences in interface configuration being reflected in the superlattice wave functions, and as a result, in the optical transition matrix elements.

In the context of the present article, it is not appropriate to present a full study of the optical properties of the superlattice. However, it is useful to compare the available absorption spectra measured by Jack *et al.*[32] with the calculated absorption spectrum. The absorption spectrum was calculated from the result of density matrix theory[44] using the method as outlined by Shaw *et al.*,[45] involving full-scale sampling of the superlattice Brillouin zone. The results are compared in Fig. 2 and show an excellent agreement in the magnitude and shape of the response, and in the cutoff energies of the first and second transitions. This agreement reflects the performance of the new EPM in describing the energies, band dispersions, and wave functions (through the transition strengths) for the superlattice in question. Note that the use of the VCA for studies of absorption may be justified, since the alloy broadening effects seen in emission spectra by Kitchin *et al.*[43] are smeared out by the summations over the full Brillouin zone in the case of absorption.

IV. SCATTERING FROM ISOLATED ANION DEFECTS

One of the most commonly observed defects in superlattices of this type are the substitutional isovalent anion defects, namely antimony atoms occupying arsenic sites in the InAs layers, written Sb_{As}, and arsenic ions occupying antimony sites within the alloy. Studies of scattering effects associated with defects have been performed using tight-binding theories (e.g., Buisson *et al.*[46] investigated antisite defects). In the present study we choose to employ a **k**-space representation for convenience in the description of the imperfect heterostructure states. In this article we shall examine in detail the process of elastic scattering from these types of defects. One naturally expects, and indeed experimental microscopy studies show, that the concentration of such defects will be greatest close to the heterointerfaces. However, before we consider the effects of the clustering of these defects at interfaces, we shall first characterize the behavior of isolated defects at various positions relative to the superlattice interfaces.

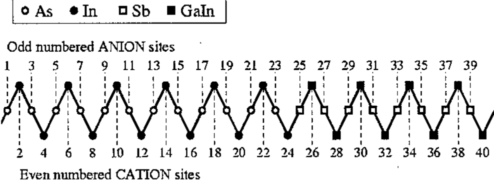

FIG. 3. Schematic diagram of the atomic spiral constituting the superlattice unit cell, showing the positions of the anions projected onto the plane containing the cations. The ionic sites are labeled with anions on odd numbered sites and cations on even sites.

We systematically study the elastic scattering lifetime of holes and electrons from substitutional anion defects located at all of the distinct possible anion sites within the superlattice cell. Figure 3 shows a schematic diagram of the atomic composition of a single perfect superlattice unit cell. The labeling of ionic site labels in Fig. 3 is used to provide us with a reference to the defect positions. For each position a full EPM calculation of a perturbed supercell of the superlattice is performed. The in-plane unit cell of the perturbed calculations is chosen to be very large ($\approx$80 000 superlattice spirals). Relaxation of the lattice around the defect atom is described using the valence force field method. In order to study the role of relaxation in determining the final magnitude of the scattering for any particular position, we shall compare the lifetime computed with full relaxation to the case where the atoms are frozen in the initial, strained, superlattice positions. Note that the lifetime is linearly dependent upon the density of scattering centers, i.e., defects (provided that the defects can still be considered isolated), and we must assume a given density for our calculations. For all of the lifetime calculations we assume a density of 10^{16} cm^{-3} defects.

First, let us consider in detail the scattering cross-section and lifetime for the Sb_{As} defect at ion site 1, adjacent to the GaInAs-like interface. These are shown in Fig. 4 as functions of the initial electron and hole wavevector. These results were calculated using the first-order expressions 9 and 10, since, as will be shown later, the first-order and nth order calculations converge for small perturbations. It can be seen that the wavevector dependence of the cross section is such that we can quote a typical value of its magnitude which applies provided the initial wavevector is not very short. In contrast, the scattering lifetime shows a strong wavevector dependence such that, for an ensemble of carriers, the effective lifetime can only be determined by averaging over some distribution of carriers throughout the band structure. The final lifetime must therefore depend upon the density of car-

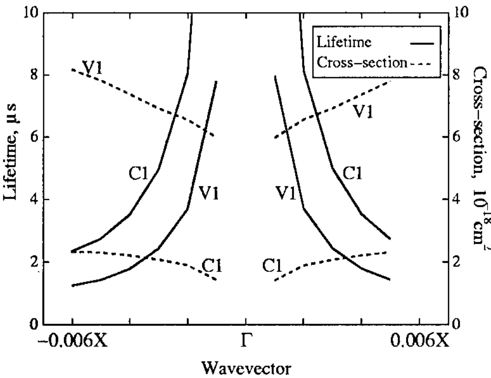

FIG. 4. Variation of the lifetime (solid lines, left-hand axis) and cross-section (dashed lines, right-hand axis) with incident wavevector for an isolated Sb_{As} defect adjacent to the GaInAs-like interface. The graphs are plotted for holes in the uppermost valence miniband, V1, and electrons in the lowest conduction miniband, C1. The lifetime assumes a concentration of 10^{16} cm^{-3} carriers at 77 K and a density of 10^{16} cm^{-3} defects.

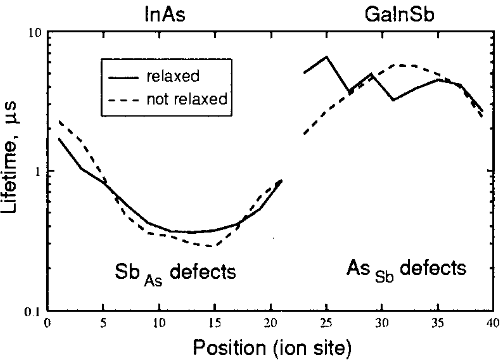

FIG. 6. Variation of the electron lifetime associated with isolated isovalent anion defects with position throughout the superlattice, for a concentration of 10^{16} cm^{-3} electrons at 77 K and a density of 10^{16} cm^{-3} defects. The labels on the position axis refer to the anion sites as numbered in Fig. 3. The lifetime is shown before (solid lines) and after (dashed lines) relaxation of the atoms in the lattice.

riers and temperature of the ensemble. Figure 5 shows the predicted temperature and carrier concentration dependence of the lifetime for elastic scattering of electrons and holes from single Sb_{As} defects at ion site 1 adjacent to the GaInAs-like interface.

In Fig. 6 we compare the lifetime of an ensemble of 10^{16} cm^{-3} electrons (at 77 K) due to a single substitutional anion defect at each of the possible ion sites throughout the superlattice. The lifetimes are compared with and without relaxation. It can be seen that the electronic lifetime is a minimum (i.e., scattering is a maximum) for Sb_{As} defects at the center of the InAs well. Examination of the charge density of the lowest conduction state in Fig. 1 shows that this state is confined in the InAs layer and has its peak at the center of the well. Not surprisingly, then, the electron scattering is predicted to be of maximum magnitude when the defects are situated at in the region where the electronic charge is most localized. The change to the lifetimes upon lattice relaxation is very small.

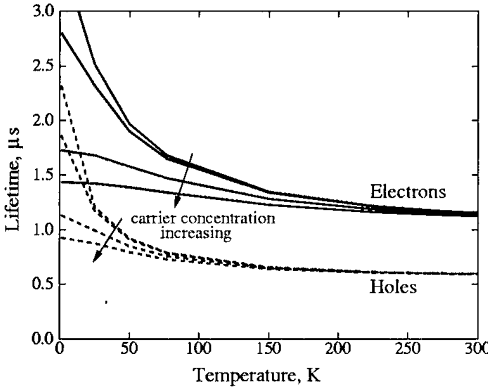

FIG. 5. Calculated lifetime (μs) vs the temperature (K) for electrons in the lowest conduction miniband, and holes in the uppermost valence miniband, due to scattering from an isolated Sb_{As} defect adjacent to the GaInSb-like interface, shown for electron concentrations 5×10^{15}, 1×10^{16}, 5×10^{16}, and 1×10^{17} cm^{-3}.

Figure 7 shows the variation of the lifetime of an ensemble of 10^{16} cm^{-3} holes at 77 K due to a single substitutional anion defect at each of the anion sites. The lifetimes computed with no lattice relaxation are seen, as in the case of the electron lifetimes, to be shortest when the defects are located at sites of maximum charge localization—in this case, As_{Sb} defects at the center of the alloy (valence) well. However, upon relaxation, there is a radical change in the lifetimes. Towards the center of the alloy layer, relaxation results in a one to two orders of magnitude increase in the hole lifetime. As a result, the minimum hole lifetime occurs for defects located adjacent to the superlattice interfaces. Furthermore, at these interface sites, the lattice relaxtaion enhances the scattering further shortening the lifetimes.

Why is the relaxation of the alloy so critical to the hole lifetime, while the relaxation of InAs hardly alters the hole lifetime? Analysis of the relaxation which occurs in these two cases indicates that the average distance which the atoms move in the two cases is very similar, though different in nature. The atoms move away from the Sb_{As} defect but are drawn in towards the As_{Sb} defects. However, tests have shown that where the relaxation patterns are swapped (i.e.,

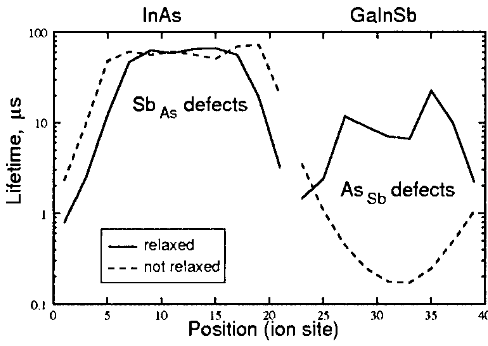

FIG. 7. Variation of the hole lifetime associated with isolated isovalent anion defects with position throughout the superlattice, for a concentration of 10^{16} cm^{-3} holes at 77 K and a density of 10^{16} cm^{-3} defects. The labels on the position axis refer to the anion sites as numbered in Fig. 3. The lifetime is shown before (solid lines) and after (dashed lines) relaxation of the atoms in the lattice.

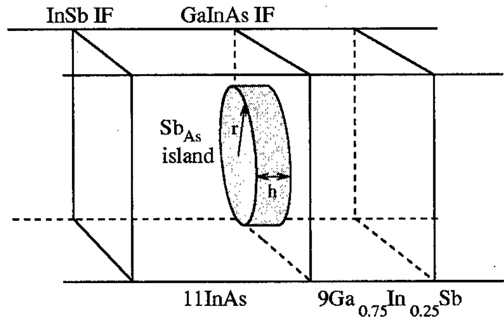

FIG. 8. Schematic diagram showing the geometry of the Sb_{As} islands considered. Inside the shaded cylinder of radius r and height h, a fraction x of the anions present are randomly replaced by Sb anions. The diagram is not to scale in the plane of the interfaces, with even the largest islands considered occupying only a very small fraction of the interfaces (and therefore being regarded as isolated scattering centers).

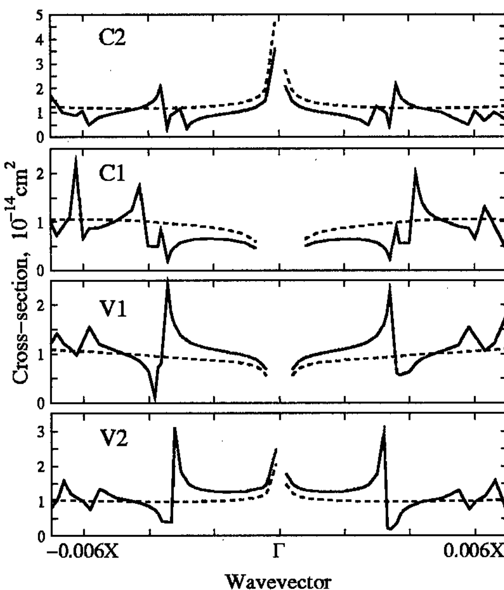

FIG. 9. Wavevector dependence of the cross-section (10^{-14} cm^2) of the 49 Sb atom island described in the text for an electron in the lowest two conduction minibands, and highest two valence minibands. The wavevector is plotted along a part of the -X-Γ-X axis. The solid lines show the full calculation including the contribution from multiple scattering events, while the dashed lines show only the first-order response.

the As_{Sb} relaxation superimposed upon the Sb_{As} defect and *vice versa*), it is still the relaxation of the alloy which results in the radical change to the lifetime. We conclude that it is in the nature of the alloy itself from which the effect originates, a large scattering cross-section contribution arising, out-of-phase with the contribution from the defect atom itself, resulting in an overall cancellation of the cross section, and corresponding increase in the carrier lifetimes.

V. SCATTERING FROM INTERFACE ISLANDS

So far we have studied in detail the behavior of single substitutional anion defects located at sites throughout the heterostructures. It is to be expected, and indeed has been observed,[26] that the concentration of these defects will be greatest adjacent to the interfaces. We now consider the case of clusters of these defects forming at the interfaces, and examine how the scattering depends upon the details of the islands. In particular we shall concentrate upon the example of islands of Sb_{As} defects protruding across the GaInAs interfaces. Figure 8 shows a schematic diagram of the cylindrical islands studied. Within the cylinder of radius r and height h, a fraction x of the As anions are considered to be exchanged for Sb.

By way of an example, we shall first examine in detail the scattering cross section for an island extending two monolayers into the InAs layer, with a radius of two lattice constants. For a swapped anion fraction of 50% the total number of Sb_{As} defects contained in the island will be 49. Figure 9 shows the variation of the scattering cross section for electrons in the lowest two conduction minibands, and highest two valence minibands, with incident wavevector for this island. The cross-section is computed using the full T-matrix expression, Eq. (7) (solid lines), and the first-order expression [Eq. (10)] (dashed lines). Clearly, it can be seen that while the approximate average magnitude of the two approaches are very similar, the fine structure of the wavevector dependence of the two results is radically different. The multiple scattering processes which are included in the T-matrix result show a series of resonances superimposed upon the linear result. It is clear that the magnitude of the discrepancy, equivalent to the contributions from the multiple scattering events, is comparable to the first-order terms at particular wavevectors. The magnitude of this discrepancy is a very sensitive function of the incident electron wavevector.

It is interesting to examine how the computed scattering cross section varies as the total number of Sb_{As} anions contained in the islands is increased. The cross section was computed for a large number of islands with different heights and radii. Since we are concerned with the typical scattering for a particular island, and not upon the specific wavevector dependence of the cross sections, we restrict ourselves to the first-order cross section of Eq. (9). Figure 10 shows the variation of the cross section as a function of n, the number of Sb_{As} defects in the island. In Fig. 10(a) points representing islands of given height and varying radius are connected, while in Fig. 10(b) islands of given radius are joined. It is interesting to note that the variation of cross section with radius follows a simple square law, while for varying heights the cross section goes beyond this. This reflects the fact that the Sb_{As} defects scatter more effectively as they penetrate further into the InAs layers, as seen in Fig. 6.

In the case of the isolated defects whose scattering properties were examined in detail in Sec. IV, it was appropriate to consider only the first-order processes described by Eq. (9). There was no significant difference between the cross section computed by the two methods. The magnitude of the discrepancy between the T matrix and golden rule calculations is dependent upon the size of the perturbation. Figure 11 shows how the magnitude of the discrepancy, as a fraction of the first-order cross section, varies with the magnitude of the first-order cross section. Since the discrepancy is

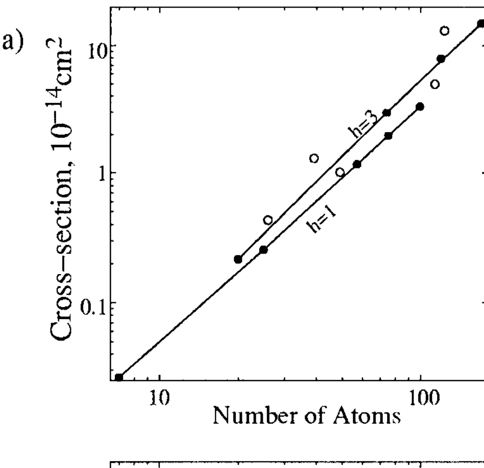

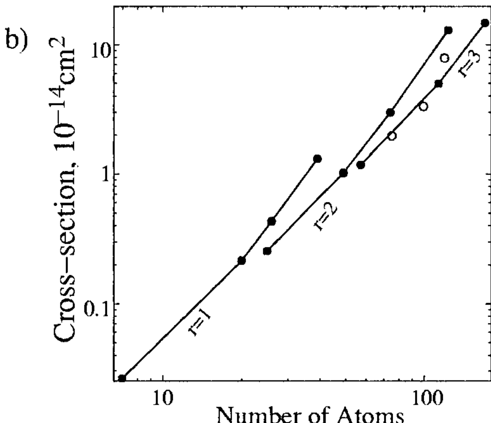

FIG. 10. Scattering cross section (10^{-14} cm^2) of cylindrical islands of varying height and radius, plotted against the number of Sb_{As} defects in the islands. In (a) points representing islands of equal height (in monolayers) are indicated by solid circles joined by lines. In (b) points representing islands of equal radii (in lattice constants) are indicated by solid circles joined by lines. The open circles represent other islands studied in each case.

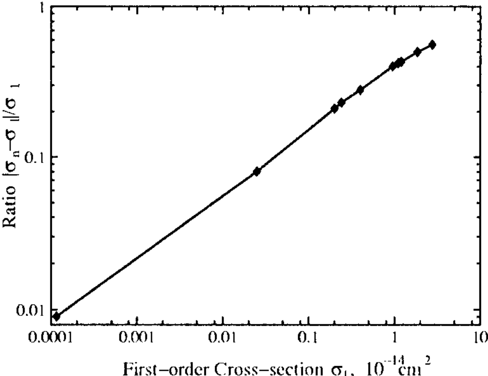

FIG. 11. Relative strength of the higher-order contribution to the scattering cross section, $|\sigma_n-\sigma_1|/\sigma_1$, is plotted on a logarithmic scale against the strength of the first-order cross section (10^{-14} cm^2), σ_1, the cross section in the golden rule approximation. The cross sections were evaluated for initial state with wavevector 0.003X.

dependent upon the precise wavevector, Fig. 11 is compared for a range of islands at a typical wavevector, namely $\approx 0.3X$. Clearly it is seen that the relative significance of the multiple scattering terms can become very large as the size of the scattering center increases. For the larger islands studied, and for the particular wavevector under consideration, the golden rule becomes a rather poor approximation.

Finally, we compare the magnitudes of the lifetimes between isolated defects and islands. For the case of electron lifetimes in the presence of Sb_{As} defects we find that for typical carrier concentrations (at temperature 77 K), the lifetime varies from 1.6 μs at the GaInAs-like interface, to 0.3 μs at the condition well center. The corresponding hole lifetimes are 0.8 and 60 μs, respectively—the minimum time occurring for defects adjacent to the interfaces. However, for a 49 atom Sb_{As} defect island the electron lifetime drops to 0.4 ps.

VI. CONCLUSION

In conclusion, we have investigated the factors which affect the elastic scattering lifetimes in antimonide-based heterostructures using a microscopic theoretical model. The lifetimes have been computed for a variety of isovalent anion defect configurations, including isolated anions and interface islands. For electrons, our calculations indicate that the scattering lifetime is a minimum at the center of the conduction well, reflecting the localization of the ground conduction miniband. However, the hole lifetime was shown to depend critically upon the lattice relaxation, resulting in a minimum lifetime for defects located adjacent to the superlattice interfaces. Clustering of defects into islands was shown to result in a dramatic reduction of the lifetime, dependent upon the shape as well as the size of the islands. Multiple scattering events were shown to have a significant impact upon the wavevector dependence of the lifetime, particularly for the larger defect islands.

The quantitative predictions of lifetimes presented in this article provide a first indication of the microscopic features of disorder which can affect dynamical properties relevant to the application of the structures in devices. This link between the microscopic properties of the superlattice imperfections and observables relevant to device performance is an essential step towards the control of performance-limiting mechanisms in devices.

In this article we have focused upon a specific structure, and with a particular type of defect. However, the theoretical techniques employed are applicable to wide range of structures and defect types, and represent a valuable generic tool in the search for an increased understanding of the role of interfaces and imperfections in determining performance indicators of heterostructure devices.

ACKNOWLEDGMENTS

The authors would like to thank the U.K. Engineering and Physical Science Research Council, D.E.R.A. (Malvern, UK), and the Office of Naval Research (U.S.A.) for financial support.

[1]A. Joullie, J. Phys. IV **9**, 79 (1999).
[2]H. Mohseni, J. Wojkowski, M. Razeghi, and W. Mitchel, IEEE J. Quantum Electron. **35**, 1041 (1999).

[3]L. J. Olafsen, E. H. Aifer, I. Vurgaftman, W. W. Bewley, C. L. Felix, J. R. Meyer, D. Zhang, C.-H. Lin, and S. S. Pei, Appl. Phys. Lett. **72**, 2370 (1998).
[4]J. R. Meyer, L. J. Olafsen, E. H. Aifer, W. W. Bewley, C. L. Felix, I. Vurgaftman, M. J. Yang, L. Goldberg, D. Zhang, C.-H. Lin, S. S. Pei, and D. H. Chow, IEE Proc.: Optoelectron. **145**, 275 (1998).
[5]I. Vurgaftman, J. R. Meyer, and L. R. Ram-Mohan, IEEE J. Quantum Electron. **34**, 147 (1998).
[6]R. M. Biefield, A. A. Allerman, and S. R. Kurtz, Mater. Sci. Eng., B **51**, 1 (1998).
[7]H. Q. Lei, C. H. Lin, and S. S. Pei, Appl. Phys. Lett. **72**, 3434 (1998).
[8]M. J. Yang, W. J. Moore, B. R. Bennett, and B. V. Shanabrook, Electron. Lett. **34**, 270 (1998).
[9]W. W. Bewley, E. H. Aifer, C. L. Felix, I. Vurgaftman, J. R. Meyer, C.-H. Lin, S. J. Murray, D. Zhang, and S. S. Pei, Appl. Phys. Lett. **71**, 3607 (1997).
[10]J. I. Malin, J. R. Meyer, C. L. Felix, J. R. Lindle, L. Goldberg, C. A. Hoffman, F. J. Bartoli, C.-H. Lin, P. C. Chang, S. J. Murray, R. Q. Yang, and S. S. Pei, Appl. Phys. Lett. **68**, 2976 (1996).
[11]R. H. Miles, D. H. Chow, Y.-H. Zhang, P. D. Brewer, and R. G. Wilson, Appl. Phys. Lett. **66**, 1921 (1995).
[12]A. N. Baranov, N. Bertru, Y. Cuminal, G. Boissier, C. Alibert, and A. Joullié, Appl. Phys. Lett. **71**, 735 (1997).
[13]C. Jenner, E. A. Corbin, B. M. Adderley, and M. Jaros, Semicond. Sci. Technol. **13**, 359 (1998).
[14]M. H. Young, D. H. Chow, A. T. Hunter, and R. H. Miles, Appl. Surf. Sci. **128**, 395 (1998).
[15]H. Mohseni, E. Michel, J. Sandoen, M. Razeghi, W. Mitchel, and G. Brown, Appl. Phys. Lett. **71**, 1403 (1997).
[16]J. L. Johnson, L. A. Samoska, A. C. Gossard, J. L. Mertz, M. D. Jack, G. R. Chapman, B. A. Baumgratz, K. Kosai, and S. M. Johnson, J. Appl. Phys. **80**, 1116 (1996).
[17]F. Szmulowicz, E. R. Heller, K. Fisher, and F. L. Madarasz, Superlattices Microstruct. **17**, 373 (1995).
[18]I. H. Campbell, I. Sela, B. K. Laurich, D. L. Smith, C. R. Bolognesi, L. A. Samoska, A. C. Gossard, and H. Kroemer, Appl. Surf. Sci. **59**, 846 (1991).
[19]D. H. Chow, R. H. Miles, J. R. Söderström, and T. C. McGill, Appl. Phys. Lett. **56**, 1418 (1990).
[20]B. R. Bennett, M. J. Yang, B. V. Shanabrook, J. B. Boos, and D. Park, Appl. Phys. Lett. **72**, 1193 (1998).
[21]E. R. Brown, E. R. Söderström, J. R. Parker, L. J. Mahoney, K. M. Molvar, and T. C. McGill, Appl. Phys. Lett. **58**, 2291 (1991).
[22]B. Z. Nosho, W. H. Weinberg, J. J. Zinck, B. V. Shanabrook, B. R. Bennett, and L. J. Whitman, J. Vac. Sci. Technol. B **16**, 2381 (1998).
[23]L. R. Ram-Mohan, I. Vurgaftman, and J. R. Meyer, Microelectron. J. **30**, 1031 (1999).
[24]G. Tuttle, H. Kroemer, and J. H. English, J. Appl. Phys. **65**, 5239 (1989).
[25]J. Wagner, J. Schmitz, H. Obloh, and P. Koidl, Appl. Phys. Lett. **67**, 2963 (1995).
[26]J. Harper, M. Weimer, D. Zhang, C.-H. Lin, and S. S. Pei, Appl. Phys. Lett. **73**, 2805 (1998).
[27]J. Harper, M. Weimer, D. Zhang, C.-H. Lin, and S. S. Pei, J. Vac. Sci. Technol. B **16**, 1389 (1998).
[28]M. J. Shaw, Phys. Rev. B **58**, 7834 (1998).
[29]M. J. Shaw, P. R. Briddon, and M. Jaros, Phys. Rev. B **54**, 16 781 (1996).
[30]M. J. Shaw, J. P. Hagon, E. A. Corbin, and M. Jaros, J. Vac. Sci. Technol. B **17**, 2025 (1999).
[31]L.-W. Wang and A. Zunger, Phys. Rev. B **59**, 15 806 (1999).
[32]M. D. Jack, B. A. Bamugratz, G. R. Chapman, S. M. Johnson, J. L. Johnson, L. A. Samoska, A. C. Gossard, and J. L. Mertz, University of California, Santa Barbara (private communication).
[33]M. Jaros, K. B. Wong, and M. A. Gell, Phys. Rev. B **31**, 1205 (1985).
[34]M. A. Gell, K. B. Wong, D. Ninno, and M. Jaros, J. Phys. C **19**, 3821 (1986).
[35]M. J. Shaw, Phys. Rev. B (accepted).
[36]M. L. Cohen and T. K. Bergstresser, Phys. Rev. **141**, 789 (1966).
[37]P. Friedel, M. S. Hybertsen, and M. Schlüter, Phys. Rev. B **39**, 7974 (1988).
[38]K. A. Mäder and A. Zunger, Phys. Rev. B **50**, 17 393 (1994).
[39]L.-W. Wang, S.-H. Wei, T. Mattila, A. Zunger, I. Vurgaftman, and J. R. Meyer, Phys. Rev. B **60**, 5590 (1999).
[40]M. Jaros, Rep. Prog. Phys. **48**, 1091 (1985).
[41]C. G. Van de Walle, Phys. Rev. B **39**, 1871 (1989).
[42]*Zahlenwerte und Funktionen aus Naturwissenschaften und Technik*, edited by K. H. Hellwege, Vol. III of ''Landolt-Börnstein,'' Vols. 17a and 22a (Springer, New York, 1982).
[43]M. R. Kitchin, M. J. Shaw, E. A. Corbin, J. P. Hagon, and M. Jaros, Appl. Surf. Sci. (accepted).
[44]P. N. Butcher and T. P. McLean, Proc. Phys. Soc. London **81**, 219 (1963).
[45]M. J. Shaw, G. Gopir, P. R. Briddon, and M. Jaros, J. Vac. Sci. Technol. B **16**, 1794 (1998).
[46]J. P. Buisson, R. E. Allen, and J. D. Dow, Solid State Commun. **43**, 833 (1982).

Interface control and band offset at the $Ga_{0.52}In_{0.48}P$ on GaAs heterojunction

C. Cai[a)] and M. I. Nathan[b)]
Department of Electrical and Computer Engineering, University of Minnesota, Minneapolis, Minnesota 55455

(Received 17 January 2000; accepted 1 May 2000)

A new switching procedure was applied in the growth of the lattice-matched heterojunction of $Ga_{0.52}In_{0.48}P$/GaAs by gas source molecular beam epitaxy. The new switching procedure exposed the GaAs surface to the Ga source instead of thermally cracked AsH_3 or PH_3 before starting the growth of the $Ga_{0.52}In_{0.48}P$ layer. The interface charge density and the conduction band offset were determined by measuring the Schottky barrier height using current versus voltage and capacitance versus voltage characteristics. The interface charge density could be reduced to near zero using the new switching procedure with an exposure time of 64 s. The value of the conduction band offset was 0.2 eV at the interface of zero charge. © *2000 American Vacuum Society.*
[S0734-211X(00)03704-5]

I. INTRODUCTION

Recently the lattice-matched $Ga_{0.52}In_{0.48}P$/GaAs (001) material system has attracted much interest as an alternative to the AlGaAs/GaAs heterostructure for high frequency and high power device applications.[1,2] The $Ga_{0.52}In_{0.48}P$/GaAs interface has an important impact on electronic properties for these specific applications. The band offset of $Ga_{0.52}In_{0.48}P$/GaAs is a crucial parameter for the design of these heterostructure devices. However, the $Ga_{0.52}In_{0.48}P$/GaAs interface is far from being well understood as for the case of AlGaAs/GaAs. The values of conduction band offset between $Ga_{0.52}In_{0.48}P$ and GaAs have been reported over a wide range from 0 to 0.39 eV.[3] In addition, the existence of interface charges has been reported for this heterostructure by our previous studies[3,4] and other research groups.[5,6] The band-offset variation and the origin of the interface charges are related to the difficult control of the $Ga_{0.52}In_{0.48}P$/GaAs interface, which shares neither the anions nor the cations. One of the reasons for the difficulty in the interface control is that the chemical bond energy difference between GaP and GaAs could cause an As/P interdiffusion process,[7] which consequently ruins the interface abruptness and causes compositional intermixing and localized strain at the phosphide/arsenide interface.[8] Another issue for achieving good quality $Ga_{0.52}In_{0.48}P$/GaAs interface is to reduce the residual incorporation of previous element V during the growth of the succeeding layer.[7] Both of the issues are strongly dependent on the switching procedure while growing the two consecutive semiconductor layers.

In this study, we grew the undoped $Ga_{0.52}In_{0.48}P$/Si-doped–GaAs heterojunctions with aluminum Schottky barrier contacts by gas source molecular beam epitaxy (GSMBE). The values of barrier heights were determined from the current–voltage ($I-V$) and the capacitance–voltage ($C-V$) characteristics. The difference between the barrier heights $\phi_{bIV}-\phi_{bCV}$, deduced from the two measurements, is significantly and linearly increased with increasing thickness of the undoped $Ga_{0.52}In_{0.48}P$ layer. In contrast to the AlGaAs/GaAs heterojunction, interface charges are observed in this experiment. The band offset and interface charge between $Ga_{0.52}In_{0.48}P$ and GaAs were determined from the $\phi_{bIV}-\phi_{bCV}$ relationship on the thickness of $Ga_{0.52}In_{0.48}P$ layer d. A new growth switching procedure from the GaAs layer to the $Ga_{0.52}In_{0.48}P$ layer was applied to improve the interface quality and reduce the charge density. We mainly changed the switching sequences of group-III and -V element sources to expose the GaAs surface to Ga flux instead of thermally cracked AsH_3 or PH_3 gas before starting $Ga_{0.52}In_{0.48}P$ layer growth. The results show that excess Ga at the interface reduces the interface charge density. The value of conduction band offset ΔE_c depends on the exposure time.

II. EXPERIMENT

A. Sample preparation

We used a Riber GSMBE system to grow the epitaxial layers to fabricate the $Ga_{0.52}In_{0.48}P$/GaAs heterojunctions. In the GSMBE, metal solids of In and Ga were used as the group-III sources, and thermally cracking AsH_3 and PH_3 were used as group-V sources. The flow rates of AsH_3 and PH_3 were 1.0 and 4.0 sccm, respectively. The details of the structure are shown in Fig. 1. All samples were grown on n-type conductive GaAs (001) substrates. A 1-μm-thick Si-doped GaAs layer ($\sim 4\times10^{16}$ cm^{-3}) was grown at 1 μm/h after growth of a heavily doped buffer layer. Subsequently, an undoped $Ga_{0.52}In_{0.48}P$ layer was grown with varying thickness d at 0.8 μm/h. The composition of $Ga_{0.52}In_{0.48}P$ lattice matched to GaAs was verified by double-crystal x-ray diffraction measurement. Figure 2 is a typical rocking curve for the ternary epitaxial film of GaInP on the GaAs with a mismatch of ~0.3%. At the top of the heterostructure, polycrystalline Al of 1200 Å was deposited *in situ* at a substrate temperature less than 50 °C. Schottky contact dots of 100, 200, and 400 μm in diameter were formed by etching Al to the $Ga_{0.52}In_{0.48}P$ surface. Ohmic contacts were made by melting indium onto the backside of the GaAs substrate.

[a)]Author to whom correspondence should be addressed; electronic mail: ccai@ece.umn.edu
[b)]Electronic mail: nathan@ece.umn.edu

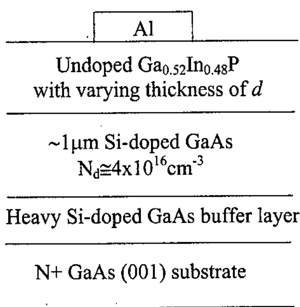

FIG. 1. Structure of the $Ga_{0.52}In_{0.48}P$/GaAs heterojunction with Al Schottky contact on top.

B. Switching procedure

During the growth interval between GaAs and $Ga_{0.52}In_{0.48}P$ in the GSMBE system, some growth conditions should be adjusted to prepare $Ga_{0.52}In_{0.48}P$ growth, such as lowering substrate temperature for $Ga_{0.52}In_{0.48}P$ growth and switching AsH_3 flow to PH_3 flow. A standard switching procedure was widely used and reported in the literatures.[5,9,10] As shown in Fig. 3(a), the GaAs surface was exposed to the P source for 16 s before the $Ga_{0.52}In_{0.48}P$ growth in the standard switching procedure. In this study, a new switching procedure [see Fig. 3(b)] was used to allow the GaAs surface to be exposed to the Ga source in order to improve the interface quality. The exposure time t_e was varied and results were compared to those from a standard switching procedure.

C. Measurements

We measured both the $I-V$ and $C-V$ characteristics to determine the Schottky barrier heights. Assuming thermionic emission of electrons over the Schottky barrier, the relationship between the current density and forward bias voltage is given by

$$J=A^{**}T^2\exp(-q\phi/k_BT)\exp(qV/nk_BT), \quad (1)$$

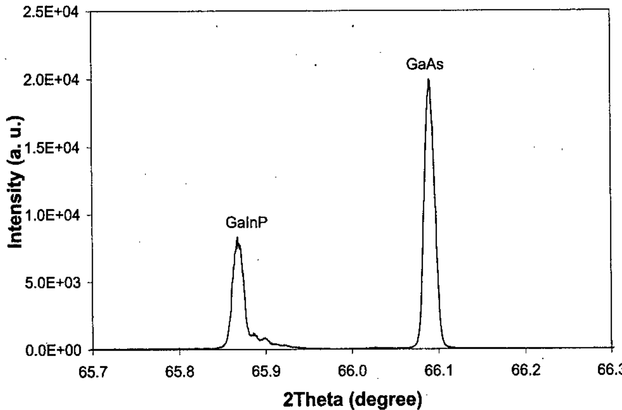

FIG. 2. Rocking curve of double crystal x-ray diffraction for the epitaxial film of $Ga_{0.52}In_{0.48}P$ on GaAs. The mismatch between the two semiconductors is 0.3%.

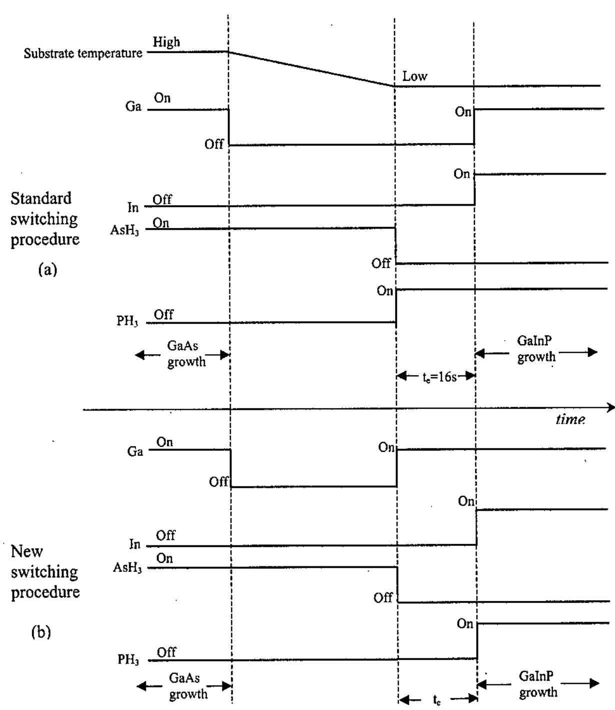

FIG. 3. Solid source and gas flow switching sequence for the growth of the $Ga_{0.52}In_{0.48}P$/GaAs heterostructure. (a) The standard switching procedure; GaAs surface is exposed to PH_3 source before starting the growth of $Ga_{0.52}In_{0.48}P$; (b) the new switching procedure; GaAs surface is exposed to Ga source before starting the growth of $Ga_{0.52}In_{0.48}P$.

where ϕ is the barrier height, A^{**} is the effective Richardson constant, and n is the diode ideality factor and is only slightly greater than unity. A^{**} is taken to be $120(m_e^*/m_e)A/\mathrm{cm}^2/\mathrm{K}^2$, where m_e^* is the effective electron mass in the semiconductor and m_e is the free electron mass. The barrier height determined by Eq. (1) is noted as ϕ_{bIV}.

The barrier height determined by $C-V$ measurements, ϕ_{bCV}, for the two-layer heterostructure shown in Fig. 1 is extracted from[3,4,11]

$$(A/C)^2-(d/\varepsilon)^2_{\mathrm{GaInP}} = (2/qN_d\varepsilon_{\mathrm{GaAs}})(\phi_{bCV}-\phi_n-k_BT/q+V_R), \quad (2)$$

where A is the area of a diode, $(d/\varepsilon)^2_{\mathrm{GaInP}}$ accounts for the undoped $Ga_{0.52}In_{0.48}P$ layer, N_d is the net donor concentration in the n-type GaAs layer, ϕ_n is the potential difference between the conduction band edge and the Fermi level of bulk GaAs doped with N_d donors/cm^3, and V_R is the reverse bias voltage.

By analyzing the conduction band of the heterostructure, the difference between ϕ_{bIV} and ϕ_{bCV} is given by[3,4,11]

$$\phi_{bIV}-\phi_{bCV}=(1/q)\Delta E_c+d(qN_{\mathrm{is}}/\varepsilon_{\mathrm{GaInP}}), \quad (3)$$

where ΔE_c is the conduction band offset, N_{is} is the number density of interface charge, and q is the electron charge.

The $I-V$ and $C-V$ measurements were performed with an HP4145 parameter analyzer and an HP4194 impedance analyzer, respectively, at room temperature in the dark.

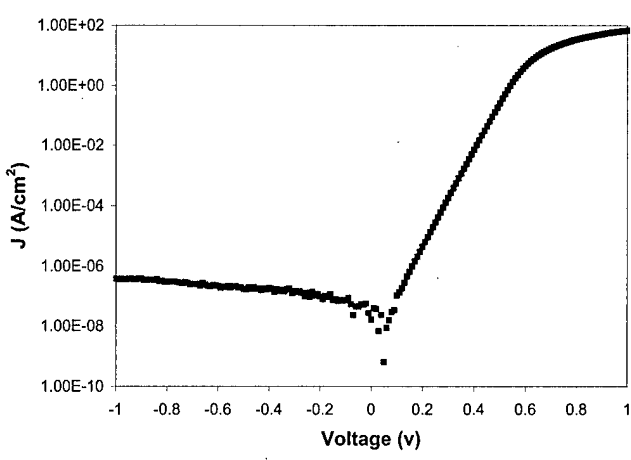

FIG. 4. Plot of $\log(J)$ vs V for the $Ga_{0.52}In_{0.48}P$/GaAs heterojunction with Al Schottky barrier. The range of current for which $\log(J)$ vs V is linear is at least three orders of magnitude.

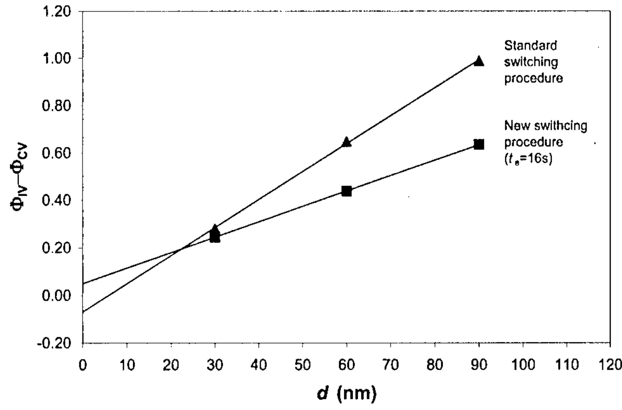

FIG. 6. $Ga_{0.52}In_{0.48}P$ thickness d dependence of $\phi_{bIV}-\phi_{bCV}$ for the samples grown by the standard switching procedure and the new switching procedure (t_e=16 s). It is a linear relationship. ΔE_c is the intercept on $\phi_{bIV}-\phi_{bCV}$ axis. The interface charge density is proportional to the slope.

III. RESULTS AND DISCUSSION

Figure 4 is a typical plot of $\log(J)-V$ for the $Ga_{0.52}In_{0.48}P$/GaAs heterojunction with an Al Schottky barrier. The range of the current for which $\log(J)$ vs V is linear is usually at least three orders of magnitude. Then, the values of the diode ideality factor n and barrier heights ϕ_{bIV} were determined by Eq. (1) from this linear region. The values of n for all samples were less than 1.1 in this study. This fact suggests that the thermionic emission is the dominant current mechanism. The plot of $(A/C)^2-(d/\varepsilon)^2_{\mathrm{GaInP}}$ vs V_R is a straight line as shown in Fig. 5. According to Eq. (2), the net donor concentration in the n-type GaAs layer N_d was determined by the slope of the straight line, and the barrier height ϕ_{bCV} was extracted from the interception on the V_R axis for each sample.

The difference between ϕ_{bIV} and ϕ_{bCV} is varied with thickness of the undoped layer d. Figure 6 shows the data of $\phi_{bIV}-\phi_{bCV}$ with d of 30, 60, and 90 nm using both the standard switching procedure and the new switching procedure with t_e=16 s. The linear relationships between $\phi_{bIV}-\phi_{bCV}$ and d are consistent with Eq. (3) for the two switching procedures. Figure 6 also suggests that the interface charge is independent of thickness d, and dependent on the growth switching procedure. The values of ΔE_c obtained from Eq. (3) for the standard and new switching procedures are observed to be -0.07 and 0.05 eV, respectively. The former is close to the value reported earlier.[3] The interface charge densities N_{is} obtained from the slopes of the straight lines are 7.7×10^{11} cm^{-2} for the standard procedure, and 4.2×10^{11} cm^{-2} for the new procedure with t_e=16 s. The new switching procedure, to expose the interface to the Ga source for 16 s, does reduce the interface charge density. This effect is thought to be the result from the excess Ga atoms at the interface, which could keep As and P from interdiffusing and reduce the residual element As.

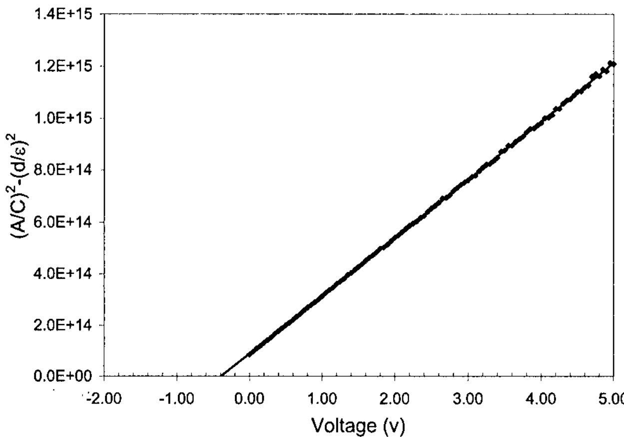

FIG. 5. Plot of $(A/C)^2-(d/\varepsilon)^2_{\mathrm{GaInP}}$ vs V_R. The straight line intercepts the V_R axis at $-(\phi_{bCV}-\phi_n-k_BT/q)$.

In order to improve the interface quality further, we increased the exposure time to 64 s for the new switching procedure. Table I lists the values of $\phi_{bIV}-\phi_{bCV}$ for five samples grown by the new switching procedure with t_e =64 s. The first three values of $\phi_{bIV}-\phi_{bCV}$ are around 0.21 eV and nearly independent of the thickness of the $Ga_{0.52}In_{0.48}P$ layer d. This fact suggests that the interface charge density is very small or nearly zero. In this experiment, ΔE_c is observed to be around 0.21 eV and it is consistent with the results obtained from the improved interfaces reported by other researchers.[5,12] However, the two samples with thicker $Ga_{0.52}In_{0.48}P$ layer (d=80, 90 nm, see Table I)

TABLE I. Experimental data for five samples grown by the new switching procedure with t_e=64 s.

d (nm)	30	40	60	80	90
ϕ_{bIV}	0.81	0.83	0.83	0.88	0.86
ϕ_{bCV}	0.58	0.62	0.62	0.44	0.36
n	1.09	1.07	1.07	1.05	1.05
$\phi_{bIV}-\phi_{bCV}$ (eV)	0.23	0.21	0.21	0.44	0.50

do not show the zero interface charge and this residual interface charge may be due to unintentional doping in the thicker $Ga_{0.52}In_{0.48}P$ layer.

IV. CONCLUSION

We investigated the $Ga_{0.52}In_{0.48}P$/GaAs heterojunction grown by GSMBE by means of $I-V$ and $C-V$ characteristics. A new switching procedure, which allowed the GaAs surface to be exposed to the Ga source instead of the group-V element source during the growth interval from the GaAs layer to the $Ga_{0.52}In_{0.48}P$ layer was applied to improve the interface quality and reduce the interfacial charge density. The results from the new switching procedure were compared to those from the standard switching procedure. We found that the interface charge could be reduced to near zero using the new switching procedure with an exposure time of 64 s. The conduction band offset ΔE_c was 0.2 eV at the interface of zero charge density.

[1]B. Pereiaslavets, G. H. Martin, L. F. Eastman, R. W. Yanka, J. M. Ballingall, J. Braunstein, K. H. Bachem, and B. K. Ridley, IEEE Trans. Electron Devices **44**, 1341 (1997).
[2]W. Liu, S.-K. Fan, T. Henderson, and D. Davito, IEEE Electron Device Lett. **14**, 176 (1993).
[3]T. H. Lim, T. J. Miller, F. Williamson, and M. I. Nathan, Appl. Phys. Lett. **69**, 1599 (1996), and references therein.
[4]C. Cai, M. I. Nathan, and T. H. Lim, Appl. Phys. Lett. **74**, 720 (1999).
[5]Y. K. Fukai, F. Hyuga, T. Nittono, and K. Watanabe, J. Vac. Sci. Technol. B **17**, 2524 (1999).
[6]M. O. Watanabe and Y. Ohba, Appl. Phys. Lett. **50**, 906 (1987).
[7]O. Schuler, O. Dehaese, X. Wallert, and F. Mollot, J. Appl. Phys. **84**, 765 (1998).
[8]J. M. Vandenberg, M. B. Panish, R. A. Hamm, and H. Temkin, Appl. Phys. Lett. **56**, 910 (1990).
[9]H. Y. Lee, M. J. Hafich, and G. Y. Robinson, J. Cryst. Growth **105**, 244 (1990).
[10]M. Usami, Y. Matsushima, and Y. Takahashi, J. Cryst. Growth **150**, 1344 (1995).
[11]T. J. Miller and M. I. Nathan, Appl. Phys. Lett. **61**, 2332 (1992).
[12]O. Dehaese, X. Wallart, O. Schuler, and F. Mollot, J. Appl. Phys. **84**, 2127 (1998).

Effects of gap states on scanning tunneling spectra observed on (110)- and (001)-oriented clean surfaces and ultrathin Si layer covered surfaces of GaAs prepared by molecular beam epitaxy

Hideki Hasegawa,[a] Noboru Negoro, and Seiya Kasai
Research Center for Interface Quantum Electronics and Graduate School of Electronics and Information Engineering, Hokkaido University, North 13, West 8, Sapporo 060-8628, Japan

Yasuhiko Ishikawa
Research Institute of Electronics, Shizuoka University, 3-5-1 Johoku, Hamamatsu 432-8011, Japan

Hajime Fujikuwa
Research Center for Interface Quantum Electronics and Graduate School of Electronics and Information Engineering, Hokkaido University, North 13, West 8, Sapporo 060-8228, Japan

(Received 17 January 2000; accepted 19 April 2000)

In an attempt to understand and control Fermi level pinning on GaAs surfaces, an ultrahigh vacuum (UHV) scanning tunneling spectroscopy (STS) study was made on (110) and (001) clean surfaces and Si covered (001) surfaces of *n*-type GaAs prepared by molecular beam epitaxy. Normal STS spectra showing conductance gaps corresponding to GaAs energy gap and anomalous spectra showing much larger gaps coexisted on all samples. The rate of finding normal spectra was very low on the initial surfaces, but it greatly increased after Si deposition particularly on the $c(4\times4)$ surface. A previous explanation of the gap anomaly by tip-induced electrostatic bend bending change is invalid. A new model based on a band bending change due to tip-induced local charging of surface states is presented where tunneling proximity makes occupancy of surface states in equilibrium with the scanning tunneling microscopy (STM) tip. Spots with anomalous spectra correspond to Fermi level pinning centers where the tip directly "writes" or "erases" single or a few electrons to and from the surface states. Away from the pinning center, such charge transfer does not take place, and normal STS spectra are obtained with Fermi level positions consistent with macroscopic band bending measured by x-ray photoelectron spectroscopy and by an UHV contactless capacitance–voltage system. No direct one-to-one correlation existed between the pinning center and any specific visual STM defect features such as vacancies, dimer-desorbed holes, dimer kinks, step etc. Pinning centers make up inhomogeneous distributions of spatially extended pinning areas of universal nature surrounding any kind of structural disorder. Si deposition is shown to be very effective in reducing the number, spatial extension and state density of such pinning areas, particularly on the initially $c(4\times4)$ reconstructed surface. © *2000 American Vacuum Society.* [S0734-211X(00)02704-9]

I. INTRODUCTION

High-density gap states at surfaces and interfaces of III–V compound semiconductors are known to cause Fermi level pinning and cause various adverse effects in electronic and optoelectronic devices. Since surfaces tend to dominate over the bulk in small structures, control of surfaces and interfaces becomes more and more important as device feature sizes are scaled down to the nanometer quantum regime.

The Si interface control layer (Si ICL)-based surface passivation method[1] is an effective approach with which to remove such gap states. In this method, an ultrathin pseudomorphic Si layer grown by molecular beam epitaxy (MBE) is inserted between the compound semiconductor and a Si-based insulator such as SiO_2 and Si_3N_4, as schematically shown in Fig. 1(a). Its role is to coherently terminate surface bonds of the compound semiconductor and to form a good interface with the Si-based outer insulator. The band states of the Si ICL which has an extremely narrow band gap due to tensile stress can be pushed from the band gap of the compound semiconductor by quantum confinement,[2] as shown in Fig. 1(b), if the ICL thickness is of the few monolayer level. The effectiveness of this method has been demonstrated in a macroscopic way in various device-oriented structures including InGaAs and InP insulated gate field effect transistors (IGFETs) and high electron mobility transistors (IHEMTs),[3–5] AlGaAs/GaAs near-surface quantum wells,[6] and InAlAs/InGaAs near-surface ridge quantum wires.[7] However, from the microscopic point of view, the mechanism for Fermi level pinning on III–V surfaces and its reduction by the Si ICL is not well understood. Scanning tunneling spectroscopy (STS) should be a powerful tool for such study, but only limited work[8–10] has been done so far on GaAs (001) surfaces in spite of its technological importance.

The purpose of this article is to carry out an ultrahigh vacuum (UHV) STS study on clean MBE-grown and Si-covered surfaces of *n*-type GaAs in an attempt to clarify the microscopic mechanism of Fermi level pinning and its reduction by Si ICL. STS spectra were taken on (110) and (001) surfaces and Si deposited (001) surfaces. All the ex-

[a]Corresponding author; electronic mail: hasegawa@rciqe.hokudai.ac.jp

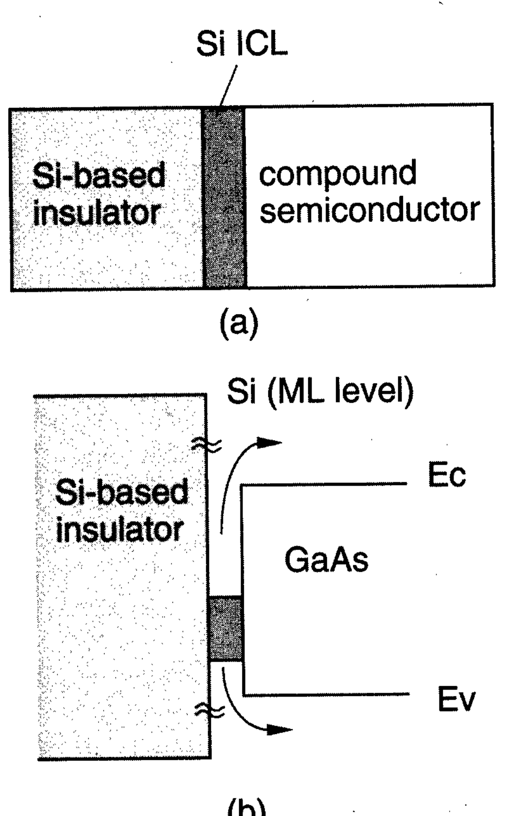

FIG. 1. (a) Concept of Si ICL-based passivation for compound semiconductor surfaces and (b) band line up of the Si ICL-based passivation structure having a monolayer-level Si.

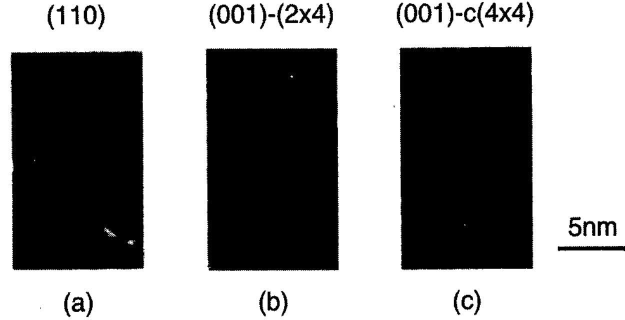

FIG. 2. STM images of initial surfaces: (a) (110)-(1×1), (b) (001)-(2×4), and (c) (001)-c(4×4).

periments were carried out in an UHV-based multichamber system.

Normal STS spectra showing conductance gaps corresponding to the GaAs energy gap and anomalous spectra showing much larger gaps coexisted on all sample surfaces. A previous explanation of the gap anomaly was shown to be invalid and a new model based on band bending change due to tip-induced local charging of surface states at pinning centers is presented. The pinning centers make up inhomogeneous distributions of spatially extended pinning areas of a universal nature. Deposition of Si ICL is very effective in reducing the number, spatial extension and state density of such pinning areas, particularly on the initially c(4×4) reconstructed surface, in agreement with our recent macroscopic study.[11]

II. EXPERIMENT

Samples were prepared and characterized without breaking UHV in an UHV-based multichamber system installed in the Research Center for Interface Quantum Electronics (RCIQE), Hokkaido University. Thick (>3000 Å) Si $(1-3 \times 10^{18}\ \mathrm{cm}^{-3})$-doped GaAs epitaxial layers were grown by solid source MBE on n^+-GaAs(001) substrates at 580 °C with a growth rate of 1.0 monolayer (ML)/s, and annealed in an As_4 flux for 10 min to achieve (2×4)β-phase reconstruction. For comparison, (110) surfaces were also prepared by MBE on (110) substrates with somewhat different growth conditions. MBE deposition of Si ICL was made on (2×4) and c(4×4) reconstructed surfaces at 300 °C at a rate of 4.9 ML/h in the same chamber using a Si K cell. For this, the (2×4) surface was prepared by reducing the As_4 flux intensity during cooling down to 300 °C, and the c(4×4) surface without reducing the As_4 flux during cooling.

STS spectra were taken at room temperature by a JEOL JSTM-4600 with electrochemically polished tungsten tips. Prior to STS measurements, scanning tunneling microscopy (STM) images were taken in the constant current mode at 0.1–0.3 nA. For STS measurements, the tip was located at a fixed position, and then the tunneling current–voltage $(I-V)$ characteristics were measured by breaking the STM feedback loop and ramping the sample bias voltage. No intentional vertical movement of the tip was made during measurements, as was done in previous work.[12] To enhance the measurement sensitivity, ramping of the sample bias was repeated 64 times at the same position, and an average $I-V$ curve was obtained. The minimum resolution of the tunneling current was 30 pA. The differential conductivity (dI/dV) was calculated numerically from the $I-V$ data. The conductivity was further normalized as $(dI/dV)/\overline{(I/V)}$, using a one-pole low pass filter technique[12] with a broadening parameter of $\Delta V = 3$ V to obtain spectra which are less sensitive to the sample-to-tip distance.

In order to obtain information on Fermi level pinning on the macroscopic scale, x-ray photoelectron spectroscopy (XPS) band bending measurements and UHV contactless capacitance–voltage $(C-V)$ measurements were carried out *in situ* at room temperature using a Perkin-Elmer PHI 5100C spectrometer with monochromatic Al $K\alpha$ radiation (1486.6 eV) and a novel UHV $C-V$ measurement system developed by the authors' group,[13] respectively. The latter allows metal–insulator–semiconductor (MIS) $C-V$ measurements at 500 kHz on free semiconductor surfaces by using a constant UHV gap maintained by a piezoelectric feedback mechanism.

III. EXPERIMENTAL RESULTS

A. STM topography

Examples of the filled state STM images of MBE-grown initial surfaces are given in Fig. 2 for (110)-(1×1), (001)-(2

×4), and (001)-$c(4\times4)$ surfaces. All of them showed well known structures with high perfection.

Deposition of Si on (001) surfaces resulted in various surface structures as already described elsewhere.[11,14] Briefly, submonolayer Si deposition on the initially (2×4) reconstructed (001) GaAs surface produced three regions, namely, the region maintaining the initial (2×4) reconstructed structure, the region where the initial missing-dimer trench was filled with Si atoms, and the hole region where initial As dimers were removed and underlying Ga atoms appeared. Further Si deposition produced Si terrace regions. On the other hand, Si deposition on $c(4\times4)$ reconstructed (001) GaAs surfaces included the initial $c(4\times4)$ region and the Si deposited terrace region. No hole region was seen after Si deposition on the $c(4\times4)$ surface, and the topology was much more ordered and smooth.

B. STS spectra

A total of 450 STS spectra were taken on various parts of initial (110)/(001) and Si deposited (001) surfaces and they indicated the following two remarkable features. First, on every surface, normal STS spectra showing a GaAs energy gap of 1.4 eV and anomalous spectra showing a much wider apparent energy gap coexisted as briefly reported elsewhere.[15] Second, the rate of finding anomalous spectra greatly reduced after Si deposition, particularly on the $c(4\times4)$ initial surface.

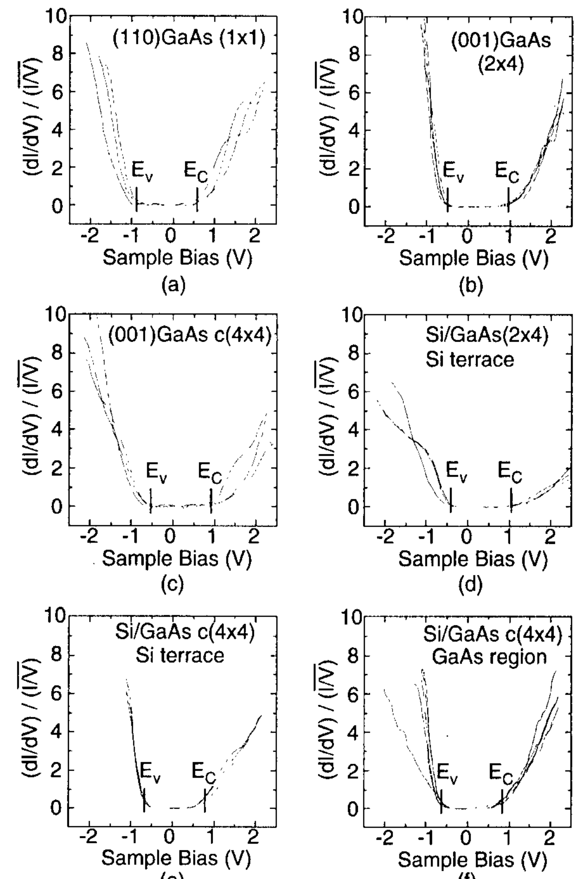

FIG. 3. Normal STS spectra taken on various GaAs surfaces.

Figures 3(a)–3(f) summarize normal STS spectra taken on various surfaces in terms of the normalized conductance defined by $(dI/dV)/(\overline{I/V})$. The characteristics in Figs. 3(a)–3(f) show that the conductance rises at the points indicated by E_C and E_V and that $E_C-E_V\sim1.4$ eV hold in all cases. On the other hand, anomalous spectra were seen at many spots on the sample surfaces. Examples are shown in Figs. 4(a)–4(f) for various surfaces where the conductance rises at E'_V and E'_C with $E'_C-E'_V$ being much larger than 1.4 eV. In some cases, E'_C could not be detected within the voltage ramp up to 2.5 V used for the measurements.

The results of STS spectra measurements performed on 400 points on various (001) sample surfaces are summarized in Table I in terms of the rate of finding a spot showing a normal STS spectrum. As seen in Table I, the rate is extremely low on the initial surfaces. The rate increased after Si deposition. Particularly, a dramatic increase was observed after Si deposition on $c(4\times4)$ surface.

From a traditional viewpoint of STS, such large conductance gaps are difficult to understand. Furthermore, both the normal and anomalous spectra show no discrete peaks of the density of states (DOS) in the gap which one might expect on surfaces with strong Fermi level pinning. However, such a large conductance gap with no DOS peaks was also observed by other workers including Bressler-Hill *et al.*[9] and Takahashi and Yoshida.[10] The present observation reproduces this, and also shows that both normal and anomalous spectra can coexist on the same surface.

One possible explanation for this anomaly is some tip-induced spurious effect. However, both normal and anomalous spectra were completely reproducible as a function of the spatial position on the surface, as verified by repeated experiments with the tip going back and forth over the STM image. Actually, reproduction of normal spectra was more difficult than of anomalous spectra on freshly MBE-grown surfaces, because normal spectra could be obtained only on limited spots, as shown in Table I. Reproduction was only possible after careful compensation for small tip drifts during measurements. After Si deposition, it became much easier to reproduce normal and anomalous spectra. Additional evidence against tip induced spurious effects is the light illumination effect found by Takahashi and Yoshida.[10] That is, under the same tip, the large conductance gap is reduced to a normal value by laser light illumination as our preliminary study also confirmed.

Finally, within the measurements done in this study, no clear direct one-to-one correlation was observed between the location of the spot showing a large gap and specific visual STM defect features such as vacancies, dimer-desorbed holes, dimer kinks, and steps, etc.

C. XPS and contactless *C–V* measurements

The result of the XPS measurement is summarized in Fig. 5(a). Both Ga *3d* and As *3d* core level peaks showed consistent movement, indicating the presence of band bending. The surface Fermi level (E_{FS}) was strongly pinned on all types

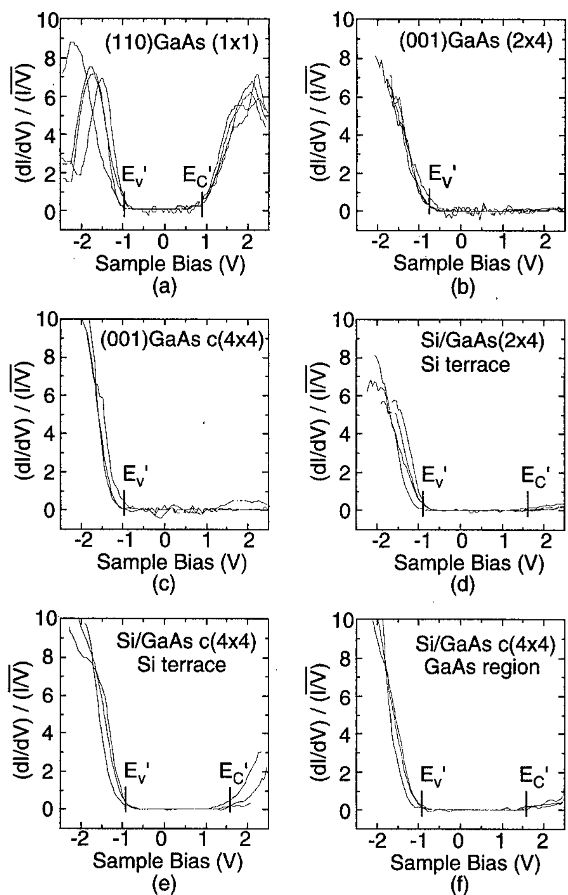

FIG. 4. Anomalous STS spectra from various GaAs surfaces.

of initial surfaces, including the (110) surface which usually shows a flat band if it is obtained by cleavage. However, MBE-grown (110) surfaces showed strong band bending, in agreement with our previous study.[16] After a 1 ML Si deposition, the Fermi level did not change appreciably on the (2×4) reconstructed initial surface. On the other hand, a clear shift of about 250 meV toward E_C was observed after Si deposition on the $c(4\times4)$ surface, indicating a decrease of band bending.

TABLE I. Rate of finding a spot showing a normal STS spectrum. (Measured points: 400.)

Surface	Measured location	Initial surface (%)	After deposition of 1/4 ML Si (%)	After deposition of 3/8 ML Si (%)
(001)-(2×4)	On an As dimer array	4	···	···
	In the hole region	10	0	33
	On the Si terrace	···	36	···
(001)-$c(4\times4)$	On $c(4\times4)$	19	12	71
	On the Si terrace	···	15	67

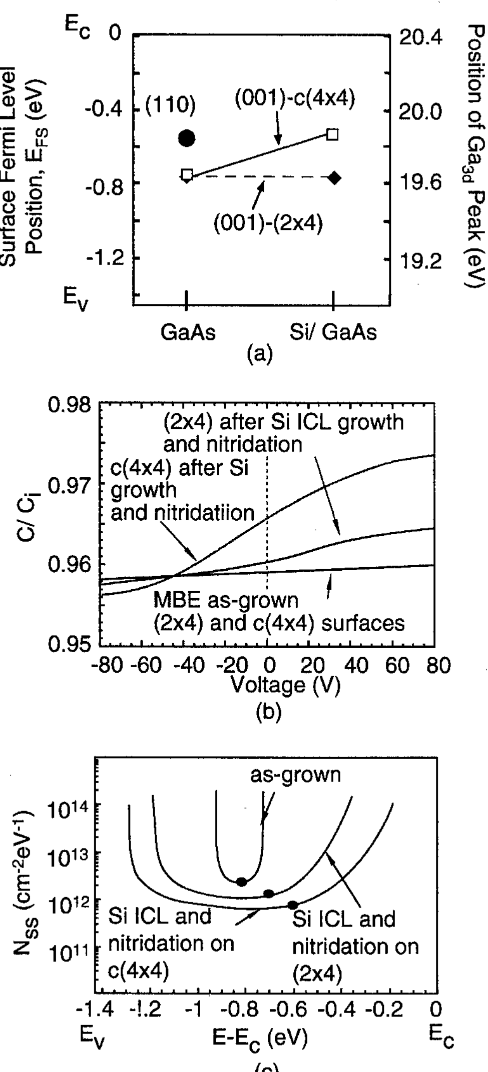

FIG. 5. (a) Summary of surface Fermi level positions on GaAs surfaces determined by the peak positions of Ga *3d* spectra, (b) UHV contactless $C-V$ curves from GaAs (001) surfaces, and (c) interface state density (N_{SS}) distributions calculated by the measured $C-V$ curves. The closed circles indicate the zero-bias Fermi level positions.

The high frequency $C-V$ curves normalized by the UHV gap capacitance C_i, obtained by UHV contactless $C-V$ measurements, are shown in Fig. 5(b). The Si-deposited surfaces shown here went through a further surface nitridation process described elsewhere[2] in order to see whether the above XPS detected reduction of pinning survives after formation of the final passivation structure shown in Fig. 1(a).

Almost flat $C-V$ curves were obtained on MBE-grown (2×4) and $c(4\times4)$ surfaces, indicating the presence of strong Fermi level pinning. After Si deposition, the capacitance showed variations with the field plate bias V, indicating a reduction of pinning. The effect was much larger on the $c(4\times4)$ initial surface, consistent with the XPS result. The interface state density distributions obtained from the $C-V$ curves using Terman's method are shown in Fig. 5(c). Sharp distributions of high density surface states existed on the initial surfaces. The distribution is widened and lowered after

Si deposition, particularly on the $c(4\times4)$ surface. The black data points in Fig. 5(c) show zero bias Fermi level positions estimated from $C-V$ curves. They are consistent with XPS results, although some further reduction of pinning took place after surface nitridation in the case of the (2×4) initial surface.

IV. DISCUSSION

A. Previous explanation of the anomalous conductance gap

At first, observation of conductance gap different from that of the bulk band gap appears very surprising. Previously, a conductance gap smaller than the bulk band gap was observed on a Si(001) surface.[17] However, this was due to the presence of a surface state band of extended nature in the bulk gap, resulting in a surface state gap. On the other hand, there is no such extended surface state band within the bulk gap on the GaAs(001) surface as shown by theory[18] and photo-emission/inverse photoemission (PES/IPES) experiments.[19] Thus, one should basically obtain a conductance gap equal to bulk band gap (1.4 eV).

From an experimental viewpoint, two other groups[9,10] reported a similar anomaly, as already mentioned. On the other hand, Parshley *et al.*[8] made a detailed STS study on highly Si-doped (001) GaAs surface in an attempt to show that kinks in the (2×4) As dimer arrays act as surface acceptors and cause pinning near midgap. Contrary to the present study, they observed a normal conductance gap. However, the STS spectra were either featureless in the gap or showed U-shaped continuous DOS spectra in spite of their effort to find a discrete DOS peak near midgap.

One explanation for an increased conductance gap may be the spreading resistance effect discussed by Flores and Garcia.[20] They argued that the spreading resistance near the tip should produce a significant voltage drop on the semiconductor side. Recently this model was suggested to be the origin of strong current dependence of STS spectra taken on a 6H-SiC(0001) surface.[21] However, it is highly unlikely that such a model applies to the present case using highly Si-doped samples.

As a more sophisticated model, Bressler-Hill *et al.*[9] argued that the STM induces changes of band bending electrostatically on the surface where high density acceptor type discrete surface states cause pinning near midgap, as illustrated in Fig. 6(a). They assumed that occupancy of the deep acceptor states is in equilibrium with the semiconductor bands and is determined by the bulk Fermi level like in thick MIS structures. They also assumed that partitioning of the applied bias between the tunneling vacuum insulator and the semiconductor band is determined by conventional one-dimensional MIS theory. Then, under a sample negative bias, the bias is totally applied between the tip and sample surface because electric field lines from the tip are always terminated by negative charge due to increased filling of acceptor states with bias. Under a sample positive bias, acceptor states are

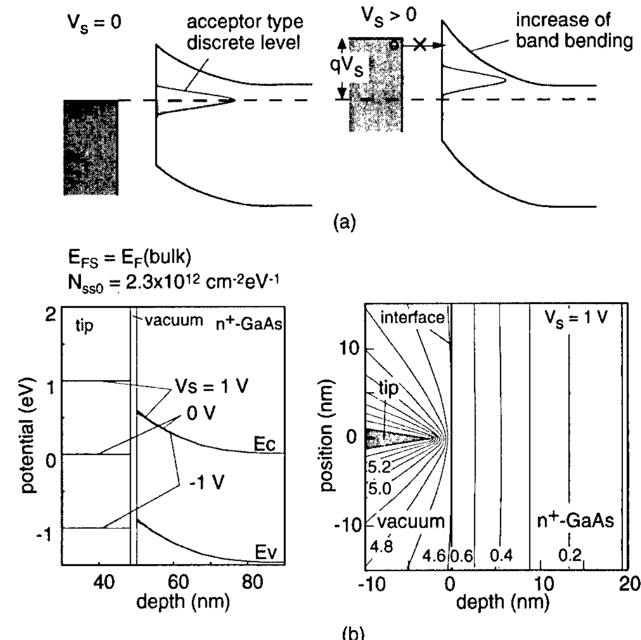

FIG. 6. (a) Previous model for anomalous STS spectra and (b) the calculated results of band bending and the potential distribution.

quickly emptied, and a substantial part of the sample bias is now consumed for increase of semiconductor band bending.

This model seems to explain the main features of the observed gap anomaly. However, it is obviously wrong, because the latter assumption means that the anomaly should also take place under positive bias on an ideal surface without surface states for the same reason. STS usually relies on the fact that the tip capacitance is small enough to allow sweeping of the surface energy without causing an appreciable band bending change, and this has been previously realized experimentally on many well-behaved semiconductor surfaces. Additionally, this model cannot explain the present experimental observation that the anomaly occurs, to a smaller extent, under sample negative bias.

In order to have further ideas on band bending electrostatically induced by the tip, a rigorous numerical calculation of the potential distribution was made on a computer on a macroscopically pinned surface of GaAs, using a successive overrelaxation (SOR) method and the following empirical DOS formulas for the disorder-induced gap state (DIGS) continuum[22,23] which consists of donor-type and acceptor-type states below and above the change neutrality point, E_{HO}:

$$N_{SS}(E)=N_{SS0}\exp\left[-\left(\frac{E-E_{HO}}{E_{0a}}\right)^{n_a}\right]$$

for acceptor-type states, (1a)

$$=N_{SS0}\exp\left[-\left(\frac{E-E_{HO}}{E_{0d}}\right)^{n_d}\right]$$

for donor-type states, (1b)

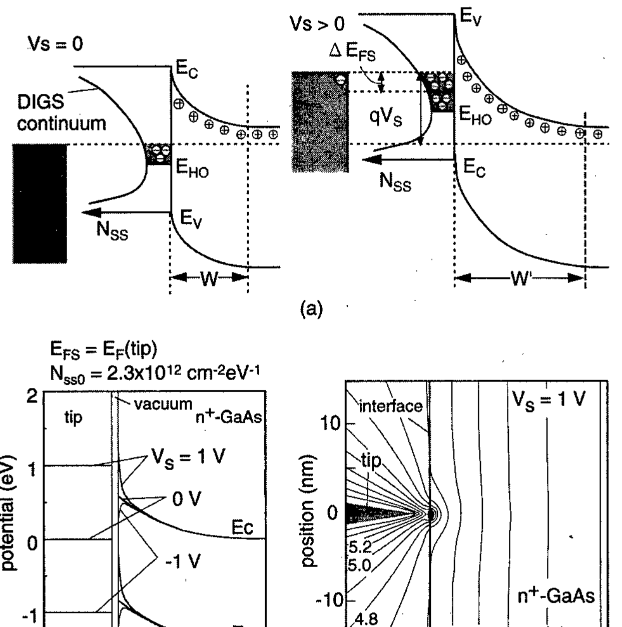

FIG. 7. (a) New model for anomalous STS spectra based on electron exchange with a DIGS continuum and (b) the calculated results of band bending and the potential distribution.

with $E_{HO}=0.8$ eV, $n_a=1.6$, $n_d=1.6$, $E_{0a}=0.1$ eV, $E_{0d}=0.1$ eV, and $N_{SS0}=2.3\times10^{12}$ cm^{-2} eV^{-1}. These formulas give a good phenomenological representation of macroscopic surface state distributions such as those shown in Fig. 5(c). It was also assumed that $E_{FS}=E_F$ (semiconductor bulk), and the tip-to-surface distance was taken to be 1 nm. The result of calculation is shown in Fig. 6(b). As seen in Fig. 6(b), the tip-induced increase of band bending is negligibly small even for the strongly pinned surface.

B. New explanation of the anomaly

Conventional STS theory for surface states tacitly assumes that the electrons tunneling into the surface states are quickly removed from these states, so that the tunneling rate *T(V)* with *V* being the tip voltage is the rate limiting factor for the tunneling current. However, since the thermal escape rate of carriers, $e_n(E)$, is rather small when the energy location, E, in the gap is deep, the validity of this assumption becomes doubtful for deep surface states. A simple analysis leads to the following expression for the tunneling current:

$$I_t=N_{SS}(E)(1-f_S)T(V). \tag{2a}$$

Here, f_S is the occupation function of the gap state at energy, E, and is given by

$$f_S=\frac{T(V)}{T(V)+e_n(E)}, \tag{2b}$$

with

$$e_n=\sigma_n v N_C \exp\left(-\frac{E_C-E}{kT}\right), \tag{2c}$$

where σ is capture cross section of the surface state for electrons, and v is the mean thermal velocity of electrons. In the case of $T\ll e_n$, one obtains

$$f_S\cong0,\quad E_{FS}=E_F(\text{bulk}), \tag{3a}$$

$$I_t=N_{SS}(E)T(V), \tag{3b}$$

which gives the basis of standard STS theory. However, when $T\gg e_n$, one obtains

$$f_S\cong1,\quad E_{FS}=E_F(\text{tip}), \tag{4a}$$

$$I_t=N_{SS}(E)e_n(V). \tag{4b}$$

In this case, local charging of surface takes place. By estimating the actual values of T and e_n for minimum tunneling currents of a few 10 pA detected in this study, it is easy to see that this case is more likely for deep surface states on GaAs.

The new model for the anomaly is shown in Fig. 7(a). It is based on electron exchange with the DIGS continuum. Since the tip can exchange electrons rather freely with the gap states, it is assumed in Fig. 7(a) that the surface quasi-Fermi level, E_{FS}, determining the gap state occupancy, comes into equilibrium with the tip Fermi level E_F (tip) rather than the semiconductor bulk Fermi level, E_F (bulk). This is a most likely situation in ultrathin tunneling MIS structures and was discussed years ago,[24] although workers in the STS community have not thought about it so far to our knowledge. In such a situation, the acceptor-type states are occupied under sample positive bias by a direct supply of electrons from the tip, and this is contrary to the model of Bressler-Hill *et al.* and also to the situation in a thick MIS system where a sample negative bias causes filling of acceptor-type states. Similarly, under sample negative bias, electrons are returned from donor-type states directly to the tip in the new model. Thus electrons are added to or subtracted from the semiconductor surface which causes "real" modification of local bend bending due to localized charging. Since the number of surface states which lie within the tunneling distance from the tip is limited, only single or a few electrons are captured. Thus the present phenomenon can be regarded as a kind of single electron charging phenomenon. According to the present model, a large tip bias V_S is required to obtain a Fermi level shift ΔE_{FS} in Fig. 7(a). The fact that $|E_V'|>|E_V|$ in the anomalous spectra shown in Figs. 4(a)–4(f) shows that not only acceptor-type, but also donor-type, gap states exist on the surface in accordance with the DIGS model.[22]

In order to confirm the above model quantitatively, rigorous numerical calculations of the potential distribution were made for the same N_{SS} distribution in Fig. 6(a), but this time assuming $E_{FS}=E_F$ (tip). The result is shown in Fig. 7(b) and it clearly shows the appearance of band bending change induced by local charging of surface states. Figure 8(a) shows the calculated relationships between the sample bias and en-

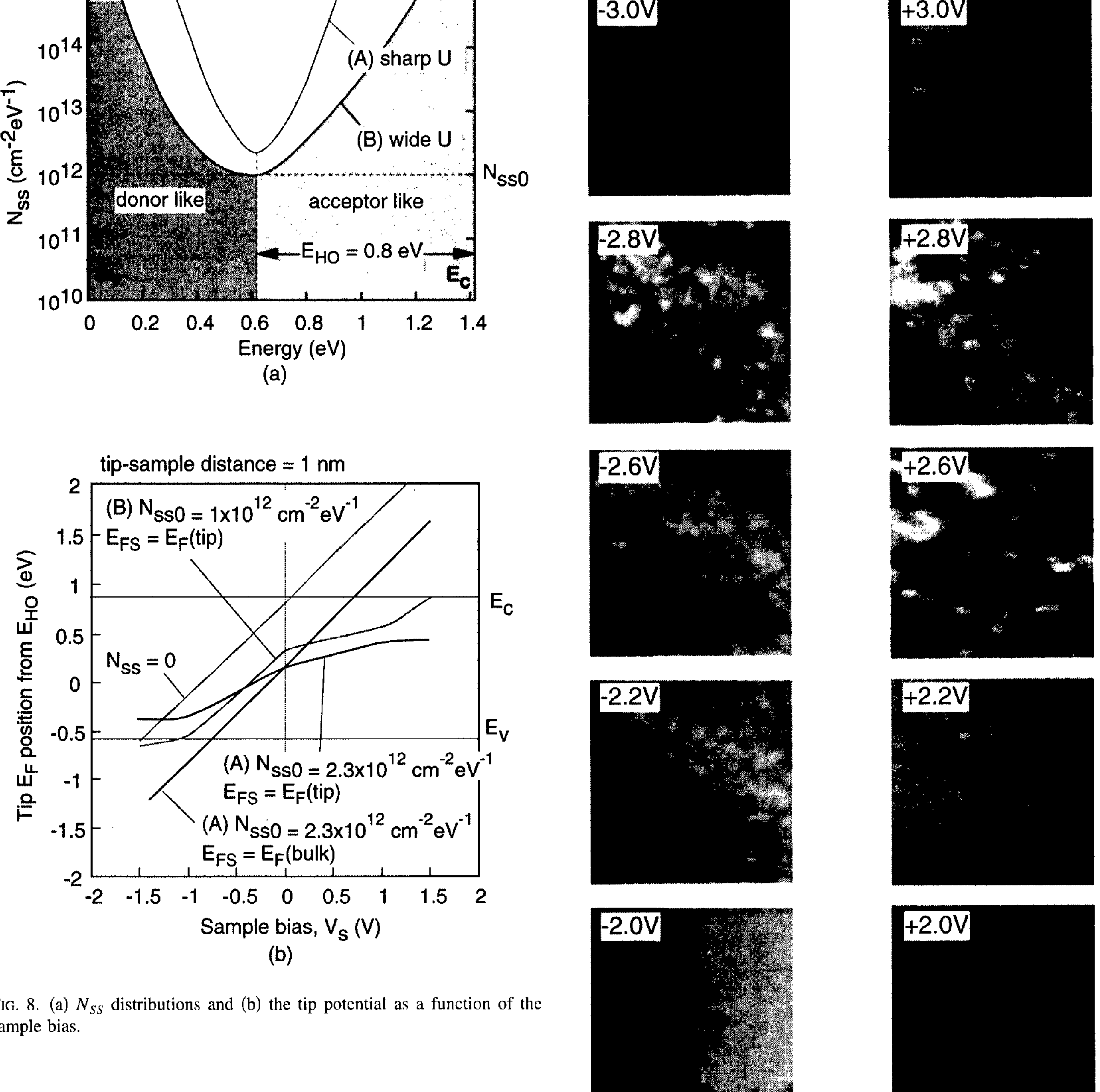

FIG. 8. (a) N_{SS} distributions and (b) the tip potential as a function of the sample bias.

FIG. 9. Sample bias dependence of STM images taken on the MBE-grown (001) GaAs surface. (a) Filled state images and (b) empty state images.

ergy position of the tip in the semiconductor band with respect to the charge neutrality level, E_{HO}, for two different surface state distributions shown in Fig. 8(b) with $E_{HO}=0.8$ eV, $n_a=1.6$, $n_d=1.6$, $E_{0a}=0.1$ eV, $E_{0d}=0.1$ eV, and $N_{SS0}=2.3\times10^{12}$ cm^{-2} eV^{-1} for the narrow U-shaped N_{SS} distribution and $E_{HO}=0.8$ eV, $n_a=2.3$, $n_d=1.4$, $E_{0a}=0.22$ eV, $E_{0d}=0.15$ eV, and $N_{SS0}=1\times10^{12}$ cm^{-2} eV^{-1} for the wide U-shaped N_{SS} distribution, respectively. In both distributions, the integral of $N_{SS}(E)$ was terminated so as to not exceed the number of the surface atom density.

The calculated results can explain various features of the observed anomalous spectra rather well quantitatively. That is, $|E_C'|>|E_C|$, $|E_V'|>|E_V|$, and $|E_C'-E_C|>|E_V'-E_V|$ The last feature reflects the position of E_{HO} and higher densities of acceptor-type states. For comparison, the result for the case of $E_{FS}=E_F$ (bulk) is also shown, and this does not explain the experiment at all.

According to the new model, anomalous behavior is obtained only when the tip hits the pinning center. Away from the pinning center, this anomaly does not take place due to the absence of charge exchange, and normal STS spectra with $E_{FS}=E_F$ (bulk) should be obtained. Thus, coexistence of normal and anomalous spectra is explained. In the normal

STS spectra, however, bend bending remains, because the band bending caused by pinning centers extends over the entire sample surface. Thus the Fermi level position can be determined from the normal spectra. According to the normal spectra in Fig. 3, $E_{FS}=E_F$ (bulk) lies 0.6 eV below E_C for the (110) surface, 0.9–1.0 eV below E_C for the (001)-(2×4) and (001)-c(4×4) initial surfaces, 1.0 eV below E_C for the Si-deposited surface on (2×4), and 0.75 eV below E_C for the Si-deposited surface on c(4×4), respectively. Taking into account the accuracy of the band bending determination by XPS, these values are in good agreement with the XPS result shown in Fig. 5(a). Thus, the normal STS spectra in Fig. 3 can be interpreted in the conventional way.

The fact that the GaAs gap is measured on the Si overlayer shows that Si band states are pushed out of the GaAs band gap due to quantum confinement in the surface vacuum-Si–GaAs quantum well, as indicated in Fig. 1(b). The other fact, that the rate of finding normal spectra dramatically increased after Si deposition, particularly on c(4×4), directly confirms the reduction of surface pinning states by Si ICL.

According to our new model, it is necessary to realize $T \ll e_n$ in order to obtain the true DOS with a normal conductance gap. However, realization of this condition becomes exponentially more and more difficult with the increase of the band gap. Thus, as compared with Si, it is much more difficult for GaAs, and requires the capability of measuring extremely small tunneling currents that are far below that of our commercial JEOL system which has a current resolution of only 30 pA. Under the condition $T \gg e_n$, the gap is increased and the DOS in the gap is multiplied by a factor of $T/e_n (\ll 1)$ with respect to the bulk band states. Thus, the STS spectra obtained by us and by Takahashi and Yoshita[10] show large gaps and no sign of gap states in the gap in spite of the presence of strong Fermi level pinning. On the other hand, the condition $T \ll e_n$ might have been realized in the work of Pashley *et al.*[8] who used a powerful and sophisticated STS system. This explains the reason why they could observe normal gaps. The U-shaped continuous STS spectra they observed seem to be consistent with the state distributions that were observed by macroscopic C–V measurements and were assumed in the calculation in this study. This also indicates that kinks are not discrete deep acceptor states, as we discussed previously.[25] Finally, the new model can obviously explain the light illumination effect reported by Takahashi and Yoshida,[10] since photoinduced carriers readily screen the surface state charge and flatten the band. However, their estimate of surface state charge may be wrong quantitatively due to a highly nonuniform field distribution near the tip shown in Fig. 7(b) which makes applicability of a simple one-dimensional calculation doubtful.

Thus, the seemingly contradicting and confusing results obtained so far on GaAs(001) surfaces can be understood in a consistent way by the new model.

C. Spatial distribution of pinning centers

Finally, if the present model is valid, the STS anomaly should provide valuable information concerning the microscopic origin of surface states by comparing the STM topology and spatial distribution of STS spectra. To this end, the tip–bias dependence of the STM images taken on (001)-(2×4) surfaces are shown in Fig. 9. Strong asymmetry exists between filled state and empty state images where very spatially irregular and bias-dependent images with dark areas are obtained under positive sample bias. A more detailed STM image under positive bias is also shown in Fig. 10(a). It shows dark areas, although the image under negative bias showed regular dimer arrays free of dark areas. STS line scans showed that these dark areas which increase in size with bias reduction correspond to areas having large conductance gaps. Previously, such a dark region was interpreted in terms of local band bending due to donor/acceptor charging. However, according to the present interpretation, charging takes place only under the tip, and disappears by emission to reestablish the situation of $E_{FS}=E_F$ (bulk) as the tip moves away. Thus, dark areas are produced only at surface states, unless some fixed charge centers exist. The observed bias dependence of images exclude the latter possibility.

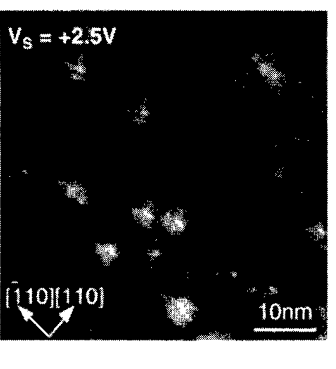

(a)

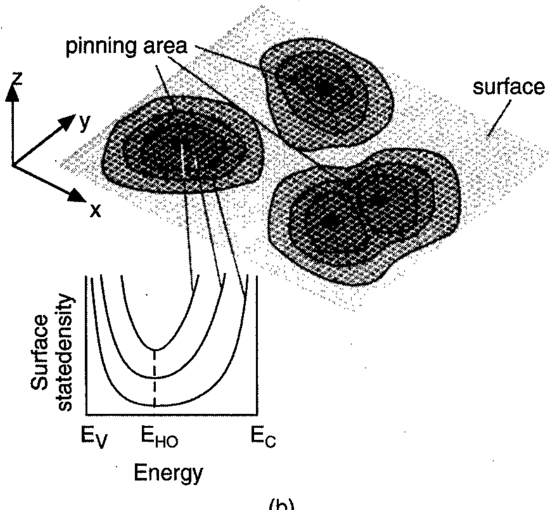

(b)

FIG. 10. (a) Typical empty state STM images of the MBE-grown (001) GaAs surface and (b) schematic illustration of spatial and energy distributions of surface states.

Attempts to find direct one-to-one correlation of the individual spot showing an anomalous spectrum with one particular type of isolated defect structure in the STM topology

such as a vacancy, dimer-desorbed hole, missing dimer, dimer kink, step, etc. have not so far been successful. Instead, the result strongly indicated that the pinning center is not a point, but forms an area. At the center of these areas, there seem to be some kinds of structural disorder. Thus, any structure disturbing the two dimensionality of the surface structure seems to lead, not to isolated discrete deep acceptors or donors, but to formation of areas of pinning centers with a gap state continuum having similar energy and spatial distributions of states with a common charge neutrality point, E_{HO}, as schematically shown in Fig. 10(b). It looks as though there exists a strong tendency to form such a spatially widened gap state continuum rather than forming a highly localized isolated discrete deep state. All these features seem to support the DIGS model[22] for pinning from the microscopic viewpoint. Further work is necessary to clarify the underlying mechanism for formation of such a continuum rather than isolated defect levels.

V. CONCLUSION

In order to clarify the mechanism for Fermi level pinning and its reduction by Si ICL, a detailed UHV STS study was made on (011) and (001) clean surfaces and Si-deposited (001) surfaces of GaAs prepared by MBE, and led to the following conclusions.

(1) Normal STS spectra showing the GaAs energy gap and anomalous spectra showing much larger conductance gaps coexist on the surfaces with surface states causing strong Fermi level pinning.
(2) The previous explanation of the gap anomaly based on the tip-induced electrostatic band bending change is invalid.
(3) The gap anomaly can be explained by a new model involving a band bending change due to tip-induced local charging of surface pinning centers by single or a few electrons. Here, tunneling proximity makes occupancy of surface states in equilibrium with the STM tip. Away from the pinning center, such charge transfer is impossible, and a normal STS spectrum is obtained.
(4) No direct one-to-one correlation exists between the pinning center and any of visual STM defect features. Pinning centers make up spatially inhomogeneous pinning areas surrounding any kind of structural disorder.
(5) Si ICL is very effective in reducing the number, spatial extension and state density of such pinning areas, particularly on the $c(4\times4)$ reconstructed surface, and leads to remarkable reduction of Fermi level pinning.

ACKNOWLEDGMENTS

The present study was supported financially in part by a Grant-in-Aid for Scientific Research Project on Priority Area "Single Electron Devices and their High Density Integration" (No. 08247101) and by Scientific Research B (No. 10555098) from the Ministry of Education, Science, Sports and Culture, Japan.

[1]H. Hasegawa, M. Akazawa, H. Ishii, and K. Matsuzaki, J. Vac. Sci. Technol. B **7**, 870 (1989).
[2]T. Hashizume, K. Ikeya, M. Mutoh, and H. Hasegawa, Appl. Surf. Sci. **123/124**, 599 (1998).
[3]S. Kodama, S. Koyanagi, T. Hashizume, and H. Hasegawa, Jpn. J. Appl. Phys., Part 1 **34**, 1143 (1995).
[4]S. Suzuki, Y. Dohmae, and H. Hasegawa, Solid-State Electron. **41**, 1641 (1997).
[5]M. Yamada, H. Takahashi, T. Hashizume, and H. Hasegawa, Jpn. J. Appl. Phys., Part 1 **39**, 2439 (2000).
[6]H. Hasegawa, S. Kodama, S. Koyanagi, and T. Hashizume, Jpn. J. Appl. Phys., Part 2 **34**, L495 (1995).
[7]H. Fujikura, S. Kodama, T. Hashizume, and H. Hasegawa, J. Vac. Sci. Technol. B **14**, 2888 (1996).
[8]M. D. Pashley, K. W. Haberen, and R. M. Feenstra, J. Vac. Sci. Technol. B **10**, 1847 (1992).
[9]V. Bressler-Hill, M. Wassermeier, K. Pond, R. Maboudian, G. A. D. Briggs, P. M. Petroff, and W. H. Weinberg, J. Vac. Sci. Technol. B **10**, 1881 (1992).
[10]T. Takahashi and M. Yoshita, Appl. Phys. Lett. **70**, 2162 (1997).
[11]M. Mutoh, N. Tsurumi, and H. Hasegawa, Jpn. J. Appl. Phys., Part 1 **38**, 2538 (1999).
[12]P. Martensson and R. M. Feenstra, Phys. Rev. B **39**, 7744 (1989).
[13]H. Takahashi, T. Yoshida, M. Mutoh, T. Sakai, and H. Hasegawa, Solid-State Electron. **43**, 1561 (1999).
[14]N. Tsurumi, Y. Ishikawa, T. Fukui, and H. Hasegawa, Jpn. J. Appl. Phys., Part 1 **37**, 1501 (1998).
[15]N. Negoro, H. Fujikura, and H. Hasegawa, International Symposium on Control of Semiconductor Interfaces, 25–29 October 1999, Karuizawa, Japan; Appl. Surf. Sci. (to be published).
[16]Y. Ishikawa, N. Tsurumi, T. Fukui, and H. Hasegawa, J. Vac. Sci. Technol. B **16**, 2387 (1998).
[17]R. J. Hamers and U. K. Köhler, J. Vac. Sci. Technol. A **7**, 2854 (1989).
[18]D. J. Chadi, J. Vac. Sci. Technol. A **5**, 834 (1987).
[19]J. E. Ortega and F. J. Himpsel, Phys. Rev. B **47**, 2130 (1993).
[20]F. Flores and N. Garcia, Phys. Rev. B **30**, 2289 (1984).
[21]V. Ramachandran and R. M. Feenstra, Phys. Rev. Lett. **82**, 1000 (1999).
[22]H. Hasegawa and H. Ohno, J. Vac. Sci. Technol. B **4**, 1130 (1986).
[23]L. He, H. Hasegawa, T. Sawada, and H. Ohno, J. Appl. Phys. **63**, 2120 (1988).
[24]E. R. Rhoderick and R. H. Williams, *Metal-Semiconductor Contacts*, 2nd ed. (Oxford University Press, Oxford, 1978), Chap. 4, p. 150.
[25]Y. Ishikawa, T. Fukui, and H. Hasegawa, J. Vac. Sci. Technol. B **15**, 1163 (1997).

Spin-dependent resonant tunneling in double-barrier magnetic heterostructures

A. G. Petukhov,[a] D. O. Demchenko, and A. N. Chantis
Physics Department, South Dakota School of Mines and Technology, Rapid City, South Dakota 57701-3995

(Received 17 January 2000; accepted 4 May 2000)

Recent advances in molecular beam epitaxial growth made it possible to fabricate exotic heterostructures comprised of magnetic films or buried layers (ErAs,$Ga_xMn_{1-x}As$) integrated with conventional semiconductors (GaAs) and to explore quantum transport in these heterostructures. It is particularly interesting to study spin-dependent resonant tunneling in double-barrier resonant tunneling diodes (RTDs) with magnetic elements such as GaAs/AlAs/ErAs/AlAs/GaAs and GaAs/AlAs/$Ga_xMn_{1-x}As$/AlAs/GaAs. We present the results of our theoretical studies and computer simulations of transmission coefficients and current-voltage characteristics of RTDs based on these double-barrier structures. In particular, resonant tunneling of holes in the $Ga_xMn_{1-x}As$-based RTDs is considered. Our approach is based on **k·p** perturbation theory with exchange splitting effects taken into account. © *2000 American Vacuum Society.*
[S0734-211X(00)04604-7]

I. INTRODUCTION

Resonant tunneling (RT) of charge carriers through semiconductor double-barrier heterostructures (DBH) has been extensively investigated both experimentally and theoretically since the pioneering work of Tsu and Esaki.[1] Currently, resonant tunneling diodes (RTDs) are being used in a variety of applications such as high-speed switching, high-speed signal generation, static random access memory, etc. (see Ref. 2 and references therein). Recent advances in molecular beam epitaxy made it possible to fabricate RTDs containing magnetic materials (such as ErAs or $Ga_xMn_{1-x}As$) as their active elements.[3,4] Introducing the magnetosensitive elements in these semiconductor devices can greatly enhance their functionality. For instance, recently discovered magnetization-controlled RT in GaAs/ErAs RTDs[3] has remarkable features such as splitting and enhancement of the resonant channels, which depend on the orientation of the external magnetic field with respect to the interface. Quantum transport in magnetic RTDs essentially involves the hole states of either ErAs or $Ga_xMn_{1-x}As$. In this work we will explore hole resonant tunneling in the presence of magnetization.

II. METHODS OF CALCULATIONS

A. Exchange field

The **k·p** method has been successfully applied by many authors to simulations of quantum transport in conventional GaAs/AlAs RTDs.[2] For instance, it was used in Refs. 5–7 to interpret experimental data of Mendez *et al.*[8] on resonant tunneling of holes in GaAs/AlGaAs DBH. The method is particularly useful for analyzing spin-dependent RT in semiconductor-based magnetic heterostructures. Our goal is to analyze spin-dependent quantum transport in GaMnAs-based magnetic heterostructures and devices, taking into account both the band structure and magnetization effects.

The first step is to construct a **k**-dependent magnetization-induced exchange operator acting on the upper valence states of a magnetic semiconductor or semimetal. In order to generate the exchange Hamiltonian matrix from the first-principle calculations for the materials described by the Kohn–Luttinger model, we will follow the procedure outlined in Ref. 9. In the absence of the spin-orbit interaction, the application of the **k·p** method results in the two sets of the upper valence bands described by the following Hamiltonians (in units of $\hbar^2/2m_0$) for spin "up" and spin "down" hole states, respectively,

$$H^{\uparrow,\downarrow}=-\gamma_0^{\uparrow,\downarrow}-(\gamma_1^{\uparrow,\downarrow}+4\gamma_2^{\uparrow,\downarrow})k^2+6\gamma_2^{\uparrow,\downarrow}(L_x^2k_x^2+L_y^2k_y^2+L_z^2k_z^2)+12\gamma_3^{\uparrow,\downarrow}\{k_xk_y[L_xL_y]+k_xk_z[L_xL_z]+k_yk_z[L_yL_z]\}, \quad (1)$$

where L_α are 3×3 matrices of the angular momentum 1, $[L_\alpha L_\beta]$ are their anticommutators, and γ_i are the Luttinger parameters. The auxiliary Luttinger parameters $\gamma_0^{\uparrow,\downarrow}$ describe Zeeman splitting at the center of the Brillouin zone while the other six parameters $\gamma_i^{\uparrow,\downarrow}$ are responsible for an additional Zeeman splitting due to the magnetization-induced difference in the effective masses of the spin up and spin down hole states. In the presence of the magnetization the total Hamiltonian of the hole states in a dilute magnetic semiconductor or paramagnetic semimetal can be represented as

$$H=H_+\otimes I+H_-\otimes(\boldsymbol{\sigma}\mathbf{b})+\lambda_{so}\mathbf{L}\otimes\boldsymbol{\sigma}, \quad (2)$$

where $H_\pm$ are given by (1) where the superscripts "$\uparrow,\downarrow$" are changed for "$\pm$"; $\gamma_i^\pm=(\gamma_i^\uparrow\pm\gamma_i^\downarrow)/2$, I is the 2×2 unit matrix, $\boldsymbol{\sigma}$ and $\mathbf{L}$ are the Pauli and orbital momentum vector operators, respectively; $\mathbf{b}$ is the unit vector in the direction of the magnetization. The second term in Eq. (2) describes the exchange field induced by magnetization. In combination with the third, spin-orbital term it is responsible for any magneto-electronic effects in magnetically active elements of the structures in question.

As an illustration of this approach we will consider the upper valence band structure of an ErAs quantum well in the

[a]Electronic mail: andre@odessa.phy.sdsmt.edu

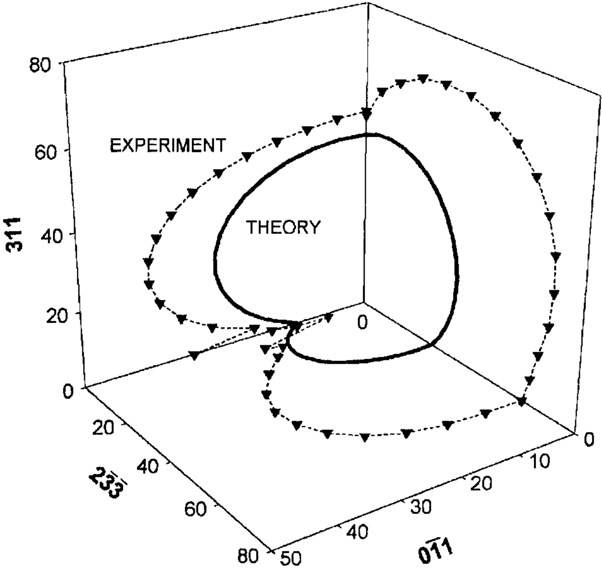

FIG. 1. Angular dependence of the Zeeman splitting (in mega-electron-volts) of the light hole channel in the ErAs-based DBH with 10 ML quantum well.

presence of magnetization induced by external magnetic fields of different orientations. Figure 1 shows experimental data, obtained for n^+ GaAs/AlAs/ErAs/Als/n^+ GaAs RTDs with 10 ML ErAs quantum well,[10] grown in the (311) direction, that are compared with our theoretical results. As we already mentioned, the experiments on RT through ErAs quantum wells revealed strong Zeeman splitting of the resonant channel corresponding to the light hole (LH) state in the quantum well. This splitting also strongly depends on the orientation of the magnetization with respect to the interface. The theoretical curves were calculated by means of the Hamiltonian (2) with the parameters fitted to the results of the first-principle linear-muffin-tin orbital (LMTO) calculations[11] and $k=2\pi/10a$, where a is the ErAs lattice constant in the (311) direction. Qualitative behavior of the theoretical curves is very similar to that of the experimental data. There is, however, a systematic quantitative discrepancy which requires further investigation.

B. Flatband solution of the Schrödinger equation

As a next step, we represent our DBH as a stack of $N+1$ flatband regions and, therefore N interfaces between them. Then we will apply the transfer matrix technique[2] to calculate the transmission coefficient and tunneling current. This technique requires solving the Schrödinger equation in each flatband region with subsequent matching of these solutions at each interface. We will restrict further consideration to the case of 4×4 Kohn–Luttinger Hamiltonian describing the LH and heavy hole (HH) states only. In each flatband region with potential V_b the wave function of a hole with energy E is a superposition of the eight plane-wave (or evanescent) solutions

$$\psi(z)=\sum_{\alpha=1}^{8} A_\alpha \mathbf{v}(k_z^\alpha)\exp(ik_z^\alpha z), \tag{3}$$

where terms in the sum are always enumerated in such way that the first four of them correspond to the probability density current form left to right while the next four terms are their "right-to-left" counterparts, $E_b=E-V_b$, and k_z^α can be found from the secular equation

$$\det|\mathbf{H}(\mathbf{k}_\parallel,k_z)-E_b\mathbf{1}|=0, \tag{4}$$

which is nothing but a multiband analog of the simple relation $k_z=\pm\sqrt{2mE_b}$ for the ordinary one-band tunneling problem. Once k_z^α are known, the eigenvectors $\mathbf{v}(k_z^\alpha)$ can be found from

$$[\mathbf{H}^{(2)}k_z^2+\mathbf{H}^{(1)}(\mathbf{k}_\parallel)k_z+\mathbf{H}^{(0)}(\mathbf{k}_\parallel)-E_b\mathbf{1}]\mathbf{v}=0, \tag{5}$$

where we represented the Hamiltonian matrix (2) as a second order polinomial in k_z. Direct application of Eqs. (4) and (5), known as the complex band structure method, is rather inconvenient and inefficient from the numerical point of view. It can be used efficiently only if the analytical solutions $k_{z,\alpha}(E_b)$ and $\mathbf{v}(k_{z,\alpha})$ are available.[12] In fact, it was used by Wessel and Altarelli[5] for the Hamiltonian (2) with zero exchange field. Clearly, this method is not suitable for our purposes. Instead, we will follow an approach suggested in Ref. 7. We will treat Eq. (5) as generalized eigenvalue problem with k_z being the eigenvalues in question.[13] This problem can be reduced to a regular eigenvalue problem for the non-Hermitian matrix:

$$\begin{pmatrix} \mathbf{0} & \mathbf{1} \\ -(\mathbf{H}^{(2)})^{-1}[\mathbf{H}^{(0)}(\mathbf{k}_\parallel)-E_b\mathbf{1}] & -(\mathbf{H}^{(2)})^{-1}\mathbf{H}^{(1)}(\mathbf{k}_\parallel)\end{pmatrix}\begin{pmatrix}\mathbf{v}\\ k_z\mathbf{v}\end{pmatrix} = k_z\begin{pmatrix}\mathbf{v}\\ k_z\mathbf{v}\end{pmatrix}, \tag{6}$$

which, in turn, can be solved by means of the standard numerical routines. Here $\mathbf{1}$ is a 4×4 unit matrix and $\mathbf{0}$ is a 4×4 zero matrix. The knowledge of k_z^α and $\mathbf{v}(k_z^\alpha)$ for certain E and $k_\parallel$ allows us to formulate boundary conditions at each interface.

C. Boundary conditions and tunneling current

The boundary conditions can be formulated by means of the following standard conventions:[14] (i) the difference in the Bloch amplitudes at the heterointerface is neglected, i.e., the envelope function is continuous across the interface; (ii) the current associated with this envelope function is also continuous. It can be shown that within the framework of $\mathbf{k}\cdot\mathbf{p}$ method the current density operator can be expressed in terms of $\mathbf{H}^{(i)}$ and k_z as follows:[6,15]

$$\mathbf{J}_z=\frac{1}{\hbar}[2\mathbf{H}^{(2)}k_z+\mathbf{H}^{(1)}]. \tag{7}$$

By applying the boundary conditions step by step at each interface from right to left we can express the amplitudes of the transmitted waves $\mathbf{t}$ through the amplitudes of the incoming $\mathbf{a}$ and reflected $\mathbf{r}$ waves

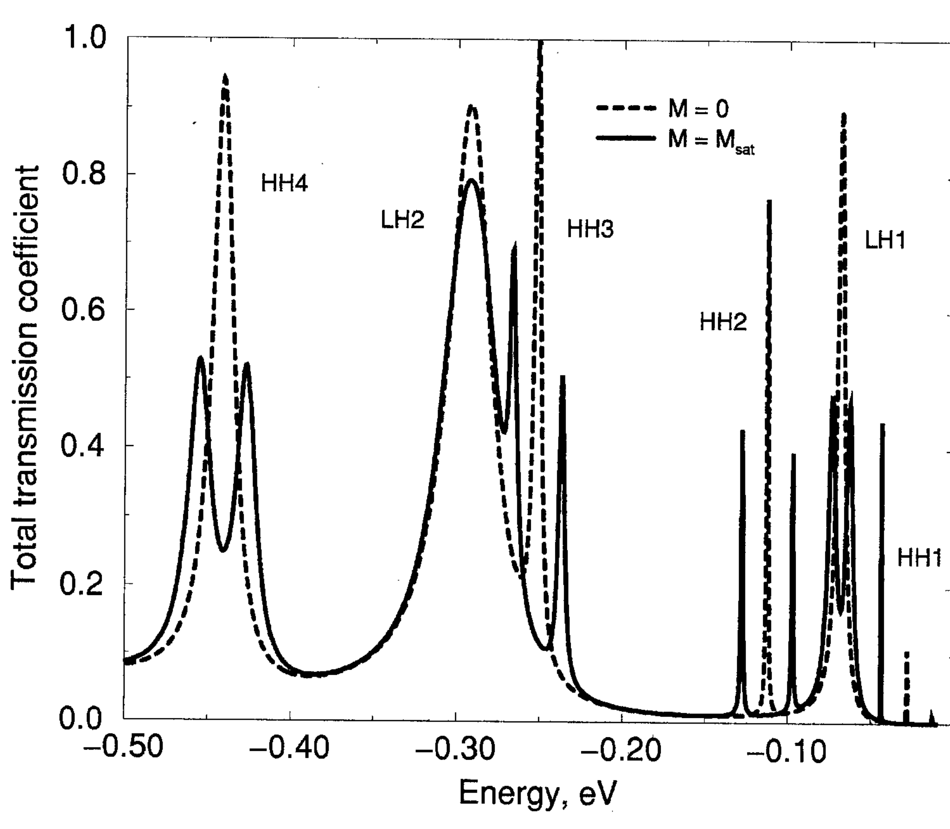

FIG. 2. Total transmission coefficient as a function of energy for GaMnAs-based DBH and $k_{\|}=(0.02\ \text{Å}^{-1},\ 0)$. Dashed line—zero magnetization, solid line—saturated magnetization.

$$\begin{pmatrix} \mathbf{t} \\ \mathbf{0} \end{pmatrix} = \prod_{j=N}^{1} \mathbf{M}_R^{-1}(z_j)\mathbf{M}_L(z_j) \begin{pmatrix} \mathbf{a} \\ \mathbf{r} \end{pmatrix} \equiv \begin{pmatrix} \mathcal{M}_{11} & \mathcal{M}_{12} \\ \mathcal{M}_{21} & \mathcal{M}_{22} \end{pmatrix} \begin{pmatrix} \mathbf{a} \\ \mathbf{r} \end{pmatrix}, \tag{8}$$

where vectors $\mathbf{t}$, $\mathbf{a}$, and $\mathbf{r}$ are four-component columns, and $\mathbf{M}_{R,L}(z_j)$ are 8×8 matrices evaluated at right and left sides of the interface j, respectively. They are comprised of the columns corresponding to different eigenvalues k_z^{α}:

$$\mathbf{M}^{\alpha}(z_j) = \begin{pmatrix} \mathbf{v}(k_z^{\alpha})\exp(ik_z^{\alpha}z_j) \\ \mathbf{J_z}(k_z^{\alpha})\cdot\mathbf{v}(k_z^{\alpha})\exp(ik_z^{\alpha}z_j) \end{pmatrix}. \tag{9}$$

In Eq. (8) the transfer matrix $\mathcal{M}$, which is the product of matrices $\mathbf{M}$, is partitioned into four 4×4 subblocks. It allows us to eliminate the reflection amplitudes

$$\mathbf{t} = (\mathcal{M}_{11} - \mathcal{M}_{12}(\mathcal{M}_{22})^{-1}\mathcal{M}_{21})\mathbf{a} \equiv \mathcal{M}'\cdot\mathbf{a}. \tag{10}$$

The transmission coefficient $T_{\mu\nu}$ between the incoming wave μ and the transmitted wave ν is

$$T_{\mu\nu} = \begin{cases} \dfrac{\mathrm{Re}(\mathbf{v}_R^{\nu\dagger}\mathbf{J}_z\mathbf{v}_R^{\nu})}{\mathrm{Re}(\mathbf{v}_L^{\mu\dagger}\mathbf{J}_z\mathbf{v}_L^{\mu})}|\mathcal{M}'_{\nu\mu}|^2, & \text{if } \mathrm{Re}(\mathbf{v}_L^{\mu\dagger}\mathbf{J}_z\mathbf{v}_L^{\mu}) \neq 0 \\ 0, & \text{otherwise} \end{cases} \tag{11}$$

Finally, the tunneling current density at zero temperature can be calculated as an integral over $\mathbf{k}_{\|}$ and energy E[16]:

$$j \propto \int_{E_F}^{\min(E_F+eU,0)} dE \int d\mathbf{k}_{\|} \sum_{\mu,\nu=1}^{4} T_{\mu\nu}(\mathbf{k}_{\|},E,eU), \tag{12}$$

where E_F is the Fermi energy in the emitter and U is bias applied to the DBH. In our calculations, the potential of the biased structure is assumed to be constant within the limits of each flatband region and is taken as the average over this region. All our actual calculations are restricted to the simplest case when a DBH is modeled with the five flatband regions corresponding to a semi-infinite emitter and collector, two finite barriers, and a quantum well.

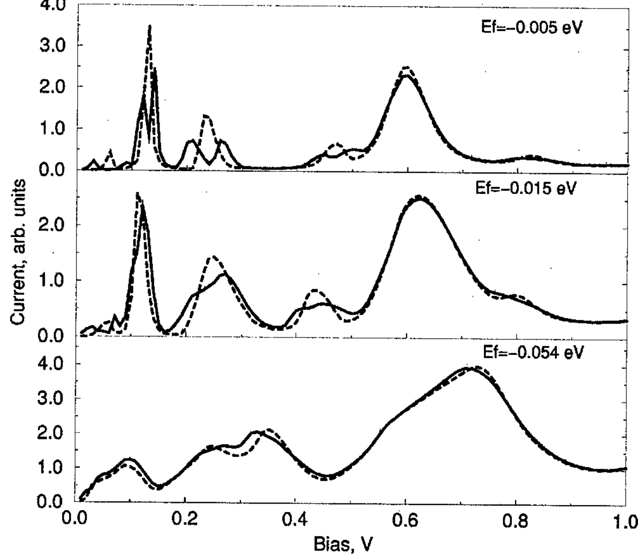

FIG. 3. Tunneling current as a function of bias for various positions of the Fermi energy levels (dashed line—zero magnetization, solid line—saturated magnetization).

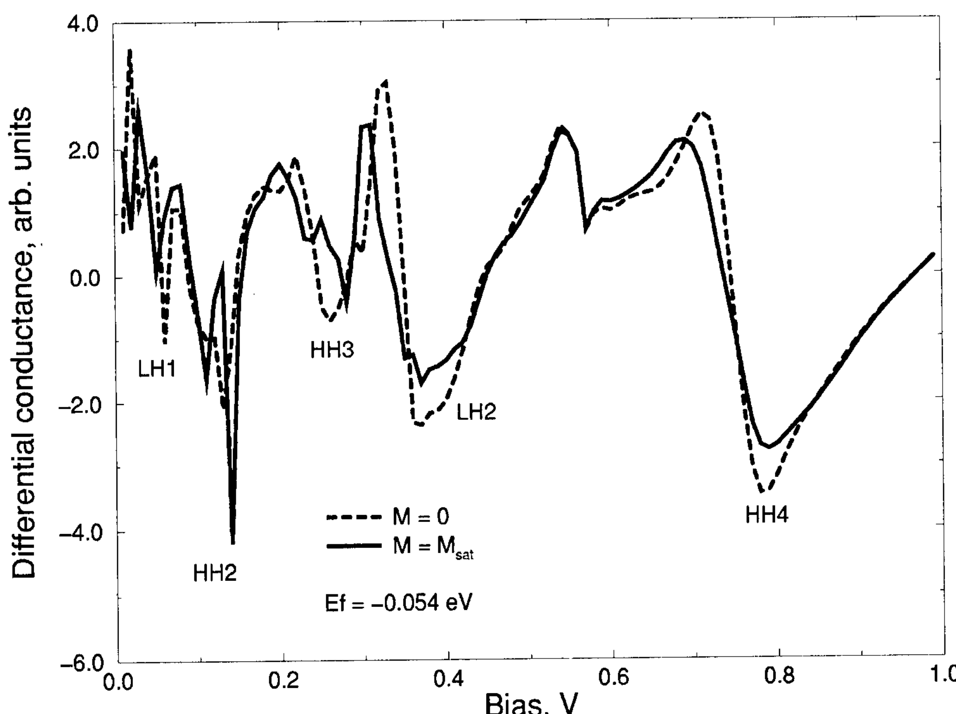

FIG. 4. Differential conductance as a function of bias for the GaMnAs-based DBH for $E_F = -0.054$ eV (dashed line—zero magnetization, solid line—saturated magnetization). HH2 and HH3 channels are clearly split.

III. RESULTS

Here we present the results of our calculations of the transmission coefficients and tunneling current–voltage ($I-V$) characteristics of hypothetical p-GaAs/AlAs/$Ga_xMn_{1-x}As$/AlAs/p-GaAs RTDs. As a first example, we will consider the transmission coefficient of the DBH with 10 Å-wide AlAs barriers and a 50 Å wide $Ga_{0.99}Mn_{0.01}As$ quantum well. Figure 2 shows the total transmission coefficient of the structure in question at zero bias for zero (dashed line) and saturated (solid line) magnetization in the quantum well, which is perpendicular to the layers. Parameters of the exchange field were determined in accordance with Sec. II A, i.e., they were fitted to the results of first-principle LMTO calculations.[17] Electronic states in the quantum well define a very sharp structure (i.e., the sequence of peaks and valleys) of the transmission coefficient. Also, there is a very pronounced Zeeman splitting of the HH) channels and the first light hole channel (LH1). Zeeman splitting of the HH ($m_j = 3/2$) channels is much larger than that of the LH ($m_j = 1/2$) channels. Also, mixing of the LH and HH channels is quite substantial due to the fact that $k_\| \neq 0$.[7,9]

It is interesting to see how this quite pronounced structure of the transmission coefficient (including Zeeman splittings) manifests itself in the $I-V$ characteristics. Figure 3 shows $I-V$ characteristics of three RTDs, based on the DBH described earlier, for three different doping levels of the p-type emitter. Zeeman splittings of the resonant channels can be clearly seen in the $I-V$ characteristics of the first RTD with $E_F = -0.005$ eV. The impact of magnetization is still quite dramatic for another RTD with a higher doping level ($E_F = -0.015$ eV). For the third RTD, however, $E_F = -0.054$ eV and the magnetization induced effects are rather modest. They can be revealed only in the differential conductance dI/dV versus voltage characteristics (see Fig. 4).

There is no surprise that both high values of the Fermi level and complex character of the band structure of the emitter make it difficult to observe a distinct RT structure and, particularly, magnetization controlled RT. On the other hand, the RTDs with the low concentration of holes in the emitter, for which the effects of magnetization are quite significant, will have relatively low current densities. One of the possible alternatives providing for the observation of stronger magnetization controlled effects would be fabrication of structures, utilizing interband spin-dependent RT, similar to those used in ErAs experiments.[3,10]

A comment is in order as to the likely effect of electrostatic band bending and internal electric fields, not accounted for here, on the calculated $I-V$ curves. The primary effect will consist in additional shifting and broadening of the resonant peaks. We believe, however, that the basic spin-dependent features of the heterostructures, considered in the present work, will not be strongly affected. We are planning to address these issues along with the strain effects in a separate article.[17] We are also planning to investigate additional spin splitting caused by the internal electric field in the quantum well (Rashba effect).[18,19]

ACKNOWLEDGMENT

This work was supported by AFOSR Grant No. F49620-96-1-0383.

[1]R. Tsu and L. Esaki, Appl. Phys. Lett. **22**, 562 (1973).
[2]H. Mizuta and T. Tanoue, *The Physics and Applications of Resonant Tunnelling Diodes* (Cambridge University Press, Cambridge, 1995).
[3]D. E. Brehmer, K. Zhang, C. J. Schwartz, S. P. Chau, and S. J. Allen, Appl. Phys. Lett. **67**, 1268 (1995).

[4]H. Ohno, A. Shen, F. Matsukura, A. Shen, K. Ohtani, and Y. Ohno, Appl. Phys. Lett. **73**, 363 (1998).
[5]R. Wessel and M. Altarelli, Phys. Rev. B **39**, 12802 (1989).
[6]C. Y.-P. Chao and S. L. Chuang, Phys. Rev. B **43**, 7027 (1991).
[7]Y. X. Liu, D. Z.-Y. Ting, and T. C. McGill, Phys. Rev. B **54**, 5675 (1996).
[8]E. E. Mendez, W. I. Wang, B. Ricco, and L. Esaki, Appl. Phys. Lett. **47**, 415 (1985).
[9]A. G. Petukhov, W. R. L. Lambrecht, and B. Segall, Phys. Rev. B **53**, 3646 (1996); A. G. Petukhov, Appl. Surf. Sci. **123/124**, 385 (1998).
[10]D. E. Brehmer, Ph.D. thesis, UC Santa Barbara, 1999.
[11]A. G. Petukhov, W. R. L. Lambrecht, and B. Segall, Phys. Rev. B **53**, 4324 (1996); W. R. L. Lambrecht, B. Segall, A. G. Petukhov, R. Bogaerts, and F. Herlach, *ibid.* **55**, 9239 (1997).
[12]L. C. Andreani, A. Pasquarello, and F. Bassani, Phys. Rev. B **36**, 5887 (1987).
[13]J. H. Wilkinson, *The Algebraic Eigenvalue Problem* (Oxford University Press, Oxford, 1965), pp. 633 and 634.
[14]M. Altarelli, in *Proceedings of Les Houches Winter School, Semiconductors, Superlattices, and Heterojunctions*, edited by G. Allan, G. Bastard, N. Boccara, M. Lannoo, and M. Voos (Springer, New York, 1986).
[15]G. Y. Wu, K.-M. Hung, and C.-J. Chen, Phys. Rev. B **46**, 1521 (1992).
[16]C. B. Duke, *Tunneling in Solids* (Academic, New York, 1969).
[17]D. O. Demchenko, A. N. Chantis, and A. G. Petukhov (unpublished).
[18]Y. A. Bychkov and E. I. Rashba, JETP Lett. **39**, 78 (1984).
[19]P. R. Hammar, B. R. Bennett, M. J. Yang, and M. Johnson, Phys. Rev. Lett. **83**, 203 (1999).

Schottky barrier tuning with heterovalent interlayers: Al/Ge/GaAs versus Al/Si/GaAs

C. Berthod[a] and N. Binggeli
Institut Romand de Recherche Numérique en Physique des Matériaux (IRRMA), CH-1015 Lausanne, Switzerland

A. Baldereschi[b]
Institut de Physique Appliquée, Ecole Polytechnique Fédérale de Lausanne, CH-1015 Lausanne, Switzerland and Dipartimento di Fisica Teorica and INFM, Università di Trieste, I-34014 Trieste, Italy

(Received 17 January 2000; accepted 6 April 2000)

Using *ab initio* calculations, we compare the effects produced on the Al/GaAs(100) Schottky barrier height by Ge and Si interface layers with thickness ranging from 0 to 2 monolayers. The dipole layers, generated by the group-IV atomic substitutions at the interface, increase/decrease the p-type Schottky barrier at the As-/Ga-terminated Al/GaAs(100) junction. Although the trends with Ge and Si interlayers are similar for coverages less than 0.5 monolayers, at higher coverages the Schottky barrier exhibits a stronger nonlinear behavior, and smaller barrier variations, in Al/Ge/GaAs(100) than in Al/Si/GaAs(100). In particular, at a coverage of 2 monolayers, the use of Ge interlayers instead of Si ones reduces by 25% the barrier tunability. These trends are at variance with those predicted by existing macroscopic band-structure models, and our results should help in discriminating between different mechanisms of Schottky barrier tuning. © *2000 American Vacuum Society.* [S0734-211X(00)00204-3]

I. INTRODUCTION

The possibility of tuning Schottky barrier heights (SBHs), and hence of modulating the transport properties of metal/semiconductor devices, by means of heterovalent interface layers has stimulated much interest in recent years.[1–8] Very large barrier modifications (0.8–0.9 eV variations) have been achieved, e.g., in metal/GaAs(100) junctions by depositing Si layers at the interface in the presence of excess cation or anion fluxes.[1–3] The mechanism behind these large barrier variations, however, remains controversial. Two types of conflicting models have been proposed which emphasize, on one hand, the *macroscopic* properties of degenerate bulk Si[2,3,9] and, on the other hand, Si-induced *microscopic* interface dipoles.[1,10,11]

The barrier modifications were first reported for junctions containing Si interlayers with thicknesses between ~10 and 100 Å.[2,4,5] To interpret such data, Nathan and co-workers[2] proposed a model based on a macroscopic description of the band alignment in metal/n^+Si/GaAs and metal/p^+Si/GaAs heterojunctions. In this model, the equilibrium bulk band gap of Si is used to describe the interlayer, and the Fermi level is assumed to be pinned at the Si/Al interface and unpinned at the Si/GaAs interface. Within this model, the maximal tunability of the barrier is given by the Si equilibrium band gap, $E_g(\mathrm{Si})=1.1$ eV, and is reached for Si thicknesses on the order of 60–80 Å, assuming a typical doping of 5×10^{19} cm^{-3} for the n^+ or p^+ layer.[2] Furthermore, even when considering a doping as high as 10^{20} cm^{-3}, this model predicts that the largest barrier changes are established at a coverage larger than 30 Å.

Cantile *et al.*,[1] however, showed subsequently that the SBH modifications in Al/Si/GaAs(100) junctions are already established for interlayer coverages as low as 2 monolayers (ML), in contrast with the above model predictions. Furthermore, based on the data reported by various groups,[1–5] the maximal barrier tunability of the Al/Si/GaAs junctions is 0.8–0.9 eV, which is significantly smaller than the Si band gap. To account for such discrepancies, Morkoç and co-workers[9] proposed a revised macroscopic model, which incorporates the effect of strain on the Si band gap and assumes that the Fermi level is unpinned at the Al/Si interface. For coverages below the critical thickness for strain relaxation (<15 Å), this model predicts a maximal tunability corresponding to the gap of bulk Si coherently strained to the GaAs lattice parameter, i.e., $E_g'(\mathrm{Si})=0.7$ eV, as obtained from band-structure calculations,[9,12] and yields a minimal value of the SBH equal to the band offset at a strained Si/GaAs(100) heterojunction: $\phi_p^{\mathrm{min}}=\Delta E_v(\mathrm{Si/GaAs})=0.39$ eV. The results of the revised model are in satisfactory agreement with the maximal tunability (0.8–0.9 eV) and minimal barrier value (0.3–0.4 eV) observed experimentally at low Si coverage (~2 Si ML).

Several authors questioned, however, the applicability of a macroscopic approach to a nanoscopic interlayer, given that the tuning takes place for coverages less than 2 ML;[1,10,13] concerning the use of a bulk band gap, in particular, we showed from *ab initio* calculations, that 2-ML-thick Si interlayers give rise to a metallic local density of states, with no detectable band gap, in epitaxial Al/Si/GaAs(100) systems.[10] An alternate (microscopic) explanation was thus suggested.[1] In this approach, tuning is associated with local

[a]Present address: DPMC, Université de Genève, 24 Quai Ernest-Ansermet, 1221 Genève 4, Switzerland.
[b]Author to whom correspondence should be addressed; electronic mail: baldereschi@epfl.ch

interface dipoles generated by replacing GaAs pairs by Si pairs at the junction. In a previous first-principle study we showed, in this connection, that microscopic interface dipoles generated by Si substitutions at As-terminated (for low Ga chemical potential) and Ga-terminated (for low As chemical potential) GaAs(100) interfaces could indeed *quantitatively* explain the Al/Si/GaAs(100) Schottky barrier tuning with 0–2 ML of Si.[10,11] In this description, the excess flux determines the anion/cation chemical potential and the relative stability of the junctions with high (As-terminated) and low (Ga-terminated) *p*-type SBHs.[10] The microscopic tuning mechanism associated with local-interface dipoles can be applied quite generally to other systems containing heterovalent interlayers, and a model was thus proposed to predict the barrier variations with interlayer coverage in terms of simple physical parameters of the host and interlayer.[11]

In view of the conflicting interpretations associated with the local-dipole and revised macroscopic models, and since both models reproduce the barrier changes established at ~2 Si ML, it would be useful to test the predictions of these models on a different group-IV interlayer. In this article, we examine the Al/Ge/GaAs(100) junction, and show that this system can help discriminating between the two models.

Unlike Si, Ge is lattice matched to GaAs and one avoids the additional, and irrelevant, complexity of strain effects. Within the revised macroscopic model, the maximal tunability should be essentially the *same* for the Al/Si/GaAs and Al/Ge/GaAs(100) systems. This is because the equilibrium band gap of Ge (0.66 eV) is practically identical to the band gap used by Morkoç and co-workers for coherently strained Si (0.7 eV). Furthermore, according to the revised macroscopic model, the maximal value of the Schottky barrier at low coverage $\phi_p^{\max}$ should be 0.1 eV *larger* in Al/Ge/GaAs(100) than in Al/Si/GaAs(100), as the Ge/GaAs(100) valence-band offset measured by Morkoç and co-workers[14] (0.49 eV) is ~0.1 eV larger than the value quoted for the strained Si/GaAs(100) system.

Using first-principles calculations we have examined the effect of Ge-induced dipole layers on the Al/GaAs(100) SBH, for interlayer coverages in the 0–2 ML range. We show here, in particular, that contrary to the predictions of the revised macroscopic model, in the local-dipole picture, replacing Si by Ge will: (i) *reduce* the barrier tunability by ~25%, and (ii) *decrease* the maximal value of ϕ_p by ~0.1 eV for an interlayer coverage of 2 ML. These trends result from the higher polarizability of Ge with respect to Si, and could be used to discriminate between the microscopic and macroscopic theories proposed for the tuning.

In contrast to the case of Si, very few experimental data are available for Ge interlayers. Measurements have been performed only on metal/GaAs(100) junctions grown in anion-rich conditions, and including Ge interlayers with thicknesses above 12 Å.[5] The interpretation of the barrier changes for coverages above 2–4 ML is a complex problem. It should be mentioned, in particular, that the barrier variations measured in Al/Si/GaAs(100) are monotonic only in the 0–2 ML coverage regime; with ~2–4 Si ML, the barrier variations saturate, and their amplitude decreases at higher coverages.[1] It has been shown, moreover, that the lattice structures of the interlayers with thicknesses above 10 Å bear no resemblance to that of bulk Si.[13] As such structures are beyond the scope of our present first-principles investigations, and since we expect similar trends for Ge interlayers, we will not attempt to discuss here the behavior of the barriers at high interlayer coverage. Nevertheless, it is interesting to note that, similarly to the trend predicted by the *ab initio* calculations at low coverage, the measurements on Ge interlayers at high coverage indicate a reduction in the amplitude of the barrier variations relative to the Si case, for interlayers having comparable thicknesses.

II. METHOD

The interface structures considered in this study are the same as in Ref. 11, with the Si atoms replaced by Ge atoms. We thus consider abrupt junctions, with As- and Ga-terminated GaAs (100) surfaces. In order to accommodate the small (1%) lattice mismatch between GaAs and Al, the Al overlayer is pseudomorphically elongated by 3% according to macroscopic elasticity theory. We introduce Ge interlayers with coverage ϑ in the 0–2 ML range at the abrupt Al/GaAs (100) junction by replacing with Ge atoms an equal number of Ga and As atoms in the two planes closest to the metal. We thus assume a fully self-compensated Ge distribution over two atomic layers, and simulate the fractional coverages $0<\vartheta<2$ ML with the virtual-crystal approximation, using $\langle \mathrm{Ga}_{1-(\vartheta/2)}\mathrm{Ge}_{\vartheta/2}\rangle$ and $\langle \mathrm{As}_{1-(\vartheta/2)}\mathrm{Ge}_{\vartheta/2}\rangle$ pseudo ions.[7]

The *ab initio* computations are performed within the local-density functional (LDF) framework, using pseudopotentials.[15] The self-consistent charge density in the junctions is evaluated within a supercell geometry,[11] using a (2, 6, 6) Monkhost–Pack *k*-point mesh.[16] A Gaussian broadening, with full width at half maximum of ~0.1 eV, is used to locate the Fermi energy.[17] The electronic orbitals in the supercell are expanded in a plane-wave basis set, with a kinetic-energy cutoff of 10 Ry. All the calculations are done at the theoretical in-plane lattice parameter of GaAs: $a=5.55$ Å ($a^{\exp}=5.65$ Å). The *p*-type SBH is calculated as $\phi_p=\Delta V+\Delta E_p$, where ΔV is the lineup of the average electrostatic potential at the interface,[18] and ΔE_p is the difference between the Fermi energy in the metal and the valence-band maximum in the semiconductor, each measured with respect to the average electrostatic potential in the corresponding crystal. The bulk band-structure calculations are performed with a 20 Ry cutoff, and using (6, 6, 6) and (12, 12, 12) Monkhost–Pack grids for the semiconductor and metal, respectively. A correction of +0.25 eV is added to the band term ΔE_p to account for spin-orbit and many-body effects.[19] This correction is the same for all systems discussed here, and amounts to a rigid shift of the theoretical LDF barrier heights. The numerical convergence on the SBHs obtained with the parameters described above is estimated as ~30 meV.

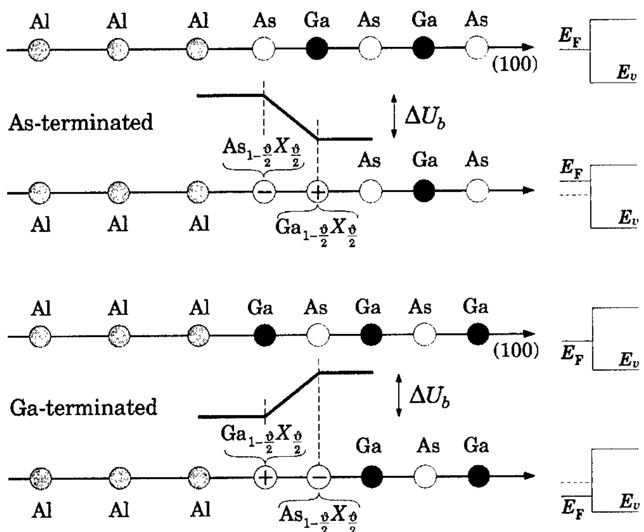

FIG. 1. Microscopic dipoles induced by group-IV atoms (X=Si or Ge) in a bilayer configuration at the As- and Ga-terminated Al/GaAs (100) interfaces. The dipole layer increases ϕ_p in the As-terminated junction and decreases ϕ_p in the Ga-terminated junction.

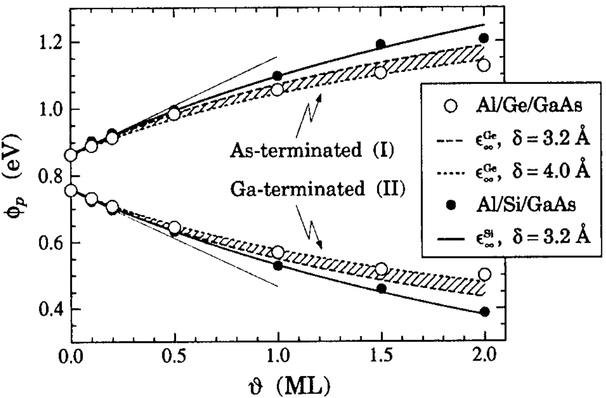

FIG. 2. Comparison of the Schottky barrier heights in Al/Ge/GaAs (100) and Al/Si/GaAs (100) (Ref. 11) junctions as a function of interlayer atomic coverage. The circles are the results of the self-consistent calculations (shifted by +0.25 eV). The curves give the predictions of the model, Eqs. (1) and (2), for Si interlayers with δ=3.2 Å (solid lines), and for Ge interlayers with δ=3.2 Å (dashed lines) and δ=4.0 Å (dotted lines). The thin straight lines indicate the model predictions in the linear regime.

III. CAPACITOR MODEL

The microscopic tuning mechanism associated with interface dipoles is illustrated in Fig. 1. As first pointed out by Harrison,[20] the substitution by group-IV atoms of two adjacent GaAs (100) planes is equivalent to a transfer of protons from the As atoms to the neighboring Ga atoms, and thus leads to a microscopic dipole in the ionic charge density. For a given coverage ϑ, the bare dipole layer associated with these point charges produces a discontinuity of the electrostatic potential, $\Delta U_b = \pm(\pi e^2/a)\,\vartheta$. As a result, the potential lineup ΔV at the interface is modified, and the Fermi level in the metal is shifted with respect to the energy levels in the semiconductor. The final change ΔV, however, is not just given by the bare discontinuity ΔU_b, but by the screened discontinuity $\Delta U = \Delta U_b/\epsilon_{\text{eff}}$, where the effective screening parameter ϵ_{eff} accounts for the response of the electrons to the bare perturbation. Thus, ϕ_p increases (decreases) by ΔU at the As- (Ga-) terminated interface, and we may write (in atomic units)

$$\phi_p^{\text{I, II}}(\vartheta) = \phi_{p,0}^{\text{I, II}} \pm \frac{\pi e^2}{a} \frac{\vartheta}{\epsilon_{\text{eff}}(\vartheta)}, \tag{1}$$

where $\phi_{p,0}^{\text{I, II}}$ stands for the SBH of the As-terminated (I) and Ga-terminated (II) interface with no interlayer, and the plus (minus) sign is for the interface I (II). In our study on Si interlayers, we found that the effective screening $\epsilon_{\text{eff}}(\vartheta)$ can be accurately described by the following capacitor-based model:[11]

$$\epsilon_{\text{eff}}(\vartheta) = 1 + (\epsilon_\infty^{\text{GaAs}} - 1) + 4\pi e^2 D_s\,\delta + \frac{\vartheta}{2}[\epsilon_\infty^X - \epsilon_\infty^{\text{GaAs}} + 4\pi e^2 (D_s' - D_s)\,\delta], \tag{2}$$

where $\epsilon_\infty^{\text{GaAs}}$ and ϵ_∞^X are the macroscopic dielectric constants of GaAs and of the group-IV material, respectively, δ is an effective screening distance of the order of the decay length of the metal-induced gap states (MIGS), and D_s, D_s' are the surface densities of states evaluated at the Fermi energy and at the position of the ionic dipole, without interlayer and with 2 ML of the group-IV atoms, respectively. The first three terms on the right-hand side of Eq. (2) correspond to the electronic screening in the linear regime, and describe the vacuum, semiconductor, and MIGS responses, respectively. The last term is a higher-order correction, which takes into account the gradual change in the electronic susceptibility due to the modifications of the host semiconductor and of the MIGS density of states with the group-IV atom coverage.

IV. RESULTS AND DISCUSSION

In Fig. 2, we show the results of the *ab initio* calculations for the *p*-type SBHs of the As- and Ga-terminated Al/Ge/GaAs (100) junctions, as a function of interlayer coverage ϑ. As expected from Eq. (1), ϕ_p increases as ϑ increases in the junctions I (As-terminated) and decreases in the junctions II (Ga-terminated). The SBH variations for the junctions I and II are practically symmetric. This shows that the effective screening, in Eq. (1), does not depend significantly on the semiconductor–surface termination. At $\vartheta = 2$ ML, the SBH modifications for the two interfaces are ± 0.26 eV, corresponding to an effective screening $\epsilon_{\text{eff}}(2) \approx 63$. In Fig. 2, we also report for comparison the calculated barrier heights in the Al/Si/GaAs (100) system,[11] which exhibit similar trends. The latter barrier modifications are in good agreement with existing experimental data on Al/Si/GaAs(100) in the 0–2 ML coverage range.[1] At very low coverage (below 0.5 ML), the SBHs of the Al/Ge/GaAs and Al/Si/GaAs systems are almost indistinguishable. At higher coverages, instead, the dipole-induced changes in ϕ_p are clearly larger for the Si case than for the Ge one: the SBH modifications at $\vartheta = 2$ are about ± 0.36 eV in the Al/Si/GaAs junctions. The corre-

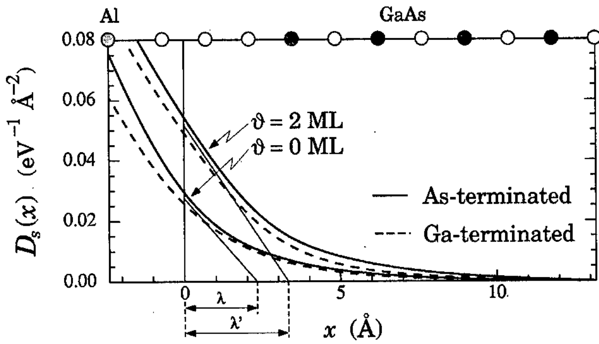

FIG. 3. Surface density of states at the Fermi energy for the Al/GaAs and Al/Ge/GaAs (100) junctions. The solid (dashed) lines correspond to the As- (Ga-) terminated interface. λ and λ' indicate the average MIGS decay length at the position of the dipole for Ge coverages $\vartheta=0$ ML and $\vartheta=2$ ML, respectively. The positions of the atomic planes are shown in the upper part of the figure.

sponding effective screening at 2 ML is thus weaker in the Al/Si/GaAs junctions [$\epsilon_{\rm eff}(2)=45$] than in the Al/Ge/GaAs junctions.

The Al/Si/GaAs barrier tuning with ϑ is well described by the capacitor model with the parameter values: $\epsilon_\infty^{\rm GaAs}=12.4$, $\epsilon_\infty^{\rm Si}=13.9$, $D_s=0.027$ eV^{-1} Å^{-2}, $D_s'=0.050$ eV^{-1} Å^{-2}, obtained from *ab initio* calculations, and using $\delta=3.2$ Å (see Fig. 2). According to the model, the effective screening in the linear regime [$\vartheta=0$ in Eq. (2)] depends only on the properties of the bare Al/GaAs interface, and should thus be the same for the Al/Si/GaAs and Al/Ge/GaAs junctions. This is in agreement with the first-principles results. The predictions of the capacitor model in the linear regime are also indicated in Fig. 2 (thin lines), and correspond to $\epsilon_{\rm eff}=28$. The linear approximation reproduces well the *ab initio* results up to $\vartheta\approx0.5$ ML. However, it overestimates the magnitude of the Ge-induced barrier changes by more than 0.3 eV at $\vartheta=2$ ML, indicating the presence of substantial nonlinear screening effects.

Most of these nonlinearities can be explained within the capacitor model in terms of a change with coverage of the semiconductor dielectric constant and MIGS density of states. In Fig. 3, we display the calculated surface density of states at the Fermi energy in the As- and Ga-terminated Al/GaAs (100) junctions, containing 2 ML of Ge and without Ge. The surface densities of states are very similar for the two terminations. At the position of the ionic dipole, we find $D_s'\approx0.052$ eV^{-1} Å^{-2} for the Al/2 Ge ML/GaAs system, i.e., a value which is almost twice as large as that without Ge ($D_s=0.027$ eV^{-1} Å^{-2}) and very similar to that of the Al/Si/GaAs system ($D_s'=0.050$ eV^{-1}Å^{-2}). The Ge dielectric constant obtained from *ab initio* calculations is $\epsilon_\infty^{\rm Ge}=18.6$, which is about 50% larger than the corresponding value for GaAs, and 30% larger than that of Si.[21] The model predictions for the Al/Ge/GaAs system obtained using the above parameter values are displayed in Fig. 2, and account for most of the nonlinearities in the barrier variations. The fact that the surface densities of states at the As- and Ga-terminated interfaces are very similar explains the observed symmetry of the barrier variations of the two types of interfaces.

The capacitor model predicts smaller barrier modifications for Ge than for Si interlayers at coverages higher than $\vartheta\approx0.5$. This derives from the higher susceptibility of the Ge interlayer, and is consistent with the *ab initio* trend. We note, however, that the amplitudes of the calculated Al/Ge/GaAs barrier variations in Fig. 2 are smaller than those predicted by the model. The difference is about 50 meV at $\vartheta\approx2$, which is slightly larger than our numerical accuracy. These deviations from the model are attributed to complex nonlinear effects related to the presence of the short-range component of the ionic potential (not accounted for in our screening model). The additional terms needed in Eq. (2) to reproduce the *ab initio* results are mainly of order ϑ, and can be accounted for reasonably well using a slightly larger value of the length parameter, i.e., with $\delta=4$ Å in Eq. (2) (see Fig. 2). We would like to note, in this connection, that only the changes with doping of the semiconductor dielectric constant and MIGS density of states have been taken into account explicitly in Eq. (2); the variation of the length parameter δ, instead, has been neglected. Such a change could be easily taken into account by replacing $(D_s'-D_s)\delta$ by $(D_s'\delta'-D_s\delta)$ in Eq. (2), where δ' corresponds to the length parameter at $\vartheta=2$. Figure 3 shows, in fact, that the MIGS decay length changes from $\lambda\approx2.3$ Å at $\vartheta=0$ to $\lambda'=3.3$ Å at $\vartheta=2$. The change in the MIGS decay length, however, turns out to be essentially the same for Ge and Si interlayers. Furthermore, with the above correction and the choice of parameters $\delta=\lambda=2.3$ Å and $\delta'=\lambda'=3.3$ Å, the model predictions would be barely distinguishable from those corresponding to Eq. (2) with $\delta=3.2$ Å. Therefore, although a correction taking explicitly into account the change of the MIGS decay length would be more physical and could be introduced, it would not improve noticeably the description of the SBH variations.

V. SUMMARY AND CONCLUSIONS

We have examined from first principles the SBH modifications induced by Ge dipole layers at the Al/GaAs (100) interface. We find that, while these barrier modifications are identical to those induced by Si interlayers at low coverage (below 0.5 ML), their magnitudes are smaller than those induced by Si at higher coverages. For a coverage of 2 ML, in particular, replacing Si by Ge reduces the barrier tunability by ~25%, and decreases the maximal value of the p-type Schottky barrier by ~0.1 eV. These differences derive from the higher polarizability of the Ge interlayer. Our predictions on the effects of Ge interface layers on the Al/GaAs(100) Schottky barrier differ from those of the existing macroscopic models, and could be used to discriminate between the conflicting theories of Schottky barrier tuning.

ACKNOWLEDGMENTS

This work was supported by the Swiss National Science Foundation under Grant No. 20-47065.96. Computations were performed at the CSCS in Manno. The authors thank A. Franciosi for stimulating discussions.

[1]M. Cantile, L. Sorba, S. Yildirim, P. Faraci, G. Biasiol, A. Franciosi, T. J. Miller, and M. I. Nathan, Appl. Phys. Lett. **64**, 988 (1994); M. Cantile *et al.*, J. Vac. Sci. Technol. B **12**, 2653 (1994); G. Gigli, M. Lomascolo, M. De Vittorio, R. Cingolani, A. Cola, F. Quaranta, L. Sorba, B. Mueller, and A. Franciosi, Appl. Phys. Lett. **73**, 259 (1998).

[2]J. C. Costa, F. Williamson, T. J. Miller, K. Beyzavi, M. I. Nathan, D. S. L. Mui, S. Strite, and H. Morkoç, Appl. Phys. Lett. **58**, 382 (1991); J. C. Costa, T. J. Miller, F. Williamson, and M. I. Nathan, J. Appl. Phys. **70**, 2173 (1991).

[3]K. Koyanagi, S. Kasai, and H. Hasegawa, Jpn. J. Appl. Phys., Part 1 **32**, 502 (1993).

[4]J. R. Waldrop and R. W. Grant, Appl. Phys. Lett. **52**, 1794 (1988); **50**, 250 (1987).

[5]J. R. Waldrop, Appl. Phys. Lett. **53**, 1518 (1988).

[6]S. De Franceschi, F. Beltram, C. Marinelli, L. Sorba, M. Lazzarino, B. H. Müller, and A. Franciosi, Appl. Phys. Lett. **72**, 1996 (1998).

[7]M. Peressi, N. Binggeli, and A. Baldereschi, J. Phys. D **31**, 1273 (1998), and references therein.

[8]G. Margaritondo, Rep. Prog. Phys. **62**, 765 (1999), and references therein.

[9]Z. Chen, S. N. Mohammad, and H. Morkoç, Phys. Rev. B **53**, 3879 (1996).

[10]C. Berthod, N. Binggeli, and A. Baldereschi, Phys. Rev. B **57**, 9757 (1998).

[11]C. Berthod, N. Binggeli, and A. Baldereschi, Europhys. Lett. **36**, 67 (1996).

[12]R. People, Phys. Rev. B **34**, 2508 (1986).

[13]L. Sorba, J. J. Paggel, and A. Franciosi, J. Vac. Sci. Technol. B **14**, 2994 (1996).

[14]M. S. Ünlü, S. Strite, G. B. Gao, K. Adomi, and H. Morkoç, Appl. Phys. Lett. **56**, 842 (1990).

[15]N. Troullier and J. L. Martins, Phys. Rev. B **43**, 1993 (1991).

[16]H. J. Monkhorst and J. D. Pack, Phys. Rev. B **13**, 5188 (1976).

[17]C.-L. Fu and K.-M. Ho, Phys. Rev. B **28**, 5480 (1983).

[18]A. Baldereschi, S. Baroni, and R. Resta, Phys. Rev. Lett. **61**, 734 (1988).

[19]C. Berthod, N. Binggeli, and A. Baldereschi (unpublished).

[20]W. A. Harrison, J. Vac. Sci. Technol. **16**, 1492 (1979).

[21]To evaluate ϵ_∞, we use the capacitor model of Peressi *et al.*, Phys. Rev. B **43**, 7347 (1991). The results are $\epsilon_\infty^{\mathrm{Ge}}=18.6$, $\epsilon_\infty^{\mathrm{Si}}=13.9$, and $\epsilon_\infty^{\mathrm{GaAs}}=12.4$.

Tunable Schottky barrier contacts to $In_xGa_{1-x}As$

C. Marinelli,[a] L. Sorba, M. Lazzarino, D. Kumar,[b] E. Pelucchi, B. H. Müller, D. Orani,[c] S. Rubini, and A. Franciosi[d]
Laboratorio Nazionale TASC-INFM, Area di Ricerca, Bldg. MM, S.S. 14, Km. 163.5, I-34012 Trieste, Italy

S. De Franceschi[e] and F. Beltram
Scuola Normale Superiore di Pisa and INFM, I-56126 Pisa, Italy

(Received 17 May 2000; accepted 31 May 2000)

$Al/In_xGa_{1-x}As(001)$ diodes incorporating Si bilayers deposited under As or Al flux were fabricated by molecular-beam epitaxy on GaAs(001) wafers for $0.2<x<0.4$. Schottky barrier heights as high as 0.75 eV and as low as -0.10 eV could be reproducibly obtained. Diodes engineered for high barrier height systematically showed a higher thermal stability than low-barrier diodes. We discuss the composition dependence of the barrier height and the observed degradation behavior vis-a-vis of the predictions of the interface-dipole model of Schottky barrier tuning. © *2000 American Vacuum Society.* [S0734-211X(00)08804-1]

I. INTRODUCTION

The transport properties of metal/semiconductor interfaces in most devices are customarily tuned by controlling the doping level of the semiconductor in the near-junction region. Scattering of carriers by ionized impurities is an unavoidable by-product of doping, reducing the carrier mobility and making ballistic transport difficult to achieve. This limitation, and the fact that available doping technology is far from satisfactory for a number of novel semiconductor materials of current interest, is stimulating research into new methods of tuning the properties of metal/semiconductor interfaces.

The possibility of controlling the transport properties of metal/semiconductor contacts by changing the local interface environment has been an elusive goal for many years. Changes in the Schottky barrier height have been reported for different treatments of the initial semiconductor surface prior to metal deposition, as well as different growth protocols.[1] Reproducibility and stability of the resulting contacts remain key issues to be addressed.[2]

One of the most promising nonconventional methods to control the Schottky barrier height involves insertion of ultrathin heterovalent layers at the interface under appropriate growth conditions. For example, Si interface layers 2 monolayer (ML) thick, inserted in Al/GaAs(001) diodes by using molecular-beam epitaxy (MBE) under As flux have been found to reduce the *n*-type Schottky barrier height ϕ_{Bn} down to 0.2–0.3 eV. Incorporation of a Si bilayer under Al flux was found instead to increase ϕ_{Bn} up to 1.1–1.2 eV.[3,4]

The above effects have been observed *in situ* by x-ray photoemission spectroscopy (XPS) in samples with thin metal overlayers, as well as *ex situ* by current–voltage ($I-V$) and capacitance–voltage ($C-V$) transport measurements in fully developed diodes.[3,4] The engineered barriers appeared stable in a relatively wide temperature range,[5] and little degradation of the internal quantum efficiency and ideality factors was observed, allowing tunability of the barrier heights in Schottky barrier photodetectors.[6]

Based on the original phenomenological considerations,[3,4] or on more recent first-principles calculations,[7–9] some authors have associated these effects with a Si-induced local interface dipole. The dipole would originate from the heterovalent character of the Si–GaAs bonds across the interface, and its direction and magnitude would depend on the cation- or anion-terminated nature of the GaAs layer.[3,4,7,8] The excess flux provided during Si deposition would determine the Ga and As chemical potentials and the relative stability of the Ga- and As-terminated surfaces.[9] This interface-dipole model of Schottky barrier tuning is potentially widely applicable, but to our knowledge its predictions have not yet been tested for any junction other than Al/GaAs.

The main purpose of the present work was to test the predictions of the interface-dipole model of Schottky barrier tuning by examining the effect of inserting Si bilayers in $Al/In_xGa_{1-x}As(001)$ junctions under cation or anion flux. In particular, we have examined the systematic variation of the barrier height with alloy composition, and the ideality and stability of the resulting, engineered contacts. A discussion on the implementation of ohmic contacts to $In_{0.38}Ga_{0.62}As$ alloys,[10] and the exploitation of such contacts in superconductor/semiconductor hybrid junctions[11] was presented earlier.

The $Al/In_xGa_{1-x}As(001)$ interface system was selected in view of the many useful similarities (for low x) and important differences (for high x) between GaAs and $In_xGa_{1-x}As$, as well as for the many applications of high-electron-mobility $In_xGa_{1-x}As$ epilayers in high-speed and optoelectronic devices.[12–14]

[a]Present address: Department of Electrical and Electronic Engineering, University of Bristol, Bristol, BS8 1TR, United Kingdom.
[b]Present address: Electronic Science Department, Kurukshetra University, 136119 India.
[c]Also with Institut de Physique Appliquee, Ecole Polytechnique Federale, PHB-Ecublens, CH-1015 Lausanne, Switzerland.
[d]Also with Dipartimento di Fisica, Universita' di Trieste, I-34127 Trieste, Italy and Department of Chemical Engineering and Materials Science, University of Minnesota, Minneapolis, MN 55455; electronic mail: francios@sci.area.trieste.it
[e]Present address: Department of Applied Physics, Delft University of Technology, P.O. Box 5046, 2600 GA Delft, The Netherlands.

II. EXPERIMENTAL DETAILS

All structures were grown by solid-source MBE in a single facility which includes interconnected chambers for III–V semiconductor growth, analysis through monochromatic x-ray photoelectron spectroscopy (XPS), and metallization. Si-doped ($n \sim 5\times10^{16}\,cm^{-3}$), 0.5-$\mu$m-thick GaAs(001) buffer layers were first grown at a substrate temperature of 600 °C with a (2×4) surface reconstruction—as determined by reflection high energy electron diffraction (RHEED)—on n^+-GaAs(001) substrates. This was followed by $In_xGa_{1-x}As$ growth at 500 °C, with an As/Ga beam equivalent pressure ratio of 17, as measured with an ion gauge located at the sample position, and at a growth rate of 1.1–1.8 μm/h. RHEED indicated a (3×1) reconstruction, as expected for the growth conditions employed.[15]

Measurements of the $In_xGa_{1-x}As$ alloy composition were performed *in situ* using XPS, and *ex situ* using x-ray diffraction (XRD). The SSX-100-301 XPS spectrometer employed Al $K\alpha$ radiation (1486.6 eV), monochromatized and focused by a bent crystal monochromator, and was operated with an overall resolution of 0.75 eV and a spot size of 300 μm. The XRD measurements were performed using a high-resolution diffractometer equipped with a Cu radiation source and a Bartels four-crystal Ge(220) monochromator, providing Cu $K\alpha_1$ radiation ($\lambda=0.154\,056$ nm) with a 12 arcsec angular divergence. Systematic comparison of XPS and XRD results for 0.5–2.0-μm-thick $In_xGa_{1-x}As$ epilayers was carried out to gauge the well-known tendency of In to segregate to the growth surface.[16]

When required, Si bilayers (1 ML=0.134 nm) were deposited onto the $In_xGa_{1-x}As$ surface at 300 °C at a growth rate of 2.4 nm/h. Calibration of the Si flux was performed as described elsewhere.[17] An anion (As) or cation (Al) flux was provided during Si deposition, with beam equivalent pressures of 4×10^{-6} and 5×10^{-9} Torr, respectively. The final Al metallizations were deposited in all cases at room substrate temperature.

The Schottky barriers were gauged *in situ* by XPS and *ex situ* by $I-V$ measurements. Samples for XPS determination of the barrier height included 50 to 200-nm-thick, Si-doped ($n \sim 5\times10^{16}\,cm^{-3}$), $In_xGa_{1-x}As$ epilayers and 2-nm-thick Al overlayers. Samples for $I-V$ determination of the barrier included 2-μm-thick, Si-doped ($n \sim 5\times10^{16}\,cm^{-3}$), $In_xGa_{1-x}As$ epilayers[18] and 150-nm-thick Al overlayers. Circular contacts, with diameter in the 75–200 μm range, were defined on the Al film by means of standard photolithography and wet-chemical-etching techniques. Linear fits of the forward bias region of log(I)–V characteristics were performed to estimate the Schottky barrier height. XPS and $I-V$ results obtained from samples with engineered interfaces were systematically compared with results obtained from samples without Si bilayers.

The stability of the engineered interfaces against thermal degradation was gauged by comparing $I-V$ characteristics obtained before and after sequential annealing cycles. To this purpose the samples were mounted onto a W strip heater by means of Mo clips and subjected to annealing cycles at increasing temperature under nitrogen atmosphere. The temperature was monitored by means of a thermocouple spot-welded to the heater. During each annealing cycle the sample temperature was kept constant for 10 s, and typical temperature ramp-up and ramp-down times were 15 and 10 s, respectively. We caution the reader that the above protocol is sensibly different from that employed in earlier degradation studies of engineered Al/GaAs diodes.[5]

III. RESULTS AND DISCUSSION

A. $In_xGa_{1-x}As$ composition and residual strain

A number of $In_xGa_{1-x}As$ epilayer standards were first examined *in situ* by XPS immediately after growth, and then *ex situ* by XRD. In Fig. 1(a) we show representative XRD spectra near the symmetric (004) reflection of the GaAs substrate for $In_xGa_{1-x}As$ epilayers with XRD-determined composition $x=0.047$ (dotted line) and 0.298 (solid line). The epilayer thickness was 2 and 1.5 μm, respectively. Both spectra have been normalized to the GaAs (004) diffracted intensity, located at the zero of the x axis in the figure. The $In_xGa_{1-x}As$-related (004) diffraction features are also shown, in an expanded scale, for the two samples. From the results shown in Fig. 1(a) and the spectra recorded near the asymmetric (224) reflections (not shown), we determined the lattice parameters in the directions parallel ($a_\parallel$) and perpendicular ($a_\perp$) to the surface.[19]

From the observed tetragonal distortion of the $In_xGa_{1-x}As$ unit cell, the known elastic stiffness constants of the material,[20] and the equilibrium lattice parameter a_0 expected from Vegard's law, we evaluated the In concentration, x, and the residual strain in the different $In_xGa_{1-x}As$ epilayers. In Table I we list the measured composition x (column 1) and the residual strain in the direction parallel to the interface $\epsilon_\parallel=(a_\parallel-a_0)/a_0$ (column 3) for a number of representative $In_xGa_{1-x}As$ epilayers of thickness h (column 2). For comparison, we also show in Table I the parallel residual strain predicted by the phenomenological expression $(\epsilon_\parallel)^2h=K=0.0037\pm0.0007$ nm (column 4) proposed by Drigo *et al.*,[21] and the lattice mismatch between the bulk $In_xGa_{1-x}As$ alloy and the GaAs substrate (column 5), derived from Vegard's law.

The results shown in Table I indicate that for the range of epilayer thicknesses studied most of the lattice mismatch is relaxed through formation of misfit dislocations at the $In_xGa_{1-x}As$/GaAs interface. The residual strain at the surface of the $In_xGa_{1-x}As$ epilayers is very small (0.1%–0.3%), so that its effect on the $In_xGa_{1-x}As$ band gap and Al/$In_xGa_{1-x}As$ Schottky barrier height is expected to be negligible in practical diodes. The predictions of the phenomenological expression proposed by Drigo *et al.*[21] are generally consistent with our experimental data.

XPS analysis of the same $In_xGa_{1-x}As$ epilayers was performed immediately after growth by measuring the integrated intensities of the Ga $3d$, In $4d$, and In $3d_{5/2}$ core level emissions and then scaling them by empirical core-sensitivity factors. The latter were obtained by comparing the

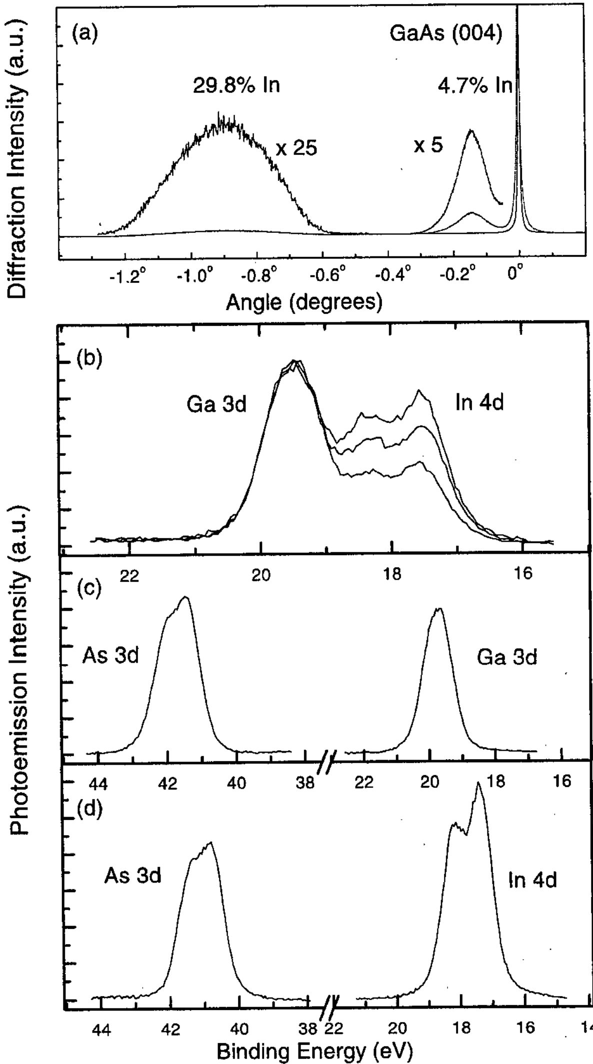

FIG. 1. (a) Representative x-ray diffraction (XRD) spectra near the symmetric (004) reflection of the GaAs substrate for $In_xGa_{1-x}As$ epilayers, with XRD-determined compositions $x=0.047$ (dotted line) and 0.298 (solid line). The epilayer thicknesses were 2 and 1.5 μm, respectively. Both spectra have been normalized to the GaAs (004) diffracted intensity located at the zero of the x axis in the figure. The $In_xGa_{1-x}As$-related (004) diffraction features are also shown in an expanded scale for the two samples. (b) Monochromatic x-ray photoemission spectroscopy (XPS) results from $In_xGa_{1-x}As$ alloys with nominal composition x 0.2, 0.3 and 0.35 showing the Ga 3d (in the 19–20 eV range) and In 4d (in the 17–19 eV range) emission features. The binding-energy scale is referred to the Fermi level E_F of the spectrometer and the spectra have been normalized to the peak intensity of the Ga 3d doublet. (c) XPS spectra for the As 3d (left) and Ga 3d (right) core doublets from a GaAs binary standard. (d) XPS spectra for the As 3d (left) and In 4d (right) doublets from an InAs binary standard.

Ga 3d, In 4d, In 3$d_{5/2}$, and As 3d intensities from binary GaAs and InAs standard epilayers grown on GaAs(001) and InAs(001) substrates. The procedure is illustrated in Figs. 1(b)–1(d). In Fig. 1(b) we show the Ga 3d (in the 19–20 eV range) and In 4d (in the 17–19 eV range) emissions from three representative $In_xGa_{1-x}As$ epilayers. The binding-energy scale is referred to the Fermi level E_F of the spectrometer and the spectra have been normalized to the peak intensity of the Ga 3d doublet.

TABLE I. Structural parameters of $In_xGa_{1-x}As$ epilayers grown by molecular-beam epitaxy (MBE) at 500 °C on GaAs(001) substrates. Column 1: indium concentration x as determined from high-resolution x-ray diffraction (XRD) data; column 2: epilayer thickness h; column 3: experimental residual strain $\epsilon_\parallel$ in the direction parallel to the interface, derived from our XRD data; column 4: expected parallel residual strain $(K/h)^{1/2}$, from the empirical expression proposed in Ref. 21; column 5: expected lattice mismatch $\Delta a/a$ relative to GaAs, from Vegard's law.

$x(\%)$	h (nm)	$\epsilon_\parallel(\%)$	$(K/h)^{1/2}(\%)$	$\Delta a/a(\%)$
4.7±0.5	2000±100	0.09±0.03	0.14±0.02	0.34
15.6±0.5	1000±50	0.18±0.03	0.19±0.02	1.12
17.7±0.5	1500±75	0.17±0.03	0.16±0.02	1.27
19.8±0.5	1000±50	0.25±0.03	0.19±0.02	1.42
29.8±0.5	1500±75	0.23±0.03	0.16±0.02	2.14
30.9±0.05	1500±75	0.25±0.03	0.16±0.02	2.21
35.2±0.5	500±25	0.33±0.03	0.27±0.03	2.52

The intensity ratio of the In 4d and Ga 3d emissions shown in Fig. 1(b) has been obtained by fitting the spectrum to a superposition of three Gaussian functions, accounting for the Ga 3d doublet and the In 4$d_{3/2}$ and In 4$d_{5/2}$ spin-orbit-split contributions, respectively. The spin-orbit splitting and the branching ratio of the two In 4d components were kept fixed at the literature values of 0.86 eV and 0.66, respectively, during the fitting process.[22] The Ga 3d and the In 3d doublets from the same alloys were also systematically monitored. Following such procedures we derived the cation intensity ratios I(In 3$d_{5/2}$)/I(Ga 3d) and I(In 4$d_{5/2}$)/I(Ga 3d) for each of the ternary alloys.

In Fig. 1(c) we show photoelectron energy distribution curves (EDCs) for the As 3d (left) and Ga 3d (right) core doublets from a GaAs binary standard, while in Fig. 1(d) we show the emission from the As 3d (left) and In 4d (right) doublets from an InAs binary standard, in arbitrary units. By normalizing the emissions from the two binary standards to the intensity of the As 3d doublet, we derived the ratio of the elemental core sensitivity factors for the two cations S(In 3$d_{5/2}$)/S(Ga 3d) and S(In 4$d_{5/2}$)/S(Ga 3d).[23] The average In concentration x within the XPS sampling depth could then be determined from either one of the following expressions:

$$x=\frac{\mathrm{I(In\,3}d_{5/2})}{\mathrm{I(In\,3}d_{5/2})+\mathrm{I(Ga\,3}d)\cdot\left[\frac{S(\mathrm{In\,3}d_{5/2})}{S(\mathrm{Ga\,3}d)}\right]}, \quad (1)$$

$$x=\frac{\mathrm{I(In\,4}d_{5/2})}{\mathrm{I(In\,4}d_{5/2})+\mathrm{I(Ga\,3}d)\cdot\left[\frac{S(\mathrm{In\,4}d_{5/2})}{S(\mathrm{Ga\,3}d)}\right]} \quad (2)$$

with the only possible difference between the results of Eqs. (1) and (2) being associated with the different escape depth of photoelectrons from the In 4$d_{5/2}$ or In 3$d_{5/2}$ core levels,[24] in the presence of a sufficiently inhomogeneous In distribution in the near-surface region.

In Fig. 2 we plot the XPS-determined values of the $In_xGa_{1-x}As$ surface composition [solid symbols, from Eq. (1), open symbols, from Eq. (2)] as a function of the XRD-derived value of the bulk In concentration. The solid line

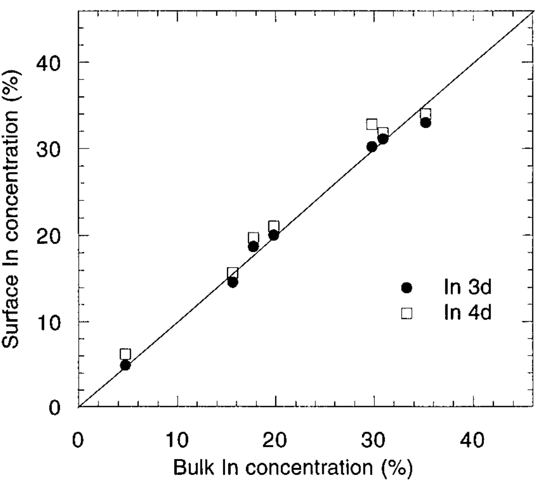

FIG. 2. XPS-determined values of the $In_xGa_{1-x}As$ surface composition [solid symbols, from In $3d$ data, Eq. (1), open symbols, from In $4d$ data, Eq. (2)] as a function of the XRD-derived value of the bulk In concentration. The solid line shows the expected trend in the absence of any surface segregation effects.

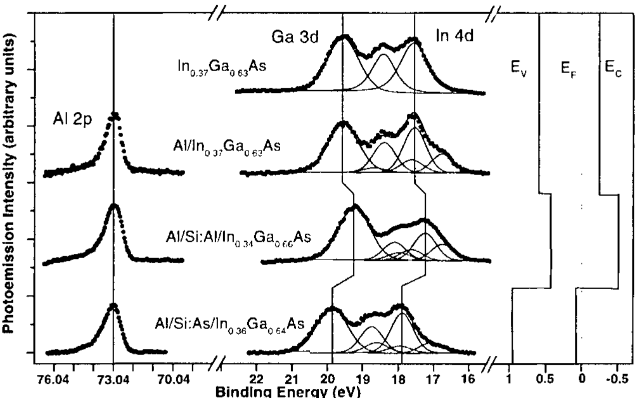

FIG. 3. XPS determination of the Schottky barrier for $Al/In_xGa_{1-x}As$ junctions. From top to bottom: Ga $3d$ and In $4d$ emission from a n-$In_{0.37}Ga_{0.63}As(001)$ epilayer prior to Al deposition; Al $2p$ (left) and Ga $3d$ and In $4d$ emissions (right) from the corresponding $Al/n-In_{0.37}Ga_{0.63}As(001)$ junction; core emissions from an $Al/n-In_{0.34}Ga_{0.66}As(001)$ junction incorporating a Si bilayer deposited under Al flux; core emissions from an $Al/n-In_{0.36}Ga_{0.64}As(001)$ junction incorporating a Si bilayer deposited under As flux. The Al overlayer was 2 nm thick in all cases. Solid symbols denote the experimental data. Solid lines show the result of a least-square fit to the data in terms of a superposition of Gaussian contributions relating to bulk (solid vertical lines) and chemically shifted Ga $3d$, In $4d_{3/2}$, and In $4d_{5/2}$ core features. The XPS-derived position of the Fermi level within the $In_xGa_{1-x}As$ band gap is also shown (rightmost section).

shows the expected result in the absence of any surface segregation effect. Throughout the composition range explored, the maximum deviation is less than 2% of x, when the In $3d_{5/2}$ data are considered (solid symbols), indicating no relevant In segregation.[25]

A somewhat larger systematic deviation (typically 3% of x) is observed in Fig. 2 when the In $4d$ data are considered (open symbols). We associate this fact with an increased experimental uncertainty, as opposed to segregation effects. Photoelectrons from the In $3d$ core levels have a shorter escape depth than those from the In $4d$ core level (see Ref. 24), so that the effect of In surface segregation would be to apparently push the $3d$-derived data (solid symbols) *above* the $4d$-derived data (open symbols) in Fig. 2, in contrast with the observations. We estimate that the uncertainty in the XPS values is about 10% of x, mostly resulting from the fitting and background subtraction procedure required to extract the In $4d$ spectral contribution [see Fig. 1(b)], as well from the determination of the elemental core sensitivity factors.

The amount of In segregation in our $In_xGa_{1-x}As$ epilayers is therefore to be considered below our detection limit, in contrast with the large indium surface segregation effects detected by XPS by other authors, which have been described as two to threefold enhancement in the In surface concentration relative to the bulk.[25] The results of Fig. 2 indicate that, for appropriate growth protocols, the well-known tendency of In to segregate to the $In_xGa_{1-x}As$ growth surface[17,25] can be effectively suppressed. This is important for the purposes of the present study, since any In surface segregation could modify the surface $In_xGa_{1-x}As$ band gap relative to the bulk and affect the $Al/In_xGa_{1-x}As$ Schottky barrier height.

B. Schottky barrier height

Schottky barrier heights were determined *in situ* by XPS for thin-overlayer samples, and confirmed *ex situ* on selected samples by depositing thick metal overlayers and performing $I-V$ measurements. Representative XPS measurements are shown in Fig. 3. The topmost spectrum (solid circles) shows the Ga $3d$ and In $4d$ emissions from a $In_{0.37}Ga_{0.63}As$ alloy prior to metal deposition. The binding-energy scale is referred to E_F. Using the analysis procedure described in the previous section, we identified three different contributions associated with the Ga $3d$ doublet, and with the In $4d_{3/2}$ and In $4d_{5/2}$ emissions (solid lines, left to right). The position of the valence-band maximum E_v was determined through a least-square linear fit of the leading valence-band edge, and is shown to the right in Fig. 3 together with the position of the conduction-band minimum E_c. The latter was obtained from the measured position of E_v relative to E_F and the known $In_{0.37}Ga_{0.63}As$ band gap.[26]

The binding energies, relative to E_v, of the Ga $3d$, In $4d_{5/2}$, and In $3d_{5/2}$ centroids are 18.86±0.06, 16.86 ±0.06, and 443.73±0.06 eV, respectively.[27] Such binding energies remain unchanged, within experimental uncertainty, for other $In_xGa_{1-x}As$ alloy compositions throughout the $0.2<x<0.4$ composition range. This is consistent with results by Hwang *et al.*,[22] from which one infers a core binding-energy variation of only 0.02 eV in the composition range examined here.

Upon deposition of 2 nm of Al onto the $In_{0.37}Ga_{0.63}As(001)$ surface, the photoemission spectra (second topmost spectra in Fig. 3) show changes in the In $4d$–Ga $3d$ line shape (right) together with the characteristic Al $2p$ doublet from metallic, elemental aluminum,[28] with centroid at 73.04±0.04 eV (left). The complex In $4d$–Ga $3d$ line shape could be reproduced with a super-

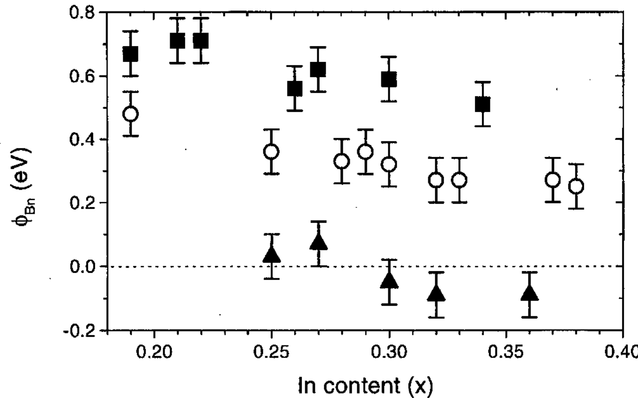

FIG. 4. XPS-derived *n*-type Schottky barrier height in $Al/In_xGa_{1-c}As$ junctions as a function of the In concentration, *x*, in the alloy. Open symbols: samples with no Si interlayer. Solid squares: junctions incorporating a Si bilayer deposited under Al flux. Solid triangles: junctions incorporating a Si bilayer deposited under As flux.

position of three bulk-related core features, at the same positions as for the clean surface, and three new chemically shifted contributions (solid lines). To simplify the least-square fitting procedure, the full width at half maximum (FWHMs), the spin-orbit splitting, and the branching ratio were kept fixed at the values determined for the $In_{0.37}Ga_{0.63}As$ epilayer prior to metal deposition.[29]

The emergence of cation-related components shifted to lower binding energies relative to the bulk components in the initial stages of Al deposition (1–5 ML) is accompanied by the emergence of As $3d$ features chemically shifted to higher binding energy relative to the bulk component (not shown), and of Al $2p$ features, shifted to higher binding energies relative to the position for elemental, metallic Al (not shown). All such trends are consistent with a partial Ga–Al and In–Al exchange reaction, leading to formation of Al–As bonds at the interface and to outdiffusion of the displaced cations into the metallic overlayer.[1,30] With increasing coverage the reaction stops and a metallic Al overlayer is formed.

For an Al coverage of 2 nm, the main core-level features in Fig. 3 (vertical solid line) correspond to the emissions from cations within the semiconductor, while the low-binding-energy features correspond to outdiffused cations. The positions of the semiconductor-related Ga $3d$ and In $4d$ features can be used to monitor the band bending and the Schottky barrier height,[31] using the previously determined core binding energies relative to E_v (Ref. 27). Analogous results were obtained using the In $3d$ and As $3d$ core levels (not shown). The *n*-type Schottky barrier height $\phi_{Bn}=E_c-E_F$ derived for the $Al/In_{0.37}Ga_{0.63}As$ junction from Fig. 3 is 0.27 ± 0.07 (Ref. 32). This value is shown in Fig. 4 together with results obtained for other $In_xGa_{1-x}As$ alloy compositions (open circles).

The $Al/In_xGa_{1-x}As$ *n*-type Schottky barrier height is seen to decrease gradually with increasing In content from 0.48 ($x=0.19$) to 0.24 eV ($x=0.38$) in the composition range examined. The decrease in the barrier mirrors the variation in the bandgap, which goes from 1.15 eV ($x=0.19$) down to 0.91 eV ($x=0.38$). For Al/GaAs junctions [E_G(GaAs)=1.42 eV] fabricated using identical conditions we determined a *n*-type Schottky barrier height of 0.78 eV (Refs. 3 and 4), further supporting the above trend. The *p*-type Schottky barrier $\phi_{Bp}=E_F-E_v$ only changes from 0.64 (Al/GaAs) to 0.67 eV ($Al/In_{0.38}Ga_{0.62}As$) through 0.66 eV ($Al/In_{0.19}Ga_{0.81}As$) in the series. This type of behavior is consistent with other existing reports on the compositional dependence of the Schottky barrier height in metal/ $In_xGa_{1-x}As$ junctions.[33,34]

Assuming transitivity of the band alignment in metal—semiconductor and semiconductor—semiconductor junctions,[35–38] our result would indicate a valence-band discontinuity relatively small and independent of *x* in $In_xGa_{1-x}As$/GaAs(001) heterojunctions. For example, from the measured Schottky barrier heights, assuming transitivity in the band alignment, we would derive ΔE_v varying from -0.08 to -0.11 eV, for hypothetical, unstrained InAs/ GaAs(001) heterojunctions.[39] This is consistent with the estimate of -0.11 ± 0.05 eV for the valence band offset, that was derived by Hwang *et al.* using the natural valence-band offset method.[22,39] Several,[40] but not all[41] calculations of the band offset at $In_xGa_{1-x}As$/GaAs(001) heterojunctions indicate that the band gap difference mainly concentrates in the conduction-band discontinuity.

C. Engineered Schottky barriers

In the lower half of Fig. 3 we show XPS results for two junctions incorporating Si bilayers deposited under anion (As) or cation (Al) or flux (first and second bottom-most spectra, respectively). Good least-square fits of the overall experimental line shapes could also be obtained in terms of superpositions of three bulk-related core features, with energy positions rigidly shifted relative to the positions observed prior to Si and metal deposition, and three contributions chemically shifted to lower binding energies relative to the bulk contributions. As described in the previous section, FWHMs, spin-orbit splitting and branching ratio were kept fixed. The presence of the Si bilayer is seen to affect the intensity and, to a lesser extent, the position of the chemically shifted components relative the bulk components. In particular, deposition of the Si bilayer under Al flux appears to lead, in general, to enhanced In and Ga segregation, in agreement with transmission electron microscopy (TEM) results, which suggest that some Al-cation exchange reaction accompanies the deposition of Si overlayers on the III–V surface for such growth conditions.[42] Deposition of the Si bilayer under As flux generally leads instead to smaller modifications of the relative intensity and position of the chemically shifted core features, as compared to the case without interlayer.

The positions of the bulk-related Ga $3d$ and In $4d$ emissions, and the position of the In $3d$ feature (not shown) have been used to derive the Schottky barrier height, with consistent results. In particular, the *n*-type Schottky barrier heights ϕ_{Bn} are 0.51 ± 0.07 and -0.09 ± 0.07 eV for $Al/Si/In_{0.34}Ga_{0.66}As$ and $Al/Si/In_{0.36}Ga_{0.64}As$ junctions incor-

TABLE II. Current–voltage ($I-V$) determinations of the n-type Schottky barrier height, and ideality factor for $Al/In_xGa_{1-x}As$ diodes incorporating a Si bilayer deposited under Al flux, and for samples with no Si interlayer. Results are shown for samples prior to and after 10 s rapid thermal annealing cycles at the indicated maximum temperature. Column 1: In concentration x. Column 2: sample type, i.e., no-interlayer sample, or diode incorporating a Si bilayer deposited under Al flux. Column 3: rapid-thermal-annealing (RTA) temperature. Room-temperature (RT) denotes as-grown samples, prior to any annealing treatment. Column 4: n-type Schottky barrier height ϕ_{Bn}. Column 5: ideality factor n.

x	Sample type	RTA (°C)	ϕ_{Bn} (eV)	n
0.2	no-interlayer	RT	0.48±0.04	1.07±0.01
"	"	200 °C	0.52±0.03	1.07±0.03
"	"	300 °C	0.54±0.03	1.09±0.04
"	"	400 °C	0.55±0.03	1.03±0.02
"	"	500 °C	0.60±0.03	1.02±0.03
0.2	Si bilayer (Al flux)	RT	0.74±0.03	1.06±0.03
"	"	200 °C	0.72±0.02	1.12±0.03
"	"	300 °C	0.72±0.02	1.26±0.03
"	"	400 °C	0.71±0.03	1.30±0.03
"	"	500 °C	0.70±0.03	1.34±0.04
0.4	Si bilayer (Al flux)	RT	0.45±0.03	1.10±0.03
"	"	200 °C	0.46±0.03	1.12±0.03
"	"	300 °C	0.47±0.03	1.18±0.03
"	"	420 °C	0.46±0.03	1.19±0.03

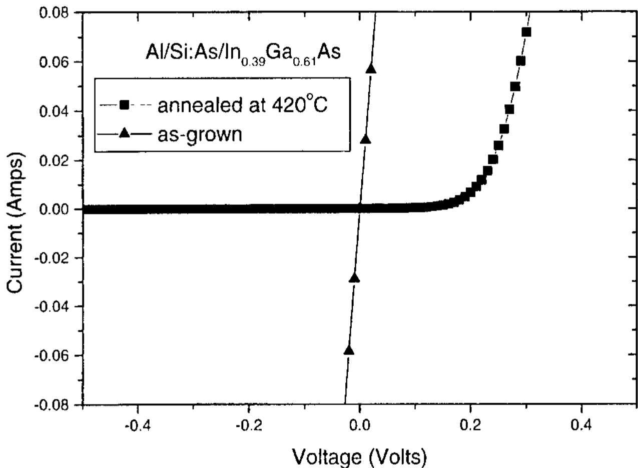

FIG. 5. Current–voltage ($I-V$) characteristics from $Al/In_{0.39}Ga_{0.61}As$ junctions incorporating a Si bilayer deposited under As flux. The as-grown junction exhibits an ideal ohmic characteristic (solid triangles) which reverts to a rectifying behavior upon annealing at 420 °C (solid squares).

porating a Si bilayer deposited under Al and As flux, respectively. These results are included in Fig. 4 together with n-type Schottky barrier heights determined by XPS for $Al/Si/In_xGa_{1-x}As$ with other x. Solid squares and triangles in Fig. 4 correspond to results obtained for junctions incorporating Si bilayers deposited under Al and As flux, respectively.

As for the samples without Si interlayer (open symbols), junctions with a Si interlayer exhibit a barrier height decreasing with increasing x (Fig. 4), so that the barrier height mirrors the band gap variation with alloy composition. More importantly, a 0.6 eV variation in the barrier height can be obtained for any alloy composition by incorporating a Si bilayer under appropriate growth conditions. The composition- and Si-induced variations in the barrier height combine to yield an unprecedented 0.8 eV range of barrier tunability (Fig. 4). In particular, junctions with Si bilayers deposited under As flux on $In_xGa_{1-x}As$ alloys with $x > 0.25$ are expected to exhibit an ideal ohmic transport characteristic.

$I-V$ measurements from representative diodes engineered for high and low n-type Schottky barrier height are shown in Table II and Fig. 5, respectively, together with results obtained from samples without interlayers. The values of the Schottky barrier height derived from transport measurements are in good agreement with the values determined by XPS summarized in Fig. 4. For example, diodes incorporating Si bilayers deposited under Al flux (Table II) exhibit n-type Schottky barrier height of 0.74±0.03 eV for $x=0.2$ and of 0.45±0.03 eV for $x=0.4$, to be compared with the extrapolated XPS values of 0.73 and 0.46 eV, respectively (Fig. 4). The corresponding ideality factors for the two diodes are 1.06±0.03 and 1.10±0.03, respectively.

In Fig. 5 we show the ideal ohmic $I-V$ characteristics from an $Al/In_{0.39}Ga_{0.61}As$ diode incorporating a Si bilayer deposited under As flux (solid triangles and thick solid line). A similar ideal ohmic behavior was observed throughout the 300–200 K temperature range, indicating that there is no residual barrier within experimental uncertainty. In the same conditions, samples with no interlayer exhibit a rectifying behavior, with $\phi_{Bn}=0.23\pm0.02$ eV. Both types of behavior are in good agreement with the expectations derived from XPS results (Fig. 4).

The effect of the Si bilayers on the $Al/In_xGa_{1-x}As$ Schottky barrier height is compellingly similar to that reported earlier for Al/GaAs junctions.[3,4] In Fig. 4 (and Table II) we observe that Si bilayers deposited under Al flux induce a ~0.25 eV increase in the n-type Schottky barrier, while Si bilayers grown under As flux yield a ~0.35 eV decrease in the barrier. For Al/GaAs(001) junctions we found bilayer-induced barrier changes of ~0.25 and ~0.5 eV, respectively.

The linearity and transferability of the bilayer-induced barrier change is fully consistent with the predictions of the local-interface-dipole model of Si-induced Schottky barrier tuning.[7–9] In this model the magnitude of the dipole is determined only by the valence difference between interlayer and junction atoms, and by the effective screening of the local electrostatic dipole. Screening depends, in turn, on the macroscopic dielectric constants of the III–V semiconductor and of the group-IV interlayer material, and is only slightly enhanced in going from Al/GaAs to $Al/In_xGa_{1-x}As$ junctions. The orientation of the dipole is determined by the termination of the semiconductor layer, which is stabilized by the cation or anion flux provided during interlayer deposition. The model would therefore predict for all $Al/Si/In_xGa_{1-x}As$ junctions a qualitatively similar dependence of the barrier change on the cation/anion flux provided during Si deposi-

tion and only a slightly decreasing magnitude of the barrier tunability range with increasing x.

We also emphasize that most other models found in the literature are difficult to reconcile with evidence that a single group-IV bilayer can cause such large variations in the barrier height and in opposite directions, and that the As and Al fluxes required to produce such an effect are much larger than those commonly employed for doping purposes. We maintain that a group-IV bilayer deposited under such conditions cannot be assimilated to a degenerately bulk-doped semiconductor with bulk-like electronic structure. First-principles calculations have shown that local density of states and electronic structure of such systems are completely at variance with the predictions of macroscopic models.[9,38,43,44]

One important word of caution is motivated by the simplistic nature of the local interface configuration postulated by the dipole model of Schottky barrier tuning. The results of Fig. 3 clearly indicate that the presence of the Si interlayer modifies the local interface chemistry and substantially affects atomic interdiffusion. The model, however, assumes abrupt metal/IV/III–V interfaces with no interdiffusion. No provision exists, for example, to account for the Al–Ga and Al–In exchange reactions that may accompany the deposition of the Si bilayer under Al flux.[42] On the other hand, recent studies replacing the Al flux with a Ga flux during Si bilayer deposition show identical Schottky barrier modifications, in the absence of any exchange reaction at the interface.[45] The implication is that not all of the chemical phenomenology which emerges from the local interface studies might be relevant to the formation of the Schottky barrier height.

D. Degradation of engineered Schottky barriers

The thermal stability of engineered Schottky barriers is of paramount importance for any possible device application, and may provide information on the nature of the interface. We subjected $Al/In_xGa_{1-x}As$ diodes engineered for high and low Schottky barriers, as well as samples with no Si interlayer, to thermal annealing cycles to different temperatures in the 200–500 °C range. The results are summarized in Table II and Figs. 5 and 6.

For the samples without interlayer, annealing cycles at temperatures as high as 500 °C yielded a gradual increase in the n-type barrier height, with little modification of the ideality factor. This type of behavior is often ascribed to AlAs formation at the interface, as a result of enhanced atomic interdiffusion.[46] Diodes engineered for high barrier exhibited instead a relatively constant Schottky barrier height and a gradual degradation of the ideality factor.

For example, an $Al/In_{0.2}Ga_{0.8}As$ diode incorporating a Si bilayer deposited under Al flux retained over 94% of its enhanced Schottky barrier after an annealing cycle at 500 °C, but showed a substantial increase in the ideality factor, that was up to 1.30 from the value of 1.06 for the as-grown junction (Table II). In the same temperature range the corresponding sample without interlayer showed a 27% increase

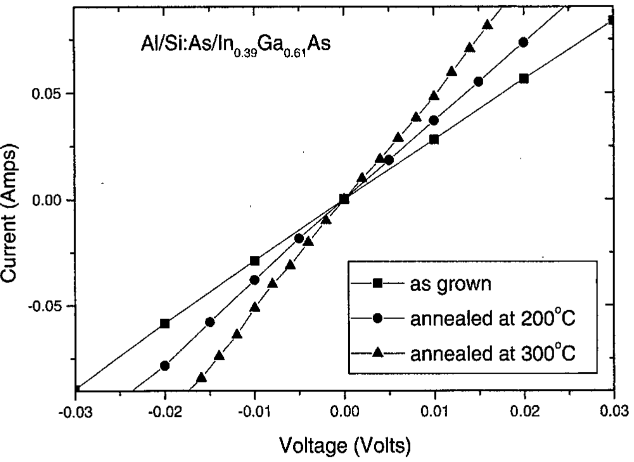

FIG. 6. $I-V$ characteristics from $Al/In_{0.39}Ga_{0.61}As$ junctions incorporating a Si bilayer deposited under As flux. Junctions annealed at 200 (circles) and 300 °C (triangles) show an ideal ohmic characteristic similar to that of the as-grown junctions (squares), but with a reduced specific contact resistance.

in the barrier height, but an ideality factor which remained at 1.02. Such a different behavior suggests that in the diodes engineered for high barrier height, defects may form in the near-interface region upon annealing, which are absent from the samples without interlayer.

The effect of annealing cycles on the diodes engineered for low barrier height is qualitatively different, and strikingly nonmonotonic. Upon annealing at 200 and 300 °C $Al/In_{0.39}Ga_{0.61}As$ diodes incorporating Si bilayers deposited under As flux, the $I-V$ characteristics remained ohmic, and exhibited a gradual decrease in the apparent specific contact resistance with increasing annealing temperature (Fig. 6). This type of behavior is usually ascribed to increased doping and/or enhanced tunneling across the barrier. Upon annealing at above 420 °C, however, the $I-V$ characteristics reverted to a rectifying behavior (solid squares and thin solid line in Fig. 5), compellingly similar to that observed in the samples without Si interlayer. This abrupt change in behavior further demonstrate that interdiffusion and doping cannot explain *per se* the results in Figs. 4 and 5.

The qualitatively different behaviors of diodes engineered for high and low barrier heights upon annealing suggest the existence of different microscopic degradation mechanisms. This, in turn, indicates differences in the initial atomic configuration and in their relative stability. The local-interface-dipole model of Schottky barrier tuning offers a simple and direct explanation of this different behavior. The relative stability of the interface dipoles leading to lower and higher n-type Schottky barriers depends on the relative thermodynamic stability of anion- and cation-terminated Si–GaAs interfaces. In the model, the relative thermodynamic stability of the two interfaces is determined by the cation- and anion-related chemical potentials.[9]

In the experiment, interfaces engineered for high Schottky barrier heights are in contact with a cation reservoir (the metal overlayer), while interfaces engineered for low barrier heights are not. As a consequence, the stability of anion-terminated interfaces is expected to be lower than that

of cation-terminated interfaces. Simply stated, arsenic atoms released upon annealing from the interface region are not going to be replaced, and the formation of an increasing number of cation-terminated bonds at the interface will lead to an increase in the barrier, i.e., to degradation. Recent preliminary studies examining the degradation of Al/n–GaAs diodes engineered for low barrier height, by means of spatially resolved photoemission spectroscopy, have indeed shown formation of localized defects related to As outdiffusion from the interface region.[47] Unfortunately, no quantitative determination of the defect-related local variation in Schottky barrier height was performed. Further spatially resolved studies, possibly in combination with ballistic-electron-emission investigations, seem clearly desirable at this time.

IV. CONCLUSIONS

We inserted by molecular-beam epitaxy Si bilayers under cation (III) or anion (V) flux in the interface region of $Al/In_xGa_{1-x}As(001)$ junctions. The resulting Schottky barrier height was determined *in situ* by means of x-ray photoemission spectroscopy, and *ex situ* through current–voltage measurements. In particular, we examined the systematic variation of the barrier height with alloy composition in the $0.2<x<0.4$ range, and the ideality and stability of the resulting, engineered contacts. The observed 0.8 eV variation of the n-type barrier height throughout the range explored was found to be in agreement with the predictions of the interface-dipole model of Schottky barrier tuning.

High-barrier junctions, incorporating Si bilayers deposited under cation flux, retained their rectifying character at temperatures as high as 500 °C. Ideal ohmic contacts, incorporating Si deposited under anion flux, reverted to a rectifying behavior upon annealing at 420 °C. The different degradation behavior lends further support to the interface-dipole model of Schottky barrier tuning.

ACKNOWLEDGMENTS

This work was supported in part by INFM under the TUSBAR Advanced Research Project and by the National Science Foundation under Grant No. DMR-9819659. One of the authors (D.K.) acknowledges support by the International Center for Theoretical Physics in Trieste, Italy, under the TRIL program. One of the authors (B.M.) acknowledges support by the Commission of the European Communities under the TMR program. Useful discussions with N. Binggeli and A. Baldereschi are gratefully acknowledged.

[1]See, for example, L. J. Brillson, in *Handbook on Semiconductors*, edited by P. T. Landsberg (Elsevier, Amsterdam, 1992), Vol. 1, p. 281, and references therein.

[2]C. J. Palmstrøm and T. D. Sands, in *Contacts to Semiconductors*, edited by L. J. Brillson (Noyes, Park Ridge, 1993); C. J. Palmstrøm and D. V. Morgan, in *Gallium Arsenide Materials, Devices, and Circuits*, edited by M. J. Howes and D. V. Morgan (Wiley, Chichester, 1985), p. 195, and references therein.

[3]M. Cantile, L. Sorba, S. Yildirim, P. Faraci, G. Biasiol, A. Franciosi, T. J. Miller, and M. I. Nathan, Appl. Phys. Lett. **64**, 988 (1994).

[4]M. Cantile, L. Sorba, P. Faraci, S. Yildirim, G. Biasiol, G. Bratina, A. Franciosi, T. J. Miller, M. I. Nathan, and L. Tapfer, J. Vac. Sci. Technol. B **12**, 2653 (1994); L. Sorba, J. J. Paggel, and A. Franciosi, *ibid.* **14**, 2994 (1996), and references therein.

[5]L. Sorba, S. Yildirim, M. Lazzarino, A. Franciosi, D. Chiola, and F. Beltram, Appl. Phys. Lett. **69**, 1927 (1996).

[6]G. Gigli, M. Lomascolo, M. De Vittorio, R. Cingolani, A. Cola, F. Quaranta, L. Sorba, B. H. Müller, and A. Franciosi, Appl. Phys. Lett. **73**, 259 (1998).

[7]C. Berthod, N. Binggeli, and A. Baldereschi, Europhys. Lett. **36**, 67 (1996).

[8]C. Berthod, J. Bardi, N. Binggeli, and A. Baldereschi, J. Vac. Sci. Technol. B **14**, 3000 (1996).

[9]C. Berthod, N. Binggeli, and A. Baldereschi, Phys. Rev. B **57**, 9757 (1998).

[10]S. De Franceschi, F. Beltram, C. Marinelli, L. Sorba, M. Lazzarino, B. Müller, and A. Franciosi, Appl. Phys. Lett. **72**, 1996 (1998); C. Marinelli, L. Sorba, B. H. Müller, D. Kumar, D. Orani, S. Rubini, A. Franciosi, S. De Franceschi, M. Lazzarino, and F. Beltram, J. Cryst. Growth **201/202**, 769 (1999).

[11]S. De Franceschi, F. Giazotto, F. Beltram, L. Sorba, M. Lazzarino, and A. Franciosi, Appl. Phys. Lett. **73**, 3890 (1998).

[12]C. J. Palmstrøm, B. P. Van Der Gaag, J.-I. Song, W.-P. Hong, S. A. Schwarz, and S. Novak, Appl. Phys. Lett. **64**, 3139 (1994).

[13]D. C. Streit, A. K. Oki, T. R. Block, M. D. Lammert, M. M. Hoppe, D. K. Umemoto, and M. Wojtowicz, J. Vac. Sci. Technol. B **14**, 2216 (1996).

[14]Y. Dohmae, S. Suzuki, T. Hashizume, and H. Hasegawa, Jpn. J. Appl. Phys., Part 1 **36**, 1834 (1997).

[15]N. Grandjean, J. Massies, M. Leroux, J. Leymaric, A. Vasson, and A. M. Vasson, Appl. Phys. Lett. **64**, 2664 (1994), and references therein.

[16]J. Massies, F. Turco, A. Salettes, and J. P. Contour, J. Cryst. Growth **80**, 307 (1987). J. M. Moison, F. Houzay, F. Barthe, J. M. Gerard, B. Jusserand, J. Massies, and F. S. Turco-Sandroff, *ibid.* **111**, 141 (1991).

[17]L. Sorba, G. Bratina, A. Franciosi, L. Tapfer, G. Scamarcio, V. Spagnolo, E. Migliori, P. Merli, and E. Molinari, J. Cryst. Growth **127**, 121 (1993), and references therein.

[18]All samples for transport measurements also included a heavily n^+-doped interface between the $In_xGa_{1-x}As$ epilayer and the GaAs substrate.

[19]The lattice tilt between overlayer and substrate, obtained from (004) reflections acquired rotating the sample by 180° about the surface normal, was found to be negligible (<0.01°). Analysis of (224) reflections, at grazing incidence or grazing exit angle, revealed only small inhomogeneities in the residual strain (<0.01%) in the two orthogonal ⟨110⟩ directions.

[20]Landolt-Börnstein, in *Numerical Data and Functional Relationships in Science and Technology*, edited by O. Madelung, Group III (Springer, Berlin, 1982), Vols. 17a and 22a.

[21]A. V. Drigo, A. Aydinli, A. Carnera, F. Genova, C. Rigo, C. Ferrari, P. Franzosi, and G. Salviati, J. Appl. Phys. **66**, 1975 (1989).

[22]J. Hwang, P. Pianetta, C. K. Shih, W. E. Spicer, Y. C Pao, and J. S Harris, Jr., Appl. Phys. Lett. **51**, 1632 (1987).

[23]Since no attempt was made to compensate for possible variations in the analyzer throughput with kinetic energy, the values of $S(\mathrm{In}\,4d_{5/2})/S(\mathrm{Ga}\,3d)=2.341\pm0.074$ and $S(\mathrm{In}\,3d_{5/2})/S(\mathrm{Ga}\,3d)=13.686\pm0.705$ determined in this study should be considered specific of the XPS spectrometer employed. However, the kinetic energy range involved is relatively narrow, so that we do not expect large variations in the analyzer throughput. Our experimental values are in fact very close to predictions based on Hartree–Fock–Slater calculations: $S(\mathrm{In}\,4d_{5/2})/S(\mathrm{Ga}\,3d)=2.214$ and $S(\mathrm{In}\,3d_{5/2})/S(\mathrm{Ga}\,3d)=13.277$, extrapolated from the value reported by J. J. Yeh and I. Lindau, At. Data Nucl. Data Tables **32**, 1 (1985) taking into account the $2j+1$ multiplicity of each doublet component.

[24]In the kinetic-energy range of interest, the escape depth of normally emitted Ga $3d$ and In $4d$ photoelectrons is 26.6 Å, see E. A. Kraut, R. W Grant, J. R. Waldrop, and S. P. Kowalczyk, Phys. Rev. B **28**, 1965 (1983). In our experimental geometry the average photoelectron collection angle is 55° from the sample normal, leading to an effective escape depth of about 15.3 Å. In the kinetic-energy range of interest, the escape depth of normally emitted In $3d_{5/2}$ photoelectrons is 15 Å, see J. M. Moison, C. Guille, F. Houzay, F. Barthe, and M. V. Rompay, *ibid.* **40**,

6149 (1989); in our experimental geometry this would lead to an effective escape depth of 8.6 Å.

[25]See Moison *et al.*, in Ref. 24.

[26]To evaluate the room-temperature band gap E_G for $In_xGa_{1-x}As$ alloys we used the empirical relation $E_G(x)=0.354+0.604(1-x)+0.475(1-x)^2$ proposed by S. Paul, J. B. Roy, and P. K. Basu, J. Appl. Phys. **69**, 827 (1991).

[27]Strain can in principle change core binding energies and affect the determination of the band alignment. See, for example, J. Tersoff and C. G. Van de Walle, Phys. Rev. Lett. **59**, 946 (1987); However, even for the thinnest $In_xGa_{1-x}As$ epilayers examined here by XPS, the expected residual strain was well below 1%. The effect of strain on the electronic states of highly strained (2%–7% in-plane strain) $In_xGa_{1-x}As$ layers has been determined through photoemission spectroscopy by a number of authors, including K. Hirakawa, Y. Hashimoto, K. Harada, and T. Ikoma, Phys. Rev. B **44**, 1734 (1991); A. Stampfl, X. D. Zhang, G. Kemister, R. C. G. Leckey, J. D. Riley, B. Usher, P. T. Orders, R. Denecke, J. Faul, and L. Ley, *ibid.* **45**, 4181 (1992). An extrapolation of such results to the present situation would indicate that the expected influence of residual strain on core binding energies and Schottky barrier height is lower than 0.05 eV.

[28]S. A. Flodstrom, R. Z. Bachrach, R. S. Bauer, and S. B. M. Hagström, Phys. Rev. Lett. **37**, 1282 (1976).

[29]The Gaussian FWHM was fixed at 1.04 eV for the Ga $3d$ doublet, and at the resolution-limited experimental value of 0.75 eV for the other five core features. The spin-orbit splitting and the branching ratio were fixed at 0.86 and 0.66 eV for both, the bulk related and the chemically shifted, In $4d$ doublets (see Ref. 22).

[30]Such a type of exchange reactions have been reported for many metal/GaAs(110) interfaces. See, for example, R. Z. Bachrach, R. S. Bauer, J. C. McMenamin, and A. Bianconi, in *Physics of Semiconductors 1978*, edited by B. L. H. Wilson (Institute of Physics, London, 1979), p. 1073; L. J. Brillson, Surf. Sci. **168**, 260 (1986); A. Kahn, L. J. Brillson, A. D. Katnani, and G. Margaritondo, Solid State Commun. **38**, 1269 (1981); J. J. Joyce, M. Grioni, M. del Giudice, M. W. Ruckman, F. Boscherini, and J. H. Weaver, J. Vac. Sci. Technol. A **5**, 2019 (1987).

[31]Since continuous, metallic Al layers, at least 2 nm thick, were deposited onto the samples, no surface photovoltage effects were observed. See M. H. Hecht, J. Vac. Sci. Technol. B **8**, 1018 (1990).

[32]The dispersion in the numerical values of the barrier height due to the use of the different Ga $3d$, In $4d_{5/2}$, In $3d_{5/2}$, or As $3d$ core levels was typically less than ±0.02 eV. The larger uncertainty quoted for the absolute value of the barrier height takes into account the additional uncertainty in the determination of the core binding energy relative to E_v, and in the determination of the alloy composition and band gap.

[33]W. Mönch, *Semiconductor Surfaces and Interfaces*, 2nd ed. (Springer, Berlin, 1995), and references therein.

[34]K. Kajiyama, Y. Mizushima, and S. Sakata, Appl. Phys. Lett. **36**, 67 (1996).

[35]J. Tersoff, Phys. Rev. B **30**, 4874 (1984).

[36]C. J. Palmstrøm and T. D. Sands, in *Contacts to Semiconductors*, edited by L. J. Brillson (Noyes, Park Ridge, 1993), p. 67. See, in particular, Fig. 48.

[37]J.-K. Lee, Y.-H. Cho, B.-D. Choe, K. S. Kim, H. I. Jeon, H. Lim, and M. Razeghi, Appl. Phys. Lett. **71**, 912 (1997).

[38]J. Bardi, N. Binggeli, and A. Baldereschi, Phys. Rev. B **59**, 8054 (1999).

[39]In InAs/GaAs junctions the valence-band maximum is expected to be higher in energy in GaAs than in InAs, with a type-II band alignment.

[40]M. Oloumi and C. C. Matthai, J. Phys.: Condens. Matter **3**, 9981 (1991), and references therein.

[41]K. J. Moore, G. Duggan, K. Woodbridge, N. J. Pulsford, and R. J. Nicholas, Phys. Rev. B **42**, 3024 (1990).

[42]E. Carlino, L. Sorba, A. Franciosi, S. Heun, and B. H. Müller, Philos. Mag. B **80**, 1055 (2000).

[43]Z. Chen, S. N. Mohammad, and H. Morkoç, Phys. Rev. B **53**, 3879 (1996).

[44]M. Peressi, N. Binggeli, and A. Baldereschi, J. Phys. D **31**, 1273 (1998), and references therein. See also A. Baldereschi *et al.*, these proceedings.

[45]B. Bonanni, M. Lazzarino, D. Orani, S. Rubini, and A. Franciosi (unpublished).

[46]N. M. Johnson, T. J. Magee, and J. Peng, J. Vac. Sci. Technol. **13**, 838 (1976); A. Bosacchi, S. Franchi, E. Gombia, R. Mosca, F. Fantini, R. Menozzi, and S. Naccarella, Electron. Lett. **30**, 820 (1994).

[47]S. Heun, T. Schmidt, J. Slezak, J. Diaz, K. C. Prince, B. Müller, and A. Franciosi, J. Cryst. Growth **201/202**, 795 (1999).

Photoemission results on intralayer insertion at III-V/III-V junctions: A critical appraisal of the different interpretations

M. Moreno[a)]
Instituto de Ciencia de Materiales de Madrid (CSIC), Cantoblanco, E-28049 Madrid, Spain, and Paul-Drude-Institut für Festkörperelektronik, Hausvogteiplatz 5-7, D-10117 Berlin, Germany

M. Alonso
Instituto de Ciencia de Materiales de Madrid (CSIC), Cantoblanco, E-28049 Madrid, Spain

M. Höricke and R. Hey
Paul-Drude-Institut für Festkörperelektronik, Hausvogteiplatz 5-7, D-10117 Berlin, Germany

K. Horn
Fritz-Haber-Institut der Max-Planck-Gesellschaft, D-14195 Berlin, Germany

J. L. Sacedón
Instituto de Ciencia de Materiales de Madrid (CSIC), Cantoblanco, E-28049 Madrid, Spain

K. H. Ploog
Paul-Drude-Institut für Festkörperelektronik, Hausvogteiplatz 5-7, D-10117 Berlin, Germany

(Received 17 January 2000; accepted 30 May 2000)

Several researchers have proposed that band discontinuities at semiconductor heterojunctions may be ''tuned'' by inserting very thin layers of foreign atoms at the interface which are thought to induce an ''interface dipole.'' Modifications of the *apparent* valence-band offset, as measured by photoelectron spectroscopy (PES), have been indeed observed upon Si insertion at GaAs–AlAs interfaces, and they have been generally interpreted as *real* band-offset changes. However, there is an alternative explanation of the photoemission results in terms of band-bending effects. Here, we present results of PES experiments designed to test the two opposing interpretations. We have examined the effect of Si insertion at polar (100) and nonpolar (110) interfaces, and we have studied the insertion of Si (*n*-type) and Be (*p*-type) intralayers. Similar results are obtained for polar and nonpolar interfaces, and effects of opposite sign are observed for Si and Be intralayers. These results can be readily interpreted in terms of a band-bending profile modification upon Si or Be insertion. Additional PES experiments performed at different substrate temperatures have allowed us to test the proposed band profiles. From the surface photovoltage effects induced at low temperature, we obtain evidence for sample band bending which is consistent with the room-temperature band profiles proposed. Hence, our results can be completely understood within a ''band-bending interpretation,'' calling into question the interpretation in terms of a ''band-offset tuning effect.''
© *2000 American Vacuum Society.* [S0734-211X(00)08104-X]

I. INTRODUCTION

Control of the magnitude of band offsets in semiconductor junctions may introduce a new degree of freedom in the design of heterojunction devices, and is thus a most desirable goal. Offsets of isovalent interfaces of type IV/IV, or III–V/III–V and II–VI/II–VI with a common anion or cation, have been found to be independent of orientation and interface quality.[1–5] At heterovalent junctions, such as III–V/IV junctions, band offsets seem to be determined by bulk properties for nonpolar interfaces, but they depend on interface microscopic details for polar orientations.[6] GaAs–AlAs interfaces, which have ubiquitous optoelectronic applications, belong to the group of common anion isovalent compound interfaces; therefore, the possibilities for changing the band offset in these interfaces are, in principle, limited. Nevertheless, it has been proposed[7,8] to modify the band discontinuity of these interfaces by inserting a group-IV (e.g., Si or Ge) intralayer, thus trying to convert the isovalent interface (III–V/III–V) into a double heterovalent one (III–V/IV+IV/III–V), so that a chance of modifying the band offset arises for polar interface orientations.

Two mechanisms have been proposed for the intralayer to induce a band-offset change. One is the establishment of charged interfaces of opposite polarity, the so called ''microscopic interface capacitor.'' Polar interfaces between heterovalent semiconductors, if ideally abrupt, should be charged. This situation is thermodynamically unstable but, if the intralayer is thin enough, the increase in the free energy of the system is small and the two heterovalent III–V/IV interfaces may remain charged,[9] and may act as the parallel plates of a microscopic capacitor [Fig. 1(a)].[10] The positively (negatively) charged interface corresponds to the side where the material is anion (cation) terminated. The establishment of this microscopic capacitor produces a potential drop at the interface, thus changing the band offset, ΔE_V, which increases or decreases depending on the stacking sequence [see

[a)]Electronic mail: mmoreno@icmm.csic.es

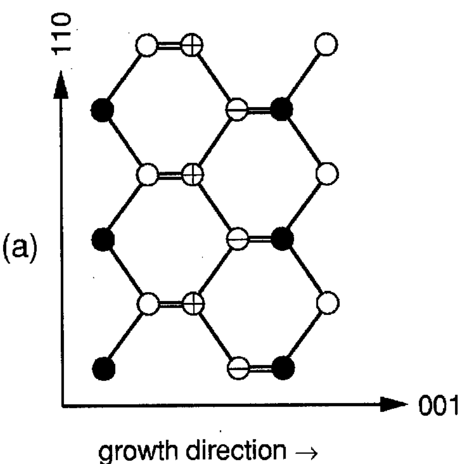

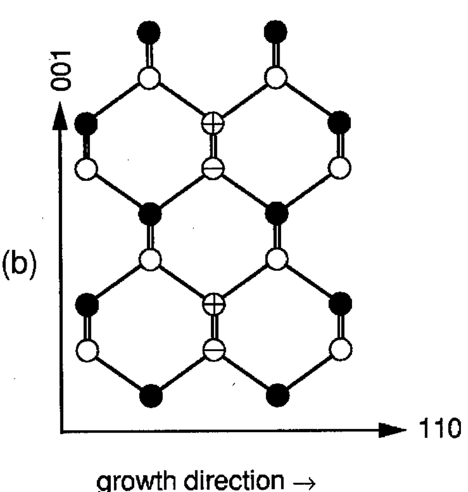

FIG. 1. Schematic representation of the charge transfer expected at (a) (100)-polar, and (b) (110)-nonpolar III–V/IV/III–V interfaces according to the Harrison microscopic interface-capacitor picture (Ref. 10).

Figs. 2(a) and 2(b)]. A second mechanism may lead to the formation of "neutral nonequivalent interfaces."[11] Reduction of the free energy of the system and neutrality are achieved through formation of point defects and atomic mixing.[10,12] Multiple interface configurations result from atomic mixing, thus producing different band-discontinuity values.[13,14] Within the microscopic-interface-capacitor picture,[10] the *polar* character of the interface plays a key role in the modification of the band offset. A polar geometry induces a charge transfer *crossing* the interface [Fig. 1(a)]. On the contrary, at nonpolar junctions the charge transfer takes place *along* but not *across* the interface [Fig. 1(b)]; thus, the layer-averaged interface is not charged. Hence, according to the microscopic-interface-capacitor model, band-offset changes are expected to occur upon intralayer insertion for polar interfaces but not for nonpolar ones.

Photoelectron spectroscopy (PES) is widely used to determine valence-band offsets at semiconductor heterointerfaces.[15–17] Determining the band discontinuity at the interface between two semiconductors, A and B, by core-level photoemission spectroscopy involves the measurement of the

(a) Interface without intralayer

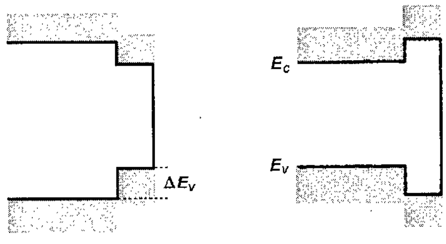

(b) Interface with intralayer (band-offset change)

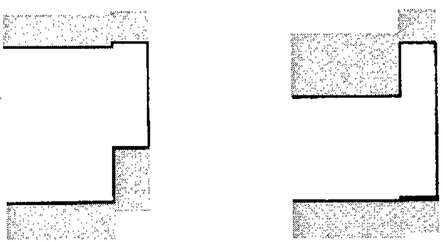

(c) Interface with intralayer (band-bending change)

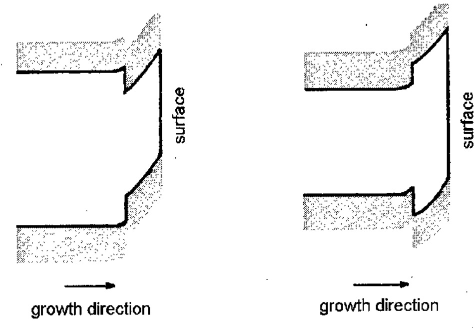

FIG. 2. Schematic band diagrams for GaAs-on-AlAs (left) and AlAs-on-GaAs (right) heterojunctions: (a) without an intralayer, and with a Si intralayer according to the two competing interpretations invoking (b) a band-offset charge or (c) a band-bending change.

separation, $\Delta E_{\mathrm{CL}} = E^B_{\mathrm{CL}} - E^A_{\mathrm{CL}}$, between two core-level kinetic energies (relative to the Fermi level): E^A_{CL} and E^B_{CL}, corresponding to each side of the interface.[15–17] The valence-band offset ΔE^*_V is easily determined by subtracting a quantity, ξ, that accounts for the difference between the respective core-level binding energies:

$$\Delta E^*_V = \Delta E_{\mathrm{CL}} - \xi, \quad (1)$$

where

$$\xi = (E^B_{\mathrm{CL}} - E^B_V) - (E^A_{\mathrm{CL}} - E^A_V),$$

$E_{\mathrm{CL}} - E_V$ being the binding energy of the core level relative to the valence band maximum (VBM). The valence-band-

offset value, ΔE_V^*, determined in such a manner is called the "apparent" offset; it only corresponds to the *real* offset ΔE_V if certain conditions are met.

Determining interface band offsets requires one to prove *interface* energy values. However, photoemission spectroscopy provides weighted energy averages of emissions that originate all along the photoemission probing depth, not only at the interface. In order to guarantee that the energy values measured by photoemission correspond to those at the interface, flat-band conditions along the photoemission probing depth must prevail. The existence of band bending in this region gives rise to a systematic error in the determination of ΔE_V. Peak centroid positions can be used to define the kinetic energy values E_{CL}^A and E_{CL}^B included in Eq. (1). This choice fixes the accuracy in determining ΔE_V, because it does not discriminate the contribution from possible chemically shifted species, surface components, etc. Depending on the complexity of the core-level peaks and of the wanted accuracy, core-level peak deconvolution is or is not required.

Modifications of the *apparent* valence-band offset, as measured by PES, have been observed upon Si insertion at GaAs–AlAs interfaces,[18–22] and the microscopic-interface-capacitor model has sometimes been invoked to explain such changes.[18] However, since photoemission is sensitive to a variety of factors, it is important to establish whether a *real* band-offset change has occurred. In fact, an alternative interpretation of the PES results for the GaAs–(Si)–AlAs system has been proposed,[19,20] which assumes that the intralayer modifies the band-bending profile without changing the band offset. By relying solely on PES, it is difficult to assess whether the variations observed in the Al(2*p*)-to-Ga(3*d*) energy separation upon Si insertion at GaAs–AlAs(100) junctions[18–22] are due to modification of the interface band offset [Fig. 2(b)], or to variation of the band-bending profile near the surface [Fig. 2(c)]. Such band-bending effects are not easily measurable, or even detectable, by photoemission spectroscopy.[23,24] Nevertheless, one approach to investigating possible band-bending effects is to introduce intralayers of different doping type, since *n*-type and *p*-type impurities induce band bendings of opposite sign.

In order to accurately determine band discontinuities by photoemission spectroscopy, it is mandatory to perform the experiment under *flat-band* conditions, at least in the overlayer. Photovoltage effects have been shown to produce steady-state conditions in which the surface band bending is reduced or eliminated. Such surface photovoltage (SPV) effects can be induced by the light used to excite photoelectrons, e.g., by synchrotron light.[25–37] In this process, soft x-ray photons excite electrons to the conduction band, leaving holes in the valence band or core levels; secondary excitations and nonradiative decay processes effectively multiply the number of charge carriers. Electrons and holes are accelerated in opposite directions (photocurrent) by the built-in field present in the semiconductor depletion region, so that minority carriers accumulate at the surface. This carrier separation produces a photovoltage which opposes the initial built-in voltage. In order to maintain a charge balance, a current of majority carriers flows to the surface (restoring current). In equilibrium, the restoring current is equivalent and opposite to the photocurrent, so that both currents cancel each other. The supply of the restoring current is limited by the depletion region resistance, which has a pronounced dependence on sample temperature. At room temperature, the restoring current is usually sufficient to quickly discharge most of the induced photovoltage. However, at low temperature the restoring currents are reduced and there is a net forward bias. The surface photovoltage tends to eliminate any initial band bending present at the surface depletion region. Hence, comparison of synchrotron-radiation PES experiments performed at room and at low substrate temperatures may provide insight into the sample band bending.

Here, we follow a three-pronged approach in order to test the two opposing interpretations which have been proposed to explain the effect of intralayer insertion, i.e., intralayer-induced band-offset changes versus modifications of the band-bending profile [Figs. 2(b) and 2(c)]. According to the microscopic-interface-capacitor model,[10] qualitatively different behaviors are expected for polar and nonpolar interfaces. On the other hand, according to the band-bending interpretation, effects of opposite sign are expected for intralayers with *n*-type and *p*-type doping behaviors. In order to check whether the above predictions agree with experimental observations, we have first examined the effect of Si insertion at polar (100) and nonpolar (110) interfaces, and second we have studied the insertion of Si (*n*-type) and Be (*p*-type) intralayers. A third type of PES experiments, performed at low temperature, has permitted us to analyze the sample band profiles. While all three types of experimental results are seen to support a band-bending interpretation, some of them are in conflict with an interpretation invoking band-offset changes.

II. EXPERIMENT

Using molecular-beam epitaxy (MBE), we have fabricated GaAs/AlAs heterojunctions on (100)-[2° off toward (111) *A*] and (110) GaAs substrates. We used epiready heavily Si-doped ($n = 1 \times 10^{18}$ cm^{-3}) substrates to prevent the samples from being charged during the photoemission measurements. First, a (0.1–0.3)-μm-thick Si-doped GaAs buffer layer was grown ($n = 1 \times 10^{18}$ cm^{-3}), followed by a 20-nm-thick undoped AlAs layer [Fig. 3(a)]. At this point, a layer of Si or Be, with a density of 2.2×10^{14} atoms cm^{-2}, was inserted in some of the samples. This two-dimensional (2D) concentration corresponds to approximately 1/3 of the atomic sites in a (100) monolayer, or to 1/4 of the atomic sites in a (110) monolayer. Finally, all samples were terminated by a 2-nm-thick, nominally undoped, GaAs overlayer [Fig. 3(a)]. The growth parameters employed are summarized in Tables I and II. The conditions for growth on (110) substrates were carefully optimized by using atomic-force microscopy to guarantee a smooth surface morphology. The Si and Be intralayers were inserted using a *pulsed low-flux* δ-doping method.[38,39] In the samples containing an intralayer

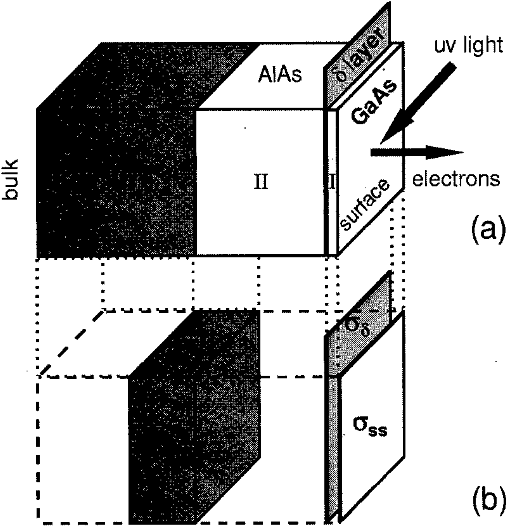

FIG. 3. (a) Schematic representation of the sample structure. (b) Model charge configuration assumed in the calculations.

of Si or Be, the overlayer was grown at a reduced substrate temperature to minimize segregation and outdiffusion of intralayer atoms.

After growth, the samples were transferred under ultra high vacuum from the MBE chamber to the PES station at the synchrotron source using a small transfer chamber. The samples were placed together in the analysis chamber, under electrical contact and grounded. We used a multiple sample holder which accommodated several samples. One of the holder positions was designed to be in thermal contact with a liquid-N_2 reservoir. The low-temperature (LT) measurements were carried out by placing the sample to be analyzed in this cooling position. The temperature at which the samples were cooled down in this way corresponds to a thermocouple reading of 220 K. Equal LT conditions were reproducibly obtained with this cooling arrangement, the actual temperature being probably lower than the nominal.

PES measurements were performed immediately after sample growth using synchrotron radiation coming from the TGM2 and TGM6 beamlines of BESSY I (Berliner Elektronenspeicherring-Gesellschaft für Synchrotronstrahlung mbH). The low-temperature experiments were performed using radiation from the TGM6 monochromator, which was located in front of a wiggler/undulator, delivering $10^{12}-10^{13}$ photons/s in the photon energy range used (40–95 eV). Electron kinetic-energy distribution curves (EDCs) were obtained for each sample. The Ga(3*d*), Al(2*p*), As(3*d*) and valence-band-edge emissions from each sample, as well as the Fermi-edge emission from a gold foil that was in electrical contact with the back side of the semiconductor samples, were consecutively recorded at a fixed photon energy. This procedure was repeated for several photon energies. Electrons were collected and counted in normal-emission geometry by an angle-resolving photoelectron spectrometer. The overall energy resolution was 150–300 meV over the range of photon energies used.

III. RESULTS AND DISCUSSION

A. Polar versus nonpolar interface orientations

Figure 4 shows Al(2*p*) and Ga(3*d*) EDC spectra recorded from GaAs-on-AlAs heterostructures with 95 eV photons. Results from samples without (closed symbols) and with (open symbols) a Si intralayer are compared for the (100) [Fig. 4(a)] and (110) [Fig. 4(b)] interface orientations. The Fermi-edge spectrum recorded on gold is also displayed. Upon Si insertion, the Ga(3*d*) peak from the GaAs overlayer

TABLE I. MBE-growth parameters of the samples studied in Sec. III A.

	GaAs/AlAs(100)	GaAs/Si/AlAs(100)	GaAs/AlAs(110)	GaAs/Si/AlAs(110)
Substrate (GaAs)				
orientation	(100)-2°→(111)*A*	(100)-2°→(111)*A*	(110)	(110)
Si doping	1×10^{18} cm^{-3}	1×10^{18} cm^{-3}	1×10^{18} cm^{-3}	1×10^{18} cm^{-3}
Buffer layer (GaAs)				
thickness	0.3 μm	0.3 μm	0.1 μm	0.1 μm
T_{subs}	590 °C	590 °C	485 °C	485 °C
growth rate	0.44 μm/h	0.44 μm/h	0.16 μm/h	0.16 μm/h
Si doping	1×10^{18} cm^{-3}	1×10^{18} cm^{-3}	1×10^{18} cm^{-3}	1×10^{18} cm^{-3}
Buried layer (AlAs)				
thickness	20.0 nm	20.0 nm	20.0 nm	20.0 nm
T_{subs}	610 °C	610 °C	505 °C	505 °C
growth rate	0.36 μm/h	0.36 μm/h	0.18 μm/h	0.18 μm/h
Si doping	⋯	⋯	⋯	⋯
Intralayer		(Si)		(Si)
2D density	⋯	2.2×10^{14} cm^{-2}	⋯	2.2×10^{14} cm^{-2}
T_{subs}	⋯	590 °C	⋯	505 °C
flux (pulsed)	⋯	2×10^{11} cm^{-2} s^{-1}	⋯	2×10^{11} cm^{-2} s^{-1}
Overlayer (GaAs)				
thickness	2.0 nm	2.0 nm	2.0 nm	2.0 nm
T_{subs}	590 °C	540 °C	505 °C	385-485 °C
growth rate	0.44 μm/h	0.44 μm/h	0.16 μm/h	0.16 μm/h
Si doping	⋯	⋯	⋯	⋯

TABLE II. MBE-growth parameters of the samples studied in Secs. III B and III C.

	GaAs/AlAs(100)	GaAs/Si/AlAs(100)	GaAs/Be/AlAs(100)
Substrate (GaAs)			
orientation	(100)-2°→(111)*A*	(100)-2°→(111)*A*	(100)-2°→(111)*A*
Si doping	1×10^{18} cm^{-3}	1×10^{18} cm^{-3}	1×10^{18} cm^{-3}
Buffer layer (GaAs)			
thickness	0.3 μm	0.3 μm	0.3 μm
T_{subs}	590 °C	590 °C	590 °C
growth rate	0.2 μm/h	0.2 μm/h	0.2 μm/h
Si doping	1×10^{18} cm^{-3}	1×10^{18} cm^{-3}	1×10^{18} cm^{-3}
Buried layer (AlAs)			
thickness	20.0 nm	20.0 nm	20.0 nm
T_{subs}	610 °C	610 °C	610 °C
growth rate	0.2 μm/h	0.2 μm/h	0.2 μm/h
Si doping	···	···	···
Intralayer		(Si)	(Be)
2D density	···	2.2×10^{14} cm^{-2}	2.2×10^{14} cm^{-2}
T_{subs}	···	590 °C	500 °C
flux (pulsed)	···	2×10^{11} cm^{-2} s^{-1}	2×10^{11} cm^{-2} s^{-1}
Overlayer (GaAs)			
thickness	2.0 nm	2.0 nm	2.0 nm
T_{subs}	610 °C	540 °C	450 °C
growth rate	0.2 μm/h	0.2 μm/h	0.2 μm/h
Si doping	···	···	···

remains at nearly the same position, while the Al(2*p*) peak from the AlAs buried layer shifts towards lower kinetic energies. Thus, the Al(2*p*)-to-Ga(3*d*) energy distance increases upon Si insertion. Remarkably, this effect is observed for *both* polar-(100) and nonpolar-(110) interfaces.

We have determined the apparent valence-band offset, ΔE_V^*, from the core-level offset, ΔE_{CL}, measured between the Al(2*p*) and Ga(3*d*) peak centroids, the "centroid" being defined as the energy value that divides the peak into two parts of equal area. We have used in Eq. (1) a value for ξ of 54.00 eV, calculated considering the well known Ga(3*d*) binding energy in GaAs (−18.86 eV) and Al(2*p*) binding energy in AlAs (−72.86 eV). The contribution of chemically shifted species and surface/interface components is expected to be small in our GaAs/AlAs heterostructures. For the heterojunctions without an intralayer, the apparent valence-band offsets are 0.50 eV and 0.48 eV for the (100) and (110) orientations, respectively. The apparent valence-band offset obtained for (100) Si-containing heterostructures is 1.12 eV, that is, for the (100) orientation ΔE_V^* increases by 0.62 eV upon Si insertion. For (110) Si-containing heterostructures the apparent valence-band offset is 0.81 eV, that is, for the (110) orientation ΔE_V^* increases by 0.33 eV upon Si insertion.

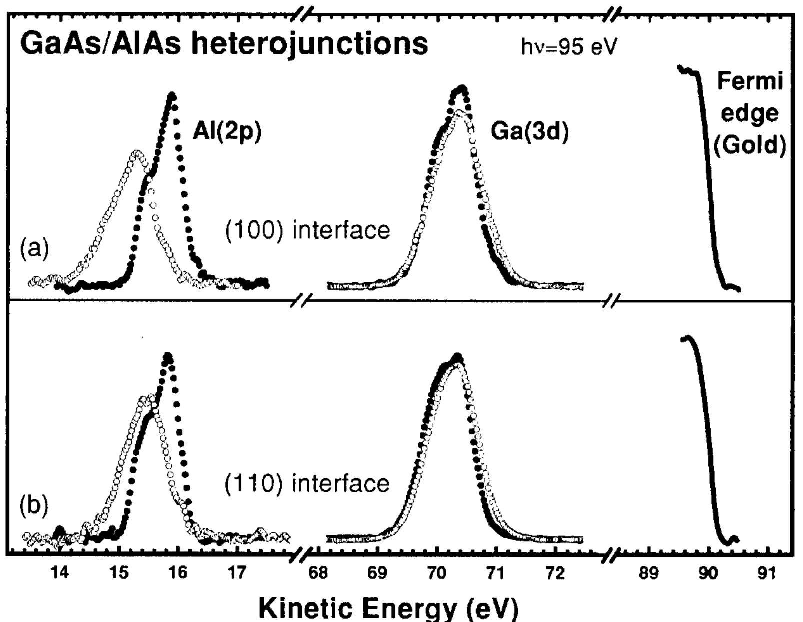

FIG. 4. Al(2*p*) and Ga(3*d*) core-level spectra recorded on GaAs/AlAs (closed circles) and GaAs/Si/AlAs (open circles) heterojunctions (GaAs on top), with 95 eV photons. Results for (a) (100), and (b) (110)-oriented interfaces. Fermi-edge spectra recorded on gold are also shown. The core-level spectra are normalized to the peak area.

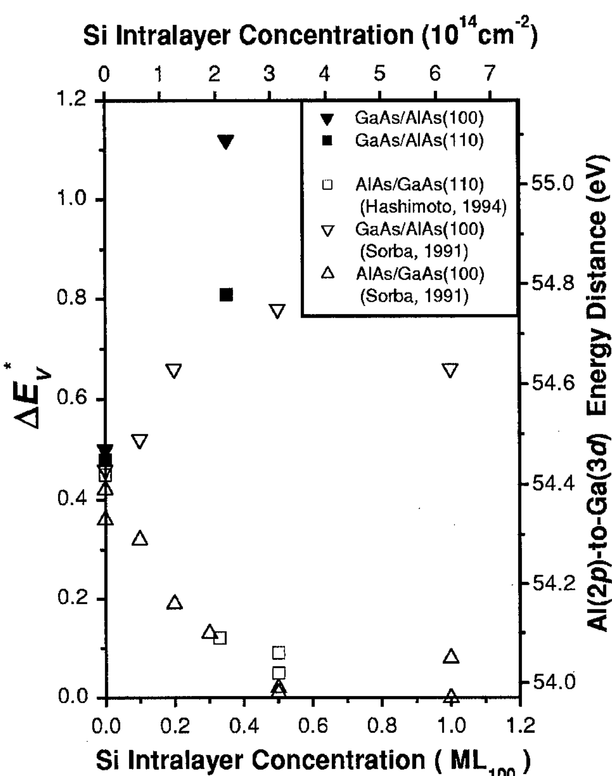

FIG. 5. *Apparent* valence-band offset and corresponding Al(2*p*)-to-Ga(3*d*) separation measured by photoemission spectroscopy on AlAs–Si–GaAs heterostructures. Our results (closed symbols) and those reported by other groups (open symbols) are shown as a function of the nominal Si-intralayer concentration for different interface orientations and stacking sequences.

Figure 5 shows a comparison of our results (closed symbols) with results obtained by other groups for the AlAs–GaAs system (open symbols). The apparent valence-band offset that we have obtained for Si-containing (100) interfaces (1.12 eV) is markedly higher than the value previously reported for the same nominal Si concentration [0.65 eV for 1/3 monolayer (ML)],[18] which we attribute to our improved method of Si deposition. Our results for GaAs-on-AlAs(110) junctions, together with the data reported[2] for the reverse stacking sequence, AlAs-on-GaAs(110), indicate that the apparent valence-band offset in nonpolar interfaces *increases* or *decreases* depending on the stacking sequence, similar to what was previously found for polar interfaces.[18]

Geometric arguments, such as those included in the microscopic-interface-capacitor model, do not explain why the band offset should change at nonpolar interfaces. The chemical asymmetry existing between each side of the interface (AlAs versus GaAs) could account for a Si-induced dipole *crossing* a nonpolar interface. However, if this explanation were valid, the same increase or decrease of the band offset should occur at the nonpolar interface independently of the stacking sequence. Muñoz and Rodríguez-Hernández predicted[40] a *reduction* of the valence-band offset at AlAs–GaAs (110) interfaces upon Si insertion. According to their calculations, the same reduction of the offset should occur for GaAs-on-AlAs and AlAs-on-GaAs junctions because, since this type of calculation does not take into account the presence of the surface, both stacking sequences are indistinguishable in the case of the (110) orientation. Thus, the *increase* or *decrease* of the apparent band offset depending on the stacking sequence observed for (110) nonpolar interfaces is explained neither by the microscopic-interface-capacitor model, nor by the chemical asymmetry of the junction, nor by the calculations of Muñoz and Rodríguez-Hernández. A model based on the establishment of ''neutral nonequivalent interfaces,'' like that recently proposed by Miwa and Ferraz,[41] could probably account for band-offset changes occurring at nonpolar interfaces. Actually, whatever the experimental result was, one could likely find a suitable ''disordered interface atomic configuration'' giving rise to a theoretical offset in agreement with experiment.[11] Arguments invoking ''neutral nonequivalent interfaces'' as responsible of band-offset changes must prove, in order to be solid, that the selected interface atomic configuration corresponds to the configuration of the real samples.

The results summarized in Fig. 5 can be readily understood within a band-bending interpretation,[19,20,22] without requiring a band-offset change altogether, as follows. The *n*-type doping character of the Si intralayer induces a sharp upward band bending in the overlayer [Fig. 2(c)]. This bending is reflected in an increase (decrease) of the Al(2*p*)-to-Ga(3*d*) energy distance measured by PES for GaAs-on-AlAs (AlAs-on-GaAs) heterostructures, as further explained below, the polarity nature of the interface being irrelevant.

B. *n*-type versus *p*-type intralayers

Figure 6 shows Al(2*p*), Ga(3*d*) and valence-band-edge spectra recorded with 95 eV photons on different GaAs-on-AlAs(100) heterostructures: (i) without intralayer (closed symbols), (ii) with a Si intralayer [open symbols in Fig. 6(a)], and (iii) with a Be intralayer [open symbols in Fig. 6(b)]. The Al(2*p*)-to-Ga(3*d*) energy separation is observed to *increase* upon Si insertion and to *decrease* upon Be insertion. The apparent valence-band offset ΔE_V^* increases by 0.59 eV upon Si insertion, and decreases by 0.19 eV upon Be insertion. The gold spectrum permits us to determine the location of the Fermi level deep in the bulk of the semiconductor samples; for equilibrium room-temperature measurements it also defines the location of the Fermi level at the sample surface. This is very useful information because it can be used as an absolute reference for the measurements performed in the different samples. The surface Fermi level is observed to lie 0.95 eV above the VBM in GaAs/AlAs(100) heterostructures without an intralayer, 0.78 eV in GaAs/Si/AlAs(100), and 1.09 eV in GaAs/Be/AlAs(100) (Fig. 6); the surface Fermi level thus approaches the VBM by 0.17 eV upon Si insertion, and shifts away by 0.14 eV upon Be insertion. Hence, the experimental results reveal an opposite behavior of the core-level separation and of the surface Fermi-level position for Si and Be insertions, which is qualitatively consistent with an interpretation in terms of band-bending effects and a doping role for the inserted impurities. They are also quantitatively consistent, as we show below.

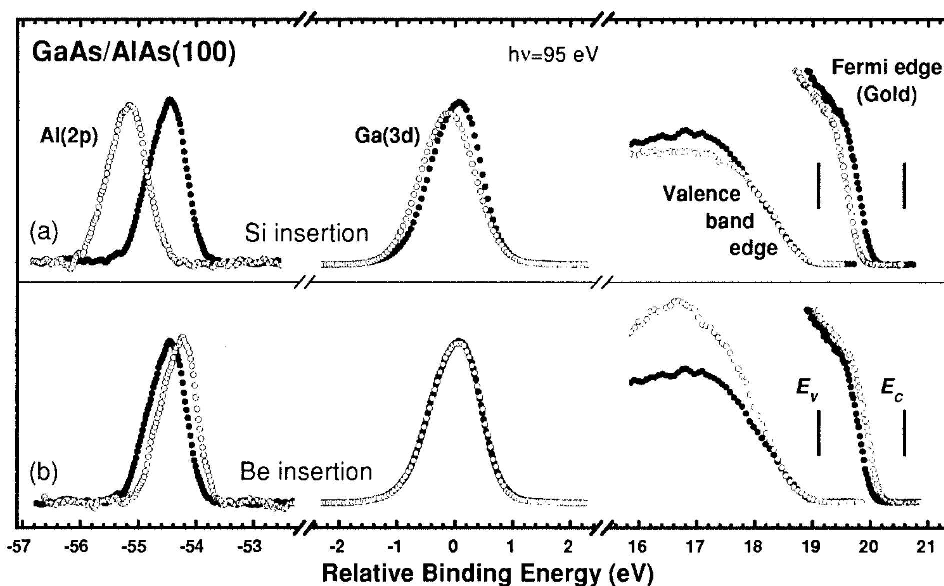

FIG. 6. Al(2*p*), Ga(3*d*) and valence-band-edge EDC spectra recorded with 95 eV photons on GaAs-on-AlAs(100) heterojunctions without (closed circles) and with (open circles) an intralayer, as well as Fermi-edge spectrum recorded on gold. The effects of (a) Si and (b) Be insertions are compared. Data are presented in a relative binding-energy scale, where the leading edges of the valence-band spectra recorded in the different samples have been aligned, and the energy zero has been arbitrarily chosen at the position of the Ga(3*d*) centroid of the sample without an intralayer. The core-level spectra are normalized to the peak area.

Our samples include three well-distinguished regions: (i) the GaAs *n*-doped substrate (region III), (ii) the AlAs buried layer (region II), and (iii) the GaAs overlayer (region I) [see Fig. 3(a)]. Some samples contain a Si or a Be δ layer at the front GaAs/AlAs interface, between layers I and II. We have calculated the band profiles along the different regions by solving Poisson's equation for *model* charge distributions appropriate to each type of sample, and introducing as input parameters the positions of the Fermi level deep in the bulk of the sample and at the surface. Deep in the bulk, the Fermi level lies close to the conduction-band minimum (CBM) due to the high *n*-type doping of the substrates. For the surface Fermi-level positions we have considered those experimentally determined for each type of sample.

In heterostructures without an intralayer we have assumed the following charge distribution: (i) a laminar charge located at the surface due to the charge trapped in surface states (σ_{SS}) and (ii) a volume charge located at the shallowest part of the Si-doped GaAs substrate, which consists of a homogeneous distribution of positively ionized Si atoms (ρ_{dep}); see Fig. 3(b). The corresponding band profile is displayed in Fig. 7(a). For heterostructures without an intralayer band bending takes place mainly along the AlAs buried layer, and the potential varies very little along the GaAs overlayer, only 0.03 V.

Accounting for the doping role of Si and Be impurities in GaAs, we have assumed that in our intralayer-containing samples a certain fraction of the inserted Si (Be) atoms becomes positively (negatively) ionized, with electrons (holes) being released to the host semiconductor lattice. Such a fraction of ionized intralayer atoms will be called the "effective doping concentration." Although the exact distribution of the intralayer atoms is unknown and some segregation and outdiffusion are expected to occur, a certain fraction of the inserted atoms likely remains localized at the interface position. For simplification, we have assumed that all the intralayer atoms acting as dopants (effective doping concentration) are confined at the interface position. Although this assumption is not expected to exactly match the real situation, since some of the outdiffused atoms could also have a doping role, it serves us to illustrate the physics of the process.

In our samples, the δ layer has been inserted at the front GaAs/AlAs interface (I/II interface), which is located only 2 nm from the surface. According to the hydrogen model, the first-orbit radius of impurity electrons (holes) in GaAs amounts to 10 nm (3 nm). Due to the close proximity of the surface, most of the impurity electrons (holes) provided by the Si (Be) intralayer are probably trapped in surface states.[42] Therefore, in our intralayer-containing heterostructures we have considered, besides a substrate volume charge ρ_{dep}, a static *capacitor-like* charge distribution [schematically depicted in Fig. 3(b)], where the electrons (holes) provided by the intralayer are trapped in surface states, thus *separated* from their parent Si (Be) atoms; a positively (negatively) charged sheet σ_{δ}, located at the interface position, represents the charge of the ionized Si (Be) atoms, and a sheet σ_{SS} represents the surface charge.

The band bending across the overlayer region can be calculated for a specific intralayer charge density or, conversely, one can calculate the intralayer charge density that produces a certain potential variation across the overlayer. We have calculated the number of ionized intralayer atoms required to induce a variation in the magnitude of the overlayer band bending that equals the changes observed in the Al(2*p*)-to-Ga(3*d*) offset displayed in Fig. 6. According to our calculations, a concentration of 2.39×10^{13} atoms cm^{-2} (7.4×10^{12} atoms cm^{-2}) must be positively (negatively) ionized to account for the experimental results obtained for insertion of Si (Be) at (100) interfaces. Figures 7(b) and 7(c) display the band profiles calculated for heterostructures with the above intralayer charge densities. It can be seen that the *n*-type Si δ layer induces sharp *upward* overlayer band bending, while

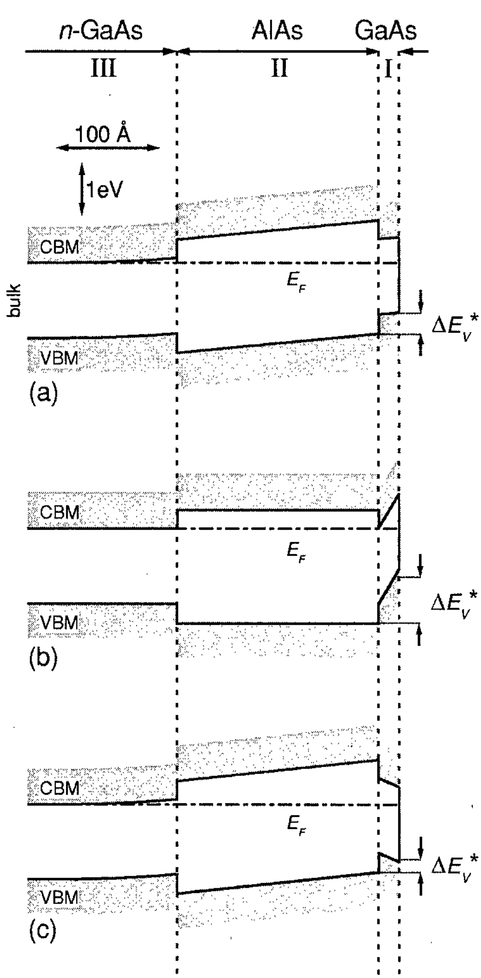

FIG. 7. Band profiles in our (a) GaAs/AlAs(100), (b) GaAs/Si/AlAs(100), and (c) GaAs/Be/AlAs(100) heterostructures. They have been calculated considering the model charge distribution shown in Fig. 3(b). An effective doping concentration of 2.39×10^{13} cm^{-2} has been assumed for the case of Si, and of 7.4×10^{12} cm^{-2} for the case of Be. The *apparent* valence-band offsets, ΔE_V^*, that would be measured by photoemission for the band profiles displayed are also shown. The horizontal lines at the right indicate the valence-band-maximum positions obtained by subtracting from the $\overline{E}_{\mathrm{Al}(2p)}$ and $\overline{E}_{\mathrm{Ga}(3d)}$ PES average energies the respective core-level binding energies.

the *p*-type Be δ layer causes *downward* overlayer band bending.

In order to understand how such intralayer-induced modifications of the band profile alter the Al(2*p*)-to-Ga(3*d*) energy separation measured in a photoemission experiment, it is important to realize that the PES signal is the result of adding up emissions from atoms located at different depths, each contribution being weighted by an exponential factor, which accounts for the attenuation of the signal due to the electron scattering. The PES average energy of a core level $\overline{E}_{\mathrm{CL}}$ can be written as follows:

$$\overline{E}_{\mathrm{CL}}=\frac{\int_0^\infty E_{\mathrm{CL}}(z)\exp(-z/\lambda)\mathrm{d}z}{\int_0^\infty \exp(-z/\lambda)\mathrm{d}z}, \tag{2}$$

where $E_{\mathrm{CL}}(z)$ is the energy of the core level as a function of the depth z, and λ is the photoelectron attenuation length. Hence, PES probes a certain volume of the sample close to the surface, strongly enhancing the signals coming from shallow regions over those originating in the deep layers. The PES average energy of the Ga(3*d*) core level, $\overline{E}_{\mathrm{Ga}(3d)}$, essentially corresponds to the value of $E_{\mathrm{Ga}(3d)}$ at the surface, being not very sensitive to energy variations along the GaAs overlayer. $\overline{E}_{\mathrm{Ga}(3d)}$ mainly reflects the variations in the Fermi-level surface pinning position. The PES average energy of the Al(2*p*) core level, $\overline{E}_{\mathrm{Al}(2p)}$, corresponds to the value of $E_{\mathrm{Al}(2p)}$ at the shallowest part of the AlAs region, being not very sensitive to energy variations along the AlAs buried layer. $\overline{E}_{\mathrm{Al}(2p)}$ is much more sensitive to changes of the overlayer band bending than $\overline{E}_{\mathrm{Ga}(3d)}$; in fact, $\overline{E}_{\mathrm{Al}(2p)}$ is shifted by the same energy amount as the magnitude of the potential drop in the overlayer. Figure 7 shows the *apparent* valence-band offsets, ΔE_V^*, that would be measured by photoemission for samples with the band profiles displayed. The horizontal lines at the right of Fig. 7 indicate the valence-band-maximum positions obtained by subtracting from $\overline{E}_{\mathrm{Al}(2p)}$ and $\overline{E}_{\mathrm{Ga}(3d)}$ the respective core-level binding energies. Note that ΔE_V^* does not correspond to the real interface valence-band offset; ΔE_V^* is strongly affected by the overlayer band bending, an upward (downward) bending of the overlayer bands resulting in a larger (shorter) value of ΔE_V^*.

From the above model calculations we infer that about 2×10^{13} Si atoms cm^{-2} (7×10^{12} Be atoms cm^{-2}) must be ionized in the Si (Be) intralayer to account for the observed Al(2*p*)-to-Ga(3*d*) offset variations on the basis of a band-bending effect. Such *effective doping* concentration has a direct relation to the *free-carrier* concentration determined by Hall-effect measurements. Hall-effect experiments indicated that the *pulsed low-flux* impurity-deposition recipe that we have used permits one to obtain carrier concentrations in the 10^{13} cm^{-2} range for Si δ-layer atomic concentrations in the high-10^{13}/low-10^{14}) atoms cm^{-2} range.[38,39] Thus, the effective doping concentrations necessary to explain the experimental results on the basis of a band-bending effect are actually achieved.

It is thus possible to successfully explain the observed *apparent* valence-band offset variations (Fig. 6) solely on the basis of intralayer-induced modifications of the overlayer band bending, with no need to include any change of the *real* interface band offset. In our interpretation the overlayer band bending results from trapping of the carriers provided by the intralayer in surface states, being thus separated from their ionized parent intralayer atoms. Segregation of intralayer atoms and *bulk* doping are not necessary for the build up of an overlayer band bending, just a separation of charges across the overlayer (overlayer capacitor effect) is needed. The band-bending interpretation provides a straightforward explanation for the fact that Si and Be intralayers induce changes of opposite sign: this can be easily understood accounting for the respective *n*-type and *p*-type doping behaviors.

The overlayer-capacitor model that we have used to illustrate the band-bending interpretation differs substantially from the interface-capacitor model previously invoked to explain the proposed intralayer-induced band-offset changes.

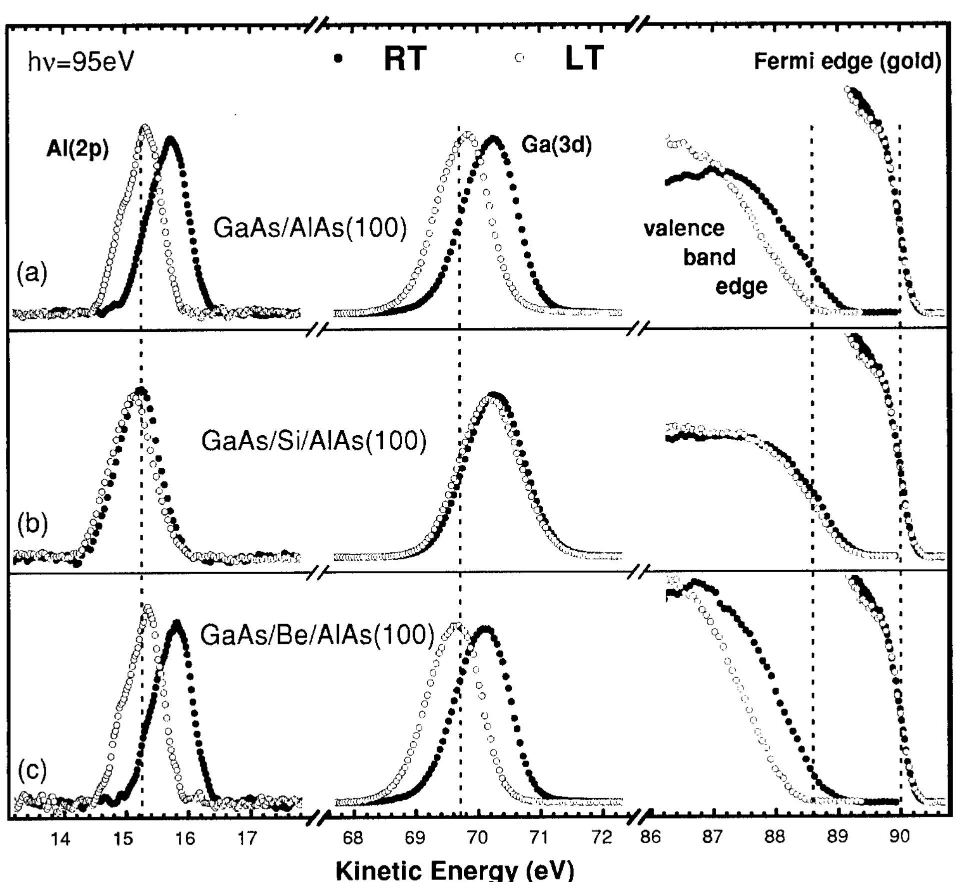

FIG. 8. Al(2*p*), Ga(3*d*) and valence-band-edge EDC spectra recorded with 95 eV photons at room temperature (closed circles) and at low temperature $T \sim 220$ K (open circles) on (a) GaAs/AlAs(100), (b) GaAs/Si/AlAs(100), and (c) GaAs/Be/AlAs(100) heterostructures. Gold Fermi-edge spectra are also shown. The core-level spectra are normalized to the peak area. The vertical dotted lines mark the kinetic-energy positions corresponding to the Al(2*p*), Ga(3*d*), and valence-band-maximum levels under flat-band conditions, as well to the *bulk* Fermi level.

The polarity nature of the interface plays a key role within the interface-capacitor model, but it is not important for the model here proposed, as long as the properties of the growth on different substrate orientations do not change the effective doping concentration. We have observed Si-induced core-level offset variations that are larger for polar GaAs/AlAs(100) junctions than for nonpolar GaAs/AlAs(110) ones (Fig. 4). This result can be well understood within the band-bending interpretation, since the strength of the overlayer-capacitor effect depends on the *effective doping* concentration of the intralayer; such a concentration is expected to be higher in (100)-oriented samples than in (110)-oriented ones, for two reasons: (i) because self-compensation is known to be more important for growth on (110) substrates[43] and (ii) because the Si-insertion recipe used here was specifically optimized for the (100) growth direction.[38] Figure 5 shows that the core-level offset variation that we have observed upon Si insertion at GaAs-on-AlAs(100) junctions is remarkably larger than the changes previously reported by other groups. Such an observation can be also explained within the band-bending interpretation: the larger effect is likely due to the higher doping efficiency of our pulsed low-flux Si-deposition technique in comparison with the growth recipes employed by other groups.

Although the position of the intralayer with respect to the surface is irrelevant within the interface-capacitor model, it plays a key role in our overlayer-capacitor model. No differences in the strength of the microscopic interface capacitor are in principle expected between the samples used in PES experiments and in devices. However, charge separation in the overlayer and the associated band bending occurs only if a certain number of the carriers provided by the intralayer becomes trapped in surface states, which requires that the intralayer is located close enough to the surface. Although such a condition is easily fulfilled in samples typically analyzed in a photoemission experiment, the relevance of the overlayer-capacitor effect is not clear for the type of heterojunctions with deeply buried interfaces that are generally used in devices.

C. Surface photovoltage effects

Surface photovoltage effects can have a strong influence on the kinetic energies measured by photoemission for core levels of semiconductor materials.[25,29,34] Figures 8(a)–8(c) show Al(2*p*), Ga(3*d*), and valence-band-edge spectra recorded with 95 eV photons at room and at low temperature (RT and LT) on GaAs-on-AlAs(100) heterostructures without an intralayer, with a Si intralayer, and with a Be intralayer, respectively. Figure 8 also shows gold Fermi-edge spectra. The LT signals from the GaAs/AlAs(100) and GaAs/Be/AlAs(100) heterostructures appear significantly shifted relative to the RT emissions. In contrast, for the GaAs/Si/AlAs(100) heterostructure the PES signals scarcely shift upon cooling (<0.1 eV). The Al(2*p*), Ga(3*d*), and valence-band-edge signals *rigidly* shift by 0.43 and 0.47 eV toward lower kinetic energies for the GaAs/AlAs(100) and

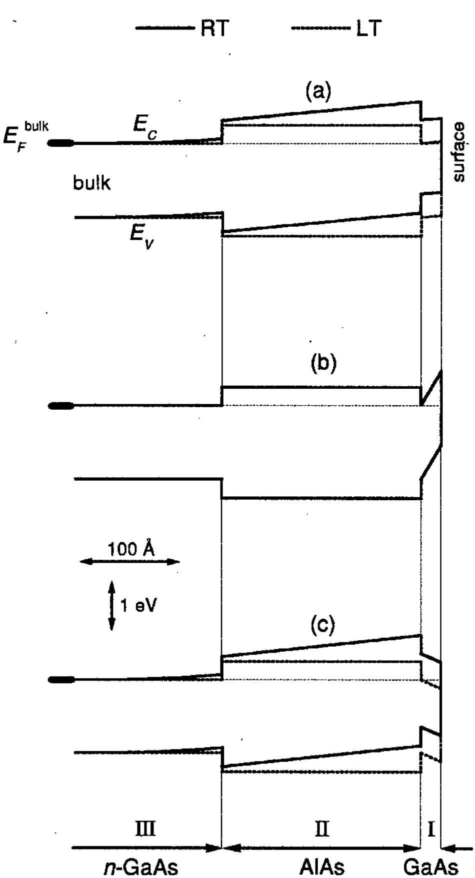

FIG. 9. Band profiles proposed for (a) GaAs/AlAs(100), (b) GaAs/Si/AlAs(100), and (c) GaAs/Be/AlAs(100) heterostructures, when illuminated with 95 eV photons at room temperature (solid lines) and low temperature (dotted lines). The horizontal dash-dotted thin lines mark the energy position of the Fermi level *deep in the bulk* of the samples.

GaAs/Be/AlAs(100) heterostructures, respectively. Noticeably, for the three types of samples, the Al(2*p*)-to-Ga(3*d*) energy separations measured at LT are *identical* to those measured at RT, and the Al(2*p*) peaks approximately converge upon cooling on a common energy position.

The shifts of the PES signals observed upon cooling (Fig. 8) can be explained by the occurrence of photoinduced nonequilibrium processes at LT, which modify the RT band profiles. Since light penetrates even into the *n*-GaAs substrate, SPV effects can in principle occur in the GaAs overlayer, the AlAs buried layer, and even in a portion of the *n*-GaAs substrate. The temperature-dependent results can be understood by considering light-induced modifications of the proposed RT band profiles (Fig. 7), so that at LT bands become completely flat in the AlAs region, and the band bending in the GaAs overlayer persists (see the LT profiles displayed in Fig. 9 as dotted lines).

According to the band profile proposed for the GaAs/Si/AlAs(100) heterostructure at RT [solid lines in Fig. 9(b)], the bands are flat along the AlAs region. There is thus no reason for induction of a photovoltage in the AlAs layer, which explains why the Al(2*p*) signal scarcely moves upon cooling in the case of the Si-containing heterostructure (Fig. 8). To the contrary, the RT band profiles proposed for the GaAs/AlAs(100) and GaAs/Be/AlAs(100) heterostructures indicate the existence of *upward* band bending in the AlAs region [see the solid lines in Figs. 9(a) and 9(c)]. Thus, a photovoltage can be induced, producing band flattening in the AlAs layer, and consequently a shift of the Al(2*p*) signal toward *lower* kinetic energies, as observed experimentally (Fig. 8).

The Al(2*p*) signal originates close to the front AlAs/GaAs interface. The kinetic energy expected for the Al(2*p*) signal if the bands were completely flat all along the *n*-GaAs substrate and the AlAs buried layer in any of our GaAs/AlAs/*n*-GaAs(100) samples is marked in Fig. 8 by a vertical dotted line, and corresponds to a value $E_k=15.24$ eV.[44] At LT the Al(2*p*) centroids appear at kinetic energies of 15.28, 15.09, and 15.29 eV for the GaAs/AlAs(100), GaAs/Si/AlAs(100), and GaAs/Be/AlAs(100) samples, respectively. The position of the Al(2*p*) peaks measured on the three types of heterostructures at LT is thus very close to the "flatband" energy. Taking into account the fact that the band profiles proposed for the AlAs layer and the *n*-GaAs substrate of the GaAs/AlAs(100) and GaAs/Be/AlAs(100) samples at RT favor the establishment of a photovoltage, it is reasonable to conclude that the bands become completely flat from the front AlAs/GaAs interface down to the deep *n*-GaAs bulk, as depicted in Fig. 9 (dotted lines). Note that the band profile proposed for the Si-containing structure is already flat at RT along this region.

The Ga(3*d*) signal and the leading edge of the valence-band spectrum mainly originate close to the GaAs surface. In a *hypothetical* situation where the bands were completely flat all along the GaAs/AlAs/*n*-GaAs(100) heterostructures, the Ga(3*d*) signal and the valence-band leading edge would appear at kinetic energies of 69.71 and 88.57 eV, respectively,[45] assuming a *constant* band-offset value upon intralayer insertion. Such flat-band energy positions are marked in Fig. 8 as vertical dotted lines. The Ga(3*d*) signals and the leading edges of the valence-band spectra for the intralayer-containing samples are seen to deviate from such flat-band positions, at both RT and LT (Fig. 8). The shifts of the Ga(3*d*) and valence-band-edge signals cannot be explained as being due to light-induced flattening of the GaAs-overlayer bands, since the constancy of the Al(2*p*)-to-Ga(3*d*) energy separation upon cooling (Fig. 8) implies that the overlayer band bending does not change. However, these shifts can be well understood as being a consequence of the light-induced flattening of the AlAs bands, which additionally causes the bands of the GaAs overlayer to be rigidly "pulled down" toward higher binding energies (as depicted in Fig. 9), so that the Ga(3*d*) and valence-band-edge signals are shifted toward lower kinetic energies. The persistence of the overlayer band bending is probably due to the role played by the interface band discontinuities, which act as energy barriers preventing the transport of the photogenerated carriers through the interface. In the three heterostructures considered, the band discontinuities existing at the front AlAs–GaAs interface restrict the spatial separation of the electron-hole pairs photogenerated within the overlayer to the thickness of the overlayer itself, which is only 2 nm. The

overlap of the electron and hole wave functions inside the thin overlayer is considerable (the Bohr's radius of free electrons is ~10 nm and of free holes ~3 nm). Therefore, the electron-hole recombination is high, and the establishment of a photovoltage in the overlayer region is ineffective.

IV. CONCLUSIONS

We have demonstrated, through the examination of polar and nonpolar interfaces, intralayers of different doping type, and photoelectron spectra recorded under conditions where a surface photovoltage exists, that no change in the band offset of the heterojunction upon intralayer insertion needs to be invoked in order to arrive at a consistent description of our results. Indeed, some of our results are in direct contradiction of the interface-capacitor model previously invoked to explain such type of photoemission data. Rather, we propose an overlayer-capacitor model in which charge separation between the surface and the intralayer builds up a strong electric field in the overlayer. Hence, the photoemission results are explained in terms of band-bending profile changes.

ACKNOWLEDGMENTS

The authors gratefully acknowledge P. Schützendübe and H. P. Schönherr for their expert MBE assistance, W. Braun for the flexibility in the beam-time scheduling, necessary to coordinate the synchrotron experiments performed at BESSY with the MBE sample growth, J. A. Martín-Gago, C. Rojas, F. Schneider, C. Polop, S.-A. Ding, and S. Barman for technical assistance during the synchrotron beam times, and H. Kostial, H. Yang, and A. Yamada for valuable discussions. One of the authors (M. M.) acknowledges financial aid from the Comunidad Autónoma de Madrid (Spain). This work was partially supported by the Spanish Dirección General de Investigación Científica y Técnica under Grant Nos. PB98-524 and PB97-1195. The work at BESSY was supported by the EU Human Capital and Mobility Programme under Contract No. CHGE-CT93-0027.

[1]C. G. Van de Walle and R. M. Martin, Phys. Rev. B **34**, 5621 (1986).
[2]C. G. Van de Walle and R. M. Martin, Phys. Rev. B **37**, 4801 (1988).
[3]S. Baroni, R. Resta, A. Baldereschi, and M. Peressi, in *Spectroscopy of Semiconductor Microstructures*, edited by G. Fasol, A. Fasolino and P. Lugli (Plenum, London, 1989), Vol. 206, p. 251.
[4]W. R. L. Lambrecht and B. Segall, Phys. Rev. B **41**, 8353 (1990).
[5]A. Baldereschi, R. Resta, M. Peressi, S. Baroni, and K. Mäder, in *Semiconductor Interfaces at the Sub-Nanometer Scale*, edited by H. W. M. Salemink and M. D. Pashley (Kluwer, Dordrecht, 1993), Vol. 243, p. 59.
[6]S. Baroni, R. Resta, and A. Baldereschi, in *Proceedings of the 19th International Conference on the Physics of Semiconductors*, edited by W. Zawadzki (Institute of Physics, Polish Academy of Sciences, Wroclaw, 1988), p. 525.
[7]A. Muñoz, N. Chetty, and R. M. Martin, Phys. Rev. B **41**, 2976 (1990).
[8]M. Peressi, S. Baroni, R. Resta, and A. Baldereschi, Phys. Rev. B **43**, 7347 (1991).
[9]D. M. Bylander and L. Kleinman, Phys. Rev. B **41**, 3509 (1990).
[10]W. A. Harrison, E. A. Kraut, J. R. Waldrop, and R. W. Grant, Phys. Rev. B **18**, 4402 (1978).
[11]A. Franciosi and C. G. Van de Walle, Surf. Sci. Rep. **25**, 1 (1996).
[12]R. M. Martin, J. Vac. Sci. Technol. **17**, 978 (1980).
[13]R. G. Dandrea, S. Froyen, and A. Zunger, Phys. Rev. B **42**, 3213 (1990).
[14]G. Biasiol, L. Sorba, G. Bratina, R. Nicolini, A. Franciosi, M. Peressi, S. Baroni, R. Resta, and A. Baldereschi, Phys. Rev. Lett. **69**, 1283 (1992).
[15]E. A. Kraut, R. W. Grant, J. R. Waldrop, and S. P. Kowalczyk, Phys. Rev. Lett. **44**, 1620 (1980).
[16]R. W. Grant, E. A. Kraut, S. P. Kowalczyk, and J. R. Waldrop, J. Vac. Sci. Technol. B **1**, 320 (1983).
[17]E. A. Kraut, R. W. Grant, J. R. Waldrop, and S. P. Kowalczyk, Phys. Rev. B **28**, 1965 (1983).
[18]L. Sorba, G. Bratina, G. Ceccone, A. Antonini, J. F. Walker, M. Micovic, and A. Franciosi, Phys. Rev. B **43**, 2450 (1991).
[19]M. Akazawa, H. Hasegawa, H. Tomozawa, and H. Fujikura, Jpn. J. Appl. Phys., Part 2 **31**, L1012 (1992).
[20]Y. Hashimoto, G. Tanaka, and T. Ikoma, J. Vac. Sci. Technol. B **12**, 125 (1994).
[21]M. Moreno, H. Yang, M. Höricke, M. Alonso, J. A. Martín-Gago, R. Hey, K. Horn, J. L. Sacedón, and K. H. Ploog, Phys. Rev. B **57**, 12314 (1998).
[22]M. Moreno, J. L. Sacedón, M. Alonso, M. Höricke, R. Hey, J. Avila, M. C. Asensio, K. Horn, and K. H. Ploog, Phys. Rev. B **58**, 13767 (1998).
[23]T. Ogama, J. Appl. Phys. **64**, 753 (1988).
[24]G. Margaritondo, F. Gozzo, and C. Coluzza, Phys. Rev. B **47**, 9907 (1993).
[25]M. Alonso, R. Cimino, and K. Horn, Phys. Rev. Lett. **64**, 1947 (1990).
[26]M. Alonso, R. Cimino, C. Maierhofer, T. Chassé, W. Braun, and K. Horn, J. Vac. Sci. Technol. B **8**, 955 (1990).
[27]S. Chang, I. M. Vitomirov, L. J. Brillson, D. F. Rioux, P. D. Kirchner, G. D. Pettit, J. M. Woodall, and M. H. Hecht, Phys. Rev. B **41**, 12299 (1990).
[28]D. Mao, A. Kahn, M. Marsi, and G. Margaritondo, Phys. Rev. B **42**, 3228 (1990).
[29]M. Alonso, R. Cimino, and K. Horn, J. Vac. Sci. Technol. A **9**, 891 (1991).
[30]T. U. Kampen, D. Troost, X. Y. Hou, L. Koenders, and W. Mönch, J. Vac. Sci. Technol. B **9**, 2095 (1991).
[31]A. Bauer, M. Prietsch, S. Molodtsov, C. Laubschat, and G. Kaindl, J. Vac. Sci. Technol. B **9**, 2108 (1991).
[32]D. A. Evans, T. P. Chen, T. Chassé, and K. Horn, Appl. Surf. Sci. **56–58**, 233 (1992).
[33]R. Cimino, A. Gearante, M. Alonso, and K. Horn, Appl. Surf. Sci. **56–58**, 151 (1992).
[34]K. Horn, M. Alonso, and R. Cimino, Appl. Surf. Sci. **56–58**, 271 (1992).
[35]D. Mao, M. Santos, M. Shayegan, A. Kahn, G. Le Lay, Y. Hwu, G. Margaritondo, L. T. Florez, and J. P. Harbison, Phys. Rev. B **45**, 1273 (1992).
[36]M. H. Hecht, Phys. Rev. B **41**, 7918 (1990).
[37]M. H. Hecht, J. Vac. Sci. Technol. B **8**, 1018 (1990).
[38]L. Däweritz, H. Kostial, R. Hey, M. Ramsteiner, J. Wagner, M. Maier, J. Behrend, and M. Höricke, J. Cryst. Growth **150**, 214 (1995).
[39]K. H. Ploog and L. Däweritz, Jpn. J. Appl. Phys., Part 1 **34**, 691 (1995).
[40]A. Muñoz and P. Rodríguez-Hernández, Phys. Rev. B **45**, 4502 (1992).
[41]R. H. Miwa and A. C. Ferraz, Phys. Rev. B **59**, 12499 (1999).
[42]J. F. Sampaio, S. L. S. Freire, and E. S. Alves, J. Appl. Phys. **81**, 530 (1997).
[43]J. M. Ballingall and C. E. C. Wood, J. Vac. Sci. Technol. B **1**, 162 (1983).
[44]This "flat-band energy" has been calculated assuming the values: $E_g^{GaAs}=1.43$ eV for the GaAs band gap, $\Delta E_V=0.47$ eV for the GaAs/AlAs valence-band offset, and $E_{Al(2p)}-E_V=-72.86$ eV for the Al(2*p*) binding energy. We have determined the valence-band offset value through PES measurements of the "apparent" offset in the GaAs/AlAs(100) heterostructure without an intralayer at RT, which give $\Delta E_V^*=0.5$ eV. In order to obtain the "real" offset, the value of the overlayer band bending (0.03 eV, calculated by solving Poisson's equation) must be subtracted.
[45]The flat-band kinetic-energy value for the Ga(3*d*) level has been calculated assuming the value $E_{Ga(3d)}-E_V=-18.86$ eV for the Ga(3*d*) binding energy.

Epitaxial oxide thin films on Si(001)*

Z. Yu,[a] J. Ramdani, J. A. Curless, C. D. Overgaard, J. M. Finder, R. Droopad, K. W. Eisenbeiser, J. A. Hallmark, and W. J. Ooms
Physical Sciences Research Laboratories-Motorola Labs, 2100 E. Elliot Road, Tempe, Arizona 85284

V. S. Kaushik
Motorola Digital DNA Labs, 3501 Ed Bluestein Boulevard, Austin, Texas 78721

(Received 17 January 2000; accepted 3 April 2000)

Over the years, the development of epitaxial oxides on silicon has been a great technological challenge. Amorphous silicon oxide layer forms quickly at the interface when the Si surface is exposed to oxygen, making the intended oxide heteroepitaxy on Si substrate extremely difficult. Epitaxial oxides such as $BaTiO_3$ (BTO) and $SrTiO_3$ (STO) integrated with Si are highly desirable for future generation transistor gate dielectric and ferroelectric memory cell applications. In this article, we review the recent progress in the heteroepitaxy of oxide thin films on Si(001) substrate by using the molecular beam epitaxy technique at Motorola Labs. Structural, interfacial and electrical properties of the oxide thin films on Si have been characterized using *in situ* reflection high energy electron diffraction, x-ray diffraction, spectroscopic ellipsometry, atomic force microscopy, Auger electron spectroscopy, x-ray photoelectron spectroscopy, high-resolution transmission electron microscopy, high-resolution transmission electron energy loss spectroscopy, capacitance–voltage and current–voltage measurement. We also present the transistor results and address the impact of the epitaxial oxide films on future generation metal-oxide-semiconductor field effect transistors. © *2000 American Vacuum Society.* [S0734-211X(00)00504-7]

I. INTRODUCTION

Perovskite-type oxide thin films are very attractive materials due to their simple crystal structures and unique ferroelectric, dielectric, and optical properties. Epitaxial ferroelectric oxides integrated with Si are very attractive for nonvolatile memory transistor applications.[1] Among the choices for ferroelectric films epitaxially grown on silicon, perovskite-type $BaTiO_3$ (BTO) is one of the most promising candidates, with desirable structural and ferroelectric properties. BTO has a tetragonal (pseudo-cubic) crystal with structure with an *a*- and *b*-axis lattice constant of 3.992 Å and *c*-axis lattice constant of 4.036 Å at room temperature. Thus, the lattice mismatch with silicon is reasonably small (~3.9%) when the BTO unit cell is rotated 45° on its [001] axis. Epitaxial $BaTiO_3$ films grown on silicon are also attractive materials for both optical waveguides[2,3] and field effect transistor (FET)[4,5] applications. However, there have been very few reports of epitaxial growth of $BaTiO_3$ thin films on Si by molecular beam epitaxy (MBE).[3,6]

The ever shrinking size of the metal-oxide-semiconductor field effect transistors (MOSFETs) in the integrated circuits demands even smaller dimensions of effective gate oxide thickness. For MOSFET applications, traditional SiO_2 gate oxide is quickly approaching its physical scaling limit due to severe direct tunneling leakage and poor reliability.[7] And it is critical to develop suitable alternative gate oxides to overcome these problems. In fact, there has been an extensive search for suitable high dielectric constant (high-*k*) gate oxides to replace SiO_2 for future-generation MOSFET applications in recent years. Among the reported high-*k* materials,[8–18] perovskite-type $SrTiO_3$ (STO) lends itself as one of the most promising candidates for alternative gate oxide with desirable structural and dielectric properties. STO has a simple cubic crystal structure and a high bulk *k* value of 300 at room temperature. The lattice mismatch between STO ($a_0=3.905$ Å) and Si ($a_0=5.431$ Å) is also fairly small (~1.7%) with STO unit cell rotated 45° around Si surface normal [001] axis. For device applications, high-quality epitaxial oxide films are expected to offer better uniformity, lower leakage, and higher reliability than amorphous and polycrystalline ones. An epitaxial oxide thin film also serves as an excellent buffer layer for subsequent heteroepitaxy of various functional oxides including ferroelectric[19] and high-T_c superconductor[20] thin films on Si substrates. In addition, single crystalline oxide thin films are expected to play an important role in silicon-on-insulator (SOI) technology. Over the years, however, the growth of single crystalline oxides on silicon has been a great technological challenge due to the easily formed amorphous silicon oxide layer on Si surface in an oxygen atmosphere, preventing the intended oxide heteroepitaxy on Si substrate. So far, there have been a few reports of successful epitaxial oxide growth (e.g., SrO, BaO, STO, BTO) on Si substrate using pulsed laser deposition (PLD),[20–22] e-beam deposition[23,24] and MBE.[16–18,25] Among the growth techniques, MBE offers the best control over the quality of the STO film and the oxide/Si interface. MBE as-grown crystalline BTO and STO films (3 unit-cell thick) on Si(001) without an amorphous interfacial layer have been reported by using *Z*-contrast scanning TEM.[16,17]

In this article, we review the recent progress in the heteroepitaxy of oxide thin films on Si(001) at Motorola Labs.

*No proof corrections received from author prior to publication.
[a]Electronic mail: a780aa@email.mot.com

Structural, interfacial and electrical properties are characterized using *in situ* reflection high energy electron diffraction (RHEED), x-ray diffraction (XRD), spectroscopic ellipsometry (SE), atomic force microscopy (AFM), Auger electron spectroscopy (AES), x-ray photoelectron spectroscopy (XPS), Rutherford backscattering spectroscopy (RBS), high-resolution cross-sectional transmission electron microscopy (HRTEM), high-resolution transmission electron energy loss spectroscopy (HREELS), current–voltage ($I-V$), and capacitance–voltage ($C-V$) measurements. Finally, MOSFET devices with epitaxial STO gate dielectrics are fabricated and tested.

II. EXPERIMENT

Commercial Si(001) wafers with sizes up to 8 in. in diameter were used in the experiment. All MBE growth runs were conducted in an upgraded V100 production-type MBE system equipped with a turbo-molecular pump and a titanium sublimation pump. The growth chamber base pressure is below mid-10^{-10} mbar. Ba, Sr, Ti metals from effusion cells and oxygen were used as deposition sources, respectively. *In situ* RHEED was used to monitor the growing surface in real time during the entire growth process. The kinetic energy of the RHEED electron beam is 15 keV. RHEED images were captured by a charge coupled device (CCD) camera interfaced with a personal computer. The as-received substrate was transferred into the growth chamber and heated to temperatures below 800 °C before being exposed to a Sr metal flux, until an ordered interface structure was formed on Si(001) surface. BTO and STO films were deposited on such ordered structure at temperatures ranging from 200 to 700 °C under up to 10^{-5} mbar O_2 partial pressure in the growth chamber. RHEED indicated that the coherent surface ordering was maintained throughout the entire growth process, especially at the initial nucleation stage. The crystallinity of the films was also characterized by XRD theta-2theta and pole-figure scans. Film thickness and refractive index were measured using a SE spectrometer. Film surface morphology was mapped using AFM with a Si probe tip. Film composition was examined by AES, XPS and RBS. High-resolution cross-sectional TEM was used to evaluate the oxide film and its interface with Si substrate. And the high-resolution transmission EELS was employed to help further identify the chemical nature of the interfacial layer. The probe size was 1.0–1.5 nm and the probe step was 0.5–1.0 nm depending on the magnification used. Electrical and interfacial properties of the STO films on Si were characterized by $I-V$ and $C-V$ measurements on the MOS capacitors. Finally, MOSFET (effective channel length $L_{\mathrm{eff}}=1.2\,\mu\mathrm{m}$) was fabricated and tested using epitaxial STO as the alternative gate oxide.

III. RESULTS AND DISCUSSION

A. $BaTiO_3$

Figures 1(a) and 1(b) are the RHEED patterns of a BTO film grown on a SrO buffered Si substrate. These streaky and bright patterns clearly indicate the smooth BTO surface and high degree of crystallinity of the film. The film thickness and refractive index are measured by SE as 217 Å and 2.17 (633 nm), respectively. XRD theta-2theta scan plotted in Fig. 2 has only BTO 200 and BTO 100 diffraction peaks at 22.3° and 45.6°, respectively, along with part of the Si 004 peak, which implies that the BTO film is *a*-axis oriented, i.e., BTO(100)//Si(001). As shown in Fig. 3, the BTO surface appears very smooth and the measured AFM rms roughness is only 4.6 Å. The simultaneous quasistatic and high-frequency $C-V$ characteristics depicted in Fig. 4 show well-behaved progression from accumulation to inversion and depletion. The interface state density (D_{it}) is only $2\times10^{11}\,\mathrm{eV}^{-1}\,\mathrm{cm}^{-2}$. The extracted dielectric constant of the film is about 14. The exact cause for this has not been determined. From the $I-V$ curve in Fig. 5, one can see that the leakage current density is below $1\times10^{-7}\,\mathrm{A\,cm}^{-2}$ at ±2 V bias. It is worth noting that the film was annealed in O_2 for 5 min at 600 °C and in H_2 (forming gas) for 15 min at 400 °C prior to electrical testing. And there was no degradation of the $C-V$ or $I-V$ performance observed due to this hydrogen exposure. Meanwhile, there was no observed hysteresis in the epitaxial BTO films. Increasing biases were applied until

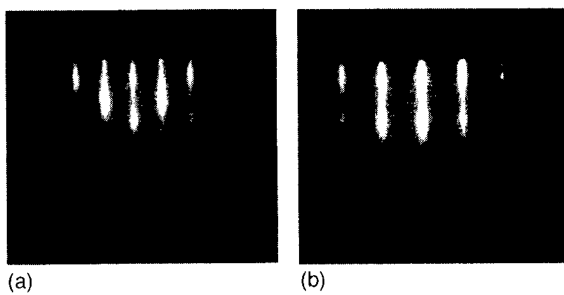

FIG. 1. RHEED patterns of a 271 Å $BaTiO_3$ film on SrO/Si(001). (a) Along SrO[110]/Si[110]; (b) along SrO[100]/Si[100].

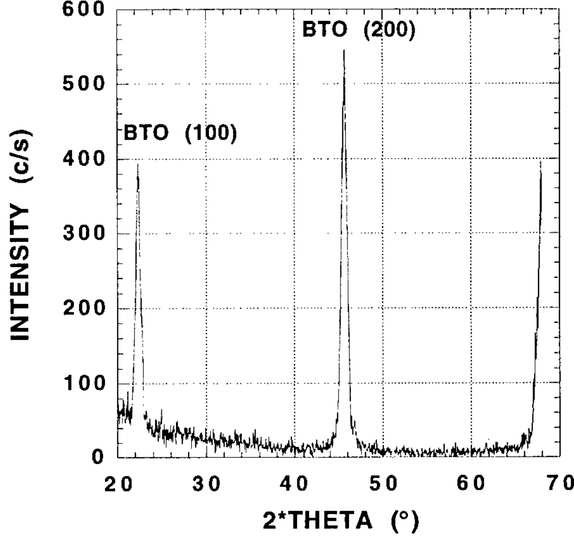

FIG. 2. XRD theta-2theta scan of the $BaTiO_3$ film. Only $BaTiO_3$ 200 and 100 diffraction peaks are observed, indicating *a*-axis orientation.

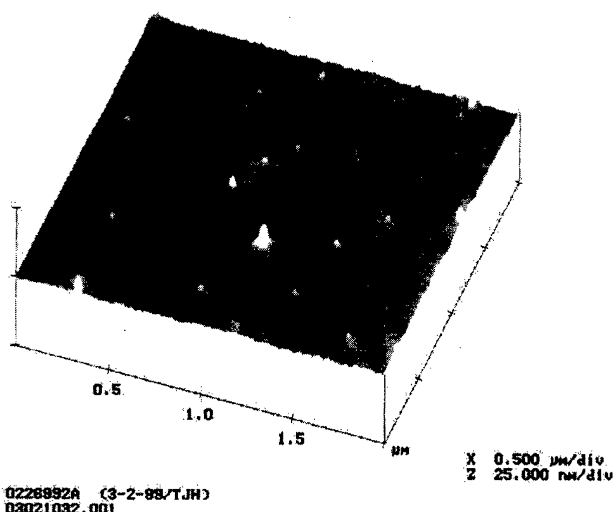

FIG. 3. AFM image of the $BaTiO_3$ film. The rms roughness is 4.6 Å.

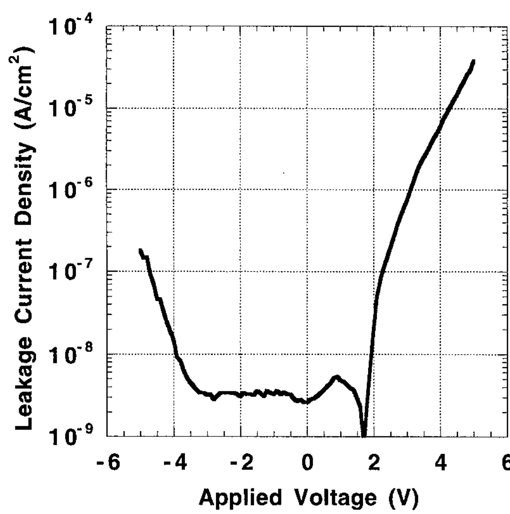

FIG. 5. $I-V$ characteristics of the BTO film. Leakage current density is below 1×10^{-7} A cm^{-2} at ±2 V.

dielectric breakdown occurred at 10 V. This is not surprising considering the *a*-axis orientation seen in the XRD (Fig. 2). Further work is planned to optimize the growth process, interface, and film structure.

B. $SrTiO_3$

Figure 6 shows RHEED patterns of an STO thin film on Si(001) along STO[100] and STO [110] azimuths, respectively. The film thickness was measured to be 145 Å by SE which also yielded a refractive index $n=2.25$ at 633 nm wavelength, which is close to the bulk value of 2.4. Routinely obtained with Kikuchi lines and Kikuchi bands, the bright and streaky RHEED patterns clearly indicate the epitaxial nature and high degree of crystallinity of the STO film. It is also noted from the RHEED zone axis that the unit cell of the STO film is rotated 45° with respect to the underlying Si substrate. The STO surface appears extremely smooth and no spotty features associated with structural defects are present in the RHEED images. XRD theta-2theta scan depicted in Fig. 7 confirms the pure (001) orientation of the epitaxial STO film. A strong STO 002 diffraction peak at 45.9° and a weaker STO 001 peak at 22.5° are the only STO

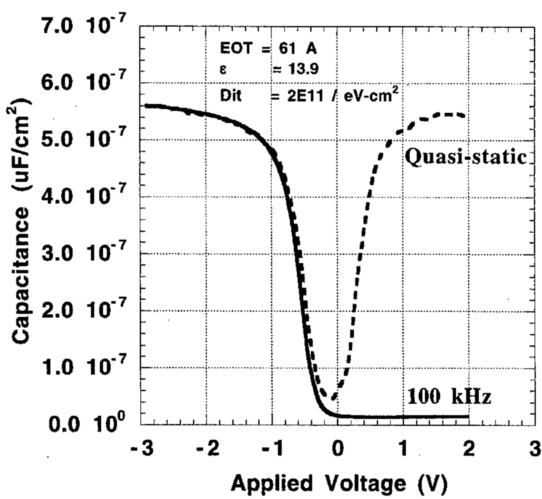

FIG. 4. Simultaneous quasistatic and high-frequency $C-V$ characteristics of the BTO film.

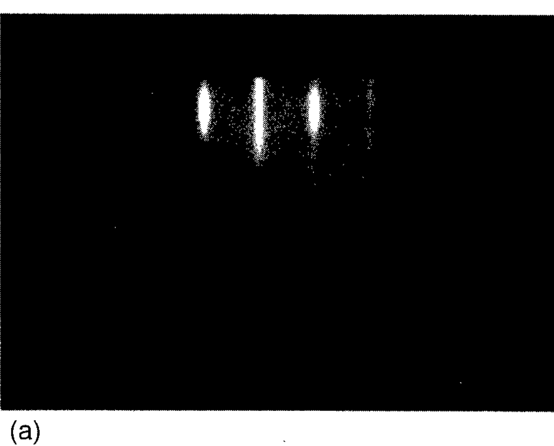

(a)

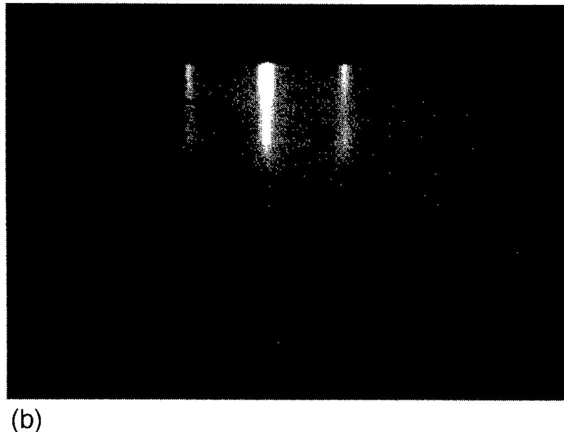

(b)

FIG. 6. RHEED patterns of a 145-Å-thick STO film on Si(001) along (a) STO[010] and (b) STO[110] zone axis.

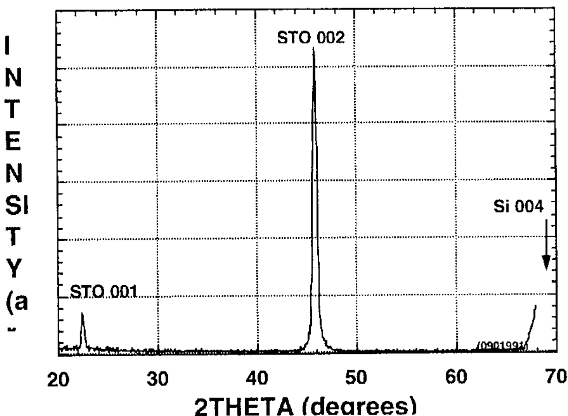

FIG. 7. XRD theta-2theta scan of a 254-Å-thick $SrTiO_3$ film. The FWHM of the STO 002 peak is 0.5°.

features in addition to the Si 004 diffraction, i.e., no extra XRD peaks from other crystalline orientations of the STO film exist in the measured 2theta range. The full width at half maximum (FWHM) of the STO 002 peak is 0.5° and the film thickness is 254 Å from SE measurement. The in-plane epitaxial relationship was also examined by x-ray pole-figure scans. Four poles corresponding to the reflections from STO{011} family planes were observed 45° apart from the Si{011} poles. Therefore, both RHEED and XRD have confirmed that perovskite oxide heteroepitaxy on Si substrate develops with STO(001)//Si(001) and STO[100]//Si[110]. In other words, the STO unit cell is indeed rotated 45° around the surface normal [001] axis with respect to the underlying Si unit cell, as predicted. The AFM image of the STO surface is shown in Fig. 8, where the smooth surface morphology is observed with no signs of micro cracks, pinholes, or grains. The measured rms surface roughness is only 1.2 Å indicating that our MBE STO films grown on Si(001) substrate one atomically smooth. In fact, the STO film surface is

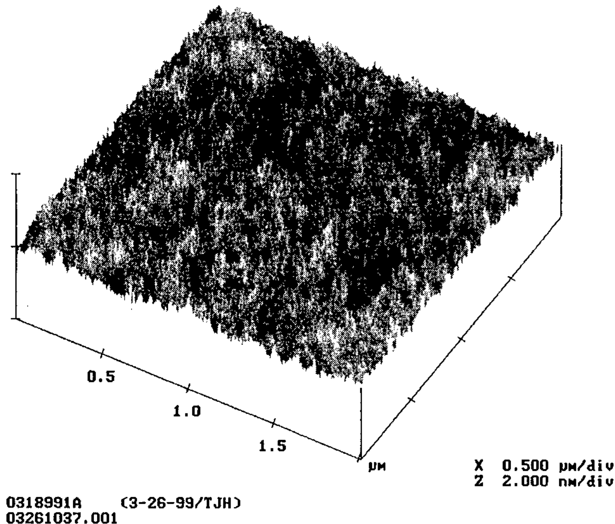

FIG. 8. AFM image of a 100-Å-thick $SrTiO_3$ film on Si(001). The rms roughness is 1.2 Å, indicating atomically smooth surface morphology.

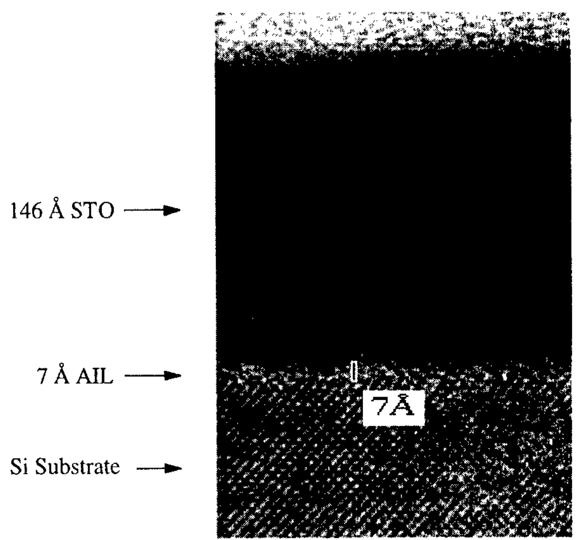

FIG. 9. High-resolution TEM image of a 146-Å-thick $SrTiO_3$ film on Si(001). An amorphous interface layer of about 7 Å is present between the two single crystals.

as smooth as the starting substrate surface. AES analysis of the epitaxial STO film on Si was performed with a $SrTiO_3$ single crystal standard placed by its side. A quick estimate of the film composition can be obtained by a careful comparison of the Auger peak intensities of Sr, Ti, and O from the STO film to those from the STO single crystal standard. Both AES and RBS studies conclude that our MBE grown films are nominally $SrTiO_3$ and are slightly Sr rich. Furthermore, AES and XPS depth profiles indicate that the film composition is fairly uniform across the entire film thickness and no server interdiffusion can be observed at the STO/Si interface.

Although it is interesting to demonstrate oxide heteroepitaxy on Si without any low-k amorphous interfacial layer (AIL), it is critical to tailor the AIL thickness to minimize the short channel effect in the MOSFET devices with a very high-k gate dielectric.[26] By systematically varying the growth conditions such as substrate temperature and oxygen partial pressure, we have produced STO films with controllable AIL thickness. Using *conventional* HRTEM, we have observed images of ~150 Å thick STO films on Si substrate with *no interfacial layer* or with AIL thickness up to 25 Å.[27] To illustrate the optimal high-k/low-k stack structure, Fig. 9 illustrates the HRTEM image of a 146 Å thick STO film on Si substrate. Notice the STO film is single crystalline and the interface between STO and Si is flat where the amorphous interfacial layer is about 7 Å. Tests on samples with different STO thickness show that the AIL thickness is independent of the STO film thickness, and it has a lower dielectric constant than the crystalline STO. XPS Si $2p$ depth profile (shown in Fig. 10) indicates that the interfacial layer is likely to be SiO_x ($x<2$). High-resolution transmission EELS (plotted in Fig. 11), on the other hand, seems to indicate that the AIL is SiO_2. The discrepancy in the results could be due to the sample preparations for the HREELS. Further work is under way to clarify the chemical nature of the amorphous interfacial layer. At any rate, the low-k amorphous interfacial layer

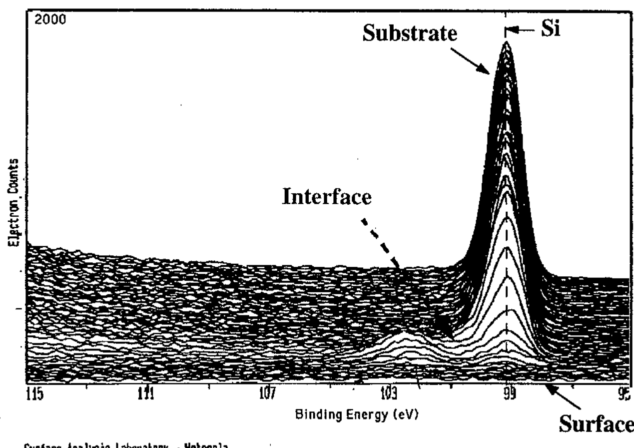

FIG. 10. XPS Si $2p$ depth profile of a STO film on Si(001), indicating the interfacial layer is likely $SiO_x(x<2)$.

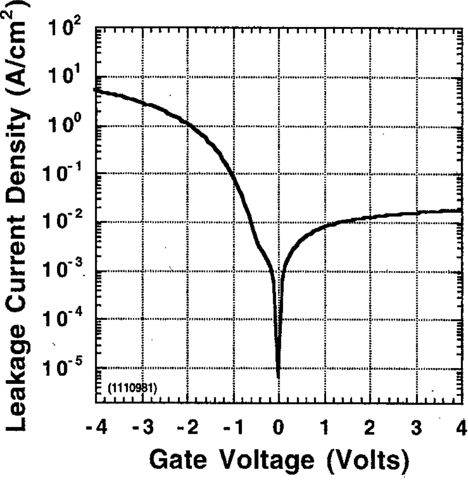

FIG. 12. Leakage current density as a function of bias voltage for an as-grown 196 Å $SrTiO_3$ MOS structure.

is either SiO_2 or SiO_x ($x<2$). This desirable high-k and low-k combination (STO/SiO_x) actually reduces the short channel effect of the high-k gate dielectric and is expected to enhance the reliability and performance of the MOSFETs.[26]

$I-V$ and $C-V$ measurements were performed on STO MOS capacitors. Figure 12 plots the leakage current density as a function of bias voltage for an as-grown STO film. The leakage current density at 1 V is below 10^{-2} A/cm^2. The $C-V$ characteristics of the dielectric film structure can be extracted from the STO MOS capacitor using a three-element model[28,29] (inset in Fig. 13), which takes into account the effects of the substrate, contact resistances as well as the parallel resistance across the capacitor. The capacitance effective thickness (CET) is then inferred from oxide $C-V$ characteristics in strong accumulation using three different methods (Hauser–Ahmed,[30] McNutt–Sah–Walstra,[31,32] and traditional $C_{OX}-C_G$). The details of electrical analysis will be published elsewhere.[33] For the 110-Å-thick STO film in Fig. 13, these three methods give oxide capacitance values of 0.033, 0.0321, and 0.0316 pF/μm^2, respectively. These capacitance values correspond to CET values of 10.5, 10.7, and 10.9 Å, respectively. Based on the above analysis, we verified that the measured STO capacitor has a capacitance effective oxide thickness of less than 11.0 Å. If we subtract the known 2–3 Å for charge quantum confinement effect at the oxide Si interface,[34] we can estimate that the 110 Å $SrTiO_3$ behaves comparably to an 8 Å SiO_2 gate insulator. The interface trap density was estimated using a method proposed by Terman.[35] By comparing the theoretical $C-V$ curve for a 10.5 Å SiO_2 gate insulator on silicon to our measured $C-V$ curve at 100 kHz, we calculated an interface state density $D_{it}=6.4\times10^{10}\,\mathrm{cm^{-2}\,eV^{-1}}$ at midgap and an oxide trap charge density of $1.2\times10^{11}\,\mathrm{cm^{-2}}$. Meanwhile, only a small shift in gate voltage (10 mV) was observed in the hysteresis of the STO capacitor using a dual $C-V$ sweep from -5 to 5 V at 100 kHz. For comparison, $C-V$ measurements were also performed on the actual FET structures, which led to a FET inversion capacitance of 0.029

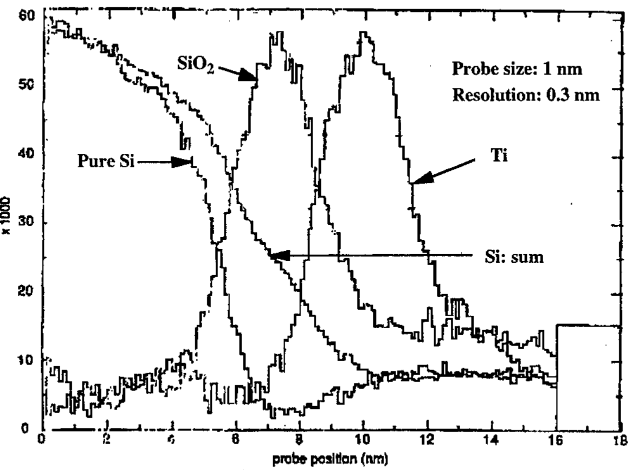

FIG. 11. High-resolution transmission EELS of a STO film indicating the AIL is SiO_2.

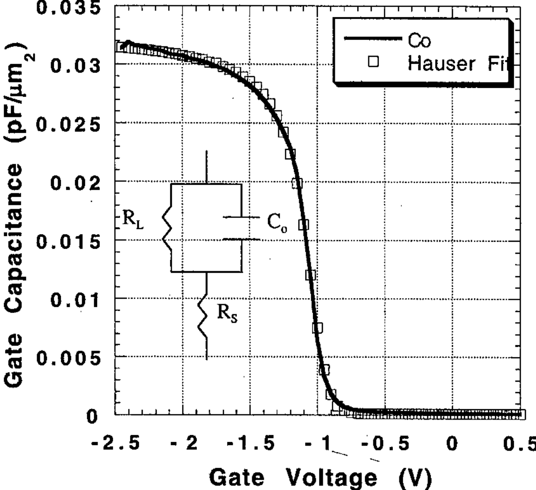

FIG. 13. $C-V$ characteristics of a 100-Å-thick $SrTiO_3$ thin film on p-type silicon with a boron concentration of $2.0\times10^{15}\,\mathrm{cm^{-2}}$ using the three-element model shown in the inset. The measurement frequency is 100 kHz.

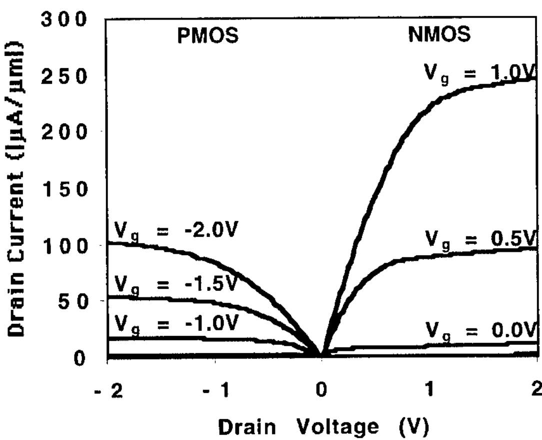

FIG. 14. Drain current–drain voltage curves for $1.2\times10\,\mu$m gate NMOS and PMOS STO gate dielectric FETs.

pF/μm^2 corresponding to a 11.9 Å CET, after subtracting the contribution from the contact pad. This number includes the contribution from the quantum mechanical effects (2–3 Å)[34,36] and a possible contribution from the gate electrode.[37] After removing these contributions, the actual effective oxide thickness for the FET is again less than 10 Å, in very good agreement with the capacitor $C-V$ results. Both n-type metal-oxide-semiconductor (NMOS) and p-type metal-oxide-semiconductor (PMOS) drain current–drain voltage curves are shown in Fig. 14. These devices have effective channel lengths of 1.2 μm. The threshold voltages of these devices are shifted toward negative values due to the low work function of the TaN gate. The peak transconductance at 1 V drain bias is 269 μS/μm and 90μS/μm for the NMOS and PMOS device, respectively. The inversion layer carrier mobility was calculated from the low field transconductance measured on $10\,\mu\mathrm{m}\times10\,\mu$m FETs. The electron and hole mobilities are inferred as 221 cm^{2}V^{-1}s^{-1} and 62 cm^{2}V^{-1}s^{-1}, respectively. In inversion, the PMOS device has leakage current three orders of magnitude better than an equivalent thickness of SiO_2 and the NMOS device has leakage two orders of magnitude better than a 10 Å SiO_2 film.[38]

IV. CONCLUSIONS

We have reviewed the recent progress in the heteroepitaxy of oxide thin films on Si substrates at Motorola Labs. The emphasis has been on the structural, interfacial and electrical properties of $BaTiO_3$ and $SrTiO_3$ perovskite-type oxide thin films grown on Si(001) surface by MBE. RHEED and XRD analysis has demonstrated high quality heteroepitaxy of these oxide films. AFM has revealed atomically smooth surface morphology. Although we have demonstrated heteroepitaxy of $SrTiO_3$ oxide films directly on Si(001) without amorphous interfacial layer by using *conventional* HRTEM, the insertion of a thin (5–7 Å) low-k interfacial layer drastically reduces the MOSFET short channel effect and improves the device performance. Therefore, the thickness of the low-k (SiO_2 or SiO_x) amorphous interfacial layer between the high-k STO and Si substrate has been controlled and optimized. We have achieved an equivalent oxide thickness less than 10 Å with an interface state density $D_{it}=6.4\times10^{10}\,\mathrm{cm^2\,eV^{-1}}$, using a 110 Å STO film on Si substrate. We also have fabricated both n- and p-channel MOSFETs with gate length $L_{eff}=1.2\,\mu$m using epitaxial STO gate dielectric. These NMOS and PMOS devices have shown excellent performance with inversion layer carrier mobilities of 221 cm^{2}V^{-1}s^{-1} and 62 cm^{2}V^{-1}s^{-1}, respectively. The leakage current in these devices is over two orders of magnitude lower than an electrically comparable SiO_2 gate dielectric. In conclusion, we have demonstrated that epitaxial perovskite oxide films grown on Si are very promising for future generation MOSFET and nonvolatile memory applications.

ACKNOWLEDGMENTS

The authors would like to thank the Physical Characterization Lab, the Surface Analysis Lab, and the Processing Team for their excellent technical assistance and Dr. H. Tompkins, Dr. J. Wang, Dr. J. Conner, Dr. P. Alluri, Dr. S. Zafar, Dr. R. Liu, Dr. S. Zollner, Dr. A. Demkov, Dr. J. Gutt, and Dr. B. Cheng for helpful discussions.

[1] D. H. Looney, US Patent No. 2,791,758.
[2] B. Hoerman, G. Ford, L. Kaufman and B. Wessels, ISIF'98, p. 102C.
[3] R. A. McKee, F. J. Walker, J. R. Conner, and E. D. Specht, Appl. Phys. Lett. **59**, 782 (1991).
[4] J. Lyu, J. Jeong, K. Kim, B. Kim, and H. J. Yo, ETRI J. **20**, 241.
[5] H. Mori and H. Ishiwara, Jpn. J. Appl. Phys., Part 2 **30**, L1415 (1991).
[6] J. Hallmark, Z. Yu, R. Droopad, J. Ramdani, J. Curless, C. Overgaard, J. Finder, D. Marshall, J. Wang, and B. Ooms, Integr. Ferroelectr. (to be published).
[7] C. Hu, Tech. Dig. Int. Electron Devices Meet. 319 (1996).
[8] I. Kizilyalli, R. Huang, and P. Roy, IEEE Electron Device Lett. **19**, 423 (1998).
[9] D. Park, Y.-C. King, Q. Lu, T.-J. King, C. Hu, A. Kalnitsky, S.-P. Tay, and C.-C. Cheng, IEEE Electron Device Lett. **19**, 441 (1998).
[10] B. He, T. Ma, S. Campbell, and W. Gladfelter, Tech. Dig. Int. Electron Devices Meet. 1038 (1998).
[11] K. Yokota, T. Yamada, F. Miyashita, K. Hirai, H. Takano, and M. Kumagai, Thin Solid Films **344**, 109 (1998).
[12] L. Manchanda, W. Lee, J. Bower, F. Baumann, W. Brown, C. Case, R. Keller, Y. Kim, E. Laskowski, M. Morris, R. Opila, P. Silverman, T. Sorsch, and G. Weber, Tech. Dig. Int. Electron Devices Meet. 605 (1998).
[13] M. Morita, H. Fukumoto, T. Imura, and Y. Osaka, J. Appl. Phys. **58**, 2407 (1985).
[14] H. Fukumoto, T. Imura, and Y. Osaka, Jpn. J. Appl. Phys., Part 2 **27**, L1404 (1988).
[15] G. Wilk and R. Wallace, Appl. Phys. Lett. **74**, 2854 (1999).
[16] R. McKee, F. Walker, and M. Chisholm, Phys. Rev. Lett. **81**, 3014 (1998).
[17] R. McKee, F. Walker, and M. Chisholm, Mater. Res. Soc. Symp. Proc. **567**, 415 (1999).
[18] Z. Yu, R. Droopad, J. Ramdani, J. A. Curless, C. D. Overgaard, J. M. Finder, K. Eisenbeiser, J. Wang, J. A. Hallmark, and W. J. Ooms, Mater. Res. Soc. Symp. Proc. **567**, 427 (1999).
[19] E. Tokumitu, K. Itani, B. Moon, and H. Ishiwara, Mater. Res. Soc. Symp. Proc. **361**, 427 (1995).
[20] F. Sanchez, M. Varela, X. Queralt, R. Aguiar, and J. L. Morenza, Appl. Phys. Lett. **61**, 2228 (1992).
[21] F. Sanchez, R. Aguiar, V. Trtik, C. Guerrero, C. Ferrater, and M. Varela, J. Mater. Res. **13**, 1422 (1998).
[22] O. Nakagawara, M. Kobayashi, Y. Yoshino, Y. Katayama, H. Tabata, and T. Kawai, J. Appl. Phys. **78**, 7226 (1995).
[23] H. Mori and H. Ishiwara, Jpn. J. Appl. Phys., Part 2 **30**, L1415 (1991).
[24] B. K. Moon and H. Ishiwara, Jpn. J. Appl. Phys., Part 1 **33**, 1472 (1994).

[25]T. Tambo, T. Nakamura, K. Maeda, H. Ueba, and C. Tatsuyama, Jpn. J. Appl. Phys., Part 1 **37**, 4454 (1998).
[26]B. Cheng, M. Cao, R. Rao, A. Inani, P. Voorde, W. Greene, J. Stork, Z. Yu, P. Zeitzoff, and J. Woo, IEEE Trans. Electron Devices **46**, 1537 (1999).
[27]J. Ramdani, R. Droopad, Z. Yu, J. A. Curless, C. D. Overgaard, J. Finder, K. Eisenbeiser, J. A. Hallmark, W. J. Ooms, V. Kaushik, P. Alluri, and S. Pietambaram, Appl. Surf. Sci. (in press).
[28]J. F. Lønnum and J. S. Johannessen, Electron. Lett. **22**, 456 (1986).
[29]K. J. Yang and C. Hu, IEEE Trans. Electron Devices **46**, 1500 (1999).
[30]J. R. Hauser and K. Ahmed, Characterization and Metrology for ULSI Technology: 1998 International Conference, p. 235.
[31]M. J. McNutt and C. T. Sah, J. Appl. Phys. **46**, 3909 (1975).
[32]S. V. Walstra and C. T. Sah, Solid-State Electron. **42**, 671 (1998).
[33]K. Eisenbeiser, J. Finder, Z. Yu, J. Ramdani, J. Curless, J. Hallmark, R. Droopad, W. Ooms, L. Salem, S. Bradshaw, and C. Overgaard, Appl. Phys. Lett. (to be published).
[34]C.-Y. Hu, D. Kencke, S. Banerjee, B. Bandyopadhyay, E. Ibok, and S. Garg, Appl. Phys. Lett. **66**, 1638 (1995).
[35]L. M. Terman, Solid-State Electron. **5**, 285 (1962).
[36]S. Jallepalli, J. Bude, W.-K. Shih, M. Pinto, C. Maziar, and A. Tasch, Jr., IEEE Trans. Electron Devices **44**, 297 (1997).
[37]C. Black and J. Welser, IEEE Trans. Electron Devices **46**, 776 (1999).
[38]C.-H. Choi, J.-S. Goo, T.-Y. Oh, Z. Yu, R. Dutton, A. Bayoumi, M. Cao, P. Voorde, D. Vook, and C. Diaz, IEEE Electron Device Lett. **20**, 292 (1999).

Epitaxial thin films of MgO on Si using metalorganic molecular beam epitaxy

F. Niu, B. H. Hoerman, and B. W. Wessels[a)]
Department of Materials Science and Engineering and Materials Research Center, Northwestern University, Evanston, Illinois 60208

(Received 17 January 2000; accepted 22 May 2000)

Epitaxial cubic MgO thin films have been deposited on single crystal Si(001) substrates by metalorganic molecular beam epitaxy. The Mg source was the solid precursor magnesium acetylacetonate and a rf excited oxygen plasma was the oxidant. The growth process involved initial formation of an epitaxial β-SiC interlayer followed by direct deposition of a MgO overlayer. The films were characterized by *in situ* reflection high energy electron diffraction, x-ray diffraction, conventional and high resolution transmission electron microscopy, atomic force microscopy, Auger electron spectroscopy, and Fourier transform infrared spectroscopy. The β-SiC interlayer had an epitaxial relationship such that SiC(001)‖Si(001) and SiC [110]‖Si [110]. The SiC interlayer showed a columnar grain structure with planar defects including twin bands and stacking faults. The MgO overlayer showed an epitaxial relationship given by MgO(001)‖Si(001) and MgO[110]‖Si[110]. No evidence of twins in the MgO layers was observed. © *2000 American Vacuum Society.*
[S0734-211X(00)06104-7]

I. INTRODUCTION

There has been increasing interest in epitaxial oxides on Si prepared by various thin film deposition methods. Epitaxial oxides can be used as optical devices, as an optical isolation layer for integrated lightwave circuits[1] or potentially as a gate insulator in ferroelectric-gate field effect transistor devices.[2] Because of the thermodynamic stability of silicon dioxide only a limited number of oxides are compatible with silicon.[3] One such oxide is MgO, which is a highly ionic, insulating crystalline solid with a rocksalt structure. Its' refractive index and dielectric constant are 1.74 and 9.65, respectively. However the lattice misfit between MgO and silicon is 22.5% which should preclude epitaxy. Despite the large mismatch, highly textured and even epitaxial films of MgO have been prepared by a number of techniques including metalorganic chemical vapor deposition (MOCVD),[4–6] pulsed laser deposition (PLD),[7–12] sputtering,[13–19] e-beam-assisted molecular beam epitaxy (MBE),[20] nebulized spray pyrolysis,[21] and sol-gel.[22] An alternative approach to deposit epitaxial MgO that may have several advantages is metal-organic molecular beam epitaxy (MOMBE). This technique utilizes metalorganic compounds as the metal source.[23–28] A major advantage of MOMBE is that the background O_2 pressure is very low ($<10^{-10}$ Torr). This potentially enables the growth of oxide thin films on clean, atomically smooth Si substrates without formation of an amorphous SiO_2 interfacial layer prior to deposition. The ultrahigh vacuum also enables *in situ* surface diagnostics such as reflection high energy electron diffraction (RHEED). One of the major challenges concerning the use of MOMBE is identification of suitable metalorganic precursors. The ideal solid precursor for MOMBE deposition should have (1) a very low background pressure at room temperature ($<10^{-7}$ Torr); (2) a single metal-containing volatile species; (3) a high sticking coefficient; and (4) long-term stability of the precursor at the sublimation temperature (no decomposition or oxidation of the source materials).

In the present work, MOMBE was employed to grow (001) oriented MgO epitaxial layers on Si. An interlayer of SiC was used to minimize formation of an amorphous silicon dioxide interfacial layer as well as to reduce stress induced by the large lattice mismatch between MgO and Si. Cubic MgO thin films have been grown on (001)Si with an epitaxial relationship of MgO(001)‖Si(001) and MgO[110]‖Si[110]. The structure, surface morphology, and composition of MgO thin films and SiC interlayer were analyzed by *in situ* reflection high energy electron diffraction, x-ray diffraction (XRD), conventional and high resolution transmission electron microscopy (TEM), atomic force microscopy (AFM), and Auger electron spectroscopy (AES).

II. EXPERIMENTAL PROCEDURE

The films were deposited in a SVT Associates SN35 MBE system equipped with a load-lock, low temperature effusion cells and an oxygen plasma source. The solid metalorganic precursor was contained in an effusion cell. The schematic of the MOMBE system has been reported elsewhere.[28] The cell temperature can be precisely controlled to less than 0.2 °C. Mg $(acac)_2$ (acac=acetylacetonate) was used as the precursor. The source flux pressure was controlled by a flux monitor. An oxygen plasma from a SVT rf plasma O_2 gun with an output energy of 400 W was used as an oxidant. The substrate was resistively heated. The substrate temperature was measured by a thermocouple calibrated by an infrared optical pyrometer.

N-type Si (100) wafers, 3 in. in diameter, with resistivities of 1–10 Ω cm were used as substrates. Prior to growth, the

a)Author to whom correspondence should be addressed: electronic mail: b-wessels@nwu.edu

TABLE I. MOMBE growth conditions for the interlayer and overlayer.

Growth conditions	Interlayer layer	Overlayer
Growth Temperature(°C)	850–950	700–900
RF oxygen plasma power (W)		300–400
O pressure (Torr)	$0-10^{-7}$	$(1-3)\times 10^{-5}$ with O plasma
Source pressure (Torr)	$1.0\times 10^{-9}-1.0\times 10^{-7}$	1.0×10^{-6}
Growth time (hours)	0.25–1	3–5
Film thickness (nm)	20–100	10–200
Growth rate (nm/h)	10–30	10–30

Si surface was chemically etched in a HNO_3:HF:H_2O (5:3:92 by volume percentage) solution for several seconds to remove the surface oxide layer and then was subsequently cleaned in methanol and acetone for 15 min. The chemically etched Si wafer was immediately placed in the system load lock and then transferred to the growth chamber pre-pumped down to a base pressure of $10^{-9}-10^{-10}$ Torr. The Si was subsequently degassed for 30 min at 200 °C and desorped for 30 min at 850 °C. The Si surface cleaned by this simple procedure showed a clear and streaky RHEED pattern with Kikuchi lines indicating the Si surface was atomically clean.

The SiC interlayer was grown on the treated Si(001) surface at a substrate temperature of 850–950 °C. The SiC layer was grown by exposing the hot silicon substrate to the $Mg(acac)_2$ at a source pressure of 1.0×10^{-7} Torr without the presence of oxygen for 1–60 min. Subsequently the MgO layer was grown on top of the interlayer at a substrate temperature of 700–900 °C at a source pressure 1.0×10^{-6} Torr and oxygen pressure 3.0×10^{-5} Torr. Table I lists the typical growth conditions for preparing the MgO film by MOMBE.

The film thickness was measured by a Tencor P-10 surface profiler. The film composition was measured by a Physical Electronics Auger electron spectrometer. The microstructure was determined by an x-ray diffractometer using Cu K_α radiation, an Hitachi HF-8100 conventional transmission electron microscope and an Hitachi HF-2000 cold field emission high resolution transmission electron microscope both operated at 200 kV. TEM samples were prepared by mechanical grinding and polishing followed by further mechanical dimpling to a thickness of less than 10 μm and final thinning in a Gatan Model 691 precision ion polishing system. The film surface morphology and roughness were examined by a Nanoscope III atomic force microscope with a Si_3N_4 tip.

III. RESULTS

A. SiC interlayer

Prior to formation of the interlayer the Si was heated to 900 °C and a reconstructed Si(001) surface was obtained. For comparison RHEED patterns from the reconstructed Si(001) 2×1 surface prior to growth are shown in Fig. 1(a) for the ⟨100⟩ azimuth and in Fig. 1(b) for the ⟨110⟩ azimuth. After exposing the reconstructed Si surface to the metalorganic precursor at 900 °C after 15 min, sharp characteristic single crystal RHEED patterns were observed as shown in Fig. 1(c) for ⟨100⟩ azimuth and Fig. 1(d) for ⟨110⟩ azimuth. RHEED analysis indicated that the interlayer was epitaxial.

Fourier-transform infrared (FTIR) measurements of the carbonized Si surface layer confirmed the presence of SiC. Figure 2 shows a FTIR transmittance spectrum from a 200-nm-thick interlayer grown on Si. A well resolved absorption peak at 798.62 cm^{-1} was observed which is in good agreement with the SiC characteristic stretching vibration [transverse optical (TO) mode] between Si and C atoms at 797 cm^{-1}.[29,30]

In order to identify the in-plane orientation of the interlayer, plan view TEM samples were examined. The Fig. 3 inset shows the ⟨001⟩ zone axis electron diffraction pattern from an interlayer grown on Si. There were two sets of diffraction patterns observed, the one with a larger lattice constant is from Si(001) substrate and the other with a smaller lattice constant is from the interlayer as determined by indexing. Using the known Si lattice constant ($a=5.430$ Å) as an internal calibration standard, we determined the lattice spacing of the interlayer to be $a=4.328$ Å. This is in excellent agreement with the lattice constant of bulk β-SiC ($a=4.349$ Å). Note that the interlayer and Si have an in-plane

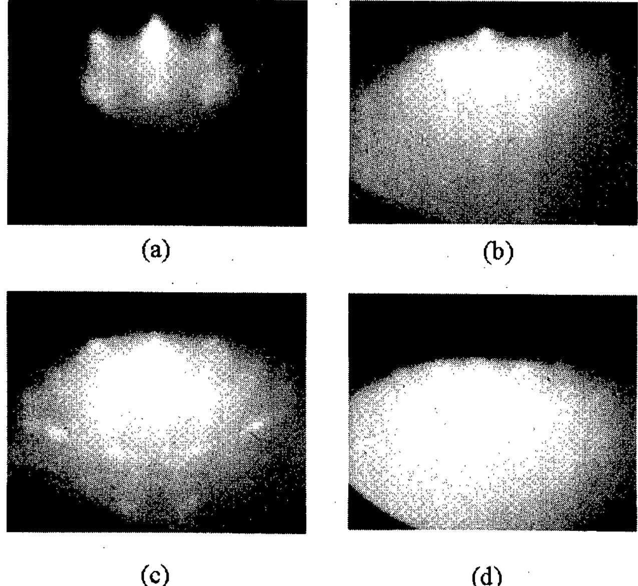

FIG. 1. RHEED pattern from Si and SiC surface. (a) From Si substrate along ⟨100⟩ azimuth; (b) from Si substrate along ⟨110⟩ azimuth; (c) from interlayer along ⟨100⟩ azimuth; (d) from interlayer along ⟨110⟩ azimuth.

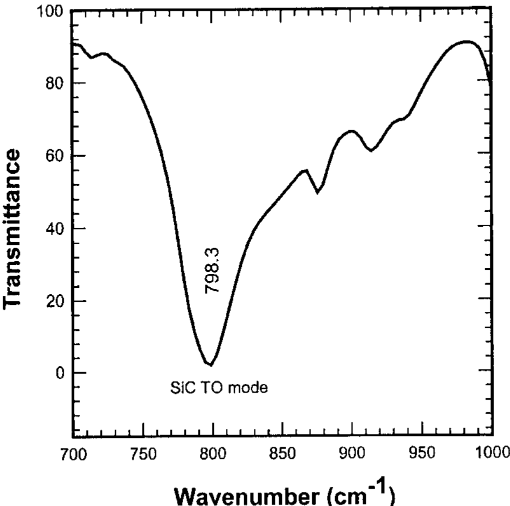

FIG. 2. FTIR spectrum from a 200-nm-thick SiC interlayer.

orientation relationship: interlayer {220}||Si{220} and interlayer {040}||Si{040}. Thus it can be concluded that the interlayer is epitaxial SiC with an orientational relationship of SiC(001)||Si(001) and SiC[110]||Si[110]. The observed streakiness of the TEM diffraction spots is possibly associated with the multiple twin band structure of SiC as we will show below. An angular broadening of the SiC diffraction spots by a few degrees was observed which indicates the SiC layer is highly (001) oriented consisting of columnar grains with low-angle boundaries. The satellite spots around Si(220) and (040) reflections actually result from double electron diffraction, which is common where two layers of crystals overlap and have a fixed orientation relationship. Figure 3 shows a bright field TEM micrograph from the interlayer grown on Si. The irregular dark spots are SiC crystallites with an average size of 20 nm. Large rectangular pits were also observed.

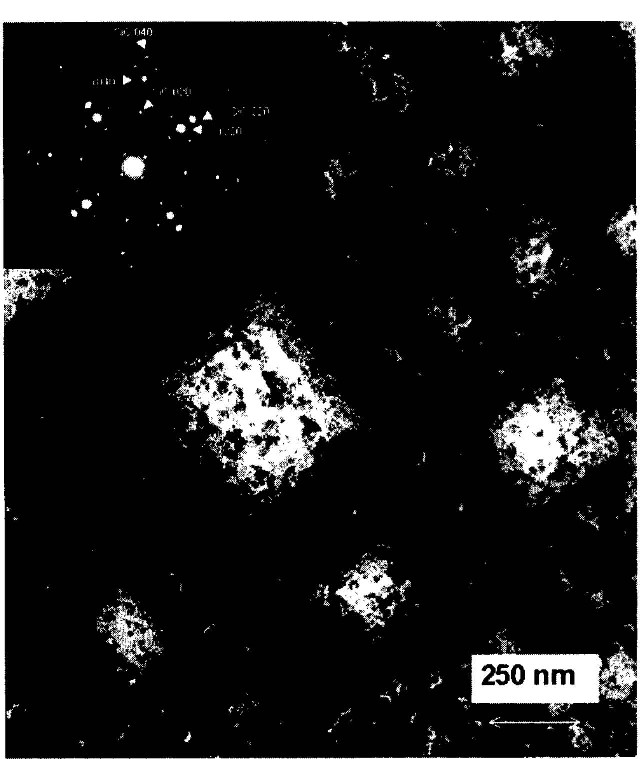

FIG. 3. Bright field TEM micrograph from the SiC interlayer. The inset is an electron diffraction pattern taken along Si ⟨100⟩ zone axis.

FIG. 4. Bright field XTEM micrograph from the film.

Figure 4 shows a bright field cross sectional TEM (XTEM) micrograph from the film. Flat and sharp interfaces between the interlayer and the MgO overlayer and the interlayer and Si and were observed. The MgO film shows columnar growth with a flat surface.

To determine whether or not an amorphous phase was present at the interface between the Si and the SiC interlayer, high resolution XTEM was used to resolve the interface. Figure 5 shows a high resolution XTEM micrograph from the same film. The electron beam direction is nearly parallel

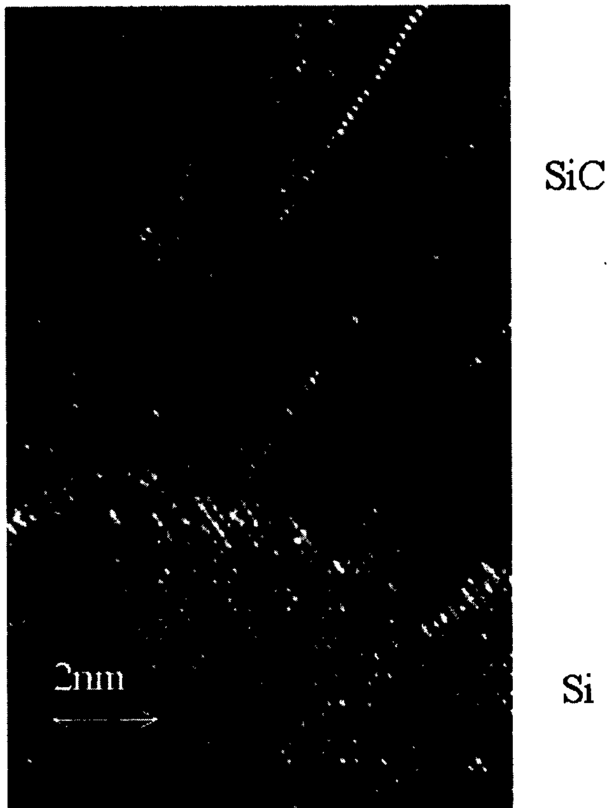

FIG. 5. High resolution XTEM micrograph from the SiC film.

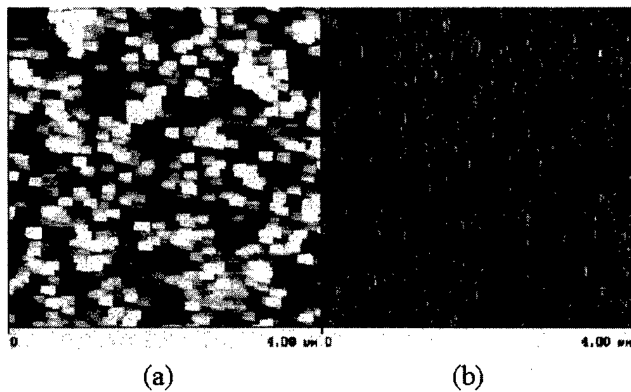

FIG. 6. AFM image from the interlayer surface. (a) Height mode; (b) deflection mode.

to the Si ⟨110⟩ zone axis. The parallel lattice fringes in Si substrate and SiC are from Si{111} and SiC{111} atomic planes, respectively. The interlayer exhibited good epitaxy with the Si substrate. No evidence of an amorphous phase was observed at the interface. Furthermore, the SiC crystallites indicated a multiple twin structure with {111} planes as twin boundaries and stacking faults.

Figure 6 shows AFM micrographs of the SiC interlayer. Figure 6(a) is taken in the height mode and Fig. 6(b) is in the deflection mode. The surface morphology consisted of a dense array of rectangular islands. The average surface rms roughness is 3.6 nm.

B. MgO epitaxial layers

MgO layers were subsequently grown on the SiC interlayer. The RHEED pattern of the MgO overlayer had cubic symmetry as shown in Fig. 7(a) for ⟨100⟩ azimuth and Fig. 7(b) for ⟨110⟩ azimuth. It was observed that the overlayer and Si surface have an epitaxial relationship: MgO(001)||Si(001) and MgO[110]||Si[110]. In some cases weak RHEED rings were also found superimposed on single crystal RHEED patterns, which indicates existence of some polycrystalline regions in the films.

To determine the chemical composition of the film, AES spectra were measured. Figure 8 shows an AES spectrum from the MgO overlayer after the surface was sputter cleaned for 5 min and a spectrum from a MgO single crystal substrate. The spectrum from the overlayer indicates the presence of only Mg and O. No carbon contamination was observed. In addition, the peak-to-peak ratio of Mg and O from the interlayer is very close to that of the MgO substrate, which indicates the interlayer is stoichiometric.

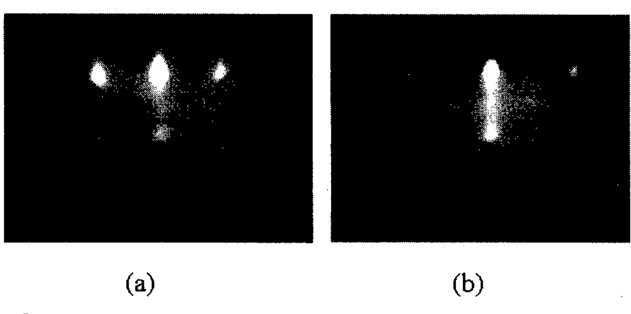

FIG. 7. RHEED pattern from surface of the MgO overlayer (a) along ⟨100⟩ azimuth; (b) along ⟨110⟩ azimuth.

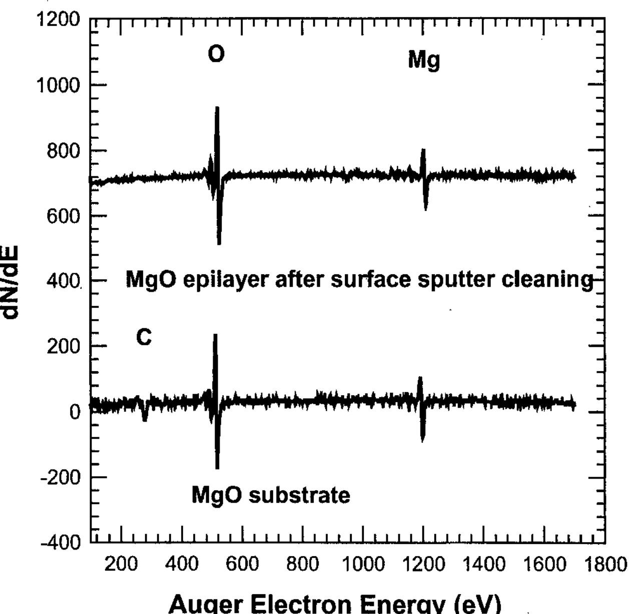

FIG. 8. AES spectra from the MgO overlayer and a MgO substrate.

XRD was used to verify phase purity and orientation as well as determine the lattice parameter of the deposited MgO. Figure 9 shows a typical θ-2θ XRD scan from the MgO layer. The dominant diffraction peak is at $2\theta=42.9°$, which corresponds to the MgO (200) diffraction. Several other diffraction peaks were observed. The peak at $2\theta=69.2°$ is attributed to the (004) Si substrate peak. The peak around 33° was attributed to the Si (002) forbidden reflection. The measured lattice spacing of MgO is 4.211 Å. The pattern confirms that the overlayer was MgO with its orientation MgO(001)||Si(001). No other phases or orientations were observed.

The epitaxial relationship between the MgO and the Si is further illustrated by TEM results. The Fig. 10 inset shows a plan view election diffraction pattern along the ⟨001⟩ zone axis from a MgO film. An additional set of diffraction spots is observed that is very close to the second set as previously shown in Fig. 3, but with a slightly smaller lattice constant. This set of diffraction spots is from the overlayer. The measured lattice constants are $a=4.328$ and $a=4.202$ Å for the interlayer and overlayer, respectively as listed in Table II. They are in excellent agreement with the respective lattice constants of β-SiC ($a=4.349$ Å) and MgO ($a=4.213$ Å). Note that the measured lattice mismatch of MgO and SiC is less than 4%. From the electron diffraction pattern it is confirmed that the overlayer is epitaxial cubic MgO with an orientational relationship of MgO(001)||SiC(001) and MgO[110]||SiC[110]. Furthermore, no twinning of the MgO layer was observed. TEM results are consistent with the RHEED and XRD results. The morphology of the film was determined from the bright field TEM image. Figure 10

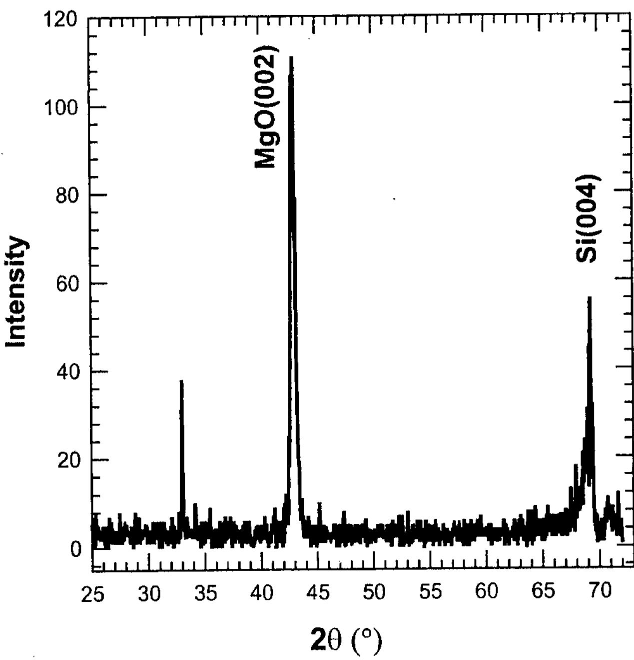

FIG. 9. XRD scan from the MgO overlayer.

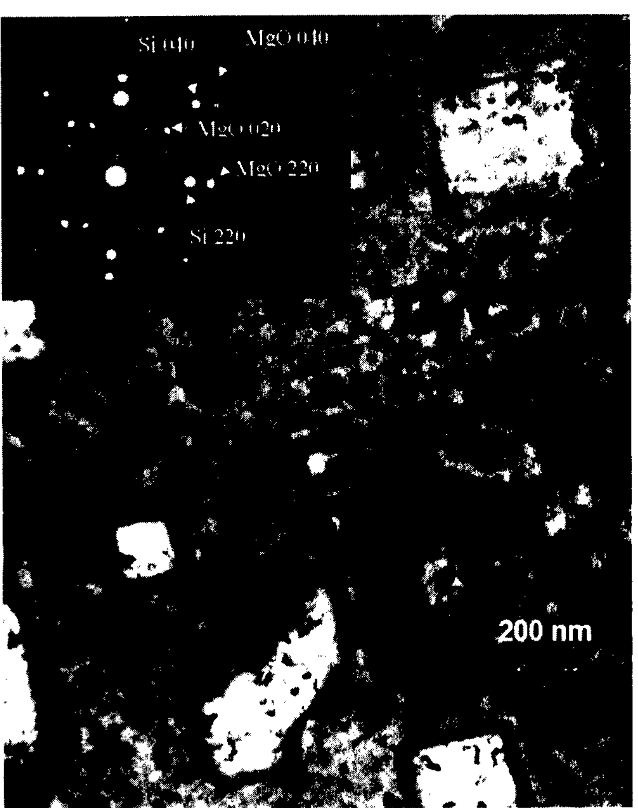

FIG. 10. Bright field TEM micrograph from the MgO overlayer. The inset is an electron diffraction pattern taken along Si ⟨100⟩ zone axis.

shows a bright field micrograph from the MgO epitaxial film. The film consists of dense small dark spots and some rectangular pits. A similar morphology was also observed in the interlayer as previously shown in Fig. 3. It is difficult to distinguish MgO crystallites from SiC crystallites because of overlapping as indicated by the moiré fringes. The rectangular pits observed in Figs. 3 and 10 have been reported to be associated with etch pits in Si substrates resulting from Si out-diffusion during carbonization.[31]

Figure 11 shows a high resolution XTEM micrograph at the interfacial area between the SiC interlayer and MgO overlayer taken with the electron beam nearly parallel to the MgO ⟨110⟩ zone axis. The parallel lattice fringes in MgO and SiC are from their {111} atomic planes, respectively. Both the SiC interlayer and the MgO overlayer exhibited a good epitaxial relationship with the Si substrate. No evidence of an amorphous phase was observed. In addition, no twinning in the MgO overlayer was observed.

Figure 12 shows the surface AFM micrograph of the overlayer. Figure 12(a) is taken in the height mode and Fig. 12(b) is in the deflection mode. Again rectangular islands were observed with average island size of 200 nm. The average surface RMS roughness is 4.9 nm.

IV. DISCUSSION

The attainment of (001) oriented epitaxial MgO films on Si by MOMBE is consistent with earlier studies that used physical vapor deposition. Using PLD, Fork *et al.* obtained (100)MgO epitaxial films on (100)Si provided that no amorphous interfacial layer was present as indicated by high resolution TEM.[9] This presumably resulted from their use of H-passivated Si as the substrate. Walker *et al.*, however, have reported that direct epitaxial growth of MgO on (100)Si resulted in formation of twinned films presumably due to large lattice mismatch between Si and MgO.[20] In order to obtain untwinned films, a thin layer of Ba_2Si several monolayer thick was needed between the Si substrate and the MgO

TABLE II. Measured lattice spacing of the interlayer and overlayer by TEM.

Atomic planes	Measured lattice spacing for SiC(Å)	Measured lattice spacing for MgO(Å)	Lattice spacing for Si(Å)[a]	Lattice spacing for cubic SiC(Å)[a]	Lattice spacing for cubic MgO(Å)[a]
{400}	1.082	1.050	1.357	1.087	1.053
{220}	1.540	1.481	1.920	1.538	1.489
Lattice constant	4.328	4.202	5.430	4.349	4.213

[a]Lattice spacings are from Ref. 32.

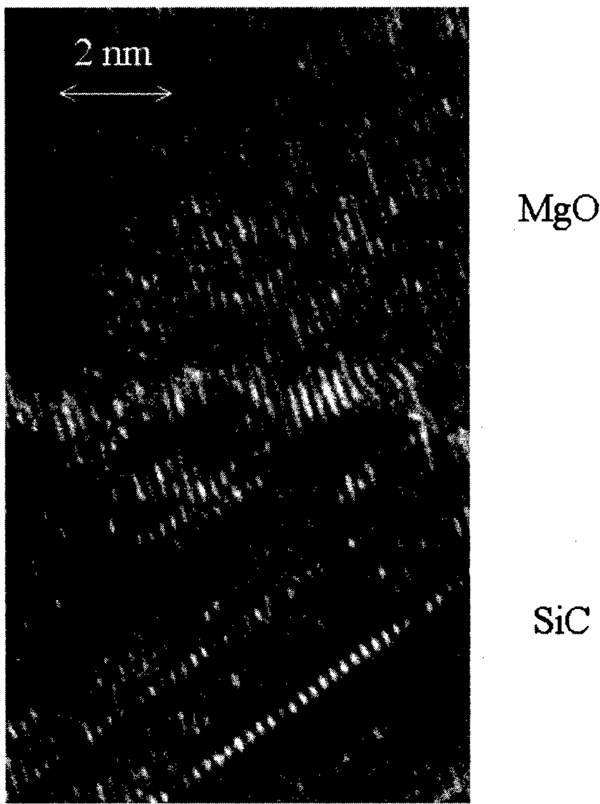

FIG. 11. High resolution XTEM micrograph from the MgO overlayer.

layer.[1] In our study, twinning of MgO layers was not observed in the RHEED and TEM studies. This presumably results from the presence of the SiC interfacial layer and the smaller lattice mismatch between MgO and SiC. A high density of twins and stacking faults, however, was observed in the SiC layer, which resulted from the large misfit of 20% between SiC and Si. Thus the SiC interfacial layer serves as a strain relaxed template for growth of epitaxial MgO that leads to untwinned films. These experiments indicate that epitaxial growth of MgO on Si requires a clean interface with low misfit stress between Si and the MgO overlayer.

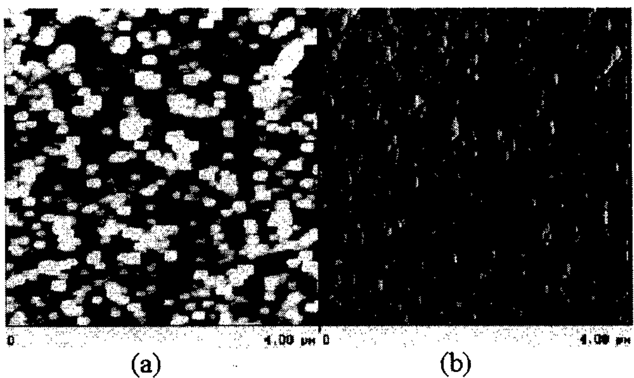

FIG. 12. AFM image from MgO surface. (a) Height mode; (b) deflection mode.

V. CONCLUSIONS

In the present work, we have demonstrated the growth of epitaxial (001)MgO on Si(001) by MOMBE. Epitaxy of the MgO was obtained by growing on a thin SiC template layer. The layer was formed by carbonization of the Si substrate using the metalorganic as the carbon source. The interlayer formed was β-SiC which had an epitaxial relationship of SiC(001)||Si(001) and SiC[110]||Si[110] with the Si substrate. The MgO overlayer showed an epitaxial orientational relationship of MgO(001)||Si(001) and MgO[110]||Si[110]. No evidence of an amorphous layer was observed between either the oxide and the SiC or SiC and Si interface.

ACKNOWLEDGMENTS

The authors are grateful to Dr. Antonio DiVenere for his technical assistance with MOMBE. This work was supported under DARPA through the MURI program for Integrated Devices for Terabit per Second 1.3 and 1.5 Micron Network Applications at Northwestern University monitored by the AFOSR under Grant No. F49 620-96-1-0262. Equipment support was provided by BMDO through the DURIP program under Grant No. F49620-96-1-0460. This work made use of the Central Facilities supported by the MRSEC program of the National Science Foundation (DMR-9632472) at the Materials Research Center of Northwestern University.

[1]R. A. McKee, F. J. Walker, and M. F. Chisholm, Phys. Rev. Lett. **81**, 3014 (1998).
[2]J. Senzaki, K. Kurihara, N. Nomura, and O. Mitsnaga, Jpn. J. Appl. Phys., Part 1 **37**, 5150 (1998).
[3]K. J. Hubbard and D. G. Schlom, J. Mater. Res. **11**, 2757 (1996).
[4]J. M. Zeng, H. Wang, S. X. Shang, Z. Wang, and M. Wang, J. Cryst. Growth **169**, 474 (1996).
[5]J. Boo, S. Lee, K. Yu, W. Koh, and Y. Kim, Thin Solid Films **341**, 63 (1999).
[6]E. Fujii, A. Tomozawa, S. Fujii, H. Torii, M. Hattori, and R. Takayama, Jpn. J. Appl. Phys., Part 1 **33**, 6331 (1994).
[7]P. Tiwari, S. Sharan, and J. Narayan, J. Appl. Phys. **69**, 8358 (1991).
[8]X. L. Guo, Z. G. Liu, X. Y. Chen, S. N. Zhu, S. B. Xiong, W. S. Hu, and C. Y. Lin, J. Phys. D **29**, 1632 (1996).
[9]D. K. Fork, F. A. Ponce, J. C. Tramontana, and T. H. Geballe, Appl. Phys. Lett. **58**, 2294 (1991).
[10]T. Ishiguro, Y. Hiroshima, and T. Inoue, Jpn. J. Appl. Phys., Part 1 **35**, 3537 (1996).
[11]S. Amirhaghi, A. Archer, B. Taguiang, R. McMinn, P. Barnes, S. Tarling, and I. W. Boyd, Appl. Surf. Sci. **54**, 205 (1992).
[12]A. Masuda, Y. Yamanaka, M. Tazoe, T. Nakamura, A. Morimoto, and T. Shimizu, J. Cryst. Growth **158**, 84 (1996).
[13]Y. Kaneko, N. Mikoshiba, and T. Yamashita, Jpn. J. Appl. Phys., Part 1 **30**, 1091 (1991).
[14]H. Shimakage, A. Kawakami, and Z. Wang, IEEE Trans. Appl. Supercond. **9**, 1645 (1999).
[15]S. Fujii, A. Tomozawa, E. Fujii, H. Torii, R. Takayawa, and T. Hirao, Appl. Phys. Lett. **65**, 1463 (1994).
[16]S. Kim and S. Hishita, Thin Solid Films **281,282**, 449 (1996).
[17]M. Tonouchi, Y. Sakaguchi, and T. Kobayashi, J. Appl. Phys. **62**, 961 (1987).
[18]Y. Li, G. C. Xiong, G. J. Lian, J. Li, and Z. Z. Gan, Thin Solid Films **223**, 11 (1993).
[19]Y. Misaki and M. Mikawa, J. Vac. Sci. Technol. A **15**, 48 (1997).
[20]F. J. Walker, R. A. McKee, S. J. Pennycook, and T. G. Thnndat, Mater. Res. Soc. Symp. Proc. **401**, 13 (1996).
[21]J. G. Yoon and K. Kim, Appl. Phys. Lett. **66**, 2661 (1995).
[22]X. R. Fu, G. M. Wu, S. G. Song, Z. T. Song, X. Z. Duo, and C. L. Lin, Appl. Surf. Sci. **148**, 223 (1999).

[23]J. P. Bade, E. A. Baker, A. I. Kingon, R. F. Davis, and J. Bachmanm, J. Vac. Sci. Technol. B **2**, 327 (1990).
[24]A. L. Kingon, K. Y. Hsieh, L. L. H. King, S. H. Rou, K. J. Bachmann, and R. F. Davis, Mater. Res. Soc. Symp. Proc. **200**, 49 (1990).
[25]D. J. Lichtenwalner and A. I. Kingon, Appl. Phys. Lett. **59**, 3045 (1991).
[26]S. Ikegawa and Y. Motoi, Thin Solid Films **281,282**, 60 (1996).
[27]K. Hayama, T. Togun, and M. Ishida, J. Cryst. Growth **179**, 433 (1997).
[28]F. Niu, B. H. Hoerman, and B. W. Wessels, Mater. Res. Soc. Symp. Proc., Vol. 606, edited by A. C. Jones, J. Veteran, S. Kaushol, D. Mullin, and R. Cooper (to be published).
[29]M. Diani, A. Mesli, L. Kubler, A. Claverie, J. L. Balladore, D. Aubel, S. Peyre, T. Heiser, and J. L. Bischoff, Mater. Sci. Eng., B **29**, 110 (1995).
[30]K. Kim, S. Choi, and K. L. Wang, J. Vac. Sci. Technol. B **10**, 930 (1992).
[31]G. Ferro, Y. Monteil, H. Vincent, and V. Thevehot, J. Appl. Phys. **80**, 4691 (1996).
[32]JCPDS-ICDD, PCPDFWIN(2.0) database, Provided by Materials Data Inc. (1998).

Hot carrier transport effects in Al_2O_3-based metal-oxide-semiconductor structures

R. Ludeke
IBM T. J. Watson Research Center, P. O. Box 218, Yorktown Heights, New York 10598

M. T. Cuberes
Department of Applied Mechanics and Engineering, University of Castilla-La Mancha, 13400 Almaden, Spain

E. Cartier
IBM T. J. Watson Research Center, P. O. Box 218, Yorktown Heights, New York 10598

(Received 17 January 2000; accepted 8 May 2000)

Over the barrier, hot electron transport across 8 nm thick amorphous Al_2O_3 layers embedded in metal-oxide-semiconductor (MOS) structures was investigated with ballistic electron emission microscopy (BEEM). The oxide field dependence of the BEEM threshold voltage V_{th}, which corresponds to the potential maximum of the barrier, was found to be dominated by image force and charge trapping/detrapping effects. The static barrier height at the $W-Al_2O_3$ interface $\Phi_B=3.90 \pm 0.03$ eV and the dynamic dielectric constant $\epsilon_{if}=1.86\pm 0.1$, which reflects the strong image force lowering of the barrier observed at both interfaces. A band offset between the Al_2O_3 and Si conduction bands of 2.78 ± 0.06 eV was deduced. Electron trap levels at energies overlapping the Si band gap and of densities in the $10^{12}\,cm^{-2}$ range were deduced to lie in the oxide near the Al_2O_3-Si interface. Their occupancy is determined by the position of the interface Fermi level. For *p*-type substrates the traps were empty (filled) for positive (negative) applied bias. Local, electrical stressing increased the interface trap charge for *n*-type substrates, but had negligible consequences on *p*-type substrates. The Al_2O_3 was readily stressed to failure upon injecting sub-nano-Coulomb of charge at electron kinetic energies in the 4–6 eV range. *© 2000 American Vacuum Society.* [S0734-211X(00)04804-6]

I. INTRODUCTION

At current rates of miniaturization of field effect transistors, scaling rules would require the thickness of present, SiO_2-based gate dielectrics to approach 1.5 nm before the end of the first decade of this century.[1] Aside from potential reliability issues at even larger thickness,[2] device design will be constrained by an ever increasing and eventually unacceptably high leakage current that results from electrons tunneling directly through the ultrathin SiO_2 layer. A practical thickness limit for SiO_2 appears to be in the 1.7–2 nm range.[3] The leakage current problem can be forestalled by the choice of a gate oxide with a static dielectric constant ϵ_0 much larger than that of SiO_2 ($\epsilon_{SiO}=3.9$). This allows an increase in thickness of the gate dielectric by a factor $\epsilon_0/\epsilon_{SiO}$, for otherwise identical design specifications, which then leads to an exponential reduction of the tunneling current. A variety of dielectric materials have been considered recently as potential gate oxide substitutes for SiO_2, including Al_2O_3.[4,5] Ta_2O_5,[6,7] and TiO_2,[8] as well as the more complex Hf and Zr silicates,[9] and $SrTiO_3$.[10] Since the barrier height is another parameter that determines the tunneling current,[11] the choice of suitable dielectrics is also somewhat constrained to those with relatively large band gaps. Large band gaps should assure interfacial barriers of sufficient height to limit both electron and hole tunneling.[12]

Al_2O_3, the dielectric studied here, meets the aforementioned criteria with a dielectric constant of 9 and a band gap of ≈9 eV. In the past it has been considered as a potential gate dielectric and some of its properties were investigated for relatively thick (40–50 nm) films.[13,14] However, little is known of the electronic properties of thin, high quality films suitable for gate dielectrics that are commensurate with sub-4-nm SiO_2. In this article we report transport studies on thin (8 nm) Al_2O_3 layers embedded in metal-oxide-semiconductor (MOS) structures. The properties, measured on a nanometer scale with a scanning tunneling microscope (STM), are relevant to device characterization and modeling, as well as to hot electron phenomena and charge trapping in the MOS structures. Specifically, we have obtained the barrier heights at both the gate-oxide and oxide-Si interfaces, the band offsets between the conduction bands of Si and Al_2O_3, as well as the dynamic dielectric response of the oxide (image force dielectric constant). We have also observed electron trapping and detrapping events, and have obtained trapped charge densities and their spatial and energetic location. Furthermore we discuss results of preliminary electrical stressing studies. These indicate a limited resistance to hot electron induced trap formation, yet an easily reached stress limit at which failure occurred. In this respect Al_2O_3 differs markedly from SiO_2, for which local breakdowns were seldom observed in spite of a propensity for electron induced trap generation.[15]

II. SAMPLE PREPARATION

The 8 nm thick Al_2O_3 films were grown by atomic layer chemical vapor deposition (ALCVD) on Si(100) substrates at

a relatively low substrate temperature of 300 °C.[5] The *n*- and *p*-doped substrates, with resistivities of 1 and 17 Ω cm, respectively, were H passivated in diluted HF just prior to their introduction into the growth chamber in order to minimize the formation of a native oxide. Postdeposition analysis indicated that the films were amorphous and stoichiometric, possessing good thickness uniformity and abrupt interfaces, and with no evidence for an interfacial silicon oxide layer. Details of the deposition and characterization methods are described in Ref. 5, including preliminary electrical characterization ($C-V$) of an annealed 8 nm film with an Al gate. Some samples were annealed after the Al_2O_3 deposition at conditions similar to those reported for thicker polycrystalline aluminum oxide films.[14]

Small, approximately 4×12 mm pieces of the wafers were mounted on substrate holders for the STM experiments. Ga–In contacts were scratched into their backside to assure low resistance contacts. Once in the ultrahigh vacuum (UHV) of the preparation chamber the samples were outgassed near 200 °C to remove volatile contaminants, including traces of water. They were then transferred into the UHV deposition chamber and mounted onto a liquid He-cooled cryostat. Thin (3 nm) W dots, 200–300 μm in diameter, were evaporated through a shadow mask with the sample held near 30 K. The tungsten was evaporated by a low power (50 mA, 1.9 kV) *e*-beam evaporator that was fitted with deflection plates to minimize potential damage from stray electron and ions.[16] The substrate was cooled so as to assure a relatively smooth and fine-grained W film. Subsequently taken STM images showed a morphology essentially identical to similarly deposited W films on SiO_2, which consisted of uniform nodules, ~2 nm in diameter.[17] After the sample warmed to room temperature it was transferred, again under UHV, onto the measurement stage of the STM located in an adjacent chamber. Once in position, a grounding contact consisting of a fine Pt–Rh wire was manipulated onto a selected metal dot for current–voltage ($I-V$) measurements and for characterization by ballistic electron emission microscopy (BEEM).[15,18] The $I-V$ measurements permitted an estimate of the quasi-static capacitance–voltage characteristics since the voltage ramp in our instrument is stepped rather than continuous.

III. BEEM FUNDAMENTALS AND OXIDE BIASING ISSUES

Briefly, in BEEM the tip of the STM is biased at V_T relative to the metal overlayer (the W dot). This imparts a kinetic energy eV_T to the electrons that tunnel from the STM tip to the metal film. The latter is thin enough to allow most electrons to traverse it ballistically. Upon reaching the far interface they may scatter back or, if they have sufficient energy to overcome any potential barrier at the interface, they may proceed into the conduction band of the underlying material (the oxide in the present case). Under favorable circumstances the electrons may reach the Si substrate and emerge from it as a detectable "collector" current I_c. In the spectrosopy mode, the scanning of the STM is interrupted

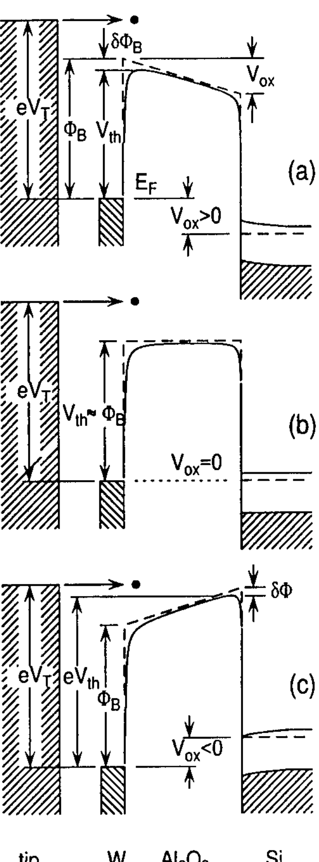

FIG. 1. Energy band diagram of a BEEM experiment on a MOS structure for three different oxide potentials: $V_{ox}>0$ (a), $V_{ox}=0$ (b), and $V_{ox}<0$ (c). The static trapezoidal barrier profiles are shown by dashed lines. The solid lines represent the dynamic or screened profile sensed by the electron. They were calculated using classical image force theory. The metal "gate" (*W*) is grounded and the STM tip bias (V_T) and applied sample bias (V_b) are referenced to it.

and I_c is measured as the tip bias is ramped over a predetermined range while keeping the feedback controlled tunnel current constant. The tip bias at the onset of a finite collector current is referred to as the threshold voltage V_{th}. V_{th} corresponds to the maximum of the potential barrier encountered by the electrons and is referenced to the Fermi level of the metal film. The relevant energies and potentials of a MOS structure probed by BEEM are shown by the energy band diagrams in Fig. 1. Three different situations are illustrated, each corresponding to a different bias V_b applied across the MOS sample. The leftmost hatched area represents the conduction band of the STM tip, whose Fermi level is raised by eV_T relative to the Fermi level E_F of the W film. The conduction band of the Al_2O_3 is offset by the intrinsic barrier potential Φ_B, which depends only on the workfunction of the metal.[14] The static profiles of the barriers are represented by dashed lines in each diagram, specifically for oxide potentials (a) $V_{ox}>0$, (b) $V_{ox}=0$, and (c) $V_{ox}<0$. V_{ox} is the net potential drop in the oxide and includes contributions from any oxide charge. The various oxide biases are achieved by applying a bias V_b between the W gate and the Si (part of this potential will be dropped across the Si, so that $V_{ox} \neq V_b$).

In any experiment involving the transmission of electrons through or over the barrier, the electron, upon entering the barrier region from either the metal or semiconductor side, perturbs their electron distribution. The altered charge distribution creates in effect a screening charge of opposite polarity at the interfaces, producing an attractive force on the electron that can be adequately described by classical image force theory.[19] The results of including the image force contributions to the barrier profiles at both interfaces are shown by the solid lines in Fig. 1. The potential barrier in the presence of a positive oxide potential is lowered by an amount:

$$\delta\Phi_B=(qV_{ox}/4\pi\epsilon\epsilon_{if}t_{ox})^{1/2}, \quad (1)$$

where ϵ and ϵ_{if} are the permittivity in vacuum and the image force dielectric constant, respectively, and t_{ox} is the thickness of the barrier. The image force induced changes in Φ_B and at the oxide–Si interface ($\delta\Phi_B$) are indicated in Fig. 1(a). It is $\Phi_B-\delta\Phi_B$ that is measured as V_{th} in a BEEM experiment for $V_{ox}>0$, or $\Phi_B-\delta\Phi_B+|V_{ox}|$ for $V_{ox}<0$. For the latter case we can obtain the image force lowering at the oxide–Si interface by subtracting V_{ox} from the measured V_{th}. A plot of V_{th} vs $V_{ox}^{1/2}$ should result in a straight line if changes in the threshold are due to image force effects. The slope of the linear plot is inversely proportional to ϵ_{if} and its zero field intercept gives the value of Φ_B. The value of ϵ_{if} is generally lower than the static dielectric constant ϵ_0 for polar materials and often is close to the optical dielectric constant ϵ_∞. The reduction reflects the inability of the polarized valence charge in the dielectric to react to the fast moving electrons.[20]

V_{th} was determined from computer fits to the data using a model calculation of the dependence of the collector current I_c on the tip bias V_T in the immediate threshold region. Differences in V_{th} of less than 50 meV were noted in the results calculated with models that either exclude[21] or included[22] quantum mechanical effects in the transmission probabilities. In our determinations of V_{th} we included them. Because of the very small collector currents measured in the Al_2O_3 layers (smaller by nearly an order of magnitude compared to SiO_2 of similar thickness[23]), it was necessary to average typically 15–20 similar spectra to achieve a signal to noise ratio sufficient to determine V_{th} within 50 mV. To avoid the possibility of threshold shifts resulting from electron trapping due to prior injections near the measurement point, a problem for SiO_2 layers,[24] sets of 25 well separated spectra were taken over 100×100 nm^2 virgin portions of the sample (as will be shown later this precaution was only warranted for n-type samples, for which modest trapping effects were measured for sequential injections at the same point on the sample).

IV. RESULTS: THRESHOLD SHIFTS

The changes in V_{th} as a function of the applied sample bias V_b for MOS samples of both conductivity types are shown in Fig. 2(a). The solid points are for the annealed n-type sample, the open points are for p-type samples. The curves are spline fits to the data points. For positive bias [condition depicted in Fig. 1(a)] the changes in V_{th} are gradual but nonlinear, possibly the effect of the lowering of the barrier by image force effects. For the n-type sample there is an obvious transition to a faster rate of increase in V_{th} for $V_b\lesssim0.5$ V that is preceded by a nearly flat segment at a slightly higher bias. This region represents the transition from inversion to flatband, as the position of the Fermi level at the interface moves from near the valence band towards the conduction band. For biases $V_b\lesssim0$ the thresholds rise rapidly as the n-type sample is in accumulation, with condition typified by Fig. 1(c). Thus the flatband voltage V_{fb} is estimated to be near 0.5 V. This transition is less obvious in the annealed p-type sample, but can be ascertained to be in the vicinity of -0.25 V, a value that is consistent with $C-V$ measurements. The importance of annealing the samples becomes apparent upon comparing the p-type data for the two cases in Fig. 2(a). Over a narrow (±0.5 V) range of V_b near zero the two curves are parallel, suggesting that annealing shifts the as-grown curve (open diamonds) to the right. However, they quickly diverge beyond this range. The rapid dropoff of the threshold for $V_b>0.5$ V cannot be attributed, as will be discussed shortly, to image force effects, but is consistent with a lowering of the threshold from a buildup of positive charge at the W–Al_2O_3 interface. Presently this explanation remains speculative.

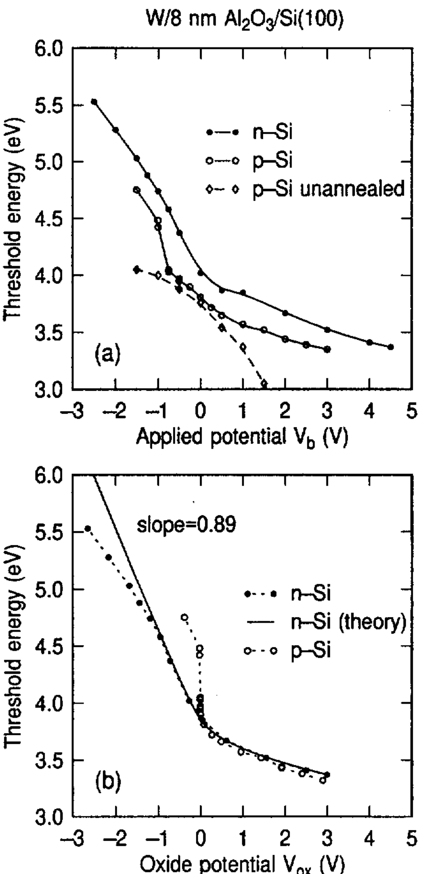

FIG. 2. Threshold voltages V_{th} measured by BEEM as a function of the sample bias V_b (a) and as a function of the oxide potential V_{ox} (b) for 8 nm Al_2O_3-based MOS structures on n (filled symbols) and p-type Si(100) substrates (open symbols).

To gain quantitative understanding of the threshold shifts

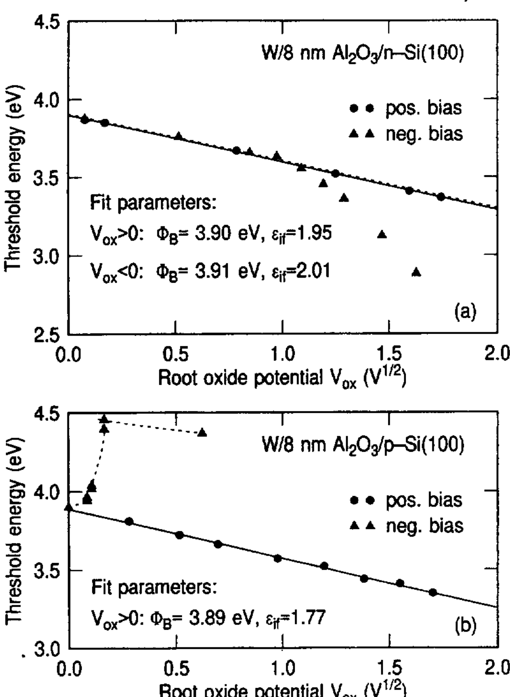

FIG. 3. Threshold voltages V_{th} measured by BEEM as a function of the square root of the oxide potential $V_{ox}^{1/2}$ for 8 nm Al_2O_3-based MOS structures on n- (a), and p-type Si substrates (b). Data for $V_{ox}>0$ are plotted as filled circles. For $V_{ox}<0$ (triangles) the reduced threshold ($V_{th}-|V_{ox}|$) is plotted on the ordinate. The straight lines are linear fits to the data, with the fitting parameters displayed in the figures.

it is necessary to plot them as a function of the oxide potential V_{ox}. With the knowledge of the flatband shifts, V_{ox} can be obtained from the well known solutions of the Poisson equation for an ideal MOS structure, provided that any existing oxide charges remain constant and localized over the bias range contemplated.[25,26] The resulting data, using V_{fb} of 0.45 and −0.25 for the annealed n- and p-type layers, respectively, are shown in Fig. 2(b). For $V_{ox}>0$ the two curves nearly overlap, suggesting the threshold changes in both samples to be of a similar origin that is intrinsic to the Al_2O_3. For negative potentials the two curves diverge drastically, implying different electronic processes occurring at the two Al_2O_3–Si interfaces, which this bias polarity explores [see Fig. 1(c)]. The initial linear rise for the n-type sample is consistent with raising the oxide-Si barrier maximum by V_{ox} (the slope is 0.89). However, for the p-type sample the rise is initially too abrupt, which implies that it is due to a buildup of repulsive negative charge near the Al_2O_3–Si interface.

V. IMAGE FORCE AND CHARGING EFFECTS

To better assess the role of image force contributions to the threshold shifts, we plot the data of Fig. 2(b) versus the square root of V_{ox} for $V_{ox}>0$. The results are shown as solid dots in Fig. 3(a) for the n-type sample and in Fig. 3(b) for the p-type sample. Their linear behavior, emphasized by the solid lines through the data points, is strongly suggestive of barrier lowering from image force effects. The lines are actually least square linear fits with intercepts that are within 10 meV for the two samples. This yields an average zero field barrier height of $\Phi_B=3.90\pm0.03$ eV. The uncertainty is based on the accuracy of determining the threshold voltages from the fits. Image force effects were also observed for SiO_2 gate oxides.[20] From the slope we deduce the image force dielectric constant $\epsilon_{if}=1.95$ for the n-type sample using Eq. (1). This value is drastically lower that the static dielectric constant $\epsilon_0\approx 9$. The latter includes contributions from the polarizable ions in the oxide. The ions, specifically their optical phonon modes cannot respond to the energetic electrons of the BEEM experiment, thereby limiting the screening effectiveness of the oxide to contributions from only the valence electrons, which is reflected in the optical dielectric constant $\epsilon_\infty\sim 2$.[27] For the p-type sample in Fig. 3(b), a slightly lower value of $\epsilon_{if}=1.77$ was obtained from the slope of the data.

The interface of greater technological concern and interest is that of the oxide-Si, which can be probed with BEEM, as mentioned previously, for $V_{ox}<0$. However for this polarity V_{ox} raises the barrier, thereby disguising subtle threshold changes that may arise from other effects. To overcome this deficiency we subtract V_{ox} from the thresholds and instead plot a field reduced threshold ($V_{th}-|V_{ox}|$) on the ordinate. For the n-type sample the results are shown by filled triangles in Fig. 3(a). A least square fit is again a straight line up to $\sim 1\ V^{1/2}$ with a slope and intercept nearly identical to those for positive bias, thereby confirming the expected presence of image force effect at the oxide–Si interface as well. As an aside, the wrong choice of V_{fb} yields unrealistic values for ϵ_{if}, and to a lesser extent nonmatching barrier heights, a dependency that can be used to fine tune the value of V_{fb}. For abscissa values greater than 1 $V^{1/2}$ the thresholds for the n-doped sample, specifically ($V_{th}-|V_{ox}|$), decrease progressively with increasing V_{ox}. This deviation from linearity was already obvious in Fig. 2, but is accentuated here because of the mode of plotting the (reduced) shifts. This barrier reduction originates from either the appearance of a positive charge near the interface or a reduction of existing negative charge. The former possibility is unlikely as a positive charge near the interface would be neutralized by electrons in the Si, since under the negative bias conditions the n-type Si is in accumulation, as illustrated in Fig. 1(c). Since the threshold dependency on V_{ox} was reversible it is further unlikely that hole traps lying high in the band gap of the Al_2O_3 would become charged, for it would be energetically unfavorable for them to discharge by merely decreasing $|V_{ox}|$. Instead we attribute the decreasing thresholds for $V_{ox}<1$ V to discharging of electron traps, an interpretation that is consistent with the data for the p-type sample, as well as electrical stressing results to be discussed in Sec. VI. The observation that the trapped charge remained constant for $V_{ox}>-1$ suggests that it preexisted the experiments.[13] Its location or more specifically the location $\bar{x}$ of the centroid of the charge distribution can be readily obtained from the slope of the linear portion of the V_{th} vs V_{ox} curve. The centroid location $\bar{x}$ of a negative oxide charge corresponds to the highest point in the

potential profile, which BEEM measures as V_{th}. The dependence of the potential maximum (i.e., V_{th}) on V_{ox} is given by $\bar{x}V_{ox}/t_{xo}$.[28,29] Thus the slope $\bar{x}/t_{ox}$ is a direct measure of the position of the charge centroid relative to the metal–oxide interface. The slope of the linear segment of the $V_{ox}<0$ curve for the n-type sample in Fig. 2(b) indicates that the charge is located near the oxide–Si interface. The measured value of 0.89 is actually an underestimate since the measured V_{th} is smaller than the actual static barrier height by the magnitude of image force reduction. Correcting the data for this effect raises the slope to nearly 1. That is, the charge is located essentially at the interface.

The threshold dependence on $V_{ox}<0$ of the p-type sample was drastically different from that of the n-type just discussed. The results, specifically those of the reduced threshold ($V_{th}-|V_{ox}|$), are shown by the filled triangles in Fig. 3(b). The threshold rises rapidly, reaches a maximum and then decreases. Over the bias range shown the charge state at the p-Si–oxide interface change from neutral (flatband) to inversion at the interface, as the Fermi level moves from near the valence band to the conduction band. We attribute the increases in barrier height to progressive charging of previously neutral electron traps near the interface. Since the trapping saturates at relatively low biases ($V_b\approx-1$ V), prior to strong inversion, the distribution in energy of the trap levels is largely confined to an interval matching the band gap of Si. The subsequent decrease of the threshold energy at a linear rate with slope close to that of the n-type sample under negative bias implies that the trap states presently under discussion are also located near the oxide–Si interface. Thus it appears that these trap states on both n- and p-type substrates are of a similar origin, and that their occupancy is solely determined by the position of the Fermi level at the oxide–Si interface. The measurements could not be extended beyond the bias ranges shown because of rapidly deteriorating signal-to-noise ratios that we associated with field enhanced trapping and detrapping events.

From the observed saturation of the trapping on the p-type sample we can make an estimate of the charge density σ_{if} at the interface. We use a sheet charge model to describe the potential profile $E(x)$ in terms of the potential $\Phi_Q(\bar{x})$ of the charge distribution, $\bar{x}$ being the location of its centroid, the image force potential $E_{im}(x)$ and the oxide potential V_{ox}:[30]

$$E(x)=\Phi_B+E_{im}(x)-qV_{ox}x/t_{ox}+\Phi_Q(\bar{x},x), \tag{2}$$

$E_{im}(x)$ includes image contributions from both interfaces and is given by[31]

$$E_{im}(x)=\frac{q^2}{16\pi\epsilon\epsilon_{if}}\sum_{n=0}^{\infty}(k_1k_2)^n \times\left(\frac{k_1}{nt_{ox}+x}+\frac{k_2}{t_{ox}(n+1)-x}+\frac{2k_1k_2}{t_{ox}(n+1)}\right), \tag{3}$$

where

$$k_1=\frac{\epsilon_{if}-\epsilon_m}{\epsilon_{if}+\epsilon_m}=-1,\quad k_2=\frac{\epsilon_{if}-\epsilon_{Si}}{\epsilon_{if}+\epsilon_{Si}}. \tag{4}$$

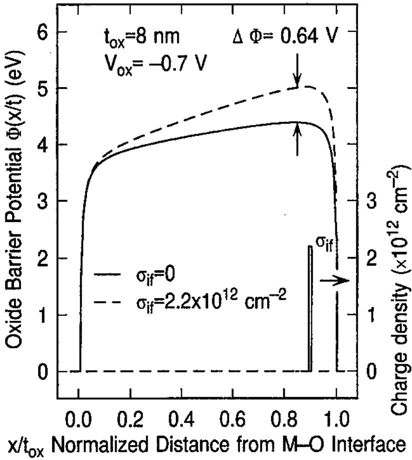

FIG. 4. Barrier profile calculated in the absence (solid line) and presence (dashed line) of a sheet charge $\sigma_{if}=2.2\times10^{12}\,cm^{-2}$ located at $x/t_{ox}=0.9$. The increase $\Delta\Phi=0.64$ eV matches the experimental value for the negatively biased p-type sample in Fig. 3(b). Image force effects at both interfaces were included.

In Eq. (4) ϵ_m and ϵ_{Si} are the dielectric constants of the metal and Si, respectively. The potential profile for a nominal barrier of $\Phi_B=3.9$ and $V_{ox}=-0.7$ V, which corresponds to the conditions for which the traps in the p-type sample are saturated, is shown in Fig. 4 as a solid line in the absence of an interface charge. A charge sheet placed at $x/t_{ox}=0.9$ requires a density of 2.2×10^{12} electrons/cm^2 to raise the back of the potential profile by 0.64 eV, the measured threshold shift. The resulting profile is shown by the dashed line in Fig. 4. The charge density is only weakly dependent on the position of the charge sheet, which is represented by the bar in the lower right of the figure.

VI. ELECTRICAL STRESSING STUDIES

Hot electron induced modifications of the dielectric or stressing may occur under seemingly benign conditions, as the measurement to determine its stress-free properties may already modify the charge balance in the oxide. Such effects have been observed in BEEM studies of SiO_2-based MOS structures, for which the mere process of measuring the threshold energy changes the threshold on subsequent scans. In this case charging of traps occurred even though the kinetic energies of the electrons injected into the conduction band were kept well below the 2 eV threshold for which new electron traps can be generated.[24,30] It was observed that contrary to the case of Al_2O_3, for which preexisting traps are located near the oxide-Si interface, those in SiO_2 were located nearer to the metal–oxide interface and stress induced traps were distributed throughout the SiO_2. It is thus relevant to investigate stress induced degradation processes in Al_2O_3 and compare these to SiO_2.

Hot electron induced changes in the thresholds of the Al_2O_3-based MOS structures were readily observed in the n-doped samples. The mere repetition of a scan at the same location on the n-doped sample could induce threshold changes. This effect is shown in Fig. 5(a). Spectrum (1) was

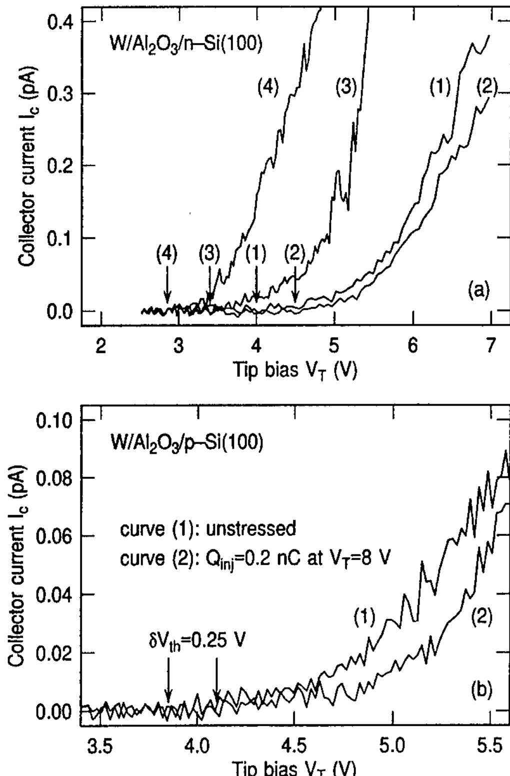

FIG. 5. BEEM spectra (I_c vs V_T) for locally stressed MOS structures on n-(a) and p-type (b) substrates. Spectra 1 and 3 in (a) and spectrum 1 in (b) are the first spectra on initially unstressed virgin locations on the sample surface. Threshold shifts after repeat scans at the same location were only observed for the n-type sample (spectra 1 and 2). Only relatively small threshold shifts were observed on the p-type sample after stressing to near oxide failure (b).

taken on a virgin portion of the sample, with spectrum (2) representing the third scan with V_{th} shifted by 0.5 V (the drift during the 4 min interval was less than 0.5 nm). The second scan exhibited a 0.3 V shift, with scans beyond the third producing no further shifts. The observed increase in V_{th} of 0.5 V was quite typical, although on occasion no changes were measured in V_{th} after similar scan sequences. On SiO_2 even less energetic injections produced shifts greater than 1 V.[24] Stressing the Al_2O_3 locally by injecting electrons at biases in the range $V_T = 8-10$ V (equivalent kinetic energy ~4–6 eV) led to oxide breakdowns after injecting as little as 0.25 nC into the oxide. The oxide invariably failed when stressed in the presence of an accelerating bias of $V_b = +2$ V. Charging effects were noted initially, accompanied by increases in the thresholds by as much as 1 V. Stress induced reductions of the thresholds prior to failure were also observed, a failure sequence that was also seen in SiO_2.[25] An example of a stressed induced threshold reduction is shown by curves (3) and (4) in Fig. 5(a). The film was stressed at $V_T = -10$ V and $V_b = +2$ V, with a total charge of 0.37 nC injected between spectra (3) and (4). The observed shift was 0.6 V. The next stressing event led to an immediate failure. We define failure as the disappearance of the conventional interfacial barrier, with thresholds becoming small and BEEM currents increasing to values comparable to the STM tip current. This stage, however, is only occasionally observed. In most cases of observed failures considerable damage occurs at the stress site, with a portion of the metal destroyed over an area a few tens nanometer in diameter. The lack of metal in the vicinity of the failure site prevented imaging of the site with the STM. However, just beyond the damaged area the oxide exhibits its usual properties. Furthermore, after a failure the MOS structure could still be biased without affecting the leakage current, and the experiments could be continued on other parts of the MOS structure.

Stressing of the p-doped samples led to very different results from those for n-doped samples, excepting the comparable ease of reaching oxide failure. Repeated spectral scans at the same spot on the sample indicated negligible charging, as V_{th} remained constant within 0.1 V, which corresponds to the accuracy of determining the thresholds from single spectral scans. Even after prolonged stressing at $V_T = -8$ V and injected charges to near failure doses, the shifts in V_{th} were only 0.25 V. The corresponding spectra are shown in Fig. 5(b). The oxide failed locally after an additional injection of only 0.04 nC.

The absence of threshold shifts for moderately stressed p-type samples and the pronounced increases in V_{th} observed for the n-type samples suggests that the additional trap levels created by stressing are of a similar nature than the interface traps present prior to stressing. This follows from the supposition that stressing creates similar traps irrespective of the type of substrate doping, and the inference that their charging is again dependent on the position of the Fermi level at the interface. Their location near the interface is also suggested from a lack of charging in the p-type samples, as charging would occur if the states were located towards the middle of the oxide, a process that is observed for stressed SiO_2 layers of comparable thickness.[24] The injected charges necessary to stress Al_2O_3 to failure are typically several orders of magnitude lower than those for SiO_2[15] a serious concern from a device reliability point of view. On the other hand, the robustness of Al_2O_3 to low voltage stressing is not yet known.

VII. DISCUSSION AND CONCLUSIONS

From the data presented thus far we can determine the band offset between the Si and Al_2O_3 conduction bands. We will use the data obtained for p-type Si, since for this sample there is negligible interface trapping for $V_{ox} \geqslant 0$. Based on the calculated position of the bulk Fermi level for 17 Ω cm B-doped Si (0.25 eV above the Si valence band), the flatband voltage of -0.25 V and the measured $\Phi_B = 3.9$ eV, we obtain a conduction band offset of $\delta E_{cb} = 2.78 \pm 0.06$ eV. The error is based on the uncertainties in the measured energies. δE_{cb} and the other relevant values obtained in our experiment are listed in Table I, together with band offsets reported earlier for thicker polycrystalline Al_2O_3 films. These earlier determinations were made by internal photoemission, a technique considerably more susceptible to model dependent and extrapolative errors. Nevertheless, our value is within 0.2 eV

TABLE I. $W-Al_2O_3$ barrier height, image force dielectric constant, and $Si-Al_2O_3$ conduction band offsets.

Si substrate	Φ_B(eV)	ϵ_{if}	δE_{CB}(eV)	δE_{CB}(eV) prior work
n type	3.90±0.03	1.95±0.1	⋯	2.95±0.1 (Ref. 13), 2.78±0.2 (Ref. 14)
p type	3.89±0.03	1.77±0.1	2.78±0.06	

of those reported earlier.[13,14,32] It should be emphasized again that the barrier heights measured at the $W-Al_2O_3$ and Al_2O_3-Si interfaces only apply in the zero field limit. For other bias conditions substantial lowering can be expected due to the strong image force effects, effects that cannot be ignored in predicting currents through MOS structures biased in either the direct or Fowler–Nordheim tunneling regimes. Since $\epsilon_{if}\approx 1.86$ for Al_2O_3 is substantially smaller that the 2.69 value in SiO_2, image force effects are more pronounced in the aluminum oxide. The reason for the lower image force dielectric constant appears to arise from a weaker electron-optical phonon coupling in Al_2O_3.[33] The parameters obtained in these experiments can now be used to simulate the data, an exercise which serves as a sort of self-consistency check. We have used Eq. (2) to calculate the maximum in the barrier potential, using the values of $\Phi_B=3.91$ eV and $\epsilon_{if}\approx 1.86$. The maxima in the potential, calculated as a function of V_{ox}, are plotted as a solid line in Fig. 2(b). The curve agrees well with the experimental data up to an oxide bias sufficient to start discharging the traps. The good fit once again confirms an image-force origin for the observed threshold shifts for both positive and negative oxide potentials.

In summary, we have investigated hot electron transport properties of amorphous Al_2O_3 layers of sufficient thickness (8 nm) to determine field dependent intrinsic properties, yet thin enough (3.5 nm equivalent SiO_2 thickness) to predictably extrapolate their suitability to thicknesses required in future generations of devices. It is however their extrinsic interface properties that seem to be most problematic. Although seemingly quite robust against bulk trap formation, the ease of achieving oxide failures, in comparison to SiO_2, as well as the presence of unacceptably large interface trap densities, are presently major obstacles to its potential usefulness as a viable gate oxide alternative.

ACKNOWLEDGMENTS

The authors would like to give special thanks to Evgeni Gusev for coordinating the sample growth. Useful discussions with Max Fischetti, Dan DiMaria, and Doug Buchanan are gratefully acknowledged. One of us (M.-T. C.) would like to thank IBM Spain for their support for an extended stay at the T. J. Watson Research Center.

[1] *The National Technology Roadmap for Semiconductors*, 3rd ed. (Semiconductor Industry Association, San Jose, CA, 1997).
[2] D. J. DiMaria and J. H. Stathis, Appl. Phys. Lett. **71**, 3230 (1997).
[3] Y. Taur *et al.*, Proc. IEEE **85**, 486 (1997).
[4] L. Manchanda *et al.*, Tech. Dig. Int. Electron Device Meeting 605 (1998).
[5] E. P. Gusev, M. Copel, E. Cartier, I. J. R. Baumvol, C. Krug, and M. A. Gribelyuk, Appl. Phys. Lett. **76**, 176 (2000).
[6] D. Park *et al.*, IEEE Electron Device Lett. **19**, 441 (1998).
[7] I. C. Kizilyalli *et al.*, IEEE Electron Device Lett. **19**, 423 (1998).
[8] S. A. Campbell, H.-S. Kim, D. C. Gilmer, B. He, T. Ma, and W. L. Gladfelter, IBM J. Res. Dev. **43**, 383 (1999).
[9] G. D. Wilk, R. M. Wallace, and J. M. Anthony, J. Appl. Phys. **87**, 484 (2000).
[10] R. A. McKee, F. J. Walker, and M. F. Chisholm, Phys. Rev. Lett. **81**, 3014 (1998).
[11] The reader should recall that the tunneling current across a rectangular barrier of height Φ_B and width t_{ox} is $I_T \propto \exp[-(8qm^*)^{1/2}\, t_{ox}(\Phi_B - V_{ox}/2)^{1/2}/\hbar]$, where V_{ox} is the applied bias and m^* the effective electron mass.
[12] Assuming a symmetric band gap alignment between Si and a gate dielectric with dielectric constant ϵ_0, an approximate criterion for the minimum band gap energy E_g is: $(E_g/2-1)^{1/2}\epsilon_0 \gg 7$. The value of 7 corresponds to SiO_2 and assumes a gate bias of 1 V, N. Szydlo and R. Poirier, J. Appl. Phys. **42**, 4880 (1971).
[13] N. Szydlo and R. Poirier, J. Appl. Phys. **42**, 4880 (1971).
[14] D. J. DiMaria, J. Appl. Phys. **45**, 5454 (1974).
[15] R. Ludeke, IBM J. Res. Dev. **44**, 517 (2000).
[16] The same system was used on ultrathin SiO_2 layers with no evidence for radiation induced damage.
[17] R. Ludeke and A. Schenk, J. Vac. Sci. Technol. B **17**, 1823 (1999).
[18] W. Kaiser and L. D. Bell, Phys. Rev. Lett. **60**, 1406 (1988).
[19] S. Sze, *Physics of Semiconductor Devices*, 2nd ed. (Wiley, New York, 1981).
[20] H. J. Wen, R. Ludeke, D. M. Newns, S. H. Lo, and E. Cartier, Appl. Surf. Sci. **123/124**, 418 (1998).
[21] L. D. Bell and W. Kaiser, Phys. Rev. Lett. **61**, 2368 (1988).
[22] R. Ludeke, A. Bauer, and E. Cartier, J. Vac. Sci. Technol. B **13**, 1830 (1995).
[23] R. Ludeke, M. T. Cuberes, and E. Cartier, Appl. Phys. Lett. **76**, 2886 (2000).
[24] H. J. Wen and R. Ludeke, J. Vac. Sci. Technol. B **15**, 1080 (1997).
[25] R. Ludeke, H. J. Wen, and E. Cartier, J. Vac. Sci. Technol. B **14**, 2855 (1996).
[26] E. H. Nicollian and J. R. Brews, *MOS Physics and Technology* (Wiley, New York, 1982).
[27] F. Gervais, in *Handbook of Optical Constants II*, edited by E. D. Palik (Academic, New York, 1991). In the kinetic energy range of 0.1–0.2 eV in which V_{th} is determined, ϵ_∞ varies rapidly from near 1 to 2.6.
[28] D. J. DiMaria, J. Appl. Phys. **47**, 4073 (1976).
[29] B. Kaczer and J. P. Pelz, J. Vac. Sci. Technol. B **14**, 2864 (1996).
[30] R. Ludeke and H. J. Wen, Appl. Phys. Lett. **71**, 3123 (1997).
[31] A. Schenk and G. Heiser, J. Appl. Phys. **81**, 7900 (1997).
[32] Reference 14 discusses an uncertainty of 0.2 eV in δE_{cb} which arises from the choice alone of the power dependence of the photoresponse.
[33] H. Froehlich, Adv. Phys. **3**, 325 (1954).

Mechanism of dopant segregation to $SiO_2/Si(001)$ interfaces

J. Dabrowski,[a] R. A. Casali,[b] H.-J. Müssig, R. Baierle,[c] M. J. Caldas,[d] and V. Zavodinsky[e]
IHP, Im Technologiepark 25, D-15236 Frankfurt (Oden), Germany

(Received 17 January 2000; accepted 31 May 2000)

Dopant atoms segregate to $SiO_2/Si(001)$ interfaces and are deactivated there. This can cause problems in fabrication of submicron microelectronic devices. On the basis of *ab initio* calculations, we propose a mechanism for donor segregation and deactivation. We argue that donor species (P and As) are trapped as threefold-coordinated atoms at interface defect sites (dangling bonds and Si vacancies) and, most significantly, in form of dopant pairs at defect-free interfaces. This pairing will dominate when dopant concentration exceeds approximately $10^{19}\,cm^{-3}$. © *2000 American Vacuum Society.* [S0734-211X(00)08504-8]

I. INTRODUCTION

In complementary metal-oxide-semiconductor (CMOS) technology, SiO_2 is placed next to doped regions of silicon.[1,2] Segregation to $SiO_2/Si(001)$ interfaces can cause redistribution of dopant atoms during fabrication of metal-oxide-semiconductor field-effect transistors (MOSFETs).[2] This can affect the device threshold voltage by up to 50%.[3] The interface can collect at least $3\times10^{14}\,cm^2$ P atoms,[4] that is, close to a monolayer, on $1\ ML\simeq7\times10^{14}\,cm^2=N_0$ for Si(001). The segregated atoms are deactivated. The transport of the dopant atoms from where they were implanted to the interface is supplied by point defects[5,6] induced by implantation damage.[2,7] Existing segregation models used in CMOS technology process simulation assume that the interface has approximately 1 ML of unspecified dopant traps.[8–11] What remains unknown is the nature of these traps and the reason why the segregated atoms do not act as shallow donors anymore.

Here, we analyze atomistic details of the segregation process. Our discussion is based on *ab initio* numerical results for P and As and on Auger electron spectroscopy (AES) measurements for P. The calculations show that segregation and deactivation of these group-V species occurs when the donor atoms acquire a triple-coordinated configuration, with three of their five electrons used in three bonds with Si neighbors and the remaining two electrons localized in a lone pair orbital. Such a geometry is energetically favorable when the donor substitutes a Si atom in an interface defect site or when it forms a nearest-neighbor pair with another donor atom close to the interface. Examination of published secondary ion mass spectroscopy (SIMS) data for phosphorus shows that dopant pairing dominates for implanted doses $\gtrsim10^{14}\,cm^2$, whereas at lower doses it is trapping at defects that prevails.

The energy gain due to pairing is $E_S^{pair}-E_S^{pair}(0)+2E_F$, where E_F is the Fermi energy with respect to the silicon valence band top and $E_S^{pair}(0)$ refers to *p*-type material ($E_F=0$); $E_S>0$ indicates that segregation is favorable. The energy gained when two donor atoms form a pair under a dimerized interface amounts to $E_S^{pair}\simeq0.6\,eV$ (computed value), assuming $E_F=0.8\,eV$ and substitutional P as the reference structure. The dependence of E_S^{pair} on Fermi level is a direct consequence of the dopant deactivation: two electrons are moved from E_F to deep states localized on lone pair orbitals of the segregated pair of atoms. The computed energy gain due to trapping at interface dangling bond sites is $E_S^{db}\simeq1.1\,eV$. Since the interface Si dangling bonds are usually occupied by two electrons, E_S^{db} does not depend on E_F, because the external reservoir (Fermi sea) is not involved in the reaction.

One might suppose that P and As atoms stick to the interface because there they can make bonds with oxygen. However, our calculations show that these species avoid such bonds if given a chance to react with silicon (i.e., Si reduces As and P). Indeed, it is known that P and As atoms are expelled from SiO_2 to silicon during thermal oxidation of Si.[2] Consequently, their segregation from bulk Si to the interface is not a simple chemical effect, but must be accompanied by a structural transformation. We find that this transformation (coordination change from fourfold to threefold) is promoted by elastic stress at the interface.

II. APPROACH

Ab initio calculations[12–17] were performed on a Cray T3E supercomputer in von Neumann Computing Center, Jülich, Germany. We used supercells of Si(001) type, with lateral dimensions from 2×2 to 4×4 (measured in translation vectors of the ideal surface). Vertically, the supercells contained six to eight Si layers and one to three oxide layers. Numerical convergence was verified by performing test calculations at plane-wave cutoff energies between 16 and 40 Ry and with Brillouin zone sampling equivalent to Γ and (1/4,1/4) points of 2×2, 3×3, and 4×4 surface cells. The data quoted

[a]Electronic mail: jarek@ihp-ffo.de
[b]Permanent address: Universidad Nacional del Nordeste, Av. Libertad 5600, 3400 Corrientes, Argentina.
[c]Present address: Depto. de Fisica, Universidade Fedoral de Santa Maria, 9711030 Santa Maria, RG, Brazil.
[d]Present address: Instituto de Fisica da Universidade de São Paulo, 05508-900 São Paulo, Brazil.
[e]Present address: Institute for Automation and Control Processes, 5 Radio str., Vladivostok 690041, Russia.

below were obtained using 40 Ry cutoff and the Γ point of 4×4. Reliability of the results was checked through comparison with geometries, electronic structures, and energy differences for test Si–O and Si–O–P structures computed with other *ab initio* codes[18–20] and with energy differences obtained by a semiempirical method (AM1[21]). The chemical potential of each donor species (P, As) was calculated from the total energy of a substitutional donor atom in the fourth Si layer below the interface in a 4×4 supercell. The position of the Fermi level was computed from total energy differences between various charge states (electron transition levels). We verified that in the absence of point defects, (0/+) transition levels coincide with the silicon valence band maximum. The estimated numerical uncertainty in energy differences is about 0.2 eV per cell due to Brillouin zone sampling and energy cutoff. Additional uncertainty of about 0.1 eV per donor atom enters due to inaccuracies in the calculation of chemical potentials for As and P.

Segregation was studied first by substituting dopant atoms for host atoms in silicon at various distances from the interface. Next, dopant atoms replacing under-coordinated Si atoms at the interface were considered. The SiO_2/Si(001) structures were designed to represent the key features of the interface with few atoms. Dimerized and undimerized interfaces were considered. In an undimerized interface, an atomic layer of SiO_2 is attached through oxygen atoms to Si(001) 1×1 surface. In a dimerized interface, up to three atomic layers of tridymite-based SiO_2 are attached through oxygen atoms to Si(001) 2×1 surface; the dimers are oxidized, as in Fig. 1(c). Finally, defects were created in bulk Si and then placed near an ideal interface. They were bonded to SiO_2 either directly (Fig. 1), or through oxygen interstitial atoms (O_i) adsorbed at the interface. The bulk defects included a nearest-neighbor P pair (P_2), O_i, Si vacancies (V_{Si}) complexed with P and O_i, and nobonded defects $113Si_2$ and $113P_2O_i$ [Figs. 1(a) and 1(b)].

Auger electron spectroscopy (AES) data were collected through native oxide layers thin enough (~15 Å) to make the interface phosphorus observable. To minimize electron-irradiation effects, the spectra were taken at low primary electron beam energy and current density. The detectable P is elemental. We found the P_{LVV} peak at 120 eV, which coincides with the position of uncharged P and is ~10 eV higher in energy than the P peak in P_2O_5.[22] The identification of the observed spectral line as due to unoxidized phosphorus is corroborated by the fact that electron-beam induced evaporation of the oxide affected neither position nor shape of this line. This is consistent with the known fact that P is expelled from SiO_2 during thermal oxidation of Si. It follows that the state of segregated P differs from the states of P donor and oxidized P: the latter are positively charged, whereas the segregated P atoms are electrically neutral. This result allows us to argue that a monolayer of efficient P traps is unlikely to exist at the interface, because P atoms bonded at such traps would have oxygen neighbors.

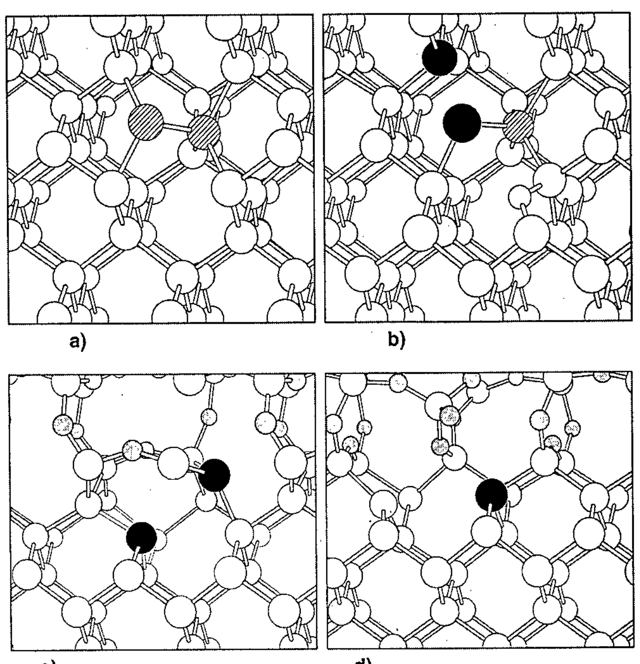

FIG. 1. Segregation to SiO_2/Si(001). Si atoms are white, O atoms are gray, P atoms are black. The P atoms are electrically neutral. Upper panels: Associated bulk defects. (a) $113Si_2$, or {113}-rebonded Si pair (dashed atoms) arranged as in the cone of a {113}-planar defect; metastable. (b) $113Si_2$ is stabilized as $113P_2O_i$. P substitutes one of the dashed atoms and its neighbor with a stretched bond. This bond breaks, leaving two threefold-coordinated P. The O_i relaxes part of the stress on the other end of the defect. When the oxygen atom is located at SiO_2/Si(001) interface, formation of this complex can lead to segregation of P (Ref. 26). Lower panels: Simple geometries of P atoms bonded at a dimerized SiO_2/Si(001) boundary. (c) P_2^*: Threefold-coordinated P atoms of a distorted nearest-neighbor P_2 pair. (d) Threefold-coordinated P atom trapped at an interface silicon vacancy.

III. SEGREGATION MECHANISM

We found that substitutional phosphorus, P_{Si}, may be weakly bonded (~0.2 eV) in the second layer under a "perfect" interface; no binding was computed in deeper layers. Formation of a coherent phosphorus silicide (SiP in zinc blend structure) also leads to no substantial energy gain. We conclude that neither attraction of substitutional donors induced by strain fields under the interface nor decreased solubility of P due to enhanced silicide precipitation under the interface are the dominant mechanisms of dopant segregation. Although we cannot exclude that these effects exist, we believe that other atomic geometries, for which we computed higher binding energies, are responsible for the segregation.

All structures with P–O of As–O bonds were unstable by at least 0.5±0.2 eV when P atoms were fourfold-coordinated, and by 0.1±0.2 eV for threefold-coordinated P. These results are in accordance with our AES data obtained through native oxide layers for segregated phosphorus and indicate that atomic geometries with donor-oxygen bonds play no important role in the segregation.

It is known that interfaces to native oxides contain much higher concentration of electrically active defects (presumably Si dangling bonds) than interfaces to thermal oxides

used as MOSFET gate dielectrics. These concentrations are $\sim 10^{13}$ and $\sim 10^{12}/cm^2$, respectively. As noted below, such dangling bonds are the preferred segregation sites. Our experiment confirms that the most efficient trapping does not involve formation of P–O bonds. However, it does not exclude that interfaces with thermal oxides may contain sites at which P atoms bonded to O reside after many dangling-bond sites have been occupied.

Reactions in which P substitutes an under-coordinated, unoxidized Si are clearly exothermic. The computed energy, gain is $\sim$1.1 eV.

Trapping on interface dangling-bond sites is limited by density of the defects. But at least two structures which can be formed without any seeds other than a "perfect" SiO_2/Si(001) boundary make it possible to cover the interface with nearly a monolayer of P (or As). The first one involves a pair of two nearest-neighbor, substitutional P atoms. We will name this pair P_2. Such a pair transforms under the interface into a pair of threefold-coordinated P atoms: the P–P bond is broken and one of the P atoms moves into the interstitial region [P_2^*, Fig. 1(c)]. This resembles behavior of certain donors in bulk III–V compounds and alloys.[23] In the second structure, which we name $113P_2O_i$ [Fig. 1(b)], an oxygen interstitial (O_i) and two threefold-coordinated P atoms combine with a {113}-nobonded Si pair [$113Si_2$, Fig. 1(a)]. The $113Si_2$ defect is built of two Si atoms that switched bonds with their neighbors,[24] as in cores of {113}-planar agglomerates of Si interstitials.[7,25] The P atoms substitute two nearest-neighbor Si atoms in $113Si_2$, and the P–P bond is broken. We focus our further discussion on the simplest of these two pair geometries, that is, on the P_2^* defect and its As analog, As_2^*. The $113P_2O_i$ complex is described in more detail in Ref. 26.

P_2^* is unstable in bulk Si, where it decays to P_2. But the P_2^* geometry is stabilized near the interface. This happens because the oxide helps to accommodate the deformation of bonds around P_2^*. The pairing energy E_S^{pair} depends therefore on the residual stress in the film, and on the possibility to relax this stress (i.e., on the oxide and interface structure). For example, $E_S^{\mathrm{pair}}(E_F=0.8\,\mathrm{eV})$ of phosphorus is 0.35 eV under a nondimerized interface and 0.46 eV under a dimerized interface with oxidized dimers [Fig. 1(c)]. The dimerized interface is favored because the O–Si–P angles become optimal in this configuration: they can approach the tetrahedral value of 109°. Such optimal angles are not feasible when the interface is undimerized, but even in this case they are closer to tetrahedral than it is possible in a P pair embedded in silicon bulk. The value of E_S^{pair} depends also on donor species, being higher for As than for P by 0.1–0.2 eV.

Pairing of dopants affects the functional form of the dependence of the number N_s of the segregated P on the concentration C_{P} of active P in bulk close to the interface. In order to estimate this effect, we assume that P can be bonded at the interface by pairing and/or trapping, that the corresponding reaction constants are thermally activated with energies E_p and E_t, and that P atoms are in local equilibrium.[9] Consider N_d deactivation sites existing under the interface.

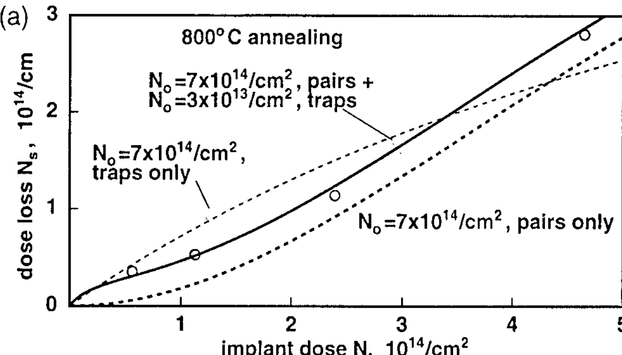

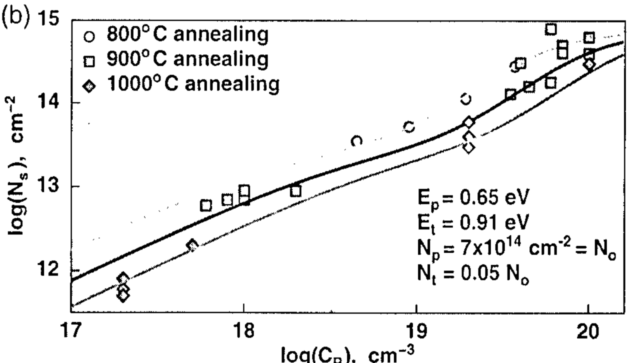

FIG. 2. Pairing and dose loss of P. The areal concentration of lost dopants, N_s, is obtained by comparison of SIMS profiles obtained first after implantation through an oxide film, then after annealing, and finally after stripping the oxide. (a) Dependence of N_S on implant dose N, SIMS data after (Refs. 4 and 28). If traps only are assumed, the dependence is qualitatively incorrect. Pairing and traps together give an excellent fit. (b) Dependence of dose loss N_s on P concentration C_{P} close to the interface, SIMS data after annealing at 800 °C [circles, after (Refs. 4 and 28)], 900 °C [squares, after (Refs. 9 and 10)], and 1000 °C [diamonds, after (Ref. 23)]. In order to reduce the number of parameters, we set $B_p=B_t=N_0$ (see the text), that is, we ignore entropy contributions other than those due to the number of lattice sites (Ref. 29).

The deactivation rate r is proportional to the number $N_f=N_d-N_s$ of free deactivation sites, while the activation rate $\bar{r}$ is proportional to the number N_s of the occupied sites: $r\sim(N_d-N_s)$, $\bar{r}\sim N_s$. The important difference between the deactivation rates for trapping and pairing is that the former is proportional to C_{P}, while the latter is proportional to C_{P}^2.

In thermal equilibrium $r=\bar{r}$ leading to $N_s-N_pC_{\mathrm{P}}^2/[C_{\mathrm{P}}^2+B_p^2\exp(-E_p/kT)]$ when segregation is dominated by pairing ($N_d=N_p$), and to $N_s=N_tC_{\mathrm{P}}/[C_{\mathrm{P}}+B_t\exp(-E_b/kT)]$ when trapping dominates ($N_d=N_t$). B_p^2 and B_t are proportional to the reaction constants for pairing and trapping. For simplicity, we neglected the small amount of P that is dissolved in the volume of SiO_2.[9] We also assumed that $N_p=N_0=1$ ML, that is, that all geometrically possible pairing sites can be occupied. The resulting functional dependence (Fig. 2) compares favorably with the published data:[4,9,10,27] the available temperature range is from 800 to 1000 °C. Numerical fit to these data yields $E_p=0.65\pm0.3\,\mathrm{eV}$ and $E_S=0.91\pm0.2\,\mathrm{eV}$. The fitted energies are compatible with our *ab initio* estimates for P pairing (0.5±0.4 eV at $E_F=0.8\,\mathrm{eV}$) and trapping at dangling-bond sites (1.1±0.2 eV).

Interestingly, the fitted value of N_t for trapping is as high

as 0.05 ML, about ten times higher than the typical density of electrically active interfacial defects created during thermal oxidation. In other words, there exists a regime of segregated P concentration between roughly 10^{12} and 10^{13} cm^2 in which the segregation can be explained neither by trapping at electrically active defects nor by pairing.

This apparent inconsistency can be reconciled when one recalls that ion implantation produces Si vacancies and interstitials. May segregated V_{Si} be responsible for the "missing" traps [Fig. 1(d)]? Combined Monte Carlo and classical potential simulations of atomic diffusion indicate that for each implanted ion, approximately one V_{Si} and one Si_i diffuses to the surface after ~800 °C anneal.[30] It is not known what happens to a vacancy once it reaches the SiO_2/Si(001) boundary, but it is clear that if the concentration of interface V_{Si} exceeds the equilibrium concentration and if the temperature is high enough for lateral diffusion, V_{Si} will annihilate at interfacial steps and/or agglomerate in complexes. We postulate that implantation at doses $10^{12}-10^{13}$ cm^2 saturates the interface with such vacancy complexes.

In order to gain insight into vacancy-related processes at SiO_2/Si(001), we performed exploratory calculations for V_{Si} segregation. We estimated that the binding energy of a single V_{Si} under the interface is ~1 (semiempirical result) and ~2 eV on more at the interface (*ab initio*). Given that *ab initio* formation energy of V_{Si} is ~3.1 eV in bulk Si, the binding energy, of more than 2 eV means that the formation energy of a single interfacial V_{Si} does not exceed ~1 eV. We did not calculate the energetics of V_{Si} complexes, but the distribution of local strain in SiO_2 near to V_{Si} sites suggests that formation of interface divacancies and/or divacancy pairs may lower the formation energy by a significant amount.

If the interface were in thermal equilibrium, the concentration of V_{Si} as high as 0.05 ML would require the V_{Si} formation energy of only ~0.4 eV. The actual formation energy is probably higher. But metastable arrangements of vacancies are well assessed on Si(001) *surfaces*. They appear when many (~10%) surface atoms are taken away, e.g., by sputtering or etching; when too many surface atoms are removed (~30%), formation of these structures may be suppressed. Metastable geometries existing on Si(001) up to 950 °C are known. Surface vacancies ("missing dimers") hardly recombine with surface adatoms, because complete annihilation of a dimer vacancy requires that two adatoms are captured. The first captured adatom is re-emitted before the second one arrives. We think that similar effects stabilize interface vacancies against recombination at interface steps and annihilation with Si and/or P interstitials. The postulated stability of vacancy complexes against recombination with Si_i is corroborated by the fact that Si_i incorporation into SiO_2 dominates over recombination of Si_i at the interface.[31] We verified that P trapping at a single V_{Si} defect segregated to a dimerized interface is energetically favorable. The corresponding energy gain amounts to 0.7±0.2 eV, in agreement with numerical fit to the data in Fig. 2. This segregation energy was computed for the vacancy structure displayed in Fig. 1(d) calculations for other geometries are in progress.

In summary, we presented an *ab initio* study of P and As segregation to SiO_2/Si(001) interfaces. A simple, physically based model of segregation was formulated. The coexistence of pairing and trapping causes a two-regime dependence of the segregation coefficient on the implant dose. We found that high dose losses are intrinsically nonlinear. We proposed that metastable Si vacancy complexes formed at the interface in the course of annealing of implantation damage are responsible for the segregation in the 10^{13} cm^2 regime.

ACKNOWLEDGMENTS

The authors thank S. Dunham, A. Fischer, P. Masri, H.-J. Osten, A. Ourmazd, and H. Rücker for discussions. This study was supported by the DFG project DA 308/5-1, Conselho Nacional de Desenvolvimento Científico e Tecnológico, Fundação de Amparoà Pesquisa do Rio Grande do Sul, and the Russian Research Program "Physics of Solid State Nanostructures." We acknowledge use of computers in von Neumann Institute for Computing, Jülich (J. D.) where most of the numerical work was done, and Laboratório de Computação Científica Avançada, University of São Paulo (R. B. and M. J. C.). Some of the calculations for Si vacancies were performed on the Cray T3E in the Computing Center, Ganching, Germany; we thank M. Scheffler for providing the computing resources.

[1]S. M. Sze, *Physics of Semiconductor Devices* (Wiley, New York, 1981).
[2]J. Dabrowski, H.-J. Müssig, M. Duane, S. T. Dunham, R. Goossens, and H.-H. Vuong, Adv. Solid State Phys. **38**, 565 (1999); http://www.ihp-ffo.de/chipps/97/Ddoc/dpg.html).
[3]H.-H. Vuong, C. S. Rafferty, S. A. Elshraghi, J. L. Lentz, P. M. Zoitzoff, M. R. Pinto, and S. J. Hillonius, IEEE Trans. Electron Devices **43**, 1144 (1996).
[4]P. B. Griffin, S. W. Crowder, and J. M. Knight, Appl. Phys. Lett. **67**, 482 (1995).
[5]P. M. Fahey, P. B. Griffin, and J. D. Plummer, Rev. Mod. Phys. **61**, 289 (1989).
[6]J. Dabrowski, in *Special Defects in Semiconducting Materials*, edited by A. Agarwala (Scitec Publ., Switzerland, 2000), p. 23.
[7]P. A. Stolk, H. J. Gossmann, D. J. Eaglesham, D. C. Jacobson, C. S. Rafferty, G. H. Gilmer, M. Jaraiz, J. M. Poato, H. S. Luftman, and T. E. Haynes, J. Appl. Phys. **81**, 6031 (1997).
[8]M. Orlowski, Appl. Phys. Lett. **55**, 1762 (1989); H. Sakamoto and S. Kumashino, SISPAD, 81 (1997); H.-H. Vuong, C. S. Rafferty, J. R. McMacken, J. Ning, and S. Chaudhry, *ibid.*, 85.
[9]F. Lau, L. Mader, C. Mazure, Ch. Werner, and M. Orlowski, Appl. Phys. A: Solids Surf. **49**, 671 (1989).
[10]H.-H. Vuong, C. S. Rafferty, J. Ning, J. R. McMacken, J. McKinley, and D. A. Stevie, SISPAD, 380 (1998).
[11]R. Kasnavi, P. B. Griffin, and J. D. Plummer, SISPAD, 48 (1998).
[12]Car-Parrinollo method, fhi97md code, Local Density Approximation, nonlocal pseudopotentials.
[13]M. Bockstodto, A. Kloy, J. Neugebauer, and M. Scheffler, Comput. Phys. Commun. **107**, 187 (1997).
[14]D. M. Coperley and B. J. Alden, Phys. Rev. Lett. **45**, 567 (1980).
[15]J. P. Perdew and A. Zunger, Phys. Rev. B **23**, 5048 (1981).
[16]D. R. Hamann, Phys. Rev. B **40**, 2980 (1989); G. B. Bachelot, D. R. Hamann, and M. A. Schlüter, Phys. Rev. B **26**, 4199 (1982).
[17]L. Kleinman and D. M. Bylander, Phys. Rev. Lett. **48**, 1425 (1982).
[18]FP-LMTO code and LCAO pseudopotential code SIESTA. SIESTA was used mostly for bulk defects (up to 128 atoms).
[19]M. Methfossel, M. van Schilfgaarde, and R. A. Casali, *Lecture Notes in Physics* (Springer, Berlin, 2000); E. Bott, M. Methfessel, W. Krabs, and P. C. Schmidt, J. Math. Phys. **39**, (1998).

[20]D. Sanchez-Portal, P. Ordejon, E. Artacho, and J. M. Soler, Int. J. Quantum Chem. **65**, 453 (1997).
[21]M. J. S. Dewar, E. G. Zoebisch, E. F. Healy, and J. J. P. Stewart, J. Am. Chem. Soc. **107**, 3902 (1985); V. A. Zayetz, *CLUSTER-Z1 Quantum Chemical Software* (ISC National Academy of Science, Ukraine, Kiev, 1990); V. D. Khavryutchenko and A. V. Khavryutchenko Jr., *DYQUAMOD Dynamical Quantum Modeling Software for Personal Computers* (JINR Dubna, and ISC National Academy of Science, Ukraine, Kiev, 1993).
[22]G. Queinolo and G. U. Pignatel, J. Electrochem. Soc. **127**, 2438 (1980).
[23]M. J. Caldas, J. Dabrowski, A. Fazzio, and M. Scheffler, Phys. Rev. Lett. **65**, 2046 (1990).
[24]J. Dabrowski, H.-J. Müssig, G. Wolff, and S. Hinrich, Surf. Sci. **411**, 54 (1998).
[25]S. Takeda and T. Kamino, Phys. Rev. B **51**, 2148 (1995).
[26]R. Baierle, M. J. Caldas, J. Dabrowski, H.-J. Müssig, and V. Zavodinsky, Physica B **273/274**, 260 (1999).
[27]Y. Sato, M. Watanabe, and K. Imai, J. Electrochem. Soc. **140**, 2679 (1993).
[28]We assume that the number of P atoms diffused to the interface is proportional to the implant dose.
[29]J. E. Northrup and S. B. Zhang, Phys. Rev. B **47**, 6791 (1993).
[30]M. Jaraiz, G. H. Gilmer, J. M. Poate, and T. Diaz de la Rubia, Appl. Phys. Lett. **68**, 409 (1996).
[31]S. T. Dunham, J. Appl. Phys. **71**, 685 (1992).

Roughening of the Si/SiO_2 interface during SC1-chemical treatment studied by scanning tunneling microscopy

M. Gotoh,[a] K. Sudoh, and H. Iwasaki
The Institute of Scientific and Industrial Research, Osaka University, 8-1 Mihogaoka, Ibaraki 567-0047, Japan

(Received 17 January 2000; accepted 19 April 2000)

The Si/SiO_2 interface morphology is observed with subnanometer resolution by an ultrahigh vacuum scanning tunneling microscope (STM). We analyze the roughness of the Si/SiO_2 interface for a chemical oxide film formed by a wet chemical process ($NH_4OH/H_2O_2/H_2O$ treatment). The oxide film is selectively removed by irradiating a field emission electron beam extracted from a STM tip at a temperature of 300–350 °C. We find that during the chemical process the roughness of the Si/SiO_2 interface increases with the treatment time. © *2000 American Vacuum Society.* [S0734-211X(00)02604-4]

I. INTRODUCTION

Most Si wafer cleaning processes have been used on conventional RCA cleaning.[1] The SC1 treatment ($NH_4OH/H_2O_2/H_2O$), which is the first step of the RCA treatment, is particularly effective for removing surface contaminants by etching the Si substrate. However, it has been reported that the surface microroughness increases in wet cleaning processes.[2] Such microroughness degrades device performance more significantly as the characteristic dimensions of devices decrease.[3] Despite the technological importance, the mechanism of roughening for wet chemical processes is poorly understood, in particular from the microscopic viewpoint.

In $NH_4OH/H_2O_2/H_2O$ solutions, etching and oxidation occur simultaneously, while keeping the thickness of the chemical oxide constant.[4] To understand the nature of the roughening during the treatment on the local atomic scale, it is necessary to directly observe the buried Si/SiO_2 interface. Gibson and co-workers pioneered the investigation of interface roughness, imaging the interfacial steps by plan-view transmission electron microscopy.[5,6] Watanabe *et al.* also observed interfacial steps using scanning reflection electron microscopy.[7,8] Although these imaging techniques are powerful methods used to characterize the interface roughness and to study the oxidation mechanism, their lateral resolution is limited to a structural scale of the order of a nanometer. In this article, we report an alternate method to observe buried Si/SiO_2 interface structures with subnanometer resolution using ultrahigh vacuum scanning tunneling microscopy (UHV-STM).[9] With this method the oxide films are removed under UHV by a locally confined, low-energy electron beam extracted from a STM tip which is used as well to observe the interface morphology.[10,11] This is effective in avoiding contamination and damage to the interface compared to the chemical etching normally used to remove the oxide films. In this article we study the microscopic roughness of the Si/SiO_2 interface for a Si(001) wafer treated by a wet chemical process.

[a]Electronic mail: gotoh31@sanken.osaka-u.ac.jp

II. EXPERIMENT

We performed experiments in an UHV chamber with a base pressure of 3.0×10^{-8} Pa equipped with a variable temperature STM (JSTM-4610 from JEOL). Samples were cut from *n*-type, (001)-oriented Si wafers. The Si(001) substrate was first cleaned by flashing to 1200 °C in order to prepare an atomically flat, clean surface; it was then thermally oxidized at ~600 °C for 1 min in oxygen at a pressure of 2.0×10^{-4} Pa to form a thin oxide overlayer. The oxide layer protects the interface during transfer of the sample through air for further treatment in SC1 solutions ($NH_4OH/H_2O_2/H_2O$). The mixing ratio of the solution was $NH_4OH:H_2O_2:H_2O=1:1:10$ and the treatment temperature was 72 °C. Finally, the sample was rinsed in flowing ultrapure water at room temperature before transferring it again into the UHV chamber. The sample was first degassed at 420 °C for 12 h and the oxide film was removed by a field emission electron beam from the STM tip at a sample voltage of 100 V and field emission currents of 100–400 nA while heating the sample (Fig. 1). Subsequently the exposed Si surface was observed with the same tip at a sample bias voltage of 3 V.

III. RESULTS AND DISCUSSION

Figure 2 shows a STM image of the thermally oxidized Si(001) surface in which two circular openings are formed by the field emitted electron beam irradiation at 450 °C for 10 (top left) and 20 s (bottom right). A sample bias voltage of 100 V and a field emission current of 100 nA were used. The Si(001) surface was, as noted in Sec. II, cleaned by flashing in UHV prior to thermal oxidation. Since the oxide film is ultrathin, the atomic steps can be observed not only on the clean Si surfaces in the open windows where alternate S_A and S_B steps are revealed, but they are seen as well on the oxide surface. Note that the exact oxide thickness cannot be measured from the STM image, but it is believed to be a few monoatomic layers. In Fig. 2, each step in the open window is continuously connected to the step on the oxide surface, and we find no scooped-out ditches and holes in the open

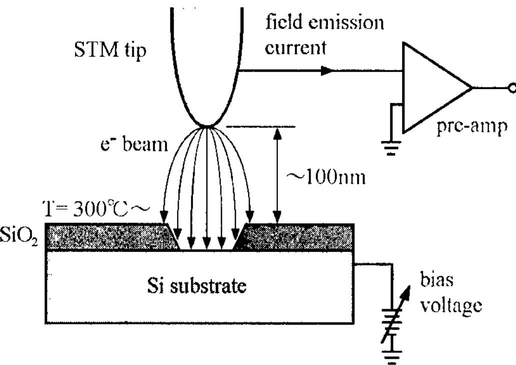

FIG. 1. Schematic diagram of the experimental setup of the silicon oxide removal by electron beam irradiation at elevated temperature using STM.

windows. Thus we consider the perturbation at the interface structure due to oxide removal to be negligible under the process conditions.

Figure 3 shows STM images of the Si(001) surface which is thermally oxidized after flash cleaning in UHV and a region where the oxide film is removed by field emitted electron beam irradiation at 350 °C with scanning the STM tip at a sample bias voltage of 100 V and a field emission current of 200 nA over the 260 nm×260 nm square region. The scanning time was 90 s, which corresponds to an area dose of 2.7×10^{4} C/cm^{2}. In Fig. 3(b), one can see that the terrace and step structure which had been formed by flashing prior to thermal oxidation is retained at the interface after thermal oxidation, although the roughness of the steep edge and the density of islands seem to be larger compared to a typical flash cleaned surface. This result may suggest that the oxide film growth accidentally corresponds to completion of oxide layers according to the previously reported layer-by-layer oxidation of Si surfaces.[8] The root-mean-square (rms) roughness of the exposed Si surface is 0.13 nm, which is comparable with that of the clean Si surfaces. Study of the dependence of the thermal oxide interface roughness on oxide thickness is in progress. We used such well-controlled surfaces covered by thin thermal oxide layers as starting surfaces for chemical oxidation by the SC1 treatment.

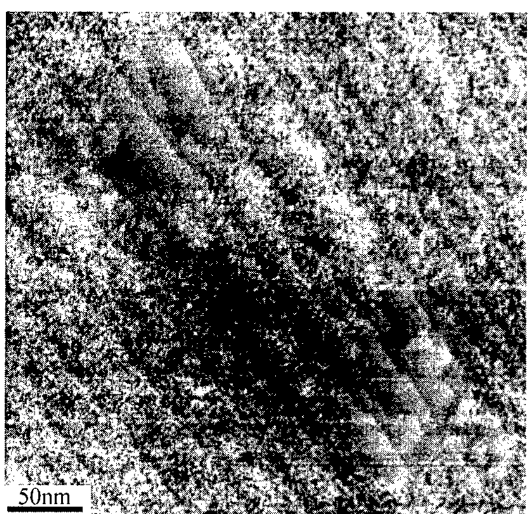

FIG. 2. 350 nm×335 nm STM images of the thermally oxidized Si(001) surface in which two circular openings are formed by field emitted electron beam irradiation with a STM tip at 450 °C for 10 (top left) and 20 s (bottom right).

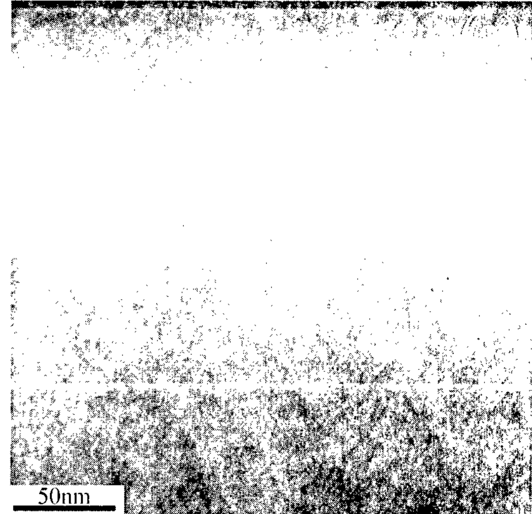

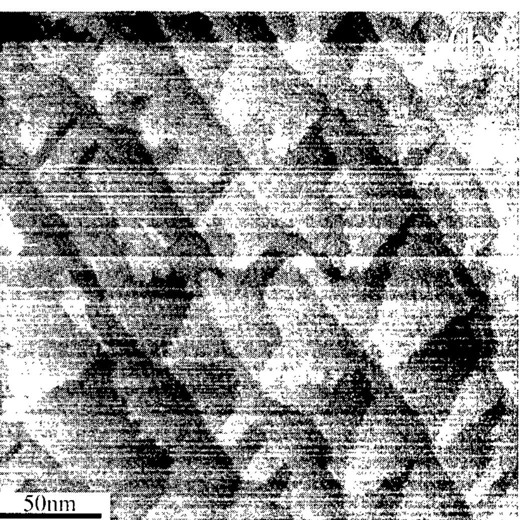

FIG. 3. 250 nm×245 nm STM images of (a) the thermally oxidized Si(001) surface and (b) a region where the oxide film is removed by field emitted electron beam irradiation at 350 °C.

In SC1 solutions, etching and oxidation of the Si surface occur simultaneously. The thickness of the chemical oxide is about 6 Å, independent of the concentration of NH_4OH and H_2O_2.[4] Figure 4(a) shows a typical STM image of the chemically oxidized Si(001) surface after the SC1 treatment for 15 min. Figures 4(b) and 4(c) show STM images of the Si/SiO_2 interfaces exposed by electron beam irradiation for the samples treated by the SC1 for 1 and 15 min, respectively. To remove the chemical oxides, the 260 nm×260 nm square regions were scanned by the STM tip at a sample bias voltage of 100 V and a field emission current of 400 nA, while heating the samples at 300 °C. The scanning time was 180 s, which corresponds to an area dose of 1.1×10^{5} C/cm^{2}. Figure 5 shows cross sections of the surfaces along the lines in

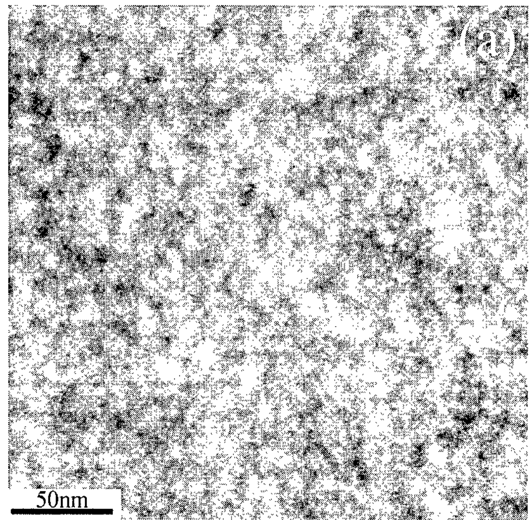

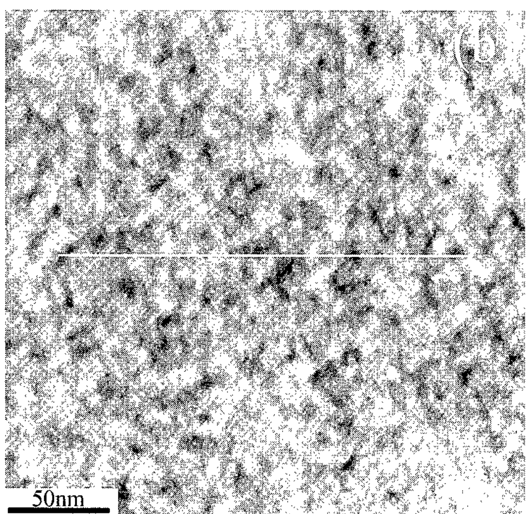

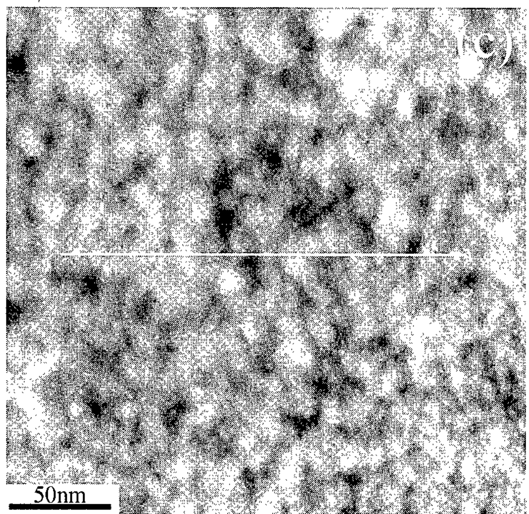

FIG. 4. 250 nm×245 nm STM images of (a) the chemically oxidized Si(001) surface and (b) and (c) regions where the oxide films formed by the SC1 treatment for 1 and 15 min are removed by field emitted electron beam irradiation at 300 °C, respectively.

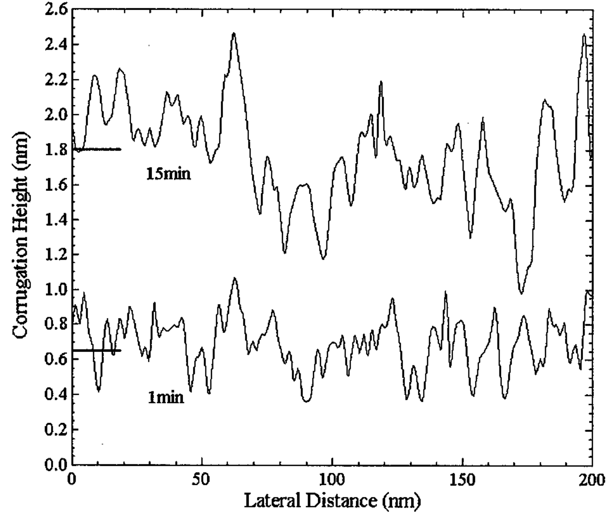

FIG. 5. Cross sections of the surfaces along the lines in Figs. 4(b) and 4(c).

Figs. 4(b) and 4(c). In the STM images in Figs. 4(b) and 4(c), we cannot find terrace and step structures, but, instead, microscopic undulation. As the treatment time increases, the interface roughness increases by coarsening of the microscopic undulation.

To quantify the roughness from the STM data we measured the rms roughness (surface width) $\sigma(L)=[\langle h(\mathbf{r})^2\rangle - \langle h(\mathbf{r})\rangle^2]^{1/2}$, where $h(\mathbf{r})$ is the surface height at position $\mathbf{r}$ and L is the horizontal length measured. Figure 6 shows the rms roughness plotted as a function of length-scale L for the samples treated by SC1 for 1 and 15 min. The rms roughnesses saturated at larger length are 0.18 and 0.29 nm for the 1 and 15 min SC1 treatments, respectively, showing that the interface roughness increases with the length of the chemical treatment. It is known that SC1 cleaning increases the surface microroughness and that the rms roughness for the 15 min SC1 treatment is comparable with the values previously reported.[12] In Fig. 6, the correlation length, at which the rms roughness reaches a constant, increases with the length of chemical treatment, implying that the lateral characteristic

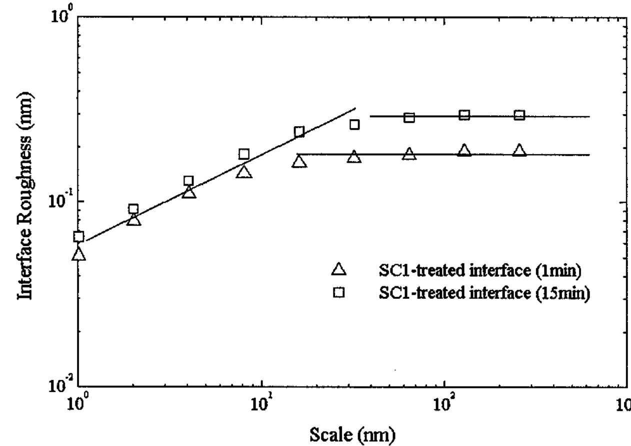

FIG. 6. Scaling analysis of the chemical oxide interface roughness for the chemical oxides treated for 1 and 15 min.

scale of the roughness also increases due to the prolonged treatment. The results shown in Fig. 6 suggest that the interface roughness follows scaling behavior.[13] Detailed analysis of the scaling behavior is in progress to determine the roughening mechanism for the wet chemical process.

IV. CONCLUSION

In conclusion, our STM based method for observation of buried Si/SiO_2 interfaces, in which oxide films are removed under UHV conditions by low-energy electron beam irradiation at 300–350 °C, is effective for measuring the microscopic interface roughness. Using this method, we have measured the roughness of the Si/SiO_2 interface caused by the SC1 treatment and found that the interface roughness increases with the treatment time.

ACKNOWLEDGMENTS

This work was supported by the Center-of-Excellence Program (09CE2005) from the Ministry of Education, Science, Sports and Culture. One of the authors (K.S.) acknowledges support from JSPS. The authors thank Dr. Nan Li for fruitful discussions.

[1]W. Kern and D. A. Puotien, RCA Rev. **31**, 187 (1970).
[2]M. Miyashita, T. Tsuga, K. Makihara, and T. Ohmi, J. Electrochem. Soc. **139**, 2133 (1992).
[3]P. O. Hahn and M. Henzler, J. Vac. Sci. Technol. A **2**, 574 (1984).
[4]M. Sakurai, J. Ryuta, E. Morita, K. Tanaka, T. Yoshimi, and Y. Shimanuki, *Extended Abstracts of The Electrochemical Society* (The Electrochemical Society, Pennington, NJ, 1990), Vol. 90-1, p. 710.
[5]J. M. Gibson and M. Y. Lanzerotti, Nature (London) **340**, 128 (1989).
[6]X. Chen and J. M. Gibson, Phys. Rev. B **54**, 2846 (1996).
[7]H. Watanabe, K. Fujita, and M. Ichikawa, Surf. Sci. **385**, L952 (1997).
[8]H. Watanabe, K. Kato, T. Uda, K. Fujita, and M. Ichikawa, Phys. Rev. Lett. **80**, 345 (1998).
[9]M. Gotoh, K. Sudoh, and H. Iwasaki (unpublished).
[10]N. Li, T. Yoshinobu, and H. Iwasaki, Jpn. J. Appl. Phys., Part 2 **37**, L995 (1998).
[11]M. Shibata, Y. Nitta, K. Fujita, and M. Ichikawa, Appl. Phys. Lett. **73**, 2179 (1998).
[12]T. Ohmi, M. Miyashita, M. Itano, T. Imaoka, and I. Kawanabe, IEEE Trans. Electron Devices **39**, 537 (1992).
[13]H. Iwasaki, A. Iwamoto, K. Sudoh, and T. Yoshinobu, Mater. Res. Soc. Symp. Proc. **367**, 159 (1995).

E' centers and leakage currents in the gate oxides of metal oxide silicon devices

P. M. Lenahan[a] and J. J. Mele
The Pennsylvania State University, University Park, Pennsylvania 16802

(Received 17 January 2000; accepted 30 May 2000)

We have made electron spin resonance and current density versus voltage measurements on a variety of thin SiO_2 films on silicon. In some of the films we have generated fairly high ($\geqslant 10^{18}\,cm^3$) densities of neutral E' centers near the Si/SiO_2 interface. Neutral E' centers are paramagnetic defects in which an unpaired electron resides in a high p-character wave function primarily located on a silicon atom bonded to three oxygen atoms. We find that the generation of these centers is consistently accompanied by the generation of large leakage currents in the oxide. We also find that the annihilation of these E' centers by a low temperature (200 °C) anneal in air is consistently accompanied by the annihilation of the large leakage currents. Many investigations have established that high electric field stressing creates leakage currents in thin oxide films on silicon. Studies of at least two independent groups have also established that high electric field stressing generates significant E' density within the stressed oxides. Our study demonstrates a strong link between E' center density and oxide leakage currents. Our results, combined with the results of the earlier aforementioned studies, strongly indicate an important role for E' centers in stress induced leakage currents. These leakage currents are a fundamental problem in the very thin SiO_2 films on silicon utilized in present day metal oxide silicon devices. © *2000 American Vacuum Society.* [S0734-211X(00)08304-9]

I. INTRODUCTION

The oxides of present day metal oxide silicon integrated circuits can be so thin that leakage currents caused by various types of stressing are a fundamental concern.[1–6] An unstressed oxide exhibits current density versus voltage characteristics consistent with the tunneling current density anticipated from the "ideal" band diagram illustrated in Fig. 1(a). However, if an oxide is subjected to stressing, for example, by a high electric field across the oxide, damage caused by the stressing can cause leakage currents to appear at relatively low oxide fields.[1–6]

These leakage currents have been extensively investigated in many experimental studies of a purely "electronic" nature.[1–6] Several investigators have suggested a link between E' centers and these leakage currents.[1–4,6,7] E' centers[8–17] are point defects in which an unpaired electron resides in a high p-character wave function strongly localized on a silicon atom bonded to three oxygen atoms. A neutral E' center is schematically illustrated in Fig. 2. Recent observations indicate that the leakage currents are caused by inelastic tunneling of conduction band electrons to defect centers in the oxide near the Si/SiO_2 boundary.[5,6] Recent work by Takagi, Yasuda, and Toriumi[6] and Yokozawa *et al.*[7] suggests that E' centers are good candidates for the centers involved in the inelastic tunneling process.

In this study we show that the generation of electrically neutral E' centers are accompanied by a large (several orders of magnitude) monotonic increase in leakage currents and that the disappearance of these E' centers via low temperature (200 °C) annealing is accompanied by a monotonic decrease in leakage currents. Recent calculations by Takagi, Yasuda, and Toriumi[6] indicate that defect densities in $\sim 10^{18}-10^{19}/cm^3$ range in the immediate (<10 nm) vicinity of the Si/SiO_2 interface ($\sim 10^{12}-10^{13}/cm^2$) would lead to leakage current densities similar to those we measured in this study. Our electron spin resonance (ESR) measurements indicate E' densities consistent with this range.

II. EXPERIMENTAL TECHNIQUES

It is possible to generate either positively charged or neutral E' centers in thin oxide films. Positively charged E' centers may be generated by exposing oxides to modest ($<10^{14}$ holes/cm^2) fluences of holes,[11–17] for example, by exposing the oxides to a moderate dose ($\leqslant$10 Mrad) of ionizing radiation. Neutral E' centers can be generated by subjecting oxides to extended periods of vacuum ultraviolet illumination (VUV).[17] These E' centers are generated very near the Si/SiO_2 boundary.[17] (Several earlier studies have shown that E' centers are generated in oxides subjected to high electric fields.[18–20] The nature of the E' charge states in the stressed oxides was not evaluated in those earlier studies.)

Since the presence of charged defects would (due to the presence of the space charge alone) alter the oxide barrier and increase oxide current [see Fig. 1(b)] we have chosen to investigate leakage currents in oxides with neutral E' centers. These centers were generated by exposing oxides to up to 120 mm of VUV illumination ($hc/\lambda \leqslant 10.2$ eV) from a 50 W deuterium lamp in a vacuum chamber. After VUV illumination, samples were transferred to the TE_{104} cavity of an

[a]Electronic mail: pmlesm@engr.psu.edu

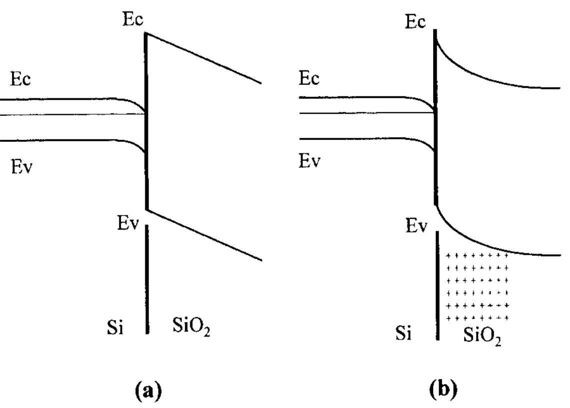

FIG. 1. Silicon–silicon dioxide band diagram near the Si/SiO_2 boundary with a positive gate potential applied. (a) No space charge is present in the oxide. (b) The effect of positive oxide charge is schematically illustrated. The presence of the positive charge will lower the barrier and increase leakage current.

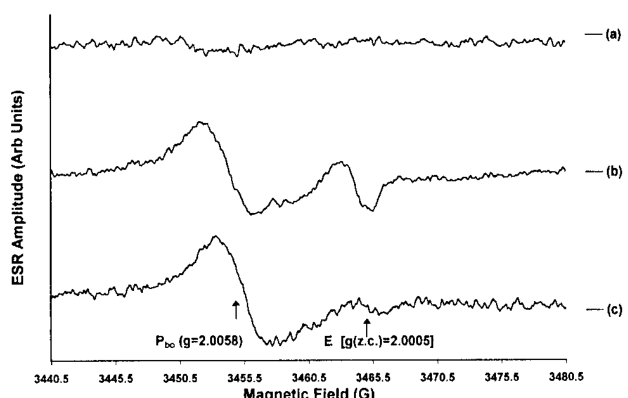

FIG. 3. (a) Pre-VUV, (b) post-VUV, and (c) post-VUV post-annealing ESR traces (40 G wide) taken on the 45 nm oxide films on silicon; the spectrometer settings were chosen so both the Si/SiO_2 interface P_b centers and the E' centers are clearly visible. A third signal, due to conduction electrons, appears on the right-hand side of both traces.

ESR spectrometer. ESR measurements were made at room temperature on oxides at x band using a Bruker spectrometer with a 300 series bridge. Our ESR spin concentration measurements are accurate to slightly better than a factor of 2 in absolute number and about $\pm 10\%$ in relative number. In order to evaluate the leakage current for the oxide film as a whole and not from isolated weak spots, we used corona discharge ions to bias the oxide surfaces and measured the corona ion induced potential using a Kelvin probe electrostatic voltmeter.[21] This approach, the measurement of oxide currents via corona ion decay, was pioneered many years ago by Weinberg, Johnson, and Lampert.[21] Taking the derivative of potential versus time we determined current versus voltage dependence: $C(dV/dt)=dQ/dt=i$. Here C is the oxide capacitance, $\epsilon_0 \kappa_{SiO_2}/t_{ox}$, where ϵ_0 is the permitivity of free space, κ_{SiO_2} is the relative dielectric constant of SiO_2, and t_{ox} is the oxide thickness. Q is charge, t is time, and i is current. Our current measurements, based on a derivative of voltage versus time, are reasonably accurate ($\pm 10\%$); however, the absolute value of the voltage may be in error by tenths of a volt.

Three very different sets of oxides have been used in this study. Oxides 5.8 nm thick were grown in NO at 850 °C and then exposed to O_2, also at 850 °C at the Honeywell Facility in Plymouth, MN. Oxides 45 nm thick were grown in dry oxygen at 850 °C at the Navy Space Warfare Center Facility in San Diego, CA. Oxides 120 nm thick were grown in dry oxygen at 950 °C at the Harris-Intersil Facility in Palm Bay, FL. All oxides were grown on (001) Si surfaces. We chose this rather wide range of oxide thicknesses in the hope that our results might be interpreted as broadly representative of the response of thermally grown oxide films on silicon.

III. RESULTS

The results of our study are qualitatively illustrated in Figs. 3–6. Figure 3 illustrates pre-VUV, post-VUV, and post-VUV–post-annealing ESR traces taken in the vicinity of the free electron $g \cong 2.002$. Here $g = h\nu/\beta H$, where h is Planck's constant, ν is microwave frequency, β is the Bohr magneton, and H is the magnetic field at resonance. The magnetic field is swept over a range which is appropriate for both widely studied metal oxide silicon ESR defects, P_b and E' centers.[13] P_b centers are silicon dangling bond centers precisely on the Si/SiO_2 boundary.[11–17,22–24] The spectrometer settings used to obtain the data in Fig. 3 are less than optimum for both the E' and P_b spectra. The settings represent a compromise, chosen so that both spectra would be simultaneously visible. Prior to VUV illumination, no ESR signals are visible. After

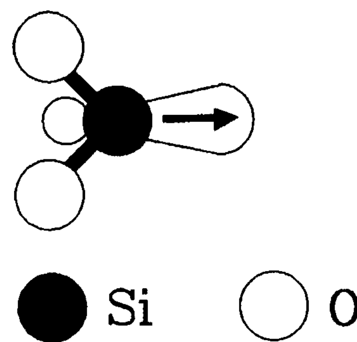

FIG. 2. Schematic illustration of a neutral E' center.

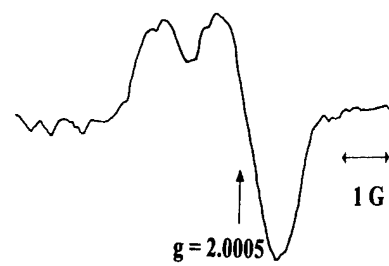

FIG. 4. 8-G-wide ESR scan, of VUV illuminated oxides, with the spectrometer settings optimized for the E' center signal.

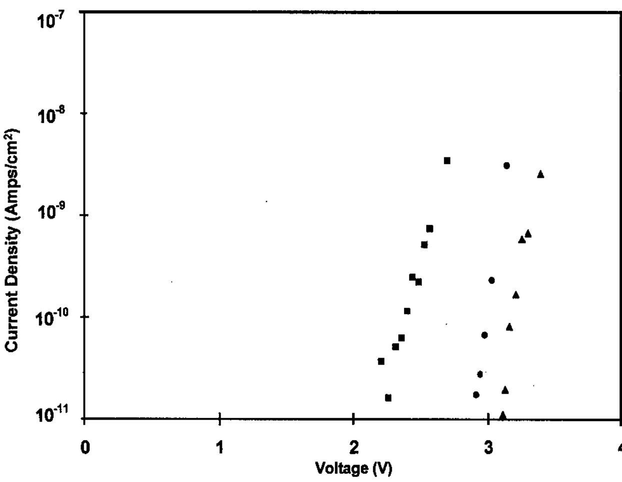

FIG. 5. Current density vs voltage measurements on the 5.8 nm oxides prior to VUV illumination (as processed), post-VUV illumination, and post-VUV postanneal at 200 °C. Circles: as processed. Squares: post-VUV illumination. Triangles: post-VUV, postanneal.

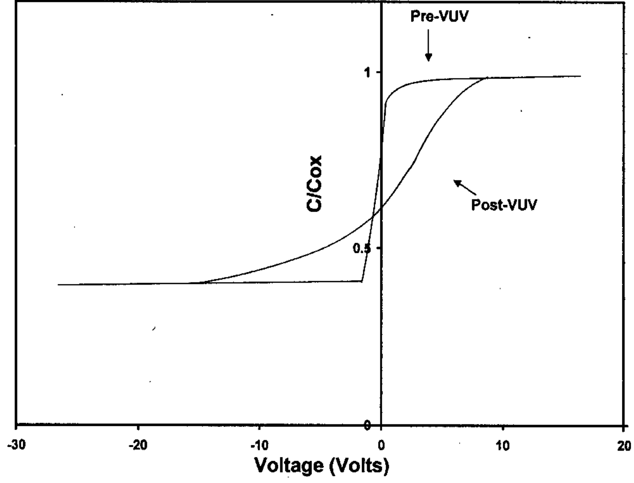

FIG. 7. Pre- and post-VUV illumination on capacitance vs voltage curves on the 120 nm oxides. Note that the two curves intersect indicating that the VUV illumination creates very little net space charge within these oxides, a result consistent with earlier observations.

illumination, strong E' and P_b signals are present. An anneal of 15 min at 200 °C eliminates most of the E' centers but does little to P_b intensity. Figure 4 illustrates a post-VUV stressing E' spectrum taken at a modulation amplitude and microwave power significantly lower than that in Fig. 3. These spectrometer settings, unlike those utilized in Fig. 3, are optimized to detect the E' center defect. With regard to the spectrometer settings of Figs. 3 and 4 some elaboration may be useful. In Fig. 3, the microwave power level chosen is too high for the E' spectrum and the modulation intensity is too low for optimum P_{b0} detection. The compromise of a microwave power setting too high for optimum E' observation and a magnetic field modulation intensity too low for optimum P_{b0} detection allows both spectra to be simultaneously observed in a single trace. In trace 4, the quite low microwave power and modulation intensity are appropriate for E' observation. The low microwave power (10^{-5} W) settings used in obtaining Fig. 4 are required for the quantification of E' center concentration.

Figures 5 and 6 show pre-VUV illumination, post-VUV illumination, and the postillumination poststressing current–voltage ($I-V$) curves for the 45 and 5.8 nm oxides. The VUV illumination greatly increases leakage currents. These currents are greatly reduced by the subsequent anneal. Figure 7 illustrates representative pre- and post-VUV illumination capacitance versus voltage curves, which indicate that essentially no oxide space charge is created by the VUV illumination; thus, the very large changes in current versus voltage characteristics illustrated in Figs. 5 and 6 are not due to space charge in the oxides. Figure 8(a) illustrates a corresponding increase in E' density with the VUV illumination; Fig. 8(b) illustrates a representative series of $I-V$ curves for the 120 nm oxide films prior to VUV stressing and for various peri-

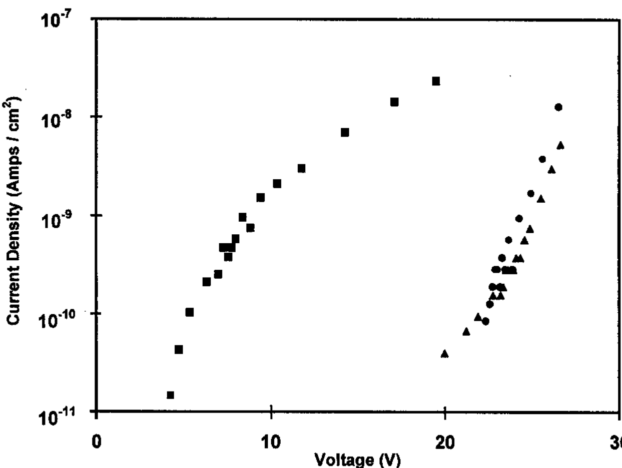

FIG. 6. Current density vs voltage measurements on the 45 nm oxides prior to VUV illumination (as processed), post-VUV illumination, and post-VUV postanneal at 200 °C. Circles: As processed; squares: post-VUV illumination; triangles: postanneal.

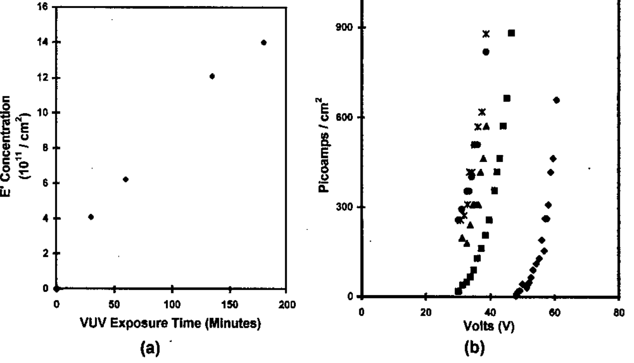

FIG. 8. (a) Plot of E' concentration vs VUV illumination time compared with (b) current density vs voltage curves at various VUV illumination times. Note the E' density and leakage currents both increase monotonically with VUV illumination time. Both sets of data were taken on the 120 nm oxide sample. Diamonds: As processed; squares: post-30 min VUV illumination, triangles: post-60 min VUV asterisks: post-135 min VUV, circles: post-180 min VUV.

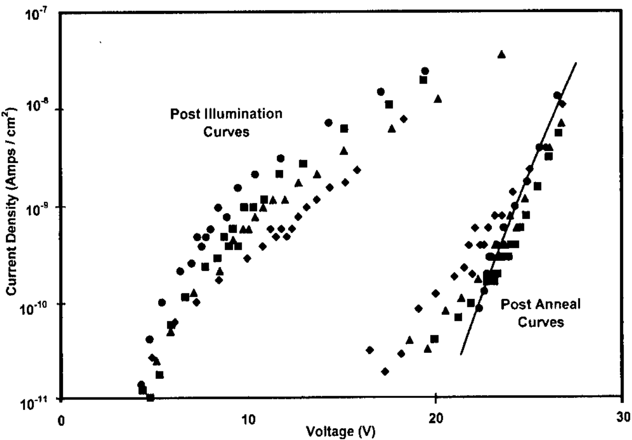

FIG. 9. Prestressed, post-VUV stressed, and post-VUV-postannealing current vs voltage curves for the 45 nm oxides are illustrated. The preillumination (as processed) curve is represented by the circles within the right side cluster of data points as well as by the trend line connecting the aforementioned points. The post-VUV illumination curves are clustered on the left-hand side of the plot (diamonds: 30 min VUV illumination; triangles: 60 min VUV; squares: 90 min VUV; circles: 120 min VUV). The postanneal curves are clustered on the right-hand side of the plot (diamonds: 15 min anneal; triangles: 30 min anneal; squares: 60 min anneal).

ods of VUV stressing. Figure 9 illustrates a representative series of $I-V$ curves for the 45 nm films prior to VUV illumination, for various periods of VUV illumination, and for post-VUV annealing. Figures 10 and 11 directly compare E' densities and leakage currents in the 45 nm oxides as a function of VUV illumination and post-VUV annealing. Note the close correspondence between E' center generation and leakage current generation, as well as E' center annihilation and the elimination of the leakage currents.

IV. DISCUSSION

Recently, Takagi, Yasuda, and Toriumi[6] modeled leakage currents in terms of inelastic tunneling of silicon conduction

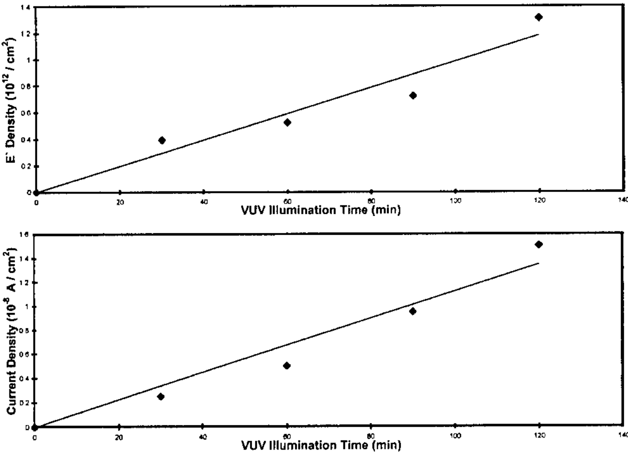

FIG. 10. (Upper) E' density vs VUV illumination time in the 45 nm oxides. (Lower) current density plotted at 17 V vs VUV illumination time for the same oxides. The choice of 17 V is arbitrary but, as Fig. 9 shows, the qualitative trend indicated is consistent with the complete data set. The lines are drawn as a guide for the eyes.

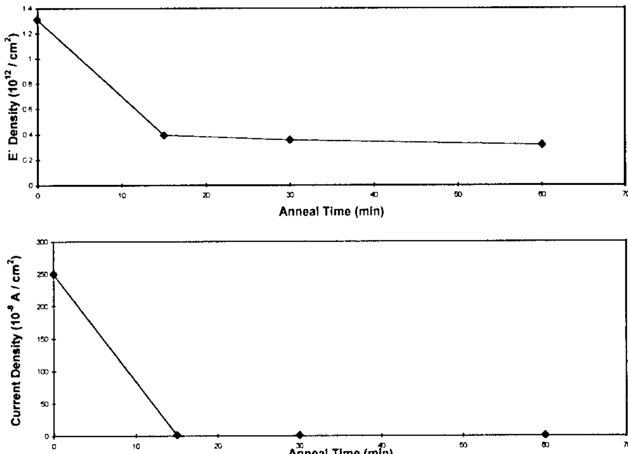

FIG. 11. (Upper) E' density vs anneal time in air at 200 °C in the 45 nm oxides. (Lower) leakage current plotted at 20 V vs anneal time for the same oxides. As in Fig. 10, the choice of 20 V is arbitrary but indicates the qualitative trend indicated by the complete data set shown in Fig. 9. The lines are drawn as a guide for the eyes.

band electrons into oxide traps which experience about ~1.5 eV relaxation upon electron capture. They also provided experimental evidence for this relaxation.[25] A fairly large relaxation would presumably occur in E' centers upon electron capture; thus these defects have been suggested by Takagi, Yasuda, and Toriumi (and others)[1–4] as possible candidates for the inelastic tunneling centers. At least two independent ESR studies have directly demonstrated strong E' center generation in a fairly wide variety of high electric field stressed oxides.[19–21]

V. CONCLUSIONS

Our results clearly demonstrate a strong qualitative correlation between neutral E' center density and oxide leakage currents in several sets of very different oxides. We believe our results provide extremely strong, albeit circumstantial, evidence that these defects, as suggested by the work of Takagi, Yasuda, and Toriumi,[6] are responsible for these leakage currents due to inelastic tunneling of silicon conduction band electrons through their levels.

It should be noted that we have generated these currents via VUV illumination, a process likely very different than the process involved in E' generation through high electric field stressing.[19–21] We used the VUV illumination scheme to simply separate space charge effects on the oxide barrier, which are generally present in high electric field stressing, from effects due to tunneling through the defect levels. Thus, although our experiment rather cleanly separates effects of space charge on the barrier, our oxides have not experienced precisely the same phenomena as the technologically important high oxide field stressing process. It should also be noted that our observations do not rule out possible roles for other defects in oxide leakage current phenomena.

Nevertheless, since it has already been established that high electric field stressing creates significant E' density, our results (linking E' centers to leakage currents) strongly sug-

gest an important, probably dominating, role for these defects in the stress induced leakage currents observed in many thin oxide films.

ACKNOWLEDGMENTS

The authors thank J. F. Conley of Dynamics Research Corporation, R. K. Lowry and D. Woodbury of Intersil, and Mike Liu of Honeywell for samples and useful discussions.

[1]J. H. Suehle, P. Chaperale, C. Messick, W. M. Miller, and K. C. Boyko, Proceedings of the IEEE International Reliability Physics Symposium, 1994 (unpublished), p. 120.
[2]J. Mc Pherson and H. Mogul, J. Appl. Phys. **84**, 1513 (1998).
[3]B. Schlund, C. Messick, J. S. Suehle, and P. Chaparala, IEEE International Reliability Physics Symposium Proceedings, 1996 (unpublished).
[4]D. J. Dumin and J. Maddux, IEEE Trans. Electron Devices **40**, 986 (1993).
[5]E. Rosenbaum and L. F. Register, IEEE Trans. Electron Devices **44**, 317 (1997).
[6]S. Takagi, N. Yasuda, and A. Toriumi, IEEE Trans. Electron Devices **46**, 348 (1999).
[7]A. Yokozawa, A. Oshiyama, Y. Miyamolo, and S. Kumasinio, Proceedings of the IEEE International Electron Devices Meeting, 1997 (unpublished), p. 703.
[8]R. A. Weeks, J. Appl. Phys. **27**, 1376 (1956).
[9]R. H. Silsbee, J. Appl. Phys. **32**, 1456 (1961).
[10]D. L. Griscom, Phys. Rev. B **22**, 4192 (1980).
[11]P. M. Lenahan and P. V. Dressendorfer, IEEE Trans. Nucl. Sci. **30**, 4602 (1983).
[12]P. M. Lenahan and P. V. Dressendorfer, J. Appl. Phys. **55**, 3495 (1984).
[13]Electron spin resonance studies of centers in amorphous oxide films have been reviewed by P. M. Lenahan and J. F. Conley, Jr., J. Vac. Sci. Technol. B **16**, 2134 (1998).
[14]H. Miki, M. Noguchi, K Yokogawa, B. Kim, K. Asada, and T. Sugano, IEEE Trans. Electron Devices **35**, 2245 (1988).
[15]T. Takahashi, B. B. Triplett, K. Yokogawa, and T. Sugano, Appl. Phys. Lett. **26**, 1339 (1987).
[16]L. Lipkin, L. Rowan, A. Reisman, and C. K. Williams, J. Electrochem. Soc. **138**, 2050 (1991).
[17]J. F. Conley, P. M. Lenahan, H. L. Evans, R. K. Lowry, and T. J. Morthorst, J. Appl. Phys. **76**, 2872 (1994).
[18]W. L. Warren and P. M. Lenahan, J. Appl. Phys. **62**, 4305 (1987).
[19]W. L. Warren and P. M. Lenahan, IEEE Trans. Nucl. Sci. **34**, 1355 (1987).
[20]H. Hazama, K. Harada, Y. Ozawa, and K. Yamabe, *Proceedings of the Workshop on Ultrathin Oxides* (Japanese Society of Applied Physics, Tokyo, 1998), Catalog No. AP982204, pp. 207–212 (in Japanese).
[21]Z. A. Weinberg, W. C. Johnson, and M. A. Lampert, J. Appl. Phys. **47**, 248 (1994).
[22]Y. Nishi, T. Tanaka, and A. Ohwada, Jpn. J. Appl. Phys. **11**, 85 (1972).
[23]P. J. Caplan, E. H. Poindexter, B. E. Deal, and R. R. Razouk, J. Appl. Phys. **50**, 879 (1979).
[24]P. M. Lenahan, P. V. Dressendorfer, K. L. Brower, and W. C. Johnson, IEEE Trans. Nucl. Sci. **28**, 4105 (1981).
[25]S. Takagi, N. Yasuda, and A. Toriumi, IEEE Trans. Electron Devices **46**, 335 (1999).

Photoemission spectroscopy of platinum overlayers on silicon dioxide films

J. W. Keister and J. E. Rowe[a),b),c)]
Department of Physics, North Carolina State University, Raleigh, North Carolina 27695-8202

J. J. Kolodziej and T. E. Madey
Department of Physics and Astronomy and Laboratory for Surface Modification, Rutgers University, Piscataway, New Jersey 08855-0849

(Received 6 April 2000; accepted 15 May 2000)

Soft x-ray photoelectron spectroscopy (SXPS) has been used to study ultrathin Pt films on silicon dioxide as model supported-catalyst materials. Using monochromatic synchrotron radiation. Pt $4f$ and Si $2p$ core level photoelectron peaks were measured as a function of platinum coverage in the range 0–10 ML. The bulk silicon and silicon dioxide film Si $2p$ peaks each show a binding energy decrease within the first ML of dosing. However, the effect is stronger for the silicon dioxide Si $2p$ peak, indicating an increased screening of the $2p$ electrons by the metal overlayer. We also observe a monotonic increase of the work function of the ultrathin film Pt/SiO_2 system with coverage from 4.52 initially to 5.58 eV at ~10 ML. The Pt $4f_{7/2}$ core level binding energy decreased from ~72.2 to ~70.9 eV between 0 and ~10 ML coverage. This binding energy shift at low dose (≤ 1 ML), the coverage dependence of the Pt line shape and intensity, and the large saturation coverage for the work function are each consistent with two-dimensional cluster-island growth. The metallic nature of the Pt overlayer with dose is quantitatively verified by nonlinear, least-squares numerical fitting of the Pt $4f$ SXPS peak line shapes with Gaussian-broadened Doniach–Sunjic functions. © *2000 American Vacuum Society.* [S0734-211X(00)05704-8]

I. INTRODUCTION

The present article presents a study of Pt metal clusters supported on thin SiO_2 films on Si wafers. The growth of metal overlayers on insulating substrates is important for characterizing supported catalysts for various chemical reactions. In addition, the Pt/SiO_2/Si system is a good simple model for a metal-oxide-semiconductor transistor structure, and thus these experiments are relevant models for electronic properties of such structures in electronics technology.

The interaction of near noble metals such as Pt with a covalent solid is expected to be relatively weak. Previous work has shown that Pt films grow as metal island clusters with a three-dimensional (3D) growth mode on vitreous carbon.[1,2] However, more recent theoretical work suggests that polarization of the metallic overlayer by an ionic solid substrate becomes increasingly important as the metal film thickness increases, and that oxide surface defects may demote cluster nucleation.[3,4] In the study of Pt overlayer clustering, the use of photoelectron spectroscopy is particularly useful because of its chemical state sensitivity, as well as its sensitivity to electrostatic charge transfer on both short and long time scales. In the present study, we have used soft x-ray photoelectron spectroscopy of the Pt $4f$ and Si $2p$ core levels to probe Pt overlayer formation on thin SiO_2/Si films, and have found clustering behavior between 0 and 10.9 ML.

II. EXPERIMENTAL DETAILS AND PROCEDURES

Thin SiO_2 films on Si were prepared by plasma oxidation techniques as outlined in earlier work.[5] There are several important features of these SiO_2 films. In particular, they are thick enough (~20 Å) to prevent direct contact between the Pt overlayer and the Si substrate during deposition at 300 K. This is important because platinum silicides are known to form at relatively low temperature.[6] Thinner films (≤ 1 nm) are likely to be more susceptible to pinhole defects which might allow Pt atoms to contact the Si substrate atoms and react, resulting in nucleation of a $PtSi_x$ phase. Previous studies[5] have shown that continuous SiO_2 films form on Si(111) at ~10 Å thickness. By using somewhat thicker films in the present study, we ensure that the Pt metal–Si interaction is minimal. Also the films are thin enough to prevent charging during the photoemission experiment. This is important for clarifying the core-hole final state potential effect on the Pt clusters, which we observe. In addition, the oxide films are flat and uniform. This is ensured by the chemical cleaning and postoxidation annealing steps taken during oxide film preparation.[5]

The SiO_2 films were transferred in air to the photoemission chamber and cleaned by annealing to ~500 °C in ultrahigh vacuum.[5] After this, platinum was thermally evaporated onto the SiO_2 substrate in the photoemission chamber (base pressure $\sim 4\times 10^{-11}$ Torr) using a thin Pt wire filament, heated resistively. During dosing, the sample was kept at room temperature. The dose time was controlled using a shutter, and the dose rate was calibrated by dosing onto a tungsten (211) crystal, which shows marked changes in the surface states upon completion of 1 ML[7] (one close-packed monolayer of Pt atoms corresponds to a coverage of 1.5

[a)]Author to whom correspondence should be addressed; electronic mail: rowe@arl.aro.army.mil
[b)]Also with the Physics Division, Army Research Office, Research Triangle Park, NC 27709-2211.
[c)]Also with the Department of Physics and Astronomy and Laboratory for Surface Modification, Rutgers University, Piscataway, NJ 08855-0849.

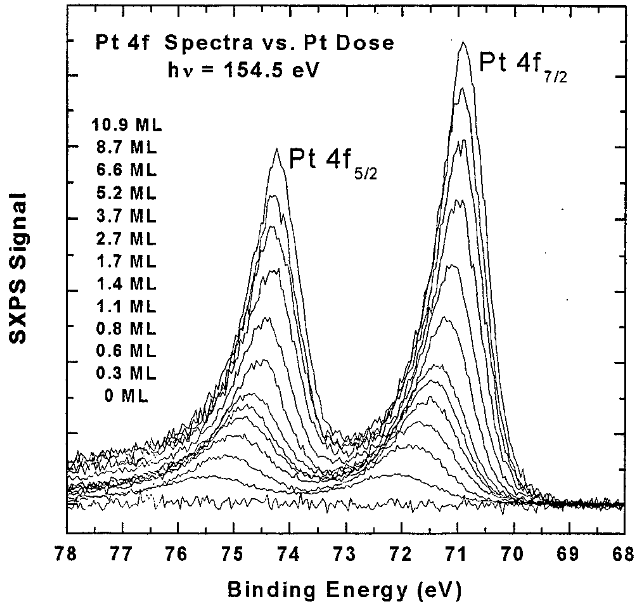

FIG. 1. SXPS Pt $4f$ data for dosing on flat, amorphous SiO_2, measured at a photon energy of 154.5 eV. The peak height increases monotonically with dose for coverages of up to ~11 ML.

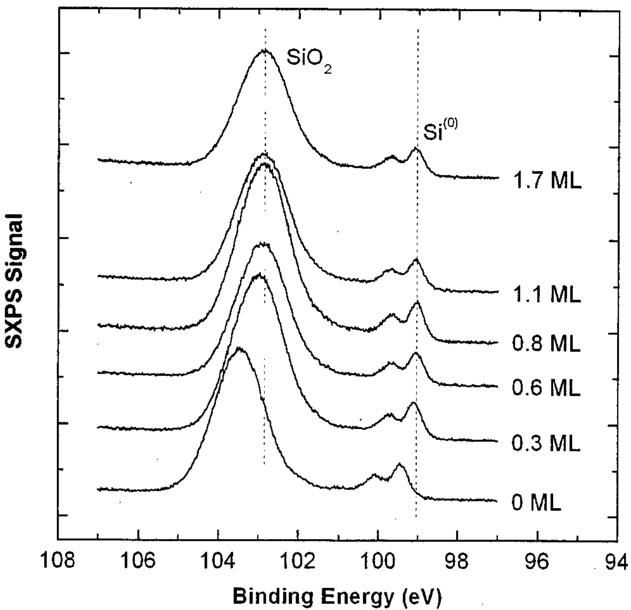

FIG. 2. Si $2p$ SXPS spectra measured at 154.5 eV photon energy for Pt doses$\leq$1.7 ML. The intensity is attenuated continuously and the positions shift until a coverage of ~0.6 ML is reached. Above this coverage, the peaks are attenuated only.

$\times 10^{15}\,cm^{-2}$). In our dosing experiments, 1 ML corresponded to 25 min, on average.

The soft x-ray photoelectron spectroscopy (SXPS) measurements were made using tunable soft x-ray light (40–200 eV) from the UV synchrotron storage ring at the National Synchrotron Light Source in Upton, NY. The U4A grazing-angle 6 m toroidal grating monochromator has recently been upgraded to a spherical grating configuration to give high resolution (<0.1 eV) over the entire range of usable energies and includes exit slit translation. The electron energy analysis was performed using a Vacuum Science Workshop, model VSW-100, 100 mm hemispherical analyzer operating at a fixed pass energy with a resolution of ~0.1 eV. The reference Fermi energy (E_F) was measured using the metal sample holder. It is important to note that this technique is very surface sensitive as a result of the short (<10 Å) inelastic mean free path of the electrons at the energies used.

III. EXPERIMENTAL RESULTS

A. Platinum 4*f* core levels

In Fig. 1 are shown several Pt $4f$ SXPS spectra obtained for Pt doses between 0 and 10.9 ML. The Pt $4f_{7/2}$ binding energy for the 10.9 ML Pt film was measured to be 70.9 eV, which compares favorably with the known Pt bulk value of 71.1 eV.[8] The platinum $4f$ signal is spin-orbit split by an energy of ~3.3 eV, allowing clear separation between the $4f_{7/2}$ and $4f_{5/2}$ peaks. These peaks shift continuously with Pt coverage in the range of 0–10.9 ML indicating a continuous change in core level binding energy due to either initial state chemistry or final state potential over this range. The Pt $4f$ peaks also become narrower as coverage increases.

B. Silicon 2*p* core levels

The Si $2p$ spectra shown in Fig. 2 each have a strong, broad peak for SiO_2, and a spin-orbit-resolved pair of narrower peaks for the Si substrate (the Si $2p_{3/2}-2p_{1/2}$ splitting is 0.60 eV). The high SiO_2/Si SXPS signal ratio is typical for a film of ~20 Å thickness, measured at 154.5 eV photon energy. The chemical shift of ~4 eV of the silicon dioxide film peak, relative to the substrate, is also typical for SiO_2 films of this thickness. The Si $2p$ spectra show a shift in the core level peak positions within the first monolayer of Pt dosing. This shift is greater for the oxide peak than for the bulk.

C. Pt/SiO_2 work function

As illustrated in Fig. 3, the work function of the Pt/SiO_2 system increases monotonically as the Pt dose is increased from 0 to 10.9 ML. From an initial value of 4.52 eV, the work function reaches 5.58 eV at maximum dose, and has a value of 4.95 eV at ~1 ML. The work function asymptotically approaches the known Pt bulk value[9] of 5.59 eV as the Pt coverage is increased. The shift from 5.58 to 4.52 eV is a 1.06 eV shift, consistent with $\Delta\Phi_{max}$ values for Pt dosing on W which are in the range of 1.00–1.05 eV.[7]

IV. DISCUSSION

A. Platinum 4*f* core levels

In order to quantify the shape and position of the Pt $4f$ SXPS line, a nonlinear least-squares fitting procedure was used. An example of the line shape analysis is shown in Fig. 4. We found that all the data could be reasonably fit with a Gaussian-broadened Doniach–Sunjic (i.e., metallic) line

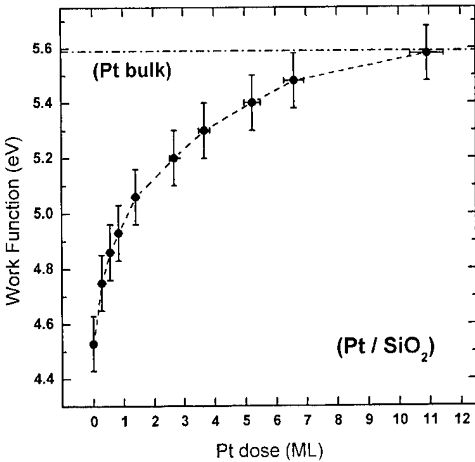

FIG. 3. Work function of the Pt-dosed SiO_2 film as a function of Pt dose, which rises monotonically until the bulk Pt value of 5.59 eV (Ref. 9) is asymptotically reached. A dashed line is drawn between consecutive points as a guide to the eye.

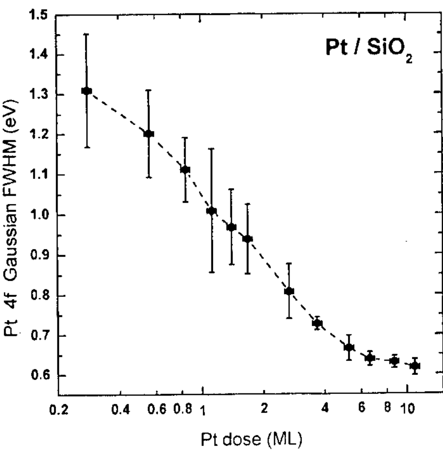

FIG. 5. Gaussian full width at half maximum (FWHM) of the Pt 4f peaks measured as a function of Pt dose. The monotonic decrease is taken to indicate that the clusters approach uniform bulk Pt by smoothly coalescing as more Pt is available, until the intrinsic bulk linewidth is approached, to within experimental resolution. A dashed line is drawn between consecutive points as a guide to the eye.

shape, with an α value[7] fixed at 0.22 and a Gaussian full width at half maximum (FWHM) which decreases monotonically from 1.3 to 0.6 eV with increasing Pt dose. The Gaussian width as a function of Pt dose is given in Fig. 5. We attribute the decreasing Gaussian linewidth to the coalescence of clusters from a distribution of cluster sizes. This interpretation is tied to our model for the Pt binding energy shift, and we return to it again, after the model is described in the following paragraphs.

With the α value and Lorentzian linewidth fixed for all of the Pt 4f fits, the only parameters that contribute to the peak area are the Gaussian width and peak height. In fact, the peak area is proportional to the product of these two parameter values. This fact allowed us to evaluate the relative Pt SXPS intensity from the fit parameters, as a function of Pt coverage. As illustrated in Fig. 6, the photon-flux-normalized SXPS Pt signal increases proportionally with dose at very low coverages (less than 1 ML). After ~0.9 ML is reached, the slope of the peak area versus dose curve drops by a factor of 2 or more, as a result of Pt signal attenuation in 3D clusters. The deviation from linearity at this point in the curve strongly suggests a cluster growth mode change from two-dimensional (2D) to 3D. As dosing continues, the Pt signal approaches the maximum intensity of bulk Pt (SXPS electrons of deeper Pt layers are scattered by the topmost Pt atoms).

Unfortunately, the nature of the Pt film growth within the first layer is not unambiguous based on the total intensity dependence on coverage. Further details of the growth mode in the first layer are obtained from the coverage dependence of the Pt 4f binding energy peak position, which is also obtained from the fitting procedure. From Fig. 1 it is clear that the Pt 4f peak position also changes as a function of coverage. A reasonable explanation for this behavior is that the Pt clusters become instantaneously charged during photoionization, and that the local electrostatic potential resulting

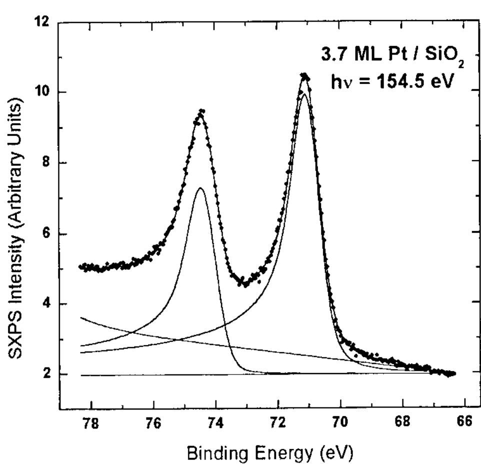

FIG. 4. Example fit of Gaussian-broadened Doniach–Sujic line shape to the Pt 4f peaks at an intermediate dose of 3.7 ML. Individual contributions to the fit are shown below the data.

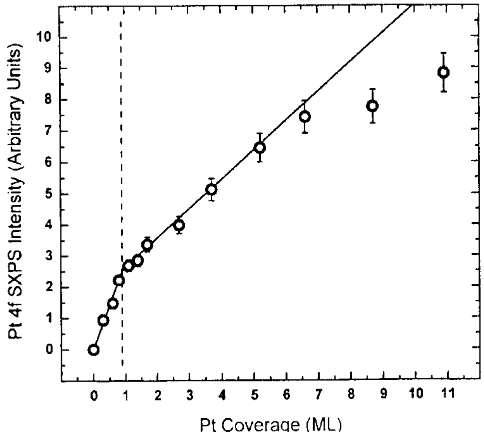

FIG. 6. Pt 4f SXPS intensity as a function of Pt dose. Note the deviation from linearity at ~1 ML (a vertical dashed bar is drawn at 0.9 ML for comparison).

from this charge depends on the size of the metal cluster as observed previously for Pt on vitreous carbon substrates.[1,2] That is, the cluster momentarily takes on the positive unit charge of the core hole. This charge is distributed at the boundary of the cluster by valence electron screening (i.e., a uniform potential of a metallic cluster is assumed). The apparent binding energy of photoemitted electrons which leave the cluster is reduced by the core-hole charge, multiplied by the local electrostatic potential resulting from screening of this charge.[1,2] Despite this instantaneous charging of the Pt clusters, no net buildup of charge (i.e., no surface charging) occurs for the film. On average, the Pt-covered surface is not charged, due to neutralization of the clusters by the slower electrons tunneling through the SiO_2 film.

For photoionized clusters of any dimensionality, the local electrostatic potential is inversely proportional to the cluster's radius. This idea can be summarized by the following equations:

$$\mathrm{BE}=\mathrm{BE}_0+\Delta\mathrm{BE},$$
$$\Delta\mathrm{BE}=q\cdot V=e\cdot\left(\frac{1}{4\pi\epsilon_0}\cdot\frac{e}{R}\right), \quad (1)$$

where BE is the observed binding energy. The other terms are defined as follows: BE_0 is the final, reference binding energy, ΔBE is the observed (coverage dependent) shift, q is charge, V is the electrostatic potential, e is the electron charge, ϵ_0 is the free-space permittivity, and R is the cluster's radius. Although the dependence of the binding energy shift on a cluster's radius R does not change with cluster dimensionality, the rate of change of the binding energy with dose does. This is because the number of atoms in a cluster will be proportional to R^2 or R^3, depending on the dimensionality (i.e., 2D or 3D growth). This dependence can be obtained from the measured binding energy shift using the following relation:

$$\Delta\mathrm{BE}\propto\theta^{-1/D}, \quad (2)$$

where D is the dimensionality of the cluster. So, a log–log plot of binding energy shift (ΔBE) vs Pt coverage (θ) will have a slope of $-1/D$. This is shown for our data in Fig. 7 with the final, reference Pt $4f_{7/2}$ binding energy (BE_0) taken as 70.7 eV, as extrapolated from our data in Fig. 1. This plot suggests that the Pt clusters prefer to grow in a two-dimensional manner below ~0.5–1 ML of Pt dose. This is consistent with the intensity dependence result of Fig. 6. At higher coverages, the binding energy shift deviates from the linear dependence of Eq. (2) due to attenuation of the lower-layer Pt photoelectron signal by scattering in the upper Pt layers, and by increased contribution from 3D cluster growth as coverage is increased.

As mentioned earlier, the cluster size dependence of the Pt $4f$ peak position leads to a peak width which depends on the distribution of cluster sizes. Low coverages present the possibility of a wide range of cluster sizes, and since each size should have a slightly different binding energy [as described in Eq. (1)], this situation gives rise to a wide SXPS peak. When the thicker Pt film coalesces to form fewer, larger clusters from this distribution, the Pt ($4f$) peak becomes narrower, as shown in Fig. 5.

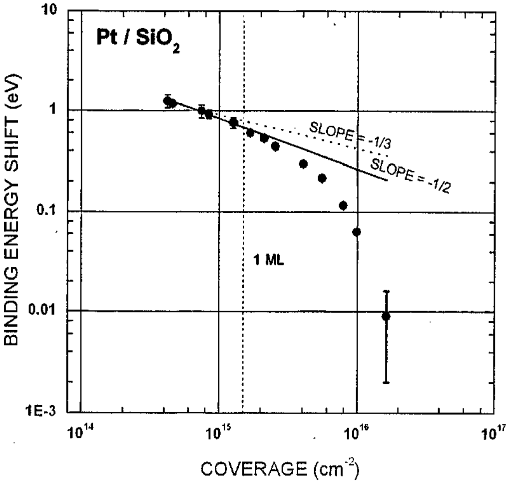

FIG. 7. Log–log plot of binding energy shift vs Pt dose reveals the growth order as the slope. Here, two-dimensional growth is implied by the slope of −1/2.

B. Silicon 2*p* core levels

As the SiO_2/Si system is covered with metal, the Si $2p$ peaks are attenuated by the Pt overlayer. In addition, Fig. 2 shows that the peak positions are sensitive to the Pt coverage within the first monolayer of dosing. Once the first ~0.6 ML of Pt is added, the bulk Si $2p$ binding energy is reduced by 0.38 eV. The nearly rigid shift of these spectra from 0 to 0.3 ML is due to pinning of the Fermi level at a different position in the Pt dosed sample compared to the clean SiO_2 surface. This pinning shift is known to occur at rather low coverage for wide band gap materials such as SiO_2.[10]

The relative positions of the substrate and film peaks in the Si $2p$ spectra are also coverage dependent. At doses greater than ~0.6 ML, the Si–SiO_2 chemical shift is constant at 3.74 eV while for 0 ML this relative shift is 3.95 eV. Thus, the Pt film reduces the SiO_2 Si $2p$ binding energy by 0.59 eV. The difference between the Pt-induced binding energy shifts for the two chemical environments of Si may be explained in terms of a localized final-state screening effect. In general, the source of the chemical shift is due in part to the transfer of valence electron density from silicon to oxygen atoms. This charge transfer gives rise to the the initial-state chemical shift effect, as the increased Coulomic attraction of $2p$ electrons with the Si nucleus increases the binding energy. However, another part of the chemical shift is due to localized screening by neighboring atoms of the positive core-hole charge created by the photoionization process. This final-state screening effect results in lower binding energies and is strongest for atoms closest to the higher-dielectric Si substrate or metallic overlayer. For thin SiO_2 films there is a final-state screening of the $SiO_2 2p$ core hole due to the Si valence electrons in the bulk Si. As the SiO_2 film thickness becomes larger than the photoelectron escape

depth this effect becomes negligible. In the case of Pt dosing, however, the SiO_2 $2p$ core hole for Si atoms nearest the surface show additional screening effects from the Pt valence electrons due to proximity of the Pt overlayer. This produces the additional shift observed. The charge screening effect of the Pt overlayer is in good agreement with previous results of Kobayashi *et al.* for Pd/SiO_2.[11] Both the Fermi level pinning and final-state screening change with Pt coverage, whereas the chemical (initial state) effect is expected to remain constant during dosing.

V. SUMMARY

In summary, the cluster growth of Pt on SiO_2 was studied using photoelectron spectroscopy. The data indicate that the growth is two-dimensional for the first 0.5–1.0 ML. This result is in contrast with previous observations of three-dimensional growth of various metals on amorphous carbon.[1,2] but agrees with several other observations of 2D growth on similar systems such as Pt/Al_2O_3, Pd/MgO, and Cu/ZnO.[12–15]

The Pt film was shown to effectively screen the Si $2p$ photoelectron core hole and lower the binding energy by roughly 0.5 eV, although the effect is stronger for the SiO_2 film which is in direct contact with the Pt. This result is consistent with results of Pd overlayers on the SiO_2/Si structure.[11]

ACKNOWLEDGMENTS

This work is supported by the Army Research Office, the Department of Energy (which operates the NSLS facility at Brookhaven National Laboratory), the National Research Council, and North Carolina State University.

[1] G. K. Wertheim, S. B. DiCenzo, and S. E. Youngquist, Phys. Rev. Lett. **51**, 2310 (1983).
[2] G. K. Wertheim and S. B. DiCenzo, Phys. Rev. B **37**, 844 (1988).
[3] A. Bogicevic and D. R. Jennison, Surf. Sci. Lett. **437**, L741 (1999).
[4] A. Bogicevic and D. R. Jennison, Phys. Rev. Lett. **82**, 4050 (1999).
[5] J. W. Keister, J. E. Rowe, J. J. Kolodziej, H. Niimi, H.-S. Tao, T. E. Madey, and G. Lucovsky, J. Vac. Sci. Technol. A **17**, 1250 (1999).
[6] B. Y. Tsui and M. C. Chen, J. Appl. Phys. **68**, 6246 (1990).
[7] J. J. Kolodziej, K. Pelhos, I. M. Abdelrehim, J. W. Keister, J. E. Rowe, and T. E. Madey, Prog. Surf. Sci. **59**, 117 (1998).
[8] J. J. Kolodziej, T. E. Madey, J. W. Keister, and J. E. Rowe, Phys. Rev. B (submitted).
[9] J. C. Riviere, Mater. Sci. Technol. **9**, 365 (1993).
[10] C. G. Vandewalle, Phys. Rev. B **39**, 1871 (1989).
[11] H. Kobayashi, T. Kubota, H. Kawa, Y. Nakato, and M. Nishiyama, Appl. Phys. Lett. **73**, 933 (1998).
[12] M. Bäumer, J. Libuda, A. Sandell, H.-J. Freund, G. Graw, T. Bertrams, and H. Neddermeyer, Ber. Bunsenges. Phys. Chem. **99**, 1381 (1995).
[13] C. T. Campell and A. Ludviksson, J. Vac. Sci. Technol. A **12**, 1825 (1994).
[14] M. Komiyashi and M. Kirino, in Proceedings of the 10th International Congress on Catalysis, Budapest, Hungary, 1992, pp. 659–669.
[15] C. Goyhenex, M. Meunier, and C. R. Henry, Surf. Sci. **350**, 103 (1996).

Intrinsic limitations on ultimate device performance and reliability at (i) semiconductor–dielectric interfaces and (ii) internal interfaces in stacked dielectrics

G. Lucovsky,[a] H. Yang, and H. Niimi
Departments of Physics and Electrical and Computer Engineering, North Carolina State University, Raleigh, North Carolina 27695-8202

M. F. Thorpe
Department of Physics and Astronomy, Michigan State University, East Lansing, Michigan 48824

J. C. Phillips
Lucent Bell Laboratories, Murray Hill, New Jersey 07974

(Received 17 January 2000; accepted 30 May 2000)

The scaling of electrical oxide thickness to 1.0 nm and below for advanced silicon devices requires a change from thermally grown oxides and nitrided oxides to deposited dielectrics which have dielectric constants, k, significantly greater than that of silicon dioxide, $k_0 \sim 3.8$. Implementation of the higher-k dielectrics into field effect transistor devices requires a processing protocol that provides separate and independent control over the properties of the Si–dielectric interface and the bulk dielectric film. Experiments to date have shown that plasma-grown nitrided oxides, ~0.5–0.6 nm thick, satisfy this requirement. This paper addresses chemical bonding issues at the Si–dielectric interface and at the internal dielectric interface between the plasma-grown nitrided oxides and the high-k alternative dielectrics by applying constraint theory. Si–SiO_2 is a prototypical interface between a "rigid" Si substrate and a "floppy" network dielectric, SiO_2, and the interfacial properties are modified by a monolayer-scale transition region with excess suboxide bonding over what is required for an ideal interface. Additionally, the defect properties at the internal interface between a nitrided SiO_2 interface layer and a bulk dielectric film reflect differences in the average number of bonds/atom, N_{av}, of the dielectrics on either side of that interface. Experimentally determined interfacial defect concentrations are shown to scale quadratically with increasing differences in N_{av} thereby establishing a fundamental basis for limitations on device performance and reliability. © *2000 American Vacuum Society.* [S0734-211X(00)08204-4]

I. INTRODUCTION

The aggressive scaling of Si complementary metal–oxide–semiconductor (CMOS) devices to gate lengths <100 nm requires an increase in gate dielectric capacitance corresponding to an electrical oxide thickness (EOT) referenced to SiO_2, of <1 nm, and eventually extending down to 0.5–0.6 nm. The direct tunneling current density, J, through SiO_2 films with a physical thickness, t_0, of ~1 nm, and at a 1 V potential drop across the oxide exceeds 100 A/cm^2. However, to maintain field effect transistor (FET) performance and reliability, the tunneling current density at an operating bias of approximately 1 V over threshold must not exceed about 1 A/cm^2. This means that physically thicker gate insulators with dielectric constants, k, greater than that of SiO_2, $k_0 = 3.8$, must be introduced into the gate stack. This integration of *alternative* deposited gate dielectrics is based on the premise that increased physical thickness, t, of these high-k insulators,

$$t = t_0(k/k_0), \qquad (1)$$

which provides the same capacitance as physically thinner SiO_2 dielectrics, will yield a tunneling current density significantly less than 1 A/cm^2. This in turn requires that conduction band offset energies and electron tunneling masses in the high-k dielectric be about the same as they are at Si–SiO_2 interfaces and in the SiO_2 dielectric film, respectively.

Introduction of gate dielectrics other than SiO_2 requires that these be prepared by deposition, rather than conventional thermal or rapid thermal growth processes. Since the Si–SiO_2 interface is continuously regenerated in a thermal growth process, the electrical properties of that interface are determined by the Si surface preparation/cleaning, the growth conditions, and subsequent thermal annealing/processing after completion of the growth phase. The electrical properties of thermally grown interfaces have been optimized for both performance and reliability, and have set the standards for performance and reliability required from alternative gate dielectrics.

Previous studies have demonstrated that the transition from thermally grown SiO_2 to deposited SiO_2 necessitates separate processing steps for interface formation and dielectric deposition.[1–9] As an example, it has been shown that direct deposition of SiO_2 by 300 °C remote plasma enhanced chemical vapor deposition (RPECVD) onto Si(100) surfaces that have been subjected to an *in situ* hydrogen plasma clean and/or an HF last rinse, resulted in highly defective

[a]Electronic mail: gerry_lucovsky@ncsu.edu

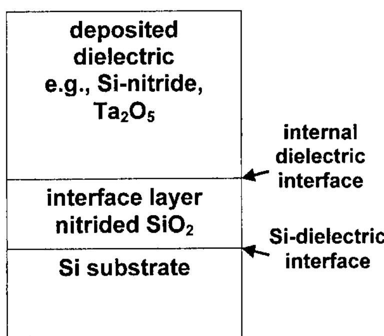

FIG. 1. Schematic representation of a stacked gate dielectric, indicating the Si–dielectric interface and the internal dielectric interface as well.

interfaces.[3] It was subsequently shown that a 300 °C remote plasma-assisted oxidation (RPAO) prior to REPCVD could be used to *in situ* clean and passivate the Si surface by growth of an ultrathin *passivating* oxide layer ~0.5–0.6 nm thick.[3] This approach has been demonstrated to give equally good results when combined with SiO_2 layers deposited by RPECVD at 300 °C, or by rapid thermal chemical vapor deposition (RTCVD), at higher temperatures, 600–750 °C.[3,7] The predeposition oxidation passivated the Si–dielectric interface against chemical attack in the form of a subcutaneous oxidation of the Si buried interface during deposition of the SiO_2 film.[1,2]

Other studies, in which deposited (i) hydrogenated Si nitride, (ii) Si oxynitride pseudobinary alloys, $(SiO_2)_{1-x}(Si_3N_4)_x$, and (iii) high-*k* dielectrics such as the Zr silicates, $(SiO_2)_{1-x}(ZrO_2)_x$ and Ta_2O_5, were substituted for RPECVD and RTCVD SiO_2, also indicated the necessity for using a predeposition, plasma-assisted oxidation step.[10–12] As shown in Refs. 3 and 7, the RPAO process of Refs. 10 and 11 formed the Si dielectric interface and a thin oxide layer that also prevented chemical attack of the substrate during film deposition. Stacked gate dielectrics formed in this way include two interfaces, the Si–dielectric interface and the internal dielectric interface, in close proximity to the Si substrate (see Fig. 1). Defects at these two interfaces play a significant role in determining device performance and reliability. This paper discusses defects at these interfaces from the perspective of constraint theory,[5] and then identifies fundamental aspects of the chemical bonding that play a role in determining the ultimate limits of device performance and reliability.

II. EXPERIMENTAL RESULTS

The devices described in this paper with hydrogenated Si nitride and Si oxynitride alloys include the remote plasma processing steps described in Refs. 9, 13–17. The devices incorporating Zr silicates and Ta_2O_5 were prepared by similar plasma-processing steps as described in Refs. 10 and 11. Interfacial oxide and nitrided oxide layers have been used in all of the devices addressed in this study. Since the focus of this paper is on the Si–dielectric interface formed in this process as well as the internal dielectric interface that is an

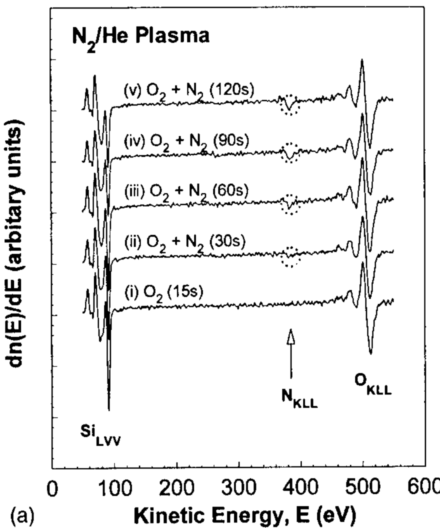

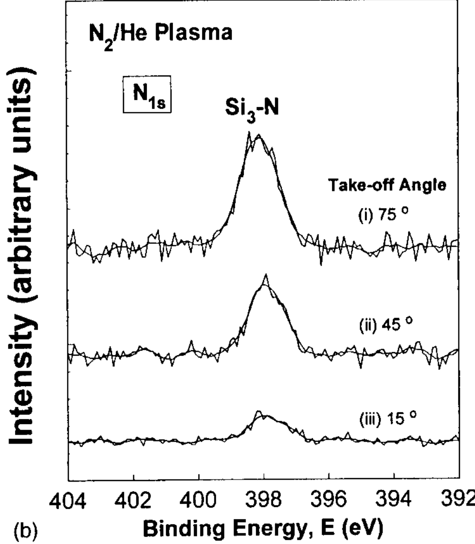

FIG. 2. (a) Differential Auger electron spectroscopy spectra as a function of electron energy for interface nitridation. Traces are included for a 15 s RPAO process, and for nitridation times ranging from 30 to 120 s. (b) Angle-resolved monochromatic N_{1s} XPS for nitrided interfaces (90 s exposure). The decrease of the nitrogen XPS feature with decreasing take off angle (with respect to the substrate) is consistent with nitrogen atoms being localized at, or in the immediate vicinity of, the Si–dielectric interface.

integral component of this interfacial oxide, the processing and characterization of these interfacial layers will be addressed in some detail. The thickness of the plasma-processed interfacial layers has been determined by on-line Auger electron spectroscopy as described in Refs. 3, 13, and 14. The processing conditions and characterizations are described in detail in Refs. 13 and 14 as well as other references cited in that paper. Figures 2(a) and 2(b) present on-line Auger electron spectroscopy (AES), and off-line x-ray photoelectron spectroscopy (XPS) data relevant to the interfacial nitridation. The combination on-line AES of Fig. 2(a), the XPS of Fig. 2(b), with the secondary ion mass spectrometry results in Ref. 14, optical second-harmonic generation (SHG) results in Ref. 17, and nuclear reaction analysis results of Refs. 9 and 14, establish that the nitrogen atoms are

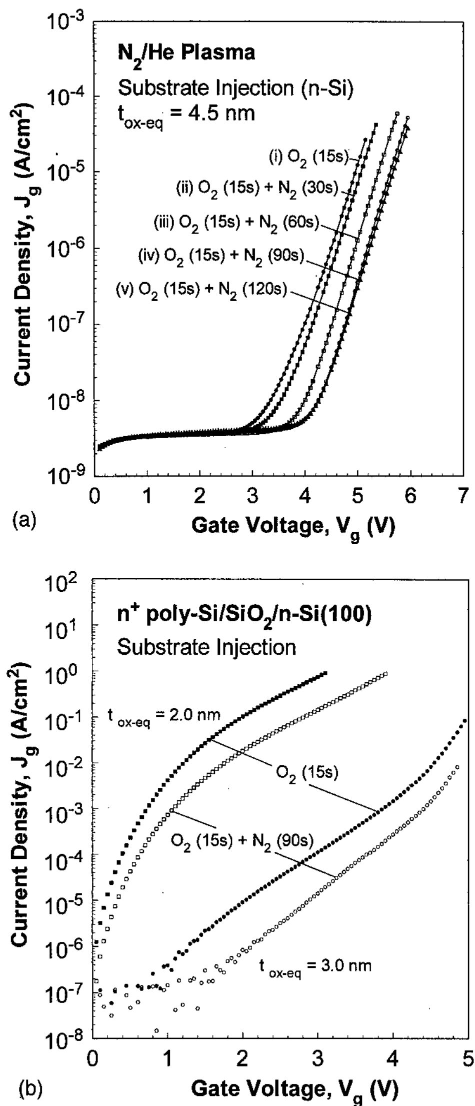

FIG. 3. Current density as function of gate voltage in (a) the Fowler–Nordheim, and (b) the direct tunneling regimes for devices with RPAO interface layers and RPECVD SiO_2 bulk dielectric films. These devices have been subjected to a 900 °C rapid thermal annealing (RTA) in an inert ambient (e.g., He).

bonded to the Si atoms at the Si–dielectric interface. In addition for a 90 s plasma-nitridation treatment[9,14] the nitrogen atom concentration of $7.5 \pm 0.5 \times 10^{14}$ cm^{-2} is equivalent to one nitrogen atom per Si(100) surface silicon atom, i.e., monolayer coverage. Figures 3(a) and 3(b) present electrical data that demonstrate the effects of interface nitridation. The data in Fig. 3(a), in the Fowler–Nordheim regime, indicate that tunneling is reduced in proportion to interface nitridation up to the monolayer level (90 s) and then saturates. The data in Fig. 3(b) indicate that reductions in the direct tunneling regime are smaller, ~10×, compared to 50–60× in the Fowler–Nordheim regime, and are effectively independent of the effective oxide thickness. The reductions in Figs. 3(a) and 3(b) are not due to shifts in the flat band voltage as determined from capacitance–voltage measurements.[10,11] The data in Figs. 4(a) and 4(b) are for device structures in

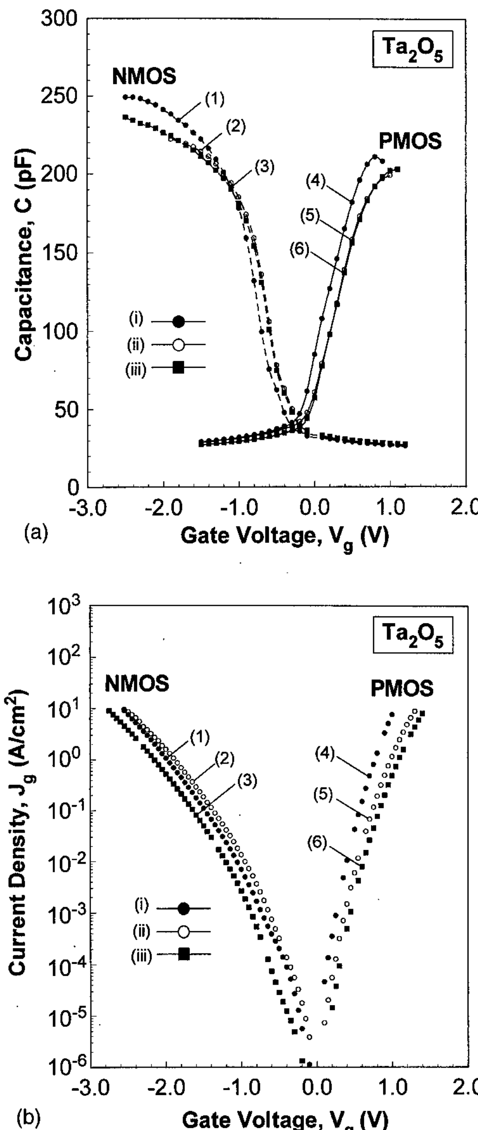

FIG. 4. (a) Capacitance–voltage, *C–V* and (b) current density–voltage, *J–V*, plots for devices with stacked gate dielectrics comprised of RPAO SiO_2 or nitrided RPAO SiO_2 and RPECVD Ta_2O_5. For comparison, these plots also include *C–V* and *J–V* traces for RPECVD Ta_2O_5 directly onto HF-last silicon substrates. These devices have been subjected to a 800 °C RTA in an inert ambient (e.g., He). The closed circles are for deposition on HF-last Si, the open circles for a RPAO SiO_2 layer, and the closed squares are for monolayer nitrided RPAO SiO_2. The EOT values are: (1) 1.09 nm, (2) 1.20 nm, (3) 1.17 nm, (4) 1.19 nm, (5) 1.30 nm, and (6) 1.29 nm.

which RPECVD Ta_2O_5, deposited at 300 °C, and subjected to a rapid thermal anneal at 800 °C replaced the RPECVD SiO_2 layers of the devices in Fig. 3. Monolayer interface nitridation has essentially the same effect on these devices with Ta_2O_5 dielectrics as it does in Fig. 3(b) with SiO_2. Additionally, the flatband voltages for the Ta_2O_5 capacitors on *n*-type and *p*-type substrates are the same to ±0.005 V as for devices fabricated on substrates from the same lot with RPECVD SiO_2 dielectrics. Initial experiments performed on devices with RPECVD Zr silicate alloy dielectrics demonstrated improved interface properties, e.g., reduced hysteresis in capacitance–voltage, *C–V*, curves, when a RPAO step

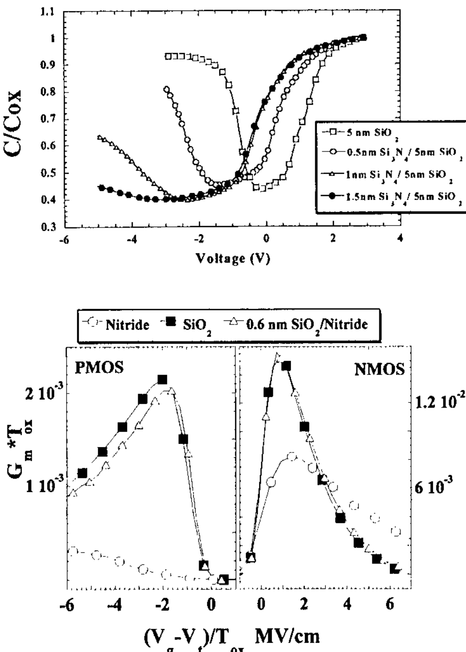

FIG. 5. (a) Negative voltage shifts of capacitance–voltage, C–V, curves for direct deposition of Si_3N_4 onto crystalline silicon. (b) $g_m - T_{ox}$ plots for NMOS and PMOS FETs with (i) RPAO and SiO_2 dielectric layers, (ii) Si_3N_4 dielectric layers deposited directly onto HF-last silicon, and with RPAO and Si_3N_4 dielectric layers. These devices have been subjected to a 900 °C RTA in an inert ambient (e.g., He).

was used prior to deposition of the Zr silicate layer.[10] High resolution transmission electron microscopy micrographs indicated subcutaneous oxidation and/or silicate formation at an HF-last Si substrate surface.

The data in Figs. 5(a) and 5(b) present another aspect of interfacial oxidation. Direct deposition of nitride layers on Si(100), or the plasma nitridation of Si(100), each prior to oxide deposition, results in highly defective interfaces as indicated by flatband voltage shifts in Fig. 5(a) and the transconductance-EOT, $G_m - T_{ox}$, plots of Fig. 5(b).[5,6,13] The insertion of a RPAO step to form approximately 0.6 nm of interfacial SiO_2 restores the $g_m - T_{ox}$ product (which is proportional to channel mobility) to values essentially equal to those in devices with Si–SiO_2 interfaces [see Fig. 5(b)].

The data in Figs. 6(a) and 6(b) demonstrated flatband voltage shifts that are attributed to fixed positive charge at the internal dielectric interface.[18,19] Each of the devices in Fig. 6(a) have RPAO non-nitrided interface layers approximately 0.6 nm thick, and then RPECVD layers of (i) SiO_2, (ii) a Si oxynitride alloy with equal formula weights of SiO_2 and Si_3N_4, or (iii) hydrogenated (~15%–20% H) Si nitride. The capacitance–voltage, C–V, curves of Fig. 6(a) with Si oxynitride and nitride dielectrics, display systematic shifts to negative voltages independent of the substrate conductivity type. The shifts are larger for the devices with nitride dielectrics, ~0.15 V, than for the devices with the oxynitride dielectrics, ~0.4 eV. These shifts are consistent with fixed positive charge levels of about 7.5 and 2×10^{11} cm^{-2} at the respective internal dielectric interfaces. This interpretation is supported by plots of hole channel mobility versus surface

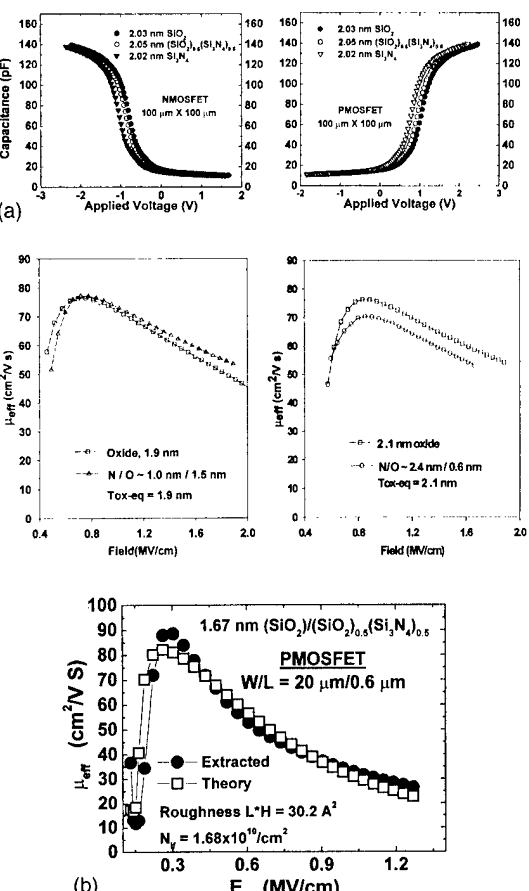

FIG. 6. (a) Capacitance–voltage, C–V, curves for NMOS and PMOS devices (EOT ~2 nm) with RPAO interfaces (~0.6 nm) and RPECVD oxide, oxynitride, and nitride bulk dielectric layers. (b) Mobility data for PMOS devices. These devices have been subjected to a 900 °C RTA in an inert ambient (e.g., He).

field in Fig. 6(b). The decrease in peak channel mobility is larger for the nitride device with the thinner interfacial layer. In addition, the magnitude of the peak channel mobilities in the devices with Si nitrides is consistent with interfacial defect levels in the low to mid 10^{10} cm^{-2} range, supporting the assignment of the flatband voltage shirts to charge at the internal dielectric interface.

Finally, Fig. 7(a) displays current-density–voltage, J–V, plots and Fig. 7(b) displays time to breakdown for devices with gate dielectrics similar to those in Fig. 6(a).[18,19] Consistent with a tunneling model discussed in Ref. 20, the tunneling current at a bias voltage of 1 V across the dielectric in substrate inversion decreases by about one order of magnitude in going from the device with oxide dielectric to the device with nitride dielectric and an additional order of magnitude in going to the device with the oxynitride dielectric. As shown in Fig. 7(b), the values of time to breakdown at a fixed bias voltage across the dielectric increase inversely as the square of the current density across the stacked gate dielectric are not correlated with flatband voltage shifts and fixed positive charge discussed previously. This reliability scaling behavior is similar to what is discussed in Ref. 21 for stacked devices with Ta_2O_5 layers and Si–SiO_2 interfaces,

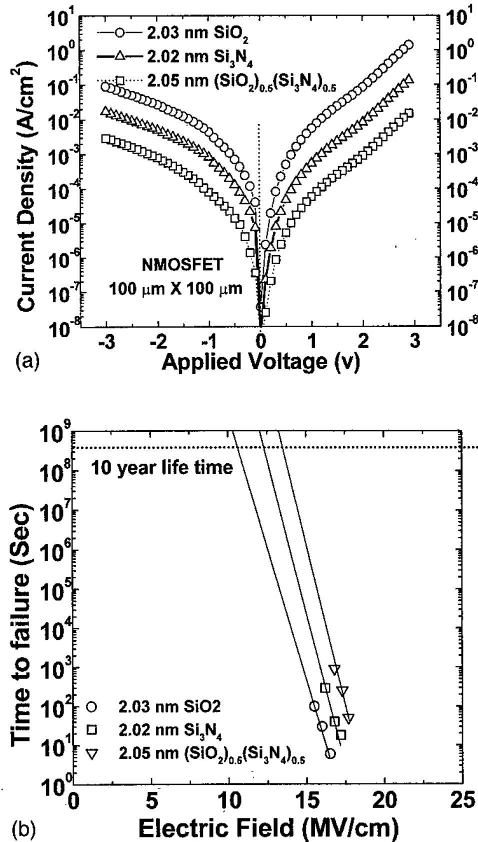

FIG. 7. (a) Current-density–voltage, J–V, plots for PMOS and NMOS FETs for the devices of Fig. 6(a). (b) Time to breakdown for NMOS devices of Figs. (a) and 6(a). These devices have been subjected to a 900 °C RTA in an inert ambient (e.g., He).

and has been attributed to a Si–SiO_2 interface controlled dielectric breakdown.

III. DISCUSSION

Several studies have addressed chemical bonding arrangements at thermally annealed Si-SiO_2 interfaces and have shown that *optimized* interfaces display transition regions ~0.3 nm thick with excess suboxide bonding arrangements different from those expected at abrupt Si–SiO_2 metallurgical interfaces. These studies include: (i) XPS on ultrathin Si–SiO_2 interfaces using monochromatic synchrotron radiation,[22] (ii) *in situ* AES,[23] and (iii) *in situ* Fourier transform infrared (FTIR).[24] From the perspective of constraint theory, these transition regions are at an interface between a "rigid" crystalline Si material and an effectively "floppy" amorphous material, SiO_2, with a random covalent network structure.[25]

Applications of constraint theory to noncrystalline solids have focused primarily on bulk glasses,[26] thin films,[27] and Si-SiO_2/Si_3N_4 interfaces.[5] Recently, both theory[25] and experiment[28] have identified a new aspect of constraint theory by demonstrating that "rigid" or "overconstrained" and "floppy" or "understrained" microstructural regions in an alloy glass are separated by monolayer scale, self-organized interface layers that are "overconstrained" with

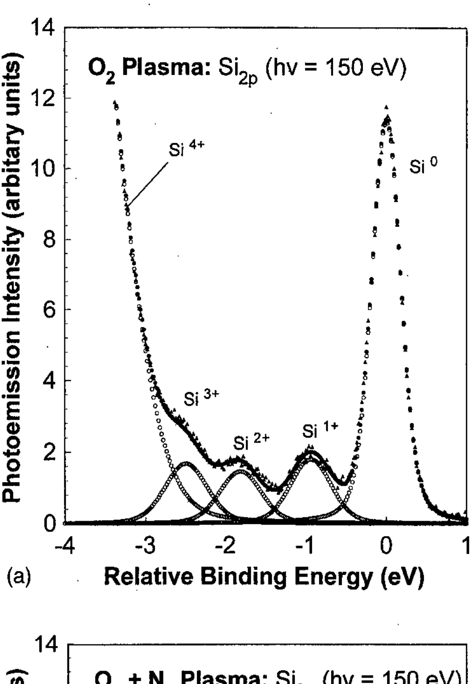

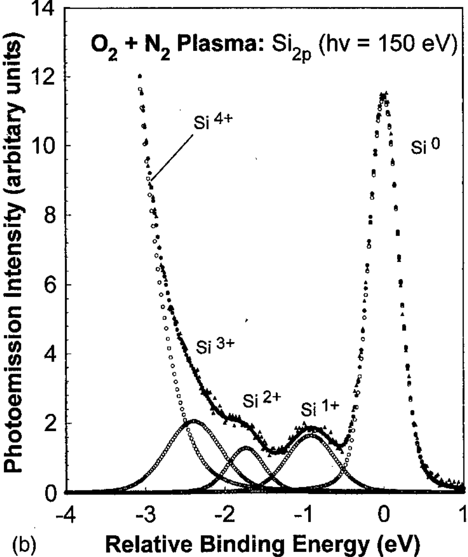

FIG. 8. (a) Synchrotron XPS data for RPAO interfaces without nitridation and (b) with monolayer interface nitridation. These devices have been subjected to a 900 °C RTA in an inert ambient (e.g., He).

respect to bonding coordination, yet not "mechanically strained." Experiments cited in Refs. 22–24, combined with the theory of Refs. 25 and 29, suggest that the interfacial transition regions in advanced Si FET gate stacks are *intrinsic*, and result in part from entropy effects. These transition regions constitute a basic limitation for the aggressive scaling of CMOS silicon devices, as well as other semiconductor devices with similar "steps" in interfacial bonding coordination.

For example, the data in Figs. 3(a) and 3(b) have been explained in terms of a model based on XPS data of Ref. 21 [see Figs. 8(a) and 8(b)]. Analysis of the interfacial features in XPS data of Figs. 8(a) and 8(b) labeled I_1, I_2, and I_3, yields concentrations of silicon atoms in suboxide bonding environments in excess of those that are required for an ideal and abrupt interface. The excess silicon atom concentrations

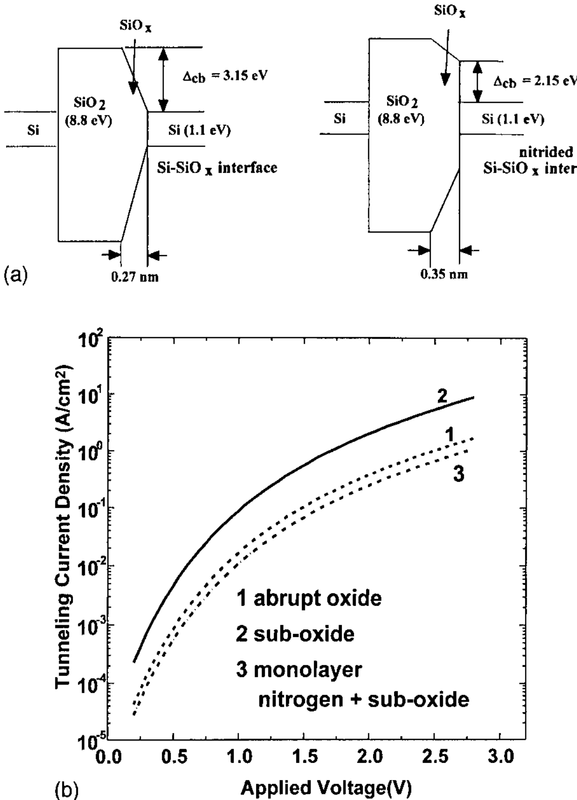

FIG. 9. (a) Interfacial band structure for tunneling calculations for RPAO and nitrided RPAO interfaces as derived from the XPS data of Fig. 8. (b) Calculated direct tunneling for devices with EOT=2 nm, for the interfaces of (a) and ideal $Si-SiO_2$ interfaces with no suboxide bonding.

have been equated to an average composition of SiO, thereby yielding converted Si areal densities into equivalent transition region widths of 0.27 nm for the non-nitrided interface and 0.35 nm for the nitrided interface.[20] Combining these XPS data with differences in optical SHG for interfaces with and without interfacial nitridation,[17] band models have been generated for the interfacial transition regions [see Fig. 9(a)]. After completing the stacked dielectrics with films of SiO_2 subject to the constraint of maintaining the same values of EOT, calculations of direct tunneling for substrate accumulation in Fig. 9(b) have yielded the reductions in the tunneling current density for devices with nitrided interfaces essentially the same as shown in Fig. 3(b).[20]

Constraint theory has also been invoked at semiconductor dielectric interfaces to explain differences in the defect densities between $Si-Si_3N_4$ and $Si-SiO_2$ interfaces.[5,6] In this application, mechanical bonding constraints at the interface have been characterized in terms of the average number of bonds per atom in the interfacial region. Following Ref. 5, the interface bonding structure is *defined* by 0.5 molecular layers of Si (0.5 atoms and two bonds), and 1.5 molecular layers of the dielectric film (SiO_2 or Si_3N_4). Interface nitridation has been taken into account by inserting one atomic layer of nitrogen between the Si substrate and SiO_2 layer. The $Si-SiO_2$ interface is used as a reference interface and is characterized by an average number of interfacial bonds/atom, $N_{av}{}^* = 2.86$. Based on the above-described model in-

TABLE I. Application of constraint theory to fixed charge at internal dielectric interfaces.

(i) Average number of bonds per atom in dielectric films, N_{av}			
SiO_2	Si_3N_4	Oxynitride alloy, $x=0.5$	Ta_2O_5
2.67	3.43	3.05	2.86[a]
(ii) Step in number of bonds/atom at internal interface with SiO_2, ΔN_{av}			
	Si_3N_4	Oxynitride alloy, $x=0.5$	Ta_2O_5
	0.76	0.38	0.19
(a) Scaling factor for defects/cm^2 scale as $[\Delta N_{av}]^2$			
	0.58	0.14	0.04
(b) Normalized ratio of defects/cm^2			
	16	4	1
(c) Fixed charge at internal dielectric interface, Q_f (cm^{-2})			
	Si_3N_4	Oxynitride alloy, $x=0.5$	Ta_2O_5
	7.5×10^{11}	2×10^{11}	$<0.6\times10^{11}$ [b]

[a]Based on an extension of the resonating bond model proposed by Phillips (Ref. 34).
[b]Estimated from $C-V$ data.

terface bonding model, N_{av} equals 3.47 for a $Si-Si_3N_4$ interface, and 2.89 for a monolayer nitrided $Si-SiO_2$ interface. As discussed in Ref. 5, the concentration of defects relative to the $Si-SiO_2$ interface scales as $(N_{av}-N_{av}^*)^2$. Based on this scaling, the defect concentration at a $Si-Si_3N_4$ interface is expected to be about three orders of magnitude higher than at a monolayer nitrided $Si-SiO_2$ interface, consistent with experimental results.[5,6] Constraint theory and the associated scaling neither predict defect concentrations, nor identify the defect bonding arrangements. Instead, they yield scaling relationships that provide a useful guideline for comparisons of the type discussed previously. In the spirit of the scaling arguments, a value of interfacial $N_{av}\sim3$ has been proposed in Ref. 5 as a demarcation between device quality and increasing defective interfaces, paralleling a similar criterion applied to defects in homogeneous amorphous thin films.[27]

Scaling theory also provides an explanation for differences in fixed charge at internal dielectric interfaces. In this application, the appropriate scaling variable is the difference in the average number of bonds per atom, ΔN_{av}, on either side of the internal dielectric interface. This model will now be applied to the $C-V$ data of Figs. 4(a) and 6(a). The interfaces being addressed are between the interfacial SiO_2 and Si nitride and oxynitride in Fig. 5(a), and SiO_2 and Ta_2O_5 in Fig. 4(a). This application of constraint theory is summarized in Table I, which includes: (i) the average number of bonds/atom, N_{av}, for SiO_2, Si_3N_4, an oxynitride alloy with a composition $(SiO_2)_{0.5}(Si_3N_4)_{0.5}$, and Ta_2O_5, (ii) the step in the average number of bonds/atom, ΔN_{av}, for internal interfaces between SiO_2 and Si_3N_4, $(SiO_2)_{0.5}(Si_3N_4)_{0.5}$, and Ta_2O_5, (iii) computed values of $[\Delta N_{av}]^2$ and normalized values of $[\Delta N_{av}]^2$, and (iv) values of fixed charge, Q_f, obtained from an analysis of $C-V$ data. The values of Q_f are obtained from the relative shifts in $C-V$ curves, as for example in Fig. 5(a). The limiting value of Q_f for the internal $SiO_2-Ta_2O_5$ interface is estimated from the accuracy of the voltage determination in the $C-V$ traces in Fig. 3(a). These data are consistent with the scaling expected from constraint theory. As noted previously and in Refs. 5 and 6, constraint theory can

be used to predict relative defect concentrations, but cannot predict the actual defect concentrations, the local bonding arrangements at the defect sites, or the energies of the defects relative to band edges.

We now turn to the reliability data in Fig. 7(b). A comparison between these data and those in Fig. 7(a) indicate that the time to breakdown at a given applied voltage increases as the square of the tunneling current decreases. Additionally, the time to breakdown does not scale inversely as the relative concentrations of Q_f at the internal dielectric interface, so that there is no experimental evidence that these internal interfaces play a significant role in intrinsic device breakdown. On the other hand, the data in Fig. 7(b) are consistent with the time to breakdown being determined predominantly by the interfacial SiO_2 layer and its interface with the crystalline Si substrate, as has been suggested in Ref. 21, which focused on devices with SiO_2 interface layers and Ta_2O_5 bulk dielectrics. The devices of Fig. 7(b) do not have nitrided Si–SiO_2 interfaces; however, as has been demonstrated in Fig. 2, interfacial nitridation reduces both Fowler–Nordheim and direct tunneling so that additional increases in time to breakdown are anticipated in devices with nitrided interfaces.

IV. CONCLUSIONS

The application of constraint theory to silicon dielectric and internal dielectric interfaces has identified fundamental limitations on the performance and reliability of FET devices that include stacked gate dielectrics. To date the only interfacial layers that have been demonstrated not to degrade FET current drive, or equivalently reduce the effective channel mobilities of both holes and electrons, are those which are either SiO_2 or nitrided SiO_2. Based on these observations, this paper has focused on stacked gate dielectrics which are comprised of a Si substrate, an ultrathin SiO_2 or nitrided SiO_2 layer, and higher-k bulk dielectric films such as Si_3N_4, a Si-oxynitride alloy [e.g., $(SiO_2)_{0.5}(Si_3N_4)_{0.5}$], or Ta_2O_5. Other research results for devices with stacked gate dielectrics have demonstrated excellent performance and reliability when the devices included an interfacial layer of SiO_2, either grown prior to deposition, or formed during a postdeposition anneal.[30,31] Therefore, the conclusions drawn in this paper extend to other stacked gate dielectric structures as well, including the devices of Refs. 30 and 31 where the interfacial layers were not prepared by RPAO.

The paper has addressed three different aspects of interface bonding and defect structure that limit device performance and reliability, (i) interfacial transition regions between the Si substrate and a dielectric film, (ii) differences in defect concentrations at interfaces between Si and different dielectric films, and (iii) differences in defect concentrations at internal interfaces between different dielectrics.

It has been shown that the interfacial transition regions with suboxide bonding in excess of what is required at an abrupt interface between Si and SiO_2 are typically about 0.3 nm thick.[22–24] These regions are formed during oxidation of the silicon substrate and minimization of their spatial extent requires a postoxidation anneal, e.g., 30 s to 1 min at 900 °C. It is particularly noteworthy that interfaces prepared by thermal oxidation at 900 °C also require an anneal at the same temperature to optimize interfacial smoothness or equivalently minimize suboxide bonding.[32] The existence of an interfacial transition region between crystalline silicon and SiO_2 is anticipated on the basis of constraint theory as has been discussed in Ref. 25. Constraint theory predicts that a transition region of the order of one molecular layer must be present at the interface between two materials in which the number of bonds/atom is different, or equivalently at which the number of bonding constraints per atom is different. The resulting interfacial region is overconstrained with respect to the lower constraint partner of the interface, and is self-organized in a way that minimizes the development of mechanical strain. Interface layers of this type have been reported within glassy alloys with microstructure composed of a floppy or underconstrained constituent, and an overconstrained bonding partner.[28] "Floppy" is defined in terms of a maximum average bonding coordination of 2.4,[26] except for SiO_2, where 2.67 is more appropriate due to unusually small bonding forces at the oxygen atom sites.[27] Values of N_{av} <2.4 (or 2.67) define a regime in which the average number of bond constraints per atom is lower than the network dimensionality.[27] These concepts, originally applied to bulk glasses, have been extended to thin film amorphous materials[27] and more recently to internal interfaces between crystalline and amorphous materials.[5] In this paper, it has been shown that control of interfacial bonding structure by interfacial nitridation can modify interfacial transition regions between Si and SiO_2 and produce significant reductions in tunneling currents, thereby improving device performance. The experiments of Refs. 22–24, combined with the theory of Refs. 25 and 29, suggest that the interfacial transition regions in advanced Si FET gate stacks are *intrinsic*, and result from entropy effects. Entropy is not a factor in the crystalline substrate, but configurational entropy is one of the most important factors in allowing for the formation of amorphous covalent random networks. Therefore, it is not surprising that it plays a role at the interface between a crystalline solid and an ideal amorphous covalent random network solid.

A second application of constraint theory as applied to Si–dielectric interfaces has been discussed in detail in Refs. 5 and 6, and deals with interfaces between Si and other dielectrics such as Si nitride. These papers demonstrate that differences in performance, e.g., channel mobilities of FETs and threshold and flatband voltages, can be understood in terms of the average number of interfacial bonds/atom. The bonding model proposed in Ref. 5 gives an average interfacial N_{av} of 2.86 for Si–SiO_2, which increases to (i) 2.89 for a Si–SiO_2 interface with monolayer nitridation, and (ii) 3.47 for Si–Si_3N_4. Based on an empirical criterion for quantification of defect formation, mostly dangling bonds in amorphous thin films, a N_{av} value of about 3 marks a boundary between device quality and defective interfaces. This is consistent with the experimental results presented in Ref. 5,

which show that interfacial defects increase as N_{av} increases following the quadratic scaling predicted by constraint theory.

Finally, constraint theory has accounted for differences in the fixed charge at internal interfaces of stacked gate dielectrics. In particular, the quadratic scaling with ΔN_{av} has accounted for differences in fixed charge at $SiO_2-Si_3N_4$, $SiO_2-(SiO_2)_{0.5}(Si_3N_4)_{0.5}$, and $SiO_2-Ta_2O_5$ internal interfaces. This interfacial charge shifts flatband voltages and therefore will also change threshold voltages in FETs, however, it does not appear to degrade reliability. If the charge is high enough, and if the interfacial layer is sufficiently thin, it can also reduce effective channel mobilities as in *p*-channel FETs with bulk Si_3N_4 dielectrics.

In conclusion, future generations of silicon-based FET devices will have to incorporate deposited dielectric layers with dielectric constants greater than that of SiO_2 in order to reduce direct tunneling currents which can be present at the scaled down operating voltages. Experiments to date indicate that these dielectrics will have to have a stacked structure comprised of an ultrathin SiO_2 interfacial layer, ~0.5–0.6 nm thick, in order to ensure device performance and reliability that is comparable to devices with thermally grown oxides of past generations of devices. This paper has shown that there are fundamental physical effects that limit the bonding structure of these interfacial oxides, both the silicon substrate and at the internal interface with high-*k* dielectric. Monolayer scale transition regions at the $Si-SiO_2$ interface are common for both homogeneous and stacked structures, and increases in direct tunneling associated with the "average SiO" interfacial composition can be reduced by incorporation of about one monolayer of nitrogen atoms bonded directly at the $Si-SiO_2$ interface [see Fig. 8(b)]. This interfacial bonding arrangement is consistent with optical SHG studies,[17] and has been confirmed by recent experiments using synchrotron XPS.[33]

Recent insights into bonding counting for silicate glasses,[34] can be extended to other non-SiO_2-based dielectrics as well, and have shown that most of the important high-*k* candidates, such as Ta_2O_5, ZrO_2, HfO_2, and Zr, and Hf silicates have values of N_{av} that, when combined with a crystalline silicon substrate, will yield interfacial values of $N_{av}<3$. This means that high defect concentrations will not result from overconstraint; however, other aspects of bonding, e.g., interfacial Si–metal atom (silicide) bonds,[35] as well as Si–O–metal atom groups, are expected to degrade performance and/or reliability. For example, fixed positive charge associated with silicide bonds, as well as second-neighbor effects on interfacial silicon atoms from different local bonding arrangements in the dielectric at the silicon buried interface, can enhance scattering of charged carriers in the channel region and decrease channel mobilities.

ACKNOWLEDGMENTS

This research has been supported in part by the ONR, SRC, and SRC/SEMATECH FEP Center.

[1] G. Lucovsky, S. S. Kim, D. V. Tsu, G. G. Fountain, and R. J. Markunas, J. Vac. Sci. Technol. B **7**, 861 (1989).

[2] S. S. Kim and G. Lucovsky, J. Vac. Sci. Technol. A **8**, 2039 (1990).

[3] T. Yasuda, Y. Ma, S. Habermehl, and G. Lucovsky, Appl. Phys. Lett. **60**, 434 (1992).

[4] S. V. Hattangady, H. Niimi, and G. Lucovsky, J. Vac. Sci. Technol. A **14**, 3017 (1996).

[5] G. Lucovsky, Y. Wu, H. Niimi, V. Misra, and J. C. Phillips, Appl. Phys. Lett. **74**, 2005 (1999).

[6] V. Misra, Z. Wang, Y. Wu, H. Niimi, G. Lucovsky, J. J. Wortman, and J. R. Hauser, J. Vac. Sci. Technol. B **17**, 1836 (1999).

[7] G. Lucovsky, J. J. Wortman, T. Yasuda, X.-L. Xu, V. Misra, S. V. Hattangady, Y. Ma, and B. Hornung, J. Vac. Sci. Technol. B **12**, 2839 (1994).

[8] G. Lucovsky, IBM J. Res. Dev. **43**, 301 (1999), and references therein.

[9] H. Niimi, H. Y. Yang, and G. Lucovsky, in *Characterization and Metrology for ULSI Technology: 1998 International Conference*, edited by D. G. Seiler, A. C. Diebold, W. M. Bullis, T. J. Shaffner, R. McDonald, and E. J. Walters (AIP, Woodbury, NY, 1998), p. 273.

[10] G. B. Rayner, R. Therrien, and G. Lucovsky (unpublished).

[11] P. K. Roy and I. C. Kizikyalli, Appl. Phys. Lett. **72**, 2835 (1998); I. C. Kizikyalli, R. Y. S. Huang, and P. K. Roy, IEEE Electron Device Lett. **19**, 423 (1998).

[12] H. Niimi and G. Lucovsky (unpublished).

[13] H. Niimi and G. Lucovsky, J. Vac. Sci. Technol. A **17**, 3185 (1999).

[14] H. Niimi and G. Lucovsky, J. Vac. Sci. Technol. B **17**, 2610 (1999).

[15] Y. Wu and G. Lucovsky, IEEE Electron Device Lett. **19**, 367 (1998).

[16] C. R. Parker, G. Lucovsky, and J. R. Hauser, IEEE Electron Device Lett. **19**, 106 (1998).

[17] G. Lucovsky, H, Niimi, K. Koh, D. R. Lee, and Z. Jing, in *The Physics of SiO_2 and $Si-SiO_2$ Interfaces-3*, edited by H. Z. Massoud, E. H. Poindexter, and C. R. Helms (The Electrochemical Society, Pennington, NJ, 1996), p. 441.

[18] H. Yang and G. Lucovsky, Tech. Dig. Int. Electron. Devices Meet. 245, (1999).

[19] G. Lucovsky, H. Yang, Y. Wu, and H. Niimi, Banpis Proc. (in press).

[20] H. Yang, H. Niimi, J. W. Keister, G. Lucovsky, and Jack E. Rowe, IEEE Electron Device Lett. **21**, 76 (2000).

[21] R. Degraeve, B. Kaczer, M. Houssa, G. Groeseneken, M. Hyens, J. S. Jeon, and A. Halliyal, Tech. Dig. Int. Electron. Devices Meet. 327 (1999).

[22] J. W. Keister, J. E. Rowe, J. J. Kolodzie, H. Niimi, N.-S. Tao, T. E. Madey, and G. Lucovsky, J. Vac. Sci. Technol. A **17**, 1340 (1999).

[23] M. Weldon *et al.*, J. Vac. Sci. Technol. B **17**, 1795 (1999).

[24] G. Lucovsky, A. Banerjee, B. Hinds, B. Claflin, K. Koh, and H. Yang, J. Vac. Sci. Technol. B **15**, 1074 (1997).

[25] M. F. Thorpe, J. Non-Cryst. Solids (in press).

[26] J. C. Phillips, J. Non-Cryst. Solids **34**, 153 (1979); **43**, 37 (1981).

[27] G. Lucovsky and J. C. Phillips, J. Non-Cryst. Solids **227**, 1221 (1998).

[28] P. Boolchand *et al.*, J. Non-Cryst Solids (in press).

[29] Y. Yu and J. Tersoff (unpublished).

[30] S. C. Song, H. F. Luan, Y. Y. Chen, M. Gardner, J. Fulford, M. Allen, and D. L. Kwong, Tech. Dig. Int. Electron. Devices Meet. 373 (1998).

[31] T. P. Ma, IEEE Trans. Electron Devices **45**, 680 (1998); X. Guo and T. P. Ma, IEEE Electron Device Lett. **19**, 207 (1998).

[32] X. Chen and J. M. Gibson, Appl. Phys. Lett. **70**, 1462 (1997).

[33] J. W. Keister, J. E. Rowe, Y.-M. Lee, H. Niimi, G. Lucovsky, and G. J. Lapeyre (unpublished).

[34] J. C. Phillips (unpublished).

[35] A. Y. Mao, K. A. Son, J. M. White, D. L. Kwong, D. A. Roberts, and R. N. Vrtis, Mater. Res. Soc. Symp. Proc. **567**, 473 (1999).

Strain-induced self-organized growth of nanostructures: From step bunching to ordering in quantum dot superlattices

J. Stangl, T. Roch, V. Holý,[a] M. Pinczolits, G. Springholz, and G. Bauer[b]
Institut für Halbleiterphysik, Johannes Kepler Universität Linz, Altenbergerstr. 69, A-4040 Linz, Austria

I. Kegel and T. H. Metzger
Sektion Physik, Ludwig-Maximilians-Universität München, D-880539 München, Germany

J. Zhu, K. Brunner, and G. Abstreiter
Walter Schottky Institut (WSI), TU München, D-85748 Garching, Germany

D. Smilgies
European Synchrotron Radiation Facility, F-38042 Grenoble Cedex 9, France

(Received 17 January 2000; accepted 3 April 2000)

We have investigated the lateral ordering of dot positions in a SiGe/Si multilayer and, for comparison, in a PbSe/PbEuTe dot superlattice using grazing incidence small-angle scattering. The two samples represent two different approaches to achieve an enhanced ordering of dot positions in semiconductor heterostructures: in the SiGe/Si sample, step bunching in the multilayer grown on a vicinal Si substrate was exploited to reduce the fluctuations in lateral dot distances. In the PbSe/PbEuTe sample the strong elastic anisotropy leads to the formation of a three-dimensional dot "lattice," exhibiting a very narrow distribution of dot distances. © *2000 American Vacuum Society.* [S0734-211X(00)00404-2]

I. INTRODUCTION

The self-organized growth of strained semiconductor nanostructures has attracted a lot of interest in recent years, both because of their physical properties as well as because of their potential for novel electronic and optoelectronic devices.[1,2] It has been realized some time ago that during the deposition of heterostructures the misfit strain can lead to islanding[2] and on vicinal surfaces to step bunching.[3] Defect free islands embedded in a higher band gap matrix material exhibit interesting electronic properties due to quantum confinement phenomena which have been used, e.g., for the fabrication of stacked quantum dot lasers. A critical issue both for fundamental research as well as for practical applications is the size and shape homogeneity of the islands.[4]

In multilayers of self-assembled quantum dots, theoretical as well as experimental work for InAs/GaAs[5] and Ge/Si systems[4] has shown that the vertical ordering of the dots may lead via their elastic strain fields to a better size homogeneity and even to a better lateral arrangement as well.[6] The self-assembly of the dot columns in multilayers results from the overlap of elastic strain fields of buried islands. The nucleation on the top surface above buried islands occurs preferentially at sites where the elastic surface strain energy exhibits local minima. However, despite the lateral ordering tendency, an increase of the islands' size has been found during the dot superlattice growth, and, furthermore, the onset of island formation was observed to occur for smaller critical thicknesses of the wetting layer with increasing number of periods.[7,8] For the InAs/GaAs and Ge/Si systems, the degree of lateral ordering which was achieved so far is, however, rather limited, a fact which has been explained recently by growth simulations.[9] It turns out that the elastic anisotropy of Si, but also of GaAs, is not sufficiently large to induce a long range lateral ordering.

In order to improve this situation for the lateral ordering for the technologically important Ge islands, two suggestions have been made: (i) to use the strain fields of misfit dislocation networks to control the nucleation of islands. However, the network is not very regular and the defects are not favorable for any applications.[10] (ii) Ordering of islands through the growth on vicinal (001) surfaces with regular ripples realized through the growth of strained multilayers.[11] In particular, regular arrays of uniform step bunches could serve as templates either for the subsequent growth of wires along the step edges or could be used to induce not only a better lateral ordering in arrays of dots, but also to achieve a better control of the dot size distribution.

For appropriate growth conditions and material parameters, step bunches form during the growth of the multilayer, which contain many monolayer steps, the terrace widths are in the range of 0.1–3 μm.[12–14] Of particular interest are regular arrays of uniform step bunches, advantageous for the deposition of regular wires and ordered dots.

On the other hand, it has been shown that for a sufficiently large anisotropy of the elastic constants of the matrix material and for the growth along an elastically soft direction, a superior lateral and vertical ordering can be achieved. This has been recently demonstrated for PbSe islands embedded in $Pb_{1-x}Eu_xTe$ spacer layers.[15,16]

In this article we present results on two different approaches to achieve a better lateral ordering of self-organized dots: First, we measured a SiGe island multilayer, which was

[a]Permanent address: Laboratory of Thin Films and Nanostructures, Masaryk University, 61137 Brno, Czech Republic.
[b]Electronic mail: gbauer@hlphys.uni-inz.ac.at

deposited on a vicinal Si substrate, leading to a step-bunched template for dot nucleation. Second, to demonstrate the potential of exploiting the elastic anisotropy of the spacer layers, we present data on a PbSe/PbEuTe multilayer. We compare results obtained by atomic force microscopy (AFM), yielding information on the morphology of the top surface only, with results of x-ray diffraction techniques, which probe the entire multilayer stack. In contrast to AFM and transmission electron microscopy (TEM), the x-ray scattering methods are nonlocal. That means that the measured signal corresponds to an integral over the irradiated sample volume. Since this volume is always much larger than the mean dot distance, this integration yields a signal averaged over the statistical ensemble of all dot configurations.

II. APPLIED METHODS

For the investigation of correlation phenomena scattering techniques are the method of choice, since the correlations in the positions of self-assembled quantum dots give rise to maxima of the power spectral density in reciprocal space.

Lateral correlations of the positions of the dots (i.e., of the dot positions *at the same interface*) give rise to a series of maxima in the power spectral density in reciprocal space in the direction $Q_\parallel$ parallel to the sample surface. From the *spacing* $\Delta Q_\parallel$ of these maxima the *mean distance* $\langle L\rangle$ of the dots is determined as

$$\langle L\rangle=\frac{2\pi}{\Delta Q_\parallel}, \tag{1}$$

whereas the *width* of the maxima contains information on the *statistical distribution* of the dot distances.

Two limiting models of the dot positions can be used. In the *short-range-order* model (SRO), the distances between the adjacent dots are random and not correlated. Then, the widths $\delta Q_\parallel$ of the satellites depend on $Q_\parallel$,

$$\delta Q_\parallel=\frac{(\sigma_\parallel Q_\parallel)^2}{\langle L\rangle}. \tag{2}$$

Hence from this dependence the root mean square deviation $\sigma_\parallel$ of the dot distances can be determined.

In the *long-range-order (LRO) model*, the widths of the satellites are independent of $Q_\parallel$, and they are inversely proportional to the size $D_\parallel$ of a laterally coherent domain

$$\delta Q_\parallel=\frac{2\pi}{D_\parallel}. \tag{3}$$

The positions and widths of the lateral satellites can be measured at any reciprocal lattice point, i.e., using various scattering geometries. For most material systems the dot distances are too small to allow an investigation using x-ray reflectivity (XRR), as the in-plane momentum transfer is limited in this configuration. Coplanar high-resolution x-ray diffraction (XRD) has been used to obtain information on the symmetry of the lateral ordering,[17] but the number of observable satellites is insufficient to definitely distinguish between SRO and LRO behavior. With grazing incidence diffraction (GID), similar analyses have been performed,[18,19] but also there a rather limited number of satellites has been observed. Furthermore, in both methods not only the positional correlations, but also the strain fields in the heterostructures influence the diffraction pattern, making the analysis ambiguous. The deformation field around the buried dots has the same translational symmetry as the dot positions and it may influence the satellite maxima. With grazing incidence small-angle scattering (GISAXS), the strain distribution in the structure plays no role, and only the material contrast is probed.[20] Furthermore, there is no limitation in the in-plane momentum transfer as in XRR, thus for the small dot distances in our samples (typically 100 nm), this method is ideally suited to obtain the positional correlation properties of the dots.

For a comparison of these results to those obtained by AFM, a two-dimensional (2D) fast Fourier transform (FFT) of the AFM images is calculated. The FFT power spectral density yields information on the preferred spatial frequencies. In addition, from the AFM images the autocorrelation function (AC) is calculated, which yields information on the size of the laterally ordered domains. In order to obtain ensemble-averaged data, the size of the scanned area must be quite large. Only if the linear size of the area is several μm's, the resolution in reciprocal space is of the order of 10^{-4} Å^{-1}, which is comparable to GISAXS but still worse than XRD and GID.

If the dot positions at *different interfaces* are correlated, but those *within the same interface* are not, the power spectral density is concentrated within sheets in reciprocal space, which are perpendicular to the correlation direction. These sheets can be observed by x-ray scattering, namely by x-ray diffraction (XRD),[17] XRR,[18] or GID.[18,21] The width of the sheets depends on the degree of the vertical dot correlation. The simplest way to observe these sheets is to perform a two-dimensional scan using XRR, however these sheets are deformed by x-ray refraction. In XRD the sheets are straight, but usually their intensity is rather low. The advantage of GID in this case consists in its depth sensitivity, which allows us to elucidate whether or not the vertical correlation improves within the stack.

If the dots are correlated both laterally and from interface to interface, the power spectral density maxima create a lattice in reciprocal space that is reciprocal to the average dot lattice. This lattice in reciprocal space can be observed by all the x-ray methods mentioned, but one has to keep in mind that, depending on the vertical divergence of the primary beam, the intensity maxima in a two-dimensional scan are projections of the points of the reciprocal dot lattice to the scattering plane.

III. EXPERIMENT

The Si/SiGe multilayer sample was grown by solid source molecular beam epitaxy (MBE) on a (001) Si substrate with a miscut of 2° along an azimuth 1.8° off the [100] direction. Twenty periods consisting of a 2.5-nm-thick $Si_{1-x}Ge_x$ layer ($x_{Ge}=0.45$) and a 10-nm-thick Si spacer layer have been

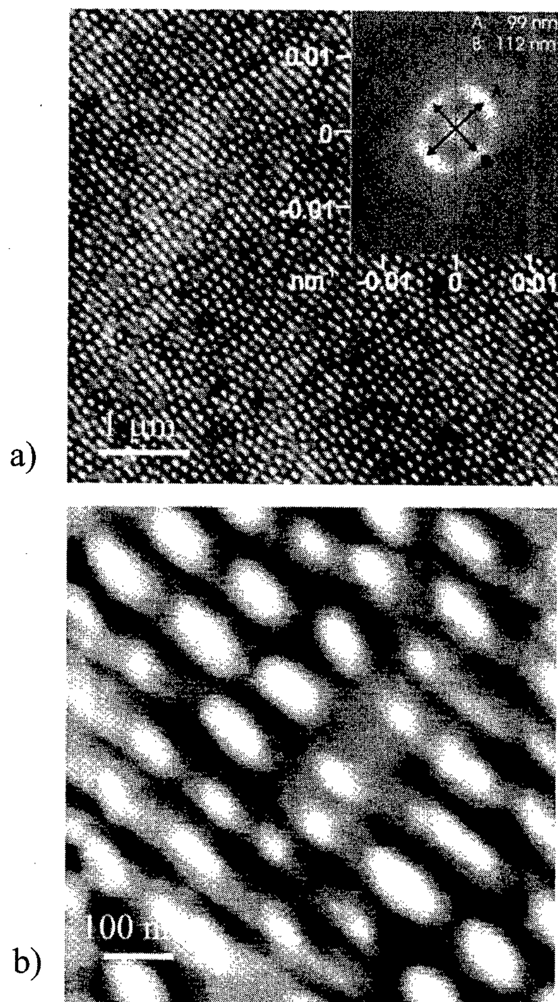

FIG. 1. (a) AFM image of the SiGe/Si dot sample. The inset shows the 2D Fourier transform of the image. The maxima "A" and "B" correspond to the average dot distances in the two (001) direction parallel and perpendicular to the miscut. (b) The close-up clearly shows that the lens-shaped islands are arranged in "chains" along steps due to step bunching.

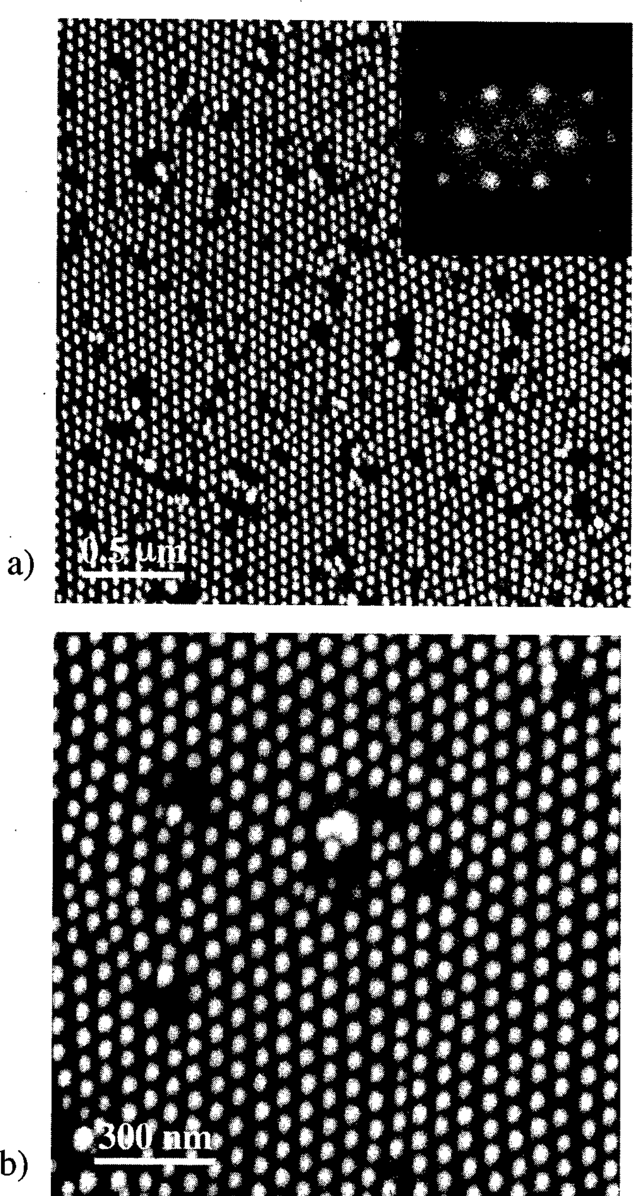

FIG. 2. (a) AFM image of the PbSe/PbEuTe sample. The dots are pyramidally shaped with (100) facets. The inset shows the 2D FFT of the image, from which the hexagonal in-plane ordering of the dot positions can be clearly seen.

grown at a substrate temperature of 550 °C. On top of the last Si layer 5 ML of pure Ge were deposited at a temperature of 500 °C.

Cross-sectional TEM shows a rippled interface structure with a period of about 120 nm and a height modulation of about 1.5 nm. The ripples are oriented along the miscut.[11] An AFM image of the sample surface is shown in Fig. 1. The edges of the images are roughly aligned with the ⟨110⟩ directions. Ge islands of about 2 nm height are aligned in rows along the step bunches, which can be clearly observed in the close-up [panel (b)]. The inset of panel (a) shows a 2D Fourier transform of the image, showing that the dot positions are correlated preferentially in two ⟨100⟩ directions, with slightly different mean distances, as indicated. From panel (b) it is obvious that the dot distance distribution perpendicular to the steps is narrower than along the steps.

The PbSe/PbEuTe sample has been grown by MBE on a (111) oriented BaF_2 with a 4-μm-thick, relaxed PbTe buffer as a virtual substrate. A 100 period superlattice (SL) stack consisting of 5 ML PbSe alternating with 47 nm $Pb_{1-x}Eu_xTe$ ($x_{EuTe}=0.07$) was grown at a temperature of 360 °C. The $Pb_{1-x}Eu_xTe$ layer thickness and composition have been chosen to fulfill the strain symmetrization condition, i.e., the net strain of one period is zero, and hence no limitation of the total SL thickness due to strain exists.[16]

For the chosen growth conditions pyramid-shaped PbSe islands with a height of about 12 nm already form in the first PbSe layer, and the dot positions become more regular with increasing number of SL periods. An AFM image of the top dot layer is shown in Fig. 2, exhibiting a pronounced hexagonal pattern of pyramids. The high degree of ordering is evident from the FFT spectrum (inset), from which we get a variation of the mean dot–dot distance $\delta L/\langle L\rangle$ of 6%.

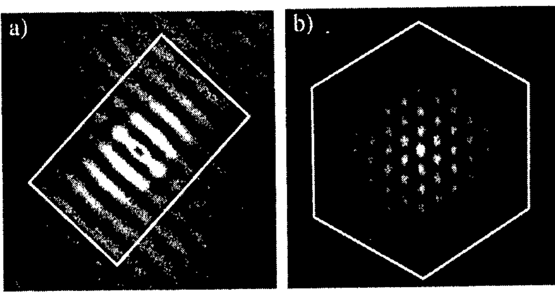

FIG. 3. Autocorrelation function of the AFM images in Figs. 1 and 2, reflecting the rectangular (a) and hexagonal (b) dot arrangement, respectively. Using a cutoff peak height of 10% of the central maximum, we obtain an average coherent domain size of $2\langle L_{[010]}\rangle \times 4\langle L_{[100]}\rangle$ for the SiGe/Si sample (a), and $6\langle L_{\langle \bar{1}10\rangle}\rangle$ for the PbSe/PbEuTe sample (b).

To get an estimate on the size of the coherent dot domains, the AC spectrums have been calculated, see Fig. 3. The dots in the SiGe/Si sample (a) are correlated in-plane in a rectangular pattern along the two orthogonal $\langle 100\rangle$ directions, whereas the AC pattern for the PbSe/PbEuTe (b) samples reflects the hexagonal arrangement of dots. In order to obtain the average coherent domain size, the heights of the side peaks along the $\langle 100\rangle$ directions in panel (a) and the $\langle 1\bar{1}0\rangle$ directions in panel (b), respectively, have been determined. Using a cutoff peak height of 10% of the central maximum, we obtain the domain sizes in units of the average dot spacings $\langle L_{hkl}\rangle$ in the respective directions SiGe/Si: $2\langle L_{[010]}\rangle \times 4\langle L_{[100]}\rangle$, with $\langle L_{[101]}\rangle = 100$ nm and $\langle L_{[100]}\rangle = 116$ nm, PbSe/PbEuTe: $6\langle L_{\langle \bar{1}10\rangle}\rangle$, with $\langle L_{\langle \bar{1}10\rangle}\rangle = 68$ nm.

IV. HIGH-ANGLE X-RAY DIFFRACTION

To obtain information on the structural parameters of the *buried* dots, we performed XRD measurements. The partially strained dots give rise to diffuse scattering in the vicinity of the coherent SL satellites, which appear due to the wetting layer and the spacer layers.

In order to investigate the SiGe dot positions, reciprocal space maps (RSMs) around the zeroth-order SL satellite have been recorded using a diffractometer in triple axis configuration and Cu K_{alpha1} radiation. They reflect mainly the more or less periodically deformed Si regions around the dots.[17,18] Figure 4 shows RSMs of the SiGe sample around the asymmetrical (044) and (404) Bragg reflections, i.e., in two orthogonal $\langle 100\rangle$ azimuths (see inset). The lower panel shows the intensity integrated along $Q_\perp$ as a function of $Q_\parallel$. In the [100] azimuth (perpendicular to the step edges) two side maxima are visible on each side, whereas in the [010] azimuth only one peak can be observed on either side. This clearly indicates the different degree of island ordering due to the step bunches. The mean dot distances for the two directions are indicated as well, and agree with the AFM results.

RSMs of the PbSe dot sample around the symmetric (111) and asymmetric (331) reciprocal lattice points are shown in Fig. 5. They have been measured in a $[11\bar{2}]$ azimuth at the Troïka II beamline at the European Synchrotron Radiation Facility (ESRF) at Grenoble, France, at a wavelength of 1.55 Å using a position sensitive detector. The large elastic anisotropy of the PbEuTe spacer material leads to three minima in the surface elastic energy density above a buried PbSe pyramid for the [111] growth direction, resulting in an ordering of the dots into a three-dimensional distorted face-centered cubic (fcc) lattice.[15] This gives rise to a large num-

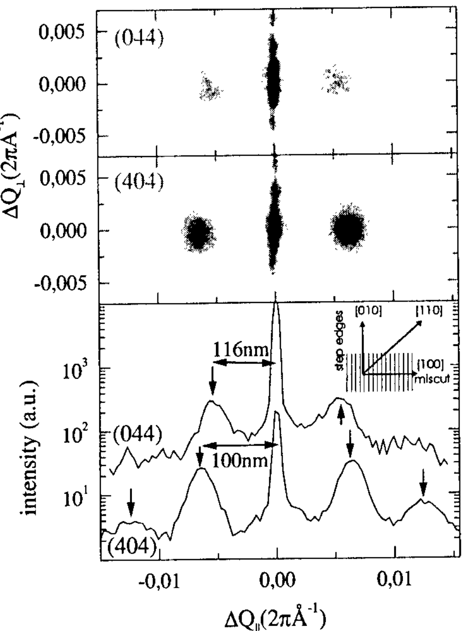

FIG. 4. XRD reciprocal space maps of the SiGe/Si dot multilayer around the SL_0 peaks of the (044) and (404) reciprocal lattice points, i.e., in the azimuth along the steps and perpendicular to it, respectively. The lower panel displays the intensities integrated along Q_z. The maps show the correlation of dot positions, which is significantly better in the direction perpendicular to the steps. The average distances between dots in the two directions are indicated in the lower panels.

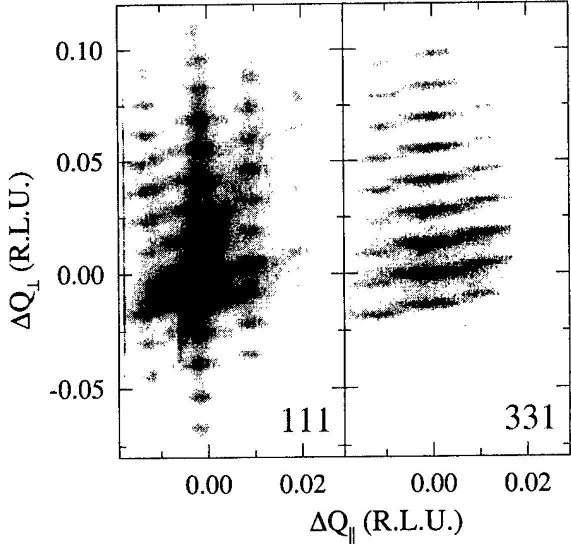

FIG. 5. XRD reciprocal space map of the PbSe/PbEuTe superlattice around the symmetric (111) and the asymmetric (331) reflection. The dots are arranged in the superlattice in a distorted fcc lattice, giving rise to a large number of satellite peaks representing the reciprocal lattice of the dot lattice.

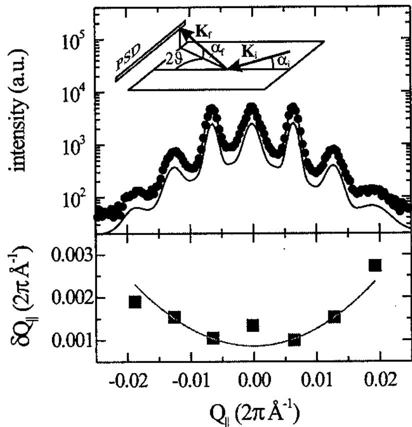

FIG. 6. GISAXS scan of the SiGe/Si dot multilayer (upper panel) in the azimuth $Q_{\parallel}$ perpendicular to the step edges. The inset shows the measurement geometry. The lateral maxima have been fitted by Gaussian peaks to determine their width, which is displayed in the lower panel. From a quadratic fit to these values the lateral correlation properties in the short-range order model have been obtained.

ber of dot satellites corresponding to the reciprocal lattice of the dot lattice, which can be observed around each Bragg reflection.

V. LATERAL ORDERING

The number of lateral satellites observed in the XRD data is, however, insufficient to obtain *quantitative* data on the lateral ordering of the dots, both for the SiGe and for the PbSe samples. Therefore we performed GISAXS measurements, which were carried out at Troïka II beamline as well. The spectra were recorded using a position sensitive detector mounted parallel to the sample surface (see inset of Fig. 6). The spectra obtained from the SiGe sample are displayed in Figs. 6 and 7 for the in-plane momentum transfer perpendicular and parallel to the step edges, respectively (note that

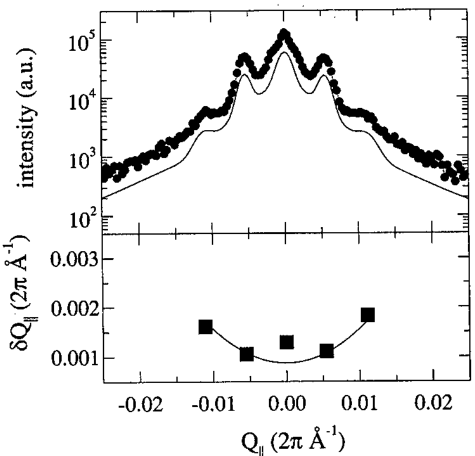

FIG. 7. Same as Fig. 6 in the azimuth $Q_{\parallel}$ parallel to the step edges. The correlation of dot positions in this azimuth is significantly worse than in perpendicular to the step edges.

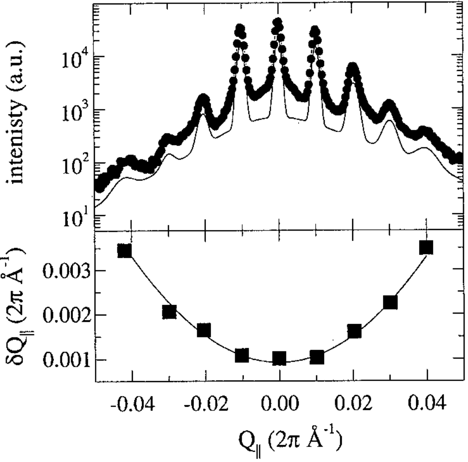

FIG. 8. Same as Figs. 6 and 7 for the PbSe/PbEuTe superlattice sample, in an azimuth $Q_{\parallel}$ parallel to $\langle 1\bar{1}0\rangle$.

this momentum transfer in GISAXS is oriented perpendicular to the azimuth of the incident beam, contrary to XRD, where it is parallel to this azimuth).

The inset in Fig. 6 shows a sketch of the GISAXS geometry. The angles of incidence and exit with respect to the surface, $\alpha_i = 1.1°$ and $\alpha_f = 0.6°$, have been chosen in order to penetrate the whole SL and thus obtain an average information over the whole stack.

The upper panels of Figs. 6 and 7 show the experimental data (dots) together with a simulation (thin solid line), where the maxima have been fitted by Gaussian peaks to determine the width along $Q_{\parallel}$. In the lower panel this width is plotted as a function of the peak position (squares). The peak width clearly increases with peak order (the central peak shape is influenced not only by the dot correlation, but also by, e.g., a long-range surface waviness, and is therefore excluded from the analysis), thus the dot positions do not follow a long-range order behavior. From a parabolic fit to these data we obtained the rms deviation of the dot distances $\sigma_{\parallel}$ in the short-range order model. In the better ordered direction (perpendicular to the step edges) we obtain $\sigma_{\parallel} = 63 \pm 7$ Å, whereas in the other direction we get a significantly worse correlation, $\sigma_{\parallel} = 88 \pm 8$ Å.

Figure 8 shows the GISAXS spectrum of the PbSe sample. Here, the degree of ordering is much higher ($\sigma_{\parallel} = 30 \pm 1$ Å), but still the SRO behavior is evident. The measurement was performed with $\alpha_i = 0.95°$ and $\alpha_f = 0.25°$.

VI. CONCLUSION

We have investigated the lateral ordering of dot positions in two different samples: In both samples, a SiGe/Si multilayer and a PbSe/PbEuTe superlattice, the growth of a periodic structure leads to the ordering of dot positions. In the SiGe/Si multilayer sample, *step bunching* during growth on a vicinal substrate is exploited to achieve an improved ordering. The experimental data clearly show that the steps formed due to the bunching process lead to an alignment of dots along the steps. The step width and hence the dot dis-

tance *perpendicular to the step edges* are very regular, whereas the dot distances *along the step edges* show a significantly higher spread.

In the PbSe/PbEuTe sample, the *large elastic anisotropy* of the material leads to a very effective coupling of dot positions in subsequent layers, leading to the formation of a three-dimensional *dot lattice*, exhibiting an even superior ordering of dot positions.

ACKNOWLEDGMENTS

This work was supported by FWF, Vienna, GMe and BMWV, Vienna.

[1]A. P. Alivisatos, Science **271**, 933 (1996).
[2]D. Bimberg, M. Grundmann, and N. N. Ledentsov, *Quantum Dot Heterostructures* (Wiley, Chichester, 1999).
[3]J. Tersoff, Y. H. Phang, Z. Zhang, and M. G. Lagally, Phys. Rev. Lett. **75**, 2730 (1995).
[4]J. Tersoff, C. Teichert, and M. G. Lagally, Phys. Rev. Lett. **76**, 1675 (1996).
[5]Q. Xie, A. Madhukar, P. Chen, and N. P. Kobayashi, Phys. Rev. Lett. **75**, 2542 (1995).
[6]F. Liu, S. E. Davenport, H. M. Evans, and M. G. Lagally, Phys. Rev. Lett. **82**, 2528 (1999).
[7]C. Teichert, M. G. Lagally, L. J. Petitcolas, J. C. Bean, and J. Tersoff, Phys. Rev. B **53**, 16334 (1996).
[8]O. G. Schmidt, O. Kienzle, Y. Hao, K. Eberl, and F. Ernst, Appl. Phys. Lett. **74**, 1272 (1999).
[9]V. Holý, G. Springholz, M. Pinczolits, and G. Bauer, Phys. Rev. Lett. **83**, 356 (1999).
[10]S.Yu. Shiryaev, F. Jensen, J. Lundsgaard Hansen, J. Wulff Petersen, and A. Nylandsted Larsen, Phys. Rev. Lett. **78**, 503 (1997).
[11]J. Zhu, K. Brunner, and G. Abstreiter, Appl. Phys. Lett. **73**, 620 (1998); K. Brunner, J. Zhu, G. Abstreiter, C. Miesner, O. Kienzle, and F. Ernst, Physica E (Amsterdam) (2000).
[12]Y. H. Phang, C. Teichert, Z. Zhang, and M. G. Lagally, Phys. Rev. B **50**, 14435 (1994).
[13]V. Holý, A. A. Darhuber, J. Stangl, G. Bauer, J. Nuetzel, and G. Abstreiter, Phys. Rev. B **57**, 12435 (1998).
[14]R. L. Headrick, J.-M. Baribeau, and Y. E. Strausser, Appl. Phys. Lett. **66**, 96 (1995).
[15]G. Springholz, V. Holý, M. Pinczolits, and G. Bauer, Science **282**, 734 (1998).
[16]M. Pinczolits, G. Springholz, and G. Bauer, Phys. Rev. B **60**, 11524 (1999).
[17]A. A. Darhuber, P. Schittenhelm, V. Holý, J. Stangl, G. Bauer, and G. Abstreiter, Phys. Rev. B **55**, 15652 (1997).
[18]V. Holý, A. A. Darhuber, J. Stangl, S. Zerlauth, F. Schäffler, G. Bauer, N. Darowski, D. Lübbert, U. Pietsch, and I. Vávra, Phys. Rev. B **58**, 7934 (1998).
[19]I. Kegel, T. H. Metzger, J. Peisl, P. Schittenhelm, and G. Abstreiter, Appl. Phys. Lett. **74**, 2978 (1999).
[20]M. Schmidbauer, T. Wiebach, H. Raidt, M. Hanke, R. Koehler, and H. Wawra, Phys. Rev. B **58**, 10523 (1998).
[21]I. Kegel, T. H. Metzger, J. Peisl, J. Stangl, G. Bauer, and D. Smielgies, Phys. Rev. B **60**, 2516 (1999).

Controlled ordering and positioning of InAs self-assembled quantum dots*

H. Lee, J. A. Johnson, J. S. Speck, and P. M. Petroff[a)]
Materials Department, University of California, Santa Barbara, California 93106

(Received 17 January 2000; accepted 25 May 2000)

An experimental approach has been developed to control the formation of InAs self-assembled islands. A lithographically defined mesa lattice on the surface was used to control the growth kinetics and island nucleation. Two distinct island formation regimes were observed from InAs islands grown on patterned GaAs (100) substrates. In the case of direct growth on patterned substrates, a type I islanding was observed, in which all the islands formed between mesas. Incorporating a stressor layer into the regrowth on the patterned substrate yielded a type island nucleation, where all the islands nucleated on top of the mesas. The possible mechanisms involved in the long range ordering and positioning of islands are discussed. © *2000 American Vacuum Society.* [S0734-211X(00)06604-X]

I. INTRODUCTION

Self-assembled quantum dots (QDs) have been intensely studied in the last several years due to their appealing electronic and optical properties.[1–3] Unique physical properties have been observed in QD structures[4,5] and device applications using QDs, such as lasers, detectors, and memories have been explored.[6–8] The self-assembled growth of QDs relies on the strain induced island formation via the Stranski–Krastanow growth mode,[3] in which island formation is the first step to minimize strain energy in coherent heteroepitaxial layers.[9] Many lattice-mismatched systems, such as InAs/GaAs, Ge/Si, and InAs/InP, have been investigated with the aim of understanding and controlling island formation.[10–21] In particular, the interplay between island nucleation and surface patterning has been studied extensively. This has been done for both larger features defined by conventional lithography[13–19] and for nano-scale inclusions patterned using electron beam techniques.[20,21] Subsurface strain fields have also been shown to play a controlling role in island nucleation, as seen in vertically stacked QDs.[2,10,11] The use of strain coupling has been extended to the highly anisotropic PbSe/PbEuTe system to produce excellent three-dimensional (3D) quantum dot lattices.[22] Despite all these efforts, the ability to control the positioning of III–V islands remains limited and this poses a great hurdle to the incorporation of QDs into devices.

We extend these ideas by using a technique, which combines lithography with *in situ* lateral strain engineering to restrict the island nucleation to mesoscopic areas of the wafer surface. In our experiments, submicron mesa arrays were fabricated using holographic lithography and wet chemical etching. Strain engineering was achieved by incorporating a coherently strain $In_{0.2}Ga_{0.8}As$ layer, which we call stressor, into the regrown structure. Due to the patterned features, the strain of the $In_{0.2}Ga_{0.8}As$ was modulated and energetically favorable nucleation sites were created on top of the mesas. Excellent long range island ordering is obtained. In this article, details of our technique will be discussed and both results of islands formed without stressor (type I nucleation) and with stressor (type II nucleation) will be presented and compared. Strong photoluminescence was also observed from these InAs QDs grown on patterned substrates.

II. EXPERIMENT AND DISCUSSION

Ordering of InAs self-assembled QDs on mesa lattices was promoted by deposition of InAs under favorable growth kinetics and thermodynamic conditions. Two distinct sets of regrowth structures, which corresponded to types I and II islanding, were studied. They are illustrated in Fig. 1. As will be shown, engineering of the regrowth structure on the mesa lattices allows a control of the island nucleation site positioning.

A. Defining the mesa lattices

Holography was used to pattern the GaAs (001) substrates, since it provided a simple and efficient method to create nanoscale mesa lattices over large areas. In this process, a GaAs substrate was first coated with photoresist (Shipley 1400-4) and then exposed in a holographic apparatus twice, with the sample rotated 90° after the first exposure. The patterns were transferred onto the GaAs substrates by wet chemical etching using $H_3PO_4:H_2O_2:H_2O=3:1:75$. The resulting pattern was a checkerboard array of square mesas. The unit cell of the lattice was 250 nm×250 nm. The mesas resembled truncated pyramids 25 nm high with a base width of 170 nm and top dimension <20 nm. Holography is very flexible, as it is easy to adjust the mesa dimensions, spacing, and orientation. In this study, we explored two different mesa lattice orientations. One lattice had its unit cell aligned along ⟨110⟩ (type A) and the other was rotated to aligned along ⟨100⟩ (type B). In these two different orientations, mesas had similar shape but were bound by different facets. After overgrowth, they showed distinct features, as described below.

*No proof corrections received from author prior to publication.

[a)]Author to whom correspondence should be addressed; electronic mail: petroff@engineering.ucsb.edu

InAs QDs

GaAs Buffer

A

InAs QDs

InGaAs Stressor

B

FIG. 1. Sample structures for two types of regrowth. (a) Schematic of the type I islanding. (b) Schematic of type II islanding.

B. Regrowth of the GaAs buffer layer on patterned GaAs surfaces

Before introduction into the molecular beam epitaxy (MBE) system, the patterned GaAs substrates were thoroughly cleaned in solvents and a fresh oxide layer was formed after a 10% HCl etch. The MBE regrowth started with a thermal desorption of the oxide layer under As_2 flux (5×10^{-6} Torr) at 630 °C. It was followed by the growth of a GaAs buffer layer at 600 °C. *In situ* reflection high energy electron diffraction (RHEED) was used to monitor the surface. Since a thin buffer layer was needed to preserve the surface patterned features, multiple growth interruptions (10 s every 5 nm) were used during the deposition to accelerate surface recovery from damages associated with processing and oxide desorption.

Figure 2 shows atomic force microscopy (AFM) images of the mesa lattices surfaces after 40 nm of GaAs was deposited on the two types of mesa patterns. In Figs. 2(a) and 2(b), the images show the evolution of lattices, which prior to regrowth had unit cell vectors parallel to $\langle 110\rangle$ and $\langle 100\rangle$ directions, respectively. Mesas in both lattices elongated in the $[1\bar{1}0]$ direction giving new mesa base dimensions on the order of 200 nm×300 nm. The mesas height was reduced to 5 nm and the top was flattened to 50 nm×200 nm. The observed anisotropic growth is quite common in MBE of III–V compounds. It is caused by the different diffusion rates in the two $\langle 110\rangle$ directions and enhanced by the multiple growth interruptions during the GaAs buffer layer deposition. Associated with this elongation, the individual mesa in the type A lattice (along $\langle 110\rangle$) has developed new facets. In this case, the facets on each mesa evolved from $\{10m\}$ to $\{11n\}$.

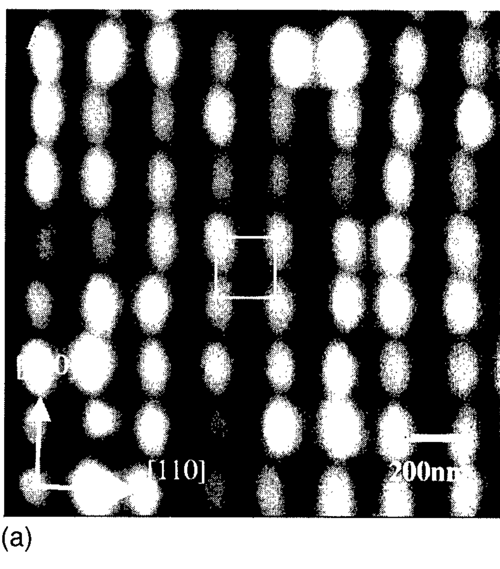

(a)

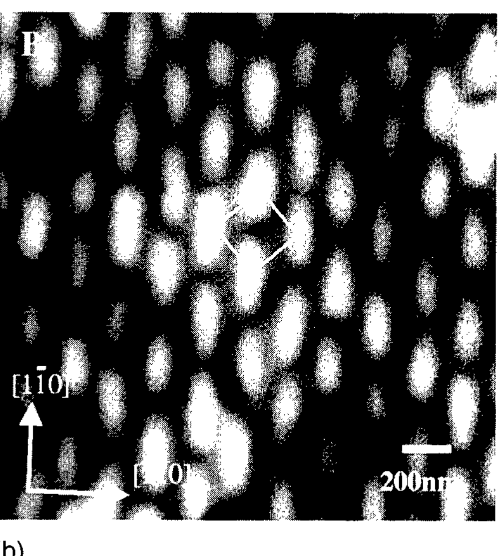

(b)

FIG. 2. AFM images of regrowth after 40 nm GaAs. (a) on type "A" mesa lattice and (b) on type "B" mesa lattice. The unit cell of each lattice is also indicated.

C. Growth of InAs island on patterned substrates

After the GaAs buffer layer was grown at 600 °C, the substrate temperature was lowered to 530 °C to deposit InAs islands. We used RHEED to monitor the island formation. The characteristic streaky to spotty RHEED pattern transition was observed after 1.7 ML of InAs were deposited, thus indicating the onset of 3D islands formation.[13,23] AFM images of InAs QDs on both mesa orientations with 40 nm GaAs buffer layer are shown in Fig. 3. These images show a type I islanding, in which the islands are formed between mesas.

As Fig. 3(a) shows, distinct one-dimensional (1D) ordered island arrays were obtained on type A mesa lattices. These preferred island nucleation sites are characteristic of type A mesa lattices only and may be a direct consequence of the mesa facet evolution during the GaAs buffer layer growth. Figure 3(b) shows the results of a growth sequence similar to

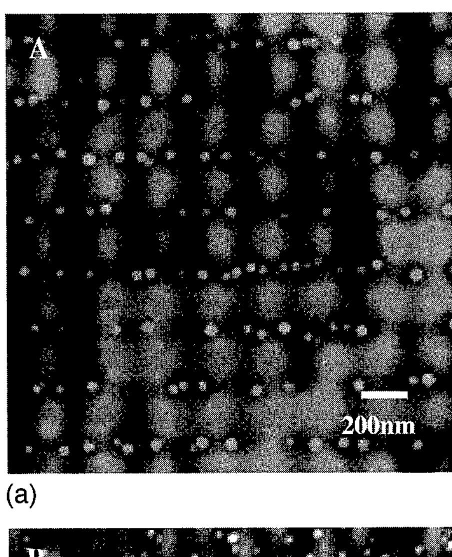

(a)

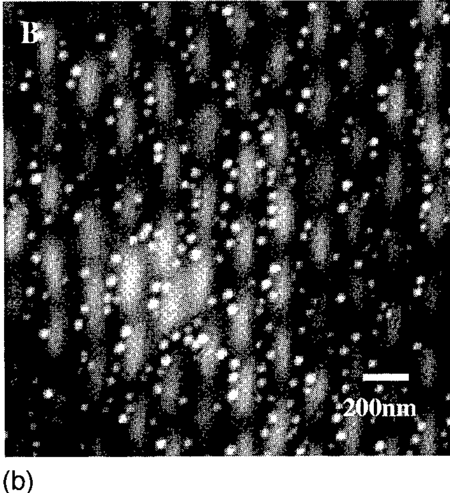

(b)

FIG. 3. AFM images of InAs QDs on (a) type "A" mesas and (b) on type "B" mesas.

that used in Fig. 3(a) but for a "B" mesa lattice. In both "A" and B type mesa lattices, all the islands were located in the valleys between the mesas. Similar results were obtained for InAs deposited on 60 nm GaAs buffer layers. The island diameter formed on patterned substrates ranged from 27 to 40 nm and their sizes appeared to be larger than on planar substrates (22–30 nm).

A possible explanation for the type I islanding is as follows. To minimize surface energy, concave regions will tend to fill and planarize upon overgrowth.[24] In the initial stages of QD deposition on the mesa arrays, the growth of the InAs wetting layer may be enhanced in the valleys due to the negative mean curvature. The wetting layer reaches the critical thickness rapidly inside the valleys, triggering the two-dimensional (2D) to 3D growth transition. Hence, the islands grow preferentially between the mesas. This explanation also accounts for the larger sized islands found between the mesas, compared to those on the planar surface.

Efficient photoluminescence (PL) was observed from type I islands after they were capped with 40 nm GaAs. The PL spectra shown in Fig. 4 were collected at 3 K with a cooled InGaAs photomultipler tube. An Ar-ion laser was used to

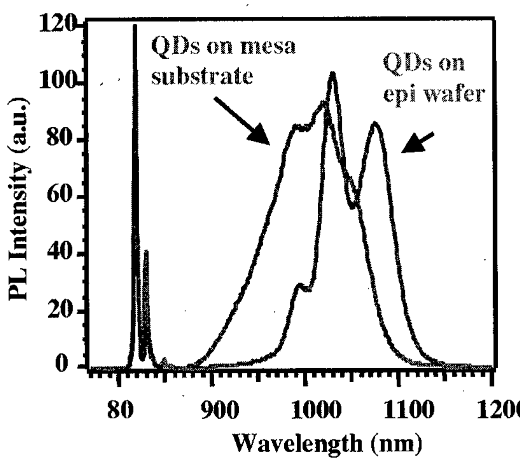

FIG. 4. Photoluminescence spectra from InAs QDs grown on patterned and unpatterned substrates at 3 K.

excite the QDs with a power density of 10 kW/cm^2. For comparison, we also show a PL spectrum of an unpatterned sample grown at the same time as the patterned sample. The PL intensity from the QDs on patterned substrates is comparable to that of an unprocessed sample. Excited states are also observed at this pumping density. The energy of the

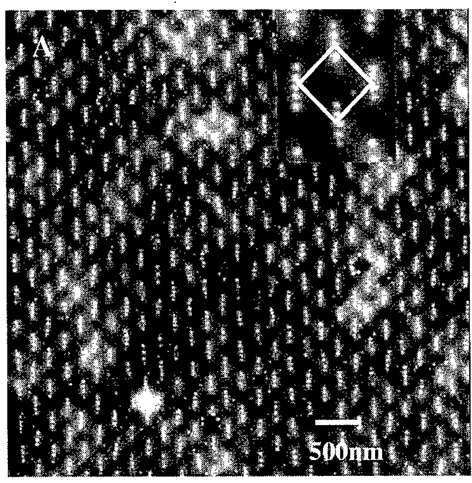

(a)

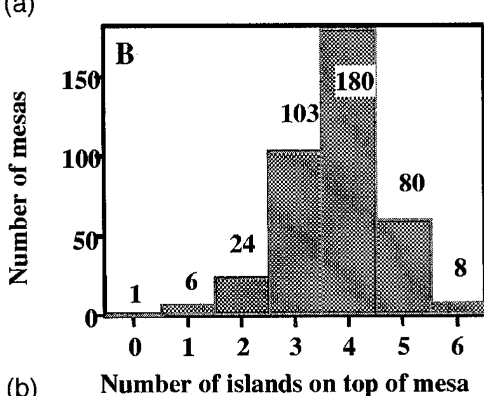

(b)

FIG. 5. (a) AFM images of InAs QDs grown on a patterned substrate with a 20 nm $In_{0.2}Ga_{0.8}As$ stressor layer. (b) Histogram of the number of islands found on top of the mesas.

ground state PL line (1.18 eV) for the InAs QDs grown on mesa lattices is blue shifted 34 meV with respect to the unpatterned sample. This also indicates that islands formed on patterned surfaces differ in size and composition. The strong PL signal observed from the InAs QDs grown on patterned substrates attests of the good quality of the InAs QDs and it indicates our regrowth surface has recovered from processing damages.

D. Growth of InAs QDs on mesa tops

A second nucleation regime can be achieved by introducing strain into the regrowth. By adding a strained $In_{0.2}Ga_{0.8}As$ layer after the GaAs buffer, the preferential nucleation of the QDs on mesa tops, type II islanding, was achieved. The sample structure, illustrated in Fig. 1(b), was a 60 nm GaAs buffer layer grown at 600 °C, followed by a 20 nm $In_{0.2}Ga_{0.8}As$ stressor layer, and 10 nm GaAs grown at 510 °C. The InAs islands were then deposited at 530 °C. An AFM image of InAs islands grown on a type B patterned substrate with stressor layer is shown in Fig. 5(a). The majority (over 90%) of InAs QDs were formed on top of mesas. Excellent island position control and long range 2D ordering were achieved with the use of a stressor layer. For this mesa size, there were on average close to four islands on top of each mesa, as indicated by the histogram shown in Fig. 5(b). Type A mesa arrays, with the same regrowth conditions, also exhibited long range QD ordering with the islands nucleating on top of the mesas.

The effect of the stressor layer on the mesa island positioning is critical. Islands on top of the mesas are analogous to the observed vertical stacking of quantum dots. Due to the patterning, the stressor layer can partially relax at the mesas peak, thus locally straining the thin GaAs barrier above the $In_{0.2}Ga_{0.8}As$. When the quantum dots are deposited, InAs preferentially accumulates where the strain energy is minimized on the growth surface,[25] i.e., at the mesa tops. The thickness and composition of the stressor layer is crucial for partial strain relaxation to occur effectively at the mesas. Indeed, for an $In_{0.2}Ga_{0.8}As$ stressor below 5 nm, all the islands are found in the valleys between mesas. The driving force to nucleate islands on top of the mesas must exceed the tendency for In to accumulate in the valleys as in type I nucleation. Detailed modeling of pattern induced strain modulation in type II structures will be discussed in a forthcoming publication.

III. SUMMARY

The present work demonstrates that control of the nucleation site positioning of InAs self-assembled QDs can be achieved by MBE deposition on a GaAs surface with a mesa lattice. Long range ordering is imposed by the presence of the mesas and/or by the introduction of a stressor layer. These techniques produce optically active QDs and provide a promising route for many device applications.

ACKNOWLEDGMENTS

This research was supported by an AFOSR Grant No. F49620-98-1-0367 monitored by Dan Johnstone. The authors wish to thank Mike Prairie (GEB), A. Romanov, and G. Beltz for their useful discussions.

[1]Y. Arakawa and H. Sakaki, Appl. Phys. Lett. **40**, 939 (1982).
[2]L. Goldstein, F. Glas, J. Y. Marzin, M. N. Charasse, and G. Le Roux, Appl. Phys. Lett. **47**, 1099 (1985).
[3]D. Leonard, M. Krishnamurthy, C. M. Reaves, S. P. DenBaars, and P. M. Petroff, Appl. Phys. Lett. **63**, 3203 (1993).
[4]H. Drexler, D. Leonard, W. Hansen, J. P. Katthaus, and P. M. Petroff, Phys. Rev. Lett. **73**, 2252 (1994).
[5]J. -Y. Marzin, J. -M. Gerard, A. Izrel, D. Barrier, and G. Bastard, Phys. Rev. Lett. **73**, 716 (1994).
[6]N. Kirstaedter, N. N. Ledentsov, M. Grundmann, D. Bimberg, V. M. Ustinov, S. S. Ruvimov, M. V. Maximov, P. S. Kopev, Z. I. Alferov, U. Richter, P. Werner, U. Gosele, and J. Heydenreich, Electron. Lett. **30**, 1416 (1994).
[7]D. Pan, E. Towe, and S. Kennerly, Appl. Phys. Lett. **73**, 1937 (1998).
[8]T. Lundstrom, W. Schoenfeld, H. Lee, and P. M. Petroff, Science **286**, 2312 (1999).
[9]J. Tersoff and F. K. LeGoues, Phys. Rev. Lett. **72**, 3570 (1994).
[10]Q. Xie, A. Madhukar, P. Chen, and N. P. Kobayashi, Phys. Rev. Lett. **75**, 2542 (1995).
[11]G. S. Solomon, J. A. Trezza, A. F. Marshall, and J. S. Harris, Phys. Rev. Lett. **75**, 952 (1996).
[12]H. Lee, R. Lowe-Webb, W. Yang, and P. C. Sercel, Appl. Phys. Lett. **71**, 2325 (1997).
[13]D. S. L. Mui, D. Leonard, L. A. Coldren, and P. M. Petroff, Appl. Phys. Lett. **66**, 1620 (1995).
[14]A. Konkar, R. Heitz, T. R. Ramachandran, P. Chen, and A. Madhukar, J. Vac. Sci. Technol. B **16**, 1334 (1998).
[15]W. Seifert, N. Carlsson, A. Petersson, L. -E. Wernersson, and L. Samuelson, Appl. Phys. Lett. **68**, 1684 (1996).
[16]R. Tsui, R. Zhang, K. Shiralagi, and H. Goronkin, Appl. Phys. Lett. **71**, 3254 (1997).
[17]T. I. Kamins and R. S. Williams, Appl. Phys. Lett. **71**, 1201 (1997).
[18]S. Jeppesen, M. S. Miller, D. Hessman, B. Kowalski, I. Maximov, and L. Samuelson, Appl. Phys. Lett. **68**, 2228 (1996).
[19]G. Jin, J. L. Liu, S. G. Thomas, Y. H. Luo, K. L. Wang, and B. -Y. Nguyen, Appl. Phys. Lett. **75**, 2752 (1999).
[20]T. Ishikawa, S. Kohmoto, and K. Asakawa, Appl. Phys. Lett. **73**, 1712 (1998).
[21]S. Kohmoto, H. Nakamura, T. Ishikawa, and K. Asakawa, Appl. Phys. Lett. **75**, 3488 (1999).
[22]G. Springholz, V. Holy, M. Pinczolits, and G. Bauer, Science **282**, 734 (1999).
[23]Y. Nabetani, T. Ishikawa, S. Noda, and A. Sasaki, J. Appl. Phys. **76**, 3347 (1994).
[24]M. Ozdemir and A. Zangwill, J. Vac. Sci. Technol. A **10**, 684 (1992).
[25]J. Tersoff, C. Teichert, and M. G. Lagally, Phys. Rev. Lett. **76**, 1675 (1996).

Growth and microstructure of self-assembled ErAs islands in GaAs

C. Kadow,[a] J. A. Johnson, K. Kolstad, J. P. Ibbetson, and A. C. Gossard
Materials Department, University of California, Santa Barbara, California 93106-5050

(Received 6 April 2000; accepted 26 May 2000)

This article concerns the microstructure of self-assembled ErAs islands embedded in GaAs. The material is grown by molecular beam epitaxy. The nucleation of ErAs on GaAs occurs in an island growth mode leading to spontaneous formation of nanometer-sized islands. Several layers of ErAs islands separated by GaAs can be stacked on top of each other to form a superlattice. A series of such samples were grown with different depositions of ErAs at a growth temperature of 535 °C. The microstructure of these samples was investigated by x-ray diffraction and transmission electron microscopy. We find that initially isolated ErAs islands with a diameter of 2 nm are nucleated. With increasing ErAs deposition, these islands branch out and form extended structures. The samples are coherent in growth directions for ErAs depositions up to 1.8 monolayers. At higher ErAs depositions defects are incorporated into the GaAs matrix. © *2000 American Vacuum Society.*
[S0734-211X(00)07404-7]

I. INTRODUCTION

This article concerns material consisting of nanometer-sized ErAs islands embedded in GaAs. The samples are prepared by molecular beam epitaxy (MBE). The ErAs islands form spontaneously during growth when a few monolayers of ErAs are deposited on a GaAs surface. These islands can be overgrown with GaAs of high quality. This allows us to stack several layers of ErAs islands on top of each other as shown in the schematic cross section in Fig. 1.

There are several motivations for us to investigate such samples. First, they provide an interesting model system for studying the epitaxy of nanocomposites. This material system is particularly interesting because the two materials involved are very different. ErAs has the rocksalt crystal structure and is semimetallic; GaAs has the zincblende crystal structure and is semiconducting. The island formation is driven by the surface chemistry rather than strain as in the case of the Stranski–Krastonow growth mode. Another motivation are the magnetic properties of these samples. The Er atoms carry large magnetic moments, which result in antiferromagnetism in ErAs bulk material at low temperatures. These large moments cause strong effects in the magnetoresistance of samples similar to the ones studied here.[1,2] The third motivation is that these samples are ultrafast photoconductors. A particular interesting aspect is that the time constants involved depend strongly on the microstructure.[3] The ultrafast properties allow us to use these materials for THz generation.[4]

In this article we investigate with x-ray diffraction and transmission electron microscopy (TEM) how the microstructure of the material changes with ErAs deposition. We address two main questions: The first question is how the ErAs islands develop with deposition. We are, for example, interested if additional material leads to the nucleation of more islands or to the growth of the existing islands. The second question pertains to the quality of the GaAs overgrowth. It is known that it is difficult to overgrow ErAs films with GaAs.[5,6] It is however possible to overgrow the ErAs islands at least if the amount of ErAs deposited is small enough.[3] Therefore we expect that at some ErAs deposition, defects will start to nucleate and the quality of the overgrowth will degrade. If the material is used for devices, a small number of defects will probably be desirable.

The information about the microstructure is important because electronic properties depend on it. For example, the dark resistivity is a very strong function of growth temperature and ErAs deposition.[1,2] Other examples are the carrier relaxation times, which are controlled by the period of the superlattice.[3]

In previous work, Palmstrøm and co-workers investigated the growth of ErAs films on GaAs.[5,6] From these studies many details of the nucleation of ErAs on GaAs are known. The ErAs nucleates in islands that are on average three to four monolayers (MLs) high. After reaching this height, the islands coalesce into a complete film. Then the growth proceeds in a layer by layer fashion. This type of nucleation behavior can be understood in the following way. The ErAs material is wetting the GaAs surface. The 3–4 MLs high nucleation sites are needed to establish the rocksalt crystal structure. Once the nucleation sites exist, the material coalesces into a complete film and the growth proceeds in the usual fashion. In their studies Palmstrøm *et al.* also showed that the ErAs grown on GaAs has in fact the rocksalt crystal structure, which is slightly distorted due to strain. Our investigations confirm these findings and extend them by focusing on island growth rather than film growth. Yamaguchi and Horikoshi also worked on thin ErAs layers sandwiched between GaAs material. They studied these layers, which were grown by migration enhanced epitaxy, with x-ray diffraction and TEM.[7]

Another body of knowledge exists due to the studies of Er-doped GaAs. It is generally found that the solubility limit

[a]Electronic mail: kadow@engineering.ucsb.edu

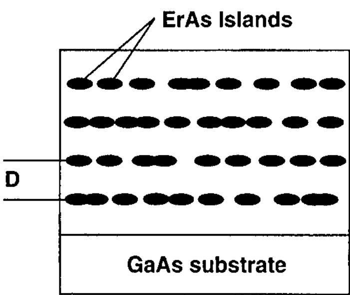

FIG. 1. Schematic cross section of the samples investigated. The ErAs islands are arranged in layers, which are stacked on top of each other forming a superlattice structure.

of Er in GaAs under typical MBE growth conditions, results in formation of ErAs precipitates for doping levels beyond approximately 5×10^{17} cm^{-3}. The precipitates have for example been studied by Peaker *et al.*[8] and by Sethi *et al.*[9]

II. EXPERIMENT

All investigated samples are superlattices of the kind shown in Fig. 1. The designs of the samples we investigated are summarized in Table I. Most of the work described here is on a series of samples with different ErAs depositions ranging from 0.6 to 2.3 ML, (samples A–F). All samples in the series contain a 10 period superlattice with 25 nm period. In addition to these samples, three other samples are included (samples G–I). Samples G and H contain AlAs etch stop layers beneath the superlattice structure. These layers were added for processing purposes and do not influence the ErAs island layers, which are of interest here. Sample I has the same ErAs deposition as sample B; it differs in the number of periods and the period itself. All samples were grown at temperatures around 530 °C. The GaAs growth rate was around 1 μm/h; the ErAs growth rate was 2.3 ML/min. The growth conditions and procedure are described in more detail in Ref. 3.

A double crystal x-ray diffractometer with an open detector was used for the x-ray experiments. During the scans source and detector were fixed, the sample was moved around the ω axis. The x-ray source generates the Cu K_α line

TABLE I. Summary of the designs of the investigated samples.

Sample	ErAs deposition (ML)	Superlattice period L (nm)	Number of periods	T_{growth} (°C)
A	0.6	25	10	535
B	1.2	25	10	535
C	1.5	25	10	535
D	1.8	25	10	535
E	2.1	25	10	535
F	2.3	25	10	535
G	1.2	5.7	40	520
H	2.4	11.3	20	530
I	1.2	40	40	535

with a wavelength of 1.541 Å. The TEM images were obtained on a JEOL 2000FX instrument. The electron energy was 200 keV.

Because both experimental techniques use diffraction, we give a brief discussion of why x rays and electrons scatter differently from the two materials in the samples. There are three possible mechanisms for that: the chemical contrast between Ga and Er atoms, the different crystal structure, and strain. The TEM data are obtained using a (002) reflection. For this diffraction condition all three mechanisms contribute. The contribution from the structure dominates because it is weak for the zincblende crystal structure of GaAs and strong for the rocksalt crystal structure of ErAs. The x-ray data, however, are taken around the (004) diffraction condition. At this condition the structure factor of the two materials is equal. Hence there is no contribution from the different crystal structures in the x-ray data presented. The only contributions are chemical and strain contrast. The chemical contrast is given by the atomic form factors f_i. The atomic form factor for x-ray diffraction scales roughly as the number of atomic electrons Z_i. This estimate gives $f_{Er}/f_{Ga}=Z_{Er}/Z_{Ga}=2.2$. The strain results from the different lattice constants of GaAs and ErAs. The bulk ErAs lattice constant exceeds the bulk lattice constant of GaAs a by 1.6%. Miceli *et al.*[10] measured the strain in ErAs films grown on GaAs. For pseudomorphic ErAs films they find that the lattice constant of the ErAs film along the growth direction b is given by $b=1.021a$. Because we use different conditions for the TEM and the x-ray data, the two experiments are sensitive to different aspects of the microstructure. With x-ray diffraction we mainly observe the GaAs matrix because most of the scattering amplitude originates from it. With TEM we mainly investigate the ErAs islands.

III. TRANSMISSION ELECTRON MICROSCOPY

Figure 2 shows plan view TEM images of three samples of the deposition series, samples B, D, and F. The images were obtained under dark field conditions using a (002) reflection. The ErAs islands appear dark. Fourier transforms of each image are also shown. The data from sample B (1.2 ML) show isolated islands, which are about 2 nm in diameter. The density of the islands is approximately 7×10^{12} cm^{-2}. At an ErAs deposition of 1.8 ML (sample D) the ErAs material forms extended, branched structures. These branches extend on average 20 nm in length, their width is around 4 nm. Scattered between these branched structures are regions of smaller, isolated islands. The last sample of the series, sample F with 2.3 ML of ErAs, appears qualitatively similar to sample D. The branched structures, however, extend further. Their average length is 30 nm, their width is unchanged. There are no regions with small, isolated islands. All three Fourier transforms show a ring around the center. For all three depositions, the radius corresponds to a length of roughly 5 nm in real space. This means that the typical length scales in the images only have a weak dependence on ErAs deposition. The rings are slightly ellipsoidal, indicating some anisotropy in the images.

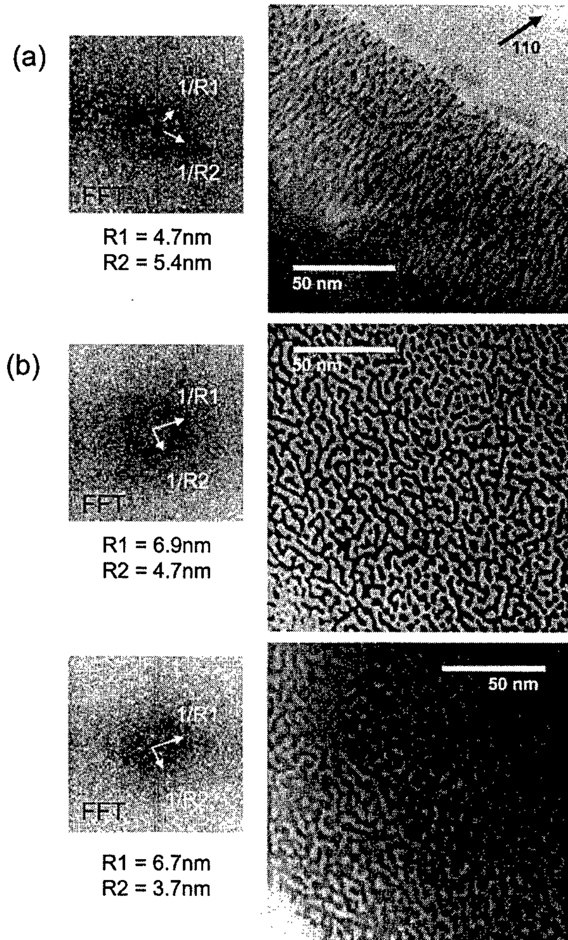

FIG. 2. Plan view TEM images of the samples B (a), sample D (b), and sample F (c). Fourier transforms of each TEM image are also shown. These images show how the ErAs islands develop as the ErAs deposition is changed.

Cross sectional TEM of sample G (1.2 ML) and H (2.4 ML) are shown in Fig. 3. The ErAs islands appear light in these two images. In the images of sample G and H, AlAs layers can be seen beneath the region that contains the ErAs islands. Sample H also contains an AlAs/GaAs short period superlattice. The superlattice of the ErAs island layers and GaAs is evident in the images of both samples. The matrix material of sample H contains dislocations. The ErAs containing layers in sample G appear smooth, while in sample H roughness appears. The onset of defect incorporation is discussed in more detail in the next sections.

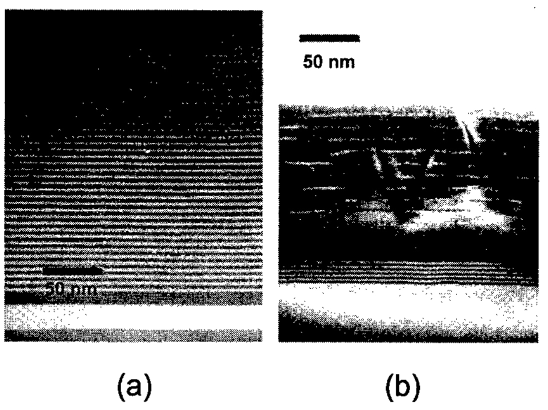

FIG. 3. Cross sectional TEM images of sample G (a) and H (b).

IV. X-RAY DIFFRACTION

Figure 4 shows an x-ray rocking curve around the (004) GaAs diffraction peak from sample I. The data contain several satellite peaks around the substrate peak. Such satellites are typically observed for superlattice structures and can be understood in the framework of kinematic diffraction theory. The satellites are spaced equidistantly. The separation of adjacent peaks is given by the **k** vector $k_D = 1/D$ associated with the period of the superlattice D. The measured period agrees within 2% with the sample design. The angular position of the zeroth order superlattice peak is shifted with respect to the substrate peak by Δk. This shift means that the superlattice is strained. The negative sign indicates that the lattice constant along the growth direction is larger than the lattice constant for bulk GaAs. This is expected because the lattice constant of ErAs is larger than the GaAs lattice constant.

A. Model

In this section we outline a simple, analytical model, which reproduces the essential features of the data in Fig. 4. We use kinematic diffraction theory and a one-dimensional model of the superlattice. The treatment follows the discussion in Ref. 11. Because the model is one dimensional, it does not take the islanding into account but the ErAs containing regions are treated as uniform layers. We make a number of further assumptions to simplify the mathematics involved. We assume in particular that all scattering occurs from the GaAs atoms. This is justified because each period of the superlattice samples discussed contains typically one to two monolayers of ErAs and 100 or more monolayers of GaAs. The point of developing this model is to obtain analytic expressions for the satellite amplitudes and the shift Δk. These allow us to develop an understanding of their meaning and how they depend on growth parameters, in particular the ErAs deposition.

At this point we need to introduce a number of quantities: $d_{(\mathrm{GaAs})}$ is the length of the GaAs section in each period of the superlattice, $d_{(\mathrm{ErAs})}$ is the length of the ErAs section. $M_{(\mathrm{GaAs})}$ is the number of monolayers of GaAs and $M_{(\mathrm{ErAs})}$ the number of monolayers of ErAs. $\langle a \rangle$ is the average lattice constant of the superlattice given by $\langle a \rangle = (M_{(\mathrm{GaAs})} \cdot a + M_{(\mathrm{ErAs})} \cdot b)/(M_{(\mathrm{GaAs})} + M_{(\mathrm{ErAs})})$. Δa is the difference between the lattice constant of GaAs a and the lattice constant b of the strained ErAs. Note that $d_{(\mathrm{GaAs})} \gg d_{(\mathrm{ErAs})}$ or $M_{(\mathrm{GaAs})} \gg M_{(\mathrm{ErAs})}$ and that $b = a + \Delta a$.

In the framework of kinematic diffraction theory the x-ray results are essentially given by the Fourier transform of the sample structure in real space. In our model the sample consists of N identical blocks of GaAs, each $d_{(\mathrm{GaAs})}$ wide, and N gaps, each $d_{(\mathrm{ErAs})}$ wide. In the limit of $N \to \infty$, the Fourier

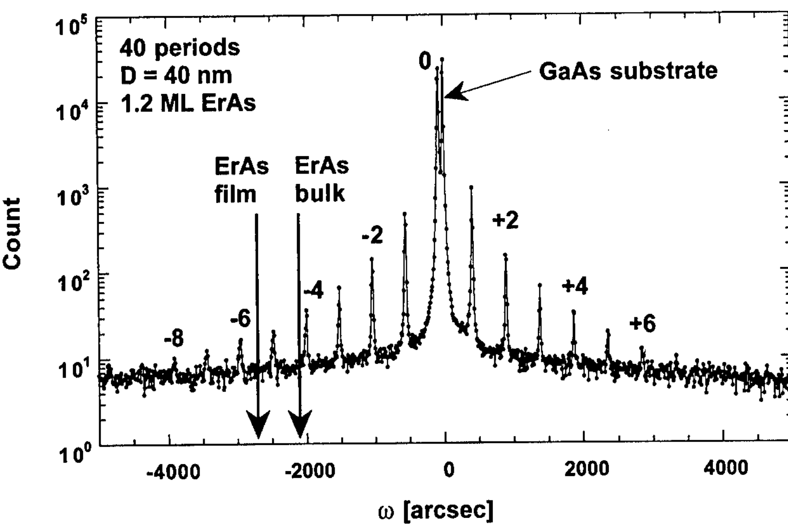

FIG. 4. X-ray scan (ω scan) around the (004) diffraction condition of GaAs of sample H. The data contain several satellite peaks, which arise from the superlattice structure. The two arrows indicate the angular positions corresponding to the lattice constants of bulk ErAs and of a pseudomorphically grown ErAs film.

transform is a series of equidistant spikes, which are spaced $k_D=1/D$ apart from each other. The scattering amplitude is only significant close to the diffraction peaks of GaAs. We denote the k value associated with the (004) diffraction condition for GaAs as $k_{(004)}$. Close to $k_{(004)}$, the magnitude of these spikes is determined by a function that we denote as T. This function T is the Fourier transform of a slit function with width $d_{(\mathrm{GaAs})}$ centered around $k_{(004)}$. For finite N, the spikes are not δ-function like, but have a finite width of $1/(N\,D)$.

The position of the spike closest to the GaAs substrate peak $k_{(004)}$ determines the shift Δk. In the case of our samples, the zeroth order superlattice peak k_0 is closest to the substrate peak. Its position is given by the average lattice constant $\langle a\rangle$ of the superlattice region, $k_0=4/\langle a\rangle$. Therefore the shift Δk can be written as

$$\Delta k=\frac{4}{\langle a\rangle}-\frac{4}{a}=2\frac{M_{(\mathrm{ErAs})}}{D}\left(\frac{\Delta a}{a}\right).$$

This means that in this model the shift Δk is proportional to the number of monolayers of ErAs deposited $M_{(\mathrm{ErAs})}$, proportional to the strain $\Delta a/a$, and inversely proportional to the superlattice period D. In particular Δk would vanish if the superlattice was unstrained.

The next question addressed is the magnitude of the satellite peaks. The peaks appear at k_n, which are given by $k_n=k_0+n\cdot k_D=k_0+n/D$, where n is an integer. The peak's magnitudes are proportional to $[T(k_n)]^2$, which can be written in the following way:

$$[T(k_n)]^2=\frac{[\sin(\pi\alpha+\pi n\beta+\pi\alpha\beta)]^2}{\pi^2(1+\beta)^2(n+\alpha)^2}.$$

α and β are the following parameters, which are both accessible from the sample design and the data: $\alpha=\Delta k/k_D$ and $\beta=d_{(\mathrm{ErAs})}/d_{(\mathrm{GaAs})}$. Note that α is a measure of the strain and that β is a measure of the chemical contrast. For the samples discussed both α and β are small compared to unity, and $\alpha\gg\beta$. β is approximately 0.01 and α is approximately 0.1. In the limit of $\beta=0$ and small α, the expression above reduces to

$$[T(k_n)]^2=\frac{\alpha^2}{n^2+2n\alpha}.$$

To first order we therefore expect the amplitude of the satellites to decrease as $1/n^2$. The next higher order results in asymmetric peak amplitudes ($[T(k_{+n})]^2\neq[T(k_{-n})]^2$). The function T^2 is symmetric with respect to $k_{(004)}$ but not with respect to k_0. The peak magnitudes are asymmetric because k_0 does not coincide with $k_{(004)}$. Hence the asymmetry is also a strain related feature. In our case, for $\Delta k<0$, the peaks with positive indices are expected to be larger than the peaks with negative indices.

The features expected from the model can be seen in the Fig. 4. The shift Δk between the substrate and the main superlattice peak is apparent and has the expected sign. The amplitudes of the satellites decay roughly as $1/n^2$. The asymmetry in the peak heights can be seen for the satellites of low order. However, for high order peaks the asymmetry is reversed. This effect is not predicted by the model. It is probably due to the scattering from the ErAs material, which we neglected in the model. The ErAs atoms should add some scattering amplitude at an angle corresponding to the position of the lattice constant of strained ErAs, which is indicated in Fig. 4. It is surprising how well our model fits the data, in particular the peak amplitudes, despite the fact that the samples contain islands and not uniform layers as assumed in the model.

Another quantity of interest is the coherence length in the superlattice. An experimental measure is the linewidth of the superlattice peaks. In the model outlined above the linewidth is given by the inverse of the total length of the superlattice $1/(ND)$. We expect to see this linewidth if the coherence length is equal or longer than the total length of the superlattice. When the coherence length becomes shorter than the total length of the superlattice, the lines will broaden. In the

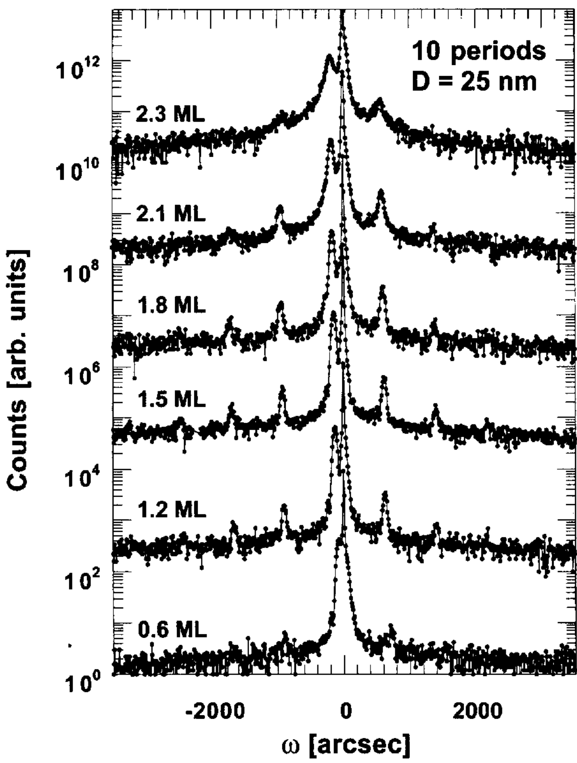

FIG. 5. X-ray scans from samples with different ErAs depositions $M_{(\mathrm{ErAs})}$ (samples A–F). Note the changes in the satellite peak magnitudes and in the strain related shift between the substrate peak and the zero order superlattice peak Δk.

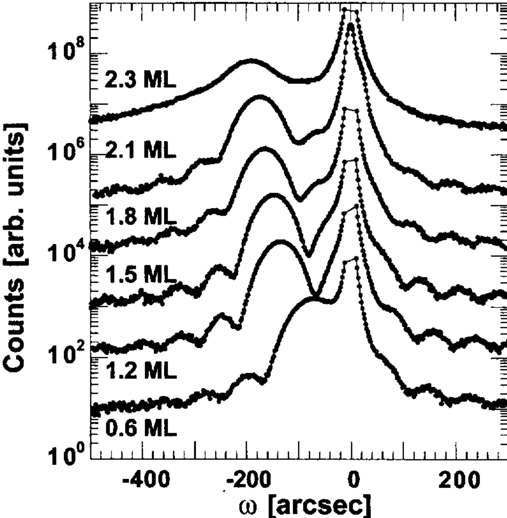

FIG. 6. X-ray scans around the substrate peak from the same samples that are shown in Fig. 5.

data we look for the onset of this broadening and take it at the point where the samples start to lose coherence. Once coherence is lost, we will not see the superlattice peaks.

B. ErAs deposition series

Figure 5 shows the x-ray data for the series of samples with different ErAs depositions (samples A–F). It can be seen that the magnitudes of the satellite peaks change with ErAs deposition. The peak magnitudes initially increase with $M_{(\mathrm{ErAs})}$, reach a maximum at a deposition of 1.8 ML of ErAs, and decrease for higher depositions. The shift Δk between the substrate peak and the zeroth order superlattice peak also changes. Δk increases monotonically with ErAs deposition. The quantitative analysis of the dependence of Δk on the ErAs deposition is discussed in a later paragraph. The linewidth of the superlattice peaks is constant up to a deposition of 1.8 ML, and it increases at higher depositions.

The onset of the increase in the linewidth gives a measure of the coherence of the samples in growth direction. From the data we conclude that the samples have coherence length in excess of 250 nm for depositions equal or lower than 1.8 MLs. We will subsequently call these samples coherent. For higher depositions the samples are semicoherent. This agrees well with the behavior of the amplitudes of the satellite peaks, which reach their maxima at the same deposition of 1.8 ML.

Shorter x-ray scans around the substrate peak of the same samples are shown in Fig. 6. The additional fringes seen in Fig. 6 correspond to the thickness of the entire superlattice. Figure 7 shows how Δk varies with ErAs deposition $M_{(\mathrm{ErAs})}$. We can fit the data with a parabolic function. For small ErAs depositions the linear term dominates. At higher values of $M_{(\mathrm{ErAs})}$, the function is sublinear. The shift Δk expected from the model, using the strain value of 2.1% measured by Miceli *et al.*,[10] equals $1.7\times 10^4\ \mathrm{cm}^{-1}$ for 1 ML of ErAs. This has the same order of magnitude as what we see experimentally. The shift predicted by the model is, however, about a factor of 4 smaller than the experimental values. The disagreement is not unexpected because in the model we make the simplifying assumption of a uniform strained layer. It would not be surprising if the strain fields of the ErAs-island layers have little to do with the strain fields of pseudomorphic films. Another factor that may lead to differences between model and experiment, is that our model uses kinematic diffraction theory and not dynamic diffraction theory.

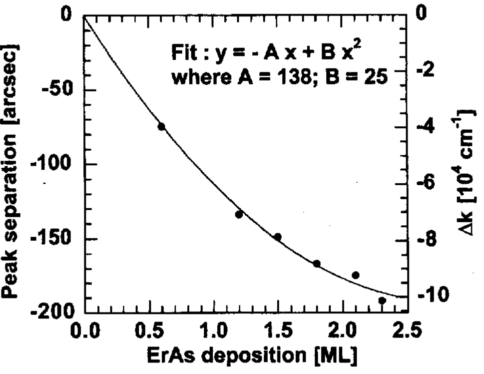

FIG. 7. Shift Δk between zeroth order superlattice peak and substrate peak as a function of ErAs deposition $M_{(\mathrm{ErAs})}$. The shift increases monotonically with ErAs deposition as expected.

V. DISCUSSION

The x-ray and TEM data give information about several aspects of the microstructure such as the GaAs overgrowth and the morphology of the ErAs islands. We believe that during the growth of these superlattice structures the GaAs overgrowth nucleates from the uncovered regions of the GaAs template around the ErAs islands. It then overgrows the ErAs islands laterally. We therefore expect to see a transition from a growth regime where the GaAs matrix is unaffected by the ErAs islands (low ErAs deposition) to a regime where the quality of the overgrowth deteriorates (high ErAs deposition) as the islands coalesce into a film. This transition is seen with x-ray diffraction, TEM, and also *in situ* with reflection high energy electron diffraction (RHEED), at least in a qualitative fashion. From the linewidth of the satellite peaks in the x-ray data, we conclude that this transition occurs between 1.8 and 2.1 ML of ErAs. The TEM data confirm this conclusion. We expect this transition point to depend on other growth parameters, in particular on growth temperature and growth rate. From the TEM images, it appears that in the regime of high ErAs deposition, dislocations nucleate from the ErAs islands layers and that the growth front roughens. The RHEED patterns are also in qualitative agreement with these findings. In the low ErAs deposition regime, we see the RHEED pattern completely recover after a few nm of GaAs overgrowth. This is not the case in the high ErAs deposition regime, where the RHEED pattern slowly deteriorates for each successive period of the superlattice. It changes from streaky to spotty and loses intensity.

Palmstrøm *et al.* show high resolution cross sectional TEM images of ErAs layers with ErAs depositions of 1, 2, and 3 in Ref. 6 (p. 95, Fig. 14). The samples are grown at a lower temperature (of 350 °C) than the samples we describe here. Those images also indicate a transition as discussed above between 2 and 3 ML of deposited material. The GaAs overgrowth of the layer with 3 ML ErAs depositions contains regions with several different crystallographic orientations. Yamaguchi and Horikoshi also investigated ErAs layers with ErAs depositions of 1, 2, and 3 ML.[7] Their samples are grown using migration enhanced epitaxy at a lower temperature of 320 °C. They also observe the transition discussed above. They can however already see dislocations in the ErAs layer with 2 ML of deposited material. Both of these studies indicate the same behavior that we observe; however, the details, especially the types of defects generated in the regime of high ErAs deposition, may be different. The transition appears to occur at approximately the same ErAs deposition despite the differences in growth conditions.

The plan view TEM images show how the ErAs islands evolve as more ErAs is deposited. Under our growth conditions, ErAs nucleates on GaAs in the form of nanometer sized, isolated islands. As more material is deposited, branched, extended islands are formed. At an ErAs deposition of 1.8 ML, these structures are clearly developed as shown in Fig. 2. There are however also regions of isolated islands. Note that these regions are only approximately 50 nm in diameter and are separated by only about 100 nm. This small length scale is unexpected because we do not think that relevant growth parameters such as temperature or Er flux vary by any substantial amount over such short distances. At the higher deposition value of 2.3 ML we find only the branched, extended islands. At this point it is not clear why the branched, extended structures are formed at higher ErAs depositions. It is noteworthy that Singer *et al.* observed somewhat similar structures for ErAs precipitates in GaAs.[8] This is particularly interesting because the ErAs is formed by precipitation during regular MBE growth with the Ga, Er, and As fluxes turned on simultaneously.

Another interesting issue is that the x-ray diffraction data agree surprisingly well with the simple model presented earlier. In particular the dependence of the satellite peak magnitudes on their order n is fit well by an $1/n^2$ dependence. Such a dependence is typical for uniform films. We speculate that the strain fields of the ErAs-island layers may be close to that of a uniform film. This would make these layers look similar to a film in the x-ray diffraction experiments we performed because they are dominated by strain effects. With the plan view TEM image of sample D [Fig. 2(b)] in mind, it seems possible that the GaAs material that grows between the ErAs islands strains to conform to the ErAs islands. If the GaAs were not strained between the ErAs islands, stacking faults were likely to form between the GaAs grown on top of the ErAs islands and the GaAs grown in between the islands due to the mismatch in the growth direction. These stacking-fault pyramids have been observed for material grown at lower growth temperature.[12] The fact that we do not observe stacking faults suggests that significant amounts of the GaAs between the ErAs islands may be strained. If true, this would result in a higher strain value than expected for a superlattice structure composed of uniform ErAs films, which is what we observe for the shift Δk. We believe that this partly explains the factor of four difference between the model and the data. Further experimentation is certainly needed to confirm or disconfirm these ideas.

VI. SUMMARY AND CONCLUSION

In summary, x-ray diffraction and TEM measurements offer insights into how the microstructure of self-assembled ErAs island in GaAs depends on the amount of ErAs deposited. The ErAs islands nucleate as isolated islands with diameters around 2 nm. At higher depositions these islands branch out and form extended structures with an average length of 30 nm. Both x-ray and TEM show that the samples are coherent in the growth direction for ErAs depositions equal to or smaller than 1.8 ML. At higher depositions, defects are incorporated into the matrix and the growth front appears to roughen. The dominating defects seem to be dislocations.

ACKNOWLEDGMENT

This work has been supported by the Jet Propulsion Lab under Contract No. 960776 and QUEST.

[1]D. R. Schmidt, J. P. Ibbetson, D. E. Brehmer, C. J. Palmstrøm, and S. J. Allen, Mater. Res. Soc. Symp. Proc. **475**, 251 (1997).
[2]D. R. Schmidt, A. G. Petukhov, M. Foygel, J. P. Ibbetson, and S. J. Allen, Phys. Rev. Lett. **82**, 823 (1999).
[3]C. Kadow, S. B. Fleischer, J. P. Ibbetson, J. E. Bowers, A. C. Gossard, J. W. Dong, and C. J. Palmstrøm, Appl. Phys. Lett. **75**, 3548 (1999).
[4]C. Kadow, A. W. Jackson, A. C. Gossard, S. Matsuura, and G. A. Blake, Appl. Phys. Lett. **76**, 3510 (2000).
[5]T. Sands, C. J. Palmstrøm, J. P. Harbison, V. G. Keramidas, N. Tabatabie, T. L. Cheeks, R. Ramesh, and Y. Silverberg, Mater. Sci. Rep. **5**, 99 (1990).
[6]C. J. Palmstrøm and T. Sands, in *Contacts to Semiconductors: Fundamentals and Technology*, edited by L. J. Brillson (Noyes, Park Ridge, NJ, 1993).
[7]H. Yamaguchi and Y. Horikoshi, Appl. Phys. Lett. **60**, 2341 (1992).
[8]K. E. Singer, P. Rutter, and A. R. Peaker, Appl. Phys. Lett. **64**, 707 (1994).
[9]S. Sethi and P. K. Bhattacharya, J. Electron. Mater. **25**, 467 (1996).
[10]P. F. Micele, K. W. Moyers, and C. J. Palmstrøm, Mater. Res. Soc. Symp. Proc. **202**, 579 (1991).
[11]G. Bauer and W. Richter, *Optical Characterization of Epitaxial Semiconductor Layers* (Springer, Berlin, 1996), p. 328.
[12]J. G. Zhu, C. J. Palmstrøm, and C. B. Carter, Mater. Res. Soc. Symp. Proc. **198**, 177 (1990).

Evolution of Si-on-GaAs (001) surface morphology towards self-organized ordered Si structures

Z. M. Wang, L. Däweritz, P. Schützendübe, and K. H. Ploog[a)]
Paul-Drude-Institut für Festkörperelektronik, Hausvogteiplatz 5-7, D-10117 Berlin, Germany

(Received 17 January 2000; accepted 6 April 2000)

Scanning tunneling microscopy studies of the restructuring of GaAs (001) surfaces induced by Si deposition have been performed. With increasing Si coverages, different reconstructions are developing. Their interaction with the surface step structures results in a distinct separation into different surface phases with different Si coverages, revealing unique Si distribution patterns. This phenomenon is explained by considering kinetically accessible thermodynamically determined structures. © *2000 American Vacuum Society.* [S0734-211X(00)00304-8]

I. INTRODUCTION

The incorporation behavior of Si atoms on GaAs (001) surfaces has been the focus of a number of studies in view of its technological importance. For coverages below 10^{13} cm^{-2}, Si confined within a few atomic layers of GaAs acts as *n*-type dopant,[1–5] providing the δ doping in practice. For high coverages, Si deposition improves ohmic contacts, tunes band gap offsets, and its study also contributes a better understanding of the first step of the Si-on-GaAs heteroepitaxy.[6–9] In Si adsorption experiments carried out on $c(4\times4)$ reconstructed surfaces,[10] "needle-like" islands were found to form by Si–As dimer exchange with the additional outermost arsenic layer. Other studies show that Si preferentially occupies the vacant second layer Ga sites in the missing dimer trenches of the $(2\times4)\beta2$ reconstructed surface.[11] Recently, there has been increasing interest in the mechanisms by which the doping atoms are incorporated into a particular region of a semiconductor material, which is critical to achieve the reduction of device sizes and an improvement of their performance. However, all the scanning tunneling microscopy (STM) studies undertaken within the above considered work show a random Si distribution across GaAs (001) surfaces. By monitoring the evolution of long- and short-range order with increasing Si coverage by reflection high-energy electron diffraction (RHEED) and reflectance difference spectroscopy (RDS), the possibility of an in-plane ordering of the Si distribution on vicinal GaAs (001)-$(2\times4)\alpha$ reconstructed surfaces was demonstrated,[12,13] and further confirmed by Raman scattering.[14] In the light of this pronounced discrepancy, the Si incorporation behavior is systematically studied in the present work by STM with different coverages, substrate temperatures and surface misorientations. During the initial stage of Si deposition, a well ordered (3×2) reconstruction is developing within the original $(2\times4)\alpha$ surface phase, and subsequently additional Si deposition above 0.3 ML (monolayer) induces a disordered asymmetric (1×3) structure $[a(1\times3)]$ coexisting with the (3×2) phase. Spatially well separated coexisting surface phases are observed in real space, (3×2) reconstructed wide terraces and $(2\times4)\alpha$ or $a(1\times3)$reconstructed regions with high step density, which indicate the achievement of distinct self-organized Si structures accompanied by step bunching. A new mechanism concerning local thermodynamic states is proposed for the step bunching in the case of two different reconstructions coexisting on the surface, which places the submonolayer epitaxy in a new light.

II. EXPERIMENT

The experiments were performed in a combined molecular beam epitaxy (MBE) and STM system with additional facilities for *in situ* RHEED and RDS analysis. Epi-ready *n*-type GaAs substrates, singular (001) or vicinal (001) with 2° miscut towards (111)A or (111)B, were transferred into the growth chamber where the oxide was thermally desorbed at 580 °C under As_4 flux. After further annealing at 600 °C for 10 min, a 300-nm-thick Si-doped GaAs buffer layer was grown at 550 °C with an As_4-to-Ga beam equivalent pressure (BEP) ratio of 23, which leads to a well ordered $(2\times4)\beta2$ surface structure as revealed by RHEED.[15] Additional growth of 100 nm Si-doped and 10 nm undoped GaAs layers was carried out at 600 °C with a lower As_4-to-Ga ratio of 15 to favor the step-flow growth mode. The last undoped layer was used to avoid any possible influence from the bulk Si doping.[16] Thereafter the substrate temperature and As_4 BEP were adjusted to achieve the $(2\times4)\alpha$ reconstructed surface, on which the surface atom mobility is high as confirmed previously by RHEED and RDS studies.[12,13] Si was deposited with a flux of about 5.0×10^{11} atoms cm^{-2} s^{-1} (calibrated by secondary ion mass spectrometry in reference samples) in pulses of 60 s and interruptions of 180 s. The Si incorporation process which is reflected in the surface structure was monitored by *in situ* RHEED and RDS. When a certain Si coverage was reached, the deposition was stopped and the resulting surface quenched by decreasing both the substrate temperature and the As_4 background pressure in order to maintain the as-grown surface structures. The unchanged RHEED pattern (judged from real-time line scan measurements) and the RDS signal during the whole process were used as criteria for correct quenching. After having the valve of the As_4 source completely closed at a substrate temperature of about 500 °C, the samples were transferred into

[a)]Author to whom correspondence should be addressed; electronic mail: ploog@pdi-berlin.de

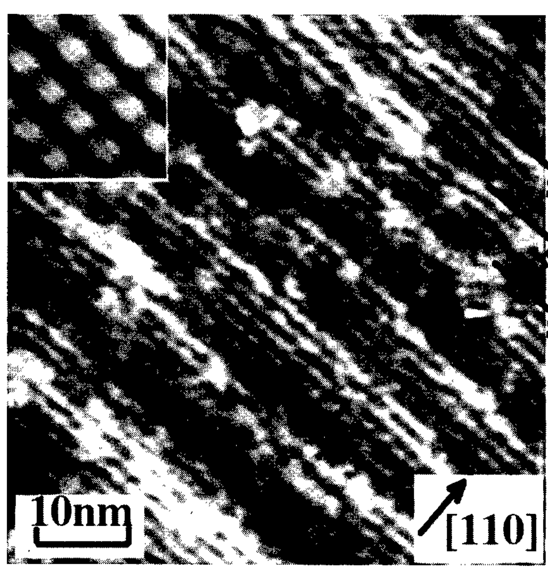

FIG. 1. STM image of GaAs (001)-(2×4)α surface with a miscut of 2° towards (111)A. The inset shows a high-resolution image of the (2×4)β2 structure on the singular surface. Some of the monolayer steps are marked by S.

the STM chamber for further analysis. STM images of filled states were taken at room temperature in the constant current mode with negative sample biases of 2–4 V and tunneling currents of 0.1–0.4 nA. We have imaged large areas at different locations on a number of samples; the images shown in the following are representative of the corresponding surface. There appears to be very little inhomogeneity across the sample surfaces.

III. RESULTS

A. Effect of the Si coverage

The surface evolution during Si deposition up to 1.5 ML was investigated on vicinal GaAs (001) samples with 2° miscut towards (111)A. The initial surface is shown in Fig. 1. The dark and light stripes running diagonally across the image are the missing dimer trenches and dimer-pair rows, respectively. The surface is (2×4)α reconstructed, as indicated by the different appearances compared to the common (2×4)β2 phase shown in the inset and also assessed by RD spectra.[17] Due to the high kink density in the dimer rows, which is characteristic of the (2×4)α structure, the dimer rows are less well resolved than on the (2×4)β2 surface.[18] The (2×4)α phase is characterized by two As dimers with a complete second Ga layer.[18,19] The exposed Ga atoms in the missing dimer rows form dimers, in contrast to the empty Ga sites in the trenches of the (2×4)β2 phase that act as favorable Si adsorption sites at low Si coverage.[20] This is an important difference between our work and previous studies by other authors.[10,11] The terraces separated by monolayer steps are about 8 nm wide, consistent with the 2° miscut.

After deposition of 0.05 ML Si, several randomly distributed (3×2) reconstructed patches have formed on the surface,[21] while the RHEED pattern changes to a (3×2) structure. Upon continuing the Si deposition, the intensity of the (3×2) RHEED pattern gradually increases and the STM study reveals that the (3×2) terraces become wider while steps are concentrated into the (2×4)α reconstructed regions.[21] Figure 2(a) shows the STM image for a Si coverage of 0.2 ML, revealing these large (3×2) reconstructed terraces separated by heavily step-bunched regions. Upon further increase of the Si coverage above 0.3 ML, the RHEED intensity of the (3×2) structure starts to decrease. The STM image shown in Fig. 2(b) for 0.5 ML Si deposition displays that the (3×2) wide terraces start to shrink and a new reconstruction, $a(1\times3)$, is developing at the step regions. Later the $a(1\times3)$ reconstruction covers almost the whole surface, shown in Fig. 2(c) for 0.8 ML Si deposition, and only some small patches as indicated by the dark triangle show disordered (3×2) appearance. Further increasing the Si coverages up to 1.5 ML, the resulting surface is characterized by a regular array of monolayer steps and terraces with all terraces $a(1\times3)$ reconstructed. This resembles the initial surface shown in Fig. 1, although the surface is now terminated by a Si–As instead of a Ga–As double layer.

The evolution of the surface morphology and its indication for Si distribution is summarized shown in Fig. 3. Previous RHEED and RDS studies have shown that the (3×2) structure is terminated by Si dimers with the dimer bond along [110] and the $a(1\times3)$ structure represents a complete Si layer covered by As dimers with dimer bonds along [$\bar{1}$10].[22,23] For the first stage of Si deposition, the (3×2) structure is developing at the expense of the (2×4)α structure, accompanied by step bunching, as shown in Figs. 3(a) and 3(b). The resulting surface for 0.1ML Si deposition shown in Fig. 3(b) is characterized by wide (3×2) reconstructed terraces and (2×4)α regions with high step density. This reveals a ribbon-like Si distribution with 1/3 ML Si covered terraces separated by uncovered step regions. The out-spreading of the $a(1\times3)$ reconstructed step regions above 0.3 ML Si deposition leads to step de-bunching as shown in Figs. 3(c) and 3(d). The well-ordered separation of two existing surface phases, (3×2) and $a(1\times3)$, indicates a distinct self-organized Si structure, 1/3 ML coverage on the terraces and 1 ML coverage at the step regions.

B. Effect of the substrate temperature

To study the influence of the substrate temperature, we concentrate on surface structures induced by 0.1 ML Si deposition on vicinal GaAs (001) samples with 2° miscut towards (111)A. Figure 4 shows large-scale STM images for Si deposition at 500, 550, and 590 °C. It is obvious that the spacing of the bunches which is equivalent to the period of Si ribbon-like self-organized structures, enlarges with increasing substrate temperature. Actually, the (3×2) and (2×4)α phases are not well separated for Si deposition at 500 °C, as evidenced by high-resolution images (not shown).

C. Effect of the substrate misorientation

The evolution of the surface morphology and consequently the Si distribution pattern changes drastically if the

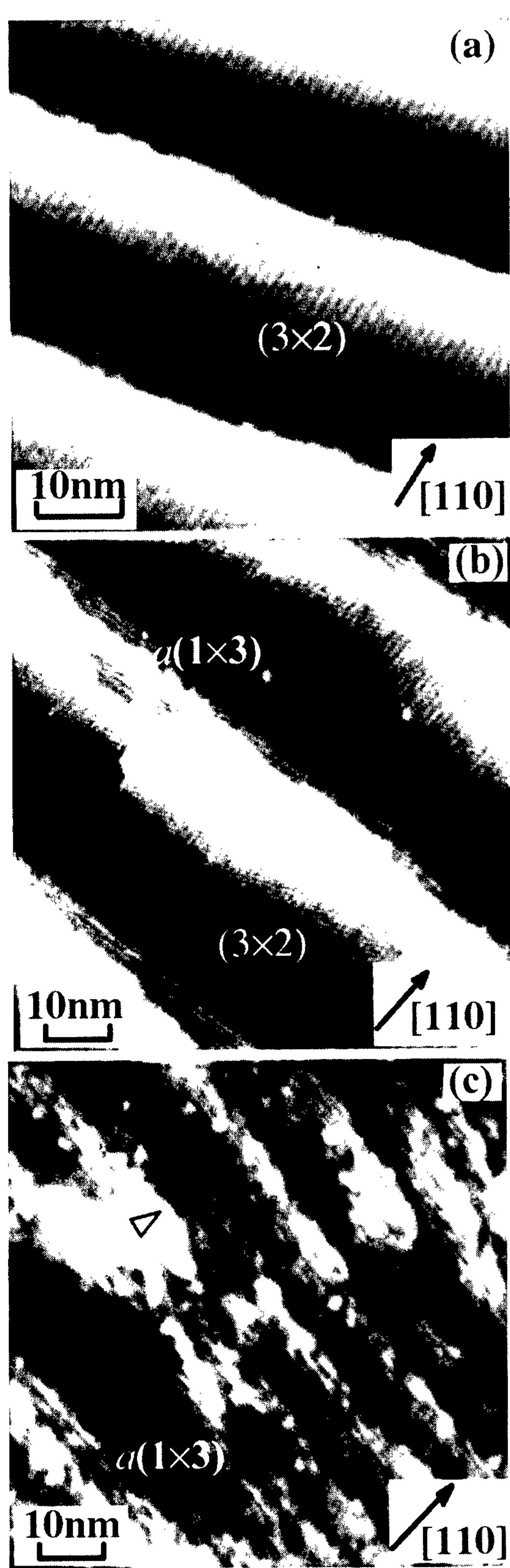

FIG. 2. STM images of vicinal GaAs (001) surface with a miscut of 2° towards (111)A after Si deposition of (a) 0.2 ML, (b) 0.5 ML, and (c) 0.8 ML at 590 °C.

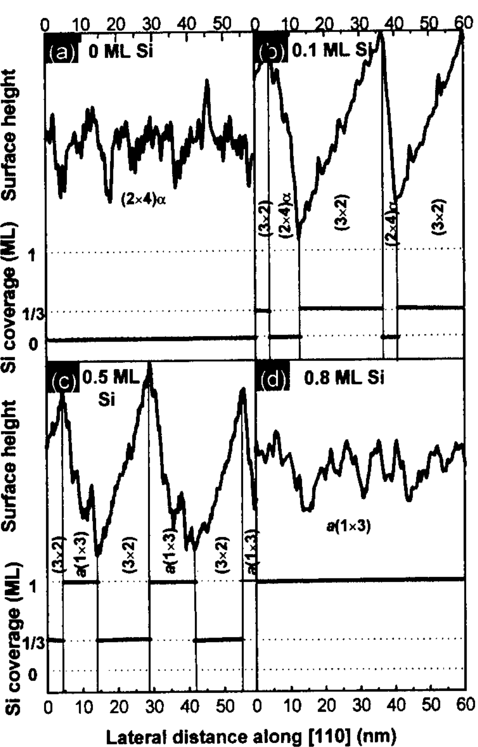

FIG. 3. Evolution of the surface height and corresponding Si distribution along the [110] direction with increasing Si coverage for vicinal GaAs (001) surface with a miscut of 2° towards (111)A.

B-type vicinal GaAs (001) surface or the singular GaAs (001) surface instead of the A-type vicinal GaAs (001) surface is used as template for Si deposition. Figure 5 shows STM images with different magnifications for 0.1 ML Si deposition on a vicinal GaAs (001) surface with 2° miscut towards (111)B. Similar to the above results on A-type vicinal surfaces, the clear separation of the two surface phases, (3×2) and (2×4)α, is observed, which is accompanied by step bunching with wide (3×2) reconstructed terraces and (2×4)α reconstructed regions with high step density. On a rough average, the bunched steps are still running along [110], as expected for the miscut towards (111)B. Compared to Si covered A-type vicinal surfaces, the step edges of Si covered B-type vicinal surfaces are extremely ragged, which results in irregular quadrangular terraces. This array of Si-terminated (3×2) reconstructed terraces defines a patterned sheet-like Si distribution. The roughness of the step edges is expected to stem from the initial surfaces, since it is well known that the edges are relatively straight for A-type steps and rugged for B-type steps.[24]

Typical STM images for 0.1 ML Si deposition on the singular GaAs (001) surface are displayed in Fig. 6. As shown in Fig. 6(a), only four monolayer levels contribute to the morphology over a 200 nm×200 nm area. The unintended miscut as determined by STM was approximately 0.2°, but with appreciable local variation. The larger magnification image of Fig. 6(b) reveals that the step edges are still (2×4)α reconstructed, marked as S_A and S_B for unintended

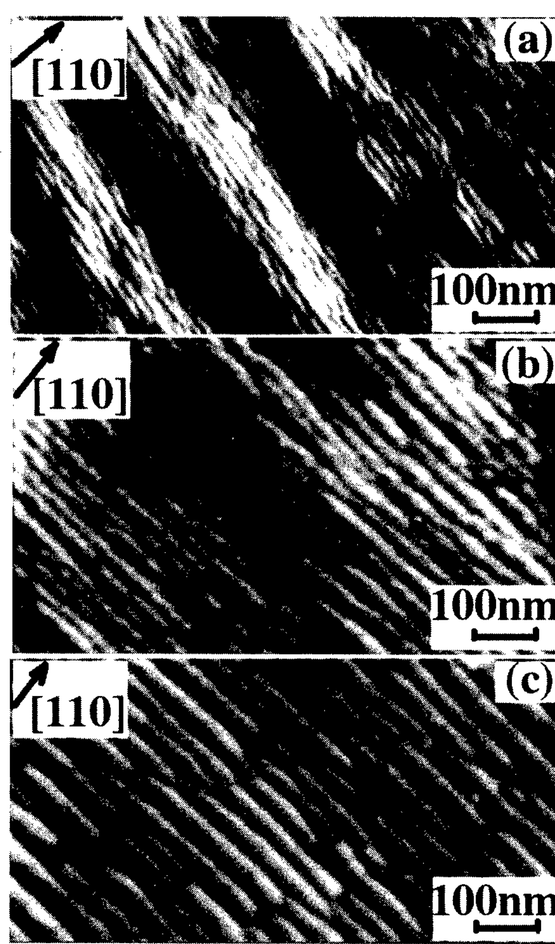

FIG. 4. STM images of vicinal GaAs (001) surface with a miscut of 2° towards (111)A after Si deposition of 0.1 ML at (a) 500 °C, (b) 550 °C, and (c) 590 °C.

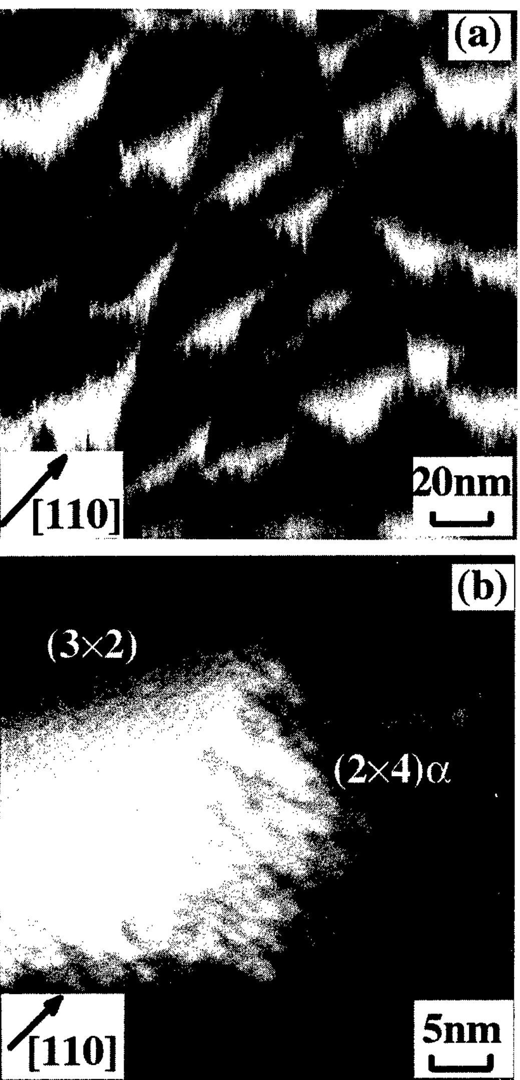

FIG. 5. STM images of GaAs (001)-(2×4)α surface with a miscut of 2° towards (111)B after Si deposition of 0.1 ML at 590 °C.

induced A-type and B-type steps, respectively, and many (2×4)α reconstructed islands are distributed on the (3×2) reconstructed wide terraces. The ordering of this (3×2) structure is, however, not nearly as good as on the terraces of the vicinal GaAs (001) surface, in particular of the A-type vicinal surface.

IV. DISCUSSION

The traditional view of submonolayer epitaxial growth is that the deposited atoms diffuse and nucleate on the immobile substrate surface. However, our experimental results clearly demonstrate another scenario: the substrate species rearrange during exposure to the impinging flux. The GaAs surface is thus quite dynamic even without Ga deposition, which is supported by recent theoretical and experimental investigations of the GaAs (001) surface under MBE conditions.[25,26] A surprisingly large concentration of Ga adatom is present for typical growth temperature even in the absence of a growth flux, e.g., 0.18 ML at 600 °C (according to Ref. 25). There is a continuous formation and dissolution of the GaAs substrate material according to thermal equilibrium. In view of the growth conditions applied in this study, it is reasonable to discuss our results in terms of thermodynamics. The deposited Si atoms induce new reconstructions of the original surface and consequently changes in surface free energy. The original structure is no longer an equilibrium state and new equilibration of the surface structure is achieved by the kinetic process. The competition between kinetic and dynamic processes results in a local equilibrium state within the surface diffusion limited scale.

Steps are the basic unit to describe the surface morphology. It has been established that the step–step interaction is the driving force for the surface evolution if the whole surface is homogeneously reconstructed, and the movement of steps is independent of the step formation energy.[27] As we observed for the original (2×4)α reconstructed vicinal GaAs (001) surface (Fig. 1) and also for the step structure when the whole surface is $a(1\times3)$reconstructed after 0.8 ML Si deposition [Fig. 2(c)], the vicinal surface in this case forms regular monolayer steps. However, to determine the surface morphology in the case that two different reconstructions coexist

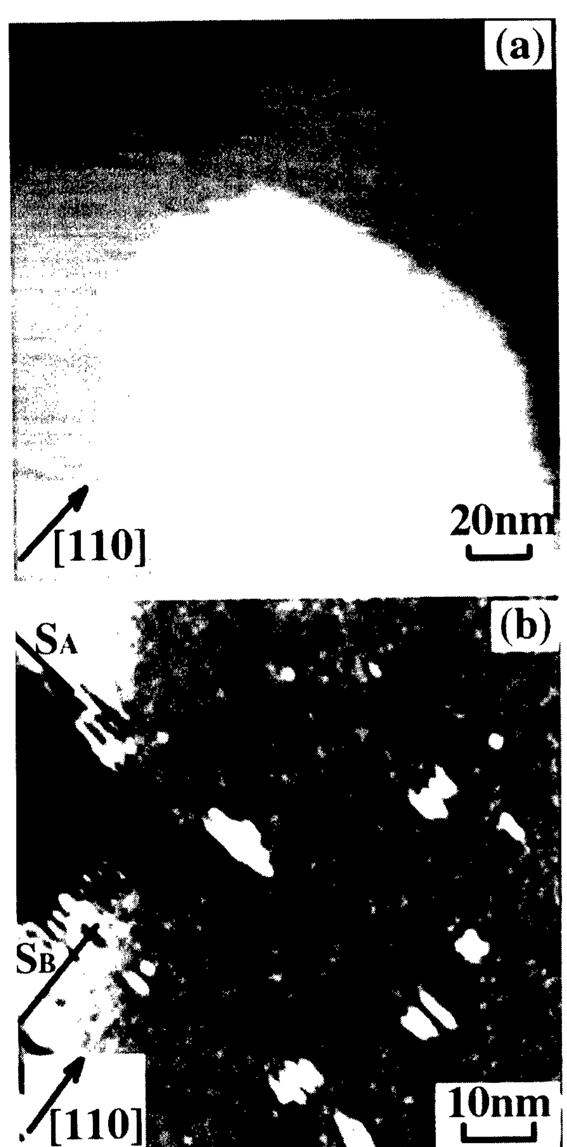

FIG. 6. STM images of singular GaAs (001)-(2×4)α surface after Si deposition of 0.1 ML at 590 °C.

on the surface [(2×4)α or $a(1\times3)$ and (3×2) in our experiment], the step formation energy must be considered. The free energy for creating a corresponding step within different reconstructed regions should be different. If the surface diffusion mobility is high, the surface atoms have the ability to diffuse over a length scale larger than the terrace width and subsequently the steps should arrange themselves to reach an energetically favorable configuration. It is expected that the steps will be concentrated in the regions of that reconstruction where the step formation energy is lower than that in other regions with another existing reconstruction, leading to step bunching as shown in Figs. 2(b) and 3. It is the interaction between the coexisting reconstructions and the surface step structure leading to the step bunching and the separation of different phases on terraces and in step regions. The period of step bunches will be directly related with the surface diffusion length, which will depend on the actual surface reconstruction[28] and the substrate temperature. When increasing the substrate temperature, the mobility of surface atoms is enhanced, and the steps can rearrange themselves on a larger length scale, leading to a larger spacing of the bunches as shown in Fig. 4. For Si deposition on the singular surface with a lot of terraces wider than 100 nm, the diffusing adatom could not always reach the step edges which causes a less ordered phase separation.

The Si-induced step bunching observed on the GaAs (001) surface indicates that the free energy to create a step within the (3×2) reconstructed regions is higher than to create a step within the (2×4)α or $a(1\times3)$reconstructed regions, which is implied also from the different appearances of the two reconstructions. The (3×2) structure is more ordered than the (2×4)α and $a(1\times3)$ structures. In general, a stronger lateral interaction between surface species is expected for an ordered reconstruction,[29] and hence a higher step formation energy.

V. CONCLUSION

In summary, Si incorporation induces new reconstructions on GaAs (001) surfaces, leading to different coexisting reconstructions. Since step formation energies are different for different surface phases, steps rearrange themselves to seek a new configuration with lowest energy, as far as this is kinetically accessible under the given preparation conditions. The dependence of this self-organization on critical growth parameters, such as the Si coverage, the substrate temperature and the substrate misorientation, was investigated. The self-organization is favored on vicinal surfaces at high growth temperature for particular coverages. The complex process at optimized conditions results in spatially well separated surface phases with different Si coverages, revealing distinct patterns of Si distribution which are challenging for improved electrical properties by reducing the elastic scattering rate and for future nanotechnology.[30–32]

The importance of our results extends beyond Si deposition on GaAs (001). Since it is a common phenomenon that atoms impinging on the substrate surface induce new reconstructions within the original surface phase, the self-organized process due to the interaction between the reconstructions and the step structures, as we have described above, is applicable in principle to other submonolayer epitaxies.

[1]E. F. Schubert, J. Vac. Sci. Technol. A **8**, 2980 (1990).
[2]K. H. Ploog, Cryst. Prop. Prep. **31**, 111 (1991).
[3]M. J. Ashwin, M. Fahy, J. J. Harris, R. C. Newman, D. A. Sansom, R. Addinall, D. S. McPhail, and V. K. M. Sharma, J. Appl. Phys. **73**, 633 (1993).
[4]K. Köhler, P. Ganser, and M. Maier, J. Cryst. Growth **127**, 720 (1993).
[5]L. Däweritz, H. Kostial, R. Hey, M. Ramsteiner, J. Wagner, M. Maier, J. Behrend, and M. Höricke, J. Cryst. Growth **150**, 214 (1995).
[6]R. W. Grant and J. R. Waldrop, J. Vac. Sci. Technol. B **5**, 1051 (1987).
[7]G. Bratina, L. Sorba, A. Antonini, L. Vanzetti, and A. Franciosi, J. Vac. Sci. Technol. B **9**, 2225 (1991).
[8]O. Brandt, G. Cook, K. Ploog, R. Bierwolf, M. Hohenstein, M. Maier, and J. Wagner, Jpn. J. Appl. Phys., Part 2 **32**, L24 (1993).
[9]A. V. Buyanov, P. O. Holtz, W. M. Chen, B. M. Onemar, T. G. Anderson, and J. Thordson, Appl. Phys. Lett. **68**, 3464 (1996).

[10]A. R. Avery, J. Sudijono, D. M. Holmes, T. S. Jones, and B. A. Joyce, Appl. Phys. Lett. **66**, 3200 (1995).
[11]A. R. Avery, J. Sudijono, T. S. Jones, and B. A. Joyce, Surf. Sci. **340**, 57 (1995).
[12]L. Däweritz, P. Schützendübe, M. Reiche, and K. H. Ploog, Surf. Sci. **385**, L917 (1997).
[13]L. Däweritz, P. Schützendübe, M. Reiche, and K. H. Ploog, J. Vac. Sci. Technol. A **16**, 1969 (1998).
[14]M. Ramsteiner, J. Wagner, D. Behr, G. Jungk, L. Däweritz, and R. Hey, Appl. Phys. Lett. **64**, 490 (1994).
[15]H. H. Farrell and C. J. Palmstrom, J. Vac. Sci. Technol. B **8**, 903 (1990).
[16]M. D. Pashley and K. W. Haberern, Phys. Rev. Lett. **67**, 2697 (1991).
[17]J. Rumberg, J.-T. Zettler, K. Stahrenberg, K. Ploska, W. Richter, L. Däweritz, P. Schützendübe, and M. Wassermeier, Surf. Sci. **337**, 103 (1995).
[18]T. Hashizume, Q. K. Xue, A. Ichimiya, and T. Sakurai, Phys. Rev. B **51**, 4200 (1995).
[19]J. E. Northrup and S. Froyen, Phys. Rev. B **50**, 2015 (1994).
[20]K. Shiraishi and T. Ito, Jpn. J. Appl. Phys., Part 2 **37**, L1211 (1998).
[21]Z. M. Wang, L. Däweritz, P. Schützendübe, and K. H. Ploog, Phys. Rev. B **61**, R2440 (2000).
[22]L. Däweritz, K. Stahrenberg, P. Schützendübe, J.-T. Zettler, W. Richter, and K. H. Ploog, J. Cryst. Growth **175/176**, 310 (1997).
[23]L. Däweritz, P. Schützendübe, M. Reiche, and K. H. Ploog, Surf. Sci. **402–404**, L957 (1998).
[24]M. D. Pashley, K. W. Haberern, and M. Gaines, Appl. Phys. Lett. **58**, 406 (1991).
[25]M. D. Johnson, K. T. Leung, A. Birch, B. G. Orr, and J. Tersoff, Surf. Sci. **350**, 254 (1996).
[26]J. Tersoff, M. D. Johnson, and B. G. Orr, Phys. Rev. Lett. **78**, 282 (1997).
[27]E. D. Williams, Solid State Commun. **107**, 681 (1998).
[28]K. Kanisawa and H. Yamaguchi, Phys. Rev. B **56**, 12080 (1997).
[29]H. Yamaguchi and Y. Horikoshi, Jpn. J. Appl. Phys., Part 2 **33**, L1423 (1994).
[30]R. L. Headrick, L. C. Feldman, and B. E. Weir, in *Delta-Doping of Semiconductors*, edited by E. F. Schubert (Cambridge University Press, Cambridge, 1996), p. 461.
[31]T. Irisawa, J. Motohisa, M. Akabori, and T. Fukui, Jpn. J. Appl. Phys., Part 1 **37**, 1514 (1998).
[32]G. E. W. Bauer and A. A. van Gorkum, in *Science and Engineering of One- and Zero-Dimensional Semiconductors*, edited by S. E. Beaumont and C. M. Sotomayor Torres (Plenum, New York, 1990), p. 133.

Atomic structure and composition of the (2×4) reconstruction of InGaP(001)

P. Vogt,[a] K. Lüdge, M. Zorn, and M. Pristovsek
Institut für Festkörperphysik, Technische Universität, Hardenbergstrasse 36, 10623 Berlin, Germany

W. Braun
BESSY GmbH, Albert-Einstein-Strasse 15, D-12489 Berlin, Germany

W. Richter and N. Esser
Institut für Festkörperphysik, Technische Universität, Hardenbergstrasse 36, 10623 Berlin, Germany

(Received 17 January 2000; accepted 15 May 2000)

In this study scanning tunneling microscopy (STM), soft x-ray photoemission spectroscopy (SXPS), and reflectance anisotropy spectroscopy were used to investigate the microscopic structure of (2 ×4) reconstructed InGaP(001) surfaces. The samples were grown lattice matched on GaAs(001) by metalorganic vapor phase epitaxy. Immediately after growth the surfaces were passivated by a thick amorphous cap consisting of a P/As double layer and then transferred to ultrahigh vacuum (UHV) analysis chambers either equipped with STM or connected to the BESSY synchrotron radiation source for photoemission experiments. Thermal desorption of the As/P capping layer at 460 °C under UHV conditions leads reproducibly to the formation of a III-rich (2×4) reconstruction, the more P-rich (2×1) could not be obtained. The low energy electron diffraction image shows a clear (2×4) pattern with sharp integer-order and fractional-order spots. STM images show rows along the $[\bar{1}10]$ direction with fourfold separation in the [110] direction, similar to the (2×4) reconstruction of InP(001). SXPS spectra of the In $4d$/Ga 3d and P $2p$ core levels demonstrate that this surface may consist of a mixed-dimer structure analogous to the one found on InP(001) and GaP(001) (2×4). Further annealing of the sample to higher temperatures degrades the surface without producing another reconstruction. The (2×4) reconstruction thus represents the most III-rich (least P-rich) stable surface for InGaP(001). © *2000 American Vacuum Society.*
[S0734-211X(00)05504-9]

I. INTRODUCTION

During the last decade the technological importance of the phosphorous based III–V compound semiconductors (InP, GaP, InGaP) has grown significantly. Especially InGaP, because of its wide range of applications in optoelectronics, has attracted a rising interest. Its main merit results from the fact that like other ternary compounds, the fundamental band gap as well as the lattice constant can be tuned via the composition parameter, e.g., the ratio between In and Ga.[1] For a composition of $x=0.52$, $In_{1-x}Ga_xP(001)$ is lattice matched to GaAs(001). Another important property of InGaP is the phenomenon of spontaneous $CuPt_B$-type bulk ordering on the group-III sublattice,[2,3] resulting in a reduced bulk symmetry and a lowering of the band gap E_0.[4] The ordering can be described by the parameter η which ranges between 0 (completely disordered) and 1 (completely ordered). Thus the ordering parameter describes a superlattice consisting of alternating gallium- and indium-rich $\langle 111\rangle_B$ planes $(In_{0.5(1-\eta)}Ga_{0.5(1+\eta)}/In_{0.5(1+\eta)}Ga_{0.5(1-\eta)})$.

Despite the technological importance of the ternary III–V materials, the atomic structure of their (001) growth planes has not yet been studied. Moreover, for (001) surfaces of binary III–V compounds rather little is known about the phosphorous based in comparison to arsenic based compound semiconductors. For InP(001), P-rich (2×1) and (2×2) and an In-rich (2×4) surface reconstruction were reported.[5,6] The In-rich (2×4) reconstruction was shown to consist of mixed In–P dimers on top of a complete second layer of In.[7] For the P-rich reconstructions of InP(001), scanning tunneling microscopy (STM)[8–12] and photoemission spectroscopy (PES)[10,12] studies were published recently. However, the atomic structure of these P-rich surfaces is not yet well understood. For GaP(001), a P-rich (2×1) and (2×4)[13] and a Ga-rich (2×4)[14] were reported. Similar to InP(001) the Ga-rich (2×4) reconstruction on GaP(001) has been shown to consist of mixed Ga–P dimers.[15]

For InGaP(001), (2×1) and (2×4) surface reconstructions during metalorganic vapor phase epitaxy (MOVPE) growth were reported,[16] analogous to the two binary systems, InP(001) and GaP(001). However, no reports concerning the atomic structure of these surface reconstructions exist. Considering binary III–As(001) and III–P(001), differences of the surface structures have been related to surface strain consistent with the different atomic radii of the individual constituents.[7] For ternary materials such as InGaP an additional degree of freedom, namely the distribution of In and Ga on inequivalent group III sites of a certain surface structure, is introduced. So far, however, these surfaces have not been analyzed. Despite this fact the reconstructions are im-

[a]Author to whom correspondence should be addressed; electronic mail: patrick@gift.physik.tu-berlin.de

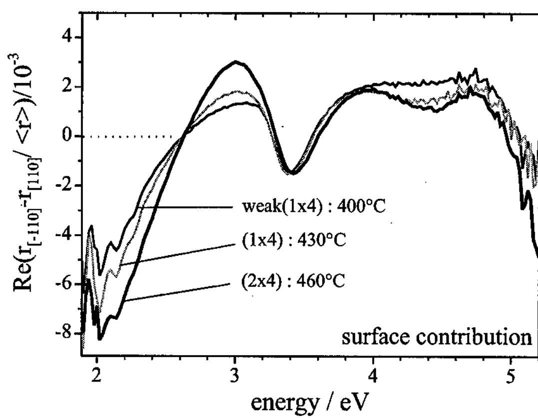

FIG. 1. Surface contributions to the RAS spectra of the InGaP(001) surface together with the corresponding surface periodicities, as obtained by LEED. At a temperature of 400 °C the LEED pattern shows a (1×4) periodicity. Annealing to 430 and 460 °C leads to a weak (2×4) and finally a clear (2×4) periodicity in the LEED patterns, respectively.

portant because it was shown recently that they influence the bulk ordering during MOVPE growth. Bulk ordering is found to develop during MOVPE growth if it takes place in the (2×1) regime, whereas it is suppressed in the (2×4) regime.[16]

Here, we report on the preparation of the well defined group III-rich (2×4) reconstruction of InGaP(001) and the corresponding atomic surface structure.

II. EXPERIMENT

The samples were grown by (MOVPE) using phosphine (PH_3), trimethylindium (TMIn) and trimethylgallium(TMGa) as precursors. The $In_{0.48}Ga_{0.52}P$ buffer layer was grown lattice matched on nominally undoped, epi-ready GaAs(001) substrate held at 650 °C, with a growth rate of 2.2 μm/h. The layer thickness of the $In_{0.48}Ga_{0.52}P$ was approximately 1.2 μm. The band-edge luminescence at room temperature (RT) was found at 665 nm (1.86 eV) which corresponds to an ordering parameter of $\eta=0.35$.[17] Directly after growth the samples were capped by an amorphous As/P double layer in order to protect them during transport through air. Under ultrahigh vacuum (UHV) condition the amorphous protection layer was thermally desorbed. The whole decapping process was monitored by quadrupole mass spectroscopy (QMS) and reflectance anisotropy spectroscopy (RAS). During the experiments the temperature of the sample was measured with a well calibrated thermocouple in contact with the sample plate. Scanning tunneling microscopy (STM) experiments were performed using an UHV-STM setup. The SXPS experiments were carried out at the TGM2 beamline at BESSY I with a total instrumental resolution (beamline plus analyzer) of 250 meV (300 meV) for the energy range of the In $4d$-Ga $3d$ (P $2p$) core levels. Additionally RAS spectra were taken with an optical setup either attached to the STM or the SXPS vessels. The reflectance anisotropy signal refers to the difference in reflectance for light polarized along the two surface symmetry axes, that is, along the [$\bar{1}$10] and [110] directions. During the decapping process two contributions have to be considered for the optical anisotropy, as monitored by RAS. The first one is the contribution of the InGaP bulk, which results from bulk ordering in the [$\bar{1}$11] direction. The second one is the anisotropy of the surface. The P-capping layer is amorphous and does not contribute significantly. In order to separate surface and bulk optical anisotropy, RAS spectra of the samples were also taken after the UHV experiments under ambient conditions. Due to the oxidation the surface becomes optically isotropic, thus only the bulk contributes to the RAS signal in this case. The surface optical anisotropy is obtained by subtracting these two spectra. For the P-rich (2×1) and the (2×4) surface reconstructions, the surface contributions to RAS are known from MOVPE experiments.[16]

III. RESULTS AND DISCUSSION

A. Surface preparation

After transfer of the InGaP(001) samples to UHV conditions the protecting As/P capping layer was thermally removed. At a temperature of 350 °C, desorption of the amorphous As layer occurred. The temperature of the sample was then held constant until no more traces of As were detectable with QMS. Thereafter the sample temperature was increased to approximately 460 °C. At a temperature of 400 °C the phosphorous started to desorb. From here on the decapping process was additionally monitored by RAS. When no more phosphorous desorbing from the surface was detectable by QMS, the RAS spectra reproducibly showed a line shape, characteristic for the (2×4) surface reconstruction (superimposed by the bulk anisotropy). The (2×1) line shape was not observed. Also very slow decapping (2 h for the desorption of the amorphous P layer) using only small temperature increments failed to produce a (2×1) surface reconstruction. The same behavior was found on InP(001) where only the In-rich (2×4) surface reconstruction can be prepared by decapping.[14]

In Fig. 1 the surface contributions to the RAS spectra of InGaP(001) are shown together with the corresponding surface periodicities, as obtained by low energy electron diffraction (LEED). Directly after desorbing the amorphous P layer at a temperature of 400 °C the LEED pattern shows a (1×4) periodicity. Further annealing to 430 and 460 °C leads to a weak (2×4) and finally a clear (2×4) periodicity in the LEED patterns, respectively.

The RAS line shape for the three different temperatures does not change significantly, but the intensities of the first minimum and maximum increase. Thus it can be concluded that due to the higher annealing temperature the surface quality improves. The RAS spectrum for the (2×4) reconstruction at RT is in very good agreement with the RAS spectra obtained for the same surface reconstruction during MOVPE growth[16] at 550 °C if the temperature dependent shift of the energetic peak position is taken into account.

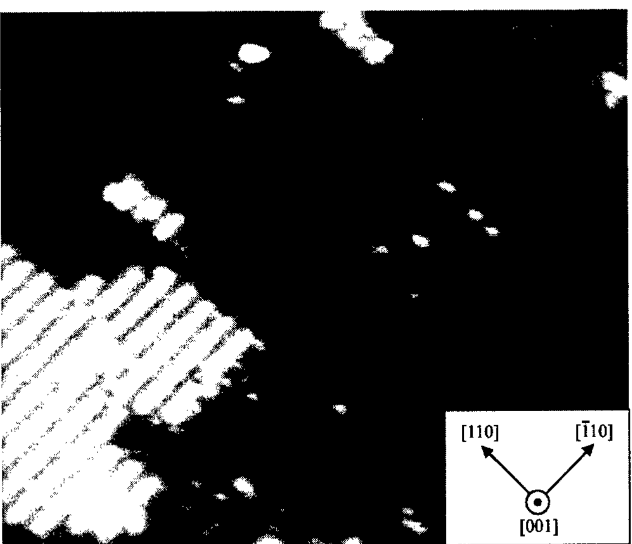

FIG. 2. STM image of the (2×4) surface reconstruction (sample bias of −3 V, scan area 40 nm ×47 nm). Clearly visible are atomically flat terraces terminated by long, straight rows separated by 1.9 nm, corresponding to the fourfold surface lattice constant.

B. (2×4) reconstruction

In Fig. 2 a STM image (40 nm × 47 nm) of the (2×4) surface reconstruction is shown. At a sample bias of −3 V, filled states are imaged. Clearly visible are atomically flat terraces terminated by long, straight rows separated by 1.9 nm, corresponding to the fourfold surface lattice constant. Along the rows a weaker pronounced corrugation with two-fold periodicity appears. The STM image is very similar to results reported on the (2×4) reconstructed InP(001) surface.[18,19]

SXPS measurements of the P $2p$ and In $4d$/Ga $3d$ core levels for the (2×4) surface reconstruction are displayed in Fig. 3. The spectra for the P $2p$ emission were taken at a photon energy (kinetic energies, referring to P $2p_{3/2}$ and In $4d_{5/2}$) of 166 eV (31 eV), and for In $4d$/Ga $3d$ at 54.5 eV (37.8 eV) which are in the range of kinetic energies of minimum electron mean free path or maximum surface sensitivity. The spectra were then analyzed by numerical deconvolution into pairs of spin orbit-split doublets which are plotted in Fig. 3 by solid lines. Each component consists of convoluted Lorenzian and Gaussian line shapes which correspond to lifetime and experimental broadening. In Table I the values for lifetime broadening, experimental broadening, branching ratio and spin orbit splitting are listed for the In $4d$, Ga $3d$ and P $2p$ core levels. For the P $2p$, (Fig. 3 right) one surface component is found. Since this component is shifted by +0.25 eV towards higher kinetic energies [lower binding energies (BE)] it must originate from P atoms that attract more charge than P-atoms in bulk InGaP.

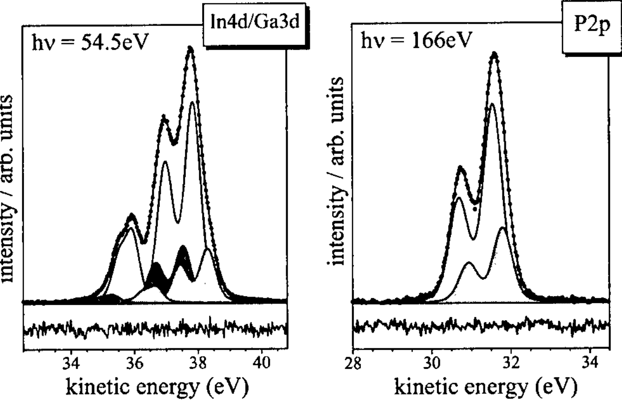

FIG. 3. Core level emission lines of P $2p$ (166 eV photon energy) and In $4d$/Ga $3d$ (54.5 eV photon energy) on the (2×4) reconstructed surface of InGaP(001). The dotted (solid) lines represent the measured data (fits). The shaded areas belong to the surface components.

TABLE I. The table shows the obtained surface core level shifts (SCLS) and the values for lifetime broadening, experimental broadening, branching ratio and spin-orbit splitting for the In $4d$, Ga $3d$, and P $2p$ core levels obtained on InGaP(001)-(2×4).

	In $4d$	Ga $3d$	P $2p$
SCLS 1. Component	+0.47	+0.73	+0.25
2. Component	−0.31	−0.61	
Gaussian broadening/eV	0.47	0.41	0.48
Lorenzian broadening/eV	0.1	0.1	0.1
Branching ratio	1.45	1.6	1.96
Spin-orbit splitting/eV	0.87	0.43	0.87

For the Ga $3d$ core level emission, two surface components are found. One is shifted by −0.73 eV towards lower, and the other +0.61 eV towards higher kinetic energies. An analogous result is obtained for the In $4d$ core level emission. Here two surface components appear also, one shifted by −0.31 eV towards lower and the other by +0.47 eV towards higher kinetic energies. These components show a clear intensity dependence on the excitation energy as expected for surface related components of the core levels. Thus it can be concluded that In as well as Ga atoms can each be found on two electronically different bonding sites on the surface.

In order to improve our understanding of the (2×4) reconstruction of InGaP(001), the results are compared to the RAS and SXPS results for the group III-rich (2×4) reconstruction of InP(001) and GaP(001) in the next paragraph.

C. Comparison to InP(001) and GaP(001)

In the following the InGaP(001) (2×4) surface is compared to the group III-rich (2×4) surfaces of the two binary materials, InP(001) and GaP(001). Both of these surface structures are explained within the "mixed-dimer" model[8] (see Fig. 5). This model consists of a group III-P dimer on top of a group III layer in which group III dimers are formed perpendicularly to the mixed dimer of the top layer.

In Fig. 4 the RAS spectra for the group III-rich (2×4) reconstructions for the two binary systems InP(001) and GaP(001) as well as for InGaP(001) are shown. It can clearly be seen from the image that the RAS line shape for all three materials is rather similar. The spectra all show a well pronounced minimum around 2.0 eV and three maxima be-

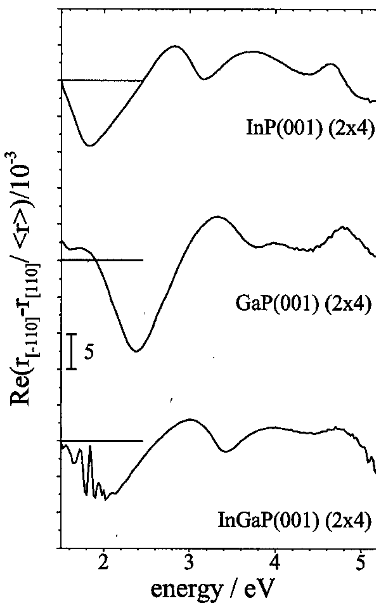

FIG. 4. RAS spectra for the group III-rich (2×4) reconstructions for InP(001) and GaP(001) as well as for InGaP(001). It can be clearly seen that the RAS line shape for all three materials is rather similar.

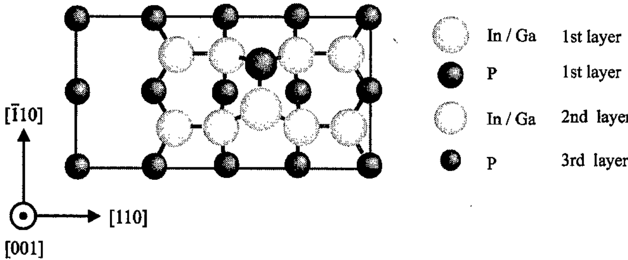

FIG. 6. Mixed-dimer model for InGaP(001) (2×4). The model consists of a group III–P dimer on top of a group III layer in which group-III dimers are formed perpendicularly to the mixed-dimer of the top layer. The group-III atoms are either In or Ga.

tween 3.0 and 5.0 eV. It has been shown that the RAS line shape is very sensitive to the atomic arrangement on the surface, in particular the minimum around 2 eV which stems from electronic transitions between surface states.[15] The structures below 2.0 eV in the InGaP spectrum arise from bulk and interface anisotropies plus Fabry-Perot interferences, since the InGaP layer is transparent below its E_0 band gap at 1.86 eV.[20] The similarity between the RAS spectra already gives an indication that the atomic surface structure for the three materials might be similar.

In Fig. 5 the P $2p$ and In $4d$ core level emission lines are shown for the (2×4) reconstructed surface of InP(001) as reported in Ref. 21. For the P $2p$ core level one surface component is found shifted 0.22 eV towards higher kinetic energies and two for the In $4d$ core level shifted +0.40 eV

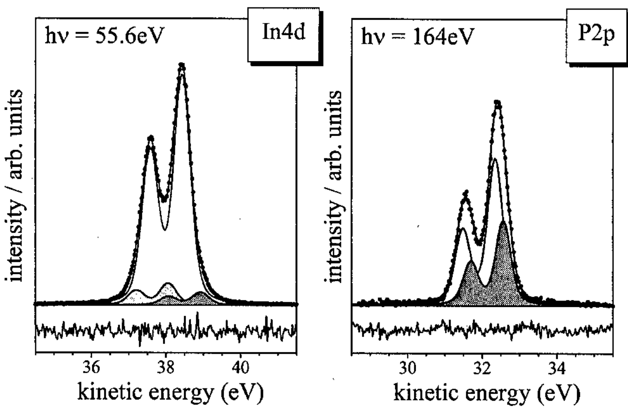

FIG. 5. Core level emission lines of P $2p$ (170 eV photon energy) and In $4d$ (55.5 eV photon energy) of InP(001) (2×4) (from Ref. 21). Dotted (solid) lines represent the measured data (fits), shaded areas the surface components.

towards higher and −0.35 eV towards lower kinetic energies, respectively. These results are in good agreement with previous works[7] apart from the energetic shift of the P $2p$ surface component which is smaller than in Ref. 7. The reason for this is probably the better experimental resolution in the first case. Similar results are obtained for the Ga-rich (2×4) reconstruction of GaP(001).

IV. DISCUSSION

The STM, SXPS and RAS results demonstrate that the atomic structure of the (2×4) reconstructed InGaP(001) surface corresponds to a similar mixed-dimer structure as known for InP(001) and GaP(001). The fact that the SXPS core level spectra reveal two surface components for Ga $3d$ as well as for In $4d$ demonstrates that the (2×4) reconstruction of InGaP(001) is formed by indium and gallium atoms, either of which can be located at two electronically different bonding sites on the surface, as well as phosphorous atoms. In Fig. 6 a mixed-dimer model for the (2×4) of InGaP(001) is shown. In the first layer, mixed In–P or Ga–P dimers are formed giving rise to a surface component for the P $2p$ core level. The high BE surface components of the In $4d$ and Ga $3d$ core levels are associated with charge depletion relative to bulk coordination, corresponding to sites with an empty dangling bond. This holds for the III site of the mixed dimer and for another four sites per unit mesh in the second layer. The remaining four sites in the second layer, beside the mixed dimer, are associated with charge accumulation relative to bulk coordination since III–III bonds occur. These sites are responsible for the low BE surface components of the In $4d$ and Ga $3d$ core level emission lines.

From the measurements described above, however, it cannot be concluded whether the arrangement of the In and Ga atoms in the second layer is random, forming In–In, Ga–Ga and In–Ga dimers, or whether there are any preferential bonding sites for the In and Ga atoms.

V. CONCLUSIONS

Our studies demonstrate that a well defined (2×4)reconstruction of partially ordered InGaP can be ob-

tained in UHV by decapping MOVPE grown samples. From the STM, SXPS and RAS results for the (2×4) reconstruction of InGaP(001) described above, a model for the atomic surface structure was derived which is related to the mixed dimer structure known from the (2×4) reconstruction of the two binary materials InP(001) and GaP(001). This structure represents the most In/Ga-rich stable surface of InGaP(001). Clear evidence for subordering of the In and Ga on the surface into inequivalent sites was not found. Also, a correlation of the (2×4) surface reconstruction to the bulk ordering was not evident. These questions could be addressed by studying surfaces of differently ordered InGaP samples.

ACKNOWLEDGMENTS

The authors gratefully acknowledge financial support of the DFG under Es127/4-1 and the technical support of the BESSY crew during the experiments. The authors also would like to acknowledge K. Horn and C.-H. Chen of the Fritz-Haber-Institute Berlin for supplying a curve fitting routine for analysis of the SXPS data.

[1]G. B. Stringfellow, J. Appl. Phys. **43**, 3455 (1972).
[2]A. Gomyo, K. Kobayashi, S. Kawata, I. Hino, T. Suzuki, and T. Yuasa, J. Cryst. Growth **77**, 367 (1986).
[3]A. Zunger and S. Mahajan, in *Handbook on Semiconductors* (Elsevier, Amsterdam, 1994), Vol. 3, Chap. 19.
[4]A. Gomyo, T. Suzuki, and S. Iijima, Phys. Rev. Lett. **60**, 2645 (1988).
[5]K. B. Ozanyan, P. J. Parbrook, M. Hopkins, C. R. Whitehouse, Z. Sobiesierski, and D. I. Westwood, J. Appl. Phys. **82**, 474 (1997).
[6]M. Zorn, T. Trepk, J.-T. Zettler, B. Junno, C. Meyne, K. Knorr, T. Wethkamp, M. Klein, M. Miller, W. Richter, and L. Samuelson, Appl. Phys. A: Mater. Sci. Process. **65**, 333 (1997).
[7]W. G. Schmidt, F. Bechstedt, N. Esser, M. Pristovsek, Ch. Schultz, and W. Richter, Phys. Rev. B **57**, 14596 (1998).
[8]L. Li, B.-K. Han, Q. Fu, and R. F. Hicks, Phys. Rev. Lett. **82**, 1879 (1999).
[9]P. Vogt, T. Hannappel, S. Visbeck, K. Knorr, N. Esser, and W. Richter, Phys. Rev. B **60**, R5117 (1999).
[10]P. Vogt, A. M. Frisch, Th. Hannappel, S. Visbeck, F. Willig, Ch. Jung, N. Esser, W. Braun, and W. Richter, Phys. Status Solidi B **215**, 737 (1999).
[11]L. Li, B.-K. Han, D. Law, C.H. Li, Q. Fu, and R. F. Hicks, Appl. Phys. Lett. **75**, 683 (1999).
[12]P. Vogt, A. M. Frisch, Th. Hannappel, S. Visbeck, F. Willig, Ch. Jung, R. Follath, W. Braun, W. Richter, and N. Esser, Appl. Surf. Sci. (in press).
[13]M. Zorn, B. Junno, T. Trepk, S. Bose, L. Samuelson, J. T. Zettler, and W. Richter, Phys. Rev. B **60**, 11557 (1999).
[14]N. Esser, W. G. Schmidt, J. Bernholc, A. M. Frisch, P. Vogt, M. Zorn, M. Pristovsek, W. Richter, F. Bechstedt, Th. Hannappel, and S. Visbeck, J. Vac. Sci. Technol. B **17**, 1691 (1999).
[15]K. Lüdge, P. Vogt, O. Pulci, M. Pristovsek, N. Esser, F. Bechstedt, and W. Richter, Phys. Rev. B Rap. Commmun. (to be published).
[16]M. Zorn, P. Kurpas, A. I. Shkrebtii, B. Junno, A. Bhattacharya, K. Knorr, M. Weyers, L. Samuelson, J. T. Zettler, and W. Richter, Phys. Rev. B **60**, 8185 (1999).
[17]P. Ernst, C. Geng, F. Scholz, H. Schweizer, Y. Zhang, and A. Mascarenhas, Appl. Phys. Lett. **67**, 2347 (1995).
[18]N. Esser, U. Resch-Esser, M. Pristovsek, and W. Richter, Phys. Rev. B **53**, R13257 (1996).
[19]C. D. MacPherson, R. A. Wolkow, C. E. J. Mitchell, and A. B. McLean, Phys. Rev. Lett. **77**, 691 (1996).
[20]J. S. Luo, J. M. Olson, S. R. Kurz, D. J. Arent, K. A. Bertness, M. E. Raikh, and E. V. Tsiper, Phys. Rev. B **51**, 7603 (1995).
[21]W. Braun *et al.* (to be published).

Understanding reflectance anisotropy: Surface-state signatures and bulk-related features

W. G. Schmidt[a)] and F. Bechstedt
Institut für Festkörpertheorie und Theoretische Optik, Friedrich-Schiller-Universität, Max-Wien-Platz 1, 07743 Jena, Germany

J. Bernholc
Department of Physics, North Carolina State University, Raleigh, North Carolina 27695-8202

(Received 17 January 2000; accepted 1 May 2000)

Using a real-space multigrid method and *ab initio* pseudopotentials we calculated the reflectance anisotropy spectra for (001) growth structures of GaP and InP as well as for stepped Si(111):H and hydrogenated Si(110) surfaces. Our results, obtained within DFT-LDA, show good qualitative agreement with recent experiments. Further improvement is achieved by using a numerically efficient GW approach with approximations for local-field effects and dynamical screening. We find the contributions to the anisotropy signal related either directly to surface states or to transitions between surface-perturbed bulk wave functions. Our results demonstrate the high sensitivity of RAS to the surface structure and chemistry and show that the optical transitions causing the anisotropy signal take place mainly in a few uppermost atomic layers of the substrate. © *2000 American Vacuum Society.* [S0734-211X(00)04104-4]

I. INTRODUCTION

Optical spectroscopy has become an important tool of surface analysis in the last years due to its high sensitivity and *in situ* applicability.[1] In particular, reflectance anisotropy spectroscopy (RAS), also called reflectance difference spectroscopy (RDS), is increasingly used to characterize static surfaces and to monitor dynamic surface processes in various environments.[2,3] To fully exploit the technological potential of RAS, a theoretical understanding of the underlying physical mechanisms and reliable schemes to calculate RAS spectra are needed. The progress in the computational modeling of RAS[4–6] has been rather slow, however. The agreement between the theoretical spectra, usually calculated by using slabs consisting of a few atomic layers, and the measured data is often unsatisfactory. This gave rise to suggestions that long-range effects, hardly accessible to slab calculations, are at least partially responsible for the surface optical anisotropy. A dynamic photon-induced localization of the initial and final states over the range of the penetration depth of light of several hundred Å was suggested to account for anisotropy signals close to the bulk critical point (CP) energies.[7] In Ref. 8 another long-range effect, the quenching of bulk-state wave functions near the surface, was made responsible for the appearance of peaks at bulk CP energies in the surface spectra. These hypotheses are currently subject to both experimental[9] and theoretical[10] investigations. The present article aims at the understanding and interpretation of the surface optical anisotropy.

Realistic surfaces, and growth structures in particular, usually contain defects such as surface steps. The latter have been shown experimentally to give rise to distinct optical anisotropies,[11–13] the origin of which is presently under debate. The theoretical description of these step-related optical anisotropies is important for a correct interpretation of RAS spectra measured during growth and contributes also to a more complete understanding of the origin of RAS in general.

In the present work we combine converged calculations based on density functional theory (DFT) in the local density approximation (LDA) with a numerically efficient approximate GW approach or a scissors operator approach to calculate the reflectance anisotropy. As model systems we study the (001)(2×4) surfaces of GaP and InP, steps on Si(111):H surfaces as well as the hydrogenated Si(110) surface. We find good agreement with experiment. Both bulk-related (''intrinsic'') and directly surface-state related (''extrinsic'') contributions in the RAS are reproduced by well-converged slab calculations. This indicates that the difficulty in theoretical modeling of RAS is not conceptual, but rather caused by: (i) convergence problems due to the large numerical expense required for calculations of surface optical properties, and (ii) the difficulty in accounting for the many-particle effects in the spectra in an efficient yet accurate manner.

II. METHODOLOGY

Our DFT-LDA calculations are performed using *first-principles* pseudopotentials[14] together with a real-space finite-difference method.[15] A multigrid technique is used for convergence acceleration. The real-space method enables efficient parallelization and is thus particularly suited for the large supercells and many electronic states required for the calculation of the surface dielectric function. The electronic wave functions were mapped on a grid with a spacing of about 0.24 Å. To model the III–V(001) surfaces we used periodic supercells containing 12 atomic layers, the bottom

a)Author to whom correspondence should be addressed; electronic mail: W.G.Schmidt@ifto.physik.uni-jena.de

layer saturated with pseudohydrogens, and a vacuum region equivalent to eight layers. The stepped Si(111):H and Si(110):H surfaces were described with symmetric slabs about 50 Å thick, separated by 14 Å of vacuum.

For the relaxation of the electronic and atomic degrees of freedom we sampled the surface Brillouin zone (SBZ) with four special **k** points in the irreducible part. The surface dielectric function was calculated with uniformly distributed **k** points corresponding to densities of 256 (GaP), 1024 (InP), and about 500 points (Si) in the full (1×1) SBZ. Further details of the DFT-LDA calculations can be found in Refs. 15–18.

Calculations within DFT-LDA neglect the quasiparticle character of electrons and typically underestimate excitation energies, an effect known as the band-gap problem.[19] For example, we calculate an indirect band gap of 0.58 eV for Si, while the room temperature experiment[20] yields 1.11 eV. A similar underestimation of about 0.5 eV occurs for the E_1 and E_2 CPs of the bulk band structure, for which we obtain 3.0 and 3.8 eV, respectively, and for the surface state energies of Si.[21,22] In order to compare the calculated RAS spectra for Si surfaces with experiment, we therefore apply an upward rigid shift of 0.5 eV to the conduction bands and renormalize the momentum matrix elements accordingly.[23] The same simple recipe has been followed in other recent *ab initio* studies of the optical properties of Si surfaces.[24,25]

Such a rigid shift (or scissors operator approach) fails, however, if the underestimation of the excitation energies in DFT-LDA is less uniform than in Si. For bulk GaP, for example, it varies between 0.6 and 0.9 eV for states close to the fundamental gap. Furthermore, as will be shown below, different shifts are obtained for bulk and surface state energies in the case of GaP and InP. Rather than applying a rigid shift as for Si we therefore use GW calculations[19] to take self-energy effects into account for the III–V (001) surface. In order to obtain accurate excitation energies, the one-electron states should be obtained by solving the quasiparticle Schrödinger equation, i.e., the local exchange and correlation potential $V^{XC}(\mathbf{r})$ used in DFT-LDA should be replaced by the nonlocal and energy-dependent self-energy operator $\Sigma(\mathbf{r},\mathbf{r}';E)$ to describe the electron–electron interaction correctly. However, even in its lowest so-called GW approximation, where Σ is expressed as a convolution of the single-particle propagator G and the dynamically screened Coulomb interaction W, its calculation remains a formidable task. In particular the large number of states entering the surface dielectric function makes calculations very expensive. Recently a linear parametrization of the quasiparticle shifts with respect to the surface localization of the corresponding electronic states was therefore suggested.[26] We used a different approach and introduced further approximations, following the schemes developed by Hybertsen and Louie[27] and Bechstedt *et al.*[28]: In first order perturbation theory the GW quasiparticle energies are obtained from the DFT-LDA eigenvalues by

$$E_{n,\mathbf{k}}=E_{n,\mathbf{k}}^{\mathrm{LDA}}+\frac{1}{1+\beta_{n,\mathbf{k}}}\{\Sigma_{n,\mathbf{k}}^{\mathrm{st}}+\Sigma_{n,\mathbf{k}}^{\mathrm{dyn}}(E_{n,\mathbf{k}}^{\mathrm{LDA}})-V_{n,\mathbf{k}}^{XC}\},\qquad(1)$$

where the self-energy operator Σ has been divided into static and dynamic contributions. $\beta_{n,\mathbf{k}}$ is the linear term of the expansion of Σ^{dyn} in energy around the DFT-LDA eigenvalue $E_{n,\mathbf{k}}^{\mathrm{LDA}}$. The static part can be further divided into two parts:

$$\Sigma^{\mathrm{st}}(\mathbf{r},\mathbf{r}')=\frac{1}{2}\sum_{n,\mathbf{k}}\psi_{n,\mathbf{k}}(\mathbf{r})\psi_{n,\mathbf{k}}^{*}(\mathbf{r}')\{W(\mathbf{r},\mathbf{r}';0)-v(\mathbf{r}-\mathbf{r}')\}$$
$$-\sum_{v,\mathbf{k}}\psi_{v,\mathbf{k}}(\mathbf{r})\psi_{v,\mathbf{k}}^{*}(\mathbf{r}')W(\mathbf{r},\mathbf{r}';0),\qquad(2)$$

representing the Coulomb hole Σ_{COH} and the screened exchange Σ_{SEX}. The $\psi_{n,\mathbf{k}}$ are the DFT-LDA wave functions and $W(\mathbf{r},\mathbf{r}';0)$ and $v(\mathbf{r}-\mathbf{r}')$ denote the statically screened and bare Coulomb potentials, respectively (see, e.g., Ref. 19 for a comprehensive review). For the practical calculation of W we model the dielectric function as[28]

$$\epsilon(q)=1+\{(\epsilon_{\infty}-1)^{-1}+(q/q_{\mathrm{TF}})^{2}+3q^{4}/(4k_{F}^{2}q_{\mathrm{TF}}^{2})\}^{-1},\qquad(3)$$

where k_F and q_{TF} represent the Fermi and Thomas–Fermi wave vectors, respectively. This expression interpolates between the correct behaviors at high and low q vectors and by construction correctly obtains the static dielectric constant for $q=0$. This model reproduces very well the random phase approximation results for semiconductors.[29] Using the LDA for W,[27] Σ_{COH} can now be calculated analytically,[28] resulting in a potential that depends on the local charge density. For the calculation of Σ_{SEX} we retain only diagonal elements in the Fourier transform of W. The local fields are included, however, by using state-dependent charge densities

$$\rho_{n,\mathbf{k}}=\int d\mathbf{r}^{3}\rho(\mathbf{r})|\psi_{n,\mathbf{k}}(\mathbf{r})|^{2},\qquad(4)$$

in the calculation of k_F and q_{TF}. The dynamic terms $\beta_{n,\mathbf{k}}$ and Σ^{dyn} in Eq. (1) can be approximated by simple integrals of the dielectric function.[28] For the practical calculation we use Eq. (3) together with a single plasmon pole approximation to describe the frequency dependence. Local-field effects are again included using the mean-density approximation, Eq. (4).

After applying this simplified GW approach to the DFT-LDA bulk band structure of GaP we obtain interband transition energies of 2.7 and 4.8 eV for E_0 and E_0', respectively. $E(X_{1c})$ and $E(X_{3c})$ are shifted to 2.2 and 2.4 eV. In the case of bulk InP, the E_0 gap at Γ changes from 0.9 eV in DFT-LDA to 1.4 eV. The transition energies E_1 and E_0' are shifted from 2.5 to 3.2 eV and from 4.2 to 5.0 eV, respectively. These values agree with the experiment within 0.2 eV. The application of this GW scheme to the surface seems problematic, since the model requires the input of the dielectric constant ϵ_{∞}. Northrup[21] and Rohlfing *et al.*[22] have shown, however, that the inaccuracies caused by the use of bulk dielectric constants for surface GW calculations are very small.

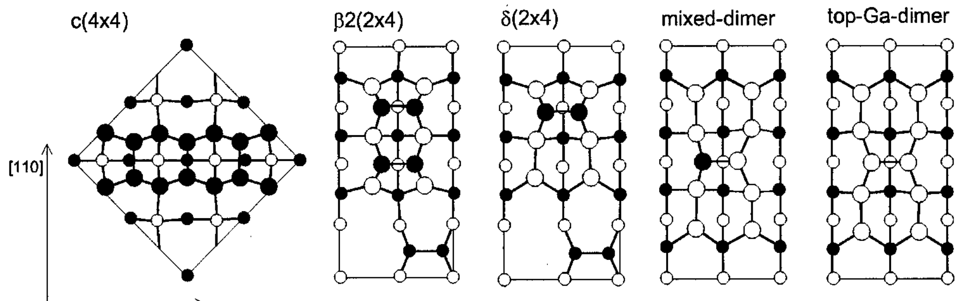

FIG. 1. Top view of GaP(001)(2×4) surface reconstruction models. The structures are ordered according to their stoichiometry. Empty (filled) circles represent Ga (P) atoms. Large (small) symbols indicate positions in the first and second (third and fourth) atomic layers.

Finally, we use the electronic structure to determine the reflectance anisotropy from the slab polarizability according to the formalism developed by Del Sole[30] and Manghi *et al.*[31]

III. RESULTS

A. GaP(001)(2×4)

Total-energy calculations[17,32,33] for GaP(001) predict a sequence of (2×4) single-dimer reconstructions for cation-rich surfaces. $\beta 2(2\times 4)$ and $c(4\times 4)$ reconstructions, known from GaAs(001), form for more P-rich surfaces. A top view of the GaP surface models is given in Fig. 1. These theoretical findings agree with the recent experiments, as discussed in detail in Refs. 17 and 33.

In Fig. 2 we show the RAS spectra calculated within DFT-LDA for the four (2×4) surface structures shown in Fig. 1. The top Ga dimer and mixed-dimer structures show a pronounced negative anisotropy in the low energy region, with minima (denoted *S* in Fig. 2) between 2.0 and 2.3 eV. The strength of this anisotropy is directly correlated with the number of Ga–Ga bonds along the [110] direction. Its magnitude is the highest for the top Ga dimer model with eight bonds, is slightly reduced, and shifted to lower energies for the mixed-dimer geometry with six cation–cation bonds, and is flattened for the δ structure with only two such bonds. The calculated spectra also show a strong dependence on the structural details at higher energies. For the $\beta 2$ geometry with three P–P dimers oriented along [1$\bar{1}$0], we find a relatively broad positive anisotropy between about 2.4 and 4.4 eV. Maxima of the anisotropy appear around 3.2 and 4.1 eV and a shoulder exists at 2.8 eV. The shape of this anisotropy is roughly preserved for the δ structure, which features one P–P dimer. Its magnitude is, however, somewhat reduced and the spectrum is shifted downwards. An even further reduction in positive anisotropy occurs for the mixed-dimer and top Ga dimer structures, featuring single Ga–P or Ga–Ga dimers, respectively, on top of a Ga-terminated substrate. The evolution of the spectra in the high energy region shows thus a correlation between the positive anisotropy and the formation of P–P dimers.

Our calculations are in accord with the available experimental data.[17,34,35] The RAS spectra measured for the Ga-rich phase of GaP(001)(2×4) feature a strong negative peak around 2.4 eV. Both the top Ga dimer model and the mixed-dimer model are thus plausible candidates to explain the Ga-rich surface phase. The measured spectrum for the Ga-rich phase shows a maximum between the energies of the E_0 and E_1 CPs. This peak, which should be observed between 2.1 and 2.9 eV in the calculated spectrum, is absent in case of the top Ga dimer structure. It appears, however, as a weak shoulder (denoted *A* in Fig. 2) for the mixed-dimer model. As will be discussed below, the agreement between the calculated spectrum for the mixed-dimer structure and the measured RAS improves substantially upon inclusion of self-energy effects, in particular with respect to the shoulder *A*. The RAS spectra thus indicate that the Ga-rich phase of GaP(001)(2×4) corresponds to the mixed-dimer geometry. This assignment is corroborated by the recently measured surface core-level shifts.[36] The spectroscopic results indicate that the extreme Ga-rich limit, which according to the total-energy calculations[17,33] is characterized by the top Ga dimer model, may actually not be reached experimentally.

The measured spectrum for the less Ga-rich (2×4) surface phase with an approximately balanced surface stoichiometry is dominated by a "camelback" spectrum with maxima between the energies of the E_0 and E_1 CPs and at E_0'.[17] No negative anisotropy appears. The only computed spectrum with no (or very little) negative anisotropy belongs to the $\beta 2(2\times 4)$ structure. Maxima appear at 3.2 and 4.1 eV,

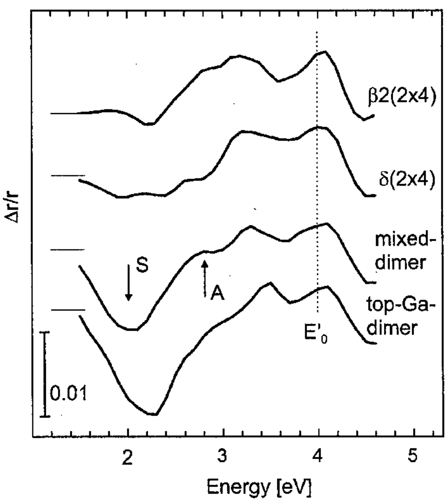

FIG. 2. RAS spectra $[\mathrm{Re}\{(r_{[\bar{1}10]}-r_{[110]})/\langle r\rangle\}]$ calculated within DFT-LDA for the four GaP(001)(2×4) surface reconstruction models shown in Fig. 1. The calculated position of E_0' is indicated.

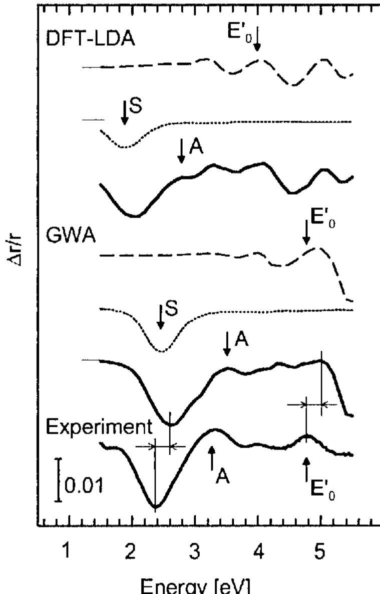

FIG. 3. RAS spectra $[\mathrm{Re}\{(r_{[\bar{1}10]}-r_{[110]})/<r>\}]$ calculated within DFT-LDA/GWA for the mixed-dimer structure are compared with the measured data (Ref. 17) for the Ga-rich GaP(001)(2×4) surface. The calculated/measured positions of E_0' are indicated. Dashed/dotted lines show the contributions to the RAS from transitions between subsurface/surface electronic states. Solid lines represent the calculations for the complete slab.

close to the calculated energies of the E_1 and E_0' CPs. Our results thus indicate that the less Ga-rich phase of GaP(001) (2×4) corresponds to the $\beta2(2\times4)$ structure.

In the following, we focus on the Ga-rich surface phase, which corresponds to the mixed-dimer structure as discussed above. This structure is reproducibly obtained in experiments.[17,35,36] To determine the origin of the optical anisotropy we spatially separated the contributions to the RAS from different slab regions. The dashed curves in Fig. 3 show the anisotropy due to transitions between the electronic states localized below the top four atomic layers. It is obvious that the surface modification of these bulk-like wave functions gives rise to strong anisotropies for high photon energies. In particular, a feature occurs near the calculated energy of the E_0' CP of the GaP bulk band structure. It depends only weakly on the actual surface structure and is present in the calculated spectra of all structures included in our study (cf. Fig. 2). Experimentally, the maximum at the E_0' CP was found irrespective of the surface preparation conditions.[17,35]

On the other hand, strong anisotropies in the low-energy part of the spectrum arise from transitions between surface localized states. In Fig. 4 we show the surface bands of the mixed-dimer model calculated in DFT-LDA, together with their orbital character. The highest occupied surface state, $V1$, slightly above the bulk valence band maximum (VBM), corresponds to the P dangling bond at the mixed dimer. $V2$ and $V3$, slightly below the VBM, are related to σ bonds between surface Ga atoms. $C1-C5$, in the upper part of the bulk band gap, arise from dangling bonds at the second-layer surface cations. [A detailed discussion of the GaP(001) surface electronic structure is given in Ref. 33.] In particular, transitions between Ga–Ga bond-related states and empty Ga dangling bonds cause the strong negative anisotropy around 2 eV. The dotted lines in Fig. 3 show the RAS induced exclusively by transitions between the valence states $V1$, $V2$ and $V3$ and the conduction states $C1-C5$. These eight states nearly completely account for the negative anisotropy observed at low photon energies. The assignment of cation-related surface states to the RAS around 2 eV corroborates the phenomenological link established by comparing the RAS of different structures as discussed above.

The optical anisotropy calculated for the complete slab (solid lines in Fig. 3) corresponds roughly to a superposition of the bulk-related features and surface peaks discussed above. This is a theoretical confirmation of the early work by Aspnes and Studna,[37] who discriminated between two components of the reflectance anisotropy: "intrinsic" contributions from surface effects on bulk wave functions and "extrinsic" contributions related to the surface structure.

In Fig. 3 two sets of theoretical data are presented, obtained in DFT-LDA and GWA. As expected from the shifts calculated for the GaP bulk band structure, we observe a distinct blueshift of the spectrum upon inclusion of self-energy effects. However, the shift is nonuniform: it amounts to about 0.6 eV for the surface-state related features (dotted

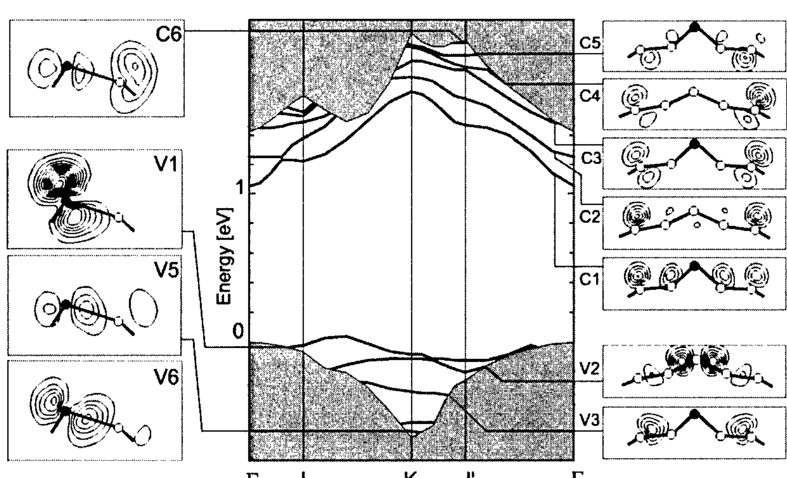

FIG. 4. Surface band structure (bound states) calculated within DFT-LDA for the mixed-dimer structure of GaP(001). Gray regions indicate the projected bulk band structure. In the left and right panels the corresponding squared wave functions at K are shown. The contour spacing is 10^{-3} bohr^{-3}.

lines) and 0.8–1.0 eV for the bulk-related ones (dashed lines). The nonuniformity of the calculated quasiparticle shifts agrees with experiment: As indicated by the arrows in the lower part of Fig. 3, the energy shift between the measured data and the spectrum calculated in GWA is nearly constant and amounts to about 0.3 eV. The inclusion of self-energy effects in the calculations not only leads to energy shifts, but also to pronounced changes in the line shape. The weak shoulder A at 2.8 eV in the DFT-LDA spectrum develops into a maximum at 3.5 eV, in good agreement with experiment.

While the agreement between the measured and the calculated spectra improves much upon inclusion of GW corrections, there remain discrepancies: the excitation energies are somewhat overestimated and the line shapes, in particular for higher energies, do not agree very well. This is not too surprising: one limitation of our study is the neglect of electron–hole interactions.[38] Furthermore, the LDA-like treatment of local-field effects in our GWA model only approximates the screening across the highly inhomogeneous surface region. Our calculations refer to zero temperature and are performed with the theoretical lattice constant (1.1% smaller than experiment), resulting in increased transition energies. Finally, the computations are performed for the ideal surface, neglecting defects and domain boundaries. Such imperfections are expected to induce distinct features in the optical anisotropy.[13]

B. In-rich InP(001)(2×4)

Similarly to GaP, cation-rich InP(001) surfaces are characterized by (2×4) single-dimer reconstructions.[33,39–41] Mixed-dimer/δ structures (see Fig. 1) form for more/less In-rich surfaces. For anion-rich surfaces $\beta2(2\times4)$ and $c(4\times4)$ reconstructions appear.[33,42] The RAS spectra for the (2×4) reconstructed InP surfaces have recently been calculated[16] and are in good qualitative agreement with the corresponding experimental results.[42–44] This holds in particular for the stoichiometric trend, which was found to be very similar to the one obtained for GaP discussed above.

More recently, however, low-temperature RAS data for In-rich InP(001)(2×4) surfaces, corresponding to the mixed-dimer structure, were measured[45,46] (see Fig. 5). The features in the low-temperature spectrum are blueshifted with respect to the 300 K measurement, and sharpened. The negative anisotropy at low energies splits into peaks at 1.9, 2.1 and 2.6 eV (denoted $S1$, $S2$, and $S3$). The high resolution achieved experimentally renders the In-rich InP surface a particularly sensitive test case for our present study on the origin of RAS features. The fine structure measured at low temperatures was not resolved in our previous calculation.[16] Furthermore, the energetic positions, in particular of the high-energy features, were not in accordance with experiment. We address these issues in the present work by using a much denser **k**-point mesh and including self-energy effects according to the GW approach discussed above.

The resulting spectra are shown in the upper part of Fig. 5. For low photon energies we obtain two pronounced negative peaks (denoted $S1/2$ and $S3$). In the high-energy region features appear close to the E_1 and E_0' energies. They form a characteristic "three-buckle" shape. Separating spatially the contributions to the optical anisotropy from different slab regions,[16,17] we find that $S1/2$ and $S3$ originate entirely from the uppermost four atomic layers. This is consistent with experiment, as the measured negative anisotropy for low energies is extremely stoichiometry dependent and therefore surface related.[42–44] The features at the CP energies arise from transitions between bulk-like electronic states that are perturbed by the surface. In earlier calculations[16,17] we have shown that these high-energy features are rather insensitive to the atomic surface structure. This agrees with experiment,[42–44] where changes in the surface conditions had very little effect on the three-buckle shape.

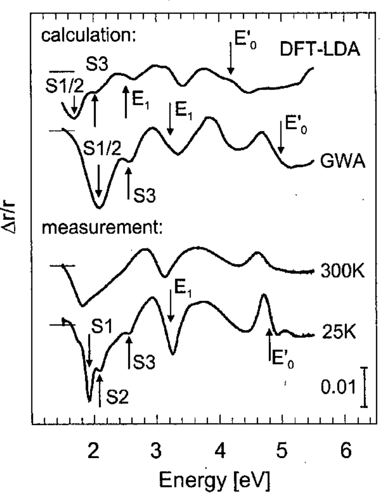

FIG. 5. RAS spectra $[\mathrm{Re}\{(r_{[\bar{1}10]}-r_{[110]})/\langle r\rangle\}]$ for the In-rich InP(001)(2×4) surface. The calculated spectra were obtained within DFT-LDA and GWA. Measurements (Refs. 45 and 46) were performed at 300 and 25 K. Bulk CP energies and surface-related features are indicated.

The major experimental features are qualitatively reproduced in the DFT-LDA calculations, although at much lower photon energies. Inclusion of self-energy effects shifts the peak positions nonuniformly to higher energies, aligning them with experiment within a few tenths of an eV. The shifts for the bulk related features are between 0.7 and 1.0 eV, somewhat larger than the shifts of 0.4–0.5 eV for the surface peaks. The changes of the line shape due to self-energy effects distinctly improve the agreement with experiment.

In order to trace the origin of the surface-related anisotropies in detail, we extended earlier calculations of the InP(001) surface electronic structure[47] to resonant surface states. We find four partially bound surface states, $V1-V4$, close to the VBM. $V1$ is formed by the bonds between first- and second-layer cations, $V2$ corresponds to the P dangling bond at the mixed dimer and $V3$ arises from the second-layer In–In bonds at the anion site of the mixed dimer (cf. left panel of Fig. 6). $V4$ is complementary to $V3$ and comparatively weakly localized at the second-layer cations at the cation site of the mixed dimer. The latter two states are degenerate with bulk bands for most parts of the SBZ (see also

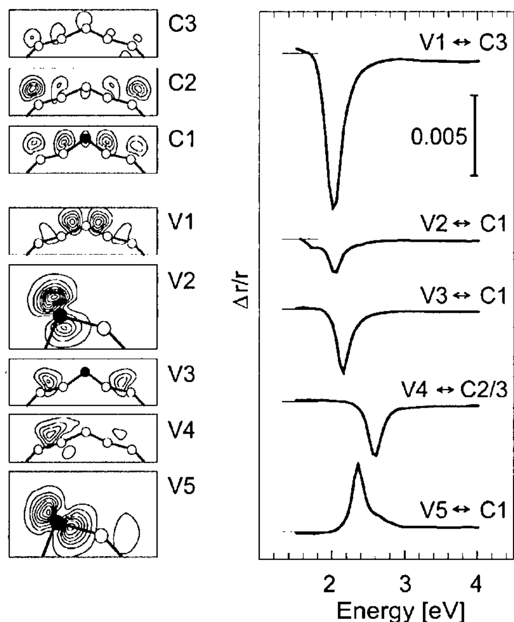

FIG. 6. (Left) Orbital character of surface states at K of the mixed-dimer geometry of InP(001)(2×4) (spacing 10^{-3} Bohr^{-3}). (Right) Calculated RAS due to transitions between these surface states.

Ref. 47). In addition, there are surface resonances. The strongly localized mixed-dimer bond $V5$ forms a very flat-band at about -0.8 to -0.9 eV. The bonds between the uppermost P and the second-layer In atoms, $V6$, disperse in energy between -1.3 and -1.6 eV. The lowest unoccupied surface states, $C1-C3$, correspond to empty dangling bonds localized at the surface cations. $C1$ is also localized at the mixed dimer (see also Fig. 5 in Ref. 16). Its energy agrees with the available inverse photoemission data.[48] In order to gain an intuitive understanding of the optical anisotropy, we investigated the existence of surface state "signatures" by calculating the RAS due to transitions within pairs of the above identified surface states. We find that some of these transitions give rise to pronounced anisotropy features, the superposition of which accounts nearly for the low-energy part of the spectrum. Figure 6 shows the calculated contribution to the RAS from transitions involving $V1-V5$ and $C1-C3$. This analysis provides a complete understanding of the surface features of the optical anisotropy: $S1$ is caused by the bonds between first- and second-layer cations. $S2$ arises from transitions mainly involving the second-layer In–In bonds. The symmetry break induced by the mixed dimer on the In–In bonds of the second atomic layer together with the dimer bond itself are responsible for $S3$.

The calculated RAS in GWA reproduces the overall experimental data rather well. The distinct contributions from $V1$ and $V3$ at 2.0 and 2.2 eV are not resolved however. Instead, we obtain one relatively broad minimum at 2.1 eV, due to the finite energy broadening necessary to account for the still limited number of wave vectors used to sample the SBZ. Apart from that, however, all experimentally found features can be identified and quantitatively described by slab calculations that take the electronic transitions within the uppermost atomic layers of the substrate into account.

C. Hydrogenated Si surfaces

As an example of step-induced optical anisotropies we study bilayer steps at the hydrogenated Si(111) surface. Since all dangling bonds are saturated, only intrinsic contributions to the RAS are expected. The two principal directions of miscut for the (111) surface are $\langle 11\bar{2}\rangle$ and $\langle \bar{1}\bar{1}2\rangle$. Assuming straight steps and barring any reconstruction, the first miscut (A in Fig. 7) gives step atoms with one dangling bond each, and the second with two dangling bonds each. In the latter case two different atomic structures are possible: a dihydride structure forms that either lies in a plane parallel (B1 in Fig. 7) or perpendicular to the step edge (B2 in Fig. 7). The optical response of these three configurations is investigated in the following. More precisely, adapting the accepted nomenclature for vicinal samples, the Si[3(111)–$(11\bar{2})$] and Si[2(111)–$(\bar{1}\bar{1}2)$] surfaces are studied, which consist of regularly spaced terraces that are three/two Si atoms wide along the $[11\bar{2}]/[\bar{1}\bar{1}2]$ direction, separated by single bilayer steps. In the following we refer to these structures as $\langle 11\bar{2}\rangle$ and $\langle \bar{1}\bar{1}2\rangle$ steps.

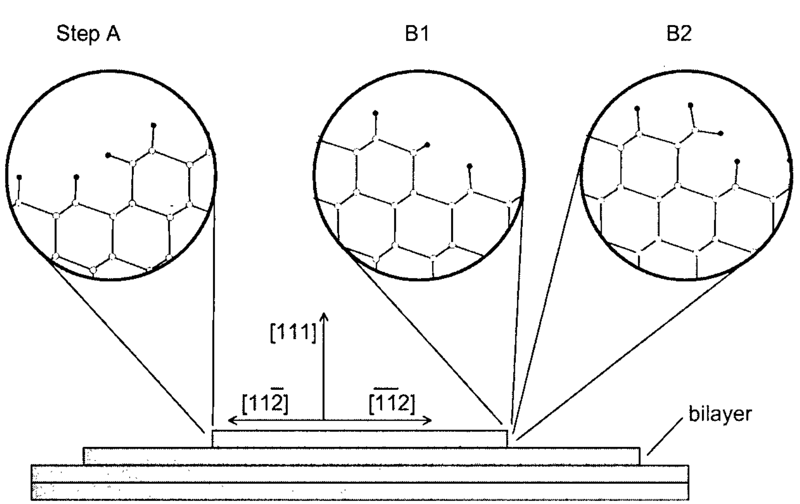

FIG. 7. Side view of the relaxed step configurations studied in this work. Empty (filled) circles represent Si (H) atoms.

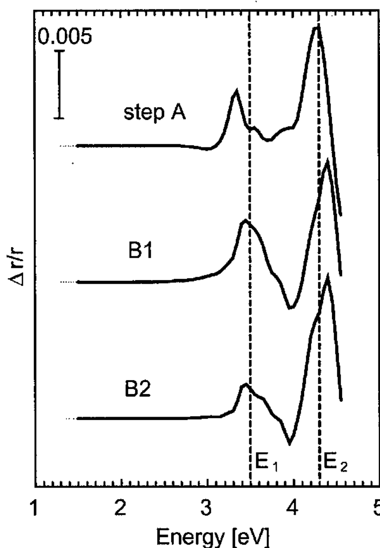

FIG. 8. Calculated RAS $[\mathrm{Re}\{(r_\alpha - r_\beta)/\langle r\rangle\}]$ for Si step geometries. The α and β principal axes lie in the surface plane and are parallel and perpendicular to the respective step edge. The labels of the curves refer to the atomic structures of Fig. 7. Bulk CP energies are indicated.

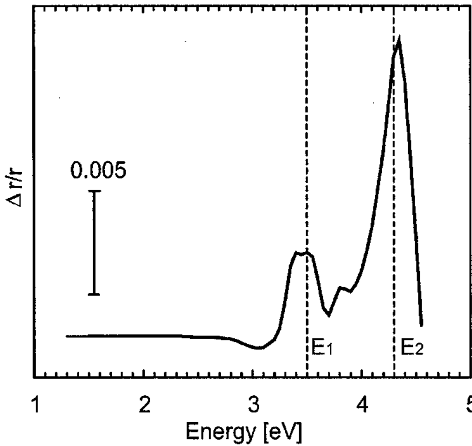

FIG. 9. Calculated RAS $[\mathrm{Re}\{(r_{[\bar{1}\bar{1}0]} - r_{[001]})/\langle r\rangle\}]$ for Si(110):H. Bulk CP energies are indicated.

The side views of the relaxed step geometries are shown in Fig. 7. All surface bonds are saturated by hydrogen. The Si atoms thus remain in bulk-like configurations and the relaxations are rather small and local. We find that the formation of a vertical dihydride structure in a plane perpendicular to the step edge (B2 in Fig. 7) is energetically preferred by 0.19 eV per step atom compared to the B1 configuration. The formation of vertical rather than in-plane dihydride structures on $\langle\bar{1}\bar{1}2\rangle$ steps is in agreement with infrared[49–51] and Raman spectroscopy.[52] The calculated RAS spectra for the three investigated step geometries are presented in Fig. 8. All steps give rise to strong anisotropy features close to the bulk CP energies. The main differences between the spectrum calculated for $\langle 11\bar{2}\rangle$ and $\langle\bar{1}\bar{1}2\rangle$ steps are a blueshift of about 0.1 eV and the occurrence of negative anisotropies at around 3 eV for the former and at around 4 eV for the latter two spectra. Based on the striking similarity of the measured step-induced RAS to that of Si(110):H it was suggested in Ref. 11 that the optical response of $\langle 11\bar{2}\rangle$ steps arises from the (110)-like regions of the stepped surface. Figure 9 shows the spectrum for the Si(110):H surface, calculated with an accuracy comparable to that obtained for the stepped surfaces. It is indeed rather similar to the RAS induced by $\langle 11\bar{2}\rangle$ steps: maxima appear at the CP energies and there is an additional shallow minimum around 3 eV. The line shape, however, in particular around the E_1 energy, is different from that calculated for the step configuration and the relative ratio of the anisotropies at the E_1 and E_2 CP energies is smaller. Furthermore, the overall similarity of the calculated RAS for all investigated step configurations suggests that one cannot explain the optical response of the $<11\bar{2}>$ stepped surface solely in terms of their (110)-like regions.

The overall similarity of all calculated step spectra indicates that the reflectance anisotropy originates from the perturbation of bulk wave functions by the formation of surface steps, rather than from electronic transitions between step-localized surface states. This picture is corroborated by our analysis separating spatially the contributions to the RAS (see Ref. 18): Electronic transitions within the uppermost 8 Å of the surface only modify the spectra, whose main features arise from transitions in deeper layers.

The calculated spectrum for Si(110):H (Fig. 9) is interesting in its own right. It clearly resembles the imaginary part of the dielectric function of Si. It is at variance with the tight-binding results of Ref. 53, but agrees rather well with experiment.[11] In Ref. 53 it was concluded that the existence of Si and H vacancies at the Si(110):H surface is a necessary condition for calculating line shapes in rough agreement with experimental data. Furthermore, it was stated that the surface local-field effect has to be included to obtain reasonable agreement with experiment. Our results, however, show that even an ideal Si(110):H surface gives rise to a dielectric function-like RAS spectrum and do not indicate a particular importance of the surface local-field effect for that surface.

A direct comparison of the data calculated for stepped surfaces with experiment is not possible, as the existing measurements[11] were performed on surfaces with considerably smaller step densities. Unfortunately, the lateral periodicities needed to accommodate wider terraces are still out of reach for *ab initio* calculations of the optical response. In Ref. 11 it was noted, however, that the anisotropy signal for Si(111):H vicinally cut toward $[11\bar{2}]$ depends nearly linearly on the step density. A similar dependence was recently obtained for Si(001).[13] Furthermore, our results, as well as earlier work,[54] show that the atomic relaxations of the step edges are rather small and local. Therefore, it is expected that our calculations can be extrapolated to allow for a meaningful comparison with the measured data.

In Fig. 10 we show the experimental data[11] for surfaces vicinally cut $\pm 5°$. The upper curve in Fig. 10 shows the RAS of the surface cut toward $[11\bar{2}]$. The main characteristics of the spectrum are the pronounced anisotropy maxima near the E_1 and E_2 CPs of the bulk band structure. This is in

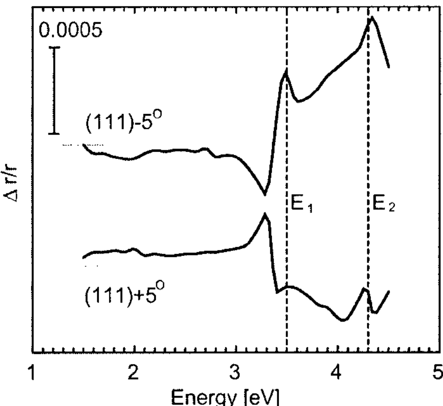

FIG. 10. Measured RAS (Ref. 11) for vicinally cut Si(111):H surfaces.

qualitative agreement with the corresponding calculated spectrum for $\langle 11\bar{2}\rangle$ steps (A in Fig. 7). The measured anisotropies are about one order of magnitude smaller than the calculated values. This can be explained partially by the lower step density: a miscut angle of $\theta=5°$ corresponds to an average terrace width n of 11 rows $[\tan\theta=2\sqrt{2}/(3n-1)]$, as opposed to the width of three rows in our calculation. Temperature effects and sample imperfections neglected in our calculation also reduce the measured anisotropy signal. The calculated line shape, in particular around the E_1 energy, is only an approximate description of the measured signal. This is not surprising, however. The neglect of excitonic effects[38] in the calculations leads to a bulk dielectric function where the E_1 peak is underestimated by about 50% and reduced to a weak shoulder of the E_2 peak. Since the step-induced reflectance anisotropy is to a large extent determined by transitions between bulk-like electronic states, the problematic description of the bulk dielectric function will cause differences in the line shape between the measured and calculated RAS spectra, in particular around the E_1 energy, even if no further approximations had been made in describing the surface. Additionally, the surface local-field effect, neglected in our study, may influence the line shape.[53] If these limitations are borne in mind, however, the agreement between experiment and theory for the $\langle 11\bar{2}\rangle$ step-induced optical anisotropy is satisfactory.

This is seemingly not the case for $\langle \bar{1}\bar{1}2\rangle$ steps. The lower curve in Fig. 10 shows data measured for the Si(111):H surface miscut 5° toward $[\bar{1}\bar{1}2]$. Yasuda *et al.*[11] assumed that the measured anisotropy is induced by bilayer $\langle \bar{1}\bar{1}2\rangle$ steps. This interpretation does not agree with the calculations. Theory predicts positive anisotropy features at the E_1 and E_2 energies, while the measured anisotropies are negative. Even considering all the limitations discussed above, it is implausible that the calculations should yield a qualitatively wrong result. From Fig. 10 it seems as if the $(111)+5°$ spectrum was an inverted and somewhat reduced version of the $(111)-5°$ spectrum. This fact has already been noted in Ref. 11. By means of infrared[49,55] and Raman spectroscopy,[52] as well as scanning tunneling microscope (STM) measurements,[56,57] it has also been demonstrated that the atomic structures of Si(111):H surfaces miscut toward $[\bar{1}\bar{1}2]$ depend strongly on the preparation conditions. In particular, a transformation of straight dihydride-terminated $\langle \bar{1}\bar{1}2\rangle$ steps into a staircase-like arrangement of monohydride terminated $\langle 11\bar{2}\rangle$ steps was observed. These newly formed steps form angles of 60°/120° with the original step edges. Assuming a complete transformation of straight $\langle \bar{1}\bar{1}2\rangle$ steps into zig-zag chains of ideal $\langle 11\bar{2}\rangle$ steps, the optical anisotropy of the surface should from pure geometrical considerations correspond to the anisotropy measured for straight $\langle 11\bar{2}\rangle$ steps, but multiplied by $-\sqrt{3}$. In reality, the optical anisotropy of remaining, not-transformed parts of $\langle \bar{1}\bar{1}2\rangle$ steps will partially cancel the signal from the zig-zag chains. A further disturbance of the "ideal" RAS spectrum can be expected from contributions due to the edges of the staircase structures. Thus, it seems likely that the optical spectrum of a Si(111):H surface miscut toward $[\bar{1}\bar{1}2]$ is an inverted, reduced, and somewhat disturbed version of the spectrum measured for a surface miscut toward $[11\bar{2}]$. Obviously, the actual spectrum will depend on the preparation conditions. This hypothesis, if correct, gives a natural explanation of the experimental findings of Ref. 11, which are seemingly at odds with our calculations. However, further experiments are needed to verify the suggested interpretation.

IV. SUMMARY

We have carried out extensive theoretical studies of the optical anisotropies of (2×4) reconstructed (001) surfaces of GaP and InP, stepped Si(111):H, and hydrogenated Si(110) surfaces. The RAS spectra calculated for the compound semiconductor surface structures show characteristic "signatures" from surface states. In particular, transitions between cation–cation bonding states and empty cation dangling bonds give rise to strong negative anisotropies at low photon energies. In addition, we find features caused by surface-modified bulk wave functions. Surface-perturbed bulk wave functions are also mainly responsible for the pronounced anisotropy features close to the bulk CP energies caused by the formation of steps on Si(111):H surfaces. Step orientation and geometry have little effect on the surface optical anisotropy. Inclusion of self-energy effects and a dense **k**-point sampling lead to a good agreement between slab calculations and experiments for the complete energy range of the spectrum. No long-range effects, such as photon-induced localization or quenching of bulk states, need to be invoked to explain the appearance of the surface optical anisotropy. The signal is mainly caused by optical transitions in the uppermost few atomic layers of the substrate.

ACKNOWLEDGMENTS

The authors thank David Aspnes, Norbert Esser, and Uwe Rossow for many stimulating and useful discussions. They

also acknowledge grants of computer time from the John von Neumann-Institut Jülich, the Konrad-Zuse-Zentrum Berlin, and the DoD Challenge Program.

[1]*Epioptics. Linear and Nonlinear Optical Spectroscopy of Surfaces and Interfaces*, edited by J. F. McGilp, D. Weaire, and C. H. Patterson (Springer, Berlin, 1995).
[2]W. Richter, Philos. Trans. R. Soc. London, Ser. A **344**, 453 (1993).
[3]D. E. Aspnes, Surf. Sci. **309**, 1017 (1994).
[4]Z. Sobiesierski, D. I. Westwood, and C. C. Matthai, J. Phys.: Condens. Matter **10**, 1 (1998).
[5]P. Chiaradia and R. Del Sole, Surf. Rev. Lett. **6**, 517 (1999).
[6]F. Bechstedt, O. Pulci, and W. G. Schmidt, Phys. Status Solidi A **175**, 5 (1999).
[7]L. Mantese, K. A. Bell, D. E. Aspnes, and U. Rossow, Phys. Lett. A **253**, 93 (1999).
[8]K. Uwai and N. Kobayashi, Phys. Rev. Lett. **78**, 959 (1997).
[9]V. L. Berkovits, P. Chiaradia, A. B. G. D. Paget, and C. Goletti, Surf. Sci. **441**, 26 (1999).
[10]R. Del Sole and G. Onida, Phys. Rev. B **60**, 5523 (1999).
[11]T. Yasuda, D. E. Aspnes, D. R. Lee, C. H. Bjorkman, and G. Lucovsky, J. Vac. Sci. Technol. A **12**, 1152 (1994).
[12]L. Mantese, U. Rossow, and D. E. Aspnes, Appl. Surf. Sci. **107**, 35 (1996).
[13]S. G. Jaloviar, J.-L. Lin, F. Liu, V. Zielasek, L. McCaughan, and M. G. Lagally, Phys. Rev. Lett. **82**, 791 (1999).
[14]M. Fuchs and M. Scheffler, Comput. Phys. Commun. **119**, 67 (1999).
[15]E. L. Briggs, D. J. Sullivan, and J. Bernholc, Phys. Rev. B **54**, 14362 (1996).
[16]W. G. Schmidt, E. L. Briggs, J. Bernholc, and F. Bechstedt, Phys. Rev. B **59**, 2234 (1999).
[17]A. M. Frisch, W. G. Schmidt, J. Bernholc, M. Pristovsek, N. Esser, and W. Richter, Phys. Rev. B **60**, 2488 (1999).
[18]W. G. Schmidt and J. Bernholc, Phys. Rev. B **61**, 7604 (2000).
[19]F. Aryasetiawan and O. Gunnarsson, Rep. Prog. Phys. **61**, 237 (1998).
[20]*Landolt-Börnstein, Numerical Data and Functional Relationships in Science and Technology* (Springer, Berlin, 1982), Vol. III, p. 17a.
[21]J. E. Northrup, Phys. Rev. B **47**, 10032 (1993).
[22]M. Rohlfing, P. Krüger, and J. Pollmann, Phys. Rev. B **52**, 1905 (1995).
[23]R. Del Sole and R. Girlanda, Phys. Rev. B **48**, 11789 (1993).
[24]L. Kipp, D. K. Biegelsen, J. E. Northrup, L.-E. Swartz, and R. D. Bringans, Phys. Rev. Lett. **76**, 2810 (1996).
[25]M. Palummo, G. Onida, R. Del Sole, and B. S. Mendoza, Phys. Rev. B **60**, 2522 (1999).
[26]O. Pulci, G. Onida, R. Del Sole, and L. Reining, Phys. Rev. Lett. **81**, 5374 (1998).
[27]M. S. Hybertsen and S. G. Louie, Phys. Rev. B **37**, 2733 (1988).
[28]F. Bechstedt, R. Del Sole, G. Cappellini, and L. Reining, Solid State Commun. **84**, 765 (1992).
[29]G. Cappellini, R. Del Sole, L. Reining, and F. Bechstedt, Phys. Rev. B **47**, 9892 (1993).
[30]R. Del Sole, Solid State Commun. **37**, 537 (1981).
[31]F. Manghi, R. Del Sole, A. Selloni, and E. Molinari, Phys. Rev. B **41**, 9935 (1990).
[32]S. Mirbt, N. Moll, K. Cho, and J. D. Joannopoulos, Phys. Rev. B **60**, 13283 (1999).
[33]W. G. Schmidt, J. Bernholc, and F. Bechstedt, Appl. Surf. Sci. (accepted).
[34]P. A. Postigo, G. Armelles, T. Utzmeier, and F. Briones, Phys. Rev. B **57**, 1359 (1998).
[35]M. Zorn, B. Junno, T. Trepk, S. Bose, L. Samuelson, J.-T. Zettler, and W. Richter, Phys. Rev. B **60**, 11557 (1999).
[36]N. Sanada, S. Mochizuki, S. Ichikawa, N. Utsumi, M. Shimomura, G. Kaneda, A. Takeuchi, Y. Suzuki, Y. Fukuda, S. Tanaka, and M. Kamata, Surf. Sci. **419**, 120 (1999).
[37]D. E. Aspnes and A. A. Studna, Phys. Rev. Lett. **54**, 1956 (1985).
[38]S. Albrecht, L. Reining, R. Del Sole, and G. Onida, Phys. Rev. Lett. **80**, 4510 (1998).
[39]C. D. MacPherson, R. A. Wolkow, C. E. J. Mitchell, and A. B. McLean, Phys. Rev. Lett. **77**, 691 (1996).
[40]W. G. Schmidt, F. Bechstedt, N. Esser, M. Pristovsek, C. Schultz, and W. Richter, Phys. Rev. B **57**, 14596 (1998).
[41]S. Mirbt, N. Moll, A. Kley, and J. D. Joannopoulos, Surf. Sci. **422**, L177 (1999).
[42]K. B. Ozanyan, P. J. Parbrook, M. Hopkinson, C. R. Whitehouse, Z. Sobiesierski, and D. I. Westwood, J. Appl. Phys. **82**, 474 (1997).
[43]D. Pahlke, J. Kinsky, C. Schultz, M. Pristovsek, M. Zorn, N. Esser, and W. Richter, Phys. Rev. B **56**, R1661 (1997).
[44]M. Zorn *et al.* Appl. Phys. A: Mater. Sci. Process. **65**, 333 (1997).
[45]T. Hannappel, S. Visbeck, M. Zorn, T. Zettler, and F. Willig, Appl. Phys. Lett. (submitted).
[46]W. G. Schmidt *et al.*, Phys. Rev. B (in press).
[47]W. G. Schmidt and F. Bechstedt, Surf. Sci. **409**, 474 (1998).
[48]S. Riese, E. Milas, and H. Merz, Surf. Sci. **270**, 833 (1992).
[49]P. Jakob, Y. J. Chabal, K. Raghavachari, R. S. Becker, and A. J. Becker, Surf. Sci. **275**, 407 (1992).
[50]S. Watanabe, Surf. Sci. **415**, 385 (1998).
[51]S. Watanabe, Appl. Surf. Sci. **130–132**, 231 (1998).
[52]M. A. Hines, Y. J. Chabal, T. D. Harris, and A. L. Harris, J. Chem. Phys. **101**, 8055 (1994).
[53]B. S. Mendoza, R. Del Sole, and A. I. Shkrebtii, Phys. Rev. B **57**, 12709 (1998).
[54]X.-P. Li, D. Vanderbilt, and R. D. King-Smith, Phys. Rev. B **50**, 4637 (1994).
[55]P. Jakob and Y. J. Chabal, J. Chem. Phys. **95**, 2897 (1991).
[56]G. J. Pietsch, U. Köhler, and M. Henzler, J. Appl. Phys. **73**, 4797 (1993).
[57]J. Flidr, Y.-C. Huang, T. A. Newton, and M. A. Hines, Chem. Phys. Lett. **302**, 85 (1999).

In situ reflectance-difference spectroscopy of doped CdTe and ZnTe grown by molecular beam epitaxy

R. E. Balderas-Navarro[a)]
Johannes Kepler Universität Linz, Institut für Halbleiterphysik und Festkörperphysik, Altenbergerstr. 69, A-4040 Linz, Austria

K. Hingerl
Johannes Kepler Universität Linz, Institut für Halbleiterphysik und Festkörperphysik, Altenbergerstr. 69, A-4040 Linz, Austria and Profactor GmbH, Wehrgrabengasse 5, A-4400 Steyr, Austria

W. Hilber
Johannes Kepler Universität Linz, Institut für Halbleiterphysik und Festkörperphysik, Altenbergerstr. 69, A-4040 Linz, Austria

D. Stifter
Profactor GmbH, Wehrgrabengasse 5, A-4400 Steyr, Austria

A. Bonanni and H. Sitter
Johannes Kepler Universität Linz, Institut für Halbleiterphysik und Festkörperphysik, Altenbergerstr. 69, A-4040 Linz, Austria

(Received 17 January 2000; accepted 25 May 2000)

We have used reflectance-difference (RD) spectroscopy (UV-visible energy range) during the growth and doping process of CdTe(001) and ZnTe(001) layers by molecular beam epitaxy (MBE). The MBE chamber is equipped with an electron cyclotron resonance cell to generate N plasma and a $ZnCl_2$ effusion cell for the *p*- and *n*-type doping, respectively. After the first stages of the growth and prior doping, different spectral features were found as we changed from Cd or Zn to Te stabilized conditions due to surface anisotropy. However, as the doping of the growing layer further increased, the RD spectra of both surfaces showed resonances around E_1 and $E_1+\Delta_1$ interband transitions due to the linear electro optic (LEO) effect. Although RD spectra exhibit similar line shapes dominated by surface transitions, differences due to the LEO can be isolated. Different Fermi level pinning mechanisms are proposed for both materials because the RD measurements of the LEO strongly depend on surface termination. © *2000 American Vacuum Society.*
[S0734-211X(00)06704-4]

I. INTRODUCTION

In the case of II–VI compounds, which are employed in the fabrication of radiation detectors (CdTe)[1] and short-wave lasers structures (ZnTe),[2] important efforts have been devoted to the doping process during molecular beam epitaxy (MBE) and metalorganic chemical vapor deposition. However, as these materials show a strong preference for one type of doping, the achievement of high *n* and *p* type conductivities is difficult.[3] Particularly for CdTe, it is difficult to control the dopant conductivity due to its tendency to form electrically active defects,[4] whereas for ZnTe only *p*-type conductivity can be achieved.[5] Therefore, a monitoring and characterization tool is of great value to investigate and control the doping process. Optical spectroscopies are well suited for this purpose as they are nondestructive, such as reflectance-difference (RD) spectroscopy, in which the difference in optical reflectivity between two mutually orthogonal polarizations is measured. The working principle of RDS is based on the fact that, as the bulk optical properties of cubic semiconductors are nominally isotropic, any observed anisotropy in the reflectance spectrum should be associated to the breakdown of the cubic symmetry at the semiconductor surface.[6] Then, by measuring the difference in reflectance for two mutually orthogonal polarizations, the bulk contribution to the sample reflectivity should cancel remaining only the surface contribution. However, there are also identified sources for bulk and interface anisotropies for zinc-blende (001) surfaces which break the four-fold rotational symmetry. We mention spontaneous ordering,[7] linear electro-optic effects,[8] dislocations,[9] and quantum confinement.[10] Among the physical mechanisms giving rise to these RD contributions, the linear electro-optic effect (LEO), through a surface electric field (SEF), is of considerable practical interest as it depends on the conductivity type and doping level of the material.[8,11,12] Until recently, the applicability of RD spectroscopy for the quantification of the SEF was limited because of the lack of an analytical model that conclusively explained the LEO line shapes. Such a model has now been developed,[13] and we will give only a brief outline. In Ref. 13 it is shown that the LEO effect in the RD spectra of zinc-blende semiconductors is due to the SEF caused by Fermi level pinning at the semiconductor surface. This SEF, in turn, induces a piezoelectric strain that leads to a change of

a)Corresponding author; electronic mail: raul.balderas@jk.uni-linz.ac.at, rbn@cactus.iico.uaslp.mx. On leave from Facultad de Ciencias; Universidad Autónoma de San Luis Potosi, Alvaro Obregón 64, San Luis Potosi, SLP 78000, México.

 0734-211X/2000/18(4)/2224/5/$17.00 ©2000 American Vacuum Society

the crystal symmetry near the sample surface from cubic to orthorhombic. For the (001) surface, such a field splits the otherwise degenerate eight ellipsoids along the Λ lines of the Brillouin zone ($\langle 111 \rangle$) into two sets of four and thereby modifies the bulk reflectivity at the E_1 and $E_1+\Delta_1$ interband transitions for light polarized along $[\bar{1}10]$ and $[110]$ principal axes. The theoretical model gives an analytical expression for the normalized change in reflectivity and was successfully tested *ex situ* for GaAs and CdTe, where the LEO component was isolated by means of photoreflectance measurements (PR).[13,14] It is noted, however, that besides the LEO contribution to the RD spectra, additional components associated to different physical origins could be present, such as surface reconstruction[15–18] and linear defects.[9] Therefore, to obtain a LEO line shape it is necessary to substract from the overall RD spectrum the non-LEO contribution. This process introduces in the final LEO spectrum a degree of uncertainty that becomes larger as the electric field strength becomes lower. In this regard, doping level determinations from RD measurements are limited to densities higher than 10^{17} cm^{-3}.

In this work we report on *in situ* measurements of RD spectra (UV-visible energy range) of both, *p*- and *n*-type, doped CdTe (001), and as well of *p*-type ZnTe (001) grown by MBE using nitrogen plasma and $ZnCl_2$ effusion cell sources. After the first stages of the growth and prior doping, significant spectral changes were found as we switched from cation to anion terminated surfaces due to surface anisotropy. However, as the doping of the growing layers further increased, the RD spectra of both surfaces showed marked resonances around E_1 and $E_1+\Delta_1$ transitions due to the LEO. Specifically, for the case of CdTe, is possible to observe the change in conductivity and therefore RD constitutes a sensitive complementary probe for the study and control of compensation phenomena.

II. EXPERIMENTAL DETAILS

The experiments were carried out in an ultrahigh vacuum (UHV) MBE chamber equipped with a 20 keV reflection high-energy electron diffraction (RHEED) system and elementary effusion cells (Zn, Cd, and Te) for growth as well with an electron cyclotron resonance (ECR) cell to generate N plasma and a $ZnCl_2$ compound source cell for *p* and *n* type doping, respectively. For more details on the plasma cell source, see Ref. 19. The shutters of the effusion cells are magnetically operated, which also enable to perform atomic layer epitaxy (ALE) growth mode in order to smooth the surface. The CdTe and ZnTe layers were grown at substrate temperatures around 300 °C on thermally deoxidized (001) GaAs epiready commercial substrates in Te-rich growth conditions. Each experiment comprises of a 0.25-μm-thick doped layer grown on top of 1 μm thick, respectively, undoped layer. For the growth of CdTe on GaAs, which has a large lattice mismatch (14.6%), a 100-Å-thick ZnTe buffer layer had to be grown first in order to inhibit (111)-oriented grains of CdTe. The final layers showed mirror-like surfaces.

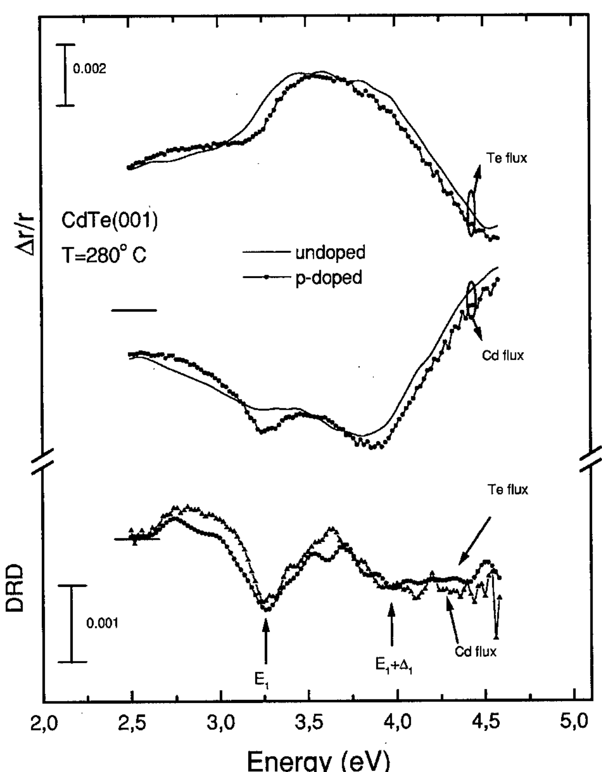

FIG. 1. *In situ* RD spectra for undoped and *p*-type (001)CdTe at two different fluxes: Te-terminated surface (top), Cd terminated (middle). Bottom: difference between doped and undoped spectra (DRD) for both Cd and Te terminations. See the text for details.

For the *in situ* RDS measurements, a commercial RDS system (ISA, Jobin-Yvon), has been attached to the MBE chamber via a near normal incidence viewport equipped with a strain free mounted Surprasil window.[19] Typical RDS spectra can be recorded from 1.5 to 5.5 eV. The RD spectra are displayed in terms of $\Delta\tilde{r}/\tilde{r}=\Delta r/r+i\Delta\theta$, where $\tilde{r}=r\exp(i\theta)$ is the complex reflectance. The quantity Δr is defined as $r_{[\bar{1}10]}-r_{[110]}$, where the directions in the indexes denote the polarization direction of the probe light along the sample principal axis. Prior to each measurement the growth was interrupted and the sample was browsed under either anion or cation flux. In the following we will first focus on RD results obtained for CdTe and then present data on ZnTe.

III. RESULTS AND DISCUSSION

First consider the RD measurements of *p*-type doped CdTe with nitrogen plasma. Figure 1 shows three sets of spectra under Cd and Te fluxes. For the sake of clarity the upper spectra were plotted vertically displaced six units. For the upper and middle spectra, solid and solid-dotted lines correspond to the undoped and doped cases, respectively. The parameters for the ECR during N doping were: pressure = 25 μbar, and a microwave input power of 30 W.[19] Undoped spectra are dominated by a broad structure around 2.5–5 eV and are sensitive as one changes from Cd to Te fluxes conditions which are attributed to transitions involving surface Te and Cd dimers and Cd–Te back bonds.[18] We

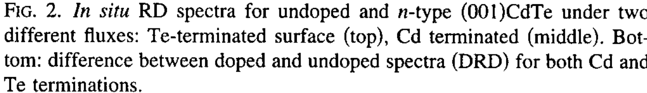

FIG. 2. *In situ* RD spectra for undoped and *n*-type (001)CdTe under two different fluxes: Te-terminated surface (top), Cd terminated (middle). Bottom: difference between doped and undoped spectra (DRD) for both Cd and Te terminations.

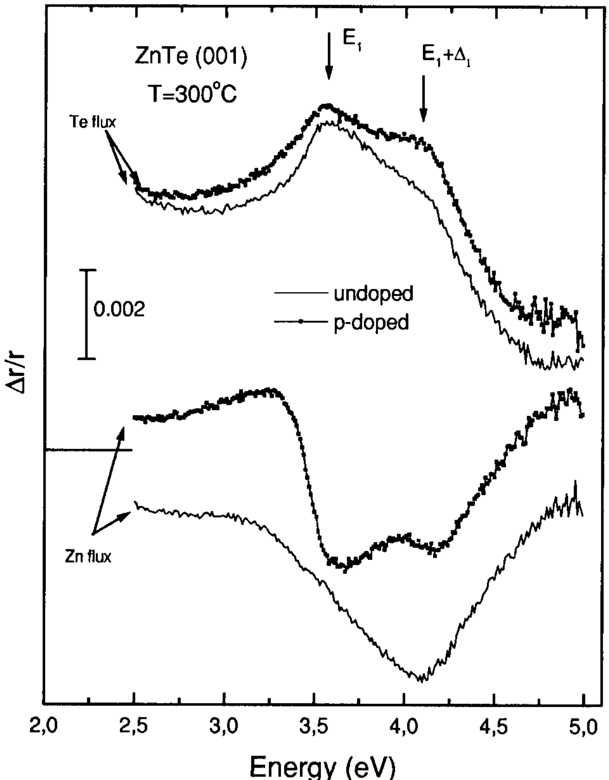

FIG. 3. *In situ* RD spectra for undoped and *p*-type doped (001)ZnTe under two different fluxes: Te-terminated surface (top), Zn terminated (bottom).

point out that the RHEED patterns of the Cd terminated and Te terminated surfaces showed (2×1) reconstructions. It is not the purpose of the present article to discuss in detail the overall evolution of the RD spectrum concerning surface termination. However, we mention that recent first principles calculations for CdTe(001), based on density functional theory,[20] suggest that the anisotropic surface electronic structure could be used in order to establish a correlation with experimental RD data and correctly identify contributions coming from dimerization.

As doping takes place we can observe an oscillation around E_1 energy predominantly under Cd termination, while the response at $E_1+\Delta_1$ is less pronounced under both terminations. These features are due to the LEO. The doped spectra also include background surface contribution. Under Te termination the E_1 transition seems to be minor because the surface optical transitions have a similar onset. By assuming that the nonelectro-optic contribution of spectra for the doped case is the same as that of the undoped one under the same flux, we isolate the LEO spectral component by substracting the undoped spectra from the doped one for both, Cd and Te fluxes. From now on we call this difference as DRD $(=[\Delta r/r]_{\text{doped}}-[\Delta r/r]_{\text{undoped}})$. The result of the substractions are shown at the bottom in Fig. 1. We note here that both line shapes are essentially the same, with the exception that the resonance around E_1 for the Te termination condition is broader than in the Cd termination case. It is important to mention here that under Cd-terminated surface the LEO component can be distinguished as an extra negative peak, whereas under Te termination, the same line shape but slightly broader, results. This indicates that for a theoretical description of RDS data, discrepancies can occur due to the built-in SEF. Only substraction of RD spectra under the same surface conditions yields unambiguously the LEO contribution. Figure 2 shows the same situation as in Fig. 1 but for *n*-type doping with $ZnCl_2$. We note, again, that both spectra are dominated by the same broad structure due to surface transitions. The bottom of Fig. 2 shows the difference spectra. We note that the line shape of the RD electro-optic component for the Cd-terminated surface corresponds to *n*-type material.[14] In contrast to *p*-type CdTe, for *n*-type material the DRD spectra for Te-terminated surface exhibits a distinct feature at $E_1+\Delta_1$: a close look at this spectra yields a background contribution that smears out the $E_1+\Delta_1$ critical point resonance. Currently we do not have an explanation for this discrepancy. From the spectra at the bottoms of Figs. 1 and 2, it is evident that the peaks have reversed their sign as the type of conductivity changed reflecting that their respective SEF are in opposite directions. This result makes RD spectroscopy a valuable complementary tool for the compensation related process during bipolar doping of CdTe.[21] We recall here that the experimental conditions of the doping cells were chosen so as to obtain carrier concentrations in the range of $n, p\approx10^{17}-10^{18}\ \text{cm}^{-3}$.

Similar RD experiments have been performed on ZnTe. The data are presented in Fig. 3. For clarity, the RD spectra of undoped ZnTe under Zn termination was vertically dis-

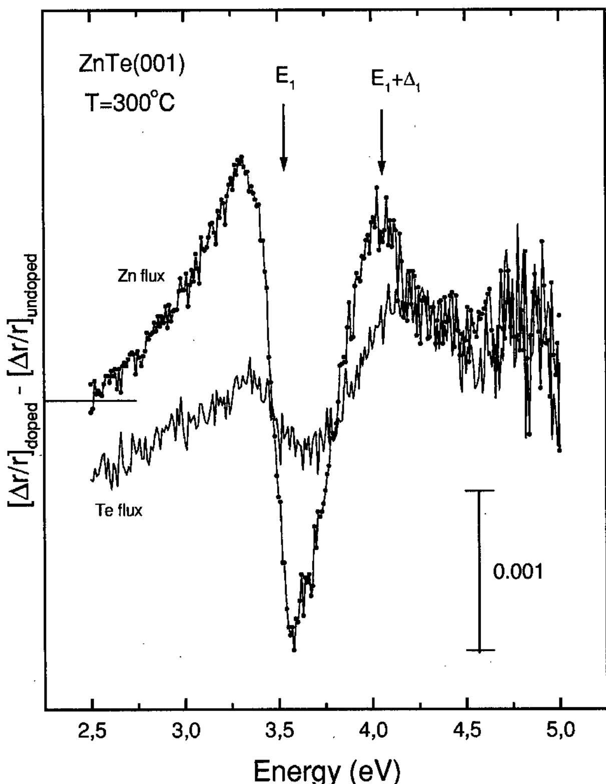

FIG. 4. Numerical differences between doped and undoped spectra (DRD) of Fig. 3 for both Zn and Te terminations.

placed −2 units. The parameters of the ECR cell are the same to that used for CdTe. For the undoped spectra, the most significant features for Te-terminated surface are a peak around 3.5 eV (E_1) and a shoulder appearing approximately at 4 eV ($E_1+\Delta_1$). In contrast, the response of Zn-saturated surface is characterized by a broad negative signal in the E_1 and $E_1+\Delta_1$ region. When compared with doped spectra we can see prominent changes for both fluxes, although it is more pronounced for the Zn-terminated spectra. The changes are evident by looking at the difference between the doped and undoped spectra, under same fluxes, as shown in Fig. 4. We note that the amplitude of the Zn-terminated spectra is around three times larger than that of the Te-terminated spectra. It is obvious that the difference in DRD spectra is not due to noise because the line shapes are similar and much smaller than the noise level. We currently explain this behavior by different Fermi level pinning positions (FLPPs). For undoped and lightly doped ZnTe the FLPP is at near midgap, whereas for heavily doped samples the FLPP is fixed by surface termination. Because Te(Zn)-induced surface states are known to be near the valence band (conduction band),[22] for *p*-type material this FLPP induces a weak (strong) SEF under Te(Zn)-rich surface conditions. The similar behavior was observed previously in doped GaAs.[23,24]

At E_1 and $E_1+\Delta_1$ transitions the magnitude of the built-in electric field can be measured by the strength of the LEO resonance. As already mentioned, it is known that the anion surface states are close to the valence band, whereas the cation surface states are close to the conduction band. For CdTe, e.g., shifting the Fermi level from near mid gap (nominally undoped) towards near the valence band (strong *p* type) should result in a different electric field under Cd than under Te termination, if the barrier height is only determined by the surface terminations. If, however, the Fermi level is pinned by intrinsic surface states, as e.g., the saturation of dangling bonds, the corresponding difference in the LEO signal, will be the same irrespectively of the surface termination. Exactly this behavior was obtained for the doping process in CdTe: the amplitudes of the DRD (bottoms of Figs. 1 and 2) are comparable. This DRD behavior is explained assigned to fixed FLPP irrespectively of dopant concentration. There still exists some controversy because the morphology, chemistry, and atomic structure of II–VI and III–V surfaces and interfaces are complex and diverse, and there is no consensus at this point on the mechanisms which dominate pinning during interface formation.[25,26] Further experiments are necessary for definite conclusions.

IV. CONCLUSIONS

In summary, we have shown in this article that *in situ* RD spectroscopy constitutes a sensitive probe for the study and control of the bipolar doping process in CdTe grown by MBE. In the case of CdTe, surface termination with either anion or cation seems to pin the Fermi level in the same position. On the contrary, for doped ZnTe under different surface terminations, we suggest that the Fermi level pinning is strongly influenced by surface conditions.

ACKNOWLEDGMENTS

This study was partially supported by the Austrian Science Foundation under Grant No. P11672-PHY. One of the authors (R.E.B.N.) gives thanks for financial support from CoNaCyT (México). K.H. is grateful for a scholarship of the Austrian Academy of Sciences.

[1] Y. Hatanaka, M. Niraula, Y. Aoki, T. Aoki, and Y. Nakanishi, Appl. Surf. Sci. **142**, 227 (1999).
[2] S. Kijima, H. Okuyama, Y. Sanaka, T. Kobayashi, S. Tomiya, and A. Ishibashi, Appl. Phys. Lett. **73**, 235 (1998).
[3] S. B. Zhang, S.-H. Wei, and A. Zunger, J. Appl. Phys. **83**, 3192 (1998).
[4] M. Niraula, T. Aoki, Y. Nakanishi, and Y. Hatanaka, J. Cryst. Growth **200**, 90 (1999).
[5] T. Baron, K. Saminasayar, and N. Magnea, J. Appl. Phys. **83**, 1354 (1998).
[6] D. E. Aspnes and A. A. Studna, Phys. Rev. Lett. **54**, 1956 (1985).
[7] B. A. Philipps, I. Kamiya, K. Hingerl, L. T. Florez, D. E. Aspnes, S. Mahajan, and J. P. Harbison, Phys. Rev. Lett. **74**, 3640 (1995).
[8] S. E. Acosta-Ortiz and A. Lastras-Martinez, Solid State Commun. **64**, 809 (1987); Phys. Rev. B **40**, 1426 (1989); Proc. SPIE **1286**, 31 (1990).
[9] L. F. Lastras-Martinez and A. Lastras-Martinez, Phys. Rev. B **54**, 10 726 (1996).
[10] L. F. Lastras-Martinez, D. Rönow, M. Cardona, P. S. Specht, P. V. Santos, and K. Eberl, Phys. Status Solidi A **170**, 317 (1998).
[11] H. Tanaka, E. Colas, I. Kamiya, D. E. Aspnes, and R. Bhat, Appl. Phys. Lett. **59**, 3443 (1991).
[12] H. H. Farrell, M. C. Tamargo, T. J. Gmitter, A. L. Weaver, and D. E. Aspnes, J. Appl. Phys. **70**, 1033 (1991).

[13]A. Lastras-Martinez, R. E. Balderas-Navarro, L. F. Lastras-Martinez, and M. A. Vidal, Phys. Rev. B **59**, 10 234 (1999).
[14]A. Lastras-Martinez, R. E. Balderas-Navarro, P. Cantú-Alejandro, and L. F. Lastras-Martinez, J. Appl. Phys. **86**, 2062 (1999); Phys. Status Solidi A **175**, 45 (1999).
[15]I. Kamiya, D. E. Aspnes, L. T. Florez, and J. P. Harbirson, Phys. Rev. B **46**, 15 894 (1992).
[16]Z. Sobiesierski, D. I. Westwood, and C. C. Matthai, J. Phys. C **10**, 1 (1998).
[17]M. Zorn, B. Junno, T. Trepk, S. Bose, L. Samuelson, and W. Richter, Phys. Rev. B **60**, 11 557 (1999).
[18]M. R. Schmid, K. Hingerl, D. Stifter, A. Bonanni, and H. Sitter, J. Cryst. Growth **184/185**, 218 (1998).
[19]D. Stifter, M. Schmid, K. Hingerl, A. Bonanni, M. Garcia-Rocha, and H. Sitter, J. Vac. Sci. Technol. B **17**, 1697 (1999).
[20]S. Gundel, A. Fleszar, W. Faschinger, and W. Hanke, Phys. Rev. B **59**, 15 261 (1999).
[21]G. Karczewski, A. K. Zakrzewski, I. Dobaczewski, W. Dobrowolski, E. Grodicka, J. Jaroszyński, T. Wojtowcz, and J. Kossut, Thin Solid Films **267**, 79 (1998).
[22]Winfried Mönch, *Semiconductor Surface and Interfaces*, Springer Series in Surface Sciences (Springer, New York, 1993), Vol. 26.
[23]M. D. Pashley, K. W. Haberern, R. M. Feenstra, and P. D. Kirchner, Phys. Rev. B **48**, 4612 (1993).
[24]D. Yan, F. H. Pollak, T. P. Chin, and J. M. Woodall, Phys. Rev. B **52**, 4674 (1995).
[25]I. M. Dharmadasa, Prog. Cryst. Growth Charact. Mater. **36**, 249 (1998).
[26]E. Ayyildiz, B. Bati, C. Temirci, and A. Turut, Appl. Surf. Sci. **152**, 57 (1999).

Surface-induced optical anisotropy of Si and Ge

U. Rossow[a)]
TU Ilmenau, Inst. f. Physik, P.O. Box 100565, D-98684 Ilmenau, Germany

L. Mantese
Physics Department, University of Texas, Austin, Texas 78712

D. E. Aspnes
North Carolina State University, Raleigh, North Carolina 27695-8202

(Received 9 May 2000; accepted 30 May 2000)

We compare surface-induced optical anisotropy spectra measured by reflectance difference/anisotropy spectroscopy of Si and Ge. Our previous work on Si has shown that we can roughly distinguish two types of contributions to the optical response of surfaces: direct contributions involving surface state transitions and indirect contributions in which the surface modifies the bulk response. We demonstrate here that this view is valid for Ge as well. For Si the indirect surface contributions exhibit three extreme, basic line shapes, which are all related to the bulk dielectric function ϵ_b or nanostructured material. We demonstrate that this line shape analysis can also be applied to Ge. © *2000 American Vacuum Society.* [S0734-211X(00)08404-3]

I. INTRODUCTION AND MODEL

The linear optical responses of surfaces and nanostructures are not yet completely understood. The surface-sensitive optical method reflectance difference spectroscopy (RDS/RAS) has recently been intensively used for surface-optical studies, in particular for characterizing surfaces and interfaces of semiconductors.[1–5] The interpretation of the spectra is in most cases very difficult since the different contributions to the signal need to be separated. Theoretical work on this subject is still in progress and only very recently quantitative agreement between measured and calculated spectra for one surface, InP(001), has been achieved.[3]

Si surfaces have also been intensively studied as a model system in the last several years.[5–9] From investigations of various Si surfaces the following picture has emerged. Surfaces can contribute to the optical response either directly or indirectly. In the former case the surfaces contribute via transitions involving surface states and near-surface modifications of the phases and amplitudes of Bloch functions due to the surface potential.[3,4,10] Direct contributions do not appear to be a significant factor in passivated Si surfaces, which makes them particularly interesting. Surfaces contribute indirectly via dynamic and many-body processes or simple microroughness. We find three types of line shapes:[11] derivativelike $(d\epsilon/dE)$;[8,12–14] ϵ-like;[12,14,15] and $1/\epsilon$-like.[11] The derivativelike line shapes show that critical point energies E_g and broadening parameters Γ obtained from optical spectra, which are generally considered to describe bulk properties, in fact depend on measurement conditions, e.g., whether normally incident light is linearly polarized parallel or perpendicular to steps. This is possible only if the excited states are mainly bulklike but are dynamically localized near the surface so that their properties are determined by a weighted average of bulk and surface potentials.[8] Such wave packets result from the finite penetration depth of the photon and are a purely dynamic phenomenon that cannot be described in the static limit. We note that the disappearance of the bound surface-state contributions in spectral regions where the final-state energy overlaps the continuum is a second case of a nominally static treatment that requires the time dependence to be included explicitly for a proper description, since the disappearance of these features in data is due to their high scattering probability (short lifetimes). The ϵ-like line shapes are due to many-body screening, specifically the surface local field (SLF) effect.[15] However, SLF contributions have been challenged by recent theoretical studies.[16] The $1/\epsilon$-like line shapes are due to microroughness and can be described by effective medium theory and the Fresnel equations.[11]

If this model describes the surface-optical response then there must be a close connection among the optical responses of surfaces, interfaces, and nanostructures, since the only difference is that localization in nanostructures is nanostructure rather than photon driven. This is discussed in more detail in Ref. 17.

The question remains as to whether Si is unique or whether other materials show similar behavior. From a comparison between Si and Ge we demonstrate that the same line shape analysis can be performed also on different materials and how difficult it is in general to separate the various contributions.

II. EXPERIMENT

Optical anisotropy measurements were performed using a RDS spectrometer that operates at near-normal incidence from 1.5 to 5.5 eV.[2] The anisotropy of the complex reflectance r is given by $\Delta r/r = 2(r_\alpha - r_\beta)/(r_\alpha + r_\beta)$, where r_α and r_β are the complex reflectances of light linearly polarized along the α and β directions, respectively. Here we report $\mathrm{Re}(\Delta r/r)$ with α along $[\bar{1}10]$ and β orthogonal to α and the surface normal.

We measured the optical anisotropy of a broad range of Si

a)Electronic mail: rossow@physik.tu-ilmenau.de

FIG. 1. Comparison of $\mathrm{Im}\langle\epsilon\rangle$ data of Si and Ge (Ref. 19). The spectral positions of E_0' and E_2 are similar but E_1 is different for the two materials.

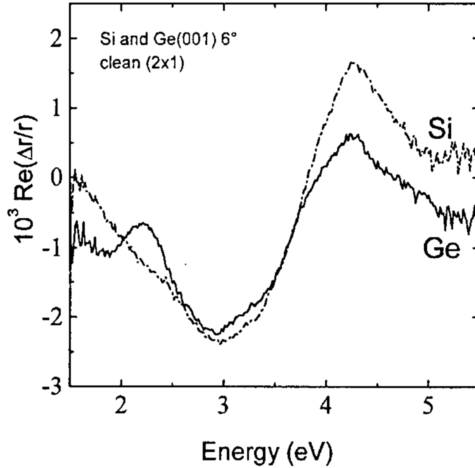

FIG. 2. $\mathrm{Re}(\Delta r/r)$ for clean (2×1) reconstructed 6° offcut Si(001) and Ge(001).

surfaces, specifically (a) vicinal (001) surfaces cut toward [110]; (b) the (113) surface, which is approximately 25° off (001) toward [110]; (c) vicinal (111) surfaces; and (d) (110) surfaces. Si samples were either chemically prepared by a RCA[18] or slightly modified RCA clean with and without a final HF dip, or were flash annealed in ultrahigh vacuum (UHV). The latter surfaces were also exposed to atomic H. Details can be found in Ref. 8.

The Ge wafers were near intrinsic n-type cut toward [110]. They were cleaned by degreasing in trichloroethylene, acetone, and methanol, then lightly etched in a 1:2:5 solution of 1% H_2O_2:H_2O:0.1% HF for 1 min at 32 °C. Then the samples were transferred into an UHV system and annealed for 2 min at 780 °C to obtain a clean (2×1) reconstructed surface. For the water immersion experiments the Ge wafers were only degreased and then left in de-ionized water for the experiments.

III. RESULTS AND DISCUSSION

As the basis for discussing the RDS spectra we use already published data for the bulk dielectric functions of Si and Ge shown in Fig. 1.[19] The bulk interband critical points E_0' and E_2 for both materials have very similar spectral positions and the line shapes around E_2 are also very similar. On the other hand, the E_1 gap of Ge is at lower energies and the spin–orbit splitting Δ_1 is much larger compared to Si.

The real part of the RDS spectra $\mathrm{Re}(\Delta r/r)$ for clean (2×1) reconstructed Si(001) and Ge(001) both offcut 6° toward [110] are shown in Fig. 2. We suggested earlier that the feature around 4.2 eV for Si is related to the E_2 gap and that the line shape is ϵ-like[17] (with additional contributions likely involving surface states in the energy range below 3 eV). This is further supported by the corresponding RDS spectrum for Ge which is similar in line shape to a feature near the same spectral position. Not so clear is the behavior of E_1 for Si. For Si we recognize a shoulder around 3.8 eV and a more pronounced feature slightly below 3.4 eV. For nanostructured Si we also found earlier shoulders in the spectral range between 3.5 and 3.8 eV and argued that this is due to a remainder of (E_0', E_1).[20,21] However, the broad feature found for Ge around 2.2 eV can be related to E_1 and $E_1+\Delta_1$ of bulk Ge. Thus either the behavior of E_0', E_1, $E_1+\Delta_1$ for Ge differs from that of Si or the situation is much more complicated. The spectrum for Ge indicates that E_0' and E_1 behave differently, i.e., the shift and weakening of these features due to the modifications induced by the surface are different. Such a different behavior of E_0' and E_1 is indeed known for Si–Ge alloys where E_1 shifts with composition but E_0' remains essentially constant, which is also expected from $\langle\epsilon\rangle$ shown in Fig. 1. On the other hand, the RDS signal for Ge vanishes with oxygen exposure while oxidized Si surfaces show RDS spectra with a derivativelike line shape.[6]

We expected to gain more insight from an investigation of Ge surfaces immersed in water. The interesting property of Ge is that the oxide is water soluble. That is, the surface immersed in water is either essentially clean or covered with a suboxide depending on pH of the solution. The resulting RDS spectra for increasing offcut angle and (113), which can be regarded as a 25° vicinal (001) surface, are shown in Fig. 3. We observe several spectral features all located near bulk interband critical points. As for the case of hydrogenated and oxidized Si surfaces the signal is increasing with offcut angle, indicating that also in this case steps contribute to the

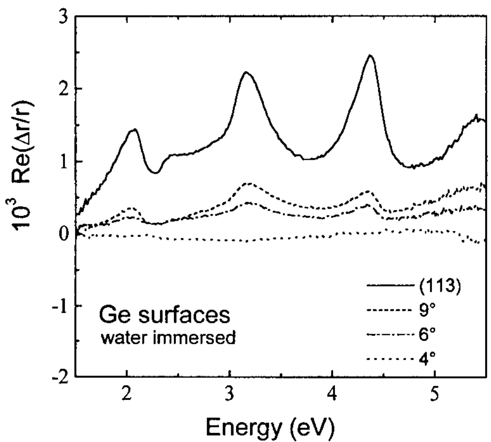

FIG. 3. $\mathrm{Re}(\Delta r/r)$ for water-immersed offcut Ge(001) and Ge(113) surfaces.

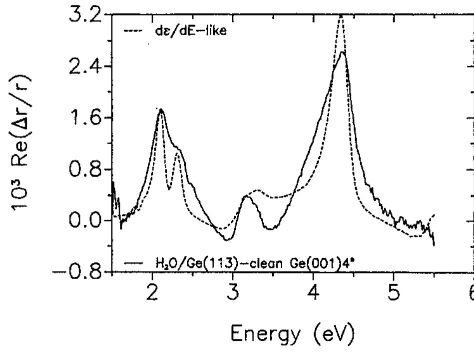

FIG. 4. Comparison of the difference $\mathrm{Re}(\Delta r/r)$ of Ge(113) in water minus clean Ge(001) 4° offcut with a derivativelike line shape.

signal. Although the character especially around 2 eV is clearly derivativelike the spectra cannot be fit based on the simple line shapes we discussed previously.

However, if we subtract a clean Ge(001) spectrum from, e.g., the spectrum for (113) immersed in water the difference spectrum can be very well fit by a derivativelike calculated spectrum based on the bulk Ge $\langle \epsilon \rangle$ data. That means that the spectra for Ge immersed in water is composed of a $\langle \epsilon \rangle$ and a $d\epsilon/dE$ part. The difficulty of the analysis arises from the fact that for derivativelike line shapes we have a complex prefactor $(-\Delta E_g + i\Delta\Gamma)$. Therefore, a linear combination of different line shapes based on real prefactors is only justified if $\Delta\Gamma$ can be neglected, which in general is not the case (Fig. 4).

IV. SUMMARY AND CONCLUSIONS

We report clean and water immersed RDS spectra for Ge and compare the spectra to that of Si. We find similarities between both materials and found evidence that the behavior around the E_2 gap is the same. The problem of the behavior of E_0' and E_1 remains unsolved. But the above shows that the line shape analysis of surface-induced anisotropy spectra works quite well not only for Si but also for Ge. The similarity between the SIOA spectra of clean vicinal Ge(001) and Si(001) surfaces on one hand and of the SIOA spectra of Si and nanostructured Si, on the other hand, indicates that the SIOA spectrum of Ge is also of the ϵ type (with additional direct contributions) and that also for the case of Ge the nanostructured dielectric function must be applied rather than the bulk dielectric function. The water immersed Ge spectra can be fit by a combination of ϵ- and $d\epsilon/dE$-type line shapes. For Si and Ge the latter is related to the steps at the surface.

This indicates that the problem of understanding the indirect contributions of surfaces to the optical response can be reduced to the problem of understanding the basic line shapes of the ϵ and $d\epsilon/dE$ types.

ACKNOWLEDGMENTS

We gratefully acknowledge financial support by the Office of Naval Research (ONR) under Contract No. N-00014-93-1-0255, and the Alexander von Humboldt Foundation.

[1]D. E. Aspnes, J. Vac. Sci. Technol. B **3**, 1498 (1985); W. Richter, Philos. Trans. R. Soc. London, Ser. A **344**, 453 (1993).
[2]D. E. Aspnes, J. P. Harbison, A. A. Studna, L. T. Florez, and M. K. Kelly, J. Vac. Sci. Technol. A **6**, 1327 (1988).
[3]N. Esser *et al.*, J. Vac. Sci. Technol. B, these proceedings.
[4]U. Rossow, K. Lindner, M. Lübbe, D. E. Aspnes, and D. R. T. Zahn, J. Vac. Sci. Technol. B **16**, 2355 (1998).
[5]Z. Sobiesierski, D. I. Westwood, and C. C. Matthai, J. Phys.: Condens. Matter **10**, 1 (1998).
[6]T. Yasuda, L. Mantese, U. Rossow, and D. E. Aspnes, Phys. Rev. Lett. **17**, 3431 (1995).
[7]J.-L. Lin, S. G. Jaloviar, L. Mantese, D. E. Aspnes, L. McCaughan, and M. G. Lagally, Mater. Res. Soc. Symp. Proc. **406**, 401 (1996); S. G. Jaloviar, J.-L. Lin, F. Liu, V. Zielasek, L. McCaughan, and M. G. Lagally, Phys. Rev. Lett. **82**, 791 (1999).
[8]L. Mantese, U. Rossow, and D. E. Aspnes, Appl. Surf. Sci. **107**, 35 (1996).
[9]J. R. Power, W. Richter, M. Palumno, G. Onida, and R. Del Sole, Phys. Status Solidi A **175**, 63 (1999).
[10]F. Manghi, R. Del Sole, A. Selloni, and E. Molinari, Phys. Rev. B **41**, 9935 (1990); R. Del Sole, Thin Solid Films **313-314**, 528 (1998).
[11]U. Rossow, L. Mantese, and D. E. Aspnes, Appl. Surf. Sci. **123/124**, 237 (1998).
[12]D. E. Aspnes and A. A. Studna, J. Vac. Sci. Technol. A **5**, 546 (1987).
[13]U. Rossow, L. Mantese, T. Yasuda, and D. E. Aspnes, Appl. Surf. Sci. **104/105**, 137 (1996).
[14]U. Rossow, L. Mantese, and D. E. Aspnes, in *Proceedings of the 23rd International Conference on the Physics of Semiconductors, Berlin, Germany,* edited by M. Scheffler and R. Zimmermann (World Scientific, Singapore, 1996), p. 831.
[15]W. L. Mochán and R. G. Barrera, J. Phys. Colloq. **45**, 207 (1984); D. E. Aspnes and A. A. Studna, Phys. Rev. Lett. **54**, 1956 (1985).
[16]W. G. Schmidt, F. Bechstedt, and J. Bernholc, J. Vac. Sci. Technol. B, these proceedings.
[17]U. Rossow, L. Mantese, D. E. Aspnes, K. A. Bell, and M. Ebert, Phys. Status Solidi B **215**, 725 (1999).
[18]W. Kern and D. A. Puotinen, RCA Rev. **31**, 187 (1970).
[19]D. E. Aspnes and A. A. Studna, Phys. Rev. B **27**, 983 (1983).
[20]U. Rossow, U. Frotscher, C. Pietryga, W. Richter, and D. E. Aspnes, Appl. Surf. Sci. **102**, 413 (1996).
[21]U. Rossow, U. Frotscher, C. Pietryga, D. E. Aspnes, and W. Richter, Appl. Surf. Sci. **104/105**, 552 (1996).

In-plane optical anisotropy of quantum well structures: From fundamental considerations to interface characterization and optoelectronic engineering

S. Cortez,[a] O. Krebs, and P. Voisin
Laboratoire de Physique de la Matière Condensée de l'Ecole Normale Supérieure, 24 rue Lhomond, F 75005 Paris, France

(Received 17 January 2000; accepted 1 May 2000)

The recently discovered in-plane optical anisotropy of (001)-grown quantum wells offers a new theoretical and experimental insight into the electronic properties of semiconductor interfaces. We first discuss the coupling of X and Y valence bands due to the breakdown of rotoinversion symmetry at a semiconductor heterointerface, with special attention to its dependence on effective parameters such as the valence band offset. The intracell localization of Bloch functions is explained from simple theoretical arguments and evaluated numerically from a pseudopotential microscopic model. The role of envelope functions is then considered, and we discuss the specific case of no-common atom interfaces. Experimental results and applications to interface characterization are presented, and the potential of the "quantum confined Pockels effect" for device applications is finally discussed. © *2000 American Vacuum Society.* [S0734-211X(00)03804-X]

I. INTRODUCTION

It was recently realized that the reduction of crystal symmetry at an abrupt heterointerface may affect quite significantly the optical properties of semiconductor quantum wells and, in particular, their isotropy with respect to the in-plane polarization of a light beam propagating parallel to the [0,0,1] growth axis. The cubic point group symmetry Td of the zinc-blend lattice is reduced to $C2v$ at an abrupt interface: it loses not only the translational invariance along the z axis, but also an element of rotational symmetry, namely the invariance by the fourfold rotoinversion around the [0,0,1] direction. The arrangement of chemical bonds in the vicinity of an interface anion, shown in Fig. 1, illustrates this symmetry breakdown which was until recently neglected in the classical envelope function theory (EFT). There are two bonds pointing forward along the [1,1,1] and [−1,−1,1] and two different bonds pointing backward along the [1,−1,−1] and [−1,1,−1] directions. The crucial point is that electrons lying on backward and forward bonds of an interface cell experience different potentials and interact with light polarized either along [110] or [−110]. In the absence of spin-orbit coupling, the threefold degeneracy of the bulk valence band with eigenfunctions X, Y, and Z is lifted by the quantum confinement into three band with symmetries X', Y', and Z, where X' and Y' refer to p-type orbitals oriented along the [1,1,0] and [1,−1,0] directions. These functions correspond to different representations of the group $C2v$, antisymmetric with respect to the planes $x'=0$ and $y'=0$. If the quantum well is symmetrical, its point group symmetry is $D2d$ and the X' and Y' representations are degenerate, but if it is asymmetrical, it retains the reduced symmetry $C2v$ of a single interface and the X' and Y' eigenstates are nondegenerate, which corresponds to in-plane anisotropy. As will be discussed further, reintroduction of the spin-orbit coupling at this point transforms the $X'-Y'$ splitting into a mixing of the heavy and light hole states in quantum well (QW) structures. Although this mixing had been discussed as early as 1985 in the tight-binding calculations of Schulmann and Chang,[1] the topic has recently attracted much attention with the experimental discovery of the related giant optical anisotropy in quantum well structures,[2] where the host materials do not share a common atom (NCA QWs), and the simultaneous development of envelope function theories[3–5] and atomistic (empirical[2,6,7] or *ab initio*[8]) calculations of this phenomenon. Optical anisotropy is sensitive to the details of interface structure, such as chemical nature of interface bonds and interface sharpness. A detailed analysis of the dichroism and birefringence of quantum wells is therefore a new and major characterization tool to analyze the properties of semiconductor interfaces.

The purpose of this article is to present recent theoretical developments of this topic, and experimental results illustrating the role of interfaces, and the effect of their detailed structure. The article is organized as follow: in Sec. II, we discuss the main features of the zone-center Bloch functions, both from symmetry arguments, and numerically using the empirical pseudopotential approach in the zero spin-orbit limit. Then we estimate the splitting of the eigenstates with X' and Y' symmetries in an interface unit cell, and introduce the envelope functions to obtain the splitting between corresponding QW states. Section III is devoted to experimental analysis of quantum wells, with special emphasis on the properties of NCA systems, and on the effect of an external electric field, or "quantum confined Pockels effect" (QCPE). In Sec. IV, we discuss the consequences of this anisotropy on the propagation of guided modes confined by the heterostructure, and the potential use of the QCPE in optoelectronic devices.

[a]Author to whom correspondence should be addressed; electronic mail: cortez@physique.ens.fr

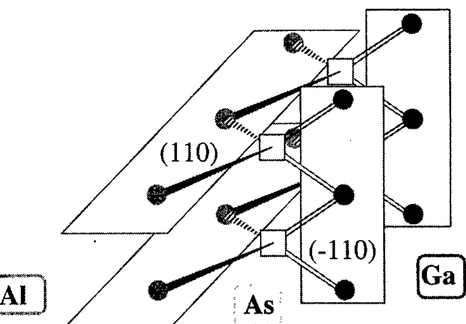

FIG. 1. Scheme of the geometrical arrangement of chemical bonds at a semiconductor interface.

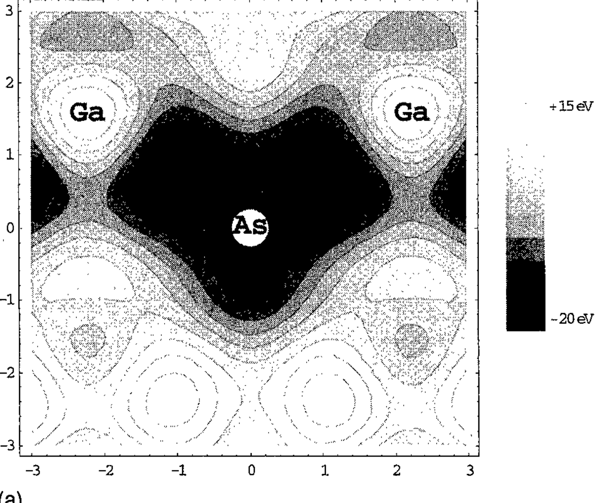

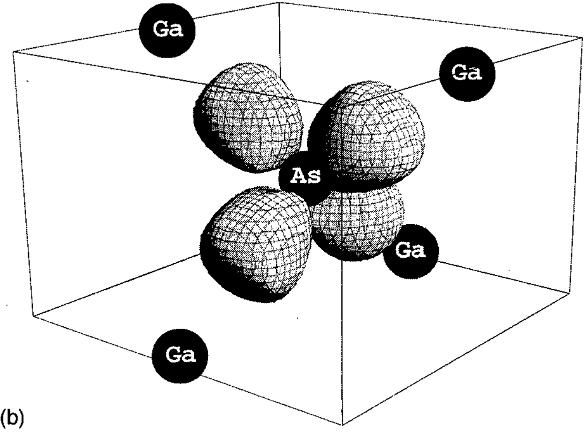

FIG. 2. Microscopic empirical pseudo-potential of bulk GaAs (a) in the plane (1,1,0); (b) three-dimensional plot of the equipotential surface at $E = -12$ eV.

II. THEORETICAL ANALYSIS OF THE SYMMETRY BREAKDOWN

A. Microscopic wave functions in the zinc-blende semiconductors

Since the properties of microscopic wave functions is the key point of this article, we first review a few general aspects. The **k·p** theory is based on the consideration of the symmetry of the zone-center eigenstates and a small number of interband matrix elements of the momentum: it generally ignores the problem of the intracell shape and localization of the Bloch functions (although, of course, the question would be implicitly solved if a complete basis were considered). However, when the crystal potential is modified on the scale of a unit cell, as for example in the case of an abrupt interface, it is intuitively evident that the matrix elements of the perturbation will be strongly dependent of the local properties of the Bloch functions. Therefore, it is crucial to use a realistic description of these functions and to examine their robustness against perturbations. The empirical pseudopotential method is based on the Fourrier series expansion of the Bloch functions, and in principle its accuracy is limited only by the number of harmonics considered in the calculation, and the careful fitting of bulk band structure. In the following, we discuss microscopic wave functions obtained in the simplest pseudopotential approach, ignoring spin-orbit interaction. Using pseudopotential form factors given in Ref. 9, we show in Figs. 2–4 a few aspects of the microscopic potential and wave functions in GaAs. As can be seen in Fig. 2(a), the potential in the plane $y'=0$, which contains the forward bonds of Fig. 1, has two deep wells nearly at the center of the Ga–As bonds. Typical figures are a well width of $L_{car}=2$ Å and a well depth of 20 eV. The equipotential surface $V(\mathbf{r})=-12$ eV, shown in Fig. 2(b), illustrates this even more obviously. The isodensity surface of the X' and Y' functions displayed in Figs. 3(a) and 3(b) show that these wave functions are strongly localized, respectively, in the backward and forward parts of the unit cell: 70% of the total X' (respectively, Y') electronic density is contained in the displayed surfaces. Conversely, the Z function [Fig. 4(a)] is equally distributed in the two parts of the cell. As for the first conduction band shown in Fig. 4(b), it does look like an antibonding combination of atomic S-like orbitals. These general features of the tetragonal bonds show little material-to-material variation: the main modification observed when using the pseudopotential coefficients of CdTe is the increased ionicity, characterized by the fact that the electron density concentrates closer to the anion, both for the valence and conduction bands.

As the intracell localization of the valence states is of central interest, it is finally interesting to justify it on the sole basis of symmetry considerations. In the following, we shall decompose the kinetic energy contribution to the Hamiltonian as a sum of its contributions along the three orthogonal directions x', y', and z. We can formally express the kinetic energy of Bloch state along the direction x' as

$$E_c^{x'} = -\frac{\hbar^2}{2m}\cdot\frac{\partial^2}{\partial x'^2} \approx -\frac{\hbar^2}{2m}\cdot\frac{1}{d_{x'}^2},$$

where $d_{x'}$ is a typical variation length of the Bloch function along the direction x'. By definition, an eigenstate of symmetry X' is antisymmetrical with respect to the plane $x'=0$ and symmetrical with respect to the plane $y'=0$, while an eigenstate of symmetry S or Z is symmetrical with respect

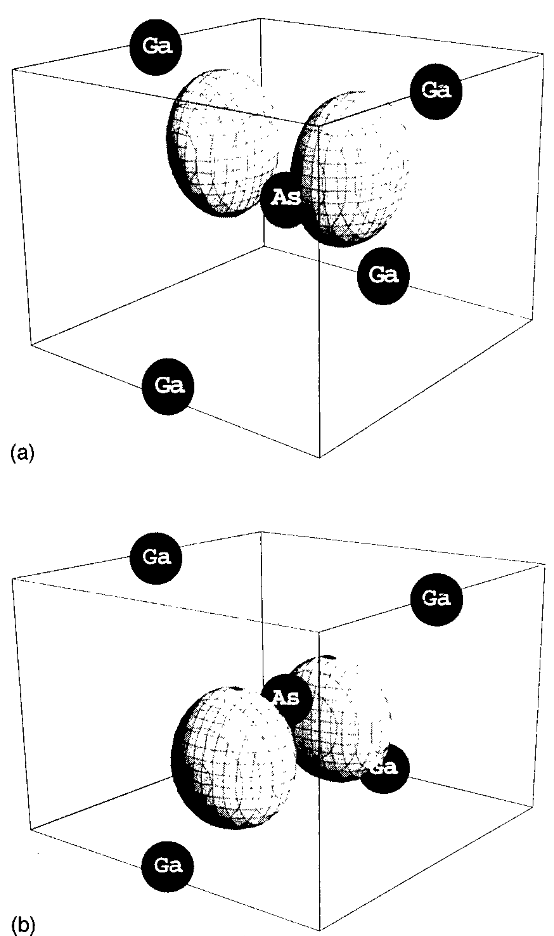

FIG. 3. Isodensity surface of the (a) X' and (b) Y' valence Bloch function at the zone center in bulk GaAs, showing their respective localization in the backward and forward half cells.

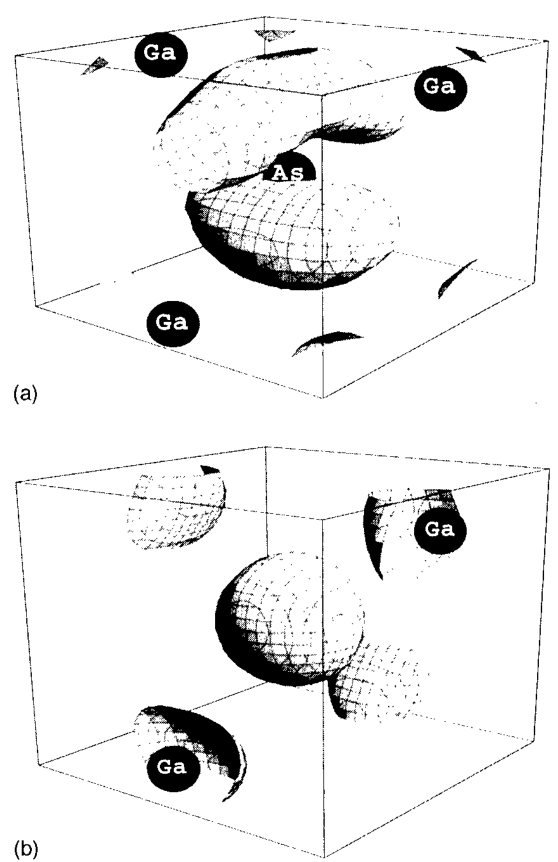

FIG. 4. Isodensity surface of the (a) Z valence and (b) S conduction Bloch functions at Γ in bulk GaAs.

to both reflections. Hence $X'(r)$ has a node in the plane $x'=0$ which contains the two backward chemical bonds. If X' was confined equally in the four potential wells, it would experience a much larger (by about four times) kinetic energy in the two backward wells where it has a node than in the two forward wells which are separated by the plane $x'=0$, and where the X' symmetry can be accommodated while retaining a constant sign inside each well. The characteristic variation length of the X' function is of the order of only $L_{car}/4=0.5$ Å in the backward region, while it would be of $L_{car}/2=1$ Å in the forward wells. Corresponding kinetic energies are of the order of 20 and 5 eV, respectively; kinetic energy acts as a strong potential repulsing the X' state out of the backward potential wells, and Y' states out of the forward wells. Another instructive way of understanding these localization properties was suggested by J. Khurgin using a tight binding point of view: if one builds solutions of X' symmetry from atomic X'_A and X'_C functions, the intersite overlap (strong, albeit usually neglected in the band structure calculations) is binding in the forward region and antibinding in the backward region.

To conclude this subsection, let us note that from the consideration of the orders of magnitude of the potential depth and length scale, the microscopic wave functions must be very robust against perturbations on the order of a fraction of eV such as a band offset, the spin-orbit interaction, or a uniaxial stress: in general, first order perturbation theory should be enough to describe the effect of such perturbations. On a more intuitive ground, Figs. 2–4 suggest that the pseudopotential coefficients are essentially related to the properties of the potential wells associated with individual bonds (including the admixion of all kind of atomic states in the bond formation).

B. Splitting of X' and Y' states at a GaAs–AlAs interface

In order to study a GaAs–AlAs interface we shall first consider an interface unit cell centered on an As atom. The symmetry plane $x'=0$ contains two backward GaAs bonds while the $y'=0$ plane contains two forward AlAs bonds. In order to describe the microscopic potential $V(\mathbf{r})$ over the interface cell, we shall rely on the pseudopotential approximation.

Let us call $V_{GaAs}(\mathbf{r})$ and $V_{AlAs}(\mathbf{r})$ the oscillatory parts of the bulk empirical pseudopotentials of these two materials, which can be viewed as some "smoothed" approximation of the microscopic potential experienced by valence and conduction electrons. The potential near the interface depends on two different phenomena: (i) The physical nature of the bonds is different in the forward and backward regions, which can be characterized quantitatively by the difference

of pseudopotential coefficients $V_{3a}, V_{3c}, V_4 \ldots$ of the semiconductors involved. This basically corresponds to a difference in the shape and depth of the potential wells corresponding to chemical bonds on both sides. (ii) There is a constant potential offset ΔV_0 between the two materials, which includes the difference of average potential of the (supposedly spatially separated) materials and the charge transfer, essentially limited to the interface bonds, which produces an electrostatic potential step at the interface. When using bulk empirical pseudopotentials, this constant offset needs to be adjusted by hand since it is not directly a bulk property of each material but rather a characteristic of the interface. We note that the interface charge transfer has the $C2v$ symmetry, hence it should also include a quadrupolar contribution. In the empirical pseudopotential picture, the charge transfer ensures (to the first order of perturbation) the continuity of the three-dimensional microscopic potential. In practice, we shall neglect the quadrupolar contribution. In this description, the microscopic potential $V(\mathbf{r})$ takes the value $V_{\mathrm{GaAs}}(\mathbf{r})$, when $\mathbf{r}$ lies closer to a GaAs bond and $V_{\mathrm{AlAs}}(\mathbf{r})+\Delta V_0$, when $\mathbf{r}$ lies closer to an AlAs bond. One should note at this point that the microscopic potential proposed here is different from the microscopic potential used in most pseudopotential calculations: the potential is associated with the closest chemical bond rather than to a combination of different atomic pseudopotentials. We introduce the function

$$\Delta V(\mathbf{r}) = V_{\mathrm{AlAs}}(\mathbf{r}) - V_{\mathrm{GaAs}}(\mathbf{r}) + \Delta V_0,$$

which has the full Td symmetry of the bulk crystal (we neglect here the small difference in bulk lattice constants). $\Delta V(\mathbf{r})$ contains all the information on the change of microscopic potential between the two bulk materials. Therefore, the microscopic potential in the interface cell can be described by

$$V(\mathbf{r}) = V_{\mathrm{GaAs}}(\mathbf{r}) + \alpha(\mathbf{r})\Delta V(\mathbf{r}),$$

where $\alpha(\mathbf{r})$ is a step function which partitions the interface cell into GaAs-like and AlAs-like regions, with the correct $C2v$ symmetry. As long as the "bond potential well" picture discussed in the previous section prevails, what matters is that $\alpha(\mathbf{r})=0$ close to the potential wells associated with the backward bonds and $\alpha(\mathbf{r})=1$ close to the potential wells associated with the forward bonds. Clearly, the unidimensional step function $Y(z)$ is a rather poor approximation of $\alpha(\mathbf{r})$. The "waffle" step function $W(\mathbf{r})$ introduced by Foreman[5] and illustrated in Fig. 5 is obviously a much better approximation. We now have to estimate the splitting of the states of symmetry X' and Y' associated with the $C2v$ symmetry of the interface cell, namely,

$$\langle X'|\alpha(\mathbf{r})\Delta V(\mathbf{r})|X'\rangle - \langle Y'|\alpha(\mathbf{r})\Delta V(\mathbf{r})|Y'\rangle,$$

where the integration is performed over the interface unit cell. It is essential to notice that this splitting corresponds to twice the $X-Y$ interface coupling $\langle X|\alpha(\mathbf{r})\Delta V(\mathbf{r})|Y\rangle$ evaluated in the H_{BF} model,[3] since $X.Y = 1/2(X'^2 - Y'^2)$. A fully numerical evaluation of this matrix element has already been attempted, but it essentially relies on our capacity to describe

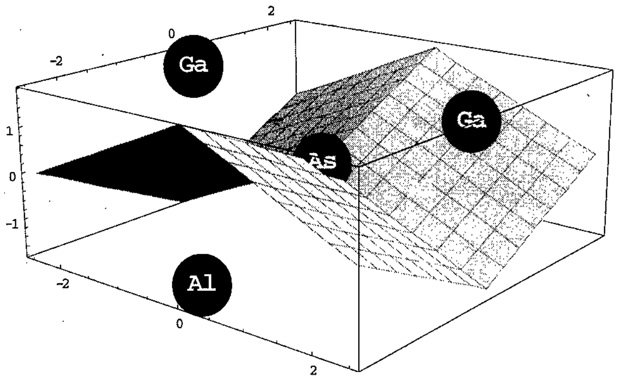

FIG. 5. "Waffle" surface used in the calculation to separate the backward and forward half cells.

correctly the difference of pseudopotential coefficients $\Delta V_0, \Delta V_{3a}, \Delta V_{3c} \ldots$ between AlAs and GaAs with a precision on the order of 0.001 Ry, which seems extremely optimistic if one compares the pseudopotential coefficients obtained in the literature for these materials. In the following, we propose a way to link the spatially dependent function $\Delta V(\mathbf{r})$ with effective parameters such as the band offsets used in the classical EFT, and therefore simplify these matrix elements. It follows from the "bond potential well" picture that the X' function entering this expression is similar to the X' function of bulk GaAs and the Y' function close to that of bulk AlAs. We note that the general features of these functions depend very little on the material. Also, if the localization of the microscopic function in the corresponding potential wells is strong enough, $\alpha(\mathbf{r})$ is close to zero in the region where Y' is nonvanishing, and close to 1 in the region where X' is nonvanishing. Within these approximations, which are discussed numerically in the following, the splitting approximates to $\langle X'|\Delta V(\mathbf{r})|X'\rangle$, which will be shown to be the valence band offset between the two materials. The correctness of this result is linked to the degree of localization of the X' and Y' functions with respect to the step change of the microscopic potential, and to the validity of this potential. In order to check this, we have calculated the degree of localization of the pseudopotential functions in a bulk GaAs unit cell. In the following, all numerical values are based on the pseudopotential form factors from Ref. 9. We obtain a strong localization of the Bloch functions: 65% of the charge of the X' state is in the upper half cell when partitioning the cell with a step function $Y(z)$, but the figure becomes 88% when using the "waffle" step function $W(\mathbf{r})$ between each half monolayer. Therefore,

$$\langle X'|\alpha(\mathbf{r})|X'\rangle \approx \langle X'|X'\rangle = 1,$$

hence

$$\langle X'|\alpha(\mathbf{r})\Delta V(\mathbf{r})|X'\rangle \approx \langle X'|\Delta V(\mathbf{r})|X'\rangle,$$

$$\langle Y'|\alpha(\mathbf{r})|Y'\rangle \approx 0,$$

hence

$$\langle Y'|\alpha(\mathbf{r})\Delta V(\mathbf{r})|Y'\rangle \approx 0.$$

We now need to define properly the valence band offset between the two materials from a microscopic point of view, and to link it with the matrix element $\langle X'|\Delta V(\mathbf{r})|X'\rangle$. We shall compare two bulk unit cells of GaAs and AlAs far from the interface. They are described by two Hamiltonians which differ only by the potential $\Delta V(\mathbf{r})$ introduced previously

$$H_{\mathrm{AlAs}}=H_{\mathrm{GaAs}}+\Delta V(\mathbf{r}).$$

The band offset is the difference of energy of the zone center ($k=\mathbf{0}$) Bloch states between these two Hamiltonians. If the Bloch functions change very little from one material to the other, a first order perturbation will directly give the difference of energy between the Bloch states in AlAs and GaAs:

$$E_v^{\mathrm{AlAs}}=E_v^{\mathrm{GaAs}}+\Delta E_v\approx E_v^{\mathrm{GaAs}}+\langle X|\Delta V(\mathbf{r})|X\rangle,$$

$$E_c^{\mathrm{AlAs}}=E_c^{\mathrm{GaAs}}+\Delta E_c\approx E_c^{\mathrm{GaAs}}+\langle S|\Delta V(\mathbf{r})|S\rangle.$$

In order to determine numerically this general result, we first need to adjust the constant coefficient ΔV_0 to reproduce correctly the valence band offset. By setting $\Delta V_0 = -0.12\,\mathrm{eV}$ and diagonalizing separately the two Hamiltonians, we can reproduce the physical offset $\Delta E_v = -0.562\,\mathrm{eV}$, which lies within 10% of the first order approximation $\langle X|\Delta V(\mathbf{r})|X\rangle = -0.525\,\mathrm{eV}$, where the function X used is the Bloch state of bulk GaAs. Intuitively, we can say that the band offset viewed by a given Bloch state $|X\rangle$ is the average value of the microscopic function $\Delta V(\mathbf{r})$ in the region where $|X\rangle$ has its maximum of density. Combining the previous results, we can conclude that the energy splitting between X' and Y' states over an interface cell is the valence band offset, which is exactly the result first predicted in the H_{BF} formalism using projection operators

$$\langle X'|\alpha(\mathbf{r})\Delta V(\mathbf{r})|X'\rangle-\langle Y'|\alpha(\mathbf{r})\Delta V(\mathbf{r})|Y'\rangle=\Delta E_v.$$

One can easily compare the above result with a fully numerical evaluation of the above matrix elements, using bulk GaAs Bloch states and expanding the function $\alpha(\mathbf{r})\Delta V(\mathbf{r})$ in the special case of a waffle interface. It yields a splitting of 0.511 eV, in close agreement with the valence band offset. The crucial point is that even this fully numerical computation requires us to first adjust properly the constant coefficient ΔV_0. We can conclude that in a nonself-consistent approach, the $X'-Y'$ splitting is essentially governed by the valence band offset at the interface, and not by the microscopic details of the change of potential between the two materials. Of course, the splitting might be reduced in the case of a smoothed interface potential, but this main feature will remain.

C. Role of the envelope functions

In order to fully understand the role of the interfaces on the electronic structure of a QW we shall present two equivalent and complementary points of view. In the case of common atom interfaces being most interesting when an electric field is applied to the heterostructure, we shall consider a microscopic potential $V(\mathbf{r})=V_{\mathrm{GaAs}}(\mathbf{r})+eFz+\alpha(\mathbf{r})\Delta V(\mathbf{r})$, and study the states corresponding to $\mathbf{k}_\perp=\mathbf{0}$. The Bloch functions change very little between two III–V materials, although the energy gaps and therefore the effective masses can be very different. The first point of view is to start from an EFT in which we neglect the coupling introduced by $\alpha(\mathbf{r})\Delta V(\mathbf{r})$ between states of opposite symmetries such as X and Y, treating it later as a perturbation. The first part can be diagonalized by a block in each subspace of symmetry X, Y, or combinations of Z and S (because of the $\mathbf{k.p}$ coupling between these states). This problem has been solved long ago in the framework of the classical envelope function theory. The upper valence states we are interested in are essentially of the form f_iX_v, f_iY_v, where the f_i are different envelope functions, plus a small contribution from higher X_c and Y_c bands of no interest here. The envelopes above already include the effect of the electric field. At this point, one should notice that a careful treatment yields exactly the same envelope functions $\{f_i\}$ for both X and Y symmetries. We shall now introduce the $X-Y$ coupling as a perturbation on the previous basis, that is evaluate the matrix elements $\langle f_iX|\alpha(\mathbf{r})\Delta V(\mathbf{r})|f_jY\rangle$, where the integration is performed over all the crystal. In order to gain some physical insight into this rather complicated function, we will make use, as in the previous section, of the fact that $X.Y=1/2(X'^2-Y'^2)$. Following the original idea of the H_{BF} model, the crystal can be partitioned into half monolayers, using appropriate (waffle-like) interfaces between them to separate the regions of space closer to a forward or backward chemical bond. The localization properties of the X' and Y' states discussed above imply that the $X-Y$ coupling can be seen as a sum over each half monolayer of the average valence band potential times the product of the envelope functions with alternating signs corresponding to forward and backward bonds. The sum takes place over each half monolayer of the crystal, not only on the interface cell. The envelope function weight is evaluated in the plane corresponding to the maximum of density of X' and Y', respectively. For simplicity, we can assume quasigermanium Block functions, and take the value of the envelopes at the center of each chemical bond. Each term of the sum essentially cancels with its neighbors, except for the small changes of the envelope function weight or the potential discontinuities. A careful treatment of these cancellations in the case of a common atom QW with two abrupt interfaces gives

$$\langle f_iX|\alpha(\mathbf{r})\Delta V(\mathbf{r})|f_jY\rangle=a/2\cdot[f_i(Z_{\mathrm{int1}})f_j(z_{\mathrm{int1}}) - f_i(z_{\mathrm{int2}})f_j(z_{\mathrm{int2}})]\cdot\Delta E_v/4.$$

The factor $a/2$ corresponds to the thickness of a monolayer, and must be introduced because of the normalization of the envelope functions. A minus sign appears because of the opposite orientation of the two interfaces. It shows that in the case of a perfect common atom QW (the well and barrier share a common atom) two envelope functions of the same symmetry are not coupled by the interfaces, which is consistent with the D$2d$ symmetry of such a system: in theory, an AlAs–GaAs QW cannot be anisotropic unless an electric field is applied along the growth direction and breaks the

symmetry of opposite interfaces. The main difference between this approach and the original $H_{\rm BF}$ model[3] is that we have taken into account the fact that the envelope functions vary slightly between two half monolayers. This change yields a model no longer dependent on the choice of the cells used to partition the crystal,[10,11] and divides the final result by a factor 2. Another point of view giving the same result without having to deal directly with the envelopes throughout the crystal is to make the summation over monolayers centered on a chemical bond rather than on an anion or a cation. In this case, the average positions of X' and Y' densities in each cell is the same, canceling any effect of slow variations of the envelopes, and leaving the sole contribution of the two interface singularities. The concepts introduced in the calculation of these matrix elements are very general and will be generalized to NCA interfaces and to the coupling between heavy and light holes.

Using the same arguments, we can determine that there is no direct coupling between $|f_iX\rangle$ and $|f_jY\rangle$ induced by the external electric field (in the quasi-Ge approximation used here): $\langle F_iX|eFz|f_jY\rangle=0$. Yet, the deformation of the envelopes due to the electric field changes the respective weights of the interface contributions, and give rise to a completely original electro-optic effect, the QCPE,[12] first observed by Kwok *et al.*[13] in electroluminescence experiments. A remarkable feature of the QCPE is that it does not rely on the inversion asymmetry of the bulk crystal, and would be observable in QWs made out of centrosymmetric hosts like Ge or Si.

D. Case of interfaces between hosts having no common atom

As first pointed in Ref. 3, the physics involved in the description of NCA interfaces (a situation encountered in the technologically important InAs–GaSb and (InGa)As–InP systems) shows striking differences with the case of common-anion interfaces: in NCA systems, the interfaces involve specific chemical bonds which do not exist in either of the hosts, and in general, the specific bonds involved at the first and second interfaces of a QW differ, so that even in the absence of external electric field, the QW retains the low symmetry of a single interface. In addition, these interface bonds usually undergo considerable strain. In this section we shall use as an example an interface having the following sequence:...–In–As–Ga–Sb.... Although InAs and GaSb are almost lattice matched, the structure contains a highly strained half monolayer composed of As–Ga chemical bonds, all lying in the same plane, let's say $y'=0$. Obviously, the potential wells associated with these bonds differ from the neigboring "bulk-like" potential wells by their native pseudopotential coefficients, and by the effect of strain. As found numerically in *ab initio* calculations,[8] the latter effect is probably the dominating one. It can be understood in terms of the kinetic energies of the different valence states. In the present example, the As–Ga half monolayer experiences a 15% tensile strain along the x' axis. Let us formally consider the effect of such a deformation ϵ on the Block states of a unit cell of bulk GaAs experiencing the same strain. The characteristic variation length $d_{x'}$ of Bloch functions along x' depends linearly on the strain, therefore the kinetic energy contribution along this direction shall be reduced by 30%. Since the valence state of symmetry X' has a node in the plane $x'=0$, most of its kinetic energy is due to the x' contribution, unlike the states Y' or Z (the latter being mixed with S states by this uniaxial strain). The total kinetic energy of unstrained GaAs valence states calculated by pseudopotentials being of 16 eV, we can expect the X' state kinetic energy to be shifted typically by an order of magnitude of -3 eV with respect to unstrained bulk GaAs. Of course, this huge effect is compensated in part by charge transfers and by the associated compressive strain along the z direction, but it is clear that it contributes by an enormous amount to the $X'-Y'$ energy splitting.

We shall not attempt here to guess an approximate geometry and microscopic potential $V(\mathbf{r})$ at the interface to compute the splitting between X' and Y' but rather show how effective parameters can be introduced to characterize an interface. Following the ideas of Sec. IV we can define an average valence potential for the states of symmetry X' in this half monolayer by taking the matrix element $V_{\rm GaAs}=\langle X'|V(\mathbf{r})|X'\rangle_{1/2\rm cell}$ over the region of space closer to the GaAs bonds, which is in practice between two waffle interfaces. The Block state X' formally used in this matrix element is similar to the Block states of InAs and GaSb since their geometrical features are essentially governed by the length of the chemical bond along x', which is imposed by the substrate, the direction z having only a very secondary effect here. One should note at this point that although we may get a physical idea of the shape of the bond QWs associated with the GaAs half monolayer, that is the pseudopotential coefficients of the strained bond, we have no means to properly fit the constant ΔV_0 in this part of the crystal since it cannot be adjusted with an experimental band offset. Hence, evaluating this potential is absolutely impossible without performing detailed self-consistent calculation because of the large charge transfer effects and the modifications of energy levels due to the strain. Therefore, we shall consider it as a characteristic of the interface, to be matched with experiments.

A NCA single interface can be viewed as two consecutive common atom interfaces with opposite orientations, yielding a $X-Y$ coupling of the following form:

$$\langle f_iX|V(\mathbf{r})|f_jY\rangle=a/2\cdot[f_i(z_{\rm int})f_j(z_{\rm int})]\cdot[(V_{\rm InAs}-V_{\rm GaAs})-(V_{\rm GaAs}-V_{\rm GaSb})]/4,$$

which is proportional to the difference of valence band offsets of the two consecutive virtual common atom interfaces, $V_{\rm InAs}$ and $V_{\rm GaSb}$ being the valence band potential in the two bulk materials. Since the high interface strain can move the X' valence energy level far from the valence energies of both InAs and GaSb, we can expect this interface coupling to be much higher than in the case of a simple common atom interface and, of course, to depend drastically on the growth sequence. Experimentally, in the case of (InGa)As–InP

quantum wells,[14] the typical order of magnitude for these interface potentials is 1 eV, which leads to matrix elements of a few meV. This means that in the zero spin orbit limit, the optical absorption spectra of such heterostructures should show a polarization dependent optical gap. As we shall now point out, this effect is strongly modified by the large mixing of valence states due to the spin-orbit coupling.

E. Spin-orbit coupling

Although the analysis of symmetry breakdown we have discussed above describes correctly the microscopic effect of interfaces, it misses the introduction of spin-orbit coupling effects. The matrix elements due to the interface symmery breakdown (a few meV) are about two orders of magnitude smaller than the spin-orbit coupling constant (a few hundred meV). Therefore, spin-orbit interaction cannot be treated as a perturbation over the states of symmetry X', Y', and Z. Instead, the interface effect can be conveniently treated as a perturbation in the traditional heavy and light hole basis that diagonalizes the spin-orbit interaction. The top valence band zone center states of a bulk material: $H+,L+,H-,L-$ are expressed as combinations of X, Y, and Z Bloch states with appropriate spins: for example,

$$H+=\frac{1}{\sqrt{2}}(X+iY)\uparrow,\quad L-=-\frac{1}{\sqrt{6}}(X-iY)\uparrow-\sqrt{\frac{2}{3}}Z\downarrow.$$

Following the procedure of section II C, we can diagonalize the Hamiltonian $H=E_c+V(\mathbf{r})+H_{so}$ in each symmetry block (with the appropriate conduction bands to take into account the **k.p** coupling) and then treat the interblock matrix elements as first order perturbations. This means that we need to evaluate matrix elements between states which are essentially of the form $|f_{Hj}H+\rangle$ and $|f_{Lj}L-\rangle$, plus small contributions from higher zone center states essentially negligible in the context of interface couplings. If we develop the Block function part of the matrix element $M^{ij}_{H+L-}=\langle f_{Hi}H+|V(\mathbf{r})|f_{Lj}L-\rangle$, the only nonvanishing contribution will be of the form $-i/\sqrt{3}\langle X|V(\mathbf{r})|Y\rangle$, which means that the heavy–light hole coupling (HH–LH) is directly proportional to the XY coupling calculated with appropriate envelope functions. In the case of a single NCA interface, we simply get

$$M_{Hi-Lj}=\frac{i}{\sqrt{3}}\frac{a}{2}\cdot[f_i(z_{\text{int}})f_j(z_{\text{int}})]\cdot[(V_{\text{InAs}}-V_{\text{GaAs}})-(V_{\text{GaAs}}-V_{\text{GaSb}})]/4.$$

The optical selection rules associated with heavy and light holes yield a specific polarization for each transition. The most striking effect in the case of NCA QW is the strong HH1–LH1 coupling arising from the different potentials at successive interfaces. A first order calculation gives a polarization rate in the energy range between the $H1-E1$ and $L1-E1$ transitions given by

$$P=\frac{\alpha_{\max}-\alpha_{\min}}{\alpha_{\max}+\alpha_{\min}}\approx\frac{2}{\sqrt{3}}\frac{M_{H1-L1}}{L1-H1}.$$

Because of sum rules, this polarization becomes almost zero at energies above the $L1-E1$ transition. It is interesting to note that the spectral width of the effect is fixed by the different confinement of heavy and light holes, while its magnitude depends on the weight of envelope functions at the interface, and specific properties of this interface.

III. EXPERIMENTAL CHARACTERIZATION OF HETEROSTRUCTURE INTERFACES

The main difference between real and ideal quantum wells is that the former do not have nominal growth sequences because of atom exchange and segregation mechanisms,[14,15] composition overshoots due to transients, and localized steps appearing at the interface. Even in the case of the most studied systems. GaAs–AlGaAs, it has been shown that interfaces have an exponential ''relaxation'' profile rather than a composition discontinuity. This implies that even nominally square, common anion QWs may actually show a small optical anisotropy associated with slightly asymmetric composition profile. Conversely, if anion exchange during the growth interruption, which is required to commute four chemical species in any epitaxial system, is highly symmetric, the symmetry of a NCA QW may be of the D $2d$ type. For instance, let suppose that the anion $A1$ is much more stable than $A2$: one may program the nominal growth sequence $C1-A1-C2-A2-(—)-C2-A2-C1-A1$, and actually get the symmetrical sequence $C1-A1-C2-A2-(—)-C2-A1-C1-A1$ because the last plane of $A2$ has been replaced by a plane of $A1$ before the growth starts again. Polarization resolved spectroscopy associated with proper modeling is a nice spectroscopic tool to elucidate these phenomena. In general, zero electric field data contain the information on the sum of the interface effects, and must be completed with the study of the QCPE which allows discrimination of the two interface contributions. Needless to mention that polarization-resolved spectroscopy is subject to many artefacts, especially when searching for polarization rates on the order of 1%. A conventional setup with careful data analysis gives a typical 0.5% limit, which can be improved—at least—one order of magnitude by using polarization modulation.

We illustrate these trends with results obtained in the (InGa)As–InP system which is of special importance because this is the key material for optoelectronics at 1.55 μm. Photocurrent spectroscopy is a nearly ideal tool in this case. Figure 6 compares the polarization spectra obtained from photocurrent spectroscopy at 77 K in (InGa)As–(AlIn)As and (InGa)As–InP QWs having similar quality and similar parameters (nominal well width of 100 Å). The former sample shows nearly isotropic properties, while the latter shows a ''giant'' dichroism corresponding to an absorption polarization rate of 10% between the $H1-E1$ and $L1-E1$ transitions. Corresponding calculations are also shown. The results in (InGa)–InP imply strongly asymmetric interface

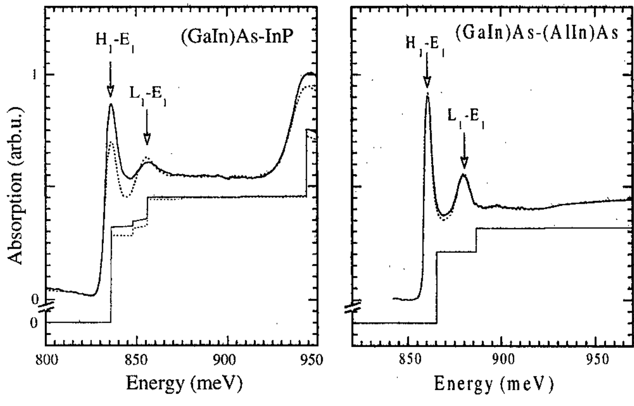

FIG. 6. Polarization-resolved absorption spectra (obtained from transmission spectroscopy at 77 K) in nominally 100-Å-thick (GaIn)As–InP (left) and (GaIn)As–(AlIn)As (right). The former shows a strong in-plane anisotropy in the spectral range between the $H1-E1$ and $L1-E1$, while the latter shows essentially isotropic properties. Displayed polarizations are along the [110] and [−110] directions, respectively. The calculated band-to-band spectra (shifted by an arbitrary 7 meV to account for exciton binding energy) are also shown.

potentials on the order of 1 eV. A more detailed insight is obtained from the analysis of the QCPE. The polarization spectra at various applied electric fields are shown in Fig. 7, together with the corresponding band-to-band calculations. The agreement is essentially satisfactory (the calculation does not include excitons, which obviously contribute to the low temperature spectra in these high quality samples). Ex-

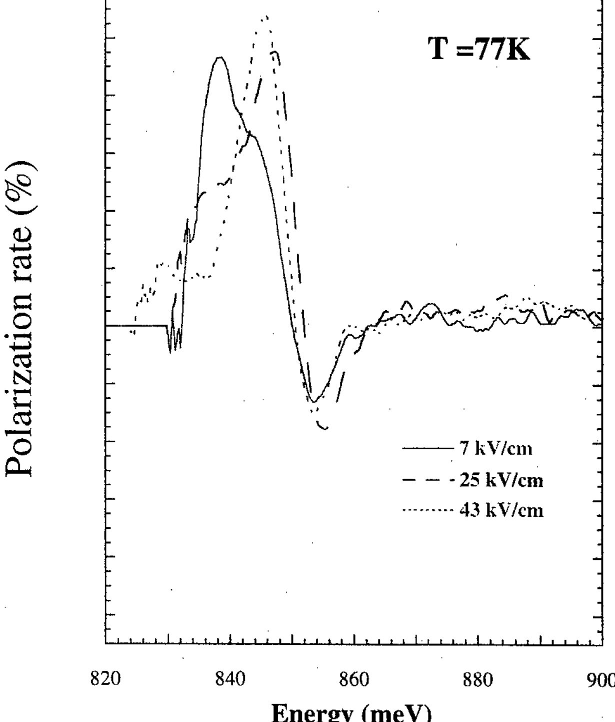

FIG. 7. Electrical field dependency of the absorption polarization ratio in the (InGa)As–InP QW of Fig. 6, showing the phenomenology of the QCPE.

citonic effects influence the QCPE in particular in the vicinity of the $H2-E1$ transition.[16] The dependency of the polarization rate on the well width is illustrated in Fig. 8. Calculations use the same set of interface potentials for the three samples ($V1 = 1.1$ eV, $V2 = -0.2$ eV). It is finally interesting to compare samples obtained with different growth techniques. In particular, the growth interruption times are in general longer in the case of an ultravacuum technique like conventional molecular beam epitaxy (MBE) or gas-source (GS) MBE than in atmospheric pressure metalorganic chemical vapor deposition (MOCVD). In Fig. 9 we show the QCPE data obtained in a top-quality (InGa)As–InP QW grown by GS-MBE. Nearly zero polarization is observed in flatband conditions, which indicates that the interfaces are close to symmetrical. Yet, in the presence of an electric field, a large polarization appears which implies an interface potential much larger than the band offset. Similar GaAs–AlGaAs or GaInAs–AlInAs wells show nearly no polarization under equivalent polarizations. This indicates that NCA QWs do have specific interface properties, but one can act on the overall symmetry of the QW with the growth procedure. Equivalent trends have recently been reported in the case of BeTe–ZnSe type II QWs.[17]

Another issue of interest is the role of interface sharpness. In the limit of a CA QW defined by a smooth cation composition profile $V(z)$, the sum of unit cell contributions is written

$$M_{HiLj} = \frac{ia}{8\sqrt{3}} \int dz\, f_{Hi} f_{Lj} \frac{\partial V}{\partial z}.$$

Again, this formula differs from Eq. (2) of Ref. 3 by a mere factor of 2, and the present result does not depend on the choice of unit cell. Obviously, as long as the symmetry of the QW is preserved, no anisotropy is generated. However, in the case of segregation profiles, which are by construction smooth and asymmetrical, some zero-field anisotropy becomes observable. Numerical estimates for a 100 Å GaInAs–AlInAs QW indicate polarization rates in the 2% range, which are within reach of careful experiments. Hence, polarization-resolved spectroscopy has a very good potential for the nondestructive characterization of burried semiconductor interfaces.

IV. IMPLICATIONS FOR OPTOELECTRONIC DEVICES BASED ON NCA QWs

The effects discussed in the preceeding sections also have a non-negligible impact on the physics of optoelectronic devices. A nearly trivial example of such impact is the situation of vertical cavity surface emitting lasers (VECSELs). In systems governed by the $D2d$ symmetry, there is no anisotropy at all and VECSEL emission has a polarization degeneracy. In practice, this means that the actual polarization of a device is totally unstable and flips randomly. Conversely, if the $C2v$ symmetry prevails, the laser emission always begins with the polarization of the largest optical absorption (or,

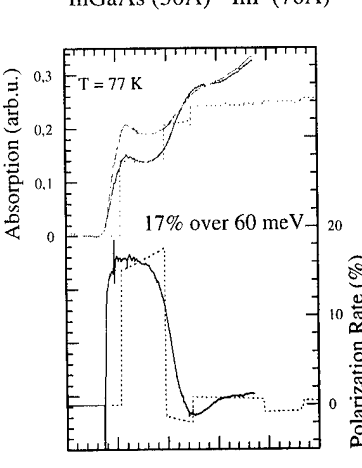

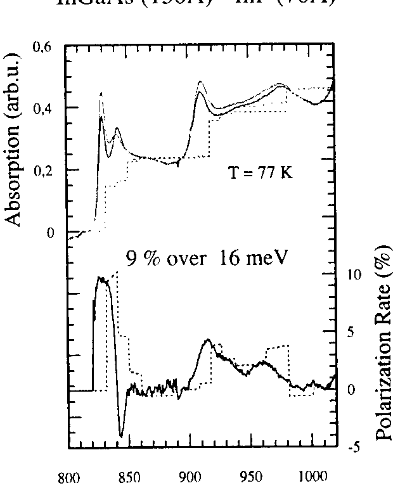

FIG. 8. Well-width dependency of the optical anisotropy in a series of MOCVD-grown (InGa)As–InP quantum wells, and corresponding calculations using the same set of "interface potentials" ($V1 = 1.1$ eV, $V2 = -0.2$ eV).

equivalently, largest gain). Such polarization stability has indeed been observed systematically in VECSELs based on the (InGa)As–InP system, as well as in blue light emitting devices based on NCA II–VI compounds. A different topic is the use (or undesired presence) of the QCPE in guided-wave optoelectronic devices. From numerical simulation of such devices, we estimate that Fabry–Pérot electro-optical modulators working in the transparency region (hence having a constant finesse) should be within reach, but the situation of guided wave devices is probably more pertinent. The guided wave counterpart of the polarization anisotropy observed in "vertical" configuration is an anisotropy of the effective optical index as a function of propagation direction. The effect observed in a waveguide containing (InGa)As–InP QWs is shown in Fig. 10: effective index of the in-plane polarized transverse electric (TE) mode for (110) and (−110) propagations clearly differ, while their z-polarized transverse magnetic (TM) mode counterpart is perfectly isotropic.[18–20] We note that these observations are fitted with the appropriate Kramers–Kronig transform of optical absorption differences, which implies that the other critical points of the Brillouin zone (namely the $E1$ and $E'1$ gaps) do not contribute significantly to overall anisotropy in these samples. The QCPE manifests itself as a linear field dependence of the optical index which adds to the quadratic dependence associated with the quantum confined Stark effect: depending on the field direction and/or propagation direction, one gets an enhanced or decreased index modulation, which is certainly relevant to the optimization of interferometric devices such as the Mach–Zehnder modulator.

V. CONCLUSION

We have discussed recent developments of the physics of rotational symmetry breakdown at semiconductor interfaces, which have quantitatively important influence on the optical properties of NCA QWs. The present approach brings support (and also, correction of some mistakes) to the heuristic H_{BF} model that we proposed in 1996. The new theory bridges the gap between the atomistic theory based on empirical pseudopotentials and the user-friendly envelope-function approach. In-fine, fully *ab initio* calculations are certainly required to determine theoretically the interface potentials, especially in the case of NCA interfaces, but effective parameters obtained by fitting experimental data can be used for a reliable engineering of anisotropy properties. This recently discovered topic has brought in a critical reexamination of the classical EFT of semiconductor heterostructures which, by construction, misses the intracell effect of the composition discontinuity. New, nondestructive experimen-

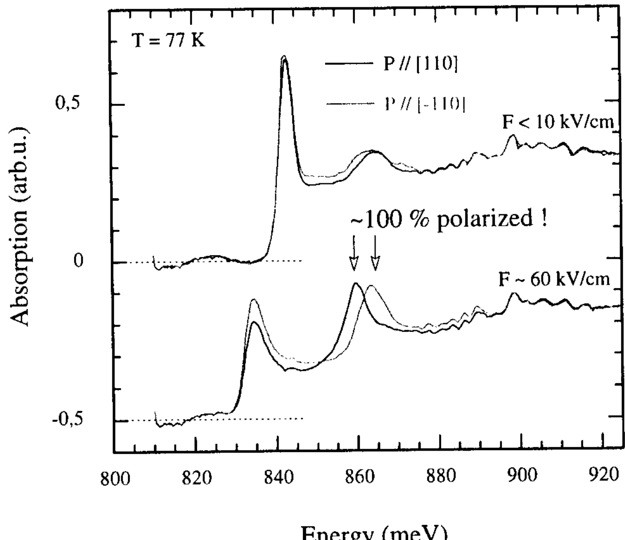

FIG. 9. QCPE spectra in a 78-Å-thick (InGa)As–InP QW grown by GS MBE. The zero-field anisotropy is weak ($D2d$ symmetry presumably induced by anion exchange), but the large Pockels effect indicate large interface potentials in this NCA system.

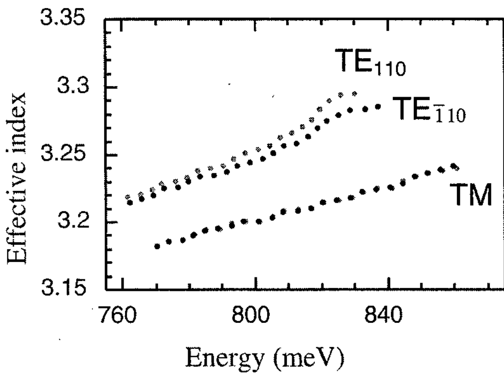

FIG. 10. Anisotropy of the TE mode effective index with respect to propagation direction in a monomode planar waveguide containing 50-Å-thick (InGa)As–InP QWs. The TM mode effective index is isotropic.

tal insight into the properties of semiconductor interfaces is allowed by polarization-resolved spectroscopy of semiconductor QWs. A completely new linear electro-optical phenomenon, the QCPE results from the reduced symmetry of interfaces and appears to have a significant impact on a variety of optoelectronic devices.

ACKNOWLEDGMENTS

The authors would like to acknowledge fruitful discussions and/or collaboration with many colleagues: E. Ivchenko, R. Magri, S. Ossicini, D. Bertho, C. Jouanin, J. M. Jancu, L. Vervoort, and A. Zunger. They express their gratitude to the epitaxists who have grown the samples used in the experimental part of this work: J. L. Gentner, D. Rondi, J. C. Harmand, J. P. André, and F. Mollot.

[1]J. N. Schulman and Y. C. Chang, Phys. Rev. B **31**, 2056 (1985); **31**, 2069 (1985).
[2]O. Krebs, W. Seidel, J. P. André, D. Bertho, C. Jouanin, and P. Voisin, Semicond. Sci. Technol. **12**, 938 (1997).
[3]O. Krebs and P. Voisin, Phys. Rev. Lett. **77**, 1829 (1996).
[4]E. Ivchenko, A. Kaminski, and U. Rössler, Phys. Rev. B **54**, 5852 (1996); E. Ivchenko, A. Toropov, and P. Voisin, Phys. Solid State **40**, 1748 (1998).
[5]B. Foreman, Phys. Rev. Lett. **81**, 425 (1998).
[6]R. Magri *et al.*, Phys. Rev. B **58**, R1742 (1998).
[7]J. M. Jancu (private communications and unpublished results).
[8]R. Magri and S. Ossicini, Phys. Rev. B **58**, R1742 (1998).
[9]E. Caruthers and P. J. Lin-Chung, Phys. Rev. B **17**, 2705 (1978).
[10]B. Foreman, Phys. Rev. Lett. **82**, 1339 (1999).
[11]O. Krebs and P. Voisin, Phys. Rev. Lett. **82**, 1340 (1999).
[12]O. Krebs, D. Rondi, J. L. Gentner, L. Goldstein, and P. Voisin, Phys. Rev. Lett. **80**, 5770 (1998).
[13]S. Kwok, H. Grahn, K. Ploog, and R. Merlin, Phys. Rev. Lett. **69**, 973 (1992).
[14]J. M. Moison, C. Guille, F. Barthe, F. Houzay, and M. Van-Rompay, Phys. Rev. B **40**, 6149 (1989).
[15]J. M. Gérard and J. Y. Marzin, Phys. Rev. B **45**, 6313 (1992); J. M. Gérard, Appl. Phys. Lett. **61**, 2096 (1992).
[16]A. Toropov, E. Ivchenko, O. Krebs, and P. Voisin, Phys. Rev. B (submitted).
[17]A. Platonov, V. Kochereshko, E. Ivchenko, G. Mikhailov, D. Yakovlev, M. Keim, W. Ossau, A. Waag, and G. Landwehr, Phys. Rev. Lett. **83**, 3546 (1999).
[18]H. Jeon, V. Kozlov, P. Kelkar, A. V. Nurmiko, C. Chu, D. Grillo, J. Han, and R. Gunshor, Appl. Phys. Lett. **67**, 1668 (1995).
[19]T. Guettler, Ph.D. thesis, Université Paris VI, 1999 (in French).
[20]T. Guettler, O. Krebs, P. Voisin, G. Faini, D. Rondi, and C. Alibert, Appl. Phys. Lett. **75**, 1890 (1999).

Optical properties of bulk and thin-film $SrTiO_3$ on Si and Pt

Stefan Zollner,[a] A. A. Demkov, R. Liu, P. L. Fejes, R. B. Gregory, and Prasad Alluri
Motorola Semiconductor Products Sector, MD M360, 2200 West Broadway Road, Mesa, Arizona 85202

J. A. Curless, Z. Yu, J. Ramdani, and R. Droopad
Motorola Physical Sciences Research Laboratories, Tempe, Arizona 85284

T. E. Tiwald, J. N. Hilfiker, and J. A. Woollam
J. A. Woollam Company, 645 M Street, Suite 102, Lincoln, Nebraska 68508

(Received 17 January 2000; accepted 5 April 2000)

We have studied the optical properties (complex dielectric function) of bulk $SrTiO_3$ and thin films on Si and Pt using spectroscopic ellipsometry over a very broad spectral range, starting at 0.03 eV [using Fourier transform infrared (FTIR) ellipsometry] to 8.7 eV. In the bulk crystals, we analyze the interband transitions in the spectra to determine the critical-point parameters. To interpret these transitions, we performed band structure calculations based on *ab initio* pseudopotentials within the local-density approximation. The dielectric function was also calculated within this framework and compared with our ellipsometry data. In the FTIR ellipsometry data, we notice a strong lattice absorption peak due to oxygen-related vibrations. Two longitudinal optic (LO) phonons were also identified. In $SrTiO_3$ films on Si, the refractive index below the band gap decreases with decreasing thickness because of the increasing influence of the amorphous interfacial layer between the $SrTiO_3$ film and the Si substrate. There is also a decrease in amplitude and an increase in broadening of the critical points with decreasing thickness. In $SrTiO_3$ films on Pt, there is a strong correlation between the crystallinity and texture of the films (mostly aligned with the Pt pseudosubstrate) and the magnitude of the refractive index, the Urbach tail below the bulk band edge, and the critical-point parameters. FTIR reflectance measurements of $SrTiO_3$ on Pt (reflection–absorption spectroscopy) show absorption peaks at the LO phonon energies, a typical manifestation of the Berreman effect for thin insulating films on a metal. The Urbach tail in our ellipsomety data and the broadening of the optical phonons in $SrTiO_3$ on Pt are most likely caused by oxygen vacancy clusters. © *2000 American Vacuum Society.* [S0734-211X(00)00904-5]

I. INTRODUCTION

Oxides with perovskite crystal structure, such as $SrTiO_3$, are important candidates for ultrathin gate dielectrics or capacitors (replacing SiO_2 and silicon nitrides) in microelectronics because of their large dc dielectric constant, or permittivity,[1] ϵ_0. $SrTiO_3$ can be grown epitaxially on Si (001), with its unit cell rotated by 45° with respect to the underlying Si substrate, resulting in a lattice mismatch of only 1.7%. Equivalent gate oxide thicknesses on the order of 10 Å with low leakage currents have been achieved.[2–6] When $SrTiO_3$ is deposited directly on Si, an amorphous nonstoichiometric interfacial layer (10–30 Å thick) is usually formed during the later stages of growth, except when the $SrTiO_3$ film is very thin.[2,6] This is undesirable, since it reduces the specific capacitance. Optical tools like spectroscopic ellipsometry can easily be adapted for in-line or *in situ* diagnostics of $SrTiO_3$ on Si, therefore understanding the optical properties of such thin films is important.

Whenever we are interested in the properties of thin films, it is usually a good idea to start with studying the bulk, both theoretically and experimentally (see Sec. II). Following Jellison *et al.*,[7] we measured the dielectric function ϵ of bulk $SrTiO_3$ from 0.03 to 8.7 eV. In comparison with *ab initio* band structure calculations based on the local density approximation using a plane wave basis set, we identify critical points in the spectra due to optical interband transitions from the (primarily) $O(2p)$ valence band to the $Ti(3d)$ conduction band at various regions in the Brillouin zone. We also study the lattice vibrations of $SrTiO_3$ by Fourier transform (FTIR) ellipsometry.

After the completion of this initial step, we discuss the optical properties of $SrTiO_3$ films grown on Si (Sec. III) and Pt (Sec. IV). We compare with data for $SrTiO_3$ films on MgO grown by molecular beam epitaxy (MBE).[7] In particular, we correlate the dielectric functions of $SrTiO_3$ films with structural properties, such as thickness and stoichiometry, crystal quality, grain size and texture in polycrystalline films, and oxygen vacancies.

II. OPTICAL PROPERTIES OF BULK $SrTiO_3$

A. Experimental procedure and results

Two bulk $SrTiO_3$ crystals, (100) oriented and $10\times10\times0.5$ mm in size, were obtained commercially from Princeton Scientific Corporation. One piece was polished on both sides (for transmission measurements), the other one on only

[a]Corresponding author; electronic mail: Stefan.Zollner@motorola.com

one side (for reflection ellipsometry). We followed the procedure of Jellison and co-workers[7] to determine the dielectric function ϵ of $SrTiO_3$ from 0.74 to 8.7 eV.

The ellipsometric angles ψ and Δ were acquired from 0.74 to 6.6 eV in 0.01 eV steps at three angles of incidence (65°, 70°, and 75°) on a Woollam VASE ellipsometer with vertical sample mounting. Our rotating-analyzer instrument uses a computer-controlled MgF_2 Berek waveplate as a compensator to improve the accuracy of the ellipsometric angles, particularly below the onset of direct absorption (at about 3.5 eV). Tests on standard samples, such as a Si substrate, indicate that the accuracy of our commercial instrument approaches or exceeds that of Jellison's two-channel polarization modulation ellipsometer,[8,9] but exceeds its spectral range (1.48–5.3 eV). For an insulator near the band gap with ϵ_1 on the order of 5–10, absorption coefficients of 2000 cm^{-1} and higher can be measured.

We also acquired the ellipsometric angles from 4.25 to 8.7 eV in 0.025 eV steps on the prototype of a commercial vacuum-ultraviolet (VUV) ellipsometer. This rotating-analyzer instrument is also equipped with a MgF_2 compensator. The entire system is purged with dry nitrogen gas to avoid oxygen and water absorption bands and has a fixed angle of incidence of 75.08°. Light from a deuterium lamp passes through a double-chamber Czerny–Turner type monochromator to provide wavelength selection and stray-light rejection. A 0.5 nm bandwidth (25 meV at 8 eV) was achieved by reducing the monochromator slit widths to ensure adequate spectral resolution for the optical features. A photomultiplier tube is used for signal detection.

The deep-UV range above 4 eV is particularly important for large band-gap materials, such as $SrTiO_3$, to reveal the critical points in the spectra, which are related to the quality and composition of the sample. Our experimental data from both instruments are displayed (as a pseudodielectric function) by the dotted line in Fig. 1.

We also measured the transmission of the two-side polished sample in the 1.0–3.4 eV spectral range, using the same VASE ellipsometer in the straight-through configuration at normal incidence. The spectral characteristics of the optical elements (Xe lamp, monochromator, and detector) were taken into account by measuring with and without sample and then normalizing the two spectra. We can measure absorption coefficients between 3 and 150 cm^{-1} with the 0.5 mm thick two-side polished sample, corresponding to transmissions (uncorrected for reflection losses) between 90% and 0.05%, limited by the dynamic range of the Si photodiode used as the detector. The logarithm of the transmission near the band gap is shown as an inset in Fig. 1 (dotted line).

B. Optical constants

It is obvious from Fig. 1 that the imaginary part of the pseudodielectric function ($\langle\epsilon_2\rangle$) is positive below the band gap of $SrTiO_3$ (around 3.2 eV), where the sample is transparent (see inset). We call this a pseudoabsorption and attribute it to the surface roughness of the sample.[7] It is thus

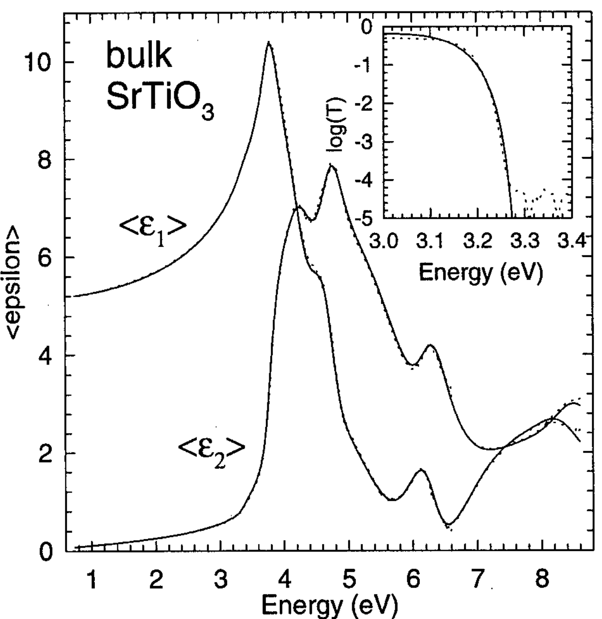

FIG. 1. Pseudodielectric function of bulk $SrTiO_3$ measured using our two ellipsometers to cover the 0.74–8.7 eV photon-energy range (dotted). The inset shows the logarithm of the measured transmission near the band gap (dotted). The solid lines show the data calculated using a model assuming a surface roughness of 24 Å and describing the $SrTiO_3$ optical constants using the Herzinger–Johs parametric oscillator model (Ref. 11) with the parameters given in Table I.

clear that Fig. 1 does not display the *true* dielectric function ϵ of the sample. To determine ϵ of $SrTiO_3$, we simultaneously fit all three data sets in Fig. 1 using a three-phase model (substrate/roughness/ambient). The roughness layer is described within the Bruggeman effective medium theory containing two phases: one with optical properties equal to the substrate (50% volume fraction), the other with optical properties equal to the ambient.[7,10] The optical constants of the $SrTiO_3$ substrate are parametrized using the Herzinger–Johs oscillator model.[11] For the transmission measurement, we also allow roughness on the back surface of the sample. We vary all parameters (those of the oscillator model and the roughness layer thicknesses) until the discrepancy between the model and the data is minimized. The resulting pseudodielectric function and transmission curve are shown by the solid lines in Fig. 1. We find a roughness layer thickness of 24 Å from the ellipsometry spectrum, similar to that of the sample used in Ref. 7 (20 Å). The transmission spectrum is not sensitive to the roughness thicknesses. We set them equal to 24 Å. The parameters of the Herzinger–Johs oscillator model obtained from the fit are given in Table I.

The agreement between our model (solid) and the data (dotted) is excellent (see Fig. 1). There is some difference near the critical points (peaks in the spectra), but it is barely visible. Once we have determined the surface roughness layer thicknesses, we can directly invert our experimental data and find ϵ as a function of photon energy without the need to assume a particular functional form for the dispersion of ϵ. In Fig. 2, we plot the absorption coefficient α determined using this wavelength-by-wavelength fit. There is

TABLE I. Parameters of bulk $SrTiO_3$ for the Herzinger–Johs parametric oscillator model. The first column enumerates the oscillators, the second and third column give the lower (EL) and upper (EU) cutoff of the oscillator with energy EC, amplitude A, and broadening Σ. The remaining columns list the so-called shape parameters describing the lower (L) and upper (U) flanks of the critical points. See Ref. 11 for a detailed description of the parameters.

No.	EL	EU	EC	A	Σ	DISC	L_{pos}	L_{amp}	L_{2d}	U_{pos}	U_{amp}	U_{2d}
0	0	1	3.323	0	50	0	0.5	0.5	0	0.5	0.5	0
1	0	2	3.750	0.253	59	0.015	0.284	0.657	−0.141	0.075	0.086	0.982
2	1	3	4.174	11.518	261	−0.713	0.125	0.017	−1	0.656	0.653	0.729
3	1	4	4.730	9.076	120	0.031	0.243	0.331	−0.308	0.195	0.221	−0.189
4	3	6	6.275	5.664	141	0.076	0.299	0.429	−0.629	0.697	0.312	−0.866
5	4	6	8.424	1.932	306	0.662	0.540	0.343	1	0.366	0	−1
6	6	6	11	167.313	0	0	0.5	0.5	0	0.5	0.5	0

a gap in our data between 3.25 and 3.37 eV, since α between 150 and 2000 cm^{-1} cannot be measured on bulk samples with our setup. Films thinner than 0.5 mm would be needed for such measurements. We partially fill this gap with data by Sata and co-workers,[12] obtained using transmission measurements on thin platelets with a thickness between 60 and 200 μm. The inset of Fig. 2 shows $\sqrt{\alpha}$ near 3.2 eV.

According to Cardona,[13] $SrTiO_3$ has an indirect band gap of about 3.2 eV. This is clearly reflected by the onset of absorption in our data in Fig. 2. A direct gap would lead to a much faster increase of the absorption; see, for example, Fig. 6.15 in Ref. 14 for InSb. Plotting α^2 near 3.2 eV also does not lead to a straight line expected for a direct gap. According to Yu and Cardona[14] (Figs. 6.17–19), plotting $\sqrt{\alpha}$ versus photon energy should result in a stepwise linear behavior related to the various phonons contributing to indirect absorption. This is not observed in our room-temperature data for $SrTiO_3$, possible because of the complicated crystal structure with many phonon modes, some of which are quite low in energy. Nevertheless, we believe that there is an indirect gap with an energy of about 3.1–3.2 eV, but we cannot determine it accurately from room-temperature data. Plotting α^2 in the 3.3–3.6 eV photon-energy range yields a reasonably straight line which crosses the energy axis at roughly 3.4 eV. We thus conclude that there is a direct gap with an energy of about 3.4 eV, just above the indirect gap at about 3.2 eV, which is in good agreement with earlier data.[15,16]

In Fig. 3, we show the dielectric function of bulk $SrTiO_3$ from 0.74 to 8.7 eV (solid lines) calculated from the parametric oscillator model used to fit the experimental data in Fig. 1. A wavelength-by-wavelength fit would result in data not distinguishable from those in Fig. 3. The agreement with the data of Jellison and co-workers[7] in the range of overlap (1.5–5.3 eV) is excellent. The symbols show the data tabulated by Gervais,[17] which were compiled from various sources. The data between 0.9 and 3.0 eV (below the gap)

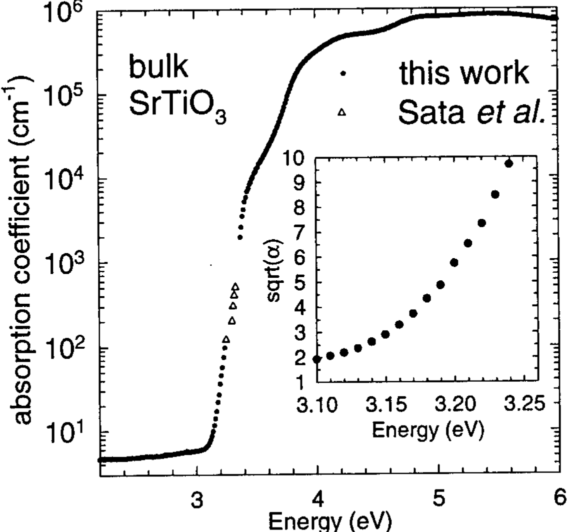

FIG. 2. Semilogarithmic plot of the absorption coefficient α vs photon energy for bulk $SrTiO_3$. The inset shows $\sqrt{\alpha}$ (in units of $cm^{-0.5}$) in the region of the indirect gap (about 3.2 eV). The gap in our data (●) is partially filled by the transmission data of Sata and co-workers (Ref. 12) (△).

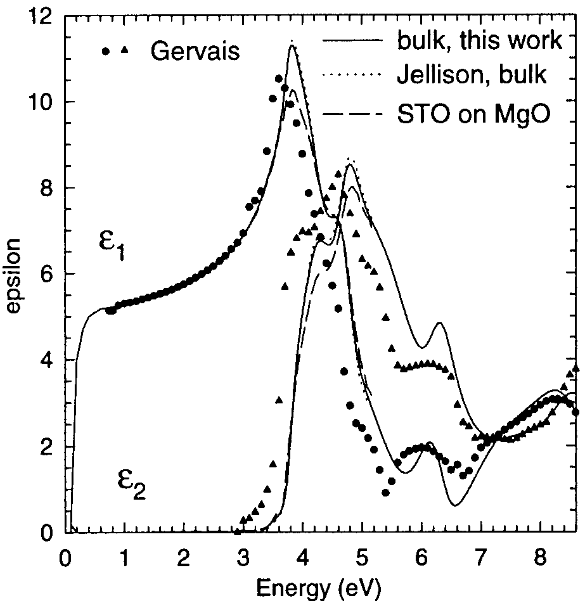

FIG. 3. Dielectric function of bulk $SrTiO_3$ obtained in this work (solid) and in Ref. 7 (dotted) using spectroscopic ellipsometry. Below 0.7 eV, the data were obtained using FTIR ellipsometry. (Symbols) Data from other techniques (Ref. 17). For comparison, the dashed line shows the dielectric function of $SrTiO_3$ on MgO grown by MBE (Ref. 7).

were determined by Cardona[13] using the minimum-deviation prism method, which is the most accurate technique to determine ϵ_1 for a transparent material. Cardona's data are no more than 0.5% higher than those of Ref. 7 and no more than 0.7% larger than ours. Below 0.9 eV, Gervais lists his own data[18] obtained by fitting the infrared spectral region near the lattice absorption using a factorized dielectric response, resulting in ϵ_1 values slightly lower than measured by us. Above the indirect gap, Gervais' data are based on UV reflectivity measurements from 2 to 30 eV combined with a Kramers–Kronig transform.[19] These data are not compatible with ours at all, although there is some resemblance near the critical points. The whole spectrum seems to be shifted toward lower energies and the resolution of the monochromator also may be a problem. The agreement gets better above 6.5 eV.

Simple numerical models are often used for metrology purposes[10] to determine thicknesses of layers (here $SrTiO_3$) on a substrate, such as Si or Pt. A Cauchy model

$$n(\lambda)=n_0+\frac{n_1}{\lambda^2}+\frac{n_2}{\lambda^4} \tag{1}$$

works well in the transparent range below 3 eV (413 nm) with the parameters $n_0=2.281$, $n_1=0.03\,\text{Å}^{-2}$, and $n_2=0.0045\,\text{Å}^{-4}$. A single Lorentz oscillator model

$$\epsilon(E)=\epsilon_\infty+\frac{A}{E_g^2-E^2-i\Gamma E} \tag{2}$$

can be used from 0.74 to 3.4 eV with the parameters $\epsilon_\infty=3.077$, amplitude $A=41.874\,\text{eV}^2$, band gap $E_g=4.466\,\text{eV}$, and broadening $\Gamma=0$. Jellison's Tauc–Lorentz model[20] with a single Lorentz oscillator broadened by an Urbach tail[21] like in amorphous semiconductors can even be used up to 3.5 eV with the following parameters: $\epsilon_\infty=1.668$, amplitude $A=230\,\text{eV}$, broadening $C=1.985\,\text{eV}$, Tauc gap $E_g=3.288\,\text{eV}$, and Lorentz oscillator energy $E_0=4.479\,\text{eV}$. We note that these parameters are not unique. They usually depend strongly on the spectral range to fit the data. Also, they usually carry little physical meaning. No constraints (for example, for ϵ_∞) were applied when fitting these parameters to the measured pseudodielectric function, but the roughness layer (24 Å) was taken into account. Due to the complex critical-point structure of $SrTiO_3$ (see below), using these simple models at higher energies than specified here leads to poor results.

C. Critical points

We have already mentioned that $SrTiO_3$ has an indirect gap at about 3.2 eV and a direct gap of about 3.4 eV. In addition, there are several other structures in the dielectric function at about 3.8, 4.3, 4.8, 6.2, and 8.5 eV. These are van Hove singularities, also known as critical points, related to optical interband transitions from the highest valence bands to the lowest conduction bands at various regions in the Brillouin zone.[14] To study these critical points in more detail, it is customary to calculate the second derivatives of the ϵ

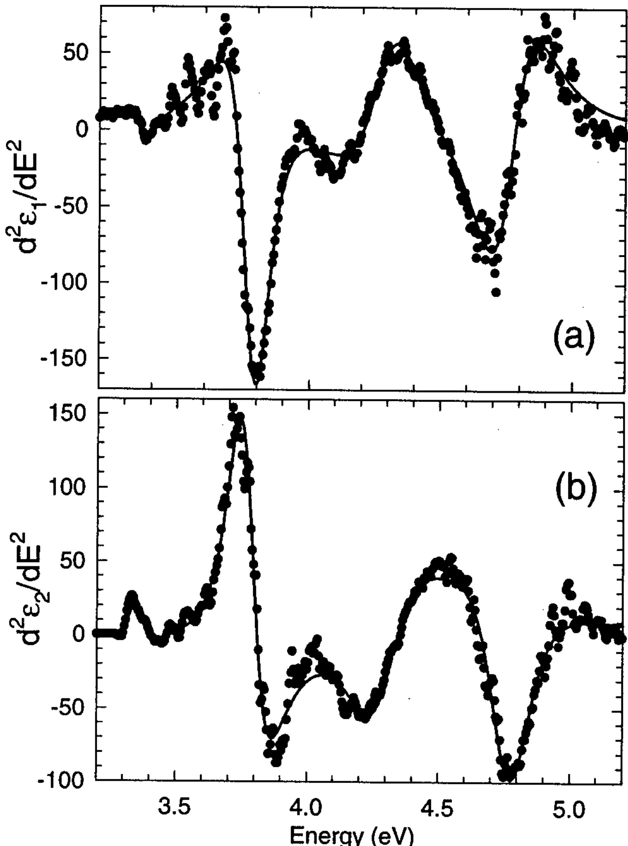

FIG. 4. Second derivative of ϵ vs photon energy in the range of critical points (symbols). The lines show the best fit to analytical line shapes with parameters given in Table II. The derivatives were calculated using the Savitzky–Golay algorithm with 20 points (in 5 meV steps) and fourth-order polynomials.

spectra, which removes the nonresonant background and amplifies the singularities. In the vicinity of the critical points, we used a two-dimensional analytical line shape[22]

$$\epsilon(\hbar\omega)=A\exp(i\phi)\ln(\hbar\omega-E_g+i\Gamma), \tag{3}$$

based on an effective mass approximation for the band structure (with several valleys) and constant (**k** independent) dipole matrix elements, to describe our data. The critical-point parameters are the amplitude A, the energy gap E_g, the broadening Γ, and a phase angle ϕ describing many-body effects and interactions of several critical points fitted with one line shape.

For our critical-point analysis, we acquired data from 2 to 6.6 eV in 0.005 eV steps at a single angle of incidence (70°) without using the compensator, averaging over 400 analyzer cycles per data point to reduce the noise. Then, we determined ϵ in a wavelength-by-wavelength fit using the known roughness layer thickness (24 Å). The derivatives were calculated using the Savitzky–Golay algorithm. Next, we determined the critical-point parameters in comparison with the analytical line shapes in Eq. (3) using a least-squares minimization with the Marquardt–Levenberg algorithm.[23] Our results are shown in Fig. 4 and Table II. Above the lowest

TABLE II. Critical-point parameters (energy E_g, amplitude A, broadening Γ, and phase angle ϕ) determined by fitting the data in Fig. 4 to the two-dimensional analytical line shapes in Eq. (3). The 90% confidence limits are in parentheses. A tentative assignment based on band structure calculations is given in the last column.

	E_g (eV)	Γ (eV)	A (1)	ϕ (°)	Theory (eV)	Assignment
E_i	3.2(1)	N/A	N/A	N/A	3.19	$\Gamma-R$
E_0	3.355(3)	0.058(3)	1.13(5)	113(5)	3.55	Γ
	3.778(1)	0.101(1)	17.17(7)	146(1)		Ti(3d)
	4.291(2)	0.177(2)	11.1(1)	320(1)	4.1, 4.4	X or Γ
	4.760(1)	0.150(1)	15.9(1)	254(1)	5.4	X
	6.15	0.15	N/A	N/A	6.8	M
	7–9	N/A	N/A	N/A		Sr(5d) and sp*

indirect (3.2 eV) and direct (3.4 eV) band gaps, we find higher gaps at about 3.8, 4.3, and 4.8 eV. At even higher energies, there are structures at 6.2 and 7–9 eV, which could not be fitted due to limitations of our software. The broadenings of our critical points are between 60 and 180 meV, not unreasonable for a crystalline material in comparison with Si.[22]

D. Comparison with theory

The most difficult task in analyzing the dielectric function of a material is the assignment of the critical points to optical interband transitions at certain points of the Brillouin zone. Usually, this is done in comparison with band structure calculations. We have therefore calculated the electronic structure of $SrTiO_3$ within the local-density approximation (LDA) using a plane-wave basis set. We used a commercial pseudopotential code (CASTEP), employing a plane-wave energy cutoff of 900 eV, ultrasoft pseudopotentials,[24] and k-space integrations with 40 special points. In general, the good agreement of the early calculations by Mattheiss[25] with our results is remarkable. Similar calculations, focusing less on the optical properties, were also performed using first-principles pseudopotentials[26] and with the linear-muffin-tin-orbitals method.[27]

The crystal structure[25] of $SrTiO_3$ consists of a simple cubic Bravais lattice with a lattice constant of $a=3.905$ Å and one molecular unit per cell [see Fig. 5(a)]. The Ti atom is located at the origin (filled), the Sr atom at the corners (shaded), and the three oxygen atoms (white, all three equivalent, i.e., related by lattice symmetry operations) at the centers of the cube faces. The space group is O_h^1. The Ti and Sr sites have the full O_h symmetry, whereas the site symmetry of oxygen is D_{4h}, that of the face center.[28] The Brillouin zone (BZ) for this lattice is shown in Fig. 5(b). The electronic energies at some high-symmetry directions of the BZ are shown in Fig. 6. In this (uncorrected) band structure, the indirect band gap is only 1.8 eV, less than the experimental band gap of 3.2 eV. This is commonly found in LDA calculations. Table III shows the energies at points of high symmetry. In this table, all conduction band energies were shifted by 1.4 eV to reproduce the experimental band gap.

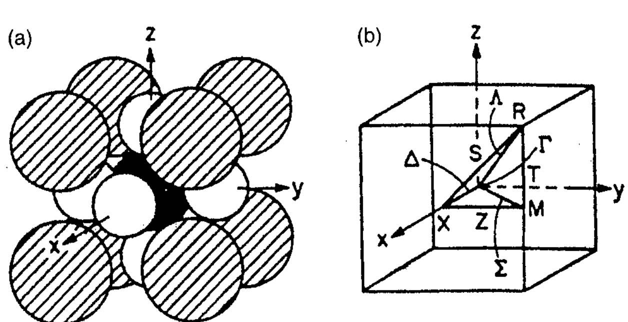

FIG. 5. (a) Unit cell for the perovskite compound $SrTiO_3$. Ti is filled, Sr is shaded, and O is white. (b) Brillouin zone for the simple cubic Bravis lattice.

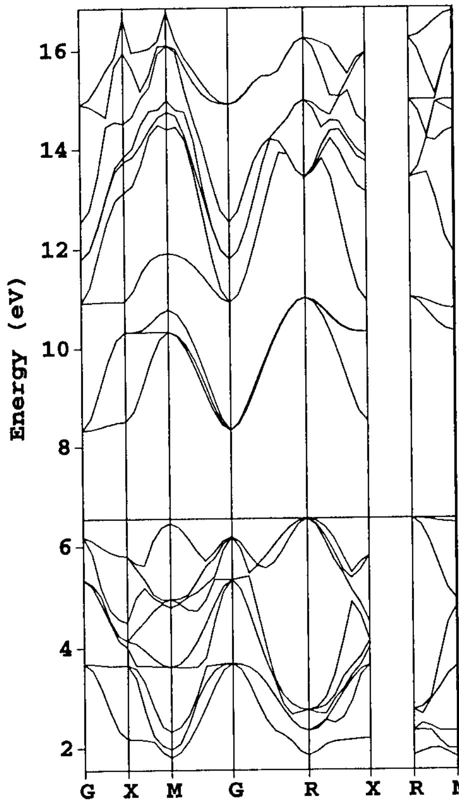

FIG. 6. Band structure of $SrTiO_3$ along some high-symmetry directions calculated using pseudopotentials with a plane-wave basis set within the LDA. The horizontal line shows the top of the valence band.

Our calculation includes the Ti(3s) (band 1, −55.5 eV in our calculation, −62 eV in photoemission[29]), Sr(4s) and Ti(3p) (bands 2–5, −32.1 eV in our calculation, −37 eV in photoemission[29]), O(2s) (bands 6–8, −16 eV in our calculation, −22 eV in photoemission), and Sr(4p) (bands 9–11, −14 eV in our calculation, −20 eV in photoemission) core states, but these bands are at least 14 eV below the valence band maximum and therefore not given in Fig. 6 and Table III. The top nine valence bands (12–20) are primarily of O(2p) character. (We do not find much charge near the Ti atoms.) They have a bandwidth of slightly less than 5 eV, in good agreement with photoemission results.[25,29] The spin-orbit splitting of the O(2p) valence bands is very small.

TABLE III. Calculated energy levels at high-symmetry points. Valence band (top), conduction band (bottom). The conduction bands were shifted by 1.4 eV to overcome the LDA band gap problem. For degenerate states, the energy is only given for the state with the lowest band index (first column). The symmetry notations were taken from Ref. 25. The last line shows the symmetry of the k point (Ref. 33).

Band		Γ		X		M		R
12	Γ_{15}	−2.85	X_1	−4.36	M_3	−4.74	R_1	−4.70
13		⋯	$X_{5'}$	−2.88	M_1	−4.57	R_{12}	−4.19
14		⋯		⋯	M_2	−4.21		⋯
15	Γ_{25}	−1.19	$X_{4'}$	−2.53	M_5	−2.92	$R_{25'}$	−3.78
16		⋯	X_5	−2.40		⋯		⋯
17		⋯		⋯	$M_{4'}$	−1.74		⋯
18	Γ_{15}	−0.36	$X_{3'}$	−2.04	$M_{5'}$	−1.58	$R_{15'}$	0
19		⋯	$X_{5'}$	−0.74		⋯		⋯
20		⋯		⋯	M_4	−0.09		⋯
21	$\Gamma_{25'}$	3.19	X_3	3.37	M_5	5.19	$R_{25'}$	5.88
22		⋯	X_5	5.18		⋯		⋯
23		⋯		⋯	M_3	5.65		⋯
24	Γ_{12}	5.79	X_2	5.81	M_1	6.77	R_{15}	8.28
25		⋯	X_1	7.80	M_2	9.26		⋯
26	Γ_{12}	6.66	$X_{3'}$	8.61	M_1	9.61		⋯
27		⋯	$X_{4'}$	8.71	M_3	9.85	R_{12}	9.85
28	Γ_1	7.39	$X_{2'}$	9.38	M_5	10.96		⋯
29		9.76		10.81		⋯	$R_{12'}$	11.11
30		⋯		11.51	M_4	11.65		⋯
		O_h		D_{4h}		D_{4h}		O_h

The lowest three conduction bands (bands 21–23) are made up of Ti($3d$) bands. They have a bandwidth of 2.7 eV. The other two Ti($3d$) bands usually follow next at higher energies, but they mix with Sr($5d$) states and antibonding Ti, Sr, and O s and p orbitals at some points in the Brillouin zone to form the higher conduction bands. See also the augmented-plane-wave calculations of Mattheiss[25] using *ad hoc* potentials for a similar discussion.

We conclude that the lowest critical points observed in our optical spectra are primarily due to transitions from the O($2p$) valence bands to the Ti($3d$) conduction bands. Therefore, oxygen or titanium vacancies will reduce the amplitude of the peaks and the refractive index below the band gap much more than strontium vacancies. This will be important for the discussion of data on thin films. Interband transitions from the O($2p$) states to the Sr($5d$) states and the sp-antibonding orbitals start at 7 eV, where they give rise to a broad hump in our VUV ellipsometry data.

It can be seen from Fig. 6 and Table III that the valence band maximum is located at the R point, i.e., at the corner of the cubic BZ. The lowest conduction band state is located at the zone center Γ, which gives rise to an indirect band gap. There is a second local valence band maximum at Γ only 0.36 eV lower, which introduces a direct band edge at Γ with an energy of 3.55 eV, in good agreement with the experimentally observed direct gap at 3.4 eV.

Our calculations find the conduction-band minimum at Γ, but the X valley, favored as the global minimum in the early literature,[25,30–32] is only slightly (0.18 eV) higher. The symmetry of the conduction band minimum at Γ is similar to that of the valence band maximum in Si. There is a small spin-orbit splitting of about 38 meV, which leads to light, heavy, and split-off electron bands at Γ (see Mattheiss[25]). This splitting is less than the linewidths of our critical points, therefore the use of a nonrelativistic band structure calculation is justified.

The band structure of $SrTiO_3$ can be integrated to obtain the dielectric function, including the matrix elements of the dipole operator based on our calculated wave functions.[14] As noted before, the conduction band energies were shifted by 1.4 eV to correct the LDA band gap error. We also added a broadening of 0.2 eV to the calculated spectrum to account for the finite lifetime of the valence and conduction band states. The result of this calculation is shown by the solid line in Fig. 7 in comparison with the experimental data (dotted). Given the simple nature of our calculation, which ignores electron–hole interactions and describes the Ti and Sr d orbitals with plane waves (without taking into account the interaction between the sp continuum and localized states), the agreement is reasonable. After correcting the conduction band energies through a rigid shift, the onset of absorption and the peak at 4.2 eV are reproduced very well. The peaks in the measured ϵ_2 at 4.8 and 6.2 eV are also present in the calculation, but blueshifted by 0.5–1 eV. Finally, the calculation correctly finds a minimum of ϵ_2 near 7 eV and a peak at 8.5 eV due to Sr-related states. All peaks except those at the highest energies (where the lifetime broadening may be larger than 0.2 eV) have approximately the correct magnitude. ϵ_1 can be ignored in this discussion, since it is related to ϵ_2 by Kramers–Kronig transform.[14]

At high-symmetry points, group theory[33] can be used to determine if transitions between particular valence and conduction band states are allowed or forbidden. At the Γ and R points, the little group of the **k** vector is O_h, therefore the

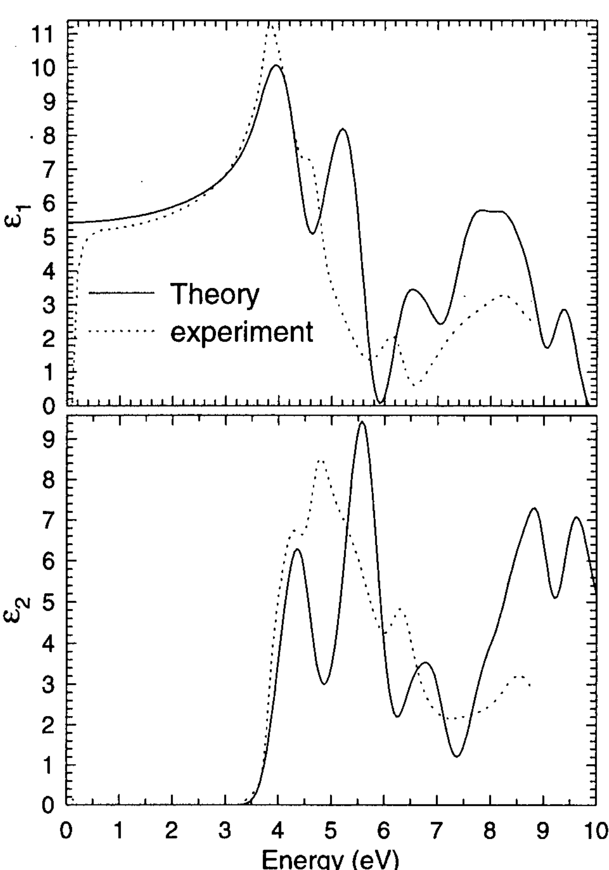

FIG. 7. Dielectric function of $SrTiO_3$ calculated from the LDA band structure in Fig. 6 (solid) in comparison with the experimental data from Fig. 3 (dotted). The conduction bands were shifted by 1.4 eV to overcome the LDA band gap problem and a lifetime broadening of 0.2 eV was added.

selection rules given by Bassani and co-workers[34] for the diamond structure can be applied. Of the possible interband transitions in Table III, only $\Gamma_{25}^{v} \rightarrow \Gamma_{1}^{c}$ is forbidden, the others at Γ are allowed. At the R point, many more transitions are forbidden. It is worth noting that all transitions from the $O(2p)$ valence bands to the lowest $R_{25'}$ conduction band (Ti related) are forbidden. This eliminates contributions to ϵ from the R point in our spectral range.

At the X point, there is a difference between the diamond and perovskite (simple cubic) selection rules caused by the absence of nonprimitive translations in $SrTiO_3$, which make all states at X doubly degenerate in the diamond structure.[33,34] To conserve parity, only transitions between even (unprimed) and odd (primed) states are allowed. At the X point, the dipole operator Γ_{15} splits into $X_{4'}$ and $X_{5'}$, which can be derived from the character tables.[35] The selection rules for optical interband transitions are obtained by reducing the tensor products of the small representations (see Table IV). For example, transitions from the highest (X_5') valence band to any of the Ti-related conduction bands (21–25) are allowed, but to the higher Sr-related conduction bands they are forbidden.

The selection rules at M are the same as those at X, since the little group is the same. At M, transitions from the highest valence band (M_4) to any of the conduction bands in

TABLE IV. Selection rules for optical dipole transitions at the M and X points of the Brillouin zone.

M_i	M_1	M_2	M_3	M_4	M_5
$M_i \otimes M_{4'}$	$M_{4'}$	$M_{3'}$	$M_{2'}$	$M_{1'}$	$M_{5'}$
$M_i \otimes M_{5'}$	$M_{5'}$	$M_{5'}$	$M_{5'}$	$M_{5'}$	$M_{1'}+M_{2'}+M_{3'}+M_{4'}$

Table III are forbidden by parity. Only transitions from the valence bands 17–19 ($M_{4'}, M_{5'}$ symmetry) are allowed.

Based on these group-theoretical considerations and by considering only the contributions from high-symmetry points, we assign the origin of the critical points given by the last column in Table II. This ignores contributions from lines, areas, and volumes with lower symmetry, which are included in the calculation of ϵ in Fig. 7.

E. Lattice dynamics of bulk $SrTiO_3$

To study the lattice dynamics of bulk $SrTiO_3$, we measured the ellipsometric angles from 250 to 7450 cm^{-1} (0.031–924 meV) at four angles of incidence (60°, 65°, 70°, and 75°) using a commercial rotating-compensator FTIR ellipsometer described elsewhere.[36] Our discussion follows that of similar measurements performed by Humlíček,[37] but covers a larger spectral range. At 0.8 eV, our FTIR measurements yield $\epsilon_1 = 5.25$, in good agreement with measurements on the near-IR/visible/UV instrument of 5.23 at 0.8 eV, see above. $\langle \epsilon_2 \rangle$ is slightly positive (0.1) because of surface roughness. At 0.2 eV, ϵ_1 drops to 4.0 because of the influence of the lattice vibrations, but ϵ_2 is still very close to 0. See the low-energy region of Fig. 3.

The ellipsometric angles ψ and Δ in the region of the oxygen lattice vibrations (from 250 to 1000 cm^{-1}), taken at four different angles of incidence, are shown in Fig. 8. ψ is close to 45° over most of this range except for a drop near 500 cm^{-1}, where the oxygen-related transverse optical (TO) phonon is located.[38] By the same token, Δ drops from large values at 250 cm^{-1} to small values at 1000 cm^{-1} except for a derivative-like structure near 500 cm^{-1} due to the same lattice vibrations. To discuss these data, we express our ellipsometric angles as a pseudodielectric function (which is close to the dielectric function ϵ for this bulk sample with very little surface roughness). These data are shown in Fig. 9 (top). Since there is no dependence of ϵ on the angle of incidence, we only show data taken at 70°.

As mentioned above, $SrTiO_3$ is a perovskite crystal with cubic symmetry (see Fig. 5). The symmetries of the normal phonon modes at the Γ point can be derived using group-theoretical methods.[28] The Ba and Ti atoms give rise to one Γ_{15} mode each, the three oxygen atoms to two Γ_{15} modes and one Γ_{25} mode. Overall, subtracting one Γ_{15} acoustic mode, we expect three Γ_{15} modes (infrared active) and one Γ_{25} mode (silent). Since $SrTiO_3$ is an ionic crystal, each Γ_{15} mode splits into a TO and longitudinal optical (LO) pair. The energies of all these modes have been determined using hyper-Raman scattering.[38] The Sr-related modes have energies of 87 cm^{-1} (TO) and 179 cm^{-1} (LO) and the Ti-related

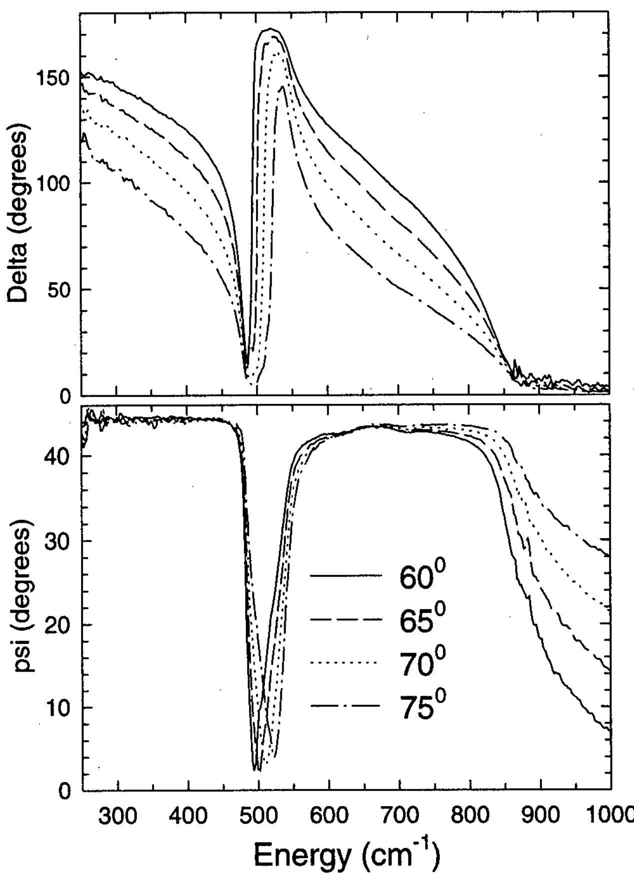

FIG. 8. Ellipsometric angles ψ and Δ at four angles of incidence in the infrared spectral region near the oxygen lattice vibrations.

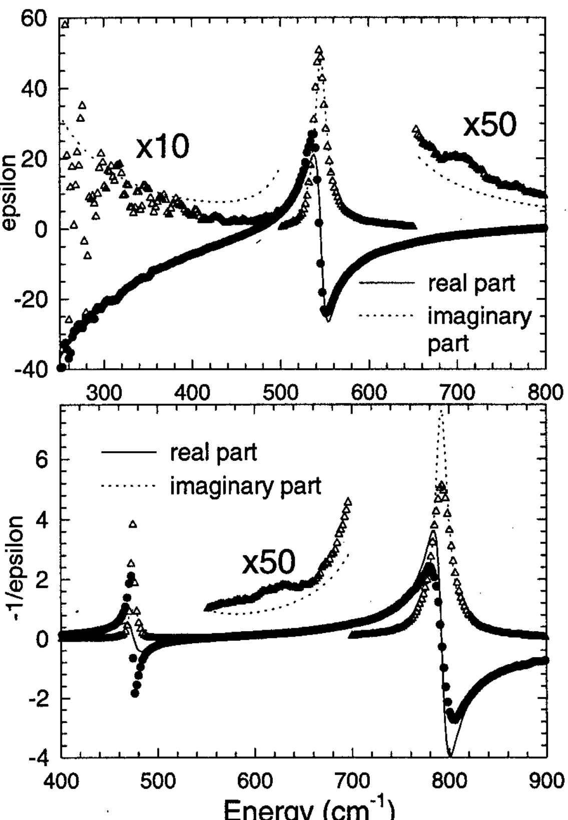

FIG. 9. Dielectric function ϵ (top) and loss function $-1/\epsilon$ (bottom) of bulk $SrTiO_3$, measured at 70° incidence (symbols) in the region of oxygen lattice vibrations, compared with a Lorentz oscillator model (lines).

modes have energies of 179 cm^{-1} (TO) and 472 cm^{-1} (LO). The silent Γ_{25} mode at 265 cm^{-1} does not influence our spectra. Finally, the oxygen-related modes are 542 cm^{-1} (TO) and 792 cm^{-1} (LO) according to the literature.[38]

Only the highest Γ_{15} mode is visible in our ϵ_2 spectra [see Fig. 9 (top)]. However, the decrease of ϵ_1 toward lower energies announces that one or more additional peaks occur below our spectral range. Therefore, our instrument cannot be used to measure ϵ_0 (i.e., the real part of ϵ at zero frequency), which is of primary technological interest, since its wavelength range is insufficient at low energies. We follow Gervais[17] and Humlíček[37] and use two Lorentz oscillators to model the dispersion of ϵ [see Eq. (2)]. Because of the limited range of our instrument, we ignore the weak Ti-related mode at 179 cm^{-1}. (Including it does not improve the agreement between data and model.) We fix the lower TO mode at $E_1 = 87\,cm^{-1} = 10.8\,meV$. All other parameters are fitted to best describe the spectrum of ϵ from 250 to 7450 cm^{-1}, although only a narrow range of the spectrum is shown in Fig. 9. The resulting parameters are: $\epsilon_\infty = 5.204$, $A_1 = 3.72 \times 10^{-2}\,eV^2$, $\Gamma_1 = 2\,meV$, $A_2 = 6.58 \times 10^{-3}\,eV^2$, and $\Gamma_2 = 2\,meV$. The oxygen-related TO phonon energy $E_2 = 67.7\,meV = 546\,cm^{-1}$ is in excellent agreement with the hyper-Raman data of Ref. 38. ϵ_1 crosses zero at 475 and 792 cm^{-1}. This is typically used as the criterion to define the LO phonon energy, again in good agreement with the literature.[38] The LO energies appear as peaks in the spectra when plotting the loss function $-1/\epsilon$ (see the bottom of Fig. 9). Our data also indicate additional structures at 700 cm^{-1} in ϵ and at 640 cm^{-1} in the loss function due to multiphonon absorption.

A comparison of the fit and the data shows that the experimental line shape is slightly asymmetric, there is more oscillator strength (absorption) at higher energies than on the low-energy side. This is also reflected in the real part of ϵ. When plotting the loss function, see the bottom of Fig. 9, we note that the calculated peak is higher than the data for the LO phonon at 792 cm^{-1} and lower for the LO phonon at 475 cm^{-1}, again an indication of the asymmetry. On the other hand, the LO peak positions are well matched between data and model. Such an asymmetric line shape is typically referred to as a Fano line shape and usually due to the interaction between a discrete state (the phonon) and a continuum, for example, free carriers.

In our case, since the $SrTiO_3$ crystal contains no free carriers, it is more likely that the asymmetry is caused by phonon–phonon interaction. Following Gervais,[17] we write ϵ based on a factorized form of the dielectric phonon response

$$\epsilon(E) = \epsilon_\infty \prod_{i=1}^{3} \frac{E_{i,LO}^2 - E^2 + i\Gamma_{i,LO}E}{E_{i,TO}^2 - E^2 + i\Gamma_{i,TO}E}. \tag{4}$$

This expression assigns different broadenings to the LO and

TO phonons. When the two broadenings are equal, the usual sum of Lorentzians is recovered.[39] Using Eq. (4) and by maintaining a 2:1 ratio of $\Gamma_{i,LO}:\Gamma_{i,TO}$, we are able to improve the agreement between our data and the model and introduce some asymmetry in the spectrum. However, measurements at longer wavelengths (below the Sr-related TO mode of 87 cm^{-1}) would be needed to clarify this point. We are not comfortable with fitting the broadening of a mode that is outside our spectral range. Measurements down to 50 cm^{-1} at the infrared synchrotron beamline in Brookhaven would be useful to study this material.[40] This has recently been done by Sirenko and co-workers.[41,42] The energies and broadenings of the low-energy phonon modes can also be studied using electric field-induced Raman scattering.[43]

III. OPTICAL PROPERTIES OF $SrTiO_3$ ON Si

After discussing the optical properties of bulk $SrTiO_3$, we proceed to those of thin $SrTiO_3$ films on various substrates. First, we note that the refractive index below the band gap of $SrTiO_3$ and $BaTiO_3$ films grown on MgO by molecular beam epitaxy is not noticeably different from the bulk.[7] However, there is a significant difference near the critical points,[7] which are broadened and have a lower amplitude. There are three possible explanations for this effect: (1) Due to a less perfect crystal structure in thin films than in the bulk, there is a scattering of the electron Bloch waves, which leads to a broadening of the critical points. This is often seen in micro-or polycrystalline semiconductors, such as Si or SiC. (2) There could be a difference in stoichiometry. Since the interband transitions originate from the O($2p$) valence band and end in the Ti($3d$) conduction band, oxygen or titanium vacancies (i.e., a change in stoichiometry) would certainly lead to a decrease of the critical-point amplitudes. (3) There could be other mechanisms for a charge transfer to Sr-related states, such as dislocations, grain boundaries[26] (in polycrystalline films), or interface states, which would reduce those amplitudes also. In similar studies on bulk $BaTiO_3$, a reduction of the refractive index in the surface region was observed after polishing, most likely due to a processing-induced damage at the surface.[44]

The $SrTiO_3$ films studied here were prepared by molecular beam epitaxy on Si(100) substrates as described elsewhere.[6] It is known that a few monolayers of $SrTiO_3$ on Si(100) can be grown without an amorphous interfacial layer.[2,6] However, in our thicker samples, we usually found an amorphous interfacial layer (10–40 Å thick) between the $SrTiO_3$ film and the Si substrate. This interfacial layer can be affected by the transmission electron microscope (TEM) sample preparation or by extended exposure to the electron beam, but careful studies of thinner films under similar conditions do not show such an interfacial layer, as noted earlier. There are several scenarios how this interfacial layer could be formed. One possibility is that, during the growth of thicker films, oxygen diffuses through the $SrTiO_3$ and reacts with the Si substrate (internal oxidation) (see Ref. 6). While the exact atomic structure and stoichiometry of this interfacial layer are not known to us, it certainly contains Si and O and could very well be a thin silicon oxide.

The $SrTiO_3$ film thicknesses were between 90 and 180 Å, measured by TEM and x-ray reflectivity. For all films, we determined the Sr/Ti ratio using x-ray fluorescence (XRF) using a methodology developed earlier[45] for $Ba_xSr_{1-x}TiO_3$ on Pt. For selected samples, the accuracy of this calibration using $Ba_xSr_{1-x}TiO_3$ XRF standards was confirmed using Rutherford backscattering and Auger spectrometry[3] (using a bulk $SrTiO_3$ standard). The films described here were usually slightly Sr rich and reduced, i.e., oxygen deficient, which could be overcome by postgrowth annealing in oxygen.[3]

The surface roughness of the films was measured by atomic force microscopy.[3,6] Typically, the rms roughness was between 1 and 5 Å, much less than for the bulk sample reported in Sec. II. Therefore, the $SrTiO_3$ film is atomically smooth and its roughness does not affect the ellipsometry analysis given below.

To verify the crystallinity and orientation of $SrTiO_3$ on Si, we measured θ–2θ x-ray diffraction (XRD) curves using a high-intensity Rigaku RU200-BH rotating-anode x-ray source and a DMAX-B goniometer, using an anode voltage of 50 kV, a beam current of 200 mA, and a divergence slit of 1°. Regardless of growth conditions, we only found the $SrTiO_3$ (100) and (200) lattice reflections.[3,6] There is no evidence for other crystalline phases in the film or a crystalline interfacial layer. The full width half maximum (FWHM) of the (200) lattice reflection usually was on the order of 1.3°, which corresponds to a film thickness of 65 Å, about half the film thickness measured by spectroscopic ellipsometry (see below). There could be some contribution to the x-ray diffraction linewidths due to lattice strain variations or dislocations, therefore the x-ray diffraction measurements underestimate the film thickness.

For all films on Si, we determined the ellipsometric angles from 0.74 to 6.6 eV, using the high-accuracy mode of the compensator as described above. The data were analyzed in a three-phase model (ambient/film/Si substrate), using the Herzinger–Johs parametric oscillator model to describe the $SrTiO_3$ film. For the thinner films (about 100 Å), there is some correlation between the thickness and the refractive index. Nevertheless, we feel that our measurements of these parameters can be trusted. This problem does not exist for films with 200 Å thickness or more. The penetration depth in bulk $SrTiO_3$ exceeds 110 Å for all wavelengths of our ellipsometer. Therefore, the $SrTiO_3$/Si interfacial layer will affect the data obtained in this three-phase model for all of our films, since the interfacial layer is not considered. For thinner films, the importance of the interfacial layer will be higher than for thicker films. In essence, this model reports an *average* dielectric function of the $SrTiO_3$ film and the interfacial layer. It is obvious that the interfacial layer thickness can be minimized by maximizing the refractive index below the band gap.

All films had a refractive index n at 632.8 nm (1.96 eV) that was significantly lower (1.85–2.23) than in bulk $SrTiO_3$ (2.39). Our best results (highest n) were obtained in slightly

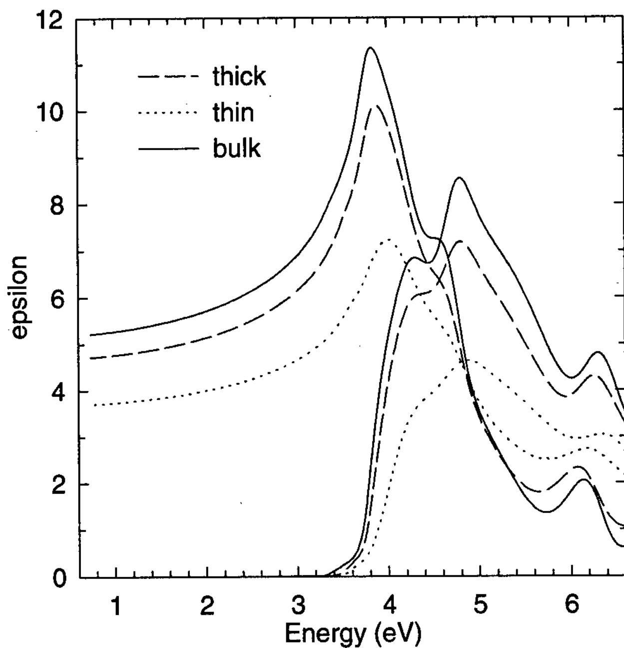

FIG. 10. Average dielectric functions of slightly Sr-rich $SrTiO_3$ films on Si determined within a three-phase (ambient/film/substrate) model. Due to the increasing importance of the interfacial layer between the film and the substrate, the average dielectric function is lower for a thinner film (110 Å, dotted) than for a thicker film (200 Å, dashed). The bulk $SrTiO_3$ dielectric function is shown by the solid line.

Sr-rich films with 200 Å thickness. For this stoichiometry, the refractive index decreases with decreasing thickness. If we stipulate that the amorphous interfacial layer has a refractive index similar to that of SiO_2 (1.4), which is considerably less than that of bulk $SrTiO_3$, then it is plausible that the average n for the film (interfacial layer plus $SrTiO_3$ film) decreases with decreasing film thickness, since the relative importance of the interfacial layer increases. To test this hypothesis, we attempted to describe the interfacial layer and $SrTiO_3$ as two different layers in the analysis of the ellipsometry data. We used our bulk $SrTiO_3$ data for the perovskite film and a Cauchy model (starting with the parameters of $SiO_2, n=1.4$, or $Si_3N_4, n=2.0$) for the amorphous interfacial layer. Unfortunately, none of these models led to a good description of the ellipsometric angles. A Bruggeman effective medium model with a mix of $SrTiO_3$ and SiO_2 to describe the film (or a mix of $SrTiO_3$ and Si to describe the interfacial layer) was also tested, but did not lead to a good agreement either. In summary, only a three-phase model (ambient/film/Si substrate) was found in good agreement with our ellipsometric angles. This model leads to an average dielectric function for the film, including the effects of the amorphous interfacial layer.

In Fig. 10, we show the average dielectric functions for two of our slightly Sr-rich $SrTiO_3$ films in comparison with bulk $SrTiO_3$. As mentioned above, ϵ_1 at 1.96 eV is lower than in the bulk for both films and decreases with decreasing thickness due to the increasing importance of the amorphous interfacial layer. However, the dielectric functions ϵ of the films cannot be represented by a scaled-down version of the bulk ϵ. In addition to the reduction of the amplitude of ϵ, there is a significant broadening of the critical points at 3.8, 4.3, 4.8, and 6.2 eV. This broadening could be due to the poorer crystallinity of the films compared to the bulk or due to confinement effects. We do not note a significant shift of the critical points or the band gap within the accuracy of our thin-film measurements. Furthermore, there is no significant absorption below the bulk band gap of 3.2 eV (i.e., no Urbach tail). The onset of strong absorption also remains about the same. (This can be seen better by normalizing ϵ_2 to the same peak amplitude for the three spectra than shown in Fig. 10.) Finally, while some of the reduction of ϵ in the films is due to the interfacial layer, there could also be a charge transfer to Sr-related states, which absorb at energies beyond our spectral range.

IV. OPTICAL PROPERTIES OF $SrTiO_3$ ON Pt

$SrTiO_3$ films were also prepared on Pt by chemical vapor deposition. For this study, a thermal oxide of 1000 Å thickness was produced on 200 mm Si (100) wafers. Then, 1000 Å thick Pt films (much less than the penetration depth of the light in our spectral range) were deposited at 450 °C by physical vapor deposition using high-purity targets, resulting in films with a rms surface roughness of less than 15 Å. The dielectric function of our Pt films prepared in this manner has been described elsewhere.[46] Their optical constants are quite different from values tabulated in the literature,[47] but consistent with ellipsometry measurements performed by others.[48] XRD measurements show that our Pt films are very strongly textured with the Pt (111) direction aligned with the growth direction. No XRD peaks other than Pt (111) and (222) plus the Si substrate peaks could be observed. The Pt grain size, determined from the FWHM of the Pt (111) peak, is about 350 Å. The FWHM of the Pt (111) rocking curves is about 3.7°, again indicating strong texture of the Pt films.

The $SrTiO_3$ lattice constant (3.905 Å) is very close to that of Pt (3.92 Å). Our best films are fully aligned with the Pt pseudosubstrate. Therefore, they cannot be studied using our XRD measurements. The texture of the $SrTiO_3$ films on Pt can be controlled by changing the deposition conditions. For those $SrTiO_3$ films with weaker texture, we observe $SrTiO_3$ (100) and (200) peaks in θ–2θ XRD scans. In this case, the average grain size of the $SrTiO_3$ grains aligned along (100) can be determined. It ranges from 100 to 200 Å. The $SrTiO_3$ films with smaller grain sizes also have weaker texture. The stoichiometry of the $SrTiO_3$ films was measured with x-ray fluorescence.[45] Some films were approximately stoichiometric, while others were significantly Ti rich (Sr/Ti ratio of 0.65 to 0.75).

The ellipsometric angles of twelve $SrTiO_3$ films on Pt prepared under different processing conditions were measured from 0.74 to 6.6 eV in the same manner as for $SrTiO_3$ on Si described above. The data were analyzed using a three-phase model (ambient/$SrTiO_3$/Pt), neglecting the small amount of surface roughness. The optical constants of the $SrTiO_3$ were again described using the Herzinger–Johs parametric oscillator model, ensuring Kramers–Kronig consis-

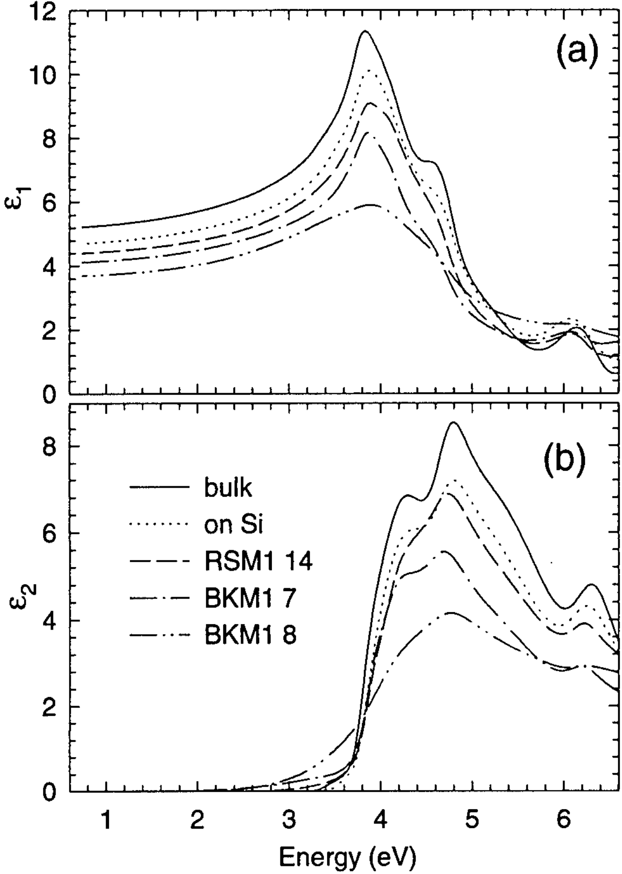

FIG. 11. Dielectric functions of polycrystalline $SrTiO_3$ films on Pt, about 230–280 Å thick, grown under different processing conditions (dashed, dot-dashed, double dot-dashed). The bulk $SrTiO_3$ dielectric function is shown by the solid line, that of the thick film on Si (see Fig. 10) by the dotted line.

tency of the optical constants while, at the same time, allowing a high degree of freedom for the dispersion of the optical constants. The film thicknesses were found to be between 210 and 280 Å. (For some films, the thicknesses were also confirmed by cross-sectional transmission electron microscopy.) The resulting (fitted) dielectric functions of the $SrTiO_3$ films on Pt are shown in Fig. 11. For comparison, we also show ϵ for bulk $SrTiO_3$ from Fig. 3 (solid) and for the thick $SrTiO_3$ film on Si from Fig. 10 (dotted).

For all films on Pt, we noticed a lower refractive index at 1.96 eV than for the thickest film on Si described earlier. The amplitudes of the critical points are also lower in the films on Pt. The films on Pt seem to have some absorption below the direct band gap (between 2.5 and 3.5 eV) indicating an Urbach tail. It is possible that this is an artifact of our data analysis, since such small values of ϵ_2 are difficult to measure for such thin films. However, since the $SrTiO_3$ films on Pt are grown at relatively low oxygen partial pressures, it is likely that they are reduced, i.e., oxygen-deficient. Linear-muffin-tin-orbital band structure calculations by Shanthi and Sarma[49] predict that oxygen vacancies act as shallow donors and dope $SrTiO_3$ with electrons. Vacancy clustering distorts the bottom of the conduction band and forms a distinct band tail in their calculations,[49] which is consistent with our experimental observations. The oxygen–vacancy related disorder also broadens the optical phonons,[50] which we discuss below.

The largest n at 1.96 eV is shown by a film that is significantly Ti rich (dashed line, Sr/Ti ratio of 0.75). This film shows an ϵ not too different from that of a stoichiometric film on Si with similar thickness (dotted). Based on our theoretical results, it is not too surprising that excess Ti (or lack of Sr) does not affect ϵ too much, since the interband transitions contributing to ϵ in our spectral range originate at the $O(2p)$ valence band and end in the $Ti(3d)$ conduction band. Sr-related states do not contribute to ϵ shown in Fig. 11.

The dot-dashed and double dot-dashed lines in Fig. 11 show ϵ for approximately stoichiometric $SrTiO_3$ films on Pt. Film number 7 (dot-dashed) is not visible in XRD because of perfect alignment with the Pt pseudosubstrate. Therefore, it is expected to have excellent crystallinity. This is also expressed in its dielectric function. All expected critical points are clearly visible, though at a lower amplitude than in the bulk or in the thick film on Si. Film number 8 (double-dot dashed) shows a strong and broad $SrTiO_3$ (200) XRD peak, indicating poor texture and a grain size of only 100 Å. The poor crystallinity expresses itself in a significant broadening of the critical points and a very strong Urbach tail below the band gap. This film also has the lowest refractive index at 1.96 eV of all films studied on Si and Pt with similar thickness.

To study the lattice dynamics of the $SrTiO_3$ films on Pt, we performed reflection absorption spectroscopy.[51] We measured the reflected intensity of the $SrTiO_3$ film on Pt (called R) and also the reflected intensity of the Pt pseudosubstrate R_0. Then, we calculate the quantity

$$1-\frac{R}{R_0}, \tag{5}$$

which should be equal to the optical density αd (where d is the film thickness) times a constant.[51] During these measurements, the angle of incidence was about 45° and the polarization state was not well defined, but the s-polarized component is expected to contribute very little to this signal.[51] A typical spectrum for a 225 Å thick film with a Sr/Ti ratio of 0.8, a refractive index of 2.20 at 1.96 eV, and good crystallinity is shown in Fig. 12. We observe two peaks approximately at the energies of the Ti- and O-related LO frequencies. There is no structure at the corresponding O-related TO frequency. This is a manifestation of the Berreman effect describing the infrared reflection response of a thin insulator on a metal, such as LiF on Ag.[52]

To compare these experiments with a model, we calculate the reflection absorption signal in Eq. (5) using our ellipsometry data analysis program.[53] We chose a polarization of 45° relative to the plane of incidence to see the effects of both s- and p-polarized beams. Since we do not have infrared ellipsometry data for the infrared dielectric function of Pt, we choose a Drude model for a typical metal with a plasma frequency of 13 eV and a broadening of 0.3 eV. The $SrTiO_3$ film is described with the same lattice dynamics model (sum

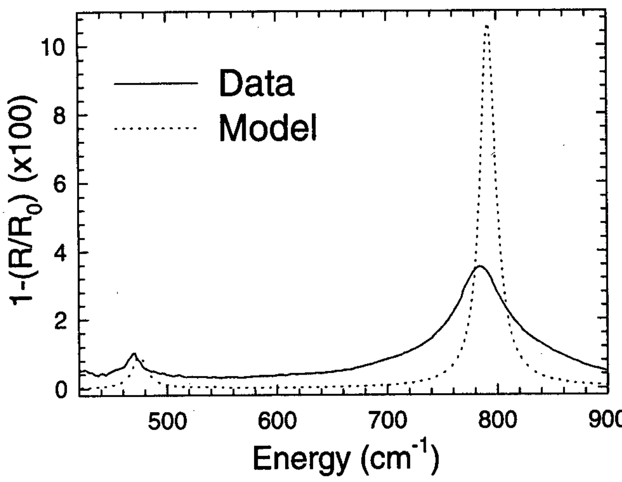

FIG. 12. Reflection–absorption spectrum (solid) of a $SrTiO_3$ film on Pt. Because of the Berreman effect, peaks at the LO phonon energies appear in this spectrum. The dashed line shows the spectrum calculated from our lattice-dynamical model for bulk $SrTiO_3$.

of two Lorentz oscillators) as in the bulk, see above. These data are shown by the dashed line in Fig. 12.

Comparing our experimental data with the model, we note that there are strong peaks in the signal due to the LO phonons. However, the LO energies are redshifted in the data compared to the model. Also, the amplitude of the LO peak at 475 cm^{-1} is approximately correct, whereas that of the peak at 792 cm^{-1} is overestimated by the model. This is not surprising in view of the bulk ellipsometry data in Fig. 9, where the LO phonon amplitudes are not correct either. However, in $SrTiO_3$ on Pt, the 792 cm^{-1} peak is broadened even more than in the bulk. The redshift and broadening compared to the bulk observed here is in contrast to infrared absorption work[50] in highly reduced $SrTiO_3$, where a blueshift and a broadening of the TO modes were observed. It is possible, though, that the TO and LO phonon shifts due to electron doping (caused by oxygen vacancies) could have different signs. The doping could screen the internal electric fields and thus change the TO–LO phonon splittings, resulting in hardening of one and softening of the other.

However, the LO redshift and TO blueshift observed in reduced $SrTiO_3$ are in contrast with the expected behavior resulting from the screening of the lattice vibrations by free electrons. In *n*-type GaAs, for example, the screening increases the LO energy and leaves the TO energy unchanged.[54] Therefore, the effects observed in $SrTiO_3$ have to be more subtle. For example, the changes of the phonon energies could also be affected by the local relaxation accompanying the oxygen vacancies.

It would be interesting the confirm our reflection–absorption spectroscopy results with infrared ellipsometry measurements, which are expected to be more sensitive, since they measure both the amplitude ratio and the relative phase of the *p*- and *s*-polarized beams.

V. CONCLUSION

We have performed extensive ellipsometry measurements over a broad spectral range to study the electronic structure, particularly the critical points, and the lattice dynamics of bulk $SrTiO_3$, in comparison with *ab initio* band structure calculations. We apply our understanding of the bulk to thin films on Si and Pt. In $SrTiO_3$ on Si, we observe a much lower refractive index below the band gap and a reduction of the critical-point amplitudes (but no shifts), particularly in thin films. Most likely, this is due to the amorphous interfacial layer between the Si substrate and the MBE-grown $SiTiO_3$ film. In $SrTiO_3$ on Pt, there is also a reduction of the low-energy refractive index, an amplitude reduction, and a broadening of the critical points, most likely due to a lower crystallinity (as in microcrystalline Si or SiC) combined with a charge transfer to Sr-related states at grain boundaries. We also observe a softening and an amplitude reduction of the LO phonons in $SrTiO_3$ on Pt in reflection–absorption measurements, which we attribute to oxygen vacancies in our films based on the growth conditions. Maximizing the crystallinity is likely to result in better electrical properties, i.e., higher resistivity and lower leakage currents through grain boundaries.

ACKNOWLEDGMENTS

The authors are grateful to C. M. Herzinger for providing the critical-point software and to Matthew Kim for supplying the $SrTiO_3$ bulk crystal. We also acknowledge stimulating discussions with Professor Josef Humlíček.

[1]Throughout this article, we follow the usual notation of lattice dynamics and call the dc dielectric constant ϵ_0, not to be confused with the permittivity of free space. The engineering literature refers to the same quantity as the relative permittivity with the symbol *k*, not to be confused with the extinction coefficient. $SrTiO_3$ is thus called a high-*k* material. Strictly speaking, ϵ_0 or *k* is not really a constant, but depends on the conditions of electrical measurements, such as the amplitude and frequency of the applied electric field, extrinsic properties such as interface states, and the thickness of the film.

[2]R. A. McKee, F. J. Walker, and M. F. Chisholm, Phys. Rev. Lett. **81**, 3014 (1998).
[3]Z. Yu *et al.*, Mater. Res. Soc. Symp. Proc. **567**, 427 (1999).
[4]Z. Yu *et al.*, J. Vac. Sci. Technol. B (in press).
[5]K. Eisenbeiser *et al.*, Appl. Phys. Lett. (in press).
[6]J. Ramdani *et al.*, Appl. Surf. Sci. (in press).
[7]G. E. Jellison, L. A. Boatner, D. H. Lowndes, R. A. McKee, and M. Godbole, Appl. Opt. **33**, 6053 (1994).
[8]G. E. Jellison, Opt. Mater. **1**, 41 (1992).
[9]G. E. Jellison and F. A. Modine, Appl. Opt. **29**, 959 (1990).
[10]H. G. Tompkins and W. A. McGahan, *Spectroscopic Ellipsometry and Reflectometry* (Wiley, New York, 1999).
[11]C. M. Herzinger and B. D. Johs, U.S. Patent No. 5 796 983 (18 August 1998).
[12]N. Sata, M. Ishigame, and S. Shin, Solid State Ionics **86–88**, 629 (1996).
[13]M. Cardona, Phys. Rev. **140**, A651 (1965).
[14]P. Y. Yu and M. Cardona, *Fundamentals of Semiconductors* (Springer, Berlin, 1996).
[15]M. Capizzi and A. Frova, Phys. Rev. Lett. **25**, 1298 (1970); Nuovo Cimento **5**, 181 (1971).
[16]K. W. Blazey, Phys. Rev. Lett. **27**, 146 (1971).
[17]F. Gervais, in *Handbook of Optical Constants*, edited by E. D. Palik (Academic, Boston, 1991), Vol. 2, p. 1035.
[18]J. L. Servoin, Y. Luspin, and F. Gervais, Phys. Rev. B **22**, 5501 (1980).

[19]D. Bäuerle, W. Braun, V. Saile, G. Sprüssel, and E. E. Koch, Z. Phys. B **29**, 179 (1978).
[20]G. E. Jellison, F. A. Modine, P. Doshi, and A. Rohatgi, Thin Solid Films **313–314**, 193 (1998).
[21]F. Urbach, Phys. Rev. **92**, 1324 (1953).
[22]P. Lautenschlager, M. Garriga, L. Viña, and M. Cardona, Phys. Rev. B **36**, 4821 (1987).
[23]J. W. Garland, C. Kim, H. Abad, and P. M. Raccah, Phys. Rev. B **41**, 7602 (1990).
[24]M. C. Payne, M. P. Teter, D. C. Allan, T. A. Arias, and J. D. Joannopoulos, Rev. Mod. Phys. **64**, 1045 (1992).
[25]L. F. Mattheiss, Phys. Rev. B **6**, 4718 (1972).
[26]S.-D. Mo, W. Y. Ching, M. F. Chisholm, and G. Duscher, Phys. Rev. B **60**, 2416 (1999); Y.-N. Xu, W. Y. Ching, and R. H. French, Ferroelectrics **111**, A23 (1990).
[27]F. M. F. de Groot, J. Faber, J. J. M. Michiels, M. T. Cryzyk, M. Abbate, and J. C. Fuggle, Phys. Rev. B **48**, 2074 (1993).
[28]D. L. Rousseau, R. P. Bauman, and S. P. S. Porto, J. Raman Spectrosc. **10**, 253 (1981).
[29]T. Higuchi, T. Tsukamoto, N. Sata, M. Ishigame, Y. Tezuka, and S. Shin, Phys. Rev. B **57**, 6978 (1998).
[30]A. H. Kahn and A. J. Leydendecker, Phys. Rev. **135**, A1321 (1964).
[31]H. P. R. Frederikse, W. R. Hosler, and W. R. Thurber, J. Phys. Soc. Jpn. **21**, 32 (1966).
[32]H. P. R. Frederikse, in *Electronic Structures in Solids*, edited by E. D. Haidemakis (Plenum, New York, 1969).
[33]G. F. Koster, Solid State Phys. **5**, 173 (1957).
[34]F. Bassani, G. P. Parravicini, and R. A. Ballinger, *Electronic States and Optical Transitions in Solids* (Pergamon, Oxford, 1975).
[35]L. P. Bouckaert, R. Smoluchowski, and E. Wigner, Phys. Rev. **50**, 58 (1936).
[36]B. Johs, J. A. Woollam, C. M. Herzinger, J. Hilfiker, R. Synowicki, and C. L. Bungay, Crit. Rev. Opt. Sci. Technol. **72**, 29 (1999).
[37]J. Humlíček, Ferroelectrics **176**, 221 (1996).
[38]V. N. Denisov, B. N. Mavrin, and V. B. Podobedov, Phys. Rep. **151**, 1 (1987).
[39]A. J. Sievers and J. B. Page, Phys. Rev. B **41**, 3455 (1990).
[40]A. Golnik, C. Bernhard, J. Humlíček, M. Kläser, and M. Cardona, Phys. Status Solidi B **215**, 553 (1999).
[41]A. A. Sirenko, C. Bernhard, A. Golnik, I. A. Akimov, A. M. Clark, J.-H. Hao, and X. X. Xi, Mater. Res. Soc. Symp. Proc. (in press).
[42]A. A. Sirenko, C. Bernhardt, A. Golnik, A. M. Clark, J. Hao, W. Si, and X. X. Xi, Nature (London) **404**, 373 (2000).
[43]I. A. Akimov, A. A. Sirenko, A. M. Clark, J.-H. Hao, and X. X. Xi, Phys. Rev. Lett. **84**, 4625 (2000).
[44]S. Trolier-McKinstry, R. E. Newnham, and K. Vedam, in *1990 IEEE 7th International Symposium on Applications of Ferroelectrics* (IEEE, New York, 1991), p. 650.
[45]T. Remmel, D. Werho, R. Liu, and P. Chu, in *Characterization and Metrology for ULSI Technology: 1998 International Conference*, edited by D. G. Seiler A. C. Diebold, W. M. Bullis, T. J. Shaffner, R. McDonald, and E. J. Walters (American Institute of Physics, Woodbury, NY, 1998).
[46]S. Zollner, Phys. Status Solidi A **177**, R7 (2000).
[47]D. W. Lynch and W. R. Hunter, in *Handbook of Optical Constants of Solids*, edited by E. D. Palik (Academic, New York, 1985), p. 275.
[48]L. Ley, T. Stark, M. Hundhausen, and H. Grünleitner, Mater. Res. Soc. Symp. Proc. (to be published).
[49]N. Shanthi and D. D. Sarma, Phys. Rev. B **57**, 2153 (1998).
[50]D. A. Crandles, B. Nicholas, C. Dreher, C. C. Homes, A. W. McConnell, B. P. Clayman, W. H. Gong, and J. E. Greedan, Phys. Rev. B **59**, 12842 (1999).
[51]H. G. Tompkins, in *Methods of Surface Analysis*, edited by A. W. Czanderna (Elsevier, Amsterdam, 1975), p. 445.
[52]J. Humlíček, Phys. Status Solidi B **215**, 155 (1999).
[53]J. A. Woollam Co., WVASE program (2000).
[54]A. Mooradian and A. L. McWhorter, Phys. Rev. Lett. **19**, 849 (1967).

Method for atomic-layer-resolved measurement of polarization fields by nuclear magnetic resonance

James G. Kempf and Daniel P. Weitekamp[a)]
A. A. Noyes Laboratory of Chemical Physics, 127-72, California Institute of Technology, Pasadena, California 91125

(Received 17 January 2000; accepted 1 May 2000)

A nuclear magnetic resonance (NMR) method of probing the dielectric response to an alternating electric field is described, which is applicable to noncentrosymmetric sites with nuclear spin $I > 1/2$. A radio-frequency electric field induces a linear quadrupole Stark effect at a multiple of the nuclear Larmor frequency. This perturbation is applied in the windows of an NMR multiple-pulse line-narrowing sequence in such a way that the resulting nonsecular spin interactions are observed as first-order quadrupole satellites, free of line broadening by the usual dominant static interactions. A simulation of the ^{69}Ga spectrum for the nuclei within the two-dimensional electron gas of a 10 nm quantum well predicts resolution of individual atomic layers in single devices due to the spatial dependence of the polarization response of the quantum-confined carriers to the applied field. This method is part of a more general strategy, perturbations observed with enhanced resolution NMR. Experimentally realized examples in GaAs include spectrally resolving electron probability densities surrounding optically relevant point defects and probing the changes in radial electric field associated with the light-on and light-off states of these shallow traps. Adequate sensitivity for such experiments in individual epitaxial structures is achieved by optical nuclear polarization followed by time-domain NMR observed via nuclear Larmor-beat detection of luminescence. © *2000 American Vacuum Society.* [S0734-211X(00)03904-4]

I. INTRODUCTION

In the early 1960s, Bloembergen and others studied the linear quadrupole Stark effect (LQSE) of the nuclear spin Hamiltonian in bulk GaAs, whereby an electric field gradient is induced at nuclear sites in proportion to the electric field at those sites.[1–3] Characterization of the spatial variation of the LQSE expected in single epitaxial structures requires high nuclear magnetic resonance (NMR) sensitivity and spectral resolution. In recent decades the phenomena of optical nuclear polarization, equilibrium and optically induced Knight shifts, and several methods of optical detection have resulted in great gains in sensitivity, spatial selectivity, and spectral resolution relative to the traditional solid-state NMR experiment.[4–12] This has allowed application of optical NMR to III–V heterostructures,[10] quantum wells[13–17] (QWs), and quantum dots.[11] Of particular relevance here are advances from our group enabling *high-resolution* time-domain optically detected NMR.[8,10] The highest spectral resolution is achieved in experiments where perturbations of the sample, such as the E field in the LQSE, are synchronized with time-suspension NMR multiple-pulse sequences to measure differences between the perturbed and unperturbed spin Hamiltonians,[18] an approach which we refer to as POWER (perturbations observed with enhanced resolution) NMR. The pulse-sequence design is conceptually similar to those used in solid-state NMR imaging,[19–21] where the perturbation is a magnetic field gradient. In recent experiments, we have probed the shallow point defects at which optical excitations localize in individual epitaxially grown AlGaAs/GaAs heterojunctions using two different examples of POWER NMR with secular, optically induced spin Hamiltonians. The radial distribution of optically switched electron density was observed as a high-resolution Knight shift distribution, and the associated changes in radial electric field were measured by the diagonal terms of the LQSE.[22]

Here we introduce a novel technique within the general class of POWER NMR, whereby a radio frequency (rf) LQSE is used to measure a third electronic property, the polarization response to an rf E field, in particular, that expected for electrons in an *n*-type GaAs QW. Our approach relies on conversion of nonsecular (off-diagonal) terms in the nuclear quadrupole Hamiltonian $\mathcal{H}_Q$ into an effective secular observable (a first-order splitting in the sample's NMR spectrum) by varying the E-field-induced interaction at twice the nuclear Larmor frequency in selected windows of a time-suspension[19,20] NMR multiple-pulse sequence. Both this transformation of a nonsecular perturbation into a high-resolution secular observable and the proposed localized measurement of dielectric response are novel aspects of this work. On bulk samples in experiments where resolution was limited by dipolar broadening, the rf LQSE has been used previously to depolarize nuclear spins in GaAs,[23,24] while the inverse of the rf LQSE has been used to realize electrically detected nuclear quadrupole resonance.[25,26] In contrast, we predict that, by employing POWER NMR and isotopic dilution, our technique can yield NMR line shapes with atomic-layer resolution that report on the rf LQSE in a GaAs QW sample. Generalizations of this spin physics may be useful in other situations where rf perturbations modulate nonsecular spin interactions.

[a)]Author to whom correspondence should be addressed.

An outline of the remaining text follows. Section II A is a description of the physical basis for the general LQSE. In Sec. II B, we derive the nuclear spin Hamiltonian pertinent to the rf effect and, in Sec. II C, we analyze the multiple-pulse techniques employed in POWER NMR. In Sec. III, we develop the form of the rf polarization response of n-type carriers in a QW and determine nuclear spin evolution due to synchronization of this response with NMR multiple-pulse line narrowing. The form obtained for the polarization response is justified by a second-order perturbation-theory treatment of a particle-in-a-box model presented in the Appendix. In Sec. IV, we present and discuss the simulated NMR spectrum, predicting resolved features due to individual atomic layers.

II. FUNDAMENTAL CONCEPTS

A. Electric-field-induced quadrupole interactions

The LQSE is a crystalline or molecular system's linear response to an E field observed as the quadrupole interaction on nuclei with spin $I>1/2$ at a site lacking inversion symmetry. The nuclear quadrupole interaction exists between the charge distribution $\rho_n(\mathbf{r})$ of a nucleus and an electric potential $V(\mathbf{r})$ arising from fields of other nuclei, the sample's electron distribution, or an applied E field. When $V(\mathbf{r})$ is expanded in a Taylor series about the nuclear position ($\mathbf{r}=0$), the overall energy of this interaction is given by the integral over the nuclear volume,[27]

$$E_{\rho,v}=V(0)\int \rho_n(\mathbf{r})d^3\mathbf{r}+\sum_i V_i\int x_i\rho_n(\mathbf{r})d^3\mathbf{r}+\sum_{i,j}\frac{1}{2}V_{ij}\int x_ix_j\rho_n(\mathbf{r})d^3\mathbf{r}+\dots. \quad (1)$$

The Cartesian position coordinates x_i and x_j, where i and j range over 1, 2, and 3, are arbitrary and the coefficients of the expansion are the derivatives

$$V_i=\left.\frac{\partial V}{\partial x_i}\right|_{r=0} \quad \text{and} \quad V_{ij}=\left.\frac{\partial V}{\partial x_i\partial x_j}\right|_{r=0}. \quad (2)$$

Since the first term in Eq. (1) is independent of nuclear orientation, it has no bearing on the NMR Hamiltonian, while the second vanishes by the inversion symmetry of the nucleus. The third term describes the energy of the nuclear quadrupole interaction that is of interest here.

When an electric field $\mathbf{E}$ is applied to the sample, the components V_{ij} of the E-field-gradient tensor may be expanded as a Taylor expansion about $E=0$:

$$V_{ij}=(V_{ij})_{E=0}+\sum_k C_{ij,k}E_k+\dots, \quad (3)$$

where the first term gives a component of the intrinsic E-field-gradient tensor and the second describes the LQSE relating the V_{ij} to $\mathbf{E}$ via the third-rank tensor $\mathbf{C}$ with components

$$C_{ij,k}=\left(\frac{\partial V_{ij}}{\partial E_k}\right)_{E=0}. \quad (4)$$

Both the matrix of $(V_{ij})_{E=0}$ and the $\mathbf{C}$ tensor describe properties of the crystalline or molecular sample and, therefore, must be invariant under symmetry transformations within the point group of that system. In the case of bulk GaAs, the crystal lattice belongs to the T_d point group, which, along with the equivalence of the coordinates, indicates that all components of $(V_{ij})_{E=0}$ must vanish, that $C_{ij,k}\neq 0$ only for $i\neq j\neq k$, and that these nonzero components are equivalent.[24]

The $\mathbf{C}$ tensor itself may be broken up into two contributing factors:

$$C_{ij,k}=R_{ij,k}+\sum_{mn} S_{ij,mn}d_{mn,k}, \quad (5)$$

where the coupling of the fourth-rank strain tensor $\mathbf{S}$ and third-rank piezoelectric tensor $\mathbf{d}$ describes the induced E-field-gradient due to a relative shift of the Ga and As sublattices with $\mathbf{E}$, and the third-rank tensor $\mathbf{R}$ describes the polarization-induced distortion of covalent electronic states in the crystal lattice. It has been shown[2,3,24] that the polarization of covalent electronic states is the dominant mechanism underlying the LQSE in GaAs, and some literature explicitly drops notation of the $\mathbf{S}$ tensor contribution by equating $\mathbf{C}$ to $\mathbf{R}$. However, the LQSE experimentally includes both terms.

Finally, we complete the form of the E-field-gradient tensor, making the particular choice of associating $k=1$, 2, and 3 with the [100], [010], and [001] crystal axes, respectively, using the Voigt notation (i.e., $11=1$, $22=2$, $33=3$, $23=4$, $13=5$, and $12=6$) to collapse the j and k indices of $\mathbf{C}$ into a single index and recalling that $C_{14}=C_{25}=C_{36}$. Thus, according to Eq. (3) and the GaAs lattice symmetry, the components of the induced E-field-gradient tensor are

$$V_{ii}=0 \quad \text{and} \quad V_{ij}=V_{ji}=C_{14}E_k \quad (6)$$

for i, j, and k a permutation of the three axes.

B. Nuclear quadrupole Hamiltonian

In order to understand and manipulate the role of the LQSE in NMR evolution, we now review the general form of the spin Hamiltonian $\mathcal{H}_Q$ corresponding to the nuclear quadrupole interaction in terms of the spherical tensor basis of operators $T_{k,q}$ with the convention[28]

$$T_{2,0}=\frac{1}{\sqrt{6}}[3I_z^2-I(I+1)], \quad (7)$$

$$T_{2,\pm 1}=\mp\tfrac{1}{2}(I_zI_\pm+I_\pm I_z), \quad (8)$$

$$T_{2,\pm 2}=\tfrac{1}{2}I_\pm^2. \quad (9)$$

TABLE I. The values of the LQSE coupling constant C_{14} and the nuclear quadrupole moment Q are listed for each isotope in GaAs. As suggested by Dumas *et al.* (Ref. 30), we use the largest reported C_{14} values, as all systematic errors in their determination tend to decrease their apparent size. Furthermore, only the product $C_{14}Q$ corresponding to each nuclear species is measurable by LQSE NMR, thus the Q values assumed by Dumas *et al.* should not be replaced by more modern values without correspondingly scaling the C_{14} values.

Isotope	$C_{14}\times 10^{-12}(\mathrm{m}^{-1})$	$Q\times 10^{29}(\mathrm{m}^2)$
^{69}Ga	2.85	1.9
^{71}Ga	2.85	1.2
^{75}As	3.16	2.9

Here I_x, I_y, and I_z are the components of the dimensionless nuclear spin angular momentum operator and $I_\pm = I_x \pm iI_y$. The spherical tensor coefficients that correspond to the $T_{k,q}$ are

$$V_{2,0} = \frac{3}{\sqrt{6}} V_{zz} = 0, \tag{10}$$

$$V_{2,\pm 1} = \mp (V_{zx} \pm iV_{zy}) = -iC_{14}(E_1 \mp iE_2), \tag{11}$$

$$V_{2,\pm 2} = \tfrac{1}{2}(V_{xx} - V_{yy}) \pm iV_{xy} = \pm iC_{14}E_3, \tag{12}$$

where the rightmost equivalence in each of Eqs. (10)–(12) follows from Eq. (6). To write $\mathcal{H}_Q$ in its most general form, we allow for arbitrary reorientation of B_0 from [001] in three successive rotations by the angles γ, β, and α about the crystal-fixed [001], [010], and [001] axes, respectively. This rotation is represented by the transformation

$$V'_{2,q}(\alpha,\beta,\gamma) = \sum_{p=-2}^{+2} V_{2,p} e^{-i(\alpha p + \gamma q)} d^2_{pq}(\beta) \tag{13}$$

of the coefficients of Eqs. (10)–(12), where the $d^2_{pq}(\beta)$ are reduced Wigner rotation matrix elements.[28,29] These spatial and spin tensor elements are inserted into the general form of the nuclear quadrupole spin Hamiltonian[28]

$$\mathcal{H}_Q(\alpha,\beta,\gamma) = \frac{eQ}{2I(2I-1)\hbar} \sum_{q=-2}^{+2} (-1)^q V'_{2,q} T_{2,-q}, \tag{14}$$

where Q is the nuclear quadrupole moment, e is the unit of electron charge, $\hbar$ is Planck's constant divided by 2π, and the expression is in units of (rad s^{-1}). Literature values of Q for each nuclear isotope in GaAs are listed in Table I, along with the measured values of C_{14} for the Ga and As sublattices in bulk GaAs.[30]

The influence of $\mathcal{H}_Q$ on NMR evolution is best evaluated in the rotating frame defined by the phase ϕ_{rf} and angular frequency ω of the applied rf magnetic field in a pulsed NMR experiment, where, in practice, $\omega = \omega_0$, the nuclear Larmor frequency. The direction of the static magnetic field $\mathbf{B}_0$ of the NMR experiment defines the z axis. To enter the rotating frame, we transform the $T_{2,q}$ operators according to

$$\tilde{T}_{2,q}(t) = U_{\mathrm{rf}}(t) T_{2,q} U^\dagger_{\mathrm{rf}}(t), \tag{15}$$

where

$$U_{\mathrm{rf}}(t) = \exp[i(\omega_0 t + \phi_{\mathrm{rf}}) I_z] \tag{16}$$

and its Hermitian conjugate $U^\dagger_{\mathrm{rf}}(t)$ are the unitary operators appropriate to this transformation. It is straightforward to show that

$$U_{\mathrm{rf}}(t) I^q_\pm U^\dagger_{\mathrm{rf}}(t) = \exp[\pm iq(\omega_0 t + \phi_{\mathrm{rf}})] I^q_\pm, \tag{17}$$

while I_z commutes with $U_{\mathrm{rf}}(t)$. Thus, according to Eqs. (7)–(9), and (14)–(17), the rotating-frame quadrupole Hamiltonian is

$$\tilde{\mathcal{H}}_Q(\alpha,\beta,\gamma) = \frac{eQ}{2I(2I-1)\hbar} \sum_{q=-2}^{+2} (-1)^q V'_{2,q} T_{2,-q} \times \exp[-iq(\omega_0 t + \phi_{\mathrm{rf}})]. \tag{18}$$

Only the term proportional to $T_{2,0}$ in Eq. (18) is stationary in the rotating frame, while effects of the oscillating terms on the spin system average to zero over time and are thus normally truncated to obtain the first-order form of $\tilde{\mathcal{H}}_Q$. The $T_{2,0}$ term gives rise to the dc LQSE and, using Eq. (13), we find

$$V'_{2,0}(\alpha,\beta,\gamma) = \sqrt{\frac{3}{2}} C_{14}[\sin 2\beta\,(E_{100}\sin\alpha + E_{010}\cos\alpha) + E_{001}\sin^2\beta \sin 2\alpha], \tag{19}$$

which, inserted into Eq. (18), yields the dependence of the secular LQSE on the orientation of the magnetic field and the components of the electric field in the crystal frame. This is needed, for example, to describe optically induced POWER LQSE experiments.[22] For the case where $E_{100} = E_{010} = E_{001}$, Eq. (19) reduces to a particular case previously presented in the context of macroscopic dc E-fields.[2,3]

The normally truncated terms of $\tilde{\mathcal{H}}_Q$ are the terms of interest here for extending POWER NMR to include the conversion of nonsecular terms into diagonal, secular observables. If the E-field perturbation of the LQSE oscillates at ω_0 or $2\omega_0$, then either the $V'_{2,\pm 1}$ or $V'_{2,\pm 2}$ coefficients, respectively, are time dependent in a way that partially cancels the time dependence of their corresponding rotating-frame operators, yielding a new static, but off-diagonal, observable in $\tilde{\mathcal{H}}_Q$. Brun *et al.*[23,24] took advantage of this resonance phenomenon to characterize the combined influence of $\mathbf{B}_0$, thermal spin-lattice relaxation and rf-E-field-induced $\Delta m = \pm 2$ transitions at $2\omega_0$ on the equilibrium magnetization of ^{69}Ga, ^{71}Ga, and ^{75}As in bulk GaAs, including its angular dependence. Investigation of $\Delta m = \pm 1$ electric transitions by the rf LQSE at ω_0 is problematic, due to possible incidental excitation of $\Delta m = \pm 1$ magnetic transitions. However, we note that recent unexplained observation[12] of optically induced NMR transitions with light pulsed at either ω_0 or $2\omega_0$ may be due to the rf LQSE induced by the photocarrier E field. For completeness, we present the angular dependence of both nonsecular terms via the general expressions for the spherical tensor coefficients:

$$V'_{2,\pm 1}(\alpha,\beta,\gamma) = \mp C_{14}e^{\mp i\gamma}[E_{100}(\cos 2\beta \sin \alpha \pm i \cos \beta \cos \alpha) + E_{010}(\cos 2\beta \cos \alpha \mp i \cos \beta \sin \alpha) + E_{001}(\tfrac{1}{2}\sin 2\beta \sin 2\alpha \pm i \sin \beta \cos 2\alpha)] \quad (20)$$

and

$$V'_{2,\pm 2}(\alpha,\beta,\gamma) = \tfrac{1}{2}C_{14}e^{\mp 2i\gamma}\{E_{100}(-\sin 2\beta \sin \alpha \mp 2i \sin \beta \cos \alpha) + E_{010}(-\sin 2\beta \cos \alpha \pm 2i \sin \beta \sin \alpha) + E_{001}[(\cos^2 \beta + 1)\sin 2\alpha \pm 2i \cos \beta \cos 2\alpha]\}. \quad (21)$$

In our present example, the $\tilde{T}_{2,\pm 2}$ interaction of $\tilde{\mathcal{H}}_Q$ is reintroduced into the secular Hamiltonian using

$$E(t) = E_0 \sin(2\omega_0 t + \phi_E) \quad (22)$$

applied parallel to $\mathbf{B}_0$ along the [001] crystal-growth axis (i.e., $\alpha=\beta=\gamma=0$), where E_0 is the positive amplitude of $E(t)$ and ϕ_E its phase with respect to ϕ_{rf}. Before considering the possible additional response in a structured sample (e.g., of the electrons in an n-type QW), which we discuss in Sec. III, we insert Eqs. (21) and (22) in Eq. (18), and substitute for α, β, and γ, to obtain the part of $\tilde{\mathcal{H}}_Q$ that is proportional to $\tilde{T}_{2,\pm 2}$:

$$\tilde{\mathcal{H}}_{Q2} = \frac{ieQC_{14}E_0}{2I(2I-1)\hbar}\sin(2\omega_0 t + \phi_E) \times (T_{2,-2}e^{-2i\omega_0 t} - T_{2,+2}e^{+2i\omega_0 t}), \quad (23)$$

where we have taken $\phi_{\mathrm{rf}}=0$. Truncating the remaining time-dependent parts of $\tilde{\mathcal{H}}_{Q2}$ yields

$$\tilde{\mathcal{H}}_{Q2} = \frac{eQC_{14}E_0}{4I(2I-1)\hbar}(T_{2,-2}e^{+i\phi_E} + T_{2,+2}e^{-i\phi_E}), \quad (24)$$

which, using Eq. (9), becomes

$$\tilde{\mathcal{H}}_{Q2} = \frac{eQC_{14}E_0}{4I(2I-1)\hbar}((I_x^2 - I_y^2)\cos \phi_E + (I_xI_y + I_yI_x)\sin \phi_E). \quad (25)$$

Though secular, $\tilde{\mathcal{H}}_{Q2}$ remains off diagonal. In the next section we describe how, using POWER NMR, $\tilde{\mathcal{H}}_{Q2}$ can be converted into a convenient diagonal form, and, we stress, isolated from other spin interactions as the dominant source of spectral structure.

C. High-resolution evolution under the rf LQSE by POWER NMR

In order to best characterize the rf polarization response to $\mathbf{E}(t)$ at $2\omega_0$ by way of Eq. (25), we would like to eliminate, in so far as it is possible, other contributions to the linewidth. These may include static contributions to the secular quadrupole interaction from the equilibrium bonding environment (absent in the bulk GaAs lattice, but not necessarily so in structured epitaxial samples), from crystal strain or even from the LQSE due to static E fields. Direct dipolar interactions of the target spin with like and/or unlike nuclei are ubiquitous, and here undesirable. Finally, a distribution of the Zeeman interaction due to inhomogeneity of the applied field, susceptibility effects or hyperfine fields can contribute to the linewidth. Multiple-pulse line-narrowing techniques provide coherent motions of nuclear spins by applying trains of resonant rf magnetic-field pulses to the sample and can be arranged so as to effectively eliminate all these interactions. We design and quantify such spin-averaged NMR experiments by replacing the time-dependent Hamiltonian governing the time evolution of the system with the time-averaged Hamiltonian $\bar{\mathcal{H}}^{(0)}$ using coherent averaging theory.[28,31] Of particular interest here are sequences for which $\bar{\mathcal{H}}^{(0)} \approx 0$, which serve as the starting point for selectively restoring small interactions, such as the rf LQSE, as the dominant source of spectral structure. The CLSW-16 sequence[19] is one such sequence consisting of a series of 16 $\pi/2$ rf magnetic pulses with alternating phases, separated by windows of free evolution of nuclear magnetization.

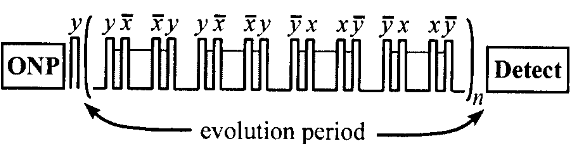

FIG. 1. The time line of the proposed optical NMR experiment. Creation of longitudinal nuclear magnetization (by optical nuclear polarization, i.e., ONP) is followed by a $\pi/2$ rf preparation pulse and the CLSW-16 NMR multiple-pulse line-narrowing sequence (Ref. 19) (rotating frame phases labeled) with synchronous E-field pulses (shaded) at twice the nuclear Larmor frequency. Subsequent detection of the surviving spin magnetization as a function of the number of repetitions n of the cycle in parentheses gives an interferogram, whose Fourier transform is the NMR spectrum of the E-field-induced spin Hamiltonian.

The CLSW-16 sequence averages to zero the chemical shift interaction, dipolar couplings, heteronuclear J couplings and quadrupolar terms that are not switched during the pulse sequence, leaving only the rotationally invariant homonuclear J-coupling between spins i and k, with Hamiltonian

$$\tilde{\mathcal{H}}_J^{ik} = J_{ik}\mathbf{I}_i \cdot \mathbf{I}_k. \quad (26)$$

Figure 1 depicts CLSW-16 during the evolution period of the proposed POWER NMR experiment timeline, where it has been modified to include the LQSE perturbation at $2\omega_0$ during the shaded windows of the sequence. Applied in this selective fashion, and using the same value of ϕ_E in all application windows, the time average of the toggling-frame representation[28,31] of $\tilde{\mathcal{H}}_{Q2}$ in Eq. (25) contributes

$$\bar{\mathcal{H}}_{Q2}^{(0)} = \frac{eQC_{14}E_0}{4I(2I-1)\hbar}\left(I_z^2 - \frac{1}{3}\mathbf{I}^2\right)\cos \phi_E \quad (27)$$

as the dominant term in $\bar{\mathcal{H}}^{(0)}$.

Note that, though derived from Eq. (25), Eq. (27) is diagonal, a transformation resulting from the positioning of the rf E field in the appropriate windows of the CLSW-16 sequence as shown in Fig. 1. Thus, for experiments that sample the magnetization only after an integral number of repeti-

tions of the cycle, its effect is analogous to the familiar static, secular quadrupolar interaction. This is the desired form of the effective Hamiltonian, splitting the NMR signal of, for example, a spin 3/2 ($I=3/2$ for ^{69}Ga, ^{71}Ga, and ^{75}As) into a triplet with $\pm 1/2 \leftrightarrow \pm 3/2$ satellite transitions split by angular frequency

$$\omega_Q = \frac{eQC_{14}E_0}{6\hbar}\cos\phi_E \tag{28}$$

from the central $1/2 \leftrightarrow -1/2$ transition. This expression for the quadrupole splitting frequency of a spin 3/2 is derived, with foreknowledge of the density matrix calculation of the NMR signal in Sec. IV, from the coefficient of I_z^2 in Eq. (27). Finally, we note that $\mathbf{I}^2 = I(I+1)$ is a number with no effect on spin evolution and choose $\phi_E = 0$.

III. APPLICATION TO *n*-TYPE QWs

The goal of this section is to describe a specific example where the polarization response of quantum-confined electrons to $\mathbf{E}(t)$ is observable with the POWER approach via rf-LQSE-induced quadrupole splittings. As above, the directions of both $\mathbf{B}_0$ and the rf E field are parallel to the [001] crystal axis. We evaluate the field at each layer of the quantum well as the sum of a homogeneous part, as would be present due to an applied voltage drop across bulk GaAs, and a part which is due to the 2D electron gas, as distorted by that homogeneous part. In the Appendix, the distribution of n-type carriers in the QW is calculated with a particle-in-a-box model of the ground-state electronic envelope $\Psi(z)$ perturbed by the E field. This wave function gives rise to the spatially varying part of the internal polarization field $\mathbf{E}_{\text{int}}$ through Gauss' law

$$\nabla \cdot \mathbf{E}_{\text{int}} = \frac{\partial}{\partial z} E_{\text{int},z} = \frac{\rho_e(x,y)}{\kappa\epsilon_0}|\Psi(z)|^2, \tag{29}$$

where $\rho_e(x,y)$ is the sheet density of charge in the QW, κ is the GaAs static dielectric constant, and ϵ_0 is the permittivity of free space. Only the E field of the quantum-confined space charge is included in $\mathbf{E}_{\text{int}}$ and the QW is taken as symmetric.[32] The perturbation theory treatment in the Appendix yields

$$\Psi(z) = a^{-1/2}\cos\left(\frac{\pi z}{2a}\right) - a^{1/2}c_0\sin(2\omega_0 t + \phi_E)\sin\left(\frac{\pi z}{a}\right), \tag{30}$$

where

$$c_0 = \frac{128 m^* a \Phi_0}{27\hbar^2\pi^4}, \tag{31}$$

$2a$ is the width of the QW, m^* is the electron's effective mass in GaAs, and $\Phi_0 = 2aeE_0$ is the linear rise in the box potential from $z=-a$ to $z=a$ provided by $\mathbf{E}(t)$ in Eq. (22). It is sufficient to treat $\mathbf{E}(t)$ as a *stationary* perturbation to the one-dimensional (1D) particle-in-a-box potential since it is weak and its frequency is much smaller than the lowest spatial Bohr frequency. After inserting Eq. (30) into Eq. (29), we integrate the resulting expression with respect to a dummy variable in place of z from $-a$ to z and from z to a. The latter of these two results is subtracted from the former, yielding

$$\begin{aligned} E_{\text{int}}(z,t) = {} & \frac{-\rho_e(x,y)}{\kappa\epsilon_0} \\ & \times\Bigg[\left(\frac{1}{a} + \frac{c_0^2 a}{2}\right)z + \frac{1}{\pi}\sin\left(\frac{\pi z}{a}\right) - \frac{c_0^2 a^2}{4\pi}\sin\left(\frac{2\pi z}{a}\right) \\ & + \cos(4\omega_0 t + 2\phi_E) \\ & \times\left(\frac{c_0^2 a^2}{4\pi}\left(\sin\left(\frac{2\pi z}{a}\right) - \frac{2\pi z}{a}\right)\right) + \sin(2\omega_0 t + \phi_E) \\ & \times\left(\frac{4c_0 a}{\pi}\left(\frac{1}{3}\cos\left(\frac{3\pi z}{2a}\right) + \cos\left(\frac{\pi z}{2a}\right)\right)\right)\Bigg]. \end{aligned} \tag{32}$$

There are three distinct components of $E_{\text{int}}(z,t)$: a time-independent component on the first line in square brackets of Eq. (32), and components at $4\omega_0$ and $2\omega_0$. Each of the three terms induces an E-field gradient with corresponding time dependence, however, we can ignore the contribution of the E field oscillating at $4\omega_0$, which is both small and off-resonance, and of the dc term, which induces a stationary component in $V'_{2,\pm 2}$ which does not cancel the time dependence of $\tilde{T}_{2,\pm 2}$. The total E field oscillating at $2\omega_0$, including the component

$$E_2(z) = \frac{-\rho_e(x,y)}{\kappa\epsilon_0}\left(\frac{4c_0 a}{\pi}\left(\frac{1}{3}\cos\left(\frac{3\pi z}{2a}\right) + \cos\left(\frac{\pi z}{2a}\right)\right)\right) \tag{33}$$

from the last line in Eq. (32), is resonant with $\tilde{T}_{2,\pm 2}$; thus, we must replace E_0 in Eqs. (27) and (28) with $(E_0 + E_2(z))$.

The contribution of $E_0(t)$ to the total E field oscillating at $2\omega_0$ is spatially homogeneous, inducing a uniform contribution to nuclear quadrupole splitting independent of z. However, the spatial dependence of $E_2(z)$ adds atomic-layer-dependent fine structure to the uniform contribution. The uniform effect provides two advantages: (1) spectral resolution of the informative satellites from the unshifted central transition, and (2) calibration of the system response to a known voltage drop. The amplitude of the distribution of $E_2(z)$ across the QW is depicted in Fig. 2, while the corresponding LQSE-induced quadrupole splitting for ^{69}Ga, calculated from Eq. (28), is indicated on the right-hand vertical axis.

IV. RESULTS AND CONCLUSIONS

The time evolution of the transverse nuclear magnetization up to time $t=nt_c$, where t_c is the duration of the CLSW-16 sequence, is calculated using the density matrix formalism as

$$\langle I_+\rangle(t) = \text{Tr}[I_+ U(t)\rho(0)U^\dagger(t)] \tag{34}$$

with

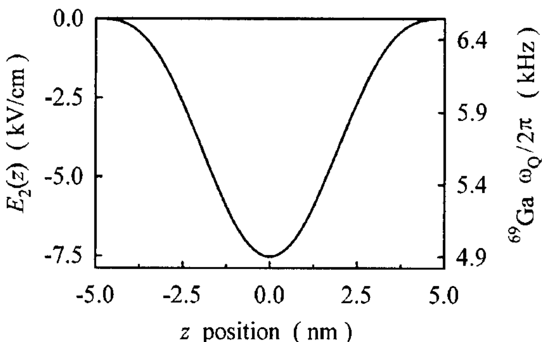

FIG. 2. The amplitude of $E_2(z)$, which is the component of $E_{int}(z,t)$ that is sinusoidally time dependent at twice the Larmor frequency of the NMR signal nucleus, is shown. The result was calculated for a symmetric 10 nm GaAs QW, assuming $\rho_e(x,y)=1.6\times10^{-3}$ C/m^2, corresponding to 10^{12} electron/cm^2, $\kappa=13.1$, and $(m^*/m_0)=0.067$, where m_0 is the electron rest mass. The amplitude of $E_0(t)$ used to obtain the result shown here was 30 kV/cm. The corresponding calculated ^{69}Ga quadrupole splitting [Eq. (28)] induced by the *total* field $[E_0(t)+E_2(z,t)]$ is shown on the right-hand vertical axis.

$$U(t)=\exp(-i\bar{\mathcal{H}}^{(0)}t). \quad (35)$$

The initial condition $\rho(0)$ of the density matrix is taken to be I_x, as results from a 90° preparation pulse prior to the start of the cycle.

In order to estimate the residual linewidth, we must consider the contribution to $\bar{\mathcal{H}}^{(0)}$ of the homonuclear J-coupling represented by $\tilde{\mathcal{H}}_J^{ik}$ in Eq. (26), which enters due to the nonequivalence of spins in adjacent atomic layers. Potter and Wu have used a novel echo-decay analysis of ^{69}Ga and ^{71}Ga NMR signals to estimate that for nearest-neighbor interactions of like spins (i.e., two-bond couplings) $J_{ik}(^{69}\mathrm{Ga})/2\pi=41$ Hz and $J_{ik}(^{71}\mathrm{Ga})/2\pi=60$ Hz.[33] Using these values, spectral features resulting from the homonuclear J-coupling have been included in a simulation where $\tilde{\mathcal{H}}_J^{ik}$ is truncated to a diagonal form by the difference in quadrupole coupling between layers. A given spin couples to a given number (between 0 and 12) of same-isotope nearest neighbors, thus spectra for each case, weighted both for the isotopic abundance of the species and for the number of ways to permute the given number of like nuclei among the twelve nearest-neighbor positions, were added. The envelope of the resulting distribution of frequency domain peaks was replaced by a best-fit Lorentzian. We expect that this gives an upper bound to the width that would result from the actual many-body dynamics, which is not tractable with known methods. Using this approach, a 200 Hz FWHM linewidth is estimated for ^{71}Ga when present at its natural isotopic abundance of 39.6%. Such a linewidth obscures some of the atomic-layer information in simulation of the resulting ^{71}Ga spectrum, as shown in Fig. 3(a). However, the same linewidth estimation procedure predicts a 10 Hz linewidth of the ^{69}Ga signal for a sample with 5% ^{69}Ga isotopic abundance, which is sufficient for atomic-layer resolution [Fig. 3(b)]. Linewidths <10 Hz FWHM have been obtained experimentally with CSLW-16,[22] proving that the other interactions can be removed to this degree in GaAs.

In simulation of the NMR experiment with the timeline shown in Fig. 1, we weighted each atomic layer's contribution to the signal expressed in Eq. (34) by the square of the QWs unperturbed ground-state envelope function at that layer. This is appropriate to optical detection methods based on the hyperfine coupling. As we have recently shown, more complex weighting may be necessary to quantitatively account for amplitude variations due to optical nuclear polarization, spin diffusion, and hyperfine relaxation.[22] Spectrally resolving individual layers would facilitate the investigation of these effects, by making information contained in the am-

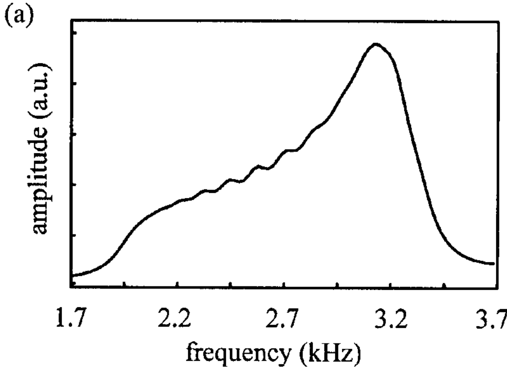

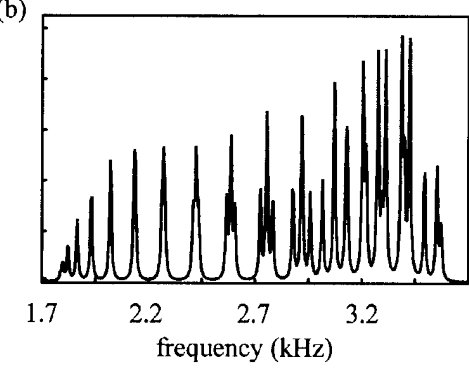

FIG. 3. (a) The simulated distribution and linewidth of ^{71}Ga quadrupole *satellites* of a 10 nm (36±1 atomic layers) GaAs quantum well (QW) with natural isotopic abundance. Central transition features (not shown) overlap at zero frequency in the rotating frame. The field distribution assumed in the simulation is the response of a quantum-confined carrier density of 10^{12} cm^{-2} to an applied rf E-field of 46 kV/cm along the [001] growth direction. The 200 Hz linewidth estimate of contributing features is discussed in the text. (b) The same simulation, but for ^{69}Ga with 5% isotopic abundance (10 Hz individual linewidths) and a 30 kV/cm rf E field. Many of the resonances due to individual atomic layers are resolved. Pairs of atomic layers that are located symmetrically across the QW center contribute identically overlapping satellites to the simulation. The largest amplitude feature corresponds to the contribution of the pair at the center of the 36-layer QW, while the smallest amplitude features correspond to atomic layers at the QW edges. Because the contribution of a 36-layer QW is combined with 1/2-weighted 35 and 37-layer contributions to the simulation, some features appear as closely spaced triplets with each line arising from a layer in a QW of each width. Finally, note that because the simulation is aliased about the $4.1\bar{6}$ kHz Nyquist frequency, the depicted structure is a reflection of the true frequency ordering of spectral lines into a mirror at the Nyquist frequency. Hence, the lines at right have the smallest net quadrupole splitting resulting from the partial cancellation of the applied field by the polarization response [$E_2(z)$ of Fig. 2].

plitude and frequency of the lines readily separable.

We summed the contributions from three separate calculations with 35, 36, and 37 atomic layers of Ga (~10 nm quantum wells) weighted by 1/2, 1, and 1/2, respectively, to obtain some sense of how predicted spectral features would be sensitive to the thickness variations typical of state-of-the-art epitaxial growth. The portion of the simulated ^{69}Ga (5% isotopic abundance) frequency domain spectrum containing satellite features is presented in Fig. 3(b), where the atomic-layer-resolved fine structure of the positive frequency quadrupole satellite is clear. The uniform contribution to the quadrupole splitting of about ~6.5 kHz due to the homogeneous rf LQSE of $E_0(t)$ is apparent in the simulated result, which is aliased around a Nyquist frequency of $4.1\bar{6}$ kHz that is practical for an experiment where CLSW-16 is used.

The simulations of Fig. 3 predict that atomic-layer-resolved spectroscopy should be possible in quantum wells using the rf LQSE with POWER NMR to provide an unprecedented local probe of electric fields and spin interactions. The analysis assumes that the LQSE coefficients measured in the bulk are also appropriate to a quantum well, a question that deserves fuller theoretical examination. From simple electrostatics, the contribution to the quadrupole interaction due to the field gradient of the envelope of the electron gas itself is negligible, in contrast to the effect calculated here, which is mediated by the LQSE dominated by covalent electrons. The particle-in-a-box model could readily be modified to include the finite well depth, which would result in finite NMR amplitude at and beyond the interface with the AlGaAs barrier. However, for several layers around the interface, it is anticipated that the heterogeneity of the bonding will lead to static quadrupole interactions whose tensors are unknown, but likely of a sufficient magnitude ($\gtrsim$20 kHz) that the multiple-pulse line narrowing as presented may fail for these few layers. Detailed simulation of these effects is possible and would aid in resolving and identifying the NMR transitions of interface layers, which has not been possible with methods applied to QWs to date.

Finally, it is worth noting that this new approach to high-resolution NMR may have useful analogs quite independent of the LQSE. For example, analogous nonsecular terms induced by sound waves (strain) are the basis for inducing transitions in nuclear acoustic resonance. The present work suggests a high-resolution analog based on the POWER approach.

ACKNOWLEDGMENTS

The authors wish to thank Michael Miller for his estimates of the linewidth contribution of homonuclear J-couplings. This work was supported by NSF Grant No. CHE-9612226.

APPENDIX

The QW is modeled as an infinite one-dimensional potential well, centered about $z=0$, where z is position along the growth direction. The quantum-confined eigenstates $\Psi_n(z)$ of the symmetric well can be categorized into even ($n=j$) and odd ($n=k$) states given by

$$\Psi_j(z)=a^{-1/2}\cos\left(\frac{j\pi z}{2a}\right), \tag{A1}$$

$$\Psi_k(z)=a^{-1/2}\sin\left(\frac{k\pi z}{2a}\right), \tag{A2}$$

where $j=1,3,5,\ldots$, $k=2,4,6,\ldots$, and $2a$ is the width of the QW. The energy of the nth state is

$$E_n=\frac{n^2\pi^2\hbar^2}{8m^*a^2}. \tag{A3}$$

An E field applied across the QW introduces a linear term in the potential well [$\Phi(z)=\Phi_0 1/2a(z+a)$ from $z=-a$ to $z=a$], which is treated as a small perturbation to the symmetric box Hamiltonian.

The first-order perturbation-theory correction to the wave function describing the ground state is

$$\Psi_1^{(1)}(z)=\sum_{n>1}\left[\frac{\langle\Psi_n^{(0)}|\left(\Phi_0\frac{z}{2a}\right)|\Psi_1^{(0)}\rangle}{E_1^{(0)}-E_n^{(0)}}\Psi_n^{(0)}(z)\right], \tag{A4}$$

where the superscripts (i) indicate ith-order perturbation corrections to the wave function and energy solutions of the Schrödinger equation. By symmetry, only the states $\Psi_k^{(0)}(z)$ of odd parity will contribute to the first-order correction of the even ground-state wave function. Inserting the expression for $\Psi_k^{(0)}(z)$ from Eq. (A2) and the corresponding energy given by Eq. (A3) into Eq. (A4) yields

$$\Psi_1^{(1)}(z)=\frac{2^6m^*a^{3/2}\Phi_0}{\hbar^2\pi^4}\sum_k\left[\frac{(-1)^{k/2}k}{(k^2-1)^3}\sin\left(\frac{k\pi z}{2a}\right)\right]. \tag{A5}$$

The term contributing at $k=4$ is only 1.6% of the magnitude of the term at $k=2$. Truncating the above series at $k=2$ yields

$$\Psi_1^{(1)}(z)=\frac{-2^7m^*a^{3/2}\Phi_0}{27\hbar^2\pi^4}\sin\left(\frac{\pi z}{a}\right). \tag{A6}$$

The sufficiency of the first-order perturbation-theory treatment of this problem is validated by derivation of the expression for the second-order correction to the ground-state wave function, which is

$$\Psi_1^{(2)}(z)=-\left(\frac{\Phi_0}{2a}\right)^2\times\sum_{n>1}\sum_{l>1}\left[\frac{\langle\Psi_l^{(0)}|z|\Psi_1^{(0)}\rangle\langle\Psi_n^{(0)}|z|\Psi_l^{(0)}\rangle}{(E_1^{(0)}-E_l^{(0)})(E_1^{(0)}-E_n^{(0)})}\Psi_n^{(0)}(z)\right]. \tag{A7}$$

Substituting the explicit forms of the zero-order wave function and energy expressions into Eq. (A7), and then taking parity considerations ($n=j$ with $j>1$ only, and $l=k$ only) into account, provides the expression

$$\Psi_1^{(2)}(z)=\frac{2^{12}a^{7/2}(m^*\Phi_0)^2}{\hbar^4\pi^8}\times\sum_{j>1}\sum_k\left[\frac{(-1)^{(j-1)/2}jk^2}{(k^2-1)^3(j^2-1)(j^2-k^2)^2}\cos\left(\frac{j\pi z}{2a}\right)\right]. \tag{A8}$$

The size of the second-order correction to the ground-state wave function can be calculated neglecting terms other than that with $(j,k)=(3,2)$, which is more than 30 times greater than the magnitude of the second-largest term in Eq. (A8). This approximation yields

$$\Psi_1^{(2)}(z)=\left(\frac{2^6m^*a^2\Phi_0}{\hbar^2\pi^4}\right)^2\frac{a^{-1/2}}{450}\cos\left(\frac{3\pi z}{2a}\right). \tag{A9}$$

The relative size of the coefficients of the second-order correction of Eq. (A9) to those of the first-order correction of Eq. (A6) is

$$\frac{48m^*a^2\Phi_0}{25\hbar^2\pi^4}=(1.62\times10^{36}\,\mathrm{J}^{-1}\,\mathrm{m}^{-2})a^2\Phi_0m_0/m^*, \tag{A10}$$

where m_0 is the electron rest mass. The three parameters determining the validity of the first-order perturbation-theory treatment are Φ_0, a, and (m^*/m_0). In the case of a 10 nm GaAs QW, where $(m^*/m_0)=0.067$, the relative size given in Eq. (A10) is $\sim(2.7\times10^{20}\,\mathrm{J}^{-1}\times\Phi_0)$, which limits Φ_0 to be less than 1.8×10^{-20} J if the second-order term is to be <5% of the first-order correction. This limit corresponds to an applied E field of ~115 kV/cm, which is well above the magnitude of the E field to be applied to the sample using the method we present; thus, the first-order perturbation-theory treatment is sufficient.

The normalized form of the QW ground-state wave function is then

$$\Psi_1(z)=(1+(ac_0)^2)^{-1/2}\left(a^{-1/2}\cos\left(\frac{\pi z}{2a}\right)-a^{1/2}c_0\sin\left(\frac{\pi z}{a}\right)\right), \tag{A11}$$

where c_0 is given by Eq. (31) and $a^2c_0^2\approx(4.5\times10^{37}\,\mathrm{J}^{-2}\times\Phi_0^2)$. Even in the case where the maximum, first-order-perturbation-theory-limited field of 115 kV/cm is applied to the QW sample, $(ac_0)^2\ll1$, and so the normalization coefficient in Eq. (A11) is set to unity.

[1]N. Bloembergen, Science **133**, 1363 (1961).

[2]N. Bloembergen, in *Proceedings of the 11th Colloque Ampere Conference on Electric and Magnetic Resonance*, Eindhoven, July 1962, edited by J. Smidt (North-Holland, Amsterdam, 1963), p. 225.

[3]D. Gill and N. Bloembergen, Phys. Rev. **129**, 2398 (1963).

[4]G. Lampel, Phys. Rev. Lett. **20**, 491 (1968).

[5]A. I. Ekimov and V. I. Safarov, JETP Lett. **15**, 319 (1972).

[6]D. Paget, Phys. Rev. B **25**, 4444 (1982).

[7]*Optical Orientation*, edited by F. Meier and B. P. Zakharchenya, in *Modern Problems in Condensed Matter Sciences* (North-Holland, Amsterdam, 1984), Vol. 8.

[8]S. K. Buratto, D. N. Shykind, and D. P. Weitekamp, Phys. Rev. B **44**, 9035 (1991).

[9]S. E. Barrett, R. Tycko, L. N. Pfeiffer, and K. W. West, Phys. Rev. Lett. **72**, 1368 (1994).

[10]J. A. Marohn, P. J. Carson, J. Y. Hwang, M. A. Miller, D. A. Shykind, and D. P. Weitekamp, Phys. Rev. Lett. **75**, 1364 (1995).

[11]D. Gammon, S. W. Brown, E. S. Snow, T. A. Kennedy, D. S. Katzer, and D. Park, Science **277**, 85 (1997).

[12]J. M. Kikkawa and D. D. Awschalom, Science **287**, 473 (2000).

[13]V. K. Kalevich, V. L. Korenev, and O. M. Fedorova, JETP Lett. **52**, 349 (1990).

[14]G. P. Flinn, R. T. Harley, M. J. Snelling, A. C. Tropper, and T. M. Kerr, Semicond. Sci. Technol. **5**, 533 (1990).

[15]S. E. Barrett, G. Dabbagh, L. N. Pfeiffer, K. W. West, and R. Tycko, Phys. Rev. Lett. **74**, 5112 (1995).

[16]S. W. Brown, T. A. Kennedy, E. R. Glaser, and D. S. Katzer, J. Phys. D **30**, 1411 (1997).

[17]P. Khandelwal, N. N. Kuzma, S. E. Barrett, L. N. Pfeiffer, and K. W. West, Phys. Rev. Lett. **81**, 673 (1998).

[18]S. K. Buratto, D. N. Shykind, and D. P. Weitekamp, J. Vac. Sci. Technol. B **10**, 1740 (1992).

[19]H. M. Cho, C. J. Lee, D. N. Shykind, and D. P. Weitekamp, Phys. Rev. Lett. **55**, 1923 (1985).

[20]D. G. Cory, J. B. Miller, and A. N. Garroway, J. Magn. Reson. **90**, 205 (1990).

[21]J. A. Marohn, D. N. Shykind, M. H. Werner, and D. P. Weitekamp, in *Review of Progress in Quantitative Nondestructive Evaluation*, edited by D. O. Thomson and D. E. Chimenti (Plenum, New York, 1993), p. 687.

[22]J. G. Kempf, B. M. Lambert, M. A. Miller, and D. P. Weitekamp (unpublished).

[23]E. Brun, R. Hahn, W. Pierce, and W. H. Tantilla, Phys. Rev. Lett. **8**, 365 (1962).

[24]E. Brun, R. J. Mahler, H. Mahon, and W. L. Pierce, Phys. Rev. **129**, 1965 (1963).

[25]T. Sleator, E. L. Hahn, M. B. Heaney, C. Hilbert, and J. Clarke, Phys. Rev. Lett. **57**, 2756 (1986).

[26]D. C. Newitt and E. L. Hahn, J. Magn. Reson., Ser. A **106**, 140 (1994).

[27]C. P. Slichter, in *Principles of Magnetic Resonance*, edited by P. Fulde (Springer, New York. 1992), Vol. 1, p. 485.

[28]M. Mehring, *Principles of High Resolution NMR in Solids* (Springer, Berlin, 1983).

[29]D. M. Brink and G. R. Satchler, *Angular Momentum*, third ed. (Oxford University Press, Oxford, 1993).

[30]K. A. Dumas, J. F. Soest, A. Sher, and E. M. Swiggard, Phys. Rev. B **20**, 4406 (1979).

[31]U. Haeberlen, *High Resolution NMR in Solids: Selective Averaging* (Academic, New York, 1976).

[32]The later assumption yields little effect on subsequent calculations presented here. We have calculated that if the initial QW wave function $\Psi(z)$ were perturbed by a large 10 kV/cm *inherent* slant in the QW potential, the largest resulting fractional shift of any single quadrupole satellite in the rf LQSE spectrum of a 10 nm GaAs QW would be only 2×10^{-2}. If, however, it is desired to characterize such deviations from the flatband condition, POWER NMR experiments in which the carrier density is modulated in synchrony with NMR multiple-pulse line narrowing are more appropriate.

[33]L. D. Potter and Y. Wu, J. Magn. Reson., Ser. A **116**, 107 (1995).

ZnSe/CdTe/ZnSe heterostructures

S. Rubini, B. Bonanni, E. Pelucchi, and A. Franciosi[a)]
Laboratorio Nazionale TASC-INFM, Area di Ricerca, Bldg. MM, S.S. 14, Km. 163.5, I-34012 Trieste, Italy

A. Garulli and A. Parisini
Istituto LAMEL del C.N.R., Via dei Castagnoli 1, I-40126 Bologna, Italy

Y. Zhuang and G. Bauer
Institut fur Halbleiterphysik, Johannes Kepler Universität Linz, Altenbergerstraße 69, A-4040 Linz, Austria

V. Holý
Laboratory for Thin Films and Nanostructures, Masaryk University, Brno 61117, Czech Republic

(Received 17 January 2000; accepted 18 May 2000)

Epitaxial ZnSe/CdTe/ZnSe heterostructures were successfully fabricated by molecular beam epitaxy on GaAs(001) wafers despite the large in-plane lattice mismatch (14.3%) between the two II–VI materials. X-ray reciprocal space maps and selected area diffraction results indicate single-phase, (111)-oriented growth of CdTe onto the lower ZnSe(001) cladding layer, and single-phase, (111)-oriented growth of the topmost ZnSe layer, with a small inhomogeneous residual strain within the CdTe layer. Cross-sectional transmission electron micrographs reveal a distribution of rotational microtwins within the (111)-oriented layers near each interface. The low-temperature near-band-edge photoluminescence from the CdTe layer is free-exciton related, and exhibits a linewidth of only 5–6 meV. © *2000 American Vacuum Society.* [S0734-211X(00)05904-7]

I. INTRODUCTION

The role of nonlinear optical materials in high-speed applications such as optical switching, amplification, frequency conversion and limiting is focusing renewed attention on CdTe. Due to its high electro-optic factor of merit, about three times as high as that of III–V semiconductors,[1] its high photorefractive parameters, and its photosensitivity in the telecommunication wavelength range when suitably doped, CdTe has important potential applications in devices as diverse as optical switches,[2,3] interconnects,[1] power limiters,[4] photorefractive gratings,[5] mostly in waveguide, etalon or doped fiber form.

Fabrication of compact waveguide structures incorporating CdTe rests on our ability to grow efficient cladding layers on high-quality CdTe. Best control of CdTe properties, including mobility, doping and carrier lifetime is afforded by epitaxial growth techniques such as molecular beam epitaxy (MBE). Although CdTe epilayers have been successfully grown by MBE on a variety of substrate materials, including Ge,[6] Si,[7–9] GaAs,[10] InSb,[11] HgTe,[12,13] and ZnSe,[14] surprisingly little effort has been devoted to date to the development of epitaxial cladding layers for CdTe.

We elected to focus on the implementation of epitaxial ZnSe/CdTe/ZnSe heterostructures by MBE on GaAs(001) wafers. Both ZnSe and CdTe are known to grow epitaxially on GaAs(001) at relatively similar growth temperatures despite the large difference in lattice parameters [5.6689 Å (Ref. 15) vs 6.482 Å,[16] for a 14.3% mismatch[17]], and in view of the difference in the refractive index of CdTe and ZnSe at 1.5 μm [2.74 (Ref. 18) vs 2.456 (Ref. 19)], such heterostructures should represent a promising intermediate step toward the implementation of epitaxial planar, unimodal CdTe waveguides on GaAs.[20]

II. EXPERIMENTAL DETAILS

ZnSe/GaAs, CdTe/ZnSe/GaAs and ZnSe/CdTe/ZnSe/GaAs heterostructures were fabricated by solid source MBE on GaAs(001) wafers using a facility which includes interconnected chambers for III–V and II–VI growth.[21] Nominally undoped ZnSe layers were grown at 290 °C using elemental Zn and Se effusion cells on undoped epitaxial (001) 2×4 GaAs buffer layers. The Zn and Se beam equivalent pressures were 6.5×10^{-7} and 1.6×10^{-6} Torr, respectively, as determined using an ion gauge located at the sample position. ZnSe growth on GaAs proceeded with a sharp, streaky 2×1 reflection high energy electron diffraction (RHEED) pattern, as expected for the Se/Zn beam pressure ratio (BPR) employed (2.5). The corresponding growth rate was 0.3 μm/h, as determined by means of a profilometer.

CdTe epilayers 0.3–0.4 μm thick were grown at 290 °C on ZnSe using elemental Cd and Te effusion cells and beam equivalent pressures of 3.9×10^{-7} and 4.1×10^{-7} Torr, respectively. During CdTe deposition on ZnSe the reconstruction changed from the initial twofold symmetry to the threefold symmetry characteristic of the (111) surface unit cell. Relatively weak half-order streaks were consistent with the 2×2 pattern expected for the CdTe(111)A surface termination.[21,22] Such a termination was reported by He *et al.* for growth conditions similar to ours.[14] The measured CdTe growth rate was 0.1 μm/h.

ZnSe/CdTe/ZnSe heterostructures were completed by growing a 1-μm-thick ZnSe upper cladding layer on top of

[a)]Also with Dipartimento di Fisica, Universita' di Trieste, I-34127 Trieste, Italy and Department of Chemical Engineering and Materials Science, University of Minnesota, Minneapolis, MN 55455; electronic mail: francios@sci.area.trieste.it

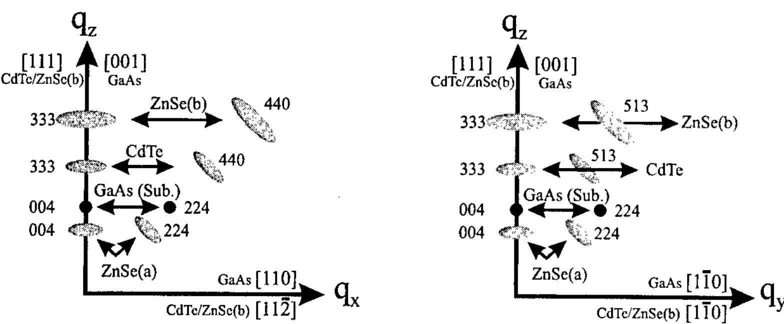

FIG. 1. Schematic diagrams of portions of the reciprocal space map expected from a ZnSe/CdTe/ZnSe/GaAs heterostructure, assuming full relaxation, (001) orientation for the GaAs substrate and lowermost ZnSe epilayer [denoted as ZnSe (a)], (111) orientation for CdTe and for the topmost ZnSe layer [denoted as ZnSe (b)]. In the diagrams q_z is along the [001] and [111] growth directions, q_x, (left panel) along the [110] direction of the (001)-oriented layer, taken as parallel to the [11$\bar{2}$] direction of the (111)-oriented layers, and q_y (right panel) along the [1$\bar{1}$0] direction of both types of layers.

the CdTe epilayer, using the same temperature and flux conditions employed to grow the lowermost ZnSe layer on GaAs. During ZnSe deposition on CdTe the RHEED pattern symmetry remained threefold, but an increased streak separation was observed relative to the initial CdTe-related pattern. This suggests that ZnSe growth proceeds with a (111)ZnSe‖(111)CdTe epitaxial relation and with large strain relaxation already in the early growth stage.[21]

In what follows we will mainly compare results obtained from two types of samples. Type A samples consisted of a 400-nm-thick CdTe layer grown on a 500-nm-thick ZnSe buffer on GaAs(001). Type B samples included a 300-nm-thick CdTe epilayer, sandwiched between two 1.3-μm-thick ZnSe cladding layers.

Reciprocal space maps from all heterostructures were recorded using a Philips MRD double-crystal x-ray diffractometer in triple axis mode, either with a 0.45 mm slit[23] or with a Ge (220) channel-cut analyzer crystal in front of the detector. The former configuration was used to detect the scattered intensity from the (001)-oriented ZnSe buffer layer in asymmetric (224) reciprocal space maps—where the peak intensities were comparatively low—with a resolution of 0.1°. The latter configuration—that provides an improved resolution of about 12 arcsec—was used in all other studies.

Cross-sectional transmission electron microscopy (TEM) studies were performed using a Philips CM30 microscope operated at 300 kV. Specimens were cut and prepared by conventional ion thinning.

Continuous wave photoluminescence (PL) experiments were performed at variable temperature using a closed-cycle He refrigerator. The CdTe layer was selectively excited using the 514.5 nm line of an Ar^+ laser with variable incident power density. The PL signal was detected using a GaAs-cathode photomultiplier and a 1 m grating monochromator, with an overall spectral resolution of 0.2 meV.

III. RESULTS AND DISCUSSION

A. Layer orientation and strain

Observation of the threefold RHEED pattern characteristic of the zinc blende (111) surface unit cell during CdTe growth on ZnSe(001), as well as during ZnSe overgrowth on the CdTe epilayer suggests dominant (111)CdTe‖ZnSe and (111)ZnSe‖(111)CdTe epitaxial relations, respectively, at the two interfaces. In order to unambiguously establish the epitaxial relations between the different epilayers, gauge strain relaxation and obtain information on the crystalline quality of the epilayers, we recorded reciprocal space maps of the scattered x-ray intensity for different Bragg reflections.

In Fig. 1 we sketch portions of the reciprocal space map expected from a ZnSe/CdTe/ZnSe/GaAs heterostructure, assuming (001) orientation for the GaAs substrate and lowermost ZnSe epilayer, and (111) orientation for CdTe and ZnSe top layers. We used labels (a) and (b) to denote reciprocal lattice points expected from the bottom-most and topmost ZnSe cladding layers, respectively. The finite full width at half maximum (FWHM) associated in the sketch with each reciprocal lattice point schematically illustrates a possible finite mosaic spread, resulting from the relaxation process.

The epitaxial relations within the interface plane used to build the sketches in Fig. 1 were as follows. For the interface between the CdTe layer and the lowermost ZnSe layer, i.e., ZnSe (a), we used [11$\bar{2}$]CdTe‖[110]ZnSe and [1$\bar{1}$0]CdTe‖[1$\bar{1}$0]ZnSe epitaxial relations, with complete strain relaxation of the CdTe and ZnSe overlayers. For the interface between the topmost ZnSe layer, i.e., ZnSe (b), and CdTe, we used [11$\bar{2}$]ZnSe‖[11$\bar{2}$]CdTe and [1$\bar{1}$0]ZnSe‖[1$\bar{1}$0]CdTe, with complete strain relaxation of the topmost ZnSe overlayer. In Fig. 1, q_z is along the growth direction and q_x, q_y are within the growth plane, i.e., in the (001) or (111) plane.

In Figs. 2–5 we show the scattered x-ray intensity distribution in reciprocal space maps near several reciprocal lattice points together with simulations. In Fig. 2(a) maps are shown near the symmetric (004) and (333) reflections, with the q_z direction parallel to the substrate normal (the GaAs [001] direction), and the q_x direction parallel to the substrate in-plane [110] direction, as in the left panel of Fig. 1. In addition to the (004) reflections from the GaAs(001) substrate and the lowermost ZnSe (a) (001)-oriented layer, the expected (333) reflections from the (111)-oriented CdTe and ZnSe (b) epilayers are indeed observed, with a separation quite similar to that expected for relaxed epilayers. The FWHMs for the CdTe (333) reflection are about 450 and 900 arcsec along the q_z and q_x directions, respectively. For the (333) reflection from the ZnSe (b) layer the corresponding FWHMs are about 400 and 2700 arcsec.

In Fig. 3(a) we show reciprocal space maps recorded near the positions expected for the asymmetric (440) reflections

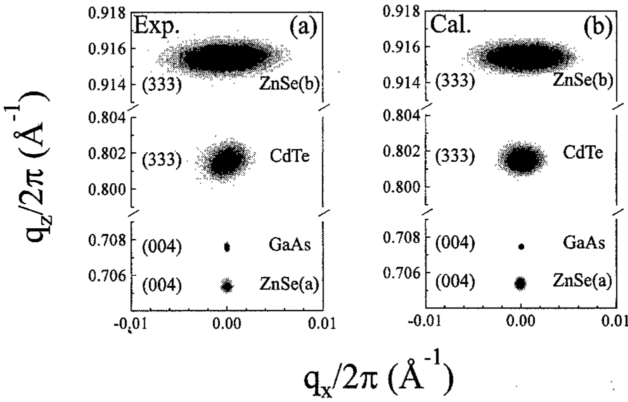

FIG. 2. Experimental (a) and calculated (b) reciprocal space maps within the q_x, q_z plane near the positions expected for the symmetric (004) reflections from GaAs substrate and the ZnSe (a) (001)-oriented epilayer, as well as for the symmetric (333) reflections from the CdTe and ZnSe (b) (111)-oriented overlayers. Intensity contours are given in steps of 10% of the maximum intensity.

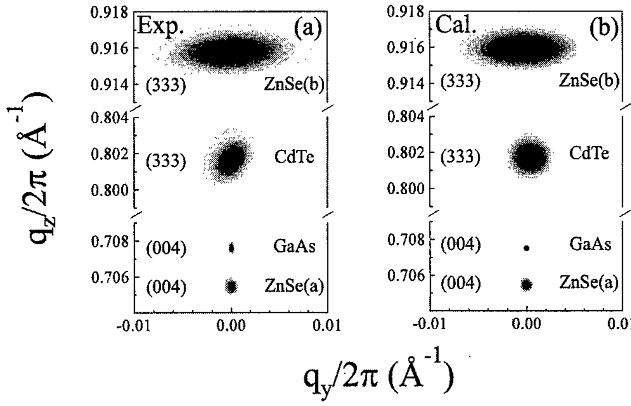

FIG. 4. Experimental (a) and calculated (b) reciprocal space maps within the q_y, q_z plane near the positions expected for the symmetric (004) reflections from the GaAs substrate and the ZnSe (a) (001)-oriented cladding layer, as well as for the symmetric (333) reflections from CdTe and ZnSe (b) (111)-oriented overlayers. Intensity contours are given in steps of 10% of the maximum intensity.

from the CdTe and ZnSe (b) (111)-oriented epilayers (see left panel of Fig. 1). Both reflections are observed, together with contributions from the (224) reciprocal lattice points from the GaAs substrate and the ZnSe (a) cladding layer. In the (224) reciprocal space maps, the shape of the intensity contours is slightly influenced by the use of a slit instead of the analyzer crystal (see experimental details section).

From the experimental positions of the subscripted maxima of the scattered intensity in Figs. 2 and 3 the in-plane lattice constants were determined as $d_{440}^{\mathrm{CdTe}}=1.1449$ Å and $d_{440}^{\mathrm{ZnSe\,(b)}}=1.0026$ Å for the (111)-oriented epilayers. The perpendicular lattice constants were also determined along the same lines as $d_{333}^{\mathrm{CdTe}}=1.2473$ Å and $d_{333}^{\mathrm{ZnSe\,(b)}}=1.0921$ Å.

In Fig. 4(a) maps are shown near the symmetric (004) and (333) reflections, with the q_z direction parallel to the substrate normal (the GaAs [001] direction), and the q_y direction parallel to the substrate in-plane [110] direction, i.e., with an azimuth rotated by 90° relative to Fig. 2(a). As illustrated in the right panel of Fig. 1, the CdTe/ZnSe (b) $[1\bar{1}0]$ azimuth is parallel to the GaAs substrate $[1\bar{1}0]$ orientation.

Finally in Fig. 5(a) we show experimental reciprocal space maps within the q_y, q_z plane near the positions expected for the asymmetric (513) reflections from the CdTe and ZnSe (b) (111)-oriented overlayers. As expected, contributions from the asymmetric (224) reflections from the GaAs substrate and the ZnSe (a) (001)-oriented cladding layer are also observed. The similarity with the sketch in the rightmost section of Fig. 1 is compelling. The in-plane lattice constants were calculated from the subscripted intensity maxima as $d_{513}^{\mathrm{CdTe}}=1.0954$ Å and $d_{513}^{\mathrm{ZnSe\,(b)}}=0.9589$ Å.

Taken together the results in Figs. 2(a)–5(a) unambiguously demonstrate that the epitaxial relations postulated in Fig. 1 were correct. Growth of CdTe with (111) orientation on ZnSe(001) therefore follows the same trend observed earlier[10] during growth of CdTe(111) on GaAs(001). The 14.3% lattice mismatch that would be expected for (001)CdTe‖(001)ZnSe growth is reduced to only −0.96% along the $[11\bar{2}]$CdTe‖[110]ZnSe during (111)CdTe‖(001)ZnSe epitaxial growth. Conversely, ZnSe overgrowth on the CdTe(111) epilayer, consistently yields single-phase, (111)ZnSe‖(111)CdTe growth, with no evi-

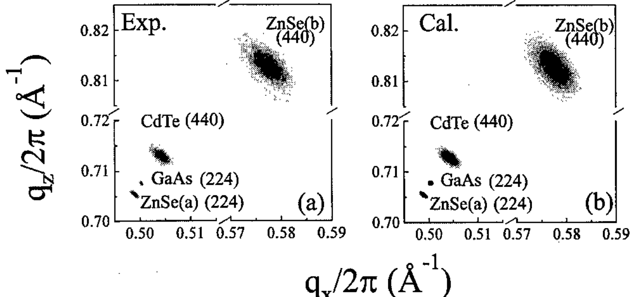

FIG. 3. Experimental (a) and calculated (b) reciprocal space maps within the q_x, q_z plane near the positions expected for the asymmetric (224) reflections from the GaAs substrate and the ZnSe (a) (001)-oriented cladding layer, as well as for the asymmetric (440) reflections from the CdTe and ZnSe (b) (111)-oriented overlayers. Intensity contours are given in steps of 10% of the maximum intensity.

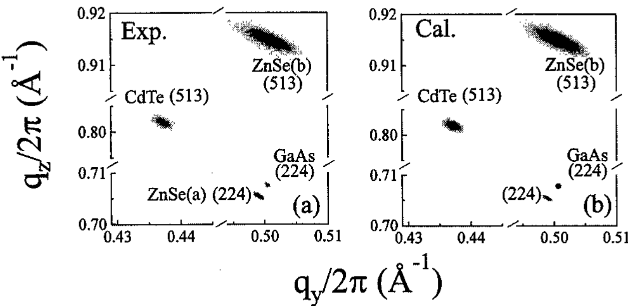

FIG. 5. Experimental (a) and calculated (b) reciprocal space maps within the q_y, q_z plane near the positions expected for the asymmetric (224) reflections from the GaAs substrate and the ZnSe (a) (001)-oriented cladding layer, as well as for the asymmetric (513) reflections from the CdTe and ZnSe (b) (111)-oriented overlayers. Intensity contours are given in steps of 10% of the maximum intensity.

TABLE I. Average residual strain in the three epilayers comprising a ZnSe/CdTe/ZnSe waveguide structure fabricated by molecular beam epitaxy on GaAs(001) wafers. The diagonal components of the strain tensors (ϵ_{xx}, ϵ_{yy}, and ϵ_{zz}) and the lattice mismatch (f_{xx} and f_{yy}) were determined from x-ray diffraction reciprocal space maps. First row: Measured residual strain for the lowermost ZnSe(001) cladding layer (a). Second row: Measured residual strain for the CdTe(111) waveguiding layer. Third row: Measured residual strain for the uppermost ZnSe(111) cladding layer (b). The reciprocal space direction is also indicated for each strain tensor component.

	$\epsilon_{xx}(\%)$	$\epsilon_{yy}(\%)$	$\epsilon_{zz}(\%)$	$f_{xx}(\%)$	$f_{yy}(\%)$
ZnSe (a)	+0.005 [110]	−0.022 [1$\bar{1}$0]	+0.035 [001]	+0.003 [110]	+0.003 [001]
CdTe	−0.242 [11$\bar{2}$]	−0.050 [1$\bar{1}$0]	−0.008 [111]	−0.960 [11$\bar{2}$]	14.3 [1$\bar{1}$0]
ZnSe (b)	−0.065 [11$\bar{2}$]	−0.044 [1$\bar{1}$0]	+0.100 [111]	−12.6 [11$\bar{2}$]	−12.6 [1$\bar{1}$0]

dence of polymorphic tendencies in the range of growth parameters explored.

Quantitative analysis of the relative positions of the maxima of the scattered x-ray intensity relative to the GaAs substrate peaks in Figs. 2(a)–5(a) allowed us to derive the average residual strain of the different epilayers within the heterostructure. In the calculations we used the following relations among the diffraction vectors (see Fig. 1):

$$\mathbf{h}_{513}=\mathbf{h}_{333}+2\mathbf{h}_{1\bar{1}0},\qquad \mathbf{h}_{440}=\tfrac{8}{9}\mathbf{h}_{333}+\tfrac{4}{3}\mathbf{h}_{11\bar{2}}. \tag{1}$$

The in-plane lattice constants for the CdTe (111) and ZnSe (b) layers were determined as $d_{1\bar{1}0}^{\mathrm{CdTe}}=4.5812$ Å, $d_{11\bar{2}}^{\mathrm{CdTe}}=2.6399$, $d_{1\bar{1}0}^{\mathrm{ZnSe\,(b)}}=4.0067$ Å, and $d_{11\bar{2}}^{\mathrm{ZnSe\,(b)}}=2.3128$ Å. From these, and from the previously determined perpendicular lattice constants, we derived the residual strain and lattice mismatch of the different epilayers.[24] We show the results in Table I in terms of the normal (ϵ_{zz}) and in-plane (ϵ_{xx}, ϵ_{yy}) diagonal components of the strain tensor. The experimental uncertainty on the determination of the strain is ±0.01%, i.e., $\pm 1\times 10^{-4}$. Both the bottom and top ZnSe cladding layers can therefore be considered largely relaxed within experimental uncertainty. A small but non-negligible residual strain appears to be present within the CdTe layer in the [11$\bar{2}$] direction, where the misfit with the underlying ZnSe layer in the [110] direction is only −0.96%.

B. Kinematic diffraction analysis and mosaic-crystal model

The experimental width of the different reflections in the reciprocal space maps carries information about the crystalline quality of the epilayers. We attempted to extract such information by simulating the measured reciprocal space maps using kinematic diffraction theory and the mosaic-crystal model.[25] In this model, mosaic blocks of average size R are separated from each other by piled-up threading dislocations with the same Burgers vector. Specifically, the threading segments of the misfit dislocations create small-angle boundaries between adjacent mosaic blocks and the blocks are assumed to be rotated with respect to each other by an angle Δ. Within each mosaic block, the scattering is assumed to be coherent, i.e., there are no dislocations and no random strain fields.

The distribution of the intensity diffusely scattered from a mosaic layer can be expressed by the Fourier transform of the correlation function $C(\mathbf{r}-\mathbf{r}')$ (Ref. 25):

$$I(q_x,q_z)=\int_{-\infty}^{+\infty}dq_y\int_V d^3(\mathbf{r}-\mathbf{r}')e^{-i\mathbf{q}\cdot(\mathbf{r}-\mathbf{r}')}C(\mathbf{r}-\mathbf{r}'), \tag{2}$$

where V is the volume of the mosaic layer. The x axis is parallel to the sample surface, the z axis parallel to the outward surface normal, and the y axis perpendicular to the scattering plane. The position vector $\mathbf{q}$ in reciprocal space is defined relative to the reciprocal lattice point $\mathbf{h}$, and the integration over q_y is performed because of the vertical divergence of the primary beam. The correlation function is defined as

$$C(\mathbf{r}-\mathbf{r}')=\langle e^{i\mathbf{h}\cdot(\mathbf{u}(\mathbf{r})-\mathbf{u}(\mathbf{r}'))}\rangle, \tag{3}$$

where $\mathbf{u}(\mathbf{r})$ is the random shift of the atom at point $\mathbf{r}$ due to mosaicity. If the layer consists of randomly positioned and randomly rotated mosaic blocks and the crystal lattice within each block is unstrained, the strain tensor of a block is purely antisymmetric and the correlation function can be expressed as

$$C(\mathbf{r}-\mathbf{r}')=P(\mathbf{r}-\mathbf{r}')\exp[-\tfrac{1}{6}\Delta^2|(\mathbf{r}-\mathbf{r}')\times\mathbf{h}|^2], \tag{4}$$

where Δ is the root-mean-square (rms) misorientation of the blocks and $P(\mathbf{r}-\mathbf{r}')$ is the probability of finding points $\mathbf{r}$ and $\mathbf{r}'$ in the same block.[25]

Simulations were performed assuming a spherical shape for the blocks with a single characteristic radius R. The values of R and of Δ were determined through a least-squares fit of the experimental data to the predictions of Eqs. (2)–(4). The simulated reciprocal space maps are shown in Figs. 2(b)–5(b). The quality of the fit is extremely comforting in view of the approximations involved in our analysis. Attempts to determine two characteristic radii (ellipsoidal shape of the blocks) were unsuccessful. In this case the fitting parameters were correlated, and this resulted in a very large statistical uncertainty in the parameters.

The values of the structural parameters obtained from the simulations are summarized in Table II. The parameters depend somewhat on the azimuthal direction of the scattering plane. Intensity maxima near different reciprocal lattice points but corresponding to the same epilayer and the same

TABLE II. Values of the structural parameters obtained by fitting the measured reciprocal space maps to the predictions of the mosaic-crystal model and kinematic diffraction theory. Intensity maxima near different reciprocal lattice points but corresponding to the same epilayer and the same azimuth of the scattering plane were fitted simultaneously. The parameters in the second, third and fourth rows correspond to the topmost ZnSe (b) epilayer, the CdTe waveguiding layer, and the (001)-oriented ZnSe (a) lower cladding layer, respectively. Column 1: azimuth. Column 2: reflections used in the fitting procedure. Column 3: average radius of the spherical crystal blocks. Column 4: root-mean-square angle of rotation between adjacent crystal blocks.

Azimuth	Diffraction	R (Å)	Δ (degrees)
$[11\bar{2}]$	ZnSe(333)+ZnSe(440)	300±50	0.43±0.04
$[1\bar{1}0]$	ZnSe(333)+ZnSe(513)	320±30	0.40±0.03
$[11\bar{2}]$	CdTe(333)+CdTe(440)	290±40	0.20±0.04
$[1\bar{1}0]$	CdTe(333)+CdTe(513)	290±30	0.13±0.03
$[11\bar{2}]$	ZnSe(004)+ZnSe(224)	920±120	0.05±0.01
$[1\bar{1}0]$	ZnSe(004)+ZnSe(224)	930±120	0.04±0.01

azimuth of the scattering plane were fitted simultaneously. The reflections used in the fitting procedure are listed in the second column of the table.

The mosaic structure of the lower, (001)-oriented ZnSe (a) cladding layer is relatively independent of the azimuth. The corresponding average mosaic block size (~0.1 μm) is a factor of 3 larger than for the (111)-oriented layers, and the rms misorientation between adjacent blocks 3–5 times lower than for the CdTe waveguiding layer and 8–10 times smaller than for the topmost ZnSe (b) cladding layer. In the mosaic model this would indicate a larger separation of dislocation pileups and smaller concentrations of threading dislocations.

The rms misorientation of the mosaic blocks Δ is larger in the topmost ZnSe (b) cladding layer than in the CdTe layer. Also, in the topmost ZnSe layer, this value does not depend on the azimuth, while the value of Δ is larger in the $[11\bar{2}]$ azimuth than in the $[1\bar{1}0]$ direction for the CdTe layer. In the mosaic model, the threading segments of the misfit dislocations create small-angle boundaries between adjacent mosaic blocks, thus a larger value of Δ means a larger density of threading segments. Therefore, in the uppermost ZnSe layer the threading segments of all families of misfit dislocations are nearly equally populated, whereas the population of these segments in the CdTe layer depends on the azimuth. The radius R of the blocks (~0.03 μm) is nearly independent of the azimuth direction, and, within experimental uncertainty, consistent for the (111)-oriented CdTe waveguiding layer and ZnSe (b) cladding layer.

C. Extended defects and interfaces

To further probe the type and spatial distribution of extended defects within the heterostructures, we performed systematic cross-sectional TEM investigations in the $[1\bar{1}0]$ zone axis common to all of the epilayers. Representative elected area electron diffraction (SAED) results are summarized in Fig. 6. In Fig. 6(a), we show an image of the different layers comprising the overall ZnSe/CdTe/ZnSe/GaAs heterostructure obtained through cross-sectional TEM in dif-

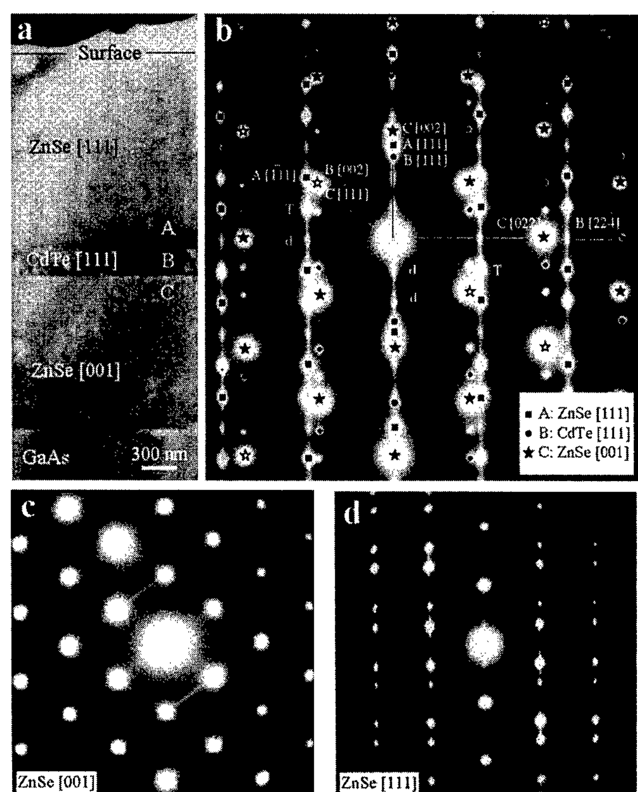

FIG. 6. Cross-sectional transmission electron microscopy (TEM) results from a ZnSe/CdTe/ZnSe/GaAs heterostructure. (a) Diffraction contrast (dark-field ⟨200⟩) image of the overall structure. (b) Selected area electron diffraction (SAED) pattern from a sampled area centered on the CdTe layer but also comprising adjacent portions of the ZnSe (a) and ZnSe (b) layers. Diffraction spots derive from the (001)-oriented ZnSe (a) layer (solid stars), the (111)-oriented CdTe layer (circles), and the (111)-oriented topmost ZnSe (b) layer (squares). Open stars denote coincident ZnSe(001) and CdTe(111) diffraction spots. In addition, type-d diffraction spots arise from double diffraction effects, while type-T spots derive from twins on the (111) growth plane. (c) SAED pattern from the lower, (001)-oriented ZnSe (a) layer. (d) SAED pattern from the topmost, (111)-oriented ZnSe (b) layer.

fraction contrast mode (dark-field ⟨200⟩). The SAED pattern in Fig. 6(b) was obtained from a sampled area centered on the CdTe layer but also comprising adjacent portions of the ZnSe (a) and ZnSe (b) layers. The resulting pattern shows diffraction spots from three inequivalent, superimposed $[1\bar{1}0]$ zone axis patterns corresponding to the (001)-oriented ZnSe (a) layer (stars), the (111)-oriented CdTe layer (circles), and the (111)-oriented topmost ZnSe (b) layer (squares).

As expected, the orientation relationships between the different layers that can be inferred from this micrograph are in agreement with those previously determined by x-ray diffraction studies. More interestingly, additional diffraction spots, some of which are denoted by "T" and "d" labels in Fig. 6(b), are also visible. Type d diffraction spots arise from double diffraction effects, while type T spots provide evidence of twinning on the (111) growth plane in both the CdTe and ZnSe (b) materials.

For what concerns the CdTe(111)/ZnSe(001) heterostructure we note that a similar, multiply twinned defect structure is shown by most $[1\bar{1}0]$ views of the CdTe(111)/GaAs(001) heterostructure, and has been associated with CdTe nucle-

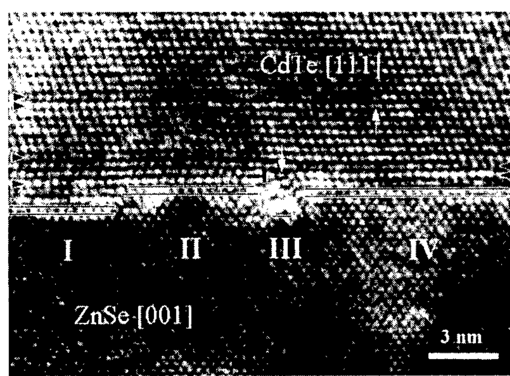

FIG. 7. High-resolution electron micrograph (HREM) of the CdTe(111)/ZnSe(001) interface, viewed along the common $[1\bar{1}0]$ zone axis (type-A sample). Interatomic channels correspond to the bright spots in the lattice fringes. The position of the interface is marked by a double horizontal line in the image. Surface steps with height ranging from 2 to 4 ml are observed to separate flat terraces, marked I–IV. Two stacking faults are observed to run at different distances from the interface on (111) planes. The stacking faults appear to be bounded by Schockley partial dislocations, denoted by white arrows. A micro twin is also clearly observed to end at the step between regions II and III.

ation at so-called direct and reverse steps of the GaAs surface.[26–28]

SAED patterns centered on the ZnSe (a) and ZnSe (b) cladding layers are shown in Figs. 6(c) and 6(d), respectively. The streaks observed in the diffraction pattern from the bottom ZnSe(001) layer indicate the presence of defects on {111} planes, namely stacking faults propagating from the (001)ZnSe‖(001)GaAs interface. Both Shockley stacking fault pairs lying on (111) and $(\bar{1}\bar{1}1)$ fault planes and single Frank stacking faults lying on $(\bar{1}11)$ or $(1\bar{1}1)$ fault planes are known to form at the ZnSe(001)/GaAs(001) interface.[29] Such defects are neither affected by strain, nor do they contribute efficiently to strain relaxation, but play an important role in II–VI device degradation, so that their concentration needs to be strictly controlled by using appropriate growth protocols.[30] An interesting implication of the results of Figs. 6(b) versus 6(c) is that the stacking faults in ZnSe giving rise to the streaking of the diffraction spots observed in Fig. 6(c) stop at the CdTe(111)/ZnSe(001) interface and will not affect the behavior of the overall heterostructure.

As to the topmost ZnSe (b) cladding layer, the SAED pattern in Fig. 6(d) still shows the presence of twins on the (111) growth plane indicating that these defects are also present in regions far from the interface with the underlying CdTe layer. It is worth noting that, in this micrograph as well as in Fig. 6(b), the observed vertical streaks suggest the presence of thin microtwins and/or stacking faults on the (111) growth planes in both the ZnSe (111) and CdTe (111) materials.

The interfaces of the CdTe layer with the ZnSe cladding layers have been examined by high-resolution electron microscopy (HREM). In Fig. 7, we show a HREM micrograph of the CdTe(111)/ZnSe(001) interface, viewed along the common $[1\bar{1}0]$ zone axis (type-A sample). Interatomic channels correspond to the bright spots in the lattice fringes of Fig. 7. The position of the interface can be detected with a small uncertainty (one atomic double layer) by the abrupt change in lattice orientation and lattice parameter and is marked by a double line in the image.

At the interface, surface steps with height ranging from two to four monolayers are observed to separate flat terraces, marked I–IV in this micrograph, indicating a measurable interface roughness. From this micrograph it appears that these interface features are not related to the presence of the stacking faults detected in the ZnSe(001) layer. Moreover, no evidence of second phases or interface reaction products was found in any of the samples examined.

The defect spatial distribution within the CdTe layer in Fig. 7 appears rather complex. Here we will limit ourselves to highlighting a feature of the observed defect arrangement that can be considered to be peculiar of the CdTe(111)/ZnSe(001) interface in the growth conditions employed, namely the coexistence in the interface region of stacking faults and microtwins on (111) CdTe planes. A typical example is given in Fig. 7 where two stacking faults are observed to run at different distances from the interface on (111) planes, as it can be easily verified by looking at the figure at a glancing angle. A microtwin is also clearly observed to end at the step between regions II and III. The stacking faults appear to be bounded by Schockley partial dislocations, denoted by white arrows in Fig. 7, having a (111) slip-plane, whereas a double extra (111) half-plane is clearly observed inside the microtwin structure.

Thus over the region III in Fig. 7 we observe the presence of a microtwin to the left and of a stacking fault to the right, suggesting that such locations—defined by opposite steps of different height—may act as nucleation sites for these defects. It is likely that stacking fault formation at such sites results from the dissociation of preexisting misfit dislocations and that, once formed, the stacking faults could propagate through the CdTe layer through a cross-slip mechanism, as should be the case for the stacking faults observed in Fig. 7 at a distance of a few nanometers from the interface. At present, however, it is not possible to ascertain the relative importance of microtwins and stacking faults in accommodating strain at the CdTe(111)/ZnSe(001) interface.

HREM observations were also performed at the ZnSe (111)/CdTe(111) interface (sample B). Representative results are depicted in Fig. 8. In this case, the interface between the two materials appears to be associated with a heavily faulted layer 3–5 nm thick, whose strong contrast has hindered any clear HREM observation of its structure. A high density of twins is observed close to the faulted interface layer in both materials. In Fig. 9, we present a bright-field TEM micrograph of the overall ZnSe(111)/CdTe(111)/ZnSe(001) heterostructure taken at a higher magnification relative to Fig. 6(a). The topmost ZnSe(111) layer clearly exhibits a higher twin density than observed in the CdTe layer.

We caution the reader that although, in principle, a distribution of rotational twins can contribute to accommodating residual strain at the interface, it is impossible at this stage to correlate the apparently higher density of twins with the different mismatch along $[11\bar{2}]$ZnSe‖$[11\bar{2}]$CdTe and

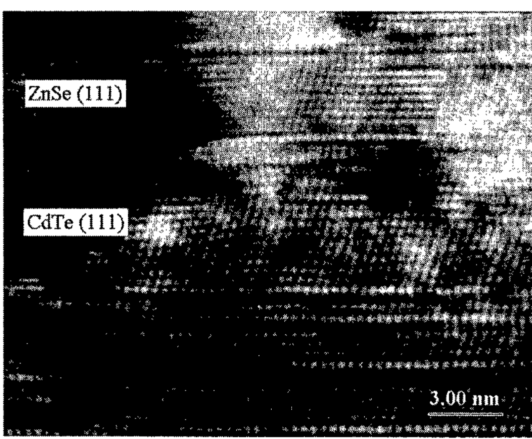

FIG. 8. High-resolution electron micrograph of the ZnSe(111)/CdTe(111) interface (type-B sample), viewed along the common $[1\bar{1}0]$ zone axis. In this case, as opposed to Fig. 7, the interface between the two materials appears to be associated with a heavily faulted layer whose strong contrast hinders any clear HREM observation of its structure. A high density of twins is observed close to the faulted interface layer in both materials.

$[11\bar{2}]$CdTe$\|$$[110]$ZnSe for the two interfaces. Multiply twinned structure can be all but eliminated from CdTe(111)/GaAs(001) using growth on vicinal substrates to cause a preferred step orientation, so that only one variant of CdTe(111) nucleates.[27,28] The implication for the present results is that surface roughness and substrate misorientation might also have an important role in determining the experimental twin distribution.

D. Optical properties

To gauge the optical quality of the CdTe epilayers, both before and after ZnSe overgrowth, we performed PL measurements as a function of excitation power density and temperature. Representative results for the near-band-edge (NBE) emission from samples A and B at a temperature of 16 K and a power density of 1 W/cm^2 are shown in Fig. 10.

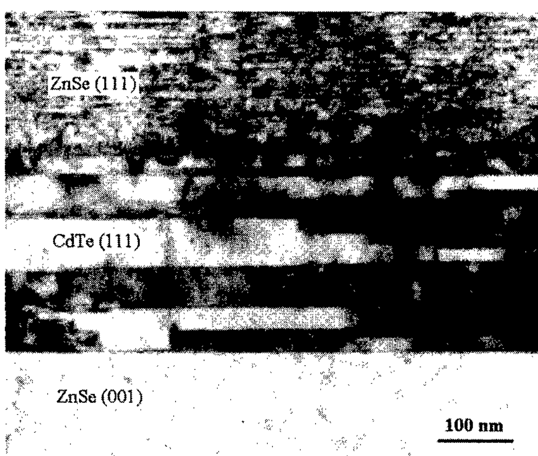

FIG. 9. Bright-field TEM micrograph of the overall ZnSe(001)/CdTe(111)/ZnSe(111) heterostructure taken at a higher magnification relative to Fig. 6(a). The topmost ZnSe (b) clearly exhibits a higher twin density than observed in the CdTe layer.

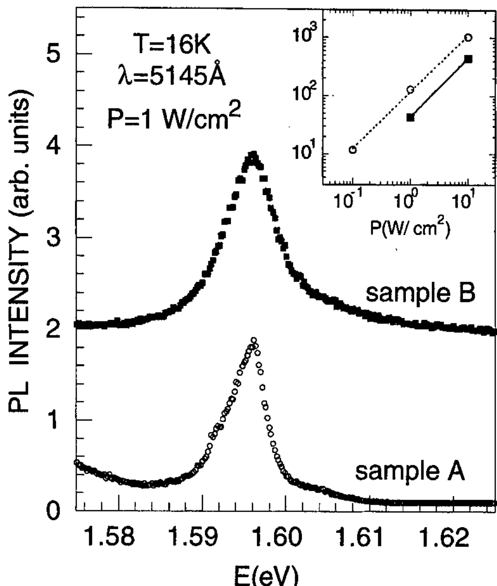

FIG. 10. Continuous wave photoluminescence mesurements at 16 K performed using the 514.5 nm line of an Ar$^+$ laser with power density of 1 W/cm^2 to selectively excite CdTe. Sample A consisted of a 400-nm-thick CdTe(111) layer grown on a 500-nm-thick ZnSe(001) buffer on a GaAs(001) wafer. Sample B included a 300-nm-thick CdTe(111) epilayer, sandwiched between ZnSe(111) and ZnSe(001) 1.3-μm-thick cladding layers. Inset: integrated near-band-edge emission from samples A (open symbols) and B (solid symbols), for different excitation power densities. Slopes are consistent with $I \propto P^n$, where I is the integrated emission intensity, P is the excitation power density, and n is found to be 0.97 ± 0.03 and 1.02 ± 0.03 for samples A and B, respectively.

The emission line, centered at 1.596 eV, corresponds to free-exciton recombination, the energy gap of CdTe being 1.606 eV (Ref. 31) and the expected exciton binding energy 10.5 meV (Ref. 32). The free-exciton origin of the NBE is also confirmed by the dependence of the PL intensity on the excitation power density. The integrated NBE from samples A and B is shown in the inset of Fig. 10 (open and solid symbols, respectively), for different excitation power densities. A linear relation with slope $n \sim 1$ in the log–log plot is expected for free-exciton recombination,[33] in agreement with the experimental observations for both samples. Biexcitonic or band-to-band emission would be expected to show a superlinear dependence of the integrated emission intensity,[33] and bound exciton emission should yield saturation effects,[33] both of which are in contrast with our experimental observations.

NBE emission in the 1.595–1.596 eV range has been observed by other groups for strain-free CdTe.[34,35] Moreover, no evidence of light-exciton recombination was observed at the highest excitation power densities explored in our samples. Such considerations suggest that the effect of the inhomogeneous residual strain within the CdTe layer—at most 0.24% along the $[11\bar{2}]$ direction—on the heavy-hole, light-hole and conduction band edge is negligible.

The FWHM of the NBE emission feature, which is usually taken as a phenomenological indicator of the epitaxial quality of the material, is 5–6 meV in Fig. 10. Such values compare well with those obtained by other authors for even

thicker CdTe epilayers on GaAs substrates,[35,36] and suggest that ZnSe overgrowth does not degrade appreciably the quality of the CdTe layer.

IV. CONCLUSIONS

We explored fabrication of epitaxial ZnSe/CdTe/ZnSe heterostructures by MBE on GaAs(001) wafers as an intermediate step toward the implementation of epitaxial planar, unimodal CdTe waveguides on GaAs. Despite the large in-plane lattice mismatch between the two II–VI materials, high-quality epitaxial structures could be produced, as indicated by our high-resolution x-ray diffraction and transmission electron microscopy results, with (111)CdTe‖(001)ZnSe and (111)ZnSe‖(111)CdTe epitaxial relations, respectively, at the two interfaces.

While the lower and topmost ZnSe epilayers were found to be largely relaxed within experimental uncertainty, a small inhomogeneous residual strain was found to exist within the CdTe waveguiding layer. Such strain has no detectable effect on the optical properties of CdTe, which exhibits dominant free-exciton emission and a promising photoluminescence linewidth of 5–6 meV, unaffected by ZnSe overgrowth.

Cross-sectional transmission electron microscopy studies revealed a distribution of rotational twins within the two (111)-oriented epilayers, probably reflecting nucleation at inequivalent step sites and therefore surface and interface roughness. Measurements in progress will ascertain the effects of the extended defect distribution—if any—on the electro-optic and waveguiding properties and assess the need to explore growth on vicinal surfaces.

ACKNOWLEDGMENTS

This work was supported in part by CORECOM, by the Consiglio Nazionale delle Ricerche of Italy under the MADESS program, and by the Commission of the European Communities under the PBULD Working Group program. The authors thank M. Martinelli, S. Pietralunga, and L. Zanella for useful discussions.

[1]R. Triboulet, E. Rzepka, A. Aoudia, G. Martel, and J.-Y. Moisan, Proc. SPIE **3178**, 22 (1997).

[2]A. Y. Hamad and J. P. Wicksted, J. Appl. Phys. **79**, 3816 (1996).

[3]D. Mayweather, M. J. F. Digonnet, and R. H. Pantell, J. Lightwave Technol. **14**, 601 (1996).

[4]S. B. Trivedi, R. J. Chen, K. Grasza, S. W. Kutcher, G. V. Nathan, W. H. Steier, D. Bacher, S. Guha, and P. Hood, Mater. Res. Soc. Symp. Proc. **479**, 179 (1998).

[5]V. I. Volkov, A. A. Borshch, M. S. Brodyn, and V. I. Rudenko, Proc. SPIE **3294**, 115 (1998).

[6]J. P. Zanatta, P. Ferret, P. Duvaut, S. Isselin, G. Theret, G. Rolland, and A. Million, J. Cryst. Growth **184/185**, 1297 (1998), and references therein.

[7]M. Kawano, A. A. Ajisawa, N. Oda, M. Nagashima, and H. Wada, Appl. Phys. Lett. **69**, 2876 (1996), and references therein.

[8]R. Sporken, F. Malengreau, J. Ghijsen, R. Caudano, S. Sivananthan, J. P. Faurie, T. van Gemmeren, and R. L. Johnson, Appl. Surf. Sci. **123/124**, 462 (1998), and references therein.

[9]S. C. Y. Tsen, D. J. Smith, J. W. Hutchins, B. J. Skromme, Y. P. Chen, and S. Sivananthan, J. Cryst. Growth **159**, 58 (1996).

[10]G. Bratina, L. Sorba, A. Antonini, G. Ceccone, R. Nicolini, G. Biasiol, A. Franciosi, J. E. Angelo, and W. W. Gerberich, Phys. Rev. B **48**, 8899 (1993), and references therein.

[11]Z. C. Feng, H. Gong, W. J. Choyke, N. J. Doyle, and R. F. C. Farrow, J. Mater. Sci. **7**, 23 (1996).

[12]J. P. Faurie, A. Million, and J. Piaguet, Appl. Phys. Lett. **41**, 713 (1982).

[13]D. J. Leopold, J. G. Broerman, G. J. Peterman, and M. L. Wroge, Appl. Phys. Lett. **52**, 969 (1988).

[14]L. He, J. Zhong, J. Lu, Z. Pong, M. Yu, J. Yu, Q. Xie, and S. Yuan, J. Cryst. Growth **101**, 147 (1990), and references therein.

[15]J. Petruzzello, J. Gaines, P. van der Sluis, D. Olego, and C. Ponzoni, Appl. Phys. Lett. **62**, 1496 (1993).

[16]R. D. Horning and J. L. Staudenmann, Phys. Rev. B **36**, 2873 (1987).

[17]We define here the lattice mismatch m between the overlayer 2 and the substrate 1 as $m=(a_{02}-a_{01})/a_{01}$ where a_{01} and a_{02} are the equilibrium (relaxed) lattice constants of the two materials.

[18]D. T. Marple, J. Appl. Phys. **35**, 539 (1964).

[19]*Numerical Data and Functional Relationship in Science and Technology*, edited by O. Madelung, Landolt-Bornstein, New Series, Group III, Vol. 17, Part B (Springer, Berlin, 1982).

[20]The number of modes in a planar waveguide is calculated as the smallest integer greater than $2d\lambda^{-1}(n_1^2-n_2^2)^{1/2}$, where d is the waveguide thickness and λ the operating wavelength. See, for example, B. E. A. Salech and M. C. Teich in *Fundamentals of Photonics*, edited by J. W. Goodman (Wiley, New York, 1991). The relatively large difference in refractive index for the two II–VI materials would produce a planar unimodal waveguide only for CdTe layer thicknesses below 0.61 μm. Ultimately, $ZnSe_{1-x}Te_x$ alloys would be preferable to ZnSe for cladding purposes.

[21]S. Rubini, B. Bonanni, E. Pelucchi, A. Franciosi, Y. Zhuang, and G. Bauer, J. Cryst. Growth **201/202**, 465 (1999).

[22]C. Hsu, S. Sivananthan, X. Chu, and J. P. Faurie, Appl. Phys. Lett. **48**, 908 (1986).

[23]See, for example, P. F. Fewster, Semicond. Sci. Technol. **8**, 1915 (1993).

[24]In-plane and perpendicular lattice strain and mismatch are defined here as follows: $\epsilon_\parallel=a_\parallel-a_r/a_r$, $\epsilon_\perp=a_\perp-a_r/a_r$, $f_\parallel=a_\parallel-a_0/a_0$, $f_\perp=a_\perp-a_0/a_0$, where $a_\parallel$ and $a_\perp$ are the measured, strained lattice constants of the overlayer, and a_r and a_0 are the the relaxed lattice constant of the overlayer material and the lattice constant of the underlying buffer layer, respectively.

[25]V. Holy, K. Wolf, M. Kasmer, H. Stanzl, and W. Gebhardt, J. Appl. Crystallogr. **27**, 551 (1994).

[26]J. Cibert, Y. Gobil, K. Saminadayar, S. Tatarenko, A. Chami, G. Feuillet, L. S. Dang, and E. Ligeon, Appl. Phys. Lett. **54**, 828 (1988).

[27]E. Ligeon, C. Chami, R. Danielou, G. Feuillet, J. Fontenille, K. Saminadayar, A. Ponchet, J. Cibert, Y. Gobil, and S. Tatarenko, J. Appl. Phys. **67**, 2428 (1990).

[28]J. E. Angelo, W. W. Gerberich, G. Bratina, L. Sorba, and A. Franciosi, Thin Solid Films **271**, 117 (1995).

[29]J.-M. Bonard, J.-D. Ganiere, S. Heun, J. J. Paggel, S. Rubini, L. Sorba, and A. Franciosi, Philos. Mag. Lett. **75**, 219 (1997).

[30]S. Heun, J. J. Paggel, L. Sorba, S. Rubini, A. Franciosi, J.-M. Bonard, and J.-D. Ganiere, Appl. Phys. Lett. **70**, 237 (1997), and references therein.

[31]J. L. Reno and E. D. Jones, Phys. Rev. B **45**, 1440 (1992).

[32]B. Segall and D. T. F. Marple, in *Physics and Chemistry of II–VI Compounds*, edited by M. Aven and J. S. Prener (North-Holland, Amsterdam, 1967), pp. 319–378.

[33]See, for example, H. B. Bebb and E. W. Williams, in *Semiconductors and Semimetals*, edited by R. K. Willardson and A. C. Beer (Academic, New York, 1972); for biexcitons see, for example, R. T. Phillips, D. J. Lowering, G. J. Denton, and G. W. Smith, Phys. Rev. B **45**, 4308 (1992).

[34]D. J. Leopold, J. M. Ballingall, and M. L. Wroge, Appl. Phys. Lett. **49**, 1473 (1986).

[35]D. J. Brinck and H. W. Kunert, Appl. Phys. Lett. **78**, 6720 (1995), and references therein.

[36]E. A. Milokhin, S. A. Dvoretskii, V. V. Kalinin, V. D. Kuzmin, Y. G. Sidorov, and I. V. Sabinina, Sov. Phys. Solid State **33**, 655 (1991).

Anisotropic strain in (100) ZnSe epilayers grown on lattice mismatched substrates

Z. Yang[a] and I. K. Sou
Advanced Materials Research Institute and Department of Physics, The Hong Kong University of Science and Technology, Clearwater Bay, Kowloon, Hong Kong, Republic of China

Y. H. Chen
Laboratory of Semiconductor Materials Science, Chinese Academy of Sciences, Republic of China

(Received 17 January 2000; accepted 15 May 2000)

We show that part of the reflectance difference resonance near the E_0 energy of ZnSe is due to the anisotropic in-plane strain in the ZnSe thin films, as films grown on three distinctly different substrates, GaAs, GaP, and ZnS, all show the resonance at the same energy. Such anisotropic strain induced resonance is predicted and also observed near the $E_1/E_1+\Delta_1$ energies in ZnSe grown on GaAs. The theory also predicts that there should be no resonance due to strain at the $E_0+\Delta_0$ energy, which is consistent with experiments. The strain anisotropy is rather independent of the ZnSe layer thickness, or whether the film is strain relaxed. For ZnSe films with large lattice mismatch with substrates, the resonance at the $E_1/E_1+\Delta_1$ energies is absent, very likely due to the poor crystalline quality of the 20 nm or so surface layer. © *2000 American Vacuum Society.*
[S0734-211X(00)05604-3]

The ZnSe/GaAs interface system offers a unique opportunity for the study of heterovalent semiconductor interfaces, as its in-plane optical anisotropy spectra show distinct resonance features near 2.7 and 3.1 eV, which are close to the E_0 and $E_0+\Delta_0$ energies of ZnSe.[1] While it is generally agreed that the 3.1 eV resonance is due to the interface state induced by the interface Ga–Se bonds,[1,2] the origin of the 2.7 eV resonance is still not very clear. This resonance was absent in the *in situ* reflectance difference (RD) spectra[2] measured at ZnSe growth temperature around 250 °C, because its strength is sensitive to temperature. The resonance is readily observable when the samples are at room temperature. In our earlier work we showed that this resonance was strong for Zn-rich ZnSe/GaAs interfaces, and much weaker for Se-rich interfaces,[1] and it was suggested that the resonance be due to the Zn–As interface bonds. Recently Hingel *et al.* suggested that this resonance could be due to anisotropic strain in the ZnSe layers grown on GaAs substrates,[3] rather than due to interface states, although the origin of such anisotropic strain was not made clear.

Recently we reported the photomodulation properties of the optical anisotropy of ZnSe thin layers grown on GaAs (100) substrates by molecular beam epitaxy.[4] Significant reduction in the strength of the RD resonance feature near the E_0 energy of ZnSe was observed when the ZnSe/GaAs interface was illuminated by a second beam of monochromatic light at photon energy below the ZnSe band gap. The resonance feature contains contributions from at least two different origins. One of them was quenched by illumination while the other changed little. The quenched one is due to the interface, and is therefore strong evidence that rules out the possibility that the 2.7 eV resonance is solely due to the anisotropic strain.

In this article we report our further study of the optical anisotropy of ZnSe epilayers grown on various lattice mismatched substrates. We show that residual anisotropic strain along the $[1,1,0]/[1,\bar{1},0]$ directions does exist in ZnSe epilayers even when the film thickness exceeds the critical thickness for strain relaxed, and that such strain will induce RD resonances at the E_0 and $E_1/E_1+\Delta_1$ energies, but not at the $E_0+\Delta_0$ energy, which is consistent with experiments.

The ZnSe/GaAs samples studied here are from the same batch we reported earlier,[1] plus two ZnSe films, one grown on GaP, and the other on a ZnS buffer layer grown on GaP, all by molecular beam epitaxy. The description of the RDS and the photomodulated RDS setup can be found in our earlier work.[4]

Figure 1 shows the RD spectra of ZnSe epilayers grown on substrates with large lattice mismatch. The thickness of both epilayers is about 230 nm and the ZnS buffer layer is about 10 nm. A well pronounced RD resonance near the E_0 energy of ZnSe, very similar to the one often observed in ZnSe films grown on nearly lattice matched GaAs substrates such as the one shown in Fig. 2(a), is clearly seen for both samples. Although we have shown by photomodulated RDS earlier that at least part of the resonance feature for ZnSe on GaAs is due to the interface states, there is another portion of the resonance which does not change with the laser illumination, and could be due to anisotropic strain. Here we clearly see that this resonance feature also exists in ZnSe layers grown on two other substrates. It is very unlikely that it is due to interface states, if there are any, at the ZnSe/substrate interface, since it is almost impossible for interface states at three interfaces, namely ZnSe/GaAs, ZnSe/GaP, and ZnSe/ZnS, which have significantly different chemical bond-

[a]On leave from the Laboratory of Semiconductor Materials Science, Institute of Semiconductors, Chinese Academy of Sciences, Box 912, Beijing 100083, Republic of China; electronic mail: phyang@ust.hk

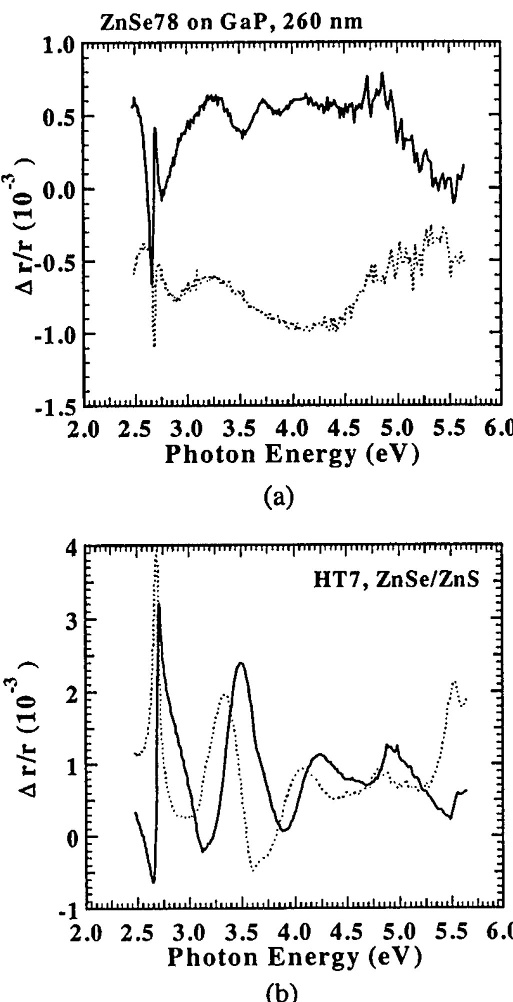

FIG. 1. Reflectance difference spectra of ZnSe thin films grown on (a) GaP substrate, and (b) ZnS buffer layer on GaP substrate.

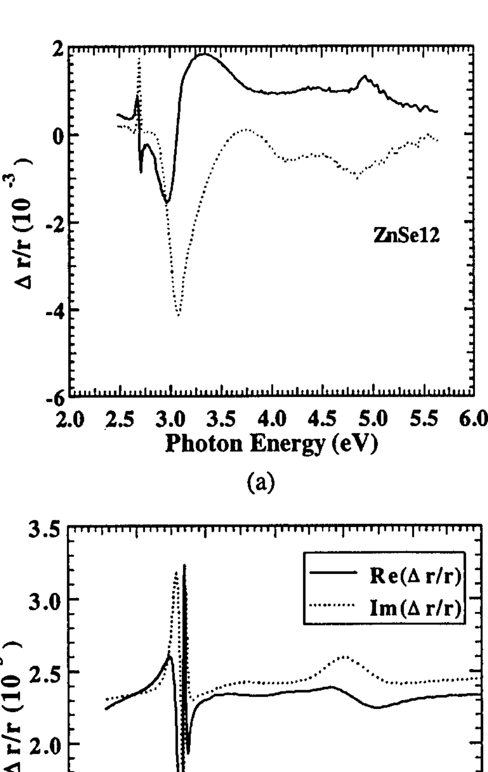

FIG. 2. Reflectance difference (RD) spectra of ZnSe thin films grown on GaAs substrate. (b) Theoretical RD spectra of the same sample.

ing and degree of lattice mismatch, to be at the same energy. Therefore there is only one possibility that we know of, that is the anisotropic in-plane strain.

To verify the existence of the strain, we performed theoretical calculations to see how such strain would induce RD resonances in other critical energy points. For simplicity, we assume that the strain is along the [1, 1, 0] direction only. Near E_0 the strain Hamiltonian for the valance bands under the framework of multiband $k*p$ theory is given by

$$\hat{H}_0=\begin{pmatrix} 0 & -i\Delta & -i\sqrt{2}\Delta \\ i\Delta & 0 & 0 \\ i\sqrt{2}\Delta & 0 & \Delta_0 \end{pmatrix}, \tag{1}$$

where $\Delta = D\epsilon_{110}$, D is the deformation potential, and ϵ_{110} is the strain. The strain will cause one Γ_8 hole band to shift by Δ and the other by $-\Delta$. The Γ_7 band, on the other hand, shifts by $2\Delta^2/\Delta_0$. Since from the observed RDS resonance strength at E_0 the estimated value of Δ is only of the order of 0.1 meV, no RD resonance is expected at $E_0+\Delta_0$. This is consistent with the earlier report,[3] and our results reported here. For ZnSe on GaP and ZnS in Fig. 1, no obvious resonances are present at the $E_0+\Delta_0$ energy either. For the ZnSe on GaAs, the resonance near 3 eV is known to be due to the ZnSe/GaAs interface state,[1-3] not the strain. So when strain was changed the resonance remained the same.[3]

For the states near the $E_1/E_1+\Delta_1$ critical points the strain Hamiltonian for the eight L states are given by

$$\hat{H}_1=\begin{pmatrix} -E_1-\Delta hk/2 & -\Delta hk \\ -\Delta hk & -(E_1+\Delta_l)-\Delta hk/2 \end{pmatrix}. \tag{2}$$

The optical anisotropy near these critical points is calculated in much the same way as the linear electro-optic effect.[5] The results are shown in Fig. 2(b) for $\Delta = 0.135$ meV. It is seen that apart from the resonance at E_0, the anisotropic strain also induces a resonance near 5 eV; which is the $E_1/E_1+\Delta_1$ critical points of ZnSe. The amplitude of the $E_1/E_1+\Delta_1$ resonance is independent of the film thickness once the thickness is beyond 100 nm, while the amplitude of the E_0 resonance oscillates with the thickness, as shown in Fig. 3. This is due to the different penetration depth of the light at the two critical energy points. The resonance can be readily observed in the experimental spectra of Fig. 2(a). Such resonance is also observed in many other ZnSe films grown on GaAs (not shown here due to limited space). The strain is rather independent of the film thickness,

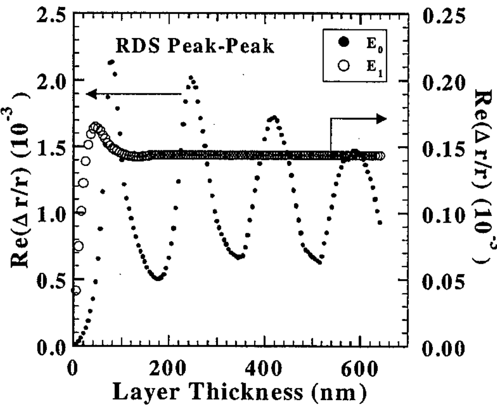

FIG. 3. Amplitudes of the E_0 and $E_1/E_1+\Delta_1$ resonances as a function of the ZnSe layer thickness.

and is present regardless whether the film is below or beyond the known critical thickness of ZnSe grown on GaAs. The amplitude ratio of the resonances at E_0 and $E_1/E_1+\Delta_1$ predicted by theory agrees quite well with the experiment, as seen in Fig. 2. Strict quantitative comparison is difficult to perform because of the interface state contrition to the E_0 resonance, and the possible nonuniform distribution of the strain, especially near the surface. The resonance near 5 eV is absent in the film grown on ZnS and GaP (see Fig. 1). This is probably because of the rather poor crystalline quality due to large lattice mismatch which could lead to a very poor surface layer. Since the penetration depth of light at 5 eV is only about 20 nm while at 2.7 eV it can reach over 1 μm of ZnSe film, the resonance at 5 eV is much more susceptible to poor quality surface layer than at 2.7 eV. For the ZnSe films grown on GaAs, the surface layer is of much better quality and the 5 eV resonance due to anisotropic strain is readily observed. Another possibility is that the strain anisotropy is not uniformly distributed throughout the film. Instead, it is probably more concentrated near the interface, and diminishes near the ZnSe surface, especially for large lattice mismatched substrates.

There are many existing indications that such strain anisotropy, although too small to be directly observed by x-ray diffraction or electron microscopy, does exist in strained ZnSe. For example, it is well known that during growth of ZnSe on GaAs, in many cases the strain release takes place along one of the [1,1,0] directions first due to the lower formation energy of the dislocation in that direction, and the strain relaxation along the $[1,\bar{1},0]$ direction takes place later (thicker film).[6] Misfit dislocations were found to be almost exclusively along the [1,1,0] direction, while micro twins were found to be almost all in the $[1,\bar{1},0]$ direction.[7] The anisotropic distribution of defects can generate anisotropic strain through the piezo-optic effects.[8] Another possibility is that such strain anisotropy could be due to the miscut angle of the (100) GaAs substrates and the different thermal expansion of ZnSe and the substrates. Further study is on the way to examine this possibility.

In summary, we show that part of the reflectance difference resonance near the E_0 energy of ZnSe is due to the anisotropic in-plane strain in the ZnSe thin films, as films grown on three distinctly different substrates, GaAs, GaP, and ZnS, all show the resonance at the same energy. Such anisotropic strain induced resonance is predicted and observed near the $E_1/E_1+\Delta_1$ energies in ZnSe grown on GaAs. The theory also predicts that there should be no resonance due to strain at the $E_0+\Delta_0$ energy, which is consistent with experiments. The strain anisotropy is rather independent of the ZnSe layer thickness, or whether the film thickness exceeds the critical value for strain relaxation. For ZnSe films with large lattice mismatch with substrates, the resonance at the $E_1/E_1+\Delta_1$ energies is absent, very likely due to the poor crystalline quality of the 20 nm or so surface layer.

This work was supported by the Research Grant Council Grant Nos. 609/95P and 6113/98P from the Hong Kong Government, and was carried out in the Zheng Gu Ru Thin Film Physics Laboratory, and the William Mong Semiconductor Cluster Laboratory at the Hong Kong University of Science and Technology.

[1]Z. Yang, I. K. Sou, Y. H. Yeung, G. K. L. Wong, J. Wang, C-x. Jin, and X.-y. Hou, J. Vac. Sci. Technol. B **14**, 2973 (1996).
[2]T. Yasuda, S. Miwa, K. Kimura, L. H. Kuo, C. G. Lin, K. Tanaka, and T. Yao, Phys. Rev. Lett. **77**, 326 (1996).
[3]K. Hingel, T. Yasuda, K. Kimura, S. Miwa, A. Ohtake, and T. Yao, J. Vac. Sci. Technol. B **16**, 2342 (1998).
[4]Z. Yang, Y. H. Chen, and I. K. Sou, Appl. Phys. Lett. **75**, 528 (1999).
[5]Y. H. Chen, Z. Yang, Z. G. Wang, and R. G. Li, Appl. Phys. Lett. **72**, 1866 (1998).
[6]H. Preis, T. Frey, T. Reisinger, and W. Gebhardt, J. Cryst. Growth 85 (1998).
[7]P. D. Brown, G. J. Russel, and J. Woods, J. Appl. Phys. **66**, 129 (1989).
[8]L. F. Lastras-Martinez and A. Lastras-Martinez, Phys. Rev. B **54**, 10726 (1996).

GaInAsP grown on GaAs substrate by solid source molecular beam epitaxy with a valve phosphorous cracker cell

D. H. Zhang,[a] X. Z. Wang, H. Q. Zheng, W. Shi, S. F. Yoon, and C. H. Kam
School of Electrical and Electronic Engineering, S2, Nanyang Technological University, Singapore 639798

(Received 17 January 2000; accepted 15 May 2000)

GaInAsP epilayers grown on GaAs substrate by solid source molecular beam epitaxy with a valve phosphorous cracker cell at varied arsenic beam equivalent pressure ratio, $f_{As}/(f_{As}+f_P)$, were investigated. It is found that the InGaAsP/GaAs can be easily grown with the solid sources, and the incorporation rate of arsenic is higher than that of phosphorous and varies with arsenic to phosphorous beam equivalent pressure (BEP) ratio, $f_{As}/(f_{As}+f_P)$. The lattice mismatch, $\Delta a/a_s$, varies from negative to positive linearly with BEP ratio and follows a polynomial expression with arsenic composition. GaP-, InP-, GaAs-, and InAs-like LO modes are observed in all samples and shift as expected. The GaP- and InP-like TO mode is observed in most of the samples while the GaAs-like TO mode is observed only in the sample with an arsenic composition of 0.96. Photoluminescence measurements reveal that the luminescence peak energy of the materials does not change significantly at high arsenic composition but increases drastically with the decrease of arsenic composition. The full width at half maximum is found to be the largest in the sample with peak energy of 1.78 eV due likely to cluster formation. All samples studied show smooth surfaces.
© *2000 American Vacuum Society.* [S0734-211X(00)05804-2]

I. INTRODUCTION

$Ga_xIn_{1-x}As_yP_{1-y}$ materials lattice matched to InP (GaInAsP/InP) and to GaAs (GaInAsP/GaAs) substrates have shown energy band gaps varying in a wide range. The former are suitable for infrared (1.3–1.6 μm) lasers and photodiodes for optical communications,[1,2] and the latter are applicable to light emitting devices which operate from visible to near infrared (0.6–1.1 μm).[3,4] Earlier, the GaInAsP/GaAs attracted relatively less attention than GaInAsP/InP as the band gap range of the commonly used AlGaAs fully covers that of the GaInAsP/GaAs, and the AlGaAs materials are thought to be much easier to grow. However, recent studies indicate that the GaInAsP/GaAs materials have many interesting properties.[5] They possess a direct band gap and high luminescence efficiency at all compositions from GaAs to GaInP ($1.42 \leq Eg \leq 1.9$ eV). Furthermore, GaInAsP/GaAs materials also show large valence-band offsets,[6] providing novel low-dimensional physical properties that are useful for photonic and electronic devices. Moreover, GaInAsP is not as easily oxidized as AlGaAs,[7] and the GaInAsP/GaAs laser diodes do not exhibit catastrophic growth of dark line defects at high optical excitation densities,[3] as opposed to what is observed for GaAs/AlGaAs lasers. There is no doubt that the lattice-matched to GaInAsP/GaAs materials deserve detailed studies.

So far, growth of the GaInAsP/GaAs has been limited to liquid phase epitaxy (LPE),[3,4,8] hydride vapor phase epitaxy,[9] organometallic vapor epitaxy (OMVPE).[10] metalorganic chemical-vapor deposition (MOCVD),[11] and gas source molecular beam epitaxy (GSMBE).[2,5] All the above techniques use gas sources. In recent years, solid source molecular beam epitaxy (SSMBE) has been attracting great attention due to environmental and economic considerations, but the growth of the GaInAsP has not been successful until the advent of the valve cracker source of phosphorous.[12] Since then, high quality GaInAsP/InP has been successfully grown in several groups[13–16] and laser diodes have also been fabricated with the quaternary material system.[17,18] To the best of our knowledge, there is no report on the GaInAsP/GaAs materials which are grown by (SSMBE). We have recently observed that growth of the GaInAsP on GaAs substrate is much easier than on InP substrate. This article will report the growth and properties of the GaInAsP on GaAs substrate by SSMBE with arsenic and phosphorous cracker cells at varied arsenic and phosphorous beam equivalent pressure (BEP).

II. EXPERIMENTAL DETAILS

Growth of the GaInAsP/GaAs was carried out in a solid source Riber 32 molecular beam epitaxy (SSMBE) system equipped with a Riber KPC250 valve phosphorous cracker cell and Riber VAC500 valve arsenic cracker cell. The purity of the phosphorous and arsenic is 7-nines, supplied by Rasa Industries of Japan. Prior to growth, oxide desorption was carried out under P_2 flux at a BEP of 5×10^{-6} Torr. The oxide desorption involves slowly ramping up the substrate temperature at a rate of 30 °C/min until the reflection high-energy electron diffraction (RHEED) pattern shows an abrupt transformation of 2×4 and 4×2 surface reconstruction. This surface transformation was adopted as a means for calibrating the substrate temperature (*Ts*) which was measured using an IRCON infrared pyrometer within suitable wavelength sensitivity and temperature range. The epitaxial GaIn-AsP layers studied were grown on semi-insulating GaAs(100) substrates at 500 °C. For the group III elements, the BEP of indium and gallium was fixed at 1.94×10^{-7} and

[a] Author to whom correspondence should be addressed; electronic mail: edhzhang@ntu.edu.sg

TABLE I. Growth conditions and compositions of the GaInAsP epilayers. The first four samples were grown at varied arsenic BEP while the rest were grown at varied phosphorous BEP. The compositions are obtained from EDX measurements.

Sample	$f_{As}/(f_{As}+f_P)$	Ga (%)	In (%)	As (%)	P (%)
1	0.05	0.60	0.40	0.31	0.67
2	0.08	0.57	0.43	0.33	0.69
3	0.10	0.59	0.41	0.44	0.56
4	0.17	0.60	0.40	0.51	0.49
5	0.18	0.61	0.39	0.52	0.48
6	0.33	0.59	0.41	0.53	0.47
7	0.38	0.58	0.42	0.67	0.33
8	0.45	0.57	0.43	0.69	0.31
9	0.56	0.58	0.42	0.77	0.23
10	0.71	0.61	0.39	0.86	0.14
11	0.91	0.62	0.38	0.96	0.04

2.0×10^{-7} Torr for all samples studied. This gives a composition of 60% gallium and 40% indium. For the group V elements, the samples studied are divided into two groups. The first group of samples employed arsenic BEP of 5×10^{-6} Torr with the phosphorous BEP varied systematically. The second group of samples, however, employed a phosphorous BEP of 1×10^{-6} Torr with the arsenic BEP varied. The thickness of the $Ga_{0.6}In_{0.4}As_yP_{1-y}$ epitaxial layers was maintained at about 1 μm on the top of a GaAs buffer layer of 100 nm.

A Philips X'pert materials research diffractometer (MRD) system using a $CuK'_{\alpha1}$ source with (004) GaAs reflection, Renisshwa micro-Raman spectroscopy, LEO 982 scanning electron microscopy (SEM) with energy dispersion x-ray (EDX), conventional photoluminescence (PL) system and atomic force microscopy (AFM) were employed to assess the quality and compositions of the samples.

III. RESULTS AND DISCUSSION

Table I shows the arsenic to phosphorous BEP ratios, $f_{As}/(f_{As}+f_P)$, and the compositions of the epilayers used in this study. The first four samples were grown at fixed phosphorous BEP with arsenic BEP varied while the rest were grown at fixed arsenic BEP but with the phosphorous BEP varied. The compositions of the samples were examined by an EDX. The indium and gallium compositions are about 40% and 60%, respectively, with an error less than 6% as the BEP of both group III elements was kept unchanged for all the samples. As the ratio increases, the arsenic composition increases monotonically while the phosphorous decreases. As seen from the table, the sticking coefficient or the incorporation rate of arsenic is much higher than that of phosphorous, especially at small ratios. For example, the incorporated As is about 31% of the total group V elements in the epilayers for the arsenic to phosphorous BEP ratio of 0.053 while the incorporated P is only 69%. At the arsenic to phosphorous BEP ratio of 0.91, however, the As composition is 95.7% of the total group V elements in the epilayer while the corresponding P composition is 4.3%. These data also indicate that the incorporation rate of As decreases with the arsenic to phosphorous BEP ratio but the incorporation rate of P increases.

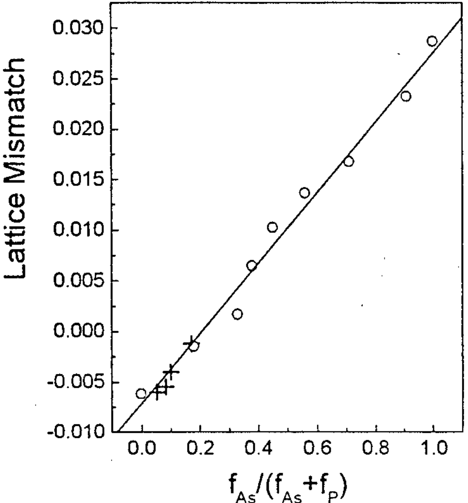

FIG. 1. Lattice mismatch as a function of arsenic to phosphorous beam equivalent pressure ratio, $f_{As}/(f_{As}+f_P)$. The open circles are from the samples grown at varied phosphorous BEP while the cross symbols are from the samples grown at varied arsenic BEP.

Figure 1 shows the lattice mismatch of the samples as a function of arsenic to phosphorous BEP ratio, $f_{As}/(f_{As}+f_P)$. The solid open circles in the figure are from the samples grown with varied phosphorous BEP while the cross symbols are from the samples grown with varied arsenic BEP. As seen from the figure, the lattice mismatch from both groups of samples varies linearly with the arsenic to phosphorous BEP ratio from negative to positive values. By adding the lattice constants of the two extreme crystals, InGaP and InGaAs, into the figure, the lattice mismatch $\Delta a/a_s$ can be described by the following expression:

$$\Delta a/a_s=(\Delta a/a_s)_{InGaP}+0.035[f_{As}/(f_{As}+f_P)] \quad (1)$$

or

$$\Delta a/a_s=(\Delta a/a_s)_{InGaAs}-0.035[f_P/(f_{As}+f_P)]. \quad (2)$$

The ideal lattice match to GaAs appears at the arsenic to phosphorous BEP ratio around 0.19. Our results also indicate that the lattice mismatch is mainly related to the arsenic to phosphorous ratio rather than the absolute BEP employed in this work.

The relationship between lattice mismatch and the incorporated As in the $Ga_{0.6}In_{0.4}As_yP_{1-y}$ from $y=0$ to $y=1$ is shown in Fig. 2. The ideal lattice match appears at an arsenic composition of about 0.525, or a phosphorous composition of 0.475. For the arsenic compositions less than the critical value, the lattice mismatch is negative, indicating a tensile strain, and it does not change significantly within this composition range. Above the critical value, the mismatch is positive, indicating a compressive strain, and it increases drastically with arsenic composition. The lattice mismatch follows well with a polynomial expression, as indicated by the solid line

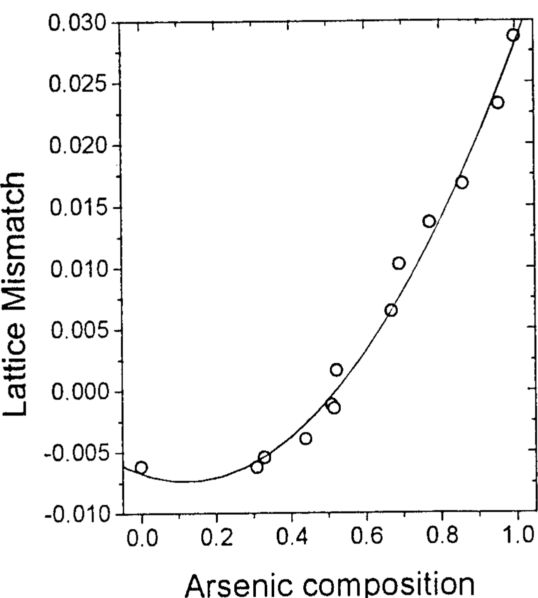

FIG. 2. Plot of lattice-mismatch vs arsenic composition. The solid line is from polynomial fit.

$$\Delta a/a_s = (\Delta a/a_s)_{\mathrm{InGaP}} - B_1 C + B_2 C^2, \tag{3}$$

where both B_1 and B_2 are constants with values of 0.011 and 0.046, respectively, and C is arsenic composition.

To verify the incorporation of phosphorous and its influence on the crystal structure, the Raman scattering was measured and the results from representatives of the two group samples which were grown at varied arsenic and phosphorous BEP, respectively, are given in Figs. 3(a) and 3(b), respectively. For the samples grown at varied arsenic BEP [as shown in Fig. 3(a)], where the As compositions are less than the critical value for the ideal lattice match, five peaks can be clearly distinguished. This observation is similar to that of Sugiura *et al.* for the GaInAsP grown by liquid phase epitaxy (LPE).[19] Peaks 1 and 2 are likely the GaP- and InP-like LO modes and peaks 4 and 5 are likely GaAs- and InAs-like LO modes. Peak 3 is likely the GaP- and InP-like TO mode. These conclusions can also be verified by the following observations. As arsenic composition or y increases, the intensity of the GaAs- and InAs-like LO modes (peaks 4 and 5) increases while the GaP- and InP-like LO modes (peaks 1 and 2) as well as their TO mode (peak 3) decreases. In addition, the five peaks also shift. As y increases, the GaP- and InP-like LO modes (peaks 1 and 2) as well as their TO mode (peak 3) shift towards a lower wave number, and both GaAs- and InAs-like LO modes (peaks 4 and 5) shift towards a higher wave number. These observations are similar to that reported by Inoshita[9] and Sugiura *et al.*[19] It should be mentioned that the Raman shift of the InAs-like LO mode (peak 5) is y dependent. It is towards a higher wave number in Fig. 4(a) because the arsenic compositions are less than 52% of the total group V elements in the epilayers.

Figure 3(b) shows the Raman results for the samples grown at varied phosphorous BEP where the arsenic compositions are more than 50% of the total group V elements in

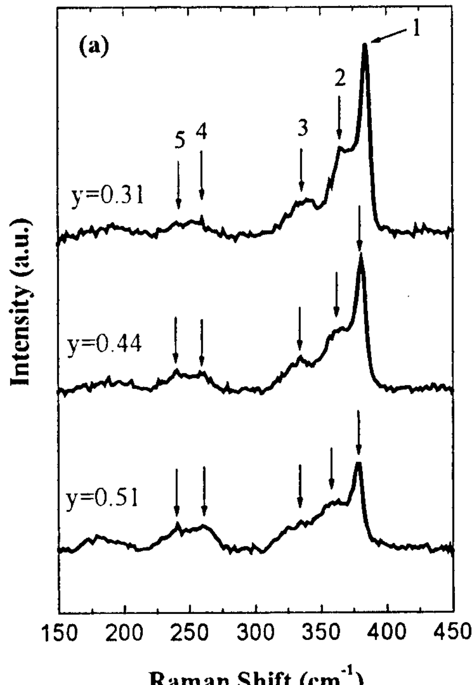

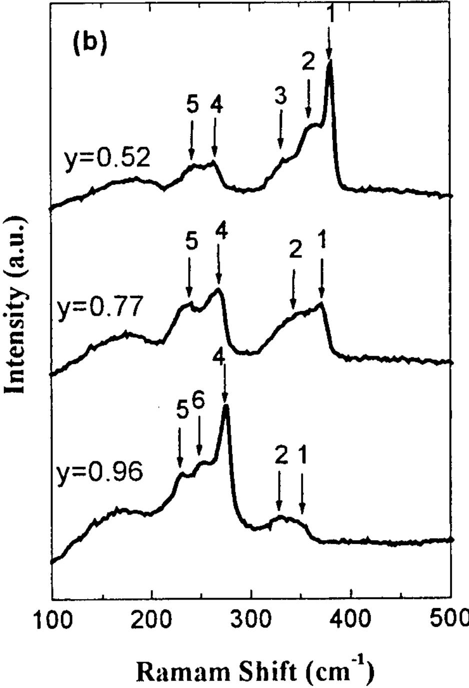

FIG. 3. Raman spectra of $In_{0.4}Ga_{0.6}As_yP_{1-y}$ (a) from the samples grown at varied arsenic BEP and (b) from the samples grown at varied phosphorous BEP. Arsenic compositions are indicated in the figure.

the epilayers. As the same as in Fig. 3(a), peaks 1 and 2 (GaP- and InP-like LO modes) continuously shift towards a lower wave number as the arsenic composition increases, and peak 4 (GaAs-like LO mode) shifts towards a higher wave number. Peak 5 (InAs-like LO mode), however, shifts towards a lower wave number. This is in agreement with previous observations.[19] Peak 3 (GaP- and InP-like TO mode) becomes hardly observable when As composition y is

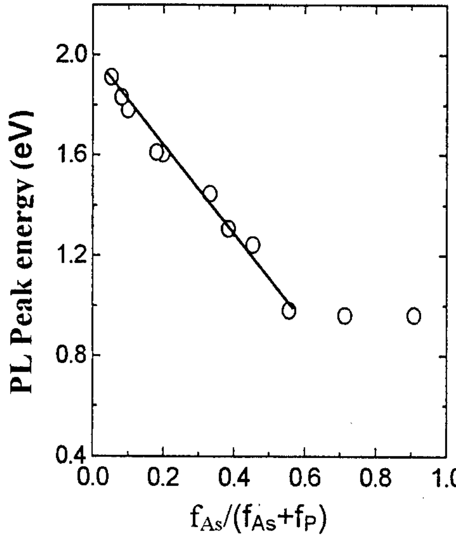

FIG. 4. Photoluminescence peak energy measured at 5 K as a function of $f_{As}/(f_{As}+f_P)$. The solid line is an aid for the eyes.

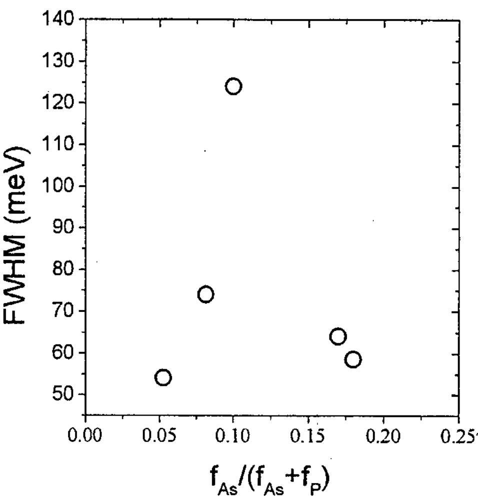

FIG. 5. Plot of full width at half maximum of photoluminescence spectra vs $f_{As}(f_{As}+f_P)$. The maximum occurs in the sample grown at a ratio of 0.1, which has an arsenic composition of 0.44 and a band gap of 1.78 eV.

greater than 0.7 due to the decrease of P composition. At $y = 0.96$, an additional peak 6 is observed at around 250 cm^{-1}, which is about 25 cm^{-1} away from the GaAs-like LO made. It is most likely the GaAs-like TO modes. The failure of observation in the other samples is mainly due to the smaller As compositions in the epilayers in which the x-ray signal of the GaAs-like TO mode (peak 6) is too weak to be observed.

The energy band gap of the materials can be approximately estimated using photoluminescence. Figure 4 shows the PL peak energy as a function of arsenic to phosphorous BEP ratio $f_{As}/(f_{As}+f_P)$. As shown in the figure, the luminescence peak of the epilayers grown at ratios above 0.5 does not change significantly, and the luminescence intensity is considerably weak. For the epilayers grown at low ratios, however, the luminescence is strong and the peak energy changes drastically. It is the highest for the epilayer grown at the smallest ratio and almost decreases linearly as the arsenic to phosphorous ratio increases up to 0.5. This decrease in band gap is mainly due to the reduction of P composition. The full width at half maximum (FWHM) of the samples is illustrated in Fig. 5. The sample grown at an arsenic to phosphorous BEP ratio of around 0.2, which has a lattice mismatch of 1.2×10^{-3}, has a relatively small FWHM. As the ratio is decreased, FWHM becomes higher. It reaches a maximum at a ratio of 0.1 that gives the epilayer peak energy of 1.78 eV. As the ratio decreases further, the FWHM starts dropping although the lattice mismatch is further accelerated. The sample grown at a ratio of 0.05 shows a FWHM value comparable to that of the nearly lattice-matched sample. It is well known that the lattice mismatch between the epilayer and substrate causes defects, such as vacancies, dislocations, and deep energy level traps, at/near the interface.[20] Such defects increase with the increase of lattice mismatch and widen the spectra. However, the defects related to the lattice mismatch are not the main origin for the widened spectrum of the sample with a luminescence peak of 1.78 eV as the mismatch of this sample is not the worst. A similar phenomenon was also observed by Mukai from the LPE grown samples, where the widened spectrum occurred at 1.75 eV and was attributed to clustering.[21]

To complete our characterization, surface smoothness of the epilayers is also examined and the average roughness as a function of arsenic to phosphorous BEP ratio is shown in Fig. 6. It is seen that the roughness varies only in a small range (2.7–9.3 nm) for samples studied but the surface of the nearly lattice-matched epilayers is smoother than that of others. It should be mentioned that the surface of the sample with widened luminescence spectrum peaked at 1.78 eV is comparable to that of other samples. This is in contrast to the LPE sample with a band gap of 1.75 eV, which is too rough to be grown thick enough, due possibly to the difference in growth technique.[21]

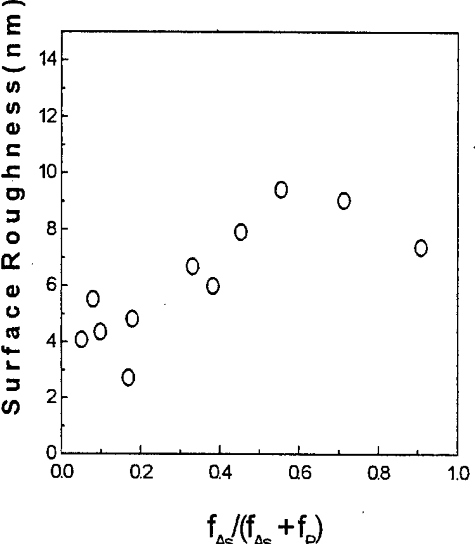

FIG. 6. Average surface roughness vs arsenic to phosphorous beam equivalent pressure ratio.

IV. CONCLUSION

In conclusion, GaInAsP materials on GaAs substrate can be easily grown by SSMBE with a phosphorous cracker cell. The sticking coefficient of arsenic is much greater than that of phosphorous, especially at low BEP, and varies with arsenic to phosphorous BEP ratio. The lattice mismatch varies from negative to positive values and can be described well by a linear relationship. It follows a polynomial expression with the arsenic composition. The lattice match of the $Ga_{0.6}In_{0.4}As_yP_{1-y}$ occurs at arsenic to phosphorous BEP ratio around 0.19 that corresponds to a y of 0.525. GaP-, InP-, GaAs- and InAs-like LO modes have been observed in all samples studied and they all shift with $f_{As}/(f_{As}+f_P)$. The GaP- and InP-like TO mode can be distinguished in the samples with y up to 0.52 while the GaAs-like TO mode can only be observed in the sample with a y as high as 0.96. From PL results, the peak energy of the epilayers increases rapidly only when arsenic composition is less than 0.52, and the linewidth of the sample with a peak energy of 1.78 eV is the largest due likely to cluster formation. All samples, including the 1.78 eV one, have a smooth surface.

[1]M. Razeghi, *The MOCVD Challenge: A Survey of GaInAs-InP for Photonic and Electronic Applications* (Hilger, Philadelphia, 1989), Vol. 1.
[2]G. Zhang, A. Ovtchinnikov, J. Näppi, T. Hakkarainen, and H. Asonen, J. Cryst. Growth **127**, 1033 (1993).
[3]D. Z. Garbuzov, N. Yu. Antonishikis, A. D. Bondarev, A. B. Gulakov, S. N. Zhigulin, N. I. Katsavets, A. V. Kochergin, and E. V. Rafailov, IEEE J. Quantum Electron. **QE-27**, 1531 (1991).
[4]O. N. Ermakov, L. S. Garba, Y. A. Golovanov, V. P. Sushkov, and M. V. Chukichev, IEEE Trans. Electron Devices **ED-26**, 1190 (1979).
[5]G. Zhang, M. Pessa, K. Hjelt, H. Collan, and T. Tuomi, J. Cryst. Growth **150**, 607 (1995).
[6]M. A. Rao, E. J. Caine, H. Kroemer, S. I. Long, and D. I. Babic, J. Appl. Phys. **61**, 643 (1987).
[7]T. Yuasa, M. Ogawa, K. Endo, and H. Yonezu, Appl. Phys. Lett. **32**, 119 (1978).
[8]T. Sugiura, N. Hase, H. Goto, K. Hiramatsu, and N. Sawaki, Semicond. Sci. Technol. **9**, 1800 (1994).
[9]T. Inoshita, J. Appl. Phys. **56**, 2056 (1984).
[10]S. H. Groves, J. Cryst. Growth **124**, 747 (1992).
[11]J. Diaz, H. J. Yi, M. Erdtmann, X. He, E. Kolev, D. Garbuzov, E. Bigan, and M. Razeghi, J. Appl. Phys. **76**, 700 (1994).
[12]G. W. Wicks, M. W. Koch, J. A. Varriano, F. G. Johnson, C. R. Wei, H. M. Kim, and P. Colombo, Appl. Phys. Lett. **59**, 342 (1991).
[13]J. N. Bailargeon, A. Y. Cho, F. A. Thiel, R. J. Fisher, P. J. Pearch, and K. Y. Cheng, Appl. Phys. Lett. **65**, 207 (1994).
[14]C. C. Wamsley, M. W. Koch, and G. W. Wicks, J. Vac. Sci. Technol. B **14**, 2322 (1995).
[15]W. Shi, D. H. Zhang, H. Q. Zheng, S. F. Yoon, C. H. Kam, and A. Raman, J. Cryst. Growth **197**, 89 (1999).
[16]D. H. Zhang, W. Shi, H. Q. Zheng, S. F. Yoon, and C. H. Kam, J. Cryst. Growth **211**, 384 (2000).
[17]J. N. Baillargeon, K. Y. Cheng, A. Y. Cho, and S. N. G. Chu, J. Vac. Sci. Technol. B **14**, 2244 (1996).
[18]M. Toivonen, A. Salokatve, M. Jalonen, J. Nappi, H. Asonen, M. Pessa, and R. Murison, Electron. Lett. **31**, 797 (1995).
[19]T. Sugiura, N. Hase, H. Goto, S. Tanaka, K. Hiramatsu, N. Sawaki, and I. Akasaki, Jpn. J. Appl. Phys., Part 1 **32**, 2718 (1993).
[20]S. Mukai, J. Appl. Phys. **54**, 2635 (1983).
[21]Q. S. Zhu, K. Hiramatsu, N. Sawaki, and I. Akasaki, Jpn. J. Appl. Phys., Part 2 **28**, L1326 (1989).

Interface tuning of the InAs/AlSb heterostructure-based quantum wells

V. M. Ichizli,[a] K. Mutamba, M. Droba, A. Sigurdardóttir,[b] and H. L. Hartnagel
Institut für Hochfrequenztechnik, Technische Universität Darmstadt, Merckstraße 25, D-64283 Darmstadt, Germany

(Received 17 January 2000; accepted 14 April 2000)

This work shows the importance of interface consideration at the barrier sides for quantum well (QW)-based semiconductor structures, on the example of the InAs/AlSb heterostructure. Various interface combinations of AlAs and InSb type have been included in an InAs/AlSb double-barrier resonant-tunneling-diode structure, and the resulting transmission functions have been calculated. A systematic comparison of the resulting structures with each other and also with the traditional case without interface consideration have been made. Clear tendencies and relationships observed in the transmission characteristics of the different structures let the interface tuning emerge as a quality tool for QW-device tayloring. © *2000 American Vacuum Society.* [S0734-211X(00)01404-9]

I. INTRODUCTION

InAs/AlSb is an attractive heterostructure for fabricating such semiconductor devices as resonant tunneling diodes (RTDs)[1] and high electron mobility transistors[2] due to the large conduction band offset and small electron effective mass in InAs. Because of both the cation and the anion change at the interface (IF) during epitaxial crystal growth, three interfaces are possible: the AlAs–IF, the InSb–IF, and a mixture of these. The type of IF influences the electrical and optical characteristics of devices based on the aforementioned heterostructure.[3,4] An InSb–IF is known to result in better device performance,[3] while the AlAs–IF is a superior hole barrier in some RTD structures.[4] In this way, a certain IF can be formed in dependence on device requirements. In other words, one can talk of interface engineering.

In our previous study,[5] we have investigated AlAs and InSb interfaces in InAs/AlSb heterostructures with one vacuum and one AlSb barrier by means of scanning tunneling microscopy and spectroscopy (STM/STS). STS measurements, i.e., local current–voltage measurements performed with a STM, are presented in Fig. 1. The only difference between the two molecular beam epitaxy-grown InAs/AlSb structures, whose STS is shown in Fig. 1, is in the interface type at the AlSb barrier, being whether AlAs or InSb interface, as described in Ref. 5. The thickness of both top InAs and underlying AlSb layers was 5 nm. One of the main reasons for the large difference between the I–V spectra taken on the AlAs– and InSb–IF regions were recognized as the large conduction band offset between them, large difference of conduction band offset between each of them with the InAs-quantum well (QW) and the AlSb barrier, and, consequently, the difference between the Eigen-energy levels. For Eigen-energy level estimation, the transmission probability was calculated and analyzed for each interface type.[5] Figure 2 shows the conduction-band offsets and Eigen-energy values derived from the maximum position of the calculated transmission line for each of the cases of AlAs and InSb interfaces. In the case of AlAs–IF, the total barrier width is made of the AlSb layer and the AlAs–IF and is larger than the barrier in the InSb–IF case, where the barrier consists only of the AlSb layer. On the other hand, in the case of InSb–IF, the width of the QW between the vacuum and the AlSb barriers is composed of InAs layer and InSb–IF and it is larger than the one in the case of AlAs–IF.

It is well known that the width of a QW and the effective electron mass strongly influences the position of the Eigen-energy levels in the QW. The current density decreases exponentially with increased barrier thickness. Thus, electrical performance of a QW-based device depends considerably on the dimensions of the QW and surrounding barriers. From all the earlier reasons, it is very important to investigate the influence of changing interface type in QW-based structures.

In this work we show how the transmission characteristics in an InAs/AlSb double-barrier resonant-tunneling-diode (DBRTD) structures can be changed through the use of different combinations of AlAs and InSb interfaces.

II. THEORETICAL COMPUTATIONS

Our previous studies on the "tungsten-tip"-vacuum-"InAs/AlSb-heterostructure"[5] have demonstrated that the interface type influences drastically the electron transport. Consequently, the latter will be even more affected by the interface type and sequence in the case of a structure with more than one semiconductor barrier. In order to get a picture of the carrier transport in such a system, transmission mechanism through it should be clearly understood. Thus, the purpose of this work was to calculate and to analyze the transmission probability through a DBRTD InAs/AlSb heterostructure in dependence on the interface type and sequence at each AlSb barrier.

A. General approach

We have calculated the transmission coefficient for a DBRTD structure with a 50-nm-thick InAs–QW and 1.7-nm-thick AlSb barriers shown in Fig. 3(a). The initial model[6]

[a]Electronic mail: hfmwe107@hrz2.hrz.tu-darmstadt.de
[b]Present address: STMicroelectronics, Marlow, England.

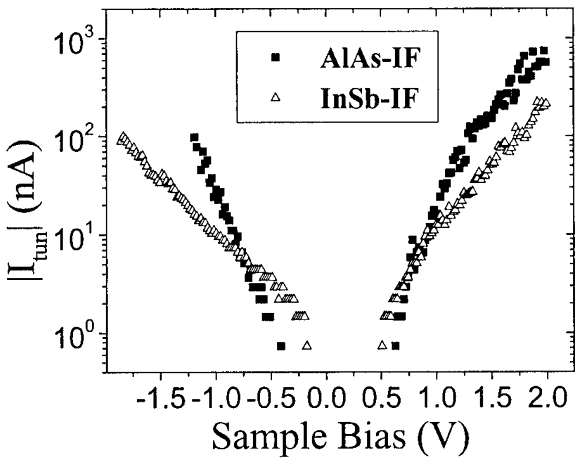

FIG. 1. STS spectra measured at AlAs– and InSb–IFs regions on the top of an InAs/AlSb thin heterostructure. Both InAs and AlAs layers are 5 nm thick.

used in this work is based on the theory of global coherent tunneling and space charge buildup. The time independent Schrödinger equation is solved by using the transfer-matrix method, the wave function is applied to evaluate the charge buildup. The initial model was modified by introducing four additional layers symbolizing interfaces at both sides of each barrier. Figure 3(b) shows an example of one such structure.

For further consideration, we would like to draw the reader's attention to the interface nomenclature system used here. Each interface combination is identified with four letters, e.g., IAIA, IIII, AIAA, etc. Letters A and I indicate AlAs and InSb interfaces, respectively. The first two letters are a sign of the left and right interfaces at the first (left) barrier, while the last two letters describe the interfaces from the left and right side of the second (right) barrier.

There are 16 possible combinations IF-barrier–IF–QW–IF-barrier-IF. We present the results of calculations for 11 of these cases shown in Table I. The behavior of the five remaining structures can easily be understood from the discussion of the ones given here. The case of traditional calculations without taking the interfaces into account, indicated as "0000" is presented in Table I as well. The dimensions of the resulting QW and barrier widths in each of the cases are

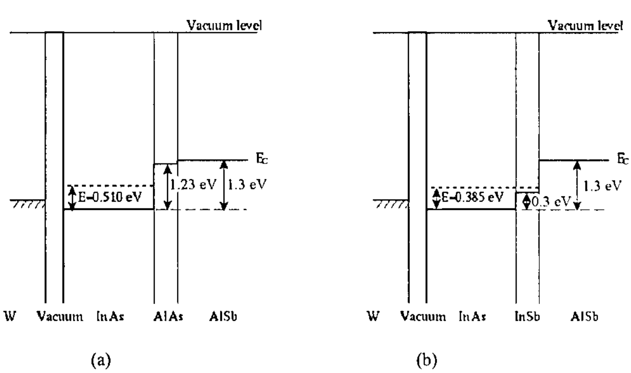

FIG. 2. Conduction band offset and Eigen-energy level values in InAs/AlSb heterostructure for the cases of (a) AlAs and (b) InSb interfaces.

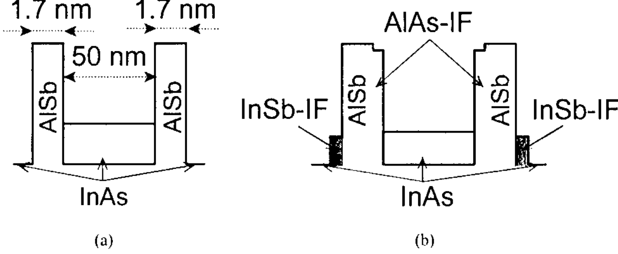

FIG. 3. Conduction band offset and layer dimensions of the considered DBRTD structure: (a) without and (b) with consideration of interfaces at the barrier sides. The dimensions of the InAs–QW and AlSb barriers are the same for both (a) and (b) structures. The thickness of InSb and AlAs interfaces are the lattice constant of the respective materials (6.5 Å for InSb–IFs and 5.66 Å for AlAs–IFs).

shown as well. All calculations were made for the case of zero bias. Hereinafter, the structures will be named according to their numbers and codes.

One sees from Table I that the transmission probability and Eigen-energy level values differ considerably for various interface combinations. However, some tendencies are present, and therefore, some conclusions can be drawn. In

TABLE I. Initial and calculated data for transmission probability analysis in DBRTD structures without and with consideration of interfaces at the barrier sides.

No.	Conduction band structure and its code***	Left and right IFs at the 1st AlSb barrier	Left and right IFs at the 2nd AlSb barrier	Eigen-level value (eV)	Transmission coefficient Log(T(E))
0	0000	No IF	No IF	0.4342	-2.3845
1	AAAA	AlAs & AlAs	AlAs & AlAs	0.3640	-4.1858
2	IIII	InSb & InSb	InSb & InSb	-	-
3	AAII	AlAs & AlAs	InSb & InSb	0.3263	-3.1602
4	AIAI	AlAs & InSb	AlAs & InSb	0.3003	-4.5372
5	AIII	AlAs & InSb	InSb & InSb	0.2704	-4.0447
6	AIAA	AlAs & InSb	AlAs & AlAs	0.3003	-5.0917
7	AIIA	AlAs & InSb	InSb & AlAs	0.2704	-4.6122
8	IAAI	InSb & AlAs	AlAs & InSb	0.3510	-4.4083
9	IIAA	InSb & InSb	AlAs & AlAs	-	-
10	IAIA	InSb & AlAs	InSb & AlAs	0.3159	-4.5018
11	IIIA	InSb & InSb	InSb & AlAs	-	-

***The first and the second letter of the structure code correspond to the interfaces from the left and right of the first (left) barrier, correspondingly. In the same manner the third and the forth letters of the code indicate the left and the right interfaces of the second (right) barrier. The code '0000' means that during calculations no interfaces were taken into consideration. In other words, the structure consists only of a QW, two spacers, and two barriers.

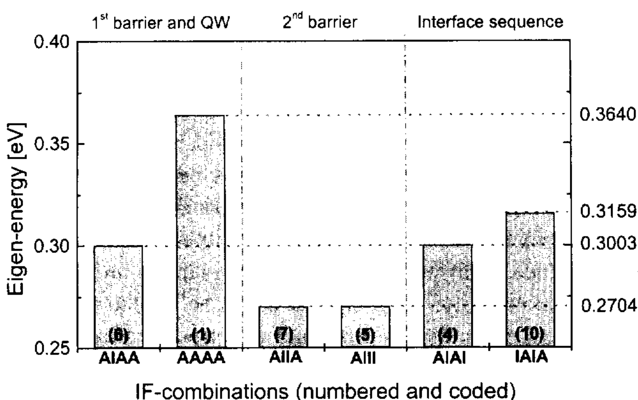

FIG. 4. Eigen-energy level dependence on the variation of QW and barrier composition and interface sequence.

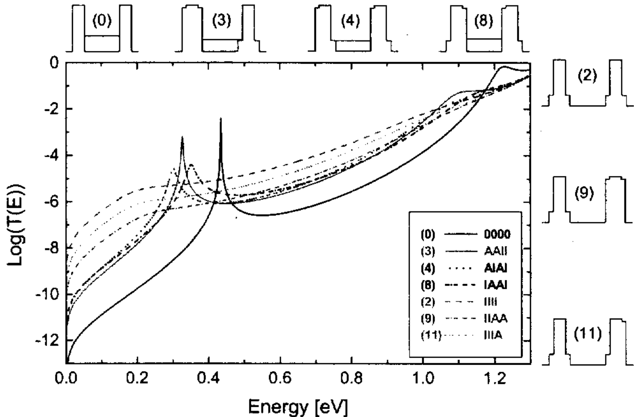

FIG. 5. Quantum confinement for various interface combinations.

the next four subsections, these different characteristics are pointed out and distinguished between the structures presented.

B. Eigen-level value

One of the most significant parameters of a QW-based semiconductor device is the Eigen-energy level. Its values change considerably with the variation of the interface combinations as can be seen from Table I. Some combinations show the same Eigen-energy level.

The Eigen-energy position depends on the nature of the modifications introduced by the interface sequence in the barriers as well as in the QW structures. Two cases illustrating these influences are shown in Fig. 4.

Structures (6)-AIAA and (1)-AAAA have the same structure of the second barrier. The sequence introduced at the first barrier-QW interface [structure (6)-AIAA] leads to a huge difference in the position of the Eigen-energy level.

Such a change is not observed for the structures (5)-AIIA and (7)-AIII where different interface sequences at the second barrier are used while keeping the same structure for the well and the first barriers. The same behavior is observed between structures (4)-AIAA and (6)-AIAI, which are shown in Fig. 4 as well.

The adopted sequence of interfaces for the whole double barrier structure also influences the Eigen-energy position. Structures (4)-AIAI and (10)-IAIA have the same thickness of both barriers and the QW. The only difference is that the first IF at each barrier structure (4) is AlAs, while structure (10) has InSb as the left IF and AlAs as the right interface at each barrier. It results in a change of Eigen-energy level of about 0.02 eV.

C. Quantum confinement

Interface combinations influence the quantum confinement as well. As seen in Fig. 5, the structures, which have InSb interface from both sides of the first (left) barrier, show no quantum confinement, although the barrier thickness in all cases changes very slightly not more than with 2 Å. The InSb-IFs at the second (right) barrier have less influence on the quantum confinement, as shown by structure (3)-AAII, which presents the best quantum confinement of all combinations with interfaces. The structure (0)-0000 calculated without interface consideration surpasses all structures with interfaces with all its parameters. However, it differs considerably from the real QW-device structures.

Let us now consider the tendency of quantum confinement variation in the structures with determinable confinement, that is all structures except those with first two InSb-IFs. Better confinement is shown by structures where the first IF is AlAs. It can be seen from transmission lines of structures (4)-AIAI and (8)-IAIA, where the second (right) barriers have the same structures, and the first (left) barriers differ in the interface sequence. The best confinement for structures with interfaces taken into account is shown by structures where both first interfaces are made of AlAs, as in the case of combination (3)-AAII.

D. Transmission maximum

In opposite to the said previously, the maximum transmission is observed for the structures, where the last two interfaces are made of InSb. Figure 6 summarizes the whole range of transmission coefficient presenting the maximum and the minimum transmission probabilities as dependent on

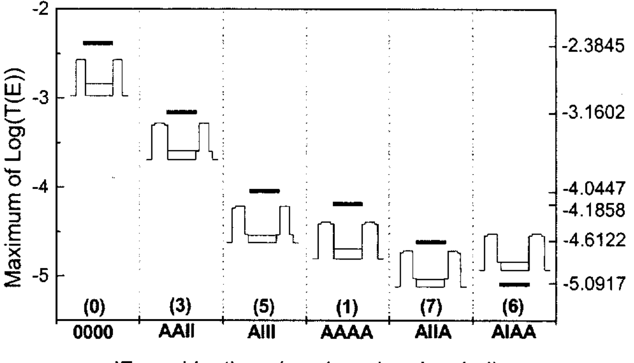

FIG. 6. Transmission maximum variation with the change of interface combinations.

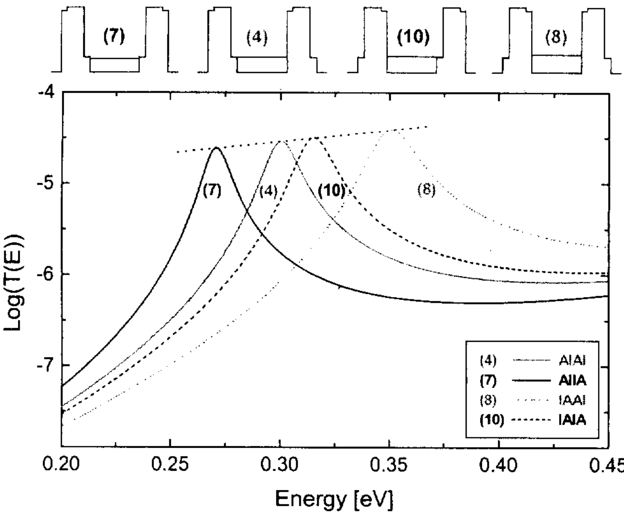

FIG. 7. Relationship between the structures, where each barrier contains one InSb and one AlAs interface.

various interface combinations. It is clearly seen in Fig. 6, that except the combination (0)-0000, the highest transmission is observed for structures (3)-AAII and (5)-AIII, because the last two interfaces are InSb. The minimum transmission probability corresponds, in general, to the structures that have AlAs for the two last interface at the second (right) barrier. It is worth noticing that the transmission probability of the structure (7)-AIAA is lower than the one of the structure (1)-AAAA due to the fact that the Eigen level in structure (7) lies lower than the InSb conduction band level, which means that the second barrier includes three layers, i.e., AlSb layer, InSb- and AlAs-IFs. In other words, the second barrier of structure (7) is thicker than the one of structure (1) because the lattice constant of InSb is 6.5 Å, which is larger than the lattice constant of AlAs (5.66 Å). Therefore, there is no contradiction to our conclusion made earlier, which states that transmission decreases with the increase of the second barrier thickness.

E. Structures with alternative interface sequence

The transmission probability calculations resulted in an interesting relationship between structures, where each of two barriers consists of one InSb and one AlAs interface surrounding the AlSb layer. Figure 7 shows this relationship: the logarithmic transmission coefficient maxima of these structures lie on one straight line, which means that the transmission probability grows exponentially with the gradual increase of the Eigen-energy level. The four structures showing progressive change of the Eigen-energy level are gathered in Fig. 7.

Apart from that, along with the increase of transmission probability, the quantum confinement decreases from structure (7)-AIIA through to structure (8)-IAAI as shown in Fig. 7. Again as described in subsection "C," the confinement is more pronounced in structures (7) and (4), where the first (left) interface of the first barrier is AlAs.

III. DISCUSSION

This work considers interfaces as a part of barriers or the QW itself in a QW-based device structure. Many physical phenomena could be included into consideration as the reasons for the transmission characteristics behavior described earlier. However, it is more reasonable to distinguish one or two criteria that could help to give a simple explanation to the influence of different interface combinations on the transmission probability. Such criteria could be related to the reflection and transmission probabilities introduced by the considered interfaces as well as the change in electron effective mass related to their presence.

From the previous section and considering the transmission through the first level of the well, it can be easily concluded that the reflection probability increases if the first or both interfaces at the first (left) barrier is InSb. This results from the relatively low conduction band offset between InAs–QW or spacer and InSb–IF (0.3 eV). Electrons in the well oscillate in this range of energies. That is why, the reflection here is much larger than in the case of a higher barrier, for instance, the AlAs–IF at the left or both sides of at the first (left) barrier. Higher barriers improve the quantum confinement. Recalling our previous study,[5] the first barrier was vacuum, and, consequently, the Eigen-energy level values was larger than in similar cases for double semiconductor barriers. For example, in the case of vacuum-QW–AlAs–IF combination the Eigen-energy level is 0.510 eV, which is even higher than the Eigen-energy level for the structure (0)-0000 (0.4342 eV) calculated without interface consideration.

The InSb–IF at the left of the second barrier also contributes to reflection, but this time within the QW. The presence of potential steps in the well is very interesting in the sense that it introduces additional reflections within the QW. In the approach of coherent tunneling where multiple reflection in the well are considered and an analogy to the Fabry–Pérot resonator applied for the transmission function, the steps give rise to additional resonators.[7] The electron effective mass in these step regions, which is different to that in the InAs part of the QW, has a strong influence on the position of the Eigen-energy levels in the resulting well. The transmission function is the one of coupled resonators which can, in certain cases, provide a poor confinement.

If the Eigen-energy level is much higher than the InSb conduction band level, then the barrier consist only of the AlSb layer, which decreases the reflection probability and increases considerably the transmission probability through the second barrier. This finally contributes to the increase of transmission coefficient and is obviously expected to result in a larger negative differential resistance in such a DBRTD structure. However, for this purpose, the large transmission should be supported by a good quantum confinement. As mentioned earlier, the quantum confinement is provided by a high first barrier. The best case of all considered structures is the combination (3)-AAII where the first (left) and barrier has AlAs–IFs at both sides, and the second (right) barrier is surrounded by InSb–IFs from both sides. Therefore, the first

(left) barrier is responsible for quantum confinement and the second (right) barrier dictates the transmission coefficient maximum changes.

IV. CONCLUSIONS

This work demonstrates how important the interface consideration is for the QW-based device modeling. It presents a further step from our first studies,[5] where the interface type variation was considered in one-AlSb-barrier structure, to the double-AlSb-barrier structure. We have shown that the variations in the interface combinations in the case of such a double-barrier structure can result in considerable changes of QW and barrier thickness, Eigen-energy level and transmission probability values. The calculation results were systemized according to the similarities in the behavior of transmission characteristics. On this basis, some important conclusions of possible physical explanation were made. The calculations of transmission coefficient with interface consideration were shown to be able to explain the reduction and sometimes disappearance of the quantum confinement, which was not possible before. The computations carried out on the basis of model function that represents only electron states in a quantum device, or in other words, only conduction band processes were taken into account. Similar computations could be considered for the case of holes. Apart from that, some common and some new fitting functions representing the resulting band profile as well as the reality of intermixing at the interface region[8] could be applied to modify calculations made in this work.

ACKNOWLEDGMENT

The authors are grateful to M. Rodriguez-Gironés Arboli for the detailed reading of the article and valuable comments and recommendations.

[1]J. R. Söderström, D. H. Chow, and T. C. McGill, J. Appl. Phys. **66**, 5106 (1989).

[2]W. Kruppa, J. B. Boos, D. Park, B. R. Bennett, and R. Bass, Electron. Lett. **33**, 1092 (1997).

[3]G. Tuttle, H. Kroemer, and J. H. English, J. Appl. Phys. **67**, 3032 (1990).

[4]S. Tehrani, J. Shen, H. Goronkin, G. Kramer, M. Hoogstra, and T. X. Zhu, *Processings of Int. Symp. GaAs and Related Compounds* (1994), Vol. 136, p. 209.

[5]V. M. Ichizli, A. Vogt, A. Sigurdardóttir, I. M. Tiginyanu, and H. L. Hartnagel, Semicond. Sci. Technol. **14**, 143 (1999).

[6]A. Sigurdardóttir, Ph.D. thesis, D17, Shaker Verlag, Aachen, Germany, 1999, p. 17.

[7]M. Büttiker, in *Resonant Tunneling in Semiconductors,* edited by L. L. Chang *et al.* (1999), p. 213.

[8]E. H. Li, Mater. Res. Soc. Symp. Proc. **450**, 353 (1997).

Surface structures and growth kinetics of InGaN(0001) grown by molecular beam epitaxy

Huajie Chen and R. M. Feenstra[a)]
Department of Physics, Carnegie Mellon University, Pittsburgh, Pennsylvania 15213

J. E. Northrup
Xerox Palo Alto Research Center, 3333 Coyote Hill Road, Palo Alto, California 94304

T. Zywietz and J. Neugebauer
Fritz-Haber-Institut der Max-Planck-Gesellschaft, Faradayweg 4-6, D-14195 Berlin, Germany

D. W. Greve
Department of Electrical and Computer Engineering, Carnegie Mellon University, Pittsburgh, Pennsylvania 15213

(Received 6 April 2000; accepted 26 May 2000)

The surface structures and growth kinetics of InGaN(0001) are studied. It is well known that during molecular beam epitaxy GaN surfaces undergo a smooth to rough transition when the growth condition is switched from Ga rich to N rich. It is found here that indium atoms have only a small effect on this transition when deposited on GaN($000\bar{1}$), but when deposited on GaN(0001) the indium acts as a surfactant and greatly extends the regime of smooth growth. Near the smooth/rough transition of InGaN(0001) growth, a bright $\sqrt{3}\times\sqrt{3}$ reconstruction is observed at growth temperature. The formation kinetics of this reconstruction are studied in detail. Scanning tunneling microscopy and total energy computations are used to study the structure of InGaN(0001) surfaces under metal rich conditions. Indium is found to occupy the top two atomic layers of the crystal; its incorporation in the second layer produces significant strain, leading to the formation of small pits on the surface and increased indium concentration inside and around the pits. © *2000 American Vacuum Society.* [S0734-211X(00)07004-9]

I. INTRODUCTION

$In_xGa_{1-x}N$ alloys have recently attracted great interest because of the successful development of InGaN/GaN based blue light-emitting devices and lasers, where InGaN is used as the active layer.[1] While the growth of high quality material and fabrication of devices have been successful, fundamental understanding of the growth, structure, and luminescence mechanism is far from complete. Issues such as indium compositional fluctuations[2] and an apparent surfactant effect due to indium [3] were investigated recently. These issues are explored here by an extensive study of the surface structure and growth kinetics of InGaN.

The basic surface structures discussed here are illustrated in Fig. 1, for the limit of very In-rich conditions. Figure 1(a) shows the previously determined structure for the N-polar InGaN($000\bar{1}$) surface, consisting of a monolayer (ML) of In bonded to a GaN bilayer.[4] For less In-rich conditions this monolayer contains a mixture of In and Ga. For the Ga-polar InGaN(0001) surface, prior theoretical studies indicate that the surface consists of either a single ML of In in the topmost layer, or one ML in the top layer plus another ML in the second layer.[5] The latter case is illustrated in Fig. 1(b). Following the notation of Ref. 5 we refer to these layers as A1 and S3, as indicated in Fig. 1(b). As discussed below, we find that the S3 layer is actually only partially occupied by In. Furthermore, we observe the formation of an array of small pits (vacancy islands) on the surface.

This article consists of three parts. First, we present a detailed study of the effect of indium atoms on the GaN surface morphology. It is well known that during molecular beam epitaxy (MBE) growth of GaN the surface undergoes smooth to rough transition when the growth condition is switched from Ga to N rich.[6–8] Here, we find that indium atoms have only a small effect on this smooth/rough transition when deposited on GaN($000\bar{1}$), but when indium is deposited on GaN(0001) the gallium flux can be reduced greatly before the growth becomes rough. Second, a $\sqrt{3}\times\sqrt{3}$ reconstruction is observed during InGaN(0001) growth near the smooth/rough transition point. This reconstruction thus serves as a useful real-time indicator during growth of when the morphology is near the smooth/rough transition, and we have studied the formation kinetics of the reconstruction in an effort to determine its structure. Finally, InGaN(0001) surfaces under metal rich conditions were studied using scanning tunneling microscopy (STM) and total energy computations. We find that the indium atoms occupy the top two surface layers. Based on theoretical results for the surface structures, we argue that strain arising from the presence of In in the second (S3) layer leads to the formation of small pits on the surface. Inside, and at the border of the pits, the surface concentration of indium is found to be larger than that far from the pits, which may lead to inhomogeneous indium incorporation in the bulk film.

[a)]Electronic mail: feenstra@andrew.cmu.edu

FIG. 1. Basic structure of In-rich InGaN surfaces: (a) $(000\bar{1})$ and (b) (0001). A1 and S3 layers are indicated in (b).

II. EXPERIMENT

The studies described here were performed in a combined MBE/surface analysis system. The growth chamber contains gallium and indium effusion cells, a rf-plasma nitrogen source, and a reflection high energy electron diffraction (RHEED) system. GaN(0001) was grown on Si-face 6H–SiC(0001) substrates, with the polish damage removed by hydrogen etching.[9] After the hydrogen etching, the substrate was introduced into the growth chamber and outgassed up to the temperature of 800 °C. A few monolayers of Si were deposited onto the surface and the substrate was then annealed to about 1000 °C until a $\sqrt{3}\times\sqrt{3}$ reconstruction was obtained.[10] GaN was directly grown on this surface at growth temperature of 670 °C. $\mathrm{GaN}(000\bar{1})$ was also grown at 670 °C, on sapphire substrates, with pregrowth nitridation of the substrate performed at 950 °C and using a low-temperature GaN buffer layer grown at 500 °C.[4] Following the GaN growth with typical thickness of 200 nm, the substrate temperature is lowered to 600–630 °C for the InGaN deposition. Typical growth rates for the GaN and InGaN are 200 nm/h. Gallium and indium flux rates were calibrated with an *in situ* crystal thickness monitor. The nitrogen plasma source was operated at a power level of 550 W and pressure of 1.8×10^{-5} Torr. The substrate temperature was measured by an optical pyrometer with emissivity set to be 0.7. After growth, the sample was quenched to room temperature, and transferred under vacuum to the analysis chamber for STM and Auger study. The base pressures of the growth and analysis chambers were in the 10^{-11} Torr range.

Auger spectroscopy was measured with a Perkin-Elmer 15-255G system. The amount of indium on the surface is determined from the indium/nitrogen peak–peak intensity ratio as measured by the Auger spectroscopy. From the known bonding arrangements for In on the surface (Fig. 1), using electron mean free paths and atomic sensitivity factors obtained from Ref. 11, and using the bulk indium composition obtained from x-ray diffraction (XRD) measurement, the amount of indium on the surface can be evaluated from a measured ratio of In 404 eV to N 379 eV Auger lines. However, when we apply this procedure to a surface for which the indium composition was confidently known from STM images,[4] the computed result from Auger data gives only about half of the expected value. The origin of this discrepancy is not well understood at present. Nevertheless, we feel that a *relative* measure of the indium surface concentration between different samples should still be reasonably accurate, and that type of procedure is used here in evaluating surface coverages. In any case, our final determinations of indium coverage are made on the basis of both STM images and Auger measurements, with the Auger results mainly being used to add confidence in the interpretation of the STM images.

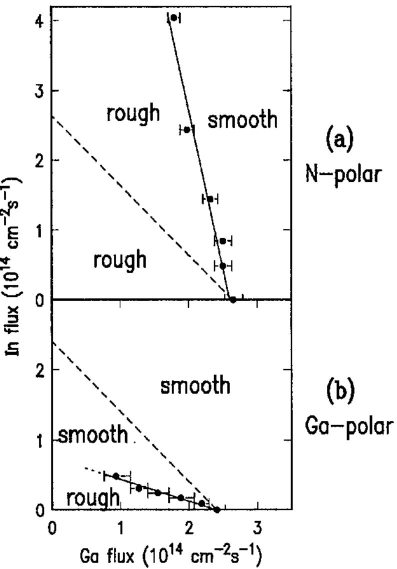

FIG. 2. Smooth/rough transition on (a) $(000\bar{1})$ face (N polar) and (b) (0001) face (Ga polar). Nitrogen flux was fixed in both experiments. Substrate temperature was 600 °C. Experimental data are shown with dots, each with an error bar. A dashed line is shown in each figure for comparison denoting the line with constant total metal flux. To the right of the transition lines (solid lines) the growth is smooth.

III. RESULTS

A. Effect of indium on the smooth/rough transition

During MBE growth of GaN, the surface undergoes a transition from smooth to rough morphology when the growth condition is switched from Ga to N-rich.[6–8] It was previously observed that the material has high quality when grown in the smooth regime;[6] it is therefore important to determine the smooth/rough transition point for GaN and InGaN. It has been reported that indium atoms serve as a surfactant, keeping the growth in the smooth regime when the gallium flux is slightly reduced beneath the transition flux.[3] However, in our prior growth of InGaN on $\mathrm{GaN}(000\bar{1})$, such a surfactant effect was not observed. Instead we found that indium atoms had little effect on the smooth/rough transition,[12] possibly due to the different polarity of GaN used in that case. In this work, a detailed study is carried out on the smooth/rough transition of InGaN growth on both the $(000\bar{1})$ and (0001) faces.

We find a dramatic difference in the smooth/rough behavior between the $(000\bar{1})$ and (0001) faces, as shown in Figs. 2(a) and 2(b), respectively. For both experiments, the nitrogen flux was kept constant. Then, a certain indium flux was applied, and gallium flux was adjusted to find the smooth/rough transition point. For comparison, dashed lines in Fig. 2 show where the total metal flux (indium+gallium) is constant. Figure 2(a) shows that for the $(000\bar{1})$ face, even when a large indium flux is applied, the gallium flux can only be reduced slightly before the growth becomes rough. In contrast, for the (0001) face, it is found that when the indium

flux is applied the gallium flux can be greatly reduced (by an amount considerably greater than that of the added indium flux) before the growth becomes rough. Thus, indium serves as a surfactant for the (0001) surface.

While this contrast between the effect of indium atoms on the surface morphology of the (0001) and (000$\bar{1}$) faces is dramatic, it is also important to realize that in order to incorporate indium into the bulk the gallium flux must be lower than the transition flux of gallium in the absence of indium.[4,13] Roughly speaking, the reason for this condition is that indium atoms tend to segregate to the surface so that when there is enough gallium the indium atoms do not incorporate.[14] Therefore, in order to grow InGaN with significant indium content, growth on the (000$\bar{1}$) face must occur in the rough growth regime whereas it can take place in the smooth regime for the (0001) face. Since one generally desires smooth morphology (implying faster surface diffusion) during growth, we conclude that the (0001) surface appears to be better suited for high quality InGaN growth.

Another implication of this surfactant effect on the (0001) surface is that more nitrogen must desorb from the surface when the gallium flux is greatly reduced in the presence of indium, since the growth is stoichiometric and now the total metal flux is lower than that during GaN growth without indium. This increased desorption could come about either as a result of higher nitrogen surface diffusivity or higher nitrogen surface concentration, where in both cases the nitrogen atoms have more chance to meet and form molecules and then leave the surface. In GaN growth, it was found that nitrogen accumulation leads to a higher diffusion barrier and hence rough growth.[7] However, as will be shown in the next part of this article, with a nitrogen rich $\sqrt{3}\times\sqrt{3}$ reconstruction the growth can still be smooth, which implies that indium lowers the diffusion barrier even when the surface has high nitrogen concentration.

B. $\sqrt{3}\times\sqrt{3}$ reconstruction on the (0001) face

During plasma-assisted MBE of GaN, reconstructions are rarely observed at the growth temperature. Some groups have reported a 2×2 reconstruction during growth,[15] although we have found previously that this structure is due to the presence of arsenic atoms in the growth environment[16] (for growth using ammonia a different, intrinsic 2×2 structure occurs [17]). For the case of InGaN growth on the (0001) face, we observe a bright $\sqrt{3}\times\sqrt{3}$ reconstruction (in the absence of arsenic) at the growth temperature. This reconstruction is observed when the Ga flux is near or below the transition point between rough and smooth growth, in the presence of indium. Figure 3 shows the corresponding RHEED pattern, which is a $3\times$structure when viewed along $(1\bar{1}00)$ azimuth and $1\times$structure along $(11\bar{2}0)$ azimuth.

We have varied the growth conditions and surface stoichiometry in an effort to determine the geometric structure of this reconstruction. For reference, various reconstructions on GaN(0001) at room temperature are well understood:[18] there are "1×1," 6×4, 5×5, and 2×2 reconstructions corre-

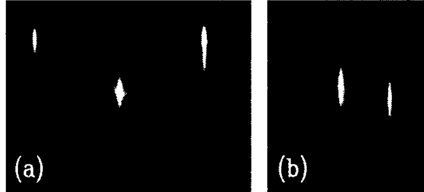

FIG. 3. RHEED pattern of $\sqrt{3}\times\sqrt{3}$ reconstruction: (a) a $3\times$structure when viewed along $(1\bar{1}00)$ azimuth and (b) a $1\times$structure along $(11\bar{2}0)$ azimuth.

sponding to different amount of gallium atoms on the surface, with the 1×1 most gallium rich and 2×2 most gallium deficient (this 2×2 reconstruction is different than the two 2×2 structures mentioned in the previous paragraph, since it is observed only during growth interrupts). Since the $\sqrt{3}\times\sqrt{3}$ reconstruction appears only when the gallium flux is reduced to near the transition point, we expect that there are *not* multiple Ga layers on the surface, so a first guess of the structure is an adlayer of indium with $\sqrt{3}\times\sqrt{3}$ structure on top of a gallium terminated GaN surface. Thus, in our first experimental effort, a GaN layer was grown in gallium rich growth conditions to obtain a flat surface. The surface showed a 1×1 reconstruction as usual when cooled down. Then the sample was heated to about 730 °C for 90 s to desorb the excess gallium. The surface then showed a faint 2×2 reconstruction when cooled down. Then indium atoms were deposited onto this surface up to a few monolayers ($1\ \mathrm{ML}=1.14\times10^{15}\ \mathrm{atoms/cm^2}$) with a rate of 0.5–2 ML/min. No $\sqrt{3}\times\sqrt{3}$ reconstruction was observed during the deposition. The same process was repeated with indium deposition carried out at the growth temperature, and again no $\sqrt{3}\times\sqrt{3}$ was observed, indicating that the indium adatoms on the gallium layer model is incorrect.

Based on the above results, it appears that nitrogen may play an important role in the $\sqrt{3}\times\sqrt{3}$ reconstruction. So for the next attempt, the nitrogen plasma source was turned on when indium was deposited and this time the $\sqrt{3}\times\sqrt{3}$ appeared very quickly. The same result occurred when indium was deposited during the GaN growth if the growth was in the nitrogen rich regime. For the latter case, it was found that the $\sqrt{3}\times\sqrt{3}$ was clearly seen when about 1/10 ML of indium was deposited, and the intensity of the reconstruction was maximum when about 1/3 ML of indium was deposited. If the gallium flux was not too small, so that in the presence of an indium flux the gallium flux is well above the smooth/rough transition point, then the intensity of the reconstruction will gradually decrease and finally disappear when more indium is deposited (consistent with the observation that the $\sqrt{3}\times\sqrt{3}$ can persist only near or below the transition point). Also, when GaN is grown in the gallium rich regime (without indium), then deposition of indium atoms does not lead to $\sqrt{3}\times\sqrt{3}$ reconstruction. Thus, N-rich conditions are required for the formation of the $\sqrt{3}\times\sqrt{3}$ structure. In the extreme case, the $\sqrt{3}\times\sqrt{3}$ reconstruction was found to persist when the nitrogen plasma is kept on but both the gallium and indium fluxes were off. Also, if indium atoms were deposited onto the GaN surface when the nitrogen plasma source was off (producing no $\sqrt{3}\times\sqrt{3}$ reconstruction), subsequently turn-

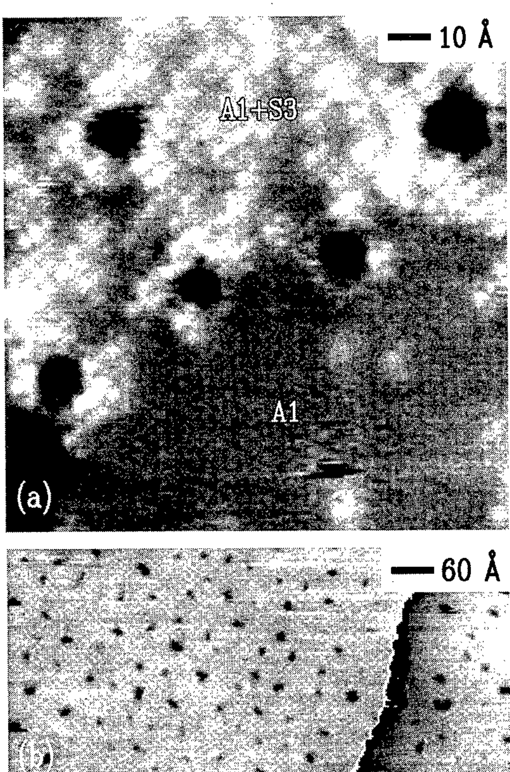

FIG. 4. STM image of InGaN(0001) surface: (a) surface containing 0.9 ± 0.2 ML of indium. Image was acquired at a sample voltage of +1.25 V, and with tunnel current of 0.075 nA. Gray scale range is 0.5 Å. Different surface regions are labeled A1 and A1+S3. (b) Surface containing 1.4 ± 0.2 ML of indium, acquired at sample voltage of −2.0 V and tunnel current of 0.075 nA. The entire surface consists of the A1+S3 structure. A split gray scale is used, with separate terraces shown on the right- and left-hand sides of the image. A gray scale range of 2.4 Å is used for both terraces.

ing on the nitrogen plasma source will make the $\sqrt{3}\times\sqrt{3}$ reconstruction appear and persist. All these experiments are carried out at the growth temperature, which was around 600 °C.

In summary, we find that the $\sqrt{3}\times\sqrt{3}$ reconstruction forms under N-rich conditions, and it contains about 1/3 ML of indium atoms. It appears to consist of a structure involving indium and nitrogen atoms, on the gallium terminated GaN surface (depending on the relative indium and gallium presence on the surface, some indium atoms can go into the gallium layer). It is worth noting that growth can still be smooth with the nitrogen rich $\sqrt{3}\times\sqrt{3}$ reconstruction, implying relatively low surface diffusion barriers for this structure.

C. STM results of InGaN(0001) surfaces under metal rich conditions

Scanning tunneling microscopy has been used to study the structure of the InGaN(0001) surface, as shown in Fig. 4. The film shown in Fig. 4(a) was grown at 610 °C, with Ga and In flux rates of 1.7×10^{14} and $4.8\times10^{13}\,\mathrm{cm^{-2}\,s^{-1}}$, respectively, well above the smooth/rough transition line. This particular film was too thin to conveniently determine its indium composition from XRD, but by comparison with other films with similar growth conditions we estimate the indium content in the bulk to be 1%–2%. The surface was known from Auger measurements to contain 0.9 ± 0.2 ML of indium. From prior theoretical work we expect the possible presence of surface structures containing In atoms either in the top surface layer or in the top two layers,[5] as illustrated in Fig. 1(b). In Fig. 4(a), we see in the lower part of the image a region of uniform 1×1 corrugation. We assign the structure of this region as having indium only in the top layer, and we refer to this structure as the ''A1 phase.''The bright corrugation maxima observed elsewhere in the image we attribute to In atoms in the S3 layer, since the height of the observed bright maxima, typically 0.2 Å above the nominal height of the 1×1 region, is consistent with theoretical result of 0.30 Å for the change in surface height induced by a second layer indium atom as discussed in the following section. The small black pits appearing on the surface appear dark (lower surface height) for both positive and negative sample bias voltage, indicating that they are some type of surface vacancy island. The pits do *not* grow with time, but rather, they have an equilibrium diameter of 10–20 Å. The depth of the smallest pits seen in Fig. 2 is typically 0.7 Å, but this value is probably limited by the shape of the STM probe tip. For the larger pits we find a depth of 2.0 Å, indicating that at least one layer of atoms is missing from the surface. In surface regions containing the pits, we find 15%–25% indium occupation of the second layer. As discussed in the next section, we believe these pits form to relieve the strain induced by incorporation of indium in the second layer. Indeed, as can be seen from Fig. 4(a), these pits are closely related to the presence of indium in the second layer.

Figure 4(b) shows a STM image obtained from an InGaN(0001) film grown with similar fluxes as that in Fig. 4(a), but with slightly lower growth temperature of 600 °C. The bulk indium content of this sample is about 4%, and the surface indium coverage is 1.4 ± 0.2 ML. In this case surface regions containing pits cover practically the entire surface, with average separation between pits of about 40 Å. We refer to this surface phase, containing pits and partial occupation of indium in the second layer, as ''A1+S3.'' The higher coverage of pits in this sample with higher indium surface concentration is consistent with the conclusion that pits are related to the indium incorporation in the second layer.

Another important feature seen in Fig. 4(a) is that the indium concentration in the second layer is higher around pits than that far from pits. This inhomogeneous surface indium concentration may contribute to the formation of the widely observed indium compositional fluctuation in the bulk InGaN.[2,19] Instead of forming from bulk properties, the indium compositional fluctuation could be grown in from the inhomogeneous surface, produced by the processes of indium surface segregation[4,5] and formation of a strained surface layer due to lattice mismatch between InN and GaN. This strain is large because the indium surface concentration is much higher than its bulk concentration.

D. Theory and discussion

The results of the previous sections are all closely related to the structure of the InGaN(0001) surface. In this section we will review some previous theoretical work on the structure of the InGaN(0001) surface as well as summarize recent theoretical results that support our interpretation of the STM images. We will also discuss the relationship between the surface structure and the expected diffusion mechanism for nitrogen on the In-covered surface.

Previous theoretical studies of the InGaN(0001) surface were performed in order to gain an understanding of indium induced morphological changes occurring on the (0001) surface.[5,20] In those studies it was shown that under conditions leading to very high concentrations of indium in the films, the (0001) surface would be close to a structural instability, and that near the core of threading dislocations intersecting the surface it would be energetically favorable to form $(10\bar{1}1)$-faceted inverted hexagonal pyramids in order to reduce strain energy associated with the dislocation. Of course, in the present case the pits seen in the films are much smaller and are not associated with dislocations; they are an intrinsic feature of the indium induced surface reconstruction. Nevertheless, the results of the previous investigations also provide guidance for understanding the origin of the smaller pits seen in the present work. A key idea emerging from that work is that the energy of indium surface segregation is comparable to the cost of forming the surface itself. In other words, the incorporation of indium into either the bulk or the S3 layer [Fig. 1(b)], where it makes either four or three compressively strained bonds with nitrogen atoms, competes energetically with morphological changes that allow the indium to be incorporated in sites where it makes fewer, but less strained, In–N bonds. In the case of the large inverted hexagonal pit formation, the indium is incorporated onto the $(10\bar{1}1)$ surfaces of the pits where it makes one or two In–N bonds. In the present case we believe that the edges of the pits in the A1+S3 phase exhibit sites where the indium atoms are bonded to just one or two nitrogen atoms, and the driving force stabilizing the formation of the pits is the relaxation of the surface strain associated with the indium atoms incorporated into the S3 layer. It is essential that the energy cost of forming the pits is sufficiently low so that the combination of pit formation and the resulting strain relief is energetically favorable.

Total energy calculations performed for a set of five structures having between 0 and 1 ML of indium in the second layer establish that there is a significant amount of strain induced by substitution of indium for gallium in the second layer. These calculations were performed in a 2×2 unit cell and the second layer contained 0, 1, 2, 3, or 4 indium atoms. In all cases the top layer consists entirely of indium. We denote the structures in this set by specifying the total indium coverage; thus the 5/4 ML structure contains $\Theta = 1/4$ ML of indium in the second layer and 1 ML of indium in layer 1 (the A1 layer). Θ is the indium coverage in the S3 layer. The energies of these five structures are plotted as a function of the Ga chemical potential in Fig. 5. Assuming the

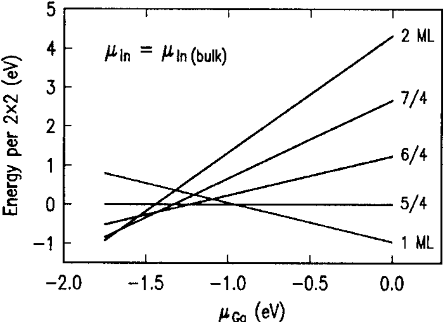

FIG. 5. Results of total energy computation for InGaN(0001) surfaces with various indium coverages, computed using a 2×2 unit cell. In all cases there is 1 ML of indium in the top layer (the A1 layer), with the remaining indium residing in the second layer (the S3 layer).

linear elasticity theory the surface energy (per 1×1 cell) of the various A1+S3 surface structures can be written as

$$E(\Theta) = E_{A1} + (E_{In} + \mu_{Ga})\Theta + E_{In\text{-}In}\Theta^2.$$

Here, E_{A1} is the surface energy of the 4/4 ML structure, E_{In} is the energy cost to incorporate a single In atom into the S3 layer (for $\mu_{Ga} = 0$ eV), and $E_{In\text{-}In}$ is the In–In interaction energy arising from overlapping strain fields. Using the calculated surface energies we obtain $E_{In} = 0.86$ eV and $E_{In\text{-}In} = 0.46$ eV. Higher order contributions in Θ are an order of magnitude smaller. The large positive value of E_{In} implies that In can be incorporated into the S3 layer only for very Ga-deficient conditions ($\mu_{Ga} < -0.86$ eV). For $\mu_{Ga} > -0.86$ eV it costs energy to incorporate even a single isolated indium atom into the S3 layer. Over a large range of chemical potentials (-0.86 eV $< \mu_{Ga} < 0$ eV) the A1 phase is the energetically preferred structure. We believe this is the 1×1 structure that is seen over large areas of the surface for the low In-content film discussed in the previous section. The atomic structure of the A1 phase is indicated schematically in Fig. 6(a).

The positive value for $E_{In\text{-}In}$ is indicative of an effective repulsive interaction between the In atoms that arises because it becomes progressively more difficult to relax the compressive strains as more indium is added to the second layer. Thus, with increasing In coverage the repulsive In–In

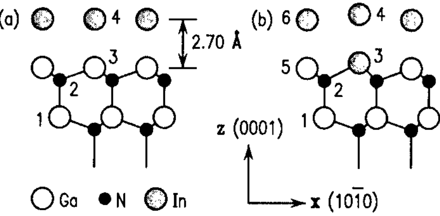

FIG. 6. (a) Schematic model of the A1 phase. The distance between the second layer gallium atoms and the first layer indium atoms is 2.70 Å. The distance between the layer 3 nitrogen atoms and the layer 2 gallium atoms is 0.68 Å. The bond angle θ_{123} is 110°. (b) Schematic model of the 5/4 ML structure. A vertical corrugation in the top layer is caused by the partial occupation of indium atoms in the second layer. This corrugation is $z_4 - z_6 = 0.30$ Å. The distance between the layer 3 nitrogen atoms and the layer 2 indium atoms is $z_3 - z_2 = 0.98$ Å. The bond angle θ_{123} is 117°.

interaction makes the In incorporation less and less favorable. In this model the gallium chemical potential has to be reduced to values below $\mu_{Ga}=-(E_{In}+2E_{In-In})=-1.78$ eV in order for all the S3 sites to be occupied by In atoms. That the In–N bonds are compressively strained, even in the 5/4 ML structure, can be seen by analyzing the atomic structure. In particular we note that the Ga–N–In bond angle θ_{123} defined in Fig. 6(b) is 117° for the 5/4 ML structure. This angle increases to 119° for the 8/4 ML structure. The optimal value for an unstrained system would be the tetrahedral angle, 109.5°. Moreover, the In–N bond length is 2.13 Å for the 5/4 ML structure and 2.09 Å for the 8/4 ML structure. In calculations for bulk InN we find the In–N bond length to be 2.17 Å. All these results indicate the existence of compressive strain, even for the low coverage 5/4 ML structure, and provide support for our contention that the pits form to relieve strain induced by the incorporation of indium in the second layer.

The second major theoretical result relating to this work concerns the smooth/rough transition of the surface morphology for InGaN(0001) compared to InGaN($000\bar{1}$). As discussed above, the clean GaN surface, both (0001) and ($000\bar{1}$), undergoes a smooth to rough transition as the Ga flux is reduced. It has been previously argued that this transition arises from a kinetic accumulation of nitrogen on the N-rich surfaces, such that the resulting Ga diffusivity is reduced and rough growth results.[7] In the present work we have found that the effect of adding indium on the smooth/rough transition is markedly different between the (0001) and ($000\bar{1}$) surfaces. We believe this difference to be correlated with the different metal (In and Ga) content of the two surfaces—1 ML for the ($000\bar{1}$) surface as pictured in Fig. 1(a), and about 2 ML for the (0001) surface as shown in Fig. 1(b). The excess metal present in the latter case may act to prevent any accumulation of nitrogen, thus preventing the associated reduction in Ga diffusivity. In addition, however, there is a separate mechanism which will act to increase the N diffusivity when 2 ML of metal is present: we find that the equilibrium position of the N atoms in this case is *between* the metal layers [i.e., between A1 and S3 layers in Fig. 1(b)], and the resulting diffusivity for the N is significantly enhanced compared to that when the N resides above the top layer.[14] Thus, we expect for both GaN and InGaN, under metal rich conditions, faster diffusion due both to the enhanced N diffusivity and the prevention of N accumulation. These mechanisms provide an interpretation of the kinetics which is in agreement with the experiment for both the clean and In-covered surfaces, of both polarity.

IV. CONCLUSION

The effect of indium atoms on the smooth/rough transition observed during MBE growth of GaN and InGaN has been studied in detail. Indium atoms were found to have little effect on this smooth/rough transition when deposited onto GaN($000\bar{1}$), but when indium is deposited on GaN(0001) GaN it is found that the gallium flux can be reduced greatly before the growth goes to rough. A $\sqrt{3}\times\sqrt{3}$ reconstruction is observed at the growth temperature. It forms and is stable under N-rich conditions. It likely consists of a structure containing indium and nitrogen atoms, residing on a gallium terminated GaN surface. InGaN(0001) surfaces under metal rich conditions were studied using STM and total energy computations. Indium is found to occupy the top two atomic layers of the crystal; incorporation in the second layer produces significant strain, leading to the formation of small pits on the surface. It is found that the indium concentration inside and around the pits is higher than that far away from the pits, which offers an alternative origin for the development of the compositional fluctuations in the InGaN bulk.

ACKNOWLEDGMENTS

This work was supported by the Office of Naval Research, Grant No. N00014-96-1-0214 (monitored by Colin Wood), and the National Science Foundation, Grant No. DMR-9615647. We thank C. D. Lee and V. Ramachandran for assistance with the MBE growth.

[1]S. Nakamura and G. Fasol, *The Blue Laser Diode* (Springer, Berlin, 1997).
[2]S. F. Chichibu, H. Marchand, M. S. Minsky, S. Keller, P. T. Fini, J. P. Ibbetson, S. B. Fleischer, J. S. Speck, J. E. Bowers, E. Hu, U. K. Mishra, S. P. DenBaars, T. Deguchi, T. Sota, and S. Nakamura, Appl. Phys. Lett. **74**, 1460 (1999).
[3]F. Widmann, B. Daudin, G. Feuillet, J.-L. Rouvière, and N. Pelekanos, Appl. Phys. Lett. **73**, 2642 (1998).
[4]H. Chen, A. R. Smith, R. M. Feenstra, D. W. Greve, and J. E. Northrup, MRS Internet J. Nitride Semicond. Res. **4S1**, G9.5 (1999).
[5]J. E. Northrup and J. Neugebauer, Phys. Rev. B **60**, 8473 (1999).
[6]E. J. Tarsa, B. Heying, X. H. Wu, P. Fini, S. P. DenBaars, and J. S. Speck, J. Appl. Phys. **82**, 5472 (1997).
[7]T. Zywietz, J. Neugebauer, and M. Scheffler, Appl. Phys. Lett. **73**, 487 (1998).
[8]V. Ramachandran, R. M. Feenstra, J. E. Northrup, and D. W. Greve, MRS Internet J. Nitride Semicond. Res. (to be published).
[9]V. Ramachandran, M. F. Brady, A. R. Smith, R. M. Feenstra, and D. W. Greve, J. Electron. Mater. **27**, 308 (1998).
[10]V. Ramachandran, A. R. Smith, R. M. Feenstra, and D. W. Greve, J. Vac. Sci. Technol. A **17**, 1289 (1999).
[11]S. Mroczkowski and D. Lichtman, Surf. Sci. **131**, 159 (1983).
[12]R. M. Feenstra, H. Chen, V. Ramachandran, A. R. Smith, and D. W. Greve, Appl. Surf. Sci. (to be published).
[13]T. Böttcher, S. Einfeldt, V. Kirchner, S. Figge, H. Heinke, D. Hommel, H. Selke, and P. L. Ryder, Appl. Phys. Lett. **73**, 3232 (1998).
[14]T. Zywietz, J. Neugebauer, J. E. Northrup, H. Chen, and R. M. Feenstra (unpublished).
[15]M. E. Lin, S. Strite, A. Agarwal, A. Salvador, G. L. Zhou, N. Teraguchi, A. Rockett, and H. Morkoç, Appl. Phys. Lett. **62**, 702 (1993); K. Iwata, H. Asahi, S. J. Yu, K. Asami, H. Fujita, M. Fushida, and S. Gonda, Jpn. J. Appl. Phys., Part 2 **35**, L289 (1996); P. Hacke, G. Feuillet, H. Okumura, and S. Yoshida, Appl. Phys. Lett. **69**, 2507 (1996).
[16]V. Ramachandran, C. D. Lee, R. M. Feenstra, A. R. Smith, J. E. Northrup, and D. W. Greve, J. Cryst. Growth **209**, 355 (2000).
[17]A. Thamm, O. Brandt, Y. Takemura, A. Trampert, and K. H. Ploog, Appl. Phys. Lett. **75**, 944 (1999).
[18]A. R. Smith, R. M. Feenstra, D. W. Greve, M. S. Shin, M. Skowronski, J. Neugebauer, and J. E. Northrup, Surf. Sci. **423**, 70 (1999).
[19]Y. Narukawa, Y. Kawakami, M. Funato, Sz. Fujita, Sg. Fujita, and S. Nakamura, Appl. Phys. Lett. **70**, 981 (1997).
[20]J. E. Northrup, L. T. Romano, and J. Neugebauer, Appl. Phys. Lett. **74**, 2319 (1999).

Growth of high-quality (Al,Ga)N and (Ga,In)N heterostructures on SiC(0001) by both plasma-assisted and reactive molecular beam epitaxy

K. H. Ploog,[a] O. Brandt, R. Muralidharan, A. Thamm, and P. Waltereit
Paul-Drude-Institut for Solid State Electronics, D-10117 Berlin, Germany

(Received 17 January 2000; accepted 1 May 2000)

We discuss the strategies essential for the growth of high-quality (Al,Ga)N/GaN and (Ga,In)N/GaN heterostructures on SiC(0001) substrates by molecular beam epitaxy (MBE) using either N_2 plasma discharge or NH_3 cracking as an active nitrogen source. Optimization of substrate preparation, nucleation, and growth conditions are the important issues to improve the surface morphology, interface abruptness, structural integrity, and electronic properties. A breakthrough in preparing the SiC(0001) surface was achieved by *ex situ* etching in H_2 at 1600 °C and subsequent *in situ* cleaning via several cycles of Ga deposition and flash-off at 800 °C. By far the best results are then obtained, when growth is initiated directly, i.e., without any specific nucleation phase, for both plasma assisted (PA)MBE and reactive (R)MBE. Using growth rates of 0.5–1.2 μm/h the optimum growth temperature T_s was found to be 700 °C for GaN. Any deviation from the optimum T_s and the optimum III/V flux ratio can be easily detected by reflection high energy electron diffraction and adjusted appropriately. Using these careful optimization strategies, both PAMBE and RMBE produce (Al,Ga,In)N heterostructures on SiC(0001) of high morphological, structural, and electronic quality in a very reproducible manner. The only difference between the two nitrogen sources is the very limited incorporation of In in (Ga,In)N in the presence of hydrogen from the NH_3 cracking on the growing surface. In PAMBE-grown (Ga,In)/GaN single and multiple quantum wells we achieved In mole fractions from 0.05 to 0.70 in 3 nm wells which very efficiently emit in the violet to yellow spectral range at 300 K. © *2000 American Vacuum Society.* [S0734-211X(00)04004-X]

I. INTRODUCTION

The recent advances and achievements in the electronic properties and device applications of modulation-doped (Al,Ga)N/GaN heterostructures grown by molecular beam epitaxy (MBE)[1–3] have strongly revived the interest in this technique for nitride growth. In this article we present some essential strategies for the growth of high-quality (Ga,In)N/GaN and (Al,Ga)N/GaN heterostructures on SiC(0001) substrates by both plasma-assisted and reactive molecular beam epitaxy, and we demonstrate that MBE is indeed a competitive technique for the growth on nitrides in terms of material quality and device relevance. We also make a critical comparison between rf plasma-assisted MBE (PAMBE) using nitrogen and reactive MBE (RMBE) using ammonia for the growth of nitrides.

II. EXPERIMENT

The growth experiments were carried out in three different custom-designed MBE systems. Two of these systems, of which one was free of arsenic, were equipped with rf plasma cells. The third one had an unheated NH_3 gas injector. Either nitrogen precursor had a purity of 5.5 N and was purified to the ppb level by commercial filters (model MONOTORR from SAES). The group III elements and dopants were evaporated from conventional effusion cells. As substrates we used on-axis, Si-face 4H or 6H–SiC(0001) from Cree Research. In the first set of growth runs the wafers were utilized as received, chemically cleaned, and outgassed, while in the second set of runs—and now routinely—after thorough *ex situ* H_2 etching at 1600 °C and *in situ* Ga deposition and flash-off, as described in Sec. III. The substrate temperature T_s, which ranged from 580 to 750 °C in various runs, was scaled by the GaAs oxide desorption temperature of 580 °C and calibrated pyrometrically. Nitride growth was initiated either with a nucleation phase (deposition of 5 nm GaN at lower temperature of 650 °C under N-rich conditions or of 5 nm AlN at higher temperature of 750 °C under stoichiometric conditions) or directly without separate nucleation phase, i.e., at growth conditions, which is now done routinely. Growth of GaN and (Al,Ga)N proceeded at substrate temperatures of 650–750 °C and growth rates of 0.6–1.2 μm/h under Ga-stable conditions. For deposition of (Ga,In)N the substrate temperature must be lowered to about 580 °C and growth must be carried out under N-stable conditions. The growth front was monitored *in situ* by reflection high-energy electron diffraction (RHEED). After growth the samples were characterized by atomic force microscopy (AFM), triple-crystal x-ray diffraction (XRD) using $Cu_{K\alpha 1}$ radiation, Raman scattering using the 514 nm Ar^+-ion laser line, transmission electron microscopy (TEM) using a JEOL 4000 EX microscope operating at 400 kV, photoluminescence (PL) and cathodoluminescence (CL) spectroscopy excited by the 325 nm HeCd laser line or using an Oxford Mono CL 2 setup, respectively, and Hall effect measurements.

[a]Author to whom correspondence should be addressed; electronic mail: ploog@pdi-berlin.de

TABLE I. Average values from various characterization techniques for 1–2 μm thick GaN layers grown by PAMBE and RMBE either without or with the optimization methods described here.

Property	Without optimization	With optimization
Roughness (nm)		
rms (3×3 μm^2)	1–10	0.2–0.7
peak-to-valley (3×3 μm^2)	15–100	4–12
X-ray width (arcsec)		
$\omega-2\theta(0002)$	40	25
$\omega(0002)$	900	100
$\omega(10\bar{1}3)$	2000	700
E_2 phonon width (cm^{-1})		
300 K	4	3
Dislocation density (cm^{-2})		
plan-view TEM	$>10^{10}$	$<10^9$
PL width (meV)		
5 K	15	7
300 K	50	40
n (cm^{-3})/μ(cm^2/V s)		
Undoped	1×10^{17}/35	1×10^{16}/--
Lightly doped	5×10^{17}/50	5×10^{17}/200
Heavily doped	2×10^{18}/100	2×10^{18}/160

III. CRITICAL ISSUES FOR IMPROVEMENT OF MATERIAL QUALITY

From our experience there are three critical issues which are essential for the improvement of the material quality during nitride MBE, i.e., substrate preparation, nucleation, and growth conditions. The individual steps will be discussed in detail, and the results are summarized in Table I.

A. Substrate preparation

Owing to the current status of the quality of commercial SiC substrate wafers, the proper preparation of the substrate surface prior to epitaxial growth is of utmost importance. As received wafers often exhibit a heavily scratched surface [Fig. 1(a)] with a peak-to-valley (ptv) roughness of 100 nm over an area of 25 μm^2 as well as a damage layer extending to 200 nm depth, both of which result from mechanical polishing. We have shown previously that this poor surface quality leads to a high density of parasitic dislocations.[4] Considerably lower dislocation densities are observed after chemomechanical polishing of the SiC substrates which removes the damage layer and decreases the ptv roughness to values around 10 nm.[5] However, the most significant improvement is achieved by etching the SiC substrates in H_2 at 1600 °C for 20 min. The surface morphology obtained after this etching step [Fig. 1(b)] is similar to that described in Ref. 6 and exhibits well-ordered arrays of unit cell high steps with a spacing of about 1 μm. The ptv roughness of these surfaces is as low as 2 nm.

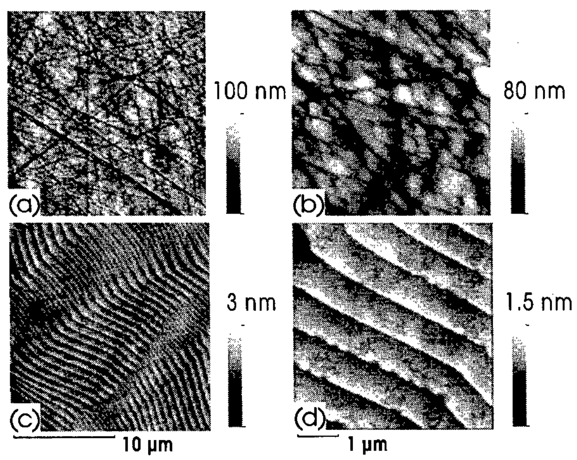

FIG. 1. AFM micrograph of: (a), (b) as-received and (c), (d) H_2 etched 6H–SiC(0001) substrate surfaces.

Next the hydrogen-etched substrates are chemically cleaned and passivated by HF dipping[6] as well as thoroughly outgassed prior to transferring them into the growth chamber. Before initiating growth, the substrates are subject to several cycles of Ga deposition and flash-off at $T_s=800$ °C to remove residual contaminants from the surface. For as-received substrates, this procedure has no visual impact on the RHEED pattern. For hydrogen-etched substrates, however, an intense ($\sqrt{3}\times\sqrt{3}$) reconstruction along the $[10\bar{1}0]$ azimuth is observed after Ga flash-off, evidencing the atomic ordering of the surface, and the contrast of the pattern improves considerably.

This improved substrate preparation procedure alone significantly reduces the dislocation density as well as the background carrier concentration (see Table I).

B. Nucleation

The nucleation phase is generally assumed to be the most critical step for obtaining high-quality GaN layers. However, at first glance the actual layer quality appears to be quite insensitive to this step. While AlN nucleation under stoichiometric conditions proceeds two dimensionally (2D) and yields immediate 2D growth of GaN, the results are virtually identical to those obtained by low-temperature GaN nucleation, which is invariably three dimensional (3D).[7] By far the best results concerning dislocation density and surface morphology for both PAMBE and RMBE are obtained, when growth is initiated directly, i.e., without a separate nucleation phase. Direct growth of GaN on SiC(0001) results in an initially spotty RHEED pattern, which becomes streaky after deposition of about 10 nm of GaN evidencing 2D growth. This streaky RHEED pattern prevails throughout growth if both stoichiometry and growth temperature are adjusted appropriately. However, any deviations from the optimum surface stoichiometry invariably cause the growth front to roughen.

C. Growth conditions

The optimum growth conditions, i.e., III–V flux ratio and substrate temperature for nitride growth are often adjusted empirically based on results from postgrowth characterization measurements. This procedure is unreliable, because the surface stoichiometry depends on both parameters which are hence interrelated. Here we show that those parameters can be controlled by *in situ* RHEED. A striking difference be-

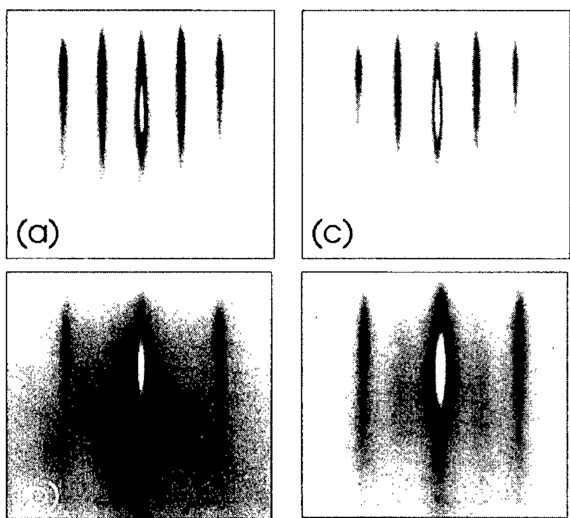

FIG. 2. RHEED patterns along the $[11\bar{2}0]$ azimuth during growth [(a) RMBE, (b) PAMBE] and during interruption [(c) RMBE, (d) PAMBE].

tween PAMBE and RMBE is reflected in the RHEED patterns observed during growth (Fig. 2). In PAMBE of GaN(0001) a (1×1) pattern is observed during growth. A transition to a (2×2) pattern occurs when the Ga flux is interrupted. The time needed for this reconstruction change is a direct measure for the excess Ga on the growth front. In our experiments, transition times between 10 and 30 s indicate the optimum surface stoichiometry. In RMBE of GaN(0001), however, a (2×2) pattern is observed during growth, the intensity of which is maximized for stoichiometric growth. This twofold reconstruction of GaN(0001), which is induced by H, vanishes for $T_s > 730\,^{\circ}C$. GaN layers grown at rates of 0.6–1.2 μm/h under these optimized conditions by either PAMBE or RMBE exhibit smooth surfaces with clearly visible atomic height steps (Fig. 3). N-stable GaN growth results in elongated transmission reflection patterns with shallow facet chevrons in RHEED and in surfaces which are rough on a microscopic (20–200 nm) scale.

When the substrate temperature for GaN growth is set too high ($T_s > 720\,^{\circ}C$), thermal etching of the surface at dislocation sites occurs, resulting in a sponge-like surface (Fig. 4) and eventually in the characteristic plateau–valley morphology often observed for MBE-grown GaN. This phenomenon manifests itself in the RHEED pattern by steep facet chevrons, which elongate during further growth towards the adjacent bulk reflections.

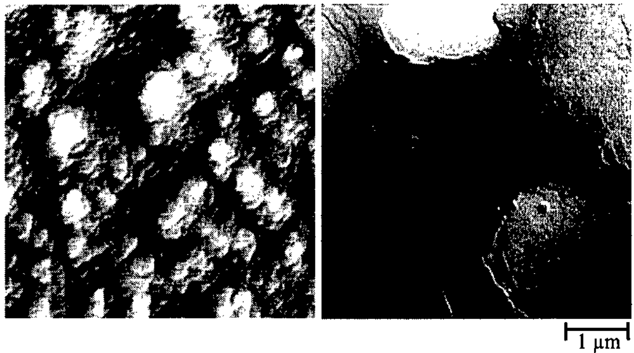

FIG. 3. Surface morphology as probed by AFM of 2 μm GaN grown by PAMBE (left) and RMBE (right) on 6H–SiC(0001).

In Table I we summarize the data from various characterization techniques to demonstrate the quality of 1–2 μm thick GaN layers grown by PAMBE or RMBE either without or with the optimization strategies discussed here. The results of our optimization strategies are self-evident, and we want to stress only a few striking points. First, and most important, the properties of GaN layers grown by PAMBE or by RMBE are literally identical in terms of quality. Both techniques yield surfaces with clearly visible atomic steps and dislocation densities below $10^9\,cm^{-2}$. There are, however, distinct differences with respect to In incorporation in (Ga,In)N, due to the presence of hydrogen. Second, using the *in situ* control of surface stoichiometry, the growth reproducibility is enhanced to a very satisfactory level.

Finally, a critical remark should be made about the long-term stability of the growth rate in PAMBE. Using rf plasma sources for active nitrogen generation in MBE, the growth rate of GaN, which can be as high as 2 μm/h, degrades with time down to 0.5 μm/h or less at the same rf power. In agreement with many users we have found that this degradation of growth rate with time does not depend on the manufacturer of the source.

IV. SELECTED RESULTS

The improvements in growth discussed before allow us to fabricate various (Al,Ga)(N/GaN and (Ga,In)N/GaN heterostructures as well as multiple quantum well (MQW) and single QW structures down to well widths of 4 monolayers with well-defined abrupt interfaces. The Al mole fraction in ternary (Al,Ga)N layers follows the gas-phase composition over the entire alloy range for both PAMBE and RMBE. A

FIG. 4. Surface morphology as probed by AFM of 2 μm GaN grown at: (a) 750 °C, (b) 730 °C, and (c) 700 °C on 6H–SiC(0001).

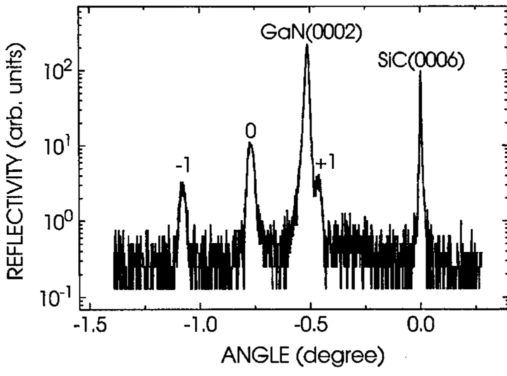

FIG. 5. Symmetric high resolution XRD scan across the GaN(0002) reflection of a ten period (3 nm $Ga_{0.55}In_{0.45}N$/10 nm GaN) MQW structure grown by PAMBE. Satellites are denoted by $\pm n$.

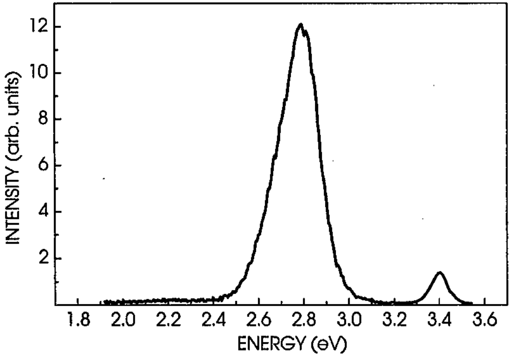

FIG. 7. Room temperature CL spectrum of 3 nm wide $Ga_{0.7}In_{0.3}N$/GaN single QW capped with 30 nm GaN.

drastic difference between the two methods exists, however, in the In incorporation in (Ga,In)N layers. With PAMBE we readily obtain (Ga,In)N quantum wells with In mole fractions up to 0.7 and emission energies spanning the spectral range from violet to yellow. Using PMBE, on the other hand, the maximum In content obtained under identical growth conditions reaches only 0.02. This striking difference is probably caused by H, present at the growth front from the cracked NH_3. The detailed mechanism responsible for this unusual behavior is not yet understood.

MBE has the clear advantage of a more homogeneous incorporation of In in (Ga,In)N QWs due to its lower growth temperature. Actually, in our experiments growth of (Ga,In)N/GaN single QWs and MQWs on a GaN buffer layer has been carried out at $T_s = 590\,^\circ\mathrm{C}$ under N-rich conditions to minimize segregation and reevaporation of In. The structural and optical properties of several samples are displayed in Figs. 5, 6, and 7. A precise determination of In mole fraction and well and barrier thicknesses in MQW structures from a comparison with simulation is possible, because sharp satellite peaks appear in the triple-crystal ω–2Θ x-ray scans (Fig. 5). Abrupt material interfaces are obtained and no deviations from periodicity exist. Deposition of the MQW structures does not deteriorate the surface morphology. As detected by AFM, even the surface of MQW

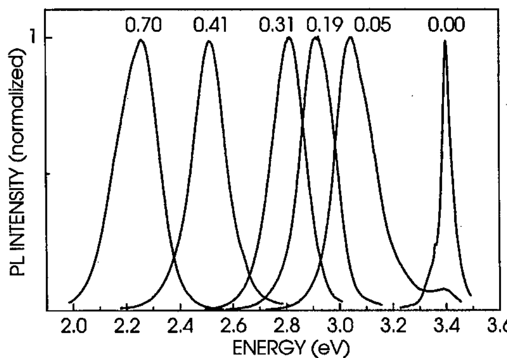

FIG. 6. Room-temperature PL spectra of (Ga,In)N/GaN MQW structures with 3 nm wide quantum wells. The In content is indicated at the top of the respective PL line.

structures containing up to 0.7 mole fraction In consists of about 100-nm-wide terraces separated by mono- and double-layer steps.

Room-temperature PL spectra of (Ga,In)N/GaN MQWs with In mole fractions from 0.05 to 0.70 (Fig. 6) exhibit QW emission bands which shift systematically from the violet to the yellow spectral range. The linewidths increase with In mole fraction from 150 to 200 meV and are only slightly broader than those from single QWs (120–180 meV). A significant part of the visible spectrum has thus been reached in a controlled way. The room-temperature CL spectrum of a $Ga_{0.7}In_{0.3}N$/GaN single QW (Fig. 7) shows that the QW emission in the blue spectral range at 2.79 eV totally dominates the spectrum. Its integrated intensity is higher by a factor of 20 than that from the GaN matrix. In addition, the emission is spatially homogeneous across the wafer down to the smallest length scale accessible in CL spectroscopy (about 100 nm). This evidences the lateral homogeneity of the sample.

Detailed time-resolved PL measurements on several series of (Ga,In)N/GaN MQW structures with systematically varied well widths and In mole fraction[8] have revealed that the optical properties of these structures are affected by both electrical polarization and alloy fluctuations. In narrow wells with high In mole fraction the alloy fluctuations dominate, while in wider wells with low In mole fraction the electrical polarization dominates.

We have fabricated several series of (Al,Ga)N/GaN MQW structures with different well widths and strain states of the constituent GaN wells to study systematically the influence of polarization induced electric fields on the optical properties.[9] As an example of the structural properties we show in Fig. 8 the ω–2Θ x-ray scan and in Fig. 9 the cross-sectional TEM image of an $Al_{0.15}Ga_{0.85}N$/GaN MQW structure grown by RMBE. The interfaces are atomically abrupt, and the dislocation density estimated from large-scale TEM lies below $10^9\,\mathrm{cm}^{-2}$. The surface morphology of these MQW structures does not change as compared to that of single GaN layers shown in Fig. 3(b).

The electric field in the GaN QWs leads to a quantum-confined Stark shift of the QW emission, which can thus fall well below the GaN bulk band gap. In addition, due to the

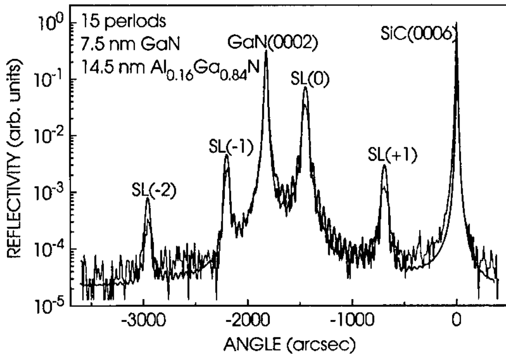

FIG. 8. Symmetric high resolution XRD scan across the GaN(0002) reflection of a 15 period $Al_{0.15}Ga_{0.85}N$/GaN MQW structure grown by RMBE (d_{GaN}=7.5 nm, $d_{(Al,Ga)N}$= 14.6 nm).

spatial separation of electron and hole wave functions, the oscillator strength of these radiative transitions can be orders of magnitude smaller than under field-free conditions. It has been suggested that heavy doping should completely screen the polarization field. However, while the QW emission energy is indeed strongly blue shifted with the doping level, the observed PL decay times clearly evidence a reduction in electron–hole wave function overlay even at the highest doping levels that we investigated ($n=1\times10^{19}\,cm^{-3}$).[9] This means that even heavy n-type doping does not produce flatband conditions in (AlGa)N/GaN MQW structures.

Of great advantage are the polarization induced electric fields in modulation-doped (Al,Ga)N/GaN heterostructures on SiC for the formation of the two-dimensional electron gas (2DEG). We have grown a series of such heterostructures by

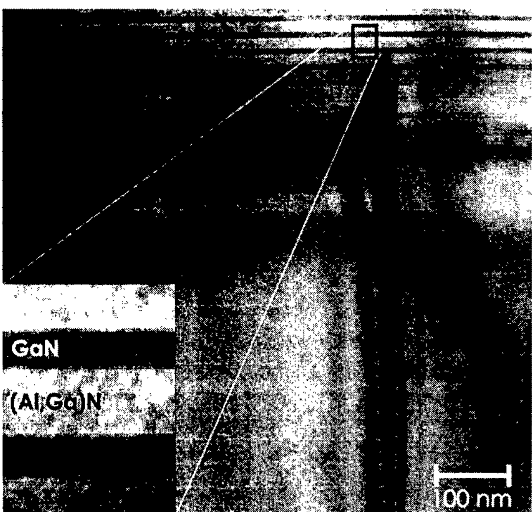

FIG. 9. Cross-sectional TEM image of the same $Al_{0.15}Ga_{0.85}N$/GaN MQW structure as in Fig. 8.

both PAMBE and RMBE to study the scattering mechanisms (dislocations, impurities, and point defects, and interface roughness in addition to phonon scattering) and their influence on the 2DEG mobility.[10] Employing our new growth strategies we have been able to reduce the density of these scatterers significantly and to obtain heterostructures which are well suited for heterostructure field-effect transistor fabrication.

V. CONCLUSIONS

Improvement of substrate preparation, nucleation, and growth conditions comprise the strategies which are essential for the growth of high-quality (Ga,In)N/GaN and (Al,Ga)N/GaN heterostructures and quantum wells on SiC(001) substrates by either PAMBE or RMBE. Both PAMBE and RMBE produce (Al,Ga,In)N heterostructures with structural and electronic properties of equivalent high quality. The major difference between the two growth techniques is the strongly limited In incorporation in RMBE grown (Ga, In)N due to the presence of H on the growing surface. On the other hand, RMBE is an extremely stable process and this technique is certainly the least expensive one for heterostructure fabrication of any of the available growth techniques.

The optical properties of (Ga,In)N/GaN QWs are affected by both electrical polarization and alloy fluctuation. Alloy fluctuations dominate in thin wells with high In mole fraction, whereas electrical polarization dominates in thick wells with low In mole fraction. The optical properties of (Al,Ga)N/GaN quantum wells are dominated by electrical polarization. Even heavy ($>10^{19}\,cm^{3}$) n-type doping does not produce flatband conditions.

ACKNOWLEDGMENTS

The authors gratefully acknowledge the active collaboration with H. von Kiedrowski, M. Reiche, and A. Trampert.

[1]Y.-F. Wu, B. P. Keller, S. Keller, J. J. Xu, B. J. Thibeault, S. P. DenBaars, and U. K. Mishra, IEICE Trans. Electron. **E82-C**, 1895 (1999).
[2]S. T. Sheppard, K. Doverspike, W. L. Pribble, S. T. Allen, J. W. Palmour, L. T. Kehias, and T. J. Jenkins, IEEE Electron Device Lett. **20**, 161 (1999).
[3]C. R. Elsass, I. P. Smorchkova, B. Heying, E. Haus, P. Fini, K. Maranowski, J. P. Ibbetson, S. Keller, P. M. Petroff, S. P. DenBaars, U. K. Mishra, and J. S. Speck, Appl. Phys. Lett. **74**, 3528 (1999).
[4]B. Yang, A. Trampert, B. Jenichen, O. Brandt, and K. H. Ploog, Appl. Phys. Lett. **73**, 3869 (1998).
[5]A. Thamm, O. Brandt, Y. Takemura, A. Trampert, and K. H. Ploog, Appl. Phys. Lett. **75**, 944 (1999).
[6]Q. Xue, Q. K. Xue, Y. Hasegawa, I. S. T. Tsong, and T. Sakurai, Appl. Phys. Lett. **74**, 2468 (1999).
[7]P. Waltereit, O. Brandt, A. Trampert, M. Ramsteiner, M. Reiche, M. Qi, and K. H. Ploog, Appl. Phys. Lett. **74**, 3660 (1999).
[8]P. Waltereit, O. Brandt, M. Ramsteiner, J. Ringling, A. Trampert, and K. H. Ploog, Inst. Phys. Conf. Ser. **166**, 453 (2000).
[9]A. Thamm, O. Brandt, A. Trampert, U. Jahn, J. Ringling, and K. H. Ploog, Inst. Phys. Conf. Ser. **166**, 461 (2000).
[10]R. Muralidharan, O. Brandt, H. v. Kiedrowski, and K. H. Ploog, Inst. Phys. Conf. Ser. **166**, 489 (2000).

Point defect modification in wide band gap semiconductors through interaction with high-energy electrons: Is reflection high-energy electron diffraction truly benign?

T. H. Myers,[a)] A. J. Ptak, B. L. VanMil, and M. Moldovan
Department of Physics, West Virginia University, Morgantown, West Virginia 26506

P. J. Treado, M. P. Nelson, J. M. Ribar, and C. T. Zugates
ChemIcon, Inc., Pittsburgh, Pennsylvania 15208

(Received 6 April 2000; accepted 26 May 2000)

Electron irradiation during reflection high-energy electron diffraction is shown to affect the materials properties of ZnSe and GaN during growth by molecular beam epitaxy. The high-energy electrons produce an electron stimulated desorption effect during growth of ZnSe, which primarily affects adsorbed Se. Se desorption rates under electron irradiation are shown to be significantly larger than thermal desorption rates. Electron irradiation also decreases ZnSe growth rates under Zn-rich conditions. The decrease can be suppressed by either growth under Se-rich conditions or by using high index substrate orientations, in this case (211)B. Electron irradiation also influences growth rates for GaN grown by rf plasma-assisted molecular beam. Characterization using Raman and photoluminescence spectroscopy along with secondary ion mass spectrometry indicate electron irradiation can have a dramatic impact on point defect and impurity content of GaN. © *2000 American Vacuum Society.* [S0734-211X(00)06904-3]

I. INTRODUCTION

Reflection high-energy electron diffraction (RHEED) is one of the most useful and undoubtedly the most widespread of the various techniques used for *in situ* monitoring during molecular beam epitaxy (MBE) growth.[1–4] While it was recognized early that RHEED could affect growing material, it has proven to be fairly benign for growth of GaAs and related III–V materials. There have been few investigations of how RHEED actually influences growth kinetics, impurity incorporation, or point defect formation. Farrell *et al.*[5] and Wu *et al.*[6] have reported that the high-energy electron irradiation occurring during RHEED affects the stoichiometry of static ZnSe and CdTe surfaces, respectively. Electron irradiation was also shown to influence surface reconstruction during the growth of CdTe.[6]

We have recently observed that RHEED can have a dramatic effect on the growth kinetics and on the incorporation of impurities/generation of point defects in ZnSe and GaN. A "stripe" associated with the position of the RHEED beam can be seen on many materials, while the effect of electron irradiation can only be seen by careful analysis on other samples, using techniques such as UV fluorescence microscopy. This article details the preliminary results of our current investigation of how high-energy electron irradiation affects the growth of ZnSe and GaN.

II. EXPERIMENT

ZnSe and GaN were grown by MBE in two separate systems at West Virginia University, one dedicated to the growth of III–nitride compound semiconductors and the other for the growth of II–VI materials. Details of the growth have been described elsewhere.[7,8] High-energy electron diffraction and irradiation studies were performed using a VE-026 electron gun from Vieetech Japan Co. Ltd. operating between 10 and 13 keV, with an electron current of ~25 μA. Studies were done in a typical RHEED geometry. RHEED images were captured and analyzed using a Si CCD camera under the control of software from *k*-Space Associates, Inc. (Ann Arbor, MI). Film growth rates were monitored *in situ* using the interference pattern observed in reflected light from a 680-nm-diode laser. UV fluorescence measurements were made on an Olympus Model BX60M Metallurgical System Microscope with a BX-FLA reflected light fluorescence attachment. A Janis SuperVaritemp dewar was used to obtain photoluminescence data using 325 nm excitation from a helium–cadmium laser with emitted light collected in a near-backscattering geometry using a 0.64-m-grating spectrometer and a GaAs photomultiplier. Imaging reflectance and Raman scattering experiments were performed at ChemIcon, Inc. (Pittsburgh, PA). Secondary ion mass spectrometry (SIMS) measurements were performed at Charles Evans and Associates (Redwood City, CA).

III. MACROSCOPIC EFFECTS OF HIGH ENERGY ELECTRON IRRADIATION: ZnSe

During our studies of the growth of ZnSe, we often observe the presence of features on the grown layers that correlate with the location of the electron beam during RHEED measurements. We typically grow on small samples, 1.5 cm by 1.5 cm, and have sacrificed sample rotation for better knowledge and control of the sample temperature during growth. If RHEED is performed during growth, the samples contain a discoloration in the form of a stripe visible to the eye. Such a stripe is readily apparent for the sample shown in

a)Electronic mail: tmyers@wvu.edu

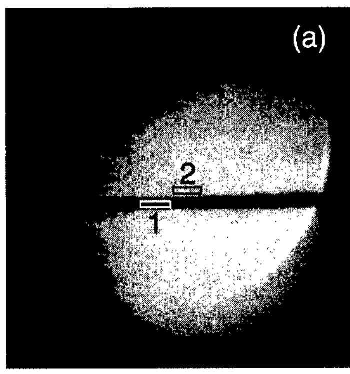

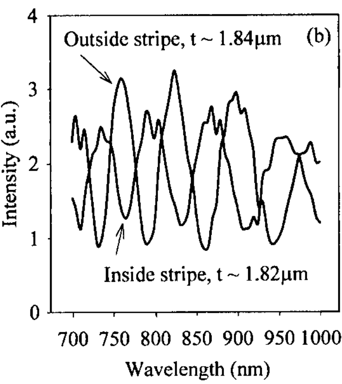

FIG. 1. (a) Reflectance image of a ZnSe layer at a wavelength of 900 nm; (b) spectral reflectance from the locations indicated by the rectangles.

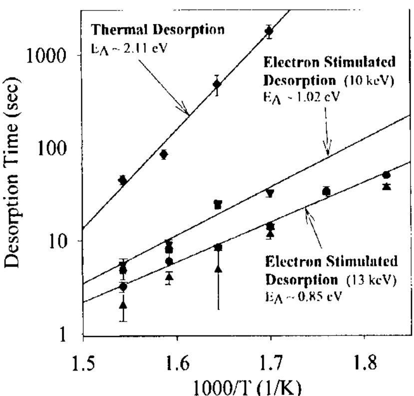

FIG. 2. Time intervals required for a Se-stable surface to evolve to a Zn-stable surface at various temperatures, with and without electron irradiation.

Fig. 1(a), which is a reflectance micrograph taken at a wavelength of 900 nm. Figure 1(b) shows the spectral reflectance taken both inside and outside the RHEED stripe. Analysis of the interference pattern indicates a slight decrease in growth rate with electron irradiation. This leads to a phase difference in the interference of the reflected light in the two regions, and provides the contrast making the stripe apparent.

Electron stimulated desorption (ESD) effects have been previously reported by Farrell *et al.* for ZnSe, and for CdTe by Wu *et al.* Electron irradiation was shown to increase Se-desorption from ZnSe and Te-desorption from CdTe static surfaces. In particular, the Se-stabilized (100) ZnSe surface exhibits either a (2×1) or a (1×1) reconstruction with an additional twofold reconstruction along the [011] direction. The Zn-stabilized surface always exhibits a $c(2\times2)$ reconstruction.[9] Thus, either the disappearance of the reconstruction along [011] or the emergence of the twofold reconstruction diffraction along the [010] direction can be used to monitor Se desorption. We chose to monitor emergence of the [010] reconstruction to indicate the attainment of a Zn-stable surface. Approximately 0.3 μm of ZnSe was grown under conditions known to produce high quality material. The growth was interrupted and the static surface exposed to a Se flux for about 5 s. The Se shutter was closed and the RHEED pattern was monitored using a CCD camera. Figure 2 indicates the times required after the Se shutter was closed for the emergence of the [010] reconstruction pattern for several substrate temperatures. Each point represents the average of five measurements. The temperature dependence is indicative of a thermally activated process, with an activation energy between 0.8 and 1.0 eV, possibly depending on electron energy. The desorption times for a strictly thermal process, one without electron irradiation, are also shown. For the latter case, the ZnSe surface was exposed to excess Se as before, but without the presence of electron irradiation. After a time, the sample was probed with the electron beam to see if a Zn-stable surface had emerged. The surface was then exposed to Se once again to produce a Se-stable surface. The process was repeated for various waiting times prior to electron beam exposure to bracket the Se thermal desorption time. The significant difference in activation energy between the two cases, 2.1 vs ~1.0 eV indicates that a large electron stimulated desorption effect is present.

As speculated by Farrell *et al.*, the ESD of Se could lead to a decrease in growth rate. To investigate this, the RHEED beam was defocused to give a stripe approximately 3 mm wide. The laser used for growth rate measurements was focused to coincide with this stripe. By turning the electron beam on and off while monitoring the film thickness evolution, the effect on growth rate could be determined at various substrate temperatures as indicated in Fig. 3(a). While increasing the substrate temperature lowers the growth rate for both Zn- and Se-stable growth, the presence of high energy electrons leads to a much more pronounced decrease in growth rate at higher temperatures for Zn-stable growth. A similar effect was not observed for Se-stable growth, as shown in Fig. 3(b), consistent with the belief that the ESD process is primarily affecting Se adatoms.

Farrell *et al.* determined a thermal activation energy of ~0.6 eV for the ESD process from 10 keV electrons in ZnSe, considerably lower than our measured value of ~1.0 eV at the same energy. This difference in activation energy may be related to the fact that we used (100) substrates off-cut 2° towards [011] with a higher step density that may have caused the Se to be more tightly bound to the surface. To further test this idea, we investigated growth of ZnSe on (211)B-oriented GaAs substrates. This orientation does not exhibit differing reconstruction depending on Zn- or Se-stable conditions, precluding RHEED desorption studies. As illustrated by the data in Fig. 3(b), there was not a measur-

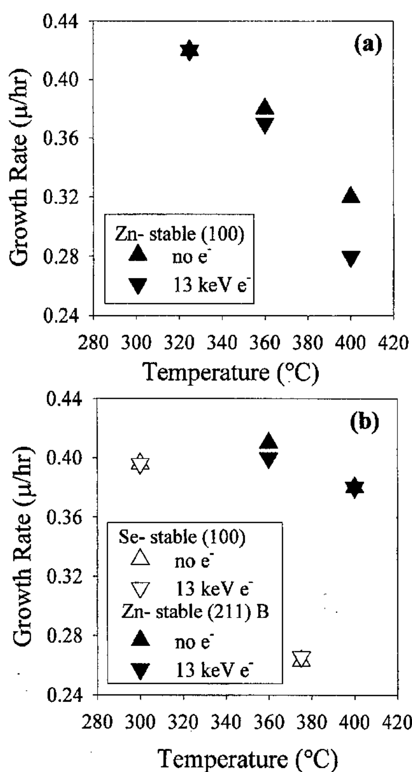

FIG. 3. ZnSe grown rates with and without electron irradiation, for various growth conditions.

FIG. 4. Integated visible fluorescence micrograph of a RHEED stripe on a GaN layer.

able difference in growth rate with and without electron irradiation up to 400 °C under Zn-stable conditions, indicating the effects of ESD were less pronounced for this highly stepped orientation.

Farrell *et al.*[5] attribute the ESD process to the generation of holes in the ZnSe, which according to Marfaing[10] will affect the more electronegative surface species, in this case Se. Simpson *et al.*[11] argue that this same process is the underlying origin of photon-stimulated effects also observed for above band-gap light illumination during growth. The observations reported here do not contradict this proposed mechanism, but also do not unambiguously resolve the underlying processes. In addition, there is little discussion in the literature on how the ESD process affects point defect formation, which is important for doping of ZnSe. We are extending the studies of the work on ZnSe reported in this article to address these two issues, with particular emphasis to see if RHEED affects the generation of point defects in II–VI semiconductors.

IV. MICROSCOPIC EFFECTS OF HIGH ENERGY ELECTRON IRRADIATION: GaN

We have also observed RHEED stripes to occur during the growth of GaN. While we do not see a pronounced decrease in growth rate due to the presence of electron irradiation, we have observed cases where there is a variation on the order of 5%. Many times the presence of an electron stimulated process is more easily determined by measuring microscopic properties. Figure 4 is a gray-scale micrograph of the integrated visible room temperature luminescence of a GaN sample exhibiting a RHEED stripe. The micrograph was taken using our UV fluorescent microscope. The contrast is provided primarily by a significant change in intensity of the so-called yellow luminescence, a band centered around 2.2 eV.

This particular sample was grown during a time when the GaN MBE system had a small air leak, resulting in the incorporation of significant amounts of carbon and oxygen, as indicated in the SIMS data plotted in Fig. 5. The scans labeled ''outside stripe'' were taken near the RHEED stripe, while the others were taken inside the stripe. There is a sig-

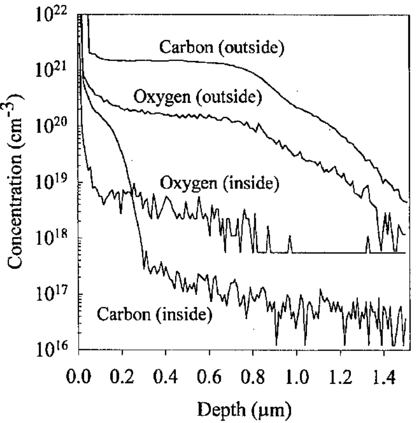

FIG. 5. SIMS of GaN indicating an ESD effect for oxygen and carbon.

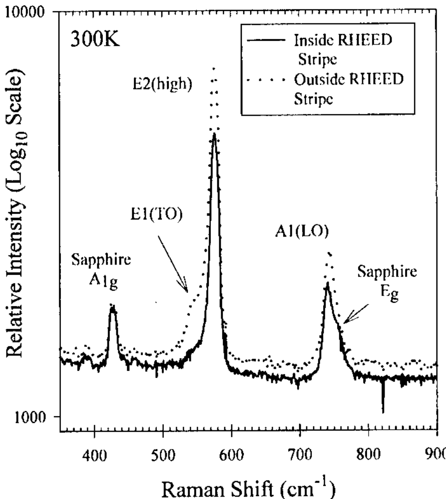

FIG. 6. Raman spectra indicating improved material quality inside the RHEED stripe.

nificant decrease in both the carbon and oxygen incorporated under electron irradiation, indicating that some type of ESD process is taking place for these impurities.

Figure 6 compares Raman spectra taken inside and outside the RHEED stripe. The presence of the $E1$(TO) resonance feature is not allowed in the Raman configuration used, and its presence in this configuration is taken to imply structural disorder.[12] This indicates the somewhat surprising result that the GaN grown under electron irradiation during RHEED has improved structural properties. This is also supported by low temperature photoluminescence (PL) measurements, as illustrated by the spectra shown in Fig. 7. PL outside the stripe exhibited: a broad donor-acceptor pair luminescence peak near 3.455 eV; the I_1 line associated with high residual background n-type doping; a strong signal at 3.400 eV that may be related to carbon; and smaller features at 3.22 and 3.26 eV that may be related to cubic inclusions. In contrast, the PL from the GaN that is inside the RHEED

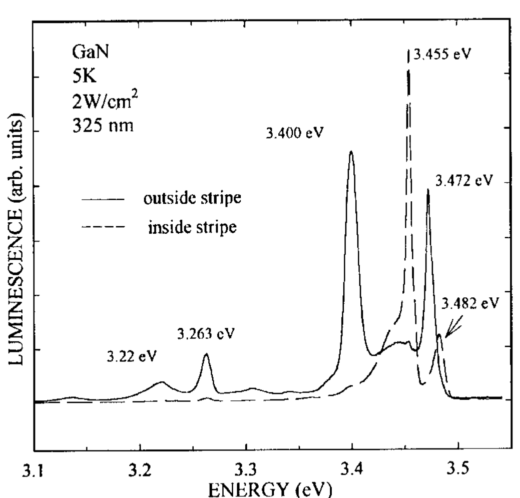

FIG. 7. PL spectra indicating improved material quality inside the RHEED stripe.

stripe region is dominated by free excitonic PL at 3.482 eV and by acceptor-bound excitonic PL at 3.455 eV. Both the A and B excitons could be resolved in temperature-dependent PL measurements (not shown). While assignment of the PL transitions is important, of primary concern to this article is the observation that completely different PL spectra were obtained inside and outside the region undergoing high-energy electron irradiation. The presence of free-excitonic transitions in the PL measurements indicated improved materials quality in the electron irradiated GaN, consistent with the Raman results. It is clear based on all of the above results that high-energy electron irradiation can have a significant impact on microscopic properties during the growth of GaN. The most interesting implication is that high-energy electron irradiation during growth can improve the materials quality of GaN.

V. SUMMARY

From the results reported here there can be no doubt that high-energy electron irradiation can affect both macroscopic and microscopic materials properties in compound semiconductors. A significant electron stimulated desorption effect is observed for Se during the growth of ZnSe. While the effects on growth rate can be minimized either by growing under Se-stable conditions or on high index orientations, this may not give the best conditions for all types of structures. In addition, it is not yet clear how electron irradiation affects point defect formation, and it may certainly modify alloy compositions.

GaN also exhibits effects related to high energy electron irradiation. An ESD effect is seen for oxygen and carbon, with small changes in growth rate occurring during electron irradiation. Raman and PL spectroscopy measurements indicate that, under certain conditions, electron irradiation during growth results in improve materials properties.

Since high energy electrons can distinctly alter surface reconstructions, surface chemistry, and epilayer materials properties, RHEED measurements must be carefully considered on a case-by-case basis to not misinterpret the observations. Indeed, if RHEED is performed during growth with sample rotation, the possibility exists to produce a periodic alloy or point defect "superlattice" structure within the material.

ACKNOWLEDGMENTS

This work was supported by ONR Grant No. N00014-96-1-1008 (monitored by Colin E. C. Wood) and by the National Science Foundation (Grant No. DMR-9806299). We would like to thank Professor N. C. Giles for the use of her facilities for PL measurements.

[1]A. Y. Cho, J. Appl. Phys. **42**, 2074 (1971).
[2]J. H. Neave, B. A. Joyce, P. J. Dobson, and N. Norton, J. Appl. Phys. **31**, 1 (1983).
[3]J. M. Van Hove, P. I. Cohen, and C. S. Lent, J. Vac. Sci. Technol. A **1**, 546 (1983).
[4]F. Briones, D. Golmayo, L. Gonzales, and J. L. Miguel, Jpn. J. Appl. Phys., Part 2 **24**, L478 (1985).

[5]H. H. Farrell, J. L. deMiguel, and M. C. Tamargo, J. Appl. Phys. **65**, 4084 (1989).
[6]Y. S. Wu, C. R. Becker, A. Waag, R. N. Bicknell-Tassius, and G. Landwehr, J. Appl. Phys. **69**, 268 (1991).
[7]Z. Yu, S. L. Buczkowski, N. C. Giles, and T. H. Myers, Appl. Phys. Lett. **69**, 82 (1996).
[8]T. H. Myers, M. R. Millecchia, A. J. Ptak, K. S. Ziemer, and C. D. Stinespring, J. Vac. Sci. Technol. B **17**, 1654 (1999).
[9]J. M. DePuydt, H. Cheng, J. E. Potts, T. L. Smith, and S. K. Mohapatra, J. Appl. Phys. **62**, 4756 (1987).
[10]Y. Marfaing, Semicond. Sci. Technol. **6**, A60 (1991).
[11]J. Simpson, S. J. A. Adams, J. M. Wallace, K. A. Prior, and B. C. Cavenett, Semicond. Sci. Technol. **7**, 460 (1992).
[12]S. D. Lester, F. A. Ponce, M. G. Crawford, and D. A. Steigerwald, Appl. Phys. Lett. **66**, 1249 (1995).

X-ray studies of group III-nitride quantum wells with high quality interfaces

P. F. Fewster and N. L. Andrew
Philips Research Laboratories, Redhill, Surrey RH1 5HA, United Kingdom

O. H. Hughes,[a] C. Staddon, C. T. Foxon, A. Bell, and T. S. Cheng
School of Physics and Astronomy, University of Nottingham, University Park, Nottingham NG7 2RD, United Kingdom

T. Wang and S. Sakai
Satellite Venture Business Laboratory, Department of Electrical and Electronic Engineering, University of Tokushima, 2-1 Minami-Josanjima 770-8506, Japan

K. Jacobs and I. Moerman
Department of Information Technology, University of Gent-IMEC, Gent, Belgium

(Received 17 January 2000; accepted 31 May 2000)

This paper reports an investigation of a variety of (InGa)N/GaN multi-quantum-well (MQW) samples grown by metalorganic vapor phase epitaxy on sapphire substrates. Dynamical scattering theory has been used to simulate the x-ray diffraction profiles so as to model the structures and to assess the quality of the grown interfaces. There is good agreement between the theoretical predictions and the experimental data. A systematic comparison of a set of ten-period MQWs with different well widths is also reported together with a discussion of the comparison between a single quantum well (QW) with five- and ten-period MQWs all with the same well and barrier widths and alloy composition. The well and barrier widths deduced from the x-ray measurements agree within experimental error with those predicted from the growth parameters, however, the In content of the wells appears to be substantially lower than that expected. This is discussed in terms of a carbon incorporation model. In the better samples, the (InGa)N/GaN interface is good to within a few monolayers—this is comparable with the best that can be achieved in (AlGa)As/GaAs QWs.
© *2000 American Vacuum Society.* [S0734-211X(00)08704-7]

I. INTRODUCTION

Group III-nitride structures are being used worldwide for both light emitting devices and high power field effect transistors.[1–3] Both types of device incorporate regions with different alloy compositions and doping levels and the performance of such devices depends critically on the interface quality. Modern x-ray diffraction techniques offer a wide variety of methods for understanding the problems involved in the growth of complex structures by heteroepitaxy and for assessing the quality of interfaces.[4,5]

The semiconductor samples used in this present work were grown at Tokushima University and Gent University by metalorganic vapor phase epitaxy (MOVPE) on sapphire substrates. After growing a suitable buffer layer of GaN, the well structures were grown and then a capping layer of GaN was produced. When growing every (In/Ga)N layer in each sample, the In/Ga supply ratio was kept constant at a level which was intended to produce $(In_{0.13}Ga_{0.87})N$. The subsequent x-ray diffraction work and theoretical modeling studies were carried out at Philips Research Laboratories and the University of Nottingham.

The object of the present exercise was to find out how closely a MOVPE-grown multi-quantum-well (MQW) structure approximates to the ideal structure planned by the grower. The parameters which were examined were In/Ga ratio in the wells, the widths of the wells, barriers, and capping layer, and the abruptness of the interfaces.

II. EXPERIMENT AND GROWTH

The MQW samples used in this work were grown by MOVPE using NH_3 as the nitrogen source and trimethyl gallium and trimethyl indium as the gallium and indium sources, respectively. The sapphire substrates were initially nitrided with NH_3 at 1100 °C and then cooled to 450 °C for the growth of a 25 nm GaN buffer layer. The bulk GaN layer, of thickness 2 μm, was grown at 1075 °C but the growth temperature was lowered to 700 °C during growth of each (InGa)N well and of the 150 nm capping layer. The cooling and heating steps at the start and end of each (InGa)N layer took several minutes during which the surface was under NH_3 but no growth was taking place. During these zero-growth periods the surface was prone to absorption of carbon-containing species from the ambient. The subsequent fate of any such species would have depended either on the relative diffusion coefficients of C in GaN and (InGa)N, respectively, or on the occurrence of surface segregation during the growth of the well.

III. CONSTANT WELL-WIDTH SUPERLATTICES

A set of three samples was grown containing one, five, and ten wells, respectively, all of which were intended to be 2.7 nm wide and separated by 7.3 nm barriers. The In con

[a]Electronic mail: Owain.Hughes@nottingham.ac.uk

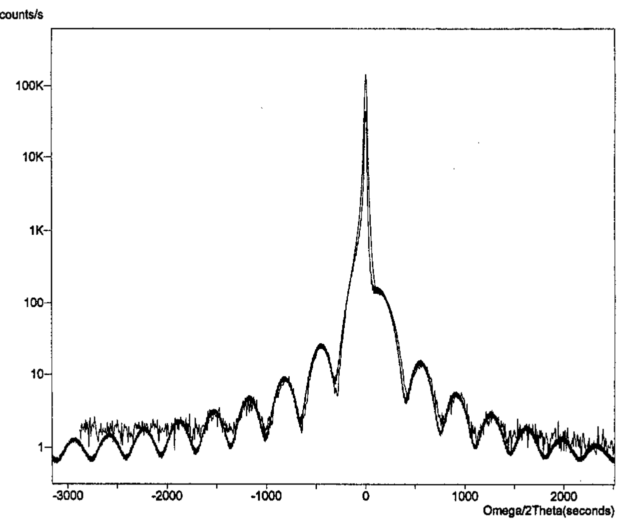

FIG. 1. $\omega/2\theta$ scattering profiles for a single 2.7 nm wide (InGa)N quantum well grown within a GaN layer. The heavy line corresponds to the theoretical profile while the faint line shows the experimental results.

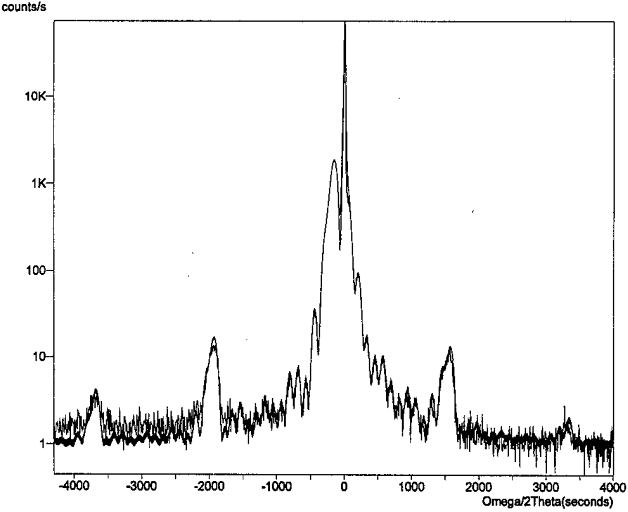

FIG. 3. $\omega/2\theta$ scattering profiles for ten 2.7-nm-wide (InGa)N quantum wells separated by 7.0 nm GaN barriers grown within a GaN layer. The heavy line corresponds to the theoretical profile while the faint line shows the experimental results.

tent, as mentioned previously, was intended to be 13%. The $\omega/2\theta$ scattering profiles obtained from these samples are shown in Figs. 1–3 together, in each case, with a theoretical profile. In the $\omega/2\theta$ technique, the angle of incidence ω is scanned from zero while the detector angle 2θ is scanned at twice the ω rate. Thus the diffraction always takes place from planes which are parallel to the sample surface.

The features to note on these plots are (a) the sharp peak at $\omega/2\theta=0$, (b) the peak at a low negative value of $\omega/2\theta$, (c) the satellite peaks which lie symmetrically about peak (b), and (d) the interference fringes which can be seen right across the profile. Peak (a) corresponds to diffraction from the GaN. Peak (b) arises from the zero-order diffraction by the superlattice and its position depends on the mean In content of the alloy in the well+barrier regions. The spacings of

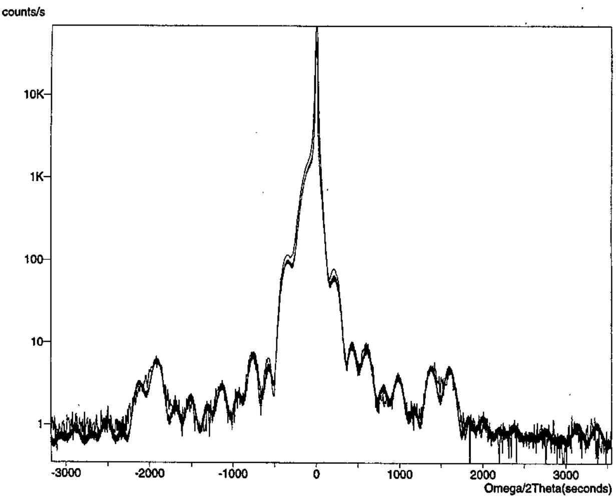

FIG. 2. $\omega/2\theta$ scattering profiles for five 2.7-nm-wide (InGa)N quantum wells separated by 7.0 nm GaN barriers grown within a GaN layer. The heavy line corresponds to the theoretical profile while the faint line shows the experimental results.

the satellite peaks (c) are, to a first approximation, dependent on the well+barrier dimension and the intensities of the peaks depend on the well widths—thus both well and barrier widths can be estimated. Finally, the interference fringes depend on the thickness of the capping layer.

Interpretation of the data obtained on the constant width superlattices was carried out by profile fitting. The simulation model used was Philips Epitaxy, which is based on the solution of the Takagi–Taupin equations.[6,7] The latter are differential equations relating the change in diffracted and incident amplitudes with depth into a crystal and they can be used as the basis of a full dynamical scattering theory. The whole structure is modeled in terms of regions of constant composition and strain as a function of depth, thus allowing complex structures with compositional grades and rough interfaces to be modeled. The Takagi–Taupin equations have been used successfully by many workers to predict diffraction profiles from graded layers.[8,9]

As can be seen in Figs. 1–3, the theoretical profiles can be fitted with considerable accuracy to the experimental data. The ten-well sample data fits best to a profile derived from a theoretical superlattice with 2.5 nm wells separated by 7.0 nm barriers. The predicted capping layer thickness was 39 nm and the In content (surprisingly) was very low at 6.4% The five-well sample data indicated identical superlattice dimensions and the In content was 6.5%. Since the single well sample data did not exhibit satellites, the dimensions of the well could not be predicted but the interference fringes gave a value of 39 nm for the capping layer.

IV. VARYING WELL-WIDTH SUPERLATTICES

A set of three samples, each containing a ten-well superlattice, was analyzed. The barrier widths were constant at 7.3 nm but the well widths were, respectively, 1.25, 2.5, and 5.2 nm. The diffraction data for the first and third samples are shown in Figs. 4 and 5. The data for the second sample is

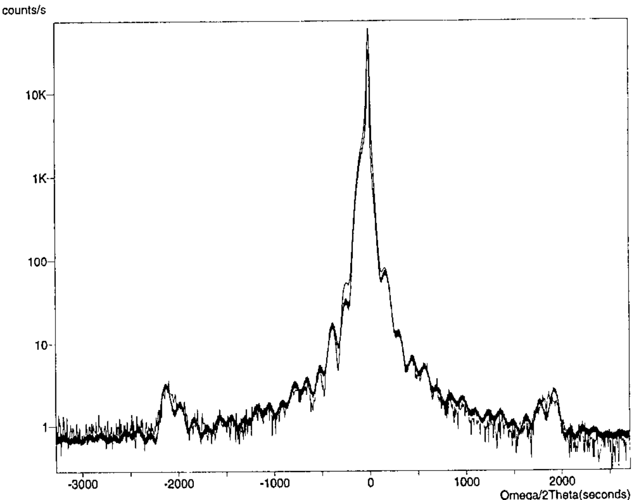

FIG. 4. $\omega/2\theta$ scattering profiles for ten 1.25-nm-wide (InGa)N quantum wells separated by 7.0 nm GaN barriers grown within a GaN layer. The heavy line corresponds to the theoretical profile while the faint line shows the experimental results.

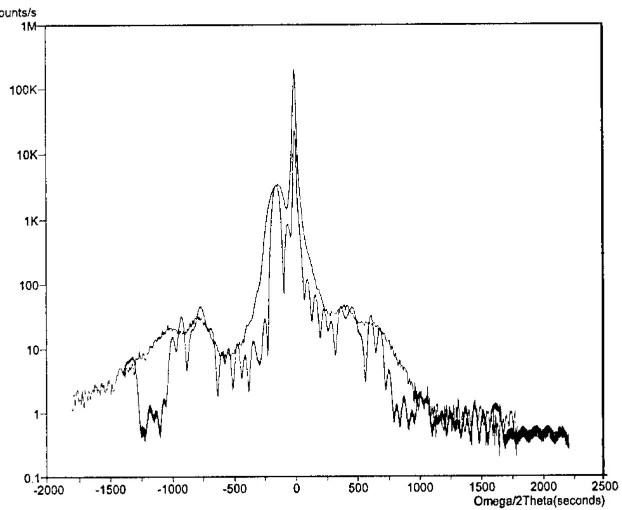

FIG. 6. $\omega/2\theta$ scattering profiles for ten (InGa)N quantum wells of varying widths and separated by 7.0 nm GaN barriers grown within a GaN layer. The heavy line corresponds to the theoretical profile while the faint line shows the experimental results.

identical to that shown in Fig. 3. Profile fitting to this set of data again gives well widths and barrier widths which are close to the intended dimensions but again the In content was found to be in the region of 6.5%.

A further set of samples was analyzed, in which the ten wells varied in width.[10] An example of data from one of these samples is shown in Fig. 6. The profile is indicative of significant variations in the period and this has been confirmed by scanning electron microscope studies.[10] The profiling procedure necessary to analyze such data fully, involves many extra fitting parameters and is incomplete at the moment. An approximate analysis has been carried out by regarding the structure as consisting of two groups of five wells, each group having constant well width. The agreement

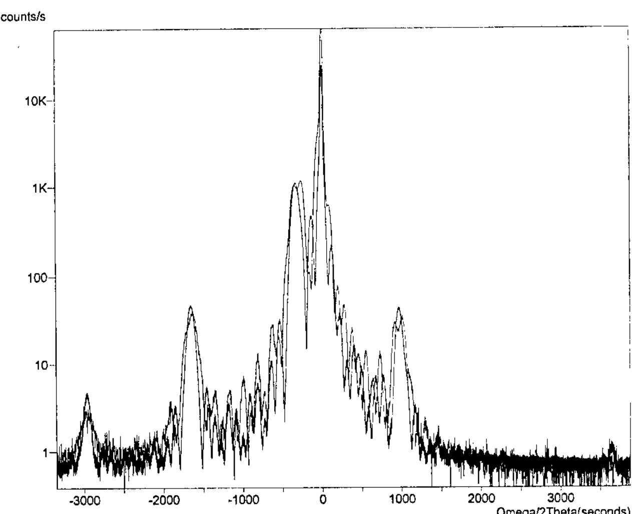

FIG. 5. $\omega/2\theta$ scattering profiles for ten 5.2-nm-wide (InGa)N quantum wells separated by 7.0 nm GaN barriers grown within a GaN layer. The heavy line corresponds to the theoretical profile while the faint line shows the experimental results.

between theory and experiment is less good but it can be seen that a reasonable fit is obtainable even with such a very approximate starting model for the well dimensions. The fit shown in Fig. 6 is based on well widths of 6.9 and 10.0 nm, respectively. A more sophisticated analysis based on ten different well widths is in hand and will be reported in the near future. The most interesting result of the approximate analysis above is that peak (b) in Fig. 6 can be modeled with some accuracy and that the indicated In content of the wells is only 3.5%—about half of the indicated content of the constant well width samples.

As a check on the calibration of the growth process, thick (1 μm) layers of (In/Ga)N were grown in the same growth reactor and the In content was found to be 13% as intended. Thus it would appear that the In deficiency reported previously is a feature only of thin structures such as the superlattices. As a further check on this phenomenon, a MQW sample was grown at very low temperature and at a very slow growth rate. The well widths were found to be accurately controllable and the In content was 13% as intended.

The above-discussed samples were grown in two different laboratories and the sapphire substrates were obtained from different suppliers. $\omega/2\theta$ profiles obtained from the substrates showed that they were of variable quality but the superlattice structures grown on them appeared to be unaffected by the quality of the underlying sapphire.

V. CONCLUSIONS

The results obtained from the above-discussed MQWs indicate that good control of well and barrier widths is achievable but, with the exception of structures grown very slowly at low temperature, the In content of the wells is much lower than was intended. There are at least three possible explanations for this effect. First, evaporation of the In could be occurring during growth. This would explain why the wells

grown at low temperature had the correct In content but does not explain why thick layers grown at high temperature also had the correct In content. Second, the effect could be caused by surface segregation. Thick samples would not suffer from In loss due to this process whereas thin structures would be affected. If this were so, however, one might have expected wide and narrow wells to have different In content whereas, in fact, the In content remained at the same level. Third, carbon incorporation could be occurring during the growth process.

Carbon has an ionic radius of 0.077 nm while the radii of gallium and indium are 0.126 and 0.144 nm, respectively. Thus if only very small amounts of C were to be incorporated onto group III sites in the (InGa)N but not in the GaN, the mean lattice parameter within the well would be reduced drastically. Thus, even though the wells do actually contain 13% In, the x-ray data would indicate that the content was much smaller. As mentioned previously, carbon could be incorporated at the free surface during the cooling down process prior to growth of the (InGa)N. During growth of the well the carbon could segregate with the growing surface and be incorporated throughout the well. When the temperature is raised prior to the resumption of the GaN growth, the excess surface carbon is desorbed and the process stops. Investigation of this possibility by secondary ion mass spectroscopy analysis is in progress.

The $\omega/2\theta$ scans shown in Figs. 1–6 have fewer satellite peaks than would be expected from MQW structures grown in materials such as GaAs/(AlGa)As. Such materials typically exhibit up to 10 or 12 satellites, which makes accurate determination of interface abruptness relatively easy. The reason for this wealth of satellites is that the atomic scattering factors of Ga and As are so similar that almost complete destructive interference occurs in the GaAs (200) diffraction. Al, on the other hand, has a very different atomic scattering factor from that of As so even small amounts of Al give rise to strong satellite peaks in the $\omega/2\theta$ scan obtained from (AlGa)As. Ga and N already have very different atomic scattering factors and the addition of In makes very little difference, hence the scarcity of satellite peaks.

The profile fitting procedures used in this work have all assumed atomically abrupt interfaces between the GaN and (InGa)N regions. An accurate estimate of the interface abruptness would need many more satellites than are available, but the fact that the fit is as good as it is [see Fig. 1(a) in particular] indicates that the abruptness is probably of the order of two or three atomic layers. Further work is in hand on modeling of MQW structures with deliberately graded interfaces which should provide a means of estimating the effect of nonabruptness on the x-ray data and hence a means of estimating the abruptness of nonintentionally graded interfaces by extrapolation.

ACKNOWLEDGMENT

The authors are grateful to the Higher Education Funding Council for England which, under the terms of the 1998 Joint Research Equipment Initiative (Project Code: JR98NOHU), provided generous funding for the purchase of the Philips X-Pert Diffractometer used in part of this work.

[1]S. Nakamura, T. Mukai, and M. Senoh, Appl. Phys. Lett. **64**, 1687 (1994).
[2]S. Nakamura, M. Senoh, S. Nagahama, N. Iwasa, T. Yamada, T. Matsushita, H. Kiyoku, and Y. Sugimoto, Jpn. J. Appl. Phys., Part 2 **35**, L74 (1996).
[3]C.-H. Chen, S. Keller, G. Parish, R. Vetury, E. L. Hu, S. P. Denbaars, U. K. Mishra, and Y. Wu, Appl. Phys. Lett. **73**, 3147 (1998).
[4]M. A. G. Halliwell, J. Cryst. Growth **170**, 47 (1997).
[5]P. F. Fewster, Crit. Rev. Solid State Mater. Sci. **22**, 69 (1997).
[6]S. Takagi, Acta Crystallogr. **15**, 1311 (1962).
[7]D. Taupin, Bull. Soc. Fr. Mineral. Cristallogr. **87**, 469 (1964).
[8]M. A. G. Halliwell, M. H. Lyons, and M. J. Hill, J. Cryst. Growth **68**, 523 (1984).
[9]A. Fukuhara and Y. Takano, Acta Crystallogr., Sect. A: Cryst. Phys., Diffr., Theor. Gen. Crystallogr. **33**, 137 (1977).
[10]N. Duxbury, P. Dawson, U. Bangert, E. J. Thrush, W. Van der Stricht, K. Jacobs, and I. Moerman (unpublished).

Charging effects in AlGaN/GaN heterostructures probed using scanning capacitance microscopy

K. V. Smith, X. Z. Dang, and E. T. Yu[a]
Department of Electrical and Computer Engineering, University of California at San Diego, La Jolla, California 92093-0407

J. M. Redwing[b]
ATMI/Epitronics, 21002 North 19th Avenue, Suite 5, Phoenix, Arizona 85027-2726

(Received 17 January 2000; accepted for publication 3 April 2000)

Charging effects in an $Al_xGa_{1-x}N$/GaN heterostructure field-effect transistor epitaxial layer structure have been studied using scanning capacitance microscopy. Voltages of ≤6 V applied between an $Al_xGa_{1-x}N$/GaN sample structure and a conducting proximal probe tip are found to create trapped charge in both doped and undoped heterostructures. Scanning capacitance measurements obtained over a wide range of bias voltages allow the charge distribution to be mapped both laterally and in depth with submicron to nanometer scale spatial resolution. Scanning capacitance imaging as a function of bias voltage performed in conjunction with numerical capacitance–voltage simulations suggests that positive charge can be trapped at the $Al_xGa_{1-x}N$ surface and within the GaN layer and negative charge can be trapped at or near the $Al_xGa_{1-x}N$/GaN interface. © *2000 American Vacuum Society.* [S0734-211X(00)00604-1]

I. INTRODUCTION

III–V nitride heterostructures have attracted intense research interest for a variety of device applications including blue light-emitting diodes and lasers,[1] visible-blind ultraviolet photodetectors,[2,3] and high-temperature/high-power electronic devices.[4–9] Although very impressive performance has been demonstrated in many such nitride-based devices, the epitaxially grown nitride materials from which device structures are fabricated typically contain high densities of extended defects such as threading dislocations as well as substantial concentrations of point defects, associated with both of which can be trap states, piezoelectric fields, and other localized variations in electronic structure. These local variations in electronic properties can exert a pronounced influence on device behavior and consequently must be characterized, understood, and controlled in nitride heterostructure materials and device engineering.

In this article, we present studies of local charging of trap states in $Al_xGa_{1-x}N$/GaN heterostructure field-effect transistor (HFET) epitaxial layer structures using scanning capacitance microscopy (SCM). The SCM technique has been applied recently to the characterization of local surface electronic structure in n-GaN epitaxial layers[10] and of local variations in threshold voltage in $Al_xGa_{1-x}N$/GaN HFET epitaxial layers.[11] By measuring capacitance properties between a conducting proximal probe tip and the sample structure of interest at a fixed tip-sample bias voltage, lateral variations in mobile carrier distributions, fixed electrostatic or trapped charge distributions, and the resulting local potential distributions can be observed at length scales ranging from <0.1 μm to several μm. Measurement and analysis of SCM image contrast as a function of applied bias voltage then enables such variations to be correlated with various features in structural morphology or with the presence of electrostatic or trapped charge concentrated in specific locations within the sample structure. In this manner we have observed and analyzed, in the studies reported here, localized charging of trap states within $Al_xGa_{1-x}N$/GaN HFET epitaxial layer structures induced by bias voltages applied via a proximal probe tip.

II. EXPERIMENT

The sample structures used in this study, shown schematically in Fig. 1, were grown by metalorganic chemical vapor deposition (MOCVD) on n-type 4H-SiC (0001) substrates. For all samples a 0.1 μm AlN buffer layer was initially deposited, followed by an undoped 1.2 μm GaN channel layer and finally the $Al_xGa_{1-x}N$ barrier layer structure. Epitaxial layer structures containing both doped and undoped $Al_xGa_{1-x}N$ layers have been characterized. The barrier layer in the undoped sample consisted simply of 230 Å nominally undoped $Al_{0.15}Ga_{0.85}N$. The barrier layer in the intentionally doped sample, used for the majority of the work described here, consisted of an undoped 30 Å $Al_{0.26}Ga_{0.74}N$ spacer layer followed by a 200 Å n-$Al_{0.26}Ga_{0.74}N$ layer doped with Si at a concentration of $3\times10^{18}\,cm^{-3}$. Even in the absence of intentional doping, the polarization fields in the strained $Al_xGa_{1-x}N$ layer will create a two-dimensional electron gas (2DEG) at the $Al_xGa_{1-x}N$/GaN interface.[12–15] The sheet carrier concentrations for these samples, determined from Hall measurements performed at room temperature, were $4.6\times10^{12}\,cm^{-2}$ for the undoped $Al_{0.15}Ga_{0.85}N$/GaN structure and $1.2\times10^{13}\,cm^{-2}$ for the doped $Al_{0.26}Ga_{0.74}N$/GaN structure.

Scanning capacitance microscopy was performed using a Digital Instruments Dimension 3100 atomic force micro-

[a]Electronic mail: ety@ece.ucsd.edu
[b]Current address: Materials Science and Engineering Dept., Penn State University, University Park, PA 16802.

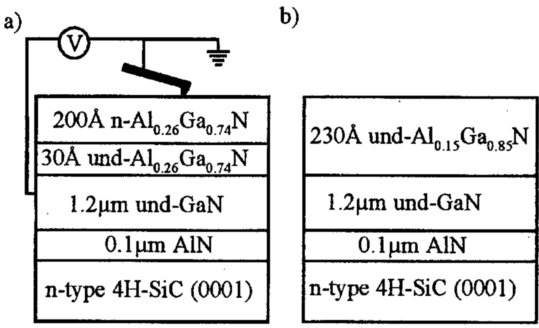

FIG. 1. Schematic diagrams of (a) doped and (b) undoped $Al_xGa_{1-x}N$/GaN HFET epitaxial layer structures. Sample and probe tip geometry and electrical connections are indicated schematically in (a).

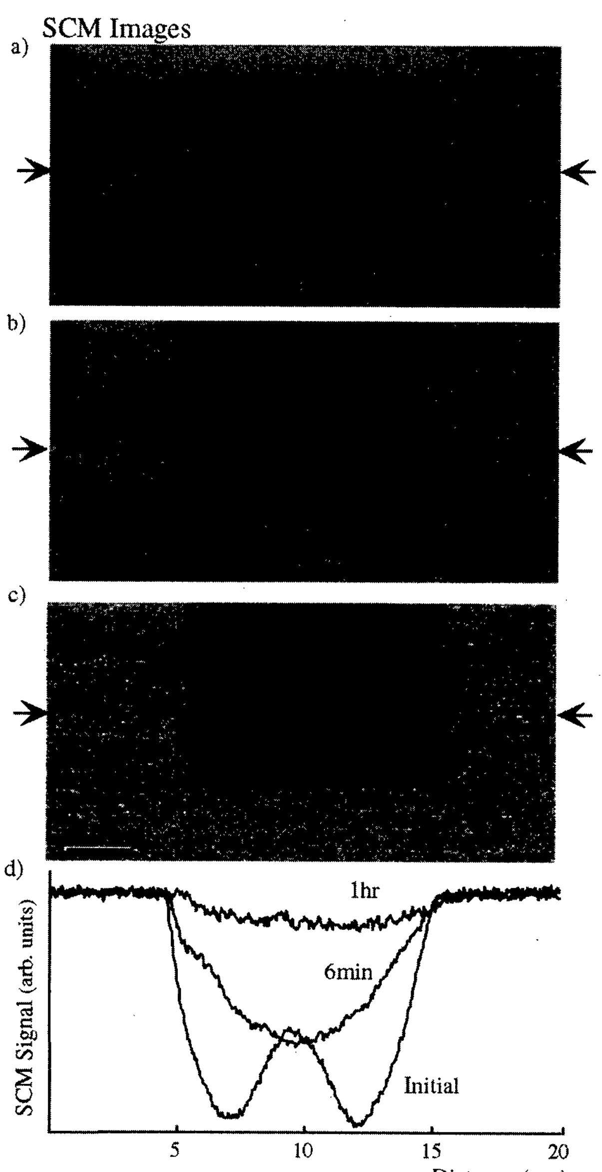

FIG. 2. SCM images obtained at 0 V dc sample bias of a locally charged region of the doped $Al_xGa_{1-x}N$/GaN HFET epitaxial layer structure and surrounding uncharged regions, obtained (a) immediately, (b) 6 min, and (c) 1 h after charging. (d) Line scans extracted from the images (a)–(c) at the locations indicated by arrows.

scope with a capacitance attachment. The ac and dc bias voltages employed during the scanning capacitance measurements were applied to the sample as indicated in Fig. 1(a). Electrical contact to the epitaxial layers was made using a conducting silver tape contact to the $Al_xGa_{1-x}N$ surface. Previous experiments have shown that there is no measurable difference between contacting the $Al_xGa_{1-x}N$ surface in this manner and contacting the GaN layer through a fully processed ohmic contact. The probe tips used in the measurements presented here were commercially available tips (Digital Instruments) fabricated from highly doped Si. In preparation for imaging, each probe tip assembly was heated at ~250 °C for 30 min to increase the thickness of the native oxide and thereby provide an insulating barrier to minimize current flow between the sample and tip during the SCM measurement. Prior to heating the probe tip and cantilever structure, the underside of the probe substrate was covered with silver paint to ensure that a good electrical contact could be made between the SCM electronics and the tip.

III. RESULTS AND DISCUSSION

Studies of phenomena such as persistent photoconductivity and of trap states in GaN, $Al_xGa_{1-x}N$, and $Al_xGa_{1-x}N$/GaN heterostructures have revealed that epitaxially grown nitride materials are typically characterized by significant densities of defects and impurities, associated with which are a variety of trap states. Filling or emptying, and consequently charging, of deep trap levels during application of large bias voltages in diodes, transistors, and other device structures can then lead to significant transient effects and frequency-dependent device characteristics. These effects can be studied on a spatially localized basis by using the conducting proximal probe tip in the SCM apparatus to apply large, localized bias voltages and observing the subsequent localized charge distribution by SCM imaging and spectroscopy.

In the studies presented here, localized regions of the sample were charged by performing a SCM imaging measurement with a relatively large dc bias voltage (typically ⩾6 V) applied in conjunction with an ac bias voltage with a typical amplitude of ~2 V. Application of a large bias voltage via the proximal probe tip is roughly analogous to the application of a corresponding bias voltage in a Schottky diode structure. Typically two or more images are obtained under these conditions, after which the scan size is increased and the dc bias voltage reduced to image the charged area along with a surrounding, uncharged region. Figure 2(a) shows a SCM image, obtained at a dc bias of 0 V, of a typical charged region and the surrounding, uncharged area in the undoped $Al_{0.15}Ga_{0.85}N$/GaN HFET structure immediately after charging as described above at a dc sample bias of 6 V. The 0 V dc bias voltage and accompanying ac modulation signal applied during imaging have only a minimal effect on the electrostatic and trapped charge distribution in the sample over the time scales probed in these studies. Figures

2(b) and 2(c) show SCM images of the same charged region shown in Fig. 2(a) obtained 6 min and 1 h after charging, respectively. A minor point to note is that a bright region is present at the center of the image in Fig. 2(a). This contrast disappears within the time (6 min) required to acquire each SCM image, and its origin is currently a subject of investigation.

Figure 2(d) shows line profiles extracted from the images shown in Figs. 2(a)–2(c). The reduction in contrast between the charged and uncharged regions with time, indicative of gradual dissipation of the trapped charge induced by the initial localized application of a large bias voltage, is clearly evident. We have confirmed that this dissipation is not induced by the SCM imaging performed after the initial charging process. The average widths of the charged regions determined from the line profiles (10.43, 10.51, and 10.94 μm for the images obtained immediately, 6 min, and 1 h after the initial charging, respectively) are consistent with a slight lateral spreading of the charge. However, it should be noted that the change in apparent size of the charged region is small compared to the total charged area (less than 1%) and that thermal drift between scans makes it difficult to obtain and compare profiles from identical locations. It should be noted that exposure to UV light removed all indication of charging.

The effects of trapped charge within III–V nitrides have been studied quite extensively. Several groups have reported persistent photoconductivity effects in GaN[16,17] and $Al_xGa_{1-x}N$/GaN heterostructures,[18,19] with the effects observed in $Al_xGa_{1-x}N$/GaN heterostructures being attributed to traps within the $Al_xGa_{1-x}N$ barrier layer in HFET structures.[18] Current collapse in GaN metal-semiconductor field-effect transistors (MESFETs) has been observed and attributed to the presence of trap states within the semi-insulating GaN layer.[20,21] In general, the locations of trap states observed in such studies are inferred based on the electrical behavior of the traps. SCM imaging performed as a function of dc bias voltage allows charge, potential, and mobile carrier distributions to be probed in three dimensions, i.e., with spatial resolution at the submicron to nanometer scale both laterally and in depth. These capabilities provide a unique and powerful method for probing the physical location of trapped charge within an $Al_xGa_{1-x}N$/GaN HFET epitaxial layer structure.

For this purpose, the doped $Al_{0.26}Ga_{0.74}N$/GaN sample, shown schematically in Fig. 1(a), was charged in the manner described above by scanning at a dc bias of 9 V. Following this process, single 10 μm line scans were acquired for dc bias voltages ranging from 0 to 10 V. Line scans for an entire series of voltages spanning this range were acquired within a few minutes of charging, thereby minimizing charge dissipation effects as well as any variations arising from tip wear or changes in environmental factors such as humidity.

Figure 3 shows a series of these line scans for a 2.5 μm charged area in the center of a 10 μm scan line. The dc bias voltage for each scan is indicated in the figure. The SCM signal is plotted in arbitrary units that remain constant for all

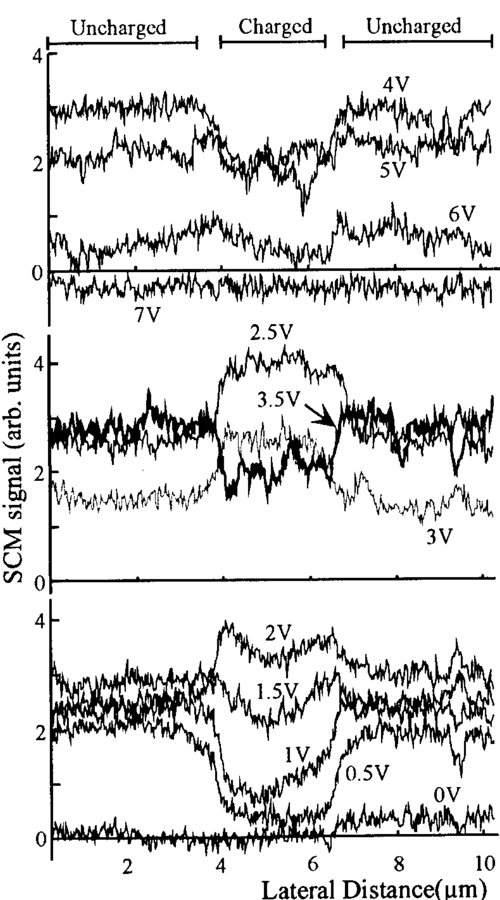

FIG. 3. SCM line scans across a 10 μm×2.5 μm sample region charged at 9 V sample bias, obtained at imaging bias voltages ranging from 0 to 7 V. Bias voltages employed during SCM imaging as well as charged and uncharged regions for all line scans are indicated.

scans. There are two important aspects to consider of the observed dependence of the SCM signal on dc bias voltage: the dependence of the absolute value of the SCM signal on bias voltage, and the contrast between the charged and uncharged regions. At the extremes of the dc bias voltage range illustrated here—<0 V and >7 V—the SCM signal shows little or no contrast between the charged and uncharged regions and the absolute value of the signal is nearly zero. In both the charged and uncharged regions, the absolute value of the SCM signal increases continuously as the dc sample bias voltage is increased from 0 V to ~2.5 V, then decreases substantially at ~3 V. Above 5 V, the signal strength in both regions decreases continuously to nearly zero as the voltage is increased. This general behavior is consistent with that previously observed in SCM studies of $Al_xGa_{1-x}N$/GaN HFET epitaxial layer structures.[11,22]

Figure 4(a) shows a plot of the SCM signal as a function of bias voltage, averaged across the uncharged (dashed line) and charged (solid line) regions within the line scans shown in Fig. 3. At sample bias voltages below 1 V, the SCM signal is larger in the uncharged region than in the charged region. As the dc bias voltage is increased to values above 1.5 V, the contrast between the charged and uncharged regions inverts, with the SCM signal from the charged region remaining

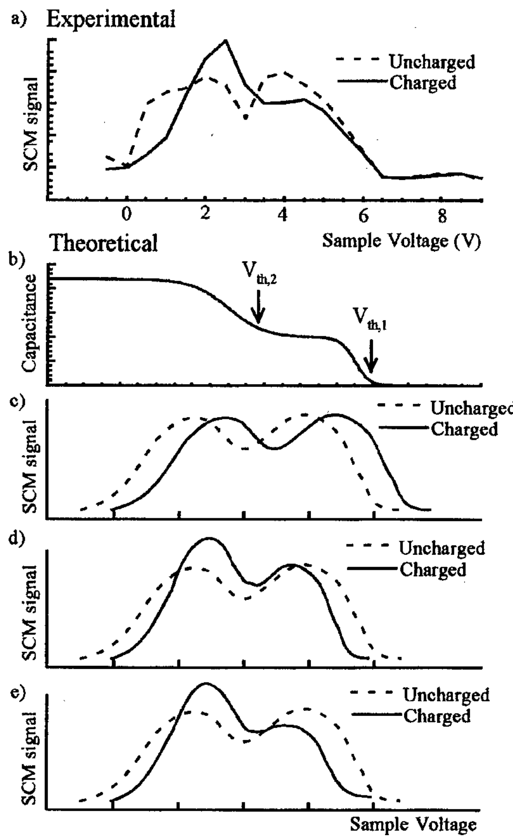

FIG. 4. (a) Measured SCM signal vs sample bias voltage for charged and uncharged sample regions derived from data in Fig. 3. (b) Schematic illustration of capacitance–voltage spectrum for a conducting probe tip and $Al_xGa_{1-x}N$/GaN HFET sample. (c)–(e) Schematic SCM signal spectra for charged (solid curves) and uncharged (dashed curves) regions of an $Al_xGa_{1-x}N$/GaN HFET sample structure for (c) positive trapped charge located at the $Al_xGa_{1-x}N$ surface; (d) positive trapped charge at the $Al_xGa_{1-x}N$ surface and negative trapped charge at or near the $Al_xGa_{1-x}N$/GaN interface; (e) positive trapped charge at the $Al_xGa_{1-x}N$ surface and within the GaN buffer layer and negative trapped charge at or near the $Al_xGa_{1-x}N$/GaN interface.

larger than that from the uncharged region until the sample bias voltage reaches 3–3.5 V. For sample bias voltages of ~3.5 V and above, the contrast reverts, qualitatively, to that observed at low sample bias voltages, with the SCM signals for the charged and uncharged regions gradually converging near zero for large positive sample bias voltages.

An analysis of the dependence of the SCM signal on bias voltage in the charged and uncharged regions can yield information about the possible locations of trap states that can become charged for large applied bias voltages. Figure 4(b) shows, schematically, a typical $C-V$ characteristic for a conducting probe tip, insulating oxide layer, and n-$Al_xGa_{1-x}N$/GaN HFET epitaxial layer structure as a function of dc bias voltage applied to the sample.[11] For sample bias voltages $V>V_{th,1}$, the 2DEG at the $Al_xGa_{1-x}N$/GaN interface is depleted and the capacitance is small. For $V_{th,2}<V<V_{th,1}$, carriers accumulate at the $Al_xGa_{1-x}N$/GaN interface and the capacitance observed is essentially that of the $Al_xGa_{1-x}N$ barrier layer and the insulating oxide layer between the conducting tip and the sample surface. For $V<V_{th,2}$, carriers spill into the $Al_xGa_{1-x}N$ barrier and towards the $Al_xGa_{1-x}N$ surface, leading to an increase in capacitance. The SCM signal is related to the slope of the $C-V$ curve, dC/dV, averaged over the ac modulation voltage amplitude.[23] The dashed lines in Figs. 4(c)–4(e) show, schematically, the resulting simulated SCM signal as a function of bias voltage for a typical $Al_xGa_{1-x}N$/GaN HFET sample structure.

To determine the locations of the traps, the effects of fixed charge layers in a variety of locations on the $C-V$ characteristics of an $Al_{0.25}Ga_{0.75}N$/GaN HFET epitaxial layer structure were simulated using a one-dimensional Poisson/Schrödinger solver.[24] A layer of trapped positive charge at the surface will change the voltage at which the charge at the surface will be depleted and the depletion region will begin to extend into the sample, yielding a shift along the voltage axis in the $C-V$ characteristics. The result is a constant shift in voltage in the $C-V$ and the SCM signal curves, as shown schematically for a positive surface charge layer by the solid line in Fig. 4(c).

If in addition to trapped charge at the surface there is trapped charge at the $Al_xGa_{1-x}N$/GaN interface or within the $Al_xGa_{1-x}N$ barrier near the interface, the threshold voltage, $V_{th,1}$ may be shifted significantly, but there will be only a relatively small effect on the voltage $V_{th,2}$ at which spillover of electrons towards the $Al_xGa_{1-x}N$ surface occurs. Negative trapped charge at or near the heterojunction interface will partially compensate the positive polarization charge at the interface and thereby reduce the sheet carrier concentration in the 2DEG. As a result, the threshold voltage $V_{th,1}$ for the charged structure will shift to a lower sample bias voltage and the $C-V$ and SCM signal characteristics near $V_{th,1}$ will change accordingly.

The effects of trapped negative charge at or near the interface will also significantly influence the $C-V$ characteristics for $V_{th,1}<V<V_{th,2}$. As the depletion depth extends below the surface and approaches the interface for increasing sample bias, the voltage necessary to deplete the 2DEG at the interface will decrease, yielding a larger change in the depletion depth and therefore the capacitance for the same voltage change compared to that in the uncharged region. This larger change in the capacitance will cause the slope of the $C-V$ characteristics and consequently the SCM signal in this region to increase, leading to the larger peak shown in Fig. 4(d) for the SCM signal near $V_{th,2}$ in the charged region.

Once the depletion depth extends below the $Al_xGa_{1-x}N$/GaN interface, the trapped charge in the vicinity of the heterojunction interface will lead simply to a constant shift in the voltage of the $C-V$ characteristics. The SCM signal in this voltage range will then depend primarily on the charge carriers within the GaN, which we have assumed to be identical for the charged and uncharged regions. The change in the capacitance for positive bias voltages in this range will therefore be the same for both regions, yielding the same slope to the $C-V$ characteristics. As shown in Fig. 4(d), the SCM signal peak near $V_{th,1}$ will therefore be of nearly identical height for both the charged and uncharged

regions, but will be shifted in voltage because of the difference in the surface and interface charge densities.

Figure 4(e) shows the result of adding positive trapped charge within the GaN layer below the 2DEG channel to the positive trapped surface charge and negative trapped heterojunction interface charge considered above. The positive charge in the GaN has little effect on the $C-V$ characteristics until the depletion region extends below the interface; thus, the SCM signal for V well below $V_{th,1}$ will not change significantly compared to that shown in Fig. 4(d). Once the depletion depth extends below the $Al_xGa_{1-x}N$/GaN interface, positive trapped charge in the GaN layer will reduce the change in depletion depth, and hence the change in capacitance, for a given change in voltage and thereby reduce the interface peak height of the SCM signal.

By comparing the experimental data illustrated in Fig. 4(a) with the simulations described above, several general trends are apparent. For $0\ V \leq V \leq 1.5\ V$, the shift between the charged and uncharged experimental curves in Fig. 4(a) suggests the presence of positive charge at the surface. The increased peak height in the SCM signal in the charged region near 2.5 V is expected for negative charge trapped at or near the $Al_xGa_{1-x}N$/GaN interface as described above. A possible mechanism for the generation of the surface and interface trapped charge is that the electrons are being forced from surface states into traps at or near the interface when large positive bias is applied. Finally, the reduced peak height near 5 V in the charged region suggests that positive charge is trapped within the GaN layer. Ionization of donor-like trap states and, hence an effective increase in n-type doping within the GaN during the charging process, can increase the amount of positive charge. Another possible factor is that negative charge at the interface will reduce the confinement of the 2DEG at the $Al_xGa_{1-x}N$/GaN interface, which allows the channel region to extend farther into the GaN layer. Such an extension of the channel region would also reduce the height of the SCM signal peak associated with depletion of the 2DEG. Finally, it should be noted that a certain amount of charging induced by the imaging process is expected in the uncharged region at large sample bias voltages, and that these effects will reduce the contrast between the charged and uncharged region. We believe that this effect is responsible for the convergence in the SCM signals observed in the charged and uncharged regions at sample bias voltages of ~5–6 V.

IV. CONCLUSION

In conclusion, we have used scanning capacitance microscopy to characterize local charging and trap states in $Al_xGa_{1-x}N$/GaN HFET epitaxial layer structures. SCM imaging as a function of applied bias voltage enables electrostatic potential, charge, and mobile carrier distributions to be probed with submicron to nanometer-scale spatial resolution both laterally and in depth. Application of large dc bias voltages during imaging was found to lead to localized, long-lived sample charging analogous to charging of deep trap states in diodes, transistors, and other device structures under large applied bias. Bias-dependent SCM imaging of charged and uncharged regions of $Al_xGa_{1-x}N$/GaN HFET epitaxial layer structures combined with theoretical analysis and numerical simulations allows information about the nature and location of various trap states to be derived. Our studies indicate that positive charge is trapped at the $Al_xGa_{1-x}N$ surface and within the GaN buffer layer, while negative charge is trapped at or near the $Al_xGa_{1-x}N$/GaN heterojunction interface.

ACKNOWLEDGMENTS

Part of this work was supported by ONR (N00014-99-1-0729 and N00014-00-1-0135, Dr. Colin Wood; DURIP award N00014-99-1-0545, Dr. John Zolper).

[1] S. Nakamura and G. Fasol, *The Blue Laser Diode: GaN Based Light Emitters and Lasers* (Springer, Berlin, 1997).
[2] J. M. Van Hove, R. Hickman, J. J. Klaassen, P. P. Chow, and P. P. Ruden, Appl. Phys. Lett. **70**, 2282 (1997).
[3] Q. Chen, J. W. Yang, A. Osinsky, S. Gangyopadhyay, B. Lim, M. Z. Anwar, M. A. Khan, D. Kuksenkov, and H. Temkin, Appl. Phys. Lett. **70**, 2277 (1997).
[4] M. A. Khan, Q. Chen, M. S. Shur, B. T. McDermott, J. A. Higgins, J. Burm, W. J. Schaff, and L. F. Eastman, IEEE Electron Device Lett. **17**, 584 (1996).
[5] O. Aktas, Z. F. Fan, A. Botchkarev, S. N. Mohammad, M. Roth, T. Jenkins, L. Kehias, and H. Morkoç, IEEE Electron Device Lett. **18**, 293 (1997).
[6] Y. F. Wu, B. P. Keller, S. Keller, D. Kapolnek, P. Kozodoy, S. P. DenBaars, and U. K. Mishra, Appl. Phys. Lett. **69**, 1438 (1996).
[7] G. J. Sullivan, M. Y. Chen, J. A. Higgins, J. W. Yang, Q. Chen, R. L. Pierson, and B. T. McDermott, IEEE Electron Device Lett. **19**, 198 (1998).
[8] S. C. Binari, J. M. Redwing, G. Kelner, and W. Kruppa, Electron. Lett. **33**, 242 (1997).
[9] R. D. Underwood, S. Keller, U. K. Mishra, D. Kapolnek, B. P. Keller, and S. P. DenBaars, J. Vac. Sci. Technol. B **16**, 822 (1998).
[10] P. J. Hansen, Y. E. Strausser, A. N. Erickson, E. J. Tarsa, P. Kozodoy, E. G. Brazel, J. P. Ibbetson, U. Mishra, V. Narayanamurti, S. P. DenBaars, and J. S. Speck, Appl. Phys. Lett. **72**, 2247 (1998).
[11] K. V. Smith, E. T. Yu, J. M. Redwing, and K. S. Boutros, Appl. Phys. Lett. **75**, 2250 (1999).
[12] A. Bykhovski, B. Gelmont, and M. S. Shur, J. Appl. Phys. **74**, 6734 (1993).
[13] P. M. Asbeck, E. T. Yu, S. S. Lau, G. J. Sullivan, J. Van Hove, and J. M. Redwing, Electron. Lett. **33**, 1230 (1997).
[14] E. T. Yu, G. J. Sullivan, P. M. Asbeck, C. D. Wang, D. Qiao, and S. S. Lau, Appl. Phys. Lett. **71**, 2794 (1997).
[15] R. Gaska, J. W. Yang, A. D. Bykhovski, M. S. Shur, V. V. Kaminski, and S. M. Soloviov, Appl. Phys. Lett. **72**, 64 (1998).
[16] M. T. Hirsch, J. A. Wolk, W. Walukiewicz, and E. E. Haller, Appl. Phys. Lett. **71**, 1098 (1997).
[17] G. Beadle, W. S. Rabinovich, A. E. Wickenden, D. D. Koleske, S. C. Binari, and J. A. Freitas, Jr., Appl. Phys. Lett. **71**, 1092 (1997).
[18] J. Z. Li, J. Y. Lin, H. X. Jiang, M. Asif Khan, and Q. Chen, J. Appl. Phys. **82**, 1227 (1997).
[19] X. Z. Dang, C. D. Wang, E. T. Yu, K. S. Boutros, and J. M. Redwing, Appl. Phys. Lett. **72**, 2745 (1998).
[20] S. C. Binari, W. Kruppa, H. B. Dietrich, G. Kelner, A. E. Wickenden, and J. A. Frietas, Jr., Solid-State Electron. **41**, 1549 (1997).
[21] P. B. Klein, J. A. Frietas, Jr., S. C. Binari, and A. E. Wickenden, Appl. Phys. Lett. **75**, 4016 (1999).
[22] K. V. Smith, E. T. Yu, J. M. Redwing, and K. S. Boutros (to be published).
[23] Digital Instruments Support Note No. 224, Rev. D (1999).
[24] G. L. Snider, computer program *ID Poisson/Schrödinger: A Band Diagram Calculator* (University of Notre Dame, Notre Dame, IN, 1995).

Depth-resolved spectroscopy of interface defects in AlGaN/GaN heterostructure field effect transistors device structures*

A. P. Young,[a] J. Bae, and L. J. Brillson
The Ohio State University, 205 Dreese Lab, 2015 Neil Avenue, Columbus, Ohio 43210-1272

M. J. Murphy and W. J. Schaff
Cornell University, Ithaca, New York 14853

(Received 17 January 2000; accepted 1 May 2000)

We report depth-resolved low energy electron excited nanometer spectroscopy from AlGaN/GaN heterostructure field effect transistors structures with AlGaN thicknesses as thin as 20 nm. By varying the voltage of a low energy electron beam in ultrahigh vacuum, we can determine whether defect induced luminescence is being emitted from the GaN buffer layer, the interfacial region where the two-dimensional electron gas (2DEG) resides, and the AlGaN barrier layer. By increasing the GaN buffer thickness, known to enhance the electron concentration of the 2DEG by reducing the dislocation density in the active region, we observed an enhancement in AlGaN luminescence, and a 20% reduction in the full width at half maximum of the near band edge peak. When a similar structure with no 2DEG is measured, we find a factor of 8 increase in midgap yellow luminescence relative to the GaN buffer emission. Taken together, these findings indicate that differences in buffer layer thickness and electrical quality can affect not only dislocation density and point defect densities, but also the optical properties of the AlGaN barrier layer and its 2DEG interface. © *2000 American Vacuum Society.* [S0734-211X(00)03504-6]

I. INTRODUCTION

Recently, there has been tremendous progress in the development of GaN based heterostructure field effect transistors (HFETs) for high power/high temperature microwave applications.[1,2] While most of the devices to date have been grown using metal organic chemical vapor deposition (MOCVD) techniques, there have also been dramatic improvements in the radio-frequency (rf) performance of molecular beam epitaxy (MBE) grown HFETs.[3] Detection and characterization of defects occur at the AlGaN/GaN interface, where electron transport takes place. Future progress in the field, depends to a large extent on the chemical identification and elimination of line defects, native point defects, and impurities near the crucial two dimensional electron gas (2DEG) interface. These defects not only reduce the 2DEG carrier densities by localizing electrons, but related trapping centers result in current hysteresis in HFET devices.[1] The source of this hysteresis is not well understood at present.

Low energy electron excited nanometer scale spectroscopy (LEEN) is one of the few techniques capable of nondestructively obtaining defect information in the near surface region (tens of nanometers) of AlGaN/GaN heterostructures.[4–6] By varying the energy of a low energy electron beam, both the recombination energy and the depth of a defect can be determined. This depth can range from just a few nanometers below the surface at a few hundred volts incident energy, up to several microns at the energies typically used in a scanning electron microscopy (SEM). In this work, we use the LEEN technique to investigate the properties of defects localized within the AlGaN barrier layer, the 2DEG interface region, and the GaN buffer layer underneath the active layers. We then attempt to correlate these measurements with the electrical properties measured previously.

II. EXPERIMENT

The high quality $Al_xGa_{1-x}N$/GaN HFET specimens of Al concentration ($x=0.36-0.42$) were grown by plasma-assisted MBE on sapphire substrates using a high temperature AlN buffer layer to control the polarity of the GaN.[1] In particular, the device structures are auto doped using the piezoelectric effect to create the 2DEG.[7] Other details of the growth procedure are presented elsewhere.[1] We examined HFETs with the following layer structure: sapphire substrate/12 nm high temp AlN buffer/ 1 or 5 μm GaN buffer/2DEG layer/25 nm AlGaN barrier/ 2 nm GaN cap layer.

The first set of specimens had 2DEG densities and mobilities of 1.3×10^{13} cm^{-2} and 1450 cm^2/V s versus 0.88 $\times10^{13}$ cm^{-2} and 1478 for one versus five micron GaN buffers, respectively. Output powers of 2 W/mm and power added efficiencies of 34% at 4 GHz were achieved from devices made from the same wafer material. The second set of specimens had either no measurable 2DEG at all or good direct current (dc) electrical characteristics, both being from within the same growth run.

The surface morphology of all specimens was quantified using a Digital Instruments Nanoscope III atomic force microscope to determine root-mean-square (rms) roughness. Linear scans over 1 μm were used for the measurement.

LEEN spectroscopy at constant power, ($I*V=$constant), was performed in ultrahigh vacuum (UHV) using electron beam energies ranging from 0.5 to 4.0 keV. Previous elec-

*No proof corrections received from author prior to publication.
[a]Electronic mail: apyoung@ee.eng.ohio-state.edu

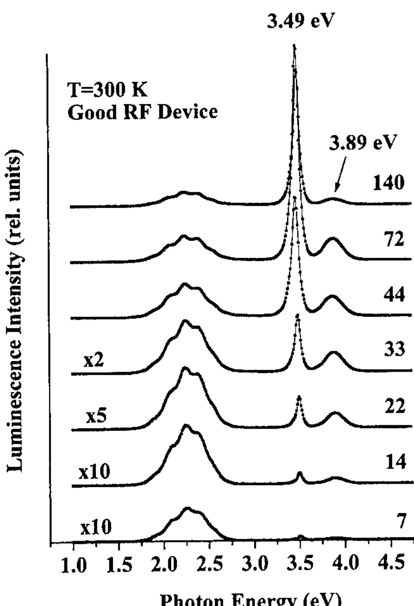

FIG. 1. Depth-dependent LEEN of HFET sample No. 689. Numbers on right are the electron beam penetration depth in nanometers. Electron beam energies ranged from 0.5 to 3.0 keV, corresponding to maximum electron penetration depths from 7 to 140 nm. All spectra were performed at room temperature.

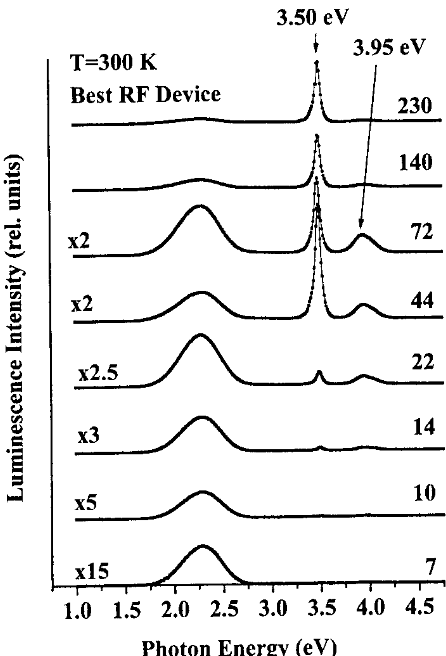

FIG. 2. Depth-dependent LEEN spectroscopy of HFET sample No. 688. At 4.0 keV, the electron beam penetrates a maximum distance of 230 nm, well into the GaN buffer of the specimen.

tron beam induced current (EBIC) measurements had shown the current to be from 0.5 to 4 μA. The beam was incident at $\approx 45°$ with respect to the surface normal of the sample inducing a spot approximately 1 mm in diameter. A Peltier-cooled S-20 photomultiplier was used to cover the range from 1.4 to 4.75 eV (885 nm$<\lambda<$261 nm). The resolution of the monochromator was $<$30 meV for all photon energies detected. The detector output was measured using standard lock-in amplifier techniques. The spectra were not corrected for the response of the detector and the optical train. Spectral energies were calibrated using lines from a Hg lamp immediately after the LEEN measurements.

III. RESULTS

As reported by Murphy *et al.*,[3] Hall measurements for the specimens from set No. 1, hereafter known as samples Nos. 688 and 689, had excellent dc characteristics and exceptional rf performance. In comparison with the excellent electrical properties of set No. 1, the specimens from set No. 2, samples Nos. 873 and 875, behaved quite differently. The measured mobility of sample No. 875 was quite good, $\mu \sim 1000$ cm^2/V s, while sample No. 873 did not have a measurable 2DEG at all, even though the only difference between the two specimens was a slight change in the way the nucleation layer was grown.

A. First set: Excellent dc and rf properties

Figure 1 shows the depth-dependent LEEN spectroscopy from sample No. 688, known to have very good electrical characteristics. Based on the calculations of Everhart and Hoff, the electron beam energies used to probe the heterostructure, 0.5–4.0 keV, correspond to penetration depths from 7 to 230 nm with the peak in the electron energy loss curve approximately one third of that depth.[8]

Clearly, from the low electron beam energy spectra, the AlGaN near band edge (NBE) luminescence peak is visible at 3.89 eV, an energy beyond the range of a HeCd laser (3.81 eV), the laser line normally used in III-nitride photoluminescence studies. The AlGaN is seen to be quite broad compared to the GaN buffer emission, having a full width at half maximum (FWHM) of 250 meV at a 77 nm penetration depth. In addition to the AlGaN peak, two other peaks are also observed in Fig. 1, the extremely broad "yellow" luminescence centered at 2.28 eV and the GaN buffer NBE emission at 3.49 eV.

Figure 2 shows the depth dependent LEEN spectra from sample No. 689, the specimen with the best electrical characteristics. This HFET specimen contains slightly less Al (36% vs 42%), and a thicker AlGaN (30 nm vs 20 nm) as determined by x-ray diffraction. Most importantly, the main difference is a 5-μm-thick buffer compared to the 0.8 μm buffer layer of the previous specimen.

Two features are apparent from the spectra. First, the AlGaN luminescence peak is a factor of two greater relative to the GaN buffer peak compared to that in sample No. 688. Second, the AlGaN peak is not symmetric, there seems to be a high energy shoulder. But, even with the high energy shoulder, the overall FWHM of the AlGaN peak is smaller (260 meV vs 210 meV) than that from sample No. 688 shown in Fig. 1.

B. Second set: Contrasting electrical properties from same growth

Figure 3 shows the depth-resolved LEEN spectra of specimen No. 873, known to have no detectable 2DEG. Similar to

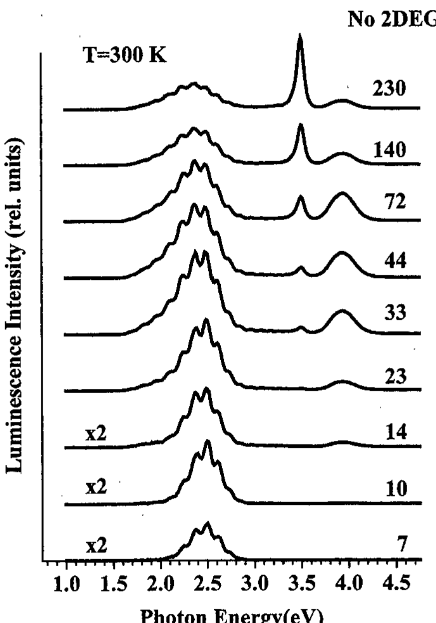

FIG. 3. Depth-dependent LEEN of HFET sample No. 873 from set No. 2. This specimen did not indicate the presence of a 2DEG from electrical measurements. The broad AlGaN peak (FWHM =300 meV), and the increased energy of the mid-gap luminescence near the surface.

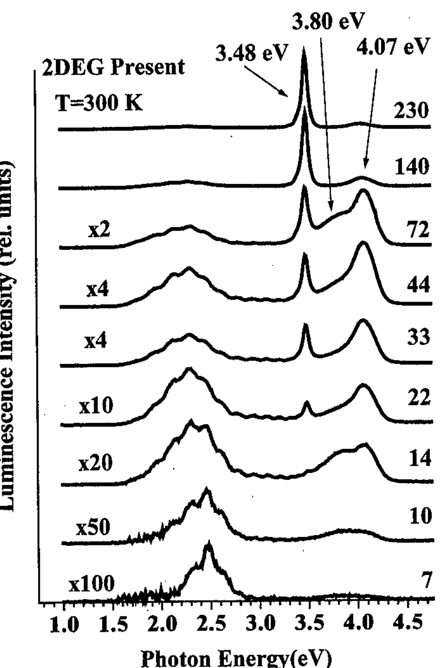

FIG. 4. Depth-dependent LEEN of HEMT sample No. 875 from set No. 2. In contrast with sample No. 873, this specimen had good electrical mobility. The split in the AlGaN peak exhibits a splitting at excitation depths corresponding to the 2DEG interface.

No. 688, the AlGaN peak is symmetric with no high energy shoulder, although the peak is broader than either sample in set No. 1, having a FWHM of 300 meV. What also stands out from the spectra is the intense midgap yellow (YL) luminescence which remains very strong, even near the surface. The YL/GaN intensity ratio is eight times higher at 77 nm for this sample than either No. 688 or 689. Furthermore, the midgap emission energy exhibits a shift to higher energy as the penetration depth decreases, from 2.37 to 2.49 eV, which did not occur in the specimens of set No. 1. In addition to the peak shift, the YL also has a much narrower FWHM near the surface, decreasing from 580 meV at 77 nm to 360 meV at a 7 nm depth. While the YL remains intense, the GaN NBE luminescence is quenched much more quickly (disappears at 23 nm) compared to the spectra from set No. 1. For the samples from set No. 1, the GaN NBE peak is still present even for a 7 nm excitation depth.

In Fig. 4, we show LEEN spectra from a similar heterostructure, No. 875 which has good dc electrical properties. In contrast with the previous three sets of spectra, the AlGaN feature in Fig. 4 has split into two peaks at 3.80 and 4.07 eV! Furthermore, there seems to be a depth dependence to the splitting, having a maximum close to the nominal interface region at ~30 nm. Also unique to No. 875, we observe a large nonradiative recombination rate near the surface in this structure (signal down by a factor of 100 at 7 nm) compared to all the other structures. This could have an impact on leakage currents and other device properties, even though the mobility was high. Finally, while the AlGaN feature shows dramatic differences with the other three specimens, the YL shows a similar dramatic shift to higher energy as the penetration depth decreases as No. 873.

IV. DISCUSSION

Within each set, the rms roughness deduced from the AFM scans and tabulated in Table I seems to anticorrelate with electrical or optical performance. AFM images show roughly spherical objects uniformly distributed over the surface. Similar to the GaN surfaces observed by Tarsa *et al.*,[9] three of the samples, Nos. 689, 873, and 875, show a similar rough granular morphology. This is most likely an indication that these samples were grown on the N-rich side of the III–V growth ratio. Compared to the other specimens, No. 688 is closer to a 1:1 stoichiometry, since it still shows some granularity, but is significantly smoother than the other samples. This suggests that the HFETs were grown on the N-rich side of the III–V ratio, but close to 1:1 stoichiometry provide the best growth condition for optimizing electrical properties. This would help to explain why we observe any luminescence from the thin Al containing region.

The high-energy features from 3.80 to 4.07 eV can either be due to direct band-to-band recombination within the AlGaN, or it can be from the 2DEG interface due to quantum

TABLE I. AFM determined rms roughness from linear scans over one μm compared with electrical features.

Sample No.	2DEG density (cm^{-2})	Mobility ($cm^2/V\,s$)	rms roughness (nm)
688	1.1×10^{13}	1478	0.24
689	8.8×10^{12}	1450	2.1
873	None	None	3.5
875	1.3×10^{13}	570	5.9

confinement. If we assume we have recombination from the AlGaN luminescence peak energy is not drastically affected by the HFET structure, then we can use the bowing parameter for bulk AlGaN to estimate the bowing parameter in this case. Following the work in Refs. 10 and 11, we first use the best-fit bowing parameter $b=0.6$ eV, and calculate the band gap using the analytical expression, $E_g(x)=E_{g,\mathrm{GaN}}+(c-b)x+bx^2$, where $c=E_{g,\mathrm{AlN}}-E_{g,\mathrm{GaN}}$. Using the value for the composition obtained via triple axis x-ray work, $x=0.36$, yields an energy of 4.2 eV. Clearly, the bowing parameter is significantly different than the 0.6 used by Steude *et al.*[10] for bulk AlGaN. Using the measured values for the Al composition ($x=0.42$ for No. 688 and $x=0.36$ for No. 689), yields bowing parameters of $b=+2.99$ and $b=+2.21$, respectively. This falls in line with the sets of measurements called Group B by Lee *et al.*[11] for AlGaN grown under suboptimal conditions. If carriers were swept into the 2DEG before recombining, this might explain the low peak energies being measured, especially if the AlGaN is of extremely high quality. More needs to be done in order to be able to decide the exact spatial location of the electron–hole recombination.

In any event neither argument would explain the splitting of this peak for specimen No. 875. Possible causes of the luminescence peak splitting could be due to: (1) AlGaN/GaN interface broadening, (2) Al segregation, (3) partial strain relaxation, (4) ordering of the AlGaN alloy. All three theories could potentially alter the band gap either in the AlGaN itself or at the interface. We cannot tell from the luminescence data alone what the reason is for the splitting. However, the strong depth dependence of the splitting is difficult to account for with strain variations alone. Cross-sectional SEM studies may reveal additional distinctions.

Finally, moving deeper into the heterostructures, we observe that all the samples have a high GaN NBE peak (3.48–3.50 eV compared to 3.42 eV in unstrained GaN). This is not due to the 2DEG confinement, since the peak does not change as the penetration depth changes. This is also not due to incomplete strain relaxation during the buffer layer's growth, since even sample No. 689 with a 5-μm-thick buffer has a relatively high NBE emission. A possible explanation is that this is due to compressive strain on the entire layer from the AlGaN barrier layer above it, or as mentioned by Lee *et al.*,[11] the thermal expansion-mismatch strain between the GaN and the substrate is a possible cause of the shift.

V. CONCLUSIONS

We have spatially resolved the electron beam induced luminescence from 20–30-nm-thick AlGaN layers embedded in nitride-based HFET device structures. Furthermore, this luminescence is sensitive to the GaN buffer layer thickness, and to the optical quality of the buffer for a given thickness. These findings indicate that differences in buffer layer thickness and buffer optical quality can affect not only dislocation and point defect densities, but also properties of the AlGaN quasi-insulator layer and its 2DEG interface. These in turn can have sizable effects on the confined electron density, mobility, and rf power output.

ACKNOWLEDGMENTS

The work of A. P. Y., J. B., and L. B. J. is supported by Office of Naval Research Grant No. N00014-00-1-0042 under the direction of Dr. Colin Wood. The work of M. J. M. and W. J . S. is supported by Grant No. N00014-96-1-1223 and No. N00014-95-1-0926 under the direction of Dr. John Zolper.

[1]L. F. Eastman, Phys. Status Solidi A **176**, 175 (1999).
[2]U. K. Mishra, Y. F. Wu, B. P. Keller, S. Keller, and S. P. DenBaars, IEEE Trans. Microwave Theory Tech. **46**, 756 (1998).
[3]M. J. Murphy, K. Chu, H. Wu, W. Yeo, W. J. Schaff, O. Ambacher, L. F. Eastman, T. J. Eustis, J. Silcox, R. Dimitrov, and M. Stutzmann, Appl. Phys. Lett. (submitted).
[4]J. Schäfer, A. P. Young, L. J. Brillson, H. Niimi, and G. Lucovsky, Appl. Phys. Lett. **73**, 791 (1998).
[5]A. P. Young, J. Schäfer, L. J. Brillson, Y. Yang, S. H. Xu, H. Cruguel, G. J. Lapeyre, M. A. L. Johnson, and J. F. Schetzina, J. Electron. Mater. **28**, 308 (1999).
[6]L. J. Brillson, T. Levin, G. Jessen, and F. A. Ponce, Appl. Phys. Lett. **75**, 3835 (1999).
[7]M. J. Murphy, K. Chu, H. Wu, W. Yeo, W. J. Schaff, O. Ambacher, J. Smart, T. J. Eustis, J. R. Shealy, and L. F. Eastman, J. Vac. Sci. Technol. B **17**, 1252 (1999).
[8]T. E. Everhart and P. H. Hoff, J. Appl. Phys. **42**, 5837 (1971).
[9]E. J. Tarsa, B. Heying, X. H. Wu, P. Fini, S. P. Den Baars, and J. S. Speck, J. Appl. Phys. **82**, 5472 (1997).
[10]G. Steude, B. K. Meyer, A. Göldner, A. Hoffman, F. Bertram, J. Christen, H. Amano, and I. Akasaki, Appl. Phys. Lett. **74**, 2456 (1999).
[11]S. R. Lee, A. F. Wright, M. H. Crawford, G. A. Peterson, J. Han, and R. M. Biefeld, Appl. Phys. Lett. **74**, 3344 (1999).

ZnO/GaN heterointerfaces and ZnO films grown by plasma-assisted molecular beam epitaxy on (0001) GaN/Al_2O_3

S. K. Hong,[a] H. J. Ko, Y. Chen, T. Hanada, and T. Yao
Institute for Materials Research, Tohoku University, 2-1-1 Katahira, Aoba-ku, Sendai 980-8577, Japan

(Received 17 January 2000; accepted 14 April 2000)

We report the structures of ZnO/GaN heterointerfaces and properties of ZnO films grown by plasma-assisted molecular beam epitaxy (P-MBE) on (0001) GaN/Al_2O_3 substrates. At first, different preparations (zinc or oxygen-plasma pre-exposures) of the GaN surface are examined and the resultant heterointerface structures and properties of ZnO films are studied. The oxygen-plasma pre-exposure of the GaN surface results in the formation of an interface layer, while the formation of interface layers is prevented by zinc pre-exposure. The interface layer is identified as single-crystalline monoclinic Ga_2O_3 through extensive transmission electron microscopy (TEM) study. The orientation relationship between monoclinic Ga_2O_3 of the interface layer and GaN and ZnO epilayers is investigated as (0001) GaN‖(001) Ga_2O_3‖(0001) ZnO and [2-1-10] GaN‖[010] Ga_2O_3‖[2-1-10] ZnO. Based on structural investigations and stability of bondings, we propose interface-bonding sequences at the ZnO/GaN heterointerfaces in zinc or oxygen-plasma pre-exposed samples: "N–Ga–O–Zn" bonding sequence for zinc pre-exposed samples and "N–Ga–(O-terminated Ga_2O_3 layer)–Zn–O" for oxygen-plasma pre-exposed ones. Lattice misfit of Ga_2O_3 against underlying GaN (against upper ZnO) is estimated as −4.7% (−6.5%) and 10.7% (8.6%) along the [010] and [100] directions of the Ga_2O_3, respectively. The structural and optical properties of ZnO films evaluated by TEM, high-resolution x-ray diffraction and photoluminescence spectroscopy consistently reveal better crystal quality of zinc pre-exposed ZnO films than oxygen-plasma pre-exposed ones. Second, the effects of high temperature annealing on ZnO films grown at low temperature on zinc pre-exposed GaN surface are studied. Surface morphology is dramatically changed by high temperature annealing; three-dimensional island morphology on as-grown ZnO layers changes into atomically flat morphology with atomic level steps and terraces through high temperature annealing. Optical properties are also improved by high temperature annealing: (i) The intensity of band edge emissions from the ZnO films increases with their full width at half maximum values being decreased. (ii) Free exciton emission from annealed films is considerably enhanced in intensity compared to as grown films. These results indicate that high temperature annealing greatly improve the crystal quality of ZnO films grown at low temperature.
© *2000 American Vacuum Society.* [S0734-211X(00)01304-4]

I. INTRODUCTION

III nitrides and ZnSe-based II–VI compounds have been successfully used for the fabrication of continuous wave laser diodes working at room temperature (RT). As a similar application for blue light emitting devices, the ZnO-based materials system has been attracting increasing attention. ZnO has a direct band gap of 3.37 eV[1] at RT in the ultraviolet (UV) region. The notable properties of ZnO are the large bond strength as indicated by a cohesive energy of 1.89 eV,[2] high melting point of 2248 K,[3] and extreme stability of excitons as indicated by large exciton binding energy of 60 meV.[4] These outstanding properties make ZnO a promising material that may be resistive against degradation during device operation and may realize excitonic laser gain at RT.

Recent investigations on ZnO have revealed that this material is quite promising for exciton-based photonic devices in the UV region.[5–8] High quality ZnO layers have been successfully grown on Al_2O_3[8,9] and spinel $MgAl_2O_4$[10] substrates by plasma-assisted molecular beam epitaxy (P-MBE). Although optical studies on the ZnO layers have demonstrated room temperature excitonic lasing[5] and high temperature stimulated emission,[6] high resolution x-ray diffraction analysis indicated the presence of degraded ZnO layers around the interface region[9] presumably due to large lattice misfit.

The use of substrates with smaller lattice misfit would improve the quality of ZnO layers around the interface region, which consequently enables to grow ZnO layers with improved crystallinity. For this purpose, we focus on GaN, which closely lattice matches to ZnO with a small lattice misfit of 1.9% and smaller thermal mismatch than ZnO/Al_2O_3. In addition to these advantages, GaN and ZnO are isomorphic. Another interesting property of the ZnO/GaN heterointerface is its heterovalent characteristics similar to the ZnSe/GaAs heterointerface.[11] Heterovalent properties of the interface would lead to the control of the band line-up of heterostructures.[12] In such heterovalent epitaxy, however, the defect generation in the overlayer is closely correlated with interface chemistry, as has been extensively studied for

[a]Author to whom correspondence should be addressed; electronic mail: skhong@imr.tohoku.ac.jp

ZnSe/GaAs heteroepitaxy[13–15] which has also a II–VI/III–V heterovalent interface.

Two kinds of interface bonds including Zn–N and O–Ga bonds would exist in the ZnO/GaN interface. The electron counting principle tells that the Zn–N bond has a deficiency of 1/4 electron per bond if we assume a four-fold coordination as it is the case of Wurtzite structure, while the O–Ga bond has an excess of 1/4 electron per bond. These excess or deficit charges would make the interface unstable, if the interface were formed solely by either type of bonds. In order to stabilize the interface, the reconstruction of the interface toward the neutralization of the interface charge would take place during growth to minimize the interface energy. Such reconstruction would induce interface dipoles leading to different band offsets[12] and would result in different defect distributions.[11] Hence, the characterization and control of the interface chemistry in heterovalent epitaxy is crucial to control the interface structure thereby improve the crystal quality of the epilayers.

Although the ZnO/GaN heterostructure has such potentially interesting properties, there have been only few reports on the growth of ZnO on GaN.[16–18] Moreover, the characteristics of ZnO/GaN heterointerface have not been clarified, yet. In this article, we report on the structures of the ZnO/GaN heterointerfaces grown with zinc or oxygen-plasma pre-exposure by P-MBE. The effects of high temperature annealing on structural and optical properties of zinc pre-exposed ZnO films will be investigated.

II. EXPERIMENT

A. Growth and sample preparations

ZnO films were grown by P-MBE on metal organic chemical vapor deposition (MOCVD) grown epi-GaN. Thickness of MOCVD–GaN was about 4 μm and the topmost surface of the {0001} GaN epilayer was a Ga-terminated face as examined by ion channeling analysis.[19] Degreasing of epi-GaN/Al_2O_3 substrates was done by acetone (for 10 min), methanol (for 10 min) in ultrasonic cleaner at RT followed by rinsing with de-ionized water and spin drying. The degreased substrate was thermally cleaned at 700–800 °C in ultrahigh vacuum for about 1 h. Zn or O-plasma pre-exposure on such a GaN surface was carried out at 700 °C for 3–5 min. After these pregrowth treatments on GaN surface, ZnO films were grown at 300–700 °C. Radio frequency (rf) oxygen plasma and a *K* cell were used as oxygen and zinc sources, respectively. Oxygen gas was supplied to the rf plasma source after being purified. We used 5N oxygen gas (bomb) and it was purified by commercial oxygen gas purifier (Liquid Gas Co., Ltd., Japan) prior to being introduced into the chamber. After purifying, purity of oxygen gas is higher than 6N and concentration of main impurities (H_2,CH_4,CO,CO_2,H_2O) are reduced in the range order of 10 ppb. The base vacuum pressure prior to deposition was 2×10^{-10} and 9×10^{-5} Torr during growth. The Zn flux was set to about 0.2 nm/s, which was monitored by a quartz thickness monitor before and after growth. Oxygen-plasma parameters were set to 350 W of power with an oxygen gas flow rate of 3.5 sccm. These source conditions for Zn and O were the same in all samples studied in this article.

Two sets of ZnO films were studied in this article. The first set of films were grown at 700 °C with a thickness of 500–600 nm by zinc or oxygen-plasma pre-exposure prior to ZnO growth (we call these samples as "Zn pre-exposed" and "O pre-exposed" samples, respectively). The growth sequence for Zn pre-exposed sample is "opening of Zn shutter for Zn pre-exposure and then turning the O plasma on and opening the shutter for ZnO growth." The growth sequence for O pre-exposed sample is "turning the O plasma on and opening the shutter for O-plasma pre-exposure and then opening of Zn shutter for ZnO growth." The second set of films with a thickness of 45 nm were prepared by Zn pre-exposure followed by low temperature (LT) (300 °C) ZnO growth and high temperature annealing at 700 °C for 30 min (we call these samples as "as-grown" and "annealed" samples, respectively).

B. Characterization of films

1. Zn or O pre-exposed samples

High-resolution transmission electron microscopy (HRTEM) on the ZnO/GaN interfaces was carried out using a JEOL JEM-ARM1250 high voltage electron microscope operated at 1250 kV. The incident electron beam was set to the [2-1-10] direction of GaN. Diffraction patterns obtained by fast Fourier transform (FFT) of HRTEM images [we call those "digital diffraction patterns" (DDPs)] were used to identify the phase of the interface layer and the orientation relationship between epi-GaN, interface layer, and ZnO film. In order to evaluate crystal quality, x-ray diffraction (XRD) rocking curve measurements were carried out. Symmetric (0002) and asymmetric (10-11) ω scans were done using a Philips X'Pert MRD high-resolution triple-axis diffractometer, which has a resolution limit of as low as 12 arc sec. Defect characterization of Zn and O pre-exposed ZnO samples was carried out using a JEOL 3010 electron microscope operated at 300 kV. Two-beam analysis was carried out under (0006) or (30-30) beam-excited conditions with cross-sectional transmission electron microscope (TEM) specimens. Optical properties were characterized by using a photoluminescence (PL) spectroscope with a 325 nm line of a 5 mW He–Cd laser at 4.2 K.

2. As-grown and annealed samples

Reflection high-energy electron diffraction (RHEED), atomic force microscope (AFM), and HRTEM observations were carried out for the investigation of the effects of high temperature annealing on ZnO films. The evolution of surface morphology during annealing was monitored by "*in situ*" RHEED observations. The surface morphology was evaluated by a combination of AFM and HRTEM observations. Cross sectional HRTEM observations were carried out along both orthogonal directions, [2-1-10] and [01-10], respectively. Optical characterization was carried out by PL and reflectance measurements using a 325 nm line of a 5 mW He–Cd laser at 4.2 K.

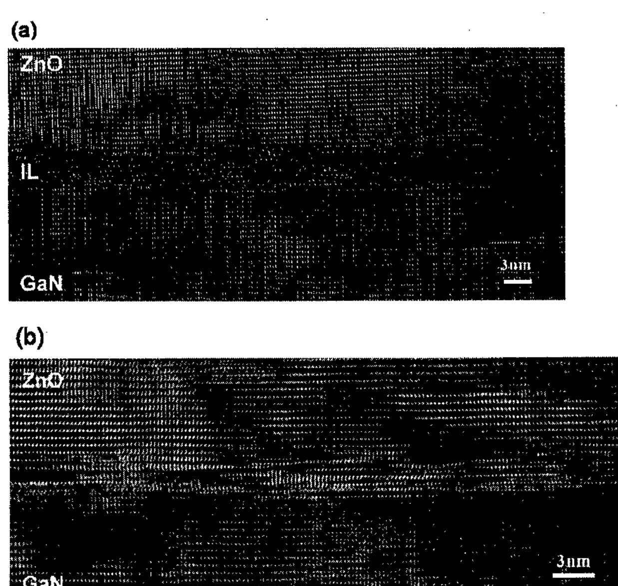

FIG. 1. Cross-sectional HRTEM micrographs of the ZnO/GaN heterointerfaces of (a) O and (b) Zn pre-exposed samples.

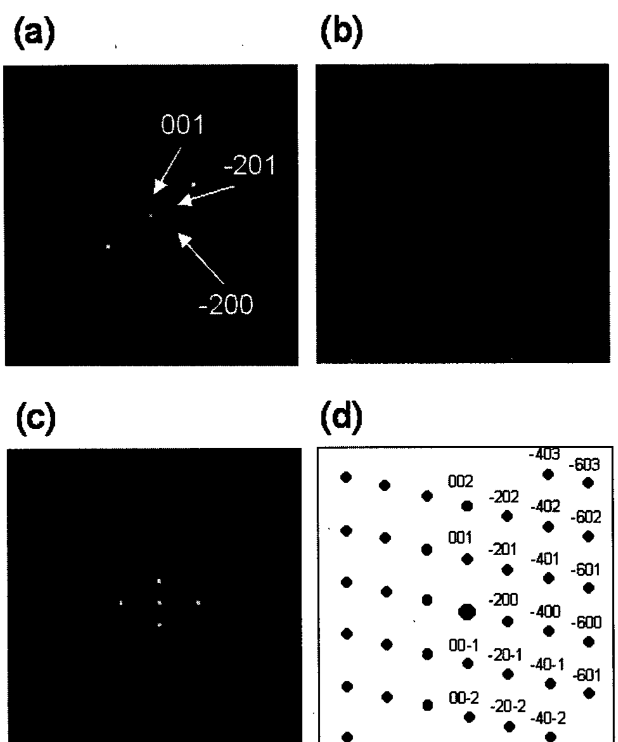

FIG. 2. (a) Digital diffraction pattern from the interface layer obtained by FFT of corresponding HRTEM image, (b). (c) Digital diffraction pattern from GaN layer, which used as a reference for evaluating reciprocal interplane distances. (d) Schematic diagram of the simulated diffraction pattern of the monoclinic Ga_2O_3 with the [010]-zone axis.

III. RESULTS AND DISCUSSION

A. Interface structures of Zn or O pre-exposed ZnO samples

1. Formation and identification of the interface layer

Figures 1(a) and 1(b) show cross-sectional HRTEM micrographs of the ZnO/GaN heterointerfaces of O and Zn pre-exposed samples, respectively. In Fig. 1(a), we could see a continuous interface layer with a thickness of about 3.5 nm at the ZnO/GaN interface. On the other hand, no interface layer was observed in Fig. 1(b). Orientation relationship between ZnO and GaN was $[0001]_{ZnO}\|[0001]_{GaN}$, and $[01\text{-}10]_{ZnO}\|[01\text{-}10]_{GaN}$ for both samples. The interface layer in the O pre-exposed samples shows different lattice images from those of ZnO and GaN.

In order to confirm the phase of the interface layer, we carried out diffraction pattern analysis. Several DDPs obtained from different regions of about 2.5 nm×2.5 nm in the interface layer showed essentially same specific diffraction pattern. Figures 2(a) and 2(b) show such a typical diffraction pattern and a corresponding HRTEM image, respectively. The distances of the diffraction planes marked by arrows in Fig. 2(a) are 0.52±0.005, 0.53±0.01 and 0.47±0.01 nm [we used DDP from the GaN layer shown in Fig. 2(c) as a reference]. We have concluded that these diffraction planes correspond to the (001), (−200), and (−201) planes of monoclinic Ga_2O_3 having spacings of 0.563, 0.594, and 0.468 nm in bulk form.[20] These three diffraction planes have the largest interplane distances and high diffraction intensity. The zone axis of the diffraction pattern was confirmed by a comparison of the experimentally obtained diffraction pattern [Fig. 2(a)] with a simulated diffraction pattern. Figure 2(d) is a schematic diagram of the simulated diffraction pattern of the monoclinic Ga_2O_3 with a [010] zone axis. The simulated diffraction pattern in Fig. 2(d) agreed fairly well with the experimentally obtained diffraction pattern in Fig. 2(a). Therefore, we conclude that the experimentally obtained diffraction pattern corresponds to that of monoclinic Ga_2O_3 with the [010] zone axis and that the orientation relationship between the monoclinic Ga_2O_3 interface layer, GaN, and ZnO epilayers could be investigated as (0001) GaN‖(001) Ga_2O_3‖(0001) ZnO and [2-1-10] GaN‖[010] Ga_2O_3‖[2-1-10] ZnO.

This epitaxial relationship would give rise to lattice strain in the Ga_2O_3 interface layer due to lattice misfits between the interface layer and the GaN substrate or the ZnO overlayer. Based on simple comparison of lattices constant and orientation relationship, the lattice misfits along the [010] (spacing, $b=0.304$ nm) and [100] (spacing, $a=1.223$ nm) axes of Ga_2O_3 against GaN [2-1-10] (spacing, $a=0.319$ nm) and the [04-40] (spacing, $2\sqrt{3}a=1.105$ nm) directions are −4.7% and 10.7%, respectively. Lattice misfits of Ga_2O_3 and ZnO along the same directions are −6.5% and 8.6%, respectively. It is likely that such a misfit strain would cause the observed slight differences in interplane distance, although more detailed analysis would be needed to elucidate the origin of these discrepancies.

In order to confirm the validity of our investigation, we discuss the possible formation of phases other than monoclinic Ga_2O_3. The largest interplane distances of diffraction planes in rhombohedral Ga_2O_3 are 0.363, 0.265, and 0.249 nm.[21] In the case of cubic Ga_2O_3, the largest distances are 0.290, 0.248, and 0.205 nm.[22] Since those values are far from the obtained interplane spacings of the interface layer, we

can exclude the existence of those phases. Here, it should be noted that monoclinic Ga_2O_3 is only a stable form among these polymorphs[23] and has a large negative heat of formation energy (−1089.1 kJ/mol at RT).[24] It is interesting to mention that a spinel (cubic) $ZnGa_2O_4$ interface layer was formed during growth of a GaN epilayer on a ZnO substrate.[25] However, the largest interplane distances of $ZnGa_2O_4$ are 0.481, 0.295, and 0.252 nm[26] and these values are also far from the measured ones, which excludes the formation of spinel $ZnGa_2O_4$ (cubic) phase in our case. Another type of compound having Ga, O, and Zn elements is homologous $Ga_2O_3(ZnO)_m$ with m being larger than 7. This family of compounds were formed by synthesis at temperatures above 1250 °C for several days.[27] The structures of these materials are orthorhombic with average lattice constants of $a=0.325$, $b=19.70$, and $c=31.40$ nm. Here, it should be noted that the lattice constants of b and c are larger than the thickness of the interface layer. Therefore, if the interface layer were $Ga_2O_3(ZnO)_m$, the a axis would be parallel to the growth direction. Even in such a case, the a (=0.325 nm) and $2a$ (=0.650 nm) values of the $Ga_2O_3(ZnO)_m$ are far from the interplane spacings of the interface layer along the growth direction in our samples. In addition, since the synthesizing conditions are completely different from our growth conditions, we can exclude the possibility of the formation of a homologous $Ga_2O_3(ZnO)_m$ phase.

Now we discuss the formation process of the interface layer. It has been known that thermal annealing in vacuum bellow at 950 °C cannot remove the oxide completely from GaN surfaces[28] (in the view point of surface spectroscopy). However, RHEED patterns (not shown here) of our substrates after thermal cleaning revealed sharp streaky pattern with a high intensity of specular beam and negligible background intensity, which imply not severe and if any, only negligible remaining of the oxide after thermal cleaning. Therefore, the initial surface reaction of oxygen with Ga-face GaN during O-plasma pre-exposure period is responsible for the formation of oxide interface layers. Hence, preventing this reaction by Zn pre-exposure is critical to suppress the oxide interface layer formation. Because no oxide layer was investigated in HRTEM observation of Zn pre-exposed samples, the possibility of the formation of the interface layer after the beginning of the ZnO layer growth can be excluded. Here, it should be noted that Ga flux during annealing of GaN is effective in removing the oxide on GaN surface.[29] It may be an interesting topic that similar phenomena will occur during Zn exposure and be remained for further study.

The formation of a monoclinic Ga_2O_3 oxide layer on MOCVD grown GaN surface by annealing under dry air ambient[30,31] and by exposure to laboratory air[32] have been reported. Amorphous or polycrystalline monoclinic Ga_2O_3 phases were formed by annealing at 450, 750 and 900 °C for 1–45 h. However, the interface layer in our sample shows single-crystalline feature. Hence, the ZnO layer on the interface layer was grown as single crystalline. Another difference in interface morphology at Ga_2O_3/GaN between the thermally oxidized case and our case using oxygen plasma is that the interface in the former is not smooth, while the latter treatment leads to the formation of atomically smooth interface morphology as can be seen in Fig. 1(a). If we assume that the initial surface condition and smoothness of epi-GaN are similar for both cases, which would be likely the case because of similar cleaning processes for removing native oxides of epi-GaN, the observed difference in the interface morphology can be attributed to the different oxidation processes, although details of the oxidation mechanisms have not been elucidated yet. Our oxide interface layer was formed by O-plasma exposure for 3–5 min at 700 °C resulting in the formation of a 3.5-nm-thick Ga_2O_3 layer, while annealing of epi-GaN under dry air ambient at temperature higher than 450 °C for 1–45 h resulted in much slower oxide layer formation according to Wolter *et al.* (they observed 500-nm-thick oxide layer formation at 900 °C for 25 h annealing).

2. Interface models in Zn and O pre-exposed ZnO samples

HRTEM study indicates that there is no interface layer at the Zn pre-exposed ZnO/GaN heterointerface. Since the topmost surface of an epi-GaN layer is a Ga-terminated one, there might be two types of possible interface bondings including Ga–Zn and Ga–O. On exposing Zn beams onto a Ga-terminated surface, Ga–Zn bonds may be formed at the surface as schematically shown in Fig. 3(a). It is likely, however, that the surface Ga–Zn bonds will be replaced with O atoms to form stronger Ga–O–Zn bonding by oxygen flux during ZnO growth, since the Zn–Ga (cation–cation) bonding is much less stable[33] compared to Ga–O and Zn–O (cation-anion) bondings. Figure 3(a) shows a schematic diagram of an interface model in a Zn pre-exposed sample. We suggest the "N–Ga–O–Zn" interface stacking sequence in the Zn pre-exposed samples.

Now we briefly discuss a possible model for the compensation of the excess bonding charges due to the heterovalence at the ZnO/GaN heterointerface. Let us assume one Ga vacancy per every four atoms at the Ga-face (0001) GaN surface on the average and transfer of 3/4 electrons per bond from three remaining Ga dangling bonds to three created N dangling bonds results in completely empty Ga dangling bonds and fully filled N dangling bonds. This surface satisfies the electron counting rule. In this model, arrangement of Ga vacancy is considered to be random. The Ga vacancy would be occupied by Zn atom during the Zn exposure which resulted in Zn–N bond on topmost GaN layer. Then, equal number of Zn–N acceptor bonds which have deficiency of 1/4 electron per bond and Ga–O donor bonds which have excess of 1/4 electron per bond would be formed. After Zn growth and charge transfer from the donor bonds to the acceptor bonds results in the compensation of the charge at ZnO/GaN heterointerface.

In the case of oxygen-plasma pregrowth treatments, a monoclinic Ga_2O_3 interface layer is formed at a ZnO/GaN

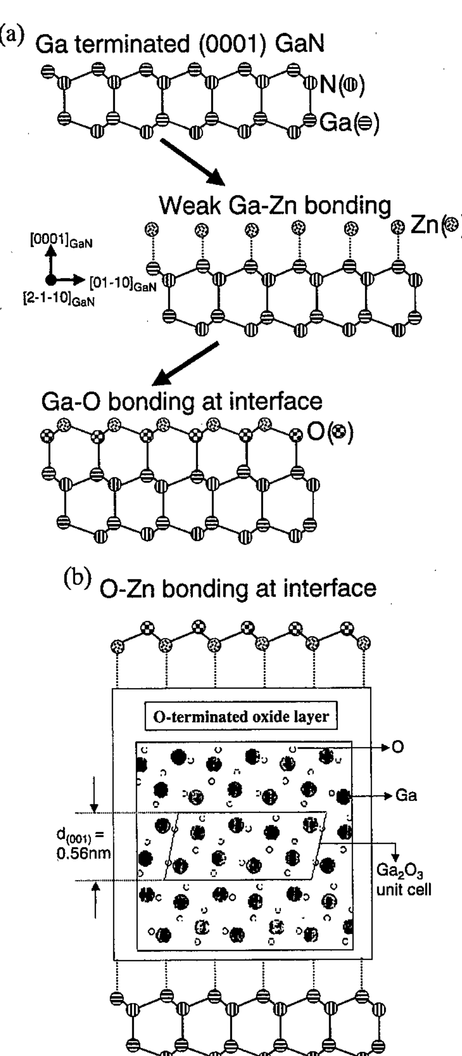

FIG. 3. ZnO/GaN heterointerface models for (a) Zn pre-exposed and (b) O pre-exposed samples.

FIG. 4. TEM micrographs showing defect structures of Zn [(a),(b)] and O pre-exposed [(c),(d)] ZnO samples. The insets are micrographs showing total ZnO layer from the interface.

heterointerface, which leads to the formation of two interfaces which includes ZnO/Ga_2O_3 and Ga_2O_3/GaN interfaces. The atomic plane of Ga_2O_3 parallel to the interface is either O or Ga planes. It is most likely that the O plane forms the Ga_2O_3/GaN interface with the topmost Ga plane of the epi-GaN. If this is the case, the Ga_2O_3 interface layer must have an O-terminated top surface, since half of the unit cell divided parallel to the interface also has an O-terminated surface and both an unit cell and half of the unit cell satisfy the ratio of Ga/O as 2/3, which matches the stoichiometry of Ga_2O_3. Other terminations do not satisfy the 2/3 ratio of the Ga/O, which implies the O terminations at half of the unit cell or one unit cell parallel to the interface are stable. Here, it should be noted that the HRTEM micrograph [Fig. 1(b)] of the Ga_2O_3 interface layer shows well-defined planes parallel to the interface with the interplane distance corresponding to one or half of the Ga_2O_3 unit cell. Therefore, we conclude that the top surface of the Ga_2O_3 interface layer is an oxygen-terminated plane. An exposure of Zn flux for ZnO layer growth will form strong and stable Zn/O stacking at the top surface of the Ga_2O_3 interface layer. We note again that the lower interface between the Ga terminated GaN and the oxide interface layer is O/Ga stacking. We propose a "N–Ga–(O-terminated Ga_2O_3 layer)–Zn–O" interface stacking sequence in O pre-exposed samples. Figure 3(b) shows a schematic diagram of an interface model for an O pre-exposed sample. Here the unit cell of the Ga_2O_3 is projected into the [010] direction.

B. Structural and optical properties of ZnO films

1. Effects of different interface structures

Figures 4(a)–4(d) are TEM micrographs showing the defects structure of Zn [(a) and (b)] and O pre-exposed [(c) and

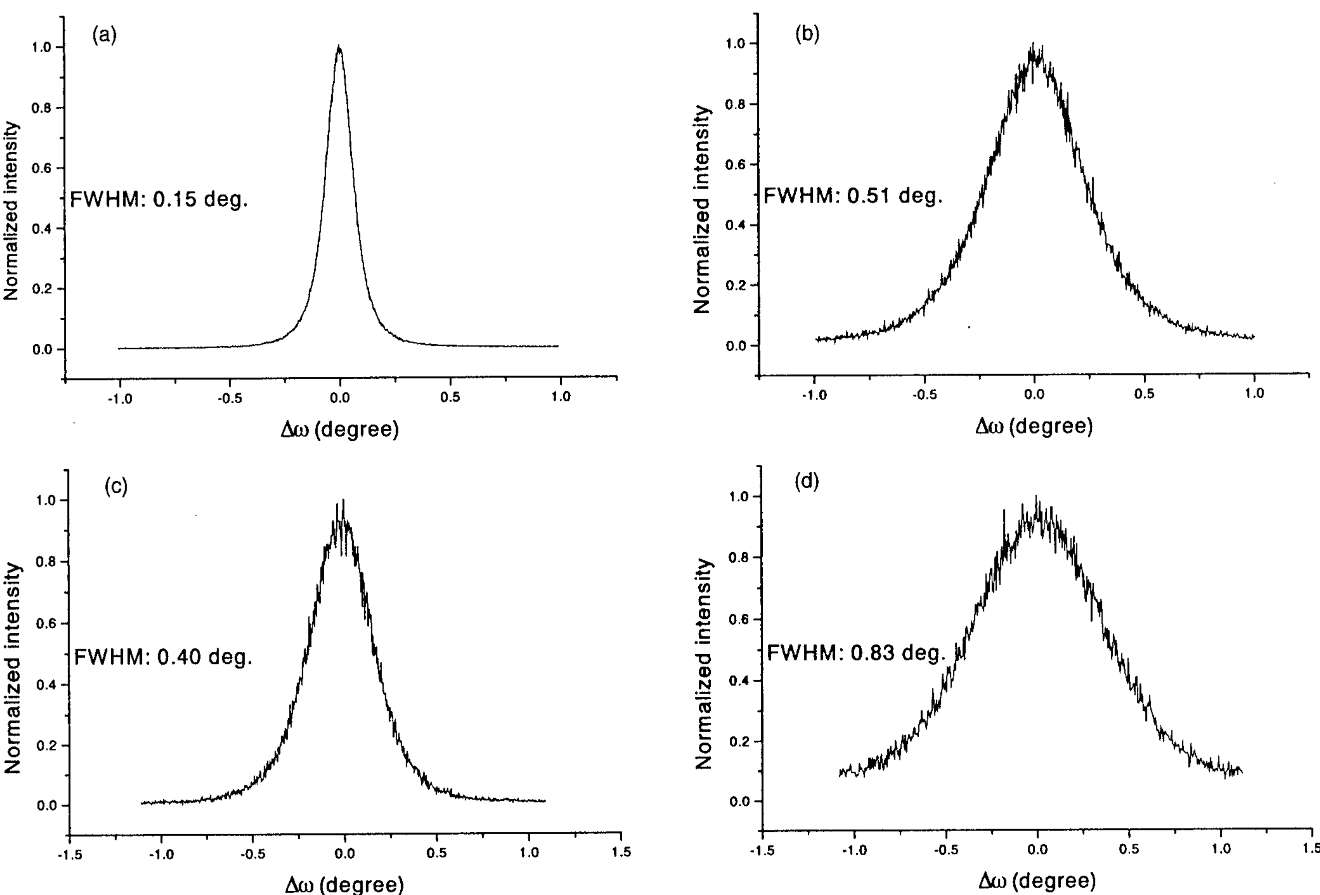

FIG. 5. XRD rocking curves of symmetric (0002) ω scans (a) and (b) and asymmetric (10-11) ω scans (c) and (d) for Zn (a) and (c) and O (b) and (d) pre-exposed samples.

(d)] ZnO samples. Overall dislocation density was higher in O pre-exposed samples than in Zn pre-exposed samples. In addition to defect density, the defect configuration in Zn and O pre-exposed samples is different. In Zn pre-exposed samples, major defects are edge dislocations parallel to the interface and high density of stacking faults on basal plane at the interface region, while in the upper region of ZnO films, major dislocations are edge types aligned along the growth directions. Such a dislocation configuration in Zn is similar as that reported by Narayan *et al.*[18] On the other hand, in O pre-exposed samples, major defects are edge dislocations parallel to the interface and low density of stacking faults on basal plane at the interface region, while in the upper region of ZnO films, major dislocations are screw or mixed types aligned along the growth direction. We estimated that total dislocation density would be low $10^{10}/\mathrm{cm}^{-2}$ to middle $10^{10}/\mathrm{cm}^{-2}$ range by considering the thickness of the TEM samples in cross-sectional view although plan-view observation is needed to assess accurate dislocation density.

Figures 5(a)–5(d) show (0002) and (10-11) ω-scan rocking curves of Zn and O pre-exposed ZnO samples. Full width at half maximum (FWHM) values of XRD rocking curves (symmetric and asymmetric scans) of O pre-exposed samples are larger than Zn pre-exposed samples; FWHM values of (0002) and (10-11) ω-scan rocking curves of the Zn pre-exposed sample are 0.15° and 0.40°, respectively; while those of the O pre-exposed sample are 0.51° and 0.83°, respectively. Defects in the films resulting in in-plane and out-of-plane disorder causes broadening of the rocking curve.[34] Therefore, larger FWHM values of O pre-exposed ZnO films implied the higher disordering and dislocation density in the films, which agreed well with the TEM results of Fig. 4.

Figures 6(a) and 6(b) show PL spectra of Zn and O pre-exposed samples. The FWHM values of band edge emission of O pre-exposed samples is larger than that of Zn pre-exposed samples. Larger FWHM values of O pre-exposed samples implied that worse crystal quality than Zn pre-exposed ones. Here, it should be noted that samples of Fig. 6 were grown at 700 °C without a low temperature-grown ZnO layer. FWHM values of band edge emission were larger than those of ZnO films,[35] which have been employed low temperature (300 °C) growth followed by high temperature (700–800 °C) annealing and high temperature growth, subsequently.

The poor crystal quality of the O pre-exposed samples revealed by TEM, XRD, and PL observations can be understood by considering the large misfits strains caused by insertion of the interface layer between GaN and ZnO films discussed in Sec. III A 1.

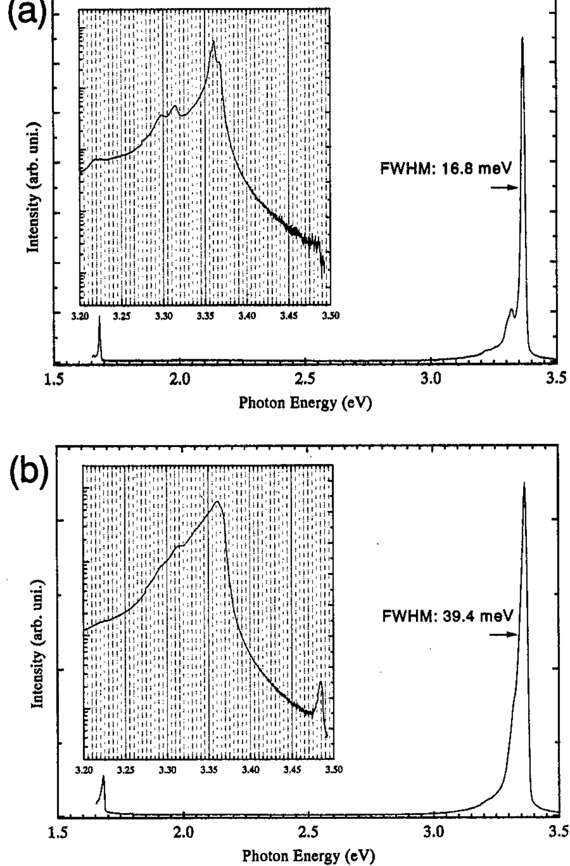

FIG. 6. PL spectra (at 4.2 K) of (a) Zn and (b) O pre-exposed samples.

2. Effects of high temperature annealing

Because Zn pre-exposed samples showed better crystal quality than the O pre-exposed samples, as discussed in the previous section, we focus on Zn pre-exposed ZnO films from now on. Figure 7 shows a RHEED pattern of a 45-nm-thick ZnO film, which was Zn pre-exposed, for as grown ZnO samples, (a) and for annealed samples, (b). The RHEED pattern of as grown sample is spotty which indicates three-dimensional island morphology. However, the RHEED pattern is changed to streaky by heating to 700 °C and sharpens with increasing annealing time. Thinner (<10 nm) and thicker (>50 nm) LT grown ZnO layers revealed difficulties in change to a streaky RHEED pattern by followed high temperature annealing. Figures 8(a) and 8(b) show surface morphologies of as grown and annealed films observed by AFM for 1 μm$\times$1 μm area. The surface morphology was significantly changed after annealing: As-grown samples show island morphology, while annealed samples show (large) step morphology. Side planes of the large steps were not determined because of absence of uniformity in aspect ratio. Root mean square (rms) values of surface roughness were 0.25 nm for the as-grown and 1.17 nm for the annealed samples. The larger rms value of the annealed sample was due to large height difference between bottom and top of the large steps. Here, it should be noted that this large step is not an atomic step. However, appearance of a sharp streaky RHEED pattern in spite of the large steps can be understood considering the finite coherent length (about 100 nm) of the electron beam (kinetic energy of 20 kV) and the existence of terraces with about 80–100 nm width between (large) steps of 4–7 nm high. Therefore, we concluded that on the terraces between the large steps in the annealed sample, only atomic-level steps must exist. These atomic-level steps were not configured out because of large height difference between top and bottom of the large step.

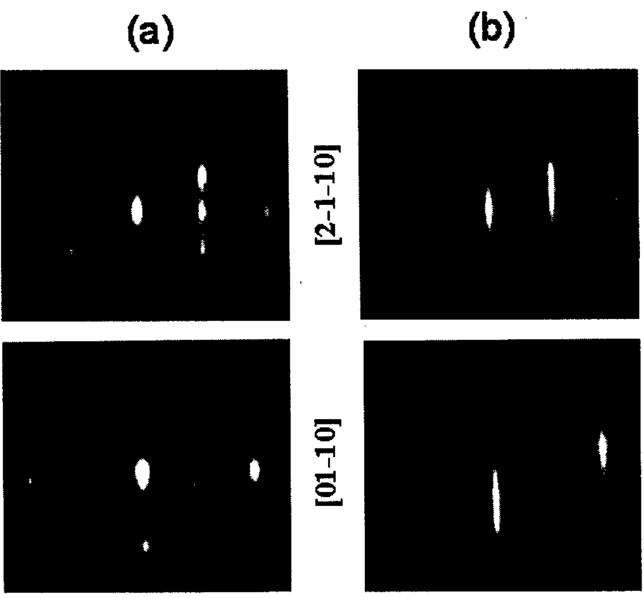

FIG. 7. RHEED patterns of (a) as-grown and (b) annealed ZnO films (film thickness=45 nm).

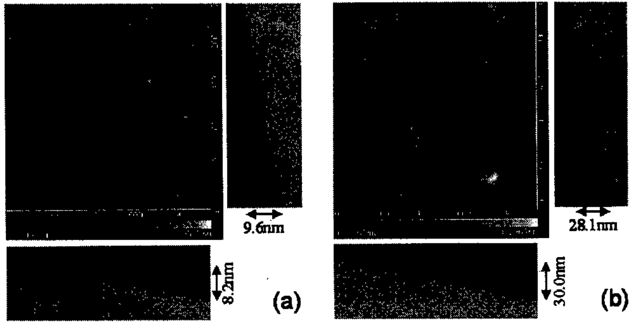

FIG. 8. AFM images showing surface morphologies of (a) as-grown and (b) annealed samples.

FIG. 9. HRTEM micrographs of as grown sample observed along the (a) [2-1-10] and (b) [01-10] directions.

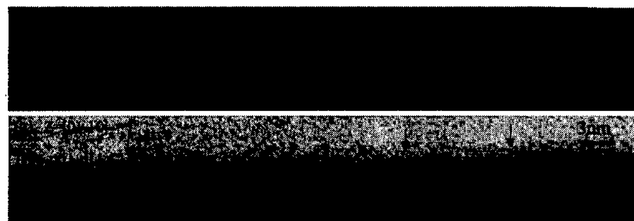

FIG. 10. HRTEM micrographs of annealed sample observed along the (a) [2-1-10] and (b) [01-10] directions.

In order to confirm flatness and existence of steps and terraces between the large steps, we carried out cross-sectional TEM observations. Figures 9(a) and 9(b) show HR-TEM micrographs of as-grown sample observed at [01-10] and [2-1-10] zone axes, respectively. Figures 10(a) and 10(b) show HRTEM micrographs of the annealed sample observed at [01-10] and [2-1-10] zone axes, respectively. Figures 9 and 10 clearly show the difference of the surface morphology between as-grown and annealed samples. The surface morphology of as-grown sample shows typical three-dimensional island morphology with average width and height of islands about 10–20 and 3–5 nm, respectively. On the other, annealed sample shows atomically flat morphology with atomic-level-height steps (as marked by arrows) and terraces. These atomic-level-height steps and terraces caused a RHEED pattern to be sharp streaky. Here, it should be noted that much smaller roughness values from AFM observations of the as-grown sample compared with HRTEM observations may caused by tip convolution (we used 20 nm diameter tip for AFM observation and it may not reveal real surface which has roughness fluctuation of 3–5 nm within short range of 10–20 nm).

Figures 11(a) and 11(b) show PL spectra (at 4.2 K) of as-grown and annealed samples. The insets show PL and reflectance spectra at around the band edge emission regions. Since the thickness of the ZnO films was thin, peaks from the GaN layer were also observed. The PL intensity from the ZnO film was increased about 2.7 times and its FWHM value was decreased from 15.5 to 11.2 meV after annealing. Differences of the PL intensity and the FWHM values can be ascribed to different crystalline qualities. Two bound exciton peaks in as grown sample observed at 3.3568 and 3.3600 eV could be assigned to I_9 and I_7 donors judging from their energy positions. While only one bound exciton peak at 3.358 eV is observed in the annealed sample. This emission line is located in between the reported energy positions of I_9 and I_8 lines. Very weak deep level emissions are observed in both samples at around 2.2 eV, which is commonly observed in bulk ZnO.

The free excitonic transition energies of bulk ZnO are marked by X_A and X_B in Fig. 11. In both reflectance spectra, abrupt decrease in reflectance is noteworthy at around the excitonic transition energies. Careful investigation show small but clear shoulders in the reflectance spectrum of the annealed ZnO layer at X_A and X_B positions, while these

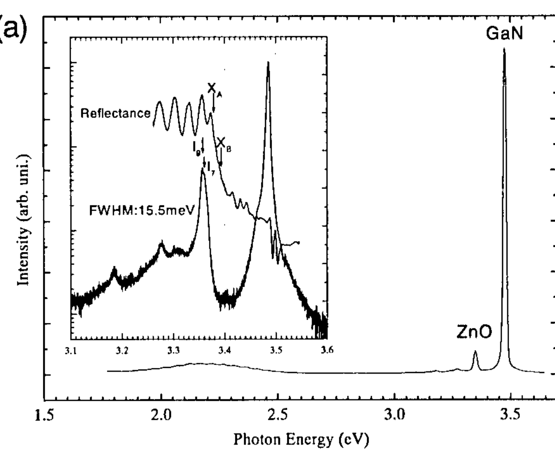

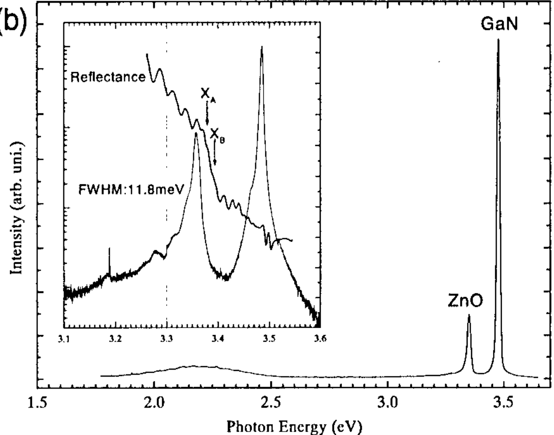

FIG. 11. PL spectra (at 4.2 K) of (a) as-grown and (b) annealed samples. The insets show PL and reflectance spectra at around the band edge emission regions.

features are rather weak in the spectrum of the as-grown ZnO layer.

As a final note, recently, we observed RHEED intensity oscillations during ZnO film growth on the low temperature grown buffer layers followed by high temperature annealing.[35] The FWHM values of (0002) XRD rocking curve (ω scan) of these ZnO films are found to be comparable to those of GaN substrate and PL at 10 K showed band edge emission with a FWHM value as narrow as 1.5 meV. Therefore, we concluded that the morphological change of the low temperature grown ZnO layers followed by high temperature annealing plays an important role for obtaining high quality ZnO films.

IV. CONCLUSIONS

In the first series of experiments, the structure of ZnO/GaN interfaces in ZnO films grown by P-MBE onto zinc or oxygen-plasma pre-exposed (0001) GaN/Al_2O_3 substrates are studied. By HRTEM observation, an interface layer is observed in O pre-exposed ZnO samples. In contrast, no interface layer is observed in Zn pre-exposed ZnO ones. The interface layer is identified as a single-crystalline monoclinic Ga_2O_3 by diffraction pattern analysis. The ZnO layer on such an interface layer is grown as a single crystal. The orienta-

tion relationship between monoclinic Ga_2O_3 of the interface layer, epi-GaN and ZnO films is investigated as (0001) GaN‖(001) Ga_2O_3‖(0001) ZnO and [2-1-10] GaN‖[010] Ga_2O_3‖[2-1-10] ZnO. We concluded that the crystalline interface layer was formed through the initial surface reaction of oxygen plasma with Ga atoms of Ga-face GaN, which can be prevented by zinc pre-exposure onto GaN substrates. Lattice misfit of Ga_2O_3 against underlying GaN (against upper ZnO) can be estimated as −4.7% (−6.5%) and 10.7% (8.6%) along the [010] and [100] directions of the Ga_2O_3. Based on the stability of bondings and structure, we propose interface models of ZnO/GaN heterointerfaces in Zn or O pre-exposed ZnO films: In the case of Zn pre-exposed film, a N–Ga–O–Zn bonding sequence is proposed, while the interface bonding sequence of N–Ga–(O-terminated Ga_2O_3 layer)–Zn–O is proposed for O pre-exposed one.

Defect configurations in the Zn and O pre-exposed samples are different. In the ZnO films with a Zn pre-exposure, major defects are edge dislocations parallel to the interface and high density of stacking faults on basal plane at the interface region, while in the upper region of ZnO films, major dislocations are edge types aligned along the growth directions. On the other hand, in the ZnO films with an O pre-exposure, major defects are edge dislocations parallel to the interface and low density of stacking faults on basal plane at the interface region, while in the upper region of ZnO films, major dislocations are screw or mixed types aligned along the growth directions. Overall dislocation density was higher in the O pre-exposed samples than the Zn pre-exposed samples. Crystal quality evaluated by XRD and PL measurements also show better crystal quality (narrower FWHM values of XRD rocking curves and of band edge emission from PL) of Zn pre-exposed samples than O pre-exposed ones, which agreed well with TEM results. Worse crystal quality of the O pre-exposed samples could be understood considering larger misfit strain caused by insertion of the interface layer between GaN and ZnO epilayers.

In the second series of experiments, effects of annealing of low temperature grown ZnO films processed with a Zn pre-exposure are studied. Surface morphology of ZnO films is significantly changed by high temperature annealing: Three-dimensional island morphology on as-grown ZnO films is changed into atomically flat surface morphology with steps and terraces by high temperature annealing. Optical properties are also improved by annealing: The FWHM value of band edge emission is decreased and its intensity is increased about three times after annealing. Free exciton emission from annealed films is considerably enhanced in intensity compared to as grown films, which indicates significant improvement of the crystal quality of low temperature grown films by high temperature annealing.

As a concluding remark, we have recently achieved high quality ZnO film growth on (0001) GaN template substrates by growing ZnO films after both Zn pre-exposure and high temperature annealing procedures of low temperature grown ZnO layers.

ACKNOWLEDGMENTS

The authors would like to thank E. Aoyagi and Y. Hayasaka, High-Voltage Electron Microscope Laboratory, Tohoku University, for the possibility to use the TEM facilities and software programs. The authors would like to thank Dr. H. Wenisch for his English grammar check for the manuscript.

[1]C. Kligshirn, Phys. Status Solidi B **71**, 547 (1975).
[2]W. A. Harrison, *Electronic Structure and the Properties of Solids* (Freeman, San Francisco, 1980), p. 173, Table 7-3.
[3]*American Institute of Physics Handbook*, 3rd ed., edited by D. E. Gray (McGraw-Hill, New York, 1972), pp. 9–19, Table 9b-1.
[4]*Properties of Wide Bandgap II-VI Semiconductors*, edited by R. Bhargava (INSPEC, The Institute of Electrical Engineers, London, United Kingdom, 1997), pp. 137, Table 1.
[5]D. M. Bagnall, Y. F. Chen, Z. Zhu, T. Yao, S. Koyama, M. Y. Shen, and T. Goto, Appl. Phys. Lett. **70**, 2230 (1997).
[6]Z. K. Tang, G. K. L. Wong, P. Yu, M. Kawasaki, A. Ohtomo, H. Koinuma, and Y. Segawa, Appl. Phys. Lett. **72**, 3270 (1998).
[7]D. M. Bagnall, Y. F. Chen, Z. Zhu, T. Yao, M. Y. Shen, and T. Goto, Appl. Phys. Lett. **73**, 1038 (1998).
[8]Y. Chen *et al.*, J. Cryst. Growth **181**, 165 (1997).
[9]Y. Chen, D. M. Bagnall, H. J. Ko, K. T. Park, K. Hiraga, Z. Zhu, and T. Yao, J. Appl. Phys. **84**, 3912 (1998).
[10]Y. Chen, S. K. Hong, H. J. Ko, M. Nakajima, T. Yao, and Y. Segawa, Appl. Phys. Lett. **76**, 245 (2000).
[11]A. Ohtake, S. Miwa, L. H. Kuo, T. Yasuda, K. Kimura, C. Jin, and T. Yao, J. Cryst. Growth **184/185**, 163 (1998).
[12]A. Franciosi and C. G. Van de Walle, Surf. Sci. Rep. **25**, 1 (1996).
[13]L. H. Kuo, K. Kimura, T. Yasuda, S. Miwa, C. G. Jin, K. Tanaka, and T. Yao, Appl. Phys. Lett. **68**, 2413 (1996).
[14]L. H. Kuo, K. Kimura, S. Miwa, T. Yasuda, and T. Yao, Appl. Phys. Lett. **69**, 1408 (1996).
[15]L. H. Kuo, K. Kimura, A. Ohtake, S. Miwa, T. Yasuda, and T. Yao, J. Vac. Sci. Technol. B **15**, 1241 (1997).
[16]M. A. L. Johnson, S. Fujita, W. H. Rowland, Jr., W. C. Hughes, J. W. Cook, Jr., and J. F. Schetzina, J. Electron. Mater. **25**, 855 (1996).
[17]R. D. Vispute *et al.*, Appl. Phys. Lett. **73**, 348 (1998).
[18]J. Narayan, K. Dovidenko, A. K. Sharma, and S. Oktyabrsky, Appl. Phys. Lett. **84**, 2597 (1998).
[19]S. Shimizu, Y. Suzuki, T. Nischhara, S. Hayashi, and M. Shinohara, Jpn. J. Appl. Phys., Part 2 **37**, L703 (1998).
[20]JCPDS card, file number 76-0573.
[21]JCPDS card, file number 74-1610.
[22]JCPDS card, file number 20-0426.
[23]R. Roy, V. G. Hill, and E. F. Osborn, J. Am. Chem. Soc. **74**, 719 (1952).
[24]I. Barin, *Thermochemical Data of Pure Substances* (VCH, Weinheim, Germany, 1989), p. 600 for Ga_2O_3 and p. 1690 for ZnO.
[25]E. S. Hellman, D. N. E. Buchanan, D. Wiesmann, and I. Brener, MRS Internet J. Nitride Semicond. Res. **1**, 16 (1996).
[26]JCPDS card, file number 38-1240.
[27]N. Kimizuka, M. Isobe, and M. Nakamura, J. Solid State Chem. **116**, 170 (1995).
[28]S. W. King, J. P. Barnak, M. D. Bremser, K. M. Tracy, C. Ronning, R. F. Davis, and R. J. Nemanich, J. Appl. Phys. **84**, 5248 (1998).
[29]M. A. Khan, J. N. Kuznia, D. T. Olson, and R. Kaplan, J. Appl. Phys. **73**, 3108 (1993).
[30]S. D. Wolter, B. P. Luther, D. L. Waltemyer, C. Onneby, S. E. Mohney, and R. J. Molnar, Appl. Phys. Lett. **70**, 2156 (1997).
[31]S. D. Wolter, S. E. Mohney, H. Venugopalan, A. E. Wickenden, and D. D. Koleske, J. Electrochem. Soc. **145**, 629 (1998).
[32]K. Prabhakaran, T. G. Andersson, and K. Nozawa, Appl. Phys. Lett. **69**, 3212 (1996).
[33]J. C. Phillips, *Bonds and Bands in Semiconductors* (Academic, New York, 1973).
[34]B. Heying, X. H. Wu, S. Keller, Y. Li, D. Kapolnek, B. P. Keller, S. P. DenBaars, and J. S. Speck, Appl. Phys. Lett. **68**, 643 (1996).
[35]H. J. Ko, Y. Chen, S. K. Hong, and T. Yao, J. Cryst. Growth **209**, 816 (2000).

Polarization effects and transport in AlGaN/GaN system

Yifei Zhang
Applied Physics Program, University of Michigan, Ann Arbor, Michigan 48109 and Department of Electrical Engineering and Computer Science, University of Michigan, Ann Arbor, Michigan 48109-2122

Yulia Smorchkova, C. Elsass, Stacia Keller, James Ibbetson, Steven DenBaars, and Umesh Mishra
Department of Electrical and Computer Engineering, University of California, Santa Barbara, California 93106

Jasprit Singh[a)]
Department of Electrical Engineering and Computer Engineering, University of Michigan, Ann Arbor, Michigan 48109

(Received 6 April 2000; accepted 26 May 2000)

The AlGaN/GaN heterostructure is important for both electronic and optoelectronic devices. In addition to having a large band gap, the heterostructure has a strong piezoelectric effect and a large spontaneous polarization. This allows one to incorporate a large electric field ($>10^6$ V/cm) and high sheet charge ($>10^{13}$ cm^{-2}) without doping. Theoretical studies are done to examine how polarization effects controls the sheet charge density. The studies also focus on how interface roughness, aluminum mole fraction in the barrier, impurity scattering, sheet charge density, and phonon scattering influence mobility. Results are compared with experimental studies on samples grown by both molecular beam epitaxy (MBE) and metalorganic chemical vapor deposition (MOCVD). We find that interface roughness is a dominant source of scattering in the samples reported. Due to the variation in growth techniques we find that the MBE samples have a smoother interface quality compared to the MOCVD samples. By carefully fitting the experimental data we present results on interface roughness parameters for MBE and MOCVD samples. © *2000 American Vacuum Society.* [S0734-211X(00)07204-8]

I. INTRODUCTION

Group III–nitride semiconductors have recently attracted wide attention in view of their application in high power devices and optoelectronic devices with wavelengths ranging from the red into the ultraviolet. These materials have direct band gaps from 1.9 eV for InN through 3.4 eV for GaN to 6.2 eV for AlN. Tremendous efforts have been devoted to the optoelectronic devices based on GaN and the related ternary alloys. For example, the blue and violet laser emission at room temperature in InGaN/GaN/AlGaN-based heterostructures under pulsed currents and continuous-wave operation[1–4] has been demonstrated. The material system is also important for high temperature-high power electronics.[5–9] In the application of high power devices such as microwave electronic devices, the performance of the devices depends on the quality of heterostructure interface formed by the materials with different band gaps as well as the quality of the materials grown.

There are two important issues that govern the AlGaN/GaN HFETs which are significantly different from HEMTs made from structures such as AlGaAs/GaAs or InAlAs/InGaAs. These issues arise from the following considerations.

(i) Polarization effects: There is a spontaneous polarization present in the structures as a result of the cation and anion positions in the lattice.[10] In heterostructures the difference between spontaneous polarization of two layers can be used to create a high density of mobile carriers. In addition to spontaneous polarization in heterostructures with strain (resulting from epitaxy) the piezoelectric effects for the nitride system are so large that effective built-in fields of $\sim 10^6$ V/cm can be produced near the interfaces.[11] These two features have been exploited to design AlGaN/GaN HEMTs with very high sheet charge. It has been found[12] that in nominally undoped HEMT structures sheet charge densities greater than 10^{13} cm^{-2} can be produced.

(ii) Interface roughness effects: Although interface roughness effects are present in other HEMT structures as well, the larger band discontinuity combined with larger effective mass in the channel makes interface roughness much more important in controlling the channel mobility.

To fully exploit the potential of spontaneous polarization and piezoelectric effect in HEMTs and other electronic and optoelectronic devices, it is important that the parameters associated with these phenomena be known accurately. It is important to know what issues control the mobility of electrons in the two-dimensional electron gas (2DEG). In particular it is important to know what effect interface roughness has on transport since the heterostructure growth has not yet been perfected. At low temperatures interface roughness is expected to be an important source of scattering in undoped samples. Thus by examining the low temperature mobility in HEMT structures we can examine the role of interface roughness scattering in nitride heterostructures.

[a)]Electronic mail: singh@engin.umich.edu

We will present results on a series of experiments on charge control and mobility studies and use a theoretical formalism to fit the data. Experimental studies are based on samples grown by molecular beam epitaxy (MBE) and by metalorganic chemical vapor deposition (MOCVD). We will use the modeling to verify how accurate parameters given in literature are and how important the role of interface quality is in AlGaN/GaN HEMTs. In Sec. II we will briefly review the experimental studies. In Sec. III we will provide details of the theoretical formalism used. In Sec. IV we will discuss the experimental results along with the theoretical fits, and we will conclude in Sec. V.

II. EXPERIMENTAL STUDIES

Results reported here are based on samples grown by MBE and by MOCVD. The two techniques would produce different quality of interfaces in general. Details of the MOCVD growth issues have been described in Ref. 13. Structures with 2–30 nm thick AlGaN layers were grown by MOCVD on 3 mm thick semi-insulating GaN on *c*-plane sapphire substrates. The growth of GaN base layers was initiated on the sapphire substrates with an approximately 20 nm thick GaN layer grown at 525 °C while the remaining GaN layer was grown at temperatures between 1040 and 1080 °C.

The MBE grown structures have been grown by rf plasma-assisted MBE. The growth was performed in a Varian Gen II MBE system. Active nitrogen for growth was supplied by EPI Unibulb nitrogen plasma source utilizing ultrahigh purity nitrogen (99.9995%) which was further purified by an inert gas purifier installed at the rf plasma source gas inlet. Elemental Ga (6N) and Al (6N) supplied from conventional effusion cells were used for the group III elements. Unintentionally doped GaN templates grown on (0001) sapphire by atmospheric pressure MOCVD were used for MBE growth of AlGaN/GaN structures. More details on the MBE growth can be found in Ref. 14.

No intentional doping was performed during growth. Double crystal x-ray rocking curve measurements ($2\theta-\omega$ scans) were used to estimate the alloy composition in the top AlGaN layer. Both (0002) and (0004) reflections were studied. Assuming coherently strained AlGaN layers and utilizing the elastic constants given by Polian *et al.*,[15] the Al concentration was calculated from the GaN and AlGaN peak separation. The carrier concentration profiles in the AlGaN/GaN heterostructures were determined using capacitance–voltage ($C-V$) measurements. The measurements were performed on the Schottky diode structures in which platinum was used for Schottky contacts while Ti/Al/Ni/Au layers were used to form the ohmic contact to unintentionally doped GaN. Temperature-dependent (13 K$<T<$300 K) Hall measurements were performed in Van der Pauw geometry on 1 cm$\times$1cm square samples.

III. THEORETICAL FORMALISM

In this section we will discuss the formalism used to understand the experimental observations. We will first give a brief discussion of spontaneous polarization and piezoelectric effect. Next we will discuss the charge control model. Finally we will discuss the mobility model.

A. Polarization effects

Nitride heterostructures have polarization charges at interfaces because of strain related piezoelectric effect and spontaneous polarization. For growth along (0001) orientation the strain tensor for coherently strained wurtzite crystals is

$$\epsilon_{xx}=\epsilon_{yy}=\frac{a_S}{a_L}-1,$$

$$\epsilon_{zz}=-\frac{2c_{13}}{c_{33}}\epsilon_{xx}, \tag{1}$$

where a_S and a_L are the lattice constants of the substrate (GaN) and the overlayer. The piezoelectric polarization is related to the strain tensor by the following relation:

$$P_{pz}=e_{33}\epsilon_{zz}+e_{31}(\epsilon_{xx}+\epsilon_{yy}). \tag{2}$$

The values of e_{31} for AlN, GaN, and InN are -0.6, -0.49, and -0.57 C/m^2.[16] The values for e_{33} are 1.46, 0.73, and 0.97 C/m^2. Using a value of $c_{13}/c_{33}\sim 0.3$ we find that the polarization produced for $Al_xGa_{1-x}N$ grown on (0001) GaN is

$$P_{pz}(x)=(-3.2x-1.9x^2)10^{-6}\ \text{C cm}^{-2}. \tag{3}$$

For completeness we note the polarization produced in growth of $In_xGa_{1-x}N$ on GaN:

$$P_{pz}(x)=(-0.89x+0.61x^2)10^{-6}\ \text{C cm}^{-2}. \tag{4}$$

In addition to the polarization induced by strain, the cation, and anion sublattices are spontaneously displaced with respect to each other producing an additional polarization. For heterostructures the difference of the spontaneous polarization appears at the interfaces. The values of the spontaneous polarization[3] are

InN: $P_{sp}=-3.2\times10^{-6}$ C/cm^2,

GaN: $P_{sp}=-2.9\times10^{-6}$ C/cm^2,

AlN: $P_{sp}=-8.1\times10^{-6}$ C/cm^2.

The two effects described above become important when heterostructures are grown. In the case of spontaneous polarization the presence of a heterostructure between materials with different spontaneous polarization values causes a net charge at the interface which causes built-in electric fields in the structure. Similarly in case the lattice constants of the components of the heterostructure are different, the resulting strain present (assuming minimal dislocation generation) causes charges at the interfaces due to the piezoelectric effect.

The magnitude and direction of the electric fields associated with spontaneous polarization and piezoelectric effect depend on the substrate, the growth orientation, and the nature of the surface (cation terminated or anion terminated). For the results given here we will discuss the most common

growth conditions employed for the nitride systems where growth is on sapphire and is along the (0001) direction with Ga terminated surface. The effective substrate is defined by the a thick overlayer that is grown on the starting substrate (sapphire). Once dislocations are generated the thick overlayer forms its own lattice and acts as a substrate for the next layers as long as the growth is coherent, i.e., overlayer thickness is small enough to generate no dislocations. The overlayer now grows with a lattice structure which fits the in-plane lattice of the substrate and has an out of plane lattice constant defined by total energy minimization. Thus a compressive strain in the plane of growth causes a tensile strain out of plane.

Consider, for example, a case where the effective substrate is GaN and an $Al_xGa_{1-x}N$ overlayer is grown coherently. The polarization is found to have the value[12]

$$
\begin{aligned}
P(x) &= P_{pz} + P_{sp} \\
&= (-3.2x - 1.9x^2)\times 10^{-6}\ \mathrm{C/cm^2} \\
&\quad - 5.2\times 10^{-6}x\ \mathrm{C/cm^2}.
\end{aligned}
\tag{5}
$$

We see that in this system the effects arising from piezoelectric effect and spontaneous polarization mismatch are comparable. Note that the two effects can have opposite directions as well as depending on the surface termination conditions and the lattice mismatch between the overlayer and the effective substrate. The electric field associated with the polarization given above is

$$F(x) = (-9.5x - 2.1x^2)\ \mathrm{MV/cm}. \tag{6}$$

We see that the built-in field and sheet charge values are very large. It is easy to produce fields around 10^6 V/cm and charge density around 10^{13} cm^{-2}.

For the heterostructure $In_xGa_{1-x}N$ grown on a GaN effective substrate the polarization charge density and field values are

$$
\begin{aligned}
P(x) &= (14.1x + 4.9x^2)\times 10^{-6}\ \mathrm{C/cm^2} \\
&\quad - 0.3\times 10^{-6}x\ \mathrm{C/cm^2}, \\
F(x) &= (15.6x + 5.5x^2)\ \mathrm{MV/cm}.
\end{aligned}
\tag{7}
$$

In this system the spontaneous polarization effect is negligible. However, the piezoelectric effect is very strong.

B. Charge control model

Our charge control model first obtains the potential profile in a HEMT structure by solving the Schrödinger equation and Poisson equation self-consistently. The Schrödinger equation yields the confined charge terms in the Poisson equation which, in turn, determines the potential profile. This potential profile is fed back into the Schrödinger equation until the solution of Poisson equation goes to convergence. The detailed formalism is described in Ref. 17.

C. Mobility model

Mobility is calculated by applying Kubo-Greenwood formula.[17] The Kubo formula[18] for the conductivity of electron under a small dc field is given by

$$\sigma_{\mathrm{dc}} = \frac{2\pi e^2\hbar}{V}\sum_n\sum_m -\frac{\partial f}{\partial E}|\langle n|v|m\rangle|^2\delta(E_n - E_m), \tag{8}$$

where f is the Fermi–Dirac distribution function, v is the velocity operator, and V is the system volume. $|n>$ is the electronic state under certain potential configuration. The summation is over all the states close to the Fermi level. The number of electronic states involved in the summation depends on the temperature. Since a finite system is chosen for our numerical study, the delta function in the Kubo formula must be treated adequately. In Ref. 17 we introduced an averaging process for the reduced momentum matrix. In this article, we use an alternative approach in which we replace the inner summation with the integral and the delta function with Lorentzian function and Eq. (8) becomes

$$
\begin{aligned}
\sigma_{\mathrm{dc}} = \frac{2\pi e^2\hbar^3}{m_e^{*2}}\sum_n \int\left(-\frac{\partial f}{\partial E_m}\right)N(E_m)|D_{n,m}|^2 \\
\times G_\Gamma(E_m - E_n)\,dE_m,
\end{aligned}
\tag{9}
$$

where m_e^* is the electron effective mass, $N(E_m)$ is the density of states function, $D_{n,m}$ is the reduced momentum matrix given by $D_{n,m} = \int\psi_n^*(\partial\psi_m/\partial x)\,d\mathbf{r}$, $G_\Gamma(E_m - E_n)$ is the Lorentzian function given by $G_\Gamma(E_m - E_n) = \Gamma/\pi[(E_m - E_n)^2 + \Gamma^2]$. The parameter Γ in the conductivity expression represents the scattering of electrons by inelastic processes such as phonons.[17] This is similar in spirit to the approach taken in deriving Mott variable range conductivity. This approach allows us to examine how phonon scattering and interface roughness scattering influence transport without treating them as independent scattering mechanisms.

We also examine mobility using the conventional approach based on the Boltzmann transport theory. The interface roughness scattering rate in the Born approximation is[18]

$$
\begin{aligned}
\frac{1}{\tau} = \frac{m^* e^2 E_{\mathrm{avg}}^2 \Delta L_z^2 L_{x,y}^2}{2\hbar^3}\int_0^{2\pi} E^{-k^2L_{x,y}^2\sin^2(\theta/2)} \\
\times[1 - \cos(\theta)]d\theta,
\end{aligned}
\tag{10}
$$

where the E_{avg} is the average field given by $E_{\mathrm{avg}} = \int Ez|\psi(z)|^2dz$.

IV. RESULTS

In the first results presented here we examine a series of samples in which the barrier layer is $Al_{0.27}Ga_{0.73}N$. The barrier thickness is altered from a high value of 50 to 6 nm. The measured sheet charge as a function of the barrier thickness is shown in Fig. 1. We find that we can get a good fit to

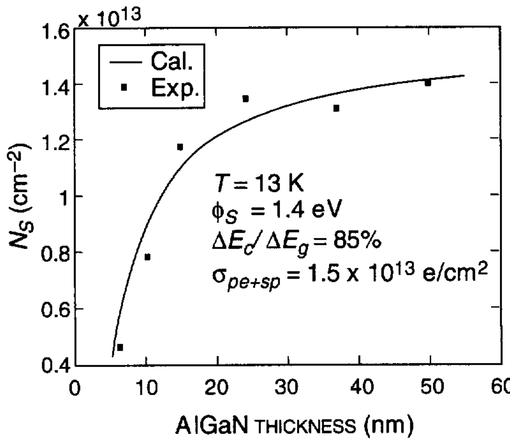

FIG. 1. Two-dimensional sheet charge density as a function of AlGaN barrier thickness. The Al mole fraction in the barrier is 27%.

the experiments with a set of parameters shown in the legend of Fig. 1. These parameters are kept fixed for the other theoretical fits. Thus the polarization charge is simply scaled with Al composition for other results according to Eq. (5).

Results of Fig. 1 show that the sheet charge is essentially unchanged as long as the barrier thickness is above 25 nm but drops rapidly as the thickness falls below this value. For barrier thickness below 5 nm the sheet charge is negligible. Of course the value of barrier thickness at which the charge in the 2D channel vanishes depends on the surface potential. In our study we find that the surface potential (Schottky barrier) is 1.4 V.

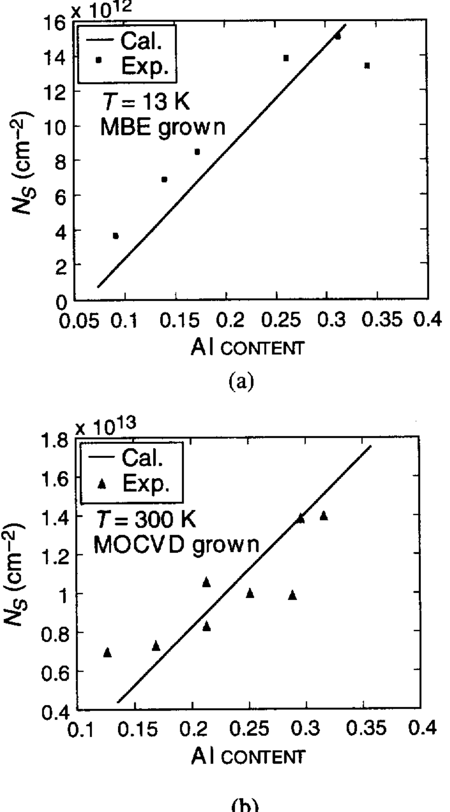

FIG. 2. Sheet charge vs Al content in the barrier for (a) MBE grown and (b) MOCVD grown samples. The solid lines are theoretical results using the charge control model presented and the parameters given in Fig. 1.

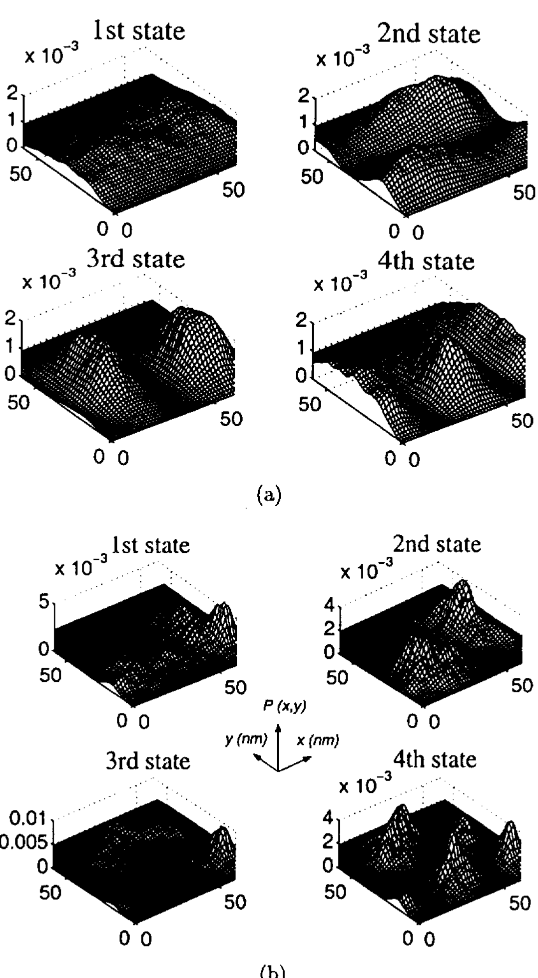

FIG. 3. Electronic states in the HEMT for an interface roughness described by a lateral extent of 15 Å and a height of 2.5 Å. (a) Results for a case where the barrier Al composition is 9%. (b) Results for a case where the barrier Al composition is 22%.

In Figs. 2(a) and 2(b) we show the results of sheet charge as a function of Al composition in the barrier for the MBE and MOCVD samples at temperature 13 and 77 K, respectively. The barrier thickness for MBE and MOCVD samples is 25 and 20 nm, respectively. We find that there is a reasonable agreement between the theoretical model and the experiments. For the MBE sample, our calculation is smaller than the experimental data. We suggest this could be caused by the Al composition accuracy measured in the experiment. By increasing the Al composition of the experimental data by 4%, we are able to achieve a reasonable agreement between our calculation and the experimental data. (More needs to be written about the Al composition accuracy.)

Figure 3 shows how interface roughness influences the electronic states. We show the nature of the wave functions of the electronic levels in the 750×750 Å region simulated. We assume that the interface roughness is described by islands that are 2.5 Å in height and have a 15 Å lateral extent.

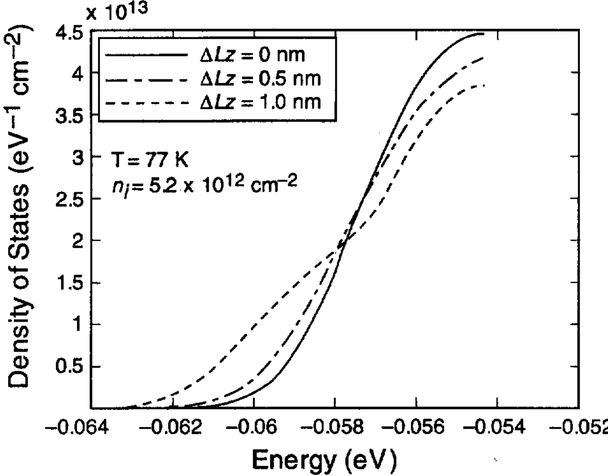

FIG. 4. Density of states in the HFET channel and the dependence on interface roughness.

Figures 4(a) and 4(b) are for cases with 9% and 20% Al composition, respectively. We see that for low Al composition sample, the low-lying states are coupled to the entire sample and only slightly vary from the wave functions for a perfect interface. This suggests at low Al content, the electron wave functions are extended and the interface roughness effect can be adequately treated by perturbation theory (Born approximation). However, at higher Al composition, we see that the low lying states are highly localized due to the very strong effect of interface disorder in the system. The Born approximation is no longer valid in dealing with the low lying states. Consequently, we use the Kubo–Greenwood formula to obtain the transport properties.

To examine the effects of interface roughness on density of states. The eigenvalues of the problem are solved and density of states is obtained using a broadening function of 20 meV. The results are shown in Fig. 4. We note that for a perfect smooth interface there is a bandtail at the low energy side arising from the finite volume used in the simulation and the broadening function. However, as the roughness increases the bandtail broadens significantly. The states at the low energy tail are localized as shown in Fig. 3.

To examine the effect of interface roughness on mobility at low temperatures we examine the mobility of the 2DEG at 13 K as a function of interface roughness island height. The interface is represented by a random placement of A and B type islands at the interface region. Here A represents the barrier region and B the GaN region. The lateral extent of the islands is kept fixed at 15 Å. In Fig. 5 we show how the mobility values change as the island height changes from zero (perfect interface) to 15 Å for various Al compositions. The sheet charge value for each composition corresponds to the results shown in Fig. 2. We see that the relative effect of interface roughness scattering increases as the barrier Al composition increases as can be expected. Also shown in the figure are the mobility values obtained from the Born approximation. We see that at high barrier composition where localization effects are significant the Kubo formalism gives a lower mobility. This is since the formalism includes phonon assisted hopping effects which are not included in the Born approximation. At low barrier compositions there is little difference between the two formalisms.

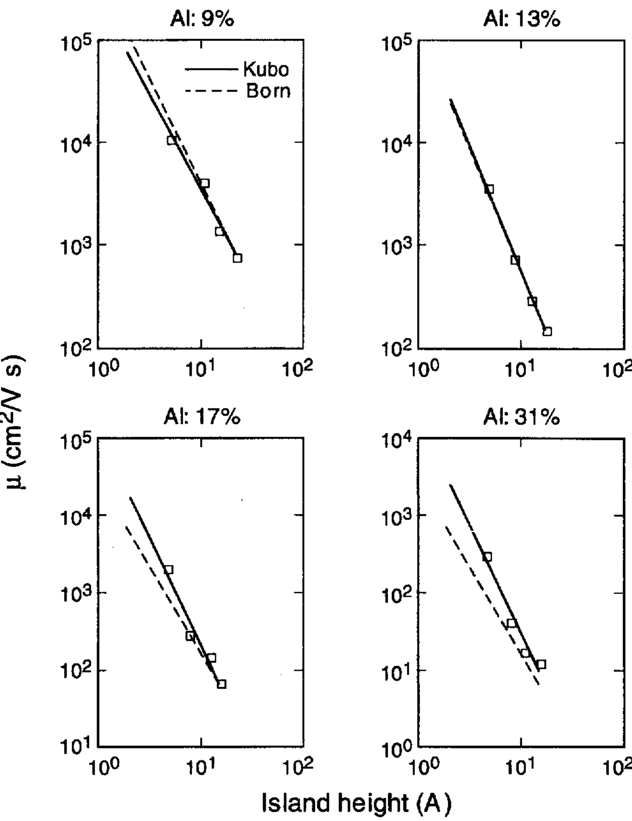

FIG. 5. Dependence of mobility in the channel on island height. Results are shown using Kubo formalism (calculated points are plotted along with a best fit) and Born approximation.

In Fig. 6 we present experimental and theoretical results on mobility versus sheet charge at low temperature. It is important to clarify how the experimental results have been obtained. The experimental results are measured for each Al composition with specific sheet charge density. The theoret-

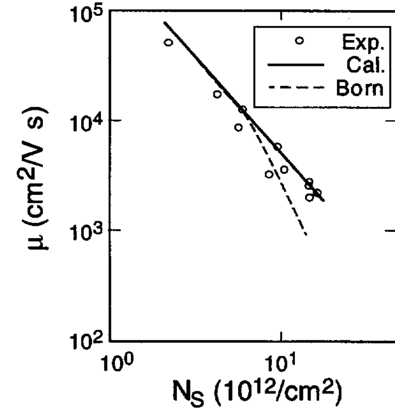

FIG. 6. Mobility vs sheet charge density. The experimental results are obtained from samples with varying Al mole fraction in the barrier region. The theoretical results use the same interface roughness parameters for all cases.

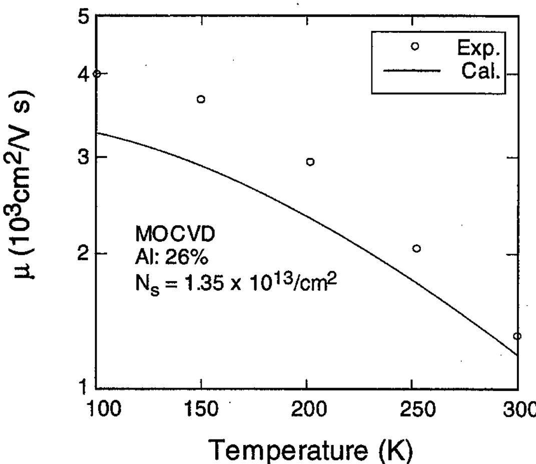

FIG. 7. Temperature dependence of mobility of MOCVD grown samples. Also shown are theoretical results.

ical results are calculated assuming that the islands describing the interface roughness have the same parameters independent of the barrier composition. Of course a higher barrier composition produces a larger potential fluctuation. The interface roughness is expected to be defined by the GaN growth and is thus expected to be the same regardless of the barrier composition. Mobility versus sheet charge results using this model is shown in Fig. 6. We find that there is an excellent agreement over the entire range of the sheet charge values. The dashed curve represents the results by using Eq. (10). We see that the Boltzmann equation based results provide good agreement at low Al composition for the reason as explained above.

In Fig. 7 we show a fit to mobility data from MOCVD samples. We find that in the cases studied, the MOCVD interface roughness value needed to explain the data is somewhat larger than the values needed for MBE samples. The value needed for MOCVD samples is 3.0 Å compared to the value of 2.5 Å for MBE samples. In both cases we assume a lateral extent of islands of 15 Å. Figure 7 shows the temperature dependence of mobility along with the theoretical fit. Results are for a sample with 26% Al content in the barrier. The sheet charge is 1.3×10^{13} cm^{-2}. The experimental results are for Hall mobility while the theoretical results are for drift mobility. Our fit gives a Hall factor of 1.2.

V. CONCLUSIONS

In this article we have presented theoretical and experimental studies on charge control and mobility in GaN/AlGaN HFETs grown by MBE and MOCVD. We find that the sheet charge density in the HFET channel is controlled by polarization effects and barrier thickness. A careful fit to the data has allowed us to provide fairly accurate values for the Schottky barrier height and the coefficients controlling the polarization charges (see Fig. 1). We have also examined the dependence of the two-dimensional electron gas mobility on interface roughness, Al composition, and temperature. A fit to the experimental data has allowed us to extract interface roughness parameters for both MBE and MOCVD grown samples. Our study illustrates the importance of interface roughness in controlling localized state density and transport.

ACKNOWLEDGMENTS

This work has been supported by Grant Nos. F001681 and F000629 from the U.S. Office of Naval Research. The work at UC Santa Barbara has been supported by the ONR IMPACT Program.

[1]I. Akasaki, H. Amano, S. Nagahama, T. Tanaka, and M. Kaike, Jpn. J. Appl. Phys., Part 2 **34**, L1517 (1995).
[2]S. Nakamura, M. Senoh, N. Iwasa, S. Nagahama, T. Yamada, and T. Mukai, Jpn. J. Appl. Phys., Part 2 **34**, L1332 (1995); S. Nakamura, M. Senoh, S. Nagahama, N. Iwasa, T. Yamada, T. Matsushita, Y. Sugimoto, and H. Kiyoku, Appl. Phys. Lett. **69**, 3034 (1996).
[3]G. E. Bulman *et al.*, Electron. Lett. **33**, 1556 (1997).
[4]M. P. Mack, A. Abare, M. Aizcorbe, P. Kozodoy, S. Keller, U. K. Mishra, L. Coldren, and S. DenBaars, MRS Internet J. Nitride Semicond. Res. **2**, 41 (1997).
[5]O. Aktas, Z. F. Fan, A. Botchkarev, S. N. Mohammad, M. Roth, T. Jenkins, L. Kehias, and H. Morkoc, IEEE Electron Device Lett. **18**, 293 (1997).
[6]M. S. Shur and M. A. Kahn, MRS Bull. **22**, 44 (1997).
[7]Y. F. Wu, S. Keller, P. Kozodoy, B. P. Keller, P. Parikh, D. Kapolnek, S. P. DenBaars, and U. K. Mishra, IEEE Electron Device Lett. **18**, 290 (1997).
[8]U. K. Mishra, Y. F. Wu, B. P. Keller, S. Keller, and S. P. DenBaars, IEEE Trans. Microwave Theory Tech. **46**, 756 (1998).
[9]R. Dimitrov, L. Wittmer, H. P. Felsl, A. Mitchell, O. Ambacher, and M. Stutzmann, Phys. Status Solidi A **168**, R7 (1998).
[10]F. Bernardini, V. Fiorentini, and D. Vanderbilt, Phys. Rev. B **56**, R10024 (1997).
[11]W. Q. Chen and S. K. Hark, J. Appl. Phys. **77**, 5747 (1995).
[12]O. Ambacher *et al.*, J. Appl. Phys. **85**, 3222 (1999).
[13]C.-K. Sun, S. Keller, T.-L. Chiu, G. Wang, M. S. Minsky, J. E. Bowers, and S. P. DenBaars, IEEE J. Sel. Top. Quantum Electron. **3**, 731 (1997).
[14]I. P. Smorchkova *et al.*, J. Appl. Phys. **86**, 4520 (1999).
[15]A. Polian, M. Grimsditch, and I. Grzegory, J. Appl. Phys. **79**, 3343 (1994).
[16]*Properties of Group III Nitrides*, edited by J. H. Edgar (INSPEC, London, 1994).
[17]Y. Zhang and J. Singh, J. Appl. Phys. **85**, 587 (1999).
[18]See, for example, D. K. Ferry, *Semiconductors* (Macmillan, New York, 1991).

CUMULATIVE AUTHOR INDEX

All authors published to date in Volume 18 are listed alphabetically with the issue (in parentheses) and page numbers following the dash. An (E) after the page number indicates Erratum.

Abadal, G.–(2) 612
Abstreiter, G.–(4) 2187
Achermann, M.–(3) 1701
Adachi, Hiroshi–(2) 1003, 1093
Adamcyk, M.–(3) 1488
Aggarwal, Sanjeev–(4) 1919
Ahn, Dong-Hoon–(2) 1085
Ahn, Kwang-Soon–(1) 140
Ahn, S.–(2) 884
Ahn, Saeyoung–(2) 933
Ahopelto, J.–(4) 1861
Akita, Seiji–(1) 104; (2) 661
Al-Bayati, Amir–(1) 445
Albers, J.–(1) 414
Alberti, A.–(2) 717
Alford, T. L.–(1) 221; (3) 1435
Alkemade, P. F. A.–(2) 706
Alluri, Prasad–(4) 2242
Almuneau, G.–(3) 1601
Alonso, Kevin–(2) 1009
Alonso, M.–(4) 2128
Alvarez, Lydia–(1) 82
Amaratunga, G. A. J.–(2) 914
Ambacher, O.–(2) 733
Ambacher, Oliver–(2) 757
Ando, Toshihiro–(2) 1089
Andrew, N. L.–(4) 2300
Andrews, A. M.–(4) 2066
Andronov, A. N.–(2) 980
Anjum, Dalaver–(4) 2011
Anselm, K. A.–(3) 1453
Anselmetti, D.–(2) 617
Aoki, Toyohiro–(3) 1598
Arai, Toyoko–(2) 648
Arie, Takayuki–(1) 104
Arkles, Barry–(4) 2011
Armour, D.–(1) 435
Arscott, S.–(1) 150
Arthur, C. B.–(2) 683
Asamizu, Hirokuni–(4) 1957
Asano, Tanemasa–(2) 877
Asnin, V.–(3) 1522
Aspnes, D. E.–(4) 2229
Athavale, Satish D.–(2) 765

Baba, Akiyoshi–(2) 877
Bae, J.–(4) 2309
Bae, Young-Ho–(2) 1006
Bai, Chunli–(1) 64; (4) 1858
Baierle, R.–(4) 2160
Baik, Dong-Ki–(2) 1085
Baik, Hong Koo–(2) 972, 1035, 1040; (4) 1953
Bailey, Glenn–(4) 1949
Baillargeon, J. N.–(3) 1453
Baklanov, M.–(1) 303
Bąk-Misiuk, J.–(3) 1697
Balasubramanian, N.–(2) 700
Balderas-Navarro, R. E.–(4) 2224
Baldereschi, A.–(4) 2114
Ball, M. A.–(3) 1583
Ballestad, A.–(3) 1488
Balooch, Mehdi–(1) 172
Bandy, Steve–(2) 968
Barsky, M.–(3) 1642
Barth, W.–(2) 896
Bashir, R.–(2) 695; (4) 2008
Bass, R.–(3) 1650
Bass, Robert–(1) 107
Bauer, G.–(4) 2187, 2263
Baumann, F. H.–(4) 2034
Beach, R. A.–(4) 2044
Beadie, G.–(3) 1614
Beaudoin, M.–(3) 1435, 1545
Bechstedt, F.–(4) 2215
Bechtler, L.–(1) 602
Bélier, B.–(1) 90
Bell, A.–(4) 2300
Beltram, F.–(4) 2119
Bendé, André Boyoguéno–(4) 1962
Bender, Hugo–(1) 242
Bennett, B. R.–(3) 1650
Bennett, J. C.–(1) 60
Bennett, Joe–(1) 503
Beresford, R.–(3) 1431
Berezovsky, J.–(4) 2057
Bernholc, J.–(4) 2215
Berry, J. J.–(3) 1692
Berthod, C.–(4) 2114
Bertness, K. A.–(3) 1426
Beton, P. H.–(1) 13
Beyer, S.–(3) 1562
Bhattacharya, P.–(3) 1706
Bhattacharya, Pallab–(3) 1502
Bian, Zailong–(1) 252
Bindley, U.–(3) 1443, 1518
Binggeli, N.–(4) 2114
Binh, Vu Thien–(2) 956
Bishop, H. E.–(2) 900
Biswas, S.–(1) 440
Blamire, M. G.–(2) 761
Bleidiessel, G.–(4) 1861
Bleiler, R. J.–(1) 440
Block, T. R.–(3) 1642, 1658
Blom, H.-O.–(4) 1906
Blum, O.–(3) 1605
Bocelli, S.–(2) 721
Bogart, Katherine H. A.–(2) 834
Boggess, Thomas F.–(3) 1623
Bohn, P. W.–(1) 144; (4) 2030
Boisen, A.–(2) 612
Bonanni, A.–(4) 2224
Bonanni, B.–(4) 2263
Bonnafé, J.–(1) 90
Booij, W. E.–(2) 761
Boos, J. B.–(3) 1650
Borden, P.–(1) 602
Boswell, F. W.–(1) 60
Boucaud, P.–(3) 1728
Bow, J. S.–(2) 729
Bower, R. W.–(2) 962
Bracker, A. S.–(3) 1650
Bradshaw, J. L.–(3) 1628
Brandow, Susan L.–(1) 107
Brandt, O.–(4) 2290
Braun, W.–(3) 1545; (4) 2210
Bridges, G. E.–(2) 626
Brierley, M.–(2) 900
Brillson, L. J.–(4) 2309
Brown, April S.–(3) 1448
Brunner, K.–(4) 2187
Bruno, J. D.–(3) 1628
Büchel, D.–(1) 418
Bukovec, P.–(2) 1097
Burden, A. P.–(2) 900, 1051
Buschert, John R.–(3) 1518
Butcher, M. J.–(1) 13
Cai, C.–(4) 2096
Cai, W. Z.–(3) 1633
Caldas, M. J.–(4) 2160
Cale, Timothy S.–(1) 267
Cano-Aguilar, O.–(3) 1553
Cantoni, M.–(4) 1915
Cardinaud, Ch.–(4) 1861
Cardon, F.–(4) 1942
Carey, J. D.–(2) 1051
Carnera, A.–(1) 519
Cartier, E.–(4) 2153
Casali, R. A.–(4) 2160
Castagne, M.–(1) 90
Caymax, Matty–(1) 405
Cerc-Korošec, R.–(2) 1097
Cerezo, A.–(1) 328
Cescato, Lucila–(2) 713
Cha, S. N.–(2) 905, 984
Chakhovskoi, A. G.–(2) 980
Chalamala, Babu R.–(4) 1825, 1919
Chang, C. M.–(2) 729
Chang, J. H.–(3) 1530
Chang, K. L.–(3) 1590, 1638
Chang, M.-C.–(1) 580
Chang, Mei–(1) 237
Chang, W.–(3) 1619
Chantis, A. N.–(4) 2109
Chao, I-Na–(3) 1720
Charlat, P.–(1) 122
Chason, E.–(3) 1431
Chassé, T.–(4) 1973
Chaudhry, S.–(1) 428
Chavarkar, P.–(4) 2066
Chee, J. K.–(2) 888, 923
Chen, Huajie–(4) 2284
Chen, Jian–(2) 1048
Chen, Jing-Yuh–(2) 751
Chen, L. C.–(4) 2057
Chen, L. J.–(4) 1929
Chen, Ling–(1) 237
Chen, Linghui–(1) 221
Chen, M. C.–(4) 1929
Chen, P. J.–(1) 580; (4) 2047
Chen, S.-F.–(2) 636
Chen, S. H.–(1) 10; (2) 911
Chen, Wen-Chang–(1) 201
Chen, Y.–(4) 2313
Chen, Y. C.–(3) 1522, 1642
Chen, Y. H.–(4) 2271
Chen, Y. W.–(4) 1903
Chen, Yefan–(3) 1514
Cheng, G. S.–(1) 10
Cheng, K. Y.–(3) 1590, 1645, 1688
Cheng, Shiou-Ying–(2) 751
Cheng, T. S.–(4) 2300
Cheng, X.-Y.–(2) 636
Cheng, Y. J.–(4) 1967
Cheung, S. P.–(2) 626
Chi, Eung Joon–(2) 1035, 1040
Chi, G. C.–(2) 729
Chia, V. K. F.–(1) 472
Chim, W. K.–(4) 1853
Chin, T. P.–(3) 1642, 1658
Cho, A. Y.–(3) 1453
Cho, Boklae–(2) 868
Cho, D. H.–(3) 1461
Cho, H.–(1) 293
Cho, M. W.–(3) 1530
Cho, T. H.–(1) 208
Cho, Won-Ki–(2) 1085
Choi, Chang-Auck–(2) 1006
Choi, Chang Ju–(2) 811
Choi, Duck Kyun–(4) 1923
Choi, Eun-Suck–(1) 262
Choi, Il Hyun–(2) 811
Choi, J. H.–(2) 888, 923, 984, 989
Choi, W. B.–(2) 888, 923, 1054
Choi, Y. S.–(2) 888, 984
Choquette, K. D.–(3) 1605
Chow, D. H.–(3) 1439
Christensen, D. H.–(3) 1510
Chuang, M. H.–(4) 1929
Chung, D. S.–(2) 1054
Chung, M. S.–(2) 919
Chung, S. J.–(3) 1583
Chung, Sukmin–(2) 868
Chung, Y. S.–(1) 197
Chuvilin, A. L.–(2) 1059
Chyi, J. I.–(3) 1453
Cich, Michael J.–(3) 1566
Cirelli, R.–(1) 317
Clarke, D. R.–(3) 1601
Clarysse, T.–(1) 361, 369, 381, 393, 435
Clarysse, Trudo–(1) 555
Coldren, C. W.–(3) 1480
Coldren, L. A.–(3) 1601
Cole, D. A.–(1) 440
Collart, E. J. H.–(1) 435, 462, 468, 493
Colonell, Jennifer I.–(2) 834
Conner, J. R.–(3) 1653
Contreras-Puente, G.–(3) 1553
Cook, J. M.–(2) 848, 856
Cooke, G. A.–(1) 493
Copeland, K. A.–(1) 307
Corbin, E. A.–(4) 2088
Correia, A.–(2) 1068
Cortez, S.–(4) 2232
Covington, Billy C.–(1) 346
Crowell, P. A.–(4) 2057
Crozes, Th.–(1) 122
Cruz, Nilson C.–(2) 713
Cuberes, M. T.–(4) 2153
Cui, Jie–(4) 2072
Cui, P.–(1) 10
Cullis, A. G.–(1) 435
Cullis, Tony–(1) 445
Curless, J. A.–(3) 1653; (4) 2139, 2242
Current, M. I.–(1) 468
Cutler, P. H.–(2) 919
Czerwosz, E.–(2) 1064

Dabrowski, J.–(4) 2160
Dagenais, M.–(3) 1619
Dai, N.–(3) 1720
Dang, X. Z.–(4) 2304
D'Arrigo, Giuseppe–(1) 576
Das, Amal K.–(4) 1847
Dash, Raj–(4) 2011
Dashiell, M. W.–(3) 1728
Davies, M.–(3) 1488
Davis, R. F.–(4) 2082
Davis, Z. J.–(2) 612
Däweritz, L.–(4) 2052, 2204
Day, P. S.–(3) 1623
De, I.–(1) 338
Debski, T.–(2) 896

Decker, M. A.–(1) 483
de Cock, G.–(1) 468
De Franceschi, S.–(4) 2119
Delaey, L.–(1) 303
Delgado, S. M.–(3) 1496
Demchenko, D. O.–(4) 2109
Demkov, A. A.–(4) 2242
de Moraes, Mário B.–(2) 713
DenBaars, Steven–(4) 2322
Deng, S. Z.–(2) 1048
Deng, Zhongsheng–(4) 2001
Dennis, M.–(1) 572
Denton, J.–(2) 695
de Rooij, N. F.–(2) 617
Deshmukh, P. R.–(2) 873
Despont, M.–(2) 617
Desse, F.–(1) 529
Desvoivres, L.–(1) 156
Detavernier, C.–(4) 1942
Dev, B. N.–(4) 1847
De Wolf, P.–(1) 361, 418, 540
De Wolf, Peter–(1) 405, 555
Dharmasena, G.–(1) 307
Díaz-Arencibia, P.–(3) 1526
Didziulis, Stephen V.–(1) 69
Dimitrov, R.–(2) 733
Ding, Ding–(1) 21
Dirscherl, Kai–(2) 621
Dłużewski, P.–(2) 1064
Dobisz, Elizabeth A.–(1) 107
Dobner, Armin–(2) 757
Domagała, J. Z.–(3) 1697
Donaton, R. A.–(4) 1942
Dong, J. W.–(4) 2057
Donnelly, V. M.–(2) 820
Donnelly, Vincent M.–(2) 834
Doolittle, William A.–(3) 1448
Dorignac, D.–(3) 1493
Dovidenko, Katharine–(4) 2011
Dowd, P.–(3) 1545
Dowsett, M. G.–(1) 493
Droba, M.–(4) 2279
Droopad, R.–(3) 1653; (4) 2139, 2242
Du, J.–(4) 1906
Duane, M.–(1) 572
Dubos, P.–(1) 122
Dupin, J. P.–(2) 956
Durrell, J. H.–(2) 761
Dziuban, J.–(2) 1115

Eberl, K.–(3) 1557
Eckert, R.–(2) 644
Edgell, M. J.–(1) 440
Edo, Ryou–(2) 774
Edrei, R.–(1) 41
Edwards, H.–(1) 566
Egelhoff, W. F., Jr.–(4) 2047
Eisenbeiser, K. W.–(3) 1653; (4) 2139
Eisenbraun, Eric–(4) 2011
El-bjeirami, Oussama–(1) 69
Elmoumni, A.–(3) 1522
Elsass, C.–(4) 2322
Emmenegger, Ch.–(2) 665
Engelmark, F.–(4) 1906
English, J. H.–(3) 1601
Eshraghi, S. A.–(1) 428
Esser, N.–(4) 2210
Etoh, K.–(1) 94
Etou, Yoshihiro–(2) 1089

Faircloth, Brian–(4) 1866
Falgayrettes, P.–(1) 90
Fang, X. M.–(3) 1720
Fang, Z.–(1) 472
Fazan, P.–(4) 1915
Feenstra, R. M.–(4) 2284
Fei, G. T.–(1) 10
Fejes, P. L.–(4) 2242
Feke, G. D.–(1) 136
Felch, S. B.–(1) 472
Feld, S.–(3) 1619
Feng, K.–(4) 1997
Feng, Shun-Ching–(2) 751
Feng, Y. T.–(2) 1048
Feng, Yan–(3) 1488
Fewster, P. F.–(4) 2300
Filip, Valeriu–(2) 937, 1073, 1077
Finder, J. M.–(3) 1653; (4) 2139
Findlay, J.–(1) 100
Fink, R. L.–(2) 968
Fitzpatrick, B. J.–(3) 1711
Flátte, M. E.–(3) 1623
Foad, M. A.–(1) 435, 462, 468
Foad, Majeed A.–(1) 445
Foisy, M.–(1) 560
Forrest, R. D.–(2) 1051
Fourmeaux, R.–(3) 1493
Foxon, C. T.–(4) 2300
Frackoviak, J.–(1) 317
Franciosi, A.–(4) 2119, 2263
Franklin, J.–(3) 1645
Frantz, Peter–(1) 69
Frey, L.–(2) 976
Friday, J. M.–(2) 900
Frisbie, C. Daniel–(2) 632
Fritz, I. J.–(3) 1605
Froyen, Ludo–(1) 242
Fu, Wenning–(3) 1467
Fuard, D.–(2) 793
Fujikuwa, Hajime–(4) 2100
Fujisaki, Yoshihisa–(1) 231
Fujita, Hiroyuki–(2) 607
Fukushima, Kimitake–(2) 607
Furdyna, J. K.–(3) 1443, 1518

Gaboriau, F.–(4) 1861
Gamo, Mikka Nishitani–(2) 1089
Ganguli, Seshadri–(1) 237
García-Cerda, L. A.–(1) 288
Garnæs, Jørgen–(2) 621
Garner, D. M.–(2) 914
Garno, J. P.–(4) 2034
Gärtner, G.–(2) 997, 1000
Garulli, A.–(4) 2263
Gaworzewski, P.–(1) 477
Gebauer, J.–(3) 1594
Gebhardt, R. K.–(4) 1973
Gebhardt, W.–(2) 733
Geer, Robert E.–(1) 252
Geittner, P.–(2) 997, 1000
Genolet, G.–(2) 617
Georgiev, Nikolai–(3) 1586
Geva, M.–(3) 1476
Ghaemi, H.–(3) 1522
Ghose, S. K.–(4) 1847
Gierałtowski, W.–(2) 1064
Gilbreath, G. C.–(3) 1609
Gilkes, M. J.–(2) 948
Gillen, Greg–(1) 503
Gnade, Bruce E.–(4) 1919
Goeckner, M. J.–(1) 472
Göhl, A.–(2) 1031
Goldberg, R. D.–(1) 435
Goldman, R. S.–(3) 1502
Gong, Qian–(1) 21
Gonsalves, Kenneth E.–(1) 325
González, L.–(4) 1980
González, M. U.–(4) 1980
González, Y.–(4) 1980
González-Hernández, J.–(1) 288
Goodall, J. G.–(1) 100
Goodman, Rory S.–(1) 191
Goorsky, M. S.–(3) 1658
Górecka-Drzazga, A.–(2) 1115
Gossard, A. C.–(4) 2197
Gossmann, Hans-J.–(1) 489
Gotoh, M.–(4) 2165
Gotoh, Y.–(2) 1018
Grabiec, P.–(2) 896
Granger, C.–(1) 514
Granger, C. N.–(1) 483
Grassi, E.–(3) 1435
Graves, D. B.–(2) 820
Gray, A. L.–(3) 1496
Gray, J. T.–(1) 580
Green, L. H.–(1) 144
Greene, L. H.–(4) 2030
Gregory, R. B.–(4) 2242
Greve, D. W.–(4) 2284
Grey, F.–(2) 612
Griesche, J.–(1) 524
Griffis, D. P.–(1) 509
Gril, R.–(1) 60
Grimaldi, M. G.–(2) 717, 721
Grober, R. D.–(1) 136
Gröning, O.–(2) 665
Gröning, P.–(2) 665
Grundbacher, R.–(3) 1642
Grützner, G.–(4) 1861
Gundlach, Heidi–(1) 252
Günther, B.–(2) 1031
Güntherodt, H.-J.–(2) 644
Guo, C.-Z.–(3) 1545
Guo, S. P.–(3) 1522, 1534
Guo, X.–(4) 1915
Guryanov, G. M.–(1) 509
Gutsche, Martin U.–(2) 765
Gwak, J.-H.–(2) 1101, 1106

Habermann, T.–(2) 1031
Haefke, H.–(2) 644
Hagmann, M. J.–(2) 1119
Hagmann, Mark J.–(2) 1009, 1014
Hagon, J. P.–(4) 2088
Hahm, Sung-Ho–(2) 1006
Haiml, M.–(3) 1701
Halicioglu, Timur–(4) 2005
Hall, E.–(3) 1601
Hallmark, J. A.–(3) 1653; (4) 2139
Hamza, Alex V.–(1) 172
Han, I. T.–(2) 905, 1054
Han, J.-P.–(4) 1915
Han, Licheng M.–(2) 799
Han, S. K.–(1) 197
Hanada, H.–(3) 1530
Hanada, T.–(4) 2313
Hansen, O.–(2) 612
Hansen, W.–(3) 1562
Hantschel, T.–(1) 361, 418
Hantschel, Thomas–(1) 555
Hara, Shigeta–(1) 7
Harris, J. S.–(3) 1480
Hartford, C. L.–(1) 401
Hartford, E. J.–(1) 401
Hartman, J. D.–(4) 2082
Hartnagel, H. L.–(4) 2279
Hasegawa, Hideki–(4) 2100
Hasenberg, T. C.–(3) 1623
Hayashi, K.–(2) 1018
Hebert, F.–(4) 2008
Hedlund, C.–(4) 1906
Heidari, B.–(4) 1861
Heitmann, D.–(3) 1562
Hellemans, L.–(1) 418, 586
Herbison, D.–(2) 914
Hernández-Calderón, I.–(3) 1526, 1542
Hernández-Ramirez, L. M.–(3) 1526
Hernández-Ramírez, L. M.–(3) 1542
Heroux, J. B.–(3) 1484
Hessman, D.–(1) 136
Hey, R.–(4) 2128
Heyn, Ch.–(3) 1562
Heyvaert, Ilse–(1) 242
Higashiwaki, Masataka–(3) 1672
Hilber, W.–(4) 2224
Hilfiker, J. N.–(4) 2242
Hill, C. J.–(4) 2044
Hillard, R.–(1) 450
Hillard, R. J.–(1) 389
Hines, Danielle–(2) 765
Hingerl, K.–(4) 2224
Hinsberg, W. D.–(4) 1874
Hirai, Nobumitsu–(1) 7
Hitzman, C. J.–(1) 440, 483
Hiyamizu, S.–(3) 1549, 1572, 1576
Hiyamizu, Satoshi–(3) 1579, 1598, 1672
Hizukuri, Masafumi–(2) 877
Ho, Paul S.–(1) 208
Hobbs, C.–(1) 293
Hoefnagels, Johann–(4) 2011
Hoerman, B. H.–(4) 2146
Hoffman, A.–(1) 41
Hoffmann, T.–(4) 1861
Hoffnagle, J.–(4) 1874
Hohmura, Ken I.–(2) 661
Hoke, W. E.–(3) 1638
Holland, E. R.–(2) 994
Holloway, P. H.–(1) 16
Holý, V.–(4) 2187, 2263
Hong, J.–(1) 283
Hong, M.–(3) 1453, 1688
Hong, S. K.–(4) 2313
Hong, S. S.–(2) 989
Hong, Soon-ku–(3) 1514
Hood, C.–(2) 900
Hoppe, M.–(1) 283
Höricke, M.–(4) 2128
Horn, K.–(4) 2128
Hosaka, S.–(1) 94
Hosono, A.–(2) 929, 976, 1081
Houle, F. A.–(4) 1874
Hsieh, K. C.–(3) 1590, 1638, 1688
Hsieh, T. E.–(2) 639
Hsing, R.–(3) 1658
Hsu, C. H.–(1) 283
Hsu, Chin-Fa–(2) 805
Hu, J.–(2) 636
Hu, Yao Zhi–(4) 1949
Hu, ZhiQiang–(4) 2027
Huang, F. K.–(1) 440
Huang, S. M.–(4) 1853
Huang, Wenhao–(4) 2027
Hudek, P.–(2) 896
Huerta, J.–(3) 1716
Hughes, O. H.–(4) 2300
Huh, Chul–(1) 55
Hung, W. C.–(2) 729
Hunt, C. E.–(2) 980
Hunter, J. L.–(1) 509
Hurt, E. H.–(4) 2082
Hwang, H. J.–(1) 458
Hwang, Ho-Jung–(1) 595
Hwang, Hyun-Deog–(2) 1085
Hwang, J. S.–(4) 1967
Hwang, J. W.–(1) 197
Hwang, W. C.–(4) 1967
Hyun, I. S.–(1) 197

Iannuzzi, M.–(2) 721
Ibbetson, J. P.–(4) 2197
Ibbetson, James–(4) 2322
Ichizli, V. M.–(4) 2279
Iguchi, Yasuhiro–(4) 1957

Ikawa, Seiji–(3) 1672
Ikossi-Anastasiou, K.–(3) 1609
Ils, A.–(4) 1915
Ilver, L.–(3) 1697
Irene, E. A.–(1) 279
Isakovic, A.–(4) 2057
Ishida, Makoto–(2) 1044
Ishikawa, H.–(3) 1576
Ishikawa, J.–(2) 1018
Ishikawa, T.–(3) 1553
Ishikawa, Yasuhiko–(4) 2100
Itoga, Kenji–(2) 774
Itoh, J.–(2) 952, 1111
Itoh, Junji–(2) 1073, 1077
Ivanov, Z. G.–(1) 25
Iwai, Hidekazu–(4) 2072
Iwamoto, Masakazu–(2) 877
Iwasaki, H.–(4) 2165

Jacobs, K.–(4) 2300
Jacobson, Dale–(1) 489
Jakob, M.–(2) 733
Jang, J. E.–(2) 1101, 1106
Jang, Jin–(2) 933
Jansen, P.–(1) 586
Jansen, Philippe–(1) 555
Jaros, M.–(4) 2088
Je, Jung Ho–(4) 1953
Jeffree, C. E.–(1) 100
Jennings, D.–(1) 462, 468
Jeon, C. W.–(1) 197
Jia, A. W.–(3) 1684
Jiang, Wei-hong–(1) 21
Jiang, Z. X.–(2) 706
Jin, Nong–(4) 2027
Jin, Sing–(1) 242
Jin, Y. W.–(2) 888, 923, 1101, 1106
Jøgensen, Jan Friis–(2) 621
Johnson, E.–(2) 700
Johnson, J. A.–(4) 2193, 2197
Johnson, M. B.–(1) 307; (3) 1583
Johnson, S. R.–(3) 1435, 1545
Johs, B.–(3) 1439
Jones, F. H.–(1) 13
Jones, K.–(1) 440
Jones, P. G. A.–(2) 900
Jonsson, L. B.–(4) 1906
Jou, M. J.–(2) 729
Joubert, O.–(1) 156; (2) 785, 793
Juang, M. H.–(4) 1937
Jung, J. E.–(2) 888, 905, 923, 984, 989, 1054, 1101, 1106
Jung, Jae Hoon–(2) 933
Jung, K. B.–(1) 16
Jung, S. J.–(2) 884
Jung, S. Y.–(2) 905, 923
Jurkovic, M. J.–(3) 1484

Kachi, Tsuyoshi–(1) 231
Kadoch, D.–(1) 572
Kadow, C.–(4) 2197
Kagadei, V. A.–(1) 454
Kaiser, S.–(2) 733
Kajiyama, Tisato–(1) 313
Kaloyeros, Alain–(4) 2011
Kaloyeros, Alain E.–(1) 252
Kam, C. H.–(4) 2274
Kamimoto, H.–(3) 1549, 1572
Kamo, Mutsukazu–(2) 1024
Kampen, T. U.–(4) 2077
Kampherbeek, B. J.–(1) 117
Kanemaru, S.–(2) 952, 1111
Kang, E. S.–(1) 458
Kang, J. H.–(2) 1054
Kang, Jeong-Won–(1) 458
Kang, Nam-Seok–(2) 1085
Kang, Tae Soo–(4) 1953
Kang, Taihee–(2) 868
Kanski, J.–(3) 1697
Karrer, Uwe–(2) 757
Kasai, Seiya–(4) 2100
Kästner, M.–(4) 2052
Kato, Y.–(3) 1684
Katzer, D. S.–(3) 1609, 1614
Kaushik, V. S.–(3) 1653; (4) 2139
Kavanagh, K. L.–(4) 2047
Kawakatsu, Hideki–(2) 607
Keenan, W. A.–(1) 472
Kegel, I.–(4) 2187
Keil, M.–(1) 307
Keister, J. W.–(4) 2174
Keller, M.–(3) 1557
Keller, Stacia–(4) 2322
Keller, U.–(3) 1701
Kelley, Tommie W.–(2) 632
Kelly, S.–(3) 1522
Kempf, James G.–(4) 2255
Khalil, N.–(1) 540
Khanin, V. V.–(1) 76
Khazov, A. Y.–(2) 900
Kikukawa, A.–(1) 94
Kim, Bongsoo–(2) 868
Kim, Boum Seock–(4) 1923
Kim, Dong-Joon–(1) 140
Kim, Gi Bum–(4) 1953
Kim, H. Y.–(2) 1054
Kim, Heon Chang–(2) 841
Kim, J1.–(2) 923
Kim, J. H.–(1) 197
Kim, J. K.–(3) 1601
Kim, J. M.–(2) 888, 905, 923, 984, 989, 1054, 1101, 1106
Kim, J. W.–(2) 888, 923, 984, 989
Kim, Jae-Sun–(1) 216
Kim, K. S.–(2) 884
Kim, Kijeong–(2) 868
Kim, M. S.–(2) 884
Kim, S. Y.–(1) 197
Kim, Seong-Jin–(3) 1680
Kim, Sung-Bock–(3) 1507
Kim, Tae-Young–(2) 1085
Kim, Yil Wook–(2) 811
Kimura, Chiharu–(2) 1024
Kinoshita, Haruhisa–(2) 1044
Kirchhoff, J. F.–(1) 440
Kitada, T.–(3) 1549, 1572, 1576
Kitada, Takahiro–(3) 1579, 1598
Kitamura, K.–(3) 1684
Kitano, Y.–(3) 1576
Kitchin, M. R.–(4) 2088
Kleiman, R. N.–(4) 2034
Klein, C.–(3) 1562
Klem, J. F.–(3) 1605
Klemens, F.–(1) 317
Klemens, F. P.–(2) 820
Klitzing, K. v.–(3) 1557
Knobel, R.–(3) 1692
Knorr, Andreas–(1) 252
Ko, H. J.–(4) 2313
Ko, Hang-ju–(3) 1514
Ko, Tze-Man–(1) 127
Kobashi, K.–(2) 1018
Kobayashi, M.–(3) 1684
Kodera, Itsuo–(2) 774
Koelle, U.–(3) 1545
Koide, Yasuo–(4) 1957
Koizumi, Satoshi–(2) 1024
Koleśnik, S.–(3) 1697
Koley, B.–(3) 1619
Kolodzey, J.–(3) 1728
Kolodziej, J. J.–(4) 2174
Kolstad, K.–(4) 2197
Kondo, T.–(2) 1018
Kopaev, Yu. V.–(3) 1668
Kopanski, J. J.–(1) 409, 414
Kortan, A. R.–(3) 1453, 1688
Kosarev, A. I.–(2) 980
Koyanagi, H.–(1) 94
Kozlovsky, V. I.–(3) 1538
Krajewski, J. J.–(3) 1688
Kramp, S.–(3) 1562
Krchnavek, Robert R.–(4) 1866
Krebs, O.–(4) 2232
Krishna, Sanjay–(3) 1502
Krüger, D.–(1) 477
Kruit, P.–(1) 117
Kucera, John-Paul–(1) 32
Kudo, Makoto–(2) 746
Kuhn, O.–(2) 612
Kuklewicz, C.–(1) 572
Kulisch, W.–(1) 418
Kumada, Teruhiko–(2) 774
Kumar, D.–(4) 2119
Kumar, N.–(2) 919
Kuo, H. C.–(3) 1645
Kuramochi, Hiromi–(4) 2072
Kurihara, Kenji–(2) 780
Kuriyama, R.–(3) 1576
Kurps, R.–(1) 477
Kurtz, S. R.–(3) 1605
Kushida-Abdelghafar, Keiko–(1) 231
Küttel, O. M.–(2) 665
Kuznetsov, V. L.–(2) 1059
Kwo, J.–(3) 1453, 1688
Kwon, O Sung–(2) 811

Labun, Andrew H.–(1) 267
Lai, J. T.–(2) 911
Lai, R.–(3) 1642
Lakhtakia, Akhlesh–(1) 32
Lambers, E.–(1) 283
Lan, Y. C.–(2) 911
Lanckmans, Filip–(1) 242
Lane, Jennifer–(1) 299
Lane, Sarah–(4) 2011
Lang, D. V.–(3) 1472
Langford, R. M.–(1) 100
LaRoche, J. R.–(1) 283
Larson, C.–(4) 1874
Larson, D. J.–(1) 328
Larson, Lawrence A.–(1) 346
Larson, M. C.–(3) 1480
Larson, P. R.–(1) 307
Larsson, P.–(1) 25
Lasell, R. A.–(1) 307
Latif, A.–(2) 761
La Via, F.–(2) 717, 721
Lay, T. S.–(3) 1453
Layadi, Nace–(1) 299
Lazzarino, M.–(4) 2119
Leclercq, J. L.–(1) 90
Lee, C. M.–(3) 1453
Lee, Dong-Gu–(2) 1085
Lee, H.–(2) 820; (4) 2193
Lee, H. W.–(2) 888, 923, 984, 989
Lee, J. G.–(1) 197
Lee, J. J.–(1) 514, 560
Lee, J. K.–(1) 208
Lee, J. T. C.–(2) 820
Lee, Jihwa–(3) 1507
Lee, John T. C.–(1) 299
Lee, Jong-Hyun–(2) 1006
Lee, Jung-Hee–(2) 1006
Lee, K. P.–(1) 293
Lee, Kyeong K.–(3) 1448
Lee, L. H.–(4) 1840
Lee, N. S.–(2) 888, 905, 923, 984, 989, 1054, 1101, 1106
Lee, N. Y.–(2) 884
Lee, Nam Yang–(2) 933
Lee, S.–(3) 1443, 1518
Lee, S. J.–(2) 1101, 1106
Lee, Se-Jong–(2) 972, 1035, 1040
Lee, Seunghwan–(1) 69
Lee, Sung-Man–(2) 972; (4) 1953
Lee, Szetsen–(2) 805
Lee, T. D.–(2) 1027
Lee, W.–(2) 900
Lee, Wei W.–(2) 799
Lee, Y. H.–(2) 1054
Lehrer, C.–(2) 976
Leite, J. R.–(4) 1991
Lenahan, P. M.–(4) 2169
Leone, Stephen R.–(1) 191
Levine, Timothy–(1) 237
Levinson, Joshua A.–(1) 172
Li, Bing-Zong–(4) 1942
Li, Guo-hua–(1) 21
Li, Hua–(1) 242
Li, J. P.–(1) 602
Li, Jianxing–(4) 2021
Li, Junwei–(4) 1858
Li, L. K.–(3) 1472
Li, M.–(2) 820
Li, M.-Q.–(2) 636
Li, Y.–(2) 994
Li, Yan–(1) 64
Li, Yufen–(4) 2001
Liang, Ji-ben–(1) 21
Liddle, J. Alexander–(1) 112
Lin, H. C.–(3) 1590
Lin, Hsi-Fu–(2) 639
Lin, I. N.–(4) 1840
Lin, M. E.–(3) 1663
Lin, W.–(3) 1534, 1711
Linder, Kojo–(3) 1502
Lindstrom, S. C.–(3) 1583
Lingel, K.–(1) 602
Lipinski, M.–(3) 1557
Lipp, S.–(2) 976
Lippens, D.–(1) 150
Lita, B.–(3) 1502
Li Tolt, Z.–(2) 968
Liu, C. C.–(2) 729
Liu, Feng-qi–(1) 21
Liu, G. T.–(3) 1496
Liu, J.–(3) 1619, 1645
Liu, R.–(4) 2242
Liu, W.–(3) 1663
Liu, W. K.–(3) 1594
Liu, Wen-Chau–(2) 751
Liu, X. W.–(4) 1840
Lo, Shih-Che–(2) 639
Loehr, J.–(3) 1619
Loesing, R.–(1) 509
Lofgreen, D.–(3) 1601
Lombardo, S.–(1) 545
Long, G. M.–(2) 914
López, M.–(3) 1716
López-López, M.–(3) 1553
Lothian, R.–(1) 283
Lourtioz, J.-M.–(3) 1728
Lu, B.–(1) 136
Lu, R. P.–(4) 2047
Lu, Y. F.–(4) 1853
Lu, Z. H.–(3) 1688
Lubyshev, D. I.–(3) 1594
Lucero, Rudy–(4) 1833
Lucovsky, G.–(4) 2179
Ludeke, R.–(4) 2153
Lüdge, K.–(4) 2210
Ludwig, K. F., Jr.–(3) 1457
Luhmann, C.–(1) 477
Luo, C.–(3) 1601
Luo, Y.–(3) 1522
Luyo-Alvarado, J.–(3) 1553

Lyman, P. S.–(3) 1638

Ma, T. P.–(4) 1915
Machala, C. F.–(1) 580
Madey, T. E.–(4) 2174
Maeda, K.–(2) 942
Maeda, Kiyoshi–(2) 653
Maex, K.–(1) 303; (4) 1942
Maex, Karen–(1) 242
Magarrell, D. J.–(3) 1623
Magee, Charles W.–(1) 489
Magel, L. K.–(1) 580
Magno, R.–(3) 1650
Mahaffy, R.–(1) 560, 566, 572
Mahapatra, D. P.–(4) 1847
Mai, Z. H.–(4) 1853
Makino, H.–(3) 1530
Malavé, A.–(1) 418
Malloy, K. J.–(3) 1496
Malyshev, M. V.–(2) 820
Malyshev, Mikhail V.–(2) 834
Mannaerts, J. P.–(3) 1453, 1688
Mannino, G.–(1) 519
Manousiouthakis, Vasilios I.–(2) 841
Mantese, L.–(4) 2229
Marabelli, F.–(2) 721
Marchiando, J. F.–(1) 409, 414
Marega, E., Jr.–(3) 1493
Marinelli, C.–(4) 2119
Marinković, V.–(1) 60
Marqués, M. I.–(2) 1068
Marrese, Colleen M.–(2) 968
Martin, Steve–(1) 252
Martini, S.–(4) 1991
Masuda, Takeshi–(2) 1044
Materer, N.–(1) 191
Mathis, S. K.–(4) 2066
Matsui, M.–(4) 1897
Matsukawa, T.–(2) 952, 1111
Matsukura, Y.–(2) 864
Matsuo, Jiro–(1) 445
May, Gary S.–(3) 1448
Mayer, Alexandre–(2) 1014
Mazel, A.–(3) 1493
McCann, P. J.–(3) 1720
McDonald, A.–(1) 572
McGill, T. C.–(4) 2044
McKerrow, Andrew J.–(1) 221
McKinley, J.–(1) 428
McKinley, J. M.–(1) 483, 514
McMacken, J. R.–(1) 428
McMurray, J. S.–(1) 549
Megía-García, C.–(3) 1553
Mele, J. J.–(4) 2169
Meléndez-Lira, M.–(3) 1553
Menchero, J. G.–(2) 741
Méndez, E. R.–(4) 1980
Mendoza-Galván, A.–(1) 288
Messier, Russell–(1) 32
Metzger, T. H.–(4) 2187
Miglio, Leo–(2) 721
Miki, Norihiko–(1) 313
Miller, D. L.–(3) 1633
Mine, Toshiyuki–(1) 231
Ming-Jr, Shiu–(2) 700
Mirin, R. P.–(3) 1510
Mishima, Tomoyoshi–(2) 746
Mishra, U. K.–(4) 2066
Mishra, Umesh–(4) 2322
Miskovsky, N. M.–(2) 919
Mitterender, Jeffrey–(1) 107
Mitura, S.–(2) 896
Miyamura, M.–(4) 2063
Miyao, M.–(3) 1724
Mkrtchyan, Masis M.–(1) 112
Moerman, I.–(4) 2300
Moffat, Harry K.–(1) 267
Moffatt, S.–(1) 519
Moldovan, M.–(4) 2295
Möller, D.–(2) 644
Monget, C.–(2) 785, 793
Moon, G. J.–(2) 884
Moon, Yong-Tae–(1) 140
Moore, R. L.–(1) 440
Moreno, M.–(4) 2128
Morgan, B. A.–(4) 2047
Morrison, M.–(4) 1874
Mosca, J. J.–(3) 1638
Moshegov, N. T.–(3) 1493
Mouli, Chandra V.–(1) 354
Mounaix, P.–(1) 150
Mount, G. R.–(1) 472
Moustakas, T. D.–(3) 1457
Mozume, Teruo–(3) 1586
Mukai, Tomonori–(1) 166
Müller, B. H.–(4) 2119
Müller, G.–(2) 1031
Murakami, Masanori–(4) 1957
Muralidharan, R.–(4) 2290
Murphy, M. J.–(4) 2309
Murphy, R. J.–(1) 501
Murrell, A.–(1) 493
Murrell, A. J.–(1) 435, 462, 468
Müssig, H.-J.–(4) 2160
Mutamba, K.–(4) 2279
Muto, Yasufumi–(2) 1003
Myers, T. H.–(4) 2295

Nagao, M.–(2) 1018
Naidenkova, M.–(3) 1658
Nakagawa, K.–(3) 1724
Nakagawa, S.–(3) 1601
Nakagawa, Tadashi–(3) 1680
Nakane, Hideaki–(2) 1003, 1093
Nakayama, Yoshikazu–(1) 104; (2) 661
Nalamasu, O.–(1) 317
Namatsu, Hideo–(2) 780
Namjou, K.–(3) 1720
Napolitani, E.–(1) 519
Nathan, M. I.–(4) 2096
Negoro, Noboru–(4) 2100
Neil, T.–(1) 514
Nelson, M. P.–(4) 2295
Nemanich, R. J.–(4) 2082
Neogi, Arup–(3) 1586
Neudeck, G. W.–(2) 695
Neugebauer, J.–(4) 2284
Newman, P. G.–(3) 1619
Ng, G. I.–(4) 1903
Ng, H. M.–(3) 1453, 1457
Nicolaescu, D.–(2) 948, 1068
Nicolaescu, Dan–(2) 937, 1073, 1077
Niedermann, P.–(1) 418
Nielsen, Lars–(2) 621
Nieveen, W.–(1) 440
Niimi, H.–(4) 2179
Nijmeijer, R.–(1) 602
Nilsson, B.–(1) 25
Ning, J.–(1) 428
Nishijima, Hidehiro–(1) 104; (2) 661
Nishijima, Y.–(3) 1576
Nishikawa, O.–(2) 942
Nishikawa, Osamu–(2) 653
Nishimoto, Clifford–(2) 968
Nishimura, Tetsuya–(3) 1586
Niu, F.–(4) 2146
Noguchi, Ko–(2) 834
Nojiri, Kazuo–(4) 1911
Northrup, J. E.–(4) 2284
Novak, S. W.–(1) 440
Nozaki, Shinji–(3) 1566
Obeidat, A.–(2) 695
Oberhofer, A.–(1) 472
Obraztsov, A. N.–(2) 1059
Obraztsova, Elena D.–(2) 1059
Ochiai, C.–(2) 976
Oehrlein, G. S.–(2) 848, 856
Oesterschulze, E.–(1) 418
Ogura, Mutsuo–(3) 1680
Ogushi, Nobuaki–(2) 774
Oh, H. W.–(2) 984
Oh, J. Y.–(2) 884
Oh, Myung Hwan–(2) 933
Oh, Se Hoon–(4) 1923
Ohlsson, O.–(1) 418
Ohno, H.–(4) 2039
Ohno, Yasuhide–(3) 1672
Ohtani, Y.–(2) 942
Ohtani, Yoshikatsu–(2) 653
Oishi, Satoshi–(2) 774
Okada, Takeshi–(4) 1957
Okigawa, M.–(4) 1897
Okuda, S.–(2) 929, 976, 1081
Okuyama, Fumio–(2) 937, 1073, 1077
Olesberg, J. T.–(3) 1623
Olson, G. L.–(3) 1439
O'Malley, M. L.–(4) 2034
Ooi, B. S.–(4) 1903
Ooms, W. J.–(3) 1653; (4) 2139
Orani, D.–(4) 2119
Ormsby, T. J.–(1) 493
Ortiz-López, J.–(3) 1553
Osburn, C. M.–(1) 338
Osten, H. J.–(1) 524
Overberg, M.–(1) 16
Overgaard, C. D.–(3) 1653; (4) 2139
Ozeki, Masashi–(4) 2072

Padežnik Gomilšek, J.–(2) 1097
Padiyar, Sumant–(1) 252
Pak, K.–(3) 1461
Palmstrøm, C. J.–(4) 2057
Pamulapati, J.–(3) 1619
Pan, Hsi-Jen–(2) 751
Pan, J. S.–(4) 1853
Pang, S. W.–(4) 1890
Paniez, P.–(1) 122
Pannetier, B.–(1) 122
Pao, Y. C.–(3) 1645
Paparazzo, E.–(1) 296
Parisini, A.–(4) 2263
Park, Chongdo–(2) 868
Park, D.–(3) 1650
Park, G. S.–(2) 888
Park, Jeong Hee–(4) 1923
Park, Jong-Bong–(1) 262
Park, Kyoungwan–(3) 1507
Park, Kyung Woong–(4) 1923
Park, Myung-Ho–(2) 1085
Park, N. S.–(2) 888, 905, 923, 989
Park, S.–(4) 2077
Park, S. H.–(2) 923, 1101, 1106
Park, Seong-Ju–(1) 55, 140
Park, Y. D.–(1) 16
Park, Y. J.–(2) 888, 923, 984, 989
Park, Y. K.–(2) 976
Park, Y. S.–(2) 1054
Park, Yeonjoon–(3) 1566
Parry, C.–(1) 493
Parsons, G. N.–(2) 683
Patel, S. B.–(1) 524
Pau, S.–(1) 317
Pavlovsky, I.–(2) 1059
Pearton, S. J.–(1) 16, 283, 293
Peidous, I. V.–(2) 700
Peignon, M.-C.–(4) 1861
Peiris, F. C.–(3) 1443
Pellerin, John G.–(1) 208
Pelucchi, E.–(4) 2119, 2263
Peoples, W.–(3) 1692
Pérez-Roblez, J. F.–(1) 288
Perry, Scott S.–(1) 69
Perusse, Scott R.–(4) 1919
Petitprez, E.–(3) 1493
Petroff, P. M.–(4) 2193
Petukhov, A. G.–(4) 2109
Pfeiffer, K.–(4) 1861
Pham, J. T.–(3) 1628
Phani, A. R.–(2) 721
Phillips, J. C.–(4) 2179
Pickrell, G.–(3) 1645
Pinczolits, M.–(4) 2187
Pinnington, T.–(3) 1488
Plavitu, Constantin N.–(2) 937
Ploog, K.–(4) 2052
Ploog, K. H.–(4) 2128, 2204, 2290
Poa, C. H.–(2) 1051
Pollak, F. H.–(3) 1522
Poulakos, M.–(1) 472
Powell, C. J.–(4) 2047
Preobrajenski, A. B.–(4) 1973
Principe, E.–(1) 440
Priolo, F.–(1) 519
Pristovsek, M.–(4) 2210
Privitera, V.–(1) 519
Prociów, E.–(2) 1115
Prodan, A.–(1) 60
Prokhorov, E. F.–(1) 288
Proost, J.–(1) 303
Proskurovsky, D. I.–(1) 454
Ptak, A. J.–(4) 2295
Purcell, S. T.–(2) 956
Py, Christophe–(2) 679

Qu, Xin-Ping–(4) 1942
Quivy, A. A.–(4) 1991

Raasch, D.–(2) 997, 1000
Rabinovich, W. S.–(3) 1609, 1614
Rabitz, H.–(3) 1530
Radhakrishnan, Gouri–(1) 69
Rafferty, C. S.–(1) 428
Raineri, V.–(1) 545; (2) 721
Rakhimov, A. T.–(1) 76
Ramaswamy, K.–(3) 1435
Ramdani, J.–(3) 1653; (4) 2139, 2242
Ramesh, R.–(4) 1919
Ramey, S. M.–(1) 389, 401
Ramšak, N.–(1) 60
Rangelow, I. W.–(2) 896
Rangra, K. J.–(2) 873
Rasser, B.–(1) 529
Ravesi, S.–(2) 717
Ray, O.–(3) 1692
Redwing, J. M.–(4) 2304
Reeves, C. M.–(1) 100
Reich, D. F.–(1) 496
Reimer, P. M.–(3) 1518
Ren, F.–(1) 283
Rennex, B. G.–(1) 409
Reuss, Robert H.–(4) 1825, 1919
Ribar, J. M.–(4) 2295
Richards, W. R.–(1) 533
Richter, W.–(4) 2210
Rietman, Edward A.–(1) 299
Riggs, R. J.–(2) 900
Rinn Cleavelin, C.–(1) 346
Ro, Jeong-Rae–(3) 1507
Roberts, R. F.–(1) 483
Robozerov, S. V.–(2) 980
Roch, T.–(4) 2187
Rohrs, Henry–(4) 1866
Ronsheim, P. A.–(1) 501

Roshchin, I. V.–(1) 144; (4) 2030
Roshko, A.–(3) 1510
Ross, Keith A.–(4) 2024
Rossnagel, S. M.–(4) 2016
Rossow, U.–(4) 2077, 2229
Roth, J. A.–(3) 1439
Rout, B.–(4) 1847
Rowe, J. E.–(4) 2174
Ru, Guo-Ping–(4) 1942
Rubini, S.–(4) 2119, 2263
Ruoff, Rodney–(4) 1866
Russell, K. F.–(1) 328
Russell, Stephen W.–(1) 221
Ryan, E. Todd–(1) 208
Rydberg, Matts–(2) 690
Ryssel, H.–(2) 976
Ryu, C. M.–(3) 1545

Sabarinathan, J.–(3) 1706
Sabarinathan, Jayshri–(3) 1502
Sacedón, J. L.–(4) 2128
Sadofyev, Yu. G.–(3) 1538, 1668
Sadowski, J.–(3) 1697
Said, R. A.–(2) 626
Saito, Yasushi–(2) 1093
Saitoh, Tadashi–(4) 1957
Sakai, S.–(4) 2300
Salamanca-Riba, L.–(3) 1711
Sallese, J.-M.–(4) 1915
Samarth, N.–(3) 1692
Samukawa, Seiji–(1) 166; (2) 834
Sanchez, M. I.–(4) 1874
Sánchez-Gil, J. A.–(4) 1980
Sandhu, R.–(3) 1658
Santiesteban, R.–(1) 483
Santos, M. B.–(3) 1583
Santoso, A.–(1) 90
Santucci, S.–(2) 721
Sarney, W.–(3) 1711
Satoh, Shinichi–(2) 774
Sawada, Kazuaki–(2) 1044
Sawicki, M.–(3) 1697
Saya, Daisuke–(2) 607
Schaepkens, M.–(2) 848, 856
Schaff, W. J.–(4) 2309
Scheer, H.-C.–(4) 1861
Schippan, F.–(4) 2052
Schlapbach, L.–(2) 665
Schmidt, K.–(1) 477
Schmidt, W. G.–(4) 2215
Schömann, S.–(4) 1973
Schön, S.–(3) 1701
Schreck, M.–(2) 1031
Schremer, A. T.–(2) 733
Schueler, B. W.–(1) 496
Schuhmacher, M.–(1) 529
Schuler, H.–(3) 1557
Schultz, B. D.–(4) 2057
Schulz, H.–(4) 1861
Schumann, M.–(4) 2077
Schützendübe, P.–(4) 2052, 2204
Segawa, Yusaburo–(3) 1514
Seidl, A.–(2) 929
Sekar, K.–(4) 1847
Sekine, M.–(4) 1897
Sekiuchi, Takashi–(3) 1514
Semet, V.–(2) 956
Senkevich, Jay J.–(1) 321
Seol, Yeo Song–(2) 811
Serena, P. A.–(2) 1068
Serpa, F. G.–(4) 2047
Shaffer, Edward O.–(1) 252
Shallenberger, J. R.–(1) 440
Shaqfeh, Eric S. G.–(1) 172
Shauly, E. N.–(1) 41
Shaw, E. M.–(3) 1623
Shaw, Jonathan–(4) 1817
Shaw, M. J.–(4) 2088
Shaw, V. L.–(2) 900
Shealy, J. R.–(2) 733
Shen, H.–(3) 1619
Shen, Jun–(4) 2001
Shen, M.–(1) 533
Sherbondy, J.–(1) 450
Sherman, A.–(4) 2016
Sherman, J. M.–(2) 695
Sheu, C. Y.–(2) 911
Sheu, J. K.–(2) 729
Shi, F.–(2) 896
Shi, W.–(4) 2274
Shih, C. K.–(1) 560, 566, 572
Shih, H. C.–(4) 1840
Shim, Jae Yeob–(2) 1035, 1040
Shim, K.–(3) 1530
Shimizu, H.–(4) 2063
Shimomura, S.–(3) 1549, 1572, 1576
Shimomura, Satoshi–(3) 1579, 1598, 1672
Shimotomai, M.–(3) 1684
Shin, I. H.–(2) 1027
Shiojima, Kenji–(1) 37
Shipitsin, D. S.–(3) 1668
Shiraki, Akiko–(1) 7
Shmelev, S. S.–(3) 1668
Shutov, M. V.–(2) 980
Sieloff, D.–(1) 514
Sigurdardóttir, A.–(4) 2279
Silva, S. R. P.–(2) 1051
Silverman, K. L.–(3) 1510
Silzars, A.–(1) 76
Simonian, D.–(3) 1472
Simonis, G.–(3) 1619
Singh, Jasprit–(4) 2322
Singh, R. K.–(1) 293
Sitter, H.–(4) 2224
Sjödin, Håkan–(2) 690
Sjölund, O.–(3) 1601
Smart, J. A.–(2) 733
Smilgies, D.–(4) 2187
Smith, H.–(1) 540, 549
Smith, K. V.–(4) 2304
Smith, L. L.–(2) 683
Smith, Paul Martin–(4) 1949
Smith, Roger–(1) 445
Smith, S. P.–(1) 440
Smith, U.–(4) 1906
Smith, Ulf–(2) 690
Smorchkova, Yulia–(4) 2322
Soares, Leandro L.–(2) 713
Sobczak, J. W.–(2) 1064
Soldatov, E. S.–(1) 76
Son, M. S.–(1) 458
Son, Myung-Sik–(1) 595
Song, Kie Moon–(2) 972, 1035, 1040
Songprakob, W.–(3) 1594
Sorba, L.–(4) 2119
Sørensen, Mads Peter–(2) 621
Sotomayor Torres, C. M.–(4) 1861
Sou, I. K.–(4) 2271
Souza, P. L.–(2) 741
Specht, P.–(3) 1594
Specht, Petra–(3) 1566
Speck, J. S.–(4) 2066, 2193
Spillers, R.–(3) 1496
Spinella, Corrado–(1) 576
Springholz, G.–(4) 2187
SpringThorpe, A. J.–(3) 1594
Spruytte, S. G.–(3) 1480
Srivastava, A.–(1) 338
Stach, Eric–(3) 1566
Staddon, C.–(4) 2300
Stangl, J.–(4) 2187
Stanton, Stuart T.–(1) 112
Starnawska, E.–(2) 1064
Stephenson, R.–(1) 361, 418, 586
Stephenson, Robert–(1) 405, 555
Stevie, F. A.–(1) 428, 483, 514
Stifter, D.–(4) 2224
Stintz, A.–(3) 1496
Stirling, S. D.–(1) 549
Stock, Stuart R.–(3) 1448
Stormer, H. L.–(3) 1472
Storti, R.–(1) 519
Streater, R. W.–(3) 1594
Streit, D. C.–(3) 1642, 1658
Stritzker, B.–(2) 1031
Ström, V.–(3) 1697
Studzinska, K.–(2) 896
Stutzmann, Martin–(2) 757
Su, T.–(2) 695
Su, Y. K.–(2) 729
Sudoh, K.–(4) 2165
Suetin, N. V.–(1) 76
Suganuma, Y.–(1) 48
Sugaya, Takeyoshi–(3) 1680
Sugii, N.–(3) 1724
Sugino, Takashi–(2) 1024, 1089
Sugiyama, Yoshinobu–(3) 1680
Sullivan, John J.–(4) 2011
Sulzbach, T.–(1) 418
Sumitani, Hiroaki–(2) 774
Sundaravel, B.–(4) 1847
Sundaresan, R.–(2) 700
Suzuki, N.–(2) 1081
Świątek, K.–(3) 1697
Syed, S.–(3) 1472

Tabat, N.–(4) 2057
Tabata, A.–(4) 1991
Tagawa, Shigeru–(2) 1089
Takabayashi, Shingo–(3) 1675
Takahara, Atsushi–(1) 313
Takahashi, K.–(3) 1684
Takai, M.–(2) 929, 976, 1081
Takeyasu, Kunio–(2) 661
Talevi, Robert–(1) 252
Tamargo, M. C.–(3) 1522, 1526, 1534, 1711
Tan, C. L.–(4) 1903
Tan, K.–(1) 560
Tan, Qi–(4) 2021
Tanaka, H.–(2) 864
Tanaka, K.–(2) 942
Tanaka, Keiji–(1) 313; (2) 653
Tanaka, M.–(3) 1461; (4) 2063
Tanaka, Takeshi–(2) 746
Tang, Jing–(4) 1858
Tanzer, T. A.–(1) 144; (4) 2030(E)
Tatsumi, T.–(4) 1897
Tatsuoka, Y.–(3) 1549, 1572
Tatsuoka, Yasuaki–(3) 1579
Tay, Sing Pin–(4) 1949
Taylor, J. W.–(1) 136
Taysing-Lara, M.–(3) 1619
Temple, D.–(1) 16
Tetz, K.–(3) 1431
Thamm, A.–(4) 2290
Thevenard, P.–(2) 956
Thimm, Peter–(4) 2024
Thompson, Phillip–(1) 503
Thorpe, M. F.–(4) 2179
Thuesen, L. H.–(2) 968
Thürer, K. H.–(2) 1031
Tian, W. -C.–(4) 1890
Tiberio, Richard–(4) 1866
Tiedje, T.–(3) 1488
Tien, Yu-Chung–(2) 805
Tiffin, D.–(1) 572
Timko, A.–(1) 317
Timmons, Richard B.–(2) 799
Timofeyev, M. A.–(1) 76
Timp, G.–(1) 317
Timp, G. L.–(4) 2034
Tiszauer, Detlev H.–(4) 1886
Tiwald, T. E.–(4) 2242
Tobin, P.–(1) 293
Tokunaga, K.–(2) 952, 1111
Tomitori, M.–(1) 48
Tomitori, Masahiko–(2) 648
Tomkiewicz, M.–(3) 1522
Tor, G.–(3) 1720
Torabi, A.–(3) 1638
Torii, Kazuyoshi–(1) 231
Toshiyoshi, Hiroshi–(2) 607
Tracy, K. M.–(4) 2082
Treado, P. J.–(4) 2295
Trenkler, T.–(1) 361, 418, 586
Trenkler, Thomas–(1) 555
Tribuzy, C. V. B.–(2) 741
Trifonov, A. S.–(1) 76
Tsai, C. H.–(2) 911
Tsai, K. L.–(2) 911
Tsai, S. H.–(4) 1840
Tsakalis, K.–(3) 1435
Tseng, Kuen-Syh–(2) 639
T-Sheng-Wang–(1) 445
Tsuji, H.–(2) 1018
Tu, C. W.–(3) 1476
Tuck, R. A.–(2) 900
Tung, C.-H.–(2) 706
Turk, B.–(3) 1472
Turner, F.–(4) 2016

Ukraintsev, V. A.–(1) 580
Umeya, H.–(3) 1684
Upham, Allan–(4) 2011

Valeyev, V. G.–(2) 1119
Vallier, L.–(1) 156
van den Berg, J. A.–(1) 435
Vandervorst, W.–(1) 361, 369, 381, 393, 418, 435, 540, 586
Vandervorst, Wilfried–(1) 405, 555
van Gestel, Maarten–(1) 252
Van Meirhaeghe, R. L.–(4) 1942
van Midden, H. J. P.–(1) 60
VanMil, B. L.–(4) 2295
Venkat, Rama–(3) 1467
Venugopal, Vijayakumar C.–(1) 32
Verhulst, Anne–(1) 405
Vettiger, P.–(2) 617
Vigneron, Jean-Pol–(2) 1014
Vijarnwannaluk, S.–(3) 1594
Vinogradov, A. J.–(2) 980
Vizcarra, R.–(3) 1645
Vogt, P.–(4) 2210
Voisin, P.–(4) 2232
Volkov, A. P.–(2) 1059
Volland, B.–(2) 896
Vorobiev, Yu. V.–(1) 288
Vorobyov, V. A.–(2) 1101
Vossough, K.–(2) 980
Vossough, K. K.–(2) 962
Vuong, H.-H.–(1) 428
Vyvoda, M. A.–(2) 820

Wada, J.–(2) 864
Wadhawan, O. P.–(2) 873
Walker, Marlon–(1) 503
Wallraff, G.–(4) 1874
Waltereit, P.–(4) 2290
Wang, Chen–(1) 64; (4) 1858
Wang, H. M.–(3) 1530
Wang, J. L. F.–(2) 706
Wang, Jianzhao–(1) 325

Wang, Jue–(4) 2001
Wang, M. T.–(4) 1929
Wang, S. B.–(4) 1997
Wang, T.–(4) 2300
Wang, T.-S.–(1) 435
Wang, W. C.–(2) 911
Wang, W. I.–(3) 1472, 1484
Wang, Wei-Chou–(2) 751
Wang, Wenwei–(4) 2027
Wang, X.-D.–(1) 560, 572
Wang, X. Z.–(4) 2274
Wang, Y.–(1) 279
Wang, Y. C.–(4) 1967
Wang, Z. M.–(3) 1633; (4) 2204
Wang, Zhan-guo–(1) 21
Ward, B. L.–(4) 2082
Waskiewicz, Warren K.–(1) 112
Watanabe, Hiroshi–(2) 774
Watanabe, Ken-ichi–(1) 7
Watanabe, M.–(2) 942
Watanabe, Masafumi–(2) 653
Watanabe, Yutaka–(2) 774
Watson, P.–(1) 317
Webb, Roger–(1) 445
Weber, E. R.–(3) 1594
Weber, Eicke R.–(3) 1566
Wei, H. Y.–(3) 1711
Wei, Q.-Q.–(2) 636
Wei, Yi–(4) 1833, 1919
Weidman, T.–(2) 793
Weigold, J. W.–(4) 1890
Weis, J.–(3) 1557
Weitekamp, Daniel P.–(4) 2255
Wessels, B. W.–(4) 2146
Westlinder, J.–(4) 1906
Whelan, C. S.–(3) 1638
Wieland, M. J.–(1) 117
Williams, C. C.–(1) 549
Williams, Kurt–(2) 765
Williamson, W. S.–(3) 1439
Wilshaw, P. R.–(2) 948, 994
Wittmaack, K.–(1) 1, 524
Wohlert, D. E.–(3) 1590
Wojtowicz, M.–(3) 1642, 1658
Woo, K. J.–(2) 884
Woodburn, Robert–(4) 1833
Woollam, J. A.–(4) 2242
Wortman, D. E.–(3) 1628
Wronka, H.–(2) 1064
Wu, C. S.–(1) 283
Wu, Hengpeng–(1) 325
Wu, L.–(1) 514

Xia, Andong–(4) 2027
Xiao, Mufei–(1) 82
Xie, Chenggang–(4) 1833
Xin, H. P.–(3) 1476
Xu, Bo–(1) 21
Xu, Huai-zhe–(1) 21
Xu, Min–(1) 127
Xu, N. S.–(2) 1048

Yam, Vy–(3) 1728
Yamaguchi, Akira–(4) 1957
Yamaguchi, S.–(3) 1724
Yamamoto, Takeshi–(2) 774
Yamane, Koichi–(2) 1003
Yamazaki, Kenji–(2) 780
Yan, Xinjian–(1) 64
Yang, A. C. M.–(4) 1840
Yang, C.-S.–(2) 683
Yang, H.–(4) 2179
Yang, Jung-Hwan–(1) 262
Yang, M. X.–(4) 1840
Yang, Rui Q.–(3) 1628
Yang, X.–(3) 1484
Yang, Z.–(4) 2271
Yaniv, Z.–(2) 968
Yao, T.–(3) 1530; (4) 2313
Yao, Takafumi–(3) 1514
Yavas, O.–(2) 976, 1081
Yavich, B.–(2) 741
Ye, C. W.–(1) 401
Ye, C. Win–(1) 389
Yee, K. F.–(1) 338
Yen, Cheng-Tyng–(1) 201
Yevstigneev, S. V.–(3) 1668
Yi, W. K.–(2) 888, 1101
Yin, J.–(3) 1431
Yoh, Kanji–(3) 1675
Yoon, Dong-Soo–(2) 972
Yoon, S. F.–(4) 2274
Yoon, Sang-Jo–(2) 1085
Yoon, Soon-Gil–(1) 216, 262
Yoon, Young Joon–(2) 972
Yoshida, Haruhiko–(3) 1586
Yoshikawa, A.–(3) 1684
Yoshimura, Shige H.–(2) 661
Young, A. P.–(4) 2309
Yu, C.–(3) 1623
Yu, E. T.–(4) 2304
Yu, Kuo-Hui–(2) 751
Yu, X.-B.–(2) 636
Yu, Y. C.–(2) 729
Yu, Z.–(3) 1653; (4) 2139, 2242
Yunogami, Takashi–(4) 1911
Yura, S.–(2) 929

Zaborowski, M.–(2) 896
Zahn, D. R. T.–(4) 2077
Zallen, R.–(3) 1594
Zang, Woo-Jae–(2) 1006
Zavodinsky, V.–(4) 2160
Zavyalov, V. V.–(1) 549
Zelaya-Angel, O.–(3) 1716
Zeng, Qingdao–(1) 64
Zeng, Wanxue–(4) 2011
Zeng, Yuxiao–(1) 221
Zeng, Z. Y.–(1) 10
Zhang, D. H.–(4) 2274
Zhang, H. X.–(4) 1997
Zhang, L. D.–(1) 10
Zhang, S.–(1) 435
Zhang, Y.-H.–(3) 1435, 1545
Zhang, Yifei–(4) 2322
Zhao, Li–(4) 2001
Zhao, R.–(3) 1594
Zhao, Rian–(3) 1566
Zheng, Bo–(1) 237
Zheng, H. Q.–(4) 2274
Zhou, Bin–(4) 2001
Zhou, W. D.–(3) 1706
Zhou, Wei–(1) 21
Zhu, D. H.–(3) 1706
Zhu, J.–(4) 2187
Zhu, P.–(4) 1997
Zhu, P. H.–(2) 636
Zhu, Shi-Yang–(4) 1942
Zhu, X. G.–(1) 10
Zhu, Y.–(1) 10
Zhu, Zuo-ming–(1) 21
Zhuang, Y.–(4) 2263
Zollner, Stefan–(4) 2242
Zorn, M.–(4) 2210
Zugates, C. T.–(4) 2295
Županc-Mežnar, Lea–(2) 1097
Zweck, J.–(2) 733
Zywietz, T.–(4) 2284

INDEX TO ADVERTISERS

Geib Refining Corp. A9
Hiden Analytical, Inc. A9, 11
INFICON. . . . . Cover 2
International Radiation Detectors A4
LK Technologies A13
Micro Photonics A3
Nano-Master A11
Omicron A9
Pfeiffer Vacuum . . . . Cover 3
Quad Group, Inc. . . . . Cover 4
Skion Corp. A1
Stanford Research Systems A7
Surface Science Spectra A15
Vat Inc. A11

Advertising Sales Office

American Institute of Physics
2 Huntington Quadrangle
Suite 1N01
Melville, NY 11747-4502
Telephone (516) 576-2440
Fax (516) 576-2481

Advertising Director: Richard T. Kobel

Advertising Sales Representative: Steven Goodman

Production Manager: Betty Aroesty

PFEIFFER VACUUM

Turbopumps Your Way

Pfeiffer Vacuum's NEW turbopumps with integrated controller

- ***Compact*** – integrated pump/controller unit for smallest footprint
- ***Simple*** – modular plug and play design, one controller for all pumps from 50-2000 l/s
- ***Economical*** – guaranteed best price/performance

Call Pfeiffer Vacuum, the largest producer of turbopumps, at **800-248-8254**, and buy precisely the vacuum you need.

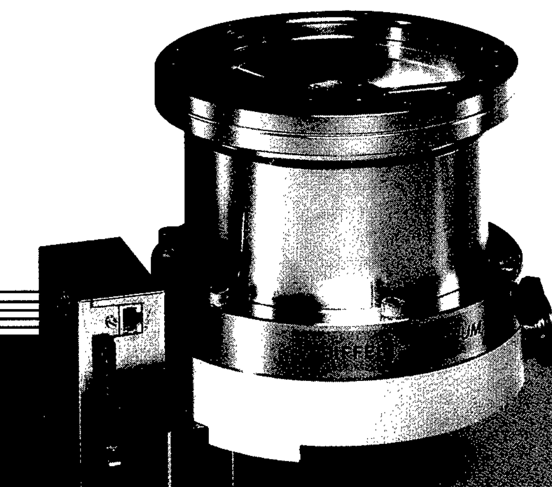

Pfeiffer Vacuum, Inc.
24 Trafalgar Square
Nashua, NH 03063-1988
Tel: 603-578-6500
Fax: 603-578-6550
www.pfeiffer-vacuum.com/turbo-drive.html

The Most Versatile Materials Characterization Tester on Earth!

Test Everything...All On One Machine

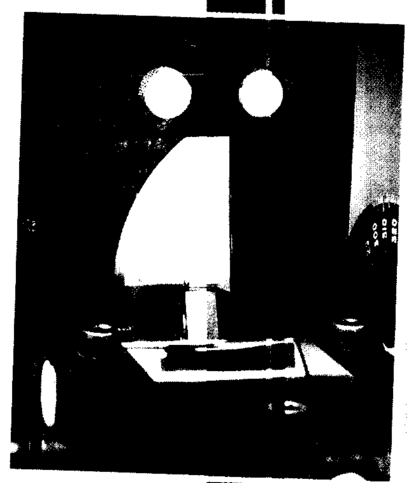

Blade Cutting Adhesion Test

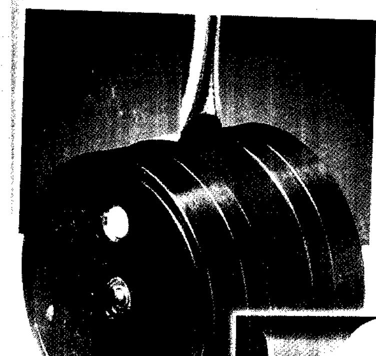

Flexible Substrate Peel Test

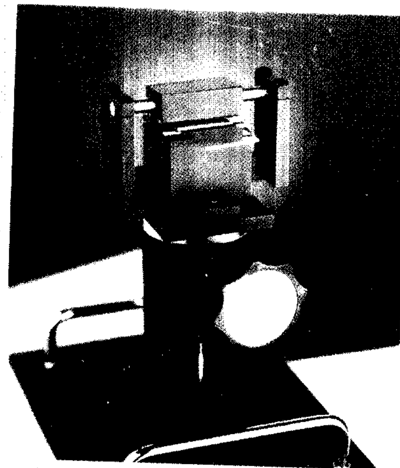

4 or 3 pt. Flexure Test

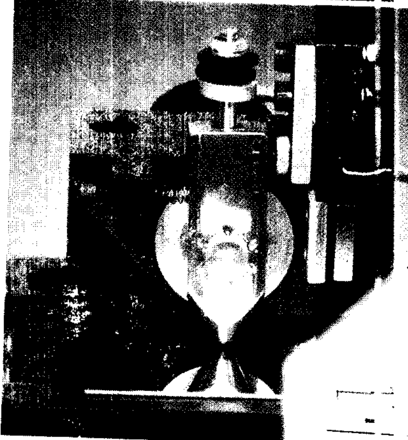

Diamond Scratch Test

NEW INSTANTANEOUS PROPERTIES TESTER

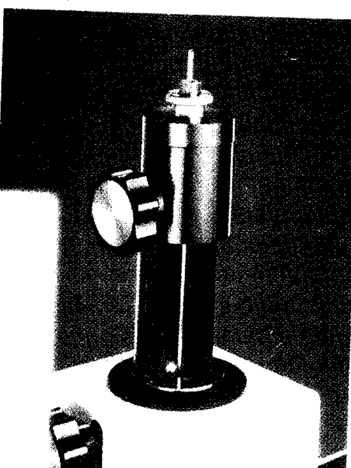

Tensile Test